Calibration and Measurement Algorithms Document for NASA's Interstellar Mapping and Acceleration Probe Mission (IMAP/CMAD)

Compiled by IMAP Project Science

Version 1.3 – October 2026

PRELIMINARY

Contents

1 Introduction **3**
1.1 Background . . . 3
1.2 CMAD Orientation . . . 3

2 Instrument Descriptions **5**
2.1 SWAPI . . . 5
2.1.1 Description and References . . . 5
2.1.2 Updates and Modifications . . . 5
2.2 CoDICE . . . 5
2.2.1 Description and References . . . 5
2.2.2 Updates and Modifications . . . 5
2.3 HIT . . . 5
2.3.1 Description and References . . . 5
2.3.2 Updates and Modifications . . . 6
2.4 SWE . . . 6
2.4.1 Description and References . . . 6
2.4.2 Updates and Modifications . . . 6
2.5 MAG . . . 6
2.5.1 Description and References . . . 6
2.5.2 Updates and Modifications . . . 6
2.6 IMAP-Lo . . . 6
2.6.1 Description and References . . . 6
2.6.2 Updates and Modifications . . . 6
2.7 IMAP-Hi . . . 6
2.7.1 Description and References . . . 6
2.7.2 Updates and Modifications . . . 6
2.8 IMAP-Ultra . . . 7
2.8.1 Description and References . . . 7
2.8.2 Updates and Modifications . . . 7
2.9 IDEX . . . 7
2.9.1 Description and References . . . 7
2.9.2 Updates and Modifications . . . 7
2.10 GLOWS . . . 7
2.10.1 Description and References . . . 7
2.10.2 Updates and Modifications . . . 7

3 Instrument Calibration **8**
3.1 SWAPI . . . 8
3.1.1 Strategy & Approach . . . 8
3.1.2 Pre-Flight Instrument Calibration . . . 8
3.1.3 In-Flight Calibrations . . . 80
3.2 CoDICE . . . 80
3.2.1 Strategy & Approach . . . 80
3.2.2 Pre-Flight Instrument Calibration . . . 80
3.2.3 In-Flight Calibrations . . . 114
3.3 HIT . . . 114
3.3.1 Strategy & Approach . . . 114
3.3.2 Pre-Flight Instrument Calibration . . . 114
3.3.3 In-Flight Calibrations . . . 120
3.4 SWE . . . 120
3.4.1 Strategy & Approach . . . 120
3.4.2 Pre-Flight Instrument Calibration . . . 120
3.4.3 In-Flight Calibrations . . . 151
3.5 MAG . . . 151
3.5.1 Strategy & Approach . . . 151
3.5.2 Pre-Flight Instrument Calibration . . . 151
3.5.3 In-Flight Calibrations . . . 164
3.6 IMAP-Lo . . . 202
3.6.1 Strategy & Approach . . . 202

3.6.2 Pre-Flight Instrument Calibration . . . 202
3.6.3 In-Flight Calibrations . . . 307
3.7 IMAP-Hi . . . 307
3.7.1 Strategy & Approach . . . 307
3.7.2 Pre-Flight Instrument Calibration . . . 307
3.7.3 In-Flight Calibrations . . . 340
3.8 IMAP-Ultra . . . 340
3.8.1 Strategy & Approach . . . 340
3.8.2 Pre-Flight Instrument Calibration . . . 340
3.8.3 In-Flight Calibrations . . . 387
3.9 IDEX . . . 405
3.9.1 Strategy & Approach . . . 405
3.9.2 Pre-Flight Instrument Calibration . . . 405
3.9.3 In-Flight Calibrations . . . 425
3.10 GLOWS . . . 425
3.10.1 Strategy & Approach . . . 425
3.10.2 Pre-Flight Instrument Calibration . . . 425
3.10.3 In-Flight Calibrations . . . 425
3.11 Cross-Calibration . . . 425
3.11.1 SWAPI & CoDICE . . . 425
3.11.2 CoDICE & HIT . . . 428
3.11.3 IMAP-Lo & IMAP-Hi . . . 428
3.11.4 IMAP-Hi & IMAP-Ultra . . . 439

4 Data Processing Algorithms 440
4.1 Data Processing Background and Approach . . . 440
4.1.1 IMAP CDF Data File Contents . . . 442
4.2 Particle Data . . . 608
4.2.1 SWAPI . . . 608
4.2.2 CoDICE . . . 687
4.2.3 HIT . . . 774
4.2.4 SWE . . . 939
4.3 Magnetic Fields . . . 976
4.3.1 Validation . . . 994
4.4 Energetic Neutral Atoms . . . 994
4.4.1 IMAP-Lo . . . 994
4.4.2 IMAP-Hi . . . 1017
4.4.3 IMAP-Ultra . . . 1017
4.4.4 All-Sky Maps . . . 1069
4.5 Interstellar Neutrals . . . 1069
4.5.1 Validation . . . 1069
4.6 Interplanetary and Interstellar Dust . . . 1069
4.6.1 Validation . . . 1114
4.7 Lyman-α . . . 1114
4.7.1 Validation . . . 1222
4.8 Error Estimation . . . 1222
4.9 Quality Flags . . . 1222

5 Data Accessibility and Usage 1223
5.1 IMAP Guidelines for Data Usage . . . 1223
5.1.1 Participation and Authorship on Papers . . . 1223
5.1.2 Coordination of Science Topics Across the IMAP Team . . . 1223
5.1.3 Coordination of IMAP Data Sharing with Outside Collaborators . . . 1224
5.2 Data Access . . . 1224
5.3 Data Processing Software . . . 1224
5.4 Data Usage Guidelines and Caveats . . . 1224
5.4.1 Summary of Latest Release . . . 1224
5.4.2 SWAPI . . . 1228
5.4.3 CoDICE . . . 1238
5.4.4 HIT . . . 1250
5.4.5 SWE . . . 1250
5.4.6 MAG . . . 1251
5.4.7 IMAP-Lo . . . 1255
5.4.8 IMAP-Hi . . . 1255
5.4.9 IMAP-Ultra . . . 1255
5.4.10 IDEX . . . 1255
5.4.11 GLOWS . . . 1260

A Appendix: Definitions and Notation 1261

B Appendix: Acronyms 1262

IMAP/CMAD 1

Introduction

1.1 Background

NASA's Interstellar Mapping and Acceleration Probe (IMAP) mission is the fifth mission of the Solar Terrestrial Probe (STP) program in NASA's Heliophysics Division of the Science Mission Directorate. As fully described in McComas et al. [2025], IMAP's science objectives explore the acceleration of energetic particles in the heliosphere and the interactions between the Sun, inner and outer heliosphere, and interstellar medium. From its orbit around the Sun-Earth 1st Lagrange point, the IMAP observatory hosts a payload consisting of ten instruments that enable both in situ and remote sensing measurements.

IMAP's Calibration and Measurement Algorithms Document (CMAD) provides a detailed description of instrument calibration efforts and results and the corresponding algorithms used in data processing. Combined, the details in the IMAP/CMAD enable any user to fully understand the scientific data they are using from the IMAP observatory. In addition to serving as a users' guide, the CMAD also documents critical details that are archived with the data set to ensure that the value of the IMAP data set persists well after the mission is successfully completed.

McComas et al. [2025] serves as the citable reference for the IMAP/CMAD. While IMAP is in Phase-E (prime mission science operations plus any additional extended mission phases), the ***IMAP/CMAD is a living document; that is, the IMAP/CMAD will remain in preliminary document status and updated periodically and as needed until the IMAP mission concludes in Phase-F and the final IMAP/CMAD is released.*** For clarity, sections that still need to be inserted are indicated in *italics*.

1.2 CMAD Orientation

The CMAD consists of the following: i) a brief introduction to the mission and overview summarizing the full details of the mission described in McComas et al. [2025]; ii) a brief and relevant description of each of the instruments in the payload, summarizing the full details of the respective instrument papers in McComas et al. [2025]; iii) detailed descriptions of the instrument calibration efforts and results; iv) detailed description of the data processing approach, software, and algorithms for each of the IMAP data products. A copy of IMAP's Rules-of-the-Road for data usage and details of data accessibility are also included.

Each instrument in the IMAP payload underwent thorough and comprehensive calibration procedures prior to final integration onto the observatory. IMAP's CMAD documents those calibration efforts, including test procedures and setups, justification, outcomes and results, and application. Details of how calibration factors are applied to each instrument include, when relevant, discussion of onboard configuration and calibration tables vs. on-the-ground calibration tables in data processing, since each instrument applies their calibration factors differently.

Several of the instruments underwent cross-calibration, since by design, all instruments that measure the same observable are designed to include overlapping measurement ranges. The following instrument-pairs were each cross-calibrated, with details captured in the CMAD: SWAPI and CoDICE; CoDICE and HIT; IMAP-Lo and IMAP-Hi; IMAP-Hi and IMAP-Ultra.

Alongside description of the measurements and calibration efforts, IMAP's CMAD also presents all relevant details of the IMAP data processing pipeline and data products. IMAP follows the familiar, NASA standard of data levels, where each increasing level of data contains increasingly processed and refined data products. For IMAP, Level-0 (L0) data correspond to "unpacked" telemetry, that have been translated and archived in human-readable common data format (CDF) files. L1 data correspond to data processed for characterization and assessment purposes, primarily for use by the instrument teams in diagnosing and assuring the instruments are operating as intended and as an intermediate step to fully-calibrated scientific data, which are provided at L2 and L3. Often, L1 data are uncalibrated or partially-calibrated, in native engineering units, and with vector data reported in instrument or spacecraft coordinate frames. L2 data products consist of instrument specific, calibrated data in physical units and coordinate frames and are intended as the lowest-level data for routine use in establishing scientific results. L3 data products are highly processed data derived further from L2 data, and some L3 products may combine data from multiple instruments. Examples of L3 data products include: all-sky ENA maps in specific heliocentric coordinate frames; combined particle spectra spanning multiple instruments' energy ranges; and particle data organized by energy, pitch angle, and gyro-phase (vs. say spin-phase and elevation angle at L2).

The CMAD describes the data processing pipeline for each instrument and higher-level data product, such that any user of IMAP data can understand how the data they are using were developed. Furthermore, the CMAD details error estimation and how error was quantified and reported for each data set. Regarding error analysis and data quality, IMAP data products also include quality flags, intended to assist users and avoid any use of poor quality or erroneous data. IMAP's CMAD also describes how quality flags are established and used for each corresponding data product.

IMAP's CMAD wraps up with details of data accessibility and usage. This section of the CMAD introduces users to the rules-of-the-road best practices for IMAP data usage. The data portal for accessing IMAP data is also provided here, with further detail provided to describe the various products provided for users on IMAP's data portal, including quicklook products and tools. Another important aspect of the algorithms and data usage included in the CMAD is the overview and description of the Combined Analysis, Visualization, and Access (CAVA) software suite, developed for user-friendly accessibility and detailed analysis of IMAP and other mission data sets.

IMAP/CMAD 2

Instrument Descriptions

2.1 SWAPI

2.1.1 Description and References

IMAP's Solar Wind and Pickup Ion (SWAPI) instrument is an electrostatic analyzer (ESA) that is designed to measure thermal plasma distributions of protons and alphas in the solar wind and light pickup ion (PUI) species (H^+ and He^+). For full details of the SWAPI instrument, refer to McComas et al. [2025] and Rankin et al. [2025].

2.1.2 Updates and Modifications

Any significant modification to SWAPI or its operations following publication of Rankin et al. [2025] are documented in this section.

2.2 CoDICE

2.2.1 Description and References

The Compact Dual Ion Composition Experiment (CoDICE) is an advanced sensorhead combining an ESA, post-acceleration (PAC) and time-of-flight (ToF), and energetic particle sensors into an extended performance payload on IMAP. CoDICE measures three-dimensional velocity distribution functions of solar wind to suprathermal ions and interstellar pickup ions, including mass and charge-state discrimination. For complete details of the CoDICE instrument, refer to McComas et al. [2025] and Livi et al. [2025].

2.2.2 Updates and Modifications

Any significant modification to CoDICE or its operations following publication of Livi et al. [2025] are documented in this section.

2.3 HIT

2.3.1 Description and References

The High-energy Ion Telescope (HIT) on IMAP is an energetic particle spectrometer that distinguishes incident ion species based on linear energy transfer (LET, or dE/dx) through an array of SSDs. HIT distinguishes elemental abundances of MeV/nuc $\sim$ 10s MeV/nuc ions from protons through Ni, measures

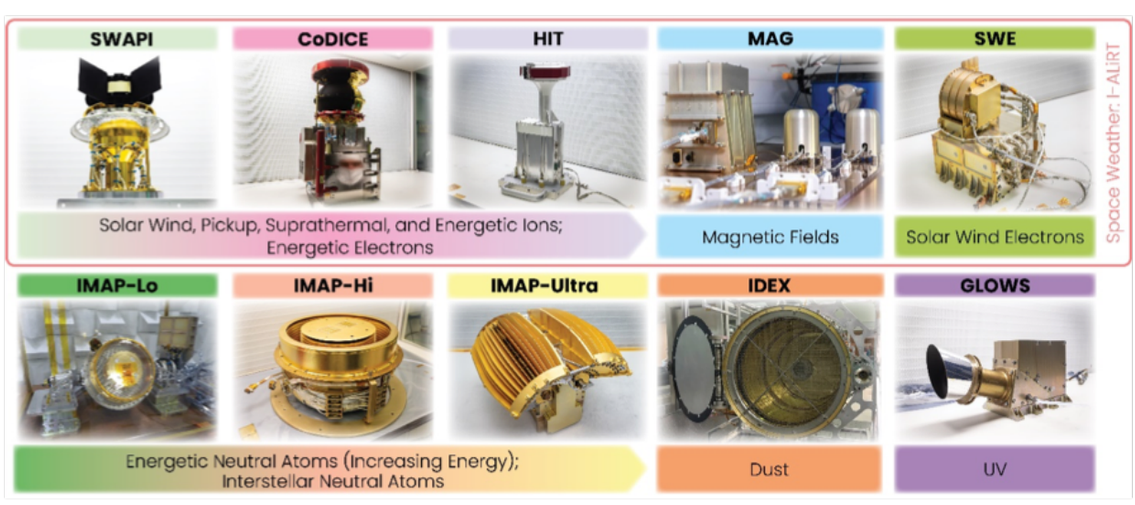


Figure 2.1: IMAP's full payload, consisting of a suite of ten instruments.

100s keV $\sim$ MeV electrons, and enables isotopic mass resolution capable of distinguishing ^{3}He from ^{4}He, an important distinction for evaluating solar particle acceleration. For full details of the HIT instrument, refer to McComas et al. [2025] and Christian et al. [2025].

2.3.2 Updates and Modifications

Any significant modification to HIT or its operations following publication of Christian et al. [2025] are documented in this section.

2.4 SWE

2.4.1 Description and References

The Solar Wind Electron (SWE) instrument on IMAP consists of an ESA specifically designed to measure the 3D velocity distribution functions of thermal to suprathermal electrons in the solar wind. SWE boasts near identical heritage from the ACE/SWEPAM instrument. For complete details of the SWE instrument, refer to McComas et al. [2025] and Skoug et al. [2025].

2.4.2 Updates and Modifications

Any significant modification to SWE or its operations following publication of Skoug et al. [2025] are documented in this section.

2.5 MAG

2.5.1 Description and References

IMAP's magnetometer (MAG) experiment consists of two fluxgate magnetometers located at different locations along a deployable, 2.5-m boom to enable very accurate stray spacecraft field characterization and removal via gradiometry. MAG measures the 3D vector magnetic field in the solar wind, known as the interplanetary magnetic field (IMF). Magnetic cleanliness was very carefully considered throughout the IMAP systems engineering and development process, and extensive efforts were taken to minimize stray magnetic fields from the IMAP subsystems and payload and characterize them prior to flight. For full details of the MAG instrument, refer to McComas et al. [2025] and Horbury et al. [2025].

2.5.2 Updates and Modifications

Any significant modification to MAG or its operations following publication of Horbury et al. [2025] are documented in this section.

2.6 IMAP-Lo

2.6.1 Description and References

IMAP-Lo is the lowest-energy range energetic neutral atom (ENA) imager on IMAP, which also covers measurements of very low energy interstellar neutrals (ISNs) below $\sim$200 eV. IMAP-Lo is a single-pixel, neutral atom imager mounted to the IMAP observatory via a pivot platform that enables the instrument to be pointed in different orientations. The viewing angle articulation is required to optimize the observability of ISNs, the trajectories of which are "lensed" by solar gravity, yielding preferential directions for different ISN species in different locations around the Sun at 1 au. For full details of the IMAP-Lo instrument and observables, see McComas et al. [2025] and Schwadron et al. [2025].

2.6.2 Updates and Modifications

Any significant modification to IMAP-Lo or its operations following publication of Schwadron et al. [2025] are documented in this section.

2.7 IMAP-Hi

2.7.1 Description and References

IMAP-Hi is the intermediate range ENA instrument onboard the IMAP observatory; it fills the energy range of 0.4 to 15.6 keV between the ranges of IMAP-Lo and IMAP-Ultra. Like IMAP-Lo, IMAP-Hi is a single-pixel, neutral atom imager, but IMAP-Hi employs two sensor heads mounted on IMAP at fixed orientations, with bore sights at 90° and 45° with respect to the spin axis. For full details of the IMAP-Hi instrument and observables, see McComas et al. [2025] and Funsten et al. [2025].

2.7.2 Updates and Modifications

Any significant modification to IMAP-Hi or its operations following publication of Funsten et al. [2025] are documented in this section.

2.8 IMAP-Ultra

2.8.1 Description and References

IMAP-Ultra is the highest-energy ENA instrument onboard the IMAP observatory. Unlike IMAP-Lo and IMAP-Hi, IMAP-Ultra is a pair of ENA cameras, each of which provides two-dimensional images of the ENA sky. Like IMAP-Hi, IMAP-Ultra's two sensor heads are oriented 90° and 45° with respect to the observatory's spin axis. For full details of the IMAP-Ultra instrument and observables, see McComas et al. [2025] and Gkioulidou et al. [2025].

2.8.2 Updates and Modifications

Any significant modification to IMAP-Ultra or its operations following publication of Gkioulidou et al. [2025] are documented in this section.

2.9 IDEX

2.9.1 Description and References

The Interstellar Dust Experiment (IDEX) on IMAP is designed to measure interplanetary and interstellar dust at 1 au. IDEX will offer unprecedented observations of the molecular, elemental, and even some isotopic composition of dust grains, revealing insights on the nature of the interstellar medium and formation of stars and planets. During IMAP's two-year prime mission, IDEX is expected to detect $\sim$ 200 interstellar and $\sim$ 1200 interplanetary dust particles. For full details of the IDEX instrument, see McComas et al. [2025] and Horányi et al. [2025].

2.9.2 Updates and Modifications

Any significant modification to IDEX or its operations following publication of Horányi et al. [2025] are documented in this section.

2.10 GLOWS

2.10.1 Description and References

The GLObal solar Wind Structure (GLOWS) instrument on IMAP is a single-pixel Lyman-α photometer designed to measure "helioglow", i.e., the backscattered light from interstellar neutrals within the heliosphere. GLOWS offers a valuable measurement in support of the ENA imagers, since the neutral background density is a critical aspect to account for considering charge-exchange processes and lifetimes during ToF of ENAs from their origins to where they are observed by IMAP near 1 au. Furthermore, because of charge-exchange between interstellar neutrals and the solar wind, helioglow observations also reveal details of distant structure within the solar wind as it floods the heliosphere. For full details of the GLOWS instrument, see McComas et al. [2025] and Bzowski et al. [2025].

2.10.2 Updates and Modifications

Any significant modification to GLOWS or its operations following publication of Bzowski et al. [2025] are documented in this section.

IMAP/CMAD 3

Instrument Calibration

3.1 SWAPI

3.1.1 Strategy & Approach

Calibration of SWAPI involved a combination of ground-based testing, cross-calibration with CoDICE, and in-flight calibrations. The ground calibrations were performed at the Princeton Space Physics Laboratory, and the strategy of the effort focused on four objectives: i) characterize instrument performance and verify SWAPI's requirements; ii) confirm functionality to demonstrate SWAPI successfully survived environmental testing; iii) establish SWAPI's response functions and validate the sensor model; iv) prepare for in-flight calibration and science operations.

A critical aspect of the SWAPI ground calibration was to determine the response function over SWAPI's azimuthal and elevation angles within the instrument FoVs. Other aspects of the SWAPI calibration tests were to determine: CEM gain curves, CEM dark count rates, UV response, energy and angular passbands, ESA k-factor, and energy resolution and response functions.

As described in Rankin et al. [2025], the following describes the various tests that were used for ground calibration of the SWAPI instrument.

- Gain Curves: optimal CEM voltages are determined by sweeping potential across one CEM while holding the other at fixed potential. Tests are conducted using both flight-like ESA voltage sweeps as well as for fixed ESA settings. Tests are performed using stable ion beams and fixed instrument orientations.
- Dark Counts: With CEMs set to their nominal operational gains, count rates are recorded in the absence of any sources, such as an ion beam or UV illumination. These tests are performed over a range of ESA voltage settings.
- UV Background: The instrument response is tested when the apertures are exposed to a UV light source. For this test, CEMs are operated at their nominal operational gain settings, and the light source is positioned at various incidence angles with respect to the SWAPI apertures. In addition to establishing the UV response functions, this test also identifies any possible light leaks in the design.
- Continuous Energy Tests: Using a fixed azimuth and elevation angle, ESA voltage sweeps are performed over a range of ion beams at different, precise energies to determine the energy efficiency curves and response functions. With these tests, SWAPI's detection efficiencies, energy resolutions, and ESA k-factors are all determined experimentally.
- Energy-Angle Passbands: Using fixed azimuth angles, SWAPI is rotated through a range of elevation angles, and at each elevation setting, a calibrated ion beam and ESA sweeps are used to determine the energy-angle response functions. The tests are performed using multiple beam energies and species to determine any energy and/or mass dependencies. These tests are used to fill out the full response functions of the instrument.
- Angular Response Functions: Using a number of azimuth and elevation angles, a calibrated ion beam at fixed energy and corresponding ESA setting is used to determine the angular response functions of SWAPI.

3.1.2 Pre-Flight Instrument Calibration

SWAPI cal report embedded below

TABLE OF CONTENTS

1. ABBREVIATIONS 3

2. SWAPI INSTRUMENT 3

3. SWAPI FM CALIBRATION OBJECTIVES 4

4. CALIBRATION FACILITY 5

4.1 Princeton Space Physics Calibration System - Overview 5
4.2 SWAPI Configurations inside the Main Chamber 7

5. ION SOURCE, BEAMLINE AND BEAM IMAGING 8

5.1 Princeton's Imaging Microchannel Plate (MCP) 9
5.2 Princeton's Absolute Beam Monitor (ABM) 9
5.3 Beam characterization during the actual SWAPI FM Pre-Flight Cal 11

6. SWAPI CALIBRATION OVERVIEW AND TEST SUMMARY 14

6.1 Calibration Test Configuration 14
6.2 Calibration Test Overview 15
6.2.1 Daily Test Flow 16

7. CHARACTERIZATION OF THE VARIOUS SWAPI SUBSYSTEMS 16

7.1 CEMs: SWAPI's Gain Curves and Pre-Launch Operating Voltages 16
7.2 CEMs: Dark Counts, UV tests, and lowest-measurable beam 19
7.3 Aperture Grid: Attenuation Factor 20
7.4 Entrance Aperture Range for Open Aperture 21
7.5 ESA Concentricity 23

8. FULL INSTRUMENT CHARACTERIZATION 23

8.1 SWAPI's Measurable Energy Range 24
8.2 SWAPI's Absolute Detection Efficiency 28
8.3 SWAPI's Energy Resolution 29
8.4 SWAPI's Voltage-Energy Conversion (K-factor) 31
8.5 SWAPI's angular response function 32
8.6 SWAPI's energy-angle response function 36
8.7 SWAPI's Azimuthal-Elevation Angle Response Function 39
8.8 Characterizing Potential Scattering 41
8.9 Comparison Between Lab Measurements and Simulation Results 43

9. DERIVING GEOMETRIC FACTORS 45

10. SUMMARY OF SWAPI KEY PERFORMANCE PARAMETERS 47

APPENDIX A. PASSBAND RESULTS: SUNGLASSES (IA = 0°) 48

APPENDIX B. PASSBAND RESULTS: OPEN APERTURE (IA = ±90°) 54

APPENDIX C. GAIN CURVES RESULTS 69

1. ABBREVIATIONS

ABM	Absolute Beam Monitor
ADE	Absolute Detection Efficiency
CEM	Channel Electron Multiplier
COIN	Coincidence counts
CoDICE	Compact Dual Ion Composition Experiment
EEPROM	Electrically Erasable Programmable Read-Only Memory
EM	Engineering Model
ESA	Electrostatic analyzer
FM	Flight Model
GSE	Ground Support Equipment
HVPS	High-Voltage Power Supply
HW	Hardware
IA	Inner Rotational Angle (equivalent to SWAPI's azimuthal angle)
IMAP	Interstellar Mapping and Acceleration Probe
JHU/APL	Johns Hopkins University Applied Physics Laboratory
LUT	Look Up Table
MCP	Microchannel Plate
NASA	National Aeronautics and Space Administration
OA	Outer Rotational Angle (equivalent to SWAPI's elevation angle)
PCEM	Primary Channel Electron Multiplier
SCEM	Secondary Channel Electron Multiplier
SG	Sunglasses
SW	Solar Wind
SWAPI	Solar Wind and Pickup Ion Instrument

2. SWAPI INSTRUMENT

The Solar Wind and Pickup Ion Instrument (SWAPI), is a top-hat electrostatic analyzer (ESA) that measures both solar wind (H+ and He++) and pickup ions (primarily interstellar He+). Its entrance aperture comprises of two regions: 1) the sunglasses (Figure 2.1a), with a custom aperture grid designed to attenuate the solar wind's intensity by ~1000 and vanes to block the nominal solar wind from entering the instrument unattenuated; 2) the open aperture through which the pickup ions enter (Figure 2.1b). Ion particles, upon entering the aperture, are steered through the instrument via the electrostatic analyzer; those that survive without prematurely scattering eventually encounter an ultra-thin carbon foil. As the incident ions interact with the carbon foil, secondary electrons are generated, and the secondaries are attracted to the positively biased secondary channel electron multiplier (SCEM). Meanwhile, the incident ions that pass through the foil are detected by the negatively-biased primary CEM (PCEM). Measurements made by both detectors within a certain time resolution (~100 ns) produce a coincidence rate (COIN). SWAPI's basic concept of operations is illustrated in Figure 2.2. Additional details about sensor components, subsystems and assembly, instrument operations, data products, and scientific objectives can be found in the SWAPI instrument paper (Rankin et al. 2019).

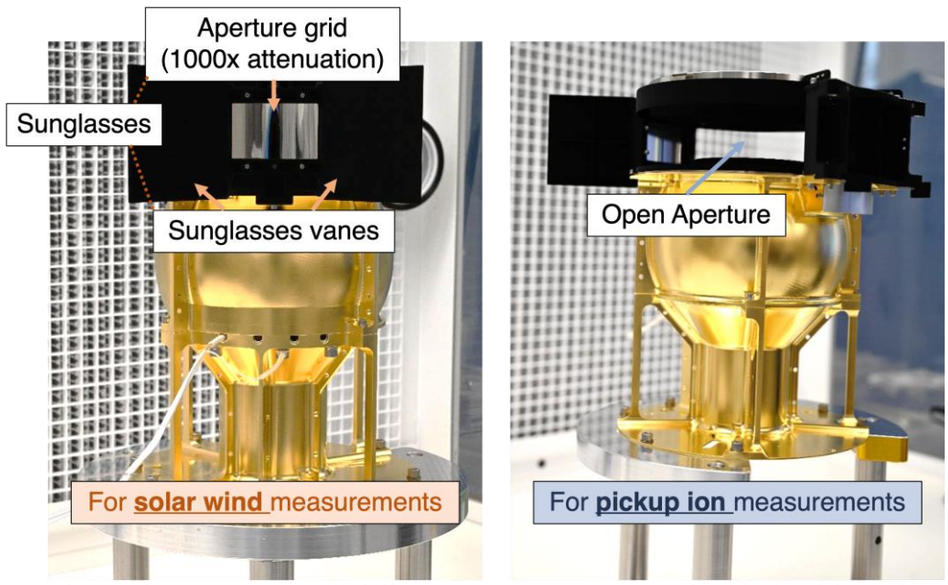


Figure 2.1. *Photo of SWAPI FM with different entrance apertures highlighted for solar wind and pickup ion measurements.*

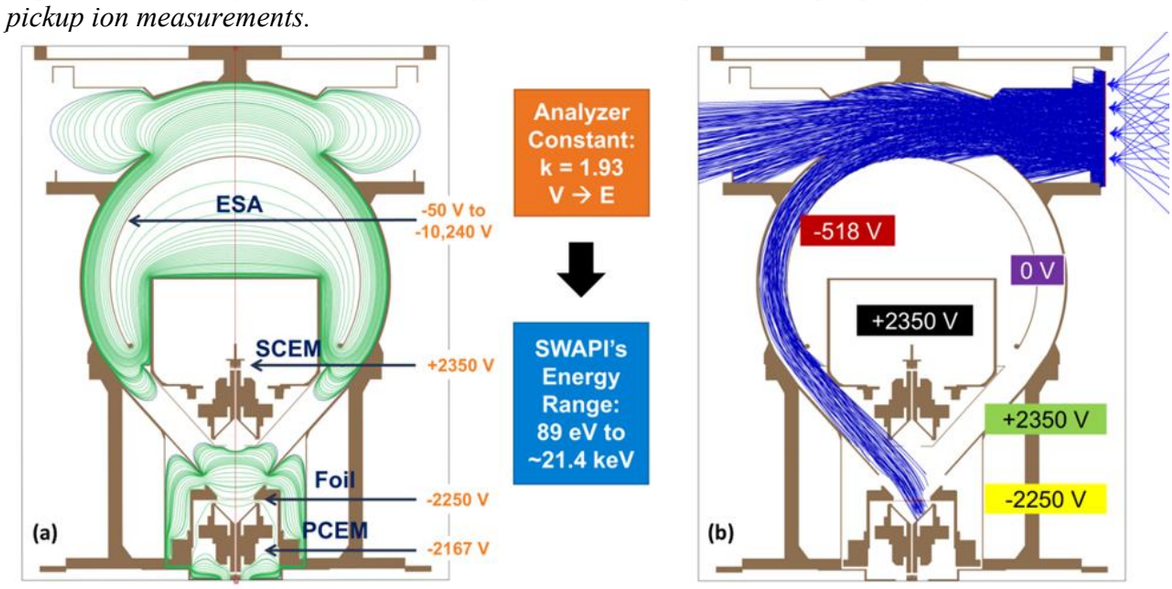


Figure 2.2. *Illustration of the basic concept of operation of SWAPI. (left) A visual representation of the electric potential inside SWAPI. (right) Trajectory of incident ions, simulated using the SIMION software (from Rankin et al. 2025).*

3. SWAPI FM CALIBRATION OBJECTIVES

The SWAPI FM calibrations (pre-environmental & post-environmental, pre-flight) were designed to characterize the instrument's performance, and verify/validate its ability to meet its science requirements and prepare for in-flight operations. All tests were constructed to achieve these

objectives (see Section 6 for an overview and summary of the testing). Rather than detailing how all of the requirements were individually met, this report is intended to provide a holistic view of SWAPI's key characteristics – from the subsystem level to the full instrument – through its ground calibrations (see Sections 7 & 8 for more details with results). The details of how these fed into specific aspects of the instrument's requirement verification and validation were delivered in SWAPI's end item data package (EIDP) and can be made available upon request (document 05899-EM-0013-SWAPI_Science_Requirements_Verification_01).

SWAPI's FM calibration objectives were broken down into the following four categories:

1) ***Verify and validate science requirements***
2) ***Acquire inputs to forward model and algorithms***

   This involved determining the full angular response, as well as the energy-angle response functions, to allow comparisons between SIMION and the calibration data, and verifying key parameters such as: SWAPI's energy resolution, the conversion factor from the optimal voltage to incident energy (k-factor), and absolute detection efficiency. These efforts not only informed the simulation results but also provided inputs to the forward model and algorithms.
3) ***Test overall instrument functionality***

   This included determination of the instrument's full energy range, signal to noise level, CEM backgrounds, UV backgrounds, scattering, sensitivity, etc. in addition to the standard response function characteristics.
4) ***Prepare for in-flight operation and calibration***

   This involved two key aspects:

   - Testing the commissioning scripts

     The tests included the initial low-voltage power-on and aliveness script, low voltage functional test script, HV ramp-up script, memory test, sequenced startup via Macro 0, flight gain curve, and nominal HVSCI operations.
   - Obtain important parameters for in-flight operations

     The key parameters included: CEM operational voltages, successful demonstration of flight-like sweeps, characterization of signal-to-noise thresholds, instrument background levels, and dynamic range capabilities.

4. CALIBRATION FACILITY

4.1 Princeton Space Physics Calibration System - Overview

All SWAPI calibration campaigns, including the cross-calibration with CoDICE and IMAP-Lo flight calibrations, took place at Princeton Space Physics Laboratory. The Princeton Space Physics Calibration System, part of the Princeton Space Physics Laboratory at Princeton University, is located in the basement of 171 Broadmead in Princeton, New Jersey. A recent configuration of the system is depicted in Figure 4.1, and a schematic diagram of the system is illustrated in Figure 4.2. Details of the facility are also summarized in the SWAPI instrument paper (Rankin et al. 2025).

The entire system is configured to provide real-time status updates, including valve states, pressures, cryo pump temperatures (on the Main Chamber and Science Chamber), turbo pump speeds (beamline and ion source sections), positioning system locations (Main Chamber and Science Chamber), and ion source settings. This data is recorded at a ~1 Hz cadence and stored in a locally hosted database. During the SWAPI calibration periods, the calibration system is time-synchronized internally but not with the instrument data acquisition system. As a result, manual time synchronization was used to ensure coordinated state motion and data collection. This process was improved for SWAPI FM cross calibration with CoDICE and for pre-cross-calibration checkout, during which the entire calibration system is time-synchronized with the instrument data acquisition system.

Full recordings of facility settings, RGA scan data, and beam diagnostics information taken during all of SWAPI's calibration campaigns (EM & FM) were recorded and have been archived. These can be made available upon request.

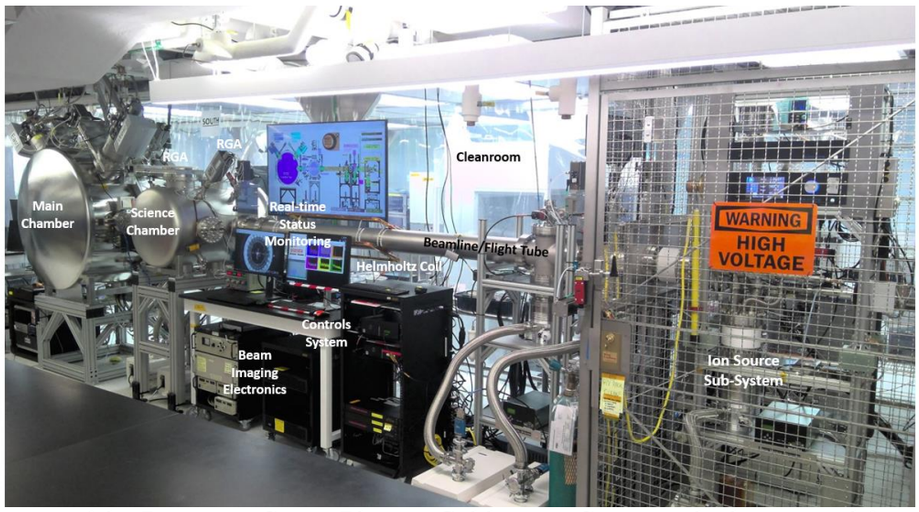


Figure 4.1. *Image of the Princeton Space Physics Calibration System, which was used for all of SWAPI's beamline calibrations (EM & FM).*

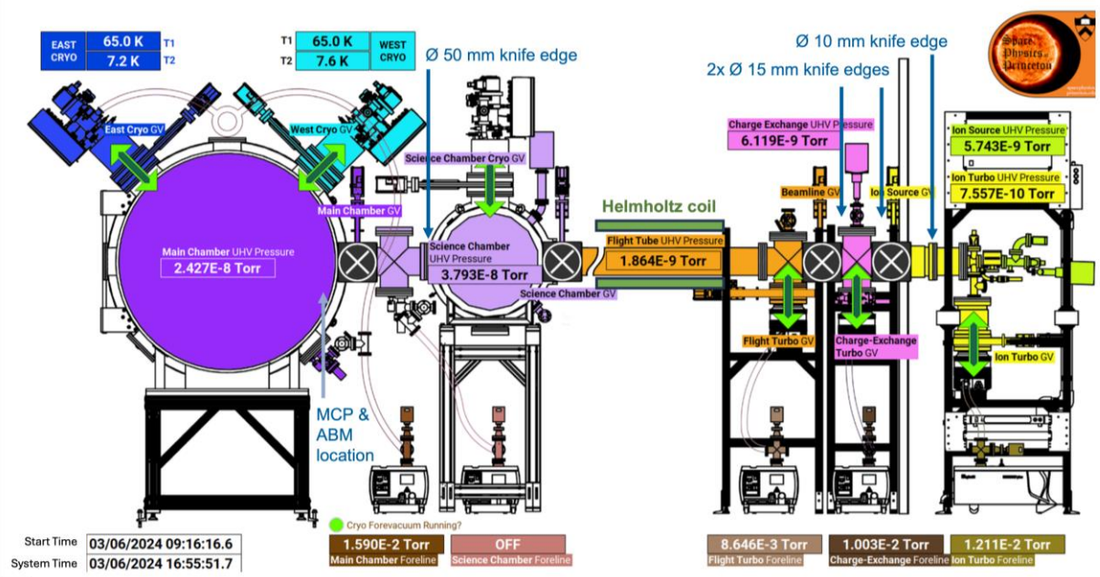


Figure 4.2*. A screenshot of the Princeton Space Physics Calibration System, used for all of SWAPI's beamline calibrations (EM & FM). No major configuration changes were made from the time of the screenshot shown up through SWAPI's Pre-Flight calibration period.*

4.2 SWAPI Configurations inside the Main Chamber

The instrument was mounted onto motion stages that allow three-axis motion: horizontal linear (translation), outer rotational (elevation angle), and inner rotational (azimuthal angles) inside the calibration chamber (see Figure 4.3). In addition, beam monitors are mounted on a 2-axis positioning system in the calibration chamber for beam calibration as well as real-time flux cross-calibration during the instrument calibrations. The beam monitors used during SWAPI calibrations are Microchannel plate detector (MCP) and a carbon-foil absolute beam monitor (ABM). Recordings of all stage orientations, along with notes on the various configurations tested have been logged, recorded, and archived. These can be made available upon request.

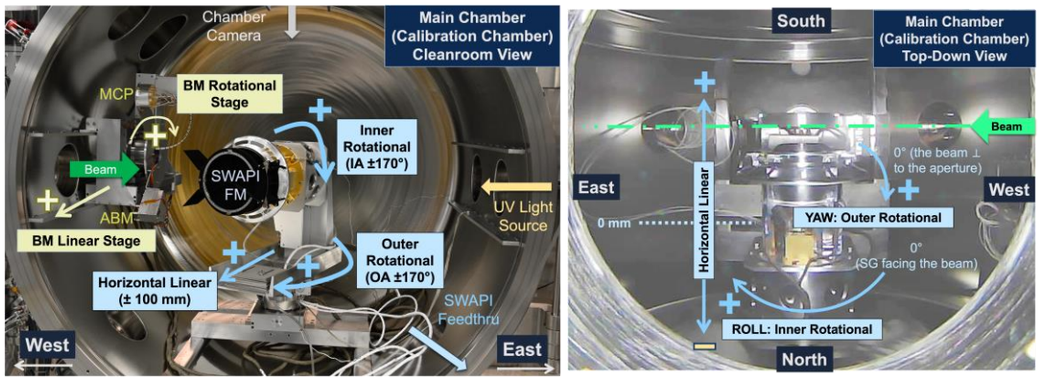


Figure 4.3. *SWAPI calibration configuration inside the chamber. (left) View from the cleanroom side. (right) Top-down view captured by the chamber camera. SG is the abbreviation for sunglasses.*

5. ION SOURCE, BEAMLINE AND BEAM IMAGING

The ion source characteristics and full operational capabilities of the Princeton beamline are described in detail by Rankin et al. (2025). Relevant to SWAPI's calibration, the Princeton system can generate stable, singly-charged ions with energies ranging from ~100 eV to ≤ 30 keV, for species dependent on gas flowed into the source which get ionized by the filement and selected by a Wien Filter before exiting the source. SWAPI was primarily calibrated with H+ and He+ from ~100 eV to ~20 keV.

Beam monitors mounted on a 2-axis positioning system in the Main Chamber were used to characterize the beam and provide real-time cross-calibration of fluxes with the instrument under test. A variety of these have been used to optimize the ion source operational settings, including: Microchannel plate detector (MCP), a carbon-foil absolute beam monitor, a conversion surface absolute beam monitor, an individual Channel Electron Multiplier, and a Faraday Cup with retarding potential analyzer capability up to 5kV biasing. However, only the MCP and carbon-foil ABM were installed in the main chamber for SWAPI's calibrations, as depicted in Figure 5.1.

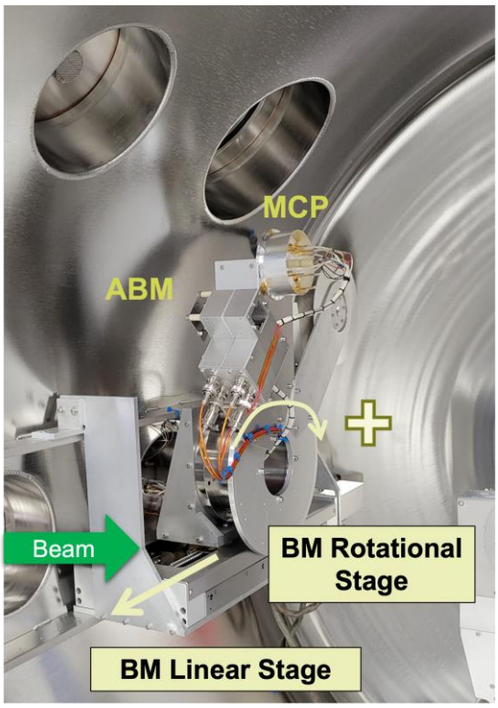


Figure 5.1. *Close up of the beam monitor (BM) detectors, ABM and MCP, inside the main chamber, mounted on linear and rotational stages.*

Prior to the instrumental test campaigns, the MCP inside the Main Chamber was used to image the full beams intended for SWAPI calibration. The ABM was used to provide baseline reference measurements for instrument calibration. During the calibration campaigns, MCP beam images were taken at the beam center as a sanity check, rather than performing full beam imaging. Additionally, ABM measurements were taken as a reference to ensure the beam reliability throughout the calibration campaigns.

In addition to using optimum beam settings and reliably characterizing the beam throughout testing, corrections must be made to compensate for the geomagnetic field – particularly for the light-element calibration at SWAPI's low-energy range. The total length of the beamline —from the nose of the ion source to the entry flange on the Main Chamber— is ~4.9 meters. Four knife-edges are positioned along the beamline to constrain the beam, ensuring that by the time it reaches the entry port on the Main Chamber, it is highly uniform, parallel, and expanded to a diameter of 6 cm. The beam diameter can be reduced as needed by placing collimators in front of the beam at the entrance flange. A lab-manufactured Helmholtz coil (Khoo et al. 2023) mounted on to the flight tube serves to counteract the Earth's magnetic field (e.g., for < 5 keV protons or < 1 keV helium).

5.1 Princeton's Imaging Microchannel Plate (MCP)

The imaging MCP used in the Princeton Space Physics Lab is a 40-mm diameter (active area) chevron-type microchannel plate detector. It consists of two MCPs stacked together with their channels angled to form a chevron shape, a resistive anode position encoder, integral anode biasing, and signal decoupling circuits. This setup allows the conversion of incoming charged particles, neutral particles, or energetic photons into four charge signals that correspond to the 2D spatial locations on the MCP. The MCP is mounted on a paddle wheel with both linear and rotational motion capability, allowing it to be positioned at various locations within the chamber for the imaging (Figure 5.1).

The MCP imaging process involved acquiring 2-D spatial measurements at 11 to 17 locations to characterize the full beam distribution. These beam calibrations were performed using Helmholtz coil (HC) current and positioning optimized for beam mapping at the MCP and ABM locations.

The beam calibration campaign performed prior to SWAPI's calibration successfully determined the optimal beam parameters that yield the most uniform beam; results for a variety of ion and neutral beam energies and species were performed, even beyond those used by SWAPI. Beyond characterizing the beam uniformity, analysis yielded a strong consensus on the beam's size: an average diameter at MCP of ~6.25 cm and a projected beam diameter at SWAPI entrance (considering beam expansion) of ~7.05 cm.

5.2 Princeton's Absolute Beam Monitor (ABM)

The absolute beam monitor (ABM) used during SWAPI FM calibrations was built in-house at the Princeton Space Physics Laboratory (Figure 5.2). This ABM consists of two Channel Electron Multipliers (CEM), a thin 0.5 $\mu g/cm^2$ carbon foil, a front bias plate, and an integrated set of front-end electronics. Thin foils are commonly used in space-based ion mass spectrometers and neutral atom imagers to generate secondary electrons. A coincidence measurement—detecting both the secondary electrons and the primary ion or neutral atom—enables unambiguous particle identification within a high-noise environment and allows characterization of particle properties via time-of-flight (TOF) techniques.

As described by Funsten et al. (2005), this method provides a simple and robust approach to determining the absolute detection probabilities of individual detectors and the overall detection efficiency of the subsystem. Importantly, this approach is independent of the incident particle flux measurements, allowing for accurate flux measurements without requiring prior knowledge of incident flux. Like SWAPI, ABM employes the same approach to determine the absolute incident flux, making it a valuable reference for flux cross calibration purposes.

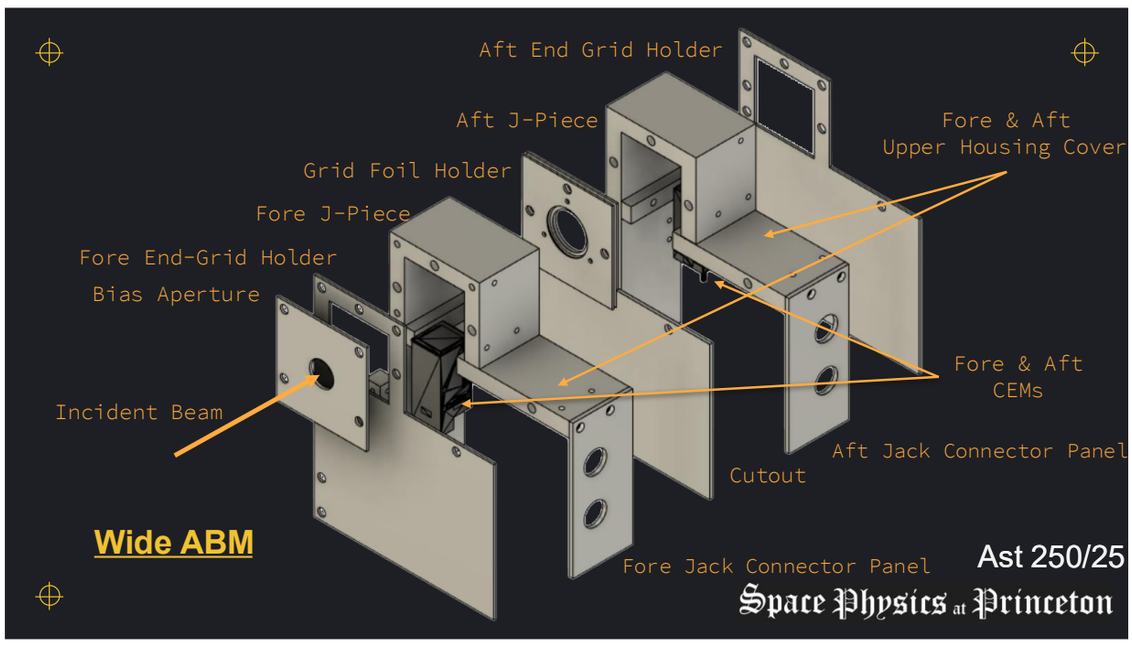


Figure 5.2. *Schematic diagram of Princeton wide absolute beam monitor modified from the original LANL design. The notation of Fore versus Aft CEMs is with respect to the incident beam and carbon foil, where Fore CEM (in front of the C-foil) locates closer to the incident beam than the Aft CEM (post C-foil).*

In general, the likelihood of detecting secondary electrons at the "Fore CEM" detector is independent of detection at the "Aft CEM" detector. Assuming negligible noise, we define N_F as the number of secondary electrons measured by Fore CEM, and N_{FA} as the number of coincidence events — i.e., detections by both Fore and Aft CEMs within a time window (typically set as 100 μs). The absolute detection probability of detector Aft CEM is then: $P_{Aft} = N_{FA}/N_F$. This probability includes effects such as energy loss on the foil and the detection efficiency of Aft CEM. Similarly, the absolute detection probability of Fore CEM is $P_{Fore} = N_{FA}/N_A$, where N_A is the number of primary particles detected by the Aft CEM.

The overall absolute detection efficiency ε_D of the ABM detector system includes the transmission probability of grid and foil (T_G , T_F) and the absolute detection probability of Aft CEM and Fore CEM, $P_{Fore}P_{Aft}$. This gives:

$$\varepsilon_D = T_G T_F P_{Fore} P_{Aft} \, .$$

The incident beam flux, N_0, is then given by: $N_0 = N_{FA}/\varepsilon_D$, effectively $N_0 = N_F N_A / N_{FA} T_G T_F$. For simplicity, we generally assume perfect transmission ($T_G T_F = 1$), yielding the formula of absolute incident beam flux as

$$N_0 = \frac{N_F N_A}{N_{FA}}$$

During both beam calibration and IMAP instrument calibrations, the performance of the ABM was closely monitored through measurements of the absolute detection efficiency (ε_D), even though this parameter

does not directly influence the determination of incident beam flux, as previously noted. A particular challenge arose when attempting to measure incident beam flux at energies near or below 100 eV, where low count statistics limit measurement reliability. This limitation stems from the use of a thin 0.5 µg carbon foil, hinting the reason for applying a conversion surface in ABM or instrument like IMAP-Lo to detect low-energy energetic neutral atoms (ENAs) and interstellar neutrals (ISNs) across few eV to 1000 eV energy range.

5.3 Beam characterization during the actual SWAPI FM Pre-Flight Cal

During the SWAPI FM Pre-flight Cal, ABM and/or MCP measurements were taken daily to characterize the beam prior to testing. The only exception was the first day of calibration, 16 September 2024, which primarily focused on verifying basic instrument functionality and conducting the full functional test since this was the first time the instrument was powered on since environmental testing. A summary of the ABM and MCP tests during the SWAPI Pre-flight FM Cal are as provided in Table 5.1.

Table 5.1. *Summary of in-house beam monitoring measurements taken during the SWAPI FM Pre-flight cal. The number of crosses indicates how many respective tests were conducted on that day.*

	Test	Day 1 (09/16)	Day 2 (09/17)	Day 3 (09/18)	Day 4 (09/19)	Day 5 (09/20)	Day 6 (09/21)	Day 7 (09/23)	Day 8 (09/24)	Day 9 (09/25)	Day 10 (09/26)	Day 11 (09/27)	Day 12 (09/28)	Day 13 (09/30)	Day 14 (10/01)	Day 15 (10/02)
MCP	**MCP Measurements - Summary**			x	x					x						
	1keV H+			x	x											
	3keV He+									x						
	4keV He+									x						
Absolute Beam Monitor (ABM)	**ABM Measurements - Summary**		x	x		x	x	x	x	x	x	x	x	x	x	x
	100 eV H+														xx	
	111 eV H+															x
	400 eV H+									xxxx	xx				x	
	1keV H+		x	x		x		xx	x		xx				xx	x
	2keV H+										xx					
	4keV H+												x		x	
	16 keV H+															
	1 keV H2+										xx			xxx		
	4 keV H2+												x			
	400 eV He+														x	
	700 eV He+														x	
	3 keV He+									xx	xx					
	4 keV He+									xxx	xx	x	x		x	
	10 keV He+															
	16 keV He+						xxx		x				x			
	18 keV He+								x							
	16 keV Ar+						x									
	~20 keV Ar+						x									
	Background									x	x	x			x	

Full Beam Imaging using MCP

Figure 5.3 shows the normalized full beam imaging results taken during the SWAPI FM pre-flight calibration, again yielding a beam diameter of ~6.25 cm at MCP (projected beam diameter of ~7.05 cm at

the entrance of SWAPI) which – being highly uniform and more than adequate to fully cover the instrument aperture – proved to be well-suited for the testing of SWAPI.

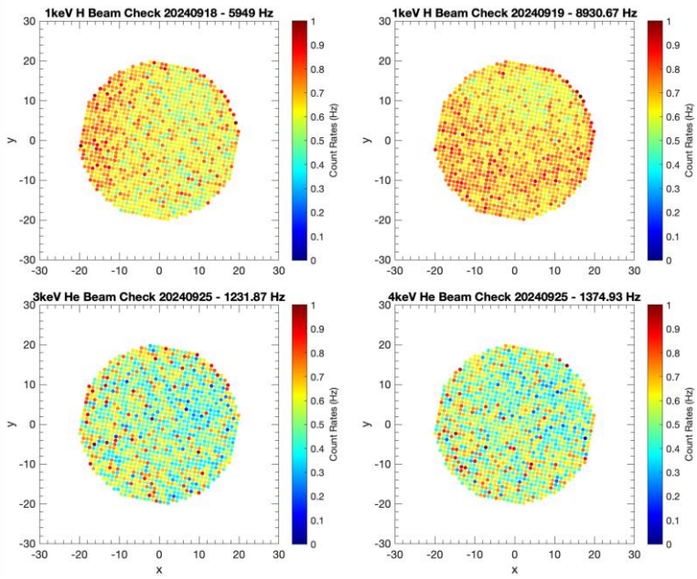


Figure 5.3. *MCP imaging at the beam center for (top panels) 1keV H+ on 18 September and 19 September 2024, as well as (bottom panels) 3keV He+ and 4 keV He+ on 25 September 2024.*

Absolute detection efficiency variation during the SWAPI FM Pre-flight Cal

Figure 5.4 shows the variation in the absolute detection efficiency (ADE) and absolute beam flux (ABF) of the ABM during the SWAPI FM Pre-flight Cal. Note that the beam parameters remained the same for all tests. The ABF was computed using the formula: ABF = $\frac{N_{FORE} N_{AFT}}{N_{COIN}\, A_{eff}}$, where A_{eff} is the effective area of the in-house ABM, 0.785 cm^2.

As reflected in the Figure 5.4 data, an interesting downward trend of absolute detection efficiency was measured over the course of calibration. One possible explanation is ABM carbon foil degradation, perhaps caused by several high-intensity beam tests conducted at the beginning of the Pre-flight Cal. However, the absolute beam flux shows variations that are consistent with the ion source pressure, suggesting that the beam variation is relatively consistent over time.

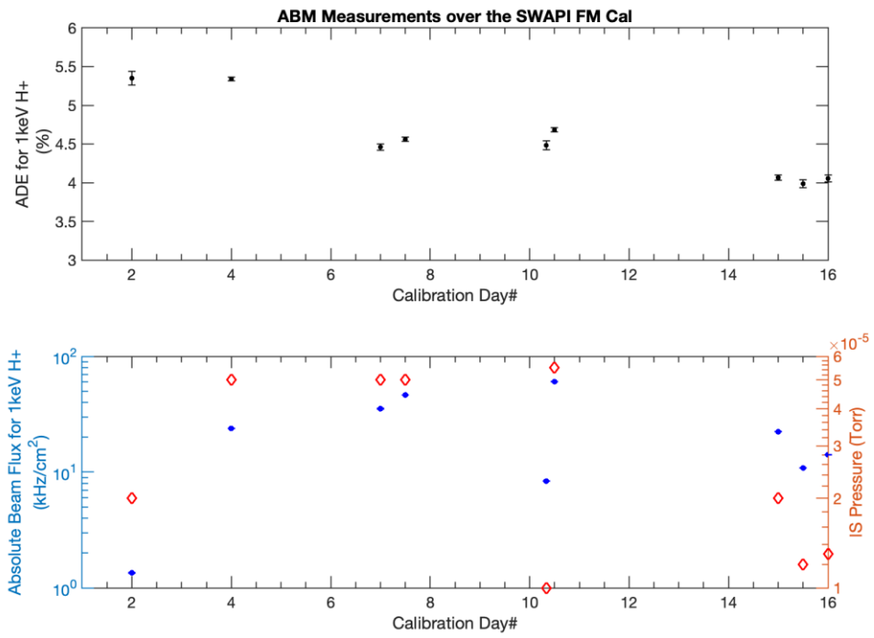


Figure 5.4. *Variation of the absolute detection efficiency (top) and the absolute beam flux (bottom) of the ABM using 1keV H+ during the SWAPI FM Pre-flight Cal. The red diamonds in the bottom panel show ion source pressure.*

Helmholtz Coil -- Gyroradius effect correction

For the SWAPI FM calibrations, it was crucial to minimize the gyroradius effect of the ion beams, which are more significant for light, low-energy species. Therefore measurements were taken in advance to optimize the HC settings (see Khoo et al. 2023 for description of methodology).

The optimal HC current and position depend on the distance between the ion source nose and the instrument location. Since the MCP and ABM are located closer to the ion source than the SWAPI instrument inside the main chamber, the HC current for MCP and ABM tests was lower than that used for SWAPI calibration, and the optimal HC position was correspondingly closer to the ion source. These optimal HC locations are marked on the flight tube, and the corresponding current values are listed on the HC power supply.

Figure 5.5 shows an example of a beam directionality test, in which SWAPI was moved from one end of the linear stage to the other while fixed at +90° azimuth and 0° elevation angle. This test used 3 keV Ar+ as a reference, as its high atomic mass results in a minimal gyroradius effect. The test involved stepping through different Helmholtz coil (HC) currents to steer low-energy proton beams toward the beam center (indicated by vertical dashed lines) or as close as possible to the 3keV Ar+ beam result.

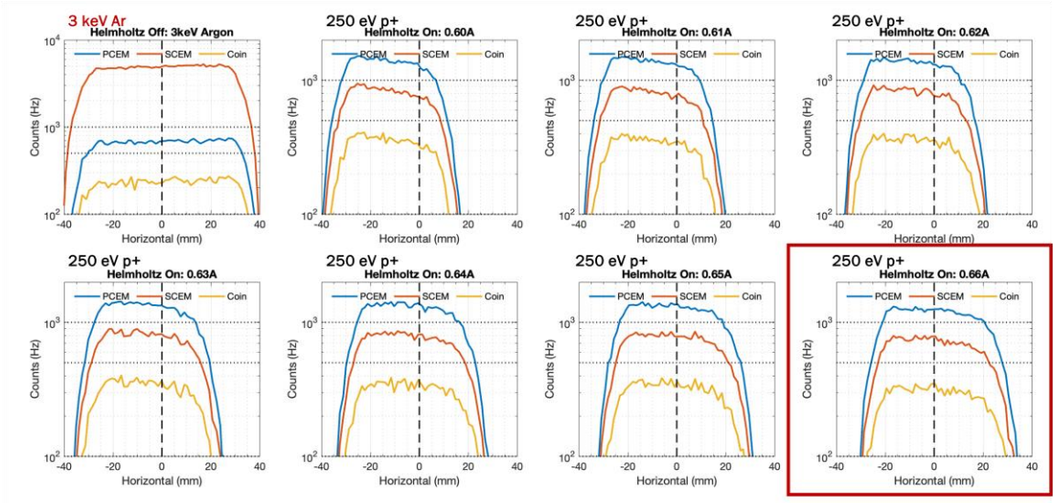


Figure 5.5. *An example of the beam directionality test taken with SWAPI fixed at +90° azimuth ("open aperture") and 0° elevation angle. The red box indicates the selected Helmholtz coil current for SWAPI calibration.*

6. SWAPI CALIBRATION OVERVIEW AND TEST SUMMARY

6.1 Calibration Test Configuration

Figure 6.1 provides schematic diagrams of the setup used during SWAPI's calibration testing. SWAPI's packetized instrument-generated telemetry was recorded through the IMAP spacecraft emulator interface using GSEOS (Figure 6.2).

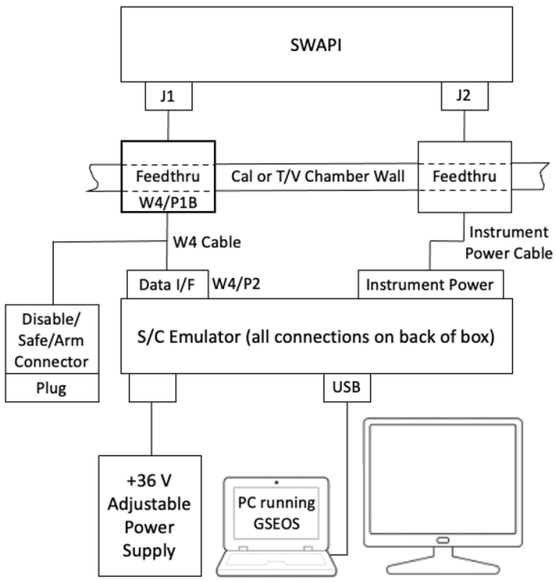


Figure 6.1. *Schematic diagram for the SWAPI instrument test wiring during its pre-flight calibration campaign.*

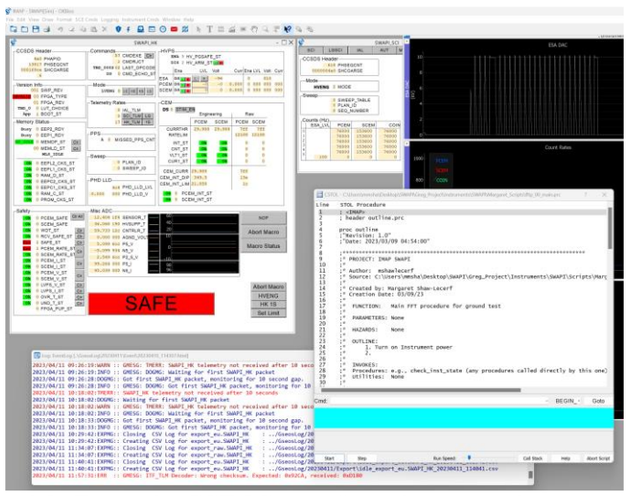


Figure 6.2. *Example GSEOS interface showing telemetry window (top screens), Event Log (bottom), and CSTOL viewer (right).*

6.2 Calibration Test Overview

The goal of the SWAPI FM Pre-flight Cal was to achieve the four key objectives outlined in Section 3. Tests were categorized by priority – high, medium, and low – and accomplished as listed in Table 6.1.

Table 6.1. *A detailed breakdown of the implemented calibration tests during SWAPI FM Pre-flight Calibration (16 September 2025 to 2 October 2025).*

High Priority Tests	Est. Hr	Status
Full Functional Test	6 hr	Done (9/16)
Gain Curves – 1 keV H+	3 hr	Done (9/17)
Gain Curves – 4 keV He+**	3 hr	Done (9/27)
High Voltage Ramp/Dwell Test	1.5 hr	Done (10/02)
Background Test	1.5 hr	Done (10/02)
Dynamic Range Test	4 hr	Done (10/01)
UV Light Leak Test	0.5 hr	Done (10/02)
Azimuthal Response → 16 keV He+ @ 0.1°/s	2.5 hr	Done (9/21)
Azimuthal Response → 1keV H+ @ 0.1°/s	2.5 hr	Done (9/23)
Full Range Energy Test → 0.1 to 20 keV, H+	2-7 hr	Done (9/18)
Full Range Energy Test → 0.1 to 20 keV, He+	2-7 hr	Done (9/27)
Full Range Energy Test → 0.1 to 20 keV, Ar+ **	2-7 hr	Done (9/21)
Full Azimuthal and Elevation Map → 1 keV H+ (1°/s)	8 hr	Done (9/23)
Full Azimuthal and Elevation Map → 16 keV He+ (1°/s)	8 hr	Done (9/28)
X-Cal Passbands→ 2 keV H+ [IA = 0°]	1.5 hr	Done (9/26)
X-Cal Passbands→ 16 keV H+ [IA = 90°]	1.5 hr	Done (9/19)
Sunglasses Passbands → 1 keV H2+ (IA = 0°)	1.5 hr	Done (9/26)
Sunglasses Passbands → 4 keV He+ (IA = 0°)	1.5 hr	Done (9/26)
Sunglasses Scattering Test→ ??? keV ??? (IA = 0°; hottest beam possible)	4 hr	Done (9/30)
Flight-like ops tests - instrument safing; flight-like sweeps; beam center-finding; fine-steps test; binary files…	3 hr	Done (10/02)

Medium Priority Test	Est. Hr	Status
Proton Passband → 0.4 keV H+ (IA = 90°)	1.5 hr	Done (9/26)
Proton Passband → 1 keV H+ (IA = 90°)	1.5 hr	Done (9/17)
Proton Passband → 10 keV H+ (IA = 90°)	1.5 hr	Done (9/19)
Helium Passband → 0.4 keV He+ (IA = 90°)	1.5 hr	Done (9/19)
Helium Passband → 0.7 keV He+ (IA = 90°)	1.5 hr	Done (9/19)
Helium Passband → 4 keV He+ (IA = 90°)	1.5 hr	Done (9/19)
Helium Passband →16 keV He+ (IA = ±90°)	1.5 hr	Done (9/24)
Helium Passband → 18 keV He+ (IA = 90°)	1.5 hr	Done (9/24)
Carbon Foil Functionality → 1 keV Ar+	1.5 hr	Done (9/16)
Nice-to-have Test		
Azimuthal Response vs ESA voltage (PB IAR) → 1 keV H+	2 hr	Done (9/20)
Solar Wind Scattering Test → 1 keV H+ (IA = 90°; 30 kHz)	4 hr	Done (10/01)
Alignment→ 16 keV H+, IA = -90°	1.5 hr	Done (9/19)
EM Continuity → 3keV He+ IA = 0°	1.5 hr	Done (9/26)
~~*Aperture Cutoff Ring (ACR) – Diagnostic Test***~~	~~*2 hr*~~	~~Done~~
*Safety Plug Test***	*2 hr*	Done (9/17)
*Proton Passband → 1 keV H+ (-90°)***	*1.5 hr*	Done (9/17)
*End of Cal Gain Curves***	*3 hr*	Done (10/02)
*Horizontal Beam Test (to compare with ABM, MCP)***	*1 hr*	Done (10/01)
Azimuthal Response vs ESA voltage (PB IAR) → 16 keV He+	*6 hr*	Done (9/24)
Multiple source tests: UV+ Ion Gauge + RGA+ Beam _ Sweep SWAPI in HVSCI	*1.5 hr*	Done (9/30)

To calibrate different aspects of its electro-optics, SWAPI was subjected to ion beams of different energies and species. The instrument was positioned at a range of rotational and translational configurations relative to the beam, depending on the specific goals of each measurement. Throughout the entire time of testing,

instrument housekeeping telemetry (e.g., voltages, temperatures, currents) and science data (e.g., PCEM counts, SCEM counts, COIN counts) were recorded by GSEOS.

6.2.1 Daily Test Flow

The test flow for each calibration day (especially during Pre-flight Cal) is summarized below:

- Perform RGA scan and ignite the beam
- Characterize and monitor the beam using MCP/ABM* at least once a day
- Power on SWAPI
- Carry out the calibration activities*
- Power off SWAPI, MCP/ABM, and ion source
- Home the instrument
- Upload all data, including SWAPI data, daily calibration checklist, RGA result, 24-hour pressure plot, and calibration system logs

**Key measurements made with main chamber ion pressure gauge OFF to minimize backgrounds*

All activities and system statuses such as the beam parameter, instrument positions, and beam monitor positions were recorded in the calibration logbook whenever a new action was taken. In addition, an RGA scan as well as a 24-hour chamber pressure plot were generated daily to ensure the chamber was clean and pressures were suitable for SWAPI's operations ($< 3x10^{-7}$ Torr for at least 24 hours before turning on high voltage). The beam was characterized and monitored by the MCP/ABM at least once per day, and occasionally multiple times (e.g., at the start and end of the calibration day). Results are presented and discussed in the later sections of this document.

7. CHARACTERIZATION OF THE VARIOUS SWAPI SUBSYSTEMS

This section discusses the characterization of each SWAPI subsystems. We begin with the CEMs, examining their gain curves and determining the best pre-launch & in-flight turn-on operating voltages. Next, we focus on the dark count measurements taken during SWAPI FM Pre-flight Cal. We then characterize the aperture grid and determine the attenuation factor near the sunglasses. Additionally, we analyzed the open aperture region and determined the effective entrance aperture range for the open aperture. Finally, we evaluated the condition of the carbon foil using a beam of 1 keV Ar+.

7.1 CEMs: SWAPI's Gain Curves and Pre-Launch Operating Voltages

Gain curves were acquired throughout the different calibration campaigns (pre- and post-environmental, leading up to delivery) to assess how the CEM gains varied over time; the results were used to determine optimal voltage settings used for SWAPI's initial in-flight operations.

In the lab, the gain curves were conducted using a slightly different method than those used in-flight. The process began by fixing the voltage of one CEM (say CEM-A) while sweeping through a range of voltages for the other CEM (say CEM-B), dwelling at each voltage step. Once the full voltage range for CEM-B was completed, the voltage on CEM-A was incremented by a fixed step, and the sweep was repeated. This continued until CEM-A also covered its full voltage range. The entire process was then repeated with the roles reversed—CEM-B was held fixed while CEM-A was swept.

Figure 7.1 shows an example of the gain curves results taken on the last day of the SWAPI FM Pre-flight Cal. The green dashed lines indicate the optimal operating voltages, which were determined from the plots as the second or third data point following the onset of the plateau region.

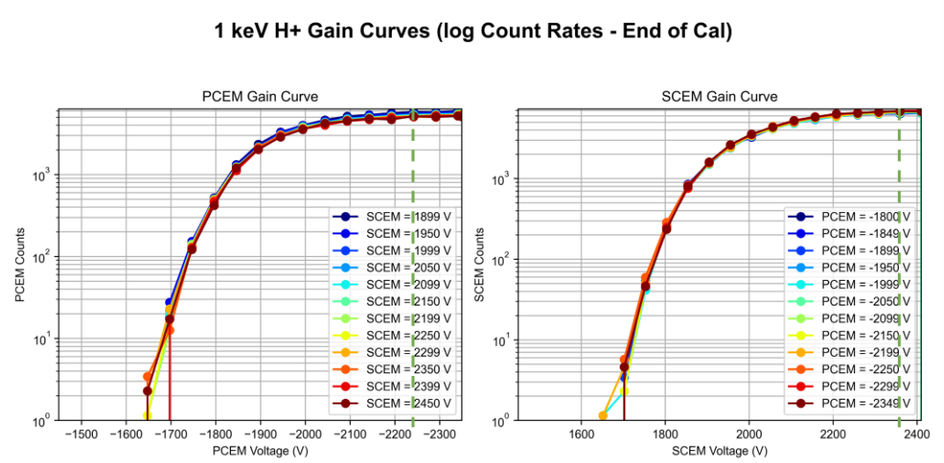


Figure 7.1. *An example of gain curves for PCEM (left) and SCEM (right) using 1keV H+.*

Figure 7.2 shows a summary of all gain curve results. To simplify the visualization, we did not plot every PCEM curve for each SCEM voltage step from every gain curve. Instead, we display on the PCEM curve corresponding to the optimal SCEM voltage, and vice versa for the SCEM curve. This approach allows us to examine the variation of the gain curves over the calibration period more clearly. Interested readers can refer to Appendix C for the full gain curve results during SWAPI Pre-flight Cal.

During Pre-flight Cal, four different gain curves were performed using 1keV H+ over a span of 15 days. On Day 1, only a single set of data was collected: SCEM voltages were fixed while PCEM voltages were swept. The reverse configuration was not performed and therefore no SCEM curve (blue) is shown in Figure 7.2b. For the remaining three gain curve tests, consistent beam parameters for 1keV H+ beam were used. However, variations in the PCEM and SCEM count rates were observed, likely due to fluctuations in the ion source (e.g., the slight variation in MCP imaging in Figure 6.6), despite efforts to maintain constant conditions such as ion source pressure. Notably, the absolute detection efficiency (ADE) remained relatively stable, with a clear shift observed between the first and second week (Day 7). This shift is likely due to the instrument being exposed to a high-intensity beam during the first week. In Week 2, the maximum CEM count rates were limited to 30 kHz to prevent overloading the detectors. The results show that the ADE values on Day 7 and Day 16 were very similar after the limits were imposed.

Additionally, we performed gain curves using 4 keV He+ and verified that the results are generally independent of the incident beam species or energy. The gain curve results obtained with 4keV He+ are provided in Appendix C. Based on these results, the selected in-flight operating turn-on operational voltages for PCEM and SCEM were -2250 and +2350 V, respectively.

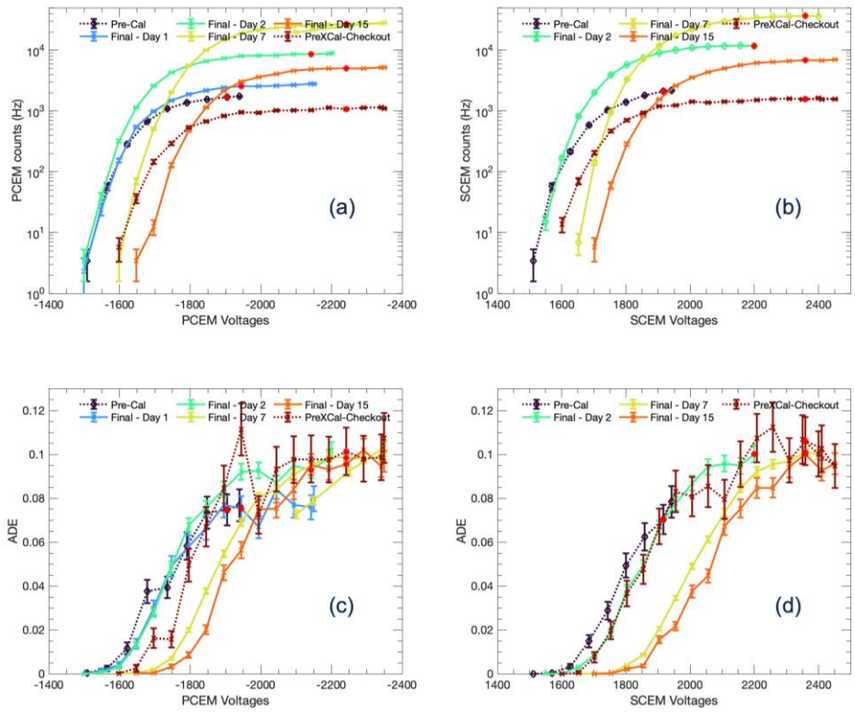


Figure 7.2. *Comparison of test results for gain curves taken between the early SWAPI FM Cal (prior to environmental testing) and Pre-flight (post-environmental tests, prior to delivery) Cal periods. (a) PCEM count rates as a function of PCEM voltages parking at the optimal SCEM voltage; (b) SCEM count rates as a function of SCEM voltages at the optimal PCEM voltage. (c) Absolute detection efficiency as a function of PCEM voltages, where the SCEM voltage is parked at the optimal voltage. (d) Absolute detection efficiency as a function of SCEM voltages where the PCEM voltage is parked at the optimal voltage. The red asterisks mark the optimal PCEM or SCEM voltage for each gain curve. These gain curve tests were performed with more steps and at higher resolution than the coarse versions that will be used in flight (see Figure 7.3 below).*

In addition, we also performed flight-like gain curves to verify the functionality of the flight gain curve scripts and ensure it adequately covers the necessary range for in-flight operating voltage assessment. Unlike the lab gain curve test – where one CEM was parked at a fixed voltage while the other was swept – the flight gain curve test stepped through a range of voltage combinations for both CEMs simultaneously. The user provides the target voltage, and the scripts generates combinations of CEMs voltages, ranging from 100 V above to 200 V below the target for each CEM. An illustration of the voltage steps is described in Figure 8.3a where the target voltages for PCEM (x-axis) and SCEM (y-axis) were 1800 V and 1850 V, respectively. The script navigates through these combinations in a ‘maze-like’ pattern to efficiently sample the voltage space. The results of the flight gain curve are also shown in Figure 7.3. They closely resemble those obtained from the lab gain curves and, importantly, cover the region near the onset of the plateau. This indicates that the flight gain curve script is sufficient for assessing the optimal operating voltages in space.

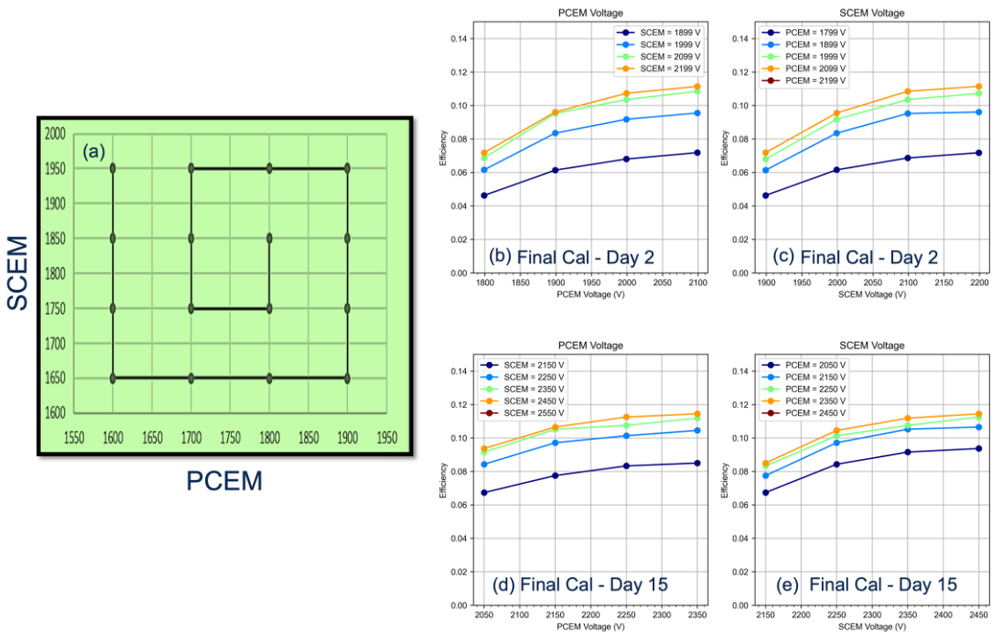


Figure 7.3*. Illustration and results of the flight gain curves. (a) Example of the flight gain curves algorithm that will step through a varying CEM voltage combination. The target voltages for PCEM and SCEM for this example are 1800 V and 1850 V, respectively. (b & c) Results of PCEM and SCEM flight gain curves taken on Day 2 of Pre-flight Cal ("Final Cal – Day 2"); (d & e) Like b & c but were taken on the last day of Pre-flight Cal ("Final Cal – Day 15").*

7.2 CEMs: Dark Counts, UV tests, and lowest-measurable beam

Dark count tests were conducted in two ways: 1) at fixed ESA settings (-100 V and -10240 V); 2) in HVSCI mode where the ESA sweeps through a wide range of voltages based on the LUT. In both methods, the SWAPI CEMs were parked at their optimal operating voltages, and the chamber gate valve was closed to isolate the instrument from the source. The main chamber ion gauge was turned off to prevent any background contamination. The results are shown in Table 7.1, which indicates that COIN rate is <0.01 Hz in both configurations (fixed ESA voltage settings and HVSCI sweep mode).

Table 7.1. *Summary of the average PCEM, SCEM, and COIN count rates in different setups for dark count tests and UV tests.*

	Test Setup	PCEM	SCEM	COIN
Dark Count	Fixed ESA (@-100 V) Beginning of the day Duration: 16 minutes	0.016 ±0.0042	0.029 ±0.0055	0.0036 ±0.0019
	Fixed ESA (@-10240 V) After UV light leak Duration: 15 minutes	0.023 ±0.0051	0.065 ±0.0085	0.0064 ±0.0027
	HVSCI (Before UV test) Duration: 10 minutes	0.015±0.0051	0.029±0.0069	0.0018±0.0019
	HVSCI (After UV test) Duration: 10 minutes	0.013±0.0047	0.025±0.0065	0±0
UV Test	Dwell @ +170 degree Duration: 1 minute	0.18 ±0.055	0.37 ±0.079	0
	Dwell @-170 degree Duration: 1 minute	0.14 ±0.048	0.18 ±0.055	0
Weak Beam	HVSCI mode Duration = 30 minutes	0.47 ±0.016	0.63 ±0.019	0.17 ±0.0096

In addition to the dark count tests, we also performed a UV light test to quantify expected background levels and look for any indication of unanticipated UV light leaks. This was done using a 1-Sun UV light source installed on the Main Chamber, downstream of the beam (recall Figure 4.3). SWAPI was parked with the inner rotational stage at ±170°, with the UV light source pointed towards the SWAPI sunglasses. The results show that both CEMs observed some real counts (e.g., higher than the dark counts reference, but still very low rates) during these tests. Importantly, there were NO coincidence triggers, highlighting the effectiveness of SWAPI's coincidence settings in filtering out background signals from the real ion detections during data analysis. Finally, we assessed the CEM detection sensitivity threshold using a very weak beam (1 keV H+ beam through the sunglasses to give < 0.5 Hz count rates). Thanks to the low dark count rates, we were able to measure an average COIN rate of 0.17 Hz, thereby exceeding SWAPI's signal to noise ratio requirement ("greater than or equal to 1 at a coincidence count rate of 0.3 Hz").

7.3 Aperture Grid: Attenuation Factor

With the CEMs parked at their optimal operating voltages, we measured the attenuation factor of the aperture grid. This was achieved by rotating SWAPI along its azimuthal axis while maintaining at an elevation angle of 0° and setting the ESA voltage to its optimal voltage, determined from the peak of a fitted ESA sweep curve. This configuration allowed the same beam to enter through different entrance apertures across an azimuthal range of ±170°, thus enabling us to characterize the instrument's full azimuthal response, including through the unattenuated open aperture and through the sunglasses grid.

Figure 7.4 shows the PCEM, SCEM, and COIN rates as a function of azimuthal angles (also refer to as inner angles) for 1keV H+ beam. Mechanically, the open aperture spans from ±20 to ±150° without accounting for the vignetting effect (see blue and orange shaded regions on the right panel of Figure 7.4; the blue and orange bars at the top represent the full mechanical extent – including vignetting – of the SW and PUI regions, respectively). The derivation of the effective aperture range is provided in Section 7.4.

As shown in Figure 7.4 (right), the COIN rate remains relatively constant in the open aperture, except near the edge of the sunglasses and the strongback. To compute the attenuation factor, we used the regions under the blue (±40° to ±120°) and orange (±12°) shaded area for open aperture and sunglasses regions,

respectively, where the COIN rates are relatively stable. The attenuation factor is defined as the average COIN rate in the open aperture region divided by the average COIN rate in the sunglasses region. This approach is justified by the comparable aperture areas of the sunglasses and open aperture region, as confirmed by SIMION simulations (not shown; refer to the instrument paper for details of the simulations). The associated uncertainties were propagated using Poisson uncertainties and can be expressed as,

$$Attenuation\ Factor, A = \frac{COIN_{OA}}{COIN_{SG}}$$

$$\epsilon_A = \sqrt{\left(\frac{\epsilon_{COIN_{OA}}}{COIN_{SG}}\right)^2 + \left(\frac{COIN_{OA} \cdot \epsilon_{COIN_{SG}}}{COIN_{SG}^2}\right)^2}$$

This yields an attenuation factor of 1212 ± 25. We note that this value falls within the reasonable range of the estimated attenuation factor based on the inspected hole area and the estimated number of holes on the aperture grid. However, the estimated attenuation factor carried high uncertainties due to the challenges in accurately measuring the hole sizes. Therefore, we adopt the empirically derived value (1212 ± 23) as the input for SWAPI's forward models.

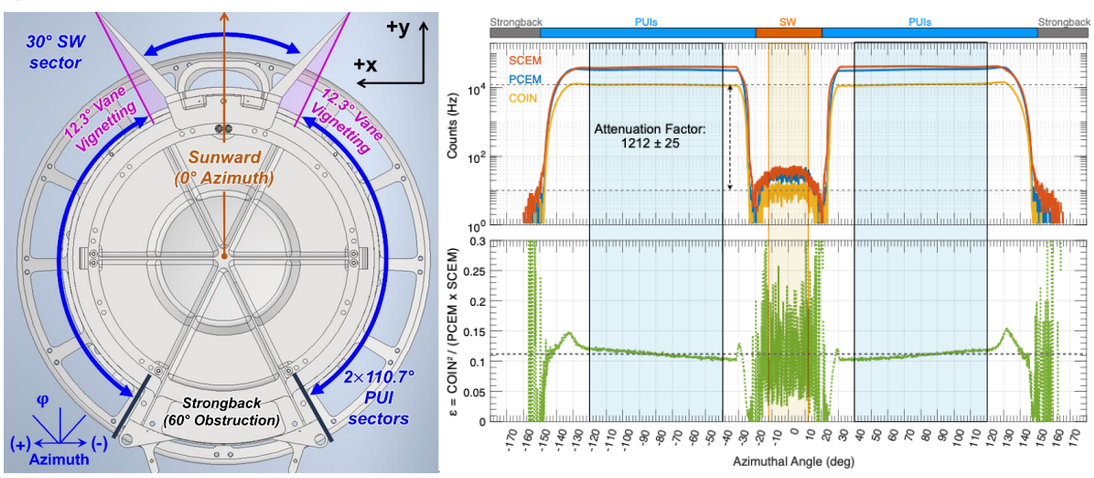


Figure 7.4. *(left) Schematics of SWAPI's entrance apertures, highlighting different regions like Sunglasses (SG), Open Aperture, and Strongback (SB). (right) PCEM, SCEM, COIN and ADE as a function of azimuthal angles (or inner angle). The incident beam for this test is 1keV H+. SWAPI was parked at the optimal ESA voltage (-504.9 V) and an elevation angle (or outer angle of 0°). The gray, blue, and orange bars along the top indicate the mechanical range for strongback (gray), open aperture (PUIs, blue), and sunglasses (SW, orange), while the shaded blue and orange highlight the regions that are unaffected by particle vignetting. (Borrowed from Rankin et al., 2025)*

7.4 Entrance Aperture Range for Open Aperture

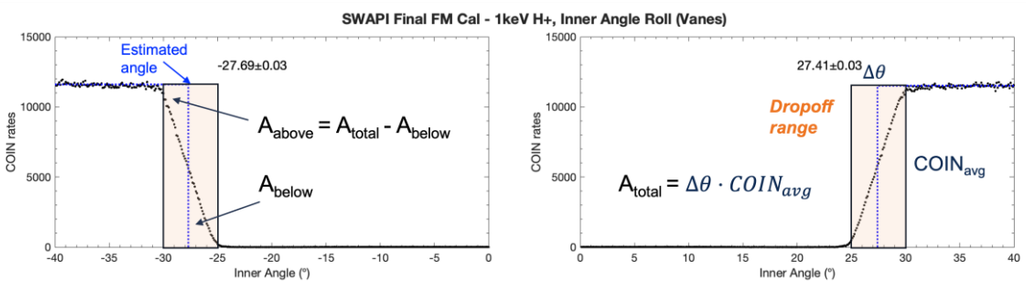
Near the edges of the open aperture, SWAPI observes a gradual, rather than sharp, transition from the open aperture to both the strongback and sunglasses region (recall left plot of Figure 7.4). This observation is attributed to the vignetting effect, which arises when parts of the instruments such as the sunglasses' vanes partially obstruct the field of view, leading to a decrease in the detected count rates near those regions. Therefore, it is necessary to empirically determine the effective aperture range to accurately characterize the instrument's response.

To define the effective aperture edges, we identified the angles at which the area below the curve (A_{below}) equal to the area confined between the curve and average count rates extended from the nearby open aperture region (A_{above}), as illustrated in Figure 7.5 below. This method provides a consistent and empirical approach to delineating the effective aperture range.

We computed the effective aperture range using the following steps:

1. Estimate average count rate (and the corresponding standard deviation) near dropoff
    - For the strongback, we excluded the pre-dropoff bump and average the flat region from ±110° to ±115°.
    - For the sunglasses, we used ±35° to ±40° to compute the average and standard deviation of the count rates.
2. Iteratively determine effective angle
    - Start with an initial guess and compute A_{above} and A_{below} until their ratio approaches 1.
    - To compute the area:
        - fit the dropoff curve with a spline function like piecewise cubic interpolation function (pchip)
            - Sunglasses: ±25° to ±30°
            - Strongback: from the intersection of the average count rate with the curve to ±150°
        - A_{below}: integrate the spline curve from the estimated angle to the end of the dropoff
        - A_{above}: A_{total} - A_{below} (see Figure 7.5)
3. Estimate Uncertainty
    - Repeat Step 2 using 10,000 randomly generated "average count rates" sampled from a normal distribution (mean and standard deviation from Step 1)
    - The final effective angle: the mean of these trials; the uncertainty is the standard deviation.

From this analysis, we determined that the effective aperture range for open aperture is -138 ± 0.05 to -28° ± 0.03 and 138 ± 0.06 to 27° ± 0.03. This gives a total open aperture range of 221° (~110° for each side), which is ~20° less than the mechanical estimate. However, we note that the mechanical estimate (Figure 7.5) does not take the vignetting effect of the sunglasses and the possible scattering effect near the strongback into the accounts. Therefore, it is reasonable to find the effective open aperture range to be smaller than what the mechanical parts allow.



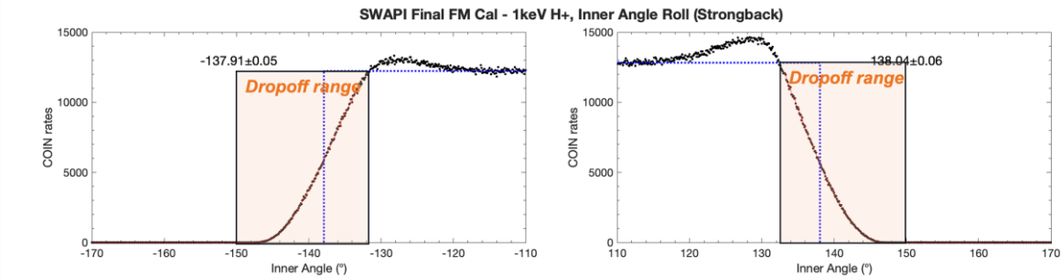


Figure 7.5. *Illustration of the effective aperture edges near the sunglasses region (top) and near the strongback region (bottom). The listed values in the plot represent the effective aperture edge angles.*

7.5 ESA Concentricity

We empirically assessed the mechanical concentricity of the ESA inside SWAPI using two empirical methods:

1. ESA sweep comparison at ±90°

   Using 1keV H+ beam, we performed ESA sweeps at ±90° (on either side of the open aperture). As shown in Figure X, the fitted curves yielded nearly identical peak ESA voltages (-506.9 ± 1.5 V at -90° vs -505.5 ± 1.4 V t +90°) as well as the FWHM ΔV (42.8 V at –90° vs 43.0 V at +90°), indicating strong symmetry.

2. Effective Aperture Range Analysis

   We also quantified the open aperture's extent on either side of the vanes using the previously described aperture range approach. The results corroborate the ESA sweep findings, confirming that the inner and outer ESAs are well-aligned and mechanically concentric.

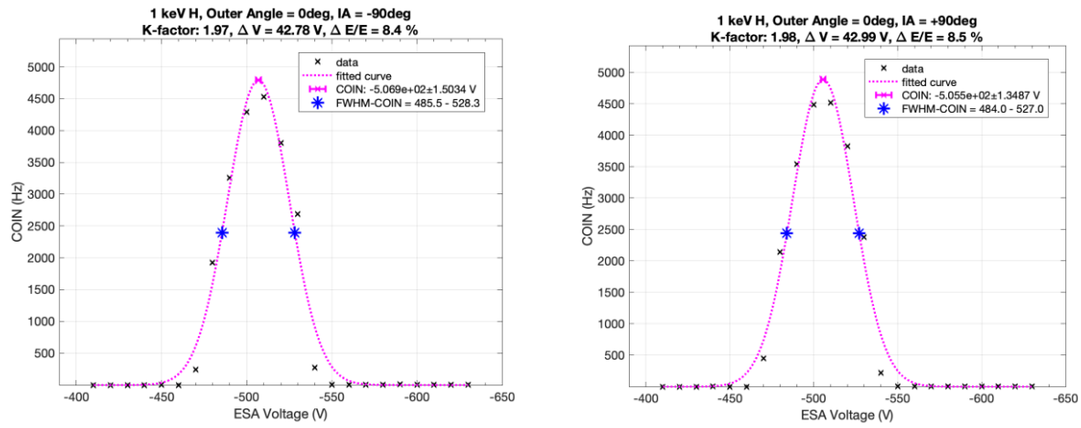


Figure 7.6. *ESA sweeps result using 1keV H+ at azimuthal angle of ±90° (both sides of the open aperture).*

8. FULL INSTRUMENT CHARACTERIZATION

This section presents the characterization of the full SWAPI instrument, focusing on key features required to validate scientific requirements and support in-flight operations. These include the measurable energy range, energy resolution, performance of flight-like sweeps and dynamic range. In addition, we also detail

inputs for forward models, such as the angular response across the full aperture, energy-angle response functions, k-factor, and absolute detection efficiency.

8.1 SWAPI's Measurable Energy Range

This section addresses the testing used to demonstrate SWAPI's ability to achieve its required energy range requirements and resolution. Tests consisted of: (1) a continuous energy calibration, in which the beam energy was set to a fixed target value and a SWAPI ESA voltage sweep was performed using a series of tuned fine steps – broader than the ESA's energy FWHM; these sweeps were repeated over a broad range of beam energies at fixed azimuth and elevation; (2) standard energy-elevation-angle passband measurements, including the upper and lower limits of SWAPI's detection range and for energies and species relevant to both solar wind and pickup ions.

We conducted three distinct continuous energy tests for H+, He+, and Ar+ during SWAPI Pre-flight Cal, covering beam energies from ~115 eV to ~18-19 keV to examine the full measurable energy range. Tests were performed with SWAPI parking at 0° elevation and +90° azimuth. Even though the tests were only performed for beams entering SWAPI's open aperture region, the results are applicable for solar wind particles, with the ~0.1% attenuation through the sunglasses being the primary distinction. Although solar wind helium is typically doubly charged (He++), we used singly charged helium (He+) in our tests, as this is what the lab setup produces.

Figure 8.1 shows COIN rates for H+ and He+ beams from the continuous energy test, plotted as a function of ESA voltage. The required energy ranges are highlighted in dark blues for solar wind H+ (top) and solar wind He+ (middle), and in dark greens for pickup ions He+ (bottom). Notably, the COIN rates fluctuate as a function of ESA voltages or incident beam energy, in contrast to the relatively stable absolute detection efficiency results (Figure 8.2; see Section 8.2 for further discussion). This suggests that the fluctuations are likely due to variation in the facility's beam generation efficiency, i.e., certain beam energies are produced more effectively than others.

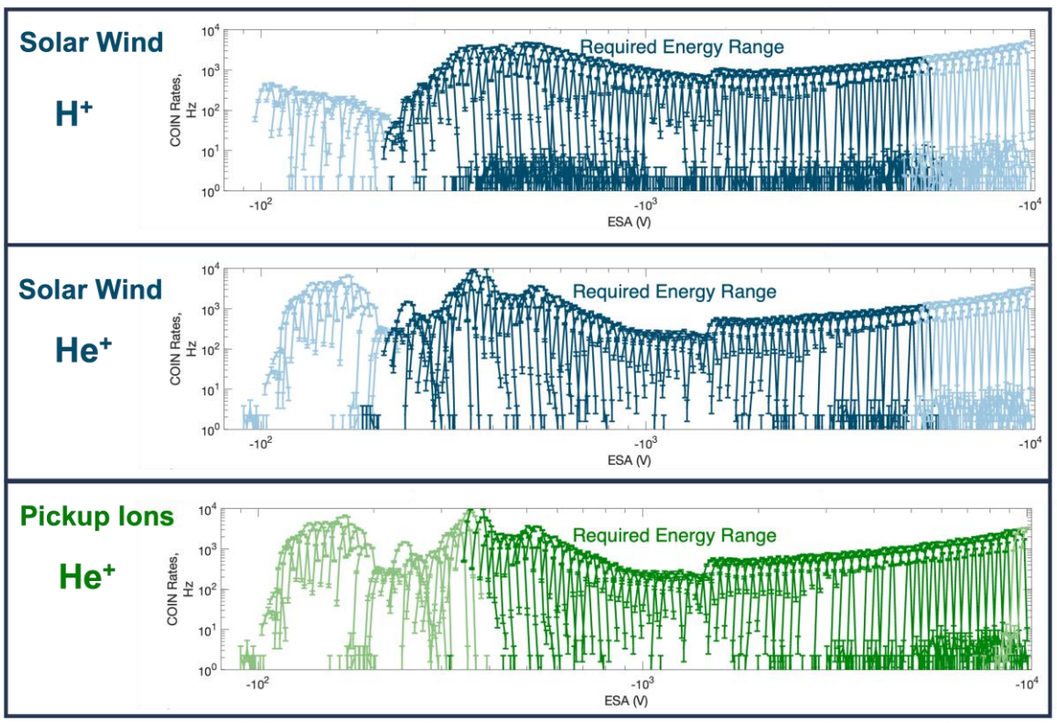


Figure 8.1. *COIN rates and the corresponding Poissonian uncertainties as a function of ESA voltages (V) from the continuous energy tests where incident beams enter the open aperture (+90° azimuthal) at an elevation angle of 0°. The required energy ranges are highlighted as dark blues for solar wind H+ (top) and He+ (middle), and as dark green for pickup ions (He+; bottom). The light blue (light green) lines show the full range of solar wind particle (pickup ions) energies that can be measured by SWAPI, effectively demonstrating that SWAPI meets its energy-range requirements with plenty of margin.*

To further characterize SWAPI's full-energy range performance, we also conducted passbands to showcase the lowest and highest energy range that can be measured by SWAPI. One of the challenges of this test was to provide a low energy beam with sufficiently high intensity. The lowest beam energy for which we can produce reliable counts (due to limitations at the ion source) are 200 eV/q H^+ and 250 eV/q He^+. The clean passbands in Figures 8.2 & 8.3 show that SWAPI can reliably measure 200 eV/q H^+ and 250 eV/q He^+ without much difference in performance compared to other energies. Figures 8.4 & 8.5 showcase SWAPI's passband measurements at its highest energy range – including at the edge of its detection capabilities -- demonstrating clean operation at high voltage and uniform performance throughout.

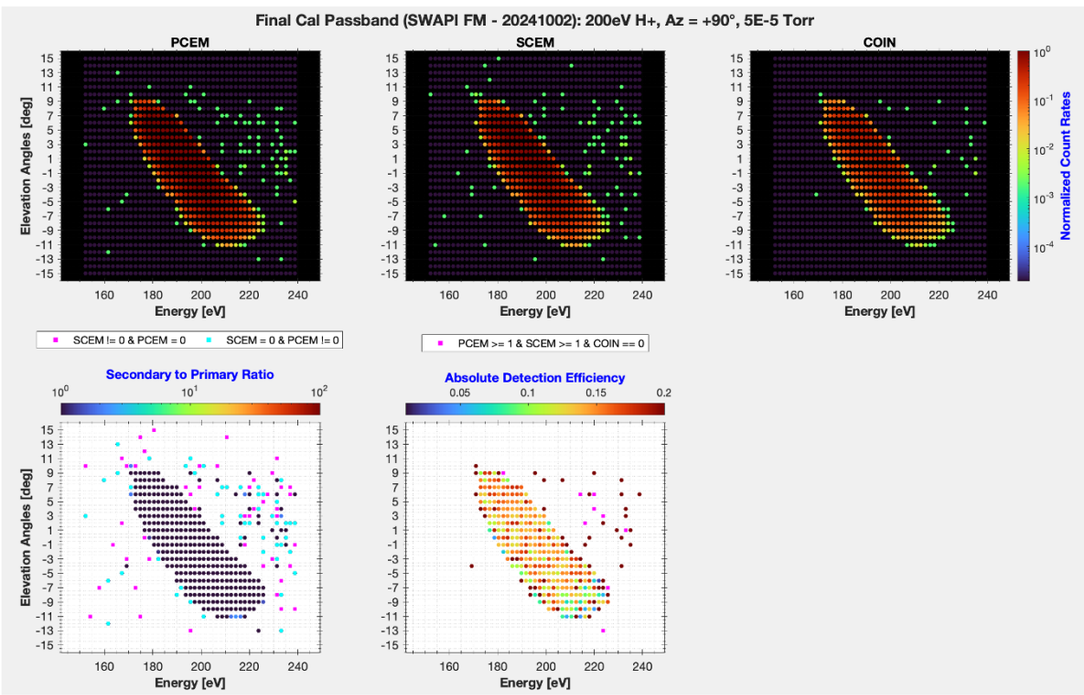


Figure 8.2. *Energy-angle response function (also known as passband) using 200 keV/q H^+ through +90° azimuth ("open aperture"). It demonstrates the lowest energy proton passband that SWAPI measured in the lab. The ESA voltage assuming the "ideal" k-factor of 1.88.*

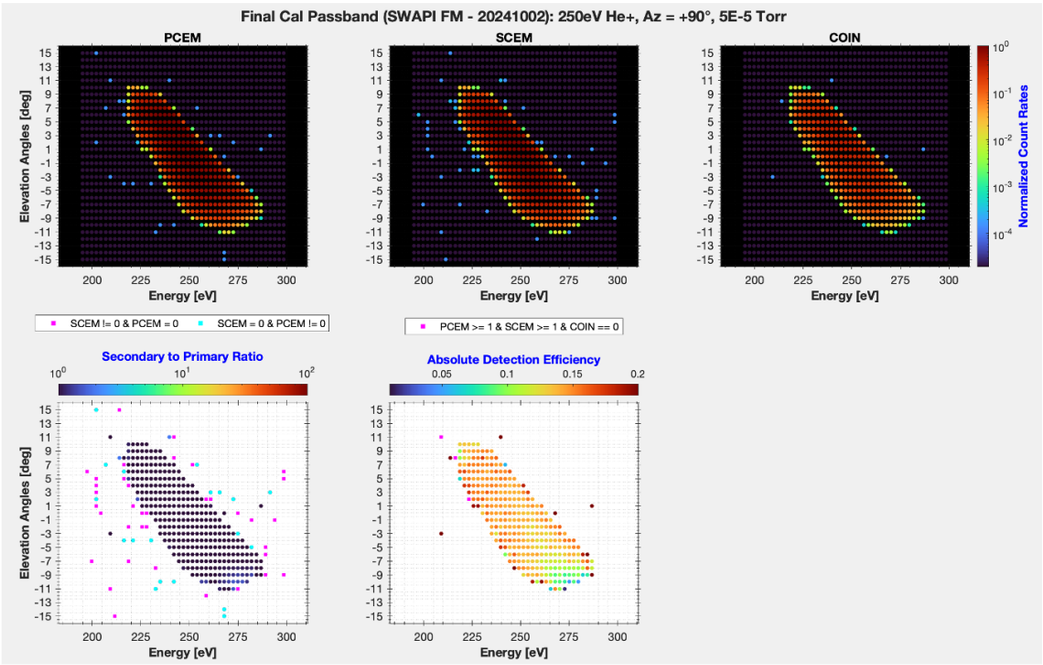


Figure 8.3. *Similar to Figure 8.2, but for 250 eV/q He^+ through +90° azimuth ("open aperture").*

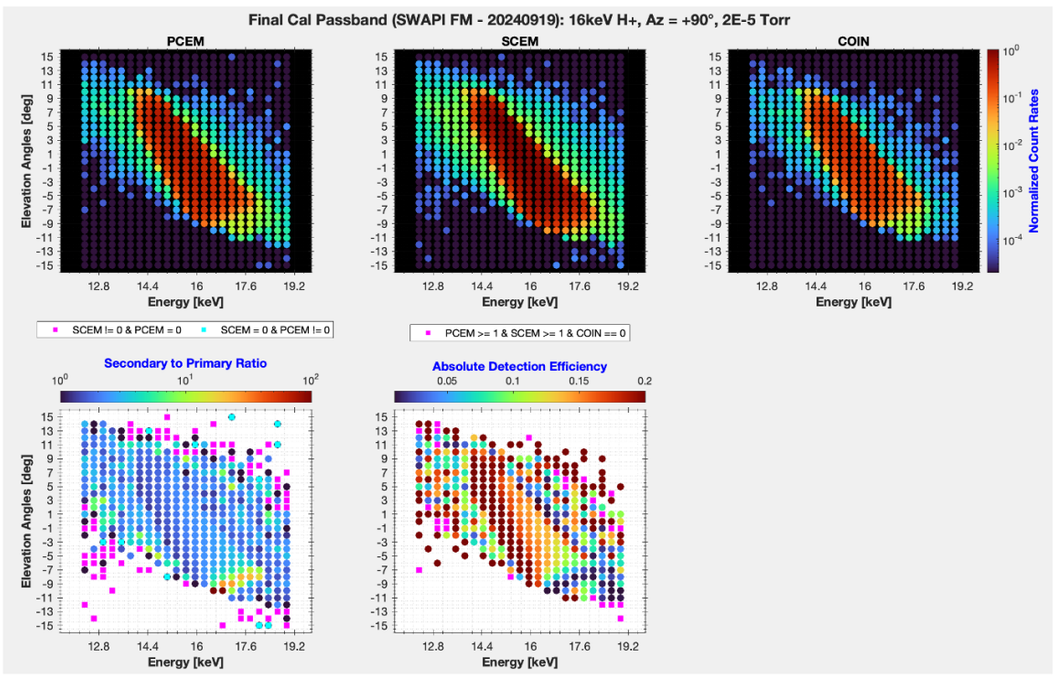


Figure 8.4. *Similar to Figures 8.2 & 8.3, but for 16 keV/q H^+ through +90° azimuth ("open aperture").*

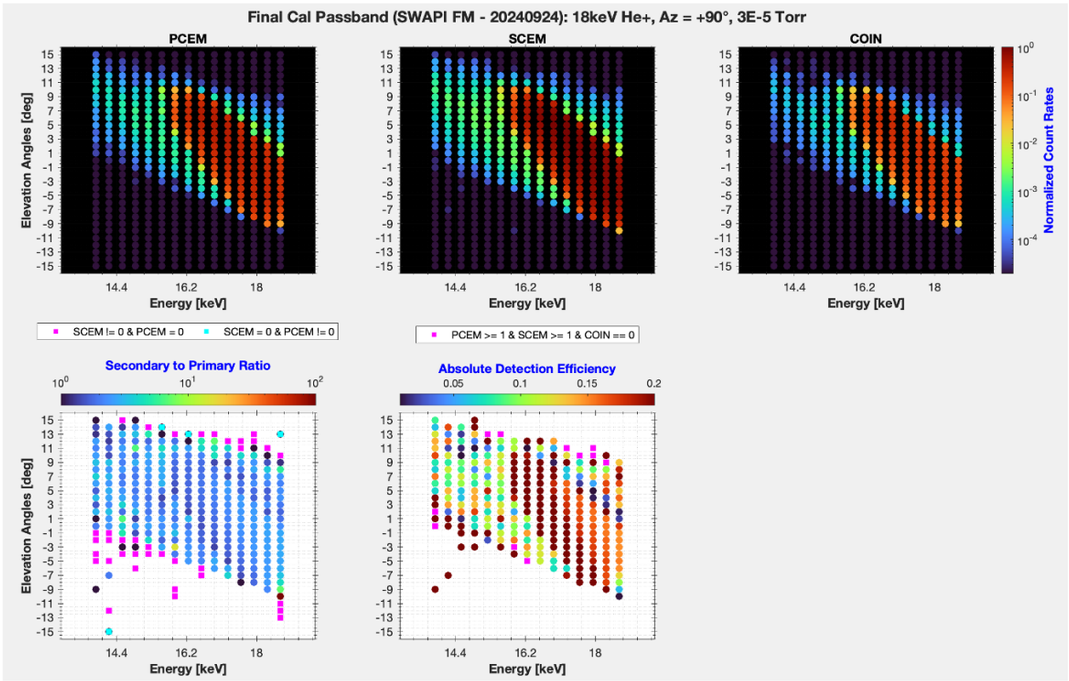


Figure 8.5. *Similar to Figures 8.2 to 8.4, but for 18 keV/q He^+ through +90° azimuth ("open aperture").*

8.2 SWAPI's Absolute Detection Efficiency

For a two-detector carbon-foil instrument like SWAPI, the absolute detection efficiency (ADE, ϵ_D) can be quantified using the coincidence count rate (COIN), and the individual detector count rates [Funsten et al. 2005; Gruntman and Morozov, 1982]. The ADE (ϵ_D) is given by:

$$\epsilon_D = T_F T_G P_A P_B$$

where T_F is the transmission factor of the ultra-thin carbon foil; T_G is the transmission factor of the nickel grid where the carbon foil resides for structural support; $P_A = \frac{C}{S}$. is the absolute detection probability of the first detector (in this case, PCEM), while $P_B = \frac{C}{P}$is the absolute detection probability of the second detector (in this case, SCEM). C is the coincidence rates measured within the time resolution (~100 ns), P and S are the count rates measured by PCEM and SCEM, respectively.

Assuming that T_F and T_G are 1—a valid approximation for SWAPI measurable beam energy, where ions can penetrate the grid and foil with minimal energy loss or straggling (except at very low energies or for heavy species), the ADE equation simplifies to:

$$\epsilon_D = \frac{C^2}{P \cdot S}$$

We used the simplified ADE equation to compute SWAPI's ADE from the continuous energy tests, as shown in Figure 8.6. Unlike the fluctuations in coincidence rates as a function of incident beam observed in Figure 8.1, the ADE remains relatively stable across the energy range for both solar wind and pickup ions, with slightly higher values for He+. Specifically, the average ADE for within the solar wind energy range (dark blues in Figure 8.6) is 0.1162 ± 0.0129 for H+ and 0.1221 ± 0.0131 for He+.

A slight concave trend is observed in the ADE curve, with marginally higher values at both low and high energies. The elevated ADE at lower energies may result from overestimating the foil and grid transmission factor (T_F and T_G), since low-energy ions are more susceptible to energy loss and straggling. To refine this assessment, further analysis using tools like Geant4 simulations is recommended to model energy-dependent transmission effects and improve the accuracy of ADE across SWAPI's full measurable energy range.

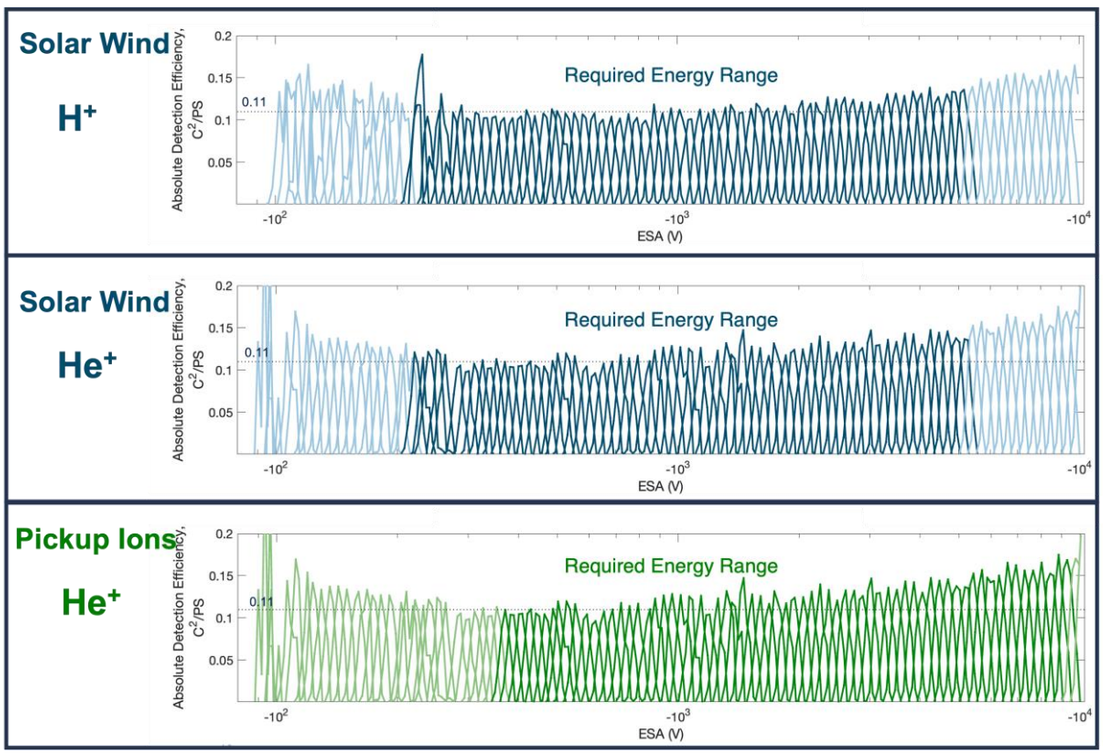


Figure 8.6. *Absolute detection efficiency as a function of ESA voltages (V) from the continuous energy tests where incident beams enter the open aperture (+90° azimuthal) at an elevation angle of 0°. The required energy ranges are highlighted as dark blues for solar wind H+ (top) and solar wind He+ (middle), and as dark greens for pickup ions He+ (bottom). The light blue (light green) lines show the full range of solar wind particle (pickup ions) energy that can be measured by SWAPI, indicating SWAPI's capability in measuring beyond the required energy range with plenty of margin. The dotted lines highlight SWAPI's designed absolute detection efficiency of 11%.*

8.3 SWAPI's Energy Resolution

As described in the SWAPI instrument paper (Rankin et al. 2025), detailed characterization of SWAPI's energy resolution is essential to meet key mission objectives. We derived the energy resolution ($\Delta E/E$) from ESA sweep results obtained during continuous energy tests. Since SWAPI is an electrostatic analyzer, $\Delta E/E$ is equivalent to $\Delta V/V$, where ΔV is the width of the ESA curve and $V = V_{optimal}$ is the optimal ESA voltage determined from the curve.

Given that the ESA sweep curve is not perfectly gaussian and often exhibits asymmetry (e.g., has a shoulder feature), we determined the energy resolution using the following steps:

1) Spline the ESA sweep curve

   Use the 'pchip' (piecewise cubic Hermite interpolating polynomial) function available in MATLAB to spline the ESA sweep curve for smooth interpolation.

2) Compute moments from the spline curve

   - I_0: Zeroth moment (total area under the curve)

- I_1: First moment (used to find the centroid)

3) Determine the optimal ESA voltage, $V_{optimal}$

$$V_{optimal} = \frac{I_1}{I_0}$$

4) Determine curve width, ΔV

   Identifying the voltage range around $V_{optimal}$ that contains a normalized area equal to:

$$erf\sqrt{\log(2)} \sim 0.761.$$

   This is done by fine stepping from both ends of the spline curve towards $V_{optimal}$, integrating the area under the two points at each step (integral under the curve divided by I_0), and finding the width where the cumulative area first meets or falls below this threshold.

5) Compute the energy resolution, ΔE/E

$$\frac{\Delta E}{E} = \frac{\Delta V}{V_{optimal}}$$

Figure 8.7 presents the energy resolution (ΔE/E) for solar wind and pickup ions as a function of incident beam energy defined as the sum of beam energy and the Matsusada output voltages. For comparison, we also include data derived from passband measurements taken at 0° and ±1° elevation angles from open aperture, ±90° azimuth. Most data are from +90°, except for 1 keV H+ and 16 keV H+ where data from both ±90° are included. Generally, the passband results shows good agreement with those from the continuous energy test.

The energy resolution is determined to be between 7% & 8.5%, particularly within the energy range relevant to solar wind particles. A closer examination of the ΔE/E curve reveals a linear relationship between beam energy and energy resolution: lower the beam energies correspond to finer energy resolution. This demonstrates SWAPI's capability to achieve high energy resolution beam even at low energy.

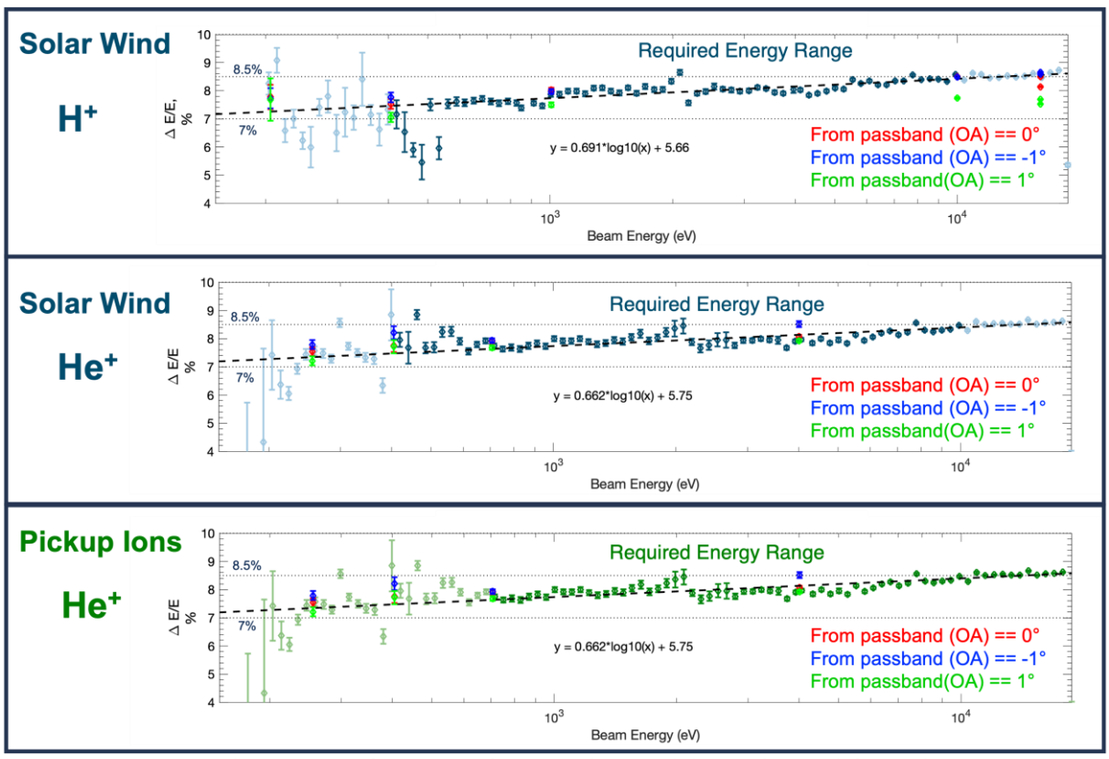


Figure 8.7. *Energy resolution as a function of ESA voltages (V), as derived from the continuous energy tests and passbands taken at open aperture (±90° azimuthal). The required energy ranges are highlighted as dark blues for solar wind H+ (top) and solar wind He+ (middle), and as dark greens for pickup ions He+ (bottom). The light blue (light green) lines show the full range of solar wind particle (pickup ions) energy that can be measured by SWAPI, indicating SWAPI's capability in measuring beyond the required energy range with plenty of margin.*

8.4 SWAPI's Voltage-Energy Conversion (K-factor)

K-factor is defined as the ratio between the analyzed beam energy and the optimal ESA voltage, $k = \frac{Beam\ Energy}{V_{optimal}}$. It is a key parameter for converting ESA voltage to beam energy, which is essential for accurate data interpretation. The K-factor is determined from ESA sweep tests, including both continuous energy tests and passbands. The beam incident energy used in the K-factor determination is the combined energy of the ion source output voltage and the Matsusada output voltage, while the optimal voltage is determined from the ESA sweep curve using the procedure described in Section 8.3.

Figure 8.8 shows the K-factors obtained from the continuous energy tests and selected ESA sweeps (specifically at 0° elevation angle and ±90° open aperture) from passbands. The results indicate a consistent K-factor, generally ranging between 1.9 and 1.95. Notably, there is a peak around ~1keV beam (1.98 for H+ and 1.99 for He+); for <1keV beams, the K-factor stays around ~1.95 (with the lowest reaching ~1.88-1.90), while above 1 keV, the K-factor gradually decreases until ~3keV, beyond which it remains relatively constant. Another notable observation is that the K-factors derived from passbands are higher than those from the continuous tests for <1keV beams, while they are more comparable for higher energy beams. This discrepancy may be attributed to poorer statistics at lower energies, leading to greater

fluctuations. Further analysis is required to fully understand this discrepancy. Based on internal discussion, we determined that 1.93 to be a good k-factor value, which is the average of the nominal value.

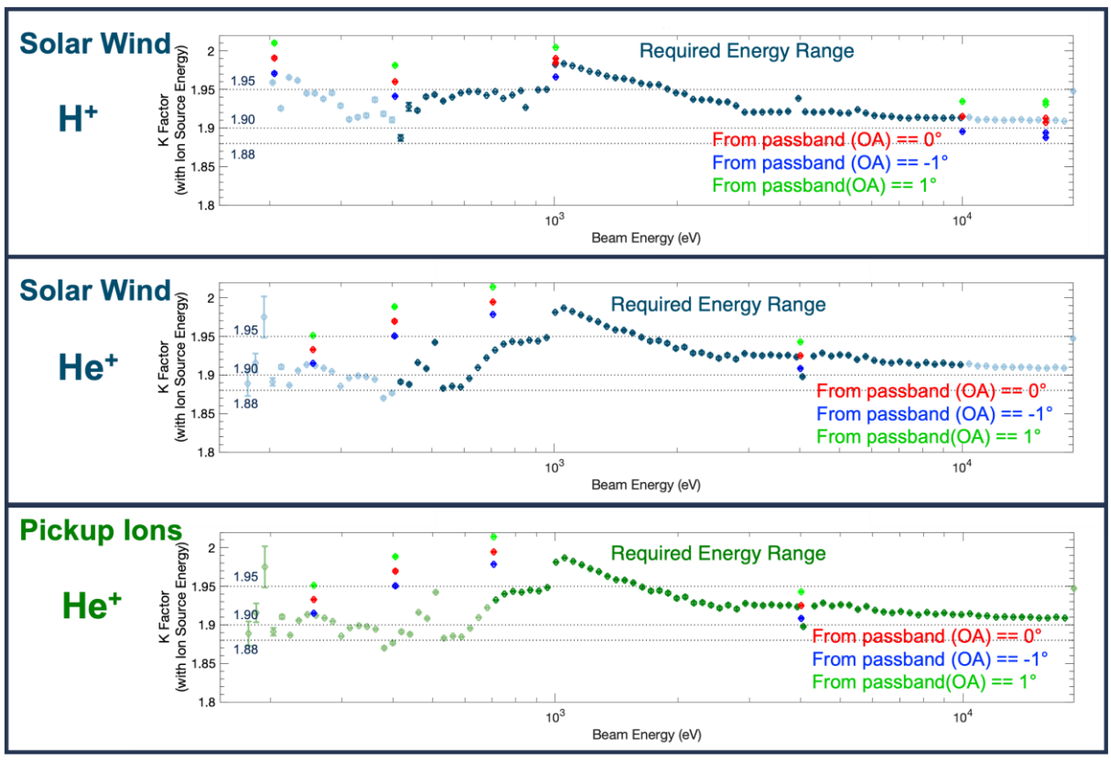


Figure 8.8. *K-factors as a function of ESA voltages (V), as derived from the continuous energy tests and passbands taken at open aperture (±90° azimuthal). The required energy ranges are highlighted as dark blues for solar wind H+ (top) and solar wind He+ (middle), and as dark greens for pickup ions He+ (bottom). The light blue (light green) lines show the full range of solar wind particle (pickup ions) energy that can be measured by SWAPI, indicating SWAPI's capability in measuring beyond the required energy range with plenty of margin.*

8.5 SWAPI's angular response function

Characterizing SWAPI's performance as a function of azimuth and elevation angles across the entire entrance aperture was essential for informing its forward model and algorithms (recall discussion about SWAPI's efficiency near the aperture edges in Section 7.4).

Figure 8.9 shows that COIN rates remain relatively flat near the open aperture until approaching the edges near sunglasses and strongback. This is expected due to the particle vignetting effect from the sunglasses as well as possible scattering near these structures. During Pre-flight Cal, this test was conducted for both 1keV H+ and 16 keV He+ (Figures 8.9 and 8.10, respectively) at an azimuthal rotational rate of 0.1°/s to ensure sufficient statistical sampling. Notably, the COIN rates and ADE for 16 keV He+ exhibit a more slanted pattern compared to those for 1 keV H+ as the instrument rotates azimuthally. This is likely a result of the fixed ESA voltage: depending on the choice of voltages, the ESA might bias the beam toward one side, creating an apparent asymmetry in detection efficiency across the aperture. Therefore, we

selected results from 1keV H+ to determine the attenuation factor (Section 7.3). It also highlights the importance of characterizing such effects by examining how the PCEM, SCEM, and COIN rates vary as a function of azimuthal angles and ESA voltages.

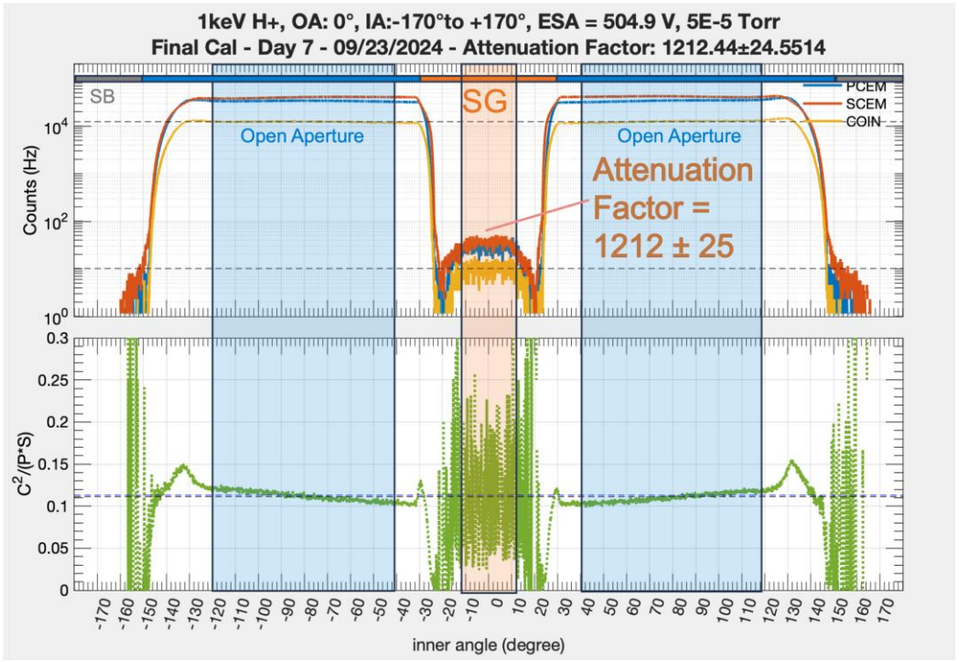


Figure 8.9. *(right) PCEM, SCEM, COIN and ADE as a function of azimuthal angles (or inner angle). The incident beam for this test is 1keV H+. SWAPI was parked at the optimal ESA voltage (-504.9 V) and an elevation angle (or outer angle of 0°). The gray, blue, and orange bars indicate the mechanical range for strong back, open apertures, and sunglasses without taking the particle vignetting into account.*

To generate the azimuthal-ESA voltage map, we perform a full rotation across the azimuthal aperture ("inner angle roll") at a fixed ESA voltage, repeating the roll for each incremented ESA voltage. The resulting azimuthal-ESA voltage map, shown in Figures 8.11 and 8.12, revealed relatively constant count rates and ADE near the open aperture across all ESA voltages.

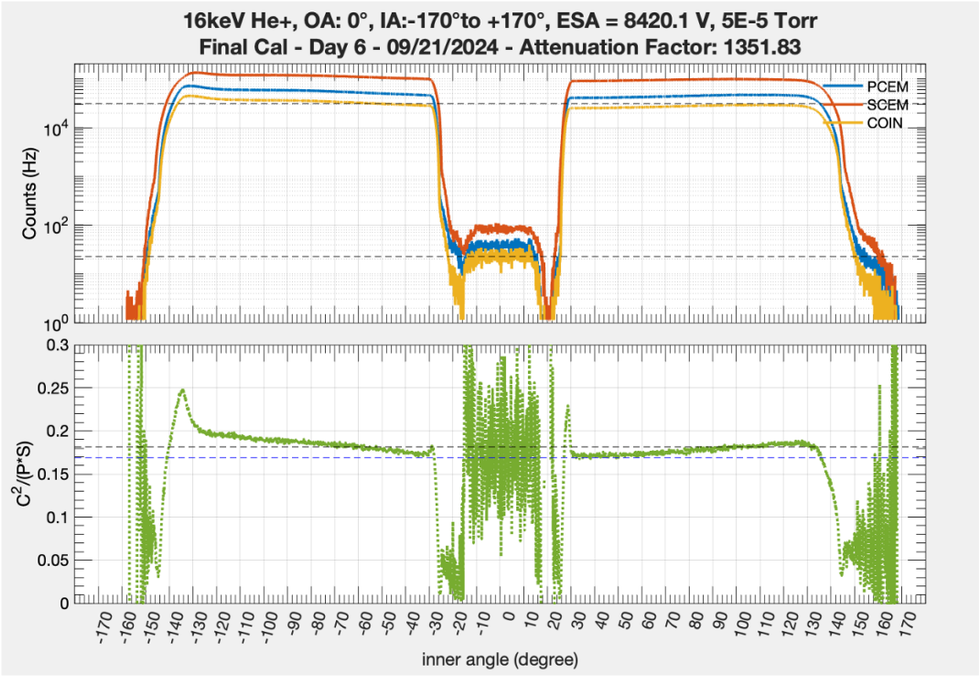


Figure 8.10. *Like Figure 8.9, but with 16 keV He+ and ESA fixed at -8420.1 V.*

A closer examination of the maps reveals intriguing features: at low (absolute) ESA voltages (-470 V), the beam enters the instrument primarily from ~±50° azimuth, near the aperture edge close to sunglasses. As the ESA voltage increases, count rates gradually fill a wider aperture range, with elevated count rates still observed near the sunglasses. At an optimal voltage, around 510-520 V, the count rates remain relatively flat, covering the full extent of the open aperture region. At voltages beyond this range, a reverse effect emerges higher count rates are measured near the strongback edge, instead of the sunglasses edge. The ADE plots support this trend, consistently showing elevated ADE values (compared to the open aperture region) near both the sunglasses and strongback edges across all ESA voltages. These results suggest an intriguing vignetting effect influenced by ESA voltage and aperture geometry. Further analysis, combining with simulations, is necessary to fully understand the underlying mechanisms.

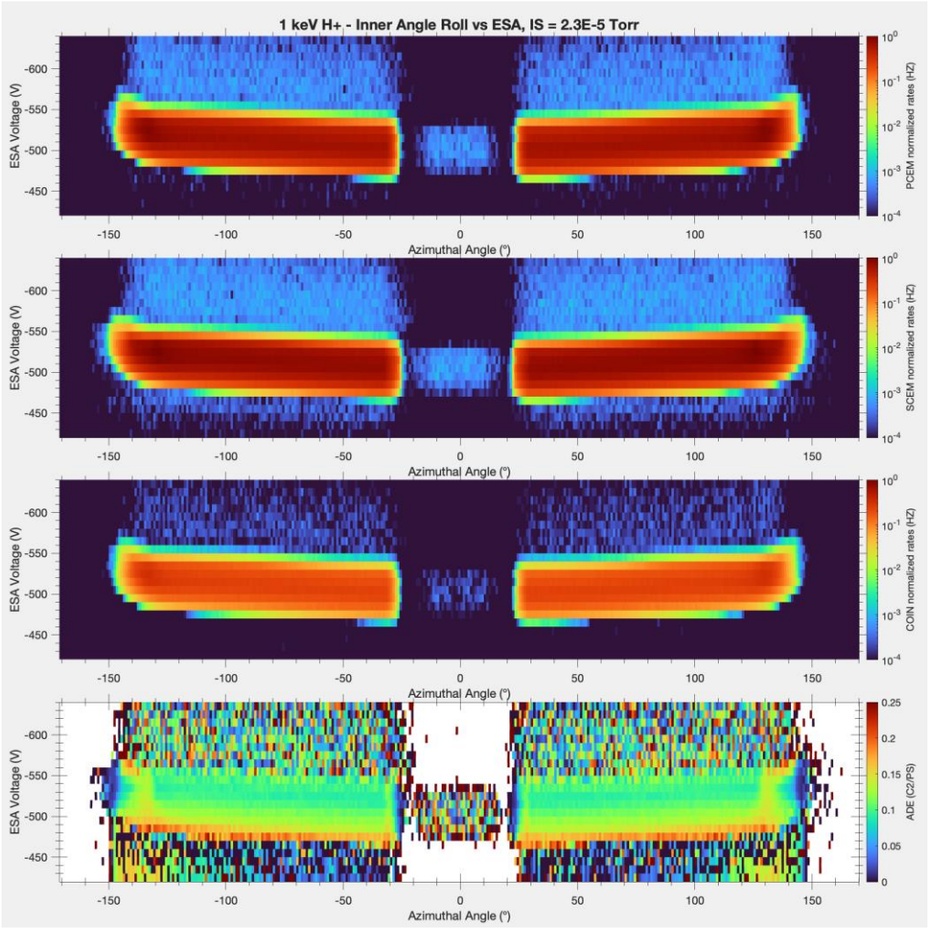


Figure 8.11. *Azimuthal-Elevation map for 1keV H+ with colorbars featuring PCEM (top) SCEM (second panel), and COIN (third panel) rates, along with the absolute detection efficiency (ADE; fourth panel), all shown as a function of azimuthal angles and ESA voltages.*

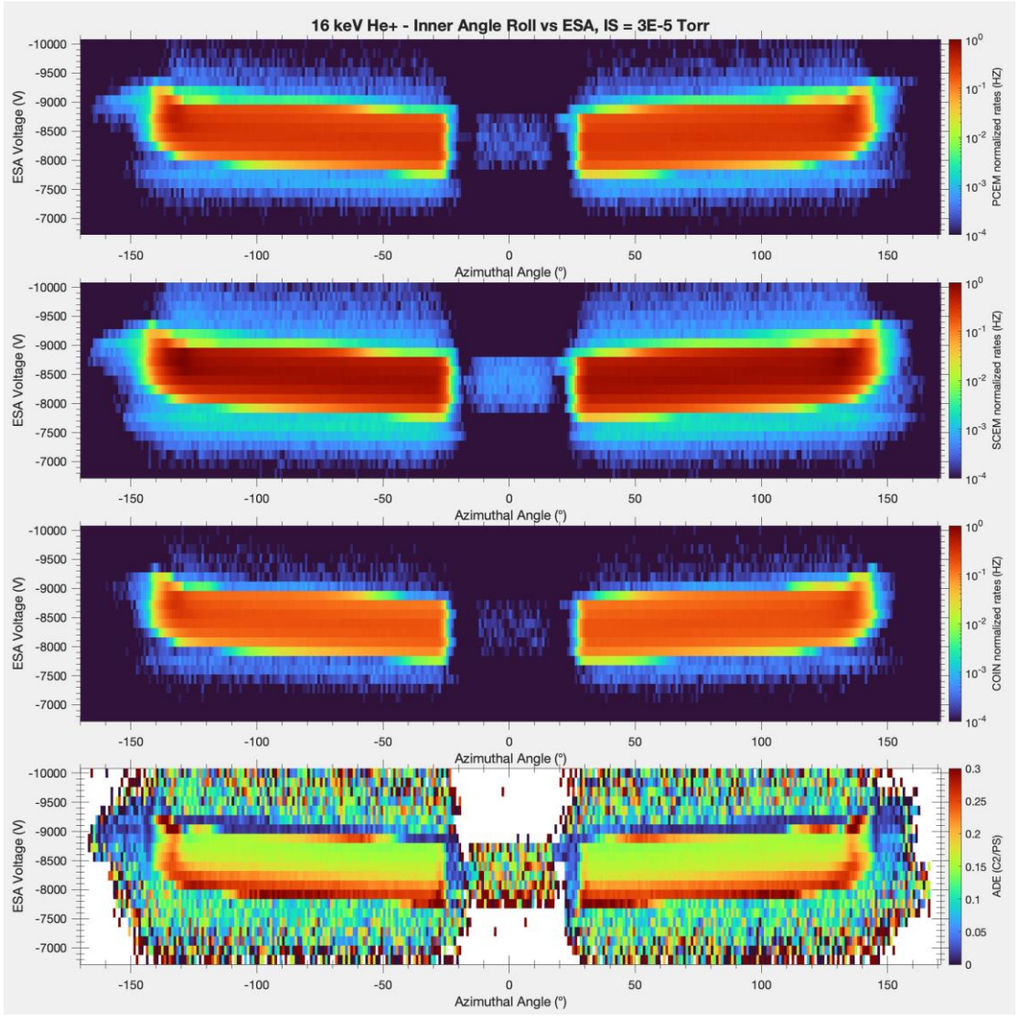


Figure 8.12. *Azimuthal-Elevation map for 16 keV He+. (top) PCEM, (second panel) SCEM, (third panel) COIN rates, and (fourth panel) ADE as a function of azimuthal angles and ESA voltages.*

8.6 SWAPI's energy-angle response function

Another key input for SWAPI's forward model (e.g., Elliot et al. 2016) is the energy-angle passband. Understanding how the instrument responds to incident particles at varying incident angles is crucial for accurate data interpretation. SIMION is used to simulate ion trajectories through the instrument and to generate ideal passbands for particles entering at different incident angles. However, the simulations do not account for effects like scattering and straggling. Therefore, it is necessary to perform laboratory measurements of the passband.

By comparing the simulated, ideal passband with the passband obtained from laboratory measurements, we can evaluate how well the simulation reproduces the instrument's actual performance and identify regions where discrepancies may exist. In addition, the current SIMION model uses a 2.5 D simulation and does not include scattering, so there could be effects in the real-world 3D instrument that are not fully captured in the model.

To generate an energy-angle map, we measured the PCEM, SCEM, and COIN rates as the instrument parked at a certain azimuthal angle, swept through a range of ESA voltage at a specific elevation angle (or outer angles based on our laboratory coordinate), and repeated the ESA voltage sweep at different elevation angles. Figures 8.13 and 8.14 show examples of the energy-angle response function for 1keV H2+ and 4 keV He+ through sunglasses (at 0° azimuth), while Figures 8.15 and 8.16 present the same but for 700 eV and 18 keV He+ through the open aperture (at +90° azimuth). Additional energy-angle response functions are available in Appendix A and B.

Notably, the passbands measured through sunglasses exhibit a narrower elevation angle range (-6° to +9°), compared to those obtained through open aperture (-10° to +10°). This is expected, as the sunglasses region has a more restricted field of view, limiting the range of incident angles at which particles can enter the instrument. Additionally, the elevation angle range for open aperture (±10°) confirms the expected functionality of the aperture cutoff ring, which restricts the passband field of view to ±10° in order to avoid direct line-of-sight with the spacecraft. Only a very small portion of beams can enter at -11° as seen in Figure 8.15 below and Appendix B (open aperture passbands).

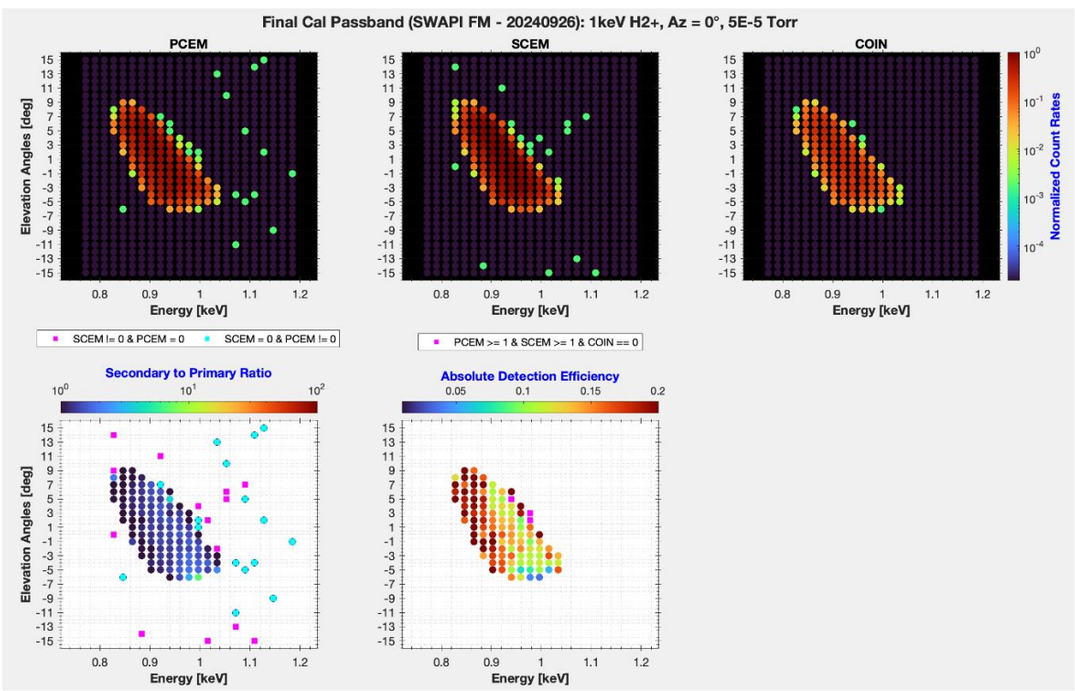


Figure 8.13. *Energy-angle passband using 1 keV/q H_2^+ through 0° azimuth ("sunglasses") to demonstrate uniform intensity across the solar wind aperture. H_2^+ is a proxy for H^+ in order to achieve the beam intensity required for reasonable statistics through this ~0.1% transmissive aperture grid. The ESA voltage is converted to energy using a k-factor of 1.88, which is the value by design.*

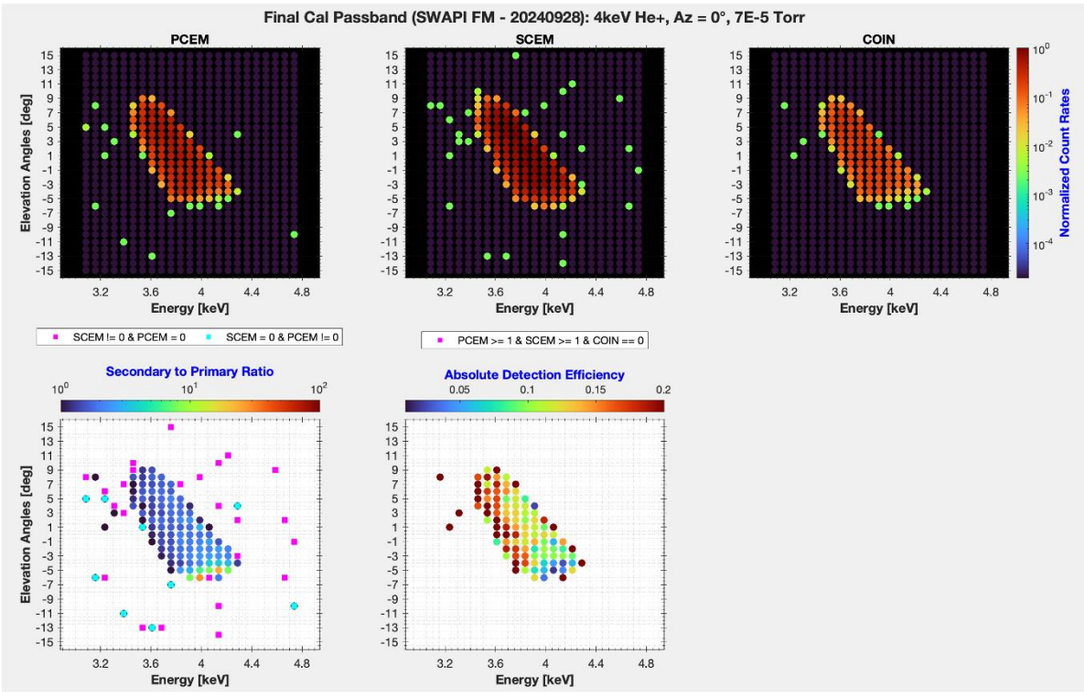


Figure 8.14. *Like Figure 8.13 but using 4 keV He+ through 0° azimuth ("sunglasses").*

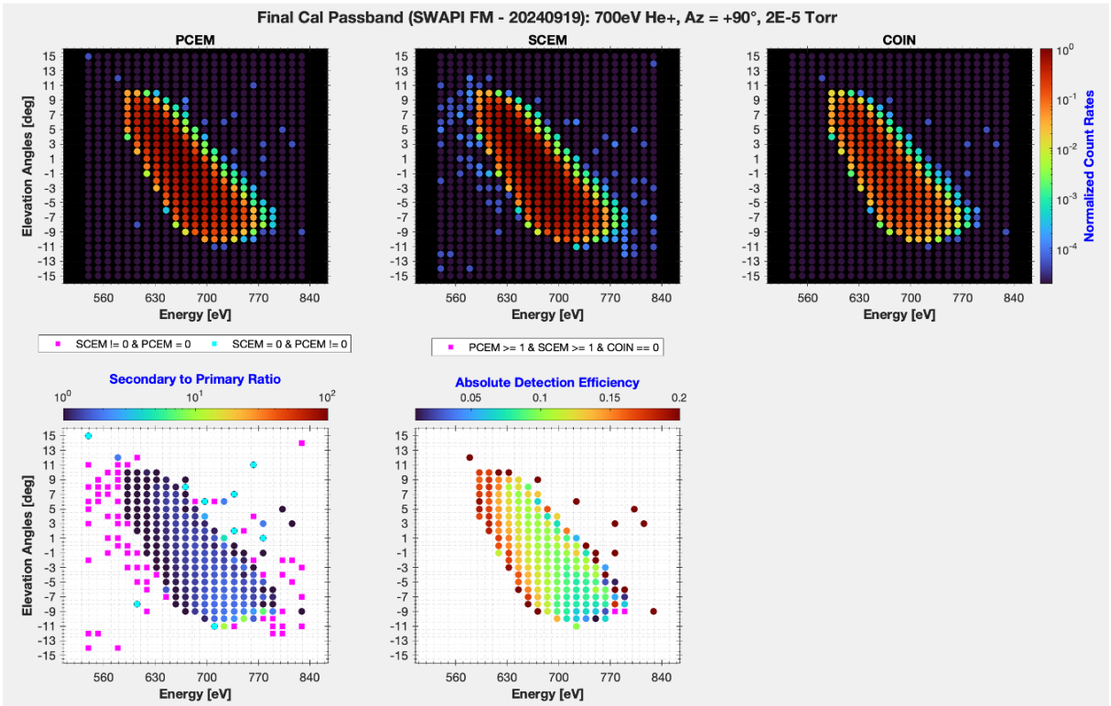


Figure 8.15. *Like Figure 8.14 but using 700 eV He+ through +90° azimuth ("open aperture").*

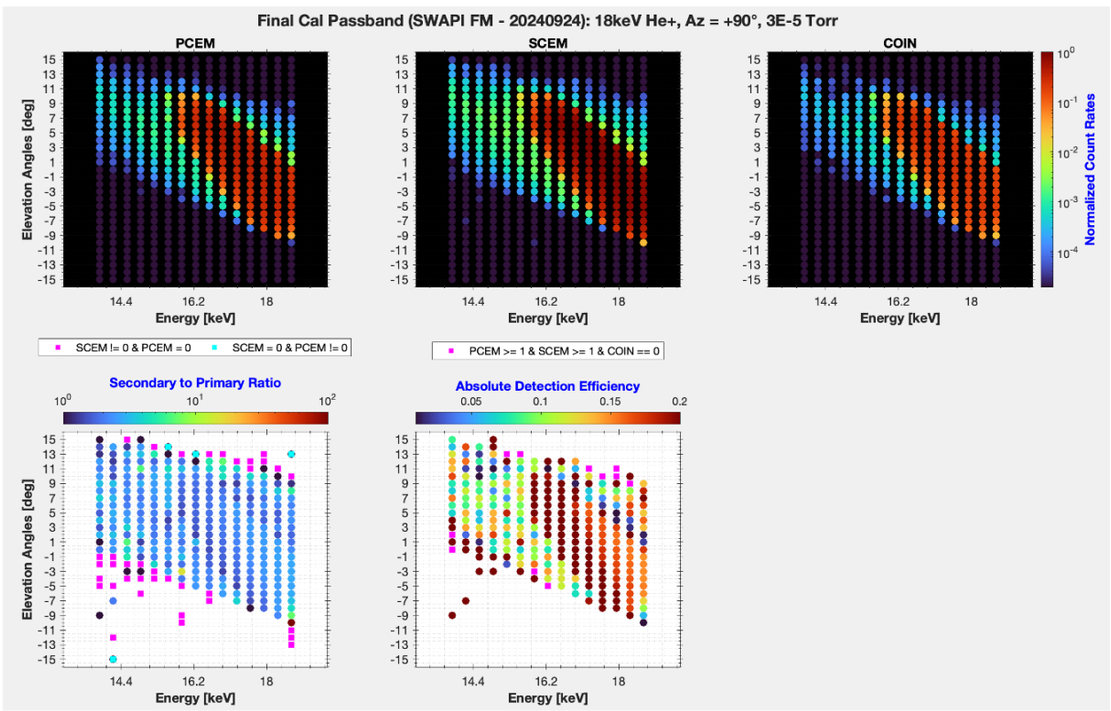


Figure 8.16. *Like Figure 8.15 but using 18 keV He+ through +90° azimuth ("open aperture").*

8.7 SWAPI's Azimuthal-Elevation Angle Response Function

In addition to ESA voltages, SWAPI's response function also varies with the direction of incident ions relative to different parts of the aperture like the strongback, open aperture, vanes, and aperture grid. To characterize this, we conducted tests to determine the azimuthal-elevation responses using both 1 keV H+ and 16 keV He+ beams, consistent with those used for the azimuthal-ESA maps.

As discussed in the sections above, the azimuthal response is sensitive to the choice of the fixed ESA voltage. Therefore, to accurately capture the response functions, we first determined the optimal ESA voltage to apply at each elevation angle. This was done by performing FWHM analysis to determine the peak location as a function of elevation angles (obtained from the passbands) and then fitting a linear fit through the energy-angle response function.

Figures 8.17 and 8.18 show the resulting azimuthal vs elevation map for 1 keV H+ and 16 keV He+, respectively. In general, PCEM, SCEM, and COIN rates remain relatively flat near the open aperture. However, the ADE plots, again, highlight enhanced detection efficiency near the sunglasses and the strongback edges. Additionally, the open aperture range becomes more constrained for >+6° elevation angles, likely due to beam obstruction by the top hat. Conversely, there is a gradual increase in the open aperture range at the negative elevation angles. These maps also confirm the general functionality of the aperture cutoff ring, which restricts the entrance elevation angle to >-10°. Only a small portion of the beam is able to enter at -11° azimuth, with no detectable signal beyond that angle. Furthermore, a relatively higher intensity is observed near the aperture edge close to the strongback, likely due to scattering processes.

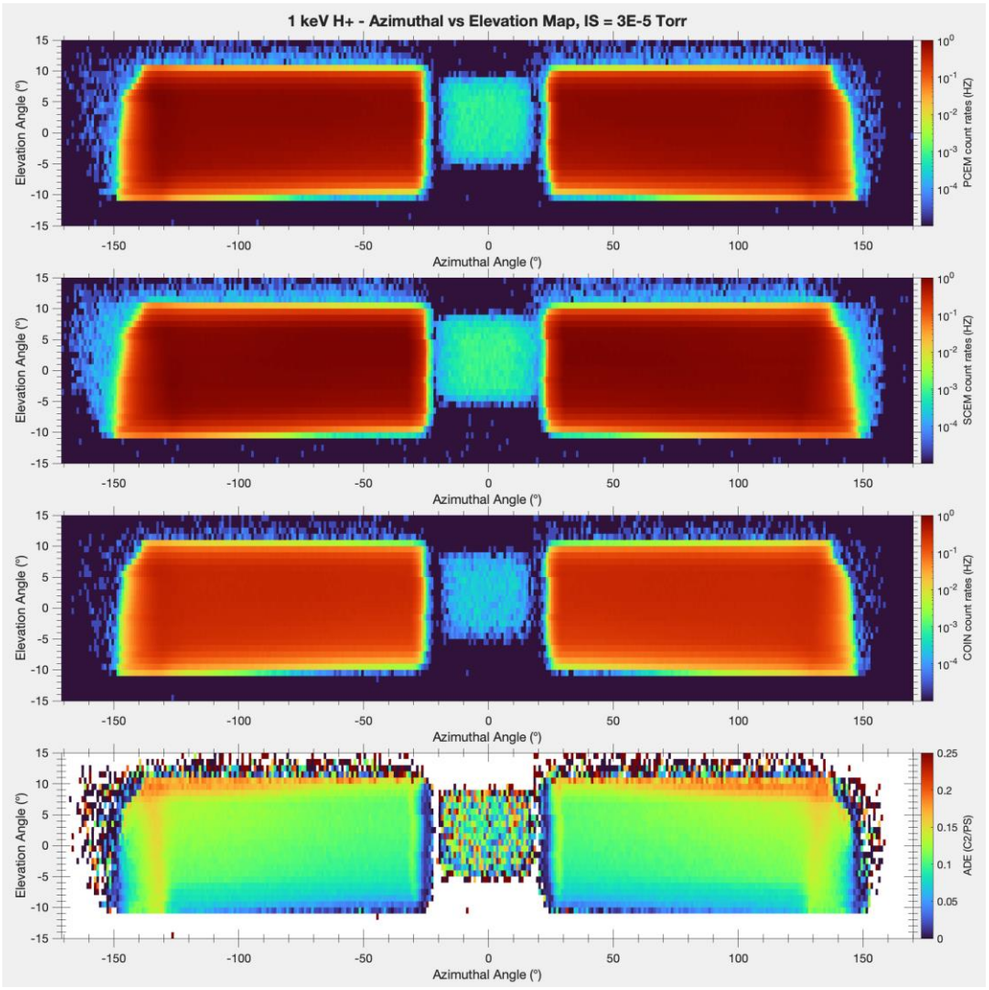


Figure 8.17. *Azimuthal and elevation map for 1keV H+. (top) PCEM, (second panel) SCEM, (third panel) COIN rates, and (fourth panel) ADE as a function of azimuthal angles and ESA voltages. The count rates are normalized to the maximum intensity measured by SCEM. Data was taken on 23 September 2025.*

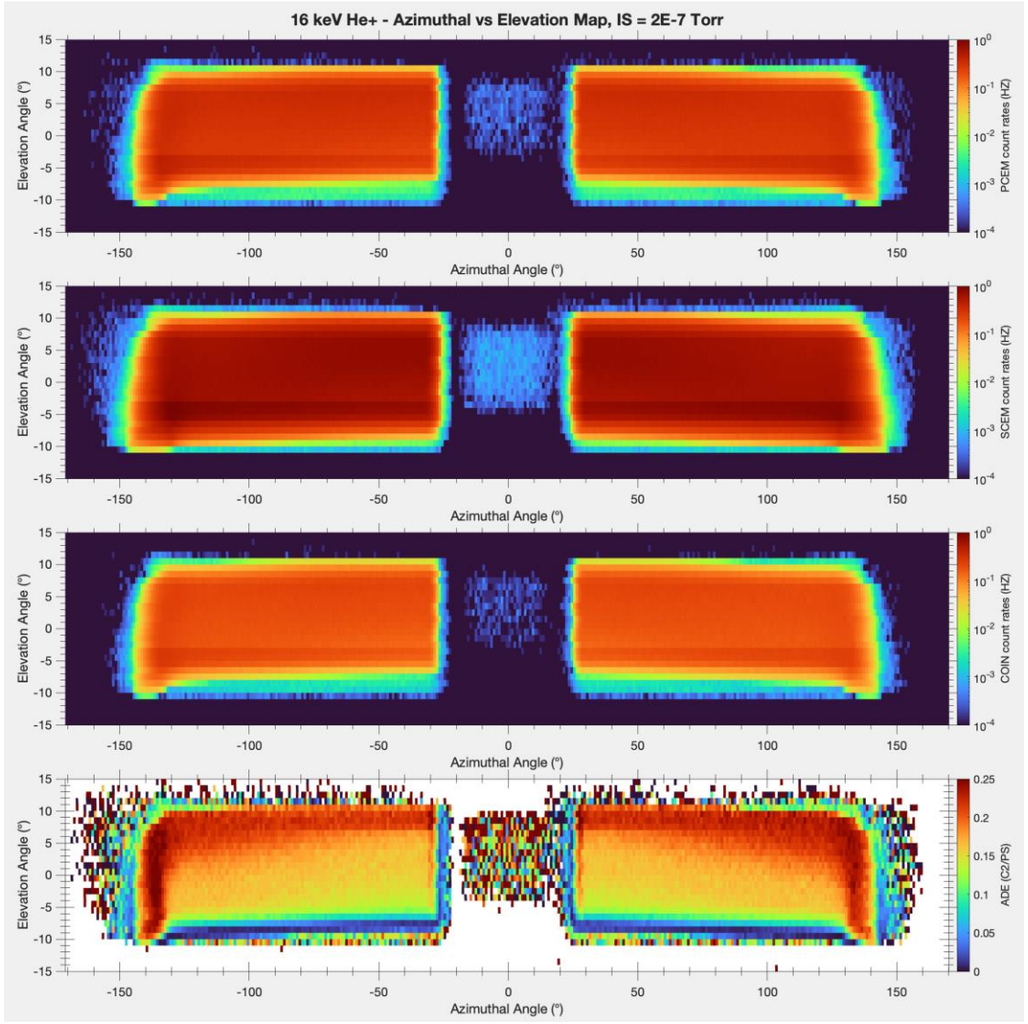


Figure 8.18. *Azimuthal and elevation map for 16 keV He+. (top) PCEM, (second panel) SCEM, (third panel) COIN rates, and (fourth panel) ADE as a function of azimuthal angles and ESA voltages. The count rates are normalized to the maximum intensity measured by SCEM. Data was taken on 28 September 2025.*

8.8 Characterizing Potential Scattering

SWAPI's sunglasses contain 21,460 holes which present opportunities for particle scattering despite the two-step design incorporating a built-in knife-edge to minimize scattering. To characterize this potential scattering effect, we conducted a "long" passband – similar to the standard passband measurement described in Section 8.6, but with a wider ESA voltage sweep over a wider range of voltage. This approach allows us to probe for scattered particles by identifying any apparent populations outside the core passband.

Specifically, we focused on the scattering effect near the sunglasses and open aperture, performing the long-passband test at 0° azimuth ("sunglasses") and +90° ("open aperture"). For the sunglasses test, we

used a 4 keV H2+ beam, chosen as a proxy for H+ to achieve the high beam intensity needed for good statistics through the ~0.1% transmissive aperture grid. ESA voltage was swept from -80V to -10,160 V in 80V steps. For the open aperture test, we used a 1 keV H+ beam, which is a lighter and low-energy species more prone to scattering, to assess the scattering effect from low-energy beam in the open aperture while acting as a proxy for solar wind measurements. The ESA voltage for the open aperture test spans from -30 V to -2830 V in ESA steps of 50 V.

Figure 8.19 shows the scattering test result through sunglasses. Aside from the core passband, no distinct secondary populations are observed. However, slightly elevated PCEM and SCEM rates are noted at lower (absolute) ESA voltages near >0° elevation angles (or outer rotational angles in the calibration lab frame). In contrast, the open aperture scattering test (Figure 8.20) reveals a shadow (low count rates) adjacent to the core population, corresponding to higher absolute ESA voltages across nearly all elevation angles. It is conceivable that these low-count populations are due to scattered, low-energy particles that require higher ESA voltage to be bent into the instrument. To further validate the scattering effect, it is necessary to compare the calibration data with the simulation results.

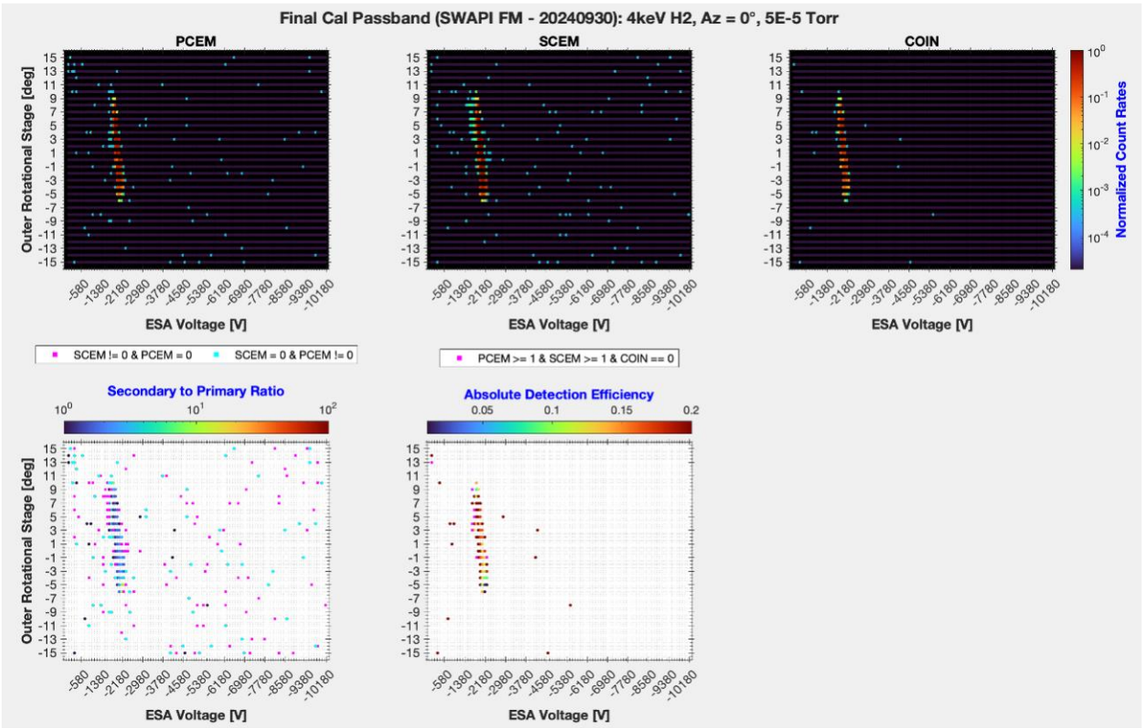


Figure 8.19. *4 keV H_2^+ passband through 0° azimuth ("sunglasses") over a wide range of ESA voltages to understand the scattering effect. For each sweep, the ESA voltage spans from -80V to -10160 V in 80V steps.*

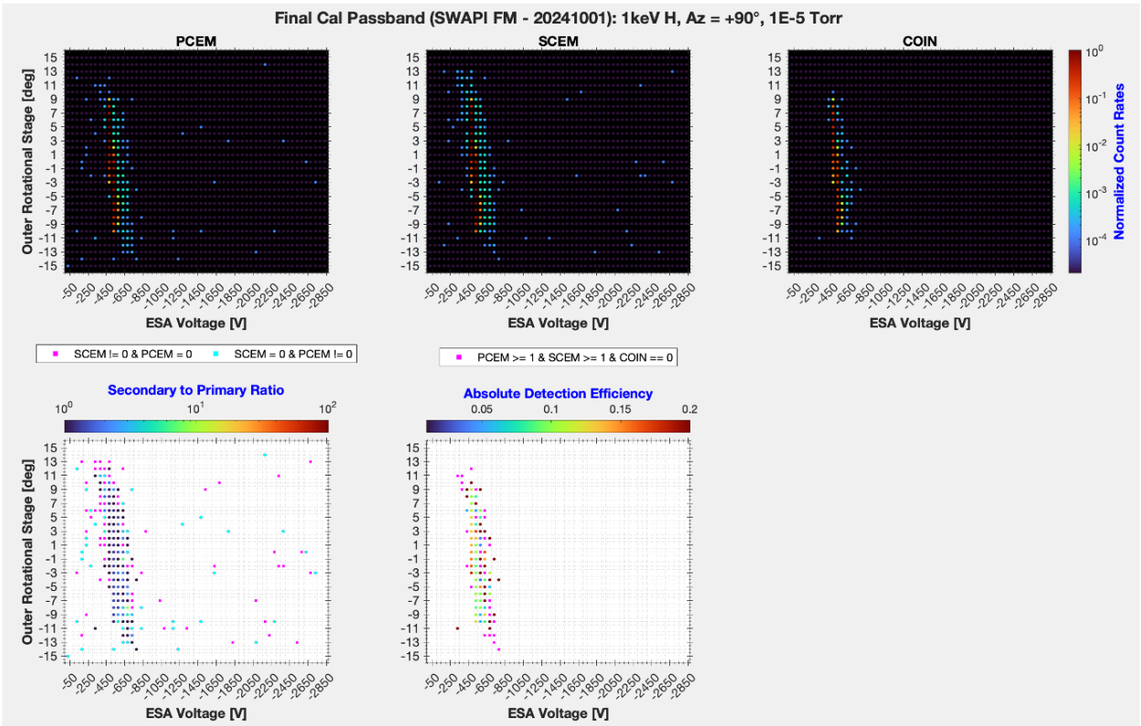


Figure 8.20. *Like Figure 8.19 but with a 1keV H+ beam entering SWAPI through its +90° azimuth sector ("open aperture"). For each sweep, the ESA voltage spans from -30V to -2830 V in 30V steps.*

8.9 Comparison Between Lab Measurements and Simulation Results

This section discusses the comparison of energy-angle passbands from the SIMION model to calibration results from the lab. Figure 8.21 shows the comparison for 250 eV, 1keV, 10keV, and 16 keV beams. Results demonstrate that the simulated results clearly match the measured response. We also verified that a 'tail-like' feature, a small divergence from the core passband on the higher ESA voltage between 1 to -3° elevation angles is a result of simulation artifact (not shown here). In addition, the measured passbands show low levels of counts due to scattering, an effect that is not taken account in the model.

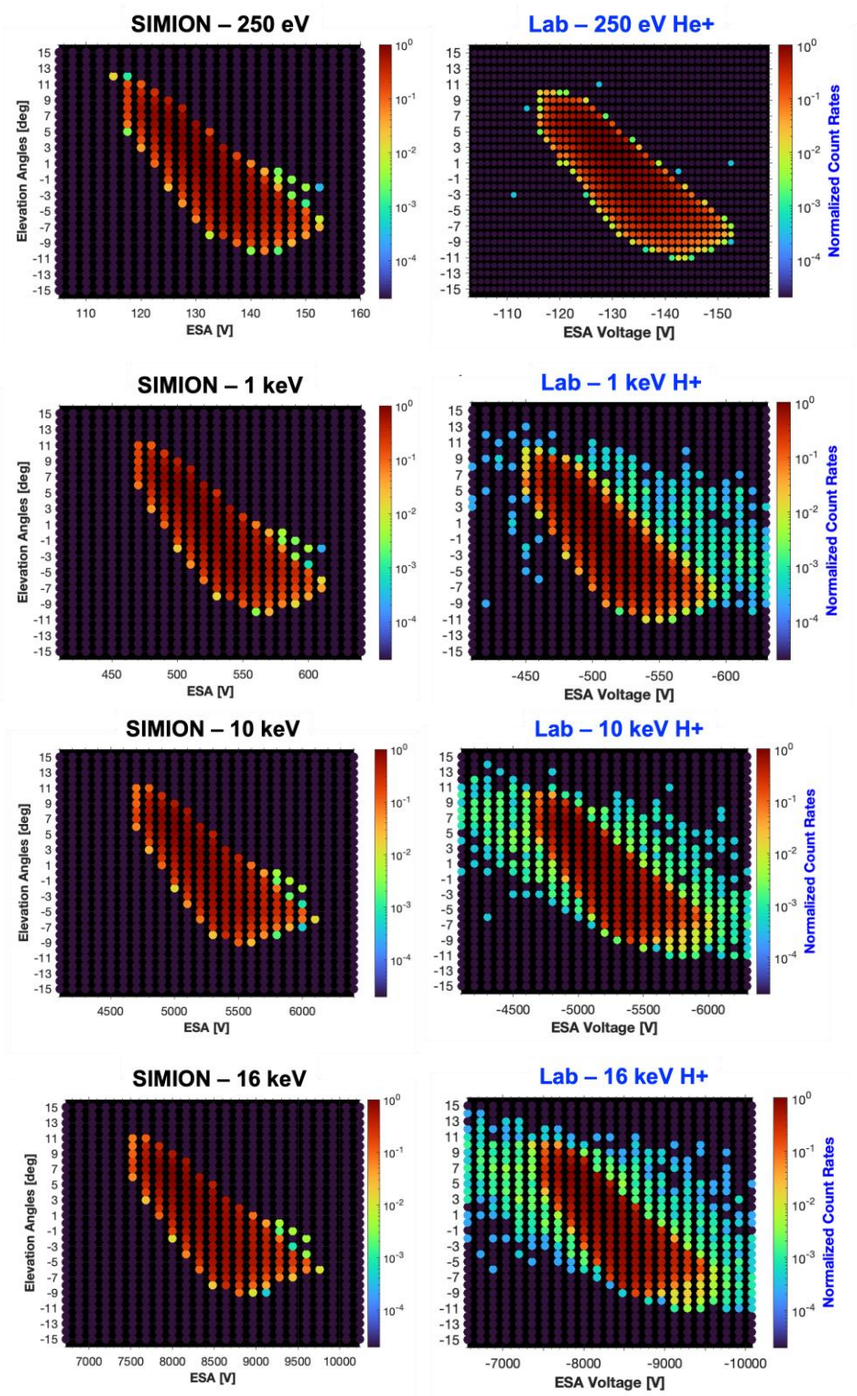


Figure 8.21. *(left) Simulated energy-angle response ("passband") using SIMION ion trajectory simulation for 250 eV, 1keV, 10 keV, and 16 keV beams. (right) Coincidence count rate measurements from the laboratory using 250 eV He+, 1keV H+, 10 keV H+, and 16 keV H+.*

9. DERIVING GEOMETRIC FACTORS

This section provides a summary of the geometric factor derivation used to verify SWAPI's ability to meet its science requirements (delivered in SWAPI's EIDP; 05899-EM-0018-SWAPI_Science_Requirements_Verification_GF). We note that the values here are only used as approximations; with respect to the full SWAPI science data pipeline, the full response function is used – comprised of these calibration inputs as well as results from the full, high-resolution electro-optical model; the details are described in the algorithms document (current version: 05899-Algorithms_AN_07).

An accurate determination of geometric factor is crucial to convert count measurements taken by the instrument to flux. In a simplified form, the relationship between counts and flux can be represented by

$$C = E\, j\, \epsilon\, G$$

where E is energy, j is the particle flux, ϵ is the detection efficiency, and G is geometric factor.

For SWAPI, the effective geometric factor, $\epsilon\, G$, can be written as

$$G_{eff} = \epsilon\, G = \epsilon A \Omega \frac{\Delta \mathrm{E}}{E}$$

where A is the aperture area, Ω is the solid angle, which is $\sin\left(\frac{\Delta\theta}{2}\right) - \sin\left(-\frac{\Delta\theta}{2}\right)]\Delta\varphi$, $\Delta\theta$ is the elevation angle, $\Delta\varphi$ is the azimuthal angle, and $\frac{\Delta E}{E}$ is the energy resolution.

Derivation of geometric factor for solar wind H+

To compute the geometric factor for the for the solar wind sun-viewing, we use a cold plasma approximation with the solar wind beam size determined by analysis using the OMNI dataset (not shown), the effective area determined by simulation (not shown), and the energy resolution, attenuation factor, as well as detection efficiency obtained from calibration data. As shown in Table 11.1, the effective geometric factor for solar wind protons is $\mathbf{1.00 \times 10^{-7}}$ **[cm² sr eV/eV]**, which exceeds the science requirement of $\mathbf{1 \times 10^{-8}}$**[cm² sr eV/eV]**.

Table 9.1 Derivation of geometric factor for solar wind H^+ using the cold plasma approximation.

Parameters	Method/Equation	Values
Solar wind beam size, $\Delta\varphi$ and $\Delta\theta$	OMNI dataset	$\Delta\varphi$ = 5° $\Delta\theta$ = 5°
Solid angle, Ω	$\sin\left(\frac{\Delta\theta}{2}\right) - \sin\left(-\frac{\Delta\theta}{2}\right)]\Delta\varphi$	Ω = 0.00761 [sr]
Energy resolution, $\frac{\Delta E}{E}$	Derived average values from continuous energy tests. *(Figure 8.7)*	$\frac{\Delta E}{E}$ = 8.081%
Absolute detection efficiencies for H^+, ϵ_{H+}	Derived average values for H+ from continuous energy tests. *(Figure 8.6)*	ϵ_{H+} = 0.1162

Effective area, $A_{sunglasses}$	1) unattenuated effective area from SIMION. *(Rankin et al. 2025)* 2) Divide that area by the attenuation factor (1212) obtained from angular response function *(Section 8.3).*	$A_{sunglasses}$ = 0.001403 [cm^2]
Effective geometric factor for solar wind, ϵG_{sw}	$\epsilon_{H+} A_{sunglasses} \Omega \frac{\Delta E}{E}$	$\mathbf{1.00 \times 10^{-7}}$ **[cm^2 sr eV/eV]**

Derivation of geometric factor for pickup ions

SWAPI's effective geometry factor for PUI's (He+) is computed using a hot plasma approximation and thus the geometric factor is dependent on azimuthal angle such that the effective area is determined by simulation (not shown) while the solid angle, energy resolution, attenuation factor, as well as detection efficiency are obtained from calibration data. As shown in Table 11.2, the effective geometric factor for solar wind is $\mathbf{2.25 \times 10^{-2}}$ **[cm^2 sr eV/eV]**, which exceeds the science requirement of $\mathbf{8 \times 10^{-3}}$**[$cm^2$ sr eV/eV]**.

Table 9.2 Derivation of geometric factor for pickup ions(He^+). Refer to GF memo for the full derivation and details.

Parameters	Method/Equation	Values
Elevation angle, $\Delta\theta$	Based on SWAPI FOV	$\Delta\theta = 20°$
Azimuthal angle, $\Delta\varphi$	Derived from calibration data. *(Section 7.4, Figure 7.5 & Section 8.5)*	$\Delta\varphi = 220.85°$
Solid angle, Ω	$\sin\left(\frac{\Delta\theta}{2}\right) - \sin\left(-\frac{\Delta\theta}{2}\right)]\Delta\varphi$	Ω = 1.339 [sr]
Energy resolution, $\frac{\Delta E}{E}$	Derived average values from continuous energy tests. *(Figure 8.7)*	$\frac{\Delta E}{E}$ = 8.081% [eV/V]
Absolute detection efficiencies for He^+, ϵ_{He+}	Derived average values for He+ from continuous energy tests. *(Figure 8.6)*	ϵ_{He+} = 0.1221
Effective area, A_{PUI}	Determine from SIMION. *(Rankin et al. 2025)*	A_{PUI} = 1.703 [cm^2]
Effective geometric factor for PUI, ϵG_{PUI}	$\epsilon_{H+} A_{PUI} \Omega \frac{\Delta E}{E}$	$\mathbf{2.25 \times 10^{-2}}$ **[cm^2 sr eV/eV]**

10. SUMMARY OF SWAPI KEY PERFORMANCE PARAMETERS

Table 10.1 presents a summary of the key performance characteristics of SWAPI that were determined from the results of SWAPI's Pre-flight Calibration.

Table 10. *Summary of SWAPI key performance parameters.*

	Parameter	Required/Designed	Goal (expected)
Solar Wind	Energy range	Solar wind H^+: 0.4-10 keV/q. Solar wind $^4He^{++}$: 0.4-10 keV/q.	Exceeds (0.1 to 20 keV/q)
	Energy Resolution	Solar wind protons H^+: < 10% Solar wind $^4He^{++}$: < 10%	Exceeds (7-8.5%)
	Energy Band per decade	Solar wind protons H^+: ≥ 5 Solar wind $^4He^{++}$: ≥ 5	Exceeds (27 energy bands per decade)
	Measurement Cadence	≤ 10 min	Full Compliance
	Geometric Factor	SWAPI effective geometric factor (at 1 keV/q SW H+): $\geq 1 \times 10^{-8}$ cm^2 sr eV/eV	Exceeds (1.00×10^{-7} cm^2 sr eV/eV) (cold plasma with 5° FWHM beam)
Pickup Ions	Energy Range	He^+ and H^+ PUIs: 0.7 keV/q - 18 keV/q.	Exceeds (0.1 to 20 keV/q)
	Energy Band per decade	He^+ and H^+ PUIs: ≥ 5.	Exceeds (27 energy bandsper decade)
	Measurement Cadence	≤ 10 min	Full Compliance
	Geometric Factor	SWAPI effective geometric factor (at 1 keV/q PUI He^+): $\geq 1 \times 10^{-8}$ cm^2 sr eV/eV for SW H^+.	Exceeds (2.25×10^{-2} cm^2 sr eV/eV) for PUI He+ (hot plasma approx.)
Dynamic Range		300 kHz to 0.3 Hz counting rates.	Full Compliance
Dark Counts		SWAPI SNR ≥ 1 at 0.3 Hz coincident count rate.	Exceeds (>10)
UV Suppression		No light leak	Confirmed
K-Factors		1.88 by design	~1.9-1.95
Total Effective Aperture Range		246° (without taking sunglasses' vignetting effect into consideration)	~211°
Sunglasses' Attenuation Factor		1000 by design	~1212 ± 25
Angular Response Function		x	Characterized
Energy Response Function		x	Characterized

REFERENCES

Elliott, H. A., McComas, D. J., Valek, P., Nicolaou, G., Weidner, S., & Livadiotis, G. (2016). The New Horizons Solar Wind Around Pluto (SWAP) observations of the solar wind from 11–33 au. *The Astrophysical Journal Supplement Series*, *223*(2), 19.

Khoo, L. Y., McComas, D. J., Rankin, J. S. (2023). Compensating for gyroradius effects in beamlines with small Helmholtz coils. *Review of scientific instruments*, *94*(3).

Funsten, H. O., Harper, R. W., & McComas, D. J. (2005). Absolute detection efficiency of space-based ion mass spectrometers and neutral atom imagers. *Review of scientific instruments*, *76*(5).

Gruntman, M. A., & Morozov, V. A. (1982). H atom detection and energy analysis by use of thin foils and TOF technique. *Journal of Physics E: Scientific Instruments*, *15*(12), 1356.

Rankin et al. (2025). Solar Wind and Pickup Ion (SWAPI) Instrument On NASA's Interstellar Mapping and Acceleration Probe (IMAP). *Space Science Reviews*, 221, 8.**. 8.**

APPENDIX A. PASSBAND RESULTS: SUNGLASSES (IA = 0°)

During the SWAPI Pre-flight Cal, we took a total of 5 passbands through sunglasses, as listed in Table A1. All passbands (in count rates and normalized rates) are listed below.

Table A1. A summary of all passbands taken through the sunglasses (0° azimuth).

Passband #	Beam Energy/Species	Passband Type	Azimuthal Angle (°)
1	1 keV H2+	Normal passband	0°
2	2 keV H+	Normal passband	0°
3	3 keV He+	Normal passband	0°
4	4 keV He+	Normal passband	0°
5	4 keV H2+	Long passband that spans over a wider range of ESA voltages	0°

Note that the count rates for these passbands are generally lower, compared to those through the open aperture, due to the 0.1% attenuation through the sunglasses. For reference, the results are shown as both count rates and normalized count rates (normalized to the highest SCEM count rates).

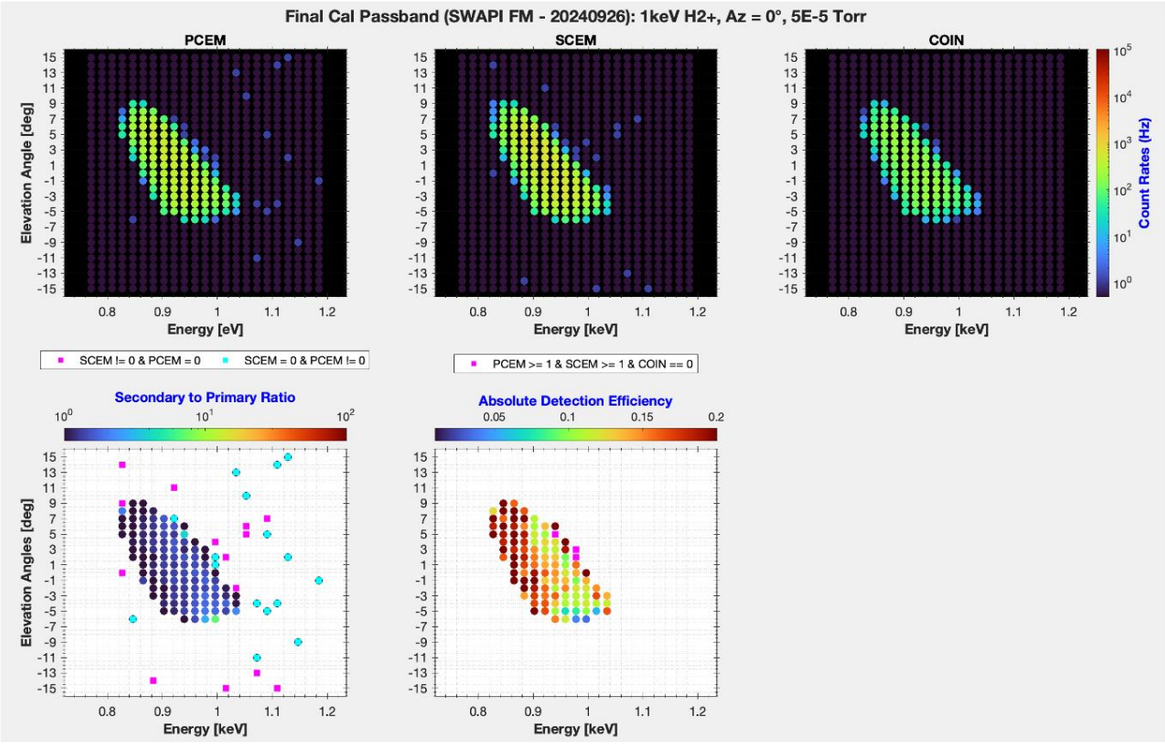


Figure A1. *1 keV H2+ passband through 0°azimuth ("sunglasses") where the y-axis shows the outer rotational stage angles (also refer to as elevation angles) and x-axis shows the ESA voltages. The color bar shows the count rates (not normalized). The ESA voltage is converted to energy using a k-factor of 1.88, which is the value by design.*

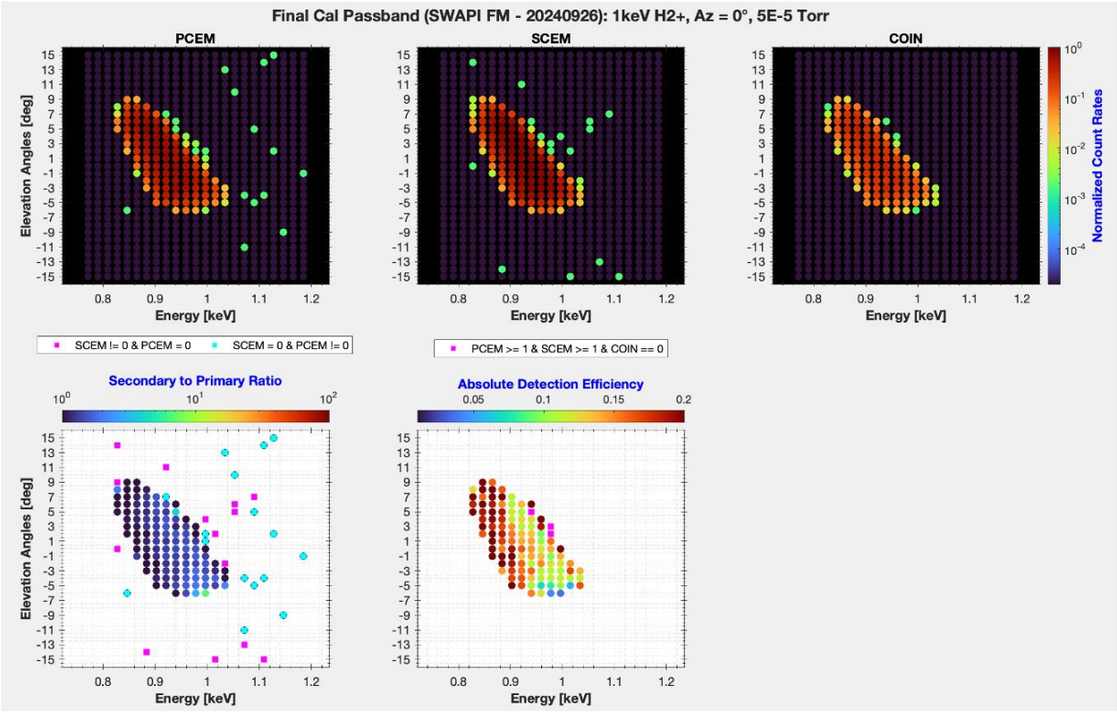


Figure A2. *Like Figure A1, but with normalized count rates.*

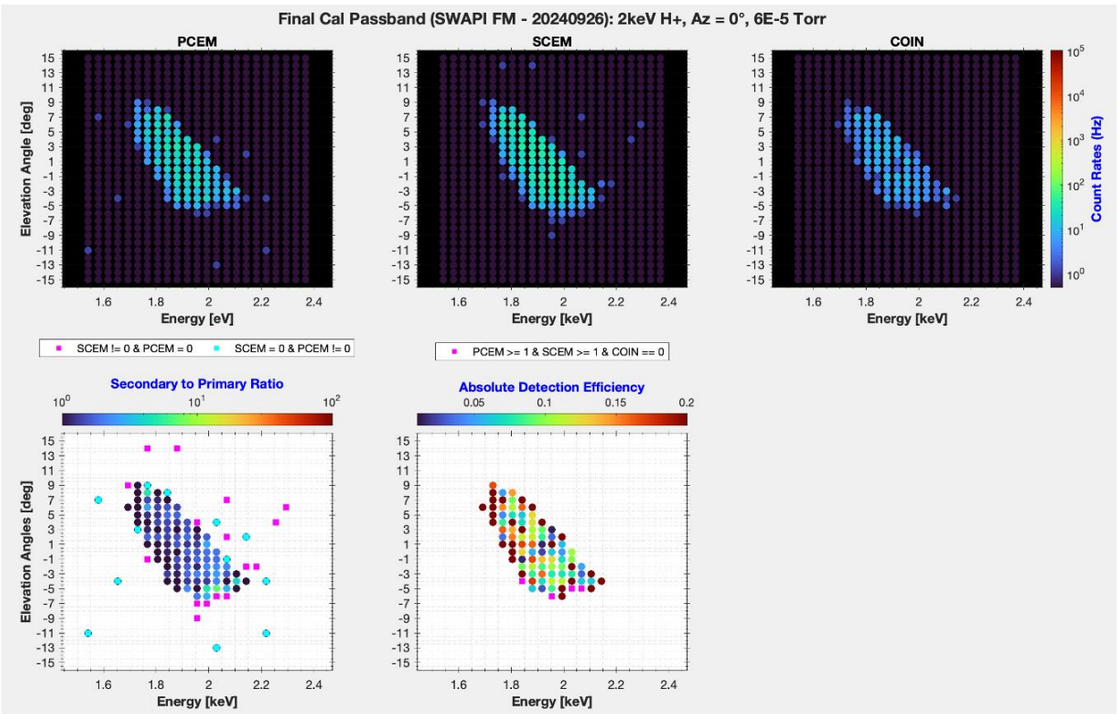


Figure A3. *Like Figure A1, but for 2keV H+.*

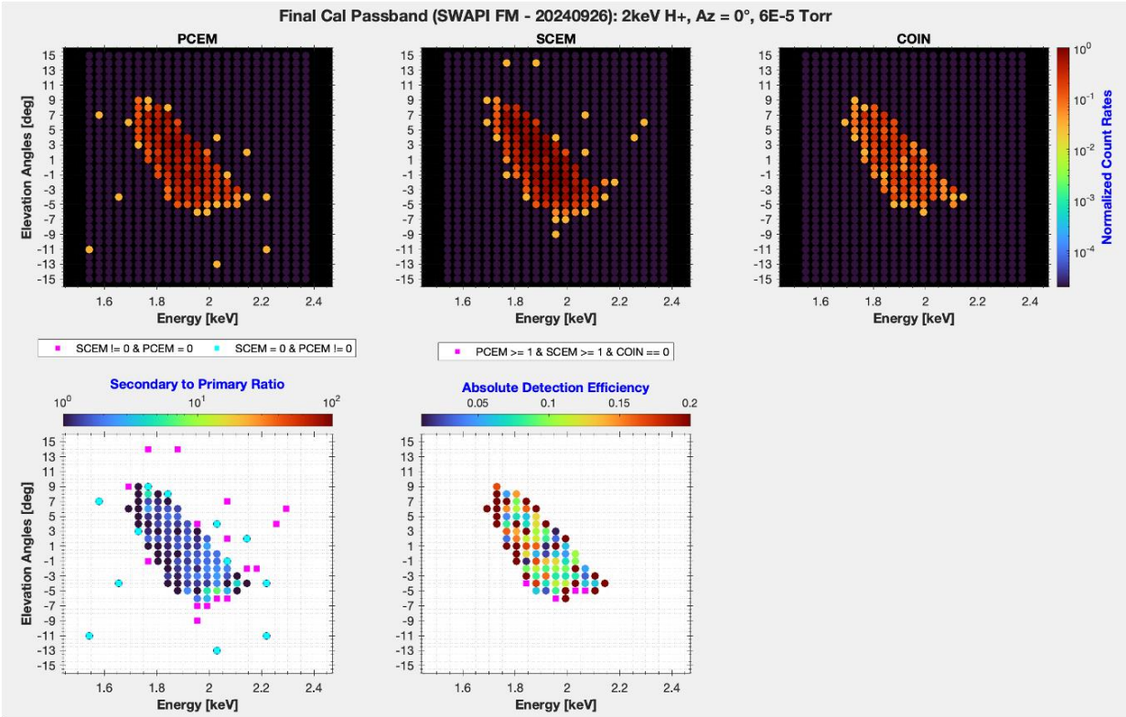


Figure A4. *Like Figure A3, but with normalized count rates.*

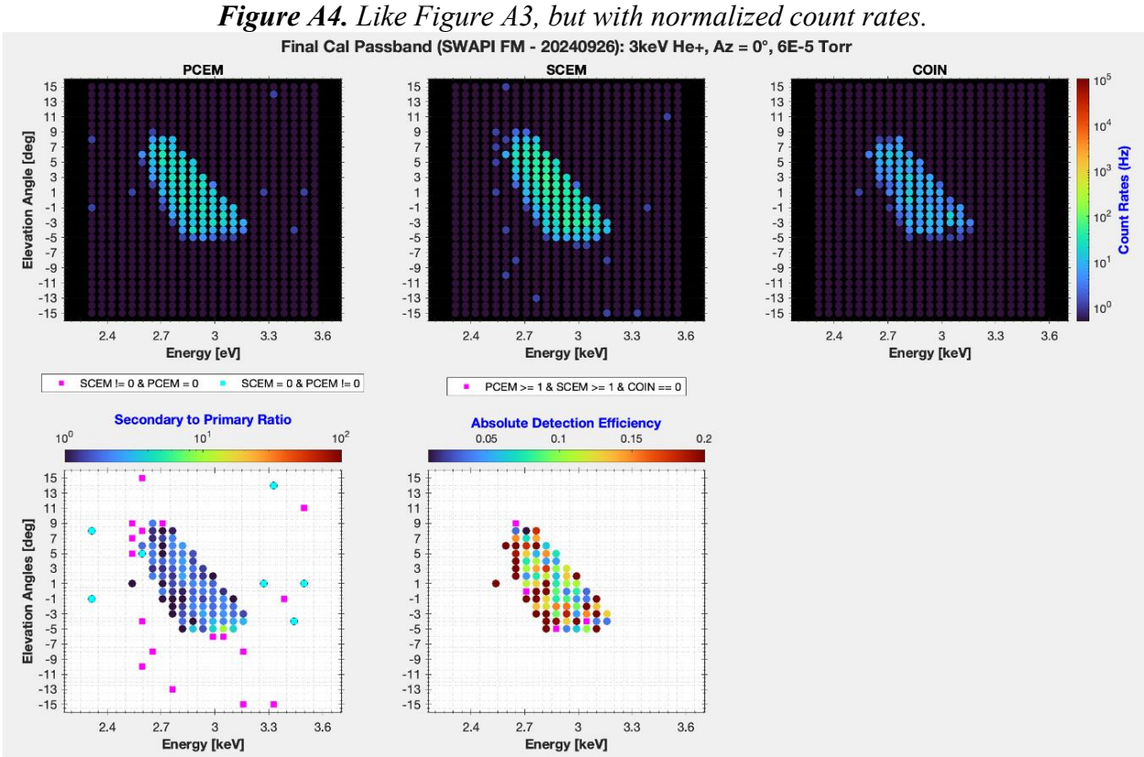


Figure A5. *Like Figure A3, but for 3 keV He+ passband through 0°azimuth ("sunglasses").*

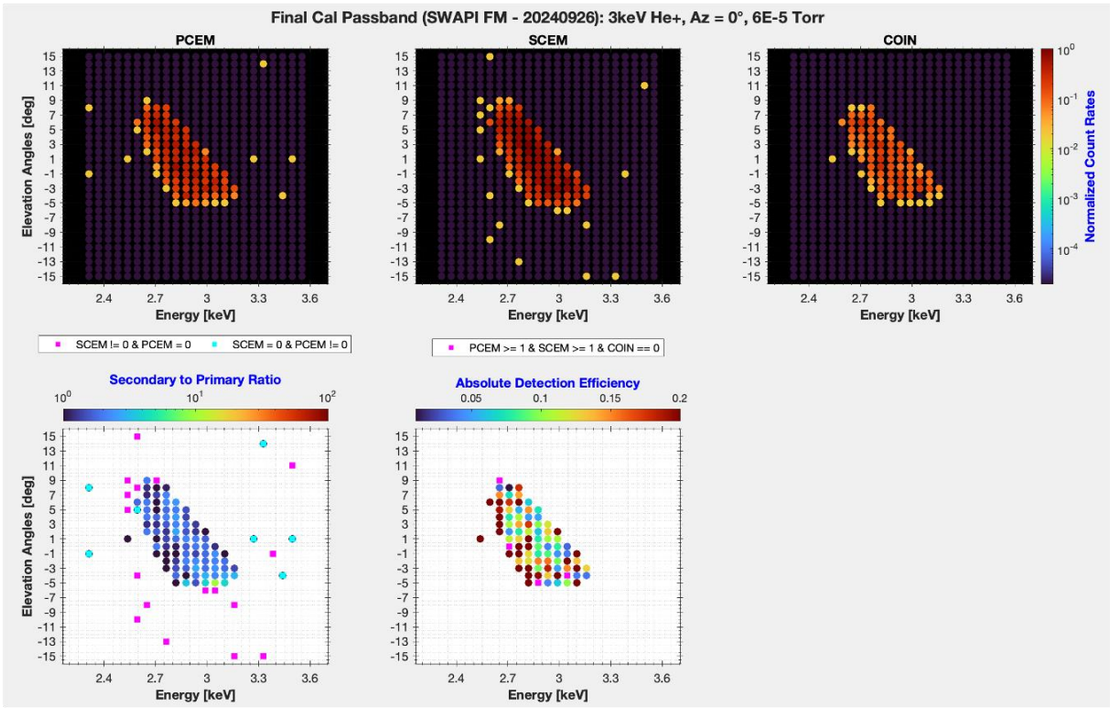


Figure A6. *Like Figure A5, but with normalized count rates.*

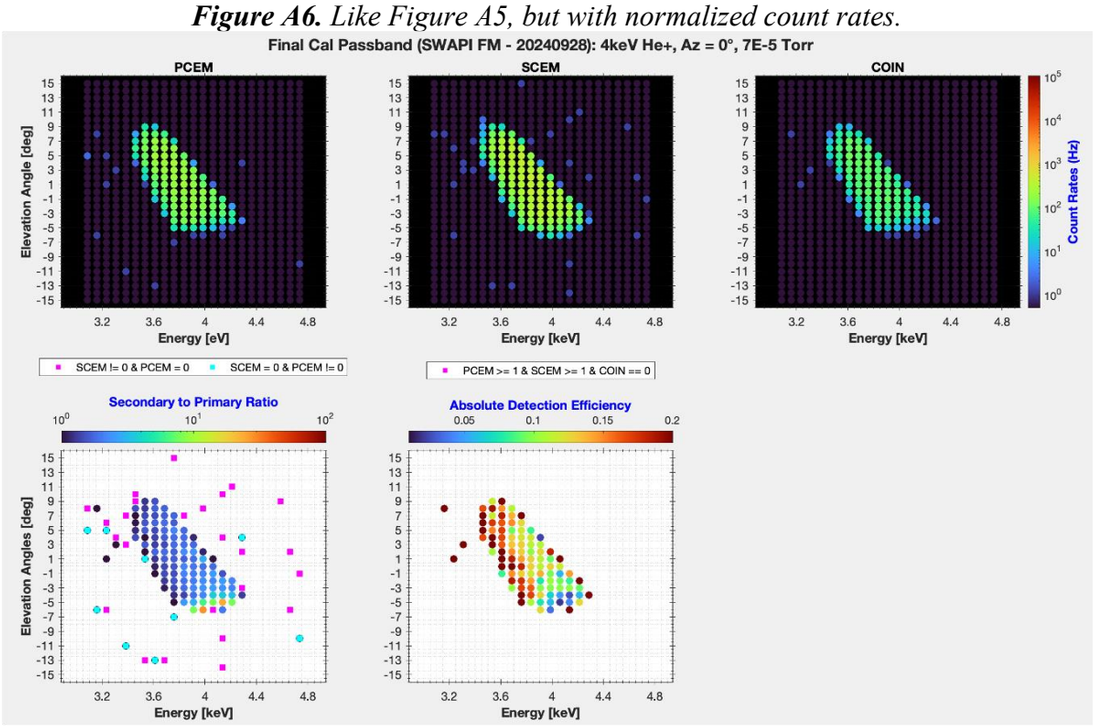


Figure A7. *Like Figure A1, but for 4 keV He+ passband through 0°azimuth ("sunglasses").*

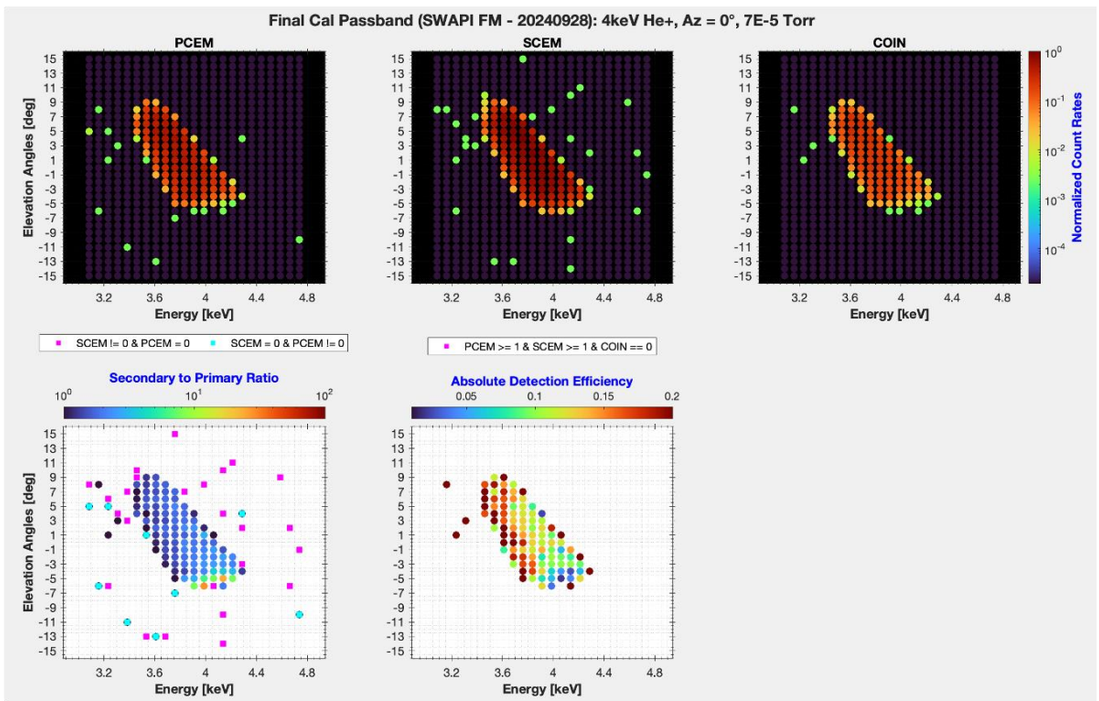


Figure A8. *Like Figure A7, but with normalized count rates.*

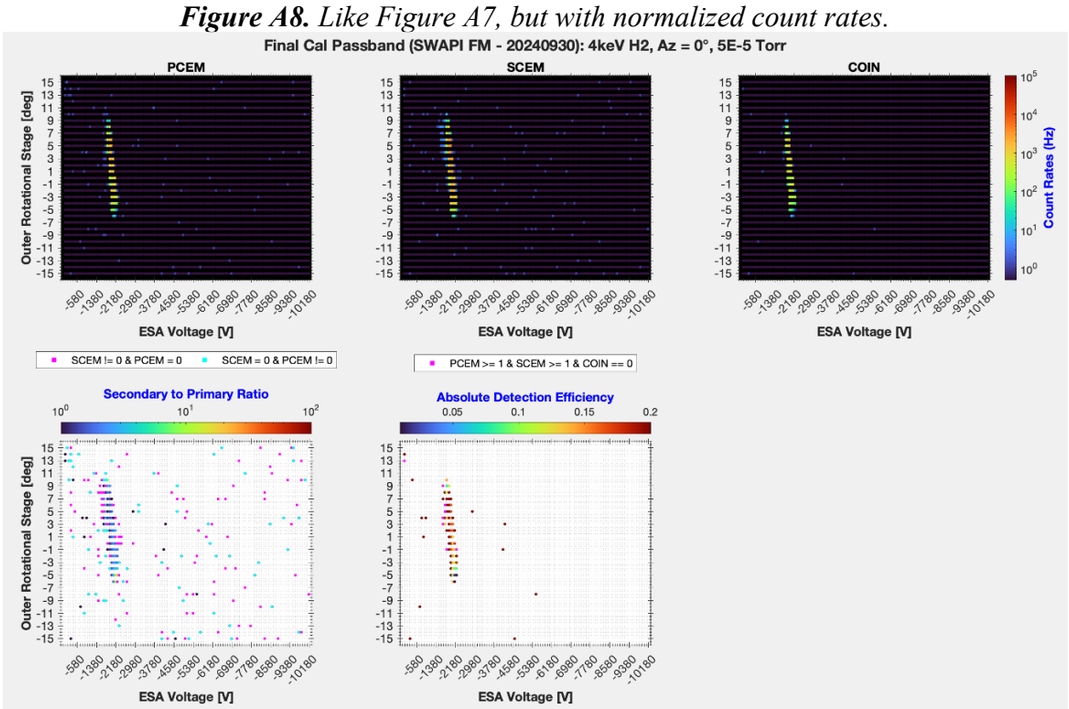


Figure A9. *Like Figure A1, but for 4 keV H2+ with a wider ESA voltage range.*

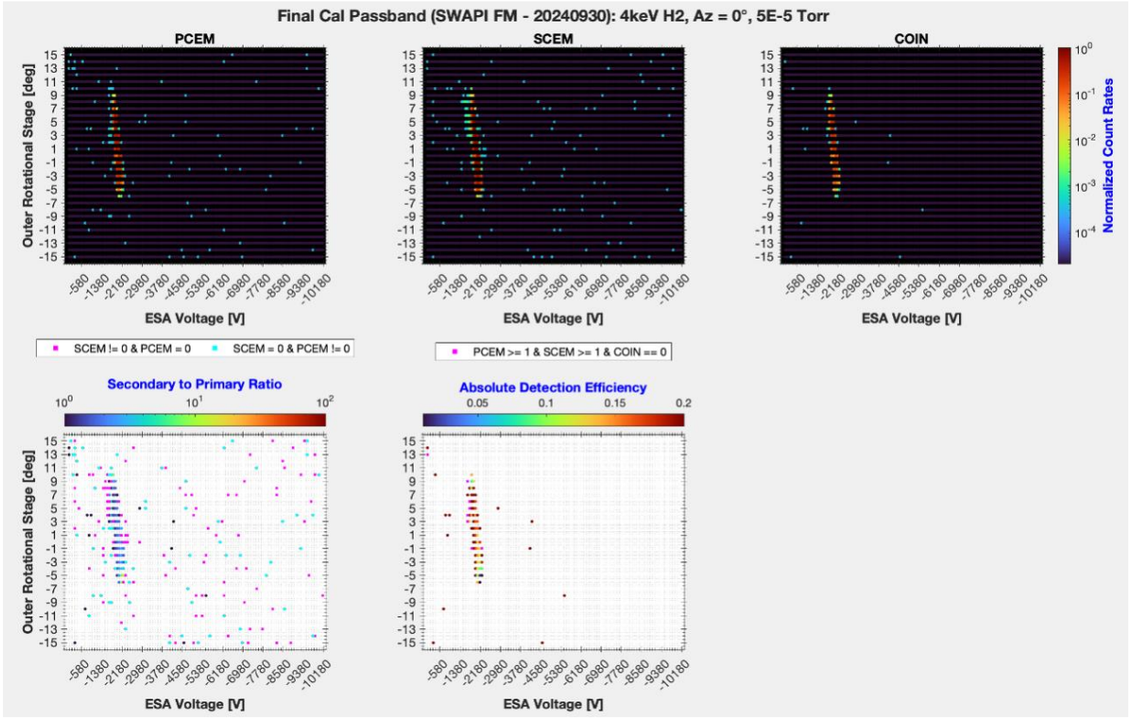


Figure A10. *Like Figure A9, but with normalized count rates.*

APPENDIX B. PASSBAND RESULTS: OPEN APERTURE (IA = ±90°)

During the SWAPI Pre-flight Cal, we took a total of 16 passbands through open aperture (±90° azimuth), as listed in Table B1.

Table B1. *A summary of all passbands taken through the open aperture (±90° azimuth).*

Passband #	Beam Energy/Species	Passband Type	Azimuthal Angle (°)
1	200 eV H+	Normal passband	+90°
2	250 eV He+	Normal passband	+90°
3	400 eV H+	Normal passband	+90°
4	400 eV H+	Normal passband	+90°
5	700 eV He+	Normal passband	+90°
6,7	1keV H+	Normal passband	±90°
8	1 keV H+	"Long passband" that spans over a wider range of ESA	+90°
9	1 keV Ar+	Normal passband	+90°
10	4 keV He+	Normal passband	+90°

11	10 keV H+	Normal passband	+90°
12,13	16 keV H+	Normal passband	±90°
14,15	16 keV He+	Normal passband	±90°
16	18 keV H+	Normal passband	+90°

Below are plots of passbands that were not included in the main text: 400 eV H+, 400 eV He+, 1 keV H+ (±90°), 1keV Ar+, 4 keV He+, 10 keV H+, 16keV H+ (±90°), and 16 keV He+ (±90°). Results are shown as both count rates and normalized count rates (normalized to the highest SCEM count rates).

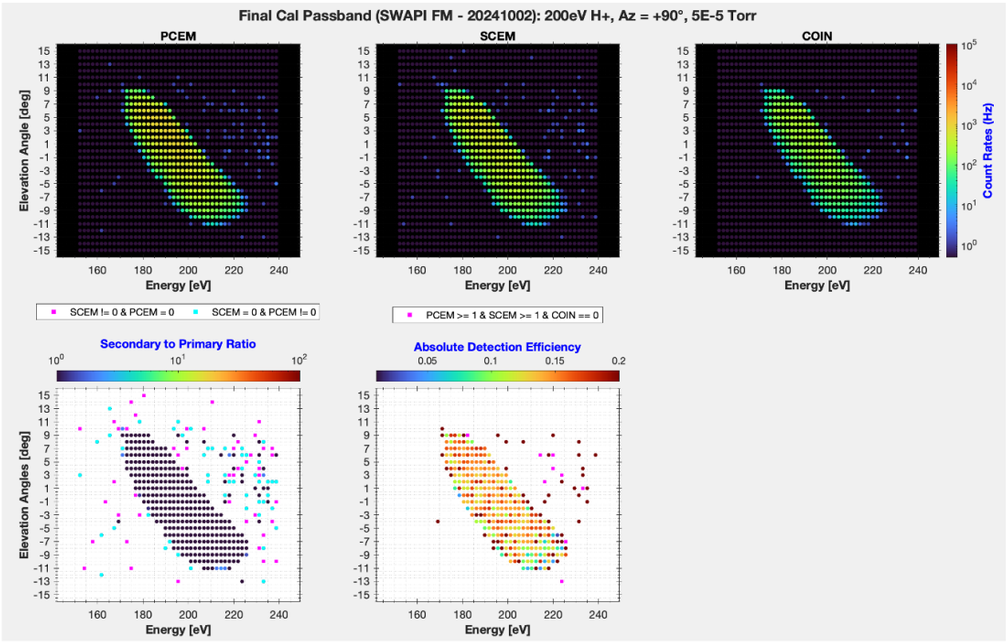


Figure B1. *200 eV H+ passband through +90°azimuth ("open aperture") where the y-axis shows the outer rotational stage angles (also refer to as elevation angles) and x-axis shows the ESA voltages. The color bar shows the normalized count rates. The ESA voltage for this plot is converted to energy using a k-factor of 1.88, which is the value by design.*

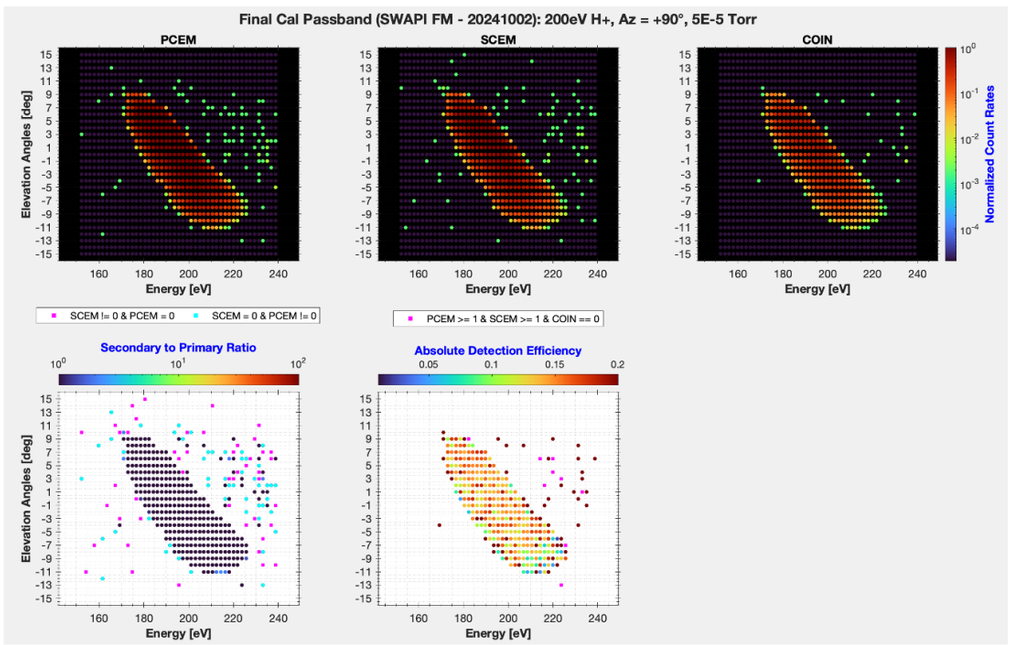


Figure B2. *Like Figure B1, but with normalized count rates.*

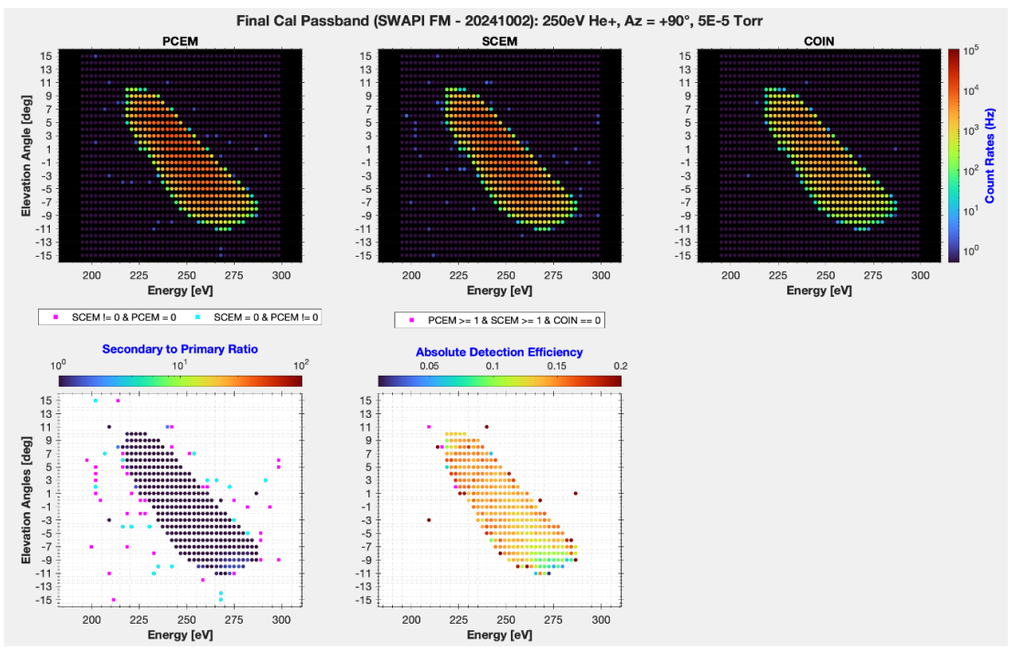


Figure B3. *Like Figure B1, but for 250 eV He+ passband through +90°azimuth ("open aperture").*

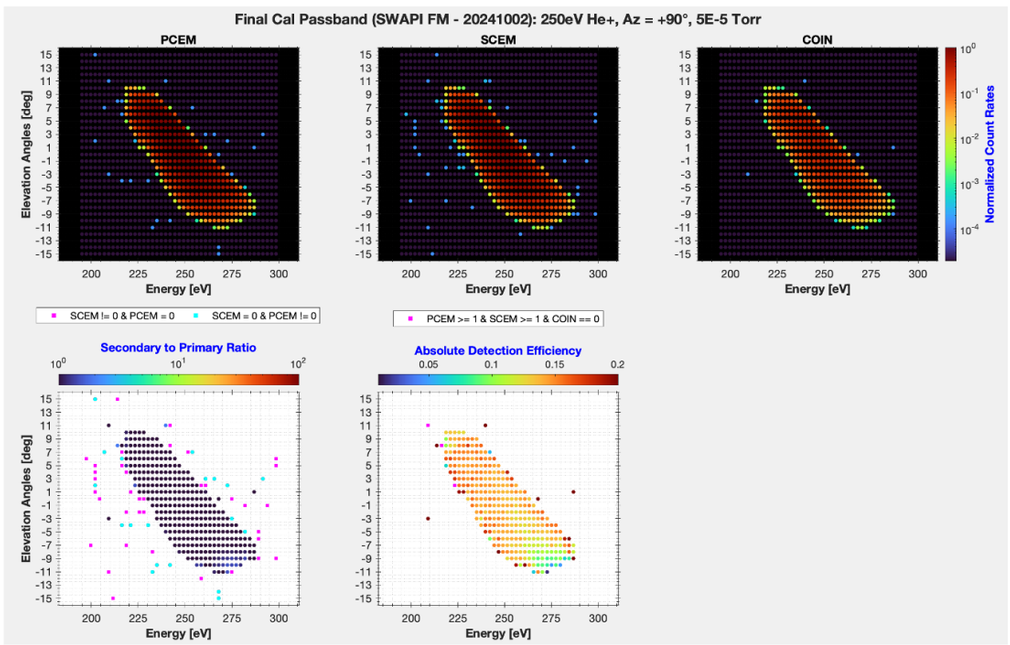


Figure B4. *Like Figure B3, but with normalized count rates.*

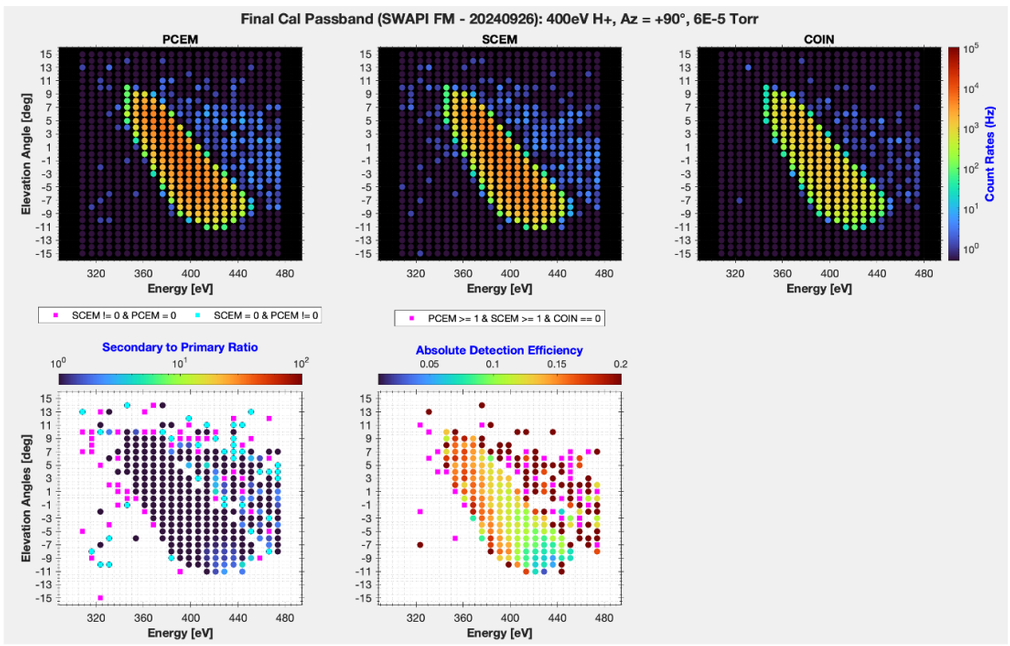


Figure B5. *Like Figure B1, but for 400 eV H+ passband through +90°azimuth ("open aperture").*

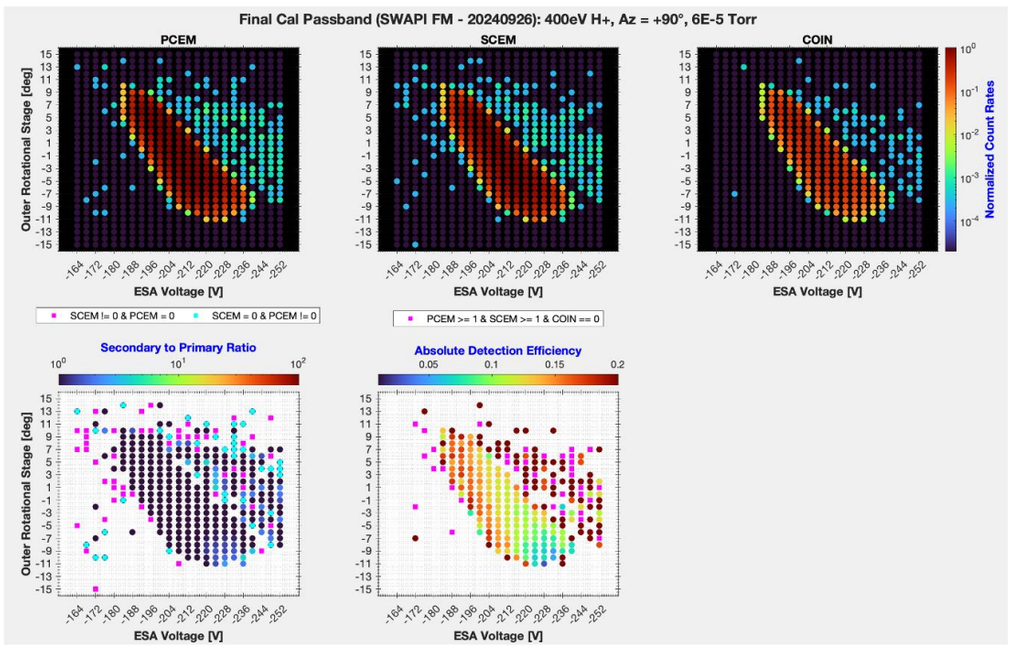


Figure B6. *Like Figure B5, but for with normalized count rates.*

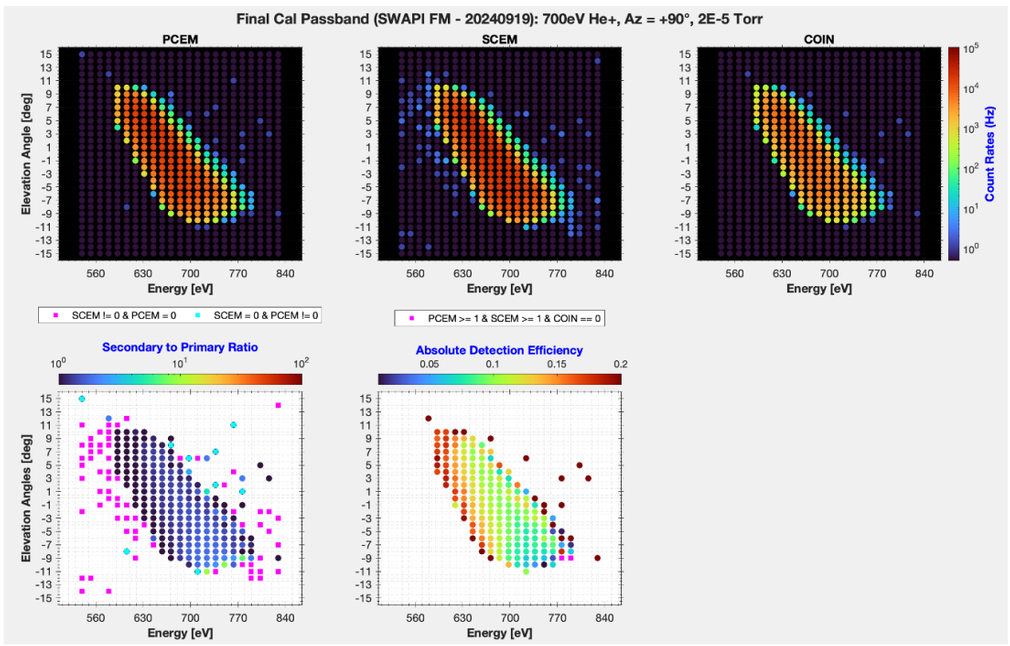


Figure B7. *Like Figure B1, but for 700 eV He+ passband through +90°azimuth ("open aperture").*

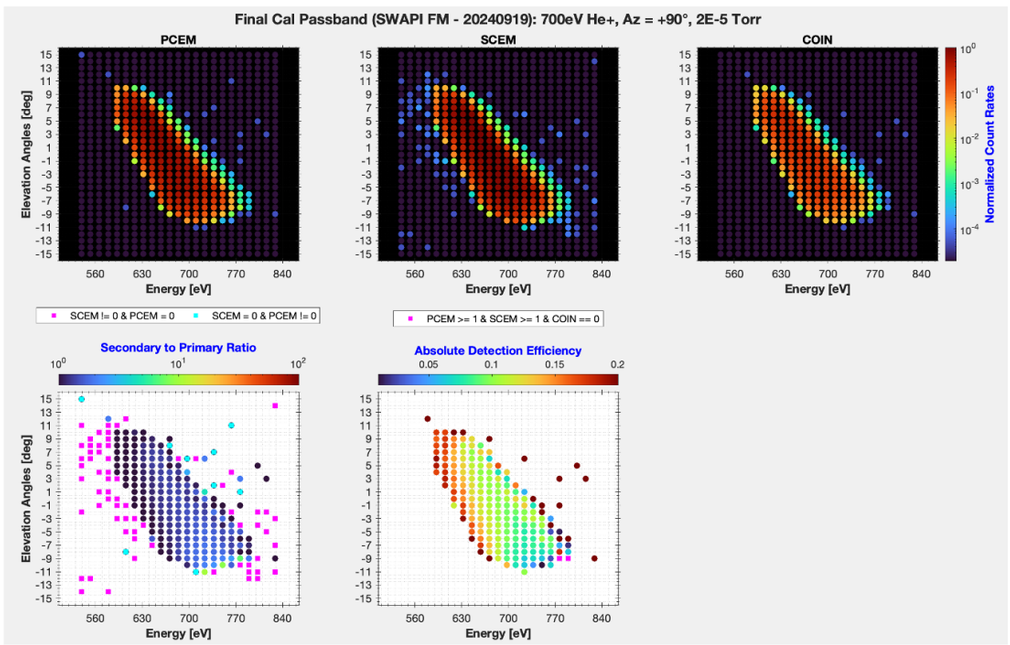


Figure B8. *Like Figure B1, but with normalized count rates.*

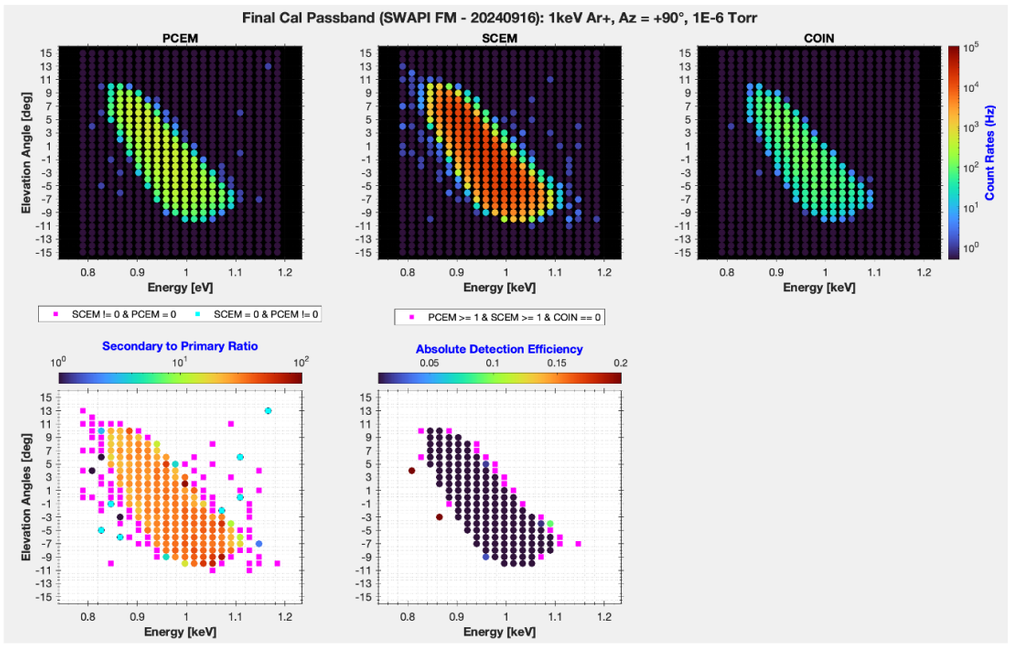


Figure B9. *Like Figure B1, but for 1 keV Ar+ passband through +90°azimuth ("open aperture").*

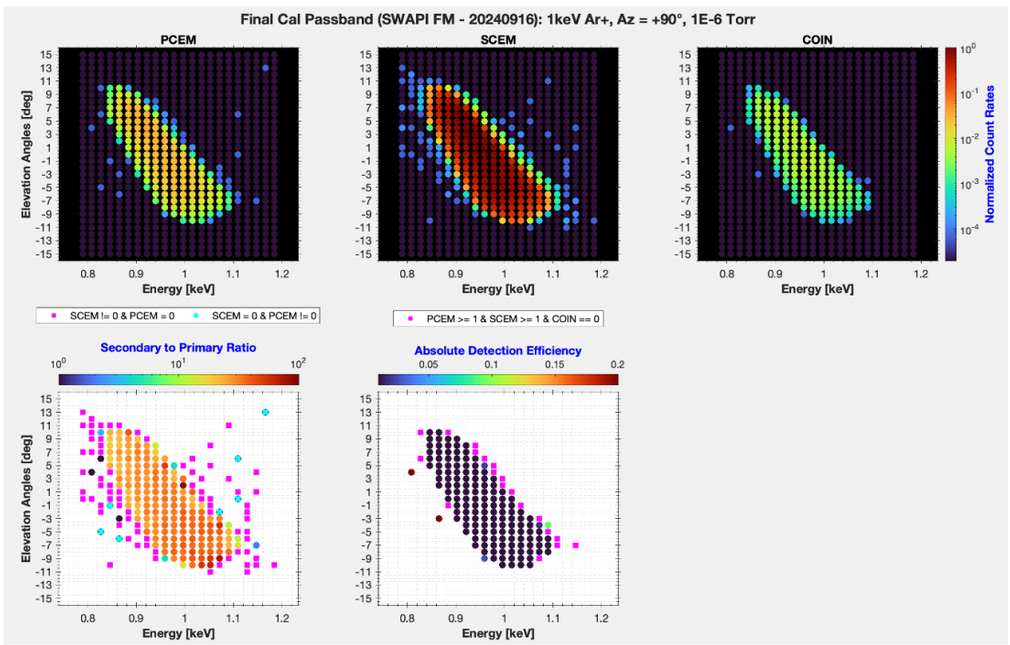


Figure B10. *Like Figure B9, but with normalized count rates.*

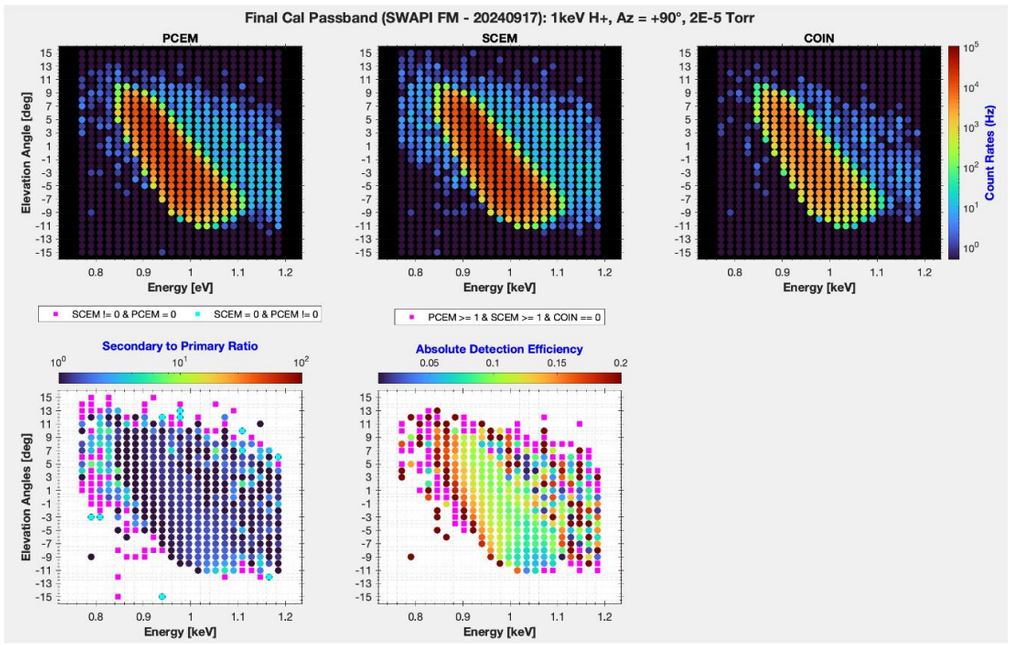


Figure B11. *Like Figure B1, but for 1 keV H+ passband through +90°azimuth ("open aperture").*

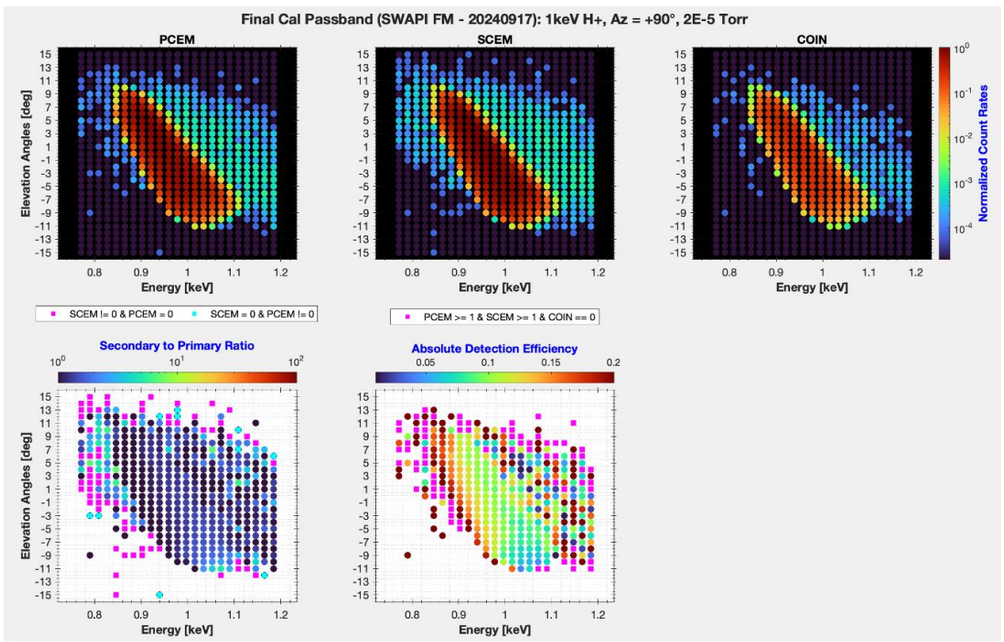


Figure B12. *Like Figure B11, but with normalized count rates.*

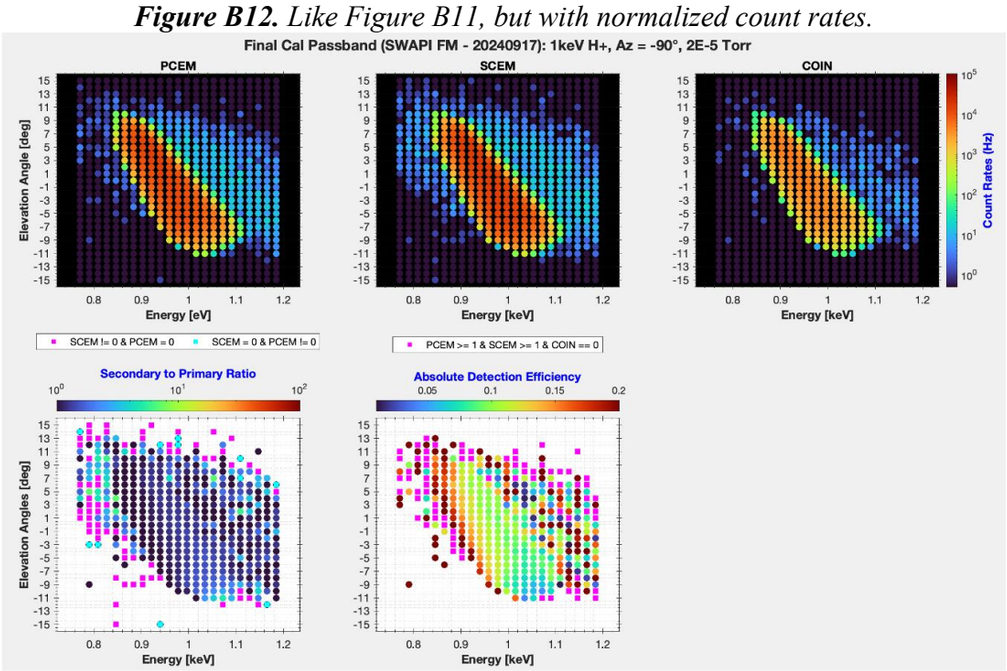


Figure B13. *Like Figure B1, but for 1 keV H+ passband through -90°azimuth ("open aperture").*

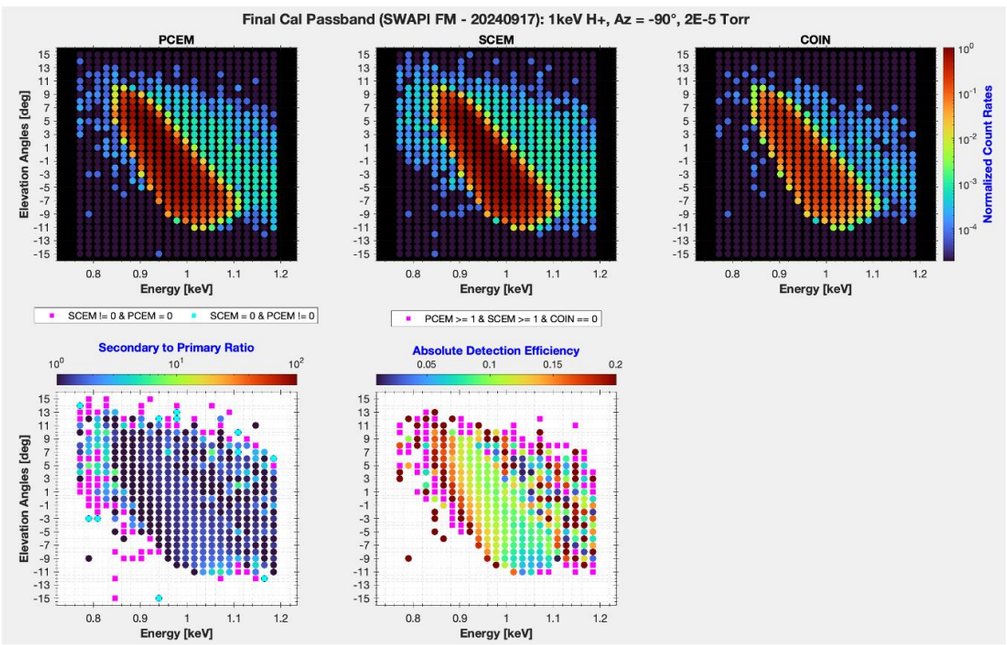


Figure B14. *Like Figure B13, but with normalized count rates.*

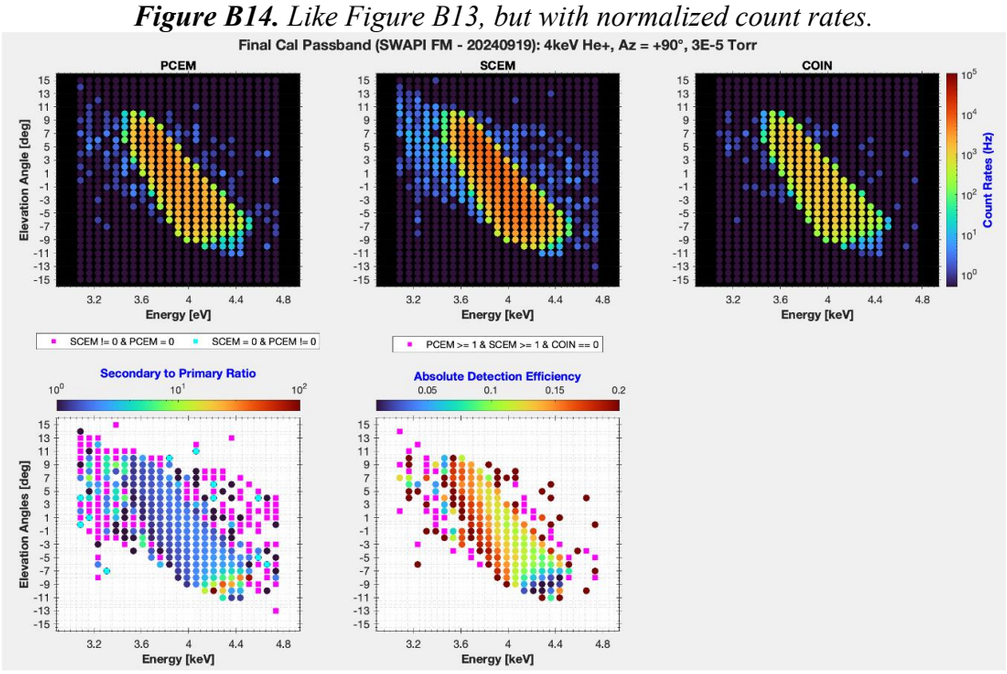


Figure B15. *Like Figure B1, but for 4 keV He+ passband through +90°azimuth ("open aperture").*

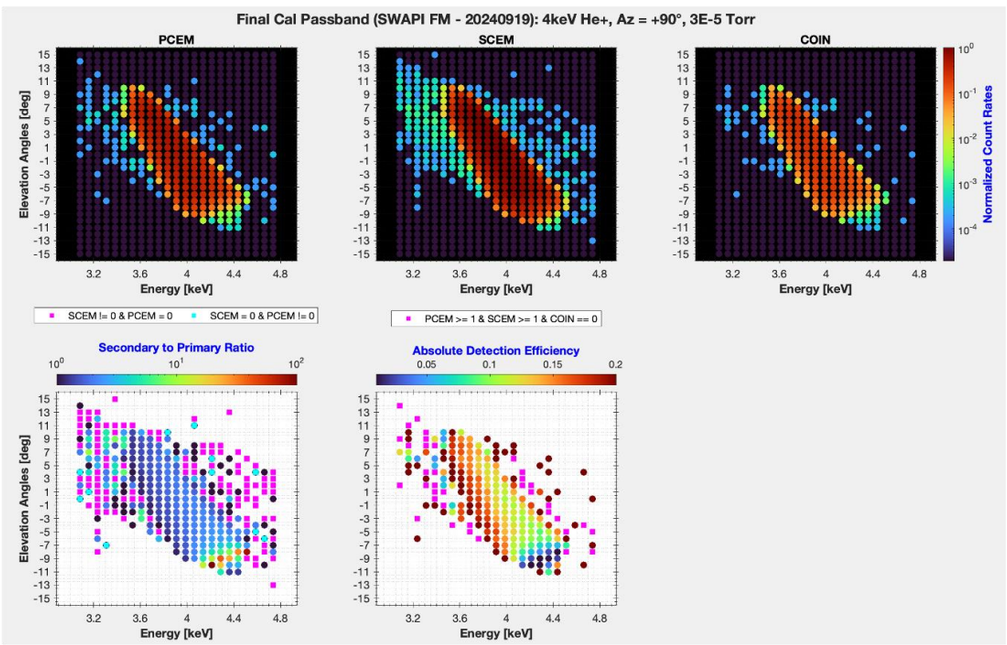


Figure B16. *Like Figure B15, but with normalized count rates.*

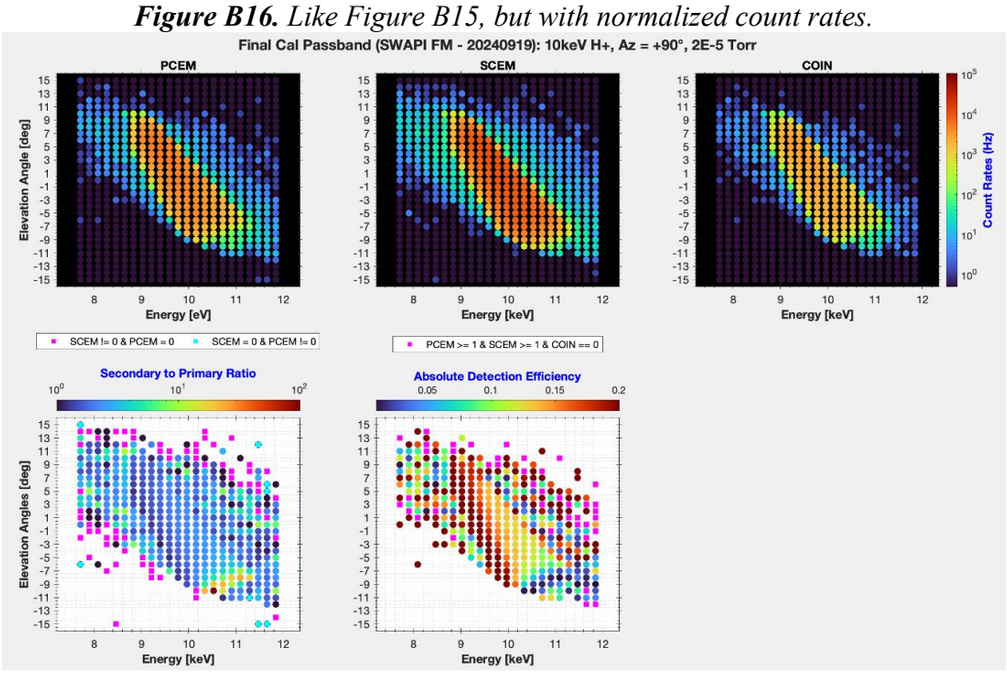


Figure B17. *Like Figure B1, but for 10 keV H+ passband through +90°azimuth ("open aperture").*

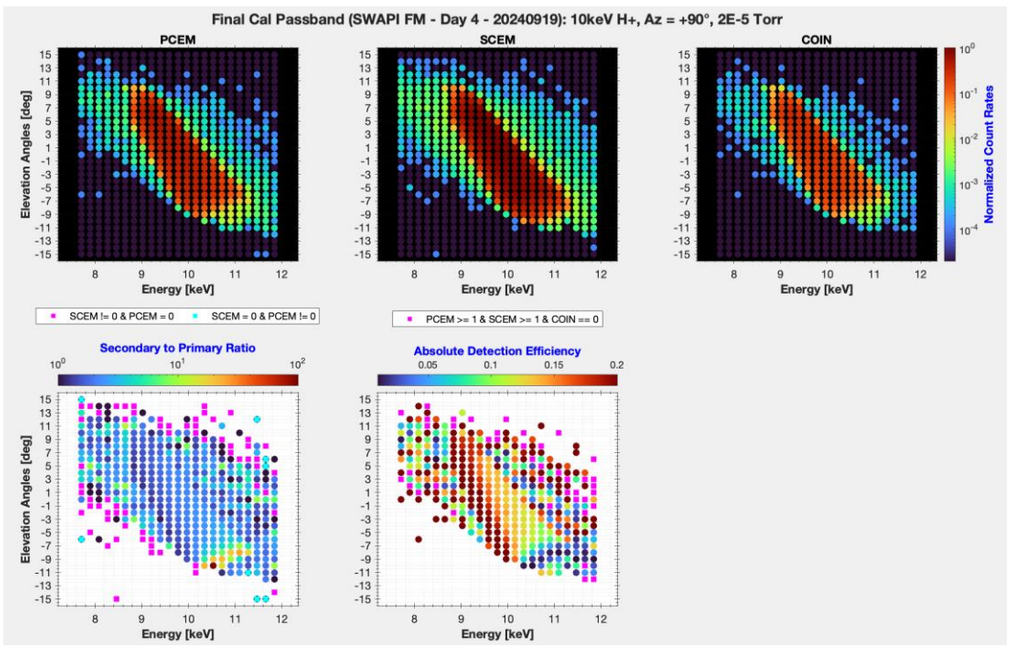


Figure B18. *Like Figure B17, but with normalized count rates.*

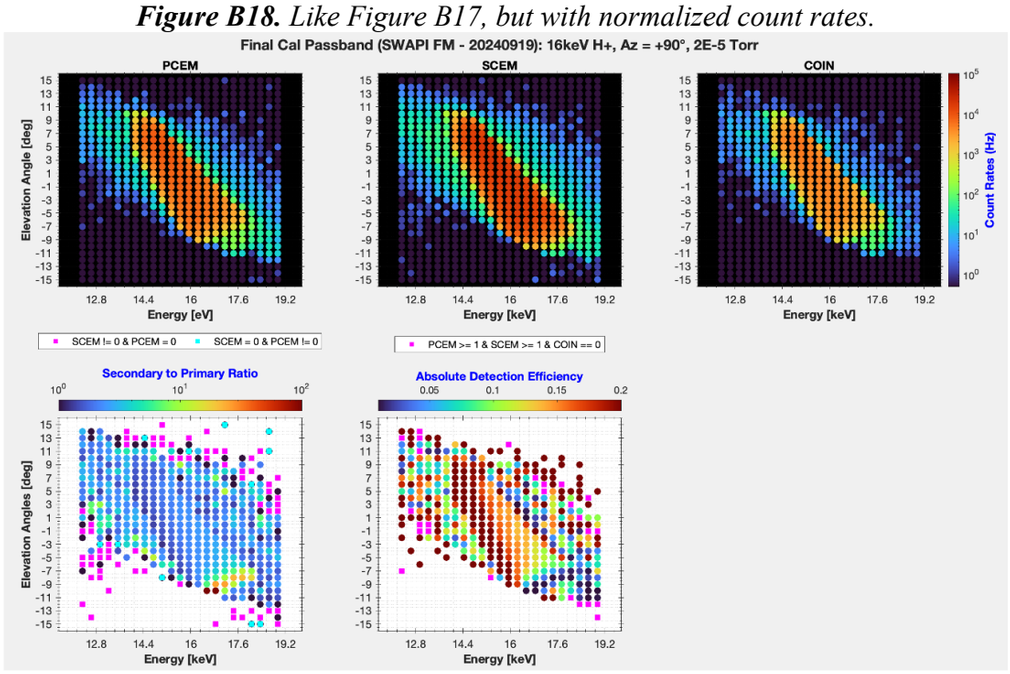


Figure B19. *Like Figure B1, but for 16 keV H+ passband through +90°azimuth ("open aperture").*

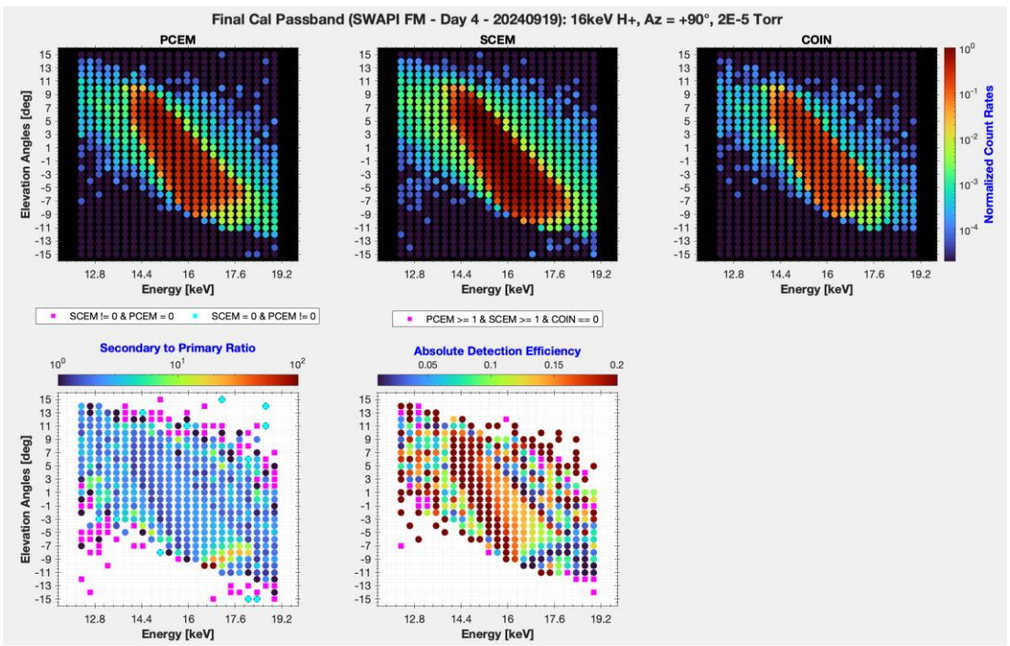


Figure B20. *Like Figure B19, but with normalized count rates.*

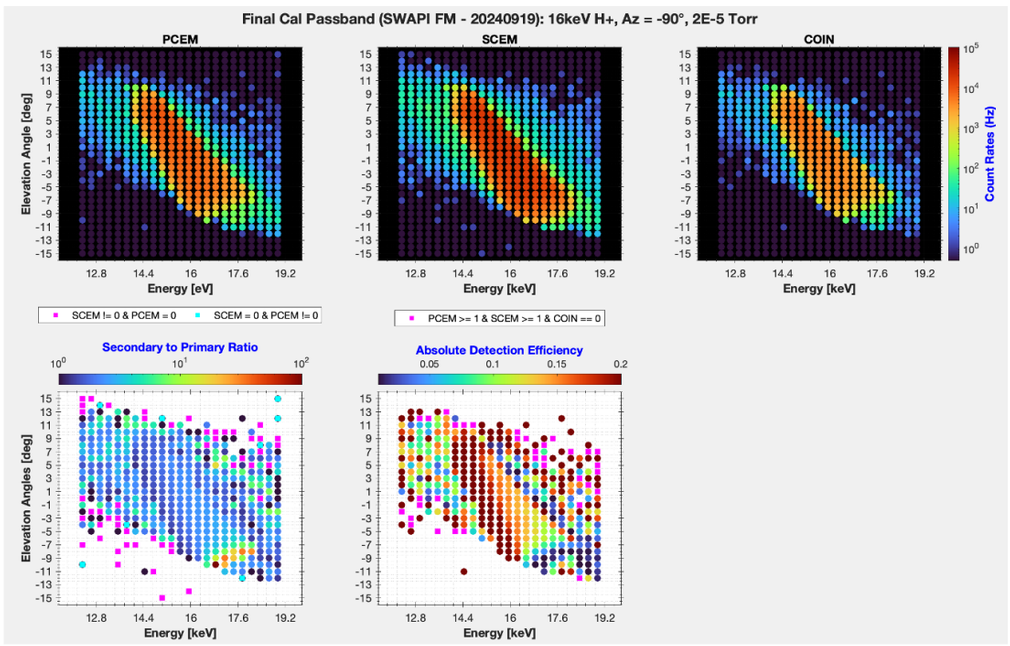


Figure B21. *Like Figure B1, but for 16 keV H+ passband through -90°azimuth ("open aperture").*

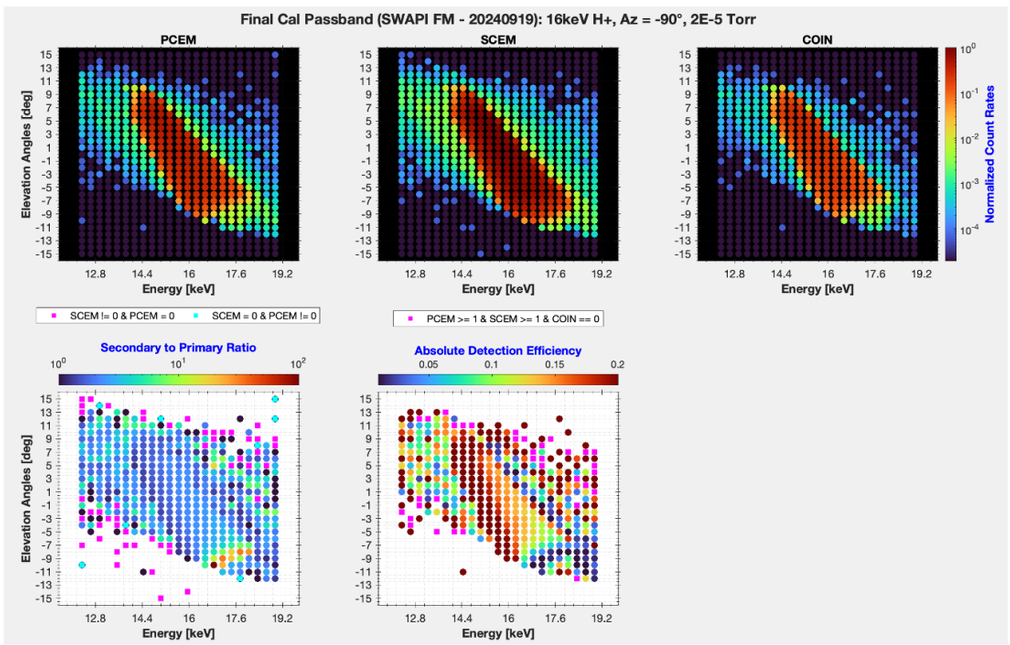


Figure B22. *Like Figure B21, but with normalized count rates.*

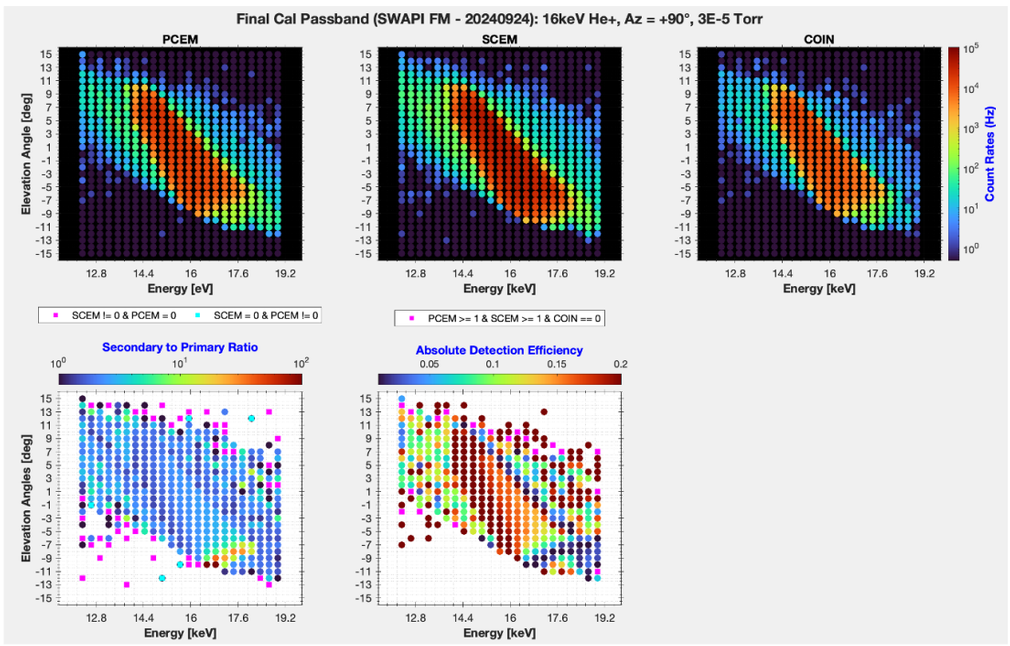


Figure B23. *Like Figure B1, but for 16 keV He+ passband through +90°azimuth ("open aperture").*

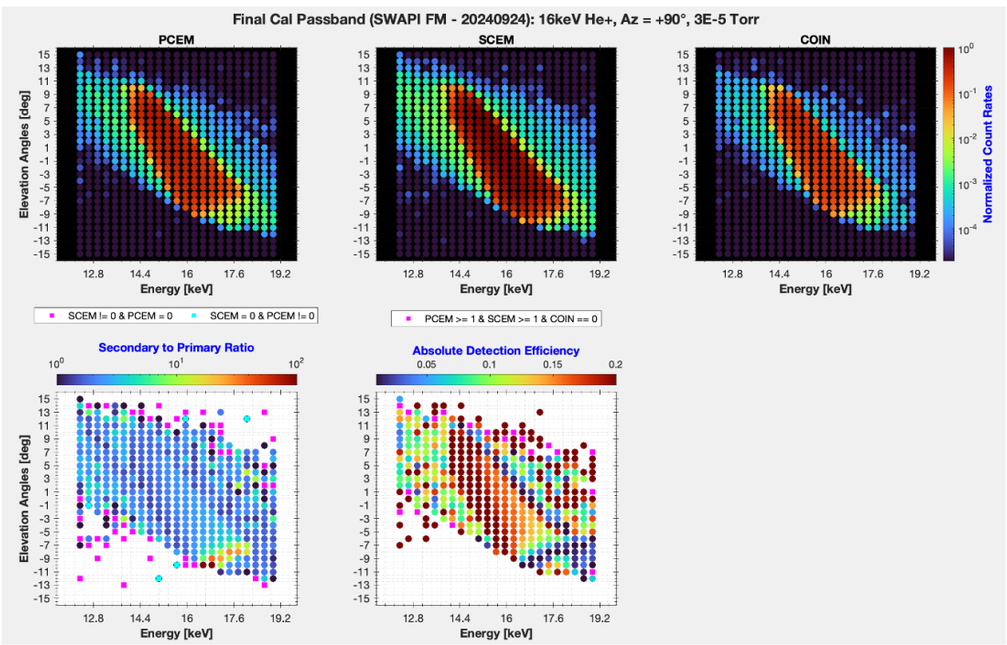


Figure B24. *Like Figure B23, but with normalized count rates.*

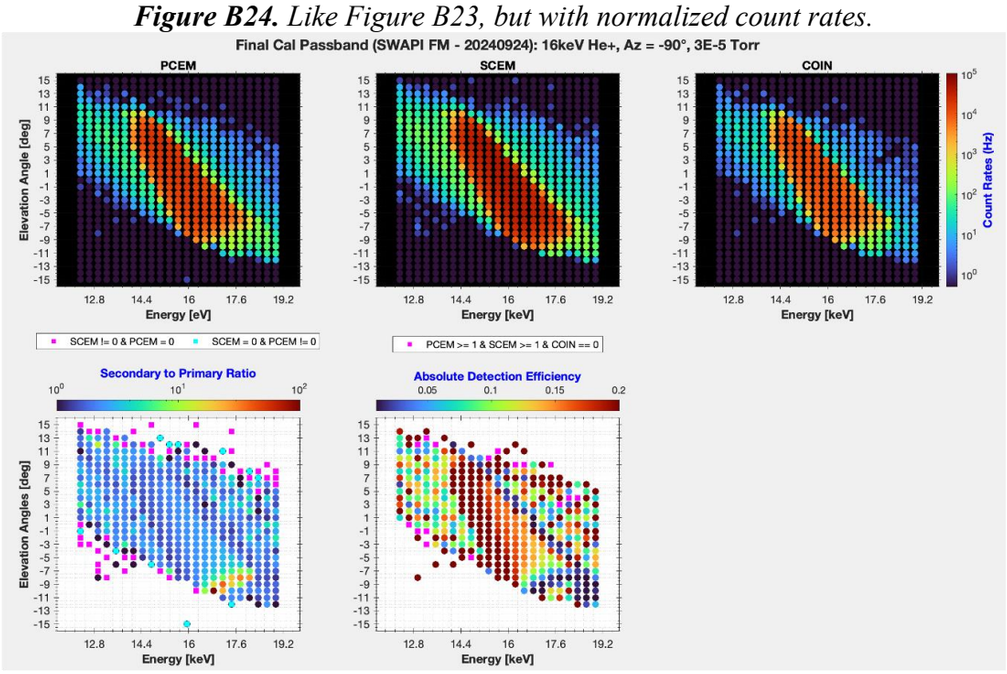


Figure B25. *Like Figure B1, but for 16 keV He+ passband through -90°azimuth ("open aperture").*

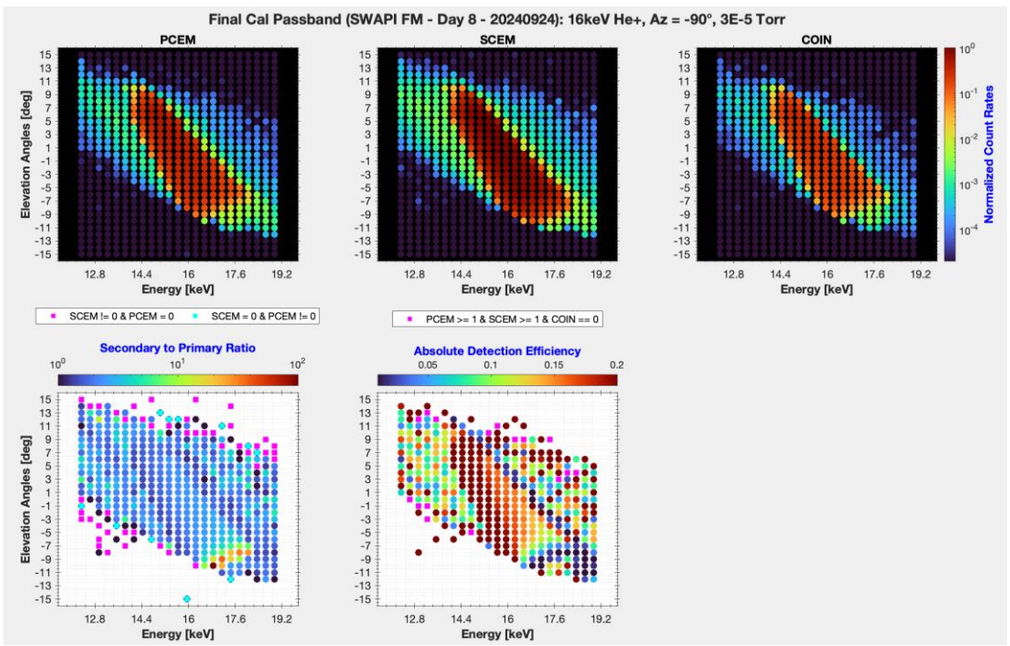


Figure B26. *Like Figure B24, but with normalized count rates.*

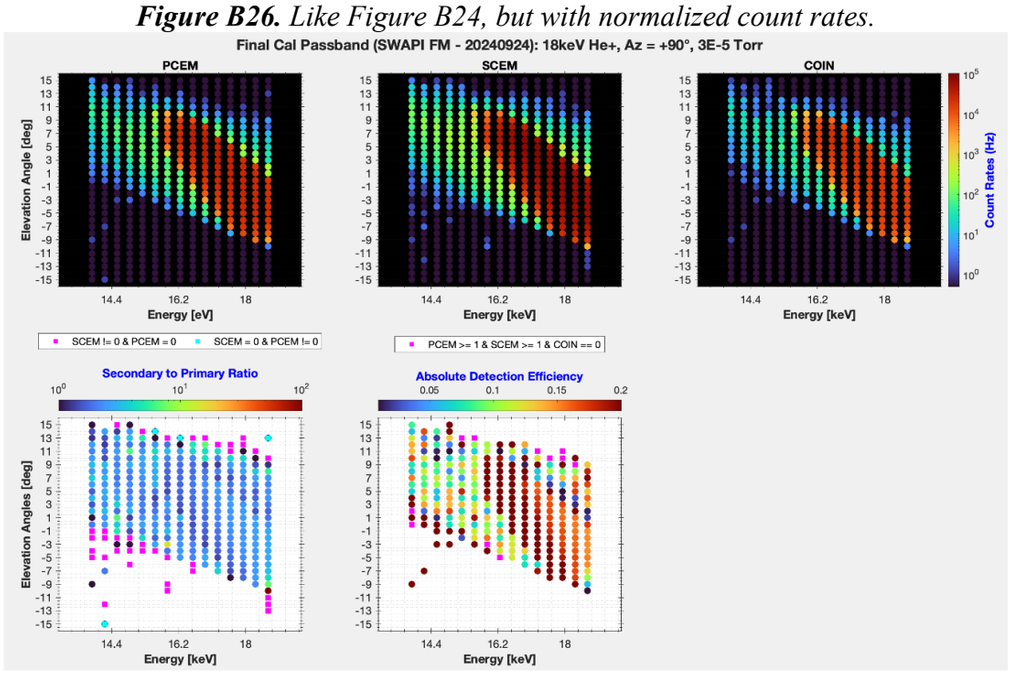


Figure B27. *Like Figure B1, but for 18 keV He+ passband through +90°azimuth ("open aperture").*

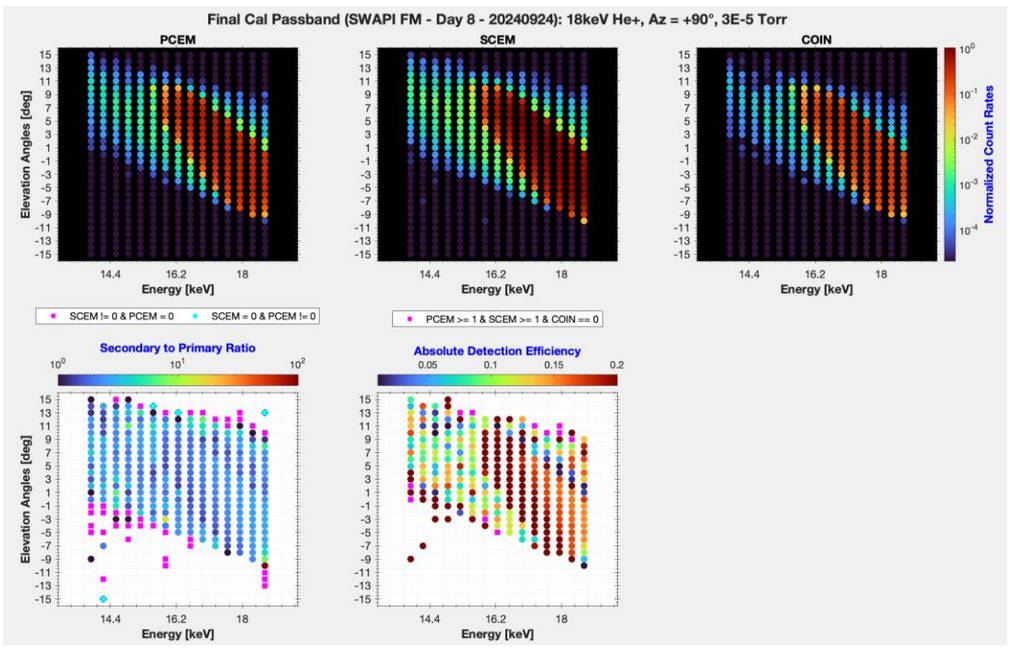


Figure B28. *Like Figure B26, but with normalized count rates.*

APPENDIX C. GAIN CURVES RESULTS

Section 7.1, Figure 7.2 summarizes all gain curves taken over the SWAPI FM calibration campaigns (pre-environmental and post-environmental, pre-flight). Below are the detailed plots of each of those individual gain curves.

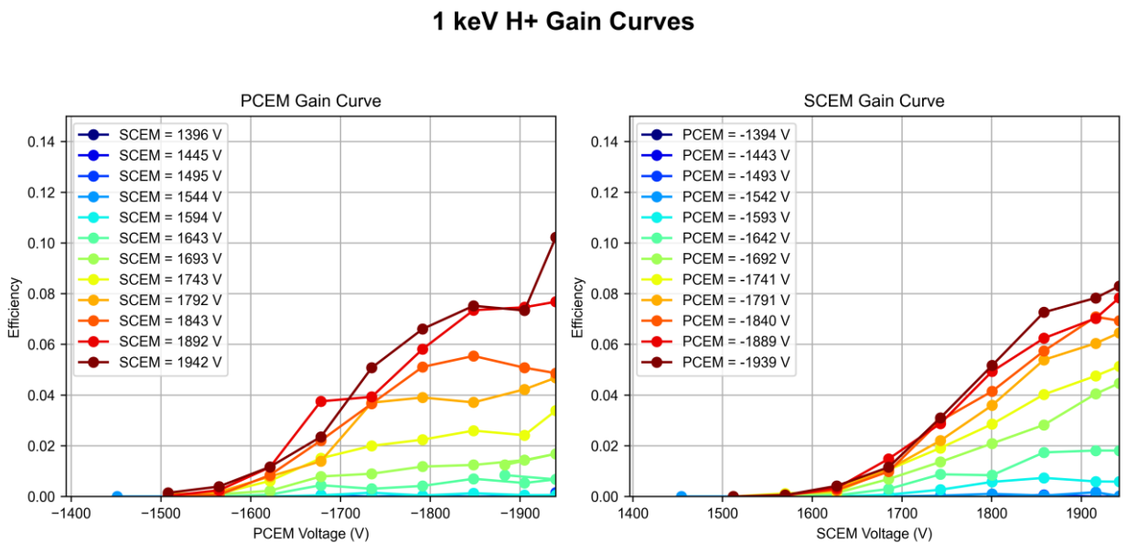


Figure C1. *Gain curves for PCEM and SCEM taken using 1keV H+ before environmental test (2024/08/14).*

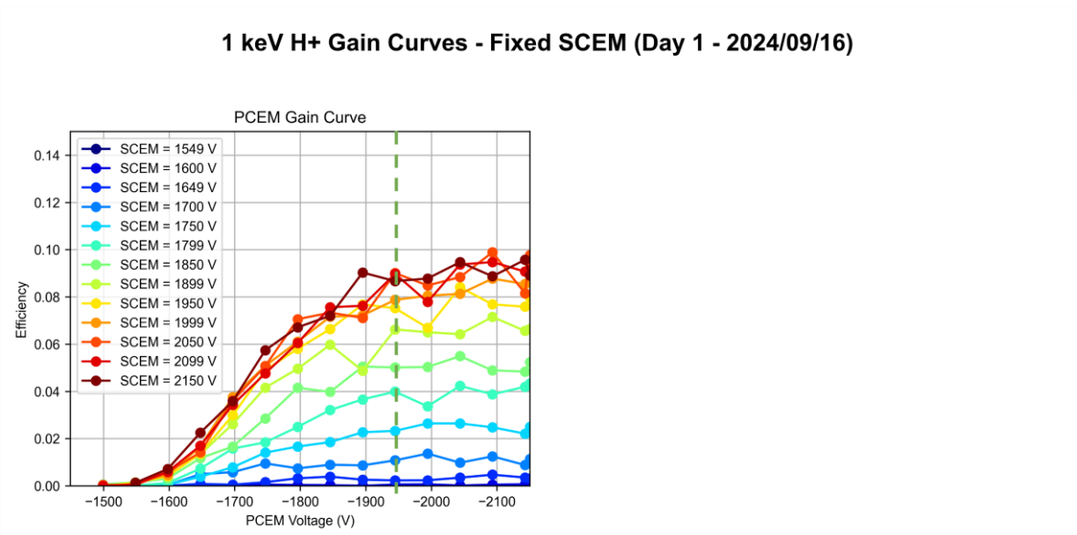


Figure C2. *Like Figure C1, but taken after environmental test, 2024/09/16 and only with PCEM curve using the same beam parameters as those taken before environmental test (Figure C1).*

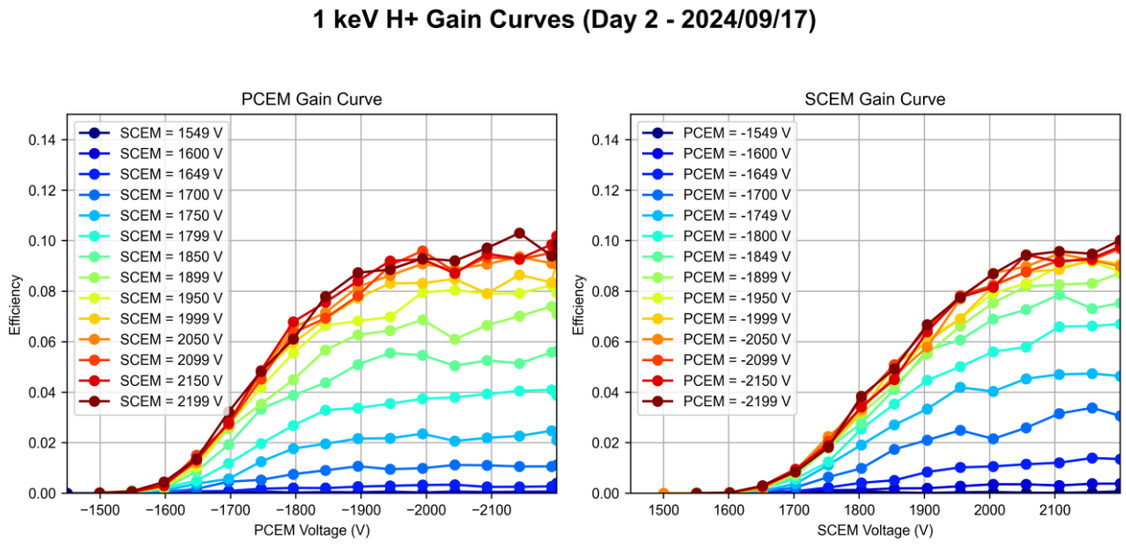


Figure C3. *Like Figure C1, but taken on 2024/09/17 with optimal beam parameters.*

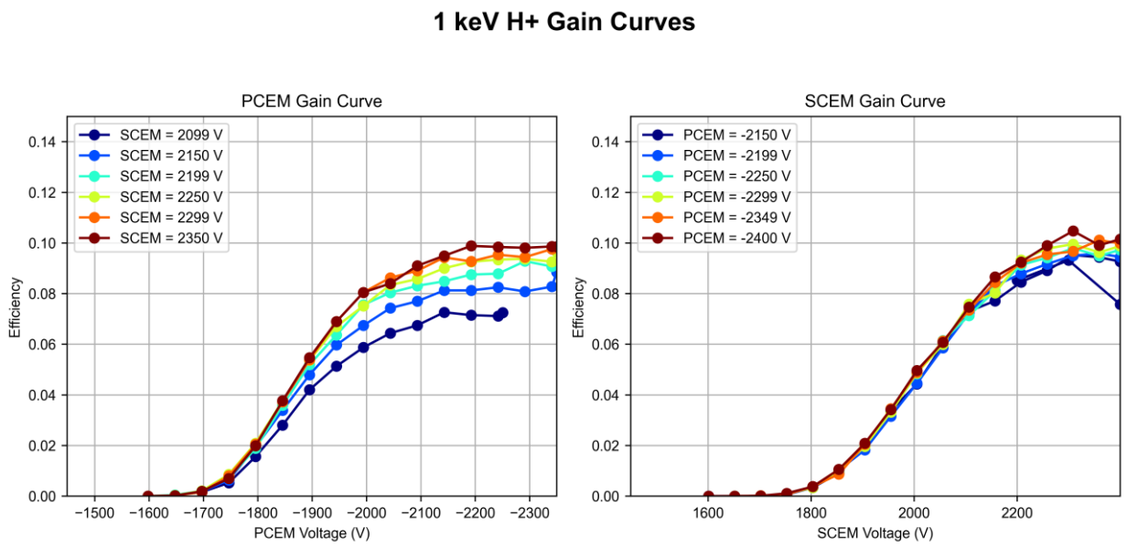


Figure C4. *Like Figure C1, but taken on 2024/09/24 with the same beam parameters as those taken on Figure C3.*

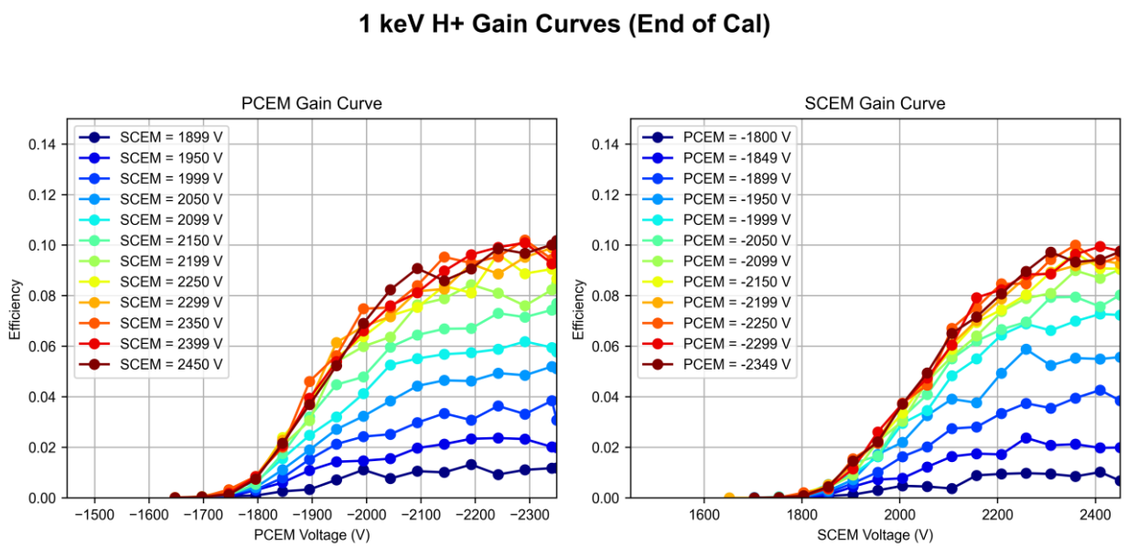


Figure C5. *Like Figure C1, but taken on 2024/09/24 with the same beam parameters as those taken on Figure C3.*

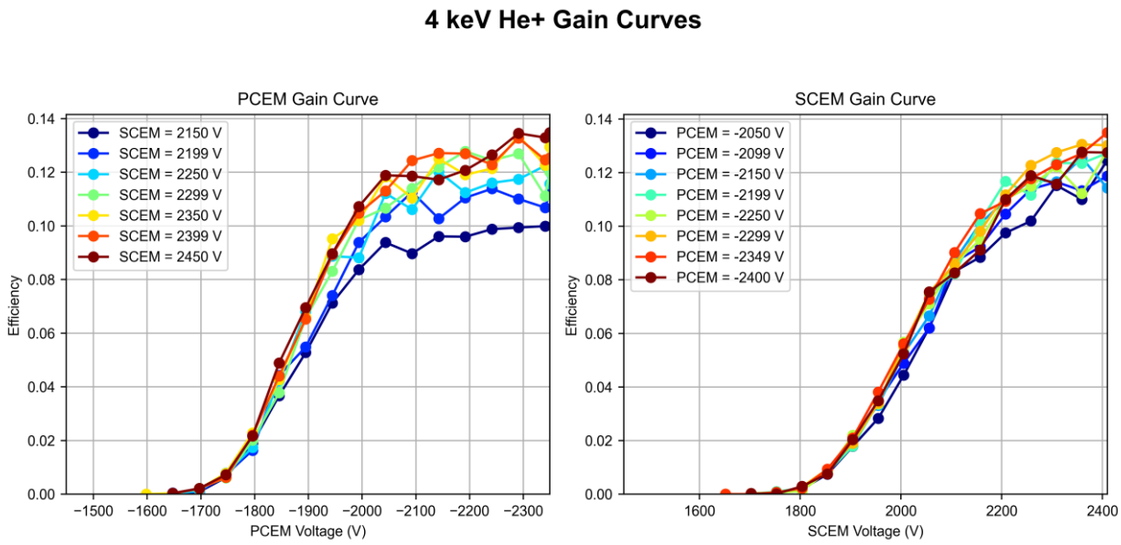


Figure C6. *Like Figure C1, but using 4keV He+, taken on 2024/09/18.*

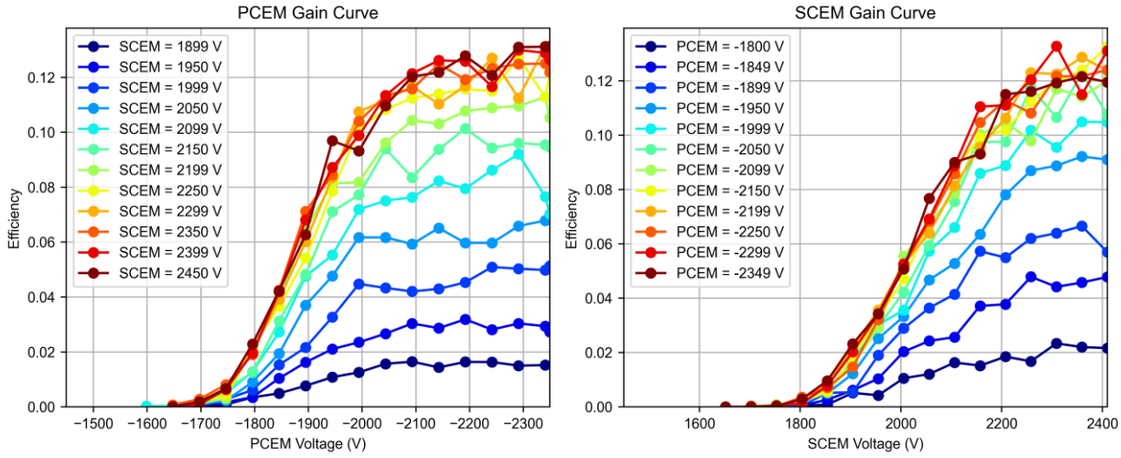


Figure C7. *Like Figure C6, but taken on 2024/09/18.*

3.1.3 In-Flight Calibrations

SWAPI in-flight calibration report to be included here.

3.2 CoDICE

3.2.1 Strategy & Approach

CoDICE employed a multi-step approach to calibrating its complex and extended-range particle instrument. First, the ESA and ToF×E subsystems were calibrated independently prior to full instrument integration and integrated sensor assembly calibration. Calibration was performed in facilities at Southwest Research Laboratory (SwRI) in San Antonio, TX. The effort focused on multiple objectives ultimately to evaluate and validate the functionality and performance of CoDICE. The following were evaluated and calibration factors and response functions established: ESA performance and response functions (including k-factor, geometric factors), collimator performance and acceptance angles, ToF×E efficiencies and response functions, mass-per-charge and mass resolutions, energy resolutions. The calibration efforts used radioactive sources for the calibration of the APD and SSD energy boards, and a pair of ion beams ranging in total from 1 to 350 keV/q with multiple ion species, including H, ^{2}H, He, N, Ne, Ar, and Kr, was used for the ESA, post-acceleration, and ToF segments.

As described in full detail by Livi et al. [2025], the following describes the various tests that were used for ground calibrations of the CoDICE instrument.

- CoDICE-Lo ESA Performance: The geometric factors and response functions were determined as a function of energy, azimuth, and elevation angles. An absolute beam monitor was used to measure the true intensity of the beam. CoDICE's ESA uses a reduced geometric factor operation (RGFO) to dynamically shift the sensitivity of the instrument as a function of energy. The RGFO functionality and ESA k-factors were all also determined from this set of calibration tests. Coincidence efficiencies, based on double and triple coincidence event rates, were also factored in and determined during this calibration procedure.

- CoDICE-Hi Collimator Performance: Collimator angular responses and foil efficiencies were tested using a 300 keV proton beam. A ^{228}Th source (αs) was also used to determine efficiencies for double and triple coincident event rates. Those lab tests confirmed the full instrument simulations using SIMION.

- ToF×E Performance: A combination of beams and radioactive sources were used to determine the mass and energy resolutions of the CoDICE-Lo and -Hi portions of the instrument. Ion beams at various energies between 1 to 80 keV/q and ion masses between 1 to 40 amu were used through the ESA and ToF segments onto the APDs. All of the azimuthal sectors were tested, including the solar wind aperture. With energy and ToF spreads, the corresponding mass and energy resolutions were determined as a function of incident ion energy. The same was conducted using ion beams and α sources through the CoDICE-Hi apertures; for those tests, the beam energy ranged from 50 to 350 keV/nuc and a ^{228}Th source was used for the α particles. All of the CoDICE-Hi apertures (and corresponding ToF paths and SSDs) were tested.

3.2.2 Pre-Flight Instrument Calibration

CoDICE cal report embedded below

INFORMATION COPY ONLY

TABLE OF CONTENTS

1. SCOPE 1

2. ABBREVIATIONS 1

3. BACKGROUND 2

3.1 CoDICE Instrument 2
3.2 Summary of Calibrations 5
3.2.1 ENERGY CALIBRATION (ECAL) *6*
3.2.2 TIME-OF-FLIGHT AND ENERGY CALIBRATION (TOFE-CAL) *6*
3.2.3 FULL FLIGHT MODEL CALIBRATION (FM-CAL) *6*
3.2.4 ESA RESPONSE TESTING (H30-CAL) *6*
3.2.5 LABORATORIES USED FOR CODICE CALIBRATION *6*

4. CODICE REQUIREMENTS TRACEABILITY 8

5. CODICE LO 9

5.1 Electrostatic analyzer performance 9
5.1.1 Relevant Requirements *11*
5.1.2 Verification Methods *12*
5.1.3 Artifacts *12*
5.2 Time of flight and energy measurement performance 17
5.2.1 Relevant Requirements *17*
5.2.2 Verification Methods *18*
5.2.3 Artifacts *18*

6. CODICE HI 22

6.1 Time of flight and energy measurement performance 22
6.1.1 Relevant Requirements *22*
6.1.2 Verification Methods *23*
6.1.3 Artifacts *23*
6.2 Geometrical acceptance evaluation 27
6.2.1 Relevant Requirements *27*
6.2.2 Verification Methods *27*
6.2.3 Artifacts *27*

7. CONCLUSION 29

INFORMATION COPY ONLY

LIST OF TABLES AND FIGURES

Page
Table 3-1: Summary of CoDICE calibration efforts. 5
Table 5-1: *A summary of low geometric factor (GF) mode performances for CoDICE-Lo evaluated by 16 keV protons. The unit used for GF is cm^2 str eV/eV. The low-GF mode will be achieved by using factor 0.7 ratio between the entrance and main electrostatic analyzer voltages.* 15
Table 6-1*: Maximum energy coverage for CoDICE Lo from test pulse measurements.* 26
Figure 3-1: CoDICE cross-section showing electro-optical design and simulations of particle trajectories through the ESA and TOF/E subsystems. CoDICE flight instrument. 2
Figure 3-2: CoDICE block diagram. 4
Figure 5-1: *Transmission responses of CoDICE-Lo instrument for (left) a solar wind sector, (center) a solar wind sector operating at low geometric factor (GF) mode, and a suprathermal sector. The top panels show positional coincidence rate (POS), the middle, double coincidence rate (DCR), and the bottom, the triple coincidence rate (TCR), respectively. The energy of the beam was fixed at 16 keV/q in these cases, and the ESA electrode voltage was scanned around the pass band. The elevation angles (El angles) are physically altered using chamber. The negative elevation angles correspond to the particles from the top cap side, while the positive angles from the electronics box side. The total counts denote the accumulated counts within 10 seconds by the whole sensor.* 13
Figure 5-2:*Dependence of the geometric factor (GF) as a function of energy per charge (eV/q) for the solar wind sector.* 14
Figure 5-3: *Dependence of the geometric factor (GF) as a function of azimuth (Az) locations on the instrument. The gray data shows the positional coincidence rates, orange, the double coincidence rates, and blue, the triple coincidence rates. The location number 1 is the solar wind sector, and the sector rotates clockwise from top-to-down view from the sensor top cap. The calculation of GF is based on the full energy-angle scan, as presented in Figure 5-1, and 8 locations out of 24 full sensor Az sectors are investigated to investigate the sensor assembling accuracy.* 14
Figure 5-4: *Dependence of the K-factor as a function of energy per charge (eV/q) for the solar wind sector.* 15
Figure 5-5*: The sensor double coincidence rate (DCR) and the triple coincidence rate (TCR) responses with fine (1°) azimuthal angle scan for the 43.5 keV and 16.5 keV proton beam. The solar wind sector is at +120° in this laboratory coordinate.* 16
Figure 5-6: *The energy-per-charge dependence of the energy and angular resolution in Full Width Half Maximum (FWHM) for CoDICE-L.* 16
Figure 5-7: *The mean TOF values in the system (in the unit of TOF channels) as a function of the incident particle's energy per nucleon for CoDICE Lo. The plotted data are selected for one RH side and one LH side for the suprathermal (ST) sector, and the solar wind (SW) direction. The beam was injected through the ESA and the post acceleration to the TOF subsystem.* 19
Figure 5-8: *Mass per charge resolutions (left) and Mass resolutions (right) for CoDICE Lo evaluated by a relevant range of particle mass (1-40) and energy (1-80 keV/q). The plotted data are selected for one RH side and one LH side for the suprathermal (ST) sector, and the solar wind (SW) direction. The beam was injected through the ESA and the post acceleration to the TOF subsystem.* 20
Figure 5-9: *The detected energy per nucleon for all APDas a function of the incident energy per nucleon. The plotted data are selected for one RH side and one LH side for the suprathermal (ST) sector, and the solar wind (SW) direction. The beam was injected through the ESA and the post acceleration to the TOF subsystem.* 20
Figure 5-10: *The detected energy resolution (in keV) for all APDas a function of the incident energy per nucleon. The plotted data are selected for one RH side and one LH side for the suprathermal (ST) sector, and the solar wind (SW) direction. The beam was injected through the ESA and the post*

INFORMATION COPY ONLY

acceleration to the TOF subsystem. 21
Figure 5-11: *The TOF vs energy count plots for the SW (1-RH3, left) and ST (17-LH7, right), accumulating several species and energies. The charage state separation capability was confirmed by using vertical separations of H_2^+, N_2^+, and Ar^{2+}+Ne^+. The beam was injected through the ESA and the post acceleration to the TOF subsystem.* 21
Figure 6-1: *The mean energy per nucleon distributions evaluated by TOF values in the system as a function of the incident particle's energy per nucleon for CoDICE Hi. The plotted data are selected for one RH side and one LH side for the suprathermal (ST) sector, and the sun-direction (LH1). The lower energy parts were evaluated by proton and Helium ion beams, and the highest end was evaluated by the Thorium 228 radioactive source.* 24
Figure 6-3:*The expected mass resolutions evaluated by combining TOF and Energy values in the system as a function of the incident particle's energy per nucleon for CoDICE Hi. The plotted data are selected for one RH side and one LH side for the suprathermal (ST) sector, and the sun-direction (LH1). The lower energy parts were evaluated by proton and Helium ion beams, and the highest end was evaluated by the Thorium 228 radioactive source.* 25
Figure 6-2: *The mean energy per nucleon distributions evaluated by Energy values in the system as a function of the incident particle's energy per nucleon for CoDICE Hi. The plotted data are selected for one RH side and one LH side for the suprathermal (ST) sector, and the sun-direction (LH1). The lower energy parts were evaluated by proton and Helium ion beams, and the highest end was evaluated by the Thorium 228 radioactive source.* 25
Figure 6-4: *The energy resolution as a function of the incident particle's total energy for CoDICE Hi. The plotted data are selected for one RH side and one LH side for the suprathermal (ST) sector, and the sun-direction (LH1). The lower energy parts were evaluated by proton and Helium ion beams, and the highest end was evaluated by the Thorium 228 radioactive source.* 26
Figure 6-6: *The TOF measurement using 300 keV H^+ beam and Thorium-228 radioactive source for all 12 apertures, confirming the whole sky coverage of the instrument. The beam test could not evaluate 180 deg channel (LH5) due to the restriction by the rotation stage motion.* 28
Figure 6-5: *The angular coverage evaluation results for CoDICE Hi. The left figure shows elevation angle scans comparing two locations in DCR using 300 keV H^+ beam due to the configuration restriction of the beam facility on the angular scan capability, this testing was conducted using prototype apertures with thin and thick (i.e., flight-like) foils without ESA installed. The right figure shows horizontal angle scans for two adjacent apertures evaluating the horizontal coverage. This testing was conducted with the full flight configuration using the Thorium-228 radioactive source.* 28

INFORMATION COPY ONLY

REVISION NOTICE

Version Identifier	Date of Issue	Summary of Changes
Rev 0 Chg 0	6/29/2025	Initial issue.
Rev 1 Chg 0	6/5/2026	Removed Export Administration Regulations (EAR) Notice upon the agreement with the project and institute. Updated values and descriptions with the latest information

INFORMATION COPY ONLY

1. SCOPE

This document contains details of how each of the science requirements have been verified for Compact Dual Ion Composition Experiment (CoDICE) Flight Module (FM) instrument on the Interstellar Mapping and Acceleration Probe (IMAP).

2. ABBREVIATIONS

AEB	APD Energy Board
APD	Avalanche Photo-Diode
BOB	Break-Out Box
CDH	Command & Data Handling board
CFD	Constant-Fraction Discriminator circuit
CoDICE	Compact Dual Ion Composition Experiment
FEE	Front-End Electronics board
FM	Flight Module
FWHM	Full-Width, Half-Max
GSE	Ground Support Equipment
IMAP	Interstellar Mapping and Acceleration Probe
LPF	Low-Pass Filter
PWA	Printed Wire Assembly
QA	Quality Assurance
QAE	Quality Assurance Engineer
SEB	SSD Energy Board
SwRI	Southwest Research Institute
SSD	Solid-State Detector
STD DEV	Standard Deviation
TOF	Time Of Flight
TP	Test Point
UUT	Unit Under Test

INFORMATION COPY ONLY

3. BACKGROUND

3.1 CoDICE Instrument

The Compact Dual Ion Composition Experiment (CoDICE, Figure 3-1) measures the 1) elemental, ionic charge state, and isotopic composition and the 3-Dimensional (3D) velocity distribution functions (VDFs) of solar wind He – Fe ions and interstellar pickup He, O, and Ne ions in the ~0.5–80 keV/q energy range in CoDICE-Lo, and 2) the mass composition and arrival direction of ~0.03–5 MeV/nuc ions in CoDICE-Hi. These measurements are required to 1) determine the LISM composition and flow properties and 2) discover the origin of the enigmatic ST tails and advance understanding of the acceleration of particles in the heliosphere.

The CoDICE sensor comprises two major sub-systems, namely: 1) an electrostatic analyzer (ESA), and a 2) Time-of-flight (TOF) vs. residual energy (E) spectrometer. CoDICE-Lo measures ions between ~0.5 and 80 keV/q that enter the collimated aperture (blue trajectories, Figure 1) and are selected and focused according to their E/q by the ESA into the Start TOF subassembly. The E/q sweeping steps up to the maximum voltage for the next stepping cycle when SW H+ count rates near ~1 keV/q exceeds a predefined threshold rate. The Start subassembly, biased at –15 kV, accelerates the incoming ions before they strike an ultra thin carbon foil (0.5 - 1 µg/cm^2) at the entrance of the TOF-E subsystem. This interaction produces secondary electrons (red trajectories) that are guided to the outer annulus of the Start MCP. The azimuthal arrival directions of the

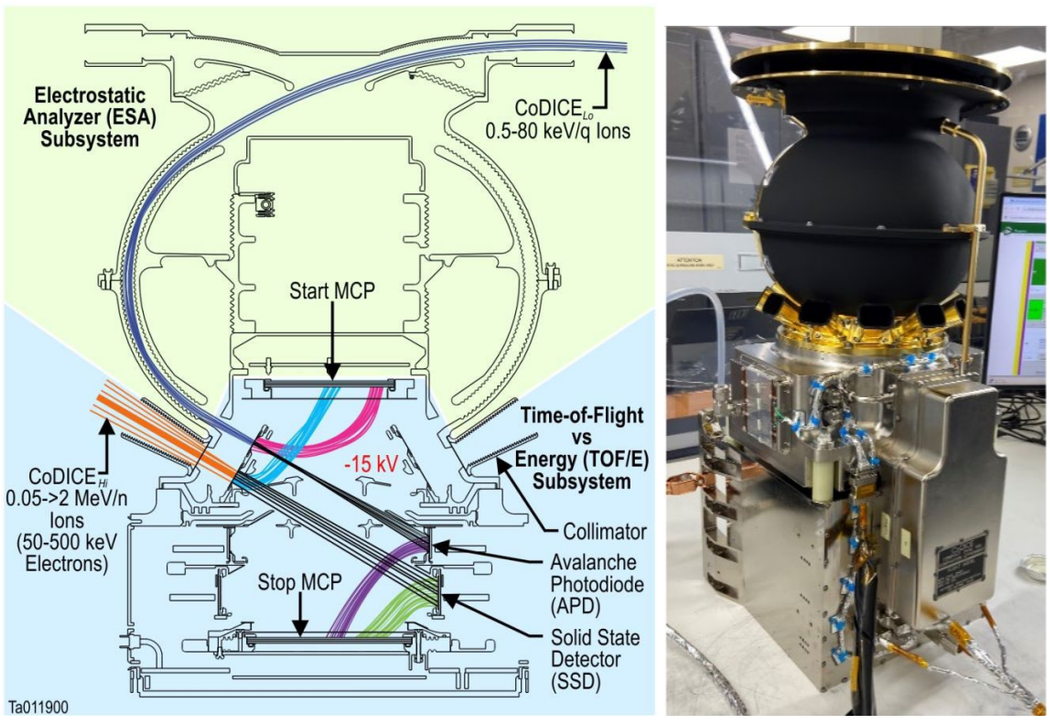


Figure 3-1: CoDICE cross-section showing electro-optical design and simulations of particle trajectories through the ESA and TOF/E subsystems. CoDICE flight instrument.

INFORMATION COPY ONLY

incoming ions are measured by a position-sensing delay line embedded within the Start MCP subassembly. CoDICE-Lo measures the full energy range as the ESA steps through all 128 voltage steps during a 4-minute interval. The mostly neutralized ions (black trajectories) then traverse a ~10.4 cm flight path and strike one of 24 Avalanche Photodiodes (APDs) where they generate secondary electrons that are guided to the center of the Stop MCP (purple). The TOF between the Start and Stop MCP signals yields the ion velocity. The residual energy E of the neutralized ion is measured by one of the 24 azimuthally distributed APDs that collectively provide 6°×360° instantaneous FOV and cover ~2.7π sr in a single SC spin. The combined measurements, E/q, TOF, and E, determine the mass (M), charge state (q), and M/q.

CoDICE-Hi measures ions between ~0.03 and >2 MeV/nuc (orange) that enter the common TOF/E subsystem through 12 separate 15°×10° FOV collimators and two 75 nm Al foils that attenuate UV light and stop low-energy (<50 keV) protons. Start and Stop MCP signals are generated by secondary electrons (light blue and green) that are produced as the ions traverse a ultra thin carbon foil (0.5 - 1 μg/cm^2) located at the TOF-E entrance and strike one of 12 SSDs distributed over 360° azimuth, respectively. Each SSD, 700 μm thick with an active area of 15×15 mm^2, determines the ion's residual energy E. The E along with the TOF, which yields the ion velocity, provides the ion mass. These secondary electrons are detected by the same MCPs shared with CoDICE-Lo, but in separate areas; Hi-Start electrons (light blue) are guided toward the center portion of Start MCP, and Hi-Stop electrons (green) are guided toward the outer annulus of Stop MCP (Figure 3-1). CoDICE-Hi covers 1.8π sr in each SC spin.

Figure 3-2 shows the CoDICE overall block diagram. CoDICE electronics box (Ebox) comprises the following major subassemblies: 1) Low Voltage Power Supply (LVPS); 2) Command and Data Handling (CDH); 3) Sensor High Voltage Power Supply (HVPS); 4) Ion-Optics HVPS; 5) Backplane; and 6) Low voltage terminal block assembly. The LVPS interfaces with the spacecraft via a nine pin D type connector. The LVPS accepts +31V nominal spacecraft primary power to create secondary voltages (+3.3V, ±5V, ±12V) for all CoDICE subassemblies. The CDH interfaces to the spacecraft RS-422 data bus via a 9 socket MDM type connector for all spacecraft commands and all instrument telemetry. The CDH interfaces to the spacecraft Arm and safe panel via a 9 pin MDM type connector for instrument Disable/Safe/Arm selection using the appropriate spacecraft-provided plugs. The CDH: 1) Provides a centralized system for command, monitoring, and control; 2) Acquires, processes, and packetizes all detector data; 3) Provides temperature, current, and voltage monitoring of the HVPS, LVPS, and the sensor; and 4) Distributes High Voltage Power Supply Safing. The Sensor HVPS has 4 HV converters, namely, 1) Sensor bulk; 2) 10-stage Start MCP; 3) 8-stage Stop MCP; and 4) APD Bias.

The Sensor Bulk supply produces a steady output voltage of +6000V. The bulk output feeds directly into the Stop Steering regulator (+3200V nominal, HV optocoupler based) which is resistor divided to produce the SSD Steering voltage (+1600V nominal). The sensor bulk provides +670V from a tap on the multiplier/filter to an additional three outputs. One of the additional three outputs (SSD Bias) also has an HV optocoupler based regulator. The remaining two of the three additional outputs (APD Optics and SSD Lens) are derived from resistive dividers for the previously mentioned tap. The 10-stage Start MCP supply produces an output voltage programmable from zero to -3400V. The current capability is up to 120 micro-amps. The 8-stage Stop MCP supply produces an output voltage programmable from zero to +5000V. The current capability is up to 120 micro-amps. The MCP Back voltage is set to a fixed voltage from +1600V

INFORMATION COPY ONLY

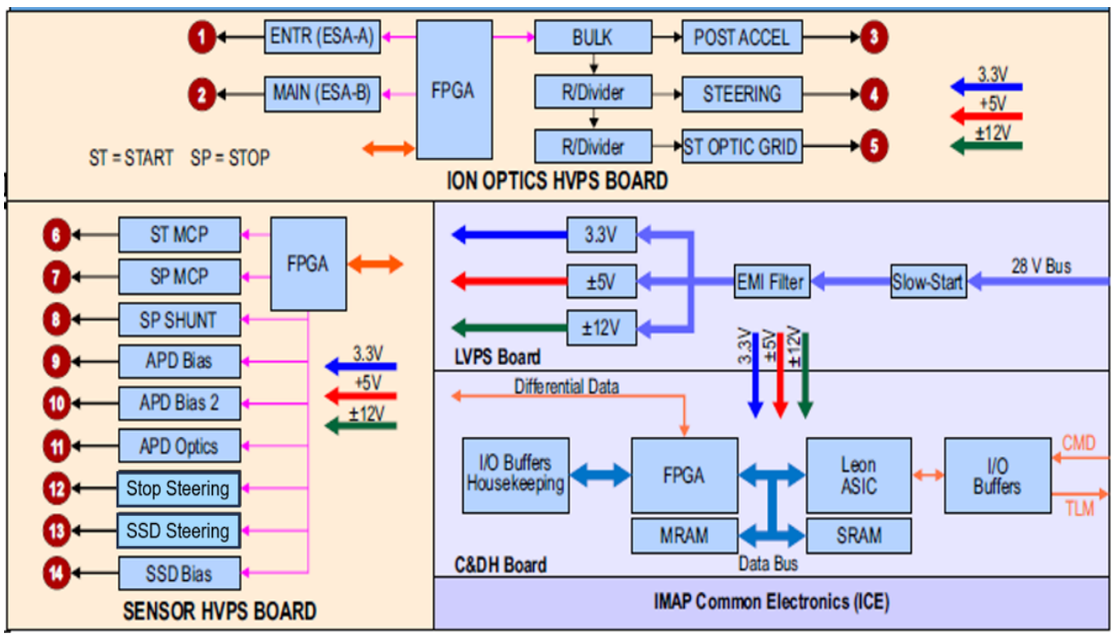


Figure 3-2: CoDICE block diagram.

by using a shunt HV optocoupler. This voltage increases as the Stop MCP voltage increases until it reaches +1600V, then it is regulated to a fixed +1600V as the Stop MCP voltage continues to increase. The APD Bias supply produces a programmable output voltage of zero to +650V. There is a slave APD Bias 2 supply producing zero to ~ +600V to bias 3 APDs that measure the solar wind. Since APD Bias 2 is a regulated voltage from APD Bias 1, it cannot generate a voltage greater than the programmed APD Bias 1 voltage.

The Ion-Optics Bulk supply produces a programmable output voltage (0V to -15500). The nominal voltage will be -15 kV. The current capability is up to 200 micro-amps. The output of this Bulk supply feeds directly into the ESA-A (Entrance) and ESA-B (Main) HV optocoupler based negative polarity stepping power supplies. This Bulk supply also feeds a resistive divider which provides the Post-Acceleration output (nominal -15 kV), the Steering output (nominal -13.24 kV) and the Start Optics Grid (nominal -2647V). The backplane routes secondary power from the LVPS to all other CoDICE subassemblies. It routes command and telemetry from and to the CDH. All electrical interfaces within the EBox are via cPCI connectors. The low voltage electrical interface to the sensor section is via a pigtail two row 51 pin MDM type connector.

The low voltage terminal block assembly provides for lower-level high voltage termination via high voltage pigtails exiting directly from the Sensor HVPS and the Ion-Optics HVPS at the EBox exterior prior to being integrated with the CoDICE sensor assembly. The higher voltages are terminated after the sensor section has been integrated with the EBox. The lower-level high voltages include: Ion-Optics HVPS voltages and the Start Optics Grid, and Sensor HVPS voltages consisting of Start MCP, Stop Steering, Stop Anode, Start Anode, APD Optics, SSD Lens, SSD Steering, Stop Grid, and Stop MCP Back.

CoDICE-Lo solar wind and pick-up ion data products are provided as 1D and 3D VDFs for

INFORMATION COPY ONLY

multiple species. CoDICE-Hi provides the arrival directions of suprathermal ions with priority given to heavy ion species. CoDICE also provides binned data products and direct event data products. The direct event data products contain the complete measurement information for each ion event that is telemetered based on the respective priority schemes, while the binned data provides counts/intensities as a function of energy, detector (APD/SSD), and spin angle at different cadences depending on the data product. Standard data-level definitions are: Level 0–the raw CCSDS packets, Level 1a: Raw count data decommutated into formatted variables; Level 1b – Counts converted to count rates; Level 2–Validated science products with count rates converted to intensities using instrument calibration factors; Level 3–Higher level science results.

3.2 Summary of Calibrations

CoDICE calibration was carried out separately for the ESA and TOF/E subsystems and then for the full sensor assembly to ensure functionality and performance characterization. The energy calibration used radioactive sources to evaluate the AEB and SEB performance and is critical for obtaining the absolute energy response. The TOF/E subsystem was also calibrated using higher energy singly charged ions without the ESA since the upper energy limit of the ESA is 80 keV/q. Finally, the full flight sensor was calibrated to evaluate end-toend performance and functionality. Table 3-1 summarizes the calibrated parameters (species, energies, locations, and angles).

Table 3-1: Summary of CoDICE calibration efforts.

	Cal. Type		Species	Energy	Az locations*	El angle
CoD-Lo	Energy	AEB only	Fe-55, Am-241	5.9 keV (γ), 14-60 keV (γ)	1-23, 15° steps	0°
	TOF-E	No ESA	H, He, N, Ne, Ar, Kr	5, 15, 40, 100, 200, 300 keV	1-23, 15° steps	0°
		With ESA	H, H2, He, N, Ne, Ar	5-80 keV (25 selected over 1-80 keV/n)	1-23, 15° steps	0°
	Full	Energy-Angle scan	H	4, 16 keV	1,3,9,11,13,21,23	-3° to 3°, 0.5° steps
		Energy-Angle scan	H, He	1, 2, 4, 6, 10, 16, 24, 43.5, 71.5 keV	1, 15	-3° to 3°, 0.5° steps
		Energy-Angle scan (Low-GF)	H	4, 16 keV	1, 15	-3° to 3°, 0.25° steps
		Fine angle scan	H, He, Ne	5, 16.5, 43.5 keV	1-23, 2° steps	0°
CoD-Hi	Energy	SEB only	Am-241, Th-228, Cf-252	59.5 keV (γ), 5-9 MeV (α), 90-130 MeV (fission)	0-15, 30° steps	0°
	TOF-E	No UV foil	H, He, N, Ne, Ar,	50, 100, 150, 200, 225, 250, 275, 300	0-15, 30° steps	0°

INFORMATION COPY ONLY

			Kr	keV		
		With UV foil	H, He, Th-228	100, 150, 200, 250, 300 keV (beam), 5-9 MeV (α)	0-15, 30° steps	0°
	Full	Fine angle scan	He, Th-228	300 keV (beam), 5-9 MeV (α)	0, 15	-10° to 10°, 1° steps
					0, 1, 7, 8, 15, 1° steps	0°

* Az location is indicated by the rate index (Table BB and CC).

3.2.1 ENERGY CALIBRATION (ECAL)

ECAL calibrates the Avalanche-Photodiode Energy Board (AEB), Solid-state detector Energy Board (SEB), and Front-End Electronics (FEE). Radioactive sources were used for the absolute energy information.

Reference: 26850.03-FEE_AEB_SEB_ECAL-01

3.2.2 TIME-OF-FLIGHT AND ENERGY CALIBRATION (TOFE-CAL)

TOFE-CAL targets the TOF, and Energy subsystem calibration without ESA section integrated. This testing was conducted in H19 lab, and confirms APD energy coverage up to 300 keV total energy.

Reference: 26850.03-TOF-E-CAL-01

3.2.3 FULL FLIGHT MODEL CALIBRATION (FM-CAL)

FM-CAL targets the full sensor assembly performance test including ESA, TOF, and Energy elements. This testing was conducted in H19 laboratory in SwRI, and confirms ESA performance up to 80 keV/q, and CoDICE high performance up to 300 keV total energy with beam and up to ~9MeV using radioactive sources. The consise and selected verions of this test were repeated before and after the vibration test (PREVIVE and POSTVIBE) to confirm the consistensy of the instrument performance.

Reference: 26850.03-FULL-FM-CAL-01, 26850.03-PREVIBE-FM-CAL-01, 26850.03-POSTVIBE-FM-CAL-01

3.2.4 ESA RESPONSE TESTING (H30-CAL)

H30-CAL targets ESA performance using wide and uniform beam in H30 laboratory in SwRI. This testing confirmed ESA performance up to ~20 keV/q, and CoDICE high performance were evaluated by using radioactive sources.

Reference: 26850.03-H30-FM-CAL-01

3.2.5 LABORATORIES USED FOR CODICE CALIBRATION

Calibration of the CoDICE instrument was conducted across two primary facilities: the H30 Ion Calibration Chamber for low-to-mid energy ranges and the SwRI High-Energy Particle Accelerator (SHERPA), located at Building H19, for high-energy characterization.

INFORMATION COPY ONLY

(a) H30 Ion Calibration Chamber



This facility is utilized for the H30-CAL calibration procedure, providing an environment for characterization of space-plasma and solar-wind instruments. Central to the laboratory is a 48" diameter by 56" axial length cylindrical vacuum chamber featuring an internal envelope capable of mounting a large 8-cubic-foot instrument suite. To facilitate precise angular and spatial mapping of detector responses, the chamber integrates a 4-axis positioning system that achieves 5µm linear and 0.01 angular accuracy. The testing environment is maintained at high vacuum in the mid 10^{-8} Torr range via all dry vacuum pumping to safeguard sensitive optical and detector surfaces against hydrocarbon contamination.

For multi-species particle stimulation, the chamber is equipped with a Duoplasmatron ion source capable of generating beams from 500 eV to 51 keV/q with a mass resolution of $M/\Delta M = 40$, supplying ions ranging from H^+ to Xe^{1+}. Complementing the ion system are Kimball Physics electron guns operating from 5 eV to 30 keV and a Krypton-line UV lamp that delivers 0.8 to 1.3 solar intensity at 123.6 nm to simulate near-Lyman-alpha solar radiation profiles. Additionally, a 3-axis Helmholtz coil array provides full magnetic field control from 0 to 9 gauss, enabling local geomagnetic field nullification or the simulation of specific planetary magnetospheric baselines during instrument verification.

(b) H19 SwRI High-Energy Particle Accelerator (SHERPA)



This facility is utilized for the TOFE-CAL and FM-CAL calibration procedures. This facility utilizes a sophisticated ion beam system designed for the precise characterization of space-borne instrumentation. The process begins with a Kimball Physics ion gun generating a low-energy beam (<5 keV), which is then refined via a gas inlet system capable of producing species ranging from H^+ to Ar^+. To ensure beam purity, an ExB (Wien) filter is employed for mass selection, allowing only specific charge-to-mass ratios to propagate. These ions are then subjected to post-acceleration to reach high-energy states up to 350 keV/q, simulating the higher-charge state ions or ions in the suprathermal energy range. All testing occurs within a massive 36" diameter by 48" axial length cylindrical chamber, maintained at a high vacuum in the mid 10^{-8} Torr range. To protect sensitive flight hardware from contamination, the system utilizes all dry vacuum pumping, ensuring a hydrocarbon-free environment critical for the TOFE-CAL and FM-CAL procedures.

INFORMATION COPY ONLY

4. CODICE REQUIREMENTS TRACEABILITY

All CoDICE science requirements flow from four mission level requirements:

MRD-L2-185: Solar Wind Composition and Charge States

The Mission shall measure solar wind composition and charge-states for solar wind densities above 3 cm3, as follows:

- Composition C/O, Mg/O, Fe/O
- Composition Accuracy > 50%
- Charge state C6+/C5+, O7+/O6+, Fe(low)/Fe(high)
- Charge state Accuracy > 50%
- Cadence ≤ 1 hour

Traces directly from the L1 baseline science requirement 4.1.1.9.

MRD-L2-18: Pickup Ion Composition

The Mission shall measure pickup ions, as follows:

- Mass Range H to Ne
- Energy range 2 - 70 keV/q
- Energy bands ≥ 5 per decade
- Mass resolution M/ΔM > 2
- Cadence ≤ 1hr for 3D VDFs
- Angular resolution ≤15° for He+

Traces directly from the L1 baseline science requirement 4.1.1.10.

MRD-L2-209: Pickup Ion Isotopic Composition

The Mission shall measure 3He+, 4He+, 20Ne+, and 22Ne+, as follows:

- Composition 3He+, 4He+, 20Ne+, and 22Ne+
- Energy range 2 - 70 keV/q
- Mass resolution (M/q)/Δ(M/q) > 10

Traces directly from the L1 baseline science requirement 4.1.1.10.

MRD-L2-19: Suprathermal Ions

The Mission shall measure suprathermal ions, as follows:

- Energy range 0.05 - 2 MeV/n
- Energy bands ≥ 5
- Mass range H to Fe
- Mass resolution M/ΔM > 4
- Cadence ≤ 1 min for H, ≤ 10 min for He, ≤ 1hr for O and Fe

Traces directly from the L1 baseline science requirement 4.1.1.11.

INFORMATION COPY ONLY

5. CODICE LO

5.1 Electrostatic analyzer performance

The performance of the CoDICE-Lo electrostatic analyzer (ESA) was characterized using an H-30 ion beam. To ensure high-fidelity measurements, the sensor was mounted on a positioning system within the vacuum chamber, providing a translational accuracy of 5 µm and an angular precision of 0.01°. Because the instrument exhibits axisymmetric performance about its rotation axis, the absolute azimuthal angle relative to the sensor aperture was omitted; instead, the evaluation focused on elevation angle performance across multiple azimuthal locations. Notably, the azimuthal coverage of CoDICE-Lo is intentionally incomplete due to internal structural constraints for secondary electrons and physical limitations in the energy detector size.

Figure 5-6 illustrates the sensor's Double Coincidence Rate (DCR, orange) and Triple Coincidence Rate (TCR, blue) responses. These data were collected via a fine 1° azimuthal scan using proton beams at two energy levels: 43.5 keV (upper) and 16.5 keV (lower). To account for the high dynamic range of the data, the counting rates are plotted on a logarithmic scale. The periodic fluctuations observed in both the DCR and TCR highlight the sensor's angular response characteristics, which are modulated by the internal carbon foil support structures.

The energy geometric factor (Energy G-factor, GE) of an electrostatic analyzer, expressed in units of cm² sr eV/eV, is determined by integrating the instrument's response over its angular and energy acceptance ranges. The calculation is performed using the following formula:

$$G_E = \frac{\Delta\varphi}{E_0}\sum_m\sum_n \frac{C_{mn}}{\Phi} E_m \cos\theta_n \Delta E \Delta\theta$$

Where:

- $\Delta\varphi$: The azimuthal angle range of interest.
- E_0: Reference energy.
- E_m: The m-th energy step.
- θ_n: The n-th elevation angle.
- ΔE: Energy step width.
- $\Delta\theta$: Elevation angle step width.
- φ: Incident beam flux.
- C_{mn}: Sensor count rate at the given energy and elevation step.

This process involves a summation over the relevant measurement increments, weighted by their respective count rates and normalized by the incident particle flux to derive the analyzer's Energy G-factor. To ensure precise evaluation of the beam flux (Φ), an Absolute Beam Monitor (ABM) was utilized to calibrate the measurement efficiency independent values by using following formula using coincidence counting of particles between detectors A and B:

INFORMATION COPY ONLY

The beam flux is determined through a coincidence measurement approach. Let C represent the incident rate and A represent the Absolute Beam Monitor (ABM) acceptance area ($\approx 1\text{ cm}^2$). The count rates on detectors A and B are defined as $C_A = \varepsilon_A C$ and $C_B = \varepsilon_B C$, respectively, where ε represents the detection efficiency. The coincidence rate between the two detectors is given by $C_{AB} = \varepsilon_A \varepsilon_B C$.During the CoDICE calibration, the electrostatic analyzer (ESA) voltages for both the entrance and main electrodes are scanned simultaneously while the beam energy remains fixed. This allows the ESA electrode voltages to be swept across the instrument's passband. The elevation angles (α) are physically adjusted using the vacuum chamber's positioning system. By convention, negative elevation angles correspond to particles entering from the "top cap" side, while positive angles correspond to the "electronics box" side.To ensure stability, the beam flux is recorded before and after each angular step following the completion of an energy scan. In the G-factor control mode, the entrance electrode voltage is reduced by a factor of $R = 0.7$ throughout the energy scan. Based on the azimuthal boresight scan (Figure D), the azimuthal detector coverage ($\Delta\phi$) is determined to be approximately 7.5°, which is the value utilized for the final geometric factor calculation.

$$C = \frac{C_{AB}}{C_A C_B}$$

$$\Phi = \frac{C}{A}$$

The beam flux is determined through a coincidence measurement approach. Let C represent the incident rate and A represent the ABM acceptance area (~1 cm^2). The count rates on detectors A and B are defined as $C_A = \varepsilon_A C$ and $C_B = \varepsilon_B C$, respectively, where ε represents the detection efficiency. The coincidence rate between the two detectors is given by $C_{AB} = \varepsilon_A \varepsilon_B C$.

During the CoDICE calibration, the electrostatic analyzer (ESA) voltages for both the entrance and main electrodes are scanned simultaneously while the beam energy remains fixed. This allows the ESA electrode voltages to be swept across the instrument's passband. The elevation angles are physically adjusted using the vacuum chamber's positioning system. By convention, negative elevation angles correspond to particles entering from the "top cap" side, while positive angles correspond to the "electronics box" side.

To ensure stability, the beam flux is recorded before and after each angular step following the completion of an energy scan. In the reduced geometrical factor mode, the entrance electrode voltage is reduced by a factor of R = 0.7 throughout the energy scan. Based on the azimuthal boresight scan (Figure D), the azimuthal detector coverage Δφ is determined to be approximately 7.5°, which is the value utilized for the final geometric factor calculation.

Figure 5-1 illustrates the transmission responses of the CoDICE-Lo instrument showing instantaneous instrument response for double coincidence rate. The results for position coincidence (signles), DCR, and TCR are largely consistent with each other. The angular resolution was ~2.2° in FWHM on average: it keeps ~2.5° up to ~10 keV/q, and decreases slightly down to ~2.0° due to the ion focusing effect at the post accleration sector. The energy resolution was ~6% in FWHM on average. It also decreases

INFORMATION COPY ONLY

from 6% at lower energy ranges down to 5% at ~20 keV/q, while it recovers back to ~6.5% at 80 keV/q. Figure 5-2 presents the dependence of the G-factor on the azimuth (Az) locations of the instrument, specifically at 4 keV/q. The gray markers represent positional coincidence rates, the orange markers indicate double coincidence rates, and the blue markers denote triple coincidence rates, all plotted on a logarithmic scale for enhanced readability. Location number 1 corresponds to the solar wind sector, with sectors rotating clockwise from a top-down view of the sensor's top cap. The graph shows that the G-factor values are consistent across different azimuth locations for each type of coincidence rate, suggesting uniform sensor performance and accurate assembly. Figure 5-3 shows the geometrical factor dependence on incident beam energy, comparing with the modeling results. The gray data shows the positional coincidence rates, orange, the double coincidence rates, and blue, the triple coincidence rates. The solid lines show H-30 beam results with lower energies (<24 keV/q) with a beam rasterizer to cover the entire area of the aperture. The broken line instead shows H-19 beam results with higher energies. The H-19 beam does not fully cover the entire acceptance area around the sensor aperture, and thus GF was underestimated by a factor of 3 for lower energies. The dotted lines show the numerical simulation results with efficiency considered, which explains the laboratory positional and double coincidence results well. The departure of the data from the modeling results at 1 keV/q could be due to the beam deflection by the geomagnetic field. The beam deflection causes the imperfect coverage of the sensor acceptance area around the aperture. Figure 5-4 summarizes the K-factor evaluation results. The data was calculated based on the triple coincidence rates, and the entire energy vs elevation-angle space was considered for the K-factor calculation. The solid lines shows H-30 beam results while the broken line shows H-19 beam results with higher energies. The low-energy side values of H-19 results were overestimated due to the geomagnetic field deflection (cf. Figure 3), while the low-energy side values of H-19 results were underestimated due to the imperfect coverage of the narrow beam. For flight, +16 keV/q result (K = 5.76) in H30 will be used for the entire energy range. Figure 5-5 shows the energy-per-charge dependence of the energy and angular resolution in Full Width Half Maximum (FWHM) for CoDICE-Lo. The solar wind sector was used for these evaluations, and the H30 beam results (solid lines) and the H19 high-energy beam results (dashed lines) are shown for comparison. The double coincidence results (orange lines) and the triple coincidence results (blue lines) are well matching each other.

Table 5-1 summarizes the performance characteristics of the CoDICE-Lo instrument operating in low G-factor mode for 16 keV protons, with the units expressed in cm² str eV/eV. The table compares the low GF and normal GF values for two sectors: Location 1 (RH3) in the solar wind (SW) and 15 (LH5) in the suprathermal (ST) sectors. The low-GF yields a reduction rate of ~0.1 in DCR and ~0.07 in TCR.

5.1.1 Relevant Requirements

- RCODICE-1047: CoDICE Lo shall measure 3D VDFs of pick-up ions He+
- RCODICE-1048: CoDICE Lo energy range for He+ shall be 2 - 18 keV/q for nominal slow solar wind conditions.
- RCODICE-1049: CoDICE Lo energy bands per decade for He+ shall be greater than or equal to 5
- RCODICE-1051: CoDICE Lo time resolution for He+ shall be less than or equal to 1 hr.
- RCODICE-1052: CoDICE Lo angular resolution for He+ shall be less than or equal to 15 degrees.
- RCODICE-1055: CoDICE Lo energy range heavy PUIs shall be 2 - 70 keV/q for nominal slow wind conditions.

INFORMATION COPY ONLY

- RCODICE-1056: CoDICE Lo energy bands per decade for heavy PUIs shall be greater than or equal to 5
- RCODICE-1062: CoDICE Lo shall measure solar wind composition and charge-states for solar wind densities above 3 cm^3.
- RCODICE-1064: CoDICE Lo solar wind composition ratio uncertainty shall be less than 50 percent
- RCODICE-1066: CoDICE Lo solar wind charge state ratio shall be C6+/C5+, O7+/O6+, and Fe(low)/Fe(high) with an uncertainty less than 50 percent.
- RCODICE-1067: CoDICE Lo cadence shall be less than or equal to 1 hr.

5.1.2 Verification Methods

Obtain calibration data through relevant apertures and demonstrate the instrument response for nominal proxy species and energies. Numerical modeling results by particle ray tracing are also used to support the laboratory experiment.

5.1.3 Artifacts

Energy-Angle passbands from CoDICE's flight calibration demonstrate a uniform response through Solar Wind (SW) and Suprathermal (ST) sector entrances across all relevant energies.

- RCODICE-1047: The angular and energy resolutions, as well as the sensor field of view, were confirmed by a relevant beam testing for the entire range of interest (Figures 5-1, 5-5, 5-6).
- RCODICE-1048: The energy range was confirmed with K>5 (Figures 5-4, 5-5).
- RCODICE-1049: The energy resolution and range were confirmed as <0.7 (Figures 5-1, 5-4, 5-5).
- RCODICE-1051: The total geometry factor of the sensor was confirmed to be above 3 x 10^-6 cm^2 str eV/eV for triple coincidence signals at 4 keV/q H equivalent (Figure 5-2, Table 5-1).
- RCODICE-1052: The angular resolution was confirmed (Figure 5-5).
- RCODICE-1055: The energy range was confirmed (Figures 5-4, 5-5).
- RCODICE-1056: The energy resolution and range were confirmed (Figures 5-1, 5-4, 5-5).
- RCODICE-1062: The total geometry factor of the sensor were confirmed to be above 3 x 10^-6 cm^2 str eV/eV for triple coincidence signals at 4 keV/q H equivalent (Figure 5-2, Table 5-1).
- RCODICE-1064: The total geometry factor of the sensor were confirmed to be above 3 x 10^-6 cm^2 str eV/eV for triple coincidence signals at 4 keV/q H equivalent (Figure 5-2, Table 5-1).
- RCODICE-1066: The total geometry factor of the sensor were confirmed to be above 3 x 10^-6 cm^2 str eV/eV for triple coincidence signals at 4 keV/q H equivalent (Figure 5-2, Table 5-1).

INFORMATION COPY ONLY

- RCODICE-1067: The total geometry factor of the sensor were confirmed to be above 3 x 10^-6 cm^2 str eV/eV for triple coincidence signals at 4 keV/q H equivalent (Figure 5-2, Table 5-1).

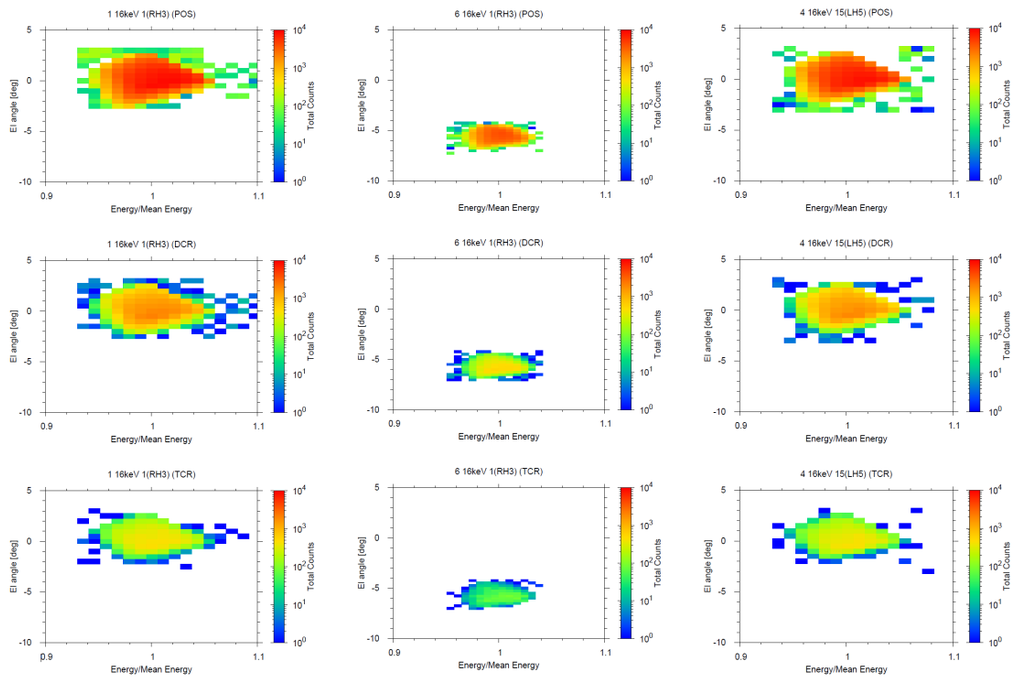


Figure 5-1: ***Transmission responses of CoDICE-Lo instrument for (left) a solar wind sector, (center) a solar wind sector operating at low geometric factor (GF) mode, and a suprathermal sector. The top panels show positional coincidence rate (POS), the middle, double coincidence rate (DCR), and the bottom, the triple coincidence rate (TCR), respectively. The energy of the beam was fixed at 16 keV/q in these cases, and the ESA electrode voltage was scanned around the pass band. The elevation angles (El angles) are physically altered using chamber. The negative elevation angles correspond to the particles from the top cap side, while the positive angles from the electronics box side. The total counts denote the accumulated counts within 10 seconds by the whole sensor.***

INFORMATION COPY ONLY

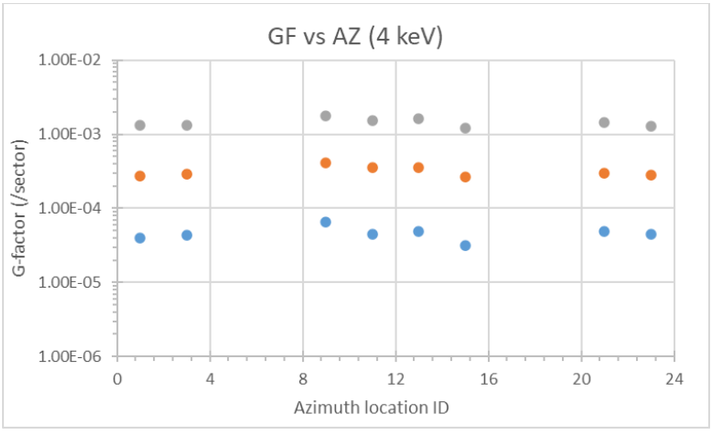


Figure 5-3: *Dependence of the geometric factor (GF) as a function of azimuth (Az) locations on the instrument. The gray data shows the positional coincidence rates, orange, the double coincidence rates, and blue, the triple coincidence rates. The location number 1 is the solar wind sector, and the sector rotates clockwise from top-to-down view from the sensor top cap. The calculation of GF is based on the full energy-angle scan, as presented in Figure 5-1, and 8 locations out of 24 full sensor Az sectors are investigated to investigate the sensor assembling accuracy.*

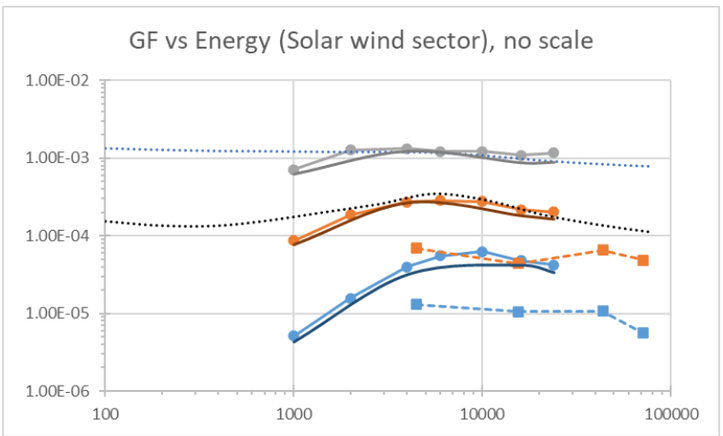


Figure 5-2:*Dependence of the geometric factor (GF) as a function of energy per charge (eV/q) for the solar wind sector.*

INFORMATION COPY ONLY

Table 5-1: ***A summary of low geometric factor (GF) mode performances for CoDICE-Lo evaluated by 16 keV protons. The unit used for GF is cm² str eV/eV. The low-GF mode will be achieved by using factor 0.7 ratio between the entrance and main electrostatic analyzer voltages.***

Sector		Type	Low GF (0.7)	Normal GF	Reduction Rate
1(RH3)	SW	DCR	2.32E-05	2.16E-04	0.107
1(RH3)	SW	TCR	3.43E-06	4.79E-05	0.072
15(LH5)	ST	DCR	2.35E-05	1.81E-04	0.130
15(LH5)	ST	TCR	3.04E-06	4.20E-05	0.072

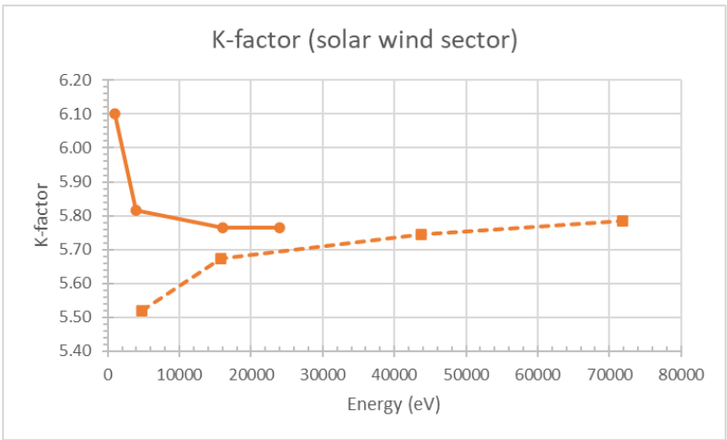


Figure 5-4: *Dependence of the K-factor as a function of energy per charge (eV/q) for the solar wind sector.*

INFORMATION COPY ONLY

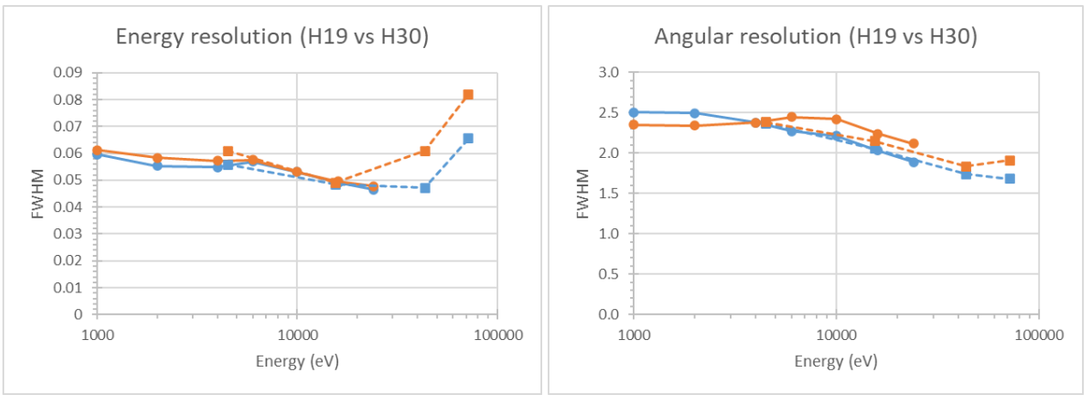


Figure 5-6: *The energy-per-charge dependence of the energy and angular resolution in Full Width Half Maximum (FWHM) for CoDICE-L.*

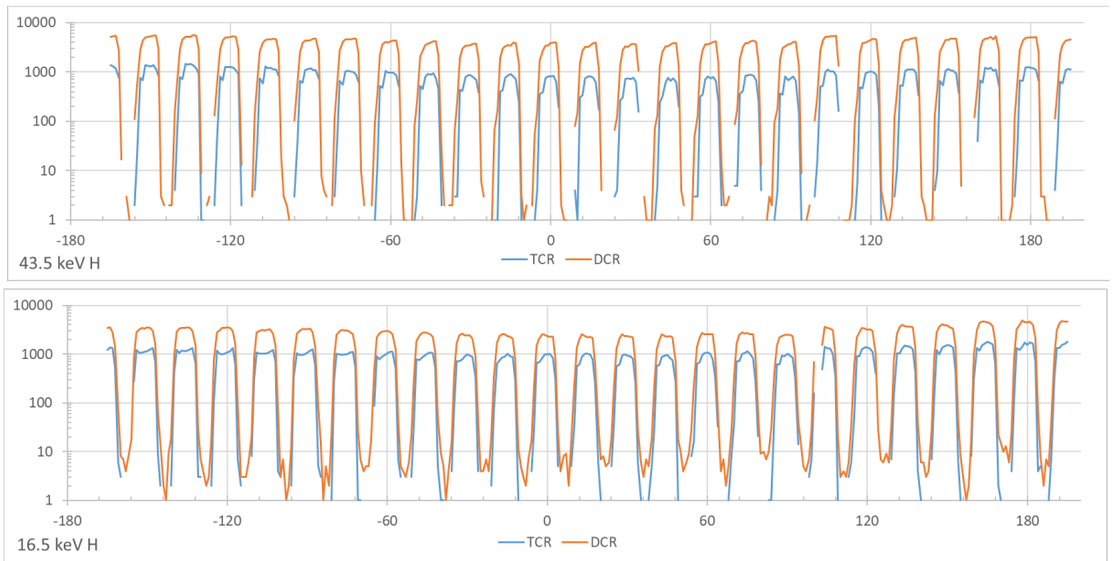


Figure 5-5*: The sensor double coincidence rate (DCR) and the triple coincidence rate (TCR) responses with fine (1°) azimuthal angle scan for the 43.5 keV and 16.5 keV proton beam. The solar wind sector is at +120° in this laboratory coordinate.*

INFORMATION COPY ONLY

5.2 Time of flight and energy measurement performance

The TOF and Energy sector performances were evaluated by injecting the particle beam through the Electrostatic Analyzer (ESA) and post-accelerating it into the TOF-E subsystem. Figure 5-7 through 5-10 summarizes the Mass and Mass per charge resolutions, representing presents the mass per charge resolution (top panel) and mass resolution (bottom panel) for the CoDICE Lo instrument, evaluated over a relevant range of particle masses (1-40 amu) and energies (1-80 keV/q). The data are shown for one right-hand (RH) side and one left-hand (LH) side from the suprathermal (ST) sector in addition to the solar wind (SW) direction. The mass per charge resolution is observed to decrease as the energy per nucleon increases, particularly beyond 10 keV/nuc, while it keeps above 10 for the entire ranges. This trend is consistent across the different sectors and directions. The bottom panel illustrates the mass resolution, expressed as ΔM/M, as a function of energy per nucleon. The mass resolution similarly shows improvement with increasing energy per nucleon due to the higher energy resolution of energy detectors, indicating increased precision in mass measurements. These figures highlight that the CoDICE Lo instrument maintains consistent performance in differentiating particle masses and charge across its operational range, effectively leveraging higher energy particles for enhanced resolution. The APD response shows a clear linear relationship above ~2 keV/nuc, where the resolution was 10-20 keV in FWHM, up to >100 keV/nuc, where the resolution improves 2-3 keV in FWHM. This indicates that the APD detectors accurately track the energy of incoming particles across the range from 1 keV/nuc to approximately 100 keV/nuc. The consistent alignment of data points across different sectors and directions (ST and SW) demonstrates the reliability and uniformity of the CoDICE Lo instrument's capabilities, ensuring precise measurements of particle energies in both the solar wind and suprathermal particle populations.

Figure 5-11 displays accumulate TOF vs E count plots for the suprathermal (ST) sector (17-LH7) of the CoDICE Lo instrument, with data accumulated for several species and energies. The x-axis represents TOF in channels, and the y-axis represents energy (both in ADC channels), with the color scale indicating the count per each channel. The charage state separation capability was confirmed by using vertical separations of H_2^+, N_2^+, and Ar^{2+}+Ne^+.

5.2.1 Relevant Requirements

- RCODICE-1048: CoDICE Lo energy range for He+ shall be 2 - 18 keV/q for nominal slow solar wind conditions.
- RCODICE-1050: CoDICE Lo mass resolution for He+ shall be M / delta M greater than 2.
- RCODICE-1053: CoDICE Lo shall measure pick-up heavy ions
- RCODICE-1054: CoDICE Lo mass range for heavy PUIs shall be 3 to 22 AMU to cover from He3+ up to Ne-22.
- RCODICE-1061: CoDICE Lo composition for PUIs He+ and Ne+ shall be 3He+, 4He+, 20Ne+, and 22Ne+ with a mass per charge resolution greater than or equal to 10.
- RCODICE-1063: CoDICE Lo shall measure solar wind elements. C, O, Mg, and Fe.
- RCODICE-1065: CoDICE Lo shall measure the solar wind charge state of C, O, Mg, and Fe.
- RCODICE-1066: CoDICE Lo solar wind charge state ratio shall be C6+/C5+, O7+/O6+, and Fe(low)/Fe(high) with an uncertainty less than 50 percent.
- RCODICE-1185: CoDICE shall provide Solar wind charge state less than 1 hour cadence, with composition C/O, Mg/O, Fe, O and charge state C6+/C5+, O7+/O6+, Fe(low)/Fe(high) to the spacecraft as part of its space weather TM packet

INFORMATION COPY ONLY

5.2.2 Verification Methods

Obtain calibration data through relevant apertures and demonstrate the instrument response in the time-of-flight and energy for a sufficient range of species and energies.

5.2.3 Artifacts

Time-of-flight and energy performance from CoDICE's flight calibration demonstrate a sufficient mass, energy, and charge state resolutions across the relevant energies and species.

- RCODICE-1048: CoDICE-Lo He+ energy range for mass analysis was confirmed by Figures 5-7, 5-8, 5-9. Note that He+ relevant range in those figures are from 4.25 to 8.25 keV/n considering the -15 kV post acceleration support.
- RCODICE-1050: The mass resolution was confirmed to be >2 by the beam testing with relevant energy per nucleon range (2 to 64 keV/n) (Figure 5-8).
- RCODICE-1053: Energy per nucleon range confirms ass coverage confirms up to mass 120 for typical slow solar wind (400 km/s), and up to mass 40 for fast solar wind (700 km/s) (Figures 5-7, 5-8, 5-9). The pick up ion cutoff can be detected up to mass 30 for slow solar wind, and up to mass 10 for the fast solar wind.
- RCODICE-1054: Energy per nucleon range confirms ass coverage confirms up to mass 120 for typical slow solar wind (400 km/s), and up to mass 40 for fast solar wind (700 km/s) (Figures 5-7, 5-8, 5-9). The pick up ion cutoff can be detected up to mass 30 for slow solar wind, and up to mass 10 for the fast solar wind.
- RCODICE-1061: Figure 5-8 (left) confirms mass per charge resolution (relevant for the singly charged pick up ions) above >10 over the relevant range (2 to 64 keV/n).
- RCODICE-1063: Typical C, O, Mg, and Fe ions in the solar wind have positive charge states of 5-6, 6-7, 8-10, and 10-16. These falls into energy per nucleon range from 3.5 keV/n upto 10.1 keV/n considerting typical range of the solar wind speed, and both mass per charge resolution >10 and mass resolution >2 requirements will be met in that energy range (Figures 5-8). Also, the energy per charge range (Figure 5-4) covers all of these elements for the slow solar wind, and C, O, Mg will be fully covered under the fast solar wind.
- RCODICE-1065: Typical C, O, Mg, and Fe ions in the solar wind have positive charge states of 5-6, 6-7, 8-10, and 10-16. These falls into energy per nucleon range from 3.5 keV/n upto 10.1 keV/n considerting typical range of the solar wind speed, and both mass per charge resolution >10 and mass resolution >2 requirements will be met in that energy range (Figures 5-8). Also, the energy per charge range (Figure 5-4) covers all of these elements for the slow solar wind, and C, O, Mg will be fully covered under the fast solar wind. Further, Figure 5-10 and 5-11 confirm charge state separation capability of CoDICE-Lo.
- RCODICE-1066: The energy per charge resolution to be less than 5% (Figure 5-5), Mass per charge and Mass resolution (Figure 5-8, RCODICE-1050 and 1061) confirms the performance to meet with this requirement.
- RCODICE-1185: This is a lower-level requirement of RCODICE-1066 in terms of the sensor performance.

INFORMATION COPY ONLY

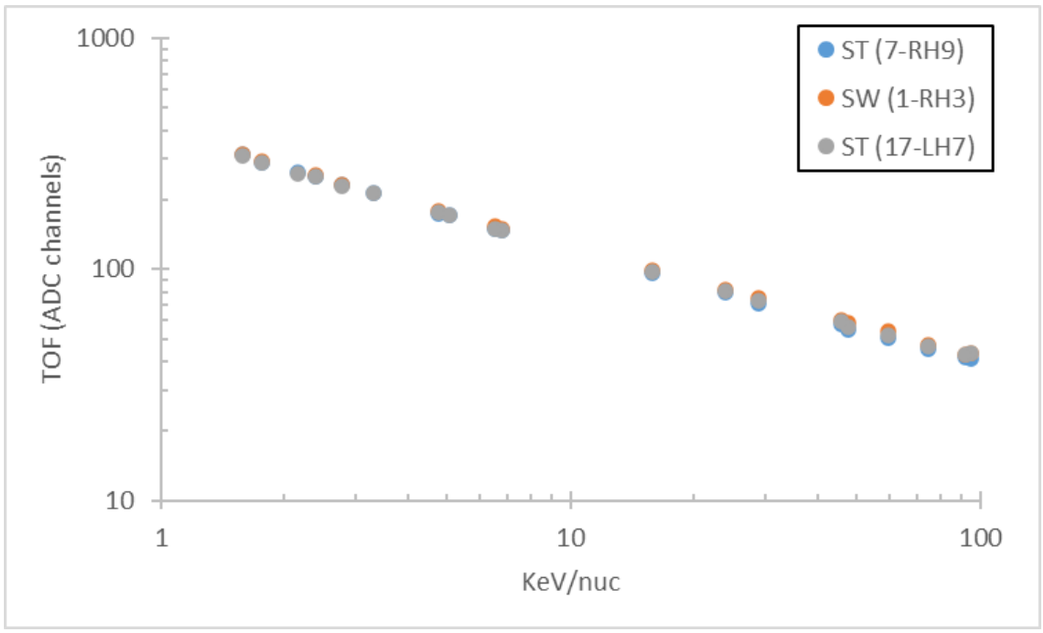


Figure 5-7: *The mean TOF values in the system (in the unit of TOF channels) as a function of the incident particle's energy per nucleon for CoDICE Lo. The plotted data are selected for one RH side and one LH side for the suprathermal (ST) sector, and the solar wind (SW) direction. The beam was injected through the ESA and the post acceleration to the TOF subsystem.*

INFORMATION COPY ONLY

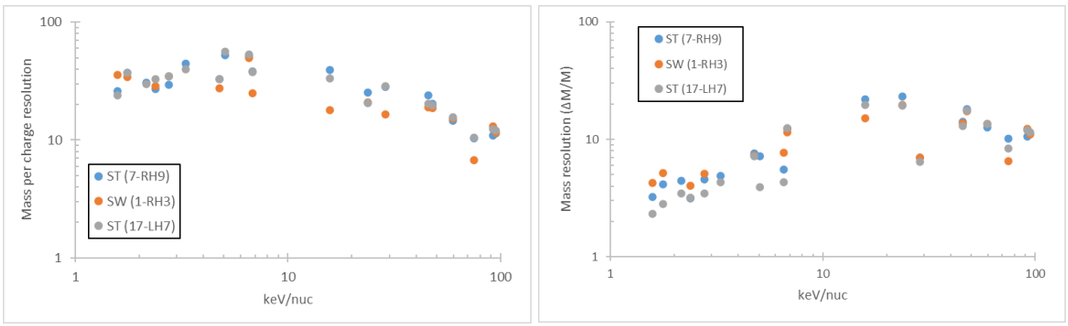


Figure 5-8: *Mass per charge resolutions (left) and Mass resolutions (right) for CoDICE Lo evaluated by a relevant range of particle mass (1-40) and energy (1-80 keV/q). The plotted data are selected for one RH side and one LH side for the suprathermal (ST) sector, and the solar wind (SW) direction. The beam was injected through the ESA and the post acceleration to the TOF subsystem.*

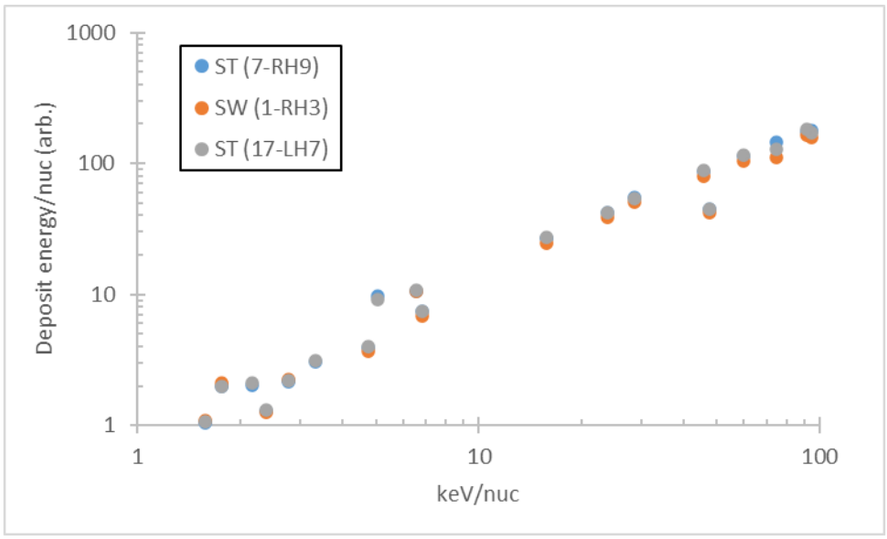


Figure 5-9: *The detected energy per nucleon for all APDas a function of the incident energy per nucleon. The plotted data are selected for one RH side and one LH side for the suprathermal (ST) sector, and the solar wind (SW) direction. The beam was injected through the ESA and the post acceleration to the TOF subsystem.*

INFORMATION COPY ONLY

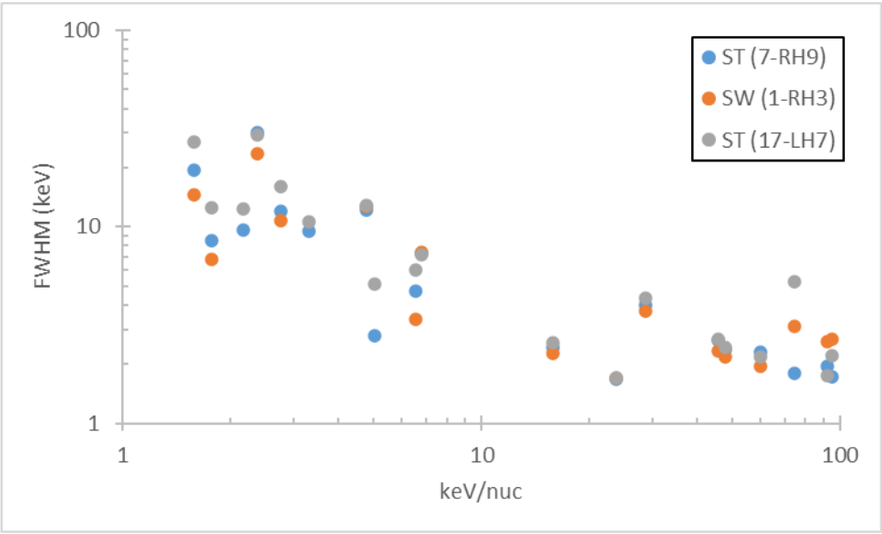


Figure 5-10: *The detected energy resolution (in keV) for all APDas a function of the incident energy per nucleon. The plotted data are selected for one RH side and one LH side for the suprathermal (ST) sector, and the solar wind (SW) direction. The beam was injected through the ESA and the post acceleration to the TOF subsystem.*

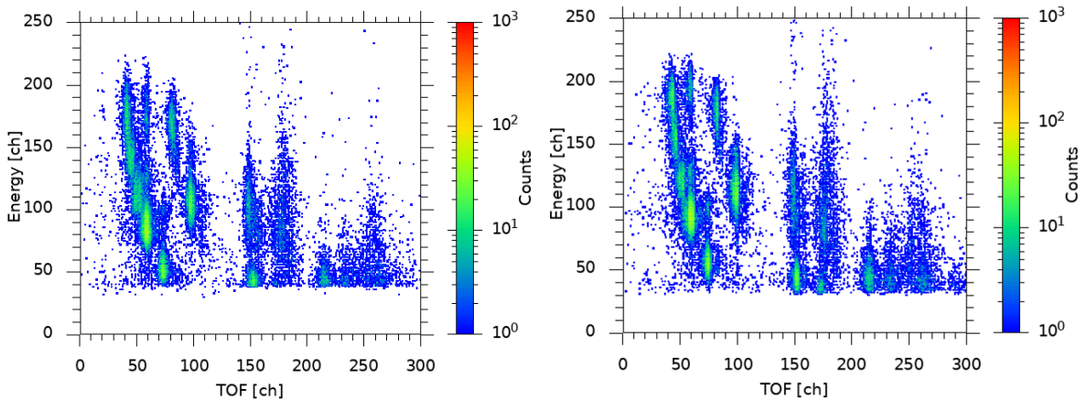


Figure 5-11: *The TOF vs energy count plots for the SW (1-RH3, left) and ST (17-LH7, right), accumulating several species and energies. The charage state separation capability was confirmed by using vertical separations of H_2^+, N_2^+, and Ar^{2+}+Ne^+. The beam was injected through the ESA and the post acceleration to the TOF subsystem.*

INFORMATION COPY ONLY

6. CODICE HI

6.1 Time of flight and energy measurement performance

Figure 6-1 through 6-4 summarizes the TOF and E performance of CoDICE Hi. The top plot illustrates the expected mass resolutions, evaluated by combining TOF and E measurements, as a function of the incident particle's energy per nucleon. The plotted data include selected measurements from one right-hand (RH) side (gray for 3-RH3) and one left-hand (LH) side (blue for 8-LH1 and orange for 12-LH4) in the suprathermal (ST) sector, along with the sun-direction (LH1). For lower energy regions, proton and helium ion beams were used, while the highest energy measurements were acquired using a Thorium-228 radioactive source. At lower energies (10 to 300 keV/n), the mass resolution stays at values around 6 to 9, while it keeps > 3 beyond 2 MeV/nuc. This trend is consistent across different sectors and directions, indicating reliable performance of the mass resolution capabilities irrespective of the measurement direction. Performance for other channels are now shown since they are similar. Overall, the figure validates the CoDICE Hi system's efficient performance in resolving mass for a range of particle energies and highlights the improved accuracy at higher incident energies. The bottom panel illustrates the energy resolution (ΔE/E) as a function of the incident particle's total energy for the CoDICE Hi system for the same selected channels from the same set of data. The energy resolution keeps around 0.1 at the lowest total energy range ~150 keV, while improving towards the highest energy range to ~0.01 due to the increase of signal charges. Overall, the CoDICE Hi system demonstrates robust energy resolution performance across a broad range of total incident energies. Based on the test pulse measurement, CoDICE-Hi will cover up to 100 to 150 MeV in total energy depending on the location. This variation was caused by the properties of charge splitting circuit on SEB.

6.1.1 Relevant Requirements

- RCODICE-1069: CoDICE Hi shall measure suprathermal ions.
- RCODICE-1070: CoDICE Hi mass resolution for suprathermal ions shall be M over Delta M greater than 4.
- RCODICE-1073: CoDICE Hi shall measure suprathermal protons.
- RCODICE-1074: CoDICE Hi energy range for suprathermal protons shall be 0.05 - 2 MeV.
- RCODICE-1075: CoDICE Hi energy bands per decade for suprathermal protons shall be greater than or equal to 5.
- RCODICE-1077: CoDICE HI shall measure suprathermal helium.
- RCODICE-1078: CoDICE Hi energy range for suprathermal helium shall be 0.05 - 2 MeV/n.
- RCODICE-1079: CoDICE Hi energy bands per decade for suprathermal helium shall be greater than or equal to 5.
- RCODICE-1081: CoDICE Hi shall measure suprathermal ions O and Fe.
- RCODICE-1082: CoDICE Hi energy range for suprathermal ions O and Fe shall be 0.05 - 2 MeV/n.
- RCODICE-1185: CoDICE shall provide the following measurements to the spacecraft as part of its space weather TM packet. - Space weather protons 1 min. cadence with 4 look directions, 4 spin sectors, an energy range of 0.05 - 2 MeV, and greater than 5 energy bands. - Space weather electron measurement less than 1 minute cadence, 4 look directions, 4 spin sectors, energy range from 0.1 - 0.5 MeV and greater than or equal to 5 energy bands.

INFORMATION COPY ONLY

6.1.2 Verification Methods

Obtain calibration data through relevant apertures and demonstrate the instrument response for nominal proxy species and energies.

6.1.3 Artifacts

Time-of-flight and energy performance from CoDICE's flight calibration demonstrate a sufficient mass, energy, and charge state resolutions across the relevant energies and species.

- RCODICE-1069: Confirmed through suprathermal particle measruements (Fig. 6-1, 6-2, 6-3, 6-4).
- RCODICE-1070: Confirmed through relevant energy per nucleon range (Fig. 6-3).
- RCODICE-1073: Confirmed through energy per nucleon performance which assimilates the propon measurement performance over relevant range (Fig. 6-1, 6-2, 6-3, 6-4).
- RCODICE-1074: Confirmed through energy per nucleon performance which assimilates the propon measurement performance over relevant range (Fig. 6-1, 6-2, 6-3, 6-4).
- RCODICE-1075: Confirmed energy resolution <0.7 for up to total energy ~9 MeV (Fig. 6-4).
- RCODICE-1077: Confirmed through energy per nucleon performance which assimilates the helium measurement performance (Fig. 6-1, 6-2, 6-3, 6-4).
- RCODICE-1078: Confirmed through energy per nucleon performance which assimilates the helium measurement performance (Fig. 6-1, 6-2, 6-3, 6-4).
- RCODICE-1075: Confirmed energy resolution <0.7 for up to total energy ~9 MeV (Fig. 6-4).
- RCODICE-1081: Confirmed through energy per nucleon performance which assimilates the Oxygen and Iron measurement performance (Fig. 6-1, 6-2, 6-3, 6-4).
- RCODICE-1185: This is a lower-level requirement of RCODICE-1069 in terms of the sensor performance.

INFORMATION COPY ONLY

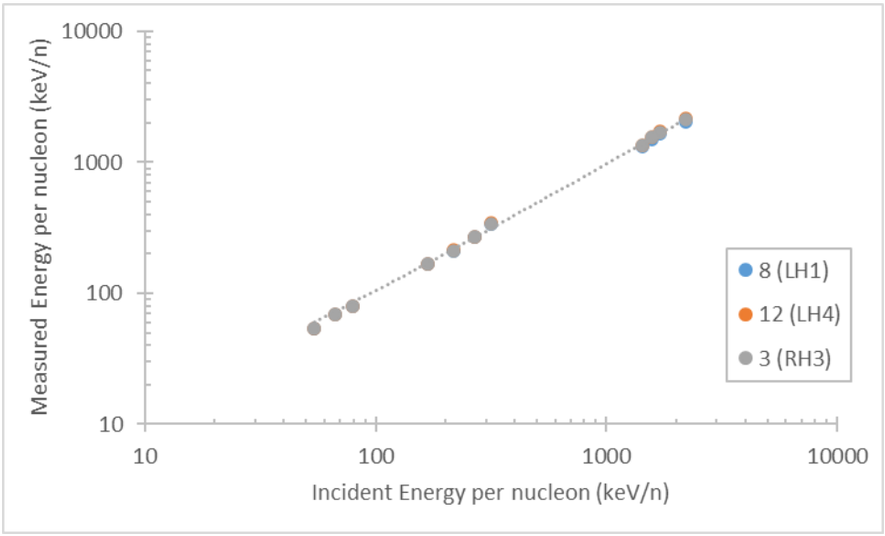


Figure 6-1: *The mean energy per nucleon distributions evaluated by TOF values in the system as a function of the incident particle's energy per nucleon for CoDICE Hi. The plotted data are selected for one RH side and one LH side for the suprathermal (ST) sector, and the sun-direction (LH1). The lower energy parts were evaluated by proton and Helium ion beams, and the highest end was evaluated by the Thorium 228 radioactive source.*

INFORMATION COPY ONLY

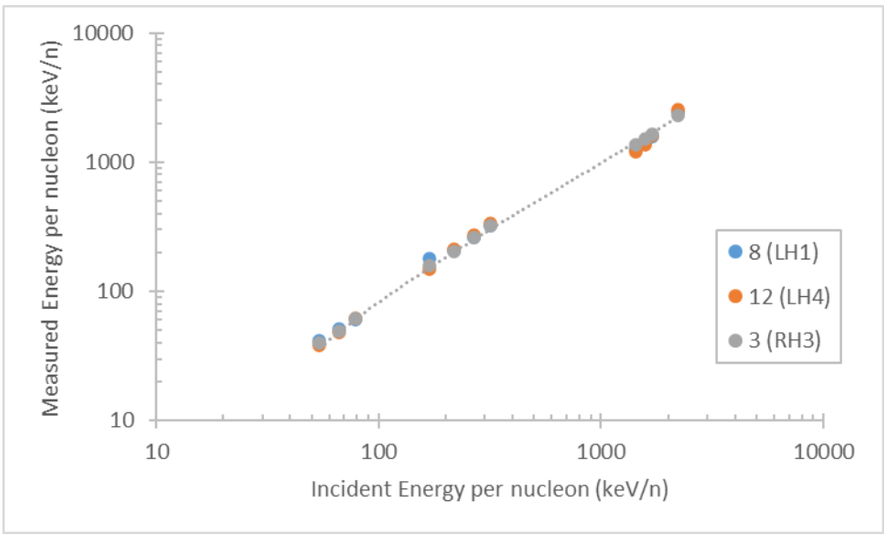


Figure 6-3: *The mean energy per nucleon distributions evaluated by Energy values in the system as a function of the incident particle's energy per nucleon for CoDICE Hi. The plotted data are selected for one RH side and one LH side for the suprathermal (ST) sector, and the sun-direction (LH1). The lower energy parts were evaluated by proton and Helium ion beams, and the highest end was evaluated by the Thorium 228 radioactive source.*

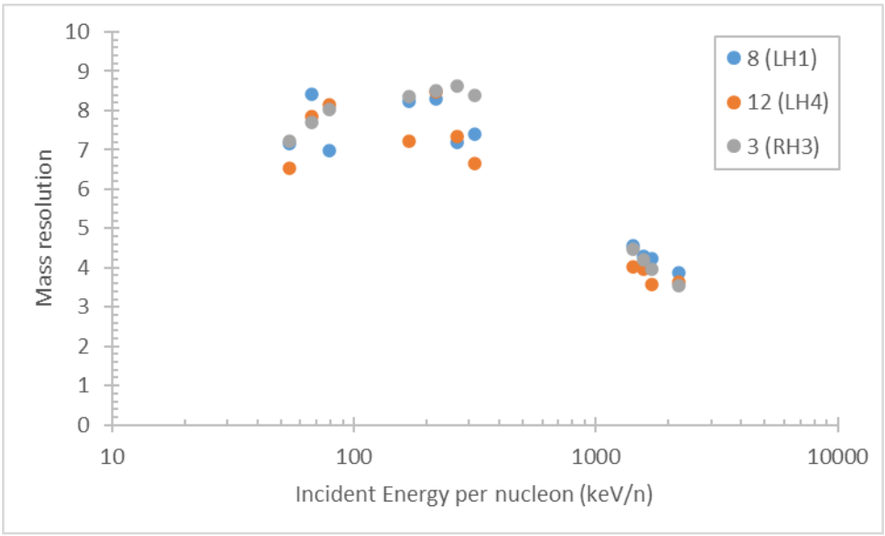


Figure 6-2:*The expected mass resolutions evaluated by combining TOF and Energy values in the system as a function of the incident particle's energy per nucleon for CoDICE Hi. The plotted data are selected for one RH side and one LH side for the suprathermal (ST) sector, and the sun-direction (LH1). The lower energy parts were evaluated by proton and Helium ion beams, and the highest end was evaluated by the Thorium 228 radioactive source.*

INFORMATION COPY ONLY

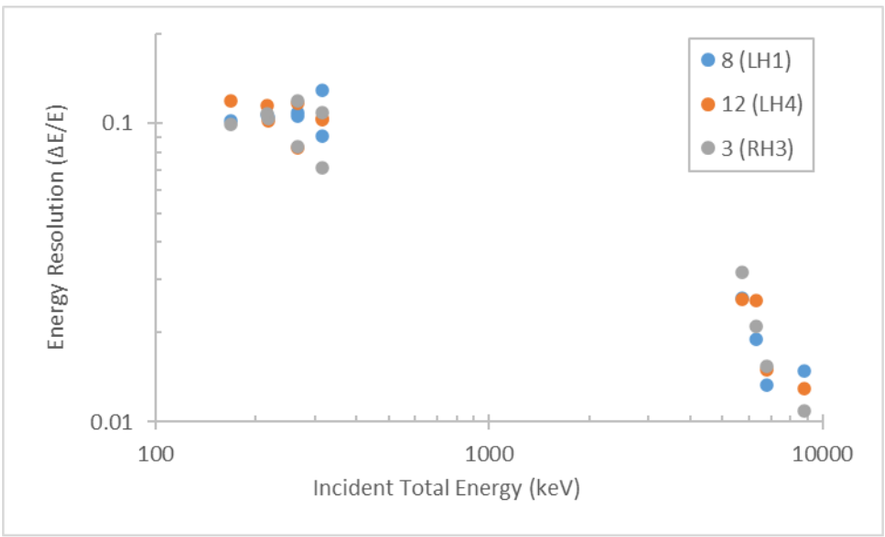


Figure 6-4: *The energy resolution as a function of the incident particle's total energy for CoDICE Hi. The plotted data are selected for one RH side and one LH side for the suprathermal (ST) sector, and the sun-direction (LH1). The lower energy parts were evaluated by proton and Helium ion beams, and the highest end was evaluated by the Thorium 228 radioactive source.*

Table 6-1*: Maximum energy coverage for CoDICE Lo from test pulse measurements.*

Channel	LH1	LH2	LH3	LH4	LH5	LH6	RH1	RH2	RH3	RH4	RH5	RH6
Rate index	8	9	11	12	13	15	0	1	3	4	5	7
Max energy (MeV)	157	139	152	121	127	146	124	108	109	103	150	122
MeV/nuc for Fe	2.8	2.5	2.7	2.2	2.3	2.6	2.2	1.9	1.9	1.8	2.7	2.2

INFORMATION COPY ONLY

6.2 Geometrical acceptance evaluation

CoDICE-Hi physical gometric factor is 0.37 cm^2 str for 12 sectors without efficiency considered, as calculated by the SIMION model. Figure 6-5 presents the angular coverage evaluation results for the CoDICE Hi instrument, with separate analyses of elevation angle scans and horizontal angle scans. The left figure showcases elevation angle scans comparing two locations in DCR using a 300 keV H^+ beam. The comparison involved prototype apertures equipped with thin (non-flight) and thick (i.e., flight-like) foils without ESA installed. The Gaussian-like curves indicate a consistent angular response nearly independent of the foil thicknesses. The right figure shows the horizontal angle scans for two adjacent apertures, evaluating the horizontal coverage using the full flight configuration with the Thorium-228 radioactive source in DCR and TCR rates. These angular coverage evaluations affirm that CoDICE Hi has reliable and consistent elevation and horizontal coverage. We also confirmed the efficiency and TOF performance uniformities using a 300 keV H^+ beam and a Thorium-228 radioactive source across all 12 apertures of the CoDICE Hi instrument (Figure 6-6). Its whole sky coverage capabilities are cnofirmed by the laboratory testing. These laboratory testing confirms this ray-tracing model from two slices on the elevation angle and horizontal angle. The uniformity of the responses over all apertures was also confirmed with the horizontal scan testing.

6.2.1 Relevant Requirements

- RCODICE-1076: CoDICE HI cadence for suprathermal protons shall be less than or equal to 1 min.
- RCODICE-1080: CoDICE HI cadence for suprathermal helium shall be less than or equal to 10 min.
- RCODICE-1083: CoDICE Hi energy bands per decade for suprathermal ions O and Fe shall be greater than or equal to 5.
- RCODICE-1084: CoDICE HI cadence for suprathermal ions O and Fe shall be less than or equal to 1 hr.

6.2.2 Verification Methods

Obtain calibration data through relevant apertures and demonstrate the instrument response for nominal proxy species and energies. Numerical modeling results by particle ray tracing are also used to support the laboratory experiment.

6.2.3 Artifacts

Angle passbands from CoDICE's flight calibration demonstrate consistent telescope geometry across all relevant energies. With the support of numerical modeling, CoDICE-Hi FOV and geometrical efficiency performances are confirmed.

- All of the requirements in this section can be met with the geometric factor > 0.004 cm^2 str from our ray-tracing model. The laboratory testing (Fig. 6-5) confirms this ray-tracing model from two slices on the elevation angle and horizontal angle, which is consistent with the gometric factor of 0.045 cm^2 str. The uniformity of the responses over all apertures was also confirmed with the horizontal scan testing (Fig. 6-6).

INFORMATION COPY ONLY

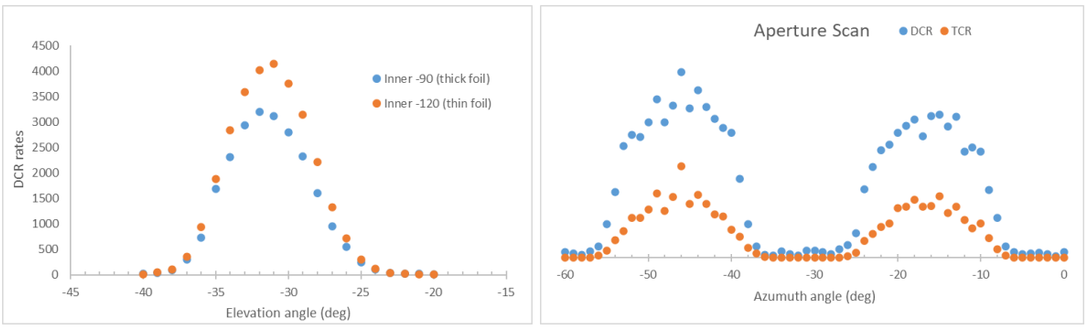


Figure 6-6: *The angular coverage evaluation results for CoDICE Hi. The left figure shows elevation angle scans comparing two locations in DCR using 300 keV H^+ beam due to the configuration restriction of the beam facility on the angular scan capability, this testing was conducted using prototype apertures with thin and thick (i.e., flight-like) foils without ESA installed. The right figure shows horizontal angle scans for two adjacent apertures evaluating the horizontal coverage. This testing was conducted with the full flight configuration using the Thorium-228 radioactive source.*

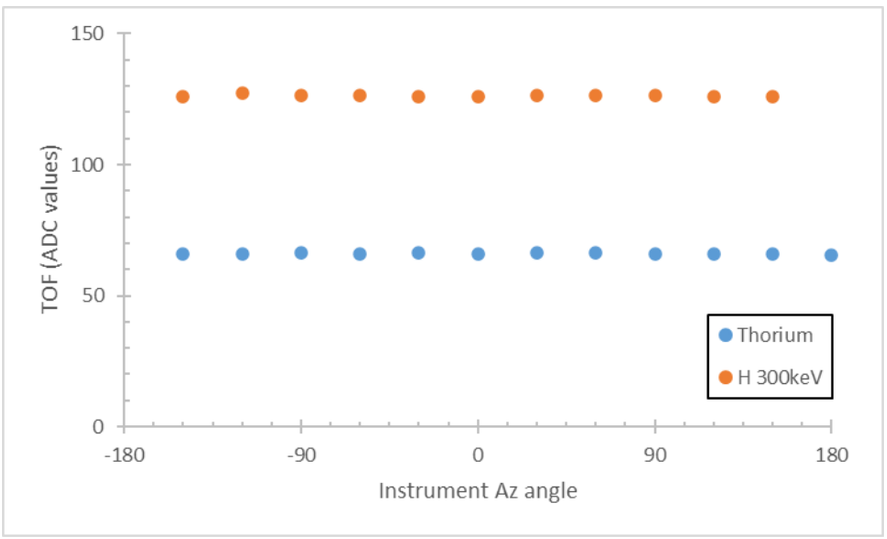


Figure 6-5: *The TOF measurement using 300 keV H^+ beam and Thorium-228 radioactive source for all 12 apertures, confirming the whole sky coverage of the instrument. The beam test could not evaluate 180 deg channel (LH5) due to the restriction by the rotation stage motion.*

INFORMATION COPY ONLY

7. CONCLUSION

CoDICE's science requirements have been verified through the combination of testing and analysis via artifacts included in this memo. Results demonstrate that the instrument will meet all of its science requirements and is expected to exceed them in many ways.

3.2.3 In-Flight Calibrations

CoDICE in-flight calibration report to be included here.

3.3 HIT

3.3.1 Strategy & Approach

HIT conducted calibrations using three different facilities plus detailed simulations of the instrument response.

The HIT response to relatively low-energy ions was studied at the Tandem Van de Graaff Facility at the Brookhaven National Laboratory (BNL). A limited run at the NASA Space Radiation Laboratory (NSRL) enabled calibration of HIT using high-energy (¿100 MeV/n) Fe beams. The HIT instrument was also tested using a ^{228}Th source. This radioactive element is known to emit a number of monoenergetic helium nuclei, making the ^{228}Th an excellent α-calibration source. The most dominant energy alphas are 5.340, 5.685, 6.288, 6.778 and 8.785 MeV; the last one is energetic enough to generate a statistically-significant signal in the L2 sensors. The full range of the HIT instrument was also simulated in Geant4, which resulted in comprehensive response functions across the full range of the instrument plus some estimate of background responses to shield-penetrating particles, such as cosmic rays.

HIT's electronics were calibrated using a series of pulser tests for the pulse-height ASIC chips. The front-end electronics

3.3.2 Pre-Flight Instrument Calibration

HIT cal report embedded below

Facility	Ion Species	Energies (MeV/n)
Tandem	H	5, 15, 20
Tandem	O	6, 7.79
Tandem	Si	4.62, 6.51
NSRL	Fe	129, 142, 149, 155, 190

Table 1: *List of ion species and energies used at the Brookhaven National Laboratory facilities.*

1 Accelerator-Beam and Radioactive-Source Tests

1.1 BNL Tandem Van de Graaff Facility

The HIT response to relatively low-energy ions was studied at the *Tandem Van de Graaff Facility* at the *Brookhaven National Laboratory* (BNL). Specifically, we used mono-energetic H, O, and Si ion beams (see Table 1), corresponding to events triggering both L3A and L3B (Range 4), events triggering only an L1, and L2 and L3 on the same side (Range 3), and events triggering only an L1 and an L2 on the same side (Range 2), respectively. The test objectives were: determine an ADC-energy calibration for each detector segment; test dynamic threshold modes; and test both high-gain and low-gain channels.

1.2 BNL NASA Space Radiation Laboratory

We also took advantage of a limited run at the *NASA Space Radiation Laboratory* (NSRL) using high-energy ($>$100 MeV/n) Fe beams. Specifically, five monoenergetic beams were used (see Table 1). In order to decelerate incident ions and obtain a spread of particle energies, we used a thin, plastic mesh material in front of the selected instrument aperture. In addition, we employed a thin copper thin copper layer to produce lighter ions by fragmentation/spallation.

1.3 Radioactive-Source Tests

The HIT instrument has also been tested using a ^{228}Th source. This radioactive element is known to emit a number of monoenergetic helium nuclei, making the ^{228}Th an excellent α-calibration source. The most dominant ones are 5.340, 5.685, 6.288, 6.778 and 8.785 MeV; the last one is energetic enough to generate a statistically-significant signal in the L2 sensors. As an example, Figure 1 shows the ^{228}Th test results for the L1A2 detector. The left panel displays the spectrum produced by the α particles, with peaks identified with the aid of simulations; a few peaks associated with internal pulsers are also visible. The resulting ADC-to-MeV calibration curve is reported in the right panel, along with the fit results.

2 Monte-Carlo Simulations

The HIT response to ions and its performance have also been investigated with the Geant4 package. The simulation implements a complete description of the electromagnetic and hadronic interactions undergone by incident ions, along with an accurate description of instrument geometry based on mechanical drawings. Simulations were also employed to help the interpretation

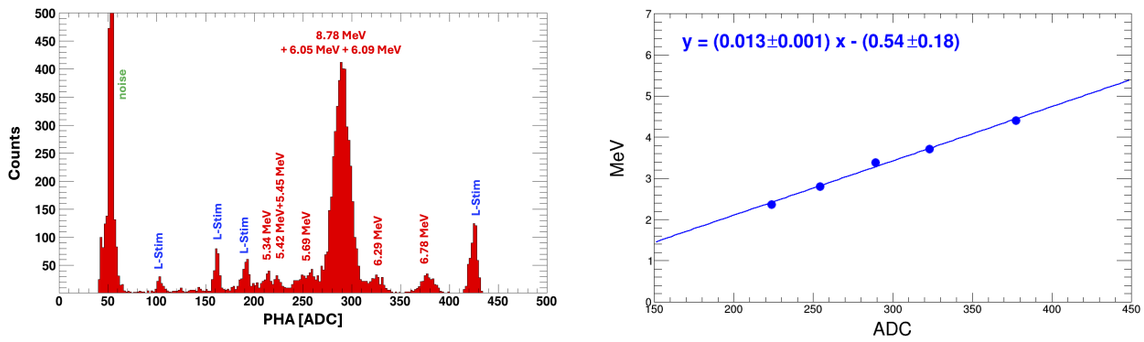


Figure 1: *Calibration of the L1A2 detector with the ^{228}Th source. Left: spectrum produced by the different α particles, with corresponding incident energy values; a few live-stim pulses are also visible. Right: the resulting calibration curve using the distributions estimated with Geant4 simulations; the fit parameters are also reported, along with corresponding uncertainties.*

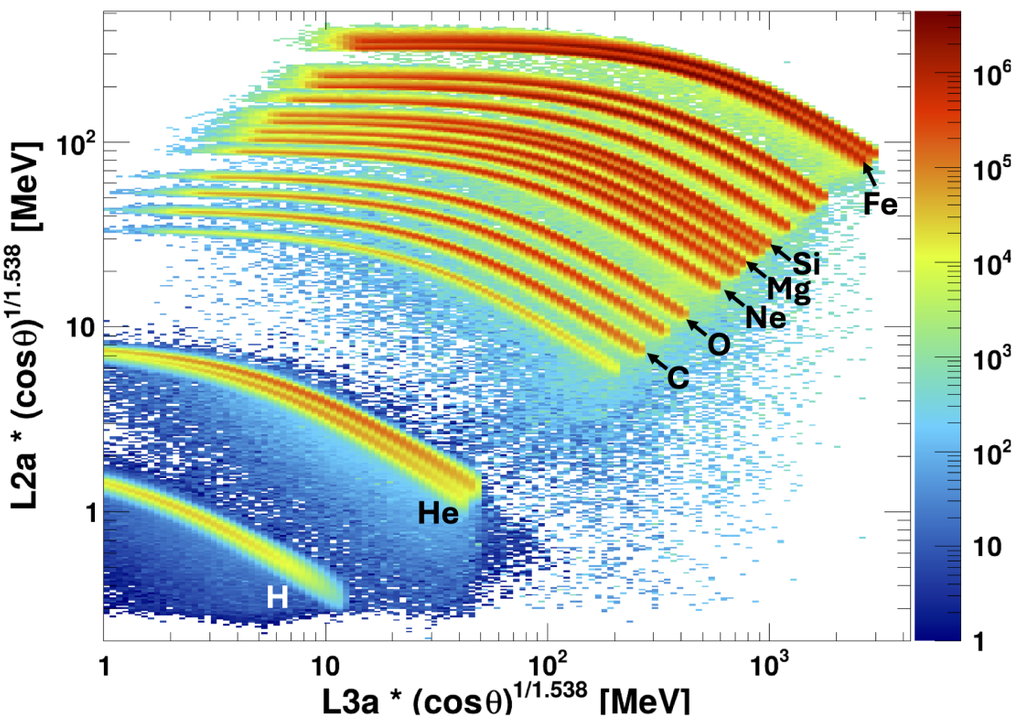


Figure 2: *Geant4 simulation of the HIT response to ions (from H to Ni) incident from the A side and stopping in L3A detector (Range 3). The tracks of most common ion species considered in the HIT requirements are marked. In the case of helium, the ^3He and ^4He isotopes are distinguishable.*

of experimental data, explore a more extensive parameter space with respect to beam tests, and develop appropriate calibration curves.

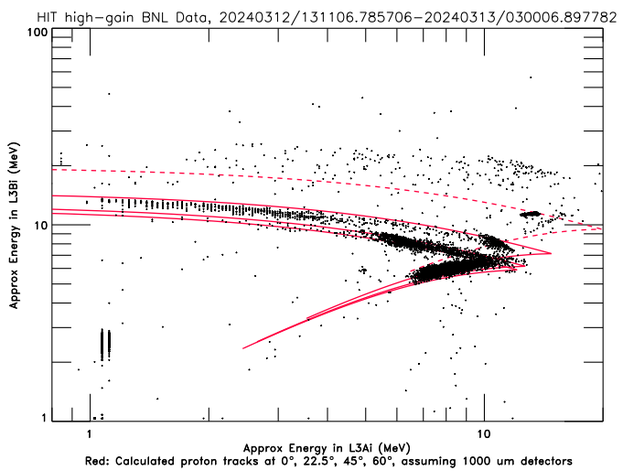


Figure 3: *L3B vs. L3A scatterplot using the proton data acquired at BNL/Tandem, incident from different detector apertures on the B side. The red curves show the expected tracks at different inclination angles.*

3 HIT Requirements

3.1 RHIT-1046: Distinguish all common energetic ion species (H, He, C, O, Ne, Mg, Si, and Fe)

This objective was achieved at BNL, using the H, O, and Si beams at the Tandem and the Fe beams at the NSRSL. The identification/classification of intermediate ion species such as He, C, Ne, and Mg was carried out by interpolation; in the case of helium, we also used the radioactive source runs. In addition, the instrument performance was verified with simulations. As an example, Figure 2 reports the simulated response to ions incident from the A side and stopping at the L3A detector. In particular, the tracks corresponding to H, He, C, O, Ne, Mg, Si, and Fe ions are marked. The distributions are corrected for the mean angle of inclination associated with the particle trajectories in the L2 segments. An identical flux intensity was assumed for all species, based on a $E^{-2.5}$ power-law spectrum; the color code indicates the number of counts in each bin. As demonstrated by the plot, the instrument energy resolution enables a clear identification of the tracks of all considered ion species with a high ($\gtrsim$90%) selection efficiency.

3.2 RHIT-1048: Measure protons over an energy range of 2–15 MeV

The HIT response to protons was extensively investigated at BL/Tandem, using different energies and apertures. Specifically, given the used energy values (see Table 1), it was possible to test the distributions corresponding to Range 2, Range 3 and Range 4. As an example, Figure 3 displays the L3B vs. L3A scatterplot, with protons incident from different detector apertures on the B side. The red curves show the expected tracks at different angles of inclination. As checked with simulations, HIT is able to measure protons with energies between $\sim$1.8 and $\sim$19 MeV, clearly encompassing the requirement energy range (2–15 MeV).

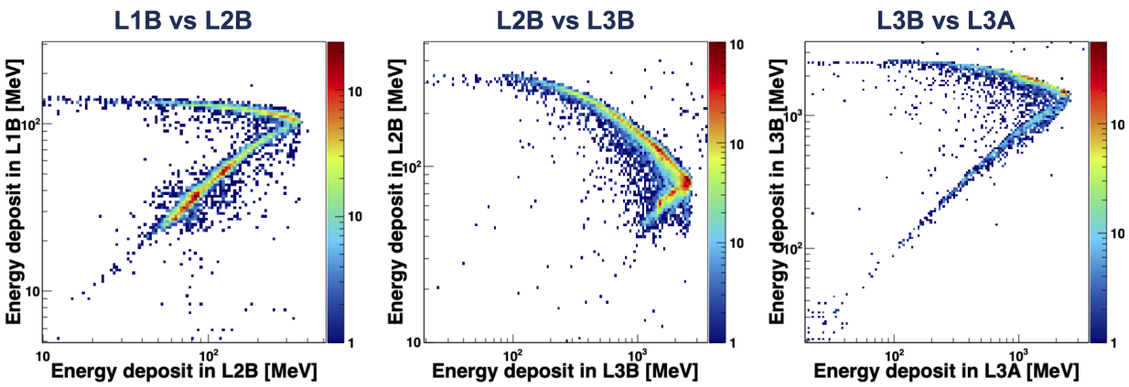


Figure 4: *Energy deposit for different detector combinations obtained with the iron beam at BNL/NSRL. Data include runs made with the beam hitting different apertures, and different iron beam energies.*

	H	He	C	O	Ne	Mg	Si	Fe
Range 2	1.8-5.7	1.8-5.9	3.1-8.1	3.6-8.9	3.8-10.5	4.1-11.4	4.1-12.0	4.7-14.5
Range 3	3.0-14.3	2.9-21.8	5.3-32.9	6.2-38.8	6.7-42.4	7.4-47.3	7.7-52.0	9.4-67.1
Range 4	12.6-19.0	12.6-57.1	23.3-123.9	27.4-127.8	31.1-146.4	34.3-160.7	37.3-166.7	51.2-200
Total	1.8-19.0	1.8-57.1	3.1-123.9	3.6-127.8	3.8-146.4	4.1-160.7	4.1-166.7	4.7-200

Table 2: *Energy ranges (MeV/n) for the different ion species, for particles entering the instrument A side and absorbed in L2A ("range 2"), L3A ("range 3") and L3B ("range 4").*

3.3 RHIT-1049: Measure helium over an energy range of 2–15 MeV/n

Since helium beams were not available at BNL/Tandem, the only He experimental data were collected with the thorium source. However, the requirement was verified by interpolation from other ion species, and by means of Geant4 simulations. Specifically, HIT is expected to measure He ions with energies between ∼1.8 and ∼57 MeV/n, clearly encompassing the requirement energy range (2–15 MeV/n).

3.4 RHIT-1050: Measure common heavy ions over an energy range of 4–30 MeV/n

The HIT response to common heavy ion species was studied at BNL, using beams of different energies (Table 1). In particular, Figure 4 displays the distributions obtained with a Fe beam at BNL/NSRL. As discussed in Section 1.2, a plastic/copper target was placed in front of the detector to provide a wide distribution of particle ranges entering the telescope. The experimental observations were supported by the Geant4 simulations, enabling a full characterization of the instrument response to the different ion species. For example, Figure 2 shows the ion tracks obtained for Range 3; they correspond to hydrogen between ∼3–14 MeV, helium between ∼2.9–18 MeV/n, carbon between ∼5.3–33 MeV/n, oxygen between ∼6.2–39 MeV/n, neon between ∼6.7–42 MeV/n, magnesium between ∼7.4–47 MeV/n, silicon between ∼7.7–52 MeV/n and iron between ∼9.4–67 MeV/n. Results are also reported in Table 2, along with the total energy ranges (including Ranges 2, 3 and 4). Specifically, we estimated that HIT is able to measure

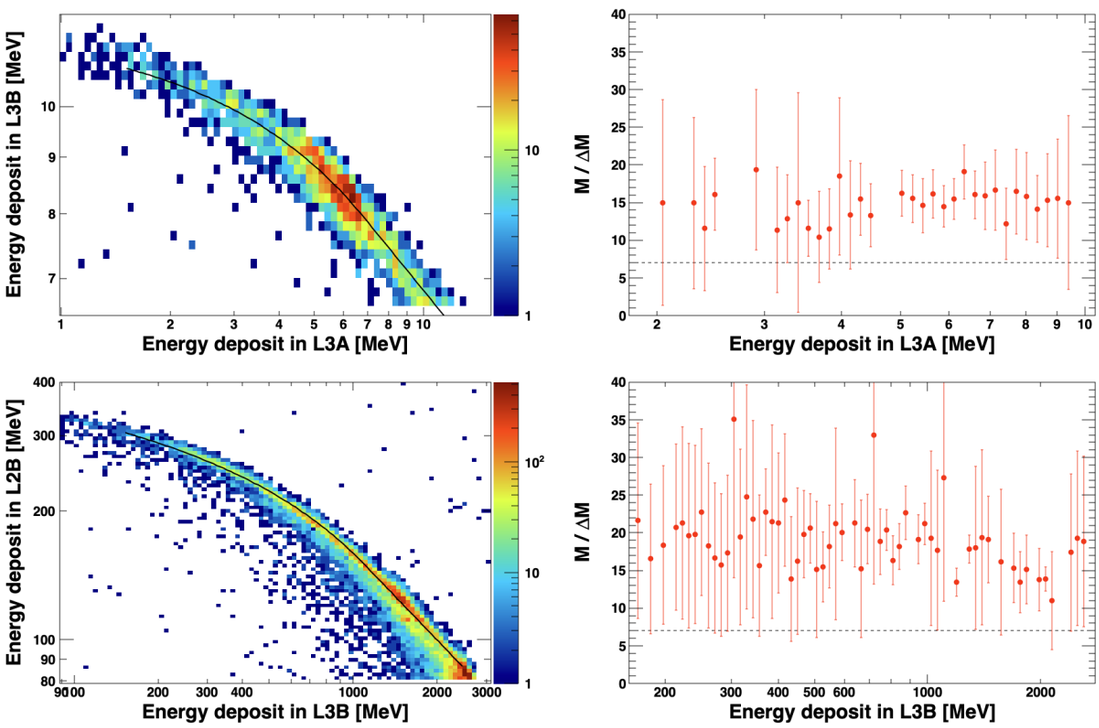


Figure 5: *Left: experimental distribution obtained for hydrogen (top) and iron (bottom) nuclei at BNL; the solid curves indicate the mean value estimated with simulations. Right: corresponding mass resolution graphs, with uncertainties; the horizontal dotted lines mark the minimum requested value, M/ΔM=7.*

carbon between ∼3.1–124 MeV/n, oxygen between ∼3.6–128 MeV/n, neon between ∼3.8–146 MeV/n, magnesium between ∼4.1–161 MeV/n, silicon between ∼4.1–167 MeV/n and iron between ∼4.7–200 MeV/n, in line with the instrument requirements.

3.5 RHIT-1051: Have a mass resolution of M/ΔM > 7 for H, He, C, O, Ne, Mg, Si, and Fe

The instrument mass resolution was investigated by combining experimental and simulation data, to get rid of the unavailability of isotope beams. Specifically, the HIT response to hydrogen and iron isotopes was studied. As a first step, the mass resolution was derived with Geant4 simulations, by comparing the energy distributions obtained for ^{1}H and ^{2}H fluxes, and for ^{54}Fe and ^{56}Fe fluxes, respectively. Subsequently, these data were scaled by a factor corresponding to the ratio between the distribution widths estimated with observations and simulations, using ^{1}H and ^{56}Fe fluxes, respectively. Results are summarized in Figure 5. The upper panels display the L3B vs. L3A experimental distribution for hydrogen based on BNL/Tandem data, and the resulting mass resolution (with errors) in terms of M/ΔM. The bottom panels report the L3B vs. L3A experimental distribution for iron based on BNL/NSRL data along with corresponding mass resolution. As evident, the obtained M/ΔM values are well above the required lower limit of 7 over the full energy range of interest. With interpolation, the M/ΔM results for He, C, O, Ne, Mg and Si ions are also expected to exceed the mass-resolution requirement.

3.3.3 In-Flight Calibrations

HIT in-flight calibration report to be included here.

3.4 SWE

3.4.1 Strategy & Approach

Calibration of SWE involved three phases consisting of: 1) characterization of the SWE sensor head using lab supplies and the EM electronics box (EBOX); 2) full instrument performance testing *prior to* environmental testing; 3) full instrument performance testing *after* environmental testing. Phases 2 and 3 ensured that the instrument performance remained unchanged by environmental test.

SWE calibrations were conducted at Los Alamos National Laboratory using a ^{63}Ni electron source and an ion beam (Phase 1) and at Southwest Research Institute's electron calibration facility using a Kimball Physics EGG-3101C electron gun. In all tests, Helmholtz coils were used to nullify the effects of Earth's magnetic field on the trajectories of the relatively low-energy electrons. At both facilities, an imaging microchannel plate was used to optimize electron beam uniformity, and translational and rotational motion stages were used to center the beams on SWE's apertures and scan over SWE's polar and azimuthal angles, respectively.

SWE's calibrations consisted of the following:

- Electro-optic simulations
- CEM detector gain quantification
- Energy and angular response functions
- Background characterization
- Geometric facter determination

3.4.2 Pre-Flight Instrument Calibration

SWE calibration report embedded below

1 Introduction

This report documents the calibration of the IMAP Solar Wind Electron (SWE) instrument, and validates that SWE meets the measurement requirements.

SWE calibration is achieved through a combination of measurements and numerical modeling. Laboratory measurements provide the most accurate description of instrument performance. However, they cannot provide a full picture of the instrument for two reasons. First, the parameter space covered by the instrument is very large in both energy and angle space, precluding measurement of each combination of parameters. In addition, determination of the instrument geometric factor is not easily obtained from the mono-energetic, approximately collimated electron beam available in the laboratory. Because of these limitations, laboratory measurements are used to validate the electro-optic model, which is then used to determine the instrument response over the full range of input particles.

The SWE calibration tests are defined by the SWE Verification and Calibration Test Plan, document CN102V-T0001 and the SWE Verification and Calibration Test Procedure, document CN102V-T0008. SWE calibration was performed in three phases: Phase 1 consisted of characterization of the SWE flight model (FM) Sensor Head (SH) using the engineering model (EM) electronics box (EBOX) and laboratory high voltage power supplies. Phase 2 and Phase 4 Calibrations were performed using the fully integrated FM SWE instrument, with Phase 2 Calibration prior to instrument environmental testing and Phase 4 Calibration following instrument environmental testing. An optional Phase 3 calibration was included in the schedule, to allow for a possible check of the calibration following instrument vibration testing, but based on vibration test signatures and functional testing of SWE following vibration this test was deemed unnecessary and was not executed.

This multiple-phase calibration scheme allowed the team to determine the effect, if any, of environmental testing on the instrument performance. In practice, no significant differences were observed following environmental tests. We note that SWE instrument EMI/EMC and magnetics testing were performed following Phase 4 calibration. These tests were expected to have an extremely low possibility of affecting SWE performance, and indeed the testing showed no areas of concern. Following EMI/EMC testing, SWE was delivered to the spacecraft for integration onto the vehicle.

1.1 Instrument Description

The SWE instrument measures the 3D distribution of solar wind thermal and suprathermal electrons from 1 eV to 5 keV. SWE (Figure 1.1.1) consists of a spherical section electrostatic analyzer (ESA) followed by seven channel electron multiplier (CEM) detectors. Electrons enter the instrument through an aperture oriented normal to the spacecraft spin axis. A positive high voltage on the inner ESA plate biases the analyzer such that only electrons within a narrow range of energies and angles pass through and are detected by the CEMs. Stepping this voltage provides coverage of the full energy range.

Electrons entering the instrument at different angles relative to the spacecraft spin axis are detected in different CEMs, yielding 21° polar angle resolution within the fan-shaped field of view (FOV). As the IMAP spacecraft spins, the FOV covers the full 0-360° range of azimuthal angles and sweeps out >95% of 4π steradians, missing only small conical holes centered parallel and antiparallel to the spin axis. Front end electronics (FEE) are co-located within the Sensor Head. The Sensor Head is mounted on top of an

electronics box module (EBOX) which contains a low voltage power supply (LVPS), high voltage power supply (HVPS), a backplane circuit board, and a command and data processing board (CDH).

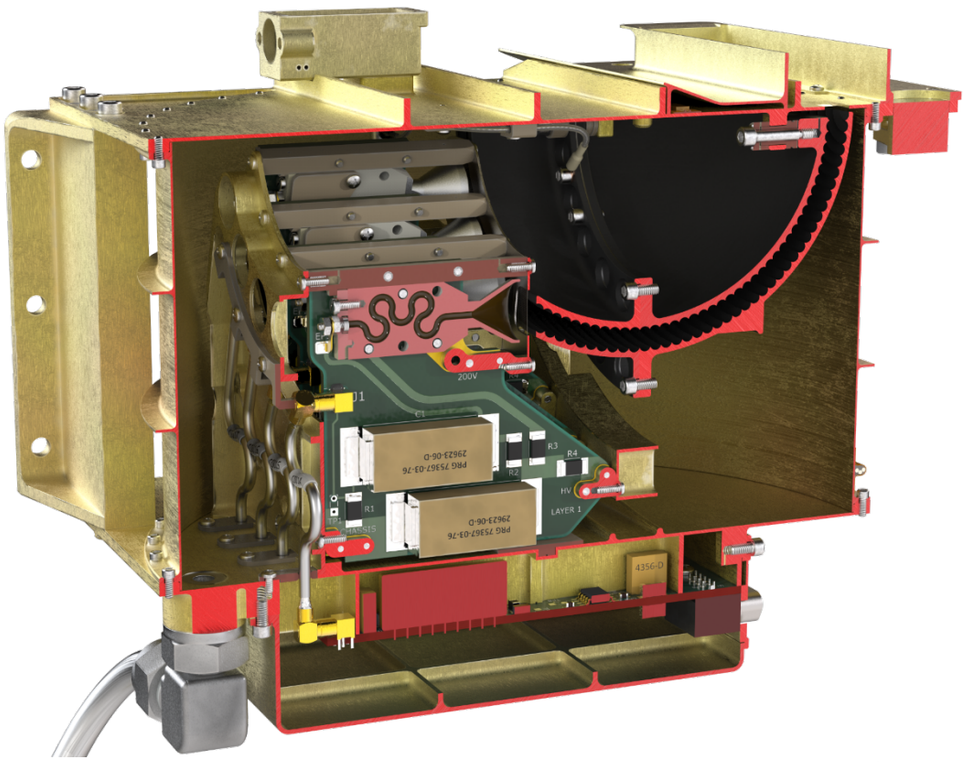


Figure 1.1.1: SWE Sensor Head cross section, showing the spherical section ESA plates followed by the CEM detectors (gold cones). The front end electronics (FEE) is at the bottom; the EBOX is not shown here.

The HVPS board includes two independent supplies to produce the high voltages required to bias the ESA (+1200 V) and the CEM detectors (up to +4200 V). The CEM voltage output V_{CEM} is commandable, with the nominal voltage at the beginning of the mission determined during CEM gain calibration. Higher V_{CEM} voltages are expected to be used as the detectors age and their gain decreases over the course of the mission. The CEM fronts are biased to +200 V, so that all electrons are post-accelerated into the CEMs by 200 V, improving detection efficiency at low energies. The CEM electron response is nearly constant over the energy range from 200 eV – 5 keV, so this post-acceleration gives a uniform response over energy. The ESA stepping supply is a dual-range supply: ESA Low Range provides voltages up to 24.5 V, and ESA High Range provides voltages above 24.5 V. The ESA voltage V_{ESA} will nominally be stepped every ~83.3 ms (consisting of 3.3 ms HV settling time followed by an 80 ms measurement interval) to provide measurements over the full SWE energy range at each measurement angle. The V_{ESA} stepping levels and timing are defined in an on-board look up table (LUT), and can be changed in flight as required. The HVPS board also includes circuitry to provide a low-level pulse discriminator threshold for the FEE preamplifier circuit, and Low-Voltage Differential Signaling (LVDS) pulser signals to provide stimulation of the preamplifiers and thus verification of the electronics performance in the absence of a particle source.

SWE has a total of six operating modes. Two of these are used for booting the instrument and starting the SWE App Flight Software (FSW), and the other four are used by the SWE App FSW, which handles the bulk of the SWE operations. Following Boot mode, SWE always transitions into low voltage engineering (LVENG) mode. In this mode, low-voltage monitors and engineering housekeeping data are collected and telemetered, and memory upload, dump, and diagnostic commands are allowed. Instrument safing from any non-boot mode will bring the instrument to LVENG mode. Low voltage science (LVSCI) mode is used to test end-to-end science data acquisition and packet generation based on stim pulse input to the FEE. In high voltage engineering (HVENG) mode, high voltages are set to fixed levels by ground command. This mode is used extensively for ground testing, and is also used during commissioning to bring up the high voltages during slow ramp-ups before the start of science operations.

Nominal SWE science operations take place in high voltage science (HVSCI) mode. A full SWE measurement is nominally performed over 4 spacecraft spins, with a lower resolution measurement each spin. However, we note that SWE measurements are not synced to the spacecraft spin, but are instead time-based measurements with the exact timing to be determined based on the actual IMAP spacecraft spin period, expected to be between 14.6 – 15.4 seconds. A “single-spin” SWE measurement is refered to as a quarter cycle, and has a length which is configurable in the FSW. The quarter cycle duration will be set to slightly longer than a spacecraft spin period, to ensure measurement over all spin angles for each energy step. Each quarter cycle includes measurement of half the V_{ESA} levels in half the spin angle bins. A full data set over four quarter cycles includes data at 24 V_{ESA} steps (24 electron energies) in 30 nominally 12-degree wide spin-angle bins.

1.2 Instrument Configuration

SWE Phase 1 calibration was performed using the flight Sensor Head with the EM EBOX. For this test, the EBOX (which contained non-vacuum compatible components) was located outside the vacuum chamber, and an isolator circuit was included between the SH and EBOX to ensure the safety of the flight hardware. This calibration phase used both laboratory high voltage power supplies and the EM HVPS from the EM EBOX. Laboratory power supplies enable biasing SWE for measurement of ions, which is desirable in calibration because the ion beam is generally more stable than the electron gun produced beam, allowing a high-resolution characterization of the SWE angular and energy response.

Calibration in Phases 2 and 4 used the fully integrated SWE flight instrument, including the FM Sensor Head mounted on the FM EBOX in flight configuration.

Most calibration data was collected in HVENG mode. In this mode, V_{ESA} does not step, and counts from each CEM detector are obtained once per second. This mode allows manual setting of the ESA high voltage, and provides more efficient data for the calibration configuration in which the spacecraft is not spinning and the input source is a monoenergetic collimated beam. Limited calibration was also performed in HVSCI mode, the nominal mode to be used in flight, allowing verification of the ESA HV stepping and of the science and real time i-ALiRT data packets.

1.3 Calibration Facilities

Phase 1 characterization was performed in the LANL W112 ion beam calibration facility. As noted above, most of the measurements in this phase used an ion beam with V_{ESA} biased negatively (nonflight

configuration) using laboratory HVPS; V_{CEM} polarity was positive for all testing. This phase also included measurements with a ^{63}Ni radioactive source, which emits electrons with an average energy of 17 keV and a maximum energy of 67 keV, including electrons in the 1 eV – 5 keV SWE energy range. For this electron testing V_{ESA} was biased positively (flight configuration) using both laboratory power supplies and the EM HVPS from the EM EBOX, providing validation of the EBOX HVPS. In addition, this phase included measurements using a UV lamp, to verify insensitivity to UV light.

Phase 2 and 4 measurements were performed in the Southwest Research Institute (SwRI) electron calibration chamber. This facility includes a vacuum chamber with a Kimball Physics EGG-3101C electron gun mounted on a port. The gun can be set to produce electrons of energies 100 eV – 10 keV. The chamber is relatively small, so two mounting configurations were required for electron beam flux to impact all 7 CEM detectors. Mounting configuration 1 provided full coverage of CEMs 1-6, at polar angles from -90 to +55 degrees. Mounting configuration 2 allowed measurements of all 7 CEMs, but with limited coverage of CEMs 1 and 7, at polar angles from -75 to +70 degrees. In addition, motion stage mechanical mounting blocked a portion of the full SWE field of view (FOV), so all CEM 1 and CEM 7 measurements were affected by the beam being partially blocked by and/or scattered off structures within the chamber.

For measurements of low-energy electrons, Helmholtz coils are required to null the Earth's magnetic field in the vacuum chamber. In Phase 1, Helmholtz coils allowed measurements of electrons down to ~2 eV. In Phase 2 calibration, the Helmholtz coils were used to zero the magnetic field at the instrument aperture. During Phase 4 calibration, an imaging microchannel plate (MCP) was installed at the location of the SWE aperture to measure the beam location and uniformity. Because of cabling issues, the MCP was only operational at times when SWE was not installed in the chamber. Based on measurements from the imaging MCP, in Phase 4 calibration the Helmholtz coils were set to provide the most uniform beam at the SWE aperture location. This optimization used different coil settings than the Phase 2 calibration, making comparison difficult but leading to more consistent angular settings. In addition, configuration 2 measurements in Phase 2 were performed with the Helmholtz coil direction reversed, and so are invalid and are not included in the analysis discussed in this report.

The electron gun beam stability varied over the course of the calibration campaign. At times, the beam was quite stable, at other times the flux varied by a factor of 2-3 on a time scale of minutes. Beam drift was mitigated by frequent repetition of normalization points, consisting of repeated flux measurements at a selected CEM, polar and azimuthal angle setting, and V_{ESA} setting. These normalizations are used to adjust counts based on the beam variation between measurements, a process that is very successful when the beam drift is relatively slow and linear. However, at times when the beam varies more erratically between normalization points correction becomes impossible, leading to uncertainties in the measurements.

Despite these uncertainties, the combination of the laboratory calibration measurements with electro-optic modeling of SWE is sufficient to determine the instrument response and validate the measurement requirements for the IMAP mission.

2 Measurement Requirements

The SWE instrument calibration campaign was designed to demonstrate that SWE meets the measurement requirements, shown in Table 2.1. These are top level, instrument specific requirements derived from mission science requirements. All Table 2.1 requirements were verified during the SWE calibration; the "Value" column shows the measured values (all of which meet or exceed the requirements), and the "Verification" column gives pointers to the sections of this report where the associated results can be found.

Table 2.1: SWE Measurement Requirements

REQ ID	Requirement	Value	Verification
RSWE-1046	Measure energies over the range of < 20 eV to > 2 keV	2 eV – 5 keV	Section 3.5
RSWE-1047	Energy resolution: $\Delta E/E < 0.17$	≤ 0.15	Section 3.6
RSWE-1048	Polar angle range from 10° – 170°	10° – 170°	Section 3.4
RSWE-1049	Polar angle resolution < 22.5° (response width, FWHM)	< 22.5°	Section 3.4
RSWE-1051	Azimuthal angle resolution ≤ 30°	≤ 30°	Section 3.6
RSWE-1052	Geometric Factor ≥ $2x10^{-4}$ cm^2 sr eV/eV	4-$8x10^{-4}$ cm^2 sr eV/eV	Sections 3.4, 3.6, 4
RSWE-1053	Dynamic range up to 500 kHz	> 500 kHz	Section 3.9
RSWE-1563	SWE measures Thermal (solar wind) Electrons	SWE measures 1 eV – 5 keV electrons	Section 3
RSWE-1182	Internal Alignment Knowledge uncertainty between Sensor boresite and mounting surface ≤ 0.7°	0.49°	Section 3.12
RSWE-1125	SWE HVSCI and HVENG modes shall be used during calibration	Calibration used HVENG and HVSCI modes	Sections 3.4, 3.6, 3.7
RSWE-1576	SWE shall have measured Voltage-Gain Curves for each detector	Initial operating voltage V_{CEM} = 2200 V	Section 3.2

3 Calibration Measurements

3.1 Initial Tests

3.1.1 CEM Conditioning

Prior to installation in the instrument, each CEM is conditioned, or burned in, by application of electrons to extract a small fraction of the total detector extractable charge (~0.1 C). The detector gain changes over the life of the CEM, with a relatively large change in gain during initial operation. CEM gains are measured at the end of this test, providing a baseline for initial operation as well as more stable and predictable future gain reduction. This procedure allows identification of any defective CEMs, and also allows selection of matched CEMs with similar gains and electrical properties. Table 3.1.1 lists the CEMs selected for SWE along with their detector gains and impedances. All detectors are Sjuts model #KBL11RS. Since all 7 detectors are driven by a single high voltage power supply, CEM selection was primarily based on matching the bias voltage required for initial CEM operation, with all selected CEMs reaching the plateau in counts at a similar voltage. We note these are not the CEMs which showed a plateau at the lowest voltage, but are a well-matched set. As secondary considerations, the selected CEMs all have relatively high gains, indicative of longer lifetime, and relatively narrow pulse height distributions, which allows optimization of the single low-level discriminator threshold setting. Two sets of flight spare detectors were also selected, the first consisting of CEM serial numbers 9, 17, 21, 24, 28, 30, and 34, and the second of CEM serial numbers 5, 8, 12, 25, 26, 33, and 36.

Table 3.1.1. SWE CEM Detectors

Position	CEM Serial #	Impedance (MOhm)	Final Gain (x 10^8)	Pulse Distribution Width
1	10	182	0.823	38%
2	19	185	0.642	48%
3	23	192	0.712	44%
4	27	183	0.815	43%
5	31	201	0.737	38%
6	32	197	0.765	52%
7	37	181	0.823	37%

3.1.2 Overvoltage Testing

Overvoltage testing was performed during Phase 1 calibration using a laboratory high voltage power supply, prior to integration with the EBOX. Only the ESA voltage V_{ESA} was tested; overvoltage test of V_{CEM} is not done, since it degrades CEM lifetime. The test was performed with V_{CEM} at +2600 V to allow monitoring of any anomalous counts. The ESA voltage was driven to 10% overvoltage level (+1320 V) and held at that voltage for a dwell time of >20 minutes. The overvoltage test was successful, with no issues observed.

3.2 CEM Gain

A first component of calibration testing is a CEM voltage-gain sweep, to determine the initial instrument operating voltage. Figure 3.2.1 shows the CEM voltage sweep results from Phase 1, 2, and 4 calibrations; note that measured CEM responses were unchanged through calibration. Phase 2 measurements were only obtained for CEMs 2-6, because of the Helmholtz coil and chamber structures issues discussed above. In Phase 1, this test was performed at a threshold setting of 4.1 V using a laboratory power supply, with a 1 keV H^+ beam input to the instrument. In Phases 2 and 4, the test was performed at threshold digital to analog convertor (DAC) values of 3400 and 3000 (4.15 V, 3.7 V), respectively, with a 1 keV electron beam input to the instrument. V_{ESA} was set to a DAC value of 770 (~215 V), appropriate for a 1 keV beam. In Phase 4, the CEM high voltage supply V_{CEM} was stepped from 1600 V to 2300 V in 100 V steps. Phase 4 calibration was performed at V_{CEM} = 2200 V. For flight, an initial operating voltage of V_{CEM} = 2200 V (DAC value 2145) was selected. We note that Phase 1 and 2 calibrations were performed at a slightly higher voltage, V_{CEM} = 2300 V (DAC value 2243).

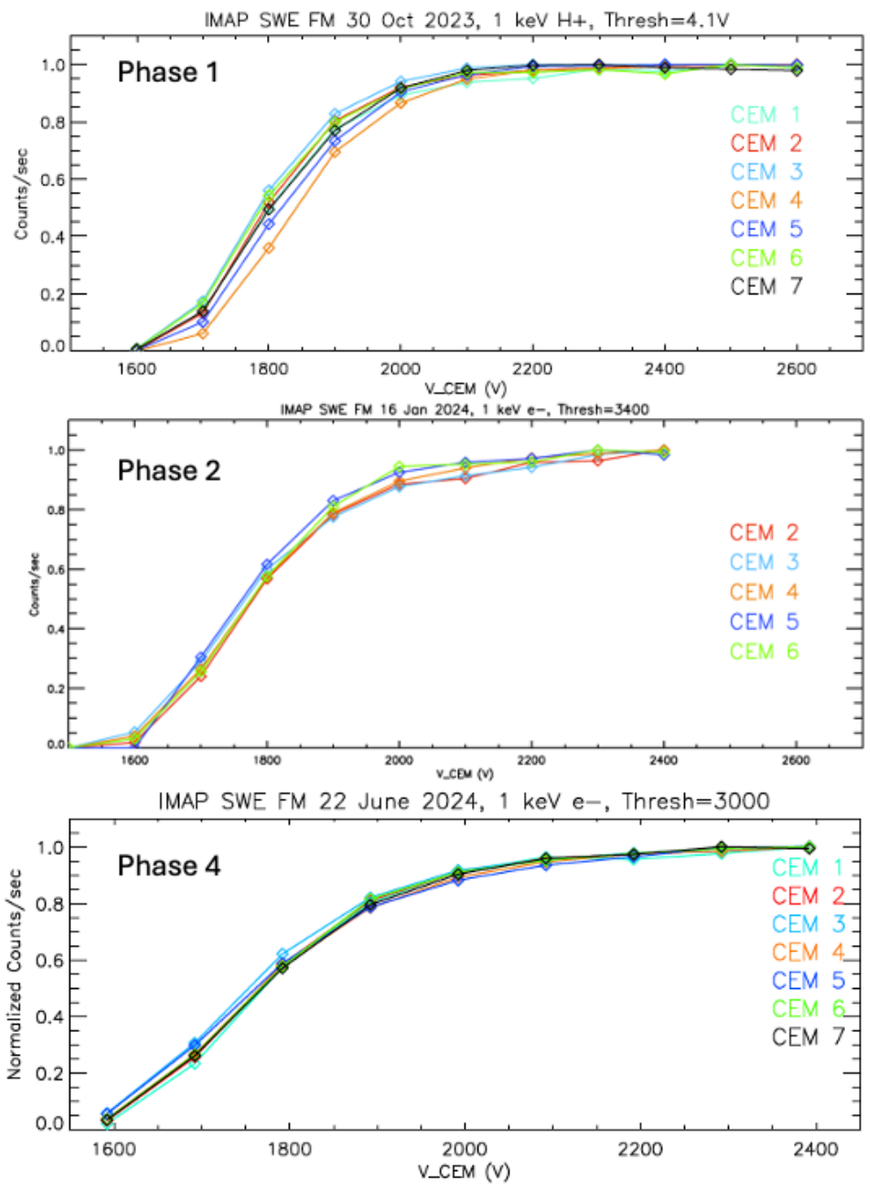


Figure 3.2.1. SWE Voltage-Gain sweeps from Phase 1, 2, and 4 calibrations. Although the x-axis scales are different, these show that CEM gains were unchanged over the calibration phases. Based on these measurements, an initial operating voltage of V_{CEM} = 2200 V was selected for calibration and for flight.

3.3 Low-Level Discriminator Threshold

With V_{CEM} set to the selected value (2200 V in Phase 4), the low-level discriminator (LLD) threshold was stepped to determine the initial operational setting. The LLD is located on the FEE board, and can be set to values from 0-4095, corresponding to voltages of 0-5 V. Only events with amplitudes above the selected threshold are counted in the electron counters. The purpose of the LLD is to eliminate noise

counts from the measurement, while retaining the maximum number of real CEM counts. As was done for the CEM gain measurements, in Phase 1 the input was a 1 keV H^+ beam, and in Phases 2 and 4 the input was a 1 keV electron beam. Figure 3.3.1 shows the Phase 4 threshold scan for CEM 2. Results from Phase 2 are very similar to those from Phase 4, and are not shown here. CEM 2 required the highest threshold value to eliminate noise counts in the other CEMs. As a single threshold setting is used for all 7 CEMs, we have selected the value that minimizes noise for all detectors, which is the value obtained from CEM 2 measurements. From these measurements, an initial LLD threshold setting of 3500 has been selected. Note that a threshold setting of ~2500 eliminates electronics noise counts, the higher value selected also eliminates cross talk between the detectors. Figure 3.3.1 also shows that at the selected threshold value, cross talk in adjacent CEMs is a factor of 100 lower than counts on the CEM seeing the electron beam, and that cross talk in other CEMs is more than a factor of 1000 lower.

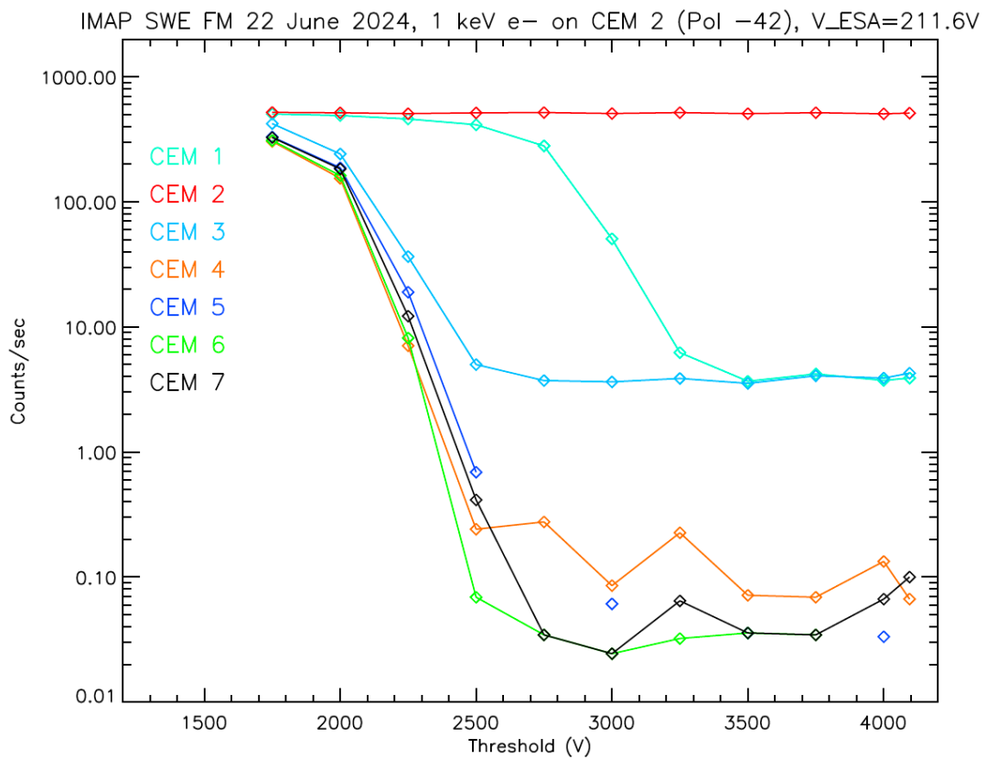


Figure 3.3.1. SWE count rate as a function of low-level discriminator threshold level, from a 1 keV electron beam incident on CEM 2 (red curve). Note that counts in CEM 2 were constant at all threshold settings. Noise counts in other CEMs are eliminated by raising the threshold. CEM 2 requires the highest threshold setting to eliminate electronics and cross talk noise.

3.4 Polar Angle Response

The polar angle response of SWE was characterized using a rotational motion stage to scan across the polar FOV. Figure 3.4.1 shows high-resolution polar scan results from calibration Phases 1 and 4. Measurements were made at 1˚ steps in polar angle using a 1 keV electron beam with V_{ESA} = 215 V and V_{CEM} = 2200 V in Phase 4 and a 1 keV proton beam with V_{ESA} = -226 V and V_{CEM} = 2300 V in Phase 1. The

azimuthal angle was fixed at 0 degrees for this measurement. Drift of the beam flux was monitored by periodic repetition of the measurement at 0˚ polar angle (CEM 4), and has been accounted for in these plots. However, variations of the beam may have occurred between these normalization measurements, leading to small variations.

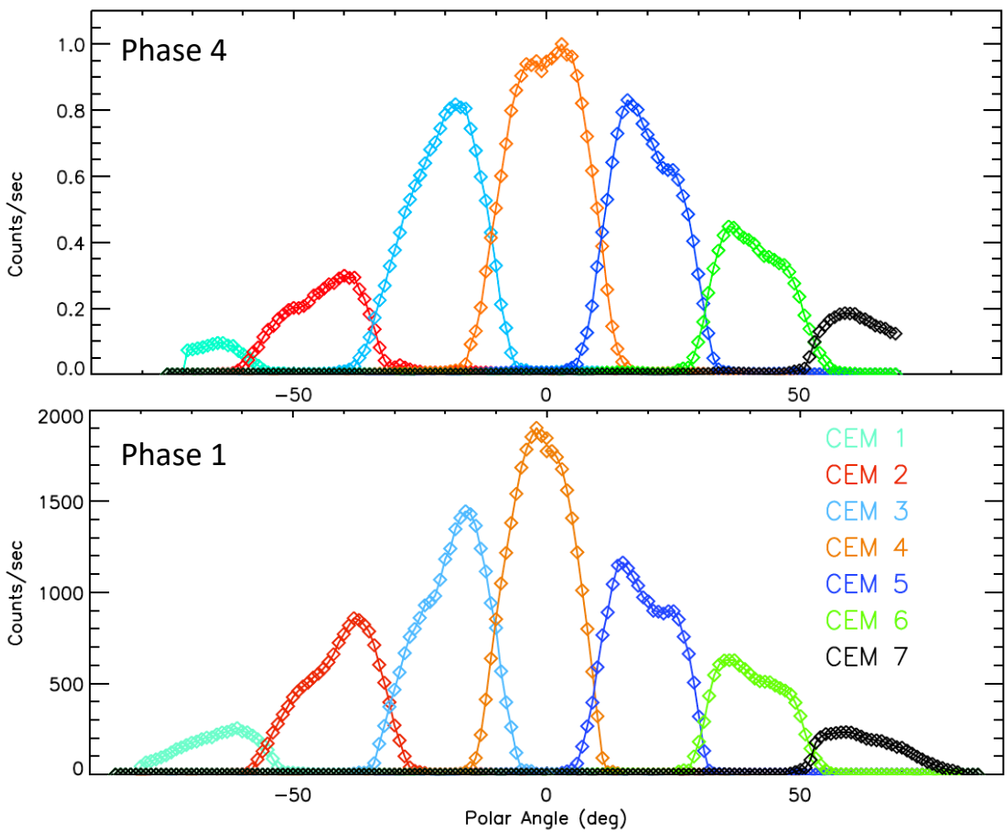


Figure 3.4.1. Polar angle response of SWE with the azimuthal angle set to 0 degrees, measured using a 1 keV electron beam in calibration Phase 4 and a 1 keV proton beam in Phase 1.

These high resolution scans demonstrate that the responses for each detector have the expected shapes and locations in angle, consistent with SIMION modeling (Section 4). The 7 detectors are generally well-separated, with some overlap at the edges of the response. The polar angle range increases away from the central CEM. Nominal angles for the 7 CEM detectors are at 0, +/-21, +/-42, and +/-63 degrees. Small variations in the response are repeatable, both in simulations and in measurements, but variations in the measurements may also result from beam variability. Phase 4 measurements are less reliable at large polar angles (CEMs 1 and 7) due to effects on the beam from structures within the vacuum chamber. Results from Phase 4 are generally in good agreement with results from Phase 1, but Phase 2 results (not shown) show some differences due to angular variations resulting from electron gun or Helmholtz coil settings.

3.5 Energy Response

SWE was designed to measure electrons from ~2 eV to 5 keV. This response was verified in two ways. During Phase 1 characterization, electron measurements were made using a ^{63}Ni electron source, which produces electrons over the full SWE energy rage, mounted in the vacuum chamber. The response to these electrons is shown in Figure 3.5.1, and shows that SWE is sensitive to electrons from 2 eV to 5 keV. Helmholtz coils are required for measurements of the lower energy electrons, which are otherwise diverted away from the SWE aperture by the Earth's magnetic field. As the ^{63}Ni energy spectrum is typically described assuming bins of constant energy width, in contrast to the SWE ~15% ΔE/E energy bins, Figure 3.5.1 shows both the raw SWE count rate, and the counts that would be expected for 1 keV-wide energy bins, demonstrating the SWE response to the full range of energies. The resulting spectrum is consistent with previous measurements using the ^{63}Ni source (i.e. from NASA Van Allen Probes HOPE), which were shown to be consistent with the known ^{63}Ni energy spectrum. Again, all electrons are post-accelerated by 200 V as they enter the CEM detectors, giving an energy-independent response over the SWE energy range. During Phase 4 calibration, the electron gun was used to verify the response of SWE to 250 eV – 5 keV electrons. Consistent measurements at lower energies were not possible with this electron gun, due to the defining parameters (extremely low beam current, low acceleration and focus voltages) being on the edge of its designed performance window. Figure 3.5.2 shows these measurements, again demonstrating that SWE is sensitive to electrons up to 5 keV. Note that the absolute counts in Figure 3.5.2 are a function of the variable electron gun flux production at different energies – this plot demonstrates that SWE is sensitive to this range of energies, but not the SWE response as a function of energy.

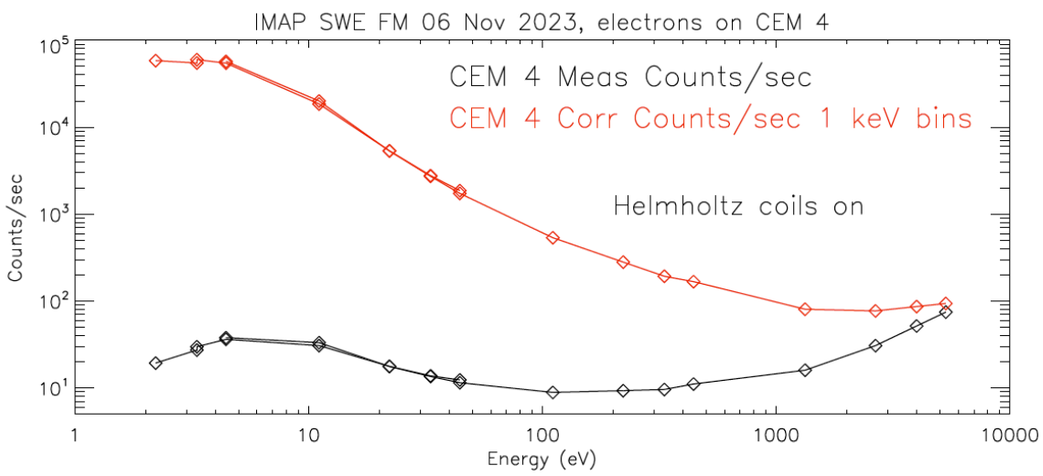


Figure 3.5.1. SWE response to electrons from a ^{63}Ni electron source (black) together with the response that would have been obtained if SWE used constant 1 keV-wide energy bins (red).

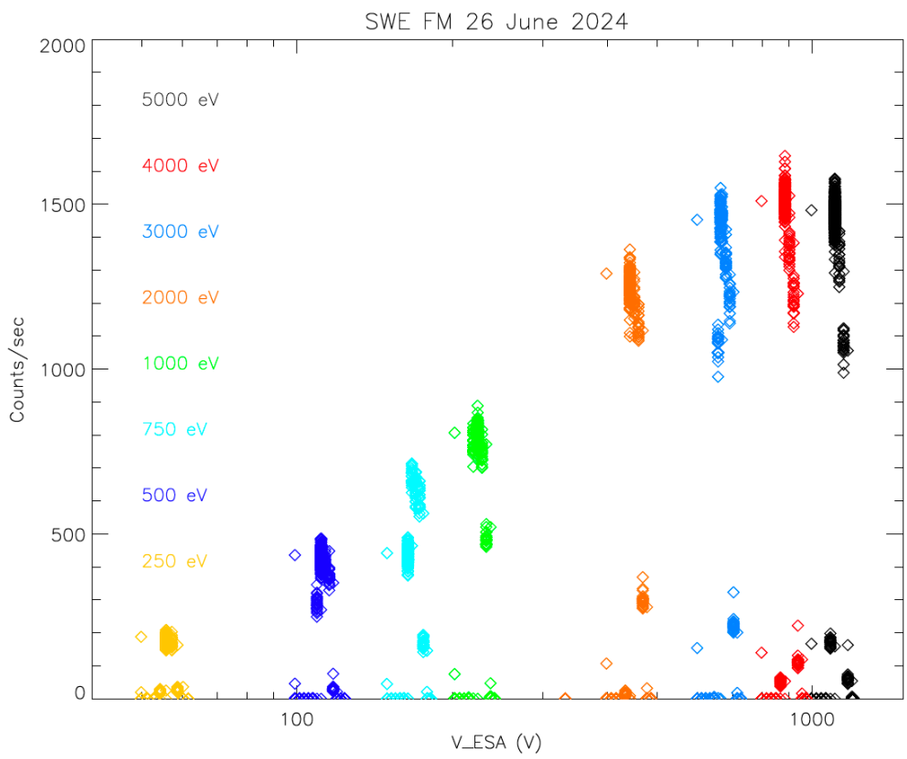


Figure 3.5.2. SWE measurements of 250 eV – 5 keV electrons from the SwRI electron gun. Note that count rate variations are due to the energy characteristics of the electron gun, and do not represent the relative energy response of SWE.

3.6 Energy-Azimuth Angle Response

Determination of the SWE response in energy and azimuth angle is accomplished by testing with a fixed energy beam over a range of angles and ESA voltages. These scans allow determination of the electrostatic analyzer constant k = particle energy / V_{ESA}, energy resolution, azimuthal angle resolution, and the coupled energy-angle response. Because it is more straightforward to change V_{ESA} than particle energy, for a given particle energy, V_{ESA} is varied to allow determination of the energy response, and the azimuthal angle of the detector is varied to give the angular response. The measurements are compared with SIMION simulation results to validate the SIMION model for use in geometric factor calculations.

Energy angle scans were performed using H^+ ions during Phase 1 calibration and electrons during Phase 2 and Phase 4 calibrations, as shown in Table 3.6.1. The table includes all scans performed, with the exception of two scans for CEM 1 which were clearly affected by chamber effects. Again, Phase 2 and 4 measurements for CEMs 1 and 7 are affected by scattering or Helmholtz coil effects and are thus less reliable than the measurements for CEMs 2-6. Primary energy-angle scan measurements were performed using 1 keV electrons, with ~3 V steps in V_{ESA} and 1.5° steps in azimuthal angle. These scans were done for all 7 CEMs. In addition, scans were done for selected CEMs at both higher and lower

electron energies, 0.5, 2.5, and 5.2 keV. Phase 1 scans used 1 keV H^+ for all CEMs, and 2 keV H^+ for CEM 6 only.

Table 3.6.1. SWE Energy-Azimuthal Angle Response Measurements.

Date	Cal Phase	CEM #	Energy	k	ΔE/E	ϕ (˚)	Δϕ (˚)
11/1/2023	1	1	1 keV H+	4.56	0.135	1.79	12.3
11/1/2023	1	2	1 keV H+	4.48	0.135	1.22	10.5
11/1/2023	1	3	1 keV H+	4.44	0.140	1.04	9.26
11/1/2023	1	4	1 keV H+	4.36	0.140	0.54	9.26
10/31/2023	1	5	1 keV H+	4.31	0.138	0.35	9.51
10/31/2023	1	6	1 keV H+	4.28	0.138	0.57	11.03
10/31/2023	1	7	1 keV H+	4.26	0.149	1.12	13.05
11/2/2023	1	6	2 keV H+	4.41	0.142	0.97	9.22
1/19/2024	2	4	1 keV	4.60	0.138	4.54	9.42
1/19/2024	2	3	1 keV	4.67	0.134	5.41	10.5
1/19/2024	2	2	1 keV	4.69	0.120	7.76	15.3
1/20/2024	2	5	1 keV	4.56	0.140	5.21	10.9
1/20/2024	2	6	1 keV	4.51	0.123	6.69	15.3
1/19/2024	2	3	2.5 keV	4.60	0.133	2.73	10.8
1/21/2024	2	1	5.2 keV	4.64	0.096	5.89	25.2
1/22/2024	2	2	5.2 keV	4.60	0.123	3.92	14.1
1/24/2024	2	7	1 keV	4.48	0.116	7.71	19.4
1/24/2024	2	6	500 eV	4.67	0.139	6.19	11.7
6/23/2024	4	7	1 keV	4.59	0.133	0.81	20.7
6/25/2024	4	6	1 keV	4.66	0.147	-0.55	13.0
6/24/2024	4	5	1 keV	4.64	0.143	-0.88	10.1
6/23/2024	4	4	1 keV	4.70	0.138	-0.87	9.5
6/24/2024	4	3	1 keV	4.77	0.141	-0.32	12.1
6/24/2024	4	2	1 keV	4.83	0.127	1.14	19.8
6/30/2024	4	4	1 keV	4.69	0.145	-0.80	9.41
6/30/2024	4	4	500 eV	4.90	0.154	-1.06	9.66
6/30/2024	4	1	1 keV	4.88	0.114	2.62	28.2

Figures 3.6.1 – 3.6.4 show examples of data from SWE energy-angle scans from Phase 4 calibration. In each case, the middle panel shows counts as a function of azimuthal angle ϕ and V_{ESA}. These plots clearly show the coupled energy-angle response characteristic of the SWE spherical section electrostatic analyzer. Data points in the left and right hand panels show these data collapsed as a function of V_{ESA} and ϕ, respectively, and are used to determine the peak and width of the response in V_{ESA} and ϕ. Lines in

these panels show Gaussian fits to the collapsed data, which are used to quantify the response as a function of V_{ESA} and ϕ. These fits provide the values given in Table 3.6.1. It is clear from these examples that the choice of a Gaussian fit can lead to some uncertainty in the fitted values, as the data are not always perfectly described by a Gaussian. Scans were performed by using the chamber motion stages to set an angle and then varying V_{ESA} over the range of interest. To track beam drift, a normalization scan at a fixed angle and voltage was performed between scans, and the change in beam over time has been incorporated into the analysis. This process was largely successful, but as seen most clearly in Figure 3.6.2 and to a lesser extent in Figures 3.6.3 and 3.6.4, there are times when the beam varied significantly during measurements at a single angle. We do not have a way to correct for these times, leading to increased uncertainty in the calculated response.

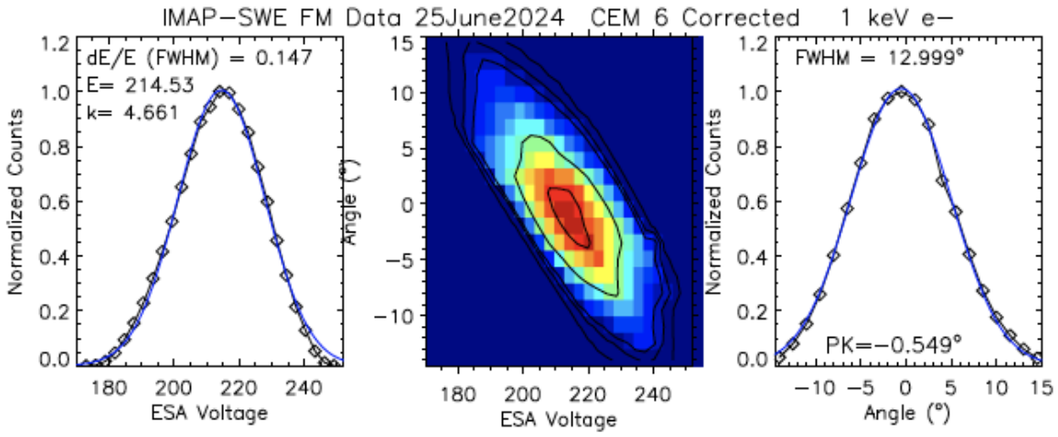


Figure 3.6.1. SWE 1 keV electron energy-angle scan for CEM 6 from Phase 4 calibration.

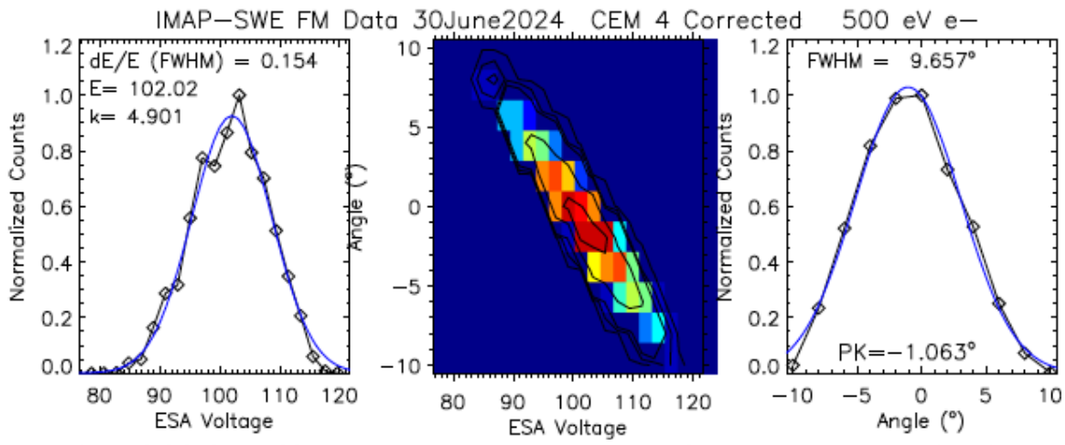


Figure 3.6.2. SWE 500 eV electron energy-angle scan for CEM 4 from Phase 4 calibration.

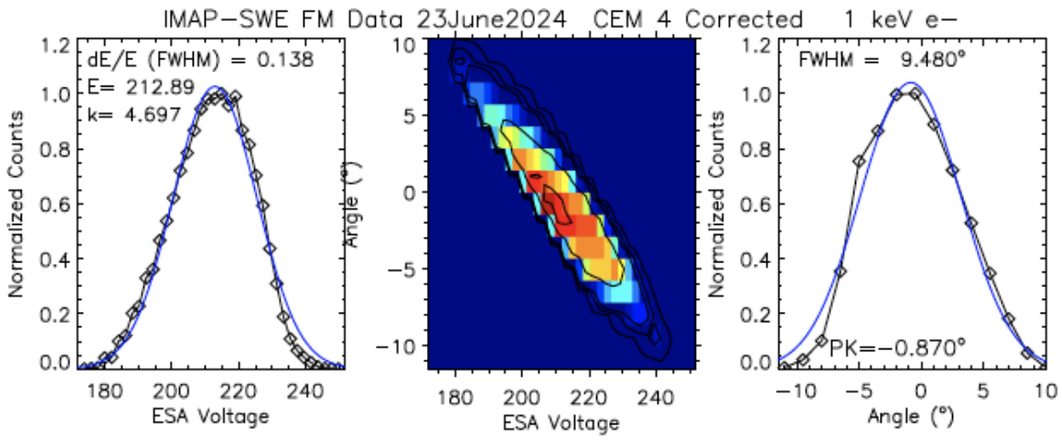


Figure 3.6.3. SWE 1 keV electron energy-angle scan for CEM 4 from Phase 4 calibration.

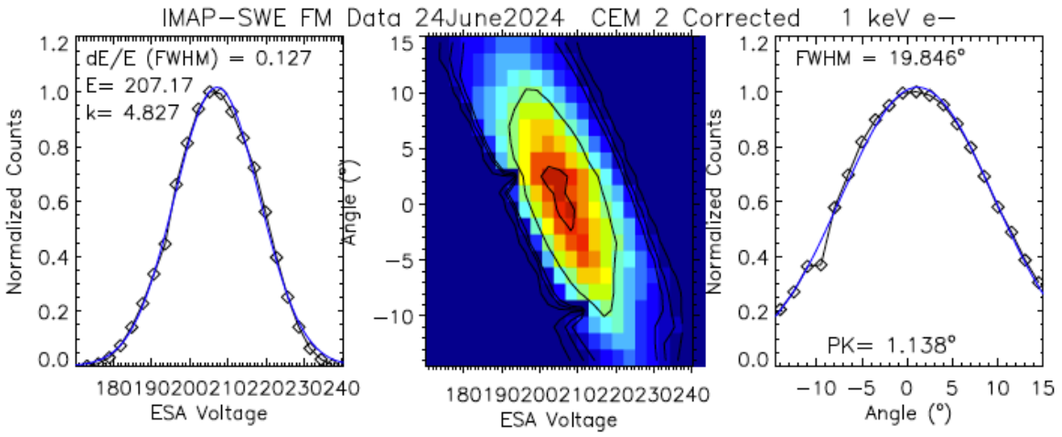


Figure 3.6.4. SWE 1 keV electron energy-angle scan for CEM 2 from Phase 4 calibration.

In general, the results of the energy-angle scans are very consistent, with very similar results observed before and after environmental testing.

Note that Phase 1 characterization was performed with H^+ ions rather than electrons. For this testing, the V_{ESA} bias voltage was negative rather than positive. However, the V_{CEM} detector bias voltage and the exit aperture grid voltage remained positive, leading to slightly different particle electro-optics. It is clear that these differences lead to somewhat different responses, with lower k factors and narrower angular acceptance ranges. Phase 1 H^+ energy-angle scan results are thus not appropriate for quantitative calibration of SWE, although they were very useful in qualitatively demonstrating that SWE functions as designed.

As discussed above, Phase 2 and Phase 4 calibrations were performed with different Helmholtz coil settings, leading to different responses, as seen by, for example, the very different azimuthal angle centers of the response in Phase 2 (large angles centered near 5 degrees) and Phase 4 (angles centered near 0). Because of concerns with the Phase 2 Helmholtz coil and electron gun settings, and because the

offset in azimuthal angles is not consistent with simulations (see below), Phase 4 measurements are deemed more accurate, and we will use the Phase 4 measurements to quantitatively describe the SWE response.

Table 3.6.1 shows possible evidence of a slight variation of the calculated k-factor with CEM number, with higher k-factors calculated for lower-numbered CEMs. This variation would result from slight misalignment of the two ESA domes, and if necessary could be accounted for in analysis. However, the difference is at most 3%, a minor variation compared to the SWE energy resolution of ~14%. In addition, the largest variations are observed for CEMs 1 and 7, for which the measurements are generally less reliable due to scattering from or blocking due to structures in the chamber.

3.7 ESA Stepping Validation

To verify that the voltages are set properly and that counts are recorded in the proper channels while stepping V_{ESA}, limited calibration was also performed with the instrument running in HVSCI mode using the nominal flight V_{ESA} stepping table. Figure 3.7.1 shows the results obtained at 5 input electron beam energies: 500, 925, 1330, 1850, and 5158 eV. At each electron energy, the motion stages were used to direct the beam to each of the 7 CEM detectors. Due to telemetry limitations, science counts in HVSCI mode are compressed from 16 bit values to 8 bit values for transmission. Counts in the figure have been uncompressed in the same manner as will be done for flight data analysis. In the nominal flight voltage table, V_{ESA} is stepped over 12 levels 15 times each in each 15-second interval (quarter cycle), to give measurements at 12 energies at each of 15 spin angles in each SWE quarter cycle and a full measurement of 24 energies at 30 spin angles over a nominal 1-minute full cycle. Because in the calibration chamber the instrument is, of course, not spinning, the 30 spin angle measurements are redundant, and thus have been averaged to obtain the values shown in Figure 3.7.1. Each data point includes measurements only from times when the beam was impacting the specified CEM for the given electron beam energy.

The nominal energy steps are shown in Table 3.7.1. This table shows that for the nominal V_{ESA} stepping, particles at 500, 925, 1330, 1950, and 5158 eV are expected to be observed at Energy Steps 17, 19, 20, 21, and 24, respectively. Figure 3.7.1 demonstrates that particles at each energy are indeed observed only at the appropriate V_{ESA} steps, and that the counts for each V_{ESA}/spin angle measurement appear in the appropriate telemetry bins.

Table 3.7.1. The nominal SWE V_{ESA} stepping look up table, including the V_{ESA} DAC values and ranges and associated voltages and energies.

Energy Step	V (Volts)	V_{ESA} DAC	ESA RANGE	Energy (eV) = V*4.75
1	0.56	94	LO	2.66
2	0.78	130	LO	3.71
3	1.08	181	LO	5.13
4	1.51	252	LO	7.17
5	2.1	351	LO	9.98
6	2.92	488	LO	13.9
7	4.06	679	LO	19.3
8	5.64	943	LO	26.8
9	7.85	1312	LO	37.3
10	10.92	1825	LO	51.9
11	15.19	2539	LO	72.2
12	21.13	3532	LO	100.4
13	29.39	100	HI	140
14	40.88	140	HI	194
15	56.87	194	HI	270
16	79.1	270	HI	376
17	110.03	375	HI	523
18	153.05	522	HI	727
19	212.89	726	HI	1011
20	296.14	1011	HI	1407
21	411.93	1406	HI	1957
22	572.99	1955	HI	2722
23	797.03	2720	HI	3786
24	1108.66	3783	HI	5266

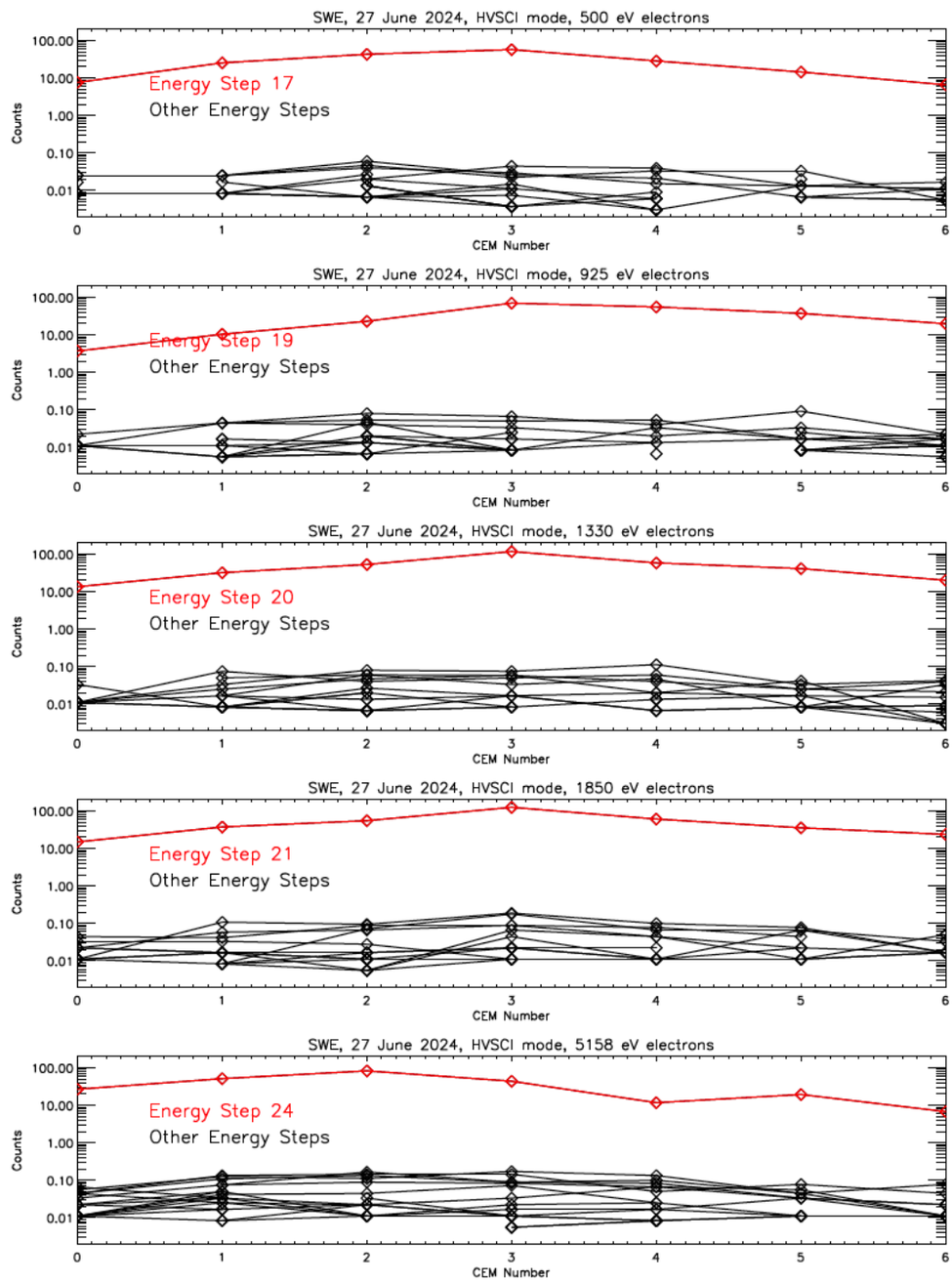


Figure 3.7.1. Average counts for the 7 SWE CEMs (numbered 0-6 rather than 1-7) for electrons at energies of 500, 925, 1330, 1850, and 5158 eV. For each energy, counts are observed only at the V_{ESA} step corresponding to that energy.

3.8 Background Noise

The SWE noise background was measured by examining CEM counts in the absence of particle input. With no particle beam present, each pixel shows < 5 Hz of noise counts. This represents < 0.5 count for each individual 80 ms energy/angle/angle accumulation. These noise rates were monitored throughout instrument testing and calibration. Figure 3.8.1 shows noise counts observed at full high voltage during thermal vacuum (TVAC) testing on 14 March 2024. Noise counts above 1 Hz were observed only at high temperatures, with the FEE temperature above 40° C and, in particular, as the temperature was reaching equilibrium at high temperature, perhaps related to noise from the temperature control circuitry.

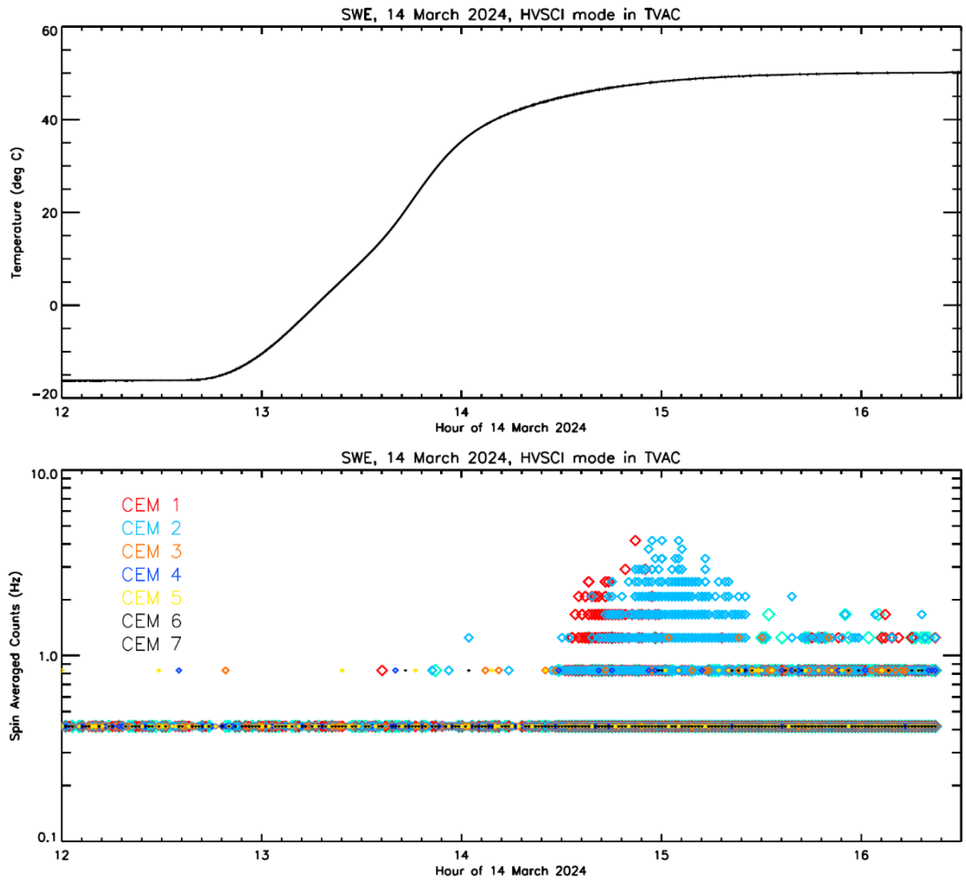


Figure 3.8.1. SWE FEE temperature (top) and background counts (bottom) at full high voltage during TVAC testing. A maximum 4 Hz count rate was observed at high temperature.

3.9 High Count Rate Test

Most calibration and testing with particle beams is performed at relatively low count rates to minimize use of CEM lifetime (the finite amount of charge that can be extracted). However, limited measurements were made at higher count rates to verify that instrument response was consistent over the expected range of count rates. For this test, measurements were made using 925 and 1000 eV electrons. Measurements covered a range of count rates, up to a maximum of 600 kHz. The time required to process each event, the deadtime, is 360 ns; applying this dead time correction (non-paralyzable model) to the measured count rates gives an actual maximum count rate of 775 kHz. Note that the deadtime correction is < 25% even at these very high rates. This test demonstrates that SWE can make measurements over a range of 775 kHz. Although we expect lower count rates (based on historical data from the heritage instruments), if such high rates are observed in flight this measurement shows that SWE can make valid measurements.

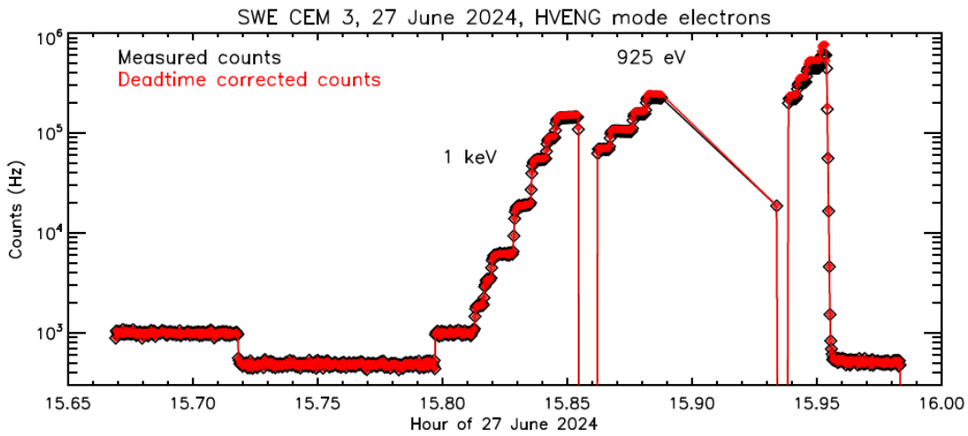


Figure 3.9.1. SWE measured (black) and deadtime corrected (red) counts in CEM 3 during testing at high count rates.

3.10 UV Sensitivity

The SWE instrument response to UV light was measured during Phase 1 characterization using a McPherson 634 UV lamp, which outputs ~0.2-Sun flux levels in the 115-165 nm wavelength range. Figure 3.10.1 shows the response of SWE to the UV lamp over the polar angle range of the instrument. We note that a small number of counts are observed at some angles, particularly in CEMs 1 and 7 when the UV light is directed at angles away from these pixels. This observation is consistent with heritage instrument observations of an occasional light signal at some angles. In addition to showing the measured count rates, the figure also indicates the counts that would be observed at full Sun UV levels in individual 0.080-second SWE measurements. The expected light signal is < 1 count/measurement for most angles, and < 5 counts/measurement at all angles. We note that the intermediate angles where highest counts are observed during this testing are unlikely to be realized in flight on the Sun-pointed IMAP spacecraft.

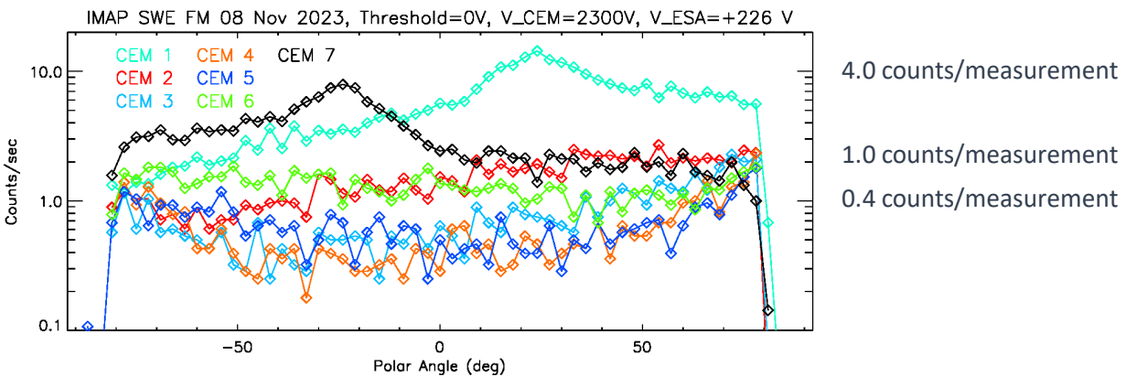


Figure 3.10.1. SWE response to UV light. This measurement shows that under expected pointing conditions SWE expects to see counts due to sunlight of < 1 count per measurement.

3.11 Microphonics Response

The SWE response to microphonics noise was measured by gently physically impacting the vacuum chamber with the instrument on at nominal voltages but with no input beam. This test, which determines if the resulting micro vibrations can generate signals in the SWE detectors or electronics, was only conducted during Phase 1 Characterization of the SWE Sensor Head. No instrument response was observed. The test was not repeated during Phase 2 or Phase 4 calibration because the electron gun was mounted directly to the vacuum chamber and we did not want to risk damaging this electron source which contains a fragile filament and precisely aligned electro-optics.

3.12 Alignment

SWE FOV alignment was confirmed through analysis. Worst case tolerance analysis was performed between the sensor aperture boresight and the SWE interface to the spacecraft. This analysis determined the worst-case tolerance impact of each sensor interface from the EBOX base to the SWE aperture for each rotational degree of freedom. The individual rotations for each axis were found to be 0.24°, 0.37°, and 0.22° for the x, y, and z axes, respectively. These maximum values for each axis were combined to determine the misalignment between the SWE interface to the spacecraft and the sensor aperture boresight. The total misalignment is 0.49°, within the 0.7° requirement.

3.13 High Voltage Power Supply Calibration

Knowledge of the measured particle energy is dependent on knowledge of the voltage applied to the ESA. Calibration of the HVPS supplies is thus an important component of the SWE calibration.

For the flight power supplies, board level calibration relating the HVPS monitor values to the HVPS output was performed over the full voltage range for both V_{CEM} and V_{ESA} (including both the ESA Low Range and the ESA High Range) at temperatures of -25° C, +25° C, and +40° C. These measurements provide knowledge of the relationship between the HV monitor values (which will be available in flight) and the actual HV levels (which for V_{ESA} determine the measured particle energy). HVPS calibration test results are given in Figure 3.13.1, which shows the error in the HV monitor values compared to the expected values over the voltage and temperature ranges.

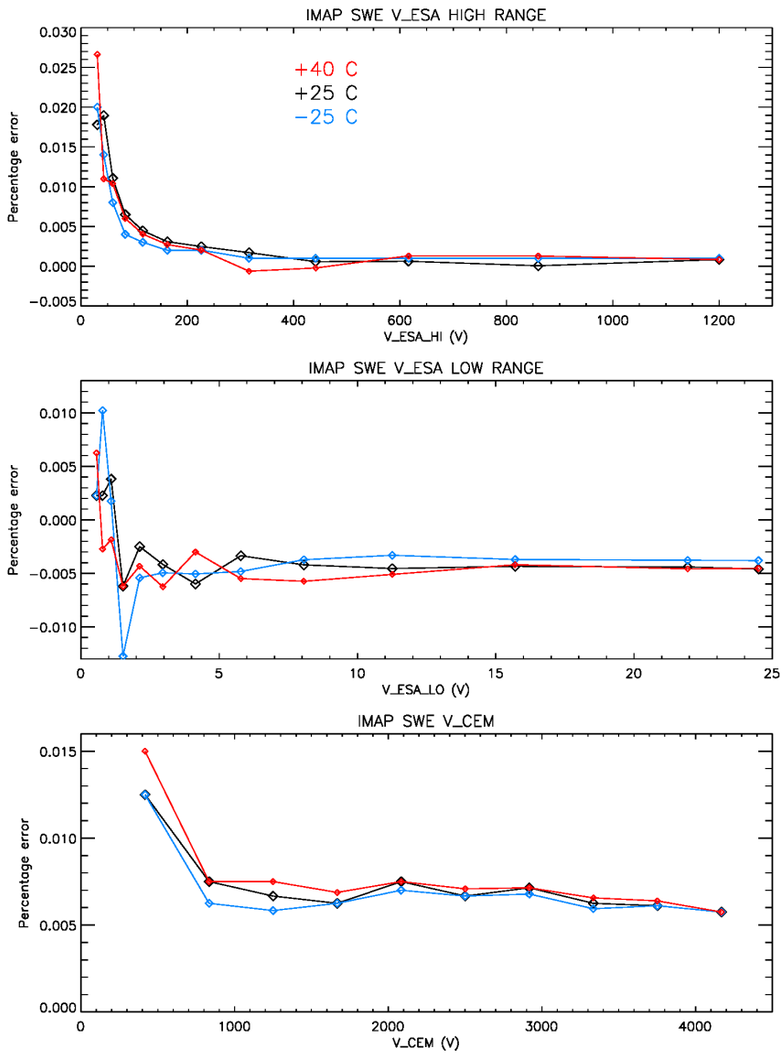


Figure 3.13.1. Percentage error in HVPS monitor values for the ESA High Range (top), ESA Low Range (middle) and the CEM (bottom) supplies.

Figure 3.13.1 show that the errors are largest at the low end of each supply, reaching values of up to 2.7% for the ESA High Range, 1% for the ESA Low Range, and 1.5% for the CEM HV. No systematic variation with temperature was observed, with small temperature variations only at the lowest end of each range. Absolute errors in the voltages were also measured, and are of the same order, highest at the low end of each range and less than 2% at all voltages and all temperatures. The small error observed in the CEM HV values will have no effect on SWE operations. The small errors in the ESA voltages will affect the measured electron energies, and can be accounted for in the analysis if necessary. However, as the energy bins are ~15% wide and are separated by ~40%, these < 3% corrections will not have a major effect on SWE analysis.

4 Electro-optic Modeling

Modeling of the SWE ESA is used to provide a full description of the SWE response and to determine the instrument geometric factors. The model is validated through comparison with electron measurements, and is then used to determine parameters that cannot be fully measured in the laboratory.

4.1 Geometry and SIMION Model

Although SWE is a high-heritage instrument, this is the first time a full electro-optic simulation of the instrument has been developed. For SWE, we used the mechanical CAD model of the instrument to develop a fully three-dimensional model in SIMION (Dahl, 2000). The model includes the entrance aperture, the inner and outer ESA plates, the ESA exit aperture and all 7 CEM detectors. The model resolution of 20 grid units per mm is sufficient to resolve the grooved analyzer plates. In the simulations, the entrance aperture and outer ESA plate are grounded, the ESA exit aperture and the CEM fronts are at +200 V, and the inner ESA plate can be varied to allow transmission of particles of a given energy.

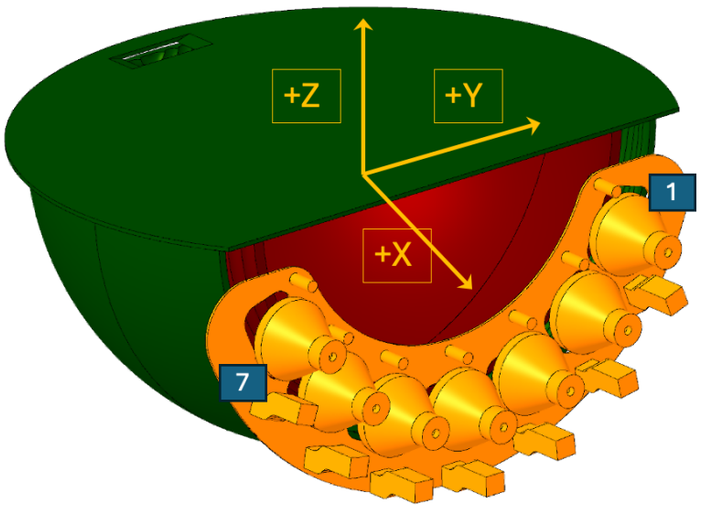


Figure 4.1.1. The SWE 3D CAD model used for electro-optic modeling. The entrance aperture is at the top left, the inner and outer ESA plates are red and green, respectively, and the CEM detectors are orange. The figure includes the SIMION coordinate system and the locations of CEMs 1 and 7.

The CAD model used to develop the SIMION model is shown in Figure 4.1.1, and a 2D cut of the SIMION model with example particle trajectories is shown in Figure 4.1.2. Both figures include the SIMION coordinate system, in which the x-axis points towards the CEMs, the z-axis points from the ESA plates toward the entrance aperture, and the y-axis completes the right-handed coordinate system with lower-numbered CEMs at more positive values of y. In Figure 4.1.2, particles pass through the entrance aperture at the bottom of the figure, then transit the ESA to reach the CEM detectors shown at the right.

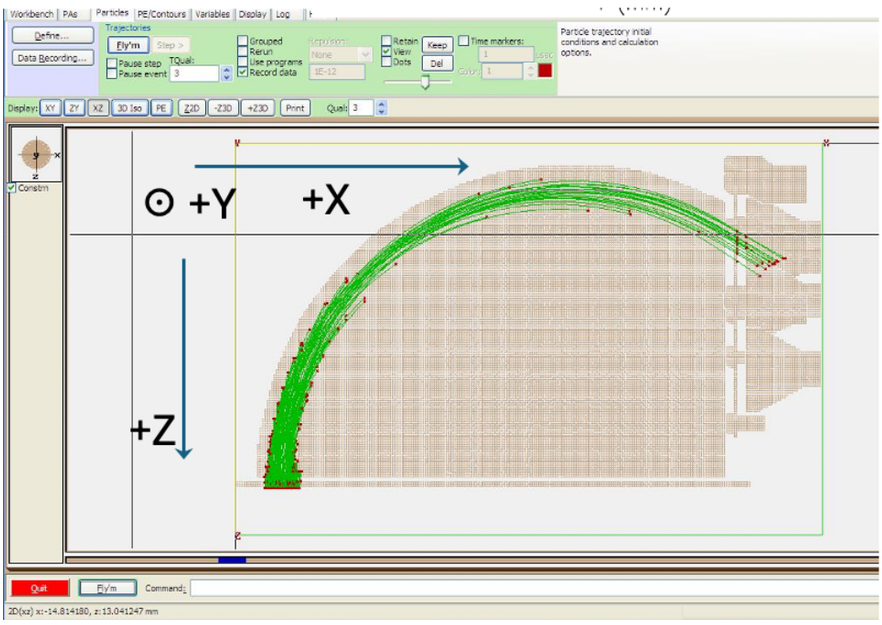


Figure 4.1.2. A cut of the SWE SIMION model in the x-z plane, with example particle trajectories shown in green and the SIMION coordinate system indicated in the upper left.

4.2 Model Results

The SIMION model is used with two different types of input. First, the particle input is designed to simulate the beam produced in the laboratory. This input provides validation of the model by allowing direct comparison with laboratory measurements. Secondly, the model is run with a random Monte Carlo input over the full instrument range, allowing determination of the instrument geometric factors. The Monte Carlo simulation included more than 10^8 electrons, of which 109,529 successfully transited the ESA and reached the detectors. This corresponds to ~15,000 valid events per CEM detector.

Figure 4.2.1 shows the results of SIMION simulation of particles entering SWE over the full entrance aperture and full range of input angles with V_{ESA} = 200 V and particles covering an energy range of 800 - 1150 eV. The figure shows the location of electrons at the CEM front location, after passing through the ESA. The simulation shows that 98.4% of electrons which transit the ESA reach the CEM detectors, verifying that the detectors are properly sized and located to optimize electron measurements. The separation of measurements on the 7 CEMs is defined by the ESA exit aperture.

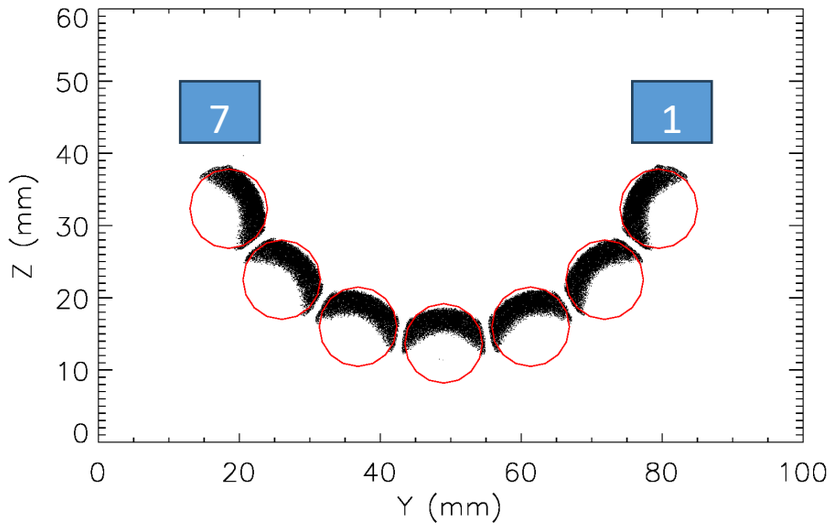


Figure 4.2.1. Locations of electrons on the 7 SWE CEM detectors.

Figure 4.2.2 shows a polar angle scan from SIMION, covering the full range of polar angles at an azimuthal angle of 0°, for comparison with calibration measurements where polar angle scans are performed at a single azimuthal angle. The figure also shows calibration measurements from a polar angle scan using 1 keV electrons (from Section 3.4). The measurements have been corrected for CEM gain, as shown above in Table 3.1.1. We note that the measurements in CEMs 1 and 7 are affected by scattering and blocking of the electron beam and so are not suitable for correlation. Also note that, as the SIMION results for CEMs 1 and 7 are from a single azimuthal angle, the results shown do not represent the peak response for these CEMs. Other than CEMs 1 and 7, the agreement between measurement and simulation is excellent. The polar angle response is also consistent with the results from the heritage Ulysses/SWOOPS-E (Bame et al., 1992) and ACE/SWEPAM-E (McComas et al., 1998) instruments.

Figure 4.2.3 shows examples of energy-angle scans from SIMION, and Table 4.2.1 summarizes the results of energy angle scans from SIMION modeling of all 7 CEM detectors. The average analyzer constant (k-factor) obtained for the 7 CEMs is 4.77, in good agreement with the value of 4.72 obtained during Phase 4 calibration. Based on the combination of measurements and simulations, we will use a SWE analyzer constant (k) of 4.75 for flight data analysis. We note that this value is consistent with the analyzer constants from the heritage instruments, which show analytic calculations of 4.3 – 6.0 (based on choosing to include or not include the analyzer plate grooves) and measured values of 4.4 – 4.8 (Bame et al., 1992, McComas et al., 1998, Barraclough et al., 2003).

The energy resolution from SIMION is slightly narrower than observed from measurements, consistent with minor additional scattering under real world conditions. Similarly, the azimuthal resolution is consistent with measurements. We note that there is an ~2° offset in the peak azimuthal angle for CEM 4 from laboratory measurements as compared to SIMION, with slightly larger errors for the other CEMs, indicating a remaining small offset in our understanding of the electron gun beam. Phase 4 calibration results are qualitatively consistent with the SIMION values, with the distribution peaking at more

positive azimuthal (ϕ) angles for CEMs away from the center. Again, the energy and angle resolution are consistent with measurements from the heritage instruments (Bame et al., 1992, McComas et al., 1998, Barraclough et al., 2003).

Taken together, the comparisons between laboratory calibration measurements and the SIMION model of the polar angle distribution and the energy/azimuthal angle distributions are sufficient to validate the SIMION model, which is then used to calculate the SWE geometric factors.

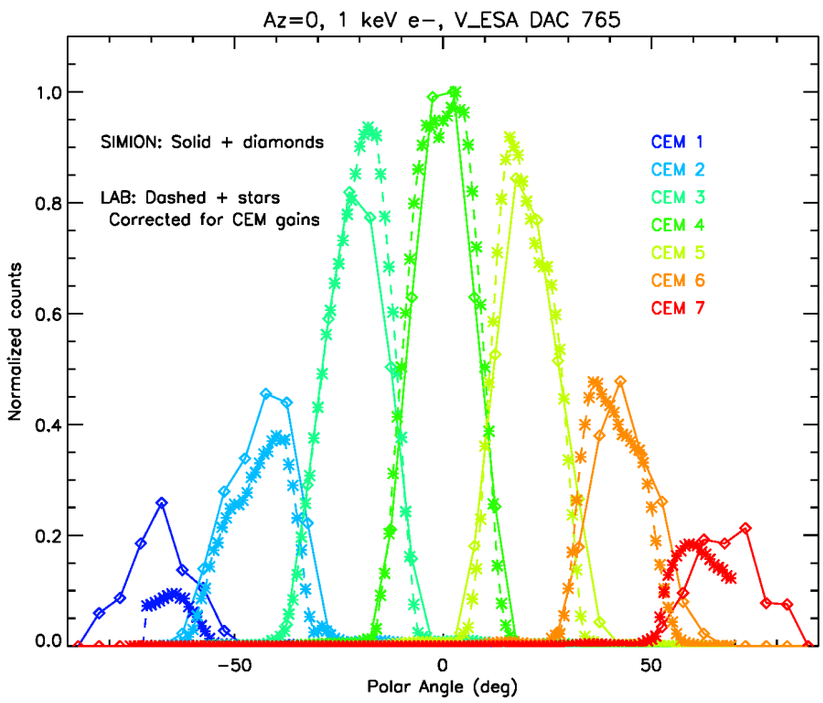


Figure 4.2.2. Polar angle scan from SWE Phase 4 calibration (dashed lines & stars) together with SIMION simulation of the same polar scan (solid lines & diamonds).

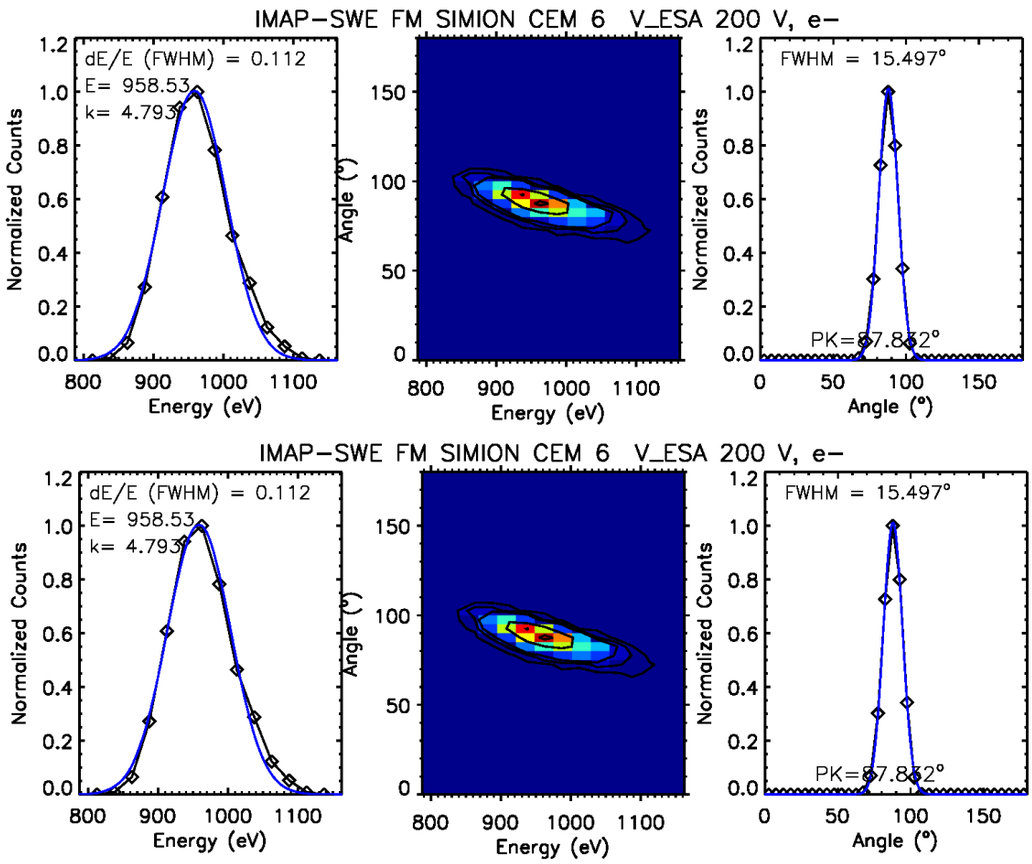


Figure 4.2.3. Example energy-angle scans from SIMION for CEMs 6 and 7, in the same format as Figures 3.6.1, 3.6.2, 3.6.3, and 3.6.4.

Table 4.2.1. SWE analyzer constant (k), energy resolution, and azimuthal angle resolution from SIMION modeling of all 7 CEMs.

CEM #	Energy	k	ΔE/E	ϕ (°)	$\Delta\phi$ (°)
1	1 keV	4.77	11.6%	6.8	36.9
2	1 keV	4.79	11.4%	2.2	15.8
3	1 keV	4.79	11.3%	1.3	11.2
4	1 keV	4.78	11.2%	1.3	9.7
5	1 keV	4.80	11.2%	1.6	11.0
6	1 keV	4.79	11.2%	2.2	15.5
7	1 keV	4.78	11.1%	7.0	35.8

4.3 Geometric Factors

The geometric factor G (cm^2 sr eV/eV) relates the measured counts C to the intensity of particles entering the instrument per unit area, solid angle, and energy. SWE geometric factors are calculated in two ways, first analytically based on the Cookbook for Spherical Analyzers (Gosling et al, 1984) and second numerically using the validated SIMION model. In both cases, the geometric factor is calculated separately for each CEM, by integrating over the range of input locations, energies, and angles. Figure 4.2.4 shows SWE geometric factors G for the 7 CEMs. The top panel shows the geometric factors calculated via both methods, and includes only these purely geometric effects. The results from the two methods agree to within 10%. The bottom panel of Figure 4.2.4 shows the SWE geometric factor including the CEM entrance grid transmission of 88%, CEM efficiency of 78%, and the CEM gain factors given in Table 3.1.1. These geometric factors are also given in Table 4.2.2. The bottom panel also includes the geometric factors from the heritage ACE/SWEPAM-E instrument (McComas et al., 1998). The SWE geometric factors are slightly higher than the SWEPAM-E geometric factors, and are also comparable to the heritage Ulysses/SWOOPS-E geometric factors (McComas et al., 1998).

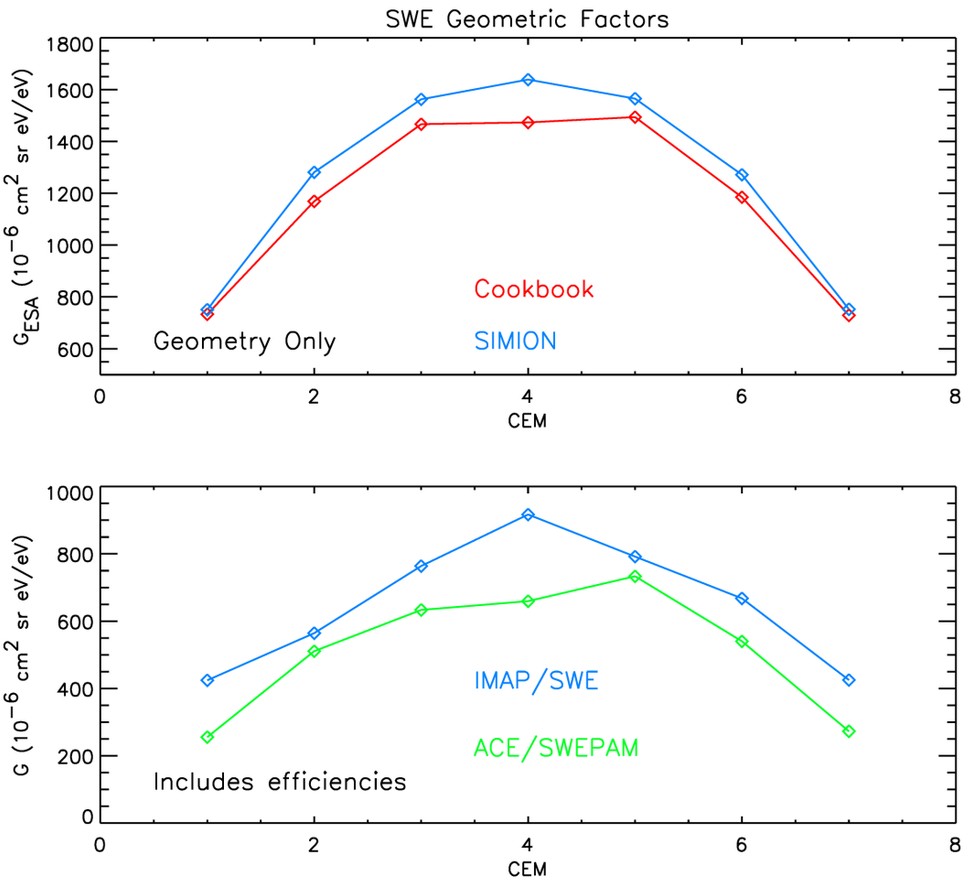


Figure 4.2.4. Top: SWE geometric factors calculated analytically and numerically. Bottom: SWE geometric factors including efficiency factors compared with the heritage ACE/SWEPAM-E geometric factors.

Table 4.2.2. SWE Geometric factors, in units of 10^{-6} cm^2 sr eV/eV)

CEM #	Geometric factor (10^{-6} cm^2 sr eV/eV)
1	424.4
2	564.5
3	763.8
4	916.9
5	792.0
6	667.7
7	425.2

5 Conclusions

Through the calibration measurements presented in this report, we have shown that the SWE instrument meets the measurement requirements as outlined in Table 2.1 and that SWE has been calibrated sufficiently to allow understanding of in-flight data. The Verification column of Table 2.1 shows the section in this report in which each requirement is verified, and the Value column shows the SWE instrument parameters obtained through calibration. SWE is capable of measuring electrons over an energy range of 1 eV to 5 keV. Energy resolution $\Delta E/E$ is < 15% (FWHM), and intrinsic angular resolution is < 22.5° in the polar direction (CEM to CEM) and < 30° (FWHM) in the azimuthal direction (within a CEM). As with all spherical analyzers, the azimuthal resolution is a strong function of polar angle, with resolution of < 15° for CEMs 2-6, and a broader measurement range for CEMs 1 and 7. The stepping high voltage power supplies cover the full energy range over 4 15-second scans, with half the energies measured in each 15-second quarter cycle, providing a full electron measurement over four 15-second spacecraft spins, with a reduced resolution measurement obtained during each 15-second spin. Since instrument data collection is independent of the spacecraft spin rate, SWE can make measurements over a range of spin rates without affecting the telemetry rate or the ability to make a measurement. The SWE geometric factors exceed the requirement, and will allow SWE to make valid measurements through the expected range of solar wind conditions. SWE has been demonstrated to be insensitive to UV light contamination, indicating operability through expected L1 conditions.

6 References

Bame, S. J., D. J. McComas, B. L. Barraclough, J. L. Phillips, K. J. Sofaly, J. C. Chavez, B. E. Goldstein, and R. K. Sakurai, The Ulysses Solar Wind Plasma Experiment (1992), Astron. Astrophys. Suppl. Ser., 92, 237-265.

Barraclough, B. L., et al. (2003), The Plasma Ion and Electron Instruments for the Genesis Mission, Space Sci. Rev., 105, 627-660.

Dahl, D. A. (2000), SIMION for the personal computer in refletion, Int. J. Mass Spectrom, 200(1-3), 3-25, doi:10.1016/S1387-3806(00)00305-5

Gosling, J. T., M. F. Thomsen, and R. C. Anderson (1984), A Cookbook for Determining Essential Transmission Characteristics of Spherical Section Electrostatic Analyzers, Los Alamos National Laboratory Report LA-10147-M.

McComas, D. J., S. J. Bame, P. Barker, W. C. Feldman, J. L. Phillips, P. Riley, and J. W. Griffee (1998), Solar Wind Electron Proton Alpha Monitor (SWEPAM) for the Advanced Composition Explorer, Space Sci Rev., 86, 563-612.

3.4.3 In-Flight Calibrations

SWE in-flight calibration report to be included here.

3.5 MAG

3.5.1 Strategy & Approach

IMAP's MAG calibration consists of a combination of ground and in-flight efforts to ultimately determine the gain matrix and offsets vector to convert the instrument measured field to the best estimate of the true vector magnetic field in space. In-flight calibrations are a critical component for MAG since the spacecraft-generated magnetic fields can only be truly estimated when operating in space.

Ground calibration of IMAP MAG was conducted at Magnetsrode facility near Braunschweig, Germany. There, all three axes of the sensors were tested to demonstrate sensitivity, orthogonality, stability, linearity, and temperature dependencies. Overall, these demonstrated the performance of the sensors satisfied the measurement requirements for the MAG instrument.

In-flight calibrations take advantage of IMAP being a spinning observatory, and procedures and results are described in the "In-Flight Calibrations" report embedded below. Furthermore, IMAP's MAG benefits from cross-calibration efforts with the SOLAR-1 mission, which launched with IMAP and were on a very close and similar outbound trajectory to L1, and the pre-existing ACE, Wind, DSCOVR, and Aditya-L1 missions already in operation around the Sun-Earth L1 point.

3.5.2 Pre-Flight Instrument Calibration

MAG cal report embedded below

IMAP PROJECT

IMAP MAG CALIBRATION INPUTS DESCRIPTION

MAG
MAGNETOMETER INSTRUMENT

project	IMAP
instrument	Magnetometer Instrument
code	MAG
organisation	Imperial College London
document title	IMAP MAG Calibration Inputs Description
prepared by	Mhairi Finlayson
approved by	Helen O'Brien
reference	IMAP-OPS-TN-ICL-017
issue	2
revision	0
date of issue	4 Jun 2026

CHANGE LOG

Date	Issue	Revision	Reason for change
25 March 2026	1	0	First release
4 Jun 2026	2	0	Updated in line with Data Release 1

Note: List of changes since first release.

CHANGE RECORD

Section(s)	Reason for change
All	All inputs updated for v2.2.0 calibration and Data Release 1

Note: Detailed changes are listed for this issue only. For previous changes, see earlier issues.

TABLE OF CONTENTS

Change Log 2
Change Record 2
Table Of Contents 2
1 Scope 3
2 Summary of Inputs to the Processing Flow 3
3 Calibration Matrices 4
3.1 Matrices used (CalibrationMatricesV9) 4
3.1 Discussion of angle determination 4
4 Spin Plane Offsets 8
4.1 Alternative Offset Optimisation 9
5 Spin Axis Offsets 12

1 Scope

This document describes the inputs used in the MAG calibration process, specifically sensor offsets calculated using techniques derived from the following references:

- Solar wind–based offset determination (Leinweber et al. [DOI 10.1088/0957-0233/19/5/055104]) – targeting spin axis offset
- Spinning spacecraft offset determination (Kepko et al. [DOI 10.1109/20.486522]) – targeting spin plane offsets and angular misalignments

These are collectively referred to as “calibration” to distinguish them from spacecraft-field cleaning techniques (see IMAP-OPS-TN-ICL-013 MAG Data Cleaning Processes for details).

The results of these Calibration techniques are used as version controlled inputs to the processing flow in IMAP-OPS-TN-ICL-013 to generate offset files used by the SDC for L2 science production.

This document applies to calibration code **v2.2.0** and the inputs used for the Data Release 1 (covering 1-Jan to 29-Apr 2026).

Release v2.2.0 · ImperialCollegeLondon/IMAP_MAG_Calibration

2 Summary of Inputs to the Processing Flow

There are three inputs to the calibration chain for producing L2 MAG data – all are under version control. The versions referenced here correspond to calibration code v2.2.0 and the inputs used for the Data Release 1 (covering 1-Jan to 29-Apr 2026).

1. Calibration Matrices (.mat): Describes sensor misalignment
   - Version used: *CalibrationMatricesV9*
2. Spin Plane Offsets (CSV): Describes offsets in X and Y (sensor frame).
   - One file per day per sensor
   - Version-controlled via: *calibration_input_release1_v001.json*
3. Spin Axis Offsets (CSV): Describes offset in Z (sensor frame)
   - 4 files per sensor covering full time period (1-Jan to 29-Apr 2026)
   - File names and versions are captured in: *calibration_input_release1_v001.json*

The calibration input files are captured in the parent metadata field of the released L2 science data files. They are archived at Imperial College London in addition to the individual offset files.

3 Calibration Matrices

3.1 Matrices used (CalibrationMatricesV9)

These matrices are in relation to the IMAP_MAG_BASE frame defined in the IMAP SPICE kernels.

MAGo

Element	Value
Theta 1	89.6895°
Theta 2	89.5617°
Theta 3	0.5700°
Phi 1	0.0000°
Phi 2	89.9403°
Phi 3	-120.5000°
Gain 1	1.0000
Gain 2	0.9991

MAGi

Element	Value
Theta 1	89.6914°
Theta 2	89.6731°
Theta 3	0.3953°
Phi 1	0.1988°
Phi 2	90.0672°
Phi 3	221.9409°
Gain 1	0.9986
Gain 2	0.9994

3.1 Discussion of angle determination

The DSRF (Despun Spacecraft Reference Frame) is used as a spin-axis-aligned inertial reference frame, in order to accurately calculate the alignment matrix.

The large coronal mass ejection (CME) on 19–20 January 2026 provided a period of high magnetic field strength, which was used to help separate the angular contribution to the spin tone from the offset contribution.

- The alignment of the spin axis (Theta 3 and Phi 3) was calculated by minimising the spin tone in the DSRF Z axis after application of the calibration matrix, and transformation into the DSRF.
- Theta 1 and Theta 2, (the angles of the X and Y axes relative to the SC Z axis) were similarly calculated by minimising the spin tone in the DSRF spin plane.
    - The Theta 1 and Theta 2 values were assessed by applying the calibration matrices, and recalculating the angles using Kepko – an ideal result of 90 degrees would indicate total agreement (see Figure 1 and Figure 2)
- Phi 2 is calculated by minimising the second harmonic of the spin – again for the CME period (see Figure 3 and Figure 4)
- The process was repeated to derive MAGi values, and then additional optimisation was performed to MAGi values to align MAGi well with MAGo over the CME, so that gradiometer can be used effectively (see Figure 5 and Figure 6)

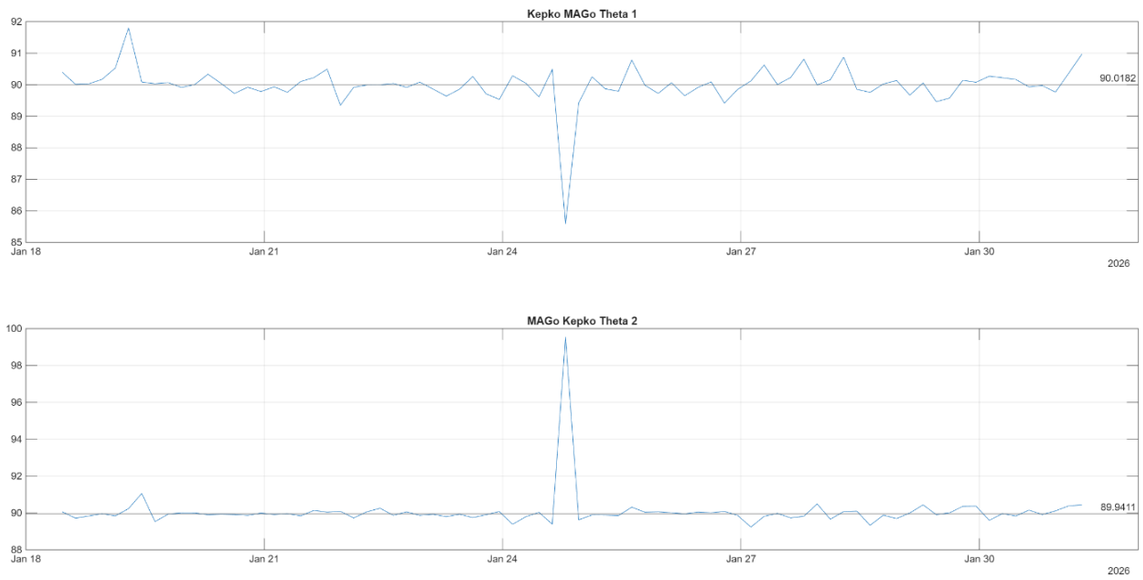


Figure 1: Quality check: MAGo Theta 1 & 2 Values calculated by Kepko following application of V9 calibration matrices. The agreement was within 0.1 degrees over the assessed time period. The data point calculated from 1am-5am on 20-Jan – a quiet period with large magnetic field – was within 0.01 degrees. This level of agreement was considered sufficient to proceed with these values.

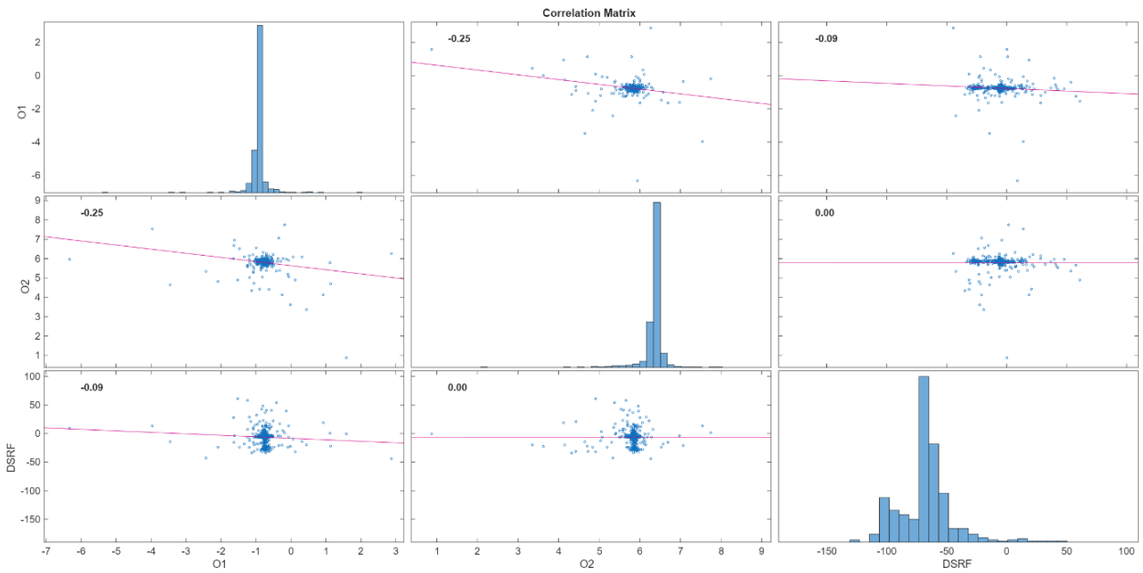


Figure 2: Quality check: MAGo Theta 1 & 2 Values: Correlation between calculated offsets and DSRF Z axis to diagnose issues with calculated angles. Note: small correlation r=0.09 between offset and DSRF Z, accepted for this release, could be target for further improvement in future. The strong correlation between Offset 1 and Offset 2 is expected (r=0.25), as that is indicative of real spacecraft interference.

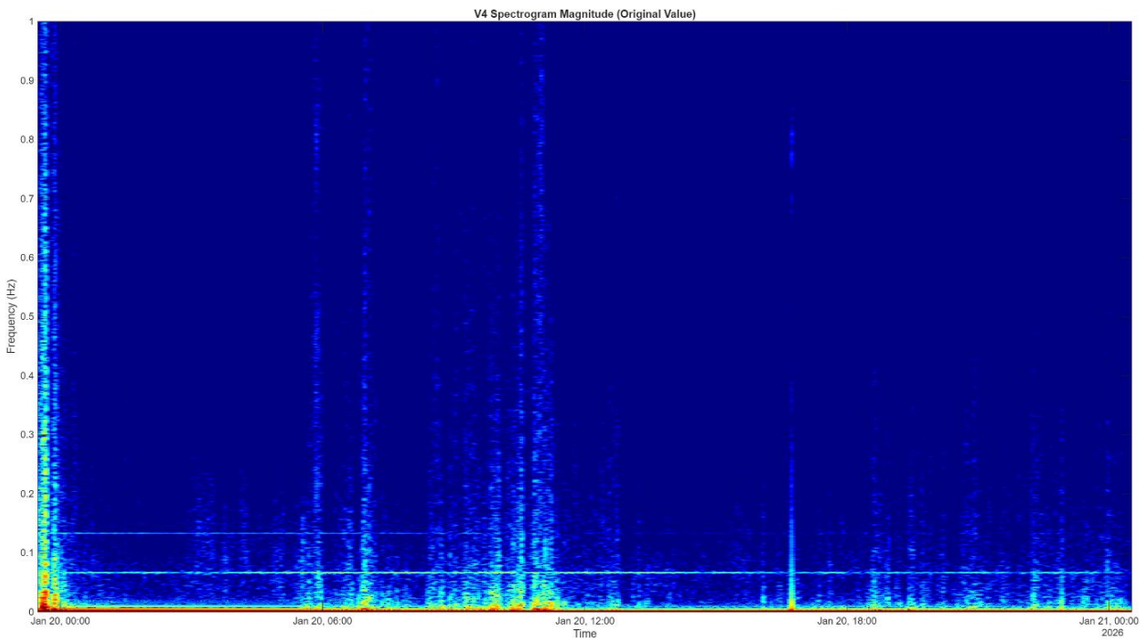


Figure 3: Plot used to identify MAG0 Phi2 angular errors. This plot clearly shows a tone at the twice the spin frequency during the CME (00:00 to 12:00 on Jan 20), this tone disappeared when the updated calibration matrix was applied, indicating greater angle accuracy had been achieved

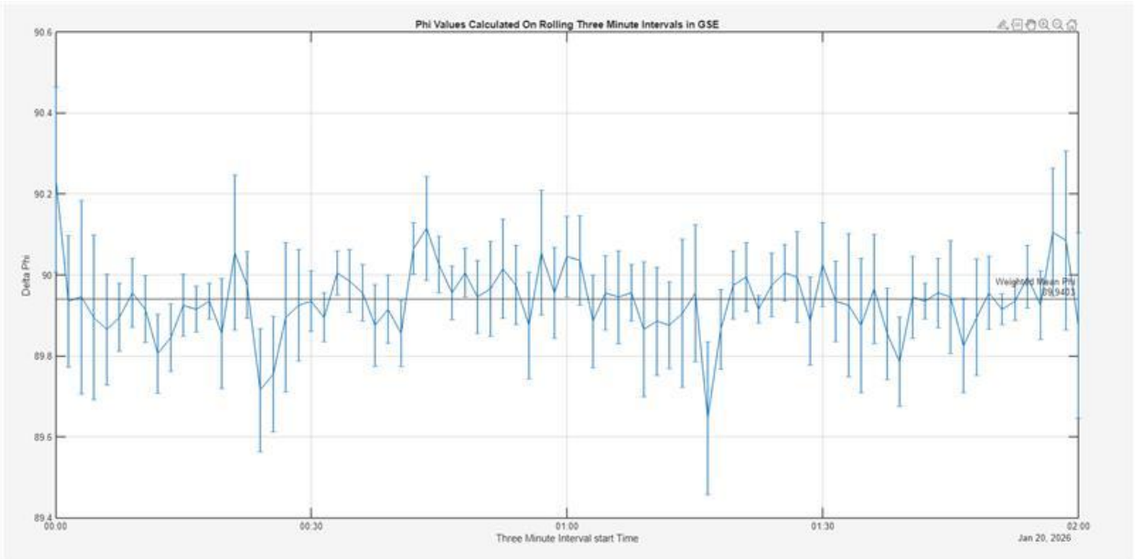


Figure 4: Plot used to identify the angle between X and Y (MAGo Phi2). Angle was optimised to minimise 2nd harmonic frequency of the spin tone, over 3-minute periods during the CME, when with a large field, the impact of angle errors are most acute. Plot shows optimised angle calculations with error bars. Final angle used is a weighted mean of these values.

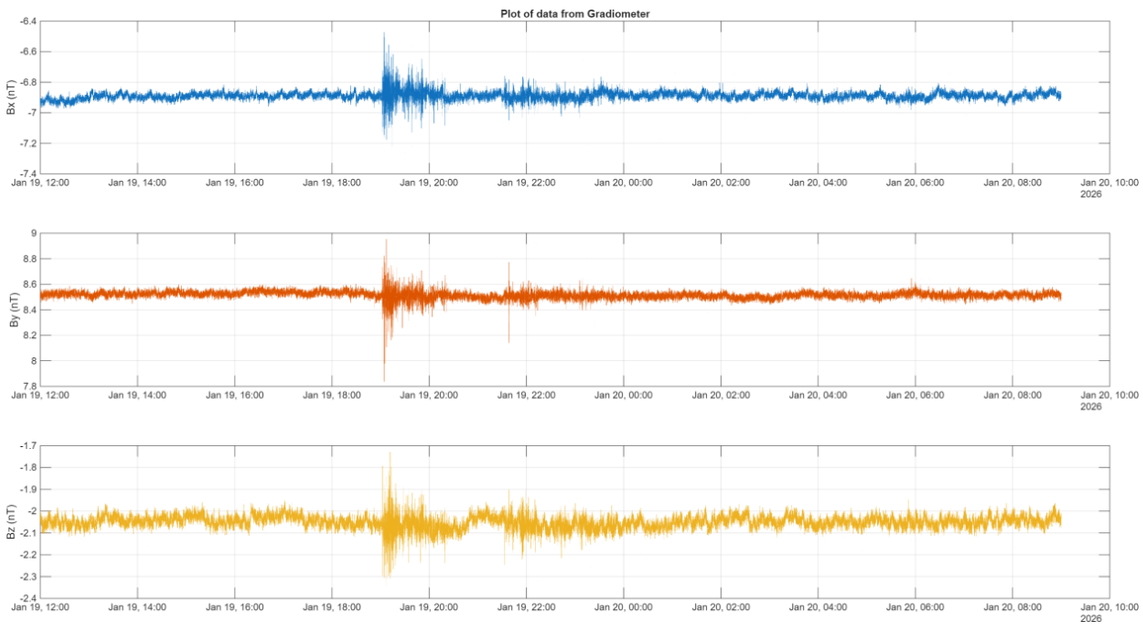


Figure 5: Quality check MAGi and MAGo co-alignment. Gradiometer over the CME using V9 matrices, indicating good alignment between MAGo and MAGi

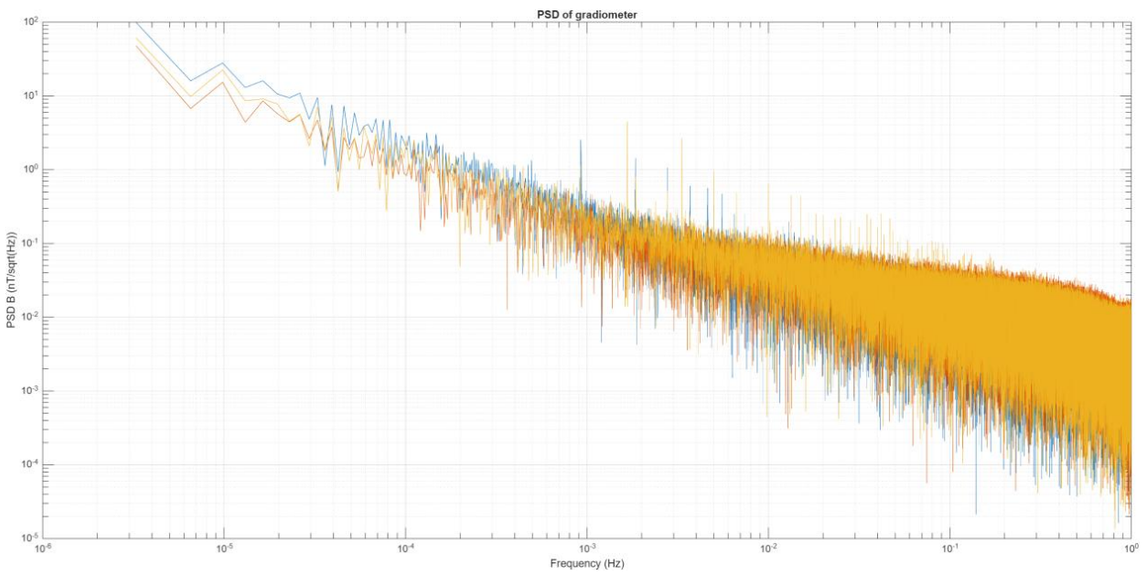


Figure 6: Quality check MAGi and MAGo co-alignment. Example PSD of the gradiometer measurement after calibration matrices applied showing decontamination heater and Hi generated signals (note these are cleaned using techniques described in TN-013), but no spin tone, indicating good angular alignment

4 Spin Plane Offsets

Kepko is used to calculate rolling offsets, using an 8 hour window with fixed angles based on the pre-calculated calibration matrices. Offset calculation is performed after pivot platform removal.

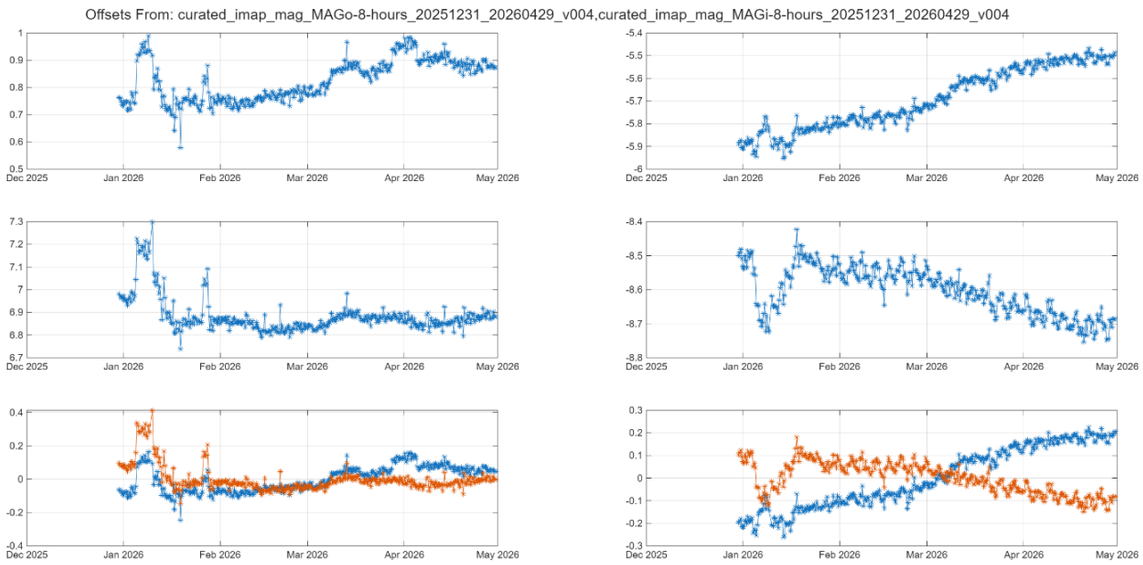


Figure 7: Plot of baseline offsets – showing overall trends during the period. Smaller time period changes are captured in the optimisation process described below. *Left:* X axis; top – MAGo, middle MAGi, bottom MAGo and MAGi with means removed *Right:* Y axis; top – MAGo, middle MAGi, bottom MAGo and MAGi with means removed

Baseline Offset	Maximum Value	Minimum Value	Mean Value	Std Dev
MAGo Offset X	0.989 nT	0.578 nT	0.826 nT	0.076 nT
MAGo Offset Y	-5.468 nT	-5.954 nT	-5.692 nT	0.134 nT
MAGi Offset X	7.297 nT	6.738 nT	6.884 nT	0.079 nT
MAGi Offset Y	-8.423 nT	-8.754 nT	-8.604 nT	0.070 nT

Table 1: Baseline spin plane offset ~~values~~metrics from 1-Jan to 29-Apr

These baseline offsets are used as input into a rolling offset optimisation strategy based explicitly on reducing spin tone. For each day, offsets are calculated on initially 3 hours of data, explicitly minimising the spin tone in the magnitude. These offsets are then applied through linear interpolation, and the general spin tone above the background is measured on an hourly basis. If the offsets do not sufficiently reduce the spin tone, then they are recalculated on progressively smaller intervals, down to six minute intervals, in order to capture the offset variations. Offset optimisation is applied post pivot platform removal, Hi and Ultra interference removal, and baseline offset application.

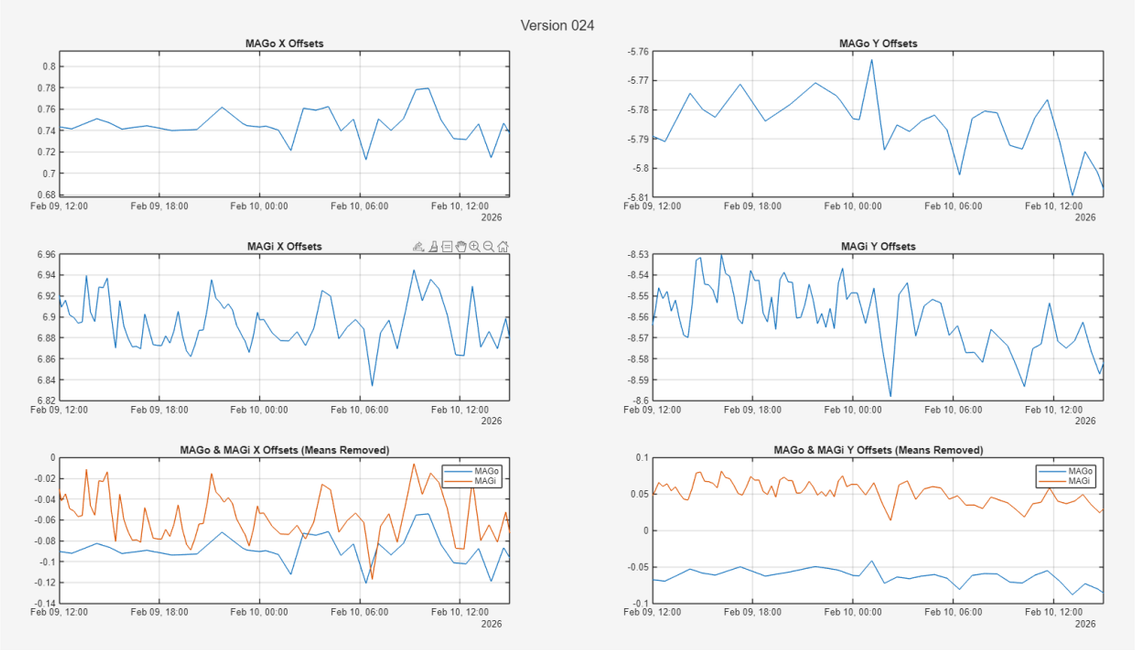


Figure 8: An example of the combined spin plane offsets applied (combination of optimised plus baseline) for 2 days in February. This indicates that MAGi is varying more than MAGo indicating real removal of spacecraft generated signals rather than noise introduced by the optimiser.

4.1 Alternative Offset Optimisation

For a small number of days in the 1-Jan to 29-Apr window, significant spin tone was visible in the components after minimisation in the magnitude. Analysis of these days indicated that raw magnitude level minimisation was likely removing real signals at that frequency, and spin tone was introduced in the components by the offset optimisation strategy. For those days, an alternative strategy has been adopted; offset optimisation to minimise the component level spin tone, over longer time intervals.

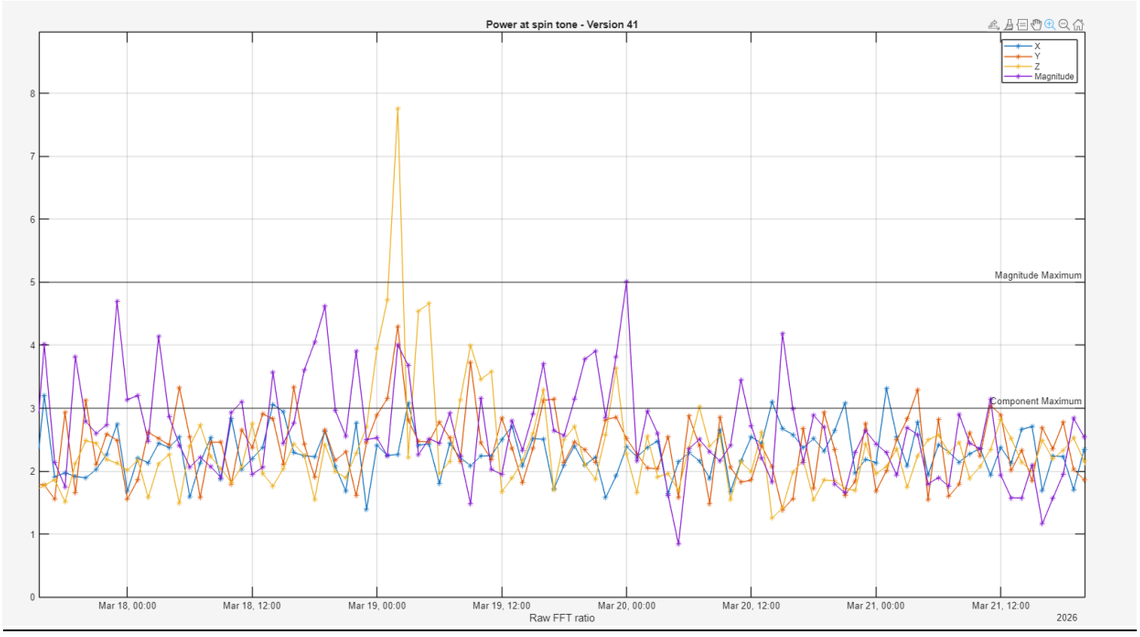


Figure 9: GSE axes plot of spin tone over background for 18-21Mar using original magnitude-spin reduction optimiser. There is enhanced spin tone in the Z axis for 19-Mar, which was introduced by the optimiser trying to suppress spin tone in the field magnitude. This was highlighted as an issue and has been resolved using the component level spin tone optimiser see Figure 12

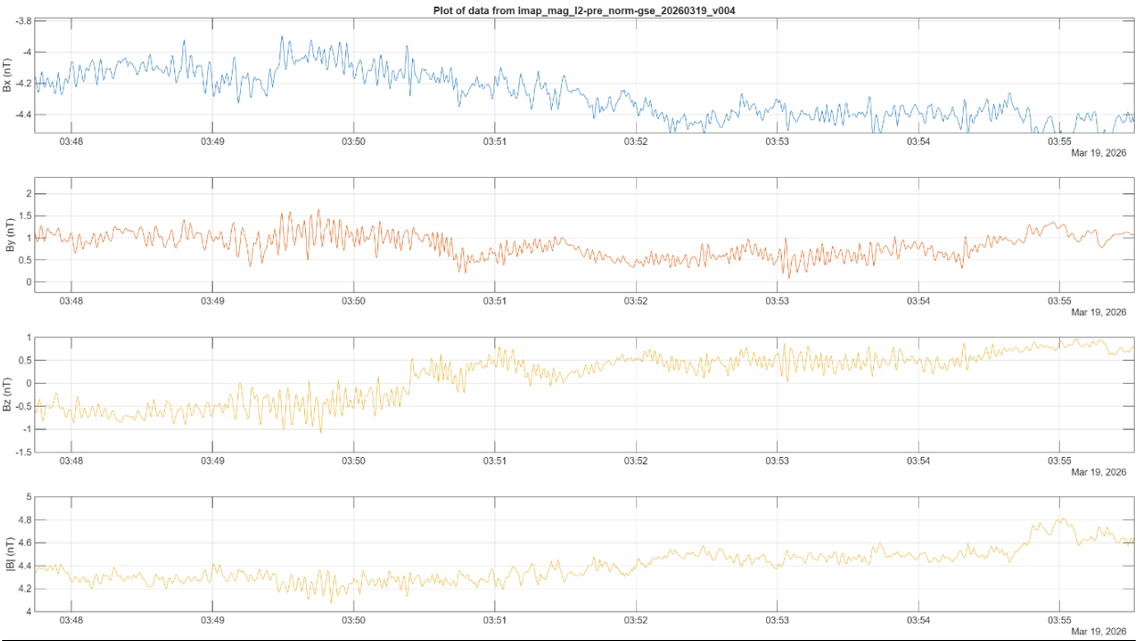


Figure 10: Time series of MAGo calibrated and cleaned data from 19-Mar. This shows solar wind power at the spin frequency – this was reducing the effectiveness of the magnitude-spin-reduction optimiser.

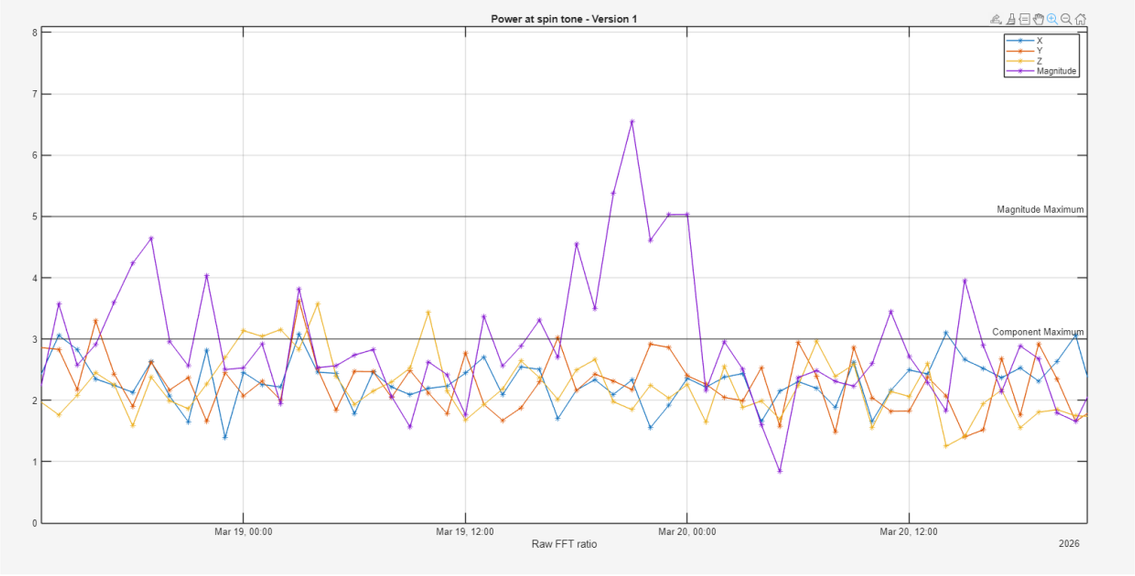


Figure 11: Spin tone after alternative offset optimisation strategy - reduction in component level spin tone, which is considered a more accurate reflection of the real science. Note: there is an associated increase in magnitude spin tone later in the day, so the approach is still not ideal. Further work could be done in this area in future iterations.

5 Spin Axis Offsets

Leinweber technique implemented code generates an offset per day and the percentage of each day which was used in the calculation. The final offset values are derived from a linear fit to the data. Days where less than 5% of the day were used are automatically excluded. Outliers are excluded automatically with a threshold of 1.5x the standard deviation using a moving mean.

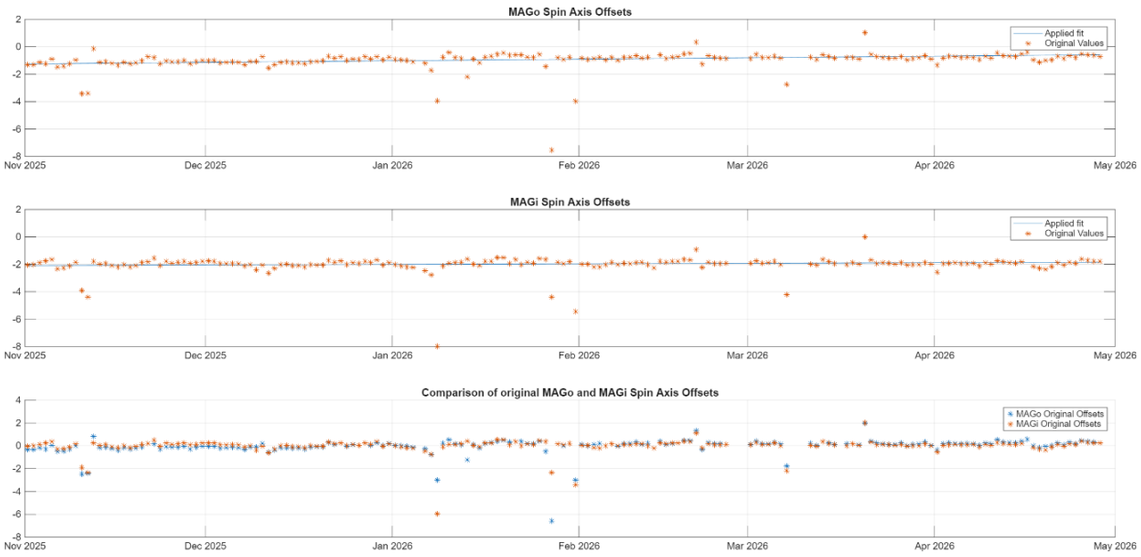


Figure 12 - Spin axis offsets with fit for MAGo and MAGi

Offset	Maximum Value	Minimum Value	Mean Value	Std Dev
MAGo Offset Z	1.250 nT	0.585 nT	0.974 nT	0.209 nT
MAGi Offset Z	2.092 nT	1.848 nT	1.990 nT	0.076 nT

Table 2 - Spin axis offset metrics from 01-Jan to 29-Apr 2026

[END OF DOCUMENT]

3.5.3 In-Flight Calibrations

The following describes the IMAP/MAG data cleaning process

IMAP PROJECT

IMAP MAG DATA CLEANING PROCESSES

MAG
MAGNETOMETER INSTRUMENT

project	IMAP
instrument	Magnetometer Instrument
code	MAG
organisation	Imperial College London
document title	IMAP MAG Data Cleaning Processes
prepared by	Mhairi Finlayson
approved by	Chris Greenaway
reference	IMAP-OPS-TN-ICL-013
issue	5
revision	0
date of issue	26th August 2026

CHANGE LOG

Date	Issue	Revision	Reason for change
12 Jan 2026	1	0	First release
29 May 2026	2	0	Updated for code v2.2.0 and data released in August 2026
4 June 2026	3	0	Focused version to be used as input for CMAD which includes descriptions of future improvements
4 June 2026	4	0	Removal of non-relevant sections for CMAD
24 Aug 2026	5	0	Updated for Release 2 and code v3.3.6

Note: List of changes since first release.

CHANGE RECORD

Section(s)	Reason for change
2	Update version of code and flow diagram
3.1	Put IMAP Lo Deltas in a table
3.3	Pre thruster and thruster removal process updated to reflect latest code version
4	Description of Trajectory Correction Manoeuvre cleaning added
5.1	Inserted plot showing pivot platform signal in L2 data

Note: Detailed changes are listed for this issue only. For previous changes, see earlier issues.

TABLE OF CONTENTS

Change Log 2
Change Record 2
Table Of Contents 2
1 Scope 3
2 Processing Flow 3
3 Features cleaned from IMAP MAG data 5
3.1 IMAP Lo Pivot Platform 5
3.1.1 Signal Characterisation 5
3.1.1 Cleaning Process 6
3.1.2 Results 8
3.2 H90 / H45/ ULTRA Decon heaters 9
3.2.1 Super-posed Epoch Analysis 9
3.3 Thrusters and pre-thruster signal removal 11
3.3.1 Signal Characterisation 11
3.3.2 Profile Characterisation 13

3.3.2.1 Pre thruster signal 13
3.3.2.2 Thruster Signal 13
3.3.3 Profile removal process 14
3.3.4 Results 15
3.3.5 Residual signal in Thruster Cleaning 16
4 Trajectory Correction Manoeuvre Cleaning 16
5 Features noted but not yet cleaned from IMAP MAG data 19
5.1 Pivot Platform Movement 19

1 Scope

This document describes the cleaning processes for features identified in the IMAP MAG data. The cleaning processes are applied to all L2 data.

This document is valid for MAG calibration code **V3.3.6 and the inputs used for the Nov 2026 data release covering 1-Nov 2025 to 31-Jul 2026.**

Release v3.3.6 · ImperialCollegeLondon/IMAP_MAG_Calibration

2 Processing Flow

Version: V3.3.6
The calibration flow is defined by the wrapper script calibrate_L2_offsets.m. This script loads the required HK and configuration settings, calls the subroutines for cleaning of specific data features and generates the final offsets, which are applied to L1C (normal mode) and L1B (burst mode) to generate the L2 data products.

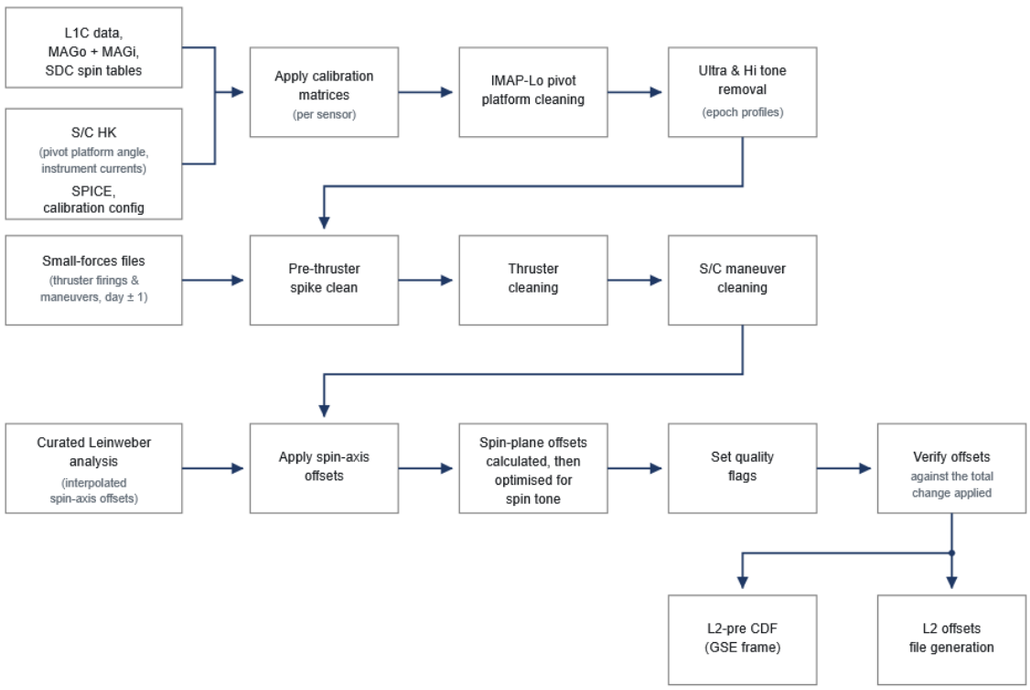


Figure 1: Calibration Code v3.3.6 Flow

The flow incorporates the following blocks:

1. Apply Calibration File (matrices): for discussion of how angles are determined see IMAP-OPS-TN-ICL-017 for further details.

2. ILO pivot platform is cleaned (see Section 3.1)

3. Ultra Decontamination Heater and HI45/90 signal removal (see Section 3.2)

4. Thruster and pre-thruster cleaning (see Section 3.3)

5. Spacecraft Maneuver Cleaning (see Section 4)

6. Apply spin axis offset correction (calculated using solar wind techniques see IMAP-OPS-TN-ICL-017 for further details)

7. Calculate and apply Spin plane offset correction (combines a baseline and spin-tone reducing optimised offset: see IMAP-OPS-TN-ICL-017 for further details)

8. The output is a file with an offset for each vector in the input L1C (normal mode) or L1B (burst mode) file. This is used by SDC to produce the final L2 products.

3 Features cleaned from IMAP MAG data

3.1 IMAP Lo Pivot Platform

The Pivot Platform (PP) was highlighted before launch as being a known magnetic contamination source. Dedicated code has been put in place to clean this signal.

3.1.1 SIGNAL CHARACTERISATION

The IMAP-Lo Pivot Platform is a component of the IMAP-Lo instrument – it moves through up to 180 degrees of motion. For the period Sep-25 to Jul-26, it had three set points and moved up to once a day. Set points are at 75 degrees, 90 degrees, and 105 degrees.

These three positions of the pivot platform each result in a different magnetic signal at MAGo (and MAGi). The difference is large, and visible in rolling spin plane offsets as well as in gradiometry. Other more complex signatures are seen during the movement itself.

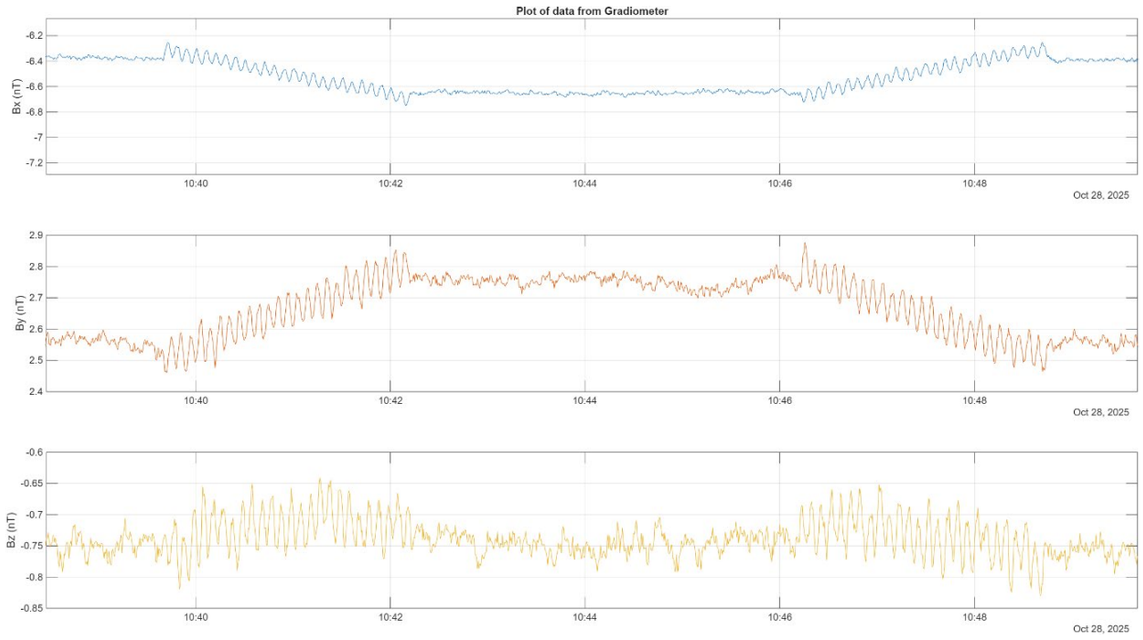


Figure 2 - ILO pivot platform movement seen in the MAG data. Figure shows the gradiometer at the time of a movement (difference between the measured field at MAGo compared to MAGi). Step change before and after movement plus more complex field signature during movement are clearly seen.

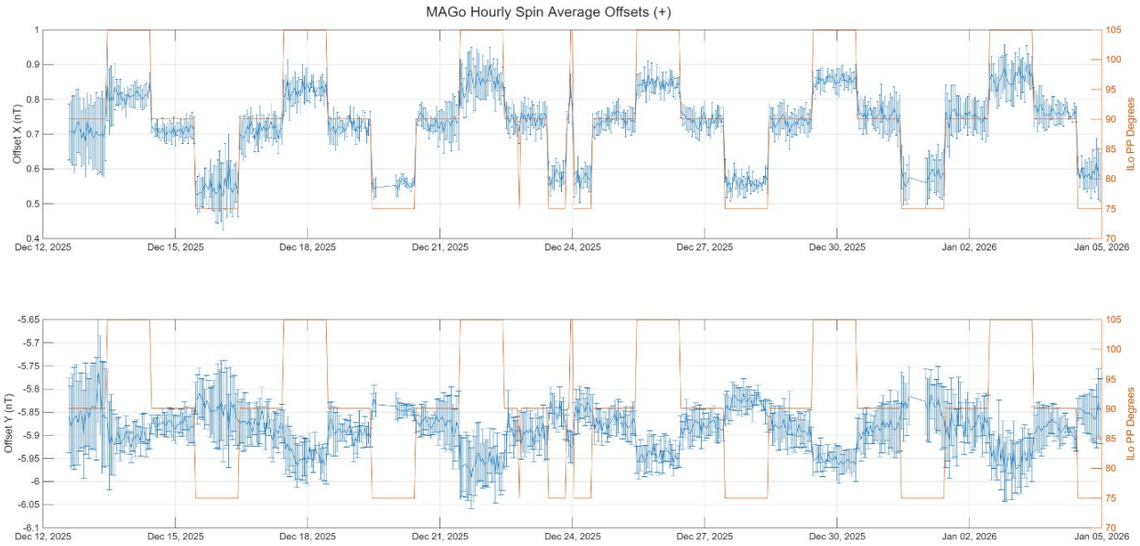


Figure 3: Rolling spin averaged MAGo spin plane offsets compared to coarse degrees of the IMAP-Lo pivot platform – shows repeating step changes associated with the pivot platform

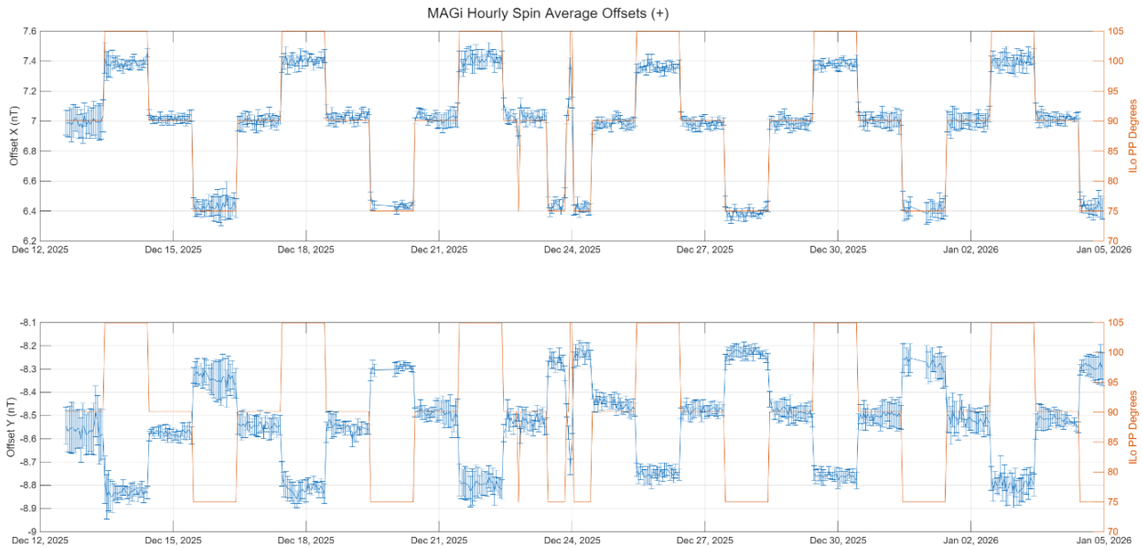


Figure 4: Rolling spin averaged MAGi spin plane offsets compared to coarse degrees of the IMAP-Lo pivot platform. The signal is larger in MAGi, consistent with MAGi being closer to the source

3.1.1 CLEANING PROCESS

Offsets from the 90 degree position have been calculated using movement data from March – April 2026 of the Pivot Platform. These offsets are pre-applied based on the housekeeping parameter ILOGLOBAL.PPM_NHK_POT_PRI which gives the degrees of position of the pivot platform. During platform movement, the offset is interpolated linearly between the start and stop positions.

The deltas used are:

MAGo	*75°*	*90°*	*105°*
Delta X	-0.1595	0	0.1197
Delta Y	0.0747	0	-0.0671
Delta Z	0.2459	0	-0.0381
MAGi			
Delta X	-0.5946	0	0.3760
Delta Y	0.2647	0	-0.2889
Delta Z	0.4930	0	-0.0122

Table 1: Table showing the deltas applied to each sensor axis based on the position of the IMAP Lo Pivot Platform

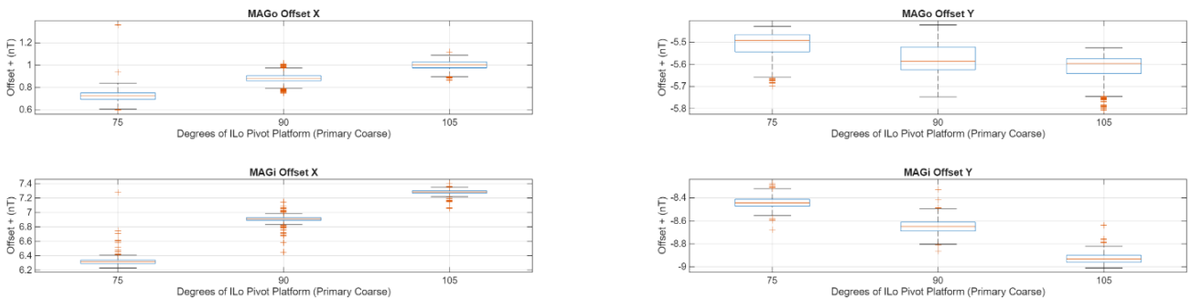


Figure 5: Deltas were determined by calculating the offset in spin plane for MAGo and MAGi at the 3 PP positions. The difference between these points is the delta used.

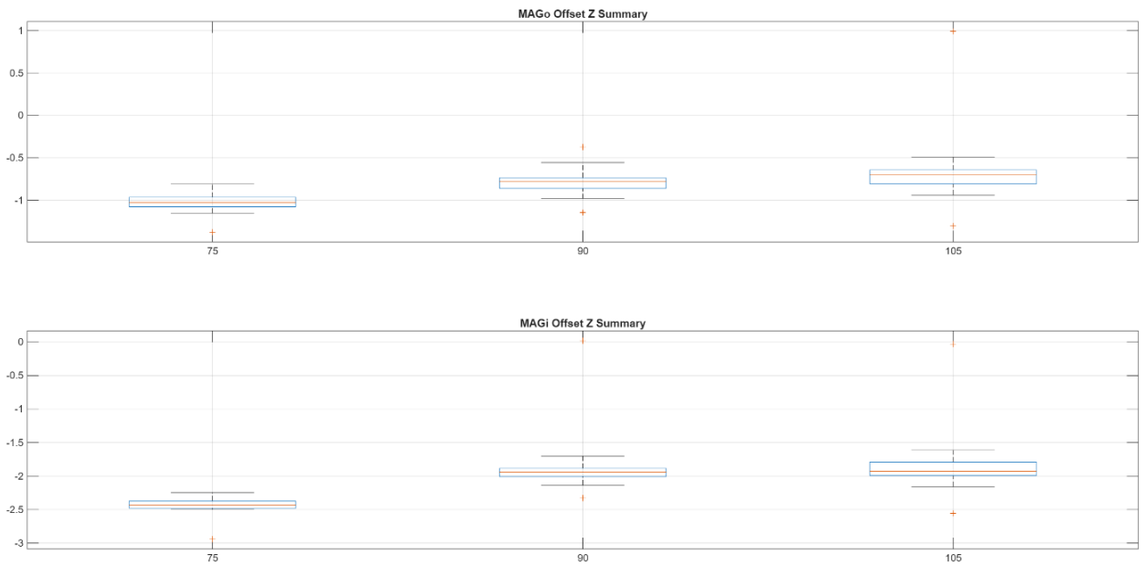


Figure 6: Offset in spin axis for MAGo and MAGi at the different PP positions

3.1.2 RESULTS

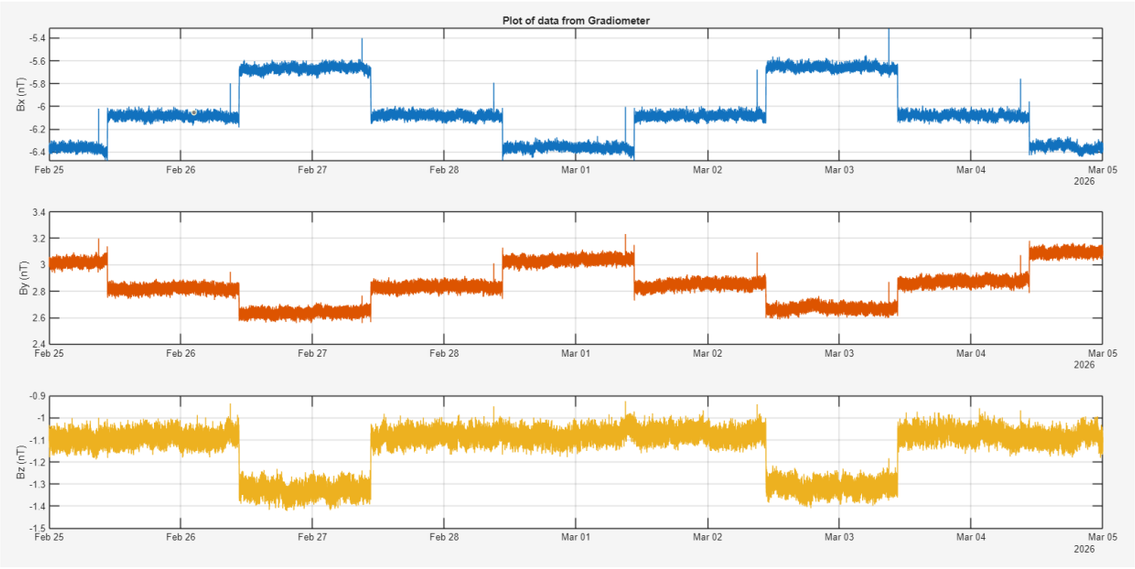


Figure 7: Gradiometer pre-PP removal, shows clear steps associated with the 3 PP positions

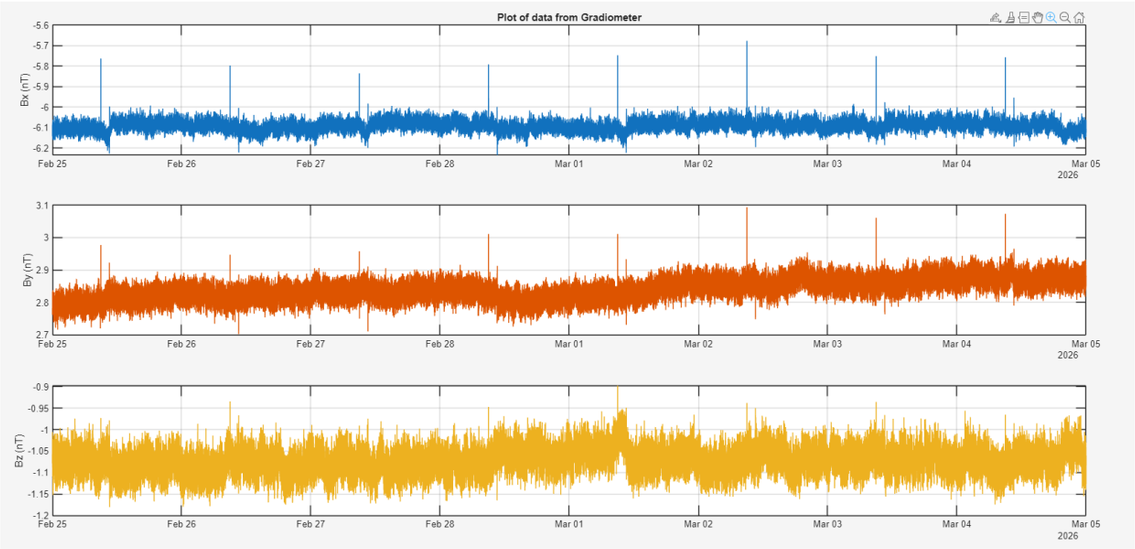


Figure 8: Gradiometer post PP removal showing steps are removed - (note spikes are from pre-thrusters and are not related to the PP)

3.2 H90 / H45/ ULTRA Decon heaters

3.2.1 SUPER-POSED EPOCH ANALYSIS

Introduced from code version 2.1.0, the superposed epoch analysis models the profile in gradiometer of the Hi45/Hi90 signal and the U45/U90 decontamination heater signal, then removes a proportion of that from the MAGo data, triggered by housekeeping data from the instruments.

One month of data was used for the analysis, from 1-Nov to 30-Nov. For the decontamination heater signal, sharp changes in U45_DECON_HTR_CURR and U90_DECON_HTR_CURR were used to identify all instances of the decontamination heaters turning on, which occurs every 10 minutes.

The gradiometer time series across all instances were averaged together, to build a profile of the impact of the decontamination heaters.

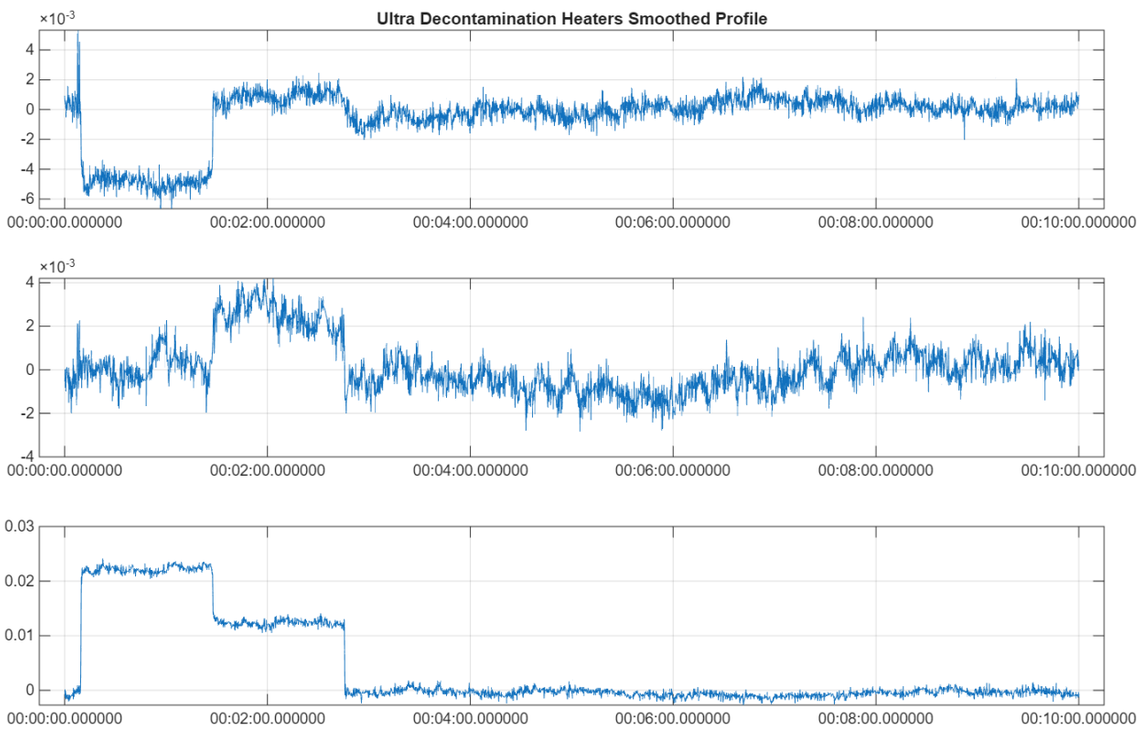


Figure 9: Ultra Decontamination Heater Profile in Gradiometer for x, y and z axes

A similar analysis was performed for the Hi-45/Hi-90 sourced signal, using H45_CURR and H90_CURR as the trigger currents to identify the feature.

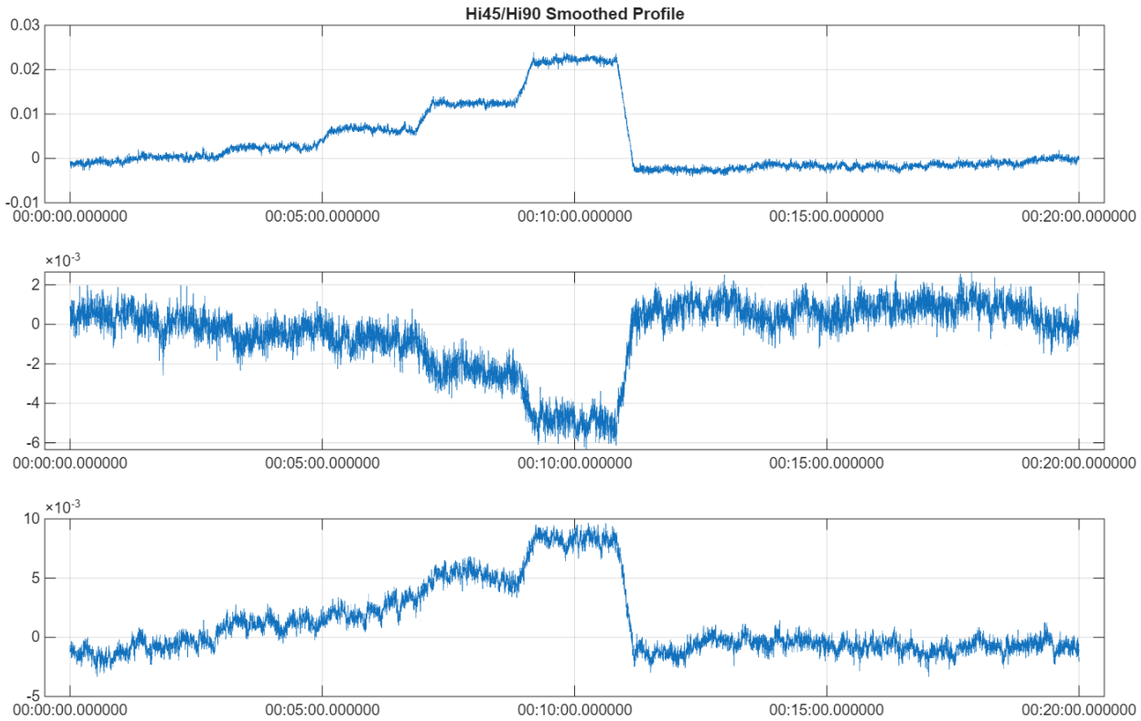


Figure 10: Hi45/Hi90 Profile in Gradiometer for x, y and z axes

A gradiometer factor was determined for removal of these signals from the original data. For the decontamination heaters, the large signal existing in the spin axis made it possible to perform a separate MAGo/MAGi epoch analysis, and calculate a gradiometer factor of 0.65 in MAGo.

The Hi45/90 interference predominately impacts the spin plane, which introduces significant complexity to performing a separate superposed epoch analysis. Instead, a gradiometer factor was calculated based on minimising spin tone in the spin plane, yielding a factor of 1.5 for MAGo.

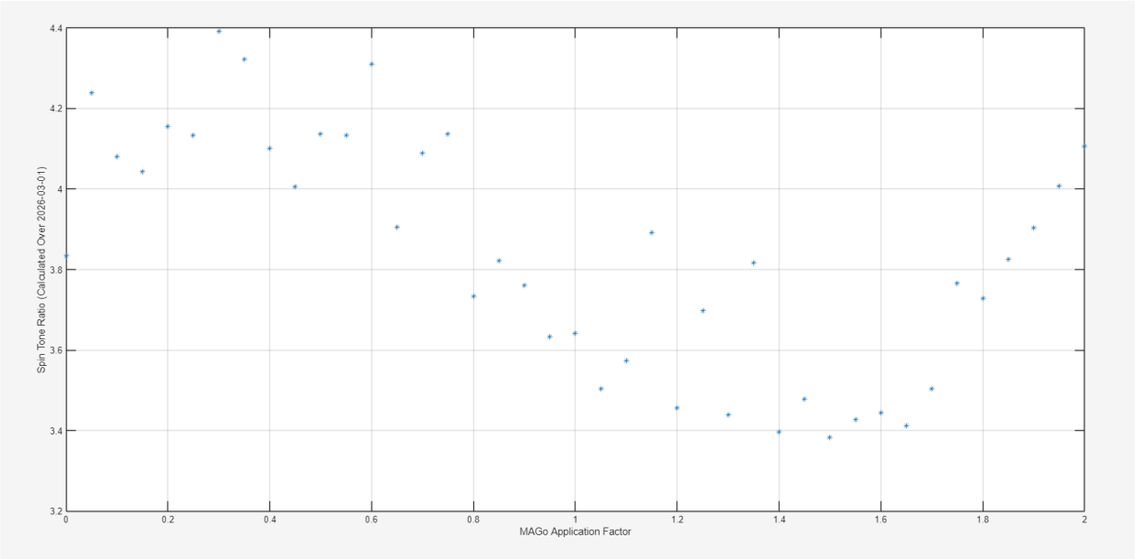


Figure 11: MAGo gradiometer factor minimisation – used for HI. A MAGo Application factor of 1.5 aligns with a minimum in the spin tone ratio

3.3 Thrusters and pre-thruster signal removal

Profile based thruster and pre-thruster signal removal was introduced in calibration code v3.3.0, in order to reduce the visible signal in the data from these spacecraft occurrences.

3.3.1 SIGNAL CHARACTERISATION

The thrusters generate a series of spikes in the MAG data when they fire. In addition, a signal (called the pre-thruster signal) is generated approximately an hour before the thrusters fire. Both signals are cleaned from the data using a pre-generated profile that is then subtracted from the data.

One hour prior to the thrusters turning on, several activities occur. One of these activities causes a noticeable short DC signal in the gradiometer. The exact source has not been located – but it is designated a pre-thruster signal for MAG cleaning purposes.

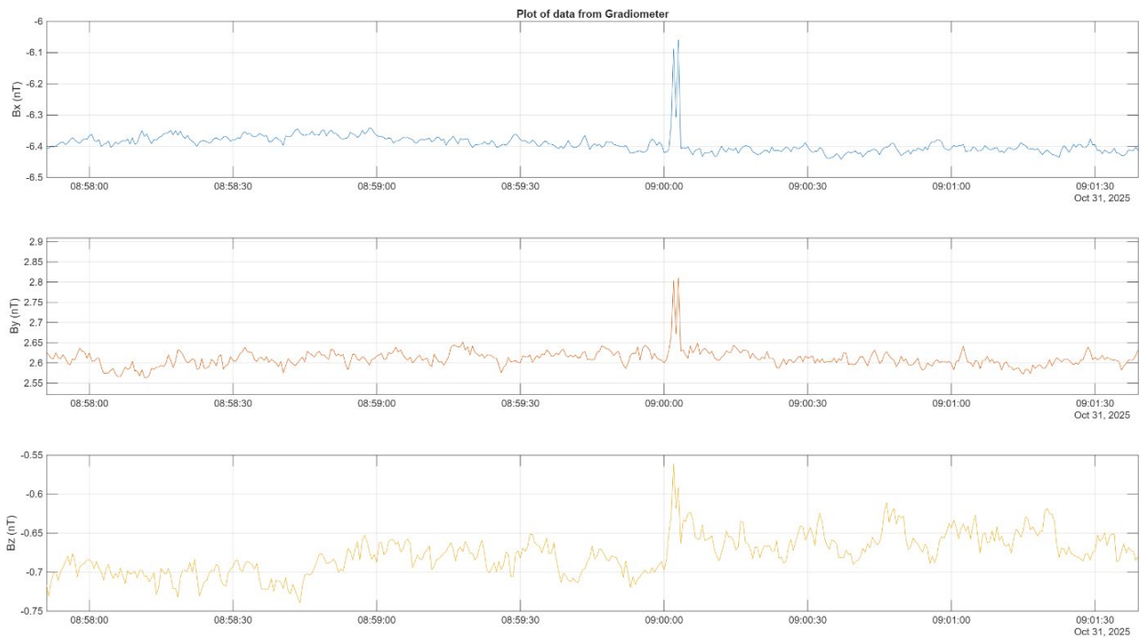


Figure 12: Pre-thruster activities seen in the delta between MAGo and MAGi

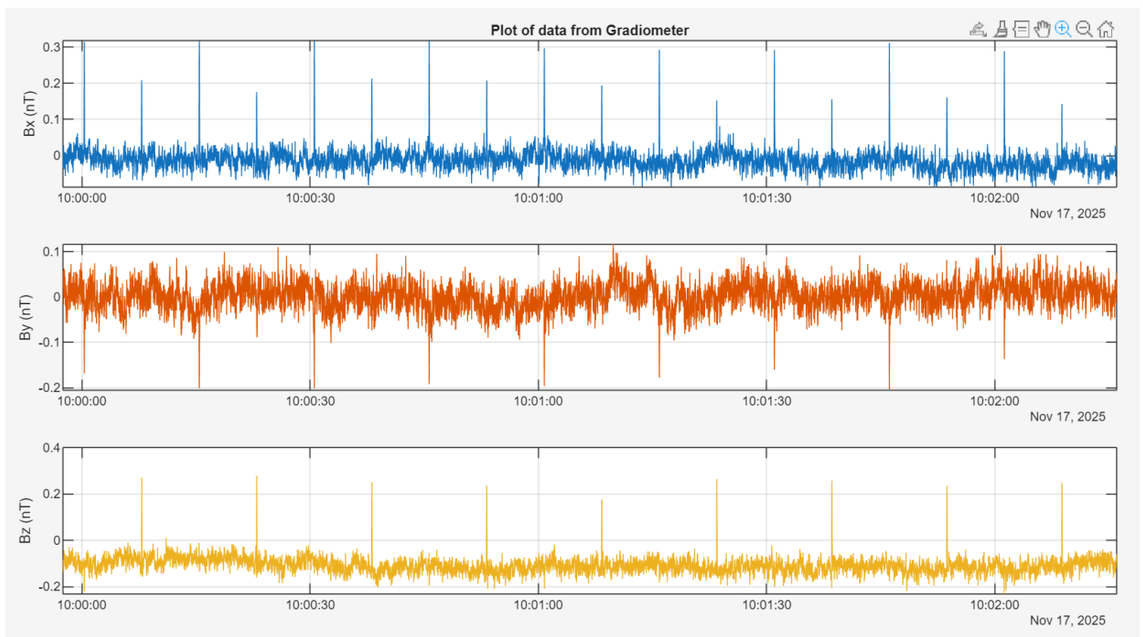


Figure 13: Thrusters firing visible in the delta between MAGi and MAGo. Seen as a series of spikes, occurs when the A1-A4 thrusters fire

3.3.2 PROFILE CHARACTERISATION

3.3.2.1 Pre thruster signal

The pre-thruster signal was characterised using data from November 2025, when both MAG sensors operated at 128Hz, to construct a high resolution profile. The delta between MAGo and MAGi was taken over every 9am period for the month, and each data period was then cross correlated and aligned, to account for the signal occurring at a slightly different time each day. The resulting profiles were added together, averaged, and smoothed, and then the baseline of the profile was subtracted to set a zero baseline. Additionally, the edges of the two distinct features were manually identified, and the profile was set to zero outside of the two peaks to prevent the addition of noise when the profile is applied.

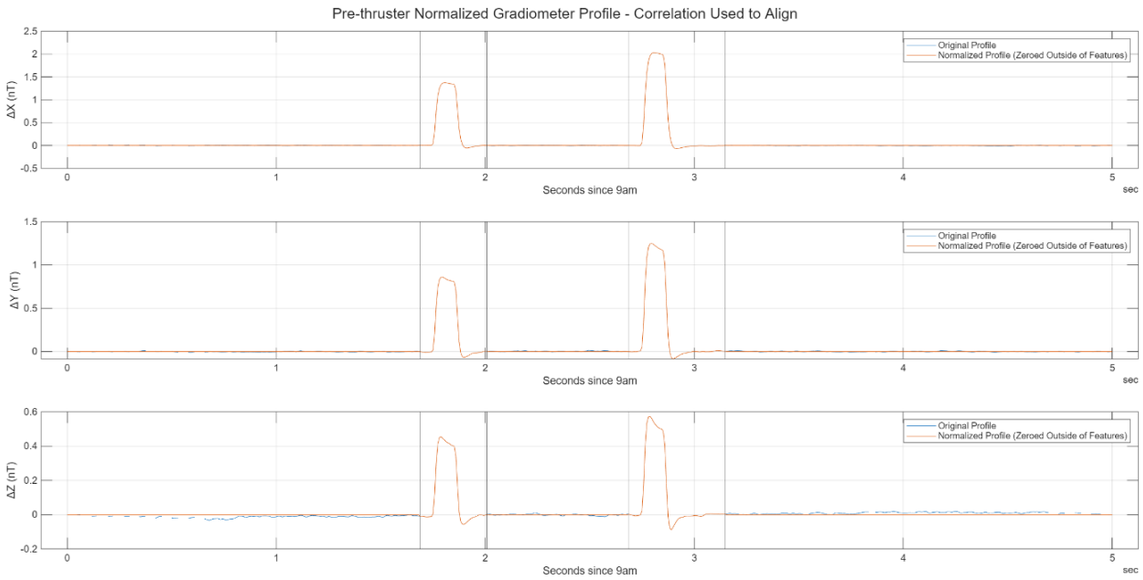


Figure 14: Pre Thruster Profile

3.3.2.2 Thruster Signal

The thruster signals were characterised using small forces tables that describe time windows and the duration of thruster firings during those time windows. The spacecraft undergoes a daily repoint, where a set of four thrusters named A1 – A4 fire in pairs to adjust the pointing of the spacecraft. This generally occurs over approximately 3-4 minutes at around 10am.

Small forces table and MAG data from November 2025 was used to construct high fidelity profiles of the thruster firings by taking the delta between MAGo and MAGi during time periods where the thrusters fired, cross correlating multiple firings, and averaging across them. The thrusters fire during the daily repoint in pairs of A1/A3 and A2/A4. Therefore, while the profiles were constructed separately, the profiles for A1/A3 and A2/A4 could not be separated or distinguished.

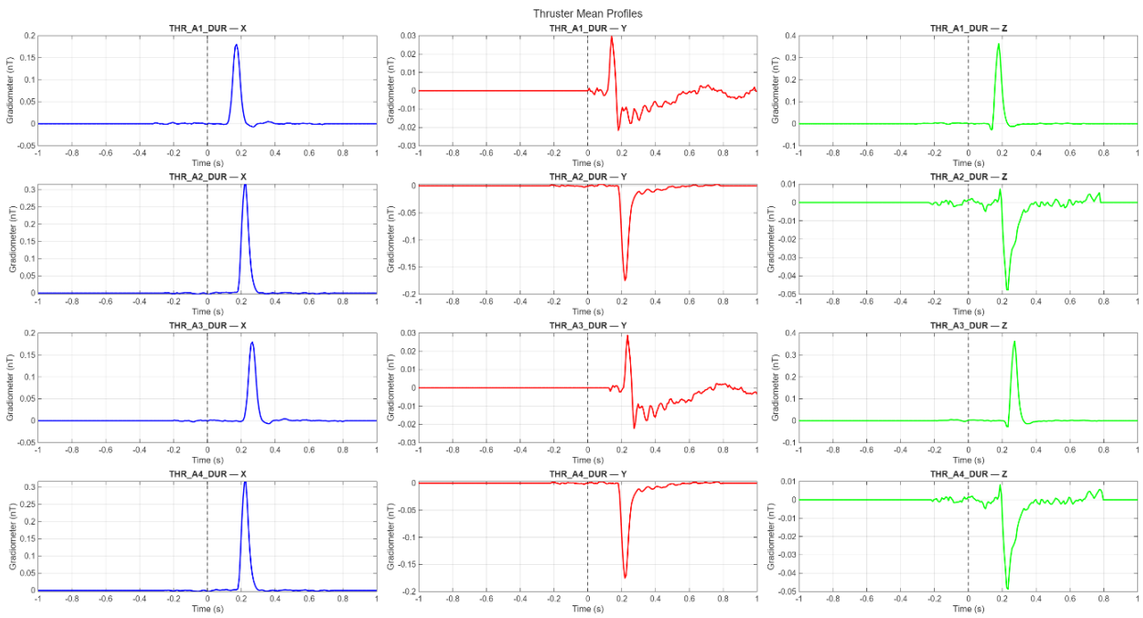


Figure 15: Mean thruster profiles in MAG X,Y,Z based on thrusters A1, A2, A3, A4

3.3.3 PROFILE REMOVAL PROCESS

The time of the pre-thruster signal is identified on any given day using the small forces table to identify the times when the control mode of the spacecraft indicates it is undergoing a repoint, and then one hour is subtracted from the repoint start time to reconstruct the time of the pre thruster signal.

The timings of the thruster firings are identified using the small forces table to identify rows where any thruster has a firing duration longer than 0ms. Thruster firings greater than 40ms are also excluded as aberrations that need to be cleaned by other means, as the profile was constructed on daily repoints where individual firings last up to 40ms.

The pre-created profile is loaded, and then cross correlation is performed in the MAG non-spinning Z axis to align the profile with the visible signal in time. This is aligned directly with a single sensors data rather than in the delta between MAGo and MAGi, as the different cadences of the two sensors in nominal operations result in a profile that does not necessarily closely resemble the constructed profile of the signal.

The profile is then filtered and downsampled onto the timeline of the sensor. For the pre thruster signal, each peak is multiplied by a distinct kappa value, and then the signal is subtracted from the sensor data.

$$Pre\ thruster\ kappa\ (Peak\ 1) = \begin{matrix} 1.1008 & 0 & 0 \\ 0 & 1.2453 & 0 \\ 0 & 0 & 0.8051 \end{matrix}$$

$$Pre\ thruster\ kappa\ (Peak\ 2) = \begin{matrix} 0.71812 & 0 & 0 \\ 0 & 0.86282 & 0 \\ 0 & 0 & 0.555 \end{matrix}$$

For the thruster removal, a kappa value has been identified for each thruster firing pair. Thrusters A2 and A3 are used to trigger thruster firing, to avoid double removal by triggering from all thrusters.

$$Thruster\ A1 + A3\ Kappa = \begin{matrix} 0.965 & 0 & 0 \\ 0 & 0.8449 & 0 \\ 0 & 0 & 0.765 \end{matrix}$$

$$Thruster\ A2 + A4\ Kappa = \begin{matrix} 0.8 & 0 & 0 \\ 0 & 0.5 & 0 \\ 0 & 0 & 1.5 \end{matrix}$$

3.3.4 RESULTS

Pre and post cleaning data is shown in Figure 18 and Figure 19 for the thruster and pre-thruster signals.

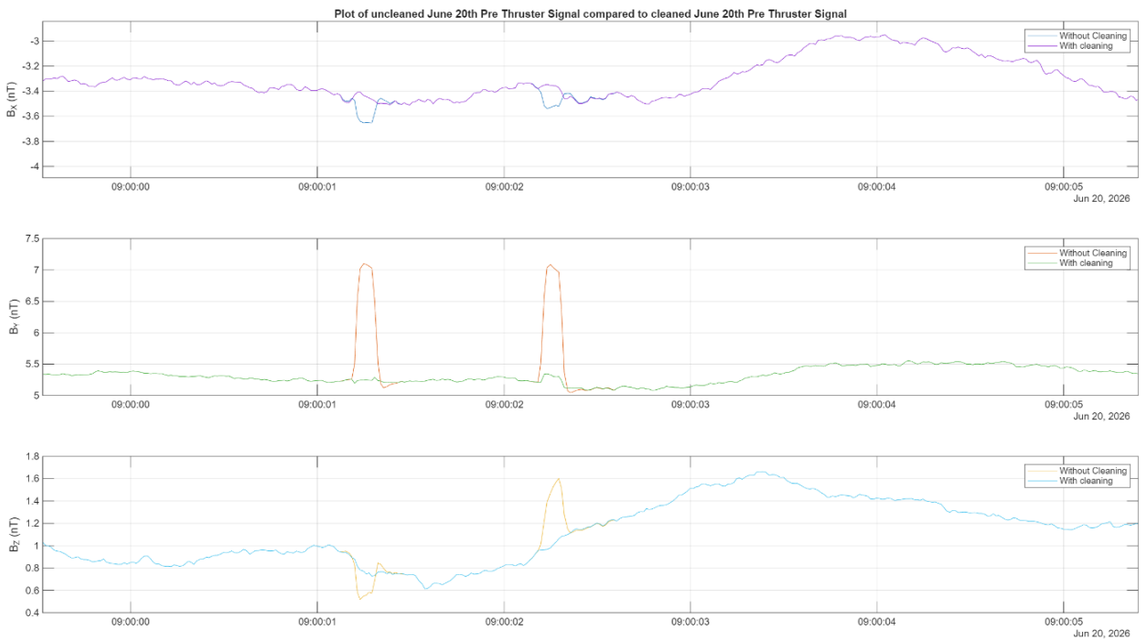


Figure 16: Pre Thruster Cleaning Results on June 20th

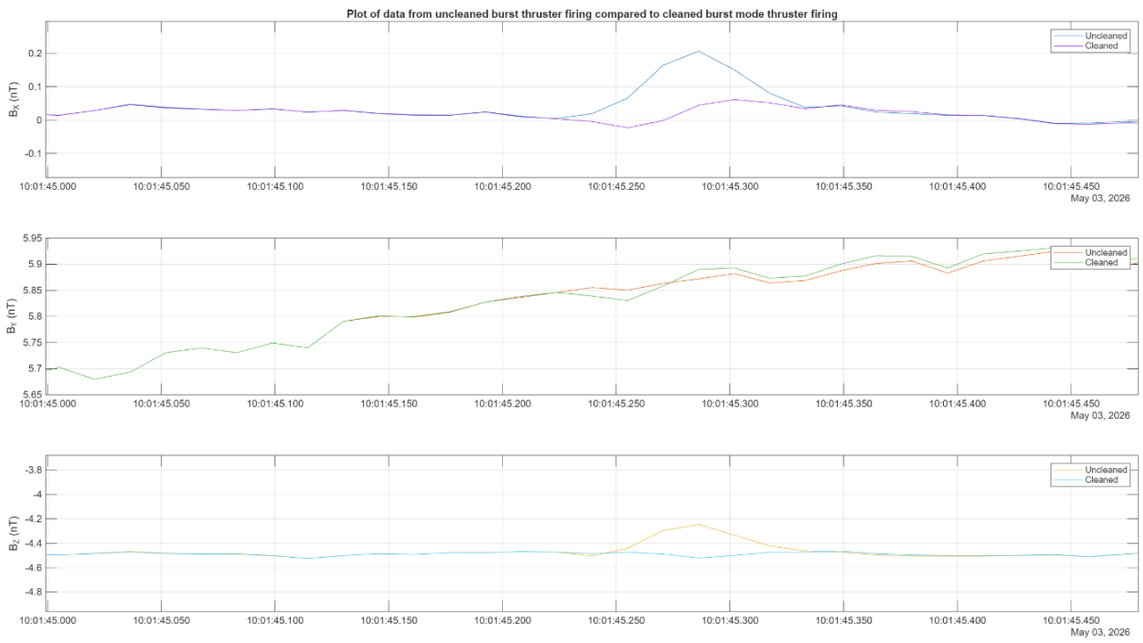


Figure 17: Thruster Cleaning results for one firing on May 3rd

3.3.5 RESIDUAL SIGNAL IN THRUSTER CLEANING

The thruster cleaning and pre thruster cleaning are imperfect and may leave residual thruster signals in the data. Improving this is a target for future updates to the cleaning process. The quality flags indicate when the thrusters are firing, and when the pre-thruster signal occurs and should be consulted before using data surrounding thruster firings.

Note: the period around the pre-thruster and thruster firings is flagged (quality flag set to 1=bad data).

4 Trajectory Correction Manoeuvre Cleaning

TCMs are rare manoeuvres which currently occur approximately once a month from Nov. 2025 to May 2026. From May 2026, trajectory correction manoeuvres cease, and new Station Keeping Manoeuvres (SKMs) will occur instead. No SKMs occurred in the time period covered by Release 2.

Trajectory correction manoeuvres are identified and cleaned from the data. The approximate timings of trajectory correction manoeuvres are manually identified and input into the calibration process. The small forces tables are then used to identify more concretely the timings of thruster firings associated with the trajectory correction manoeuvres.

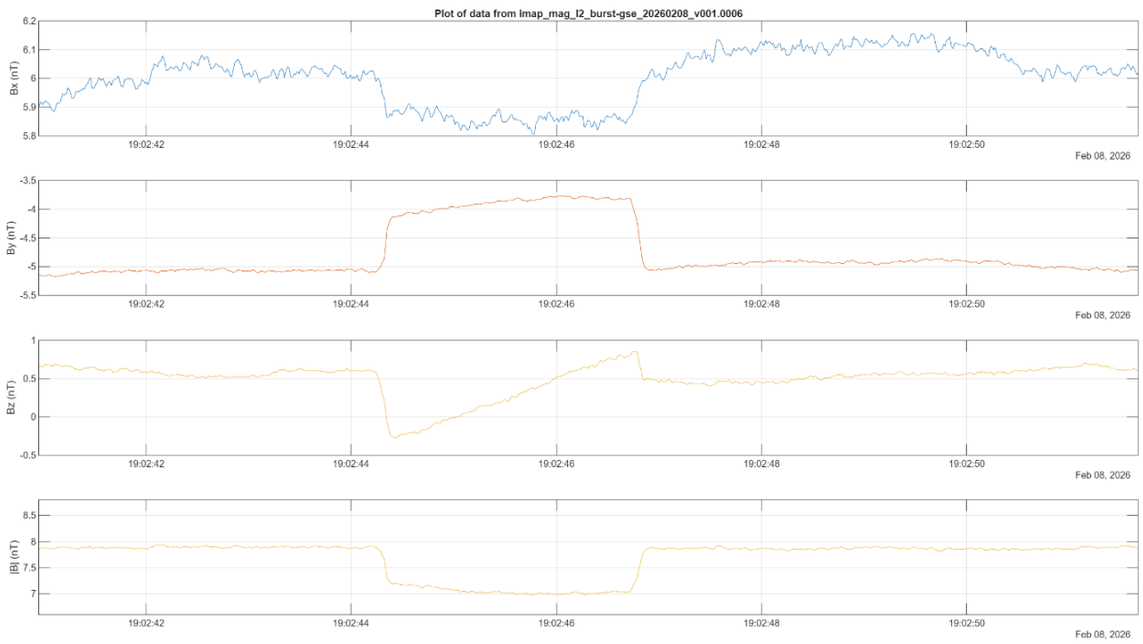


Figure 18: Single thruster firing during a TCM in GSE data shows the rectangular shape of the event, with sloped edges

A variation on the gradiometer technique is used to remove the signal. When the sample cadences of the MAGo and MAGi signals are the same – as in normal mode data - the delta between MAGo and MAGi is calculated during a thruster firing, multiplied by a kappa value determined by the type of thruster being cleaned, and subtracted from the data.

$$Thruster\ R1\ Kappa = \begin{matrix} 0.8 & 0 & 0 \\ 0 & 0.7 & 0 \\ 0 & 0 & 0.5 \end{matrix}$$

$$Thruster\ R4\ Kappa = \begin{matrix} 1.1 & 0 & 0 \\ 0 & 0.7 & 0 \\ 0 & 0 & 0.6 \end{matrix}$$

When the sample cadences differ, the delta between MAGo and MAGi does not accurately reflect the true shape of the signal, and MAGo cannot be well cleaned using the standard gradiometer strategy. Instead, MAGi is cleaned first, by downsampling and filtering the MAGo data onto a MAGi timeline, and subtracting a fraction of the delta from MAGi.

Then, the delta between MAGo and MAGi is recalculated based on a cleaned MAGi. The rising and falling edges of the signal are identified by finding peaks in the second derivative of the signal and cleaned by directly subtracting the delta from the cleaned MAGi. The flat top of the signal is cleaned by subtracting a linear interpolation between the offsets to MAGi at the start and end of the flat top of the event.

There is no impact on the structure of the data – the L2 data remains at the same high cadence throughout the event. However, some real high frequency information is lost when normalising to MAGi.

All Trajectory Correction Manoeuvres are flagged with a quality flag of 1 to indicate bad data, and should not be used for science.

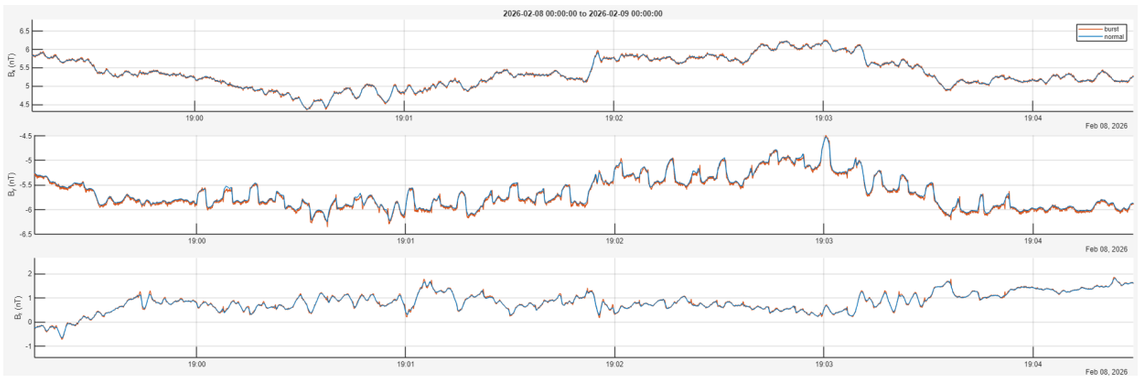


Figure 19: Cleaned normal and burst mode MAG data in the GSE frame. Component level signals of about 50pT remain in the data

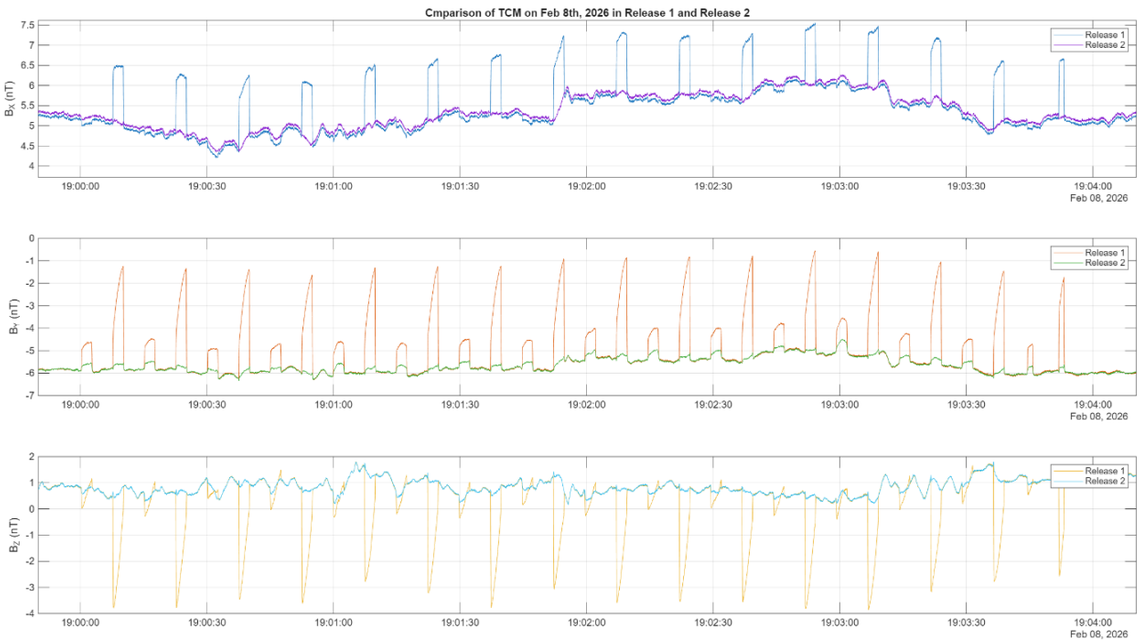


Figure 20: Comparison of Release 1 and Release 2 Data on Feb 8th, 2026 shows the effect of TCM cleaning

5 Features noted but not yet cleaned from IMAP MAG data

5.1 Pivot Platform Movement

During movement of the IMAP-Lo Pivot Platform, oscillations are seen in the MAG data for a short period of time approximately 2 minutes long.

Note: the period around the pivot platform movement is flagged (quality flag set to 1=bad data).

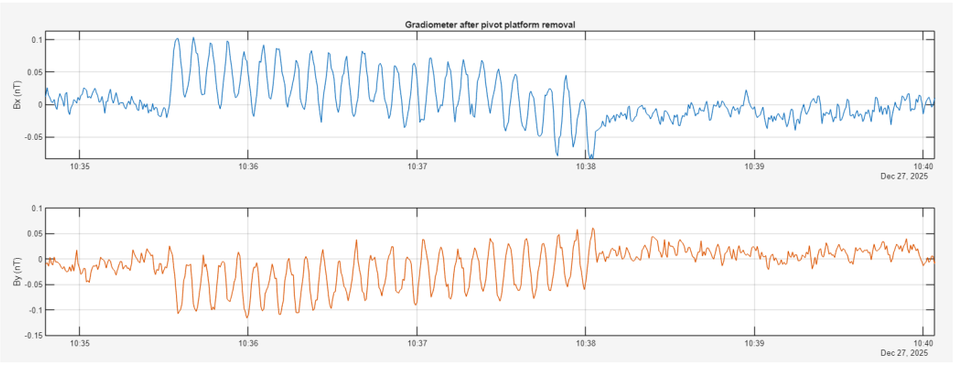


Figure 21 - Oscillation seen in gradiometer during movement of the PP – this is not currently cleaned from the data

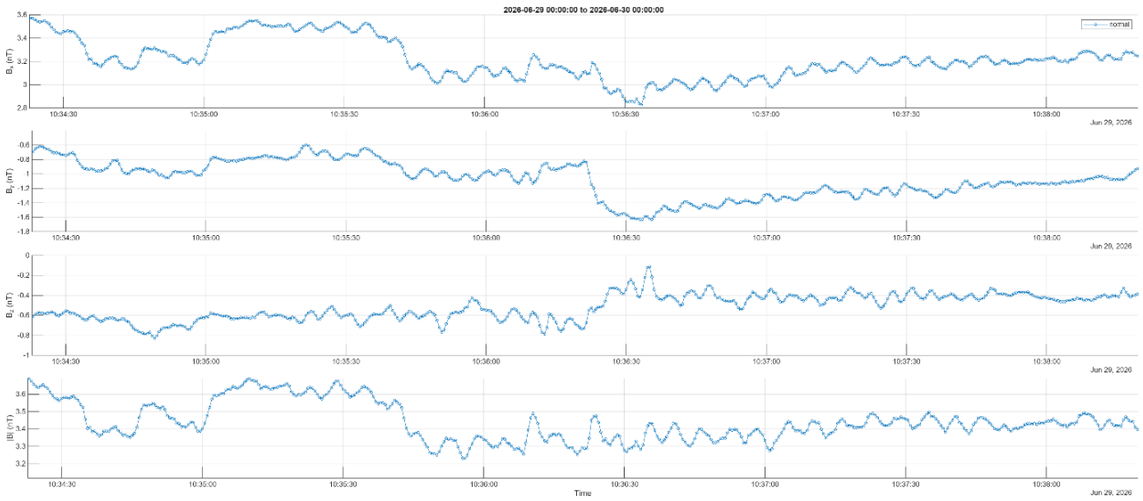


Figure 22: Oscillation visible in normal mode June 29th data

[END OF DOCUMENT]

The following describes the IMAP/MAG data calibration inputs

IMAP PROJECT

IMAP MAG CALIBRATION INPUTS DESCRIPTION

MAG
MAGNETOMETER INSTRUMENT

project	IMAP
instrument	Magnetometer Instrument
code	MAG
organisation	Imperial College London
document title	IMAP MAG Calibration Inputs Description
prepared by	Mhairi Finlayson
approved by	Chris Greenaway
reference	IMAP-OPS-TN-ICL-017
issue	3
revision	2
date of issue	14th October 2026

CHANGE LOG

Date	Issue	Revision	Reason for change
25 March 2026	1	0	First release
4 Jun 2026	2	0	Updated in line with Data Release 1
6 Aug 2026	3	0	Updated for Data Release 2
17 Sep 2026	3	1	Spin axis offset updated wording
14 Oct 2026	3	2	Updated with commentary on SPICE for Data Release 2

Note: List of changes since first release.

CHANGE RECORD

Section(s)	Reason for change
Changes to SPICE from Data Release 1	Added a note to explain the changes in this data from the previous data release, reflecting the SPICE updates that will occur

Note: Detailed changes are listed for this issue only. For previous changes, see earlier issues.

TABLE OF CONTENTS

Change Log 2
Change Record 2
Table Of Contents 2
1 Scope 3
2 Changes to SPICE from Data Release 1 3
3 Summary of Inputs to the Processing Flow 3
4 Calibration Matrices 5
4.1 Matrices used (CalibrationMatricesV9) 5
4.1 Discussion of angle determination 5
5 Spin Plane Offsets 9
5.1 Baseline Spin Averaged Offsets 9
5.1.1 Process 9
5.1.2 Offsets used 10
5.2 Spin Optimised Offsets 10
5.2.1 Process 10
5.2.2 Offsets used 16
6 Spin Axis Offsets 16

1 Scope

This document describes the inputs used in the MAG calibration process, specifically sensor offsets calculated using techniques derived from the following references:

- Solar wind–based offset determination (Leinweber et al. [DOI 10.1088/0957-0233/19/5/055104]) – targeting spin axis offset
- Spinning spacecraft offset determination (Kepko et al. [DOI 10.1109/20.486522]) – targeting spin plane offsets and angular misalignments

These are collectively referred to as “calibration” to distinguish them from spacecraft-field cleaning techniques (see IMAP-OPS-TN-ICL-013 MAG Data Cleaning Processes for details).

The results of these Calibration techniques are used as version controlled inputs to the processing flow in IMAP-OPS-TN-ICL-013 to generate offset files used by the SDC for L2 science production.

This document applies to calibration code **v3.3.0** and the inputs used for Data Release 2 (Nov 1st 2026 – July 31st 2026).

Release v3.3.0 · ImperialCollegeLondon/IMAP_MAG_Calibration

2 Changes to SPICE from Data Release 1

The transformations to the data from the spacecraft reference frame into inertial reference frames (GSE, RTN, GSM) have been updated for data release 2.

For all MAG data from start of mission to July 8th, the spin phase has been altered by approximately 1.03° to reflect the true spin phase of the spacecraft. In addition, the spin axis has been updated to repoint by approximately 0.4°, again to reflect the true pointing of the spacecraft.

From July 8th to July 31st 2026, the spin phase of the spacecraft has been updated by approximately 2.33° to reflect the true spin phase of the spacecraft.

This has no impact on the magnitude of the MAG data, or on the data in the frequency domain, as it is an inertial transformation. However, it does have a substantial impact on the components of each vector in the time domain, of the order of 0.5nT in high fields.

3 Summary of Inputs to the Processing Flow

There are three inputs to the calibration chain for producing L2 MAG data – all are under version control. The versions referenced here correspond to calibration code v3.3.0 and the inputs used for the Data Release 2 (covering 1-Nov 2025 to 31-Jul 2026).

1. Calibration Matrices (.mat): Describes sensor misalignment
    - Version used: *CalibrationMatricesV9*
2. Spin Plane Offsets (CSV): Describes offsets in X and Y (sensor frame).
    - One base spin plane offsets set per sensor
    - One optimized spin plane offsets set per sensor
3. Spin Axis Offsets (CSV): Describes offset in Z (sensor frame)
    - 1 file per sensor covering the full time period

The calibration input files are captured in the parent metadata field of the released L2 science data files. They are archived at Imperial College London in addition to the individual offset files.

4 Calibration Matrices

4.1 Matrices used (CalibrationMatricesV9)

These matrices are in relation to the IMAP_MAG_BASE frame defined in the IMAP SPICE kernels.

MAGo

Element	Value
Theta 1	89.6895°
Theta 2	89.5617°
Theta 3	0.5700°
Phi 1	0.0000°
Phi 2	89.9403°
Phi 3	-120.5000°
Gain 1	1.0000
Gain 2	0.9991

MAGi

Element	Value
Theta 1	89.6914°
Theta 2	89.6731°
Theta 3	0.3953°
Phi 1	0.1988°
Phi 2	90.0672°
Phi 3	221.9409°
Gain 1	0.9986
Gain 2	0.9994

4.1 Discussion of angle determination

The DSRF (Despun Spacecraft Reference Frame) is used as a spin-axis-aligned inertial reference frame, in order to accurately calculate the alignment matrix.

The large coronal mass ejection (CME) on 19–20 January 2026 provided a period of high magnetic field strength, which was used to help separate the angular contribution to the spin tone from the offset contribution.

- The alignment of the spin axis (Theta 3 and Phi 3) was calculated by minimising the spin tone in the DSRF Z axis after application of the calibration matrix, and transformation into the DSRF.
- Theta 1 and Theta 2, (the angles of the X and Y axes relative to the SC Z axis) were similarly calculated by minimising the spin tone in the DSRF spin plane.
    - The Theta 1 and Theta 2 values were assessed by applying the calibration matrices, and recalculating the angles using Kepko – an ideal result of 90 degrees would indicate total agreement (see Figure 1 and Figure 2)
- Phi 2 is calculated by minimising the second harmonic of the spin – again for the CME period (see Figure 3 and Figure 4)
- The process was repeated to derive MAGi values, and then additional optimisation was performed to MAGi values to align MAGi well with MAGo over the CME, so that gradiometer can be used effectively (see Figure 5 and Figure 6)

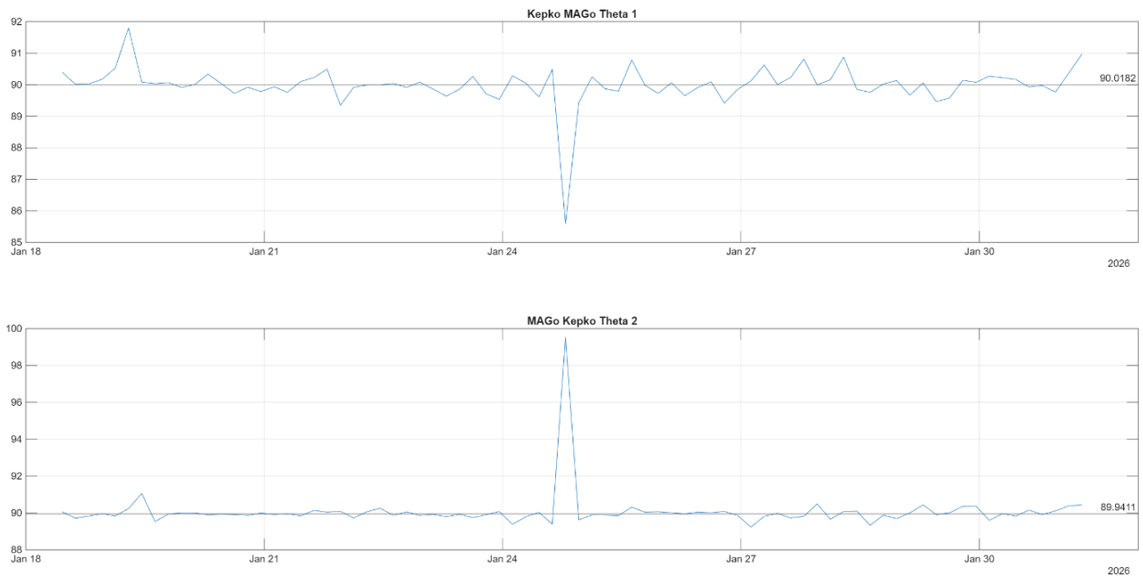


Figure 1: Quality check: MAGo Theta 1 & 2 Values calculated by Kepko following application of V9 calibration matrices. The agreement was within 0.1 degrees over the assessed time period. The data point calculated from 1am-5am on 20-Jan – a quiet period with large magnetic field – was within 0.01 degrees. This level of agreement was considered sufficient to proceed with these values.

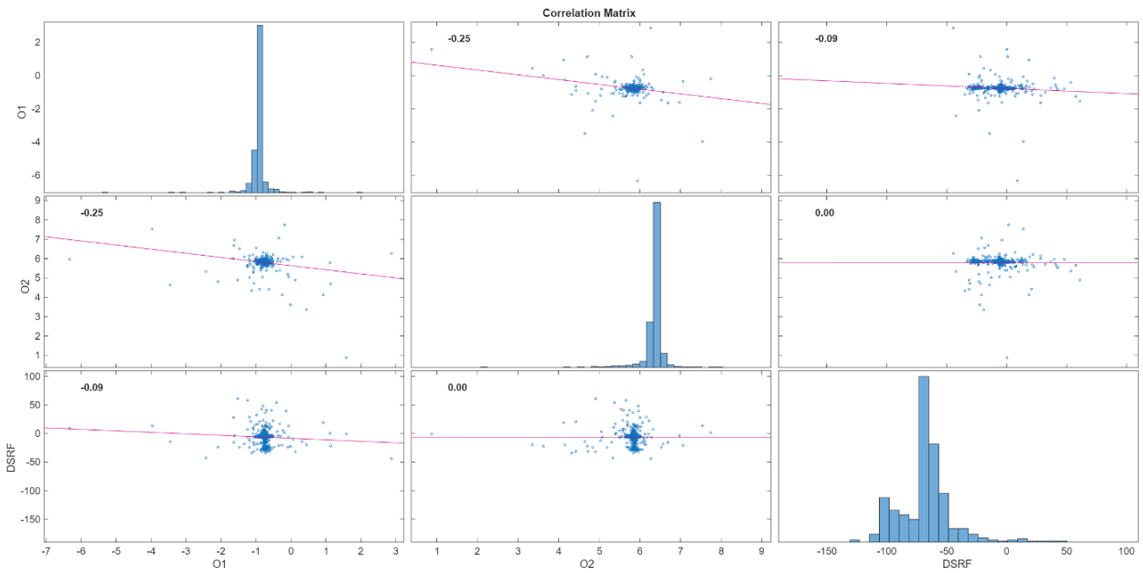


Figure 2: Quality check: MAGo Theta 1 & 2 Values: Correlation between calculated offsets and DSRF Z axis to diagnose issues with calculated angles. Note: small correlation r=0.09 between offset and DSRF Z, accepted for this release, could be target for further improvement in future. The strong correlation between Offset 1 and Offset 2 is expected (r=0.25), as that is indicative of real spacecraft interference.

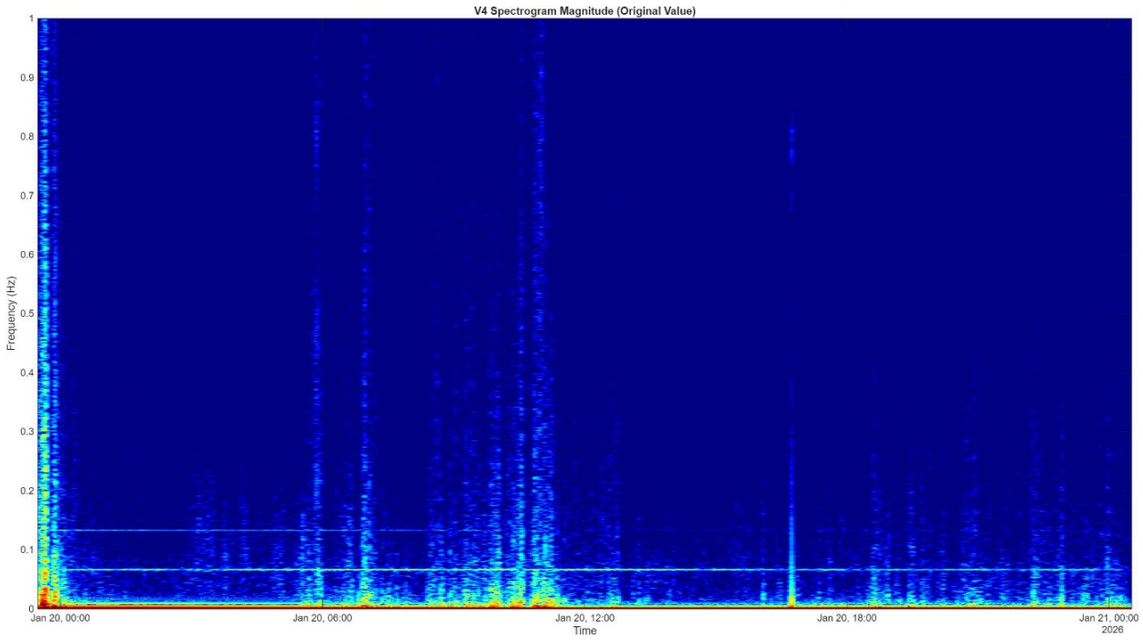


Figure 3: Plot used to identify MAG0 Phi2 angular errors. This plot clearly shows a tone at the twice the spin frequency during the CME (00:00 to 12:00 on Jan 20), this tone disappeared when the updated calibration matrix was applied, indicating greater angle accuracy had been achieved

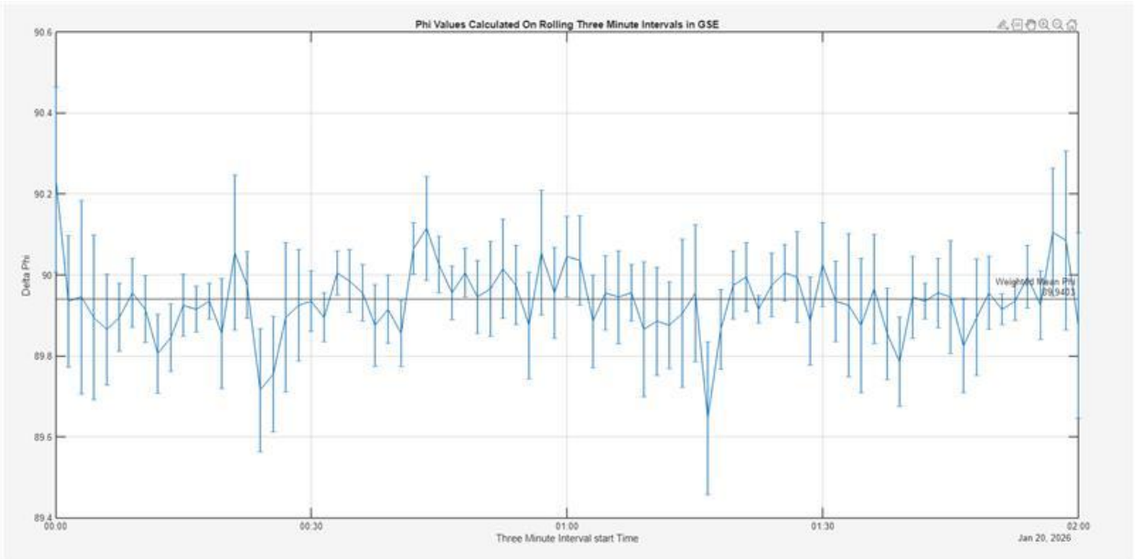


Figure 4: Plot used to identify the angle between X and Y (MAGo Phi2). Angle was optimised to minimise 2nd harmonic frequency of the spin tone, over 3-minute periods during the CME, when with a large field, the impact of angle errors are most acute. Plot shows optimised angle calculations with error bars. Final angle used is a weighted mean of these values.

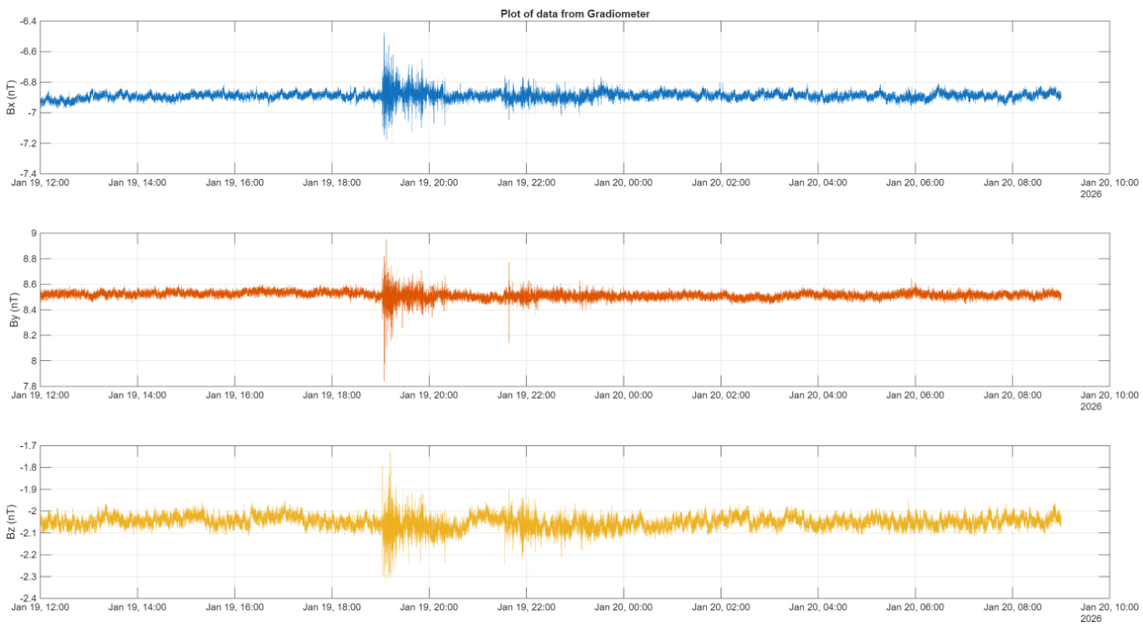


Figure 5: Quality check MAGi and MAGo co-alignment. Gradiometer over the CME using V9 matrices, indicating good alignment between MAGo and MAGi

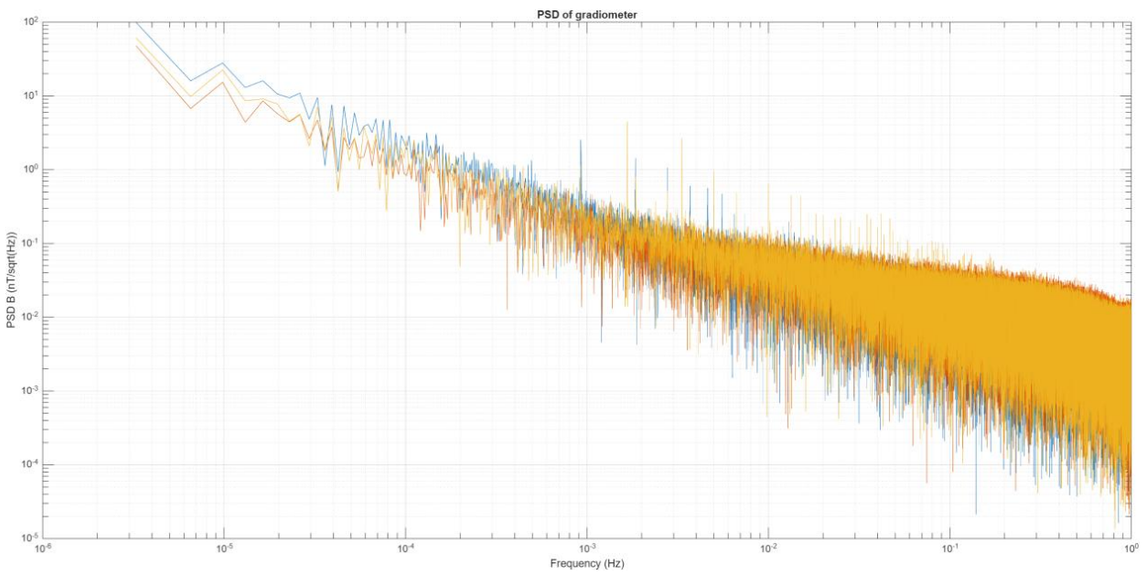


Figure 6: Quality check MAGi and MAGo co-alignment. Example PSD of the gradiometer measurement after calibration matrices applied showing decontamination heater and Hi generated signals (note these are cleaned using techniques described in TN-013), but no spin tone, indicating good angular alignment

5 Spin Plane Offsets

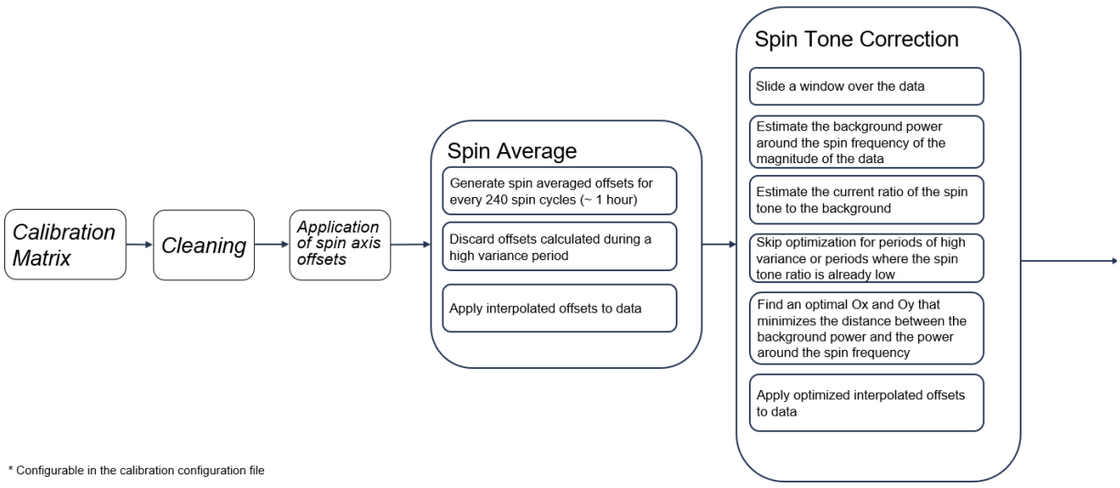


Figure 7: Flow chart outlining the progression of data through the spin plane offset determination process

5.1 Baseline Spin Averaged Offsets

5.1.1 PROCESS

A baseline set of offsets is determined in the spin plane using spin averaging. For each day, the SPICE transformation from the IMAP_MAG_BASE reference frame into the inertial despun reference frame is used to determine the angle of misalignment between the MAG Z axis and the true spin axis. This angle is approximately 0.2°, however has varied slightly over the course of the mission.

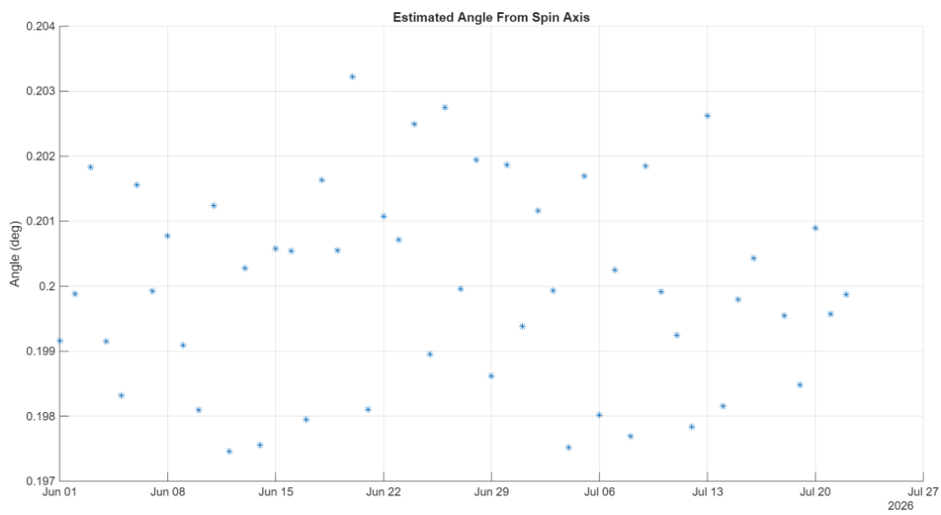


Figure 8: Example of estimated angle of MAG Z from spin axis in June

This angle then determines a transformation matrix from the MAG data, with calibration matrix applied, into a spacecraft spin aligned reference frame, where the Z axis aligns with the true spin axis as defined by the IMAP DPS frame.

In a spin aligned reference frame, the offsets can be determined as the mean of the X axis and Y axis data respectively. This is determined for IMAP MAG every 240 spins, which is approximately one hour of data. The spin aligned offsets are then transformed back into the IMAP_MAG_BASE reference frame using the inverse of the spin aligned reference frame transformation. The Z component is discarded as the spin axis offset is determined by alternate methodology described in section 4.2, and only the X and Y components are kept.

5.1.2 OFFSETS USED

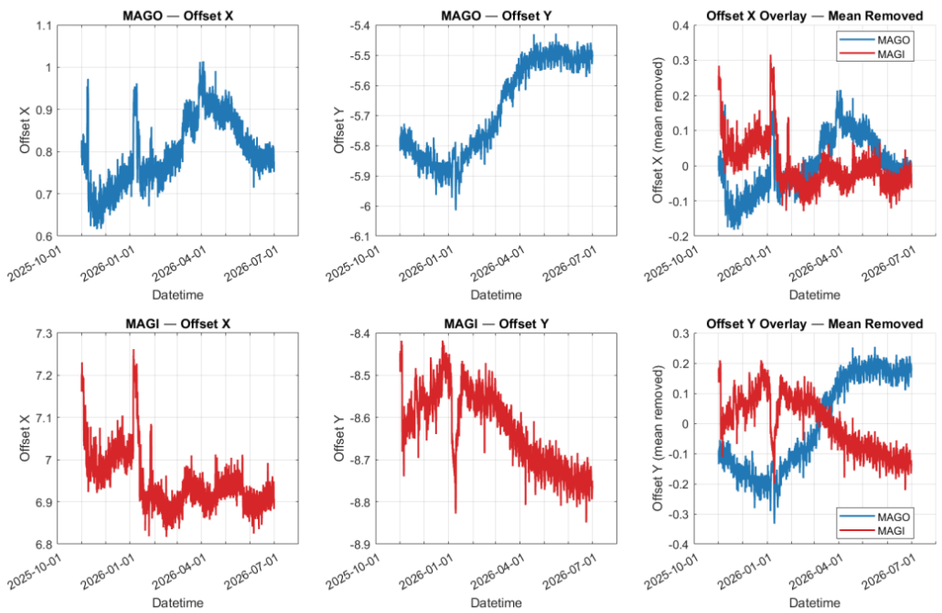


Figure 9: Spin averaged offsets from Nov-01 2025 through Jun-30 2026 showing offset drift over time

5.2 Spin Optimised Offsets

5.2.1 PROCESS

After the baseline spin plane offsets have been applied, residual spin tone remains in the data.

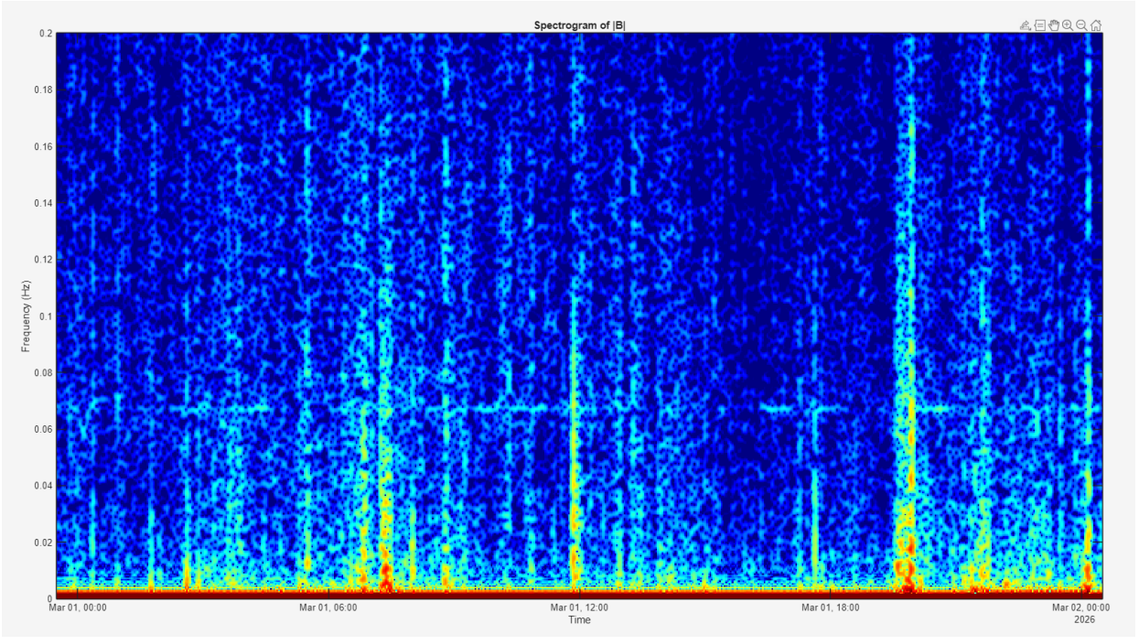


Figure 10: Example March 1st data with spin averaged offsets applied on an hourly basis displays visible intermittent power at the spin frequency in |B|. The power at the spin frequency in the components is generally not measurably above the background.

This power at the spin frequency in |B| emerges as IMAP MAG is sensitive to small fluctuations in the offsets (at the level of 20-30pT) over short periods of time (10-15 minutes). A minimisation approach is utilised to remove these small offset variations, aiming to minimise the power at the spin frequency above the background in |B| by changing the offsets. In general, the spin tone correction functionality only operates when it will measurably reduce the power at the spin frequency and attempts to do so with the smallest change.

The minimisation function operates on short time intervals of 10 minutes, stepping 5 minutes forwards to construct new intervals. It initially estimates the background power at the spin frequency by taking the median power of nearby frequencies, omitting the power at frequencies close to the spin frequency. The raw background power is multiplied by a configurable value to create a background level for the minimisation function to target, to prevent over minimisation. In the Release 2 IMAP MAG data this configurable value is set to 3.5.

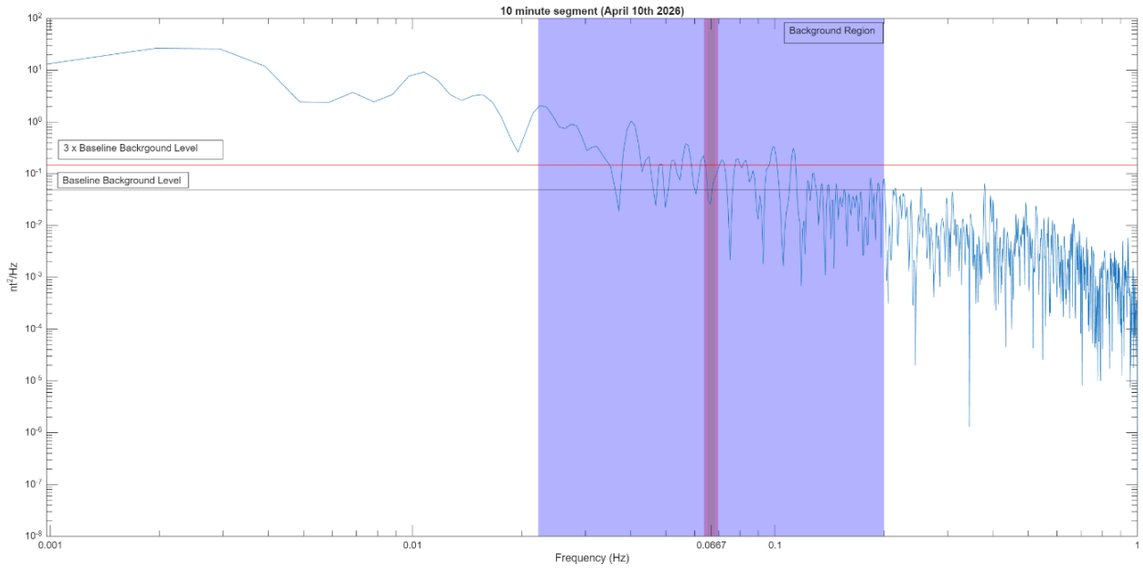


Figure 11: An estimation of the baseline background level, taken as the median of surrounding power estimates. The baseline background level is multiplied by a configurable value, to determine the actual level the minimiser attempts to target.

Intervals are then excluded or included from optimisation based on their suitability for optimisation, and their pre-existing spin tone.

An interval is excluded from optimisation if it is determined to have suitably low spin tone already. If the bandpower around the spin frequency already falls below 3.5 times the calculated baseline background level, then further optimisation for this interval is not required and it is excluded from analysis. An interval is also excluded from the offset optimisation process if the variance of the detrended |B| field is too high. High variance in the detrended |B| field is indicative of time periods where the results of the minimisation process are poorly determined with high error as the assumptions of the process – that the |B| field remains approximately constant – are violated. To avoid applying excessively large corrections, and corrections with high error, these intervals are omitted from analysis.

The output of the offset optimiser is also capped at 60 pT, and outputs higher than that are set to zero for both spin plane axes.

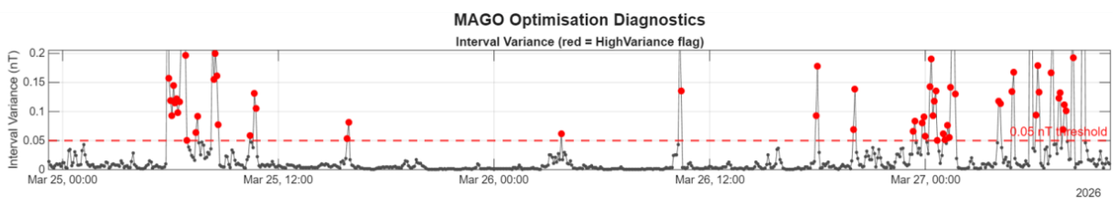


Figure 12: Example of exclusion of intervals due to the variance of |B| in the interval exceeding 0.05nT^2

Condition	Percent of MAGo intervals with condition detected in March 2026 with v3.3.0
High Variance of |B| (Above 0.05 nT^2)	17.05 %

Low Spin Tone (below 3.5 x background)	44.61 %
Determined Offset Exceeded Cap (above 60 pT)	0.23 %

For an interval that remains, the offset values in the spin plane that minimise the following objective function are calculated.

$$BandpowerSpinFrequency\ of\ |B| - EstimatedBackgroundPowerSpinFrequency\ of\ |B| + RegularizationWeight * (O_x^2 + O_y^2)$$

This objective function measures the difference between the real power in the interval at the spin frequency, and the expected power at the spin frequency based on the surrounding frequencies. The objective function additionally includes a small weighting based on the values of the offsets themselves, to encourage lower offset values. The value used for Release 2 is $1e^{-6}$.

Configuration Parameter	Purpose	Currently Selected Value
Bandwidth	Configure the width of the band around the spin frequency to encompass the possible spin periods	0.003
Minimum Tone Ratio	Configure a minimum ratio of the spin frequency to the background, below which optimization won't be performed, to prevent over optimisation	3.5
Target Multiplier	Multiplier of the baseline median background, to create a target background power to compare to in the optimisation	3.5
Regularisation Weight	Artificially inflate the value of the objective function when selected offset values are high – implemented to incentivize low input from the optimiser	1e-6
Maximum Amplitude (of Offset)	Cap the values that the offset optimizer can output – prevent divergence from spin average baseline offsets	0.1 nT

Window Minutes	Configure the size of the window in minutes that an offset is calculated over	10
Step Minutes	Configure the step in minutes by which the window slides	5
Variance Threshold	Threshold value of the variance of detrended |B| - above which no offset will be computed	0.05
Hard Zero Cap	Threshold of offset output, over which the value will be zeroed as it is considered to be an erroneous output.	0.06

Table 1: Table of input parameters for the Release 2 calibration using v3.3.0

This technique effectively reduces the spin tone in the data. In the sample month of March 2026, it reduced the mean ratio of the power at the spin frequency to the background power from 7.8 to 2.7.

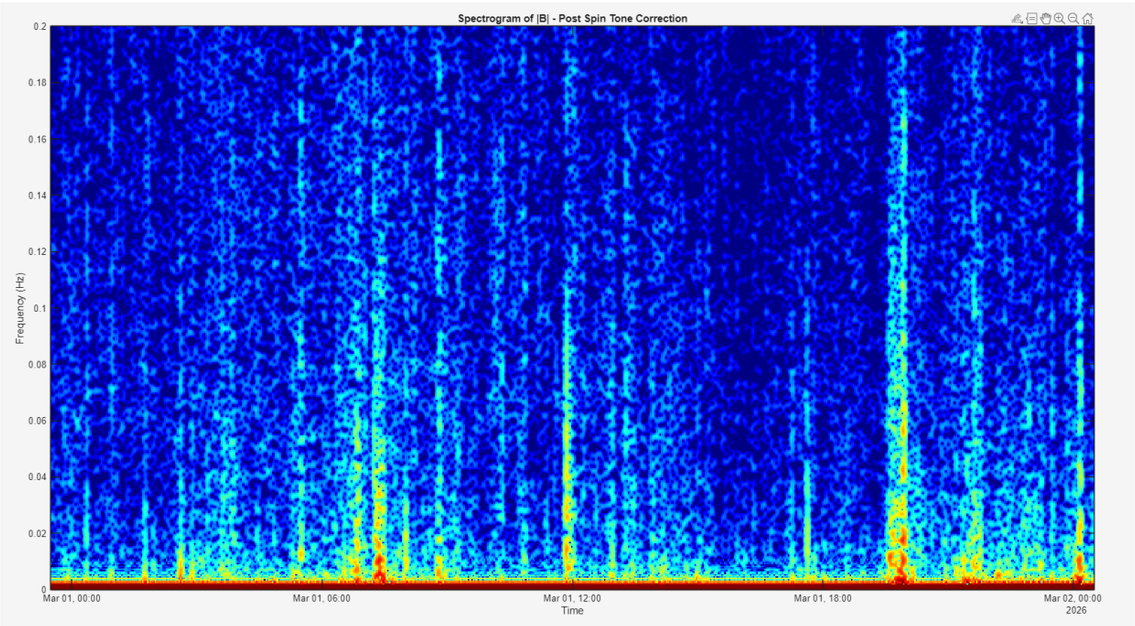


Figure 13: Example spectrogram of |B| on March 1, 2026 after the application of the optimised offsets. Can be compared to fig. 8 to show clear qualitative improvement

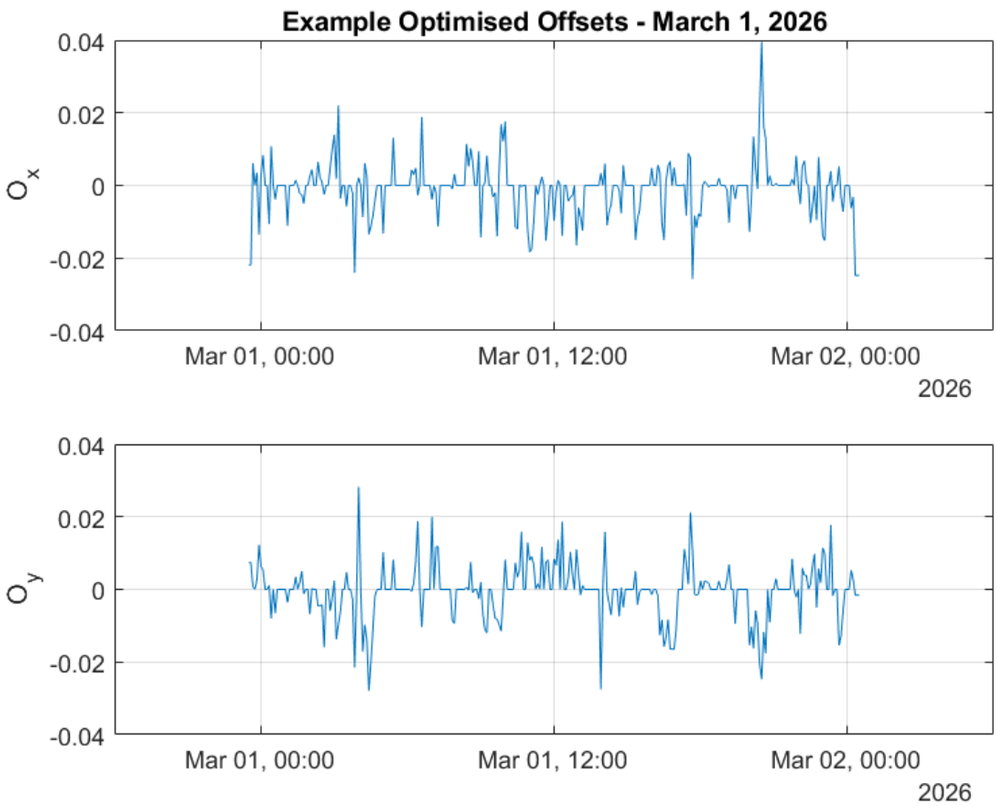


Figure 14: Example small scale offsets calculated through this methodology

5.2.2 OFFSETS USED

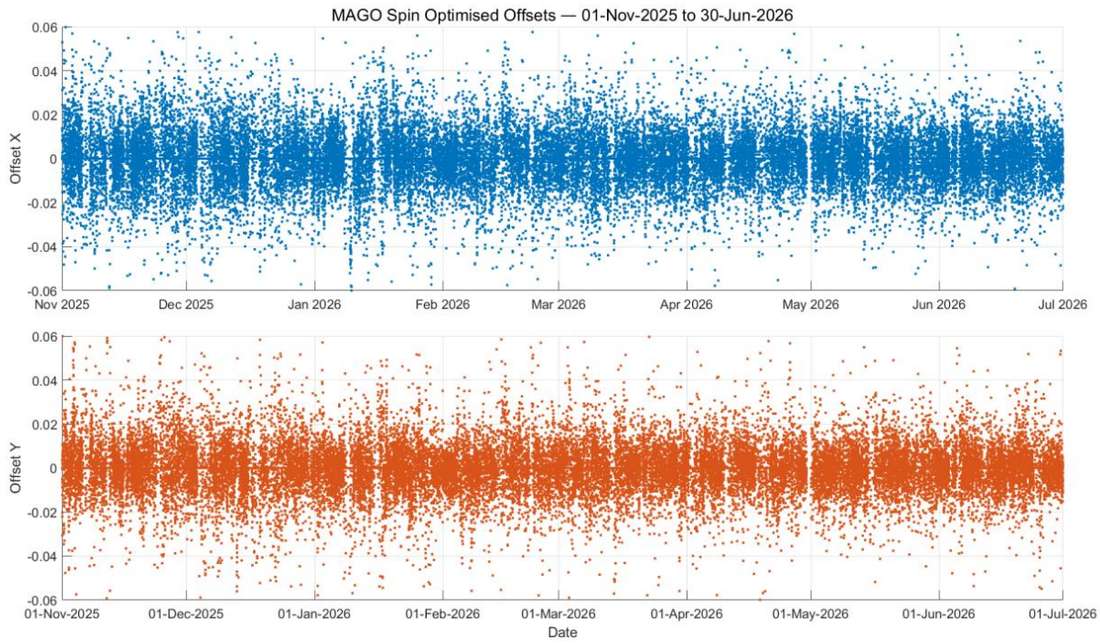


Figure 15: Interpolated and applied spin plane MAGo offsets output from the spin tone optimisation process

6 Spin Axis Offsets

Code using the Leinweber technique for interval selection combined with the Davis Smith equation for offset determination generates an offset per day. The spin axis X and Y offsets were assessed in comparison with the more accurately known spin average assessed offsets. Sets of offsets were discarded where the X and Y offsets fell further than 0.15 nT away from the known spin plane offset, under the assumption that when X and Y are well determined, the Z offset would also be more accurate.

A linear fit was taken to the data, with a hinge point on January 15th, 2026 – after the spacecraft underwent Lissajous Orbit Insertion - as all offsets stabilised more after this point, and a hinge was visible in the X and Y known offsets.

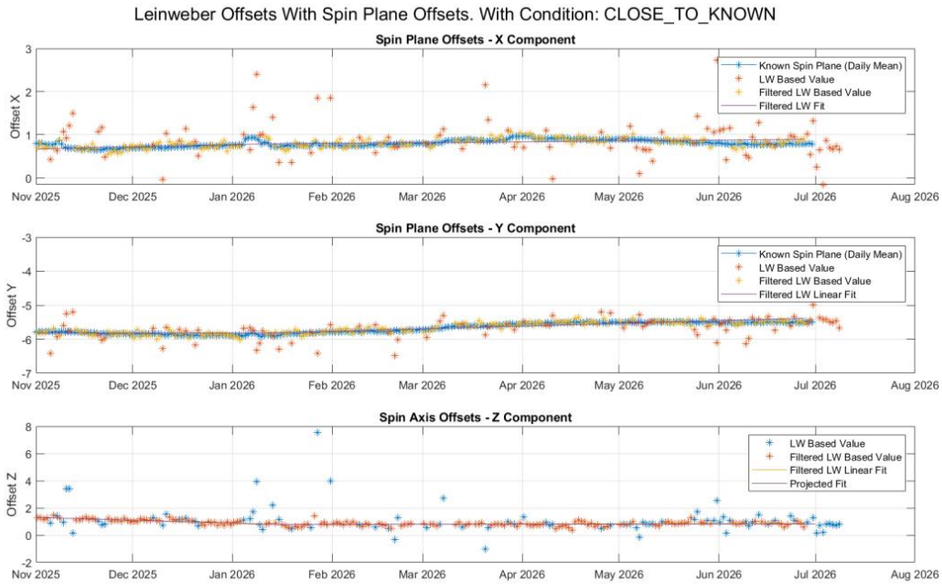


Figure 16 - Spin axis offsets with fit for MAGo

Offset	Maximum Value	Minimum Value	Mean Value	Std Dev
MAGo Offset Z	1.307 nT	0.784 nT	0.877 nT	0.143 nT
MAGi Offset Z	2.177 nT	1.854 nT	1.959 nT	0.076 nT

Table 2 - Spin axis offset metrics from 01-Nov 2025 to 30-Jun 2026

[END OF DOCUMENT]

3.6 IMAP-Lo

3.6.1 Strategy & Approach

IMAP-Lo was calibrated at Princeton's Space Physics Laboratory. Cross-calibration with the IMAP-Hi instrument was conducted at Los Alamos National Laboratory's beam facility. The IMAP-Lo instrument itself was built-up and tested in four stages: time-of-flight, pre-calibration-1, pre-calibration-2, and final calibration.

The purposes of the IMAP-Lo calibrations were to determine the response functions of the instrument, the energy loss and efficiency of the conversion surfaces, time-of-flight efficiencies through the ultra-thin foils, and geometric factors.

3.6.2 Pre-Flight Instrument Calibration

IMAP-Lo cal report embedded below

1. INTRODUCTION

This document describes the calibration process for IMAP-Lo instrument and select subsystems. Here we describe tests performed and subsequent data analysis characterizing the instrument functionality, showing that the instrument meets or exceeds all engineering requirements.

This is a living document, for the most up to date revision please contact one of the following:

- Jonathan.bower@unh.edu
- Nathan.schwadron@unh.edu
- Mitchellshen@princeton.edu
- F.rahmanifard@unh.edu

1.1 Instrument Overview

Excerpt from UNH-IMAP-Lo-27850-6002-Data-Product-Algorithms-v7-NAS.docx.

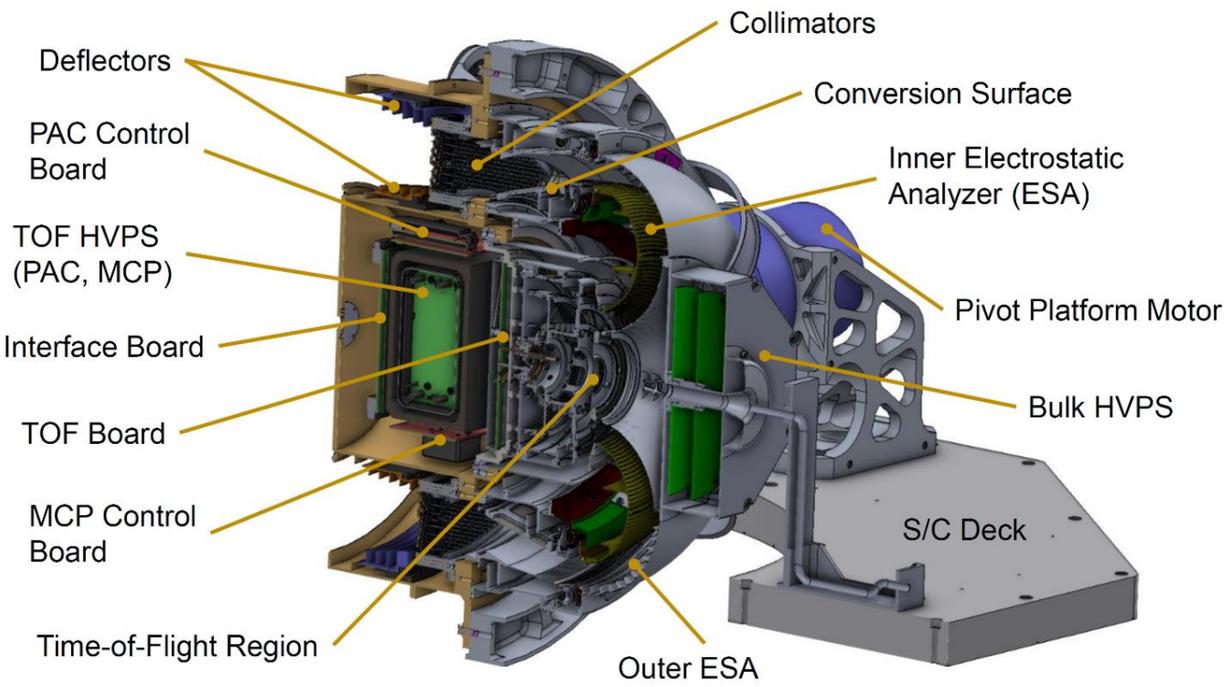


Figure 1.1.1: Cutaway diagram of IMAP-Lo showing instrument components and mounting to spacecraft deck via a dedicated pivot platform.

IMAP-Lo is a single-pixel neutral atom image that delivers measurements of ISN atoms (H, He, O, Ne, and D) resolved by energy and angle, tracked over > 180◦ in ecliptic longitude and energy-resolved global full sky maps of ENA H from 40 eV to 1 keV. IMAP-Lo is built on the heritage of IBEX-Lo, flown on NASA's Interstellar Boundary Explorer (IBEX), but with much greater collection power due to lower backgrounds at Lagrange point 1 (L1) and increased geometry factor, duty cycle, and collection efficiency. It also includes a pivot platform, which enables IMAP-Lo to track the ISN flow over almost the entire year, enabling much better sampling of ISN populations than was possible for IBEX-Lo. With the pivot platform in the default position (instrument FOV at 90◦ to spin axis, identical to IBEX-Lo), IMAP-Lo views both heliographic poles every spin and creates a full sky map every six months. During the first

year, the high-resolution mode is used for cross calibration with IBEX, with a 90◦ pivot angle on even DOYs to observe ENAs and alternating the pivot angle between 57◦ and 105◦ on odd DOYs to sample ISN populations. After the first year, the high-throughput mode will be used, and IMAP-Lo will continue to observe ENA populations on even DOYs (at 90◦ and 135◦) and on odd DOY will move through pivot angles 60◦ to 160◦ to sample specific particle populations.

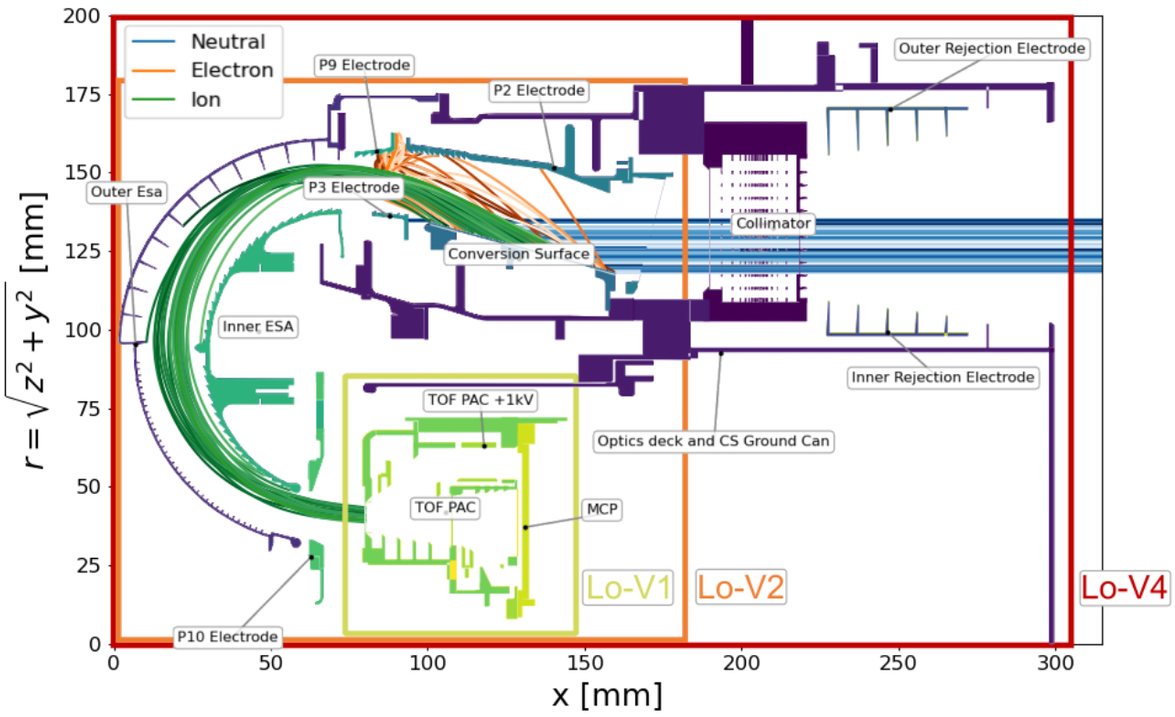


Figure 1.1.2 IMAP-Lo sensor cross section showing different instrument configurations calibrated

IMAP-Lo (Figure 1.1.1) is comprised of deflectors (DEF), collimators, conversion surfaces (CS), time-of-flight (TOF) subsystems, an electrostatic analyzer (ESA), a star sensor (STS), and a pivot platform (PPM). Figure 1.1.2 depicts a cutaway drawing of the IMAP-Lo instrument subsystems overlaid with SIMION ray-tracing. Neutrals enter the instrument from the right in this geometry, they pass between the two rejection electrodes, which sweep away charged particles, and pass through the collimator with 9◦ FWHM FOV. The neutrals then strike and reflect off of the conversion surface, where a certain fraction of them convert to negative ions. The specularly reflected negative ion is pre-accelerated into a toroidal ESA, and filtered according to energy-per-charge, while electrons are removed by a ring of magnets behind the P9 pusher electrode. Scattering of incoming particles and photons on the ESA surfaces is minimized by fins in the outer ESA, a Cu-black surface, and a 3-bounce design. After passing through the ESA, ions are post-accelerated into the TOF subsystem, where they pass through two consecutive 1-µg C foils that produce secondary ions which are guided to the outer/inner annular start sections of the chevron configuration microchannel plate (MCP). The ions continue to the central stop section of the MCP. The stop measurement combined with the two start measurements produces three independent TOF measurements. Triple-coincidence measurements achieve dark rates ≤ 1 count/day.

IMAP-Lo cycles through a series of 7 energy steps, which differ depending on the instrument stepping mode (e.g., high-resolution mode, $\Delta E/E \approx 0.7$, expected throughput = 0.14, or high throughput mode, $\Delta E/E \approx 1.1$, expected throughput = 0.29, respectively) and are defined by tables loaded on the instrument. The high-resolution mode is similar to IBEX-Lo and will be used in the first year for cross-calibration. The cadence is two spins per energy step, so with the spacecraft spinning at ~ 4 RPM, it takes ~ 3.5 minutes to sweep through the full energy range.

Figure 1.1.3 shows a basic block diagram with the components of the instrument as well as the data transfer between them. The Interface Board is the single point of contact to the S/C through the IMAP-Lo ICE (IMAP Common Electronics). It handles all power conditioning for the sensor and star sensor, parses incoming commands to the sensor electronics, HV supplies and the star sensor, and directs data from the sensor electronics and star sensor to the ICE.

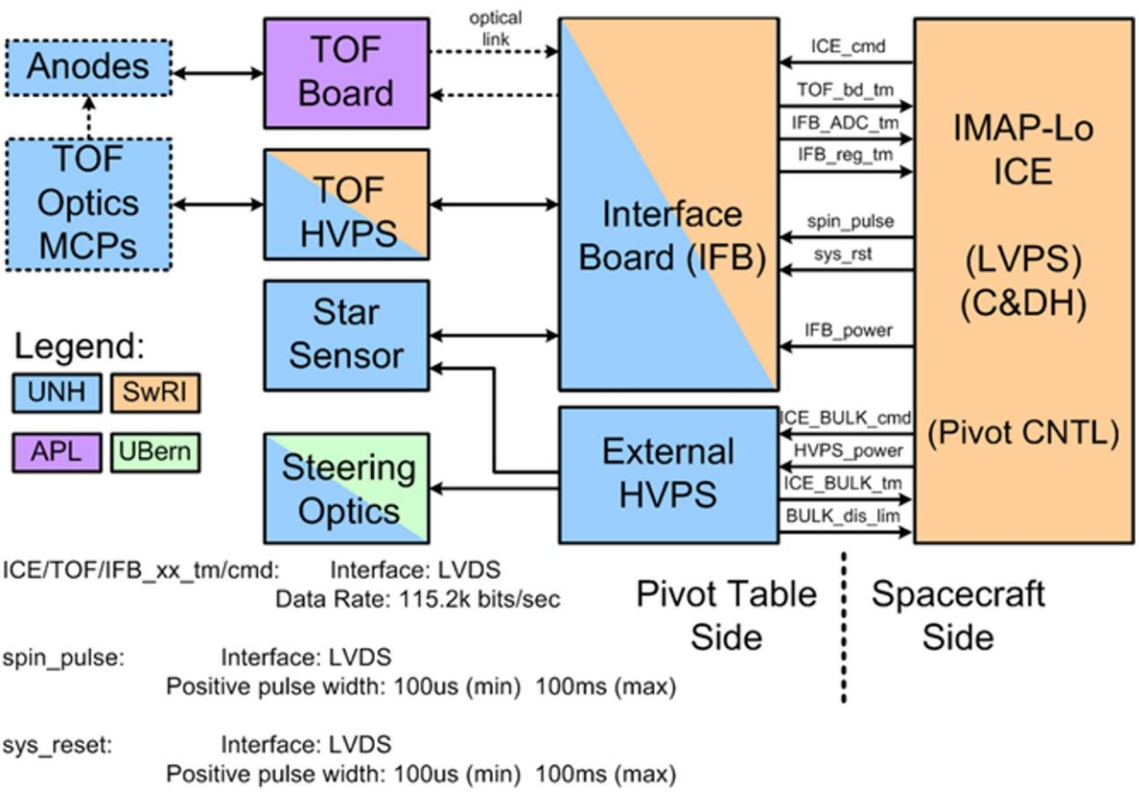


Figure 1.1.2: IMAP-Lo basic block diagram

The Direct Events, Monitor Rates and TOF Board Housekeeping generated on the TOF Board are transmitted to the Interface Board over a single 115.2kbit/sec optical serial interface. The Interface Board can be thought of as a "bent pipe" where the TOF Board data is guided to the ICE via the Interface Board TOF BD TM channel. Star Sensor data and Interface Board Housekeeping are digitized on the Interface Board and sent to the ICE via the IFB ADC TM channel, also at 115.2kbits/sec. Finally, Interface Board register data is sent to the ICE via the IFB REG TM channel, again at 115.2kbits/sec.

The IMAP-Lo TOF mass analysis system is designed to allow the clear separation between light and heavy neutral atoms and to suppress accidental background events using coincidence techniques. After passing through the electrostatic Energy Analysis System and a final potential grid the negative ions that have been produced on the Conversion Surface are post-accelerated to 12keV, added to their original energy by a positive post-acceleration (PAC) high voltage (UPAC) of 12 - 16 kV applied to the entrance foil of the IMAP-Lo TOF Mass Analysis System. The ions pass through the entrance foil (C-Foila), followed by the passage of a second foil (C-Foilc), and then reach a MCP detector in its Stop section Anode b. During the passage of each foil secondary electrons are released with a species and energy dependent efficiency. They are accelerated and steered towards two separate sections of the MCP (Starta Anode a and Startc Anode c).

In addition, the Stop anode is sub-divided into four quadrants for better background suppression and diagnostics of individual MCP segments. The Stop position of incoming particles is obtained through a Delay Line configuration with a Delay TOF measurement in TOF3. Therefore, a valid Triple Coincidence event also involves TOF3 as a fourth measurement. Because each of the Anode signals (A, C, B0, and B3) is shared between two of the TOF measurements, a valid Triple Coincidence event also satisfies the so-called Checksum condition TOF0 + TOF3 = TOF1 + TOF2 with a fidelity that reflects solely electronic jitter, i.e.,

$$| TOF0 + TOF3 - TOF1 - TOF2 | \leq 1ns$$

PHA Events that satisfy equation (1), which provides additional background suppression, are called Golden Triple Events.

1.1.1 Changes from Heritage

There are a few notable high-level differences between IMAP-Lo and its heritage instrument, IBEX-Lo, as listed below.

1. Pivot Platform
   The IMAP-Lo instrument is designed with a pivot platform that will enable instrument articulation in a range of 60-165° relative to the spacecraft spin axis. This enables IMAP-Lo to point at different ISN populations, greatly expanding the ISN collection time over the course of each year of the mission, enabling the breaking of the parameter tube degeneracy present with IBEX-Lo, and facilitating greater separation of different ISN populations.

2. Collimator Field of View
   IMAP-Lo features a broader collimator field of view (9°) than IBEX-Lo (7°), which increases the geometric factor over that of IBEX-Lo.

3. Wider Energy Window
   IMAP-Lo will have a programable energy window. In addition to the high-resolution mode ($\Delta E/E$ = 0.7), which is comparable to IBEX-Lo, it will also have a highthroughput mode with a wider energy window ($\Delta E/E$ = 1.1), which increases the geometric factor.

4. No High Angular Resolution Quadrant
   Unlike IBEX-Lo, IMAP-Lo will not have a high angular resolution quadrant, resulting in an increase of the geometric factor by a factor of 1.2.

5. Better Processor
   IMAP-Lo will have a much better processor than IBEX-Lo, enabling much more flexibility with the instrument tables (e.g., can have multiple on-board tables to put the instrument into modes for science data collection, calibration, etc.).

6. Star Sensor
   The star sensor is identical to that of IBEX but with the successor photomultiplier (PMT) model by Hamamatsu and a filter that suppresses red and infrared radiation > 500 nm in order to reduce the sensitivity to the diffuse background from the Milky Way and Zodiacal Light.

1.2 IMAP-Lo Measurement Requirements

The IMAP-Lo relevant performance requirements validated by this test plan are summarized in Table 1.2.1. Results described in this document either fully validate the requirements, or require additional testing and / or analysis.

Table 1.2.1 Summary of IMAP-Lo performance requirements from the Requirements Specification.

	H ENAs	Neutral H and D	Neutral He	Neutral O and Ne
Energy Range	500 - 1000 eV	10 - 40 eV	30 - 150 eV	400 - 700 eV
	RLO-1047	RLO-1058	RLO-1067	RLO-1077
V&V Section	4.6.3	4.6.3.1	4.2.3	4.6.4
dE/E	<70%	<120%	<120%	<120 %
	RLO-1048	RLO-1059	RLO-1068	RLO-1078
V&V Section	4.6.3.3	4.6.5, 4.6.3.3	4.6.3.3	4.6.4
Angular resolution	< 18 degree FWHM	<10 degree	< 10 deg	< 10 deg
	RLO-1051	RLO-1061	RLO-1070	RLO-1080
V&V Section	3.2	3.2	3.2	3.2
Geometric Factor	> 6e-5 cm^2 sr eV/eV @ 500 eV	> 3e-5 cm^2 sr eV/ eV between 10 - 40 eV	> 1e-4 to 1e-5 cm^2 sr eV/eV H between 30 - 150 eV	>1.5e-4 cm^2 sr eV/eV O >7e-5 cm^2 sr eV/eV Ne
	RLO-1053	RLO-1063	RLO-1073	RLO-1083 RLO-1084
V&V Section	6.1	6.1, 4.6.5	4.2.3,6.3 Requires additional analysis	6.2,6.3 Requires additional analysis

ENA flux calibration:	H ENAs X-Cal W/ IMAP-Hi	
	Absolute accuracy +/- 25%	RLO-1599: V&V Section: 5
	relative accuracy of +/- 10%	RLO-1598 V&V Section: 5

2. CALIBRATION OVERVIEW

The IMAP-Lo calibration philosophy is to follow IBEX-Lo heritage in calibrations as much as possible. The instrument assembly and integration are not all conducted at once but done in steps. Furthermore, the team is developing a full sensor model which is used to validate simulations at each calibration step. Additionally, following IBEX-Lo heritage, the overall calibration plan is as follows:

1. **Key subsystems characterized/calibrated separately**
   - Collimator/deflection system,
   - Conversion surfaces,
   - TOF subsystem,
   - Star sensor
2. **PreCal1**
   - No Entrance System
   - Accurately determine the flux of particles entering the instrument and the respective detection rates. Subsequently, the actual conversion surface/ESA/detector efficiency are determined through analysis of these data.
3. **PreCal2:**
   - Take calibration measurements with fully assembled sensor, including collimator and deflector subsystem, prior to environmental testing (instrumental level)
4. **Final Cal:**
   - Same as PreCal2 but after environmental testing (instrumental level)
5. **Cross-Cal:**
   - Take calibration measurements together with IMAP-Hi at the same neutral atom beam
   - As per observatory schedule, this also validates the instrument performance post observatory acoustic and vibration tests but prior to observatory thermal vacuum (TVAC) test.

The overarching IMAP-Lo calibration objectives are to:

- Verify IMAP-Lo performance requirements related to energy range, dE/E, angular resolution, and geometric factor
- Ensure proper functioning of all detector segments
- Ensure accurate species differentiation (H, D, He, Ne, C, O)
- Determine the factors required to convert measured ISN/ENA count rates into physical units of incident flux
  - Requires determination of the instrument Geometric Factor (for different species)
- Characterize sensitivity to backgrounds:
  - Charged particle deflection by deflectors
  - Possible internal backgrounds

The structure of this document follows the calibration sequence as outlined above. We start by discussing subsystem testing of the Collimator, TOF and Conversion surfaces where we outline key findings that feed into instrument level calibration and the determination of the instrument detection efficiency. Sensor level calibration outlines our primary calibration facility and gives an overview of each of the calibration events, then walks through key results. The key findings from sensor level testing, namely energy response and detection efficiency, are then integrated with the absolute GF, determined in collimator subsystem testing, and TOF detection efficiency to calculate the instrument species dependent geometric factors.

2.1 Calibration Sequence

Here, we outline the sequence of calibration events that occurred in the lab leading to the delivery of the IMAP-Lo FM. The organization of this report follows roughly in line with the sequence of events. An abridged testing flow is shown in **Figure** .

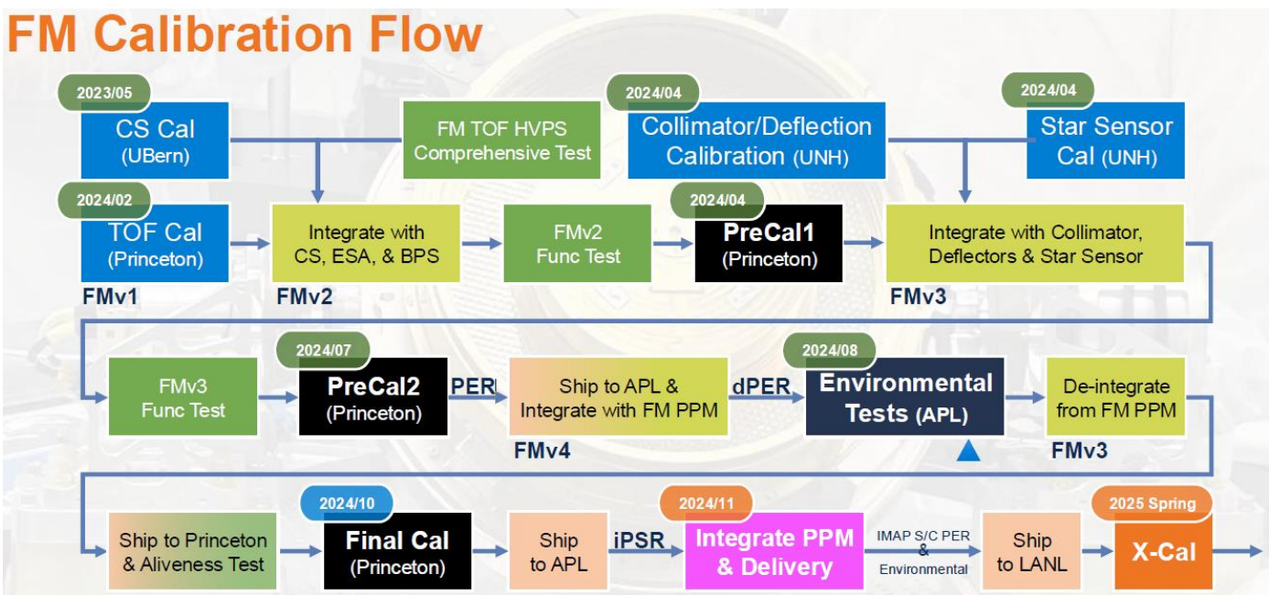


Figure 2.1.1: Abridged testing and calibration flow, indicating what objects are being tested, and which facilities are being used.

2.2 IMAP-Lo Geometric Factor

The geometric factor is effectively a measure of the instrument's collection power and is used to determine incident fluxes from measured count rates. The factors included in the GF are determined through instrument calibration, subsystem calibration, energy response modeling and geometric measurement.

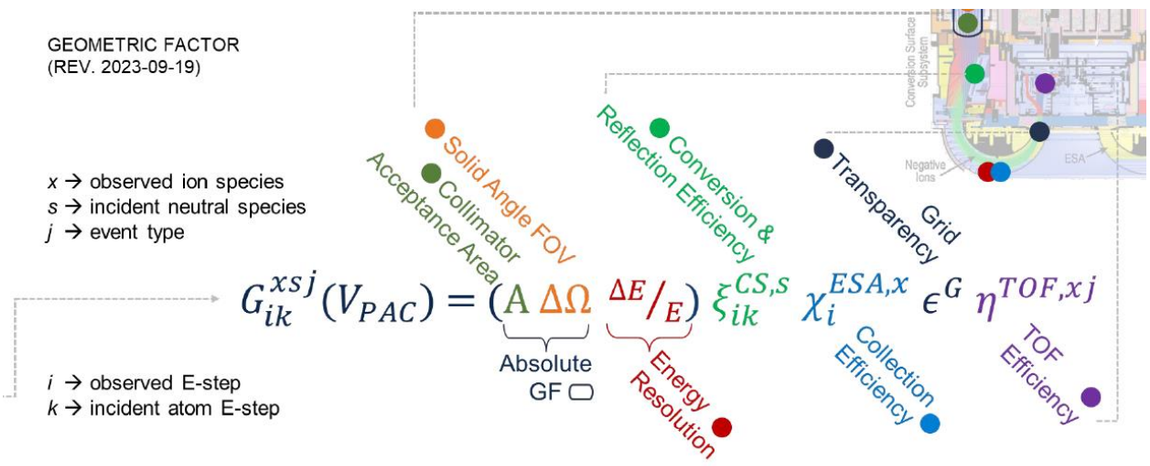


Figure 2.2.1 A description of the geometric factor

Table 2.2.1 Geometric Factor terms

Parameter	Description	Verification Test
AΔΩ	Absolute Geometric Factor Collimator [cm2 sr] acceptance area and solid angle FoV, measured in Collimator Subsystem Calibration	Collimator Subsystem calibration
ΔE/E	Energy Resolution: Given by the mean energy and energy passband of the ESA-CS subsystem for a given species, energy step and mode. Determined through model deconvolution of Differential Energy Response (DER1) calibration results.	Sensor Level Calibration (PreCal1,PreCal2, FinalCal)
ξ χ	**Conversion-Collection Efficiency:** The probability that a given species will scatter off the conversion surface and convert to a negative ion and recoil with a trajectory and energy that will survive through the ESA. In IMAP-Lo FM calibration, the conversion and reflection efficiency (green) and the ESA-collection efficiency are determined together. External determination of the conversion efficiency, performed during conversion surface subsystem calibration, is used as a sanity check for the full FM calibration ESA-CS efficiency.	Sensor Level Calibration (PreCal1,PreCal2, FinalCal)
ε	**Grid Transparency:** Combined transparency of all grids and spokes that intercept the particle path. This includes the P2 spokes, the P10 grids and spokes and the TOF entrance grids and spokes. The Collimator grid transparency is accounted for in the absolute GF, while the grids internal to the TOF are accounted for the in TOF efficiency (see TOF efficiency document)	Component Inspection
η	**TOF Efficiency**: including the grid transparencies within the TOF subsystem. Given is the pure TOF efficiency. This quantity is determined from the TOF PHA and rates according to the TOF sub-system level calibration. These efficiencies are determined separately for Event Types j, e.g. Triple and Any Double and separately for detected species x. There is no energy dependence	ToF Subsystem Calibration

	because the energy in the TOF is mostly determined by the post-acceleration voltage. The combined grid transparency (C-foil support grids and spokes) is given separately.	

3. SUB-SYSTEM LEVEL CALIBRATION

3.1 TOF Sub-system

Excerpt from E. Moebius ***IMAP-Lo_TOF-Cal_T101_Analysis_Dr4a.docx***

The IBEX-Lo and IMAP-Lo Time-of-Flight (TOF) subsystem is a triple-TOF system that provides superior noise and background suppression through a triple coincidence requirement and the ability to check the three TOF measurements for consistency with a single particle passage through the system. Figure 0.1 shows a schematic depiction of the three TOF measurements and the additional identification of the sensor quadrant hit by the particle via a Delay Line measurement.

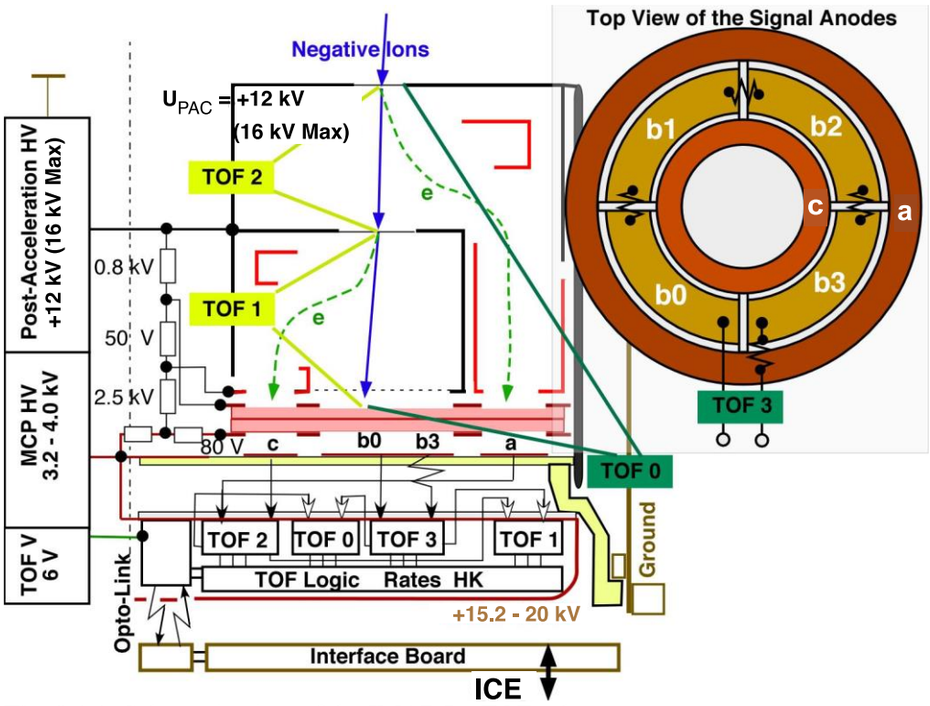


Fig. 3.1.1: Schematic view of the IMAP-Lo TOF subsystem
Left: Radial cut, along with electronic and HV block diagram. *TOF0* represents the TOF all the way from the first foil (Signal a) to the MCP (Signal b0), while *TOF1* is the second leg from the second foil (Signal c) to the MCP (Signal b3), and *TOF2* the first leg from the first (Signal a) to the second foil (Signal c). MCP Signals a and c feed directly into *TOF2*, and MCP Signals b0 and b3 feed directly into *TOF3*. *TOF0* and *TOF1* obtain the timing signals from outputs of the *TOF2* and *TOF3* TOF chips.
Right: Top View of the MCP Anode with the Delay Lines between quadrants b0, b1, b2, and b3 as well as at the end (b3 output) indicated.

As can be seen from Fig. 0.1, the TOF measurements are taken as:

$$TOF0 = T_{b0} - T_a$$
$$TOF1 = T_{b3} - T_c \qquad (3.1.1)$$

$TOF2 = T_c - T_a$

And the Delay Line:

$TOF3 = T_{b3} - T_{b0}$

The three measured TOFs can be related to the speed v_i of the passing ion after its energy loss in foil 1 and/or 2 in the respective TOF leg as:

$$v_1 = s_1/(TOF1 - T_{10}) \quad (3.1.2)$$

$$v_2 = s_2/(TOF2 - T_{20})$$

where s_1, s_2 are the lengths of the flightpaths in leg 1 and 2 and T_{10}, T_{20} are the timing offsets at a measured flight time of the ion $\tau = 0$ ns for *TOF1* and *TOF2*, respectively. Likewise, there is an offset T_{00} for *TOF0*. These offsets are due to the combination of the following delays:

1. delays in the electronics
2. slightly different lengths of each signal line to the preamplifiers on the TOF board
3. the secondary electron flight times
4. different Delays, according to each of the 4 quadrants hit, in the Delay Line applicable to *TOF1* and TOF0.

Measured 1D TOF spectra and their 2D cousin, 2-dimensional distributions based on a combination of the measured TOFs, can be assembled from the Direct Event data produced by IBEX-Lo and IMAP-Lo and are thus available for any test and calibration run on the ground or from flight data. These TOF products carry key information on the instrument performance and source distributions measured that can be extracted from them. In the following, we will describe which information can be obtained, followed by a description how each of these items can be extracted, and, in some cases, which calibration activities are most important for their generation.

3.1.1 TOF subsystem calibration setup and tasks

The TOF subsystem is exposed to positive ion beams with energies ranging from 7 to 16 keV. The observations are mostly concentrated in one quadrant augmented by a roll scan to test the instrument response in all quadrants.

Note: During the TOF calibration only one quadrant (Q3) was fully functional. The remaining three quadrants produced valid TOF1 events, but no TOF0 and TOF2 events because the connection for Start A was not functioning for these quadrants. Therefore, not all tasks could be completed during the TOF calibration.

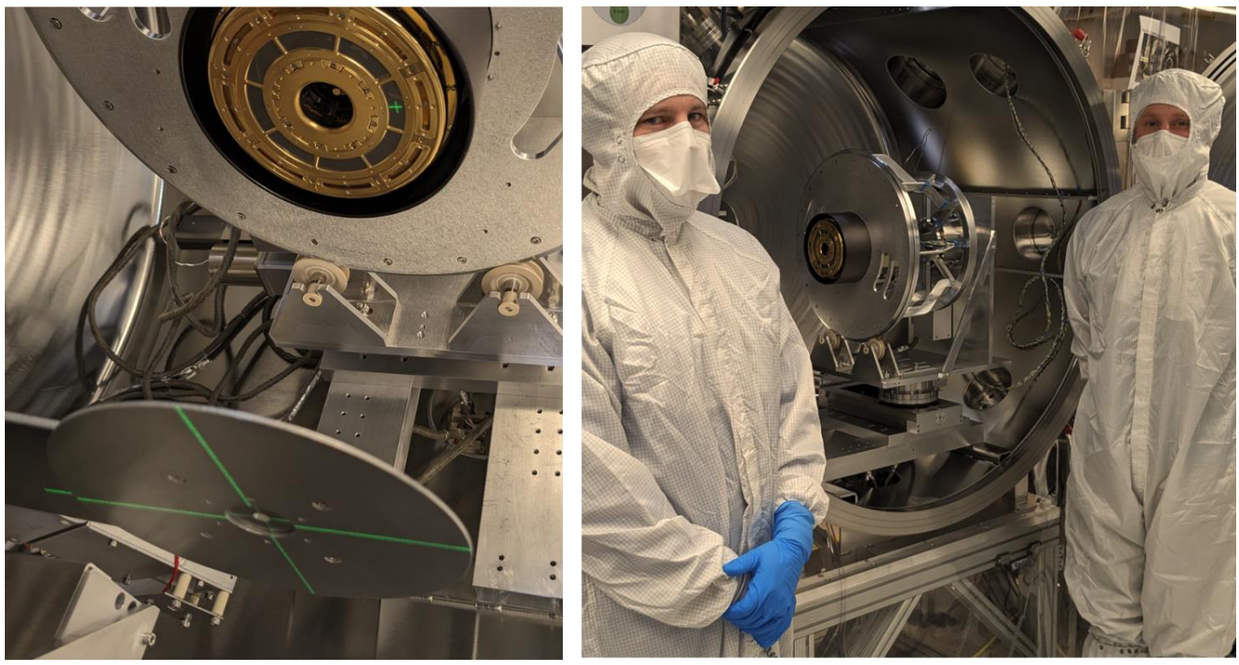


Figure 3.1.2 IMAP-Lo TOF calibration test setup and installation

The following quantities are determined during the TOF subsystem calibration

a) Species identification with TOF0, TOF1, and TOF2 (section 3.1.2)
b) TOF3 position determination, suggested quadrant boundaries, and peak locations (section 3.1.3)
c) Limits for Checksum condition (section 3.1.4)
d) Offsets for TOF = 0 (section 3.1.5)
e) TOF resolution (section 3.1.6)
f) Determination of "ghost" features in TOF spectra and 2D plots (section 3.1.7)

3.1.2 Identification of Different Species

TOF spectrographs, when combined with an electrostatic analyzer (ESA) and/or post-acceleration (PAC), provide the mass/charge (M/Q) of the incoming particles, in the case of IBEX-Lo and IMAP-Lo also directly M because these instruments use negative ions for detection and identification, which can only be singly charged. Therefore, we use only singly charged ions during the TOF subsystem calibration. However, here, we provide beams at energies commensurate with PAC voltages to be used in flight. We cover a wider range in this calibration to obtain TOF peak locations, resolution, and TOF efficiencies for an extended range. The energy at the entrance to the TOF subsystem is thus not determined by the PAC voltage, which is not applied during this set of tests, but by the beam energy E_{Beam}. Then, the TOF τ_i in each leg can be described as:

$$\tau_2 = s_2/v_2 = \sqrt{2(E_{Beam} - \Delta E_{F1})/M}$$
$$\tau_1 = s_1/v_1 = \sqrt{2(E_{Beam} - \Delta E_{F1} - \Delta E_{F2})/M} \quad (3.1.3)$$
$$\tau_0 = s_1/v_1 + s_2/v_2$$

v_1 and v_2, s_1 and s_2, and τ_1 and τ_2, are the actual speeds, length of the flight path, and TOFs in the legs of *TOF1* and *TOF2*, respectively. The TOF across the full length of *TOF0* has to be found by summing τ_1 and τ_2, because the energies and thus the speeds in the two legs are different. The reason is that either only the energy loss in one foil (ΔE_{F1}) for *TOF2* or both foils ($\Delta E_{F1} + \Delta E_{F2}$) for *TOF1* modifies the particle energy.

To compare the measured TOF (*TOF0, TOF1, TOF2*) with the simulated flight times (τ_0, τ_1, τ_2) the TOF offsets need to be added:

$$TOF0 = T_{00} + \tau_0$$
$$TOF1 = T_{10} + \tau_1 \quad (3.1.4)$$
$$TOF2 = T_{20} + \tau_2$$

For a given PAC voltage and entrance foil thickness, the particle energy upon passage of the TOF system is fixed and known. Thus, the TOF $\tau \approx \sqrt{M}$. In order to obtain a solid mass dependence of these peak locations, values for He and Ne are also obtained, along with their mutual resolution. With H, D, He, and O, a set of species that is separated by factors of 2 in mass (H, D, and He) and by a factor 4 for O from He so that a direct identification of the respective species peaks is possible, first without the precise knowledge of their TOF values and of their energy loss. Their precise measurements in the TOF calibration can then be used to validate the simulation with the actual measurements. Based on these comparisons, the actual energy loss values for each of the species at several different PAC voltage values can then be determined and compared with models of the energy loss in matter. In turn, this knowledge allows a better determination of the actual energies of the incident particles in each of the two TOF legs.

The TOF spectra for several species are compiled in Figure 3.1.3 for 12 keV ions, a) H+ (Run030), b) H2+ (Run032), c) He+ (Run031), d) Ne+ (Run045), and e) O+ (Run046). TOF spectra plots for the light ions (H^+, H_2^+, and He^+) demonstrate that very clean spectra can be obtained with Triple coincidence measurements. The O+ and Ne+ spectra contain additional step features at shorter TOF than expected for O+ and Ne+, which points to contamination with other species in the delivered beam. Water group ions contribute to the beam in the O to Ne mass range before mass selection, but they are not completely removed. These features are discussed further in section 3.1.6. No electrons are seen in the TOF spectra during the TOF calibration with positive ions.

There is a visible trend toward broader TOF peaks from lower to higher masses. This trend is strongest in TOF0s and TOF1s, which involve energy loss in both C foils. However, even O+ and Ne+ at 12 keV show a remarkably narrow TOF peak in TOF2, or a much-improved TOF resolution, due to the reduction in foil thickness from 2 to 1 µg/cm compared with IBEX-Lo.

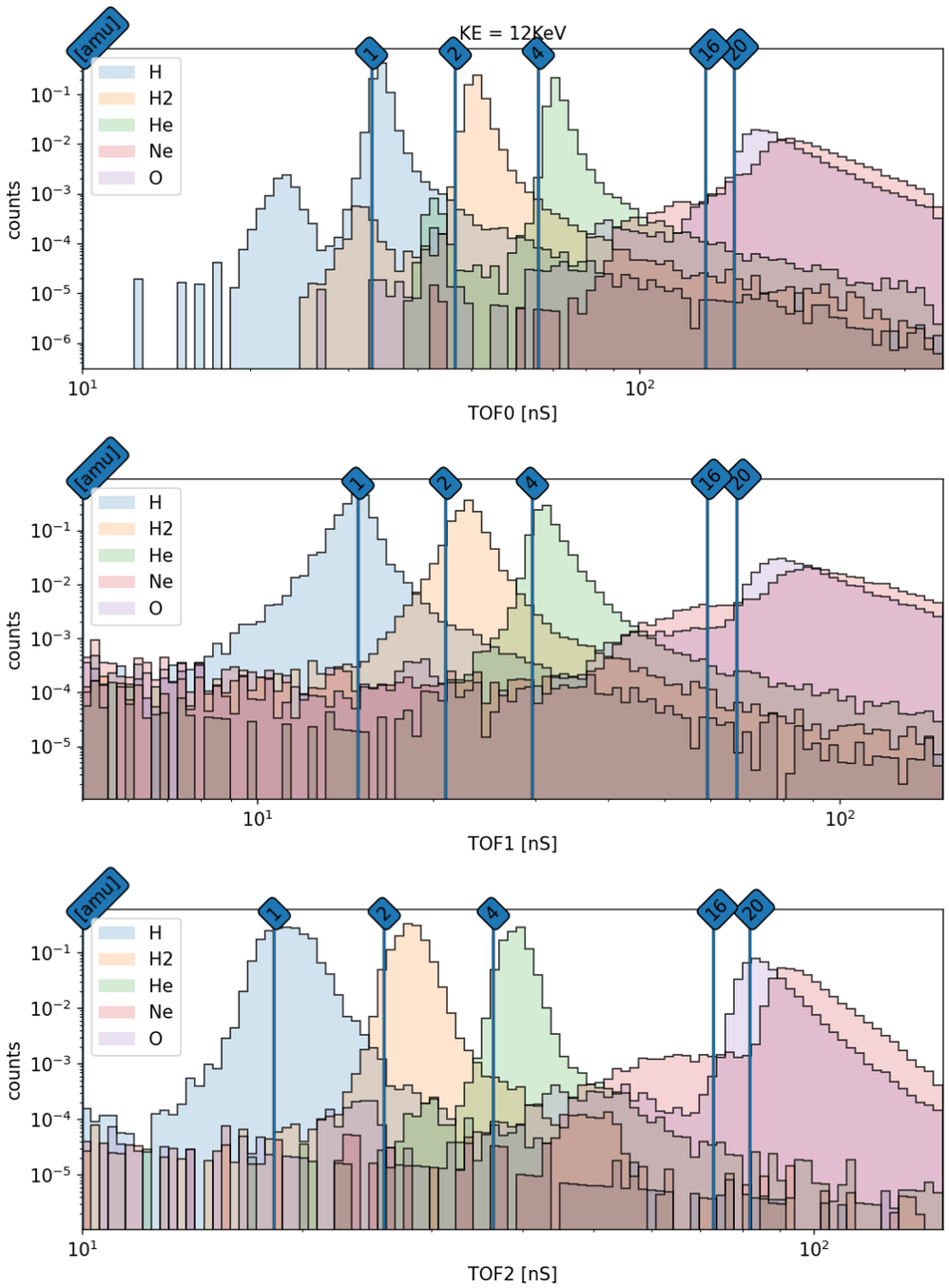


Figure 3.1.3: TOF spectra from T101 R030 with 12 keV H+ ions based on Silver Triples.
Top left: *TOF0s* (from 1st foil to the MCP) spectrum
Top right: *TOF1s* (from 2nd foil to the MCP) spectrum
Bottom left: *TOF2* (from 1st to 2nd foil) spectrum
Bottom right: *TOF3* spectrum for Type 0101 DEs (valid TOF1 and TOF3)

TOF Peak Locations and TOF Resolution

The peak location and FWHM can be determined for light ions with a simplified center of mass approach. For the heavy ions (C, O, Ne) a fit with a skewed Gaussian or an asymmetric kappa distribution has to be performed. In the following, we compile the peak values and TOF resolution for the light ions.

The TOF peak values and widths (FWHM) for 12 keV measurements are compiled in Table 3.1.1, along with the estimated mass resolution of the TOF subsection. The peak location was determined as the center of mass of the TOF distribution within the set TOF boundaries for each species. The FWHM was obtained as the number of all H events divided by the number of events in the 1 ns bin around the peak TOF value.

Table 3.1.1a 12 keV H TOF Values Run030

	TOF0s		**TOF1s**		**TOF2**	
TOF(H^+)	36.29	ns	17.57	ns	19.02	ns
ΔTOF (FWHM)	2.18	ns	2.34	ns	3.38	ns
M/ΔM	8.31		3.75		2.81	

Table 3.1.1b 12 keV H_2 TOF Values Run032

	TOF0s		**TOF1s**		**TOF2**	
TOF(H_2^+)	52.96	ns	25.89	ns	28.13	ns
ΔTOF (FWHM)	3.86	ns	3.09	ns	3.16	ns
M/ΔM	6.86		4.19		4.45	

Table 3.1.1c 12 keV He TOF Values Run031

	TOF0s		**TOF1s**		**TOF2**	
TOF(He^+)	73.16	ns	34.54	ns	39.22	ns
ΔTOF (FWHM)	4.95	ns	3.92	ns	3.76	ns
M/ΔM	7.38		4.41		5.22	

The TOF peak locations and their resolution obtained from the TOF calibration are the final values for TOF2 because the Signal board does not significantly influence these values, and no other changes of the TOF subsection, including electronics, have been made. However, TOF3, TOF0s, and TOF1s may change slightly due to tolerances in the delay line implementation. Also, the TOF resolution reflects solely the TOF subsection for a beam with a narrow energy distribution. PreCal1, 2, FinalCal, and XCal measurements also include the effects of a broader energy and angle distribution from the CS. Therefore, section 4.5.1 provides updated plots and values.

TOF Selection Limits for H and C&O

Determining the TOF distributions enables the definition of the left boundaries (LB) and the right boundaries (RB) of the TOF ranges in which the H and C&O distributions are selected. These boundaries are relevant for the LUT that feeds into the ICE software for the onboard selection of Direct Events into the H and C&O Histograms and for the data processing pipeline on the ground. We need such boundaries for PAC voltage levels of 12, 10, and 7 kV. 12 kV is the nominal operational value, 10 kV is the first step

during commissioning, which will be maintained for a few weeks, and 7 kV is the contingency value in case of problems with the high voltage.

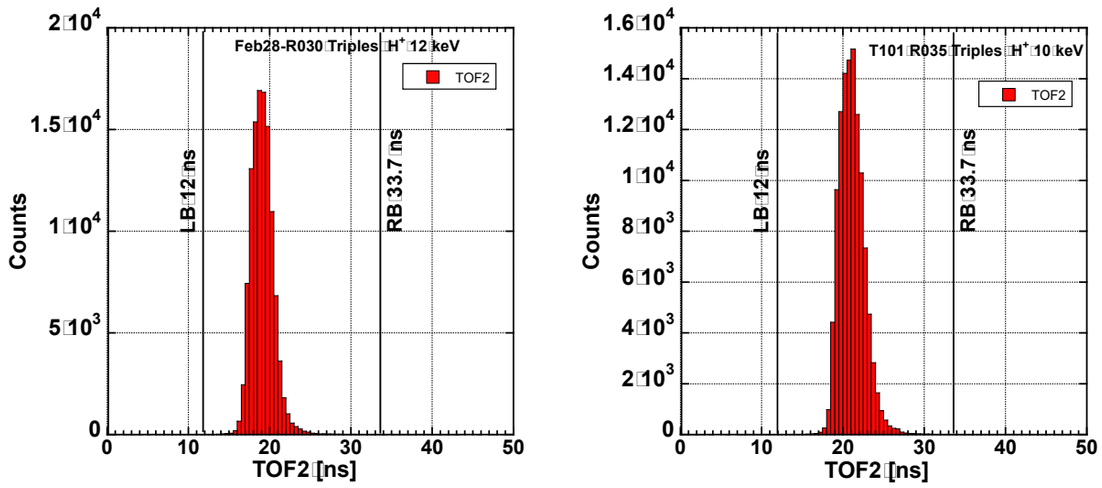


Fig. 3.1.4 H^+*TOF2* distributions for a 12 keV (left) and 10 keV (right) H^+ beam. The LB and RB TOF2 values are indicated by vertical lines.

Figure 3.1.4 shows the TOF2 distributions for a 12 and 10 keV H^+ beam. LB and RB limits for H based on IBEX-Lo values are indicated by vertical lines.
As can be seen, the LB and RB limits in TOF2 are appropriate for 12, 10, and 7 keV H. Similarly, the LB and RB limits in TOF0s are appropriate for 12, 10, and 7 keV. Only the bounding cases (12 and 7 keV are shown). Unsurprisingly, the IBEX-Lo values can be used as these wide ranges were chosen to accommodate PAC voltages between 16 and 7 kV, and the IMAP-Lo TOF section is identical in its design and dimensions to the IBEX-Lo version. The thinner foils in IMAP-Lo only shift the species peaks very slightly toward shorter TOF values and so does the higher acceleration voltage into the ESA in High Throughput Mode. However, the IBEX-Lo ranges also include a PAC voltage of 16 kV, which accommodates the shifts toward shorter TOF values. The same applies to the C&O ranges. Here, the RB is just short of the maximum TOF values accepted as valid so that the entire elongated TOF tail of the heavy ions is within the selection range.

Table 3.1.2 contains the final LB and RB limits for H and C&O in TOF2 and TOF0s. The values are shown in DN, as directly extracted from the telemetry stream, and in ns. The ICE will mainly use the TOF2 limits (with Species selector = 2) to fill Direct Events into the H and O Histograms. The data processing pipeline on the ground also use the identical values to flag Direct events as H or O so that a direct comparison between the Direct Events and Histogram events is possible.

Table 3.1.2: TOF LB and RB Limits for H and C&O Selection

	H Limits in DN	**H Limits in ns**	**C&O Limits in DN**	**C&O Limits in ns**
TOF2 LB	35	12	185	61.9
TOF2 RB	100	33.7	510	170.1
TOF0s LB	70	24.6	390	132.4

TOF0s RB	190	65	1050	354.6

3.1.3 TOF Ghost Features, Uncorrelated Background, and Beam Impurities

Figure 3.1.5 shows sample *TOF1* vs. *TOF0* and *TOF2* vs. *TOF0* 2D scatterplots obtained with the IMAP-Lo EM TOF section at the UNH accelerator, using a 16 keV H_2^+ beam. Although not taken with the FM, this example illustrates well which additional background features become visible when very high single rates are observed. It also demonstrates the power of a triple TOF system to suppress uncorrelated background and to separate additional features from the expected TOF peaks of the incoming particles.

These plots include only Golden Triple events as defined above. Shown is an example when the TOF subsystem showed an extremely high count rate on Start A, i.e., the start signal for TOF2 and TOF0 (30,000 – 50,000 cts/s). This condition led to modestly high chance coincidence rates in these two TOF channels, while the H_2^+ peak was still very prominent.

In the two 2D TOF scatterplots in Fig. 3.1.5, the chance coincidences due to the Start A counts show up most prominently as a streak parallel to the TOF0 axis at the correct TOF location for the incoming H_2^+ ions in TOF1 in the left panel, consequently, as a diagonal streak in the right panel, where these events are seen as correlated locations in TOF0 and TOF2. These two streaks also extend to shorter TOF values than expected for the H_2^+ beam.

In addition, there are two more prominent streaks, extending from the H_2^+ peak to longer TOF values. They stretch along two diagonal lines in TOF1 vs. TOF0 with different slopes and are found as a line parallel to the TOF0 axis and as a diagonal line with a shallow slope in TOF2 vs. TOF0. These streaks stem from particles that suffer substantial energy loss in either C-Foil. The steep diagonal line in TOF1 vs. TOF0 and the line parallel to the TOF0 axis in TOF2 vs. TOF0 are produced by substantial losses in Foil 2 (indicated as Scattering in Foil 2), and the shallow diagonal lines in both scatterplots are produced by substantial losses in Foil 1 (indicated as Scattering in Foil 1). Note, energy loss in C-Foil 1 affects TOF0, TOF1, and TOF2, while energy loss in Foil 2 only affects TOF0 and TOF1.

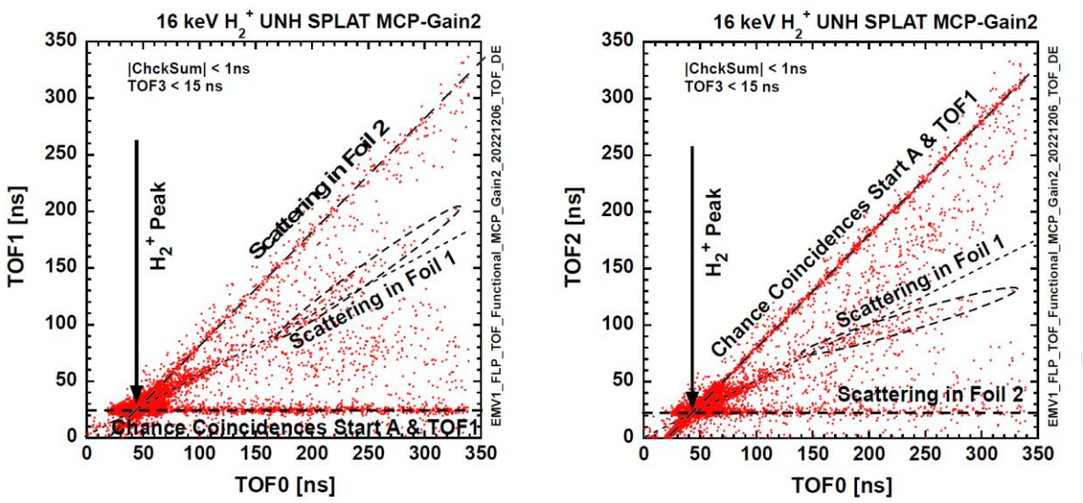


Figure 3.1.5: 2D scatterplots of Golden Triples with TOF3 > 15 ns removed. **Left** *TOF1* vs. *TOF0*, **Right** *TOF2* vs. *TOF0.* Except for the H_2^+ Peak (≈10,000 Counts total) tails from scattering in Foil1 and Foil 2 are seen. Also visible is the trace with chance coincidence counts combining the very high Start A Rate and valid *TOF1* events (horizontal on the left and diagonal on the right). No counts with *TOF1* or *TOF2* > *TOF0* are visible. The streaks of events, marked as Chance Coincidences Start A & TOF1 as well as Scattering in Foil 1 and in Foil 2, are emphasized with dashed lines. In addition, the slender ellipses with yellow highlighting indicate the regions expected for C^+ and O^+.

It should be noted that with the choices for the ChckSum condition and TOF3 used here, there are no events in the upper half of either plot above the 45° diagonal line. Such events would be the sign of the pile-up of signals from more than one particle passing the TOF system simultaneously and then violating the ChckSum condition. They have been successfully eliminated by applying both the ChckSum and TOF3 conditions.

3.1.4 Determination of Detection Efficiencies

The TOF detection efficiencies are an essential part of the IBEX-Lo and IMAP-Lo geometric factors. Because of the Triple TOF design, all three individual Signal Efficiencies can be determined as ratios of the detected Triple Coincidence Rate $R_{\text{GoldenTriple}}$ and the Double Coincidence Rate R_{TOFn} that does not contain the respective Signal:

$$Eff_A = R_{\text{GoldenTriple}}/R_{\text{TOF1}}$$
$$Eff_B = R_{\text{GoldenTriple}}/R_{\text{TOF2}} \quad (3.1.5)$$
$$Eff_C = R_{\text{GoldenTriple}}/R_{\text{TOF0}}$$

which can then be combined to form the Triple Coincidence efficiency as:

$$Eff_{Triple} = Eff_A * Eff_B * Eff_C \quad (3.1.6)$$

The efficiencies in Eqn. (3.1.5) and (3.1.6) are computed in the IMAP-Lo TOF Analysis Pipeline.

Species-Dependent Signal Efficiencies is described in a separate Memo by *R. Murphy* and in *R. Murphy's* Master Thesis.

Additional calibration of the TOF unit at the sensor level is discussed in section 4.3: Sensor Level TOF Calibration

3.2 Collimator and Deflection System

Excerpt from F. Rahmanifard 27850-1048-Collimator-Optical-Comp-R0C0 and IMAP-Lo-Coll-FoV_PointSpread_AbsGF_27850-6004_03.19.2025

The collimator consists of a stack of 21 identical grids with etched hexagon holes. The 4 spokes separating these hexagon patterns can be seen in Figure 3.2.2. On the top there is a pre-collimator that provides a triangular structure on top of the hex sides. The Lo collimator is assembled on a thick base plate by stacking grid sheets, spacers, and the pre-collimator. The as-built dimensions have been validated on the parts level before assembly within tolerances. The FOV= 8.71 deg is obtained using the hex width (w = 5 mm) and the total height of the collimator stack (h = 27.93 mm).

To find the absolute GF of the IMAP-Lo collimator, we used cad model's measurements of the inner and outer radius of the collimator (in addition to w and h). The absolute GF is the multiplication of the area of the collimator, solid angle and transparency

$$T = \frac{1}{\left(1+\frac{d}{w}\right)^2} \qquad (3.2.1)$$

where d is the grids' line width. To have the final value for the absolute GF (2.1770.028 cm^2 sr), we remove the effect of spokes and incomplete hex patterns using CAD model measurements of the spoke sizes as well as the distance between the last grid of the collimator with the inner and outer edges of CS.

Optical measurements were performed after stacking and tightening of the collimator pins. The height of the collimator is further measured after torquing to ensure accurate field of view. We have a full record of the grids as built values including the hex width and gridline width. The as built values are very accurate and well within tolerances. Further measurements were performed at the time of stacking. Therefore, **we skip measuring the hex width and gridline width**.

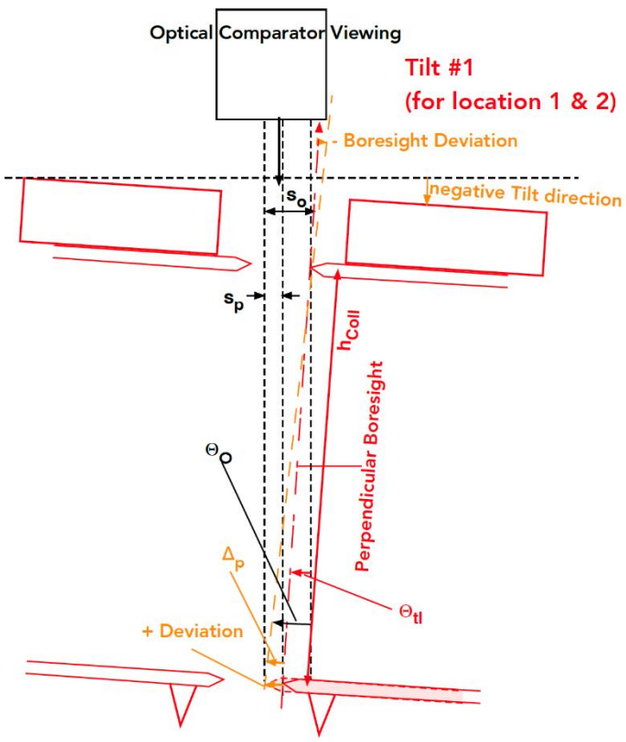
Furthermore, UNH facility provides 2D measurements, which makes it impossible to diagnose any lateral offsets. However, based on our previous measurements at PEI, confirming a standard deviation for the lateral offsets which falls well within spec, we trust that our stacking method provides the needed precision in this front. Furthermore, during the stacking Dino-Light camera was used to examine any possible lateral offset in the middle grids and between the top grid and the pre-collimator, reporting no visible offsets. Therefore, **we skip determination of any lateral offsets between the grids.**

The goals of the validation of the IMAP-Lo collimators on the Optical Comparator are:

1) Validation of the correct relative positioning of the bottom and top grid pattern (a.k.a. perpendicularity)

2) Validation of the position of the pre-collimator relative to the top collimator grid

1) provides any possible offset of the absolute reference frame with respect to the spoke alignment 2) provides confirmation that the entire pre-collimator is outside the FoV, as required, so that we can trust the FoV and absolute GF obtained as explained above.



Figı

A schematic cut through the collimator channel tilted by the angle θ_{tl} is shown in Figure 3.2.1. Measured is the offset s_o as seen from the bottom of the collimator to the top, where this offset exceeds the expected offset due to the tilt angle θ_{tl} by s_p. From these values we can calculate the boresight angular shift from perpendicularity Δ_p:

$s_p = h_{coll}\sin(\Delta_p)$.

$\theta_o = \arcsin(s_o/h_{coll})$

$\sin(\Delta_p) = \sin(\theta_o) - \sin(\theta_{tl})$ (3.2.2)

$\Delta_p = \arcsin(\sin(\theta_o) - \sin(\theta_{tl}))$

3.2.1 UNH Optical Comparator Measurements

A front view of the Optical Comparator is shown in Fig. 3.2.2. The Lo collimator is placed on a metal rail in a vertical position. This configuration allows for moving the Lo collimator in the x, y, or z directions (see red arrows in Figure 3.2.2 Left). Figure 3.2.2 Right shows the IMAP-Lo FM collimator on the comparator rail. The optical system, which acts as a precision microscope, is in front of the rail. This optical comparator provides 2D measurements in the x and y directions. Moving the rail in the z direction

(front/back) allows for focusing on different layers to make the appropriate measurements. All movements, lighting options, and different parts of the profile projector are explained in its operation manual (MITUTOYO, PH-350H). The measurement procedures are controlled by a QM-DATA200 unit.

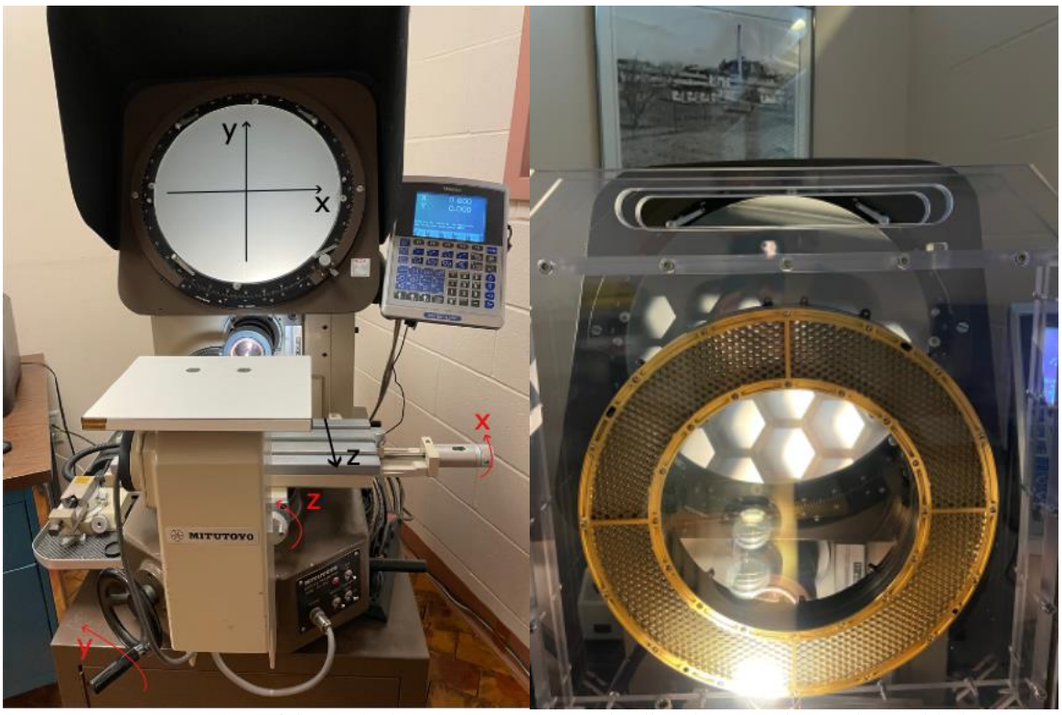


Figure 3.2.2 Left Front view of the Optical Comparator. x, y, and z directions are shown along with the handles used to move the rail in each direction. **Right** The low collimator on the rail and its magnified image on the screen.

To evaluate perpendicularity, edge-to-edge measurements were taken between corresponding hexagonal patterns in quadrants Q0 through Q3 (for example see Figure 3.2.3). The collimator was mounted on a rail with the pre-collimator side facing the operator. Measurements were performed in two primary configurations: first with Q0 and Q3 at the bottom (facing the operator) and then with Q1 and Q2 at the bottom. In both setups, the collimator was tilted at +4° and -4° about the x-axis using angle blocks. At each angle, offsets in the x-direction (Δx) were recorded for each quadrant. These offsets were used to calculate biased and unbiased perpendicularity deviations using reference equations outlined in techNote-CollimatorV3. Results showed a deviation of 0.001° ± 0.038° in the x-direction and -0.012° ± 0.022° in the y-direction, both of which fall well within specification. This confirms that the relative positioning of the top and bottom grids meets the required perpendicularity criteria.

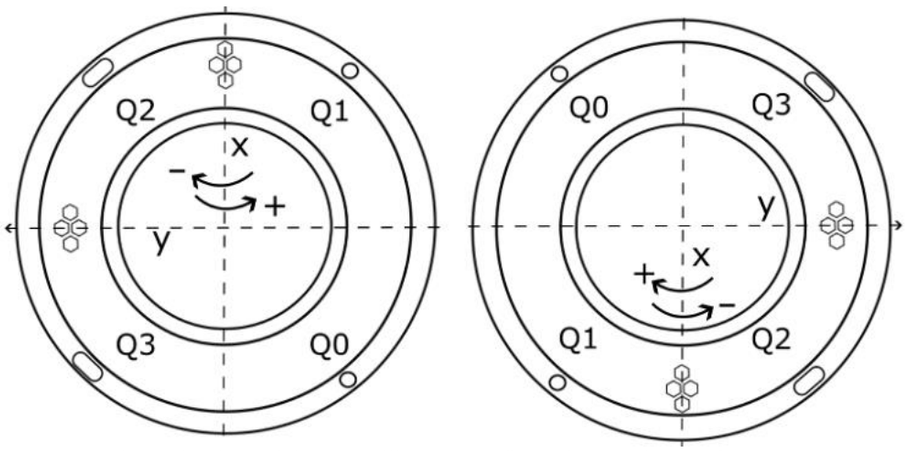


Figure 3.2.3 Schematic view of the Lo collimator configuration used to perform measurements between vortices with a ±4° rotation around the x axis in **Left)** Q0 and Q3 and **Right)** Q1 and Q2.

In addition to edge measurements, alignment of the vortex patterns between the top and bottom layers was also assessed. The collimator was positioned to bring quadrants Q0 and Q1 into view, followed by Q2 and Q3, with the same ±4° tilt applied about the y-axis. Measurements were taken along the y-direction to determine the offset between vortex centers at the top and bottom layers. These values, combined with zero-tilt baseline readings, enabled the calculation of angular deviations. The resulting data further supported the conclusion that the grid alignment remains within acceptable limits.

Lastly, measurements were conducted to verify the placement of the pre-collimator relative to the top grid layer. With the collimator positioned to bring Q3 into view, the optical comparator was focused on the top layer directly beneath the pre-collimator. Measurements were taken across multiple visible edges of a single hex, and when necessary, adjacent hex features were used. The observed offsets were symmetrical across the pre-collimator rib width and fell within defined tolerances. This confirmed proper alignment of the pre-collimator with respect to the top grid.

In conclusion, the optical comparator measurements validated all three test objectives. The measured offsets and computed angular deviations were within specified limits, confirming that the collimator assembly satisfies the required alignment criteria for grid perpendicularity, vortex pattern matching, and pre-collimator placement.

3.2.2 Ion Suppression Verification

Excerpt from IMAPLo_EM_DeflCol_Deflection_Test_Report.pdf

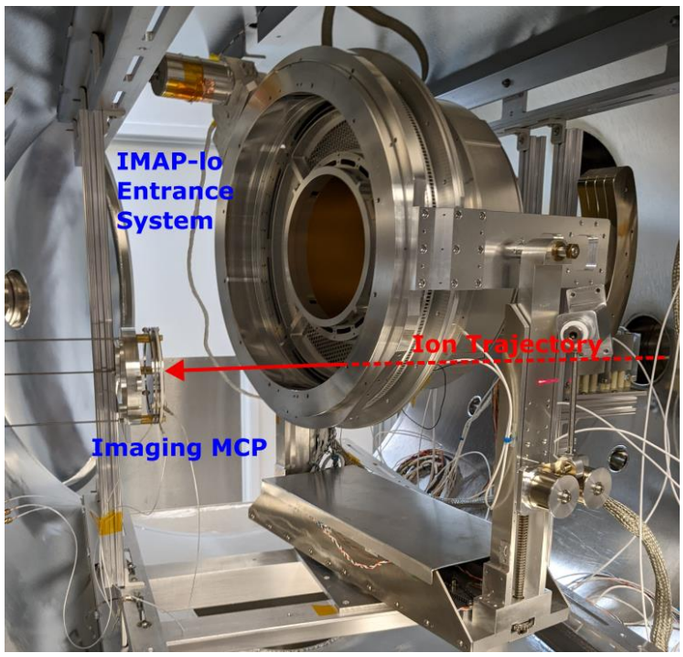


Figure 3.2.4 Test setup for entrance system ion beam calibration

The IMAP-Lo entrance deflection system was tested at the University of New Hampshire's M145 Ion Beam Chamber on November 16, 2022. The objective of the test was to evaluate the effectiveness of the deflector system in suppressing unwanted charged particles from passing through the collimator. Specifically, the team aimed to confirm that the system could reduce the beam throughput to less than 0.2% of its original value under nominal operating conditions.

The EM deflection system and collimator were loaded into the optics deck which was then mounted to the vacuum safe 5-axis table inside the chamber and aligned such that a beam from the line can strike a lab MCP detector located on the far end of the chamber from the beam. The deflectors were wired to two 5kV lab high voltage supplies.

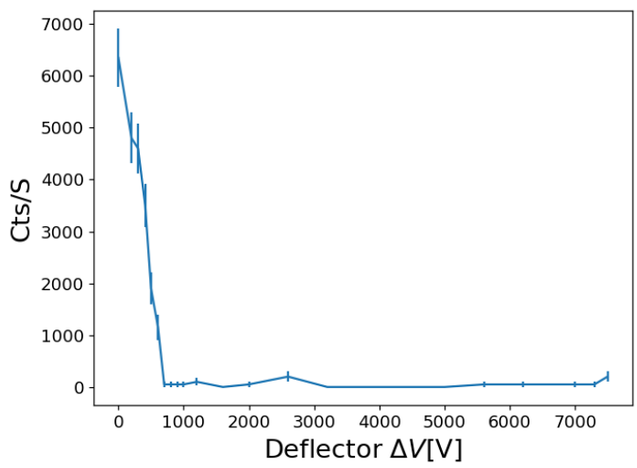


Figure 3.2.5 Deflector Voltage ramp Ion suppression

Testing was conducted in multiple stages using a 2 keV ion beam. Initially, baseline measurements were taken with the deflectors turned off to establish a reference for the natural count rate and beam alignment. The deflectors were then powered with their nominal voltages +4 kV at the inner electrode and −3.5 kV at the outer electrode and the entrance system was rotated through a ±6° range in both pitch and yaw directions. Count rate data was

collected using a high-resolution Microchannel Plate (MCP) detector, and results were post-processed for analysis. Figure 3.2.5 shows the reduction of count rate on the imaging MCP as the deflectors were ramped up to their operational voltages (dV = 7500V across the deflection gap). For a 2kV Ion beam, we see near total suppression at ~10% operational voltage dV~=700V.

The test demonstrated that the deflection system significantly suppressed the count rate, with a maximum suppression ratio of 600±400 at a 0° pitch. Across the full ±6° pitch range, the suppression ratio consistently remained above 97%. The highest observed count rate with deflectors off was between 6000–7000 counts per second, while the minimum with deflectors on dropped to approximately 10 counts per second. These results validated the deflector's ability to redirect charged particles away from the detector with high efficiency. Additionally, the count rate versus deflector voltage results showed strong agreement with both analytical models and simulation data.

3.3 Conversion Surfaces

Excerpt from J. Sokol, J. Gasser EM 27850-006 IMAP-Lo_FM_ConversionSurfaces

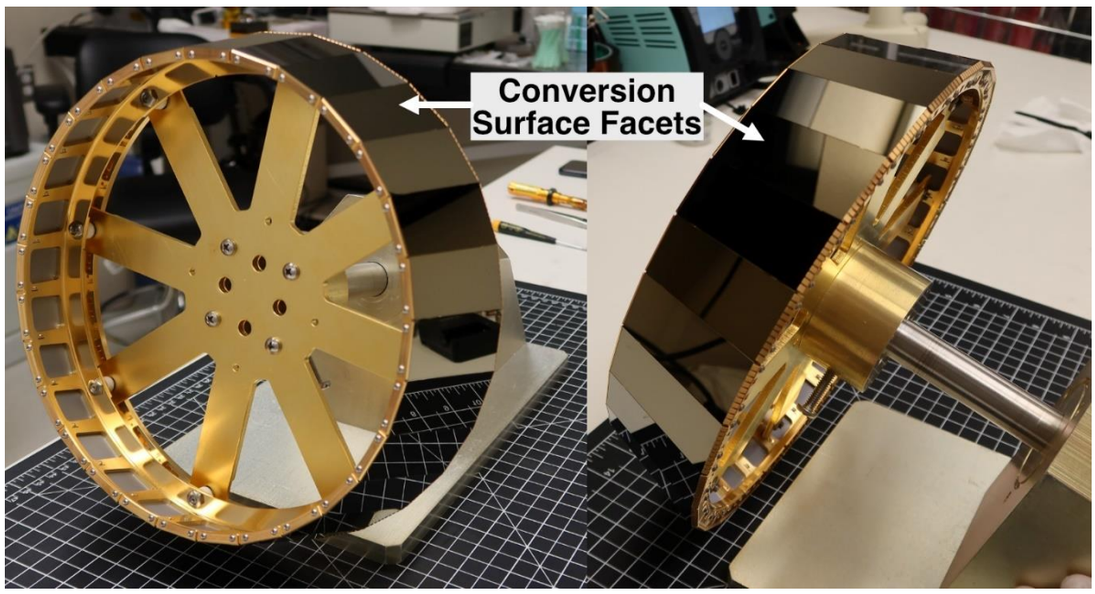


Figure 3.3.1 CS facet and installed on the P1 carousel

The IMAP-Lo Flight Model (FM) Conversion Surface (CS) development involved the fabrication and evaluation of Diamond-Like Carbon (DLC) film deposited on a substrate cut out of highly polished Silicon wafer. Ten CS coating sets were prepared, producing 70 flight facets, 10 witness facets, and 10 test samples. These components were assessed for uniformity in surface roughness, film thickness, and ion conversion efficiency.

Three (Qt. 3) test samples of the FM CS were measured for conversion efficiency in the ILENA facility at the University of Bern. The conversion efficiency for four incident beams was measured: hydrogen, helium, neon, and oxygen. The negative ion yield and angular scatter distribution in polar and azimuth directions were determined. All three samples show consistent results for the negative ion yield and the

angular scatter distribution within the statistical variation. The FM CS characterization (negative ion yield and angular scatter distribution) agrees with the Engineering Model (EM) CS characterization within the statistical variation. The IMAP-Lo CS characterization (negative ion yield and angular scatter distribution) is in agreement with the IBEX-Lo CS characterization according to available data for IBEX-Lo.

3.3.1 Conversion Surface Facets

The IMAP-Lo Conversion Surfaces (CS) consist of Diamond-Like Carbon (DLC) films deposited on highly polished Silicon wafers. These wafers, supplied by Virginia Semiconductor, are 3-inch, single-side polished with a backside etch and surface roughness ≤5 Å, as confirmed by AFM at SwRI. Slight roughness variation (~2 Å) from center to edge is attributed to the polishing process.

Wafers were diced into CS facets and 2x2 cm² test samples by Micro Precision Engineering (MPE), and each was laser-serialized. The test samples are used at the University of Bern's ILENA facility due to their compact size. DLC coating was applied using Plasma Ion Immersion Deposition (PIID), combining Argon plasma etching, DLC deposition, and Hydrogen termination in a single uninterrupted chamber process. Substrates were meticulously cleaned via wet (DI water, IPA, acetone) and dry (UV-Ozone) methods before coating. All processing occurred at SwRI. Each coating run processed up to two sets, with each set comprising 7 assembly facets, 1 witness facet, and 1 test sample. After coating, AFM measured surface roughness and VASE measured film thickness. Coated parts were stored in a UV-protected purge cabinet.

Table 3.3.1 CS Physical Properties

CS Parameters - FM Witness Facets			
Set #	**SN**	**Surface Roughness Rq [Å]**	**Film Thickness [nm]**
6	IM-VW-FM-108	3.33 ± 0.04	46.47
7	IM-VW-FM-096	3.28 ± 0.08	45.41
8	IM-VW-FM-080	3.29 ± 0.08	46.04
9	IM-VW-FM-073	3.46 ± 0.11	46.29
10	IM-VW-FM-062	3.38 ± 0.17	45.21
11	IM-VW-FM-061	4.07 ± 1.07	47.41
12	IM-VW-FM-118	3.39 ± 0.06	47.09
13	IM-VW-FM-111	3.47 ± 0.12	46.76
14	IM-VW-FM-049	3.64 ± 0.08	47.26
15	IM-VW-FM-137	3.59 ± 0.09	47.69
Mean ± Standard deviation		**3.49 ± 0.24**	**46.56 ± 0.84**

Between January–February 2023, ten FM coating sets (#6–15) were produced in six runs, yielding 70 assembly facets, 10 witness facets, and 10 test samples. Surface roughness values ranged from 3.09 Å to 4.07 Å, with a mean of 3.49 ± 0.24 Å (witness facets) and 3.30 ± 0.16 Å (test samples). Film thickness ranged from 45.21–47.93 nm, averaging 46.56 ± 0.84 nm and 46.87 ± 0.71 nm respectively—all within the acceptable limits (Rq ≤ 10 Å; thickness 35–55 nm). Results are summarized in Table 3.3.1.

FM CS surface properties align closely with those of the earlier Engineering Model (EM) CSs produced in July 2022, confirming consistency in fabrication and performance standards. EM samples were also evaluated for conversion efficiency at ILENA in August 2022.

3.3.2 Conversion and Scattering Properties

Excerpt from IMAP-Lo Memo xxx-xx C Surfaces - Rev 2-3.pdf

The ILENA test facility has been described in detail in Wahlström et al. 2013 and Gasser et al. 2021, Sokol et al., JAP, 2024. A positive ion beam of desired gas species is accelerated to a few 100 eV/q, mass filtered, and directed onto the CS test sample. The particle beam scattered off the surface is recorded using a 2D imaging detector that can be rotated around the test sample in the polar coordinate. The negative ion yield is measured by alternatingly accepting or rejecting the negative ion component in the scattered beam, while the neutral atoms component is always recorded.

The negative ion yield η has been determined for hydrogen and oxygen at a few energies in a range from 200 eV to 1000 eV per atom. To account for and subtract the negative ion contributions from particle sputtering off the CS, the same measurement has also been conducted using the noble gases helium and neon, as they do not form stable negative ions, and thus cannot be directly measured. For hydrogen at energies below 600 eV and oxygen below 400 eV, molecular ions (H2+, O2+) at twice the nominal energy have been used as the source beam (see Gasser et al. 2021). Measurements have been done at an incidence angle of 8° relative to the surface plane.

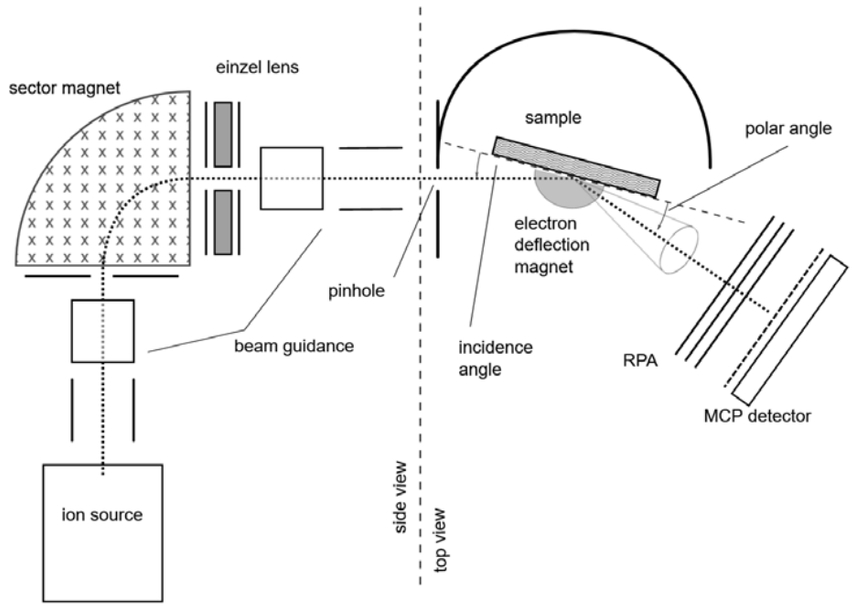


Figure 3.3.2 Schematic of the ILENA experiment setup. The detector covers angular scattering cone of 21° x 21° (adapted from [Gasser et al., 2021])

An overview of the test results for three FM samples (IM-VW-FM-061, IM-VW-FM-093, IM-VW-FM-110) and two EM test samples (IM-VW-EM-036, IM-VW-EM-039) is shown in Figure 3.3.3. The negative ion yield η (left column subplots), polar scatter FWHM (middle column), and azimuthal FWHM (right column) are presented for the tested species hydrogen, oxygen, helium, and neon (from top to bottom). For H and O, the shown η represents the values with subtracted sputter contribution. For He and

Ne, the shown η represents the negative sputter yield instead of direct charge conversion efficiency. Measurements were done at energies per atom: 195 eV, 250 eV, 390 eV, 500 eV, 780 eV and 100 eV [Sokol et al., JAP, 2024]. The measurement series for H and He at sample IM-VW-FM-061 was repeated (dashed lines) to validate the uncertainty of the experiment conditions in the first measurement run. Missing data points in the azimuthal FWHM plots indicate that the distribution half-maximum was beyond the size of the detector, which is 21 x 21 deg. The measured values for η are in agreement between the tested samples within the experiment uncertainties. For all tested EM and FM samples, η values are within the range ηH = 2% ± 0.5%, ηO = 9% ± 0.5% at 200 eV and ηO = 13.5% ± 1.5% at 1 keV. The sputter contributions amount to 1.5%-3% for He, and 3%-5% for Ne.

The angular distribution widths show some discrepancy for some data points, e.g., sample EM039 shows considerably narrower He and Ne scatter than the rest, and the oxygen azimuth FWHM for sample EM-036 is about 2 deg larger. The three tested FM CS samples show scatter distribution results mutually in agreement. A few single misaligned data points (He at 780 eV) should be considered outliers. Apart from these, the plots in Figure 3.3.3 show consistent angular scatter results between the tested EM and FM CS samples. Given the high requirements on sample positioning accuracy in the ILENA as well as on the stability of the experiment conditions, the deviations in angular scatter distribution widths reported here are probably rather an artifact of the limited precision of the experiment setup than a sign of considerable structure variations among the CS test samples.

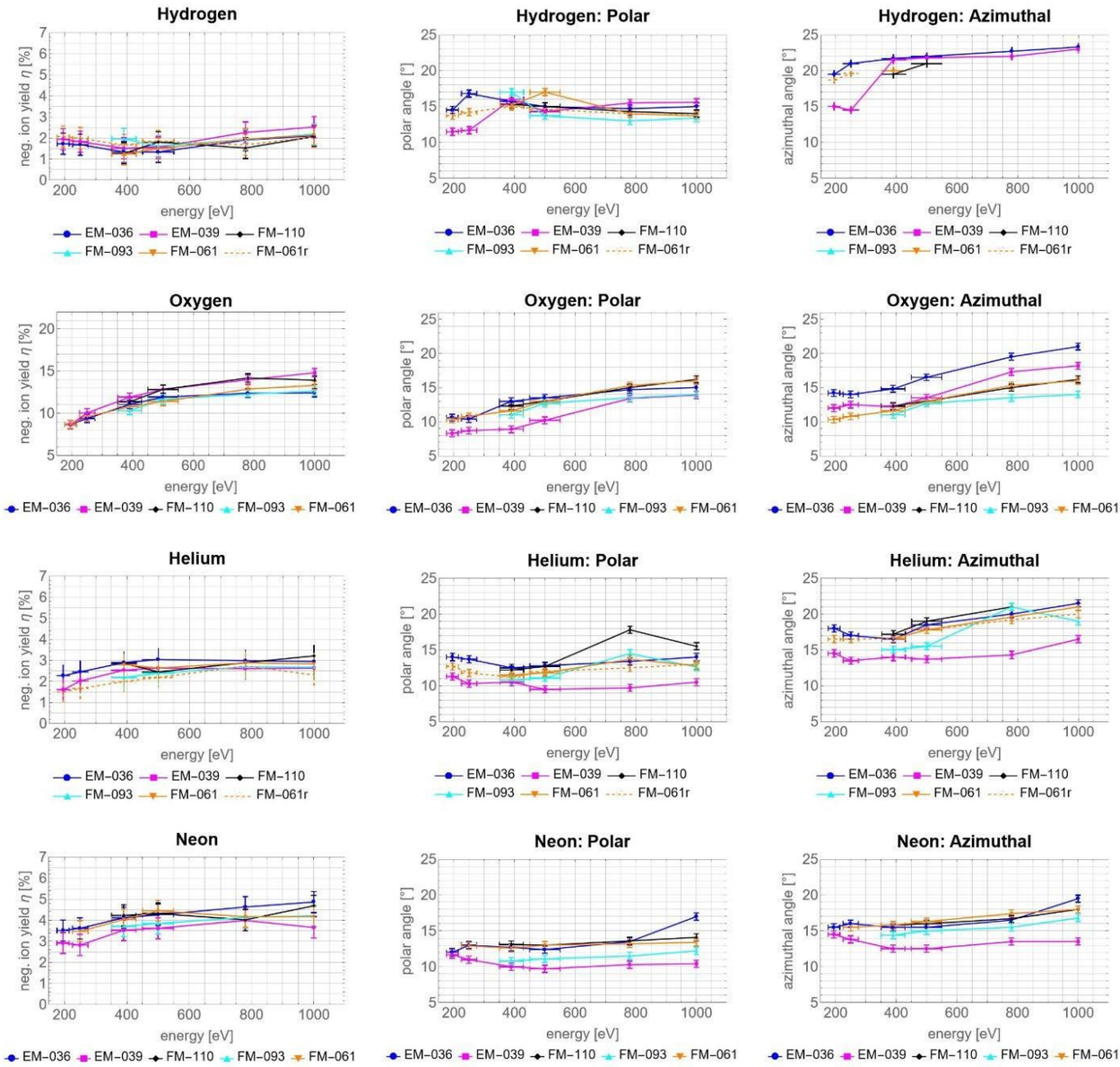


Figure 3.3.3 Overview of the results from conversion efficiency measurements for the FM and EM CS test samples. Negative ion yield (left column), angular scatter distribution FWHM in polar (middle column) and azimuthal (right column) direction for hydrogen, oxygen, helium, and neon (from top to bottom). Measurements were done at α = 8° incidence angle.

4. SENSOR LEVEL CALIBRATION

This section outlines the effort and findings from sensor-level calibration of the IMAP-Lo FM. Sensor level calibration represents the most critical phase in the overall validation process, integrating all key subsystems involved in neutral detection (CS, ESA, TOF), and evaluating their combined performance. This stage builds upon prior subsystem calibrations and focuses on verifying end-to-end functionality, including energy response, species differentiation, background suppression. Calibration was performed at the Princeton Space Plasma laboratory in three major campaigns: PreCal1, PreCal2, and FinalCal, each designed to incrementally test the instrument in increasingly flight-like configurations.

For these tests the instrument was installed on a rotation stage with 3 axes of motion. An ion beam of a desired species/energy is generated using an electron bombardment source and neutralized in a charge exchange cell. Remaining ions are removed using a Helmholtz coil, and the neutrals are collimated using a knife edge plate prior to targeting the instrument. A carbon-foil ABM is used to determine incident beam flux. Calibration system information, beam energy and species with estimated beam flux are provided in the next section.

Calibration of the instrument effectively focuses on determining baseline detection efficiency, (associated with the TOF foils, instrument grids and spokes and electronics), and the energy-angle ESA-CS conversion collection efficiency. A brief description of key types of test-runs completed in each of the calibration campaigns follows:

1. MCP Response Curve – variation of MCP voltage for given beam and ESA parameters; this test precedes each calibration campaign (at beginning of the beam tests) to check that MCP response curve has not changed. The MCP response curve for a given species is collected at each power up where an incident beam is available.
2. DER1: Differential Energy Response, Fine – Determination of differential energy response of each energy step; Fixed Beam E (for a given E-Step) and ESA voltage varied in 10% steps around center E of given E-Step.]
3. DER1a: Differential Energy Response, Beam Scan – Determination of differential energy response of an energy step; Fixed E-Step and beam energy is varied in 10% steps around center E of given E-Step. ABM flux measurements are collected for each assigned beam energy.
4. DER2: Differential Energy Response, Steps – Determination of response of other energy steps (due to spill-over of particles into other energy steps from sputtering/scattering); Fixed Beam E (given E-Step) & ESA voltage variation according to E-Steps; conduct for H, D, He, O, Ne (could add C measurements if time allows)
5. Roll Response – For ESTEP 7 and a 930 eV H beam, rotate the instrument around instrument symmetry axis (roll) to determine functionality of all CS facets and determine any variation of conversion and collection efficiency through the ESA-CS.
6. Elevation Angle Scan – For ESTEP 7 and a 930 eV H beam we rotate the instrument around the beam position on the CS to determine variation of the conversion-collection efficiency for neutral collisions with different incident angles.
7. Linear Scan – For ESTEP 7 and a 930 eV H beam we vary the horizontal stage position to determine the variation of the conversion-collection efficiency for neutrals at different positions along the CS. This test also works as a targeting validation at the beginning of testing.

8. Background – For a given energy mode and energy step, no input beam or chamber ion gauge, we collect events to measure the instrument's internal background.

In the following subsections, we outline the three test campaigns performed with the sensor, then present key calibration results and their data processing steps.

4.1 Test Facilities

Excerpt from M. Shen ***Princeton Space Physics Calibration Facilities***

IMAP-Lo Sensor, and TOF subsystem has been tested at the Princeton Space Physics Calibration facility, referred to as PSPL (Princeton Space Physic Laboratory) in this document. The PSPL test system consists of two high vacuum calibration chambers, referred to as "Main chamber" and "Science Chamber", and a post-accelerated electron impact ionization source capable of producing a large diameter, highly uniform, and parallel ion beam of any desired species, at energies up to ≤ 30 keV. The Princeton Calibration system is shown in Figure 4.1.1. Ions generated at the beam source are neutralized in a 1-foot length charge-exchange vessel with neutral nitrogen gas, operated at mTorr range, prior to traveling down a 16ft flight tube through the science chamber and into the 4ft diameter main chamber housing IMAP-Lo.

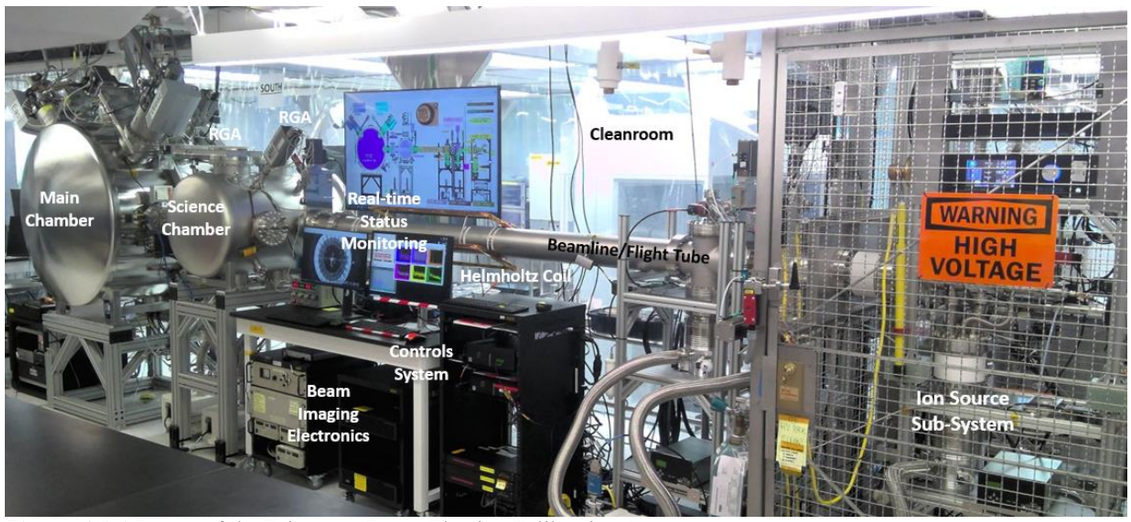


Figure 4.1.1 Image of the Princeton Space Physics Calibration System

The ion source used at Princeton is an electron impact ionization source manufactured by PREVAC Scientific (model IS-40E1). It is a two-lens, extractor-type, focused, differentially pumped ion gun capable of rastering up to a 10 mm × 10 mm area at 120mm flight distance. Ion species are selected from a mixed source gas supply consisting of a neutral gas mixture of hydrogen, deuterium, helium, neon, and argon, balanced with nitrogen. Beam intensity is controlled via source gas pressure and filament current allowing for a highly stable beam with intensity variations of <10% over day-Long timescales. A Wien filter integrated into the ion optics selection of ion species from the input source gas. With residual gases in the system and appropriate the source can also provide water group species from ambient water vapor or room air, including oxygen (O^+), hydroxyl cation (OH^+), and water (H_2O^+).

The Princeton system can generate stable ion beams with energies ranging from approximately 10 eV to ≤30 keV. Beams with energies ≤5 keV are produced by the ion source when it is operated at neutral ground

(0 V), while higher-energy beams (5–30 keV) are achieved by floating the ground using a Matsusada high-voltage power supply (model AU-30R1), thereby introducing post-acceleration. Neutrals are generated from the mass filtered, post-accelerated ion beam in a 1-foot length charge-exchange vessel, using 5N purity 99.999% N2 gas. Mediator gas pressures in the charge-exchange vessel is controlled by a precision leak valve (VAT 59.0 UHV All-Metal Variable Leak Valve), which holds the vessel at ~1*10-3T. The exact delivered neutral flux is dependent on the charge exchange cross section of the incident ion species and energy, we estimate the percentage of neutralized particles per mTorr in the differential pumping section as

$$(J_n/J_i) \times 100\% = 1 - \exp(-l\,\sigma_{CX} N) \qquad (4.1.1)$$

where J_n/J_i represents the ratio of neutral particle intensity to charged particle intensity, l is the path length of ion beam, σ_{CX} is the charge exchange cross section, and N is the density of N_2 at 1 atm (760,000 mTorr). By assuming $\sigma_{CX} = 10^{-16}$ cm^2 (*Lindsay and Stebbings, 2005*), i.e., lower limit of the cross-section for H^+ to N_2, it results in ~11.2% of H^+ ions will be neutralized. The count rate and charge exchange efficiency are qualitatively consistent with experimental studies using MCP (Micro-Channel Plate) and ABM (Absolute Beam Monitor) in Princeton Space Physics Laboratory. A caveat is that these calculations need further detailed experimental revisions for laboratory and space applications.

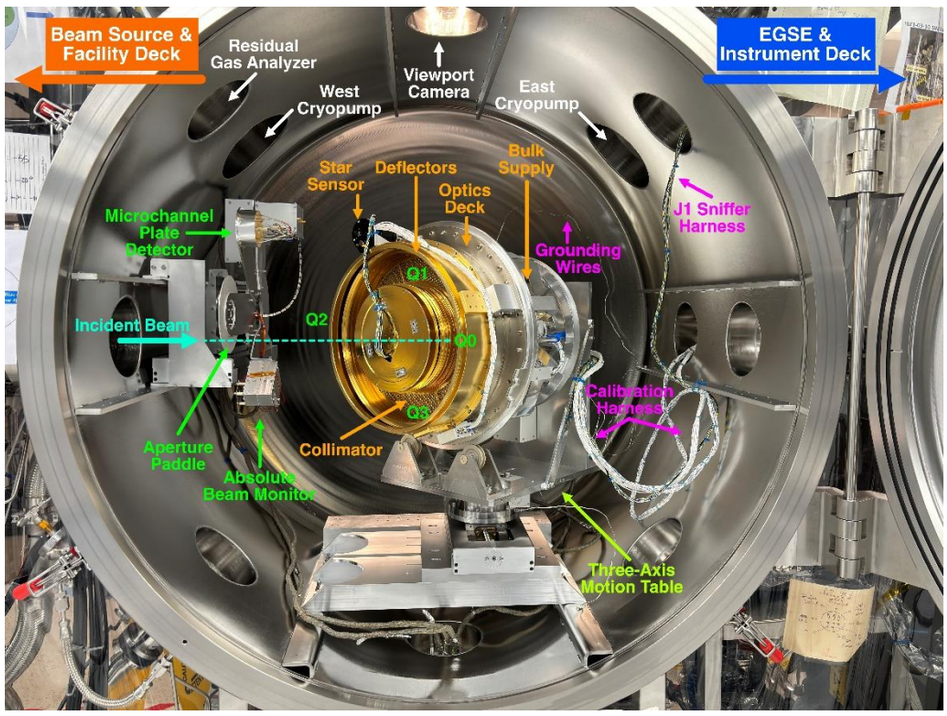


Figure 4.1.2 Image of the IMAP-Lo FM sensor installed and tested in Princeton Space Physics Calibration System.

A Helmholtz coil is mounted on the flight tube and is used either to cancel the Earth's magnetic field in ion operating mode or as an ion dump to prevent ions from entering the chamber during neutral beam operation. The total length of the beamline from the ion source nose to the entry flange of the Main Chamber is 16 feet. Knife-edges placed along the beamline shape the beam such that, by the time it reaches

the chamber entry port, it is highly uniform, parallel, and expanded to a diameter of 57 mm. This beam size can be reduced to any smaller, practical diameter using collimators installed at the entrance flange, such as the 14 mm collimator used during final calibration. Beam monitors mounted on a two-axis positioning system inside the Main Chamber are used both for beam calibration and for real-time flux cross-calibration during instrument testing. The diagnostic suite includes a microchannel plate detector (MCP), a carbon-foil absolute beam monitor, a conversion surface absolute beam monitor, a channel electron multiplier, and a Faraday cup with retarding potential analyzer capability up to 5 kV bias.

The IMAP-Lo instrument is mounted on a 3-axis positioning system inside the Main Chamber, which has a 4-foot diameter, as depicted in Figure 4.1.2. Leveraging the capabilities of high-energy ion beam (for Time-Of-Flight subsystem calibration) and low-energy neutral beam (including Pre-Cal 1, Pre-Cal2, Final Cal) provided by the Princeton Space Physics Laboratory, we're able to determine IMAP-Lo sensor response function and geometric factor through the measurements, thus fulfilling the calibration and sensor requirements.

4.1.1 Beam Flux Monitoring with ABM

During the major IMAP-Lo calibration campaign at PSPL, only the carbon-foil Absolute Beam Monitor (ABM) was used to determine the absolute beam flux. The ideal reference devices—a channel electron multiplier (CEM) and a conversion surface ABM provided by the University of Bern—were not employed during FM instrument calibrations due to facility operation constraints and limited chamber space. However, both reference devices were utilized during earlier neutral beam calibration activities conducted prior to instrument calibration. The C-foil ABM consists of two CEMs, a thin 0.5 μg carbon foil, a bias plate, and an integrated set of front-end electronics. As described by Funsten et al. [2005], space-based ion mass spectrometers and neutral atom imagers commonly use a thin foil to generate secondary electrons. A coincidence measurement—detecting both the secondary electrons and the primary ion or neutral atom—enables unambiguous particle identification within a high-noise environment and allows characterization of particle properties via time-of-flight (TOF) techniques. A simple and robust approach of the absolute detection probabilities of individual detectors and the overall detection efficiency of the subsystem, independent of the incident particle flux. Namely, a series of formulas was provided to determine incident beam flux for IMAP-Lo calibration, where the flux is independent of the efficiency and thus minor in performance of the referenced ABM.

In general, the likelihood of detection of secondary electrons at Fore CEM detector is independent of those for Aft CEM detector. Assuming the absence of noise, we certainly know that a total number of N_F secondary electrons measured by Fore CEM directly, following by the coincidence measurements of N_{FA} in a time window (typically set as 100 μs). Hence, the absolute detection probability of detector Aft CEM is given as $P_A = N_{FA} / N_F$ which includes effects such as energy loss on the foil and the detection efficiency of Aft CEM. Similarly, the absolute detection probability of Fore CEM is $P_F = N_{FA} / N_A$. It is also known that the absolute detection efficiency ε_D of the CEM detector subsystem includes the probability $T_G T_F$ that incorporates the transmission of grid and foil and the subsequent probability $P_F P_A$ for registration of a coincident event. Given $\varepsilon_D = T_G T_F P_F P_A$, the number of incident beam flux on the ABM is simply $N_0 = N_{FA} / \varepsilon_D$, effectively $N_0 = (N_F N_A)/ (N_{FA} T_G T_F)$. For simplicity, we typically assume ideal transmission, making the formula of determining absolute incident beam flux as

$$N_0 = (N_F N_A)/ N_{FA} \qquad (4.1.2)$$

During both the beam calibration and IMAP-Lo calibrations, we closely monitored the ABM performance through measurements of the absolute detection efficiency (ε_D), even though this parameter does not directly influence the determination of incident beam flux, as previously noted. A particular challenge arose when attempting to measure incident beam flux at energies near or below 100 eV, where low count statistics limited measurement reliability. This limitation stems from the use of a thin 0.5 µg carbon foil, highlighting the reason for using a conversion surface in IMAP-Lo to detect low-energy energetic neutral atoms (ENAs) and interstellar neutrals (ISNs) across few eV to 1000 eV energy range.

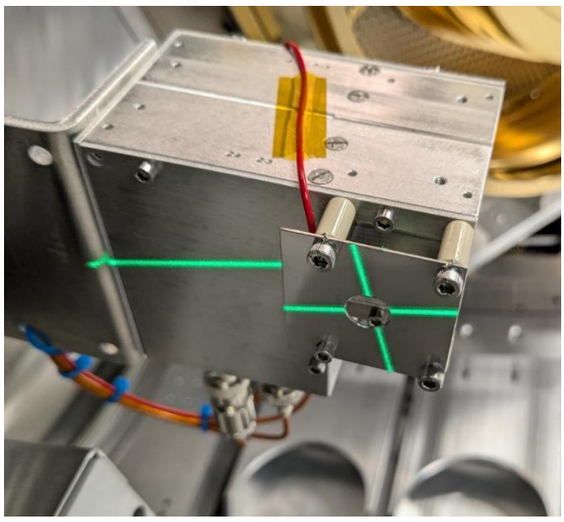


Figure 4.1.3 Front view of C-foil ABM mounted on a paddle in the PSPL main chamber in front of the IMAP-Lo sensor (golden reflection in the background). We used laser for precise beam alignment before chamber pumping down.

4.2 Calibration Activities Overview

The following qualitatively describes the three test campaigns executed during the IMAP-Lo FM calibration 2024-2025. Not described here is EM testing executed at PSPL in preparation for FM calibration and Post-FM Delivery EM calibration planned for August 2025.

For each of the test campaigns, the instrument was installed on the 3-Axis positioning system, and coarsely laser aligned prior to pump down. Following 48 hours at high vacuum (less than *1x10-6 torr),* the instrument was powered on and baseline functional testing of the HV (MCP, PAC, Bulk) and ToF electronics was performed. The instrument was then brought up to full operation HV on the ESA, MCP, PAC and the Deflectors and targeting was confirmed by sending a neutral beam into the instrument through a collimating aperture plate and scanning the linear position of the instrument across the beam. Following verification of the positioning, the instrument roll angle was varied to verify functionality of each MCP quadrant and the axial electrostatics. Finally, functionality of the instrument HV science mode, which steps through the instrument ESA settings with a cadence associated with a simulated spin pulse, was tested. At the end of each test day, the instrument was powered down, and on each subsequent test day, following power on, a MCP gain curve was collected.

4.2.1 ***PreCal1***

PreCal1 took place at the Princeton Space Plasma laboratory in April 2024. In the PreCal1, ESA and CS subsystems were integrated with the TOF unit and the PAC HV supply to test the instrument's full

electrostatics without the entrance system (collimator and deflectors). Here, we got the first look at the end-to-end functionality of the instrument's electrostatics and a determination of the energy response and collection efficiency without the effects of the collimator. In this configuration, the angle of incidence of the ion beam can be varied and the angular dependence of the collection efficiency can be deduced.

Due to timeline constraints, not all of the FM instrument components needed were available prior to testing. The test was instead conducted with the instrument in FMv2-hybrid configuration, comprised of the FM TOF and ESA-CS subsystems and EM HVPS, LV datalink Board and the EBOX. The entrance system in this configuration is replaced with an aperture plate, designed based on the CS geometry to illuminate one Full CS at a time without spillover into neighboring facets. The Mask enables:

1. Absolute calibration at the center of each energy step at one Facet of each quadrant through apertures with 5 mm diameter (Apertures A)
2. Relative calibration for the energy and sputtering response at one Facet of each quadrant through rectangular apertures (13.2 mm radial and 19.6 mm azimuthal, Apertures B), which illuminate a single Facet with 0.5 mm margin on each side.
3. One single wider rectangular aperture (20.42 mm radial and 19.6 azimuthal, Aperture C) to illuminate this single Facet at its inner and outer edge and in the center as well as in the center at up to ±9o from the boresight direction radially by means of a restricted incoming beam.

The home location for PreCal1 targeted quadrant 0, offset 15 degrees CCW from the targeting fiducial mark on the aperture mask. The home aperture mask window is approximately 2.6cm^2 (13.2x19.6mm).

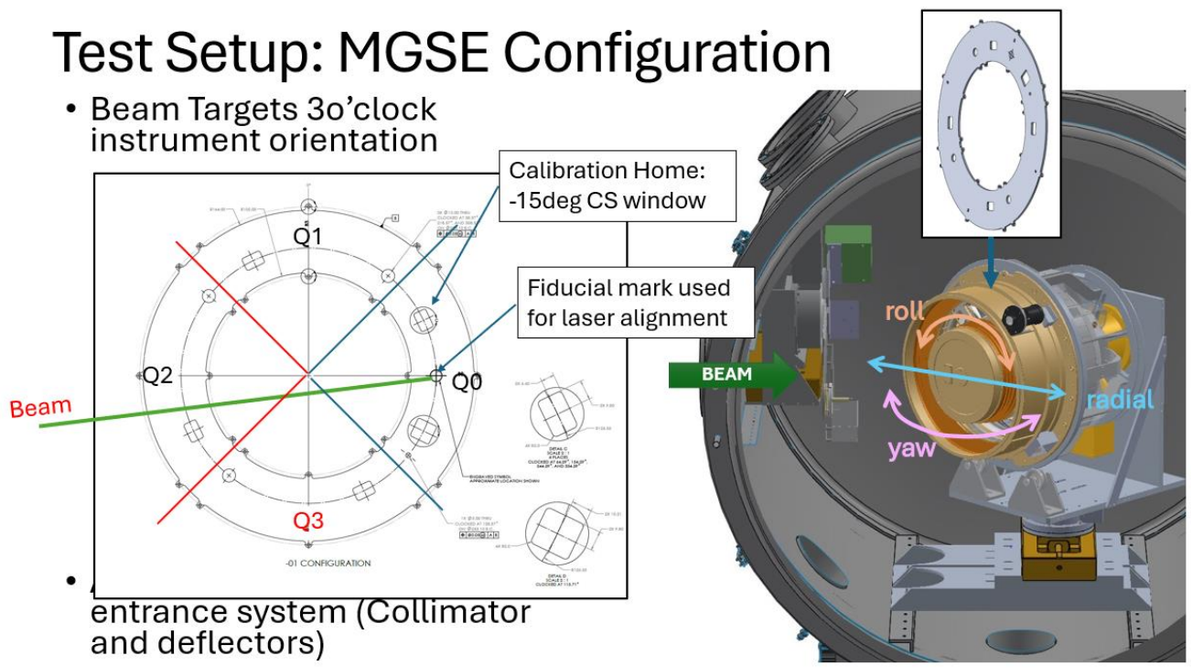


Figure 4.2.1 PreCal1 Test configuration

Early in Pre-Cal1, we found that the observed instrument energy response deviated drastically from expectation. For energy step 7, observations of the "fine-stepping" energy response (DER1) could be

matched to the instrument electrostatic model, though because of high voltage limitations, full validation of the High-Throughput mode is impossible (cannot raise U+ beyond the nominal Estep7 set voltage). DER1 response measurements for all other energy steps deviated from the modeled response. We determined three possible causes of the deviation.

1. Modeling/understanding of the energy response is fundamentally incorrect
2. Electrostatic voltages were incorrectly assigned (either through hardware or software)
3. The energy distribution of incoming particles is different than expectation

In-situ measurements of the electrostatics voltages in the ion optical path validated that the electrodes were functioning correctly, and thus ruled out possible cause #2. Through further testing and associated simulation during pre-cal1, we found that the instrument's energy response was consistent with a low energy (100eV) incident neutral distribution (see Figure 4.2.2).

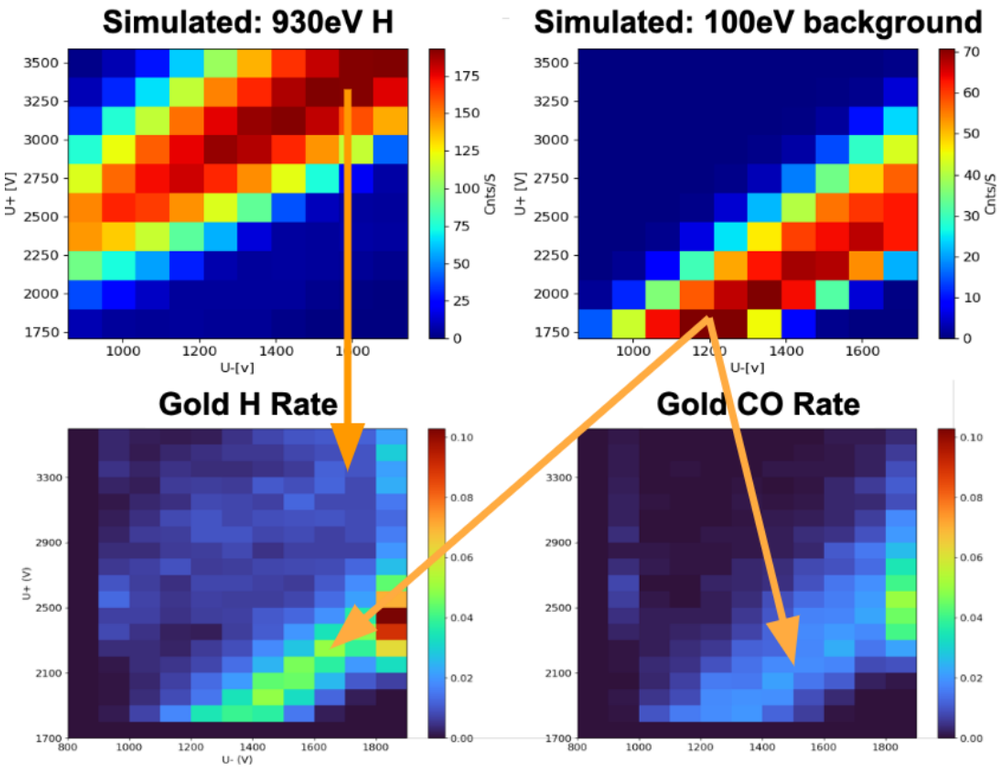


Figure 4.2.2 2D U+ U- scans observed (bottom) and simulated (top) showing low energy neutral background observed during PreCal1

A neutral background "hotspot" had been observed previously by the facilities team, but the rates were expected to be negligibly low. Measurements of the source background using the Princeton ABM showed the spatial non-uniformity (previously described as a hot spot) of the background at slightly higher rates than previously measured. This effect was attributed to the age of the ion source filament. Replacing the filament reduced the observed source background, and gave us a calibration test location to avoid the background as much as possible. These two changes yielded higher fidelity results for Estep 7 energy

response, but still no clear response function for lower energy steps, which were still seemingly dominated by some low energy particle distribution. We determined that the difference in the background rates between the ABM and the instrument could be explained by the difference in efficiency between the two detectors, (foils should have very low efficiency to measure 100eV particles). At this point, observations led us to believe that the instrument's electrostatics were functioning properly, and that the ESA-CS energy response was as expected, though not fully validated. Figure 4.2.2 compares the simulation results of instrument response to what had been measured. We noticed that the ambient background neutrals from the sources seems to be around 100eV (all species, indicating neutralized before Wien filter) and was more intensive than the charge exchange neutrals (which was set to be 930eV H). This proves that it indeed has an unexpected, strong background beam but also validates how well the instrument response model was set up and trained.

4.2.2 PreCal2

PreCal2 took place at PSPL in August 2024 prior to instrument level environmental tests. The objective of the PreCal2 test campaign was to verify the full functionality of the FM sensor, including the FM EBOX, and to perform an end-to-end calibration of the sensor with the collimator and deflectors installed. The test setup largely replicated that of PreCal1, using the same positioning system, but now with the FM entrance system. The FM TOF was integrated with the Conversion Surface sub-assembly, the ESA, the collimator, and the deflection electrodes. A 14 mm aperture plate was used to collimate the incident beam, ensuring that a single conversion surface was illuminated through the collimator. The instrument was aligned to face the beam directly, without varying yaw or radial positioning during calibration.

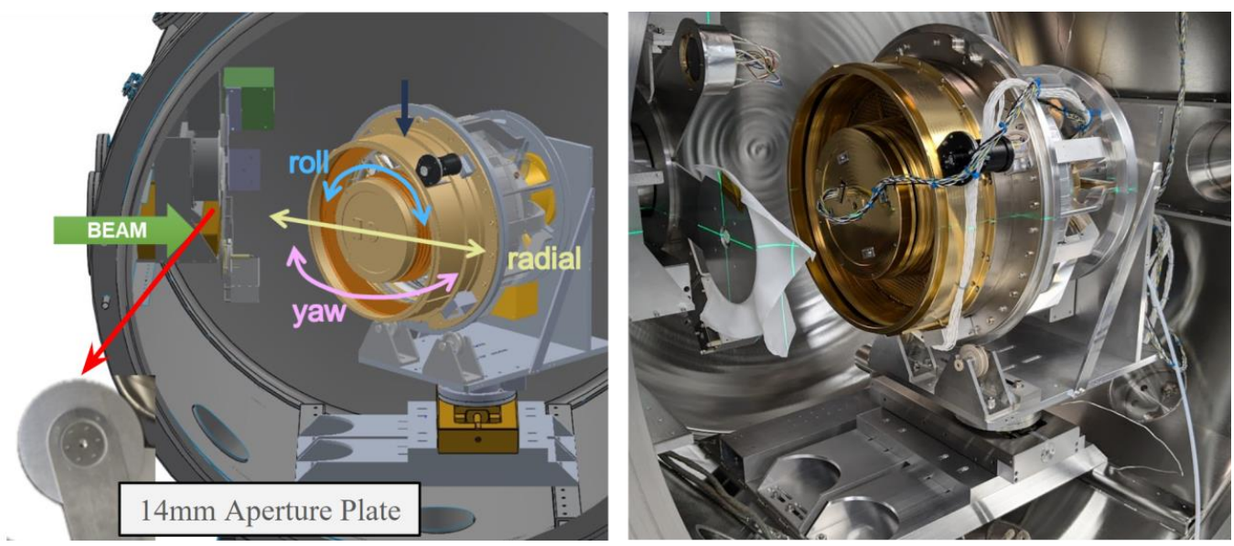


Figure 4.2.3 Test configuration used for FinalCal and PreCal2

Several functional tests were successfully completed. These included verifying the full functionality of the sensor's ion optics, performing overvoltage margin testing of the PAC to 13kV and verifying the star sensor operation at vacuum. We additionally verified the operation of the deflector electrode for ion suppression. For the deflector test, an uncollimated 930 eV hydrogen ion beam was targeted into the instrument with the ESA set to Estep 7 and the deflector voltages were ramped to operational voltage.

This resulted in a systematic decrease in ion signal count rate from about 77 cts/sec to approximately 70 cts/sec when the deflectors were powered on. Ambient neutrals still exist in this beam configuration, so we only expect to see a systematic decrease, associated with the deflectors being brought online driving a decrease in the scattered ion signal.

Our total testing time was ultimately limited by functional issues of the TOF electronics where we found that the TOF board would experience a commanding breakdown each day after approximately six hours of operation. This issue was diagnosed and fixed prior to environmental testing, believed to be temperature-related and tied to the opto-link. As a mitigation strategy, we restricted the output of direct events to only silver triples during certain tests, which allowed additional testing time, by reducing data traffic through the opto-link, at the cost of incomplete calibration data. Another issue identified was a 150V offset in the MCP voltage depending on the coupling mode between the PAC and the MCP power supply (MCP high-Low track anomaly). Although stable when voltages were not adjusted, this finding required additional investigation time which further reduced our overall test suite. This signal was ultimately found to be a non-issue and can simply be managed in the power-on sequence to ensure consistent performance (a few flight rules in space operation).

As with PreCal1, we again ran into the issue of separating charge-exchange hydrogen from source background neutrals, initially limiting our ability to assess the instrument's energy response below Estep 7 (930eV H). As a workaround, the team used molecular hydrogen (H_2) at twice the energy as a proxy for atomic hydrogen which worked to greatly expand the available calibration steps. H_2 dissociates before CS scattering due to field interaction, allowing a 1000 eV H_2 beam to simulate a 500 eV H beam. This approach follows assumptions made in ILENA scattering measurements (Wurz 1997, Schlathölter 1995). Although this solution introduced uncertainties in incident beam flux and made us reevaluate our scattering dynamics, it enabled a broader range of calibration measurements. Using the H_2 beam, the team determined the instrument's hydrogen energy response across Estep 3 to 7. A clear increase in the energy passband was observed for HiTh mode compared to HiRes mode. Preliminary estimates of total collection efficiency aligned with expectations for Estep 6 and 7. However, a greater-than-expected drop in efficiency between Estep 7 and 3, as well as a closer convergence between HiRes and HiTh at Estep 3, suggests that incoming flux estimations may need refinement. We were still unable to collect statistically meaningful energy response curves for Estep 1 and 2, but the additional observations down to 110eV H provided a solid foundation of energy response data leading into environmental testing and Final Cal. Finally, preliminary measurements of the instrument's geometric factor (GF) and energy resolution were broadly consistent with design expectations.

4.2.3 FinalCal

Instrument FinalCal was performed at the Princeton Space Plasma Lab in October 2024 using the full FM instrument configuration. The test setup was functionally identical to the one described in PreCal2.

The test campaign began with baseline functional testing and instrument alignment verification followed by full instrument functionality testing to validate instrument performance following environmental testing. Most of the full instrument functional testing from the PreCal2 campaign was repeated, including verifying science mode operation, roll response, and ion suppression using an H_2 beam at Estep6.

After verifying nominal operation, we performed comparison testing between the H and H_2 energy-voltage response at Estep7 to help evaluate the validity of using H from H_2 dissociation in our energy response calibration. Here we compared instrument response (Estep7 DER) to a beams of 930 eV H and 1860 eV H2. Results in both the HiTh and HiRes modes were statistically identical, confirming our assumption that H2 dissociates prior to colliding with the conversion surface and allowing us to use the H_2 beam as the standard for H calibration for the rest of testing. This had the added benefit that the beam could be operated at higher voltages, allowing us to avoid some of the issues we ran into operating the beam source system at low energies.

In addition to the H from H2 beam validation at energy step 7, we also performed a test to see if any of the input H2 survived to the TOF. Initially, we expected to see a small signal of H2 at twice the H energy as the dissociation rate is expected to be ~80% prior to the CS [Wurz 1997], but ultimately, we saw no H2 signal. Further reading concluded that H2 does not create a metastable negative ion and thus has a short lifetime [Heber 2006], suggesting the H2- converted at the CS does not survive to the TOF. This will ultimately impact the total collection efficiency, representing a reduction in the observed collection efficiency associated with the dissociation efficiency (20% reduction assuming an 80% dissociation efficiency), but since we have no literature on how the dissociation efficiency changes with energy, we are forced to assume 100% dissociation efficiency prior to CS scattering. This question will be further investigated in PostFM delivery CS scattering calibration slated for Summer 2025.

In an effort to push the system to energies below 100eV, we performed several tests using the system deceleration stage. In the PSPL ion beam source ions are generated by an electron bombardment source, accelerated to their extraction voltage (0-5kV) then undergo an optional post acceleration. Since our sensor level testing all takes place below 1kV the second acceleration stage is normally grounded. For this testing we flipped the polarity of the second acceleration stage in an effort to decelerate the ions instead. In this mode, the final beam energy would be determined by V_source-V_decel. In testing the instrument energy response to decelerated H and O, we found high energy contamination in our energy response signal, indicating that ions were being neutralized in the deceleration region in addition to the charge exchange cell. This high energy contamination meant that the deceleration stage in its current setup would be minimally beneficial toward instrument calibration, so its usage was abandoned moving forward. In effect this limited our measurement of the instrument energy response of H below 50 eV and O below 500eV.

The full suite of calibration testing was thus slightly abridged, but we were able to collect and characterize the instrument energy response, roll response and MCP gain to H, O, He, Ne and D in the following energy steps and modes:

Table 4.2.1 Summary of Final Cal tests. Tests run with H2 are highlighted in green, tests executed with H are highlighted in cyan.

Test	Species	Emode	Estep	Beam KE [eV]
MCP Gain	H/H2	HiTh	6	415/930
	O	HiTh	7	930
	He	HiTh	7	930
Roll Response	H/H2	HiTh	6	415/930
DER1	H/H2	HiTh, HiRes	3	55/110

			4 5 6 7	110/220 230/460 465/930 930/1860
	O	HiTh, HiRes	7 6 6.5	930 415 700
DER2	O	HiTh, HiRes	-	930
	Ne	HiTh, HiRes HiRes	- -	700 400
	He	HiTh, HiRes	-	130

Throughout the campaign, background measurements were interspersed with science testing to monitor instrument noise levels.

4.3 Sensor Level TOF Calibration

During PreCal1 through Cross-Cal, the IMAP-Lo sensor includes the conversion surface (CS) and ESA subsystems. Thus, the tests are performed with neutral atom beams targeting specific locations on the CS. Now, negative ions pass through the ESA and, after post-acceleration by a positive voltage, enter the TOF section. All tests described here involve this configuration. The observations are primarily concentrated in one quadrant, augmented by a roll scan to test the instrument response in all quadrants. PreCal2, FinalCal, and CrossCal also include the collimator subsystem, which is transparent to the analysis of the TOF subsystem data. Its presence is only relevant for determining the combined CS conversion and ESA collection efficiency because the collimator transparency has to be included in that analysis. However, the TOF subsystem analysis is not affected.

The following quantities are determined and updated over the TOF subsystem calibration in section 3.1

a) Species identification with TOF0, TOF1, and TOF2 (section 4.1.1.1)
b) TOF3 position determination suggested quadrant boundaries and peak locations (section 4.5.1.2)
c) Limits for the Checksum condition (section 4.5.1.3)
d) Offsets for TOF = 0 (section 3.1.5)
e) TOF resolution (section 3.1.6)

Determination of “ghost” features in TOF spectra and 2D plots (section 3.1.7)

4.3.1 TOF Detection Efficiency

Excerpt from E. Moebius, IMAP-Lo_Pre&FinalCal-TOF-Sect_Analysis_Dr3a.docx

An important part of the IBEX-Lo and IMAP-Lo geometric factor are the TOF detection efficiencies. Because of the Triple TOF design all three individual Signal Efficiencies can be determined as ratios of the detected Triple Coincidence Rate $R_{\mathrm{GoldenTriple}}$ and the Double Coincidence Rate R_{TOFn} that does not contain the respective Signal:

$$Eff_A = \frac{R_{\mathrm{GoldenTriple}}}{R_{\mathrm{TOF1}}} \quad Eff_B = \frac{R_{\mathrm{GoldenTriple}}}{R_{\mathrm{TOF2}}} \quad Eff_C = \frac{R_{\mathrm{GoldenTriple}}}{R_{\mathrm{TOF0}}} \tag{4.3.1}$$

$$Eff_{Triple} = Eff_A \cdot Eff_B \cdot Eff_B \tag{4.3.2}$$

The individual double TOF efficiencies are as follows:

$$Eff_{TOF0} = Eff_A \cdot Eff_B \quad Eff_{TOF1} = Eff_C \cdot Eff_B \quad Eff_{TOF2} = Eff_A \cdot Eff_C \qquad (4.3.3)$$

The efficiency allowing any of the 3 Double TOF conditions to be valid reads:

$$Eff_{AnyDouble} = Eff_{TOF0} + Eff_{TOF1} + Eff_{TOF2} - 2 \cdot Eff_{Triple} \qquad (4.3.4)$$

It should be noted that the actual efficiencies are species-dependent (see below). Taking the rates to determine the efficiencies shown in Eqns. (4.3.1) through (4.3.4), while providing a good overview and suitable for continuous monitoring throughout the mission, will not provide the absolute TOF efficiencies for H^-, O^-, or other species separately. Figure 4.3.1 shows the TOF efficiencies for Golden Triples in green and for any Doubles (*TOF0*, *TOF1*, or *TOF2*) in black as a function of the bias voltage across the MCP stack, obtained from Cross-Calibration runs T106R006 for H and T106R027 for O. Also shown are the Triple Rate, H or O Rate, and the total rate.

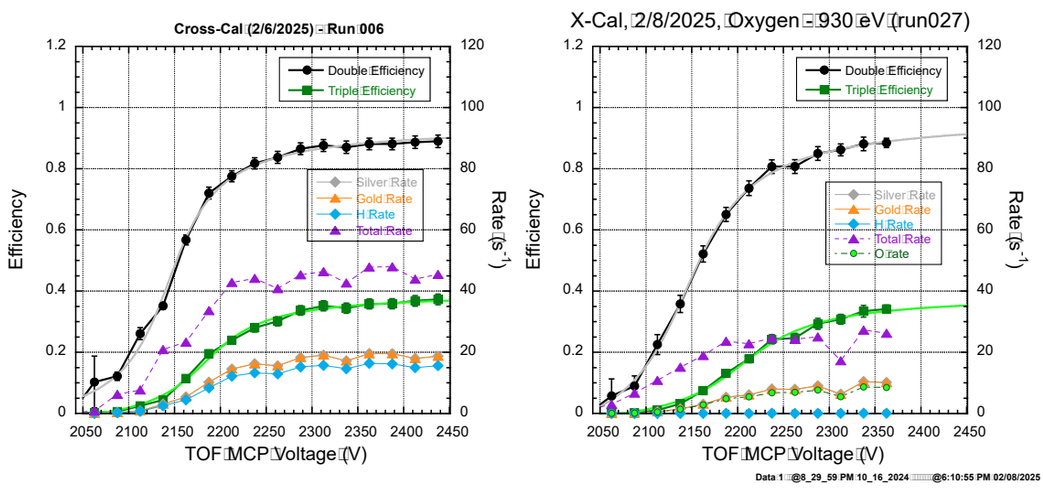


Figure 4.3.1 TOF efficiency curves and observed rates as a function of the bias voltage across the MCP stack for T106R006 (930 eV H) (left) and T106R027 (930 eV O) (right). Shown are the Triple (green) and any Double (black) efficiencies, along with the Triple, H or O, and total rates.

The efficiencies for H^- and O^- are different. While H reaches a plateau beyond about 2300 VO reaches plateau values at around 2350 V. However, both plateau values reach around 35% for the Triple efficiency (Eff_{Triple}) and 88% for the Any-Double ($Eff_{AnyDouble}$) efficiency. Both efficiency curves have been fitted by the following function:

$$Eff_k(U_{MCP}) = a_0 + a_1 \cdot Arctan(a_2 \cdot (U_{MCP} - a_3)) \qquad (4.3.5)$$

The coefficients for the fits according to Eq. (4.3.5) to each of the curves in Figure 4.3.1 are compiled in Table 4.3.1.

Table 4.3.1: Fitting Parameters for the H and O MCP Efficiency Curves

	H 930 eV	**O 930 eV**

	All Double Efficiency	Triple Efficiency	All Double Efficiency	Triple Efficiency
a_0:	0.434±0.011	0.169±0.004	0.406±0.007	0.163±0.006
a_1:	0.325±0.012	0.144±0.005	0.363±0.010	0.144±0.010
a_2:	0.025±0.003	0.020±0.002	0.019±0.001	0.016±0.002
a_3:	2143.8±2.8	2183.6±2.9	2144.2±1.9	2205.7±4.6

It should be noted that any electrons that are detected in the TOF system will systematically reduce the derived efficiencies because electrons have very low efficiencies for the generation of secondary electrons in the C-foils. Electrons can affect the efficiencies even when their peak is excluded using the TOF thresholds because, like any other species, their TOF distributions have tails. Analyzing *TOF2* distribution for quiet observation times with IBEX-Lo, shows there is a noticeable background near the H^--peak that can be attributed to the tail of the electrons, whose peak has been suppressed with a threshold in the IBEX CEU. Including these electrons in the Triple and Double Rates unwittingly reduces the deduced TOF efficiencies for H^- substantially. This effect may not be important during the calibration runs because the signal rates generated by the neutral beam are always larger than the electron rates. However, in flight, this may be different. In these cases, the method for determining the efficiencies described in a separate Memo by *R. Murphy* and in *R. Murphy's* Master Thesis should be used.

Also, some of the factors that determine the overall TOF detection efficiency are not contained in these quantities. The full account of the detection efficiencies can be found in the document "IMAP-Lo Time-of-Flight Efficiency Determination and other Factors that Influence the Rate of Detected ENAs" by *E. Möbius, N. Schwadron, and D. Heirtzler*.

Species-Dependent Signal Efficiencies

For the reasons described above and because the production of secondary electrons and scattering in the C-foils influence the detection efficiencies, they are species and energy-dependent. A species-dependent analysis of the signal efficiencies should be performed in the detailed post-processing using the Branching Analysis in section 4.5.1.5. For a given PAC voltage, there is very little dependence on the ESA step, but the efficiency of different ion species can be quite different, and often the influence of electrons must be subtracted, as demonstrated above.

4.3.2 Limits for Checksum Condition

Checksum Criterion for Triple Coincidence Events

We may define the following Checksum (*ChckSum*):

$$ChckSum = TOF0 + TOF3 - TOF1 - TOF2 \quad (4.3.6)$$

Based on Eq. (3.1.1), *ChckSum* can be written as:

$$ChckSum = (T_{b0} - T_a) + (T_{b0} - T_{b3}) - (T_{b3} - T_c) - (T_c - T_a) = 0 \quad (4.3.7)$$

Because of inevitable noise on each signal and small yet variable electronic delays, the actual observed values vary around 0 ns. Figure 4.3.2 shows distributions of *ChckSum* as obtained during the Final Cal roll scan T105R009, used already for the *TOF3* and TOF offset analysis in sections 4.5.1.2 and 4.5.1.3. All Silver Triples (Type 1111 & 1110) are used. *ChckSum* is shown in data number DN2 in the left panel, while the right panel shows *ChckSum* for the same selection in ns, both based on the Sniffer data. It seems surprising that the two shapes are different. However, the difference is due to the choices in the conversion from DN to ns values. For all 4 TOF values, the conversion reads

$$TOF_n\,[ns] = a_n + b_n \cdot TOF_n\,[DN2] \quad (4.3.8)$$

The constants have been optimized to minimize the effects of non-linearities in the ADCs, which are fully present in the DN2 values. Because of the linearities, H and C&O show up as two almost separate distributions in the *ChckSum* DN2 value distribution. The larger peak is for H, and the smaller one is for

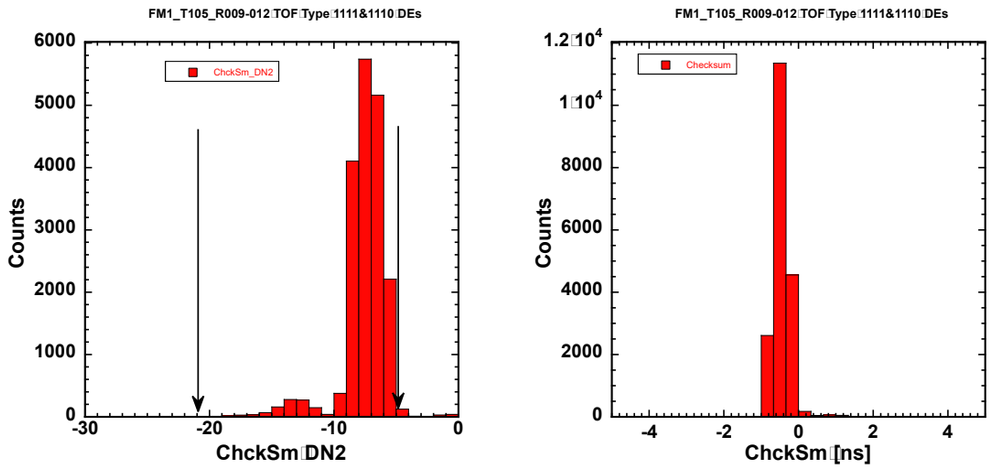


Fig. 4.3.2 Checksum distribution from the Silver Triples of the roll scan T105R009-012 in data number (DN2) as in the telemetry for Golden Triples on the left and in ns, calculated from the Sniffer data on the right.

C&O. In the converted distribution, the differences are washed out.

Golden Triples are selected as such by the ICE onboard if they fulfill the *ChckSum* condition:

$$LB < ChckSum_{DN2} < RB \quad (4.3.9)$$

Here, *LB* = -21 and *RB* = -5.

After shifting $ChckSum_{DN2}$ into the range 0 – 15 by using:

$$ChckSum_{Telemetry} = ChckSum_{DN2} + 21 \quad (4.3.10)$$

$ChckSum_{Telemetry}$ is transmitted as a 4-bit value in the telemetry.

The boundaries *LB* and *RB* are shown in Figure 4.3.2 as down arrows. A small fraction of the H distribution is clipped by *RB* when using the above values, which are currently implemented in the LUT. Moving *LB* slightly to the right reduces the fraction of failed *ChckSum* events. Using *LB* = -20 reduces the fraction from 1.3 % to 0.7 %, with no further reduction by moving farther to the right. While this change would increase the number of Golden Triples by ≈ 0.6 %, the gain would be marginal as the events that fail the *ChckSum* condition are transmitted as Silver Triples, which only results in a 0.06 % increase in the telemetry used for all Triple DEs because Silver Triples use approximately 10 % more bits than Golden Triples. Thus, the recommendation is to leave *LB* as is now.

4.3.3 Quadrant Identification via the Delay Line Signal

For the identification, whether a particle hits Quadrant 0, 1, 2, or 3 (signal terminals b0, b1, b2, and b3), the signal delays between individual quadrants, indicated by the Delay Line symbols on the top view in the upper right of Figure 3.1.1, are used, as described in detail in section 3.1.3. It should be noted that the Anode Board was replaced after the TOF Calibration. Therefore, the Delay values obtained from TOF calibration will be updated in this section using data from a roll scan of the entire TOF section during Final Calibration. The values obtained here will be relevant for analyzing the flight data.

Evaluation of the TOF Calibration Measurements

Figure 4.3.3 shows a *TOF3* histogram in DN2 (left) and ns (right), obtained with the IMAP-Lo FM in a complete roll scan covering the entire TOF entrance range in the roll angle α. The roll scan was broken up in 4 consecutive runs (T105R009 – 012).

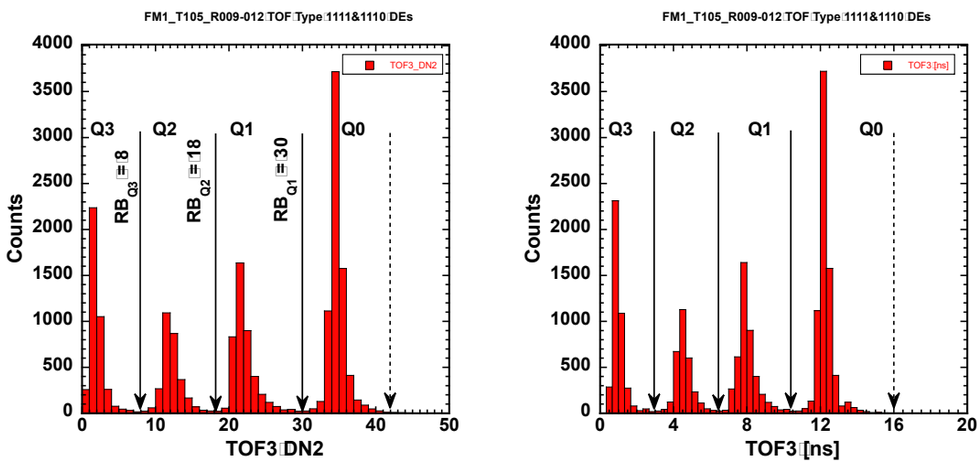


Figure 4.3.3 *TOF3* distribution from the Roll scan (T105R009-012) when all 4 quadrants were illuminated in sequence. The quadrant designations and the right boundaries for Q3, Q2, Q1, and Q0 are shown.

From the *TOF3* spectra, we can obtain the following information:

For clarity, let us repeat some crucial information from section 3.1.3 here. The individual peaks are separated by twice the signal delay between two neighboring quadrants, i.e.

$$TOF3_{Q3} - TOF3_{Q2} = 2\Delta\tau_{23}$$
$$TOF3_{Q2} - TOF3_{Q1} = 2\Delta\tau_{12} \qquad (4.3.11)$$
$$TOF3_{Q1} - TOF3_{Q0} = 2\Delta\tau_{10}$$

The individual TOF3 values for each quadrant include the final timing delay $\Delta\tau_{Fin}$ and are determined as:

$$TOF3_{Q0} = \Delta\tau_{Fin} + \Delta\tau_{10} + \Delta\tau_{12} + \Delta\tau_{23}$$
$$TOF3_{Q1} = \Delta\tau_{Fin} - \Delta\tau_{10} + \Delta\tau_{12} + \Delta\tau_{23} \quad (4.3.12)$$
$$TOF3_{Q2} = \Delta\tau_{Fin} - \Delta\tau_{10} - \Delta\tau_{12} + \Delta\tau_{23}$$
$$TOF3_{Q3} = \Delta\tau_{Fin} - \Delta\tau_{10} - \Delta\tau_{12} - \Delta\tau_{23}$$

As can be seen from eq. (4.3.11), the TOF3 values decrease from quadrant 0 to quadrant 3. This figure also evidently shows that TOF3 values above approximately 15 ns are unphysical and, thus, should be a reason for removing such events from the analysis if seen in the data.

For all events except Event ID 1111 (Silver and Golden Triples), the TOF3 values will be compressed to 2 Bits in the Flight data, i.e., just marking the quadrant position (Q0, 1, 2, 3). The peak values obtained in this calibration run will be used to ensure that the correct peak TOF3 value for each of the quadrants can be retrieved on the ground. By obtaining these values in flight from Event Type 1111, this information can be monitored throughout for its stability.

Because the Stop signal for TOF0 is taken from b0 and the Stop signal for TOF1 from b3, these measured TOF values are affected by the delays between the quadrant anodes. Thus, when combining events from more than 1 quadrant, the following values should be used instead:

$$TOF0s = TOF0 + TOF3/2$$
$$TOF1s = TOF1 - TOF3/2 \quad (4.3.13)$$

TOF0s and *TOF1s* have the delay line effects removed and represent the correct time required for a particle to move from the first foil to the anode board (*TOF0s*) or the time for a particle to pass from the second foil to the anode board (*TOF1s*).

It should be reemphasized here that the measured *TOF0* and TOF1 values cannot be negative. Therefore, *TOF0s = TOF0 + TOF3/2* will show no events with values < Min(*TOF3/2*). However, *TOF1s = TOF1 – TOF3/2* may attain slightly negative values up – Max(*TOF3/2*). It is important to note that with delay line effects removed and the checksum applied, TOF0s and TOF2 are the only independent measurements.

The peak locations in TOF3 are relevant for the data analysis on the ground because each of the 4 positions is transmitted for all DE types, except for Silver and Golden Triples, solely as a 2-bit value. Knowledge of the peak locations enables the correction of TOF0 and TOF1 for the Delay Line effects. During the roll scan, all 4 quadrants were illuminated so that all 4 peaks could be determined with comparable counting statistics. Therefore, we will also use the peak values from this determination in section 4.5.1.4 for the TOF Offsets in TOF0 and TOF1, where 0 ns TOF does not produce positive TOF values for all 4 quadrants.

The TOF3 values shown in Figure 4.3.3 (right, in ns) are used to compute the quadrant peak locations, which are compiled in Table 4.3.2, together with the total number of counts detected, the standard error, and the standard deviation. Because the TOF3 distributions for each quadrant are relatively narrow, the peak center location is obtained as the center of mass of the peak distribution.

$$TOF_{nQk} = \sum_L^R TOF_{ni} \cdot C_{ni} / \sum_L^R C_{ni} \quad (4.3.14)$$

The index *n* denotes the TOF channel number (*n* = 3 in this case), *Qk* is the quadrant, C_{ni} is the number of counts in each TOF bin, and *L* and *R* are the left and right boundaries for each sum.

The resulting TOF3 peak positions Qn are compiled in the 3rd column of Table 4.5.1.2, along with the standard error and standard deviation in columns 5 and 6.

The right boundaries (RB) for Q3, Q2, and Q1 are shown in DN2 on the left of Figure 4.3.3 and in ns on the right.

The RB values in DN2 are also compiled in the rightmost column of Table 4.5.1.1.

DN2 has the data number resolution transmitted in the telemetry. The vertical dashed line indicates beyond which values TOF3 is unphysical, which is used as a limit in the TOF3 threshold.

Table 4.3.2 Quadrant Peak Locations and Boundaries in TOF3 From Final Cal (T105R009-012)

	All	Peak(Qn)		StdErr(Qn)	StdDev(Qn)		RB DN2
Q0	7428	12.31	±	0.005	0.47	ns	N/A
Q1	4338	7.92	±	0.009	0.53	ns	30
Q2	3023	4.51	±	0.008	0.49	ns	18
Q3	4087	1.02	±	0.005	0.30	ns	8

4.3.4 TOF Offsets

Each TOF section has a specific offset, i.e., 0 ns TOF does not necessarily correspond to 0 on the measured TOF scale. These offsets are due to the finite flight times of the secondary electrons to the MCPs, electronic delay and processing times, and the different delay times for each of the 4 quadrants on the Stop Anode B. To relate the measured TOF values to simulated flight times of ions, these offsets must be determined by a combination of simulations and calibrations.

The most reliable method to determine the total offset is to use electrons that are accelerated from the ESA into the TOF section by the PAC voltage as a background signal. The flight times of 12 keV electrons across TOF0 is 0.89 ns and across TOF1 0.405 ns. These values must be subtracted from the electron TOF peak to obtain TOF = 0 ns in these two TOF sections. TOF2 does not produce a visible e TOF peak because the secondary electron delays shift TOF = 0 ns to negative values in the TOF measurement. Therefore, we determine only the Offsets for TOF0 and TOF1 here and rely on simulations for the TOF2 offset, which will be discussed at the end of the section.

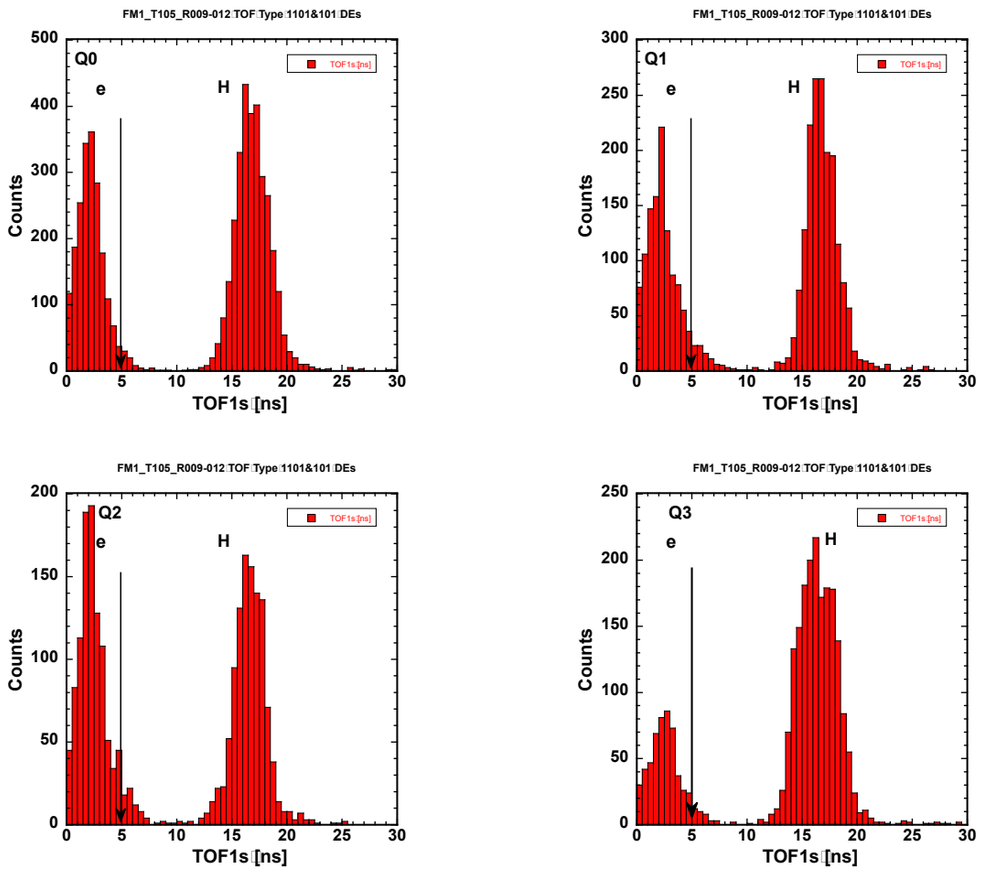


Figure 4.3.4 TOF1s distributions of Type 1101 & 0101 DEs, which contain TOF1 and TOF3 for T105R009-012, separate for each quadrant. The arrow indicates the right limit for the mean position determination of the electron peak.

To obtain electron peaks with good counting statistics, we analyze the data from the slow roll scan during Final Calibration (T105R009-012), which shows approximately equal distribution of counts in each quadrant as seen in Figure 4.3.3. Electrons are substantially suppressed compared to negative ions among Silver Triples because of their extremely low efficiencies to produce secondary electrons and the fact that the *TOF2* electron peak has a negative TOF value. Therefore, DE Type 1101 & 0101, events which contain a *TOF1* and a *TOF3* but no *TOF2*, and Type 1101 & 1001, events which include a *TOF0*

and *TOF3* but no *TOF2*, have to be used to analyze electron TOF distributions. We start with the *TOF1* distributions because here, as we will see, the electron peak is visible in all four quadrants.

Figure 4.3.4 shows the *TOF1* distributions separately for quadrant Q0 through Q3 from the top left to bottom right. function of *TOF1s,* which corrects for the delay line effects. Both peaks now remain in the same position for each quadrant. The H^--peak and the e-peak are well visible in each of the TOF spectra. The e-peak is comparable to the H^--peak in height in this DE Type selection.

The resulting e-peak locations in TOF1s are listed in column 5 of Table 4.3.3, along with the standard errors in column 7.

Column 8 of Table 4.3.3 shows the *TOF1s* e-peak values obtained by adjusting the *TOF1* e-peak values from column 2 for the delay line effects, using the *TOF3* peak values obtained from Table 4.3.2. The uncertainties in column 10 combine the *TOF3* peak uncertainties and the standard error from the left column. The differences between the values in the middle and right sets of columns far exceed their standard errors. The second row from the bottom contains the averages and standard deviations of both *TOF1s* e-peak value sets. These two averages are different by less than the standard deviations of either set. The last row shows the *TOF1s* e-peak value calculated for the electron events in all four quadrants. This value falls between the two averages. It should be noted that the *TOF3* quadrant positions obtained from all electron events (not shown here) are noticeably different from the values in Table 4.3.2 but vary within the standard deviations of the two e-peak sets. Thus, some systematic uncertainties are in these values, which may be related to a signal height dependence of the delay line values. Therefore, we adopt the larger uncertainties of the standard deviations as the uncertainty for the e-peak determination. The average between the two values in the 2nd row from the bottom equals the *TOF1s* value obtained from electrons in all 4 quadrants 1.66 ns. For any TOF analysis with *TOF1* data, only the *TOF1s* values will be used. Therefore, the average e-peak value of 1.66±0.40 ns is a useful value. Interestingly, the average *TOF1s* e-peak location was obtained in the Memo "IMAP-Lo TOF-Spectra Analysis" from compiling several runs during PreCal1 to between 1.70±0.34 and 1.75±0.34 ns, i.e., close to the value reported here. During the PreCal1 runs, mainly Q1 produced usable e-peak counts. Thus, we adopt the new value.

To obtain the offset for *TOF1s* = 0 ns, we must subtract the modeled electron flight time across *TOF1* by 0.4 ns. Any uncertainties here are small compared with the standard deviation of 0.4 ns.

The 0 ns offset in TOF1s is thus 1.26±0.40 ns.

Table 4.3.3: TOF1 and TOF1s Electron Peak Positions in all 4 Quadrants

	***TOF1e* [ns]**			***TOF1s* e(Qn)[ns]**			***TOF1se* (Qn) calc**		
Q3	2.48	±	0.055	2.15	±	0.105	1.96	±	0.055
Q2	4.14	±	0.047	1.89	±	0.130	1.88	±	0.048
Q1	5.35	±	0.048	1.54	±	0.147	1.39	±	0.049
Q0	7.07	±	0.035	1.51	±	0.119	0.92	±	0.035
Av & Stdev				**1.77**	±	0.31	**1.54**	±	0.48
TOF1s e				***1.66***	**±**	***0.40***			

Looking at Fig. 4.5.1.4a, we see that the electron signal in Q0 extends up to 12 ns in *TOF1*, while the H^- signal in Q3 starts at about 12 ns.

Therefore, the ideal TOF1 threshold value will be the equivalent DN2 value for 12 ns.

Figure 4.5.1.5a shows the *TOF0* distributions separately for quadrant Q0 through Q3 from the top left to the bottom right. The H^--peak and the e-peak are well visible in the TOF spectra of Q2 and Q3. The e-peak is reduced relative to the H^--peak in height by about a factor of 2 in this DE Type selection. In Q2, the e-peak appears cut-off at 0 ns. In Q1, the cut-off has moved to 3 ns, and the peak height is much reduced, and in Q0, no e-peak is to be seen. Eyeballing, the H^--peak is at about 37 ns in Q3 and shifts to about 25 ns in Q0. Because these are linear shifts of the *TOF0* signal due to the delay lines between the quadrants, the e-peaks shift by identical amounts and thus are negative *TOF0* values in Q1 and Q0. In Q2, e-peak is just above 0 ns and clipped.

Following the steps for *TOF1*, the *TOF0s* distributions are processed in the same sequence as in Fig. 4.5.1.5a, now corrected for the delay line effects. The H^--peak and the e-peak, when visible, now remain in the same position for each quadrant. Because only the e-peak in Q3 is well-isolated, the analysis for their mean position values is performed only with the *TOF0s* spectra.

The resulting e-peak locations in TOF0s are listed in column 2 of Table 4.3.4, along with the standard errors in column 4.

It is obvious that, except for the peak value from Q3, the other values are unphysical, and there is no entry for Q0 because no peak is visible here. According to the shift of the H^--peak from quadrant to quadrant, the e-peaks should move progressively toward lower and then negative values. However, the opposite occurs because of the clipping of the events at 0 ns. Also, the average, here over Q3 – Q1, and standard deviation are not useful. Therefore, only the e-peak value from Q3 can be used, and it is shown again at the bottom of the table along with the standard deviation uncertainty between all 4 quadrants from Table 4.3.3. For reference, the *TOF0* e-peak values for all 4 quadrants are shown in column 5, along with the standard error in column 7, calculated based on the *TOF0s* value in Q3. Using the *TOF3* peak values obtained from Table 4.3.2, the measured e-peak value in Q3 is adjusted for the delay line effects according to Eq. 4.5.1.7.

Table 4.3.4: TOF0s and TOF0 Electron Peak Positions

	***TOF0s* e(Qn)[ns]**			***TOF0* (Qn) calc**		
Q3	**2.74**	±	0.095	2.29	±	0.095
Q2	3.35	±	0.071	0.68	±	0.095
Q1	4.53	±	0.154	-1.13	±	0.095
Q0	0.00	±		-3.40	±	0.095
Av & Stdev	**2.65**	±	0.91			
***TOF0s*(e) used**	***2.74***	±	***0.4***			

Following the arguments for *TOF1*, any TOF analysis with *TOF0* data will only use the *TOF0s* values. Therefore, the measured e-peak value in Q3, which is adopted also as the average value for all quadrants, of 2.74±0.40 ns is taken. To obtain the offset for *TOF0s* = 0 ns, we must subtract the modeled electron flight time across *TOF0* by 0.89 ns. Any uncertainties here are small compared with the standard deviation of 0.4 ns.

The 0 ns offset in TOF0s is thus 1.85±0.40 ns.

The runs from PreCal1, reported in the Memo "IMAP-Lo TOF-Spectra Analysis", returned a value between 6.78±0.41 ns and 6.62±0.54 ns for the average *TOF0s* location of the e-peak, i.e., starkly different from our finding using the roll scan. However, the usable events for the e-peak were concentrated in Q2, which, according to our new analysis, shows a clipped e-peak. Also, events in Q1 and Q0, which were used then, are even more heavily clipped. Therefore, we adopt the new value from our analysis of the roll scan T105R009-012.

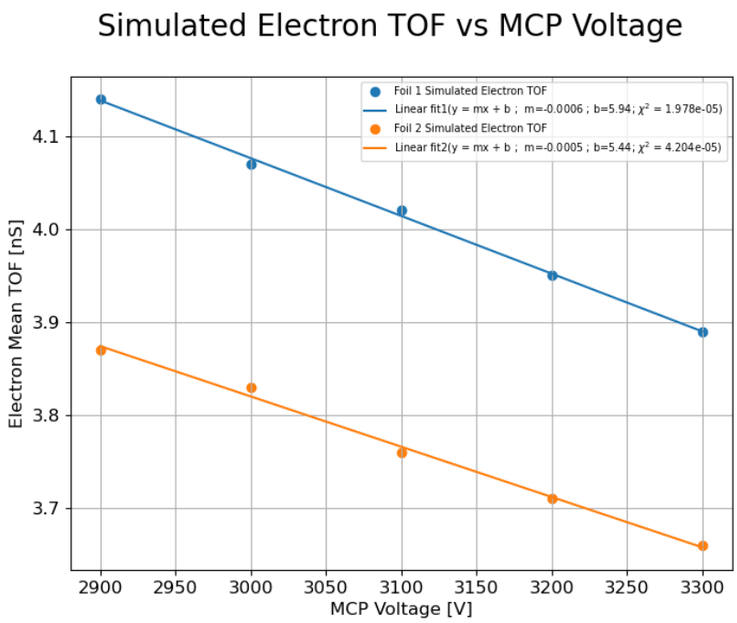


Figure 4.3.5 Simulated flight times of secondary electrons from Foil 1 to the MCP (blue) and from Foil 2 to the MCP (orange) as a function of MCP bias voltage.

The roll scan data did not produce a usable e-peak in *TOF2*, which is unsurprising for two reasons. First, the secondary electron efficiency of electrons is very low, and *TOF2* is based on two secondary electron signals, which squares the low efficiency. Second, the Start A signal comes from secondary electrons that have a longer travel time to the MCP than the secondary electrons from Start C. Figure 4.3.5 shows the simulated average secondary electron flight times for Start A in blue and Start C in orange as a function of MCP bias voltage, which also provides the electron acceleration. For the MCP bias voltage applied for operation, 3100 – 3150 V, the difference in flight times is 0.25 ns.

Therefore, we adopt as TOF2 offset the value -0.25 ns.

4.4 Branching Ratios and Sputtering Response

Excerpt from E. Moebius IMAP-Lo_Pre&FinalCal-TOF-Sect_Analysis_Dr3a.

Noble gas species, such as He and Ne, can only be detected and analyzed via sputter products for the conversion surface for an instrument with charge conversion to negative ions. With the IBEX-Lo and IMAP-Lo diamond-like carbon surface, the relevant sputter products are C from the CS and O and H from the ever-present water layer. Therefore, the knowledge of the branching ratios between O, C, and H for Ne and He as a function of incoming energy E_{Beam} and diagnosing ESA step E_{ESA} is crucial. In particular, it is essential also to have this information for O, which produces converted O^- at the incoming energy

reduced by a small percentage and sputter products at lower energies because, in flight, ISN Ne is observed together with ISN O.

Calibration Runs Performed

Several runs with Ne and O were performed during final calibration (T105) and cross-calibration (T106), and several He runs were performed during final calibration. In the following, we will discuss the results from Ne and O runs during final calibration, followed by those from cross-calibration. We will then compare the results in a consolidated representation as a function of E_{ESA}/E_{Beam}, which was used for IBEX-Lo flight data with ISN He to obtain an improved in-flight relative calibration of the sensor system to incoming He (Schwadron et al., 2022, Swaczyna et al., 2023). Finally, we will present the branching analysis for the He runs during the final calibrations.

Branching Analysis

Individual TOF peaks (H, C, and O) are modeled for the analysis using an asymmetric kappa function. C and O are more challenging to decompose than H, as they typically partially overlap. The representation of the asymmetric kappa function shown in Eq. 4.4.1 is used.

$$N(t,\kappa) = \frac{A}{((t-t_0)^2\beta+1)^{\kappa+1}},$$

$$\kappa = \frac{1}{2}(\kappa_r+\kappa_l) + \frac{1}{2}\frac{t-t_0}{|t-t_0|}(\kappa_r-\kappa_l). \tag{4.4.1}$$

A is a normalization factor for the peak height, t_0 represents the peak location in TOF, b describes the width of the peak, analogous to $b = 1/2s^2$ in a Gaussian, and k_l and k_r describe the tails on the left and right side of the peak, respectively. The asymmetric kappa function has a more gradual fall off of a kappa function while also capturing the shape of the slow-TOF tail within the TOF spectra. It thus represents well TOF-peaks shaped by energy and angle straggling in the C foils of a TOF section with a steep rise in front of the peak and an extended tail toward longer TOF values.

The function in Eq. 4.5.1.14 was tested on IBEX-Lo TOF spectra taken with C and O beams to provide shapes for the spectra of the individual species that are found in combination in most of the calibration runs. To obtain the best parameters, minimum chi-square fits were performed, which provided an initial set of bounding values for the parameters during the fits of the combined spectra.

A sample fit to a *TOF2* histogram for T105 run 105 with Ne at 700 eV into ESA Step 5 is shown in Figure 4.4.1.

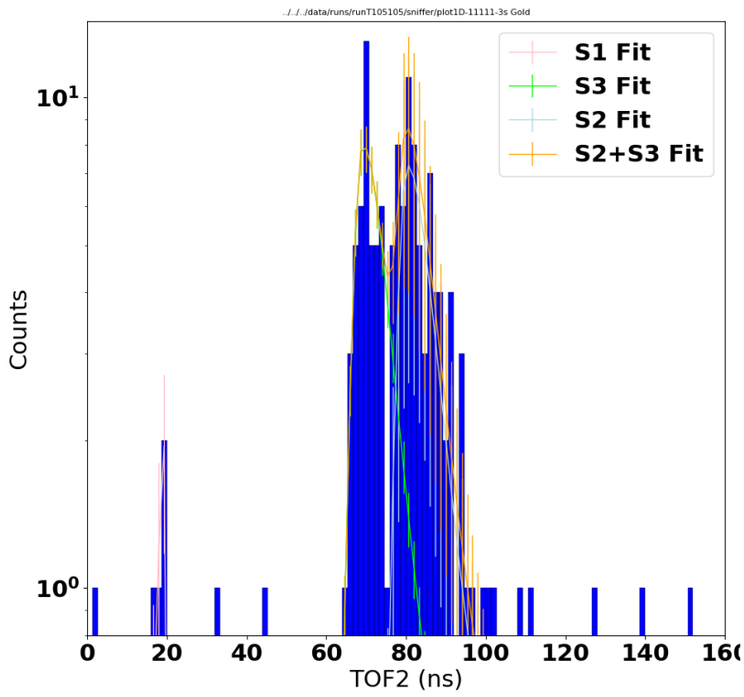


Fig. 4.4.1 *TOF2* histogram in ns for T105 run 105 (Ne 700 eV) into ESA Step 5 with the resulting fit to the H, C, and O peaks. The individual *k* functions and the combined C and O functions are shown.

The contribution of each species is calculated as the integral under each of the three *k*-functions, with the sum of all three normalized to 100%. The uncertainty for each contribution is the combined fit and Poisson statistics error.

4.4.1 Ne And O Branching Results

During the Final Calibration, Ne beam runs at 700 eV and 400 eV (T105 Runs 105 and 110) showed C percentages of about 40–50% in E-Steps just below the beam energy, with TOF0s and TOF2 results closely matching, and O dominating at the highest energies, suggesting a small contamination from water group molecules. For the O beam run at 460 eV (T105 Run 101), the C contribution was minimal near the beam energy but increased at lower E-Steps, with TOF0s indicating a C contamination roughly five times higher than TOF2, again pointing to molecular contamination. In all runs, H became dominant at the lowest E-Steps, but this lower energy range is less critical for in-flight Ne and O analysis.

During Cross Calibration at LANL, Ne and O beam runs revealed significant molecular contamination, particularly in O beams, affecting the measured C/O branching ratios. TOF0s data consistently showed higher C contributions than TOF2 data, attributed to contamination artifacts, while TOF2 results—used for final branching ratio compilations—were more reliable. Compared to Final Calibration, the C/O ratios from Cross Calibration appeared lower by about a factor of two, suggesting that Final Calibration may have also suffered some contamination despite cleaner-Looking beams, albeit with lower counting

statistics. 2D scatterplots confirmed visible molecular contamination features in both Ne and O runs, with O beams being more strongly affected.

Because none of the runs were taken with exactly the same beam energies during the different calibrations, the ESA and beam energies had to be normalized to directly compare the branching ratios from the different runs. We used a scheme employed by Schwadron et al. (2022) and Swaczyna et al. (2023) to obtain an improved in-flight calibration of the relative detection efficiencies of IBEX-Lo for the ISN He flow for this comparison. In the following, we present the individual branching ratios as a function of the normalized ESA energies E_{ESA}/E_{Beam} for the results from all calibration runs.

Ne Branching Results

Figure 4.4.2 shows the C/O ratios obtained with Ne beams as a function of E_{ESA}/E_{Beam} obtained from Final Calibration, Cross-Calibration, and IBEX-Lo calibration.

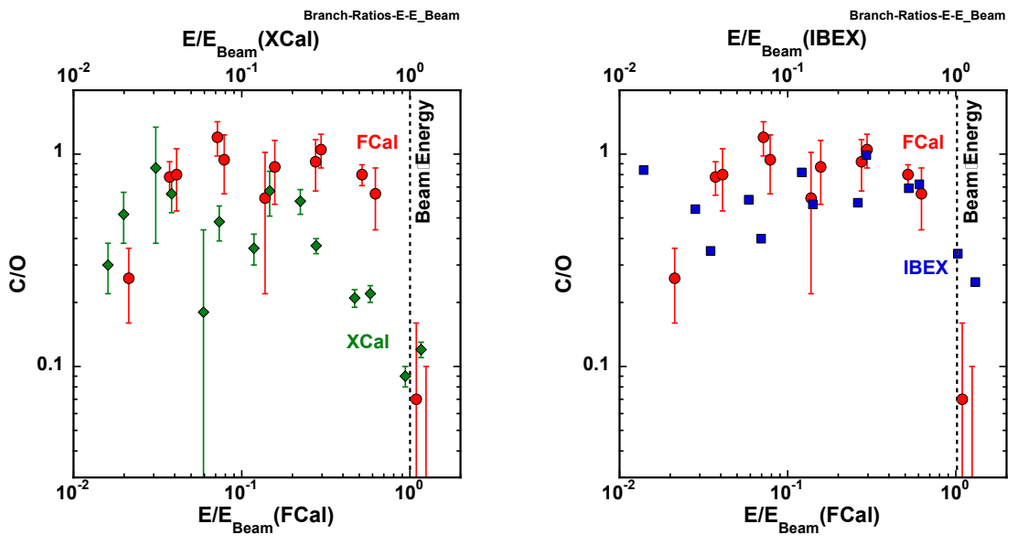


Figure 4.4.2 C/O ratios obtained with Ne beams as a function of E_{ESA}/E_{Beam} from Final Calibration and Cross-Calibration (left) and from Final Calibration and IBEX-Lo Calibration (right).

As indicated above, all results were taken from the *TOF2* histograms to avoid the impact of molecular contamination of the branching results. The comparison of the Final Calibration results with those from the Cross-Calibration and from the IBEX-Lo Calibration indicates that C/O ratios observed during Cross-Calibration are consistently lower by factors of 2-3 than those from Final Calibration, and that the results from Final Calibration agree with those from the IBEX-Lo Calibration. To emphasize the results between the beam energies and a factor of 4 below, the same results are shown on a linear scale in both axes in Figure 4.4.3.

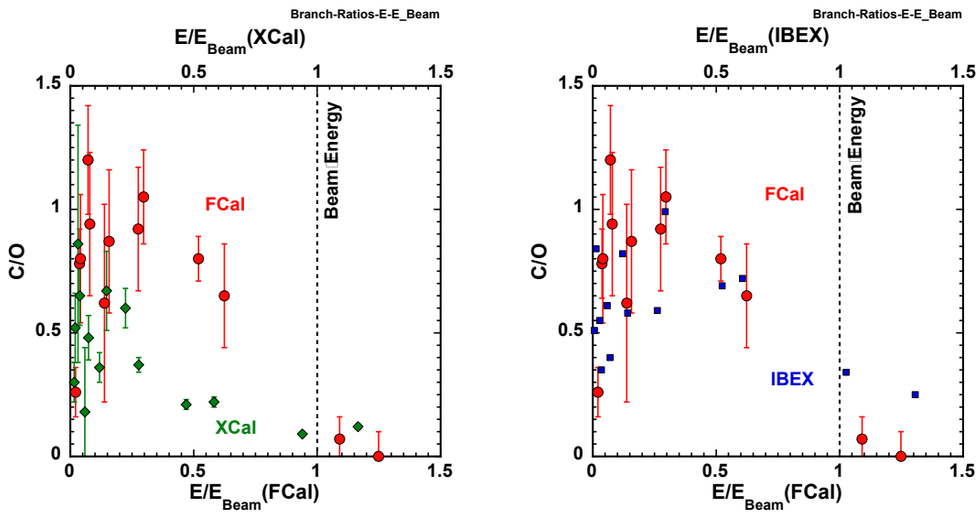


Figure 4.4.3 C/O ratios obtained with Ne beams as a function of E_{ESA}/E_{Beam} from Final Calibration and Cross-Calibration (left) and from Final Calibration and IBEX-Lo Calibration (right). This figure shows the same results as Fig. 4.4.2 but on a linear scale to emphasize the results in the highest ESA steps.

Because the IMAP-Lo instrument had been on the spacecraft for an extended time after Final Calibration, undergoing various spacecraft integration and test activities, was then transported to Los Alamos, and installed in the LANL accelerator chamber without another vacuum bakeout, it was suspected that the conversion surface may have been contaminated with a substantially thicker water layer. Therefore, Figure 4.4.4 shows the H/C ratio as a function of E_{ESA}/E_{Beam} obtained from Final Calibration, Cross-Calibration, and from the IBEX-Lo calibration. H comes from the water layer, as does O, while C comes from the diamond-like C layer of the conversion surface.

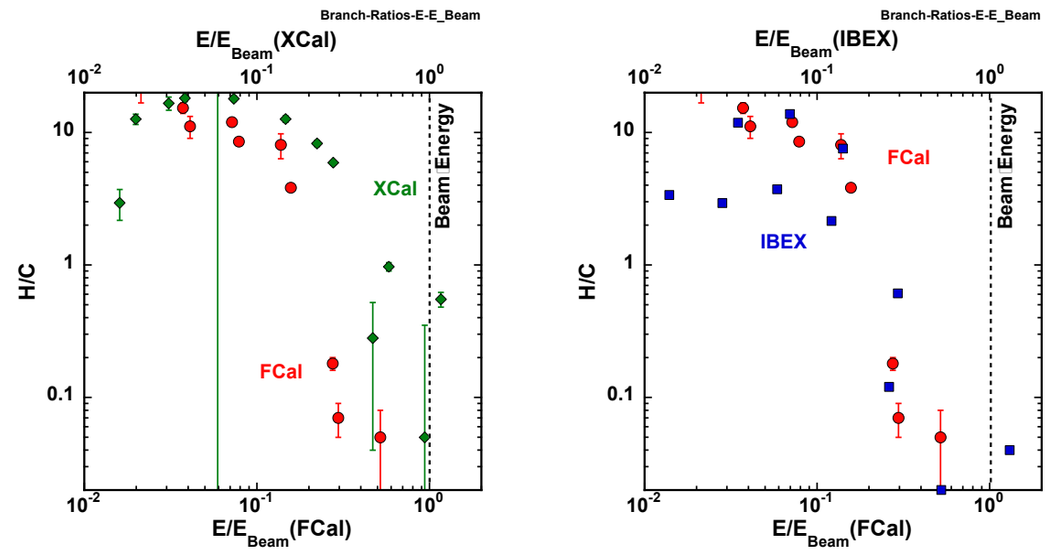


Figure 4.4.4 H/C ratios obtained with Ne beams as a function of E_{ESA}/E_{Beam} from Final Calibration and Cross-Calibration (left) and from Final Calibration and IBEX-Lo Calibration (right).

Indeed, the H/C ratio is higher throughout almost the entire energy range during Cross-Calibration than during Final Calibration, and the Final Calibration results agree better with the IBEX-Lo results. It should be noted that, generally, the IBEX-Lo results show a larger scatter than the IMAP-Lo Final Calibration and Cross-Calibration results as two groups. This scatter may be because each ESA step data point was obtained in an individual run during the IBEX-Lo Calibration, while ESA steps were automatically changed during the entire run with a set beam energy. Any branching ratios from the IBEX-Lo Response Function files that were obtained by interpolation have been eliminated. Table 4.4.1 shows a compilation of all branching ratio results with Ne beam energy and ESA energy combinations from IMAP-Lo Final Calibration and Cross-Calibration, along with all available combinations from the IBEX-Lo calibrations. Shown are the beam energy (E_{Beam}), ESA energy (E_{ESA}), and E_{Beam}/E_{ESA} for each of the calibration sets, followed by the H/O, C/O, and H/C ratios with the uncertainties obtained in the Chi-square fits for the IMAP-Lo results. For the IBEX-Lo results, no uncertainties are available right, but they can be obtained by applying the same procedure to the original calibration data. The ESA energies relevant to obtaining the ISN Ne/O ratios in-flight are highlighted in yellow.

Table 4.4.1 Branching Ratios obtained with Ne beams

Ne Beam		Final Calibration							Cross-Calibration								IBEX Calibration					
E_{Beam} [eV]	E_{ESA} [eV]	E_{ESA}/E_{Beam} (FCal)	H/O	ΔH/O	C/O	ΔC/O	H/C	ΔH/C	E_{Beam} [eV]	E_{ESA} [eV]	E_{ESA}/E_{Beam} (XCal)	H/O	ΔH/O	C/O	ΔC/O	H/C	ΔH/C	E_{Beam} [eV]	E_{ESA} [eV]	E_{ESA}/E_{Beam} (IBEX)	H/O	C/O	H/C
700	14.91	0.02	6.51	1.94	0.26	0.10	24.71	7.99	930	16.40	0.02	0.88	0.16	0.30	0.08	2.94	0.77	2300	16.00	0.01	2.46	0.51	4.87
700	28.70	0.04	8.86	3.14	0.80	0.26	11.12	2.09	930	31.57	0.03	14.27	7.84	0.86	0.48	16.60	1.88	2300	32.00	0.01	2.82	0.84	3.37
700	55.11	0.08	8.03	2.40	0.94	0.29	8.52	0.58	930	60.62	0.06	15.45	12.56	0.18	0.26	83.90	99.14	2300	65.00	0.03	1.62	0.55	2.93
700	109.96	0.16	3.32	1.07	0.87	0.29	3.83	0.23	930	120.96	0.12	11.46	1.81	0.36	0.06	32.25	2.85	2300	135.00	0.06	2.28	0.61	3.72
700	207.59	0.30	0.07	0.02	1.05	0.19	0.07	0.02	930	228.35	0.22	4.98	0.62	0.60	0.08	8.26	0.44	2300	279.00	0.12	1.76	0.82	2.15
700	436.32	0.62	0.00		0.65	0.21	0.00		930	479.95	0.47	0.06	0.05	0.21	0.02	0.28	0.24	2300	601.00	0.26	0.07	0.59	0.12
700	873.86	1.25	0.00		0.00	0.10	0.00		930	961.24	0.94	0.00	0.03	0.09	0.01	0.05	0.30	2300	1206.00	0.52	0.01	0.69	0.02
400	14.91	0.04	11.94	1.94	0.78	0.14	15.32	1.41	750	16.40	0.02	6.59	1.68	0.52	0.14	12.62	1.13	2300	2361.00	1.03	0.00	0.34	0.01
400	28.70	0.07	14.39	2.47	1.20	0.22	11.95	0.77	750	31.57	0.04	11.73	2.11	0.65	0.12	18.15	1.04	460	16.00	0.03	4.10	0.35	11.86
400	55.11	0.14	4.96	3.08	0.62	0.40	8.06	1.72	750	60.62	0.07	8.71	1.49	0.48	0.09	17.97	0.83	460	32.00	0.07	5.46	0.40	13.80
400	109.96	0.27	0.17	0.05	0.92	0.25	0.18	0.02	750	120.96	0.15	8.46	1.91	0.67	0.16	12.64	0.70	460	65.00	0.14	4.41	0.58	7.56
400	207.59	0.52	0.04	0.03	0.80	0.09	0.05	0.03	750	228.35	0.28	2.18	0.13	0.37	0.03	5.92	0.22	460	135.00	0.29	0.61	0.99	0.61
400	436.32	1.09	0.00		0.07	0.09	0.00		750	479.95	0.58	0.21	0.02	0.22	0.02	0.97	0.07	460	279.00	0.61	0.01	0.72	0.01
		2.18					0.00	0.00	750	961.24	1.17	0.07	0.01	0.12	0.01	0.55	0.07	460	601.00	1.31	0.01	0.25	0.04

O Branching Results

Figure 4.4.5 shows the C/O ratios obtained with O beams as a function of E_{ESA}/E_{Beam} obtained from Final Calibration, Cross-Calibration, and IBEX-Lo calibration. To evaluate for H, Figure 4.4.6 shows the H/O ratios obtained with O beams as a function of E_{ESA}/E_{Beam} obtained from Final Calibration, Cross-Calibration, and IBEX-Lo calibration. We compare the H contribution with that of O here because the incoming beam is O.

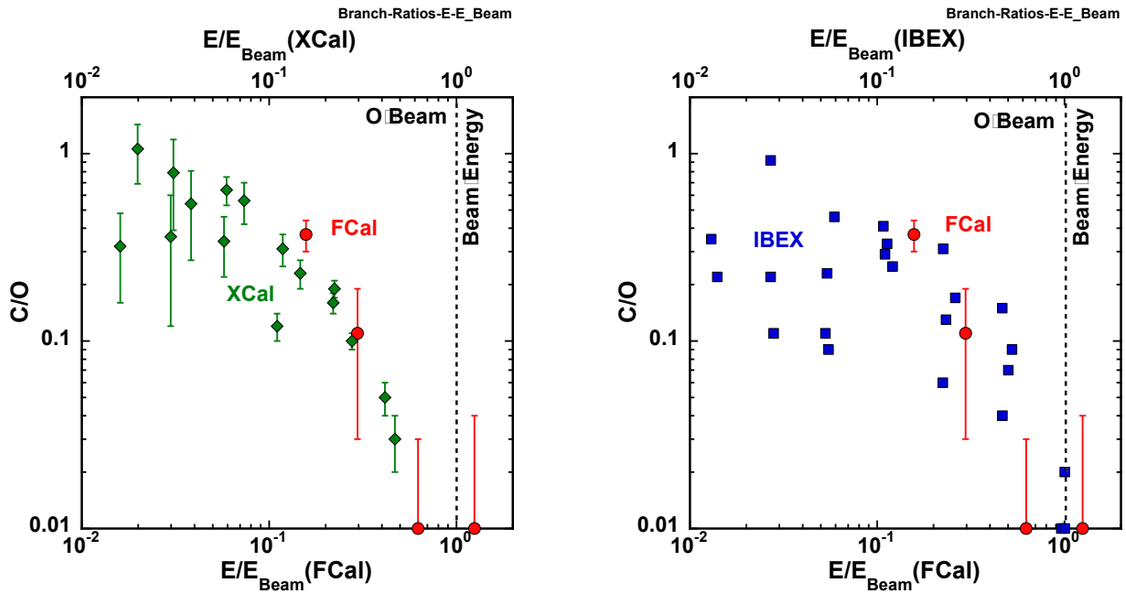


Figure 4.4.5 C/O ratios obtained with O beams as a function of E_{ESA}/E_{Beam} from Final Calibration and Cross-Calibration (left) and from Final Calibration and IBEX-Lo Calibration (right).

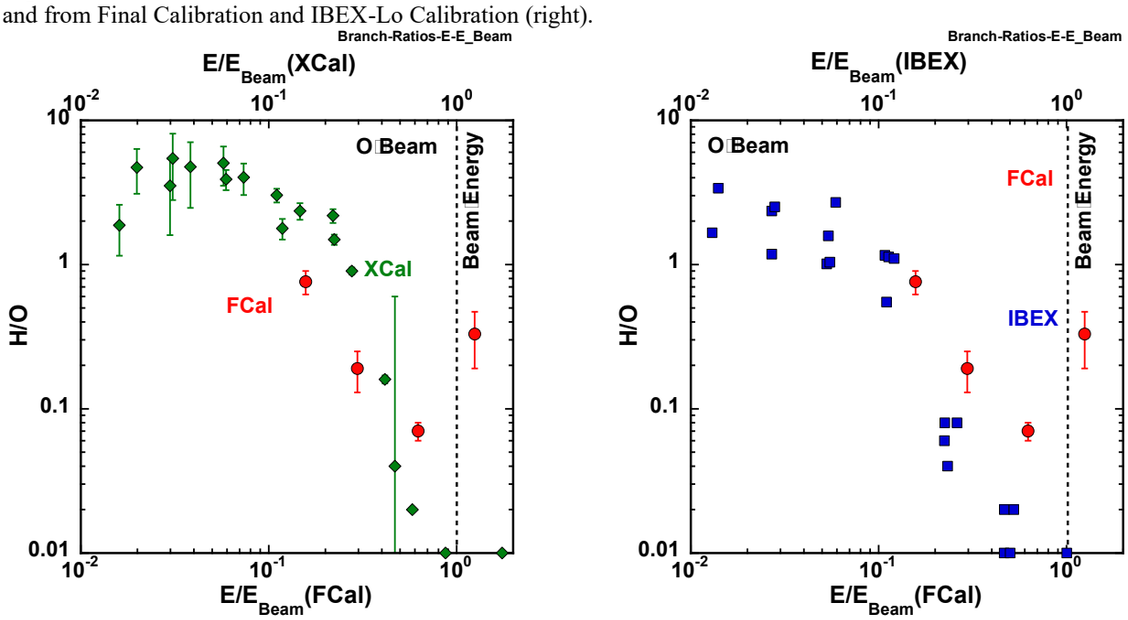


Figure 4.4.6 H/O ratios obtained with O beams as a function of E_{ESA}/E_{Beam} from Final Calibration and Cross-Calibration (left) and from Final Calibration and IBEX-Lo Calibration (right).

The branching ratios obtained with O beams from Final Calibration and Cross-Calibration with IMAP-Lo, along with the available results from IBEX-Lo calibrations, are compiled in Table 4.4.2 The format is identical to Table 4.4.1.

Table 4.4.2 Branching Ratios obtained with O beams

O Beam		Final Calibration							Cross-Calibration								IBEX Calibration					
E_{Beam} [eV]	E_{ESA} [eV]	E_{ESA}/E_{Beam} (FCal)	H/O	ΔH/O	C/O	ΔC/O	H/C	ΔH/C	E_{Beam} [eV]	E_{ESA} [eV]	E_{ESA}/E_{Beam} (XCal)	H/O	ΔH/O	C/O	ΔC/O	H/C	ΔH/C	E_{Beam} [eV]	E_{ESA} [eV]	E_{ESA}/E_{Beam} (IBEX)	H/O	C/O	H/C
		0.02							930	16.40	0.02	1.87	0.72	0.32	0.16	5.82	2.11	2300	16	0.007	4.4	0.4	10.2
		0.04							930	31.57	0.03	5.44	2.64	0.79	0.40	6.85	0.80	2300	32	0.0139	3.4	0.2	15
		0.08							930	60.62	0.06	3.90	0.62	0.64	0.11	6.13	0.33	2300	65	0.0283	2.5	0.1	23.8
700	109.96	0.16	0.76	0.14	0.37	0.07	2.02	0.16	930	120.96	0.12	1.78	0.29	0.31	0.06	5.68	0.48	2300	135	0.0587	2.7	0.5	5.9
700	207.59	0.30	0.19	0.06	0.11	0.08	1.83	1.34	930	228.35	0.22	1.49	0.12	0.19	0.02	7.96	0.52	2300	279	0.1213	1.1	0.3	4.34
700	436.32	0.62	0.07	0.01	0.01	0.02	4.55	5.32	930	479.95	0.47	0.04	0.56	0.03	0.01	1.26	16.33	2300	2361	1.0265	0	0	0.42
700	873.86	1.25	0.33	0.14	0.01	0.03	29.70	84.43	930	961.24	0.94	0.00	0.00	0.01	0.00	0.37	0.13	1200	16	0.0133	1.7	0.3	4.77
		0.04							750	16.40	0.02	4.71	1.62	1.06	0.37	4.44	0.27	1200	32	0.0267	1.2	0.2	5.5
		0.07							750	31.57	0.04	4.76	2.29	0.54	0.27	8.76	1.37	1200	1206	1.005	0	0	0.26
		0.14							750	60.62	0.07	4.02	0.99	0.56	0.14	7.20	0.52	600	16	0.0267	2.3	0.9	2.56
		0.27							750	120.96	0.15	2.35	0.31	0.23	0.04	10.08	0.97	600	32	0.0533	1	0.1	9.52
		0.52							750	228.35	0.28	0.90	0.05	0.10	0.01	8.59	0.74	600	65	0.1083	1.2	0.4	2.82
		1.09							750	479.95	0.58	0.02	0.00	0.03	0.00	0.57	0.07	600	135	0.225	0.1	0.3	0.27
		2.18							750	961.24	1.17	0.00	0.00	0.01	0.00	0.38	0.18	600	279	0.465	0	0.1	0.04
									500	16.40	0.03	3.51	1.91	0.36	0.24	9.79	3.86	600	601	1.0017	0	0	0.38
									500	31.57	0.06	5.05	1.53	0.34	0.12	14.79	2.20	290	16	0.0552	1	0.1	12.2
									500	60.62	0.11	3.02	0.33	0.12	0.02	25.05	3.85	290	32	0.1103	0.5	0.3	1.88
									500	120.96	0.22	2.18	0.24	0.16	0.02	13.94	1.62	290	65	0.2241	0.1	0.1	0.95
									500	228.35	0.42	0.16	0.01	0.05	0.01	2.95	0.34	290	135	0.4655	0	0	0.62
									500	479.95	0.87	0.01	0.00	0.01	0.00	0.58	0.14	290	279	0.9621	0	0	0.31
									500	961.24	1.75	0.01	0.00	0.01	0.01	1.04	0.66						

The C/O ratios appear comparable between all three calibrations. However, it should be noted that only the four highest energy steps are available from an O beam run during Final Calibration and that, here, sputtering is not very effective yet. Also, the IBEX-Lo results show even more substantial scatter in the O beam runs. The H/O ratio appears noticeably higher from the Cross-Calibration results than from the Final Calibration results, whereas the IBEX-Lo results either show almost the same H/O ratio as the IMAP-Lo Final calibration results or are considerably lower. Note that during the O beam runs, O comes mainly from the beam as atoms converted to O^-, and H is a sputter product from the water layer. Typically, the combined CS conversion and ESA collection efficiency is substantially higher than the CS sputter and ESA collection efficiency. The presence of HO and/or H_2O contamination in the beam, which is more prevalent at LANL because of charge exchange in the atmospheric rest gas with water remnants, is likely not the main reason for the greater than a factor of 2 difference during Cross-Calibration as we see only a small contamination of molecular fragments. Also, these fragments are seen during Final Calibration and Cross-Calibration.

In summary, the increased contributions of O and H in the Cross-Calibration runs suggest a more substantial water layer during Cross-Calibration, which is likely responsible for the differences in the branching ratio results. As pointed out above, this scenario is plausible because the IMAP-Lo instrument had been vacuum-baked out before Final Calibration and had been under vacuum substantially longer before the Ne and O runs than was possible during Cross-Calibration. In flight, the instrument will outgas for several weeks before HV commissioning starts.

4.5 Roll Response

In roll response calibration testing we observe the instrument count rate while varying the incident beam position in roll (around the instrument symmetry axis). The roll variation clocks the instrument to target different conversion surfaces and will show any axial variations (see figure below). Angular spread is assumed to be small so the beam cast on the collimator should be roughly 14mm in diameter.

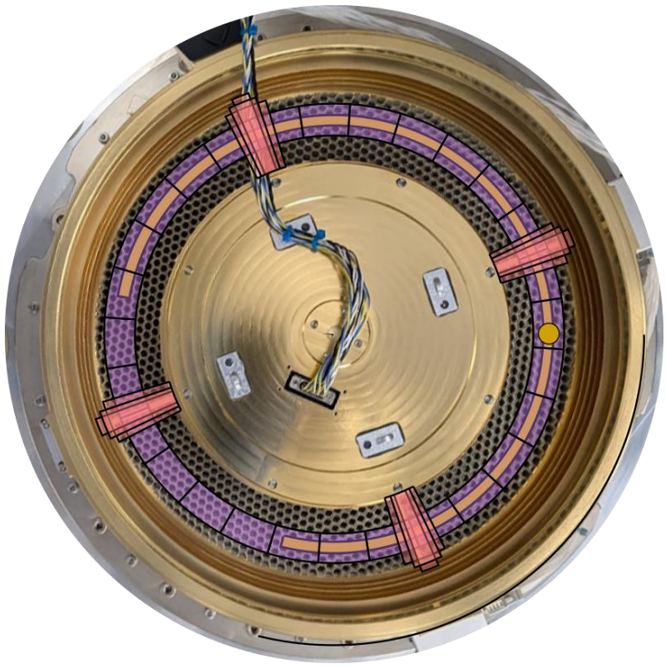


Figure 4.5.1 IMAP-Lo Entrance System Structures

In Figure 4.5.1 we can see a diagram of the instrument entrance system from the Precal2 and FinalCal test setup with relevant structures overlaid, in the instrument home position (roll = 0 deg at Quadrant 0). Positions of the overlaid structures compare photo with the instrument CAD model, and while not exact, this should be relatively accurate to the test setup. Collimator spokes are indicated in red, with the three boxed associated with the p2 grid spokes (widest of the 3 red boxes) and the collimator spoke (skinniest of the three boxes in center). The purple-segmented donut indicates the approximate location of the 28 CS facets, each covering (~12.8deg). A 14mm beam targeting the 3 o'clock position is shown as a yellow dot in Quadrant 0 (Q0), and the available targeting range for the PreCal2 and FinalCal testing is indicated by a yellow bar through the CS facets, following a counterclockwise rotation (Q3 Q0 Q1 Q2).

In instrument Final Cal, eight movements of the instrument rotation were performed and were logged in eight separate test runs [R009,R010,R011,R012,R034,R035,R036,R037]. Runs were collected by triggering the record file, and the rotation stage start and stop points simultaneously using two operators. The stage was actuated with the rotation stage clocking at 1deg/sec for runs [R009, R010, R011, R012] and 0.1deg/sec for runs [R034, R035, R036, R037]so, the stage position is simply inferred from the Sniffer count rate time stamp. Since the data collection was performed by hand, there will be some offset between the actual instrument position and the inferred clock position this effect though is assumed to be small (<1sec). We also alleviate any systematic bias that this method may introduce by repeating the data collection runs in the positive and negative directions. Finally given that we will ultimately be averaging the axial response across all measurements, any skew of the angles will only impact our qualitative interpretation of the detection efficiency (ie where exactly we see the shadow of the collimator spokes). Our total range in roll angular variation was [-104, 170]deg.

The silver count rates from the four run data set are binned in 2deg bins and averaged according to their roll angles. We use a count error taken from the total counts observed in a given bin. An important note is that the instrument count rate data only shows up every 2.5 seconds (translated directly to degrees, so the results are very course and some of the observations noted in the conclusions are susceptible to the averaging and smoothing techniques used. Successive runs are averaged to give high spatial resolution of the instrument roll response.

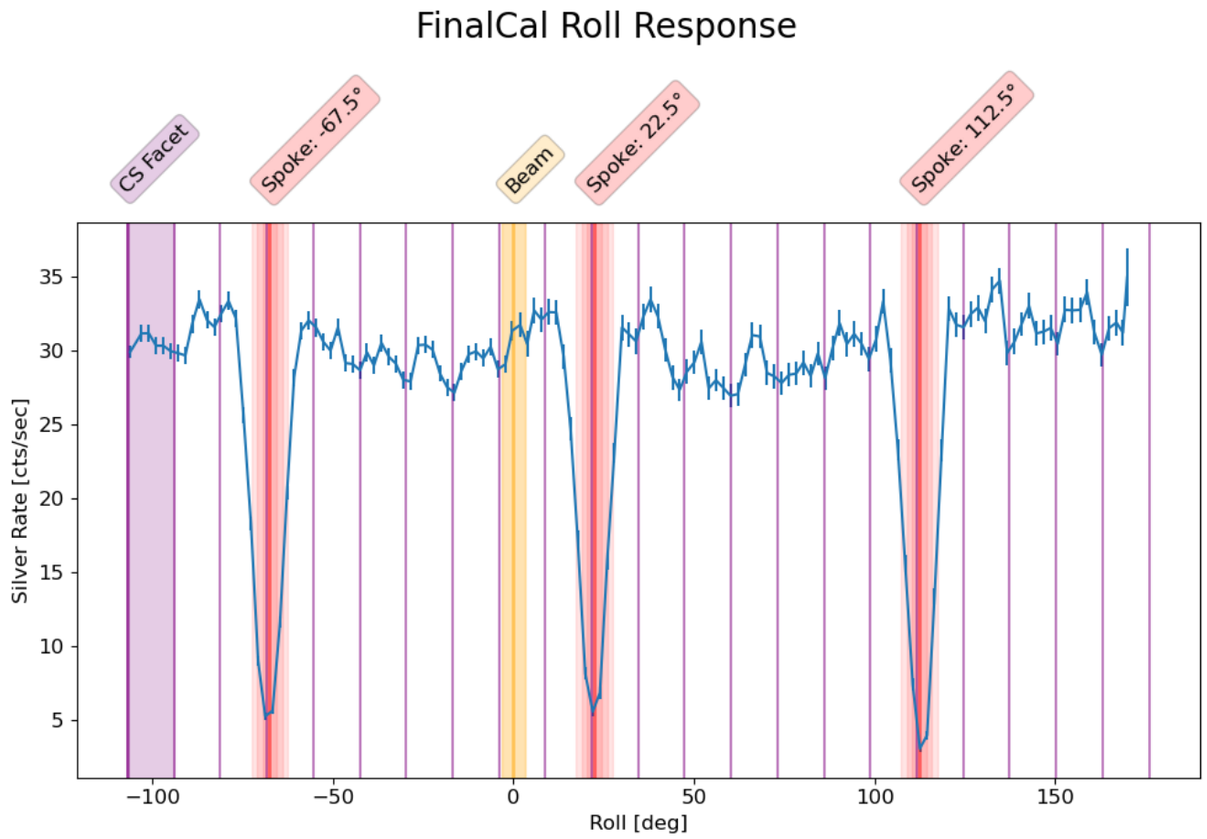


Figure 4.5.2 Final Cal Roll Response, where 3 spokes separate quadrant 3 (Q3), Q0, Q1, and Q2 from left to right. This roll response was performed with the neutral beam collimated by a 14mm collimator paddle.

In Figure 4.5.2 we can see some axial variation in collection efficiency across the collimator spokes, with about an 8% reduction observed between the spoke region and the quadrant center. This aligns reasonably with simulation results, which predicted a 5% reduction in collection efficiency due to the presence or absence of the p2 conical grid field (we don't have in IMAP-Lo eventually). Conversion efficiency remained consistent across surfaces within a 5–10% range, though notable variation—also around 5–10% — was detected across the surfaces of the CS facets, particularly from the center to the edges. While quadrant-to-quadrant collection efficiency appears relatively uniform.

Upon normalizing for TOF effects, most of the observed variation across quadrants and CS facets diminished, suggesting that azimuthal dispersion through the ESA—likely driven by field asymmetries—is the main cause of the variation. Although ions continue to reach the TOF, those with large oblique angles are more likely to be lost, which may contribute to a greater separation between HiTh and HiRes DER modes at the quadrant centers compared to the edges.

4.6 Differential Energy Response

The differential energy response (DER) characterization of the IMAP-Lo instrument is essential for understanding how the sensor electrostatics and CS respond to particles across instrument energy steps and mode. This response determines the instrument's ability to resolve energy-dependent fluxes of ENAs and ISNs, which is central to IMAP-Lo's scientific mission. The DER assessment involves a combination of controlled beamline measurements, detailed modeling, and simulations to quantify how particle detection rates vary with incident energy. The results provide the necessary transfer functions to deconvolve observed count rates into physical energy spectra and are integral to establishing energy-dependent geometric factors and response matrices used in science data processing.

Instrument electrostatics are controlled by the bulk power supply by assigning the ESA U+ and U- voltages. ESA U+ and U- voltages are defined as the highest positive (p10) and highest negative (p2/CS) electrode voltage, respectively. Voltages for both High-Throughput and High-Resolution modes for all 7 energy steps, as well as the simulated center energies for each step, are available in the IMAP-Lo Voltage stepping table 27850-2018. An abridged reference of the voltage stepping table is shown below.

High Throughput Mode

Electrodes:	Gem # [Hk3]	voltages[V]						
		Step 1	Step 2	Step 3	Step 4	Step 5	Step 6	Step 7
Conversion Surface (P1)	1	-28.19	-54.37	-104.46	-205.58	-396.43	-811.60	-1572.68
P2 Electrode	2	**-30.55**	**-58.92**	**-113.19**	**-222.75**	**-429.54**	**-879.40**	**-1704.06**
P9 Electrode	9	-5.59	-10.79	-20.72	-40.78	-78.64	-161.00	-311.98
Inner ESA (P5)	5	42.91	82.76	159.00	312.90	603.38	1235.30	2393.70
P10 Electrode	10	**61.91**	**119.41**	**229.42**	**451.48**	**870.61**	**1782.40**	**3453.85**

High Resolution Mode

Electrodes:	Gem # [Hk3]	voltages[V]						
		Step 1	Step 2	Step 3	Step 4	Step 5	Step 6	Step 7
Conversion Surface	1	-12.60	-24.30	-46.69	-91.88	-177.18	-362.73	-702.88
P2 Electrode	2	**-13.65**	**-26.33**	**-50.59**	**-99.56**	**-191.98**	**-393.03**	**-761.60**
P9 Electrode	9	-2.50	-4.82	-9.26	-18.23	-35.15	-71.96	-139.43
Inner ESA	5	27.93	53.87	103.50	203.68	392.77	804.11	1558.17
P10 Electrode	10	**40.30**	**77.73**	**149.34**	**293.89**	**566.72**	**1160.24**	**2248.26**

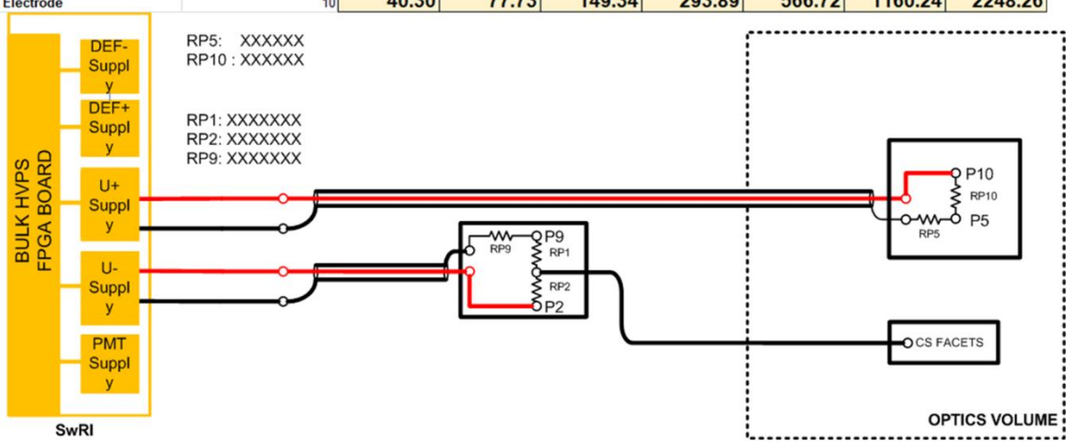


Figure 4.6.1 Block diagram of the resistor network of driving the ion optics

In this voltage configuration, negative polarity electrodes (CS/P1, P2, P9) have voltages assigned by the U- supply and a resistor chain and as such have a fixed relative voltage. The positive polarity electrodes (Inner ESA/P5, P10) are similarly assigned by the U+ supply. Energy steps, and energy scans (DER1 and DER2) are set by increasing or decreasing U+ and U- voltages while keeping the relative electrode voltage,

U+/U-, constant. While the positive and negative electrodes have a fixed relative voltage to one another, the U+ voltage and the U- voltage can be set independently, allowing for multiple electrostatic "modes":

Table 4.6.1

Voltage Mode	HiTh	HiRes	Background
|U-/U+|	0.49	0.34	27
Recoil dE/E	1.09	.71	NA

The exact voltages for each electrode, and in-turn the U+ and U- resistor chains, were defined by simulation which was optimized to yield the highest collection efficiency through the ESA for the HiTh mode. The voltages of each of the energy steps were then defined such that the center energy of the recoil ions accepted through the ESA would match IBEX-Lo. Any differences in the energy step centers between IBEX-Lo and IMAP-Lo are expected to be driven by differences in the CS scattering properties.

IMAP-Lo achieves different energy resolutions by changing/tuning the U+ and U- voltage, and adding/reducing pre-acceleration into the ESA. The ESA has a geometrically fixed dE/E = 0.7, but by lowering the voltage of the CS, converted neutrals gain energy in the region between the CS chamber and the ESA, focusing the distribution and changing the energy resolution of the ESA-CS subsystem as a whole. This method has its limitations though, as the further the |U-/U+| ratio strays from the nominal value (HiTh = .49) the fewer ions enter the ESA with observable energy-angle pairs. An important note is that, since the instrument electrostatics were optimized to the HiTh mode, the HiRes mode is achieved by detuning the electrostatics, and as such is not expected to have as high an ESA-CS conversion collection efficiency as observed by IBEX-Lo. Background mode is then achieved by setting the U- voltage so high that all ions generated from the CS are pre-accelerated so high that they simply collide with the outer ESA. Secondary particles and scattering are suppressed in the ESA through light fins and iridite blackening.

The second major factor that determines the instrument energy response is the scattering interaction of the neutrals on the CS. While the nominal energy resolution of the ESA-CS to recoil ions is easily tunable through the electrostatics, the conversion surface scattering adds another layer of complexity to consider, as any energy loss or energy dispersion on the conversion surface will drive variations in the effective energy resolution. CS scattering effects were studied at the subsystem level prior to sensor level calibration, but since the actual detection efficiency is determined by both the probability for the CS to convert a neutral to a negative ion, and the ability for that ion to be observed through the ESA, those observations require simulation to relate back to sensor level calibration results.

4.6.1 Analysis

The data analysis involves several key stages. First, raw data from the instrument sniffer and system logs are imported and preprocessed into structured dataframes. This includes computing count rates, direct event (DE) rates binned by time-of-flight (TOF) for different species (H, O, D), and synchronizing system logs with experimental runs based on timestamp alignment. Next, DER runs are selected, and instrument/system settings are averaged based on ESA voltage. Then, we calculate the particle flux incident to the collimator, using the ABM rates, and the Total collection efficiency and ESA-CS collection efficiencies using the species dependent count rates.

In the case of the instrument energy response described below, redundant DER runs (repeated species, energy step, Estep mode, beam energy) are grouped and averaged. The resulting voltage-energy response calibration runs are fit and deconvolved using the instrument electrostatics and surface scattering simulator to determine the instrument energy response functions and GFs.

4.6.1.1 Incident Particle Flux

We calculate the particle flux incident to the collimator using the ABM measured flux density, from the ABM rate and aperture, and the open area of the aperture plate.

$$R_{inc} = \frac{R_{ABM}[Cts/sec]}{A_{ABM}[cm^2]} * A_{coll}[cm^2] \quad (4.6.1)$$

For FinalCal and PreCal2, the aperture plate, A_{coll}=1.539cm2 for our 14mm diameter collimator aperture. While for PreCal1, the effective beam size incident to the CS is defined by the target position on the aperture mask and which beam aperture is used. For all Calibration testing, the ABM has an area A_{ABM}=.785cm2 (1cm diameter aperture) and the ABM rate (A_{ABM}) are absolute beam rate (formula provided in Sec. 4.1.1 Beam Flux Monitoring).

4.6.1.2 H from H2 Beam

For all observations here where EStep < 7, H2 is used in place of H. We choose H2 as our primary mode to determine the instrument response function here as we found that the incident H2 beam has a much higher purity and intensity than H, yielding a response function that is much closer to expectation. We thus have some work to do to infer the incident H flux from the ABM measured rates.

H2 is assumed to dissociate prior to collision with the conversion surface, so the H beam energy is assumed to collide with roughly half the energy of the generated H2 beam [Wurz 1997, Schlathoelter 1995] with a resulting energy of the dissociated particles given by:

$$E = \frac{E_0}{2} + \frac{E_D}{2} \pm \sqrt{E_0 E_D}\cos\alpha \quad (4.6.2)$$

here E_0 is the incident particle energy (beam energy), E_D is the dissociation energy (4.52eV) for H2, and α is the angle between the molecular axis and incident beam direction. Here α is isotropic, So, while the mean energy of the resulting H2 will be approximately half the incident energy, there will be some energy and angle dispersion which we will have to consider in the modeling of these results. The average incident beam energy is simply given by

$$\overline{E}^{H} = \sum_{N=1}^{M} \frac{1}{N}\left(\frac{E_0^N}{2} + \frac{E_D^{H2}}{2} \pm \sqrt{E_0^N E_D}\cos\alpha^N\right) = \frac{\overline{E}_0^{H2}}{2} + \frac{E_D^{H2}}{2} \quad (4.6.3)$$

This should make H energy response to H2 incident beam straightforward to determine (though there are still some questions about how the dissociation might impact the energy loss and dispersion processes, to be addressed in further analysis and simulation) but it complicates the determination of the detection efficiency. The ABM only measures counts/sec integrated across all energies and species, and its unknown how a measured flux of H2 incident beam might relate to the H flux on the CS. While we can parse the species and energy in the instrument, any contamination of other species and energies outside of what we desire to send in will effectively impact our measurement of incident beam flux and skew our observed energy response. In addition, the ABM has its own energy and species dependent efficiency further

complicating the matter. Early observations from Final-Cal comparing the H vs H2 energy response suggest that the instrument energy response to H from H2 at twice the desired energy is comparable to H energy response.

4.6.1.3 Flux Of Incident H

Next, we determine the flux of incident H from the ABM measured flux. As identified in PreCal1, there exists some low energy background generated from the ion source that contaminates the primary neutral beam component. Here, the issue that arises is that we have a mix of particle species entering the instrument from this background, but a reference flux from ABM doesn't provide species or energy determination. We use knowledge of the incident beam composition from the instrument to infer the incident H flux from the total incident ion flux (here we assume it to be just H and O, O here contains basically all heavy ions AMU > 6).

As far as estimating the incident flux is concerned, we have to make the assumption that for a given incident beam setting, the fraction of H and O being produced is constant. The variation we see in our observations can then be explained by the ESA passband overlapping or suppressing different components of the incident beam. We will then use the O and H components that the instrument observed to infer the fraction of O to H of the incident beam.

$$R_{inc} = R_{HInc} + R_{OInc} \quad \rightarrow \quad R_{HInc} = R_{Inc}(1 - R_{OInc}/R_{inc})$$

$$R_{OInc}/R_{inc} = \frac{R_{CS}^{O}}{R_{CS}^{O} + R_{CS}^{H}} = \frac{1}{1 + R_{CS}^{H}/R_{CS}^{O}} \tag{4.6.4}$$

To back out the fractional components of the incident beam, the difference in conversion efficiency and measurement efficiency of the two species must be considered. For that we incorporate the ToF and CS efficiency.

$$R_{CS}^{H}/R_{CS}^{O} = \frac{R_{DE}^{H}\epsilon_{cs}^{H}\epsilon_{TOF}^{H}\epsilon_{foil}^{H}\epsilon_{ESA}\epsilon_{grids}}{R_{DE}^{O}\epsilon_{cs}^{O}\epsilon_{TOF}^{O}\epsilon_{foil}^{O}\epsilon_{ESA}\epsilon_{grids}} \tag{4.6.7}$$

Given that the ABM has no resolution of energy, and the instrument does, we need to make some critical assumptions about the instrument's energy coverage. We assume that for a given incident beam energy, the voltage setting where we see the highest O rate represents the total incident O, i.e., total coverage of the incident energy distribution. We make a similar assumption to determine the incident H rate. The TOF efficiency for a given species is taken from the “silver” efficiency where the O/H is at a maximum. The relative O/H conversion efficiency is determined from CS subsystem calibration, where we assume a 15 deg incident angle and an incident energy associated with the center beam energy assigned for the calibration run in question.

4.6.1.4 ESA-CS Conversion Collection efficiency

In calibration, we measure the total collection efficiency as a function of beam energy, beam species and instrument voltage configuration. The total H collection efficiency ϵ_{TOT} for a given beam energy and voltage setting is governed by the ratio of the observed count rate to the particle flux incident to the collimator, as measured by the ABM. In reference to the definition of the instrument GF (Section 2.2), this measurement includes effects of the instrument conversion efficiency, ESA-CS collection efficiency,

the TOF efficiency and the grid transparency through which the beam of incident neutrals and recoil ions pass through:

$$\epsilon_{TOT} = \xi\chi\epsilon_{grid}\eta_{tof} = R_{Hsilver}/R_{HInc} \tag{4.6.8}$$

We calculate the ESA-CS collection efficiency to allow for comparison between the instrument model and our observed values.

$$(\xi\chi)_{ESACS} = \frac{R_{Hsilver}}{(R_{HInc}\epsilon_{grid}\eta_{tof})} \tag{4.6.9}$$

For the calibration events, the grid transparency parameter ϵ_{grid} is dependent on the test setup. For instance, in FinalCal, the grid transparency includes the collimator grid transparency, the p10 grids and spokes and the TOF entrance grids and spokes. Notably, we do not include the collimator or p2 spoke effective transparency because we make the assumption that we are shooting a beam straight through the collimator entrance. For each of the calibration events, we have the following effective grid transparencies:

Table 4.6.2

Test	Grid/spoke	Transparency
PreCal1/X-Cal	p10	0.85
	ToF Entrance	0.68
	Total	0.578
PreCal2/Final Cal	Collimator	0.69
	p10	0.85
	ToF Entrance	0.68
	Total	0.39882

In instrument X-Cal we make the assumption that the beam fires directly through one of the collimator hexes and thus the collimator grid transparency can be ignored.

4.6.2 Instrument Simulation

Excerpt from IMAP-Lo Instrument simulator document

Here, we outline the functionality and construction of the IMAP-Lo electrostatics and conversion surface scattering simulations. All of the electrostatics simulations discussed here are performed with SIMION ion simulation software in conjunction with a numerical model of the conversion surface scattering effects generated for this calibration effort. The bulk of the simulation effort has targeted the various IMAP-Lo calibration campaigns, but we also expand into the functionality of IBEX-Lo. Having directly comparable simulations relating IMAP and IBEX allow us to supplement the IMAP-Lo calibration results with similar results from the IBEX-Lo calibrations, providing a sanity check for IMAP-Lo results and additional well of data to fill in knowledge gaps.

Ultimately, we simulate the response function of the ESA-CS subsystem for neutrals incident to the conversion surface using a three-stage Monte-Carlo approach. To start, we define a probability distribution

of neutral particles which best represents the incident calibration beam, and fly the neutral particles to collision positions on the CS. The second stage utilizes calibration observations to account for surface scattering interactions on the CS, while the third stage simulates the ion flight through the optical path of the ESA.

A supplemental model of the instrument TOF unit has been created using SIMION and SRIM to study scattering effects through the ToF Foils. TOF trajectory and foil scattering simulation has not been integrated with the full instrument electrostatic model. Instead, particle observability is determined by impact location on the ToF entrance foil and the TOF detection efficiency is considered using calibration results.

The simulation electrostatic geometry of both the IBEX-Lo and IMAP-Lo models, is defined by an axially symmetric cross section of the instrument generated from vertexes of the instrument SolidWorks models. The full 3D model is then generated by rotating the cross section, assuming cylindrical symmetry along the instrument's boresight. This introduces several key simplifications:

1. The CS is assumed to be a smooth cone rather than a carousel of facets.
2. The spokes of the P2 electrode do not exist

Fields in the CS chamber will thus be simplified, removing any fringing effects. These asymmetries are expected to slightly impact the recoil ion trajectories, which, based on roll response calibration, may reduce collection efficiency by upwards of 5%.

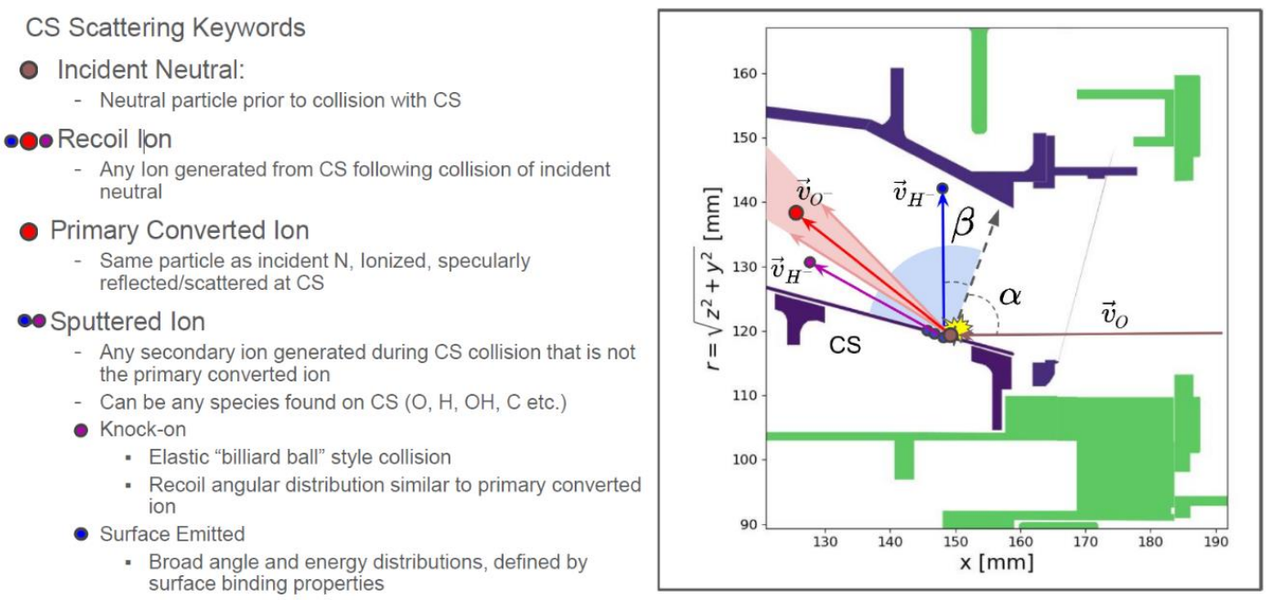


Figure 4.6.2 Cartoon illustration of coversion surface scattering and ionization

To simulate the CS scattering effects, we develop a Monte-Carlo method to apply scattering modulation functions measured in CS subsystem calibration to incident ion distributions so that we may determine

recoil ion distributions to feed back into instrument electrostatic simulations. Calibration has shown that energy loss, conversion efficiency and recoil angular scattering widths all vary according to the particle velocity incident to the CS surface plane. Basically, for a mono-energetic beam, higher energy particles, hitting close to perpendicular to the surface plane will lose more energy, have a higher chance of conversion, and scatter to a wider angular distribution when compared to a lower energy beam scattered in small angles from the surface plane. Here, calibration observations for O and Ne show a linear relationship between velocity perpendicular to the conversion surface and angular recoils scattering FWHM [Neuland 2014]. Using this relationship, each particle's incident velocity is used to define unique scattering probability distribution which are then sampled to give us a distribution of ions recoiling from the conversion surface. The conversion efficiency, defined as a function of incident velocity [Wahlstrom 2008], is simply incorporated as a weight factor for each particle in the final integration.

For a given incident neutral particle, the nominal recoil angle is determined by reflecting the incident particle velocity vector around the surface normal at the point of collision, calculated from the cross-sectional geometry. A sample of this reflection technique can be seen in the figure above, showing double bounces (specular reflection) and subsequent straight-line trajectories. The first bounce (yellow-blue) illuminates the P9 electrode and outer ESA and the second bounce (blue-red) reflects back to the P3 electrode and ToF can housing. This process has been expanded to verify the 3-bounce background suppression of the ESA via simulation. A similar process is used to calculate *v_perp*, by taking the dot product of the particle velocity vector along the surface normal vector.

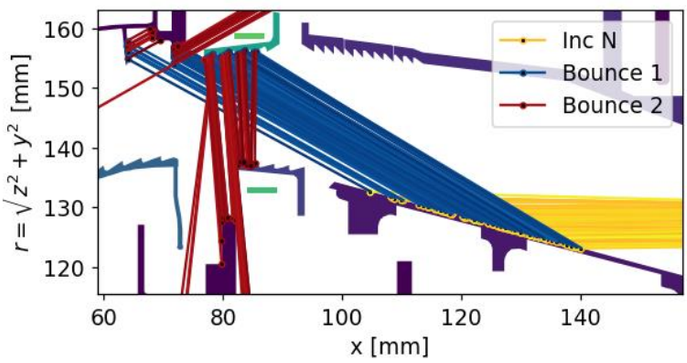


Figure 4.6.3 Specular Bounce Motion in CS chamber

The specularly reflected recoil velocity and *v_perp* are then used in conjunction with the scattering modulator functions to define the final energy and angles for the recoil ion population. The recoil ion energy (*Ke*) and elevation angle (theta) probability distributions, which control the form of the angle/energy dispersion, are chosen to be Poisson distributions.

$$y(x1) = \frac{a(xk^2)^k \exp -xk^2}{N * k!}$$

for

$$x = (x1 - c)/b \text{ and } N = \frac{k^k * \exp -k}{k!} \qquad (4.6.10)$$

While the Azimuthal angular dispersion is given the form of a normal distribution. These functional forms are chosen heuristically to represent conversion surface scattering results. Sample angular scattering distribution functions simulated and observed can be seen in Figure 4.6.4 Angular Scattering at the conversion surface. On the left we see for a tightly collimated input angular distribution (blue) the recoil ion angular distribution scatters to large FWHM (orange) in azimuth (phi) and elevation (theta). The peak of the elevation angular distribution is offset from the incident angular distribution by 30 deg due to

specular reflection at the 15 deg CS. On the right we see CS scattering angular distributions observed at Illena, and the simulated 2D scattering cone.

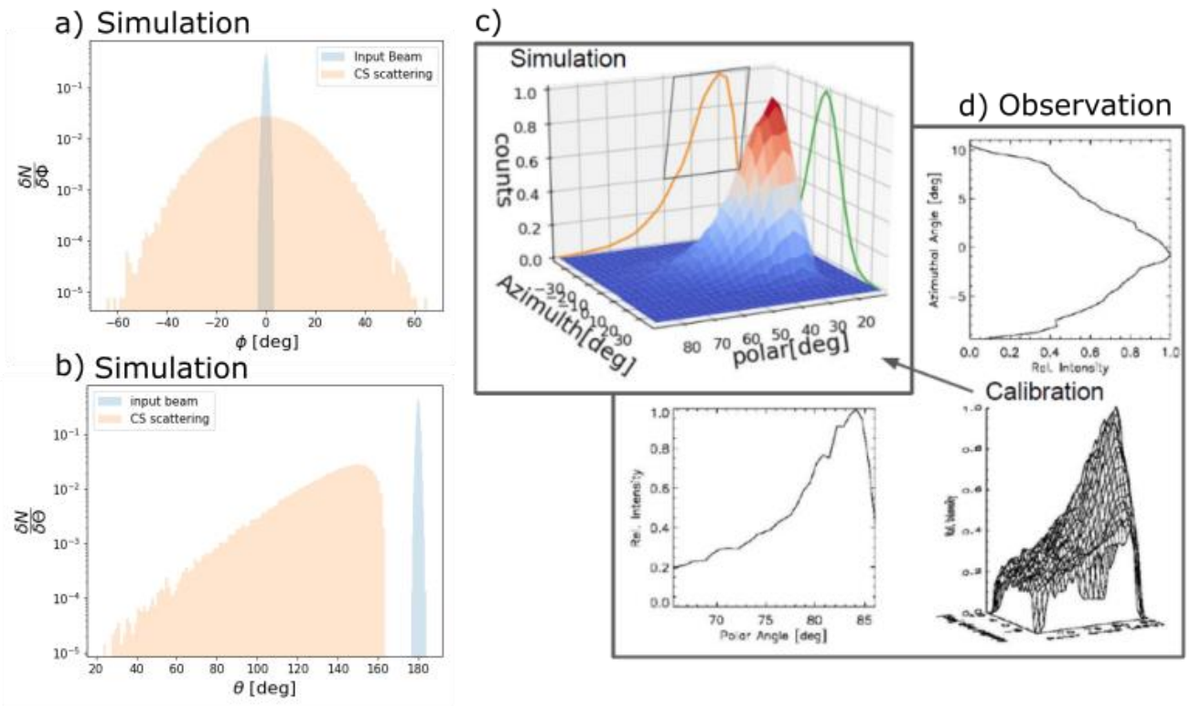


Figure 4.6.4 Angular Scattering at the conversion surface

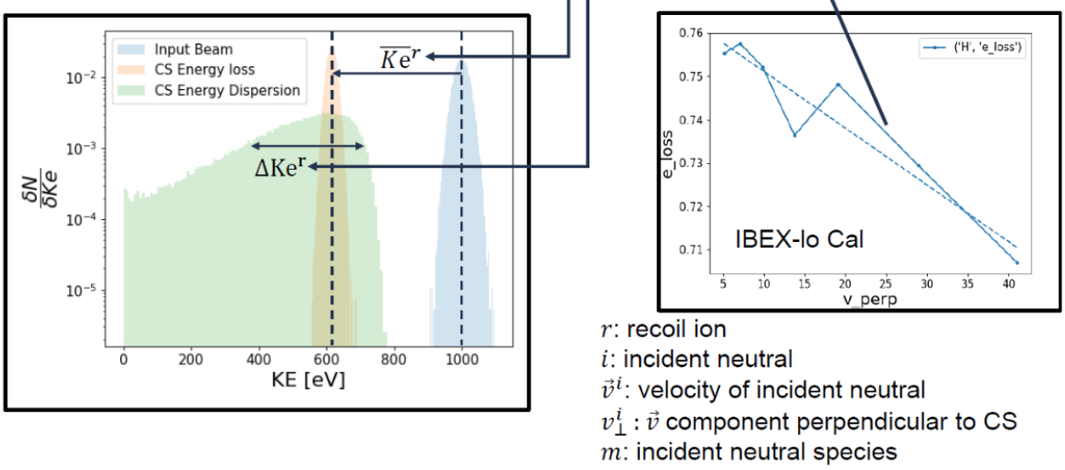
A particles final recoil energy and angle are calculated by first sampling the normalized pdf then modulating the resulting values according to the CS scattering calibration results, and IBEX-Lo calibration results, using the incident neutral perpendicular velocity. These modulation functions define key components of the recoil ion distributions.

- Ke: peak of resulting Poisson distribution determined by CS calibration energy loss curve and incident neutral v_perp
- θ: fwhm of poisson distribution determined by CS scattering calibration curves and incident neutral v_perp
- phi: fwhm of recoil Gaussian distribution.

A demonstration of this process is shown in Figure 4.6.5 Simulated CS energy Loss and Dispersion, where we see on the right, the IBEX-Lo calibrated mean energy loss, as a function of velocity perpendicular to the CS. These data were measured during IBEX-Lo Final Cal (for Esteps 1-7), and v_perp is simply calculated from the energy step center and an assumed straight-line collision on the CS of 15deg. We linear fit the data which we take as our CS scattering modulator function, and we assume an energy dispersion FWHM as half of the mean energy loss. We currently have no direct observations of the CS energy dispersion, so this will be a key calibration factor for IMAP-Lo. Now a calibration beam at 1000eV +- 50eV is defined and flown into the instrument model (blue). For each particle, we calculate an energy

loss according to the perpendicular collision velocity. If we assume no energy dispersion this shows up as a systematic shift to lower energies (orange). Finally, we introduce energy dispersion using the PDF, defined above, giving us the final energy distribution. In this scheme, the recoil ion energies are all coupled according to the incident ion collision energy and angle.

Process	Constrained by	Dependent on	Mod Function	Free Parameters
CS Energy Loss	IBEX-Lo Cal	$\vec{v}^{\mathrm{i}}(\mathrm{Ke}, \phi, \theta, \mathrm{m})$	$\overline{Ke}^r = a_1^{\mathrm{m}} v_\perp + b_1^m$	a_1^{m}, b_1^m
Energy Dispersion		CS Energy Loss	$\Delta\mathrm{Ke}^{\mathrm{r}} = c_1^m \overline{Ke}^r$	c_1^m



r: recoil ion
i: incident neutral
$\vec{v}^i$: velocity of incident neutral
$v_\perp^i$: $\vec{v}$ component perpendicular to CS
m: incident neutral species

Figure 4.6.5 Simulated CS energy Loss and Dispersion

The CS scattering measurements, along with IBEX-Lo observations are taken as a baseline to model the CS scattering effects. The full set of baseline modulator functions can be seen in Figure 4.6.6 Baseline modulator fit functions and linear fit parameters for use in the CS scattering simulator. Displayed data points for ionization efficiency (b), and angular scattering (c,d) are averaged from all FM and EM CS scattering measurements. Energy loss (a) comes from IBEX-Lo calibration. For a given species, we now have 4 energy dependent functions that determine the recoil ion distribution, and in conjunction with the ESA voltage and incident neutral beam energy distribution, we can simulate ion trajectories through the ESA and determine ESA-CS collection efficiency. The ESA-CS collection efficiency is measured in calibration as a function of beam energy and ESA mode and voltage.

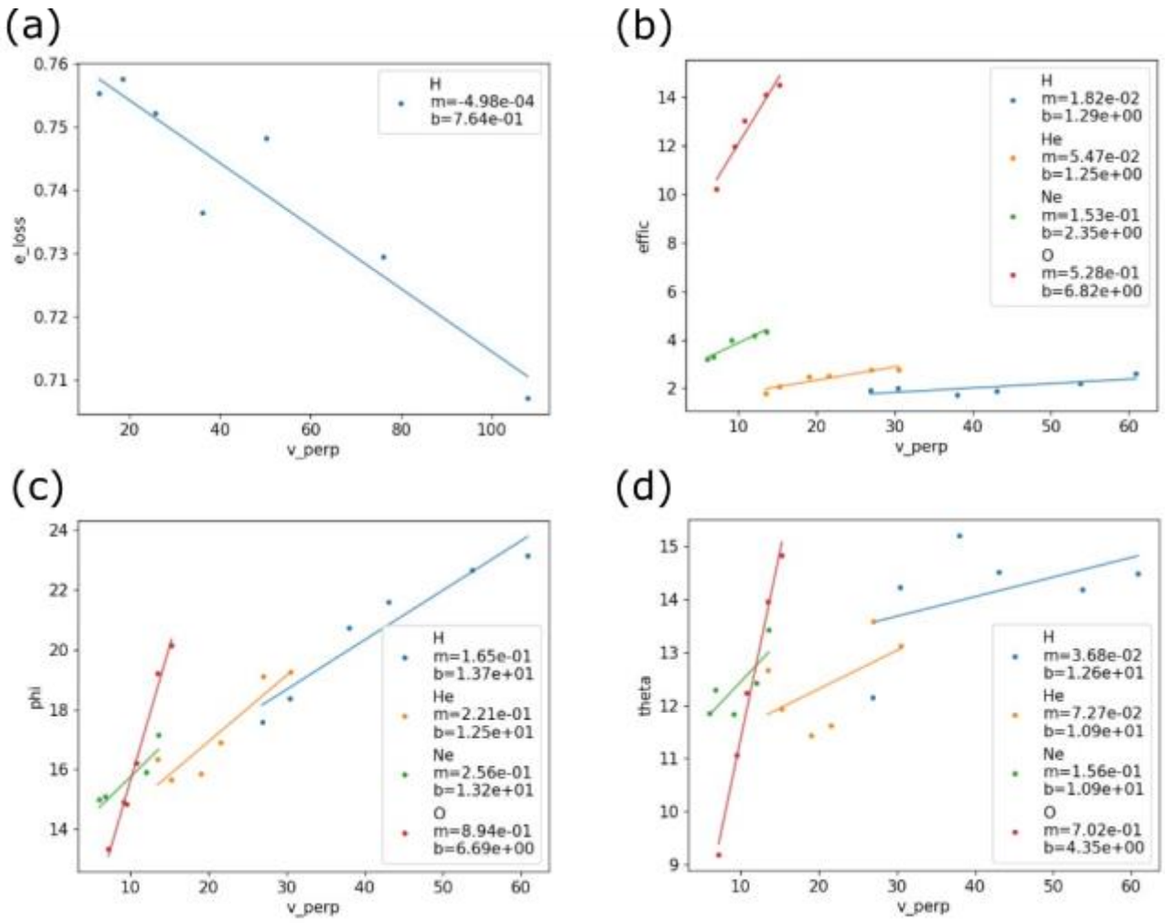


Figure 4.6.6 Baseline modulator fit functions and linear fit parameters for use in the CS scattering simulator. Displayed data points for ionization efficiency (b), and angular scattering (c,d) are averaged from all FM and EM CS scattering measurements. Energy loss (a) comes from IBEX-Lo calibration.

4.6.2.1 Calibrating the Model

The model can now be calibrated against the ESA-CS collection efficiency DER observations. For a given DER1 or DER2 calibration measurement, a beam of the calibration energy and species is simulated with some assumed energy distribution (generally a gaussian with 5-10% energy dispersion). CS scattering is calculated according to the previously described methods using the CS calibration modulation functions (shown above) as a baseline, and the recoil ion trajectories are simulated for each voltage configuration measured. The simulated ESA-CS collection efficiency for each of those points is calculated and the results are compared to observed values. We quantify the modeled goodness of fit based on the normalized collection efficiency, to compare how well the simulation represents the shape of the DER curve, according to the absolute ESA-CS collection efficiency. The normalized collection generally drives simulated energy loss and dispersion, while the total collection efficiency drives the angular scattering and conversion efficiency. We quantify the model-data offset using the chi-square residuals and we vary the modulator functions randomly until the model closely represents the observed DER measurements. With this method, the final results for the modulator functions may deviate from the original modulator

function parameters, general knowledge of the CS scattering properties is used to constrain fitting. Aside from varying fit parameters, the actual form of the modulator functions can be adjusted to improve fit accuracy.

4.6.3 H Energy Response

The DER measurements yield voltage dependent curves which we can relate to the energy response function. Here we define the parameter

ESA Voltage [E6 norm] $|_{Emode} = U+_{En}/U+_{E6}|_{Emode}$

which simply allows us to visualize the variation of the total collection efficiency with the HiTh and HiRes modes centered on the same value of ESA U+ voltage at the center peak of ESA step 6. This parameter is indirectly related to the incident particle energy, in that the energy response curves for a given step will be mirrored around an Estep peak. The DER1 curves do not yield the energy response functions directly because they do not include the energy dependent effects of scattering at the conversion surface, but we do get direct information about the electrostatics functionality.

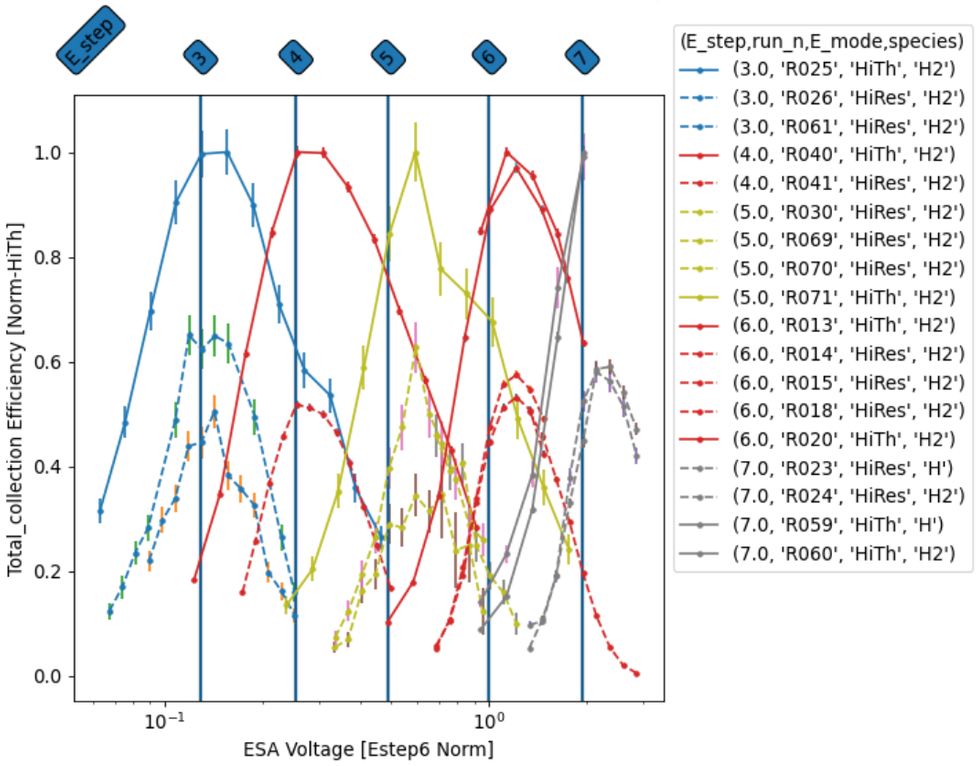


Figure 4.6.7 Normalized calibration results of H DER1 energy response measurements taken during FinalCal

In Figure 4.6.7 Normalized calibration results of H DER1 energy response measurements taken during FinalCal, we see DER measurements for Esteps 3-7 for incident neutral H energies; Estep3: 55eV (blue), Estep4: 110eV(red), Estep5: 230eV(yellow), Estep6: 465eV(orange), Estep7: 930eV(gray). In the case of Esteps < 7, the displayed results come from an H2 incident beam at twice the beam energy. For energy step 7, we have redundant measurements for a 930eV H beam and a 1860eV H2 beam showing good

agreement between the energy response functions, validating the use of molecular H2 as a proxy for a H beam. While it's possible that the instrument response to H2 could deviate from the H response at lower energies, we were unable to collect any other H2 to H comparison measurements due to the low energy source background. Based on our knowledge of the H-H2 dissociation process, any modification in the energy distribution in the H from H2 beam should be of the order of the H2 dissociation energy (4.6 eV) so is expected to be less than a 10% effect at Estep3.

We can also see redundant measurements for HiRes mode Esteps [3,5,6], showing offsets in peak height between the redundant measurements, showing statistical fluctuations in the ABM flux. The incident beam flux is needed to compare measurements with different incident rates, but with such a low energy beam, and the ABM being a foil-based detector, without any pre-acceleration, coincidence measurement statistics for several of the calibration runs are very low. This effect, along with questions about the H-H2 dissociation efficiency will ultimately limit our knowledge of the total detection efficiency.

The peak locations of the high throughput (solid lines) and High resolution (dashed lines) modes show good agreement, suggesting that the HiTh and HiRes electrostatics operate as predicted. Vertical lines are overlaid to indicate expected energy response peak locations, assuming a 30% energy loss. We can see a systematic shift of the peak locations to higher U+ voltages which seems to increase with higher energy steps, indicating that we are overestimating the energy loss by approximately 10%. We also see a consistent 50% reduction in the total collection efficiency for the HiRes mode as compared to the HiTh mode which is slightly larger than expected. Based on the initial assumptions about the energy dispersion and angular scattering at the CS, we estimated that we should see a ~20% reduction in peak collection efficiency between the HiTh and HiRes modes. The difference from predictions that we see is likely driven by an underestimation of the energy dispersion and the recoil angular scattering, which were predicted to be small due to the tightly collimated incident beam.

4.6.3.1 Final Cal DER H Modeling

Next, we calibrate the model using the observed DER1 energy response measurements shown above. As laid out in Section 4.6.2. Redundant DER measurements, same incident beam species and voltage configurations and step, (e.g. R026 and R061 shown above) are grouped and averaged to raise statistics and minimize simulation time. We start by setting up our instrument simulator environment to reflect the test setup in question, here we will be discussing results from H DER measurement in FinalCal, but this process has also been performed using H calibration measurement from PreCal2. In the case of Final cal, the instrument simulator, including the entrance system, is initialized and a 14mm diameter (centered on the CS to represent the collimating aperture) neutral ion beam, of the given species and energy is flown to the CS. The beam is assumed to have a 5% dE/E and 2deg angular spread.

Test setup particle populations and particle energy distributions for 4 beam energies can be seen in Figure 4.6.8 Incident Neutral and recoil ion energy distributions before (orange) and after (green) CS scattering. Here we can see particle energy distribution before (orange) and after (green) the CS scattering process. For calibration runs with H2, energy dispersion is added per Schlathoelter 1995, as described in Section 4.6.1.2, to account for the dissociation process. In comparing the H vs H2 energy distributions, you can see how the dissociation process increases the width of the effective incident energy distribution. The recoil ion distributions show the systematic energy loss and additional dispersion, as well as a low energy tail associated with sputtering.

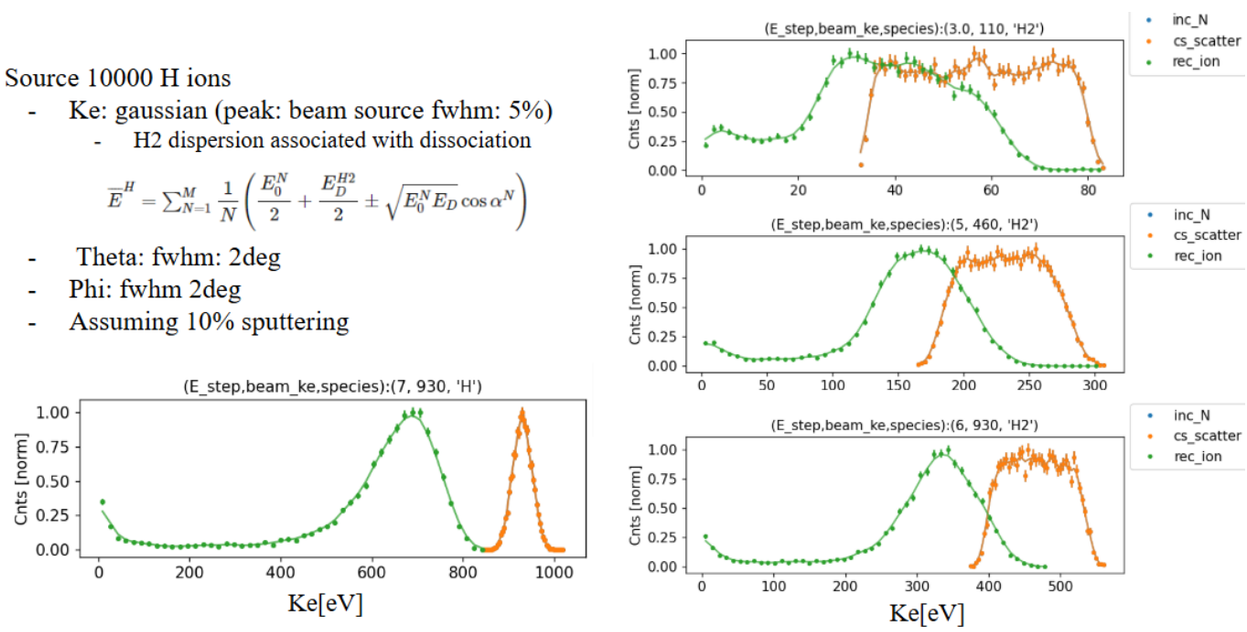


Figure 4.6.8 Incident Neutral and recoil ion energy distributions before (orange) and after (green) CS scattering

For each beam energy, neutrals are flown into the CS and the numerical scattering processes are applied to generate recoil ion particle populations. The ESA voltage is set according to each configuration of DER curve and the recoil ions are flown and ESA-CS collection efficiency for the given point is determined from the ions that survive to the TOF. The resulting simulated DER curves are then compared to observed values, and the process is repeated for new CS scattering processes.

Following this iterative process, we end up with a simulator response shape that closely agrees with calibration results. For both Hi-Th and Hi-Res modes. Simulation-Observation comparison plots showing peak normalized HiRes (a) and HiTh (b) DER curves, for ESteps 3-7, are shown in Figure 4.6.9 Simulated DER1 H Results. Here, observed (solid lines) and simulated (dashed lines) H ESA-CS collection efficiencies are overlaid, with matching colors indicating the species/energy step being compared. We can see in terms of shape, the peak location and response with match very closely. We do see some systematic deviation in the low voltage tails of the HiTh mode, suggesting that we may be underestimating the sputtering or dispersion slightly. FinalCal observations led to the implementation of a new form for the energy loss function, resulting in a strong agreement between the energy loss and response shape.

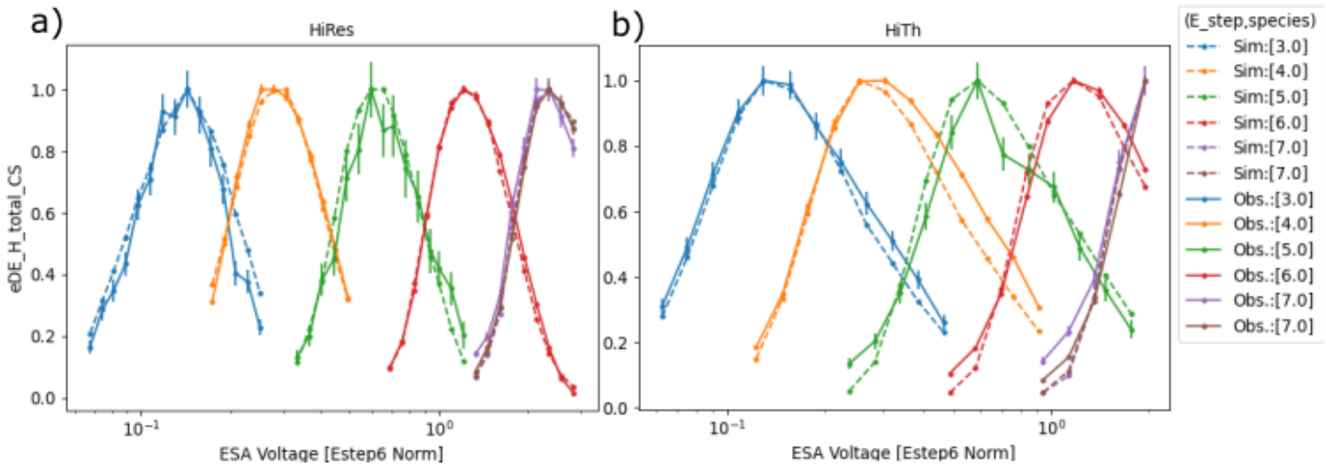


Figure 4.6.9 Simulated DER1 H Results

To quantify the variation of the ESA-CS collection efficiency across energy step we take the peak height of the simulated and observed DER curves. This parameter gives us a good idea of the relative difference between the HiTh and Hi-Res modes and a rough measure of the ESA-CS collection variation with energy. An important note here is that these are not exactly the peak collection efficiencies of the instrument energy response functions because the input beam energies are not at the nominal Estep center and we have beam related dispersion effects. Results can be seen in Figure 4.6.10 ESA-CS Peak Collection Efficiency showing observed (solid lines) and simulated (dashed) ESA-CS collection efficiency peaks for HiTh (orange) and HiRes(blue) modes.

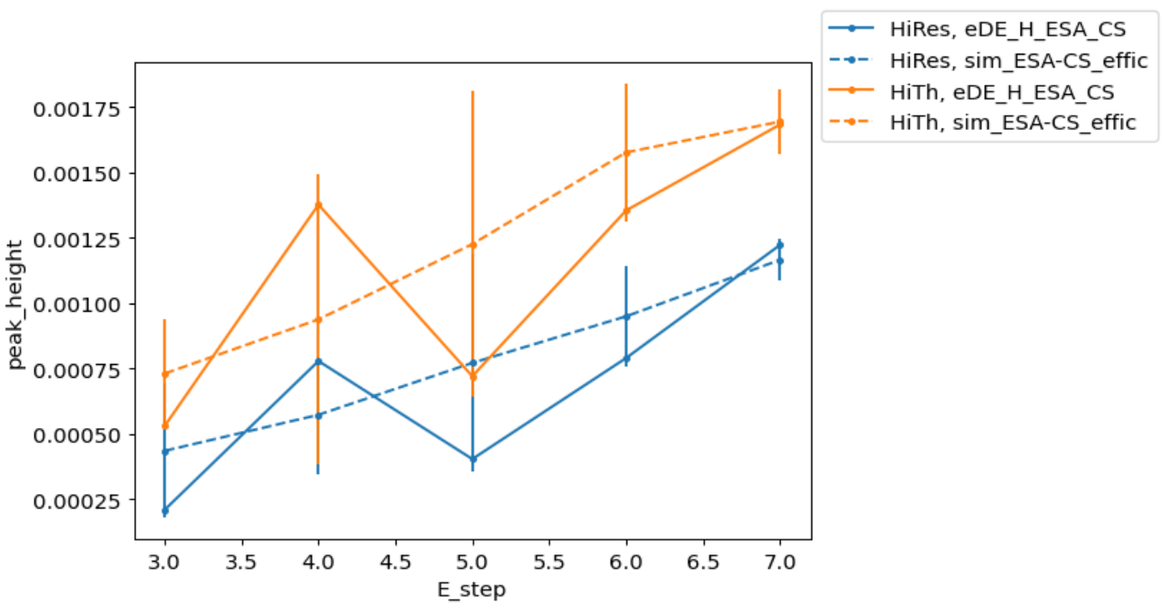


Figure 4.6.10 ESA-CS Peak Collection Efficiency

The separation in collection efficiency between HiTh and HiRes modes is fairly well represented, and the overall variation with energy is also ESA-CS collection efficiency is also well captured. However, there are observed offsets associated with fluctuations in the observed collection efficiency. For the most part, these variation are assumed to be due to low statistics in the reference ABM fluxes, but the relative increase in the collection efficiency for Estep4 has been observed in multiple runs and. If these fluctuations are confirmed to be real, the form of the energy-conversion efficiency modulator function will need to be updated. For now, the error of the collection efficiency should be considered to be as high as approximately 50%.

Following model calibration against IMAP-Lo H and H2 DER1 results, we take the CS scattering modulation functions defined by the and perform a sanity check against the IBEX-Lo calibration results FinalCal results. We make the assumption here that the CS scattering processes are identical between the two instruments. While we expect to see some differences due to random differences in the CS scattering and conversion properties, the overall functionality should be similar. We use H DER measurements taken during IBEX-Lo FinalCal [BERN 2008], and simulate the instrument response (using the IBEX-Lo electrostatics model) to a neutral particle population recoiling from the ELENA neutralization surface. Simulated and observed DER1 measurements from IBEX-Lo FinalCal can be seen in Figure 4.6.11 IBEX-lo DER1 Simulation-Calibration Comparison. Here simulation results are normalized to IBEX-Lo Estep5 peak height. The simulator shows good agreement in the shape of the energy response curves with the IBEX-Lo results. The total collection efficiency though is lower by nearly a factor of 10, largely driven by underestimation of the incident beam flux which was documented during IBEX-Lo Cross calibration.

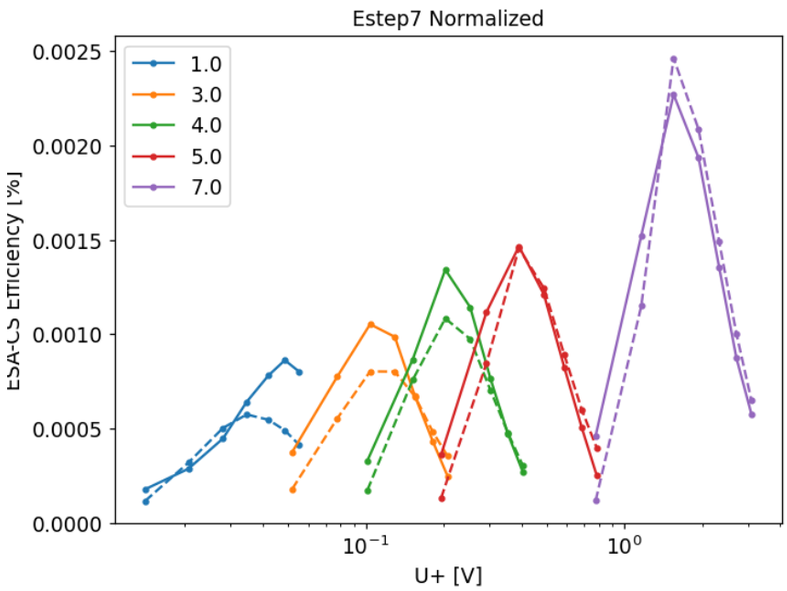


Figure 4.6.11 IBEX-lo DER1 Simulation-Calibration Comparison

4.6.3.2 H Calibrated CS Scattering Functions

We implement several changes to the functional form of the CS scattering functions based on our FM calibration results and new knowledge about the CS scattering processes. First off, for angular scattering FWHM, we use an experimentally derived “rollover function” as defined in Wurz 2006. Modulator functional forms are seen in Table 4.6.2. After attempting several different functional forms for the energy loss which did not adequately resolve both the DER1 peak locations and the distribution widths, we ended up calculating energy loss values from the FinalCal DER results. Following in the footsteps of the IBEX-Lo calibration, we estimate an energy loss for each step, based on the known incoming beam energy, the voltage of the DER1 peak location and the nominally accepted recoil ion energy for said peak voltage

(which can be easily simulated). These energy loss values are then interpolated with a cubic poly-interp using scipy.interpolate.interp1d. The efficiency is kept as a linear function. The resulting fit functions and parameters can be seen in Table 4.6.2.

Table 4.6.2 H CS scattering functions (IMAP-Lo FM FinalCal)

Process	Mod Function	Fit Parameters
CS Energy Loss (ke eloss)	$\overline{Ke}^r = scipy.interp1d(x, y, cubic)$	(x_n, y_n) = [(25.9 , 0.726), (36.3 , 0.765), (50.4 , 0.806), (76.3 , 0.828), (108.3,0.808)]
Energy Dispersion	$\Delta\overline{\mathrm{Ke}}^{\mathrm{r}} = c_1^m \overline{Ke}^r$	$c_1^H = .5$
Ionization Efficiency (effic)	$e^r = a_2^{\mathrm{m}} v_\perp + b_2^m$	$a_2^{\mathrm{H}} = .003$ $b_2^H = .051$
Sputtering Probability	$\mathrm{N}_{\mathrm{sput}}^{\mathrm{r}} = \mathrm{s}^{\mathrm{m}}\mathrm{N}^{\mathrm{i}}$	$\mathrm{s}^{\mathrm{H}} = .2$
Elevation Angular Scattering FWHM	$\Delta\theta^{\mathrm{r}} = \Delta\theta_0 \left\{1 - \exp\left(-\left(\frac{v_\perp}{v_c}\right)^{2b}\right)\right\}\left(\frac{v_\perp}{v_c}\right)^{2a}$	$(\Delta\theta_0, v_c, a_3^{\mathrm{H}}, b_3^H) =$ $(.92, 2, .153, 1.5)$
Elevation Angular Scattering FWHM	$\Delta\phi^{\mathrm{r}} = \Delta\phi_0 \left\{1 - \exp\left(-\left(\frac{v_\perp}{v_c}\right)^{2b}\right)\right\}\left(\frac{v_\perp}{v_c}\right)^{2a}$	$(\Delta\phi_0, v_c, a_4^{\mathrm{H}}, b_4^H) =$ $(1.16, 36, .224 , 1.5)$

Figure 4.6.12 shows the resulting CS scattering modulator functions, with observation data from CS scattering calibrations overlaid to show where the FM model calibration deviates from the subsystem calibration values. In Figure (a) we see the cubic polynomial interpolation of average energy loss values, the magnitudes of ~70% are roughly in line with IBEX-Lo calibration, though we see higher fractional energy loss for lower energy steps as compared to higher energy steps. The reported energy loss values from IBEX-Lo showed an inverse effect, which could be caused by the IBEX-Lo calibration results not including energy-angle coupling in their CS scattering-energy loss estimations. We know from CS subsystem calibration that higher energy particles will scatter to larger recoil angles on average which will have a lower acceptance probability through the ESA driving a shift in the apparent energy loss based on selection bias. This effect is magnified in IBEX-Lo calibration where the incident neutral beam has large energy and angular dispersion from the MEFISTO neutralizer.

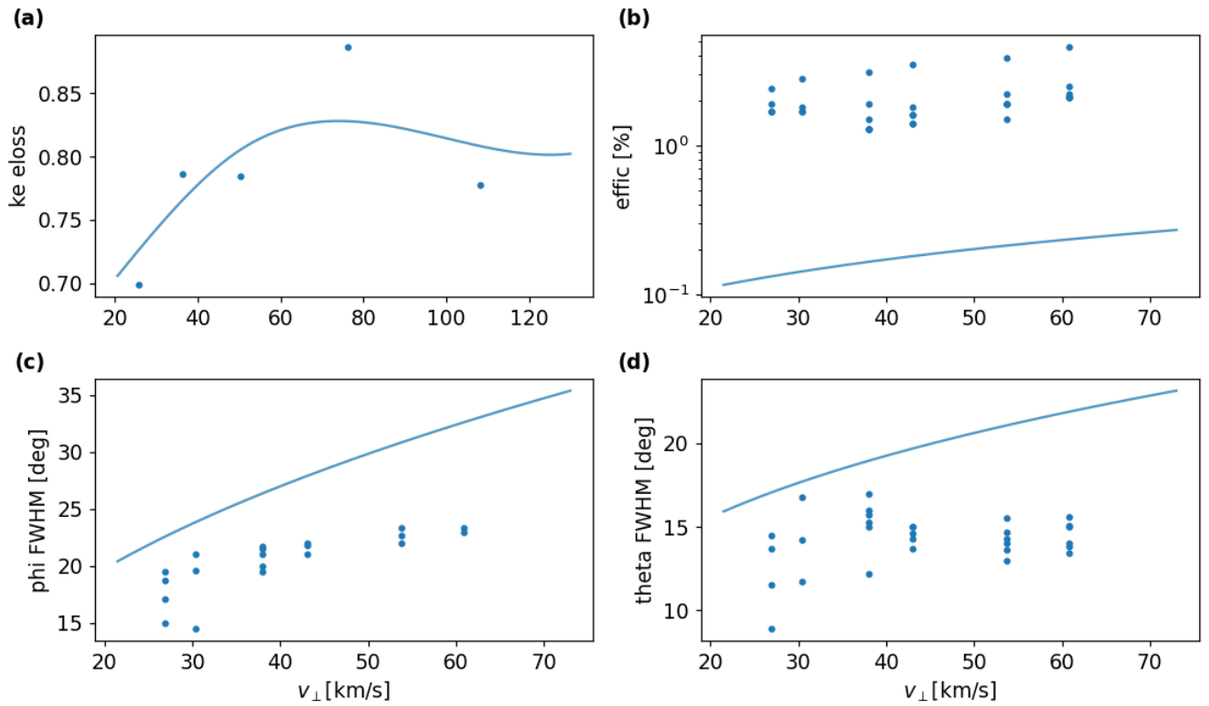


Figure 4.6.12 Calibrated CS scattering velocity functions (lines). response functions are overlayed on CS scattering observations (points) for reference. The discrepancy between the observed points and simulated lines indicate model optimized results that differ from our subsystem calibration results.

The angular scattering modulator functions (c) and (d) show increased scattering FWHM as compared to the CS scattering observations. This isn't too surprising, because in CS subsystem calibration H recoil distributions routinely exceeded the detector FoV (21deg), forcing the FWHM to be determined from extrapolation and thus prone to underestimation. The surprising result here is that the conversion efficiency (b) we observe is approximately a factor of 10 lower than the CS subsystem calibration result. The cause of this offset has not yet been determined and will be investigated further in post FM delivery CS scattering calibration (summer 2025). Similar ESA-CS survival probabilities were observed in IBEX-Lo FM calibration, leading us to believe that our process here is sound. Several possibilities exist for the conversion-reflection efficiency being so much lower than anticipated.

1. Conversion surface Ionization efficiency is overestimated in CS subsystem calibration
2. Recoil ion scattering angles are much larger than expected
3. We have a much larger rate of sputtering than expected
4. Negative ion yield measured during CS subsystem is not representative of the conversion efficiency

In CS subsystem calibration, the reported ionization efficiency is determined by measuring the fraction of the recoil particles that are negatively charged. This parameter is fundamentally different from the reported conversion-reflection efficiency here which is a measure of the fraction of negative ions that recoil as compared to the incident neutral particle population. The critical assumption in the CS calibration is that

every incident particle survives the bounce process, making the relative measure of the ionization efficiency equivalent to the conversion-reflection efficiency. What this parameter does not account for is lost to the CS though adsorption. Previous literature suggests that the ionization efficiency and the conversion-scattering efficiency should be equivalent, but this process may depend on the actual conversion surfaces in question, their substrate, smoothness and coating.

The other option essentially boils down to a larger fraction of particles being lost due to their recoil angular scattering on the CS. CS subsystem calibration has a limited FoV, and since the recoil scattering angles increase for larger incident angle, the baseline measurements are collected at a incident angle of 8 deg. Here these 8 deg results are extrapolated to 15deg based on the parametrization of recoil scattering against $v_{\perp}$. It is possible that this parametrization doesn't hold for 15deg incident angles, leading us to underestimate the recoil scattering. Direct measurements of the conversion-scattering efficiency and recoil scattering distribution at 15 degs are planned for post-FM delivery.

4.6.3.3 Energy Response Calibration Error

Excerpt from ***20250516_FinalCal H_ESA-CS Error Estimation Bower.docx***

We estimate the error associated with the ESA-CS conversion collection efficiency ($\xi\chi$) using the model fit accuracy, variation between the CS facets, and observation statistics from the instrument and the ABM count rates. There errors reported here feed directly into the GF, and constitute the bulk of the estimated error.

The variation of the CS facets, we estimate from the roll response measurements shown in Section 4.5, Figure 4.5.2. We calculate an average count rate for each of the CS facets (marked by purple vertical lines) not obstructed by the spokes, and calculate the standard error of the mean from the resulting count rates.

$$\delta_{CSfacet} = \frac{\sigma_R}{\overline{R}} = .042 \qquad (4.6.11)$$

Here N is the number of unobstructed facets we observed (15). \sigma_R is the standard deviation of the count rates, \bar{R} is the average count rate of all N facets. Next we estimate the fit error of the calibrated instrument simulator by calculating the standard estimate error from the observation and simulation ESA-CS collection efficiency shown in Section 4.6.3.1 Figure 4.6.9. The standard error of the estimate is given by:

$$\delta_{ESA-CS}^{Estep,Emode} = \sqrt{\frac{\Sigma_{n=0}^{N}(\xi\chi_n^{obs} - \xi\chi_n^{sim})^2}{N(\xi\chi_{max}^{sim})^2}} \Bigg|_{Estep,Emode} \qquad (4.6.12)$$

Here, for a given step and voltage mode, we have N observed ($\xi\chi obs$) and simulated ($\xi\chi sim$) ESA-CS conversion collection efficiencies measurements. We calculate the relative error using the maximum ESA-CS collection efficiency (ξχ^sim_max) as our normalization factor. Finally, the statistical error of the observed H counts and the total ABM coincidence counts for the test runs in consideration are calculated.

$$\delta N_{ABM} = \frac{1}{\sqrt{N_{ABM}}}$$

$$\delta N_{IMAP-lo} = \frac{1}{\sqrt{N_{IMAP-Lo}}}$$

(4.6.13)

The total error is determined by adding the previous 4 error measurements in quadrature. The resulting errors can be seen in Table 3.6.4, all of the resulting values are relative errors.

Table 3.6.4 H Estep-Emode Calibration Error

E_mode	E_step	dESA-CS	dN_abm	dCS-Facet	dN_IMAP-lo	Total Rel. Error
HiRes	3	0.39	0.577	0.04	0.06	0.70
HiRes	4	0.27	0.020	0.04	0.02	0.27
HiRes	5	0.31	0.017	0.04	0.09	0.32
HiRes	6	0.11	0.001	0.04	0.01	0.11
HiRes	7	0.04	0.001	0.04	0.02	0.06
HiTh	3	0.17	0.577	0.04	0.04	0.61
HiTh	4	0.36	0.020	0.04	0.01	0.36
HiTh	5	0.27	0.017	0.04	0.06	0.28
HiTh	6	0.10	0.001	0.04	0.01	0.11
HiTh	7	0.03	0.001	0.04	0.01	0.05

4.6.3.4 H Energy Response Functions

With the IMAP-Lo instrument model calibrated, we can now determine the H energy response functions of the ESA-CS collection from simulation. These response function fits can then be fed directly into the determination of the H geometric factor. To generate these curves, a uniform (flat) energy distribution is defined with an upper bound in energy 2.5x the expected ESA passband center for a given step. To account for the collimator response, the incident neutral particle population uniformly covering collimator exit is defined with angular spread associated with the collimator FoV (9x9deg FWHM Gaussian). This is a slight simplification, as it doesn't include the collimator edge effects, expected to be a small effect, direct implementation of the collimator FoV is planned in additional iterations of the simulator. Incident neutrals that hit the conversion surface are scattered according to the calibrated CS scattering model and the recoil ion trajectories are propagated to the TOF. Surviving particles are binned according to their incident neutral energy and yielding the instrument detection efficiency as a function of incident neutral energy.

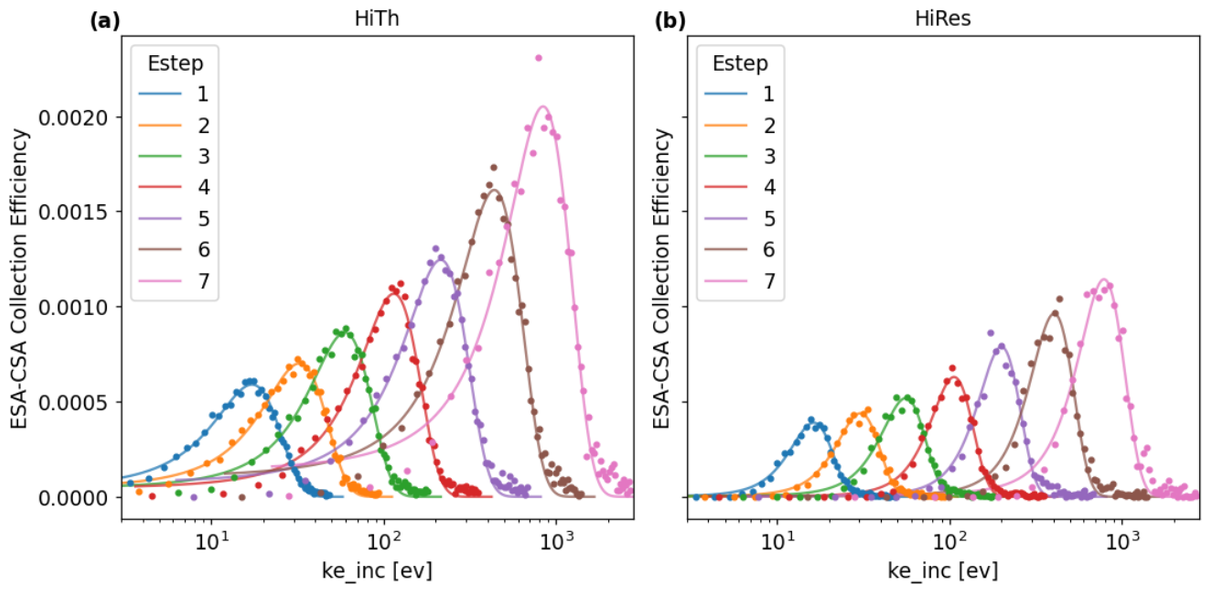


Figure 4.6.13 Model predicted H instrument response functions determined from CS scattering model fit to H and H2 DER1 measurements from FinalCal [PSPL 2024]

Table 4.6.4 H Energy response parameters determined from gaussian distributions fit to modeled energy response functions. Extrapolated Estep values indicated by **

E_mode	estep	peak [eV]	fwhm [eV]	de_e	Effic_ESA-CS Mean |FWHM|	Error Effic_ESA-CS	p0['a','x0','sigma']	p0_err
HiRes	**1****	16.33	10.78	0.66	3.14E-04	NA	[3.89045837e-04 1.63285280e+01 4.57952884e+00]	[9.89917516e-05 1.72087448e-02 2.26461447e-02]
HiRes	**2****	30.47	20.12	0.66	3.54E-04	NA	[4.38614770e-04 3.04730207e+01 8.54915086e+00]	[0.0002669 0.01435541 0.01831059]
HiRes	3	55.76	37.97	0.68	4.18E-04	0.70	[5.18260005e-04 5.57730958e+01 1.61294226e+01]	[0.0009584 0.01609461 0.02083546]
HiRes	4	106.26	69.31	0.65	5.08E-04	0.27	[6.29097720e-04 1.06283504e+02 2.94289070e+01]	[0.00344788 0.01836809 0.02399327]
HiRes	5	200.04	130.10	0.65	6.36E-04	0.32	[7.88237930e-04 2.00011130e+02 5.52337354e+01]	[0.00928949 0.01713908 0.02250074]
HiRes	6	404.96	272.03	0.67	7.77E-04	0.11	[9.62622378e-04 4.04859947e+02 1.15504197e+02]	[0.03851489 0.01844697 0.02534967]

HiRes	7	787.29	565.11	0.72	9.22E-04	0.06	[1.14263827e-03 7.87201212e+02 2.39974360e+02]	[0.13292328 0.02091848 0.02885354]
HiTh	**1****	17.19	17.73	1.03	4.76E-04	NA	[5.89570693e-04 1.71957216e+01 7.52898623e+00]	[0.00019892 0.01356994 0.02228351]
HiTh	**2****	32.36	32.36	1.00	5.65E-04	NA	[7.00517158e-04 3.23729128e+01 1.37421978e+01]	[0.00052802 0.01153368 0.01824901]
HiTh	3	59.48	57.18	0.96	6.96E-04	0.61	[8.62507733e-04 5.94864154e+01 2.42791882e+01]	[0.00195245 0.01349505 0.02081633]
HiTh	4	114.41	107.03	0.94	8.61E-04	0.36	[1.06688675e-03 1.14404657e+02 4.54534004e+01]	[0.00580131 0.01118865 0.01785659]
HiTh	5	213.70	211.86	0.99	1.04E-03	0.28	[1.24524106e-03 2.13754873e+02 8.99716991e+01]	[0.02337545 0.01420873 0.02280553]
HiTh	6	437.36	440.44	1.01	1.70E-03	0.11	[1.61171559e-03 4.37360126e+02 1.87134726e+02]	[0.07017751 0.01199105 0.01982356]
HiTh	7	838.88	850.61	1.01	2.73E-03	0.05	[2.05072206e-03 8.38851936e+02 3.61064426e+02]	[0.25331923 0.01406093 0.02269158]

The simulated energy response curves are fit with gaussian distributions, the resulting energy response curves are shown in Figure 4.6.13 with resulting fit parameters shown in Table 4.6.4. An important note here is that Esteps 2 and 1 have not been measured directly using the IMAP-Lo FM, and thus rely on extrapolation of the CS scattering parameters to low energies. The CS scattering model has been validated against Estep1 IBEX-Lo FM DER1 results, but model agreement for Estep1 has not been shown.

4.6.4 O Energy Response

We follow the same process outlined in the determination of the H energy response to determine the O energy response. Here we use DER1 energy response curves generated while observing 460/500eV, 700 eV and 930eV O and H2O neutral beams.

There are a couple key differences which we have to account for in the O energy response calibration. For hydrogen, we can estimate the low energy background by examining the relative H/O fluxes; however, because oxygen sputters both O and H, we cannot use this method to correct the incident beam flux to account for the low energy source background. As a result, the oxygen detection efficiency is determined directly from the ABM flux without any correction. Additionally, mass selection for heavy ions is challenging, as Wien filters have lower resolution for larger ions, which likely leads to some contamination from neighboring species. However, in terms of collection efficiency, this is not a significant issue since we expect minimal differences between O, OH, and H_2O in the conversion efficiency and CS scattering.

We use Ne as a proxy to estimate the sputtering contribution, as Ne has a similar mass to O and produces only sputtered recoil ions, making it a suitable reference for assessing O sputtering. By comparing the CS scattering subsystem conversion efficiency of O and Ne, we estimate the total sputtered fraction to be approximately 0.3, which includes both sputtered H^- and O^- ions. Since our focus is on the contribution of sputtered O in the O energy response, we further refine this estimate using DER2 Neon results obtained with 400 eV and 700 eV beams. From these tests, the relative rates of H to O were determined and averaged across the voltage scans, yielding an H/O fraction of 3.8. Combining these two supplemental calibration results, we estimate an O-O sputtering probability of approximately 8%.

As with the H calibration results, DER1 O Rates, counts and detector efficiencies are determined and combined for in voltage sub steps. In Figure 4.6.14 we can see observed energy response measurements for Estep6 (c/d), Estep6.5 (b) and Estep7 (a) to neutral beam energies of 460/500eV, 700 eV and 930eV respectively. Estep 7 O and Estep 6.5 H2O results show clear peaks at the approximate voltage we expect from our energy loss results from IBEX-Lo Calibration. We do see some systematic skew of the response curves to lower energies, likely associated with low energy source contamination and/or sputtering.

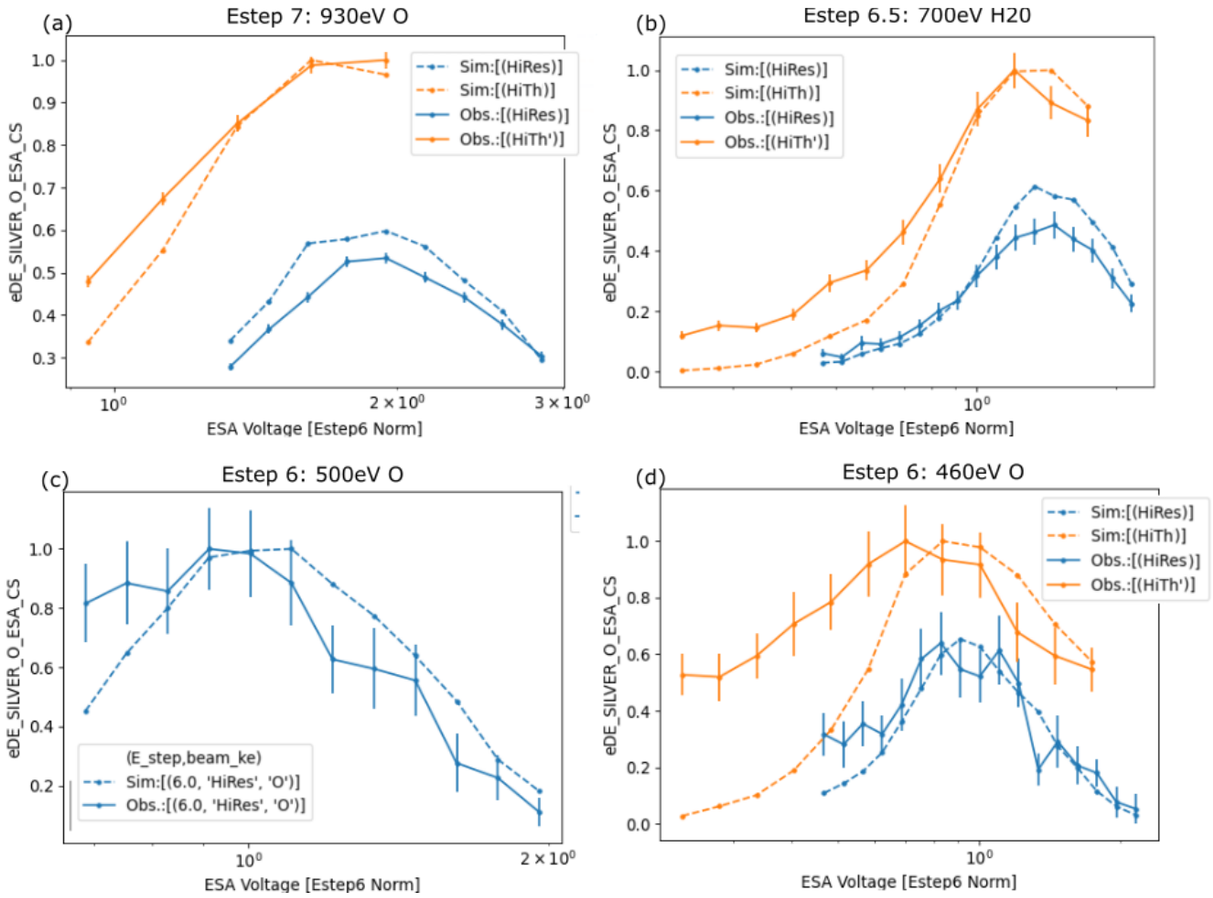


Figure 4.6.14 O DER1 Energy response curves collected during FinalCal

Due to the limitations described previously, we were only able to collect response curves down to Estep 6 before background signals began to dominate. To supplement our modeling below Estep 6, we incorporated the IBEX-Lo oxygen ESA-CS collection efficiencies to construct a version of the conversion

efficiency modulator function that more accurately reflects the instrument's response at low energies. The IBEX-Lo results were implemented by normalizing ESA-CS collection efficiency to Estep 6.5, where we have a directly comparable measurement from the IMAP-Lo final calibration. This approach assumes that the relative conversion efficiency between Estep 6 and Estep 1 is consistent between the two instruments. By doing so, we eliminate systematic differences between the IBEX-Lo and IMAP-Lo calibration test setups, allowing us to estimate the Conversion efficiency down to Estep 1. Resulting extrapolated ESA-CS collection efficiency peaks can be seen in Figure 4.6.15.

Following the regression of the CS scattering model, we observe strong agreement between the model and experimental data, though not with the fidelity of the calibrated H model. In Figure 4.6.14 (a) and (b), the model accurately reproduces the peak location and width, with the observed oxygen (O) energy loss of approximately 40%, which is consistent with results from IBEX-Lo. In Figure 4.6.14 (c) and (d), the model continues to perform well in the region where U+>Upeak+U^+ > U^+_{\text{peak}}U+>Upeak+, although there appears to be significant contamination from low-energy particle populations in the Estep 6 HiTh mode. The separation between HiTh and HiRes modes is also well captured, indicating that the angular scattering behavior is accurately represented. This supports the conclusion that the CS subsystem angular scattering fit results can be used directly with confidence.

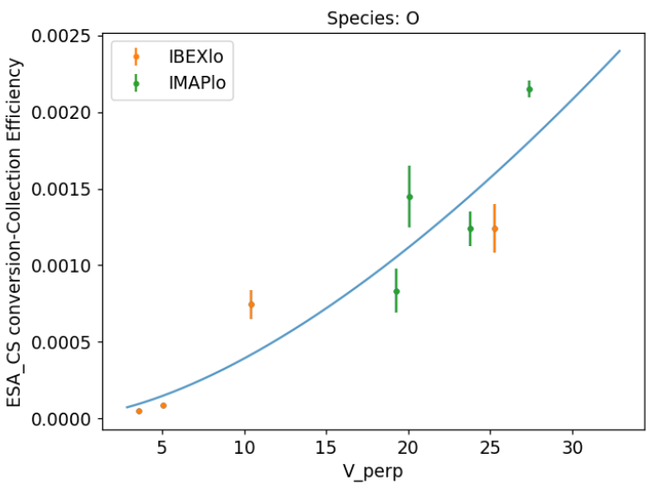


Figure 4.6.15 ESA-CS collection efficiency extrapolated with IBEX-lo FinalCal results

The resulting fit functions and fit parameters for the calibrated CS scattering model can be seen in Table 4.6.5.

Table 4.6.5 O CS scattering model calibrated

Process	Mod Function	Fit Parameters
CS Energy Loss (ke eloss)	$\overline{Ke}^r = a_1^m v_\perp + b_1^m$	(x_n, y_n) = (-0.00162, 0.62)
Energy Dispersion	$\Delta\overline{\mathrm{Ke}}^{\mathrm{r}} = c_1^m \overline{Ke}^r$	$c_1^O = .5$
Ionization Efficiency (effic)	$e^r = a_2^m v_\perp + b_2^m$	$a_2^O = .003$ $b_2^O = .051$
Sputtering Probability	$\mathrm{N}_{\mathrm{sput}}^{\mathrm{r}} = \mathrm{s}^{\mathrm{m}}\mathrm{N}^{\mathrm{i}}$	$\mathrm{s}^{\mathrm{H}} = .2$

Elevation Angular Scattering FWHM	$\Delta\theta^{\mathrm{r}} = \Delta\theta_0\left\{1-\exp\left(-\left(\frac{v_\perp}{v_c}\right)^{2b}\right)\right\}\left(\frac{v_\perp}{v_c}\right)^{2a}$	$(\Delta\theta_0, v_c, a_3^O, b_3^O) = (.06, 2.5, .317, 1.5)$
Elevation Angular Scattering FWHM	$\Delta\phi^{\mathrm{r}} = \Delta\phi_0\left\{1-\exp\left(-\left(\frac{v_\perp}{v_c}\right)^{2b}\right)\right\}\left(\frac{v_\perp}{v_c}\right)^{2a}$	$(\Delta\phi_0, v_c, a_4^{\mathrm{H}}, b_4^H) = (.245, 7.9, .29, 1.5)$

Now again, with the model calibrated to the O DER response curves we can now determine the O energy response functions of the ESA-CS collection from simulation. To generate these curves, a uniform (flat) energy distribution is defined with an upper bound in energy 2.5x the expected ESA passband center for a given step. To account for the collimator response, the incident neutral particle population uniformly covering collimator exit is defined with angular spread associated with the collimator FoV (9x9deg FWHM Gaussian). Incident neutrals that hit the conversion surface are scattered according to the calibrated CS scattering model and the recoil ion trajectories are propagated to the TOF. Surviving particles are binned according to their incident neutral energy and yielding the instrument detection efficiency as a function of incident neutral energy.

The resulting energy response functions and fit parameters can be seen in Figure 4.6.16 and Table 4.6.7 respectively. Here the response functions are fit with a log modified gaussian of the form:

y(x) = a*(x*\sigma*\sqrt{2*\pi})^{-1}\exp{-(\log(x) - \mu)^2/(2\sigma^2)} (4.6.14)

Fit parameters for the energy response functions are available in the

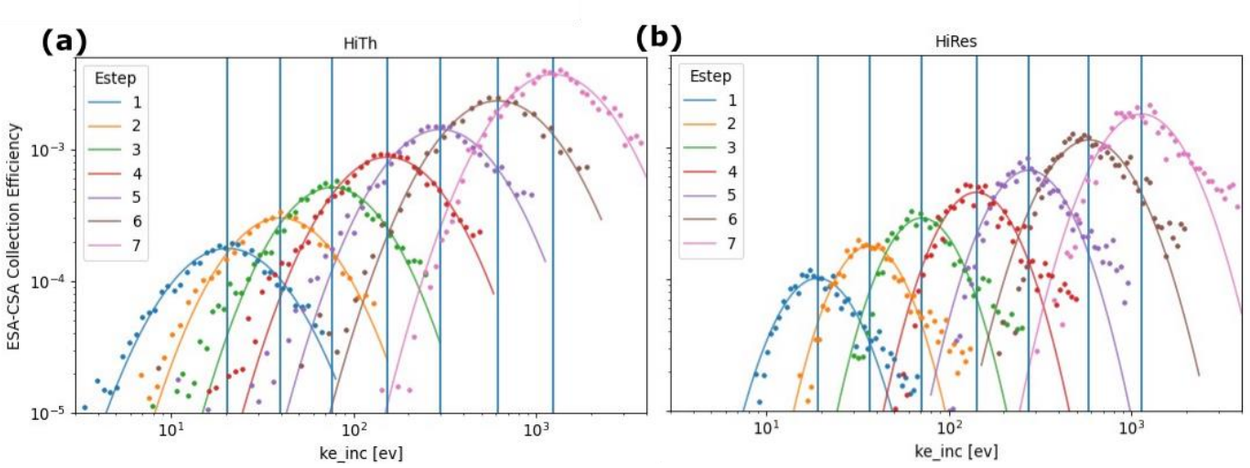


Figure 4.6.16 O Energy Response functions (a) HiTh mode and (b) HiRes Modes

Table 4.6.6 O Energy Response Parameters. Extrapolated results are indicated by Estep**

E_mode	estep	peak [eV]	fwhm [eV]	de_e	Effic_ESA-CS Mean |FWHM|	p0[a,sigma,mu]

HiRes	**1****	19.19	20.56	1.07	7.85E-05	[2.33682783e-03 4.35718181e-01 3.14433977e+00]
HiRes	**2****	36.75	35.68	0.97	1.39E-04	[0.00708144 0.3973185 3.76230749]
HiRes	**3****	71.21	71.68	1.01	2.26E-04	[0.02317395 0.4111746 4.43472341]
HiRes	**4****	141.41	147.08	1.04	3.53E-04	[0.07467691 0.42375507 5.13148341]
HiRes	**5****	274.00	297.01	1.08	5.18E-04	[0.22283057 0.44032831 5.80680964]
HiRes	6	585.03	702.29	1.20	8.71E-04	[0.90550887 0.48351008 6.60523335]
HiRes	7	1135.06	1344.40	1.18	1.37E-03	[2.71377238 0.47737851 7.26239252]
HiTh	**1****	20.43	33.68	1.65	1.30E-04	[0.00708839 0.63798117 3.42445785]
HiTh	**2****	39.72	61.50	1.55	2.23E-04	[0.02179638 0.60513381 4.04795327]
HiTh	**3****	76.48	113.25	1.48	3.83E-04	[0.06792887 0.58210501 4.67582685]
HiTh	**4****	153.53	240.64	1.57	6.45E-04	[0.24749292 0.61144643 5.40767708]
HiTh	**5****	298.46	471.76	1.58	1.04E-03	[0.78669072 0.61584467 6.07780049]
HiTh	6	615.24	1018.79	1.66	1.70E-03	[2.82551282 0.64048518 6.83253819]
HiTh	7	1242.82	1967.91	1.58	2.73E-03	[8.59302422 0.61660314 7.50534532]

The final results yield energy step centers that are roughly in line with the IBEX-Lo observations. However, the high levels of dispersion observed in the final calibration DER curves result in much wider energy passbands than initially expected; for instance, the 0.7 and 1.1 modes are more in line with 1.0 and 1.5, respectively. Consequently, the resulting response functions are highly asymmetric compared to the H results, a characteristic likely driven by the elevated dispersion.

4.6.5 D-H Conversion Efficiency

Due to time constraints during Final-Cal, we were unable to perform a full suite of calibration tests to determine the D detection efficiency and energy response. Our baseline assumption, the same assumption made in the IBEX-Lo observations, is that D and H conversion and scattering efficiency are comparable and can be ignored. Rather than rely on that assumption wholesale, we chose to perform a spot check determination of the relative conversion collection efficiency and a single measurement of the DER1 energy response.

We estimate the relative conversion efficiency for H-D using a 330eV D-H ion beam. Molecular DH ion beam at this energy will dissociate prior to the CS, and yield a ~110eV H beam and a 220eV D beam, which we will observe in Esteps 4 and 5, respectively. This specific beam energy/energy step was chosen out of convenience, because it provided high enough flux to collect the measurement in a reasonable amount of time.

We make the key assumption: for this beam configuration, all of the observed H and D is generated from a pure H-D beam and should make up equal parts of the beam composition. The relative conversion efficiency can then be measured by comparing the maxima of the H and D DER curves. We eliminate energy dependence of the conversion-collection efficiency by expressing the D collection efficiency relative to H at the same energy step:

$$\frac{\xi\chi_D}{\xi\chi_H} = \frac{\xi\chi_D^{DH-E5}}{\xi\chi_H^{DH-E4}} \frac{\xi\chi_H^{H2-E4}}{\xi\chi_H^{H2-E5}} \tag{4.6.15}$$

We find relative errors for the relative efficiencies for the two modes from the counting statistics of the considered measurements added in quadrature.

$$\delta\left(\frac{\xi\chi_D}{\xi\chi_H}\right) = \sqrt{\frac{1}{N_D^{DH-E5}} + \frac{1}{N_H^{DH-E4}} + \frac{1}{N_H^{H2-E5}} + \frac{1}{N_H^{H2-E4}}} \tag{4.6.16}$$

Looking at the TOF spectra, we see clear separation of the D signal from the H signal. Species rates are accumulated in TOF0, TOF1, and TOF2 bins, as described in the TOF calibration document. The reported species dependent ESA-CS efficiencies are selected for species according to their TOF2 measurement, as it should be the least impacted by energy loss.

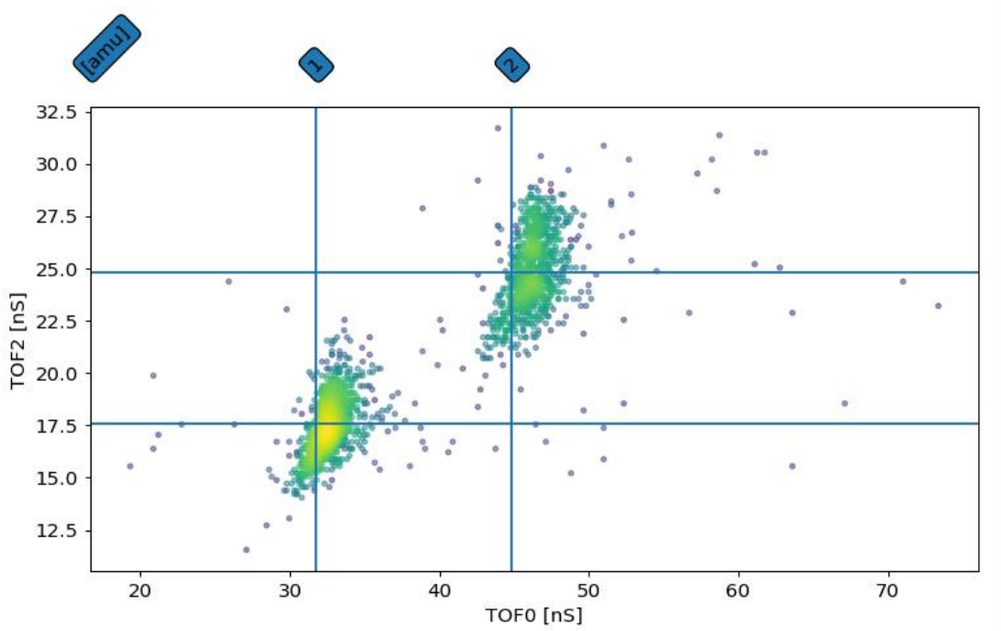


Figure 4.6.17 D-H 2D TOF spectra, overlaid lines indicate the expected mass location for the H (amu=1) and D (AMU= 2) peaks

In comparing H-D DER curves we can see that the energy response for D is similar to the H energy response.

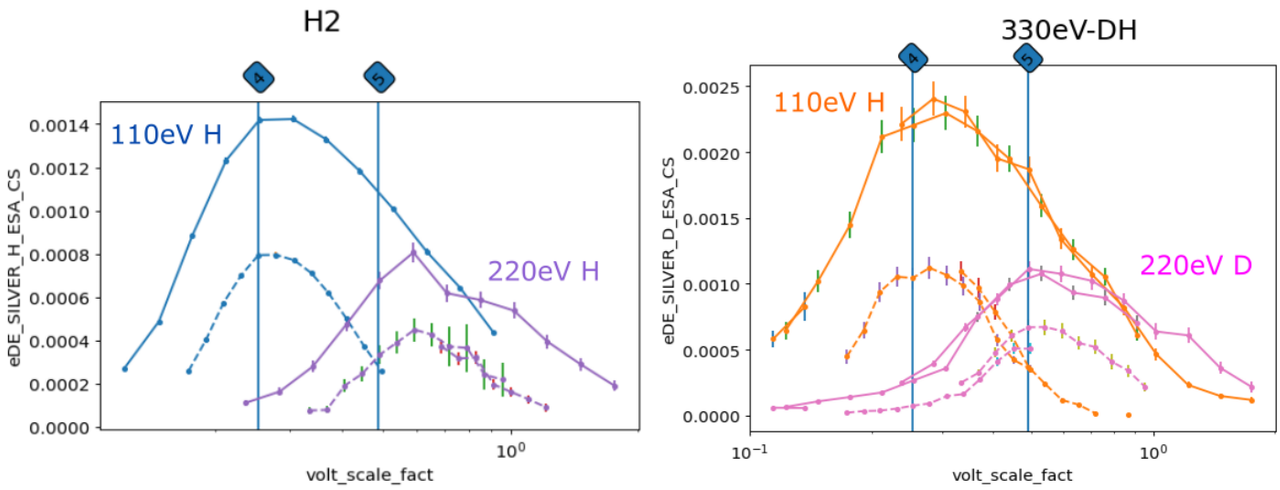


Figure 4.6.18 DER1 Energy voltage curves of 220eV Estep 5 H (Left, purple) and D (right, pink), compared to 110eV Estep4 H (blue/orange)

In Figure 4.6.18, we can see that there is a large decrease in the collection efficiency in the Estep5 D response as compared to the Estep4 H. Our baseline assumption is that conversion-collection efficiency

decreases with lower energy steps, but in the case of our H2 energy response curves, we also see an increase in the collection efficiency in Estep 4 relative to Estep5. We find relative errors for the relative efficiencies for the two modes from the counting statistics of the considered measurements added in quadrature.

Table 4.6.8

E_mode	$\xi\chi D/\xi\chi H$	$\delta\,(\xi\chi D/\xi\chi H)$
HiRes	0.944	0.199
HiTh	0.821	0.156

We use this spot check of the relative ESA-CS conversion-collection efficiency to calculate the instrument GFs for D based on the H geometric factors. This relies on the assumption that the scattering and conversion effects on the CS are similar between the two species across all energy passbands. With the limited results we do have, it appears that D scattering is more reflective of the H scattering and conversion processes than O, but we have not performed validation of this assumption across multiple energy steps. Ultimately, the D conversion collection efficiency and thus the GF should be given increased errors in accordance with this assumption.

Here we technically meet the required accuracy for the conversion efficiency calibration requirement though there are still some questions to be addressed. Additional post-delivery calibration will probe further into the specifics of the D collection efficiency and any deviations between the energy dependence of the H-D response should be identified. Post-FM EM calibration will attack this question from two sides, the first at MEFISTO by expanding CS scattering calibration to lower energies and to include a D scattering results, and the second at PSPL performing further characterization of the EM response. These measurements will work as a hinge point to relate the EM D response to the FM and eliminate any differences between the surfaces or geometries between the two systems.

4.7 Instrument Background

IBEX-Lo has shown a ubiquitous internal background of ≈0.007 Cts/s, particularly in the lowest 4 E-Steps [Galli et al., 2017]. In a detailed study in orbit and a TV Test with the IBEX-Lo ETU, this background could be attributed to the inner edge of the electrode P10, which was then modified for IMAP-Lo as compiled in a Technical Memo [Möbius et al., 2020]. During Final Calibration and Cross-Calibration, extensive Background runs were performed in various configurations. We will first discuss the Background Runs during Final Calibration, then the ones during Cross-Calibration, followed by a combined evaluation of all runs.

The run parameters and instrument conditions for all Background runs during Final Calibration are compiled in Table 4.7.1.

Table 4.7.1: Final Calibration Background Run parameters

Run	ESA	MCP	Beam	Total Accum [s]	Total TOF #DEs	Total Type 1111	Total H-	
2		72	no	925	158	1	0	
3		72	no	1219	199	3	0	
22		72	no	649	180	0	0	
32		72	no	611	156	0	0	
74		72	no	854	337	2	0	
76		72	no	977	397	0	0	
77		72	no	976	431	2	0	
93		72	no	809	266	1	0	
102		72	no	1525	594	4	0	
116	E7	Set 72	930 eV He, scatt	3539	1296	3	0	
136		72	no	2014	854	5	0	
149	E7	72-82	no	2166	2626	2	0	
150	DER2 HiThr	72	no	4195	1546	4	0	
151	DER2 HiRes	72	no	4210	1607	5	0	
152	DER2 HiRes	82	no	2106	7980	9	0	
All Final Cal			*Sum*	*26775*	*18627*	*41*	*0*	
			Sum(Accum t)	***26775***	***6.96E-01***	***1.53E-03***	***3.73E-05***	***1/s***
Background Mode								
73	BckGrd Mode			855	353	0	0	
153	BckGrd Mode	72	E5 H2 beam	4241	1655	1	0	
				5096	***3.94E-01***	***1.96E-04***	**1.96E-04**	**1/s**
			Total Accum t	***31871***			***3.14E-05***	*1/s*
IBEX-Lo				***30 C on IFB***	***594***	*H- BackGrd*	***3.30E-04***	*1/s*

The first column shows the Run number. The 2nd and 3rd columns show the sensor settings for the ESA and the MCP bias voltage. The 4th column contains the beam and chamber settings. The remaining columns contain the total accumulation time, the total number of any Direct Events, Silver Triple Events, and Direct Events that fall into the H- box. While there are, on average, Double Coincidence TOF Rates of 0.4-0.7 1/s and total Silver Triple Rates of about 1.6 10^{-3} 1/s, no event was detected in the H- TOF box in almost 32,000 s as the total accumulation time of all types of Background runs. Thus, an upper limit of 3.73 10^{-5} Counts/s could be established at room temperature during Final Calibration for all regular Background Runs. This upper limit compares with an H- Background Rate of 3.3 10^{-4} 1/s observed with the IBEX-Lo sensor during its Thermal Vacuum Test at 30 C measured on the Interface Board. Therefore, any comparable internal Background is approximately lower by one order of magnitude in IMAP-Lo.
This cleanliness of Silver Triple events is also demonstrated in Figure 4.7.1, which shows a TOF2 versus TOF0s scatterplot of all Direct Events accumulated in all Background Runs compiled in the upper portion of Table 4.7.1.

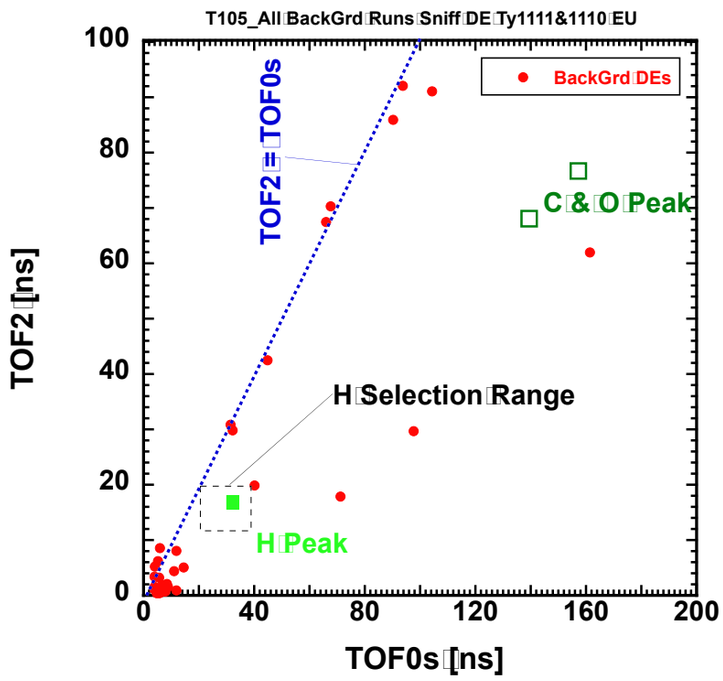


Figure 4.7.1: All Silver Triple Events from the Final Calibration Background Runs in a TOF2 versus TOF0s scatterplot. None of the events falls into the H- selection box. Most of the events can be attributed to electrons.

It can be justified that also the Background Mode Runs, in which the ESA is detuned to exclude any negative ions from reaching the TOF section, can be added to the total accumulation time because the main internal background in IBEX-Lo has come from the electrode P10 between the ESA and the TOF section. This background has been persistently in IBEX-Lo in flight and during the Background Mode runs with the sensor. Adding these two runs at the bottom of Table 4.7.1 to the total accumulation time reduces the upper limit for the H- rate to 3.14 10^{-5} 1/s.

5. CROSS-CALIBRATION WITH IMAP-HI

Excerpt from M. Shen ***IMAP-Lo_X-Cal Test Report.docx***

This section describes the steps performed in IMAP-Lo FM CrossCal sensor calibration with the IMAP-Hi 45 FM, which took place at the Los Alamos National Laboratory (LANL) in February 2025. **The goal of the CrossCal test was to verify the full functionality of the FM sensor after spacecraft environmental testing (acoustic and vibration, but not thermal TVAC yet) and to compare measured beam fluxes determined by both the IMAP-Lo and IMAP-Hi instruments, with the requirement of a relative beam flux accuracy of <10% between the two sensors and an overall absolute accuracy of the resulting geometric factor <25%.**

CrossCal was performed with 500, 750, and 930eV neutralized ions at the LANL facility, which the former two energies are the two lowest IMAP-Hi settings and the latter 930eV is the highest ESA step 7 of High-Throughput mode from IMAP-Lo. Leading into CrossCal, the sensor itself had undergone spacecraft integration for spacecraft acoustic and vibration environmental testing. It was de-integrated from the spacecraft and shipped to LANL for CrossCal and reintegrated later for spacecraft thermal environmental testing. Neither FM EBOX nor Pivot Platform (PPM) traveled with the FM IMAP-Lo sensor. Since the Cross-Calibration of IMAP-Lo and IMAP-Hi happened after spacecraft-level environmental tests of acoustic and vibration, it was considered worthwhile to leverage this beam calibration time under vacuum to verify the full functionality of the sensor prior to any cross-calibration activities. In detail, this included verification of the electronics functionality, HV functionality, sensor background, and detection efficiency.

The incident beam provided by the LANL facility targeted the sensor such that a single conversion surface was illuminated through the collimator. It targeted the 12 o'clock position of the sensor in the LANL chamber, i.e., the center of quadrant 0, where the assigned facet was tested in the FM final calibration. As a reference, the star sensor was located at approximately 7 o'clock in this configuration (see Fig. 2.1.1). During CrossCal, a Carbon-foil absolute beam monitor (ABM) and an imaging Micro-Channel-Plate (MCP) were used to check the beam intensity and uniformity.

Figure 5.1 illustrates the chamber setup with both the IMAP-Lo and IMAP-Hi 45 flight models (FMs) mounted on a large crane inside the LANL vacuum chamber. The IMAP-Hi electronics box (EBOX) was included in the vacuum and pumped down during the cross-calibration, whereas the IMAP-Lo EBOX remained outside the chamber but within the cleanroom environment. The alignment of the pencil-like neutral beam is indicated, with the beam aimed at the center of the conversion surface facet of Quadrant 0 on IMAP-Lo—the same facet previously targeted and calibrated during the Final Calibration at Princeton. The absolute beam monitor (ABM) and microchannel plate (MCP) detector are also shown; the ABM was routinely used before and after each critical cross-calibration (X-Cal) measurement. For motion control, two degrees of freedom—vertical and rotational—were employed to enable precise beam targeting. This allowed both sensors to be rotated in and out of the beam path, enabling them to measure the same neutral beam under identical chamber conditions during the campaign.

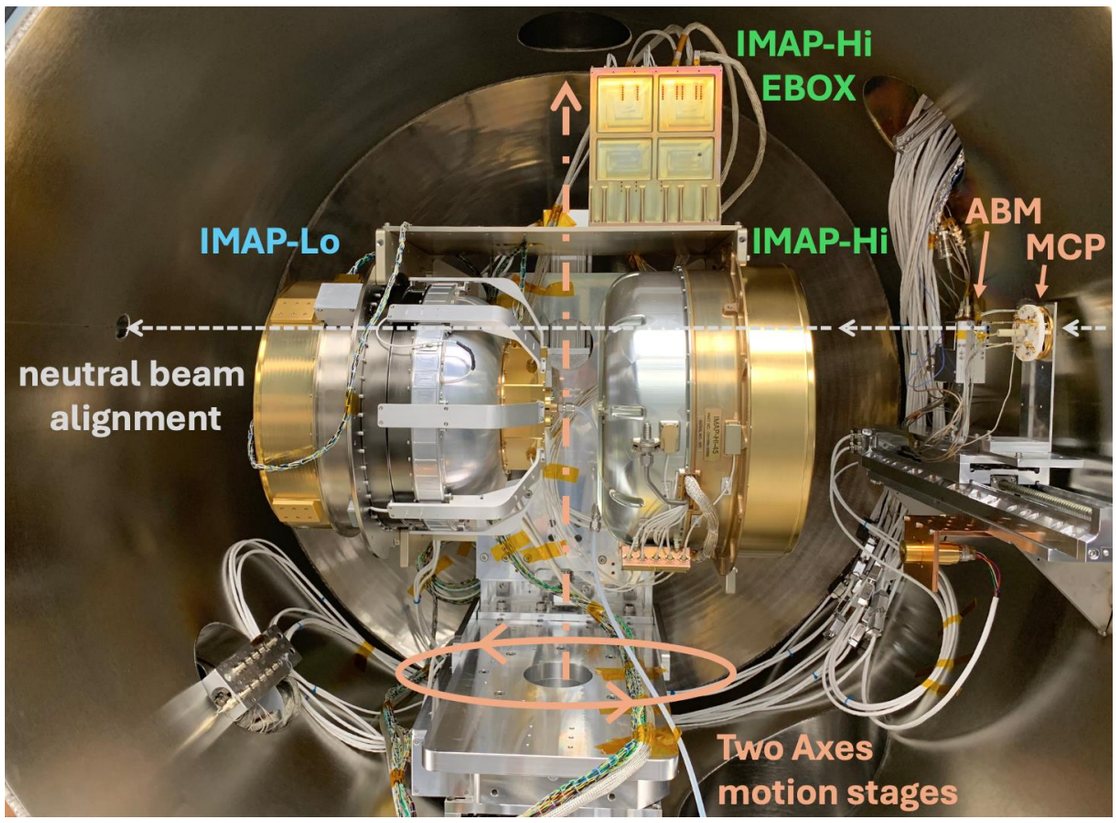


Figure 5.1 Chamber configuration of IMAP-Lo and IMAP-Hi 45 cross-calibration at LANL. Referenced ABM and MCP are denoted. Two motion stages were implemented to perform vertical and rotational motions to rotate two sensors in and out to the neutral beam.

The success criteria for the IMAP-Lo/IMAP-Hi cross-calibration required that the incident flux of the same neutral beam be determined within variations of less than 10% in relative intensity and less than 25% in absolute intensity, measured for at least two of the three calibration energies (500 eV, 750 eV, 930 eV). The "same beam" was defined as having less than 10% variation in beam intensity, as measured by the ABM before and after each cross-calibration activity, a level of stability expected to be under 5% based on LANL's experience. Each sensor was required to complete a scan at normal incidence, collecting statistically meaningful data with less than 5% uncertainty.

Similar to PreCal1, PreCal2, and Final Cal, a series of measurements of the differential energy response to several different neutral beam species and energies were conducted. The aim was to collect supplemental calibration data to be used in conjunction with previous results to improve the final instrument calibration factors. This effort was focused primarily on the H O and Ne.

List, and brief description, of tests encompassing CrossCal, heritage from FinalCal:

1. MCP Response Curve – variation of MCP voltage for given beam and ESA parameters; this test precedes each calibration campaign (at beginning of the beam tests) to check that MCP response curve has not changed; this is an instrument operation check that allows proper calibration measurements to be taken; conduct with H and O

2. Beam Alignment Response – For ESTEP 7 and a 930 eV H beam, raster the instrument along instrument's radial axis (lift) with linear motion to determine functionality of center CS facet at 12 o'clock and determine any variation of conversion and collection efficiency through the ESA-CS.
3. Differential Energy Response, Fine – Determination of differential energy response of each energy step; Fixed Beam E (for a given E-Step) and ESA voltage varied in 10% or 20% steps around center E of given E-Step for HiRes or HiTh mode respectively; conduct for H and O
4. Differential Energy Response, Steps (optional) – Determination of response of other energy steps (due to spill-over of particles into other energy steps from sputtering/scattering); Fixed Beam E (given E-Step) & ESA voltage variation according to E-Steps; conduct for H, D, He, O, Ne (could add C measurements if time allows)

In summary, during CrossCal we accomplished 45 runs with 10 HV ramps, 13 functional tests (including HV science mode with flight software version 4.3), 6 Cross-Cal key measurements as defined above, followed by 16 additional science measurements leveraging the unique high intensity collimate neutral beam (pencil beam) at LANL facility. The additional science measurements are:

- Oxygen Runs
  - MCP response (930 O, MCP SP 63 – 78)
  - Hi-Res 930 Oxygen DER1
  - Hi-Res 930 Oxygen DER2
  - Hi-Res 750 Oxygen DER1
  - Hi-Res 750 Oxygen DER2
  - Hi-Res 500 Oxygen DER1
  - Hi-Res 500 Oxygen DER2
- Neon Runs
  - Hi-Thru 750 Neon (TOF spectra, long integration)
  - Hi-Thru 750 Neon DER2
  - Hi-Res 930 Neon DER2
- Flight-like Runs
  - Threshold settings functional
  - Hi-Res DER1 with 930 H (MCP SP 76)
  - Hi-Res DER2 with 1100 H (MCP SP 76)
  - Flight Sim (MCP SP 76 + HVSCI + 930 H)

Figure 5.2 shows the results of sweep scans ("snake scans") performed with 930 eV, 750 eV, and 500 eV neutral hydrogen beams to achieve precise beam alignment onto the center of the IMAP-Lo conversion surface (CS) facet at Quadrant 0 (positioned at 12 o'clock in the figure). During the final calibration at Princeton, a 14 mm diameter paddle was placed in front of the sensor to constrain the beam size, thereby illuminating the entire CS facet. In contrast, at LANL, the neutral beam had a much smaller diameter (~3 mm), resembling a pencil beam. Under this configuration, it became essential not only to illuminate the full CS facet but also to precisely target its center to optimize conversion efficiency. To determine the optimal alignment coordinates, multiple sweep scans were conducted at various beam energies (930 eV, 750 eV, and 500 eV H). The scan results are depicted in Figure 5.3. A distinct hexagonal pattern is visible, particularly in the 930 eV H beam scan, which we suspect arises from the mechanical structure of the collimator—specifically, the 3 mm beam diameter interacting with the 1 mm thickness of each honeycomb hexagonal element.

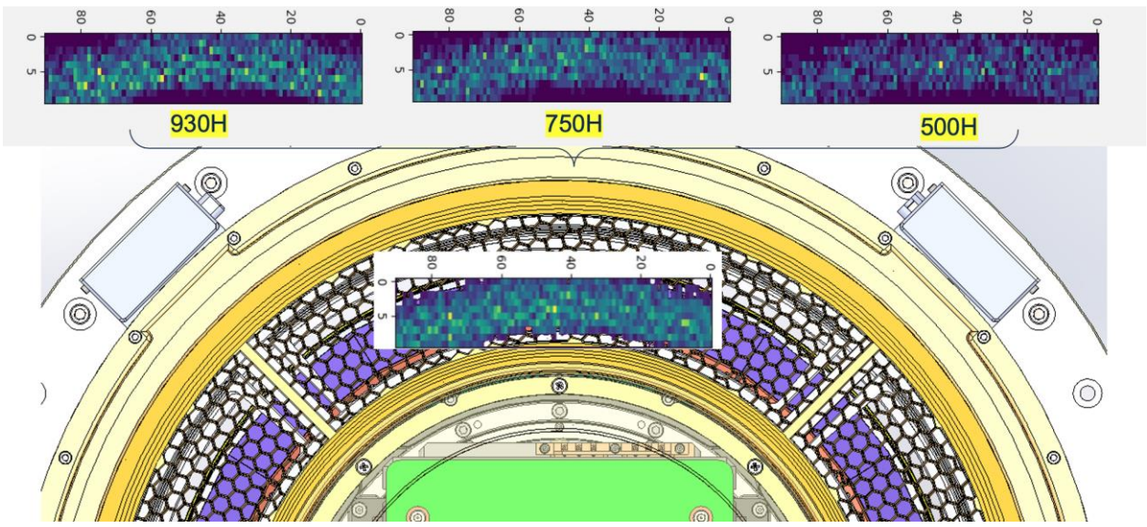


Figure 5.2 Sweep scans (snake scans) result averaging 930eV, 750eV, 500eV neutral H beams for precise beam alignment to center of IMAP-Lo CS facet at Quadrant 0 (12 o'clock in this figure).

Figure 5.3 presents a comparison of three differential energy response curves obtained while measuring a 930eV hydrogen neutral beam. The green and black curves correspond to IMAP-Lo calibration campaigns conducted at LANL (cross-calibration, X-Cal) and Princeton (Final Calibration), respectively. The cyan curve represents reference measurements from the IBEX era, calibrated at the University of Bern. Notably, the energy width of the response broadens progressively from LANL to Princeton to Bern, reflecting differences in neutralization methods: both LANL and Princeton employed charge-exchange neutralization, while Bern used surface neutralization. Despite this, the Princeton IMAP-Lo and Bern IBEX-Lo calibrations exhibit similar central peak positions. In contrast, the LANL curve is shifted toward higher U^+ (eV), suggesting either a higher energy beam or instrumental effects. We attribute this shift to beam characteristics at LANL, where a narrow, pencil-like beam was used—unlike the Princeton setup, which illuminated the full conversion surface (CS) facet. Conversion efficiency and the spatial distribution of recoil ions are known to be highly sensitive to the precise impact location of neutral particles on the CS facet. Overall, the measurements are consistent, mutually supportive, and provide a robust foundation for instrument calibration.

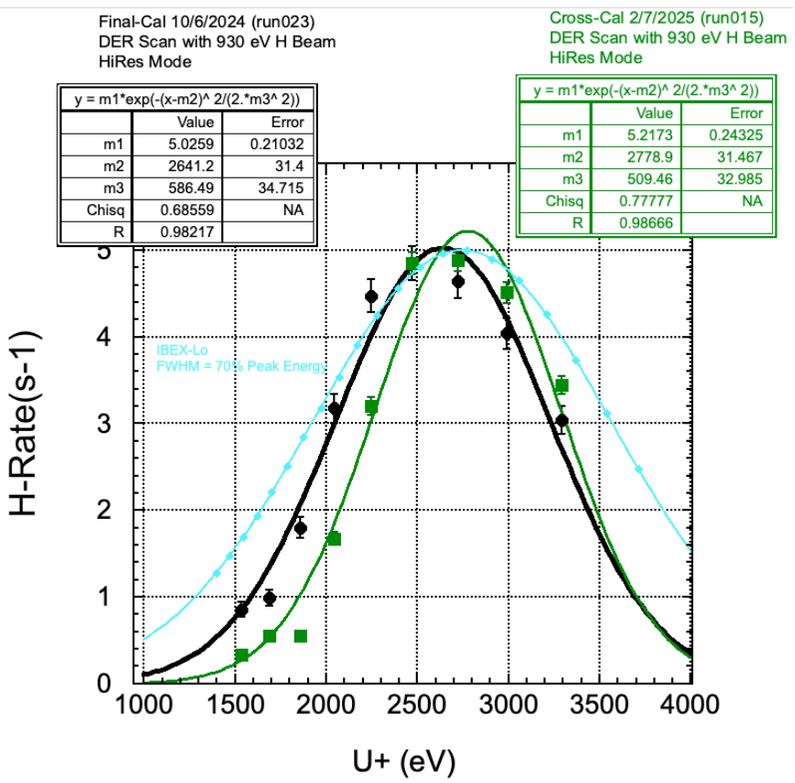


Figure 5.3 Differential energy response of 930eV hydrogen beam measured by IMAP at LANL (X-Cal, green), at Princeton (Final Cal, black) and IBEX at Bern (cyan). Effectively, this is a comparison of three neutral beam facilities (LANL, Princeton, and University of Bern). The differences in width and peak position are likely due to differences in the energy spectra and geometric width of the neutral beams delivered by the different facilities. The LANL beam can be considered a very narrow pencil beam with almost a delta function in energy. The Princeton beam covers an area of 14 mm diameter with also a delta function in energy. The Bern beam is divergent in angle and has a broad distribution in energy.

5.1 Measuring the Incident Beam Flux

At instrument cross calibration, it is essential to use geometric factors determined in final calibration to estimate observed beam rates in cross-calibration and thus compare it with the other sensor as well as the referenced beam monitor. A starting point for being able to interpret the beam measurements during cross-calibration is having a precise response function. Given a spatially uniform differential energy flux, *J (E, α, β)* [see Schwadron et al., IBEX SOC, 2009], the counts observed are given by

$$C = \Delta t \int dE \int d\Omega \, R_i \, J(E, \alpha, \beta) \qquad (5.1.1)$$

where the energy level is i, and the angles α and β are the velocity incidence angles. We integrate over these through the $d\Omega$ integral. Here, we estimate the response function for pure conversion of neutral atoms,

$$R_i = G_i \, E \, P(\alpha, \beta) \, T_i(E) \qquad (5.1.2)$$

where *Gi* is the geometric factor with units of cm^2 sr eV/eV, and P and Ti are the point spread function and the transmission function, respectively. Note that both *P* and T_i are defined as differential probabilities with unit norm:

$$\int d\Omega\, P = 1$$
$$\int dE\, T_i = 1 \qquad (5.1.3)$$

For simplicity, we consider a cylindrically symmetric point spread function and account for the angle θ off of the bore-sight axis. The point spread function varies linearly in angle θ from a maximum at $\theta_0 = 0^\circ$ to 0 at $\theta_1 = 9^\circ$. This implies an approximation for *P(θ)*

$$P(\theta) = P_0\left(1 - \frac{\sin(\theta)}{\sin(\theta_1)}\right), \quad for\ \theta \le \theta_1$$
$$= 0 \quad , \quad for\ \theta > \theta_1 \qquad (5.1.4)$$

where the point spread function is written as

$$P_0 = \frac{1}{2\pi}\frac{sin\theta_1}{sin\theta_1[1-\cos(\theta_1)/2]-\theta_1/2} \qquad (5.1.5)$$

The transmission function is a normalized Gaussian

$$T_i(E) = \frac{1}{\sigma_i\sqrt{2\pi}} exp\left[-\frac{(E-E_i)^2}{2\sigma_i^2}\right] \qquad (5.1.6)$$

where E_i is the peak-energy and σ_i is the peak width.

For the beam response, we consider a beam that is essentially a delta function in energy and angle. The beam differential flux is expressed as

$$J_b = \frac{R_b}{2\pi\delta A_b}\delta(E - E_b)\delta(cos\theta - 1) \qquad (5.1.7)$$

Note that the beam is not uniform over the instrument. Therefore, there is another factor ξ that multiplies the transmission function and represents the beam area over the effective area of the instrument:

$$\xi = \frac{\delta A_b}{A_{tot}} \qquad (5.1.8)$$

The integrated response at ESA level *i* provides an estimate of observed count rate in the beam as

$$\frac{C_i}{\Delta t} = \frac{R_b}{A_{tot}} G_i E_b P_0 T_i(E_b) \qquad (5.1.9)$$

For the total effective area and solid-angle on IMAP-Lo, we find $d\Omega A_{tot} = 2.18 \pm 0.03\ sr\ cm^2$.
In general, the observed count rate is also expressed in simpler terms

$$\frac{C_i}{\Delta t} = \frac{R_b}{d\Omega A_{tot}} G_i E_b T_i(E_b) \qquad (5.1.10)$$

whereas the beam rate for comparison with the referenced ABM yielding

$$R_b = \left(\frac{C_i}{\Delta t}\right) \times \frac{d\Omega A_{tot}}{G_i E_b T_i(E_b)} \quad (5.1.11)$$

and $C_i/\Delta t$ is the count rate which IMAP-Lo instrument measures.

5.2 Conclusion

Figure 5.2.1 summarizes the IMAP-Lo cross-calibration results conducted alongside the IMAP-Hi 45 sensor at LANL. The left panel displays the measured beam rates (solid curves), inferred from the incident flux recorded by both instruments. These rates account for each sensor's geometric factor and response function. The dashed lines represent the mean count rates from the Absolute Beam Monitor (ABM), recorded before and after each beam measurement. For IMAP-Lo, the 500 eV and 930 eV beams align with its highest two ESA steps—steps 6 and 7, respectively. In contrast, for IMAP-Hi, the 500 eV and 750 eV beams correspond to its lowest two ESA steps—steps 1 and 2, respectively. This results in a slight deviation in IMAP-Lo's 750 eV measurement from the ABM rate, as the geometric factor at this energy had to be interpolated between two ESA steps. To address this complexity, we intentionally conducted differential energy response (DER) scans rather than single-point measurements, enabling a more robust characterization of IMAP-Lo's geometric factor matrix and response function. The right panel of Figure 5.2.1 shows the inferred incident fluxes normalized to the ABM reference rates. These results confirm that the relative flux accuracy is within ±10%, and the absolute flux accuracy is within the mission requirement of ±25%.

Overall, we observe good agreement across the three energy measurements, particularly for the 500 eV and 930 eV beams. According to the success criteria jointly defined by both the IMAP-Lo and IMAP-Hi teams—as well as the mission requirement of ±25% absolute flux accuracy and ±10% relative flux accuracy—the cross-calibration (X-Cal) campaign successfully met all specifications.

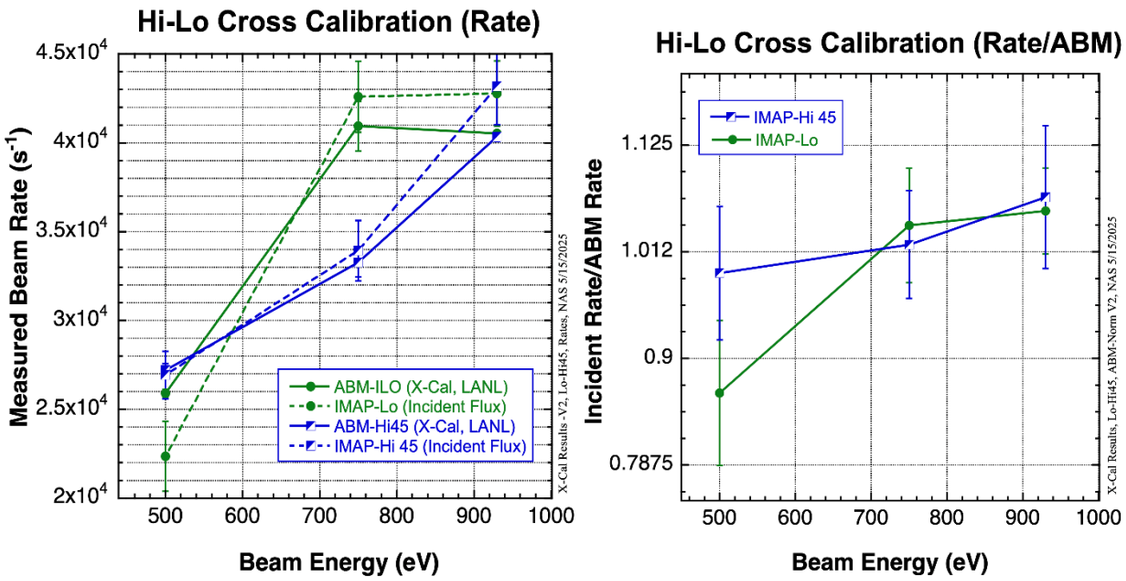


Figure 5.2.1 Charts of IMAP-Lo/IMAP-Hi cross calibration with one another in comparison to the reference ABM beam rate. *Left*: measured beam rate among; *Right*: normalized to the ABM rate as a comparison.

6. INSTRUMENT GEOMETRIC FACTORS

The instrument geometric factor can now be calculated by simply multiplying the ESA-CS collection efficiency with the TOF efficiency, the total grid transparency and the absolute GF. The complete table can be seen in ***IMAP-Lo_GF_bower_V004.xlsx.*** The grid transparency values are shown below:

Table 6.1

Grid Name	Trans [%]	Reference	Comments
p10 grid and spokes	0.85	20240804_p10_P2_GridsNspokes_SR.pdf	[.91 (12/17/2024)] [.89(12/17/2024 per Fatemeh txt)]
p2 Spokes	0.9363	20240804_p10_P2_GridsNspokes_SR.pdf	Also per supplemental document
ToF Entrance Grid	0.682	20250313_ToFEnterance_GridsNspokes_CF.pdf	
Coll spokes	1.041666667	Model, calibrated from same study I did looking at p2 spokes	value is >1 because the total open area of the collimator, and thus the coll spokes are included in the absolute geometric factor, the P2 spoke though
			Total Transparency
			0.565388656

6.1 H Geometric Factors

We now use the response functions, grid transparency shown above with the Absolute GF (see supplemental documentation) to calculate the H GF. The ESA-CS collection efficiency used is taken as the mean collection efficiency observed across the FWHM of the Energy response function.

Table 6.1.1 H Geometric Factors

Hydrogen	value	Unit	Ref	Comment		
TOF Efficiency	0.25	%	Final Cal 12/18/2024			
Absolute GF	2.18 ± 0.03	cm^2sr	Optical Measurements 3/19/25			
Total Grid Transparency	0.565	[%]				
E_mode	estep	scale_fact	de_e	Effic_ESA-CS Mean |FWHM|	GF	Relative Error
		[U+_n/U+_6]	[ke/ke]	[%]	[cm^2stkeV/keV]	
HiRes	1	0.0347	0.660437263	3.14E-04	7.03E-05	N/A
HiRes	2	0.067	0.66027447	3.54E-04	7.93E-05	N/A
HiRes	3	0.1287	0.680887516	4.18E-04	9.66E-05	0.70

HiRes	4	0.2533	0.652318365	5.08E-04	1.12E-04	0.27
HiRes	5	0.4884	0.650363345	6.36E-04	1.40E-04	0.32
HiRes	6	1	0.671765806	7.77E-04	1.77E-04	0.11
HiRes	7	1.9378	0.717792995	9.22E-04	2.25E-04	0.06
HiTh	1	0.0347	1.031331214	4.76E-04	1.66E-04	N/A
HiTh	2	0.067	0.999966761	5.65E-04	1.92E-04	N/A
HiTh	3	0.1287	0.961323182	6.96E-04	2.27E-04	0.61
HiTh	4	0.2533	0.935456862	8.61E-04	2.73E-04	0.36
HiTh	5	0.4884	0.991428725	1.00E-03	3.38E-04	0.28
HiTh	6	1	1.007046859	1.30E-03	4.44E-04	0.11
HiTh	7	1.9378	1.013986565	1.65E-03	5.69E-04	0.05

6.2 O Geometric Factors

Table 6.2.1 O Geometric Factors

Oxygen	**value**	**Unit**	**Ref**	**Comment**		
TOF Efficiency	0.3	%	Final Cal 12/18/2024			
Absolute GF	2.4	cm^2sr	F. Rahmanifard 8/30/24			
Total Grid Transparency	0.565388656	[%]				
E_mode	estep	scale_fact	de_e	Effic_ESA-CS Mean |FWHM|	GF	Comments
		[U+_n/U+_6]	[ke/ke]	[%]	[cm^2stkeV/keV]	
HiRes	1	0.0347	1.071309787	3.14E-04	1.37E-04	Extrapolated
HiRes	2	0.067	0.970804261	3.54E-04	1.40E-04	Extrapolated
HiRes	3	0.1287	1.006618112	4.18E-04	1.71E-04	Extrapolated
HiRes	4	0.2533	1.040054729	5.08E-04	2.15E-04	Extrapolated
HiRes	5	0.4884	1.084004096	6.36E-04	2.81E-04	Extrapolated
HiRes	6	1	1.200429453	7.77E-04	3.80E-04	
HiRes	7	1.9378	1.18442498	9.22E-04	4.45E-04	
HiTh	1	0.0347	1.648405491	4.76E-04	3.19E-04	Extrapolated
HiTh	2	0.067	1.548444987	5.65E-04	3.56E-04	Extrapolated
HiTh	3	0.1287	1.480666338	6.96E-04	4.19E-04	Extrapolated
HiTh	4	0.2533	1.567389314	8.61E-04	5.49E-04	Extrapolated
HiTh	5	0.4884	1.580610222	1.00E-03	6.47E-04	Extrapolated
HiTh	6	1	1.655930152	1.30E-03	8.77E-04	
HiTh	7	1.9378	1.58342707	1.65E-03	1.07E-03	

6.3 Ne Geometric Factors Hi-Resolution

To determine the instrument geometric factor for Ne, we follow the IBEX-lo methodology to measure and calculate the instrument conversion collection efficiency. For sputtered populations, ESA-CS conversion collection efficiency is measured using DER2 energy response scans, where the instrument simply steps through the nominally defined energy steps, with a beam of fixed incident energy. The geometric factor (GF) values presented here are derived from the Final Calibration runs for Hi_Resolution mode, using 700 eV (Run 105) and 400 eV (Run 110) neutral neon beams. Resulting geometric factors presented along with comparable IBEX-lo GFs can be seen in Table 6.3.1. Here, the first column indicates the E-Steps corresponding to the energy of the incoming beam. As such, these two runs directly cover E-Steps 6 and 7, while the remaining GF values are extrapolated.

For detailed calculation of the Ne geometric factors, see ***GeoFactor_Ne_V01.xlsx.***

Table 6.3.1 Ne Sputtering Geometric Factors

Incident Energy	Observed E-Step	GF Triple [cm^2sr keV/keV]	Uncertainty [cm^2sr keV/keV]		IBEX GF Triple [cm^2sr keV/keV]	IMAP/ IBEX
2	1	1.34E-06	9.1635E-07	Extrapolated	5.79E-06	0.23
2	2	6.71E-07	4.591E-07	Extrapolated	2.04E-06	0.33
3	3	8.04E-07	5.5027E-07	Extrapolated	2.35E-06	0.34
4	1	2.97E-05	2.0271E-05	Extrapolated	1.59E-04	0.19
4	2	1.34E-05	9.1541E-06	Extrapolated	6.85E-05	0.20
4	3	5.14E-06	3.521E-06	Extrapolated	1.56E-05	0.33
4	4	9.36E-07	6.4634E-07	Extrapolated	2.63E-06	0.36
5	2	3.73E-05	2.5519E-05	Extrapolated	1.91E-04	0.20
5	3	1.62E-05	1.1071E-05	Extrapolated	6.93E-05	0.23
5	4	1.05E-05	7.225E-06	Extrapolated	3.06E-05	0.34
5	5	1.89E-06	1.3879E-06	Extrapolated	5.32E-06	0.35
6	1	8.27E-06	7.5062E-06		0.00	
6	2	1.24E-05	1.1238E-05		1.65E-04	0.08
6	3	1.06E-05	9.6238E-06		2.19E-04	0.05
6	4	1.01E-05	9.1926E-06		6.55E-05	0.15
6	5	8.84E-06	8.4015E-06		4.45E-05	0.20
6	6	1.42E-06	1.597E-06		8.01E-06	0.18
7	1	1.05E-05	9.4233E-06		0.00	
7	2	1.59E-05	1.4141E-05		3.77E-05	0.42
7	3	2.43E-05	2.1436E-05		1.17E-04	0.21
7	4	2.03E-05	1.8069E-05		1.45E-04	0.14
7	5	1.87E-05	1.7391E-05		4.75E-05	0.39
7	6	1.28E-05	1.3528E-05		3.61E-05	0.35

7	7	8.76E-07	1.4451E-06	Extrapolated	9.29E-06	0.09

Compared to IBEX-Lo, the instrument has undergone several enhancements, including a higher absolute geometric factor and increased transparency across all subsystems. Despite these improvements, the GF values obtained here are significantly lower than those reported for IBEX. This discrepancy arises primarily from the collection/conversion efficiency (derived through comparisons between ABM-measured count rates and the rates recorded by the instrument) which yields smaller values than those from IBEX calibration measurements. The discrepancy between the IBEX-lo and IMAP-lo determined conversion scattering efficiency is still being resolved, but we have identified several factors that could be contributing to the difference.

One possible explanation for the lower sputtering collection efficiency is a reduced water layer on the conversion surface. In previous studies of conversion surface sputtering, Hughes et al. (2009) demonstrated that ionization efficiency decreases rapidly with decreasing surface adsorbates. Given that IMAP-lo underwent a thorough bakeout, and that Ne Sputtering measurements took place after nearly 2 weeks in hi-vac, the sublimation of H20 from the CS could be the cause for the reduced conversion collection efficiency. A comparison to IBEX-lo sputtering measurements controlling for time in vacuum has not yet been completed.

Additionally, differences in calibration facilities and assumptions further complicate direct comparisons. As indicated above, our methodology to determine the ESA-CS conversion-scattering efficiency follows IBEX-lo calculations directly, which could be introducing some systematic problems. IMAP-Lo calibrations were conducted using a mono-energetic pencil beam, which may include unquantified background contributions. In contrast, IBEX calibrations used a broader beam with large angle and energy spread and determination of the geometric factor relied on assumptions of angular isotropy and a flat energy distribution in their methodology. In the case of the IBEX-lo measurements, the resulting conversion-collection efficiency and energy response is deconvolved from the incident beam properties based on this assumption that the incident beam is uniform and effectively covers all phase space the instrument observes. In the case of IMAP-lo calibration the mono-energetic pencil beam yields a single measurement point from which the instrument energy response must be extrapolated. This process of extrapolation, described and demonstrated in Section 4.6.3, has been shown to be effective in determining the instrument energy response to primary-converted particles, but for sputtered observed species the process is not so straightforward. As we revert to the IBEX-lo method for direct measurement of the ESA-CS collection efficiency, we attempt to account for the fundamental differences in our test setups, but it is likely that there are still unaccounted for differences making the GFs calculated here not directly comparable to the results presented in IBEX-lo calibration.

We are currently investigating the instrument response including a deeper understanding of what the geometric factor represents for sputtered neutrals such as Ne. At this point, measurement of the instrument response to O and H have shown that the IMAP-lo response functions as expected and the total collection power will be higher than IBEX-lo in accordance with its design. While we still need to resolve our methodology, we have no reason to believe that the sputtering collection efficiency will be any different. Consequently, the GF values reported here should be considered preliminary and subject to revision.

7. CONCLUSION

The calibration campaign for the IMAP-Lo FM instrument was executed successfully, confirming that the instrument meets or exceeds all design and performance requirements necessary for flight readiness. The calibration strategy adhered closely to IBEX-Lo heritage, while accommodating design enhancements unique to IMAP-Lo, aiming to improve sensitivity, while reducing background.

Subsystem-level calibrations spanning the collimator and deflection system, conversion surfaces, TOF subsystem, and star sensor demonstrated performance within or exceeding specification tolerances. Notably, the collimator measurements confirmed precise geometric alignment and validated the absolute geometric factor calculations. Conversion surface characterization yielded consistent negative ion yields and angular scatter distributions across tested samples, demonstrating similarity to IBEX-Lo legacy and affirming the uniformity and effectiveness of the DLC coatings used in flight facets. TOF subsystem calibration verified accurate species separation and timing resolution, with triple-coincidence detection confirming low background rates and high mass discrimination.

Sensor-level calibration activities formed the core of the performance validation effort. These included a structured sequence of tests, PreCal1, PreCal2 and FinalCal, each designed to incrementally validate the instrument in increasingly flight-like conditions. The results from these activities provided comprehensive characterization of the sensor's energy response, detection efficiency, and background suppression. The geometric factors for hydrogen and oxygen were quantified, and roughly matched expectations, facilitating accurate flux conversions from measured count rates. Calibration accuracy was verified in CrossCal conducted in tandem with the IMAP-Hi instrument using the same neutral beamline. This step allowed for relative calibration between instruments to be verified, ensuring consistency in measured fluxes and calibrated energy responses.

Timeline restrictions and system availability meant that we were unable to collect direct energy response and collection efficiency measurements at all energy steps, notably missing Estep1 and 2 for H and Esteps 1,2,3,4,5 for O. But, our detailed modeling approach, coupled with supplementation of IBEX-Lo calibration and close adherence to heritage has allowed us to perform detailed extrapolation of our directly observed calibration results to low energy steps. Without direct validation of these detection efficiencies, questions still remain, which we hope to address through future modeling efforts and targeted subsystem and EM testing. We plan to conduct additional testing focused on the low-energy scattering properties of the CS at MEFISTO. Improved low energy calibration will enhance the fidelity of our instrument response models for both IBEX-Lo and IMAP-Lo increasing the reliability of both past and future data interpretations. Additionally, in-flight cross-calibration with IBEX-Lo during the early phase of IMAP-Lo operations will provide a valuable opportunity to systematically validate our relative calibration factors and ensure continuity between the two missions.

In comparing the Instrument Geometric factors between IBEX-Lo and IMAP-Lo we estimate a ~4x increase in collection power (for comparable voltage modes DE/E = .7), driven primarily by increased FoV, and grid transparency. Reduced carbon foil thickness of 1ug, as compared to 2ug foils on IBEX-Lo, allows us to also reduce the nominal PAC voltage to 12kV, from 16kV used on IBEX-Lo, while retaining comparable mass resolution and detection efficiency. This opportunity provides a more robust post acceleration operational mode, ensuring optimal functionality of the PAC HVPS for longer.

In conclusion, the IMAP-Lo FM instrument has been rigorously calibrated through a comprehensive test campaign. It is now fully prepared for integration into the IMAP spacecraft, with a robust understanding of its performance characteristics. These calibrations will directly support the mission's ability to deliver transformative measurements of energetic neutral atoms and interstellar particles throughout its operational lifetime.

8. REFERENCES

Eckstein, W. (1987). Direct Recoil Sputtering and Secondary Ion Production. Nuclear Instruments and Methods in Physics Research, B27, 78–93.

Neuland, M. B., Riedo, A., Scheer, J. A., & Wurz, P. (2014). Self-supporting CVD diamond charge state conversion surfaces for high resolution imaging of low-energy neutral atoms in space plasmas. Applied Surface Science, 313, 293–303. https://doi.org/10.1016/j.apsusc.2014.05.206

Wahlström, P., Scheer, J. A., Wurz, P., Hertzberg, E., & Fuselier, S. A. (2008). Calibration of charge state conversion surfaces for neutral particle detectors. Journal of Applied Physics, 104(3). https://doi.org/10.1063/1.2957064

Kudriavtsev, Y., Villegas, A., Godines, A., & Asomoza, R. (2004). Calculation of the surface binding energy for ion sputtered particles. https://doi.org/10.1016/j.apsusc.2004.06.014

Hofer, W. O. (n.d.). 2. Angular, Energy, and Mass Distribution of Sputtered Particles. Topics in Applied Physics (Vol. 64).

Galli, A., P. Wurz, N. A., Schwadron, et al., The Downwind Hemisphere of the Heliosphere: Eight Years of IBEX-Lo Observations, ApJ, 851:2, 2017.

Allegrini, F., et al., Energy loss of 1–50 keV H, He, C, N, O, Ne, and Ar ions transmitted through thin carbon foils, Rev. Sci. Instr., 77, 044501 (2006).

Schwadron, N.A., Möbius, E., D. J. McComas et al. 2022. Interstellar Neutral He Parameters from Crossing Parameter Tubes with the Interstellar Mapping and Acceleration Probe Informed by 10 yr of Interstellar Boundary Explorer Observations ApJS, 258:7.

Swaczyna, P., M. Bzowski, S. F. Fuselier, et al. 2023. Relative In-Flight Response of IBEX-Lo to Interstellar Neutral Helium Atoms, ApJS, 266:2.

Wurz, P., Schletti, R., & Aellig, M. R. (1997). Hydrogen and oxygen negative ion production by surface ionization using diamond surfaces. *Surface Science*, *373*(1), 56–66. https://doi.org/10.1016/S0039-6028(96)01146-6

Schlathölter, T., & Heiland, W. (1995). Charge exchange of swift molecules H2+, H2, CO2+ and CO2, at Pd(111) surfaces. *Nuclear Inst. and Methods in Physics Research, B*, *100*(2–3), 352–355. https://doi.org/10.1016/0168-583X(94)00847-7

Heber, O., Golser, R., Gnaser, H., Berkovits, D., Toker, Y., Eritt, M., … Zajfman, D. (2006). Lifetimes of the negative molecular hydrogen ions: H2-, D2-, and H D. *Physical Review A - Atomic, Molecular, and Optical Physics*, *73*(6). https://doi.org/10.1103/PhysRevA.73.060501

Wurz, P., Scheer, J., & Wieser, M. (2006). Particle Scattering off Surfaces: Application in Space Science *. *Surface Science and Nanotechnology*, *4*, 394–400. https://doi.org/10.1380/ejssnt.2006.394

Sokół, J. M., Lin, J., Fuselier, S. A., Eliason, T., Gomez, J. E., Rodriguez, B., … Schwadron, N. A. (2024). Diamond-like carbon conversion surfaces for space applications. *Journal of Applied Physics*, *135*(18), 1–15. https://doi.org/10.1063/5.0203686

H. O. Funsten, R. W. Harper, D. J. McComas; Absolute detection efficiency of space-based ion mass spectrometers and neutral atom imagers. Rev. Sci. Instrum. 1 May 2005; 76 (5): 053301. https://doi.org/10.1063/1.1889465

Hughes, P. P., Coplan, M. A., DeFazio, J. N., Chornay, D. J., Collier, M. R., Ogilvie, K. W., & Shappirio, M. D. (2009). Scattering of neutral hydrogen at energies less than 1 keV from tungsten and diamondlike carbon surfaces. *Journal of Vacuum Science & Technology A: Vacuum, Surfaces, and Films*, *27*(5), 1188–1195. https://doi.org/10.1116/1.3196788

3.6.3 In-Flight Calibrations

IMAP-Lo in-flight calibration report to be included here.

3.7 IMAP-Hi

3.7.1 Strategy & Approach

IMAP-Hi calibration was conducted at Los Alamos National Laboratory' Space Plasma Instrument Calibration Facility. Flight sensor calibration was split into four steps, with background characterization and gain estimation acquired in each task:

- Step 1: Deflector and ESA subsystems characterization
- Step 2: Collimator subassembly characterization, including foil coverage and deflector subsystem tests
- Step 3: Sensor response function characterization over full entrance aperture
- Step 4: Cross-calibrations with IMAP-Lo and IMAP-Hi; this included full end-to-end evaluation of the IMAP-Hi Ebox performance and science operations at nominal high voltages.

3.7.2 Pre-Flight Instrument Calibration

IMAP-Hi cal report embedded below

IMAP-Hi Calibration Report

Version No. 2

CN106V-R0002

Paul Janzen

April 2, 2026
Approved By: Dan Reisenfeld

Los Alamos
NATIONAL LABORATORY

Executive Summary

ID	Parameter	Requirement	Calibration Result
RHI-1046 RHI-1053	Measure H ENAs	—	H ENAs measured
RHI-1047 RHI-1054 RHI-1060	Energy range	≤ 0.5 keV to ≥ 10 keV	Measured 0.5 keV to 17.78 keV
RHI-1048 RHI-1055 RHI-1061	Energy resolution	$\leq 70\%$ $\Delta E/E$, FWHM	$42 \pm 3\%$
RHI-1049 RHI-1057 RHI-1062	Angular resolution	$\leq 6^\circ$ FWHM	$\leq 4.5^\circ$ FWHM
RHI-1051	S/N	≥ 50 at 1 keV	68
RHI-1596 RHI-1597	Geometric factor	≥ 0.001 cm^2 sr eV/eV at 1 keV ≥ 0.01 cm^2 sr eV/eV at 10 keV	0.00115 (0.00114) at 1 keV Hi45(Hi90) 0.0132 (0.0149) at 10 keV Hi45(Hi90)
RHI-1544 RHI-1545 RHI-1601 RHI-1602	Calibration accuracy	±10% relative ±25% absolute	±6.7% relative ±22% absolute
RHI-1139	HVSCI (science) mode	Must be tested	Was tested
RHI-1140	Voltage-gain curves	Taken for each detector	Taken for each detector
RHI-1197 RHI-1630	Boresight alignment	$\leq \pm 0.70^\circ$ tolerance $\leq \pm 0.11^\circ$ knowledge	$\pm 0.2^\circ$ $\pm 0.05^\circ$

This memo summarizes the calibration of the IMAP-Hi45 and -Hi90 sensors. Results are compared to performance requirements, as listed in Table 1. Previous documentation (e.g., the Hi45 PSR) has indicated that RHI-1596 and RHI-1597 also imply a required conversion foil coverage of better than 95%. Both Hi45 and Hi90 meet requirements.

RHI-1046	IMAP-Hi shall measure H ENAs for Hi-res Skymap.
RHI-1053	IMAP-Hi shall measure H ENAs for Energy Spectra.
RHI-1047	IMAP-Hi energy range for H ENAs shall be less than or equal to 1 keV to greater than or equal to 10 keV.
RHI-1054	IMAP-Hi energy range for H ENAs shall be less than or equal to 0.5 keV to greater than or equal to 10 keV.
RHI-1060	IMAP-Hi energy range for H ENAs shall be less than or equal to 1 keV to greater than or equal to 10 keV.
RHI-1048	IMAP-Hi energy resolution for H ENAs shall be less than or equal to 120 percent (delta E / E FWHM).
RHI-1055	IMAP-Hi energy resolution for H ENAs shall be less than or equal to 70 percent (delta E / E FWHM).
RHI-1061	IMAP-Hi energy resolution for H ENAs shall be less than or equal to 120 percent (delta E / E FWHM).
RHI-1049	IMAP-Hi angular resolution for H ENAs shall be less than or equal to 6 degrees FWHM.
RHI-1057	IMAP-Hi angular resolution for H ENAs shall be less than or equal to 18 degrees FWHM.
RHI-1062	IMAP-Hi angular resolution for H ENAs shall be less than or equal to 12 degrees FWHM.
RHI-1051	IMAP-Hi signal to background noise for H ENAs (Hi-res Skymap) shall be greater than or equal to 50 at 1 keV for an assumed H ENA flux of 100 $(\text{cm}^2\ \text{sr}\ \text{s}\ \text{keV})^{-1}$.
RHI-1056	IMAP-Hi signal to background noise for H ENAs (Energy Spectra) shall be greater than or equal to 20 at 1 keV for an assumed H ENA flux of 100 $(\text{cm}^2\ \text{sr}\ \text{s}\ \text{keV})^{-1}$.
RHI-1596	IMAP-Hi geometric factor shall be greater than or equal to 0.001 cm^2 sr eV/eV at 1 keV.
RHI-1597	IMAP-Hi geometric factor shall be greater than or equal to 0.01 cm^2 sr eV/eV at 10 keV.
RHI-1544	IMAP-Hi shall have an ENA flux calibration relative accuracy of ±10% in the energy range 0.5 to 1 keV.
RHI-1545	IMAP-Hi shall have an ENA flux calibration absolute accuracy of ±25% in the energy range 0.5 to 1 keV.
RHI-1601	IMAP-Hi shall have an ENA flux calibration relative accuracy of ±10% in the energy range 5-10 keV.
RHI-1602	IMAP-Hi shall have an ENA flux calibration absolute accuracy of ±25% in the energy range 5-10 keV.
RHI-1139	"IMAP-Hi HVSCI (SCIENCE) Mode shall be used during instrument calibration to set the instrument into a known state and acquire data. This mode will also be used during commissioning."
RHI-1140	IMAP-Hi shall have measured voltage-gain curves for each detector.
RHI-1197	IMAP-Hi internal alignment knowledge uncertainty between sensor nominal boresight and the mounting surface shall be less than or equal to 0.11 degrees.
RHI-1630	The IMAP-Hi instrument shall be developed so that the instrument alignment feature relative to the effective boresight of the IMAP-Hi FOV is within ± 0.70 degrees (per axis).

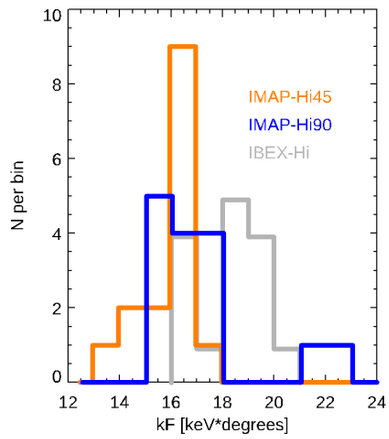
Table 1: Mission requirements addressed in calibration.

Instrument Overview

IMAP-Hi's overall design and function are detailed elsewhere. In the framework of the calibration, instrument function is most clearly described by tracing the path of ENAs through the sensor:

- First encountered are positive and negative deflectors, intended to deflect charged particles out of the instrument's field of view.
- Second is a mechanical collimator (at spacecraft potential) that limits the field of view of the sensor.

- Third is a set of conversion foils which convert a fraction of incoming ENAs to positive ions. Passage through a conversion foil has the side effects of some scattering and some energy straggling. The foils used are listed in Table 2.



	Hi45			Hi90	
Serial	Coverage (%)	k_F (keV°)	Serial	Coverage (%)	k_F (keV°)
SN423	99.9	16.6 ± 0.3	SN459	99.6	17.0 ± 0.2
SN426	99.9	16.9 ± 0.5	SN444	99.0	21.9 ± 0.1
SN425	99.9	16.9 ± 0.3	SN452	99.8	17.2 ± 0.3
SN431	99.6	16.5 ± 0.4	SN460	99.8	17.0 ± 0.3
SN430	99.7	16.4 ± 0.3	SN445	99.6	16.9 ± 0.4
SN433	99.8	16.1 ± 0.6	SN447	99.6	16.5 ± 0.4
SN428	99.8	15.2 ± 0.4	SN450	99.6	15.8 ± 0.5
SN443	99.3	17.6 ± 0.3	SN453	99.4	15.7 ± 0.3
SN422	99.6	14.1 ± 0.3	SN458	99.2	15.4 ± 0.4
SN427	99.8	13.8 ± 0.4	SN435	99.5	15.0 ± 0.5
SN436	99.7	14.9 ± 0.5	SN457	99.7	15.7 ± 0.3
SN420	99.6	15.7 ± 0.4	SN454	99.9	16.1 ± 0.3
SN424	99.7	16.9 ± 0.2	SN455	99.8	16.6 ± 0.3
SN434	99.8	16.4 ± 0.4	SN440	99.8	22.2 ± 0.1
SN429	99.8	16.5 ± 0.1	SN456	99.4	17.1 ± 0.2

Table 2: Specifications of flown conversion foils as installed, listed in order looking into the sensor clockwise from the cable tray.

- Fourth is an electrostatic analyzer (ESA), stepped through various voltages during science data collection, which passes a limited range of ion energies to the detector section. The ESA also limits unwanted signal created by light and by ENAs that remained neutral after passing through the conversion foils. The standard set of ESA voltage settings used in calibration and intended for flight are listed in Table 3.
- Next is the detector section, which is biased 8 kV negative to accelerate the ionized ENAs inward:
  - an entrance foil, which passes the ion, converting some fraction of the ions back to ENAs. Also generated by the ion are secondary electrons, on both sides of the foil.
  - an exit foil some distance later, which behaves like the entrance foil in the described aspects.
  - two channel electron multipliers (CEM A and CEM B), located and biased so that electrons generated on the rear of the entrance foil arrive at the mouth of CEM A and electrons generated on the front of the exit foil arrive at CEM B. The CEMs then have some probability (detection efficiency) to produce discriminated pulses from the initial electron.

ESA Energy Step	Nominal Central Energy (keV)	Inner ESA (V)	Outer ESA (V)
Background (0)	—	0	0
1	0.575	-472	+122
2	0.80	-713	164
3	1.10	-1047	213
4	1.50	-1564	270
5	2.50	-2089	718
6	3.75	-2893	1232
7	5.70	-4147	2034
8	8.52	-5948	3185
9	12.8	-8650	4911

Table 3: Approximate final central energies and ESA settings for IMAP-Hi. Original values for ESAs 1, 2, and 4 were 0.50, 0.75, and 1.65 keV, respectively.

  - one microchannel plate stack (MCP C), located behind the exit foil, upon which arrive both the original ENA (now scattered through a total of three foils and present as either an ion or a neutral) and secondary electrons generated on the rear of the exit foil. Both the secondary electrons and the original ENA may generate "C" pulses.

- The detector then reports some combination of A, B, and C hits inside a maximum coincidence window length. Timing information is kept between A, B, and the first C hit ("C1"), and also between the first two C hits (C1 and C2), if there are at least two C hits in the coincidence window.

Hi90 has entrance foil SN09 (99.4% coverage, k_F 16.1 ± 0.3) and exit foil SN11 (99.5%, 16.1 ± 0.3). Hi45 is likely some combination of two of the many foils labelled SN1 and SN2 (probably both 99.8%, k_F 18.1 ± 0.3 and 19.7 ± 0.2).

A *coincidence event* is defined as at least two hits being registered during one coincidence window – either from two detectors each registering a hit, or the C detector registering two hits. *Calibration products* are then formed out of sets of various coincidence events, using a qualification scheme based on the relative times of the A, B, C1, and/or C2 hits ("times-of-flight", or TOFs). The reason for a TOF-based qualification scheme is to minimize the amount of background/noise mistakenly identified as ENAs, while still correctly registering most ENA-created coincidence events as ENAs. The reason for more than one calibration product is that remaining backgrounds may be significantly different for different coincidence events, to the point where it makes sense to define a "cleanest" calibration product and a "best statistics" calibration product, in the same sense that IBEX-Hi calibration results were reported in the instrument paper for "qualified triples" and "summed doubles".

The TOFs are smeared due both to the variety of trajectories through the detector possible due to scattering and passage through the ESA, and, to a lesser degree, to the range of times for electrons to travel to the CEMs from the foils. As a result, energy resolution better than that provided by the ESA is not really possible from detector TOFs, although separating H signal from heavier atoms (He, O) is feasible. IMAP-Hi has no requirements concerning detection of any species other than H.

Although the exact specification of calibration products is likely to be modified during commissioning, when actual backgrounds in space are observed, the following initial scheme was used to analyze calibration data:

Calibration Product 1, the lowest-background data product:

- ABC1C2 quadruple coincidence, and ABC1 and AC1C2 triple coincidence (BC1C2 is excluded as it's less clean).
- if A and B are present, $t_B - t_A$ must be in the range 15 to 90 ns.
- if A and C1 are present, $t_C - t_A$ must be in the range -20 to 70 ns.
- if B and C1 are present, $t_C - t_B$ must be in the range -50 to 20 ns.
- if C1 and C2 are present, $t_{C2} - t_{C1}$ must be in the range 16/2 to 80/2 ns.

Calibration Product 2, the better-statistics data product:

- AB, AC1, and BC1C2 coincidences, using the same time ranges as Calibration Product 1.

Note that the sum of both products is required to address RHI-1596 and RHI-1597. This choice of calibration products was arrived at during calibration by observation of the sensors: C1C2 was generally compromised by ringing in the MCP line and by the design of the "discriminator" handling both the C1 and C2 pulses. The software used to analyze the calibration results was written with the likelihood in mind of quick reanalysis being needed for differently defined calibration products.

For Lo-Hi cross-calibration, for instance, a different choice of calibration product was necessary to replace the sum of Calibration Products 1 and 2, due to background in the C2 signal that was not present earlier during calibration:

Calibration Product 3, the more stable combined better-statistics data product:

- AB, ABC1, ABC1C2, AC1, and AC1C2 coincidences, using the same time ranges as Calibration Product 1 but enforcing no range limit on $t_{C2} - t_{C1}$ if C1 and C2 are present.

Product 3 has a slightly larger geometric factor than the sum of Products 1 and 2. Use of Product 3 also resolved an issue during calibration when a power outage and ensuing warmup of the cryopumps exposed the Hi45 sensor to different conditions than the usual nitrogen purge. Thereafter, until the next vent, the sensor performance was slightly different, specifically in terms of the number and nature of C2 pulses (ABM detection efficiencies also increased, suggesting the general (temporary) deposit of material with higher secondary electron yield than normally present after a purge and pumpdown). Diagnostics and subsequent amelioration are somewhat difficult due to the extremely limited nature of the discriminator that was chosen to replace a standard CFD in the front-end electronics. Between this situation and the somewhat similar odd C2 behaviour exhibited by Hi45 during Lo-Hi cross-calibration, it seems that the course of action for greatest reproducibility of results is to disregard C2 pulses when defining Calibration Products, as is the case for Cal Product 3.

Calibration Overview

IMAP-Hi calibration had numerous phases, split by environmental testing and fixing issues arising from environmental testing. The calibration plan is laid out in CN106V-T0015, the IMAP-Hi Assembly, Integration, and Test Plan. The philosophy followed IBEX-Hi calibration. Testing was nearly identical for Hi45 and for Hi90, with minor modifications made due to time limitations. The bulk of the time was spent putting a neutral hydrogen beam into IMAP-Hi at normal incidence. The beam was generated from the LANL ion beam facility by neutralizing a fraction of the H^+ beam with buffer gas (simply residual gas in the beamline after the bending magnet, or, at lower beam energies, residual gas plus room air leaked in via a leak valve) and deflecting the remaining ions out of the path with magnets. A 2 mm circular aperture was standard at the entrance of the calibration chamber, resulting in a 2-3 mm beam at the instrument entrance. Beam flux was recorded with the same absolute beam monitor (ABM) used for IBEX-Hi calibrations, and occasionally with a Quantar imaging MCP. The use of a buffer gas to produce the neutral beam necessitated a small beam size (2 mm diameter) to allow for differential pumping. Because the neutral beam is small and neutral, and the IMAP-Hi entrance aperture is vast, it was necessary to move the instrument across the beam rather than the beam across the instrument.

During calibration, IMAP-Hi was mounted on a series of motion stages as shown in Figure 1. A linear stage translated IMAP-Hi across the neutral beam horizontally; an axial rotational stage ("FERRIS") rotated IMAP-Hi to change which conversion foil was in the beam; and two rotational stages (azimuth and polar) changed the orientation of IMAP-Hi with respect to the beam. The axial stage rotated through the range 0 - 360°, allowing each of the conversion foils to be placed into the beam.

During all calibration prior to cross-calibration, the sensor was run using COTS HVPSes for all high voltages (this allowed better current monitoring and faster current trips), and using the "fast DE" line coming directly from the front-end electronics (FEE) and bypassing the CDH software. The downsides of this approach include not running the exact voltages allowed by the precision of the flight HVPS commanding, and not holding the FSW developers' feet to the fire until late in the testing.

The purpose of calibration extends beyond simply meeting the requirements listed at the start of this document, although many of the calibration activities can be tied back to the mission requirements levied, with enough pondering (note though, for example, that calibration in the central part of the IMAP-Hi energy range

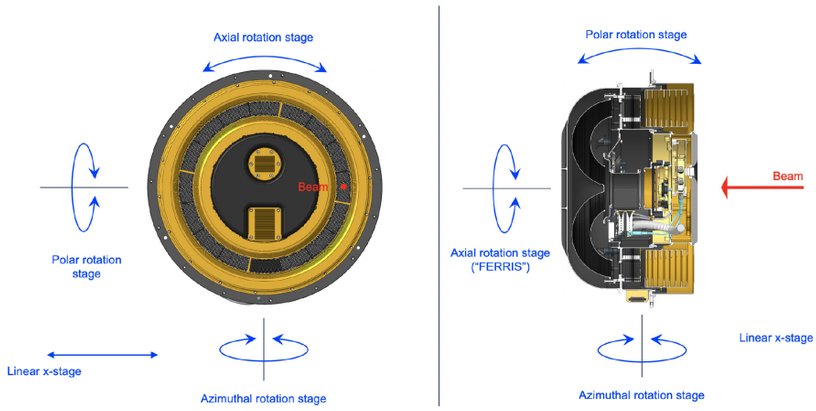


Figure 1: Sketch of IMAP-Hi indicating motion stages during calibration

was painstakingly performed despite the lack of any requirement on calibration accuracy except in energy regions overlapping IMAP-Lo and IMAP-Ultra).

Phase 1 This phase was intended primarily to characterize the electro-optics of the ESA.

At this time, the collimator was not yet installed. This allowed very straightforward characterization of the conversion foils and ESA; in particular, for the 2–3 mm neutral hydrogen beam spot used, it was easy to study ESA throughput starting at any point on the conversion foils without having to consider the transmission through the collimator for that size beam, which would depend greatly on the exact location of the beam with respect to the collimator's hexagonal holes. Neutral hydrogen beams, created by buffer-gas-neutralizing a H^+ beam created in a microwave ion source ($\Delta E < 2$ eV) and charge-to-mass selected by a bending magnet, were aimed at selected points on the foils at various energies and angles—points at the centre of the panes as well as points at the edges. Locations tested are shown in Figure 2. The ESA was run at the settings specified in Table 3. The inner ESA voltage was also swept for a neutral hydrogen beam at a fixed location and at a few fixed beam energies, specifically to test and refine the electro-optic model of the ESA.

Additional testing during this phase, necessary prior to the installation of the collimator, included deflector testing and characterization of the angular acceptance of the ESA. And, as in all phases of calibration, background count rates were monitored.

The general time frame of Phase 1 calibration was November 2023 to mid-February 2024.

Phase 1b/Phase 2 Mainly this phase was intended to characterize the collimator and to confirm instrument survival after environmental/vibe testing.

With the collimator installed, the collimator angular acceptance could be characterized and the final deflector testing could be conducted. Additionally, this phase was used to image the conversion foils and determine the percentage of holes. The entrance aperture was rastered across a N_2^+ beam produced at an energy in the middle of the ESA 7 bandpass (5.0 keV, which is close to the centre of the bandpass if straggling in the carbon foil is not considered). If carbon foil was present, the energy-straggled beam exiting the foil would be made of neutral N and N^+ outside the energy bandpass of the ESA, whereas any N_2^+ passing through a hole in the conversion foil would transit the ESA and be detected.[1]

The general time frame of Phase 1b calibration was late December 2023 (Hi45) and late January to February

[1]This means of characterizing foil holes came around after a suggestion by Frederic Allegrini to use Ar^+ or a similar heavy ion, with the idea that energy straggling would get rid of any ion that hit foil. The use of a molecular ion instead came about when Corey Tucker and Paul Janzen found the bright N_2^+ beam.

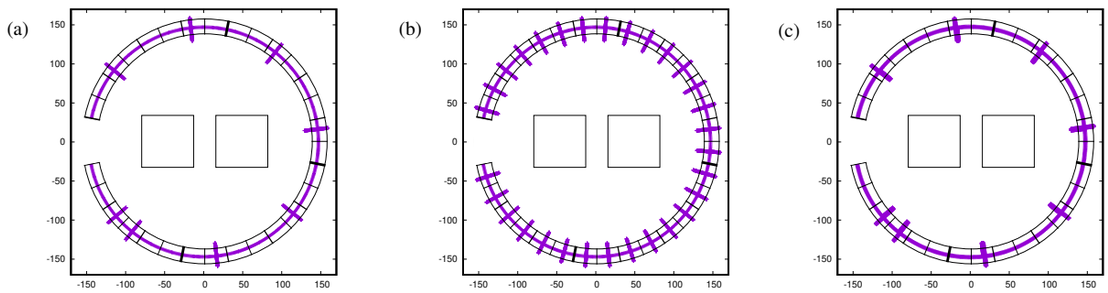


Figure 2: Diagrams of conversion foil coverage during Phase 1a and New Phase 1a as taken from the motion stage logs, overlaid on a schematic of the conversion foils. In this sketch, the squares notionally represent the vents of IMAP-Hi, and the thickest bars between foils show the location of structural ribs, whereas the thinnest bars correspond to the thin ribs between panes of a single foil assembly. The cable tray gap is evident on the left-hand side of each plot. The left two plots show the quick (a) and full (b) scans from Phase 1a; the right plot (c) shows coverage in New Phase 1a. Phase 1a included dwells, not explicitly shown in these plots, at various points to improve statistics. New Phase 1a, when the collimator was installed, included more rastering instead.

2024 for Hi90. Phase 2 on the final FMs occurred on September 24-25, 2024 (Hi45) and September 30-October 1, 2024 (Hi90).

New Phase 1 The carbon foils on IMAP-Hi sure had some problems surviving vibe. They failed after original Phase 1, and then they failed again after half a year or so of redesign. As a result, the calibration schedule once IMAP-Hi stopped falling apart got squeezed.

Given that Phase 1 original calibration is mainly a characterization of the ESA bandpass and of deflector ion rejection, and the ESA and deflectors positioning did not change through environmental/vibe, an abbreviated phase 1 beginning with the collimator already installed was deemed sufficient, in addition to prior Phase 1 work. Testing procedures were similar to that in Phase 1, but abbreviated. Because the collimator was installed, the sensors needed to be rastered across the beam. Locations tested are shown in Figure 2.

The general time frame of New Phase 1 calibration was September 2024 for both Hi45 and Hi90. Phase 2 was wedged in before Phase 3.

Phase 3 This phase constituted final calibration, to identify the specific behaviour of the flight CEMs, MCPs, and foils, with all conversion foils entirely scanned at most central ESA energies and normal incidence. Figure 3 shows the foils scanned at energies where, to save time, not all conversion foils were scanned.

The small neutral beam size fills only a small part of the entrance aperture of IMAP-Hi and so to calibrate the entirety of the sensor, the instrument must be moved through the beam. The motion of the sensor across the beam is referred to as a "snake" scan, and was performed by rastering the instrument horizontally at 1 mm/s, from beam fully off the sensor radially on one side to fully off the sensor radially on the other, then rotating in axial ("FERRIS") by 0.555°, which is a displacement of approximately 1.5 mm at the conversion foils, and rastering horizontally at 1 mm/s the other way, followed by another axial rotation, etc. The pattern of the "snake" is illustrated in Figure 4. A single conversion foil pane could be entirely measured in about a quarter hour. While IBEX-Hi had large enough collimator holes to allow clear imaging of the collimator in this process, IMAP-Hi's collimator spacing does not allow such an image.

The general time frame of Phase 3 calibration was October 2024 for both Hi45 and Hi90.

Cross-calibration: Hi90/Ultra, Lo/Hi45 Cross-calibration itself is addressed in another memo. Its relevance to this document is that during this phase, the IMAP-Hi sensors were used in "flight" configuration, with all HV supplied by the EBox, with commanding through the CDH, and with analysis done on CDH-created packets as opposed to the "fast DE" stream straight from the FEE. This is the phase during which HVSCI mode was tested.

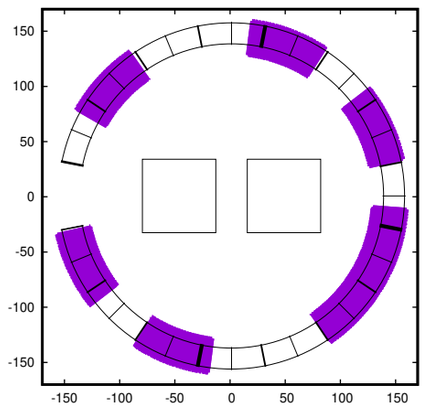


Figure 3: Foils studied in Phase 3 at energies where not every foil was hit.

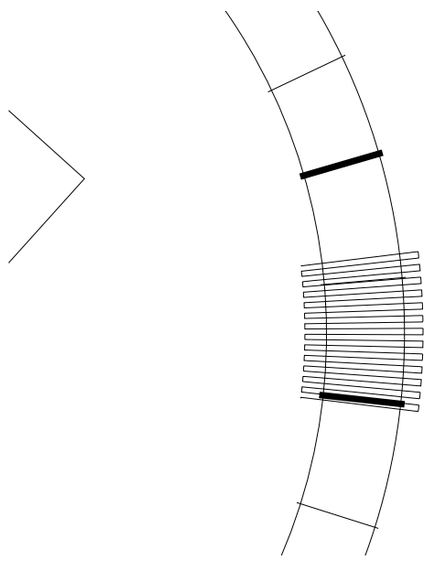


Figure 4: Closeup of a snake scan on one foil.

Hi90/Ultra cross-calibration occurred at the start of November, 2024. Lo/Hi45 cross-calibration occurred at the start of February, 2025.

Various modifications were made to hardware and software through calibration activities.

The front-end electronics (FEE) underwent development during Phase 1, including hardware modifications to change the performance of the discriminators and programming modifications to reduce the number of "mangled" (unparseable) direct events sent from the FEE. A note of relevance here is the default state of the FEE's Delay Line Disable register, which changed from enabled to disabled at some point before New Phase 1. This register functionally shifts coincidence windows, except for C1-C2, by 4 ns. In any analysis using data prior to the change in default state of this register, the qualified coincidence TOF ranges are wide enough to ignore this shift.

Note that *two* different qualification schemes exist in the IMAP-Hi data processing, once the CDH's FSW gets involved. There is a loose qualification scheme implemented by FSW to choose which events to store in the SCI_DE packets: this is necessary to stay within telemetry limits and to avoid being overrun by potential backgrounds. Following that, the TOFs listed above are used by ground processing as an additional, tighter limit. Events telemetered down but not used directly for science are used to study backgrounds.

FSW was updated continuously through calibration, but mainly after the end of Phase 3 (that is, through cross-calibration activities).

The length of the coincidence window was changed from 500 ns to 1000 ns after calibration, by SwRI, to work around a bug in the FEE FPGA involving misreported longer, valid TOFs (500 ns was already a needlessly long coincidence window, so this should not affect calibration much; count rates are low enough that no meaningful dead time correction is required in either case). Because the coincidence counters are either 9-bit counting at 1 ns, or 10-bit counting at 0.5 ns, this means that all the counters now may "alias" or wrap around inside the TOF window.

Gain Curves (RHI-1140)

Gain curves were taken in every phase of calibration. Gain curves for the two CEMs and the MCP in Hi45 and Hi90 during Phase 3 are shown in figures 5.

Except for Hi45/Lo cross-calibration, which tested gains using the voltage stepping sequence of the onboard macros, gain tests were generally performed with all detectors except the one under study at nominal operating voltage. The performance of the detector was determined by looking at the direct events and summing all *qualified* coincidence events involving the detector in question (*e.g.*, for detector A, qAB + qAC1 + qABC1 + qAC1C2 + qABC1C2). The reason for doing so is that *total* counts per detector do not exhibit a clear gain plateau due, presumably, to signal-generated ion feedback background. The greater the voltage across the detector, the more ions are created which are accelerated away from the detector towards the U-Can, where they create secondary electrons then detected by both the original detector and other detectors. In particular, the MCP is a prolific generator of counts in CEMs A and B when it is at operating voltage. Additionally, the MCP pulse-counting system is designed to register multiple hits per incidence particle, and when the original pulse gets larger (due to increased operating voltage), "ringing" also gets larger and more likely to be detected as the second pulse. This can have a secondary effect, if TOF qualification is applied to C2, of *decreasing* the apparent MCP efficiency as its operating voltage goes up, because ringing outside the valid TOF range starts to disqualify C1C2 coincidences. Note that the limited functionality of the FEE circuit intended to behave as a constant-fraction discriminator in setting a threshold is likely a minor contributing factor to these issues. (On IBEX-Hi, the three CEM detectors were separated to ensure that ion feedback from one CEM cone could not produce signal in another CEM; nonetheless, we had "burst" issues where the electron pulse exiting the rear of the CEMs could still apparently cause a signal in the other CEMs.)

The plan on orbit is to run gain tests in the same fashion as for IBEX-Hi and step all detector voltages together. This is to limit test duration to a reasonable number of hours, given that the input signal in space is not a bright lab beam but whatever ENA signal exists. A representative comparison gain test using this voltage ramping scheme was run during Lo-Hi cross-cal, to aid in analysis. If necessary, of course, on-orbit gain tests could be run the same way as the calibration gain tests, at the cost of additional time.

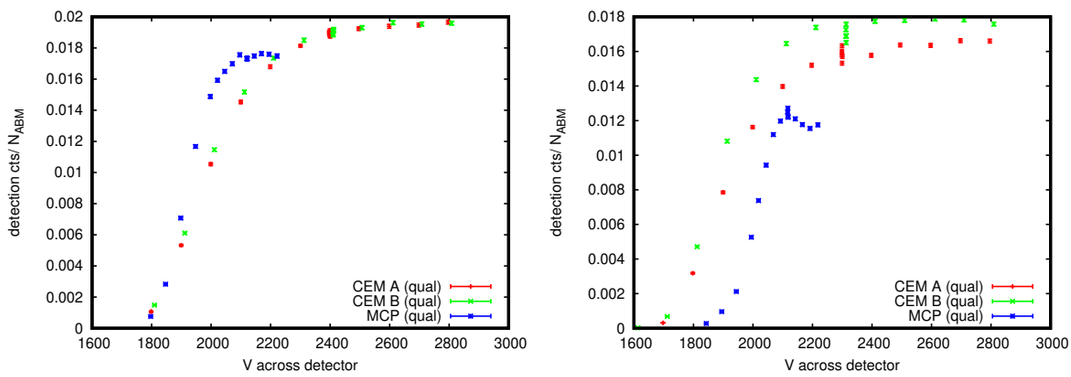


Figure 5: Gain curves taken during Phase 3 calibration for Hi45 (October 12, 2024, left plot) and Hi90 (October 26, 2024, right plot). Data shown was collected at ESA step 7 with a 5.7 keV neutral H beam, and is normalized to ABM linearly interpolated between data taken immediately prior and after. Statistical error bars based on counts seen are plotted but are comparable to symbol size. Operating voltages were 2.3 kV (CEMs A and B, Hi90), 2.4 kV (CEMs A and B, Hi45) and 2.125 kV (MCPs). "CFD" settings were 25 mV in all cases except for Hi45 MCP, which was 22.5 mV.

Energy Response and Energy Resolution (RHI-1047, 1048, 1054, 1055, 1060, 1061)

Energy response is largely a function of the ESA, with very minimal differences amongst various Calibration Products. The detector section does show somewhat differing behaviour as a function of the axial angle (*i.e.*, which conversion foil is being struck), and there are minor differences in energy straggling between conversion foils. Nonetheless, the basic energy response as measured in Phase 1 remains the same through the remainder of calibration.

Energy response was measured in two ways. Improvement of the SIMION electro-optics model, and characterizing the range of performance of the detector section, is most quickly accomplished with data collected by keeping the beam energy fixed, and shifting the voltages on the inner and outer ESA to move the energy passband. This data is collected for a sequence of locations on the conversion foils. At the detector, this functionally provides data with the incoming ion's direction varying across the full range of acceptance. While these measurements are crucial to developing a model, they are not in themselves sufficient for full calibration of the sensor at its intended ESA settings. One reason is that the ionization probability and secondary electron emission characteristics of the carbon foils inject a nontrivial amount of energy dependence into the overall response function, which is not captured in characterizing the system at one energy.

Therefore, in Phase 1a and in New Phase 1, scans were taken over samplings of conversion foils across the entire entrance aperture at a range of energies from 500 eV to 14.54 keV. Energies chosen included the central energy of each bandpass, and logarithmically spaced energies between, to favour increased calibration information at the lower-energy side of the energy response, which is where most of the flux is expected during the mission. The first sacrifice due to time constraints was data on the high-energy side of the energy response, as uncertainty here has the least scientific impact. The second sacrifice was widening the steps between consecutive energy measurements.

The LANL facility accelerating voltage comes from a 60 kV supply; at energies below 6 keV, a different beam tuning configuration was developed and implemented to maintain better stability and reproducibility at voltages far from the designed values of the supply.

Shown in Figure 6 is the energy response of all 9 standard ESA settings of IMAP-Hi, as determined in New Phase 1. The data product used was Coincidence Products $1+2$; the result is not particularly sensitive to choice of data product. Counts were always normalized to ABM flux interpolated linearly between ABM measurements. In Phase 1 and New Phase 1, the entire foil surface was not scanned. Instead, a representative subset of the conversion foil surface was studied and results were extrapolated to the entire surface.

Shown in Figure 7 are the fuller data collected over more energies in original Phase 1. Absolute values

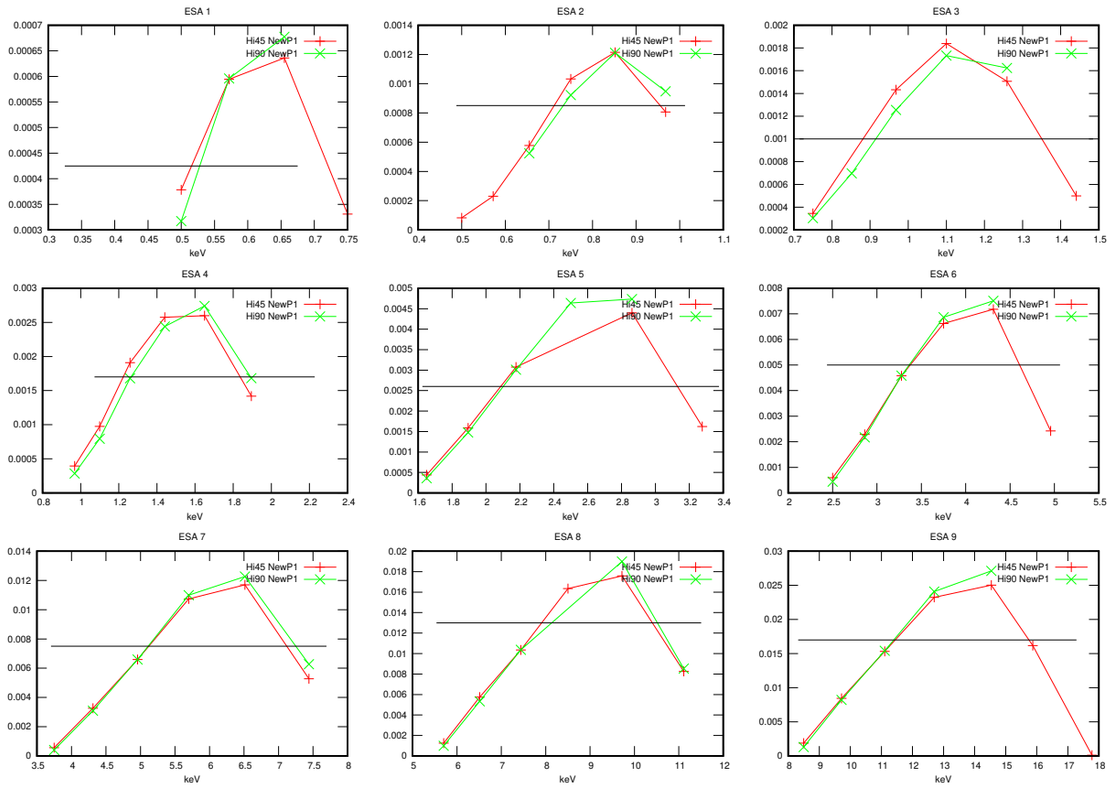


Figure 6: "New Phase 1" energy response of the IMAP-Hi units. The black line shows the requirement limit of $\Delta E/E_c = 0.70$ FWHM. IMAP-Hi meets the requirement as long as the FWHM of the curve is inside the black bar. Plotted is the sum of Calibration Products 1 and 2. The lines connecting the points are only to guide the eye, and may be misleading (*e.g.*, at ESA 5) where data at intermediate energies were not taken or processed.

between Phase 1 and New Phase 1 are not expected to be exactly the same, as parts of the sensor other than the ESA were different (detectors, detector operating voltages, foils) and the FEE programming and circuitry were different as well. It is the *shape* of the energy response that we expect to be generally the same.

In all cases, the FWHM of the ESA response is less than 0.7 of the central energy, meeting the requirement. Indeed, $(\Delta E)_{\mathrm{FWHM}}/E_c = 0.42 \pm 0.03$ for all ESA energy settings, using either approach to fitting the energy spectrum described later in the analysis concerning the geometric factor (that is, piecewise-linear or Gaussian). Much of the 0.03 variation arises simply from the choice of E_c.[2] ESA 1 appears to peak at a higher energy than designed, which is possibly due to design calculations expecting a different energy straggling in the conversion foil.

Angular Response and Alignment (RHI-1049, 1057, 1062, 1197, 1630)

Angular response was checked after sensor installation in the calibration chamber for every phase of calibration in which the collimator was installed. This was necessary to confirm the angle offsets required for the ENA beam to strike the instrument at normal incidence. Testing involved performing "snake" scans on a single conversion foil pane at 2° increments in azimuthal and polar, from −4° to +4°, with additional snakes performed at (az, polar) = (±2°, ±2°). The usual energy was 5.7 keV, at the centre of the ESA 7 passband. Count rates seen

[2] In scientific analysis of the data, $(\Delta E)_{\mathrm{FWHM}}$ is not used for anything, although the energy response $T(E)$ is used in the "flux (intensity) correction" step when the energy response is deconvolved. The E_c values are used merely to choose the energies at which the deconvolved intensity is reported.

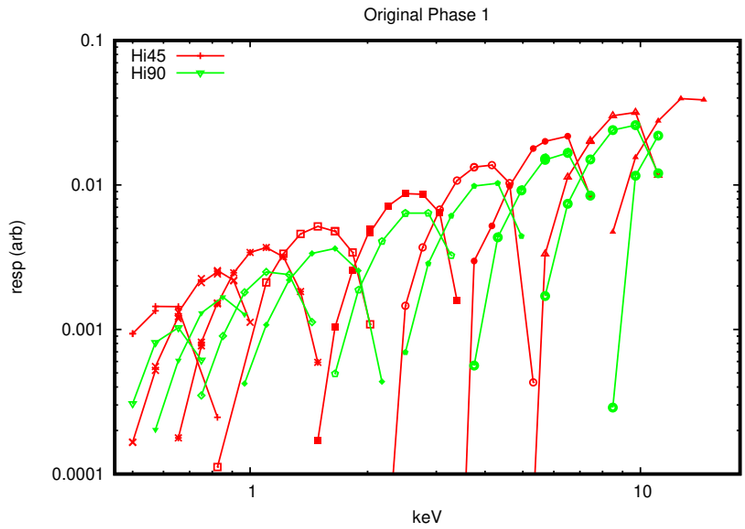


Figure 7: Energy response of IMAP-Hi as measured in original Phase 1, prior to vibe failure (so with different foils and detectors to the delivered units). The data points at each measured energy are plotted; the lines connecting the points are only to guide the eye.

were normalized to ABM count rates linearly interpolated in time from ABM measurements before and after the snake, to determine an average detection efficiency over the foil pane. This was then plotted against angle. The immediate need in calibration was to determine normal incidence, so the data in azimuthal angle with polar at zero or expected closest-to-normal, and the data in polar angle with azimuth at zero or expected closest-to-normal, were fit separately to the function $f(\theta) = \max\{0, a(1 - |x - b|/c)\}$ with fit parameters a, b, and c. The immediate need in calibration was an accurate b. A nonzero b could arise either from a misalignment of the sensor with respect to the beam (optical measurements suggested a potential 0.35° offset in azimuthal angle and a potential offset in polar angle of up to 0.8°) or from a misalignment of the collimator, with a mounting angle offset from the baseplate or a skewing of the various collimator plates in assembly being considered plausible issues and "coning" of the collimator not being considered plausible. To separate these two sources, the same set of snake scans were taken on a foil pane 180° axially away from the first one. A b with consistent magnitude and sign would be consistent with the former issue, and a b with a reversed sign would be consistent with the latter. Additionally, for Hi45, data was taken on a foil 90° from the first two foils.

For the purposes of meeting mission requirements addressed in this document, c, the response FWHM, is the interesting fit parameter. The simple form of $f(\theta)$ will not quite capture the actual collimator response, which has hexagonal symmetry and "tails" extending to larger angles before the response drops fully to zero. Additionally, the neutral beam itself has a small amount of divergence, measured in summer 2024 to be approximately 0.1° at the energies used to study angular response. Vignetting of holes in the conversion foils could possibly create angular response in addition to the collimator's, which would not be generally applicable to the entirety of the entrance aperture. Finally, the expectation going into calibration was that previous *optical* tests on the collimator would inevitably be of higher precision than ENA measurements, and that the ENA-based angular response investigation would simply verify the optical testing to within the ENA-based method's uncertainty.

A table of fit parameters b (angle offset) and c (FWHM) is shown below, with the caveat that the uncertainties derived from 5 points fitting a 3-parameter function are likely understated. The data used in fitting was the sum of Calibration Products 1 and 2, although the fit was not sensitive to the particular choice.

Date	Vibe	Sensor	Beam Energy	Axial Angle	Az Angle offset	FWHM (Az)	Polar Angle offset	FWHM (Polar)
Sep 5/24	pre	Hi45	5.7 keV	36° – 48°	0.31 ± 0.06	4.61 ± 0.10	-0.05 ± 0.01	4.47 ± 0.02
		Hi45	5.7 keV	216° – 228°	0.32 ± 0.02	4.62 ± 0.03	-0.38 ± 0.07	4.51 ± 0.12
Oct 12/24	post	Hi45	5.7 keV	36° – 48°	0.32 ± 0.02	4.62 ± 0.03	-0.10 ± 0.07	4.38 ± 0.11
Sep 17/24	pre	Hi90	12.7 keV	36° – 48°	0.34 ± 0.02	4.61 ± 0.03	-0.35 ± 0.07	4.41 ± 0.11
		Hi90	12.7 keV	216° – 228°	0.36 ± 0.04	4.56 ± 0.06	-0.36 ± 0.07	4.35 ± 0.12
Oct 3/24	post	Hi90	1.65 keV	36° – 48°	0.34 ± 0.01	4.63 ± 0.02	-0.40 ± 0.02	4.53 ± 0.03

From this table:

- There is repeatability per sensor of better than 0.1° and knowledge of better than 0.07° of beam direction, meeting alignment requirements.
- The two sensors' angular responses are slightly different, and of the two, Hi90 is better behaved (or at least, slightly more expected and more consistent between the two panes), given prior knowledge of stage alignment with respect to beam. Both are within alignment tolerance.
- The collimator response is expected to go from a FWHM of 4.0° across the sides of the hexagon to a FWHM of 4.1° across the corners.

  According to mechanical drawings, the flat side of the hexagon should be vertical at an axial angle of either 42° or 222°, suggesting that the polar FWHM should be about 0.1° greater than the azimuthal FWHM. This is the opposite of what is seen. It is worth noting that a left-right mirror reflection of one drawing would have the result of shifting the flat side of the hexagon to horizontal, which would match the observations. However, with the resolution of this issue absent, it means that fitting the observed angular response to the actual (axial-angle-dependent) collimator response, rather than to $f(\theta)$, is problematic.

  What can be done is to use the theoretical collimator response to generate data near ±4°, ±2°, and 0° for the corner and side cases, and to see what FWHMs result from a fit of $f(\theta)$. Doing so yields values for c in the 4.41 - 4.47 range along the sides and in the 4.46 - 4.53 range across the corners. Adding in the known beam divergence of ≈ 0.1° for energies of ≈ 2 keV and above results in FWHM values entirely comparable to those observed.

The conclusion is that the observed collimator angular response matches the designed and expected response to within the accuracy of the ENA calibration for Hi90 and nearly so for Hi45. The plan therefore is to use the design values as the best ones to model the collimator angular response.

Regardless, it is evident from the data in the table and the plots shown in Figure 8 that the angular response of both Hi45 and Hi90 is less than 6° FWHM, as required.

Signal to Background (RHI-1051, 1056)

Backgrounds are a key concern for IMAP-Hi, as they were for IBEX-Hi, because the heliospheric ENA signal rate is so low. A comparison to IBEX-Hi is worthwhile in evaluating the meaningfulness of this requirement. On IBEX-Hi, great care was taken for detector cleanliness (only ceramics used–no plastic, and a separate vent path for the detectors to minimize contamination from the rest of the instrument). Backgrounds for the cleanest data product ("qABC") on the order of 0.3 /ks were observed in testing, which even at this low count rate were considerably higher than predicted. A relation between background rates and level of ambient background radiation was observed, and the backgrounds on orbit were seen to be on the order of 50 /ks, varying with the cosmic ray background, leaving IBEX-Hi with a signal to background of roughly 1:1 for the cleanest data product. Good science was nonetheless accomplished with IBEX-Hi. The IMAP-Hi design eschewed the severe cleanliness design of IBEX-Hi but added more functional time-of-flight resolution to the detector, specifically to separate now-expected on-orbit backgrounds more cleanly from the signal. Definitely, the backgrounds observed on IMAP-Hi during ground calibration are larger than they were on IBEX-Hi.

EM issues related to high background rates occupied much of the EM analysis time and effort, with the main outcome being gold-plating the U-Can to reduce secondary electron production on its surface. Although the peak and typical times-of-flight of "ion feedback electrons" will not be in the qualified TOF ranges, the tail of the distribution may be.

RHI-1051 combined with RHI-1596 yields a maximum background count rate in units of /s, with the understanding that maintaining the required S/N allows the allowed background count rate to increase in proportion to the sensor's geometric factor. The signal count rate inferred for RHI-1051 is 0.1 /s, implying an allowable background rate of 2/ks for a data product with a geometric factor just meeting the RHI-1596 requirement.

Backgrounds are slightly dependent on the TOF range under consideration: in theory, the "qualified" TOF range could be narrowed to just the middle of the H ENA TOF peak, to improve S/N at the cost of reduced geometric factor. At present, the qualified windows are fairly large to improve geometric factor and to avoid complications with the FEE delay line setting. Backgrounds observed in the "qualified" TOF range have varied

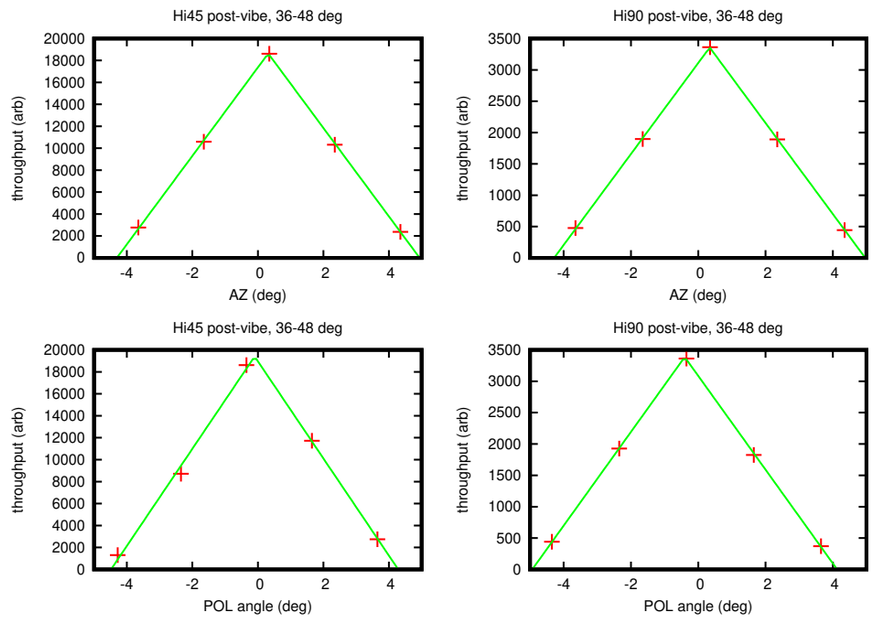


Figure 8: Angular scan data taken after vibration testing for Hi45 (October 12, 2024, left plots) and Hi90 (October 3, 2024, right plots).

Test	Duration	lA	lB	lC	qAB	qAC	qBC	qCC	qABC	qACC	qBCC	qABCC	CP1 (/ks)	CP2 (/ks)	CP3 (/ks)
Hi45 Sept 3	4560s	1673	2489	11274	26	14	176	99	1	0	4	0	0.22	9.7	9.7
Hi45 Sept 4	3789	4165	3789	21565	68	15	140	458	2	2	9	0	1.06	24.3	26.7
Hi45 Sept 12	2531	849	944	11502	10	6	54	167	0	1	8	0	0.40	9.5	9.9
Hi45 Oct 12	2700	1544	1918	9142	21	4	51	173	0	0	2	1	0.37	10.0	10.4
Hi45 x-cal	12600	-	-	-	23	26	241	33312	2	24	453	4	2.38	39.8	6.3
Hi90 Sept 18	3573	850	9239	14256	11	8	185	105	1	0	6	0	0.28	7.0	5.8
Hi90 Sept 21	4615	796	9830	13197	17	7	199	82	1	0	7	0	0.22	6.7	6.5
Hi90 Oct 1	3122	639	8798	25067	6	2	76	448	0	0	2	0	0	3.2	3.5
Hi90 Oct 5	3600	789	8163	15215	11	6	172	142	1	0	3	0	0.28	5.6	5.6

Table 4: Various background collection intervals over the course of calibration, including the Hi45 background data during cross-calibration with Lo that indicates a shift in the primary background TOF for C1C2. Singles counts are not included in the RAW_DE-based cross-calibration analysis.

over time, but have generally been observed to decrease over time that the sensor is left under vacuum. Whether or not we have seen a background rate plateau is debatable, because accurately determining backgrounds at the < 10 counts/hr level takes a lot of time, and time was at a premium during calibration.

Background data is presented in Table 4. Cal Product 1 exceeds the requirement but Cal Products 2 and 3 do not meet it. Unfortunately, Cal Product 1 does not have sufficient geometric factor on its own to suffice as the sole data product: at 1 keV, Cal Product 1 has approximately 0.55 the geometric factor of Cal Product 2, for both sensors. But the specific reason for multiple calibration products to exist is to use the lower backgrounds of one and the greater count rate of another to do better than either on its own.

Traditionally, the combined S/N ratio for multiple calibration products has been calculated by weighting each product's S/N by the product's geometric factor. Although this methodology appears to have been accepted, it is not a particularly logically meaningful quantity. The intent from a science perspective of the specifications RHI-1051 (S/N) and RHI-1596 (geometric factor) is to set a maximum allowable uncertainty on observed Poisson signal rates, in terms of easily measured laboratory quantities. Unfortunately, these specifications do not achieve this goal when products with different S/N and geometric factors are combined without also specifying an exposure time. Background (if identified and subtractable on average) increases the Poisson uncertainty, as does a smaller geometric factor, which lowers the number of count seen. The fractional uncertainty in the background-

subtracted signal formed by combining two Cal Products with different geometric factors and S/N depends on total counts seen and thus depends on exposure time.

Using the traditional combination of Cal Product S/N (that is, deciding that weighting S/N by geometric factor is sensible), applied to the total time interval of the last two background tests during cal (not cross-cal), yields a combined S/N of 34 for Hi45 and 103 for Hi90, which average to 68 for the whole IMAP-Hi sensor. Much of the difference between the sensors comes down to two background Cal Product 1 counts being observed for Hi45 in a little under an hours and a half, compared to one for Hi90 in a little under two hours. Poisson statistics are obviously very significant at this count level.

In summary, we consider the S/N requirement, RHI-1051, sufficiently met by both Hi45 and Hi90 by the use of a combination of calibration products. From IBEX-Hi, we also believe that ground-based background tests are not particularly indicative of background rates on orbit, that meeting this S/N requirement on orbit is not a prerequisite to completing the scientific goals of IMAP-Hi, and that the way the combined S/N requirement is traditionally calculated is not useful.

Tests for backgrounds from sources other than background radiation or the detectors themselves were performed as part of calibration.

- No counts were attributable to vibrations associated with the motion stages.
- UV tests with a 15 W mercury lamp (254 nm) produced total count rates similar to or less than seen with IBEX-Hi, with no significant coincidence count rates in the qualified TOF ranges. Based on IBEX-Hi's on-orbit performance, this is sufficient, particularly as IMAP-Hi will not see the two brightest UV sources seen by IBEX-Hi, the Earth and Moon. With the IMAP-Hi sunshade, the non-direct UV signal ("helioglow") is predicted to produce a negligible signal rate in the Calibration Products of less than 10^{-4}/ks, based on observations in calibration.
- The deflectors were tested to confirm the expected ion rejection, both before and after the collimator was installed, by sending in ion beams over angular ranges shown by SIMION simulations to be the most challenging to reject. Testing included running the deflectors at lower voltage than nominal to confirm significant HV margin. At no point, with the deflectors operational, was ion signal detected above the noise floor of the detector system. For the ion beam used (≈ 60 kHz), this corresponds to a minimum ion suppression factor of 1.5×10^7, which is more than an order of magnitude above that required to suppress expected on-orbit solar wind particle rates to a level negligible compared to the S/N requirement.
- ENAs other than hydrogen (helium, oxygen) may in theory produce signal mistaken for hydrogen. Beams of helium at 4.55, 5.2, 5.8, 5.92, 6.75, 7.69, 8.77, 10, 11.4, 13, 14.82, and 16.9 keV; oxygen at 5.8, 10, and 16.9 keV; and neon at 10 and 13 keV were used to characterize sensor response (specifically, detection efficiency and TOF signatures). This may allow some IMAP-Hi science involving heavy ENAs, but mainly it correlates large TOF peaks outside the "qualified H" region to very minuscule additional signal inside the "qualified H" region and allows subtraction of any such observed heavy ENA signal from the hydrogen ENA map to well below the S/N requirement.
- Finally, the ESA biasing scheme for IMAP-Hi is intended to narrow the ΔE compared to IBEX-Hi, which uses nearly the same ESA geometry. This biasing scheme biases the inner and outer ESAs at opposite polarities, whereas IBEX-Hi biased both negative (or at ground). As a result of the IMAP-Hi biasing scheme, it will not be possible to run background tests in space that completely reject positive ions created on the outer ESA by incoming ENAs that exit the conversion foils as neutrals, thus creating a new background during the background test that is not present at science ESA operating voltages. This increased background was observed on IBEX-Hi during background tests until the outer ESA was biased at least 40 V negative, and it is likely to be worse on IMAP-Hi due to the increased bias of the detector section, which pulls in positive ions from the ESA. Putting pockets in the outer ESA as per IBEX-Lo to solve this issue (and lessen UV effects) was considered early in the design phase but rejected due to lack of IBEX-Hi heritage; the inner and outer ESAs are grooved and coated with Ebanol-C, which helps somewhat. To at least be able to quantify this effect, measurements were made during the calibration campaign with various-energy neutral beams incident on the sensor with the inner and outer ESAs both at ground (as per background test ESA voltage settings). Additional signal with the ESAs "off" from the beams used was always within a factor of two of 2 counts/Ms per particle/s of beam, for Calibration Product 3, regardless

of whether the beam was 655 eV H, 12.7 keV H, or 11.4 keV He: a detection efficiency, during background tests, of ENAs that remain neutral on exit from the conversion foil but then ionize on the outer ESA of about 2×10^{-6}. Direct applicability of this test to on-orbit background tests may be limited inasmuch as the flight HVPS may not be able to reach zero volts (rather than some small non-zero voltage), and due to limitations in the housekeeping data to measure that small remaining voltage accurately.

Geometric Factor (RHI-1596, 1597)

IMAP-Hi has a requirement that geometric factor is at least 0.001 cm^{2}sr eV/eV at 1 keV and 0.01 at 10 keV. Because these two energies match none of the ESA step nominal central energies, it is necessary to interpolate between the ESA energy steps to show that this requirement is satisfied.

For ESA setting j with central energy E_j, and a beam at $E = E_j$ normally incident and entirely covering the conversion foil area,

$$\text{ENAs detected} = \text{ENAs incident} \frac{G_j}{A} T_j(E_j) E_j P(0,0)$$

where G_j is the geometric factor, A is the sensor entrance area, $T_j(E)$ is the energy response of the sensor at ESA setting j, and $P(\theta, \phi)$ is the angular response. Normalization is such that $\int T_j(E) dE = 1$ and $\int P(\theta, \phi) d\Omega = 1$.

$P(0,0)$, when the point spread function is normalized, is just 1 over the total solid angle acceptance, if the collimator lets in all particles at normal incidence. In this normalization, the actual peak collimator transmission, $\tau = 0.6944\ {}^{+0.0074}_{-0.0105}$, either is incorporated into A, which becomes the net transparent area of the foils (116.76 cm^2) rather than the total foil area (168.14 cm^2),[3] or is incorporated naturally into the ratio of ENAs detected to ENAs incident. The latter approach is taken here. The design specification for the IMAP-Hi collimator is 0.00631 sr. As discussed earlier with respect to RHI-1049, calibration shows within uncertainty that the design specification was met. Thus, $P(0,0) = 158.5$. [In comparison, IBEX-Hi had a field of view of about 0.0146 sr and a foil area of approximately 156.5 cm^2. The reduction in geometric factor compared to IBEX-Hi due to a narrower collimator field of view but larger foil area is roughly a factor of 2.3.]

E_j is basically declared by fiat within the energy response of step j, but it is nominally near the peak energy response of the ESA at the given energy step. Setting E_j a little on the low side is good for minimizing the flux correction factor later on in science operations center analysis.

To approximate the energy response function as measured in Phase 1/New Phase 1, the simplest two approaches are:

1. fit to a Gaussian, whereupon the value of the normalized energy response at the peak energy is just $1/\sqrt{2\pi}\sigma$. The fit isn't bad – it's better than trying a Gaussian fit for IBEX-Hi's energy response, in particular.

2. simply do a piecewise linear fit between calibration energies. This approach is likely to underestimate the energy response between the calibrated energies near peak transmission.

An improved, less simple approach is discussed in the Appendix discussing the final Flight Calibration Products and response function. The uncertainty in determining the energy response is estimated as approximately the difference between these two modelling approaches (usually at or below 10%) in quadrature with the difference between Phase 1 and New Phase 1 (usually at or below 10%: note that Phase 1 occurred before vibe failures and thus was not a calibration of the final flight hardware). The actual energy response will lie inside this range and requires simulations to determine the most accurate value.

Values obtained in calibration are shown in Table 5. [In comparison, IBEX-Hi typical had $T(E_c)E_c$ values around 1.6, because the energy acceptance was broader. Narrower energy acceptance lowers the geometric factor of IMAP-Hi compared to IBEX-Hi by about a factor of 1.3].

The Phase 3 "snake scans", correlated to ABM measurements, produce maps over the conversion foils of fraction of ENAs detected. An exact comparison requires scaling each (r, θ) pixel by r/r_0 to correct for unequal area sampling. This effect for scans at central energy was found to affect the average detected ENA fraction by less than a per cent. Additionally, some "snake scans" did not cover every foil at some central energies due

[3] There's an additional "unobstructed sensor area" value that occasionally gets stated, which ignores the collimator transmission at normal incidence but includes the 70% transmission of the nickel support grids for the entrance foils to reach a sensor area of 117.7 cm^2.

Sensor	ESA	$T(E_c)E_c$	Variation (model)	Variation (cal phase)
Hi45	2	1.76	8%	7%
	3	2.22	2%	3%
	4	2.13	6%	8%
	5	2.10	2%	1%
	6	2.03	1%	4%
	7	2.18	6%	10%
	8	2.17	10%	8%
	9	2.06	20%	20%
Hi90	2	1.70	20%	7%
	3	2.03	6%	—
	4	2.20	8%	9%
	5	1.92	8%	3%
	6	1.87	5%	2%
	7	2.39	8%	—
	8	1.79	—	2%
	9	1.82	—	—

Table 5: Values for $T(E)E$ at nominal central energies from Phase 1 and New Phase 1 calibration, modelled as Gaussian and piece-wise linear. No data is shown for ESA 1 because the full energy response could not be characterized: the ESA 1 energy response goes well below the 500 eV lower limit for calibration at the LANL beam facility. Time constraints limited calibration at the high-energy side of various energy steps, particularly for step 9.

to time constraints.[4] Such scans have been scaled by the relative sensor performance on the foils seen to the overall performance at other energies, interpolated to the energy under study. The scaling factor is slightly energy-dependent but is always within 5% of unity. Sample "snake" scans covering all conversion foils are shown in Figure 9.

The geometric factor finally depends on the Calibration Product chosen. The results plotted in Figure 10 show Calibration Product 3, which has a slightly larger geometric factor than the sum of Calibration Products 1 and 2.[5] [The most commonly used data product from IBEX-Hi was the "qualified triples", for which the detector-section efficiency was $\varepsilon_A\varepsilon_B\varepsilon_C \approx 0.13$. In comparison, Calibration Product 3 for IMAP-Hi, which includes a number of double coincidences, has a detector-section efficiency of $\varepsilon_A(\varepsilon_B + \varepsilon_C - \varepsilon_B\varepsilon_C) \approx 0.54$, which

[4]Every conversion foil was completely scanned in Phase 3 at central energies for ESA energy steps 2, 3, 4, 5, 8, and 9 for Hi90, and for steps 3, 4, and 5 for Hi45. Partial scans, as illustrated in Figure 3, were performed at all other central energies (and numerous energies between the central energies, with the exception of ESA 1's central energy, which was not scanned at all for Hi90).

[5]that is, when the C2 pulses are behaving correctly.

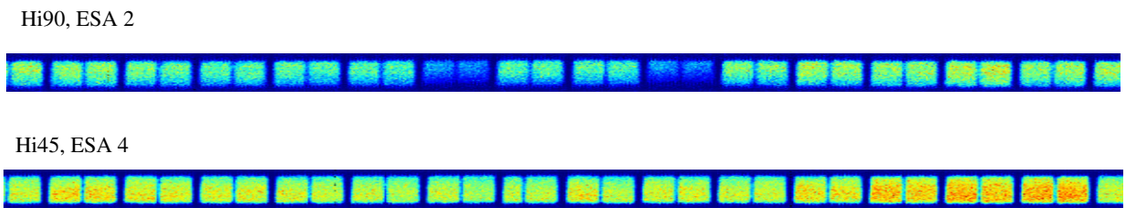


Figure 9: Sample "snake" scans, with axial angle shown in the horizontal direction and radial distance shown in the vertical direction. The cable tray has been removed from the range of angles shown. The top scan is of Hi90 at ESA 2. At this low an energy, the presence of two thicker conversion foils is obvious (it becomes less evident as the ENA energy increases). The bottom scan is of Hi45 at ESA 4. Calibration Product 3 is the one shown, but the pattern is the same for any of the Calibration Products.

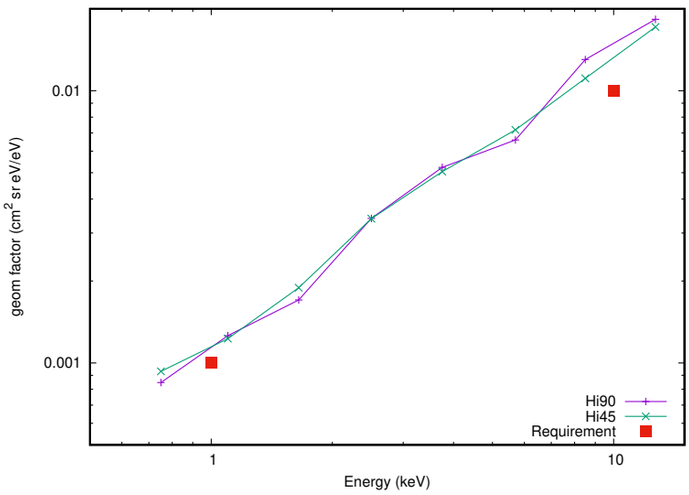


Figure 10: Geometric factor for Hi45 and Hi90 compared to requirements. The slight "wobbles" in the Hi90 plot are directly related to the variation in $T(E)E$ shown in Table 5 at ESAs 4 and 7.

is an improvement of about a factor of 4.2 over IBEX-Hi's triples-only data product.]

After interpolation between the E_c of the ESA energy steps, the geometric factor of IMAP-Hi's Calibration Product 3 at 1 keV is 0.00115 (0.00114) cm^2 sr eV/eV and at 10 keV is 0.0132 (0.0149) cm^2 sr eV/eV for Hi45 (Hi90). Uncertainties are discussed in the following section. IMAP-Hi thus exceeds the geometric factor requirements at 1 keV and at 10 keV. The sum of Calibration Products 1 and 2 also exceeds requirements, but by a narrower margin than Calibration Product 3.

Accuracy of Calibration (RHI-1544, 1545, 1601, 1602)

Satisfying the accuracy requirements has two parts, relative (10%) and absolute (25%).

The 10% relative accuracy requirement is taken to refer to individual measurements during the calibration, such as Phase 3's single-pane "snake" scans or Phase 1's scans at one energy over parts of the entrance aperture. This requirement is addressed by looking at the following factors:

1. Knowledge of incident beam

   (a) Beam drift

   ABM data were taken before and after each interval when the Hi45 or Hi90 sensor was placed in the beam. If the before and after ABM count rate differed by more than 5%, the data was retaken. Additionally, analysis of sensor performance always was performed with count rate linearly interpolated in time between the preceding and following ABM measurements. This step removes the predominant feature of LANL beam instability: a fairly linear slow drift, often associated with room temperature during the day.

   There was a period of beam instability (roughly October 29-30 2024, the conclusion of Hi90 Phase 3 calibration at energies 8.5, 10.39, and 12.7 keV) that was eventually traced to a failed function generator used for beam rastering. Even during this period, no data with a before/after difference of greater than 8% was kept.

   In summary, monitored beam drift during calibration did not contribute more than a ±4% uncertainty.

   (b) Neutrality of beam

   The ABM is agnostic as to whether the incoming beam is charged or neutral, so it will report an incorrectly high flux if the neutral beam contains an appreciable charged fraction. To check for

presence of ions, beam was typically put on the Hi sensor once all high voltages were up except for the deflectors, which were kept at ground. The count rate was then monitored as the deflector voltages were turned up. In no case was a statistically significant difference observed in count rate as the Hi sensor began to reject ions. Conservatively, a 2% shift would have been statistically significant in any of these (morning) checks.

(c) Accuracy of Absolute Beam Monitor

The absolute beam monitor used for IMAP-Hi calibration was the very same one used for IBEX-Hi calibration;[6] it had just been left (unused) in the LANL calibration chamber for the last nearly twenty years. An initial check in September 2023 of the ABM efficiency for protons at around 4 keV and 28 kHz found ε_A and ε_B to be within a couple per cent of their values during IBEX-Hi calibration in 2007.

During IBEX-Hi calibration, ABM performance was routinely checked against the detection efficiency of a Quantar imaging MCP, for which lab personnel (Ron Harper) had a long and well-tested estimate of performance, which aligned well with published detection efficiencies (specifically, Peko and Stephen's 2000 paper in NIM B, `https://doi.org/10.1016/S0168-583X(00)00306-2`). Also, the performance was routinely checked against a windowless SSD at energies $\geq$ 20 keV. In this way, throughout IBEX-Hi cal, the ABM was validated to $\leq 2\%$. Unfortunately, the windowless SSDs and up-to-date institutional knowledge of Quantar performance were not available during IMAP-Hi cal, by which time the long-ignored ABM was apparently deemed fully proven.

The design of the ABM is such that calculated flux is largely immune to actual changes in detection efficiency of the two ABM chambers. However, trending efficiency against time and against beam energy (and species) offers a good diagnostic inasmuch as sudden changes in ε are most likely due to a configuration error in the signal-processing electronics. Unfortunately, the electronics chain was modified numerous times during IMAP-Hi calibration, changing its gain. On October 21, 2024, lab personnel failed to notice a pump failure and applied HV to the ABM for two hours at rough vacuum. This markedly increased the ABM detection efficiencies, at least until the next venting on October 23 (this time period covers the end of Hi45 Phase 3, at energies 8.5, 10.39, and 12.7 keV).

The signal-processing chain amplifies the ABM's two CEM outputs and feeds this into two constant-fraction discriminators, which output stretched logic pulses. These pulses are counted directly; the A pulse is also sent to the start of a TAC, and the B pulse is delayed by a length of wire and sent to the TAC stop. The TAC produces a "valid conversion" pulse if a B is found after an A within the set time range (typically, 500 ns for IMAP-Hi calibration): this was sent to another counter. The TAC spectrum was observed periodically to confirm that the full ABM response, including "B" electrons created on the rear of the ABM foil and also on the rear wall of the ABM, was fully inside the coincidence window. A couple of the longer-TOF TAC data sets are shown in Figure 11, for 500 eV hydrogen and for 4.55 keV helium.

Misconfiguration of the electronics could include:

i. insufficiently long coincidence window, which would drop valid coincidence events, resulting in underestimated ε_A and ε_B and overestimated flux. (This did occur for at least some foil hole characterization studies using N_2^+.)

ii. not setting the CFD stretched pulse length to the same duration as the TAC coincidence window: if the CFD pulses are shorter, then one coincidence count may correlate to multiple single counts, again resulting in flux overestimation.

iii. poor matching of amplification with CFD thresholds, which could lower ε_A or ε_B but likely not in such a way as to affect calculated flux.

iv. forgetting to turn on the bias for the entrance aperture, which would allow collection of secondary electrons from outside the ABM. This would increase N_A and result in an overestimate of flux. Indeed, the entrance aperture bias of +40V still allows a small number of outside electrons in; testing indicated this effect never caused even as much as 3% shift in flux, and so it was not explicitly dealt with.

[6] *Eos Trans. AGU*, **87**(52), Fall Meet. Suppl., Abstract SM13A-0345 (2006).

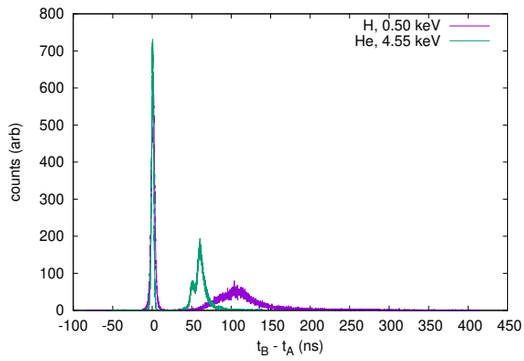


Figure 11: ABM diagnostic data (TOF spectrum) taken for 500 eV hydrogen and 4.55 keV helium.

Non-uniformity of ABM response over its entrance area could be an issue: if ε_A or ε_B depend on where an incident ENA strikes the ABM foil, and the beam does not always hit exactly the same parts of the foil, the flux may be misdetermined. This was tested extensively during the development of the ABM design and variation was kept at under 5% over the entire entrance aperture. The problem is minimized by using a small beam (2-3 mm; still large compared to the entrance aperture grid spacing of 20 lpi) positioned at the same spot each time on the ABM.

Dead time effects are ignorable: the TAC has a 1μs fixed processing time and the singles count rates were always kept below 50 kHz.

A final note concerning the ABM is the need to apply an ≈5% correction to the flux calculated simply by $N_A N_B / N_{AB}$ due to the transmission of the entrance grid, as was determined during IBEX-Hi calibration.

In conclusion, we estimate a ±4% accuracy on ABM measurements during IMAP-Hi calibration, and note that many potential issues with the ABM result in an overestimate of beam flux.

(d) Actual energy of beam

It has long been asserted that the energy spread of the LANL beam is under 2 eV. This was not verified during the IMAP-Hi calibration campaign as the sensor's energy acceptance is very broad in comparison. For the same reason, no study was made of possible beam energy shift or spread due to the conversion from H^+ to neutral H by interaction with gas in the beam column.

(e) Temperature dependency of FEE TDC calibration

During ground calibration, it was not understood that the time-to-digital converters in the sensor front-end electronics were somewhat sensitive to temperature. This was discovered early in commissioning, when the signal in the entire valid TOF range disappeared until the TDCs were recalibrated after a large temperature swing, in a significantly colder temperature range than in the lab.

TDC calibration was a somewhat haphazard affair. It occurred every time the FEE was powered on, but FEE power was generally left on for long periods as the EM EBox tended to hang every few hours for quite some time after initial power-on, but rarely thereafter. FEE temperature monitors were inoperative for at least some phases of calibration. Lab temperature varied over the course of the day (somewhere it should be logged along with the particulate counter). However, the AB and AC TOFs for triple and quadruple coincidences were continuously monitored during calibration, and checked thereafter, and never showed any obvious shifts. Therefore, we provisionally assign no additional uncertainty to possible temperature-dependent TDC behaviour.

2. Statistical accuracy of calibration

ABM measurements were collected over at least 50 seconds, resulting in statistical uncertainties of flux of under 2% worst-case and typically well under 1%. IMAP-Hi calibration data was collected so that at least

1000 counts contributed to any calibrated quantity (*e.g.*, counts over a pane), even at the most challenging lowest energies. The result is a $\leq$3% statistical uncertainty.

Adding all of these uncertainties together in quadrature results in a total of 6.7%, which is under 10% and meets requirements.

The 25% absolute accuracy requirement is taken to refer to the uncertainty in inferring the overall sensor performance, at all energies and conversion foil locations and angles, from the individual measurements taken during calibration. This requirement is addressed by looking at the following factors:

1. Accuracy of individual calibration measurements

   We take this to be the 10% "relative" requirement.

2. Accuracy of the angular acceptance

   Since calibration data essentially matched that expected from the collimator design specifications, we use the reported collimator inspection tolerances to arrive at an uncertainty of $< 2\%$ in solid angle acceptance.

3. Accuracy of the approximation that angular acceptance and energy acceptance are independent

   As with IBEX-Hi, which had broader angular acceptance but also broader $\Delta E/E$, Phase 1 testing included measuring the angular response of the ESA over a range broader than the collimator angular acceptance, prior to installation of the collimator. This particular concern is also very amenable to analysis by simulation.

   Also as with IBEX-Hi, simulations were run (by Dan Reisenfeld) for collimated monoenergetic ENA beams entering perpendicular to the conversion foils (as in calibration) as well as for for initially isotropic monoenergetic ENA distributions entering the collimator. The simulations included the collimator response, energy straggling and scattering in the conversion foil, and ESA throughput across each of the ESA settings, but did not include any energy-dependent ionization fraction from the conversion foil or position-dependent detector response. These simulations found a correction factor of less than 1% at low energies, up to about 5% at the highest energies of IMAP-Hi. The values are shown in Table 6. The uncertainty is the accuracy of the simulation, which, as for IBEX-Hi, was under a couple per cent at worst.

ESA	integrated isotropic:beam throughput ratio
1	0.99284 ± 0.00200
2	0.99136 ± 0.00170
3	0.99078 ± 0.00149
4	0.98859 ± 0.00117
5	0.97525 ± 0.00079
6	0.96598 ± 0.00057
7	0.95561 ± 0.00043
8	0.94978 ± 0.00034
9	0.94876 ± 0.00030

Table 6: Correction to integrated transmission for an isotropic signal (over the FOV of the collimator) compared to a monodirectional beam as used in calibration. Uncertainty is from the statistics of the Monte Carlo simulation.

   The factors in this table are incorporated into the geometric factor reported. On IBEX-Hi, which used a wider FOV, the correction was nearly 10% at its highest energy range (similar to ESA setting 6).

4. Accuracy of inferring energy response from a limited number of energies and locations on conversion foils

   For ESA energy steps 2-9, the discussion addressing RHI-1055 is germane, particularly the level of reproducibility between original Phase 1 and New Phase 1 in Figures 6 and 7, and in the values listed in Table 5. Conservatively, the accuracy is better than 15%; further lowering of this uncertainty is likely to follow with simulations convolving the sensor response with the range of energy spectra expected on orbit. In such simulations, the calibration of the steep low-energy side of the response is rather critical inasmuch as there tends to be much more flux at lower energies than at higher in space.

High accuracy is not claimed for the calibration of ESA energy step 1 (nominal E_c of 500 eV, actual peak transmission energy closer to 600 eV), because calibration with a meaningful H^0 beam intensity at energies below 500 eV is not possible in the LANL facility, and a non-negligible fraction of the expected ESA 1 response is at energies below 500 eV.

5. Accuracy of inferring overall detection efficiency at some energies from measurements on a limited number of conversion foils

   Analysis of the Phase 3 "snake" data comparing the performance over a limited number of foils (see Figure 3) to the performance overall shows a correction factor consistent per sensor and calibration product to better than ±2% over all energies.

6. Fundamental reproducibility of sensor behaviour

   In calibrating the sensor, it is worth considering the degree to which the sensor *can* be calibrated, and what limits are placed by variation of sensor performance due to factors such as air/humidity exposure and CEM/MCP aging. Such factors fundamentally limit the validity of any calibration, even if the requirements themselves apply only to the sensor at the instant of delivery. HOPE, part of the heritage of the detector section design, appears to have experienced absurd efficiency changes as a result of space weather conditions – changes which would severely limit the science return if also suffered by IMAP-Hi. Further, although the IMAP-Hi U-Can was gold-coated to reduce noise, the fastidious care taken with IBEX-Hi to limit volatiles outgassing near the detectors was not taken with IMAP-Hi.

   The detector section efficiencies themselves can be trended over time, as with IBEX-Hi, as long as there have accumulated statistically significant signal counts and negligible or accurately subtractable backgrounds. For example, if N_{ABC} is the number of signal counts detected by all three detectors and N_{AB} is the number of signal counts detected by at least A and B, $\varepsilon_C = N_{ABC}/N_{AB}$. This trending can identify slow changes in efficiency of the detectors; IBEX-Hi has shown it can be done to a few per cent.

   Changes in performance of the ESA are not expected without mechanical deformation of the structure. Any difference due to the HVPS not supplying the correct voltages can be detected from housekeeping data, and modelling can assist in determining the new performance.

   Changes to the conversion foils on orbit cannot be directly identified.

   One check on sensor behaviour, and in particular on part of the sensor upstream from the detectors, for which on-orbit efficiency cannot be tracked, is data taken for each sensor before and after vibe testing. Part of calibration intended to help refine sensor modelling involved placing a fixed 5 keV neutral beam on one spot on the sensor, while stepping the ESA E_c through a range energies which would transmit the beam. Data is shown in Figure 12 for Hi45 at the centre of one foil and for Hi90 at the centre at the inner edge of one foil; incident event were taken to be any qualified coincidence. The Hi45 "before" data has been uniformly scaled to account for altered collimator transmission (Hi45 was mounted about 0.35° differently in both azimuth and polar prior to vibe) and a 50 V different operating voltage on CEM A. The Hi90 data shown is treated exactly the same before and after, since neither the mounting nor the operating voltages were changed, and is consistent overall to within $\leq \pm 5\%$.

Overall, adding the various uncertainties in quadrature, it seems reasonable to assert an absolute calibration uncertainty of 22%, which is less than the requirement of 25%.

Testing of HVSCI Mode (RHI-1139)

HVSCI mode was run, with beam, for Hi90 during Hi-Ultra cross-calibration and for Hi45 during Lo-Hi calibration. This requirement was levied essentially as a response to IBEX calibration and delivery, when FSW did not have the capability of operable HVSCI at any point during calibration. The requirement for IMAP-Hi served its purpose in helping guide revisions to FSW based on discoveries during testing, and identify quirks in the FSW logic.

Figure 13 shows some data from HVSCI testing for each sensor: the inner and outer ESA voltages, and the NHK-reported science step. Counts observed in SCI_DE and SCI_CNT packets were consistent and reported counts as expected for the beam energies used.

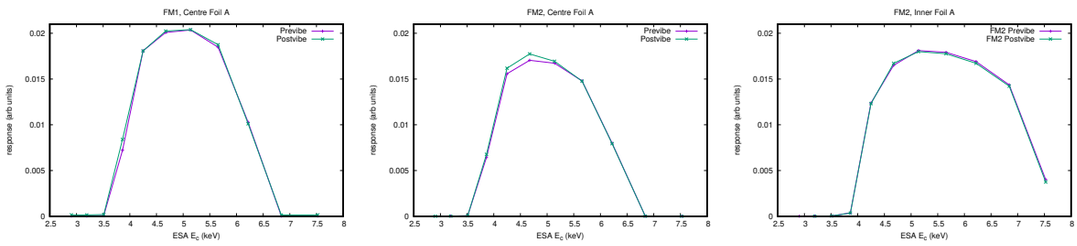


Figure 12: Characterizations of the Hi45 ("FM1") and Hi90 ("FM2") sensors before and after vibe testing, indicating general reproducibility of the sensors. The lines are to guide the eye: data was taken at the marked points only. The vertical scales of the Hi45 data have been scaled as discussed in text.

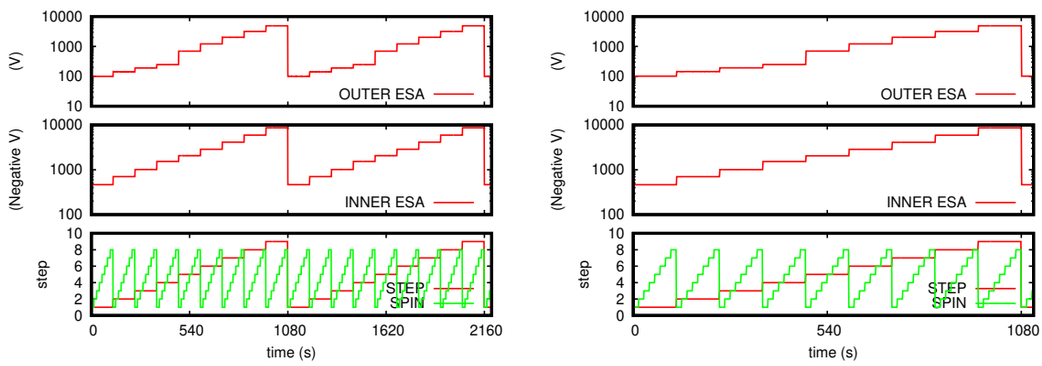


Figure 13: HVSCI data taken during cross-calibration for Hi45 (February 8, 2025, left plot) and Hi90 (November 4, 2024, right plot).



Figure 14: Sample "snake" scans using N_2^+ to show the presence of holes in the foil, with axial angle shown in the horizontal direction and radial distance shown in the vertical direction. The cable tray has not been removed from the range of angles shown. The top scan is of Hi45 and the bottom of Hi90, after all vibe testing. The colourbar is linear but due to ABM misconfiguration may not be the same for both sensors.

Conversion Foil Coverage Over 95%

Each sensor was rastered across an N_2^+ beam at the central energy of ESA 7. Beam hitting the conversion foil is broken into individual nitrogen atoms or atomic nitrogen ions outside the bandpass of the ESA; beam passing through holes in the conversion foil transits the ESA and is detected with high efficiency, at long time-of-flight. A comparison of the detected count rate (scaled by detector efficiency, determined by the ratios of A, B, and C detections in the coincidence events) with incident beam brightness (as determined by the ABM with a sufficiently long coincidence window) at any particular point on the conversion foils provides the hole fraction of the imaged area. These scans were done before and after vibration testing.

Sample final scans are shown in Figure 14 for Hi45 and Hi90, in a format similar to that of Figure 9. Unfortunately, the ABM was not set to an appropriately long coincidence window for the final scans. ABM measurements were still used to normalize all collected data to beam brightness, but the conservative worst-case foil coverage was calculated by scaling the integrated counts over the entire foil area to the highest normalized count rate observed and assuming 100% transmission at the highest normalized count rate. Compared to incident beam, the foil coverage is then $> 99.3\%$ for Hi45 and $> 98.8\%$ for Hi90.

Appendix

Final Calibration Products

Commissioning tests after launch revealed that C1C2 TOF data no longer resembled its behaviour during calibration. Hi45 C1C2 TOF shows a single sharp pulse at short times suggestive of ringing and similar to what was seen in Lo-Hi cross calibration, which happened after integration and de-integration with the spacecraft. Hi90 C1C2 TOF shows a jumbled series of peaks. Neither features any obviously resolvable ion/neutral TOF peak. Accordingly, C2 was deemed not useful for science.

Additionally, AC1 and AC1C2 counts are not very numerous to begin with, and were found to have a background in the qualified TOF region difficult to analyze.

This leaves, of Calibration Product 3, the AB, ABC1, and ABC1C2 coincidences. AB double coincidences have a higher background than ABC1 triple or ABC1C2 quadruple coincidences. Accordingly, the flight calibration products are:

Flight Calibration Product 1: ABC1C2 quadruple coincidence and ABC1 triple coincidence

- $t_B - t_A$ must be in the range 18 to 80 ns.
- $t_C - t_A$ must be in the range -10 to 70 ns.
- $t_C - t_B$ must be in the range -50 to 20 ns.

Figure 18 shows a histogram of FCP1 data binned by $t_B - t_A$ and $t_C - t_A$.

Flight Calibration Product 2: AB double coincidence

- $t_B - t_A$ must be in the range 18 to 80 ns.

In short, we require both A and B to register. The presence of C correlates to a significantly lower-background product than the absence of C. However, if detector C were to change its behaviour drastically, the *sum* of FCP1 and FCP2 should remain unchanged as long as the performance of CEMs A and B remains constant. The only drawback of combining FCP1 and FCP2 in this fashion would be the higher background of FCP 2 now associated with the single calibration product.

Energy Response

The energy response of each sensor was modelled by fitting a functional form derived from simulation to the New Phase 1 calibration data. In the simulation, an initial, normally incident ENA beam filling the entrance aperture was "flown" through the entrance foils with scattering and energy loss modelled, but not accounting for charged-state fraction (*i.e.*, every exiting particle was assumed to be a singly charged positive ion). Initial particles were randomly assigned location and energy, over a range for each ESA step. SIMION was then used to model the transmission through the ESA to the detector entrance. Finally, an empirical formula was used to model the fraction of the initial beam exiting the conversion foil as an ion ($2.241 \times 10^{-6}x^4 - 1.2638 \times 10^{-4}x^3 + 2.0389 \times 10^{-3}x^2 + 6.5251 \times 10^{-3}x + 5.7847 \times 10^{-2}$, where x is energy in keV when $x \geq 0.9$ keV, and a continuous linear extension to 0 at 0 keV for lower energies, as per the instrument paper and references therein). Energy-dependent foil scattering and the fixed potential difference accelerating ions into the detector caused the simulations to produce slightly different energy response shapes by ESA step.

The simulation used a k_F value for the entrance foils of 18 keV°. Exact behaviour varies somewhat from foil to foil; also, the detector section following was not simulated here. For these reasons, the simulation output (fraction of ENAs incident on the conversion foil that reach the start of the detector section as singly charged positive ions) was fit to the calibration data allowing the energy both to shift and to scale – that is, E was replaced with $\alpha E + \beta$. Typical scaling was well within 2% of unity and typical shift was under a few per cent of E_C, not exceeding 100 V, except at the two highest ESA steps. The fit parameters were allowed to vary from ESA step to ESA step rather than being forced to adhere to a constant factor or offset from the model, because the modelled energy dependence of the carbon foils, both in straggling and in exiting ion fraction, were insufficiently reliable at the quality of the calibration data – to say nothing of how the detector section was not modelled at all in this simulation.

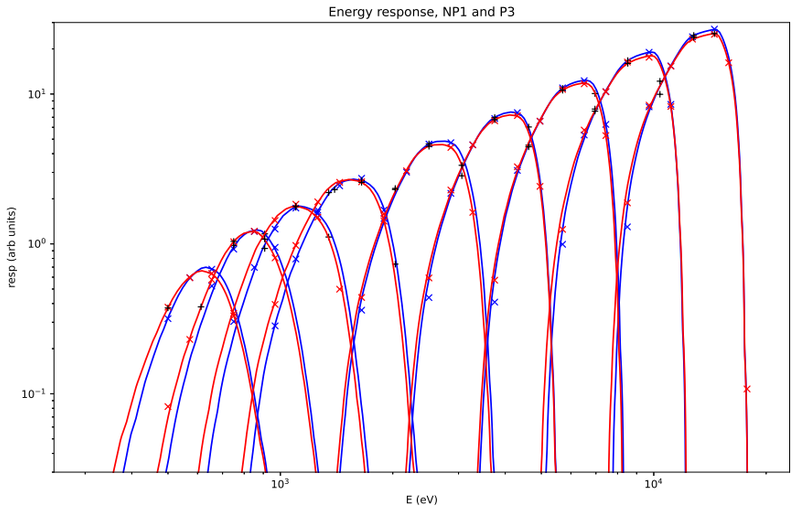


Figure 15: Simulated energy response fits to Hi45 (red X) and Hi90 (blue X) New Phase 1 data for the sum of FCP1 and FCP2. Black crosses indicate Phase 3 energy information, scaling to match the New Phase 1 data at each ESA step's E_C. In this plot, the energy response has not been normalized to integrate to unity (as in `T_CP.txt`) and instead relates directly to the integral over the covered area of detection efficiency of the sum of FCP1 and FCP2 events.

This functional form was an excellent fit to the Phase 1 data for both sensors, both for original Phase 1 and the shorter New Phase 1, as illustrated in Figure 15. Original Phase 1 covered a much larger number of energies and was used to validate the choice of functional fit, although the exact fit parameters were different for original Phase 1 compared to New Phase 1, as is expected due to differences in foils. It is evident from Figure 15 that there is a slight energy response difference between Hi45 and Hi90. It is also worth noting that the energy response was resolvably different for final calibration products 1 and 2 for both sensors, mainly at lower energy. Specifically, AB coincidences (lacking a C detection) have a peak response at slightly higher energies and detect slightly higher energy ENAs in general. Inasmuch as the SDC was not set up to deal with different energy responses for different Calibration Products, energy response at the lower end of the ESA bandpass is more critical than the response at the higher end for typical energy spectra, and combining products prior to flux correction and Compton-Getting correction is generally superior from a statistical perspective, it is probably best to use the fit to the sum of FCP1 and FCP2 rather than the different fits for the two calibration products.

Response Function

The response function is captured in the following text files, which are similar to the files provided for IBEX-Hi:

`coll_resp.txt` The collimator response for both Hi90 and Hi45, based on a simulation of the collimator as per its design specifications.

Theta (rows, polar) goes from 0 to 5.5 deg. in .05 deg steps; phi (columns, az) goes from 0 to 30 in 1 deg steps. $\theta = 0$ corresponds to normal incidence.

$\phi = 0$ corresponds to the CORNER of a hexagon. There is then symmetry every 30 degrees for the hexagon, which is why data are provided only 30 over degrees.

Numbers are the fraction of particles that pass through, starting at 1.0 for normal incidence. Clearly normalization is in order: recall that the $\Delta\theta\,\Delta\phi$ bins of this file are not of equal solid angle and need to be scaled by $\sin(\theta)$.

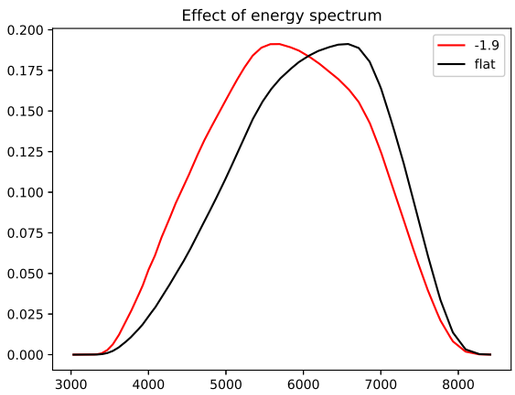


Figure 16: Simulation of Hi-90's ESA step 7, showing response as a function of energy (black) as well as the relative amount of signal seen as a function of energy when the sensor response is convolved with an incoming signal of spectral index 1.9. The horizontal axis is in eV; vertical scaling is arbitrary.

This file is not actually directly needed for data processing, and indeed cannot be used accurately without information currently lacking in this document, which is the exact as-mounted angle the hexagon sides make with respect to a known spacecraft axis. The important features in this file are the angular acceptance, which could be modelled with cylindrical symmetry without scientific concern, and the overall solid angle, which is incorporated into the `G_values.txt` *file later on.*

`E_centre.txt` This file lists the nine nominal central energies of the nine standard ESA steps, for both Hi90 and Hi45, in eV.

Based on calibration, several of the central energies were revised from the initial baseline values to those provided in Table 3. Specifically, E_C for steps 1 and 2 shifted from 500 eV to 575 eV and from 750 eV to 800 eV, and ESA step 4's E_C shifted from 1650 eV to 1500 eV.

In ground processing, the algorithms for "flux correction" and the Compton-Getting correction require modelling the flux or intensity *vs* energy continuously over multiple ESA steps. As a result, given data from multiple ESA steps, the intensity can be reported at any desired energy inside the overall IMAP-Hi bandpass. The energy most characteristic of the data from a single ESA step is not the peak of the energy response, but rather, the peak of the energy response convolved with the energy spectrum of the observed ENAs. For expected spectra (*e.g.,* $\propto E{-}1.9$), this energy is lower, as is shown in Figure 16. E_C were selected with this spectrum in mind.

`G_values-[45,90].txt` These two files list the overall "geometric factors", in units of cm^2 sr eV, for FCP1 and FCP2, by nominal ESA step.

The assumption is that both FCP1 and FCP2 share a common energy response, as provided in the `T_CP-[45,90].txt` files.

At ESA step central energies for which Phase 3 data spanned only a part of the entrance aperture, overall geometric factor was inferred by scaling by the average of the total:partial area-integrated detection efficiency for all energies at which full coverage data for that sensor was taken.

No Phase 3 data were collected at Hi-90 ESA step 1. To determine a geometric factor, the reduced ESA step 1 central energy data from New Phase 1 was scaled (prior to normalization) by the ratio seen at ESA steps 2-6 central energies between reduced Phase 3 and reduced New Phase 1. This proved to have less uncertainty than attempting to base the Hi-90 ESA step 1 geometric factor on the Hi-45 ESA step 1 Phase 3 data.

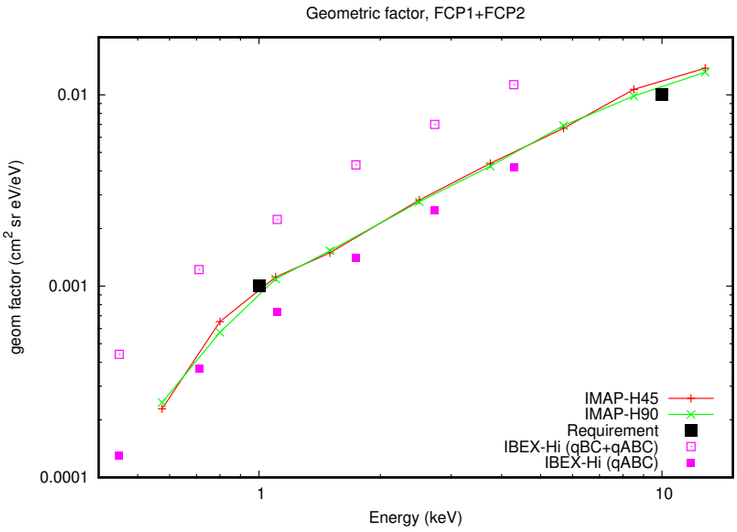


Figure 17: Geometric factors for flight calibration products. This is similar to Figure 10. IBEX-Hi geometric factors are shown for comparison: bear in mind that IBEX-Hi suffers from larger backgrounds and a smaller fraction of useful exposure time than IMAP-Hi, though.

The whole "geometric factor" framework ceases to be particularly intuitive the instant that the energy response is broad enough to warrant a "flux correction": what does it really mean to state a specific geometric factor if the next step of processing is to scale the counts by 1.10 to get the "real" answer?

The geometric factors for the sum of FCP1 and FCP2 are shown in Figure 17.

`T_energies.txt, T_CP1-[45,90].txt, T_CP2-[45,90].txt, T_CP-[45,90].txt` These files provide the normalized energy response.

`T_energies` has nine columns, one per ESA step, of the central energies for which the function fit to the calibration data was evaluated. Linear interpolation will suffice between the points.

`T_CP*-[45,90]` each has nine columns, one per ESA step, of the normalized response of the Hi45 or Hi90 sensor at the corresponding energy in `T_energies`. CP1 and CP2 correspond to Flight Calibration Products 1 and 2; CP corresponds to their sum.

These files are expected to be used to generate fit functions for flux correction and the Compton-Getting correction, but otherwise are unlikely to be used directly.

The two calibration products have slightly different energy responses, moreso at low energies. The differences even at low energies are minimal enough to ignore, probably.

For a given neutral flux N [/cm^2/sr/eV/s], Hi response (number of counts/s) is the integral over energy and solid angle of Hi_G(ESA) $\times$ Hi_T(ESA, energy) $\times$ Hi_PSF(θ, ϕ) $\times$ HI_E_central(ESA) $\times N$.

Normalization is $\int \mathrm{PSF} d\Omega = 1$ and $\int T(E) dE = 1$ for each ESA setting.

The quality of the calibration, the general behaviour of the overall geometric factor, and the accuracy of the entrance foil and SIMION simulation mean that interpolation of sensor performance to ESA voltages different from those calibrated (but within the calibrated range of energies) is possible within the required uncertainty limits.

Calculating and Trending Detection Efficiency

Individual detector performance can be assessed in space by looking at ratios of ENA-generated (*i.e.*, background-subtracted) count rates.

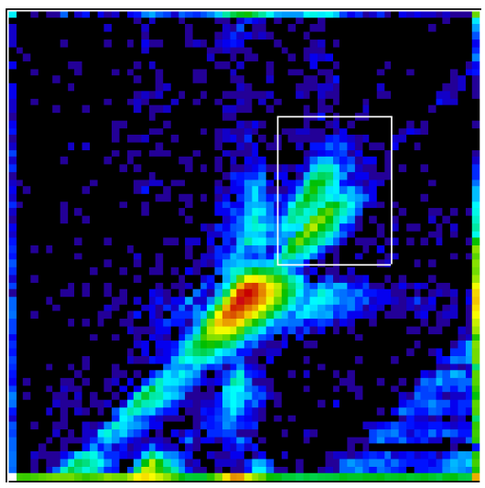


Figure 18: Two-dimensional time-of-flight histogram of Hi-90 data, with AB TOF horizontal and AC TOF vertical. The "valid" H ENA TOF region is shown by the white box. Inside the white box are two "blobs". The one at shorter AC TOF (*i.e.*, lower) indicates when detector C first triggered on a secondary electron. The blob at longer AC TOF indicates when the first C detection occurred later (*i.e.*, due to the initial particle). Zero TOF (for intended ENA detection, as opposed to other processes) is near the centre of this plot.

- the detection efficiency of detector C is, more or less, the ratio of FCP2 to the sum of FCP1 and FCP2. (The odds of both A and B detecting an incident particle, regardless of what C does, are $\varepsilon_A\varepsilon_B$; the odds of A, B, and C detecting an incident particle are $\varepsilon_A\varepsilon_B\varepsilon_C$.)
- detector C may detect a secondary electron and/or the initial particle (as an ion or as a neutral). Since C2 is noisy, we cannot infer much about the efficiency of detecting the initial particle, but some information about the efficiency of detector C at detecting the secondary electron can be inferred by the relative number of counts in the two "blobs" in the time-of-flight (TOF) plot of AB *vs* AC1, inasmuch as counts appear in the "later" blob only if the secondary electron was not detected first. See Figure 18.
- the detection efficiency of detector B can be inferred from the ratio of background-subtracted (AC + ACC) counts to the sum of FCP1 and background-subtracted (AC + ACC) counts. This is analogous to the calculation of the efficiency for detector C, but less precise, because there are fewer (AC + ACC) counts than (AB) counts and proportionately more background to subtract.
- by the same logic, the detection efficiency of detector A could be inferred from the FCP2 (ABC + ABCC) counts and the background-subtracted (BC + BCC) counts. However, the latter cannot be determined in space since the background greatly dominates the ENA signal: both appear at the same TOF.

  General trending of detector A can be done by looking at the total number of events involving an A, compared to the total number of events involving a B. The counts in this total are almost entirely of background, but it does provide a monitor sensitive to many but not all possible changes in detector A.

Baseline detection efficiency values are provided by energy from calibration in Figure 19. Phase 3 data at the energy closest to E_C were used. The efficiency of a given detector (A, B, or C) was taken as the ratio of (area-integrated detection efficiency for events containing hits from A, B, and at least one C within the qualified TOF ranges – emphi.e. FCP1) to (the sum of area-integrated detection efficiencies for all events containing hits from the other two detectors within qualified TOF ranges, whether or not the given detector registered a hit). For example, for detector B, this would be (ABC1 + ABC1C2) / (AC1 + AC1C2 + ABC1 + ABC1C2).

This discussion applies to detection efficiency and is relevant in terms of detector aging. It does not monitor the entirety of the sensor – in particular, there is no way post-launch to directly evaluate aging of or harm to the entrance foils.

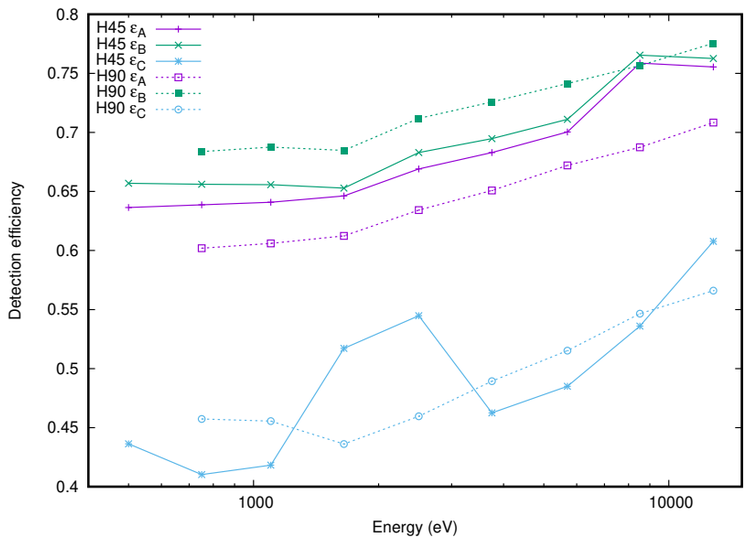


Figure 19: Individual detection efficiencies inferred for the three parts of the detector section from calibration, using ratios of coincidences from phase 3 data near the central energy of the ESA bandpass. Detection efficiency here refers to the probability of detecting an ion that has already transitted the ESA and has entered the detector section.
The two unusually high points (1650 and 2500 eV) of Hi-45 ε_C correspond to the earliest data taken in phase 3 after installing Hi-45; the Hi-45 data at 8520 eV, with slightly high ε_A and ε_B were collected shortly after a vacuum system failure.

Revision Log

April 25, 2025 Initial release.

April 29, 2025 Very minor wording clarifications; always call the foils at the entrance of the sensor "conversion foils", as opposed to the "entrance foil" at the start of the U-can. Provide hard numbers and an executive summary supplied for those who don't want to infer on their own.

April 2, 2026 Mention the TOF window quirk between calibration and operation. List foil specs. Include conversion foil N_2^+ plots and the completed isotropic/beam correction simulations. Add Appendix describing final response function.

3.7.3 In-Flight Calibrations

IMAP-Hi in-flight calibration report to be included here.

3.8 IMAP-Ultra

3.8.1 Strategy & Approach

IMAP-Ultra was calibrated at Johns Hopkins Applied Physics Laboratory's Accelerator Facility, including an ion beam and radioactive sources. IMAP-Ultra was also cross-correlated with IMAP-Hi at Los Alamos' Space Plasma Instrument Calibration Facility.

Ultra calibrations consisted of:

- Pulse-height thresholds
- Time-of-flight by pulse-height energy range and resolution
- Time-of-flight by pulse-height mass resolution
- Time-of-flight by pulse-height angular resolution
- Microchannel plate sensitivity
- UV rejection capability
- UV and ion beam responses
- Dead-time characterization and correction
- Efficiency factors and signal-to-noise ratios
- Determination of full response function (response vs. energy and azimuthal and elevation angles) and corresponding efficiencies
- Determination of projected area, accumulation time, and geometric factor

3.8.2 Pre-Flight Instrument Calibration

IMAP-Ultra calibration report embedded below

1. Introduction

1.1 Instrument Description

This document describes a series of tests performed and data analysis results that demonstrate that the IMAP-Ultra (referred to as Ultra from here on out) instrument suite, comprised by two Ultra sensors (i.e., Ultra90 and Ultra45) meets and exceeds its requirements. These tests include:

- energy calibration
- angular response measurements
- deflection plate characterization
- foil characterization
- flat fielding

The tests used calibrated pulsers, particle beams, and shutter & external radioactive calibration sources to stimulate the instrument. Calibrations determine all channel specific parameters needed to convert channel specific count accumulations into calibrated intensity images, i.e., the species, energy, and angle dependent response function.

The Ultra instrument suite comprises two sensor heads—one mounted at 90° to the spacecraft spin-axis and the other at 45° anti-sunward—with charged-particle deflection, variable slit apertures, a foil-based (Time Of Flight) TOF imager, and energy subsystems (SSDs). Each sensor has two identical entrances composed of a deflection system, variable aperture (VA), slit, and start foil. Particles (**Figure 1**) enter the deflection system, where the strong electric field between alternating grounded and HV (up to 8 kV) plates deflects charged particles into the serrated plate surfaces, effectively eliminating their forward scattering. Energetic Neutral Atoms (ENAs) proceed through a stepper motor-driven VA, which provides a variety of Geometric Factor (GF) configurations either with or without additional UV filtering (provided by an 8 μg/cm^2 Si and polyimide foil). The ENAs enter the detector through the start foil (≤ 2 μg/cm^2 grid-supported C foil that runs the length of the entrance slit) producing secondary electrons. Shaped electrodes generate the electric fields (red potential contours) to accelerate and steer the secondary electrons (green trajectories) into the Start (Micro Channel Plate) MCP, producing both 1D Start position and Start timing. The particle continues through the

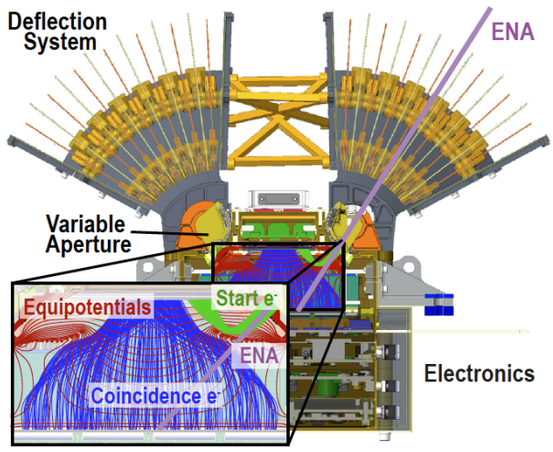


Figure 1: Ultra cutaway showing major elements: charged-particle deflection plates; front MCP assembly with two 1D start anodes servicing two entrance slits, and one 1D coincidence anode; variable aperture mechanisms servicing each entrance slit (detailed in inset); two stop MCPs imaged using 2D anodes; and a strip of SSD detectors between the two stop MCPs.

sensor to the back plane, where it passes through a stop foil (1 μg/cm^2 C, 3 μg/cm^2 Si, and 5 μg/cm^2 polyimide) and strikes the Stop MCP, producing both 2D Stop position and Stop timing. Both Start and Stop (time-delay) anodes identify position to 1 mm, resulting in ~ 2° angular resolution at the higher energies (> 30 – 40keV for protons), and more than sufficient to meet IMAP angular resolution requirements. The combined Start– Stop positions determine the ENA trajectory and, together with TOF, determine its velocity. The Stop MCP also records pulse height, which, with the TOF, yields a rough determination of particle species: light (H, He) or heavy (e.g., O, Ne, Fe). Secondary electrons backscattered from the Stop MCP foil are accelerated and guided by the electrostatic potentials onto the coincidence region of the start-coincidence MCP (blue trajectories). The valid event logic requires that the coincidence pulse follow the stop pulse within a 8-10 ns window, for a 4 ns valid event coincidence window (MCP TOF-only mode). A row of SSD detectors also located at the back plane, between the two stop MCPs, records the energy deposited for the particles that hit them. The energy deposited on SSD, together with TOF derived from the Start time and an SSD stop taken from the SSD portion of the coincidence anode, yields TOFxE, sufficient to identify the particle species (H, He, O, Ne, or Fe).

Instrument Angle Definitions & JENI (near-copy of Ultra sensor) Scattering Profiles

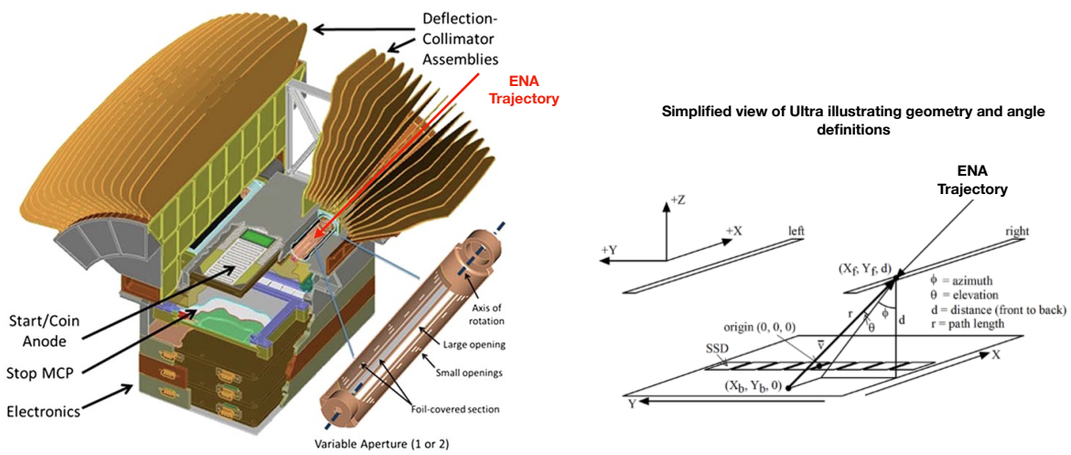


Figure 2: Ultra sensor geometry and angle definitions.

1.2 Ultra Measurement Requirements

Table 1 depicts the level-3 requirements that Ultra must meet or exceed such that IMAP can achieve its baseline science. And it is these requirements that guide the calibration philosophy outlined in this document. The right most column in Table 1 maps the requirement to specific tests.

Table 1: IMAP-Ultra measurement requirements

Ultra Level-3 Requirements			
Parameters	**Requirements**	**Goals**	**Calibration Activity**
Measured particles	ENAs	ENAs	Maps requirements to specific tests in this document
		Ions and electrons	
Energy range (RULTRA-1047; -1053; -1059)	5 keV – 40 keV (H)	3 keV – 300 keV (H; TOFxPH and TOFxE) 40 keV – 300 keV (O; TOFxPH) 50 keV – 300 keV/q (H; TOFxE) 80 keV – 300 keV/q (He; TOFxE) 120 keV – 300 keV/q (O; TOFxE)	See section 4.2
		1 keV – 1 MeV (H^+) 2keV/nuc – 5 MeV (He & O) 30 – 700 keV (electrons, SSD only)	
Energy Resolution, $\Delta E/E$ (RULTRA-1O48; -1054; -1060)	≤0.7 for 5 keV to 40 keV (H)	<14% (> 10 keV H)	See section 4.2
Masses resolved (RULTRA-1046; -1052; -1058)	MCP based mass resolution to differentiate H (lights) from O (heavies)	MCP-based: H(lights), O (heavies) SSD-based: H, He, O, Ne, Fe ($M/\Delta M \cong 2$)	See section 4.3
Angular resolution (RULTRA-1049; -1056; -1061)	≤6° (H at ≥10 keV)	≤2° : E≥10 keV H ≤7° : E≥15 keV O ≤15˚ : electrons	See section 4.4
Signal to Noise Ratio (SNR) (RULTRA-1051; RULTRA-1055)	> 20 at 10 keV for an assumed H ENA flux of 0.2 $cm^{-2}sr^{-1}s^{-1}keV^{-1}$	~10 to 1000 (energy dependent) Geometric Factor (GF) (cm2 sr) × $\varepsilon_{trasmission}$ 0.006-0.15 (high res, low background) 0.6 (high sensitivity)	See section 4.6 and 5.6
ENA flux calibration relative accuracy (RULTRA-1540)	relative accuracy of ±10% in the energy range 5 to 10 keV	relative accuracy of ±10% in the energy range 5 to 10 keV	See section 8
ENA flux calibration absolute accuracy (RULTRA-1541)	absolute accuracy of ±25% in the energy range 5 to 10 keV.	absolute accuracy of ±25% in the energy range 5 to 10 keV.	See section 8

ENA and ION SCIENCE Mode use (RULTRA-1131)	ENA and ION SCIENCE Mode shall be used during instrument calibration to set the instrument into a known state and acquire data. This mode will also be used during commissioning.	During calibrations we were using the instrument in ion science mode (i.e. without HV applied on the deflection blades), since our beam was not neutral
Time resolution (RULTRA-1050; RULTRA-1057)	Integrated observation time for H ENAs shall be greater than or equal to 270 days over a 2 year period	See section 11
Pointing Definition (RULTRA-1191)	IMAP-Ultra shall perform instrument measurements integrated as part of a spin-stabilized observatory with the observatory principal axis (spin-axis) pointed nominally at the incoming solar wind.	This is addressed at the s/c level
Observation Time at a Given Attitude (RULTRA-1558)	IMAP-Ultra shall integrate adequate counting statistics to characterize the portion of the sky observed within 90 days, assuming the observatory spin axis remains within ~10 degrees of the Sun vector while processing uniformly through the ecliptic during that period (repointing frequency is not constrained by Ultra).	Meeting the SNR requirements, satisfies this one as well

2. Chronological Order of Calibration Activities

The purpose here is to organize the document based on the order of tests that occurred in the lab with Ultra FM1 & FM2 (i.e., 90 and 45). **Figure 3** offers a graphical representation of this order and matches the calibration procedure spreadsheet, which is a more detailed list of tests in a checklist-like format to guide those in the lab. In summary, the tests can be categorized into four major categories:

- Demonstrating Ultra meets its measurement requirements
    - Stimulate the instrument with beams of different ion species (H, He, N) that span 5 – 50 keV (and beyond if time permits) over Ultra's full field of view.
    - Stimulate the instrument with radioactive disk sources (e.g., Am-241, Bi-207) to derive SSD energy calibration curves.
- Characterize the SSDs, MCP backplane and deflection system E/q cutoff efficiencies by stimulating the instrument with a combination of externally mounted degraded, i.e., broad energy spectrum, Am-241 sources and monoenergetic ion beams.
- Characterize Ultra's response to its shutter sources used for in-flight calibration

- Characterize response to background signals generated by UV photons. This will aid in determining the SNR, which will be analysis based. Ultra will be stimulated with a UV source and ions from monoenergetic ion beams.

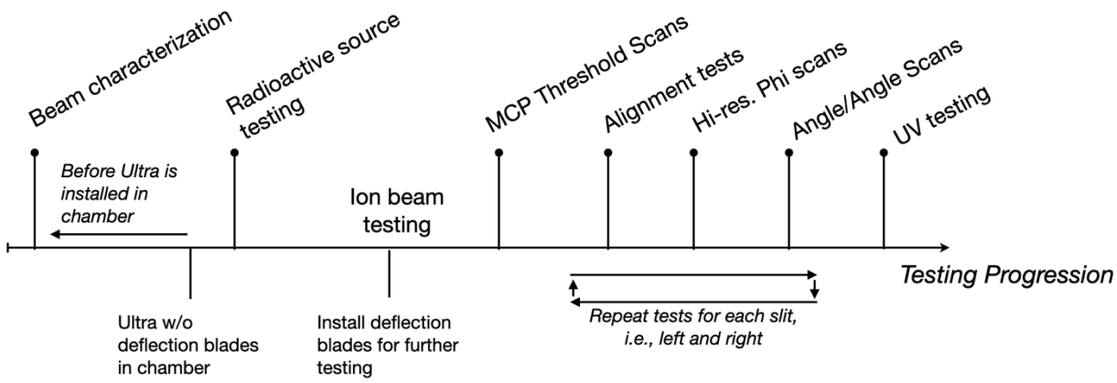


Figure 3: Testing progression of Ultra.

3. Calibration Activities

3.1 Beam Characterization

Independently monitoring the ion beam, i.e., its stability, uniformity, and divergence is critical to the success of deriving the full response function. Before Ultra FM units are installed in the chamber for calibrations, the beam is characterized using an Absolute Beam Monitor (ABM) and a microchannel plate (MCP) beam imager. The ABM will be used for the stability measurements (how the beam intensity changes with time) and the MCP imager will map out the uniformity and divergence. MCP beam imagers are placed both at the location of the ABM and the location where Ultra's aperture will be fixed (**Figure 4**). Comparing the spatial profile between these two locations aids in the interpretation of the calibration results. The beam intensity and uniformity is being spot checked throughout the angle/angle tests to ensure any dynamics are properly folded into the analysis and derivation of the response function. Those additional tests are detailed in section 3.7. MCP 1 in **Figure 4** is used throughout the FM testing to check beam uniformity, while MCP 2 is used only during the beam characterization part to determine i) the uniformity of the beam at the Ultra location, and ii) the particle density at Ultra location relative to the ABM one. Our beam characterization tests using both MCPs, prior to beam testing of the FM, revealed that MCP2 measures 80% of the particle density the MCP1 measures, and there is only very weak dependence in energy. Therefore we have used that 80% factor in our efficiency calculations discussed in Section 4. Also in Section 4 we decide in more detail the ABM and MCP1 measurements taken

during FM beam testing to monitor beam stability and uniformity, and how these measurements inform the calculation of Ultra efficiencies.

3.2 Radioactive Source Testing Purpose and Setups

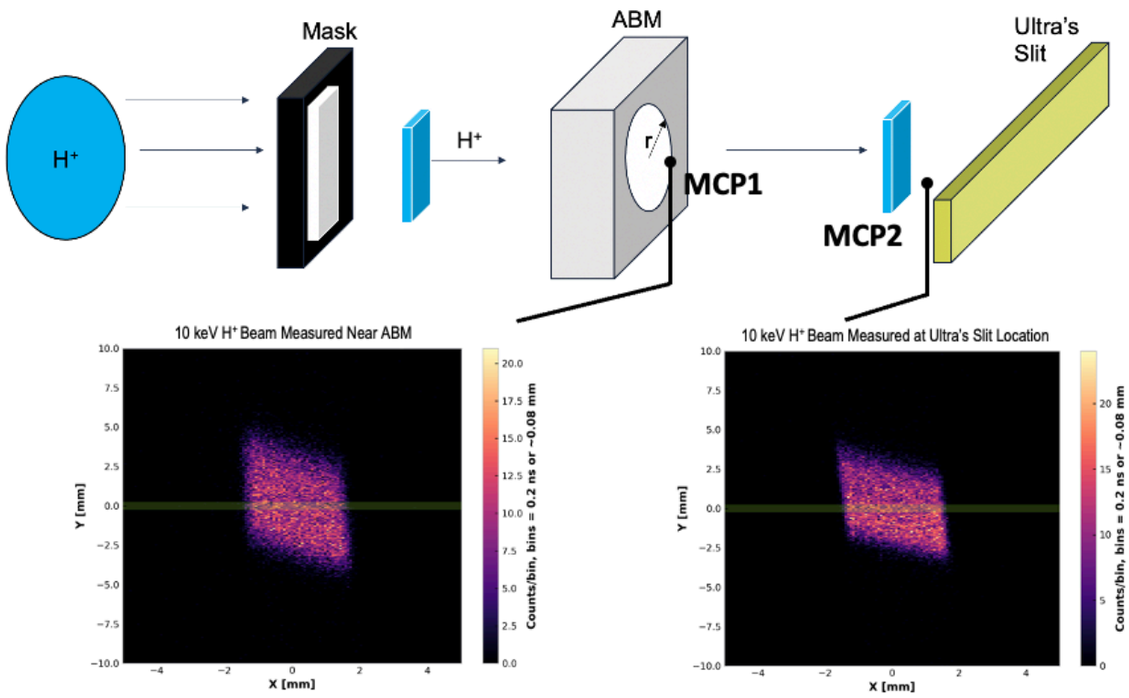


Figure 4: Setup for APL's accelerator ion beam characterization, and measurements taken by the two MCP beam imagers monitoring beam uniformity.

Prior to installing the deflection blades, radioactive source testing is performed with the primary objective to determine to the various imaging parameters (i.e., timing and position offsets) and calibration curves (e.g., that transform data numbers to physical quantities like energy and TOFs) before the time-consuming angle/angle tests. Although source testing alone is insufficient to demonstrate that Ultra meets its requirements, sources are helpful in determining Ultra's performance at the higher energies and to difference species.

Radioactive Disk Sources: The purpose of using the electron disk source and X-ray lines from other sources (e.g., Am-241 & Bi-207) is to perform energy calibration of the SSDs, which is used to convert the DN output associated with an individual particle event into units of energy (keV). This represents the amount of energy deposited by a particle in a detector pixel, but does not necessarily represent the total kinetic energy of that particle. Energetic particles may penetrate a detector or otherwise leave the active volume of a pixel without depositing all their energy, and these effects will be accounted for elsewhere, i.e., with calibration curves, when processing the instrument data. This calibration of the SSDs is a useful, but preliminary step. The primary calibration of the SSDs is to relate DNs to a deposited energy, along with energy loss in dead layers, which will be accomplished by analyzing the relationship between TOF (velocity) and SSD DN for protons, alphas, and other species.

Double Geordi Fixture with undegraded and degraded Sources: This test fixture (**Figure 5ii**) allows us to simultaneously stimulate both slits with each source centered on one of the stop MCPs with the purpose of quantifying the backplane and producing continuous TOF×E tracks. Degraded and undegraded Am-241 have been used. By filling the backplane with particles, the entire start, and stop areas are covered with events that satisfy start, stop, and coincidence requirements. This way we can test and calibrate the performance at the edges of the MCPs and create MCP PH gain maps across both MCPs. With degraded sources, we accumulate continuous TOFxE tracks and check them against the TOFxE spots acquired ion beam testing.

Characterization with sources before and after vibration: For this, we place the shutter in the source position. This can be done for both shutters at the same time since we can sort the data by left or right start slit. Data is collected for sufficient duration to get good statistics over the whole back plane. We use the same intervals for the post-environmental characterization. Additionally, a so-called source arm is being mounted to both Ultra 90 and 45 during TVAC testing so that rates as a function of temperature can be monitored.

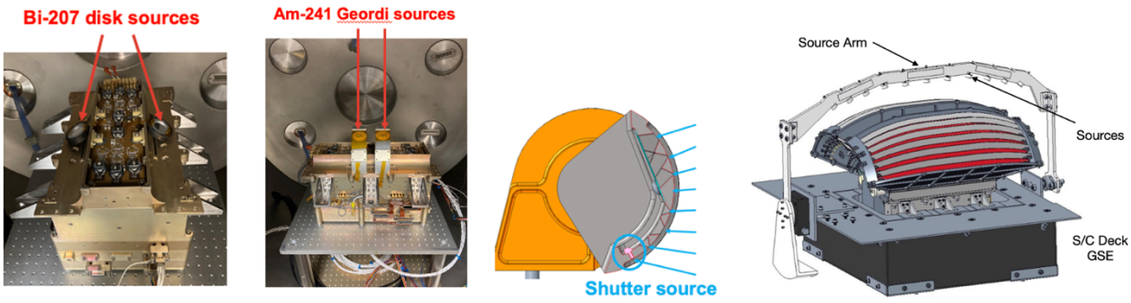


Figure 5: The various source setups that have been used during the Ultra EM and FM calibration campaigns. From left to right: i) Bi-207 disk sources, ii) Am-241 Geordi sources, iii) shutter source and iv) source arm with Am-241 disk sources.

3.3 Monoenergetic Ion Beams Testing Purpose and Setup

Monoenergetic Ion Beams: Ultra is mounted such that the long dimension of its aperture slit is parallel to the floor (perpendicular to the long dimension of the beam). The APL ion beam does not fill the area of the slit and therefore Ultra is being translated along the x-coordinate at a slew rate optimized for counting statistics and test timeliness. Ultra is also mounted to two orthogonal rotation stages such that the slit's FoV can be rotated in both the phi and theta angles (see **Figure 2** for definitions of Ultra's geometry and angle definitions). We stimulate the instrument with ion beams of different species and energies to verify the energy and angular response of the instrument and verify that Ultra meets its measurement requirements (**Table 1**) and to fully characterize its

energy and angular dependent measurement efficiencies, which are critical for science analysis in-flight and for deriving SNR (see Section 4 for more details on the derivation of efficiencies).

Angle-angle ($\phi - \theta$) scans: These scans make up the bulk of the testing, since they are critical for obtaining the angle and energy dependent response function for properly converting counts to physical units. The preferred method for obtaining the angle/angle response function is to choose a ϕ angle (the choice of which is described in) and then discretely step Ultra in θ over the full FoV (and slightly beyond; for reference we chose ~ -52° to +52° in 4° increments). For each discrete step a "X-scan" is performed to ensure the beam illuminates full slit and thus the MCP back plane. The length of Ultra's slit in the $\hat{x}$-direction is 80 mm, therefore the scan starts at -60 mm relative to the center and ends at +60 mm. **Figure 6** shows the various motions that Ultra is undergoing during the angle-angle scans. **Figure 7** shows an example matrix of angle-angle scan performed during the ion beam testing calibrations for both slits of Ultra45 and Ultra90 for energies 40, 20, 10, 7, and 5 keV protons. More limited tests were also performed for different species. The choice of phi and theta angles is discussed in Section 3.3.2.

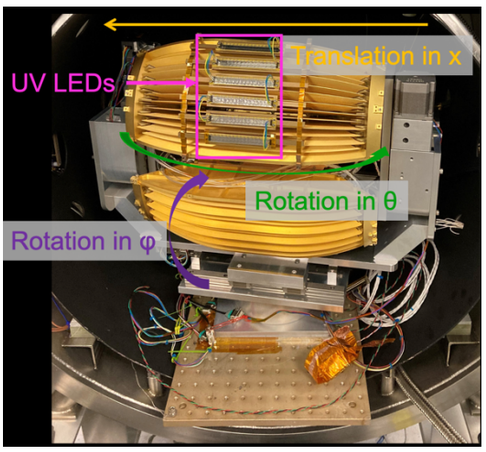


Figure 6: Depiction of rotations in theta and phi angles, as well as translation of Ultra, while in the chamber performing angle-angle tests. Occasionally UV LEDs are used (see Section 5 for those tests).

	Theta Angles →																
Phi Angles ↓	**0**	-52	-44	-36	-28	-20	-12	-9	-6	0	6	9	12	20	28	36	44	52
	8.86	-52	-44	-36	-28	-20	-12	-9	-6	0	6	9	12	20	28	36	44	52
	17.72	-52	-44	-36	-28	-20	-12	-9	-6	0	6	9	12	20	28	36	44	52
	26.58	-52	-44	-36	-28	-20	-12	-9	-6	0	6	9	12	20	28	36	44	52
	35.44	-52	-44	-36	-28	-20	-12	-9	-6	0	6	9	12	20	28	36	44	52
	44.3	-52	-44	-36	-28	-20	-12	-9	-6	0	6	9	12	20	28	36	44	52
	53.16	-52	-44	-36	-28	-20	-12	-9	-6	0	6	9	12	20	28	36	44	**52**

Requires ABM & Beam Image
Requires ABM measurement

Figure 7: Example matrix of angle-angle scans performed during proton beam testing for both instruments and slits.

3.3.1 Alignment Test

To ensure proper alignment of Ultra before the time intensive angle-angle and high-resolution ϕ-scans, we inspect the start & stop count distributions as a function of θ angle for the following energies: 40, 20, 10, 7, and 5. Specifically, Ultra is mounted in the optimal location based on the beam characterizations using the double MCP beam imagers and then rotated in ϕ to ~35.44° (approximately normal incidence to the foil, with no blade shadowing). Next, Ultra performs x-scans for the following θ values: -2° to +2° in 0.5° steps. Here are monitoring locations of the start and stop count distributions and noting the locations of physical structures (e.g., foil frames, nubs,

MCP edges, etc.) in Ultra that block particles. **Figure 8** illustrates start distributions and that a good indicator for proper alignment is the symmetry about x = 0. Alternatively, one can plot the Xstart vs Xstop distributions and look for foil frame and nub locations. The distributions should also follow a linear trend with essentially no curvature.

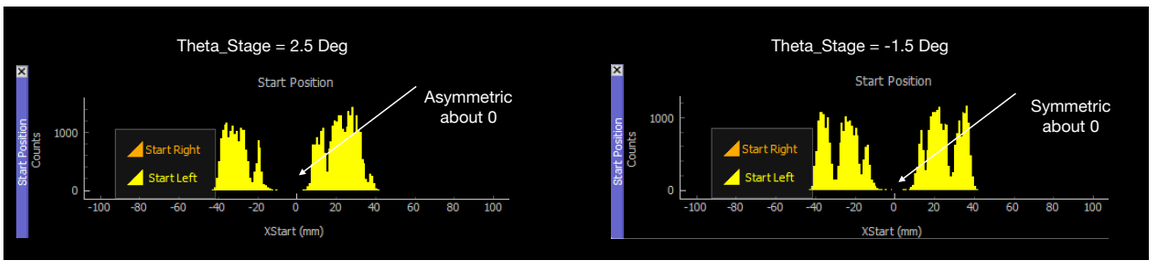


Figure 8: Start count distributions for different theta motion stage values. Theta -1.5 on the motion stage is closest to true zero in the instrument frame.

3.3.2 Hi-Resolution ϕ-Scans

Before proceeding with the angle-angle tests, a high-resolution ϕ-scan is performed to locate optimal ϕ angles for all subsequent θ-scans (θ-scans discussed next). **Figure 9** illustrates the valid events as a function of ϕ angle recorded from the rotational stage for one of the FM45 ϕ-scans. The periodic decrease in events is due to shadowing from the deflection blades. Vertical red dashes spaced every 4.43° represent the ϕ values used for the θ-scans. Additionally, 0.1° increments were chosen for the phi scan.

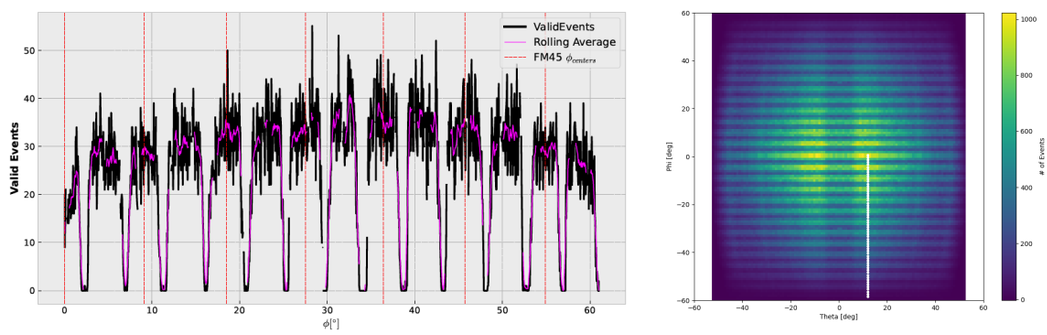


Figure 9: Valid events as a function of ϕ (in motion stage coordinates), rotation stage incremented in 0.1° steps

Note: The High-Resolution ϕ-scans are performed for each slit configuration (left vs. right), before the angle-angle tests are performed for that particular slit

The theta and phi angles were carefully chosen to adequately map out the response function, while optimizing the testing time so all energies are covered for each slit for both sensors. The distribution of thetas are shown in **Figure 10** and the phi distribution is shown in **Figure 9**. A

higher density of thetas are placed near 0° to characterize large slopes in that area. The response function has a gradual slope in the phi direction and therefore seven angles are sufficient. For the angle-angle tests, we measure the following energies: 40, 20, 10, 7, and 5 keV and in that order.

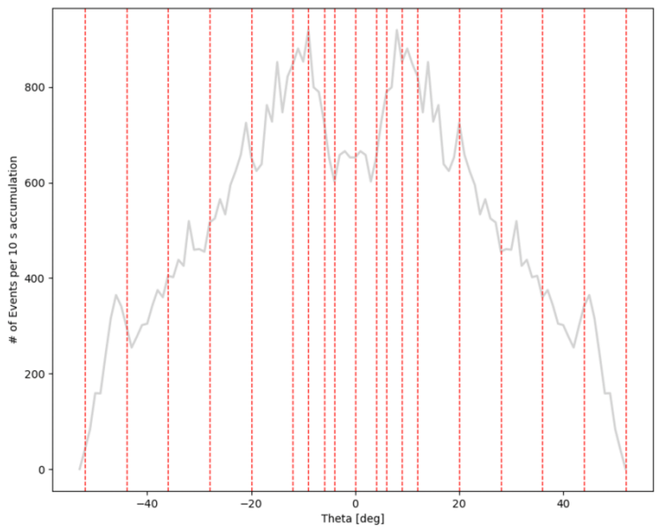


Figure 10: Distribution of simulated events (using SIMION) vs theta (θ)with red vertical dashed lines representing angles in the matrix found in Figure 7.

Below is a list of requirements with additional details (note that each bullet may not necessitate its own test since a particular measurement can be used to satisfy multiple requirements. More details can be found in the calibration procedure):

- *Energy Range & Resolution (Section 4.2):* At a minimum, 5 – 40 keV H^+, a proxy for neutral H (since Ultra does not differentiate between charged and neutral particles) is used (see threshold plan in **Table 2**). Also tests at higher energies H+ were performed for limited phi and theta angle pairs.
- *Masses Resolved (Section 4.3)* . We conducted tests to verify that MCP PH distributions are clearly separated among the different species with the same velocities or times of flights.
- *Angular resolution (Section 4.4):* Ultra is mounted to a three-axis motion stage that has the capability of rotating the instrument in both elevation (θ) and azimuthal (ϕ) coordinates and thus we can estimate the FWHM of the valid event distributions for each angle.
- *Signal-to-Noise Ratio (SNR) (Section 5):* To derive a realistic SNR requires knowledge of the measurement efficiencies as a function of beam energy and incident angle. The tests used to demonstrate energy range & resolution as well as angular resolution performance will also be used here, but in addition, a characterization of the beam (temporal and spatial uniformity) will be independently measured and compared to data obtained by Ultra. The comparison will reveal what fraction of ions are being lost in the sensor volume due to scattering, energy straggling, etc.

- *Test uniformity of front foils and MCP gain uniformity (Section 4.4.5):* The energy and angular response testing and translations along the instrument x-coordinate reveals the uniformity of the front foils and Pulse Height (PH) differences on the backplane MCPs depending on incident phi and theta angles of the beam.
- *SSD testing (Section 6)*: We have also characterized the eight SSDs by stimulating them with H^+ starting around 30 keV and going up to 100 keV and N+ (up to 170 keV) to define TOFxE tracks. The tracks will help define the channelized boxes used to telemetry mass resolved rates as a function of energy.

By using monoenergetic ion beams we can also accomplish several additional goals, including:

- Verify the FSW calculation of angles, and verify that those angles remain fixed for translations along the slit (note that, while in flight, we will collect discrete event data and we can independently characterize any deviations that exists)
- Verify the parameters required for species identification, for use in populating FSW species look up tables (LUTs)
- Verify the energy loss in foils.
- Verify the raw time of flight (TOF) and corrected TOF (cTOF)
- Verify DN to keV conversion of SSD pulse heights
- Verify MCP pulse height dependence on species and energy
- Quantify the angular resolution as a function of ion species and energy, and quantify the contributions of angular scattering, electron optics, and possible position non-linearities to that angular resolution
- Determine flat fielding response function (convolved geometric + measurement efficiencies as a function of θ and ϕ) and validate analytical & particle simulation models

4. MCP Calibrations

4.1 Pulse Height Threshold Test

Before we begin ion beam calibrations, it is crucial that thresholds are properly set to their optimal values. Below are a series of steps we will follow to set the thresholds on the CFDs and analyze the data.

Each Ultra sensor was characterized with an alpha source (test procedure 7523-1090) in vacuum prior to integration with its electronics stack. Anode amplifier output signals were passed through the vacuum wall to air-side COTS electronics, e.g. DSO, CFD and NIM Logic. It was found that CFD thresholds of 10-20mV were sufficiently high to obtain acceptable timing jitter and not so high as to require excessive MCP HV for efficient detection. This experience informed the initial

settings of the CFDs in the instrument electronics. All channels were set at 4DN above the noise level except StartPosition, which was set 2DN above noise[1].

Initial settings of MCP HV were also determined in previous subassembly test procedures but were checked and refined using proton beams and shutter sources during the calibration campaign. Where possible HV settings were determined relative to where the normalized counting rate of an anode signal versus the HV of the associated MCP achieved a plateau. For example, when only one side is stimulated the efficiency of the Left (Right) Start foils and associated regions of the Front MCP can be determined by the ratio of image-mode basic-rates counters

$$Start\ Left(Right)\ Efficiency \stackrel{\text{def}}{=} \frac{StartLeft(Right)WindowStopCoinCoincidence}{WindowStopCoinCoindience}$$

Figure 11 below shows this ratio for 5keV beam and the shutter source on Ultra45 Right side. The chosen operating level, 3.8kV, is approximately 50V above the onset of the plateau for 5keV beam. Higher energy and/or heavier projectiles produce more secondary electrons and would lead to an earlier plateau (see the alpha particle points) partly due to the larger input to the MCP. This is an even larger effect on the Stop MCP since the particle produces its secondary electrons on that surface.

During the calibration campaign the Stop MCP HV levels were varied for scans at a reduced set of angular steps. It was found that the HV needed to be raised by ~50V (4DN) for proton energies at 10keV and below. From the reduced set of angular steps at various HV levels correction factors were obtained that were applied to the already collected full angle-angle scans.

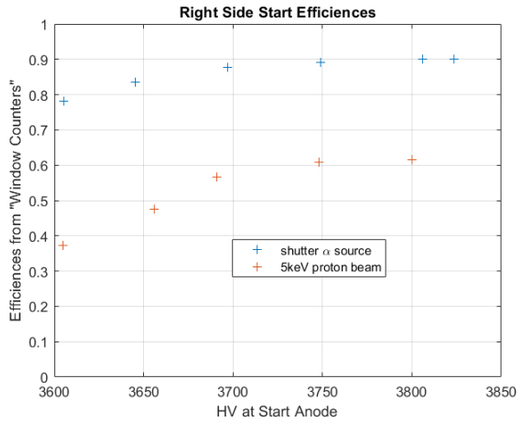
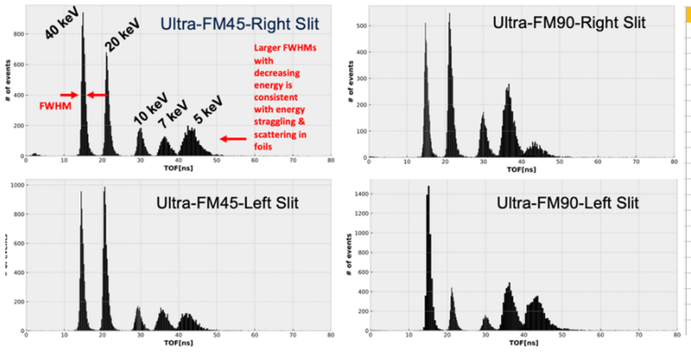


Figure 11: Efficiency from "window counters" as a function of start anode HV for 5keV beam and the shutter source on Ultra45 Right side

[1] The instrument CFD threshold sensitivity was ~ 5mV/DN for Start and Discrete Coincidence channels while for Stop and Position Coincidence channels it was ~ 2.5mV/DN. Note a higher threshold (~20mV) was used for the Start Full anode due to low level x-talk between Bottom Coincidence and Right Start Full seen in a beam test of the Engineering Model in January 2023.

4.2 Ultra TOF x PH Energy Range and Resolution

In order to satisfy IMAP mission L2 requirement of ***high energy resolution all-sky maps*** of Hydrogen energetic neutral atoms (MRD-L2-14) Ultra shall measure Hydrogen neutral atoms of 5 – 40 keV energies with an energy resolution ΔE/E (FWHM) ≤0.7 for an angular resolution ≤18°x18°.



FM	Slit	Energy[keV]	TOF FWHM [ns]	Peak[ns]	dTOF/TOF	dE/E
45	Right	5	4.6	43.2	0.11	0.21
45	Right	7	2.9	36.4	0.08	0.16
45	Right	10	1.8	30.1	0.06	0.12
45	Right	20	1.7	21.2	0.08	0.16
45	Right	40	1.3	15.0	0.09	0.17
45	Left	5	4.5	42.3	0.11	0.21
45	Left	7	2.7	36.0	0.08	0.15
45	Left	10	1.7	29.5	0.06	0.11
45	Left	20	1.2	20.7	0.06	0.12
45	Left	40	0.9	14.6	0.06	0.12
90	Right	5	4.4	43.3	0.10	0.20
90	Right	7	3.1	36.1	0.09	0.17
90	Right	10	1.8	30.2	0.06	0.12
90	Right	20	1.3	21.4	0.06	0.12
90	Right	40	1.3	15.2	0.09	0.17
90	Left	5	4.5	43.5	0.10	0.21
90	Left	7	2.7	36.4	0.07	0.15
90	Left	10	1.8	29.9	0.06	0.12
90	Left	20	1.3	21.2	0.06	0.12
90	Left	40	1.0	14.9	0.07	0.14

Figure 12: Beam calibrations covered the requirement range using 5-40 keV monoenergetic H+ beams. TOF distributions plotted for both slits of each unit, and ΔE/E calculation (right table) confirm energy resolution, i.e. ΔE/E ≤ 0.7 for high energy resolution maps, within 5 - 40 keV.

As it can be seen in Figure 12, both Ultra45 and Ultra90 can achieve a much better resolution than required (from 0.11 to 0.21 depending on the energy. In the lab, we use monoenergetic and directional H^+ beams with relatively high intensities (compared to heliospheric ENAs). This is important to note because Ultra does not have pre-assigned energy channels; therefore, we will need to make choices on how to bin the data in energy space to ensure good statistics. Nonetheless, theoretical analysis based on previously observed heliospheric intensities (from IBEX and INCA data) indicate that an energy resolution of ΔE/E of ~ 0.4 should be adequate for good statistics, i.e. satisfying the SNR requirement (see section 5) for 6 deg angular resolution, which is much better than the spatial resolution of the high energy resolution maps. Therefore Ultra meets requirements RULTRA-1047; -1048; -1053; 1054; -1059; -1060.

4.3 Ultra TOF x PH Mass Resolution

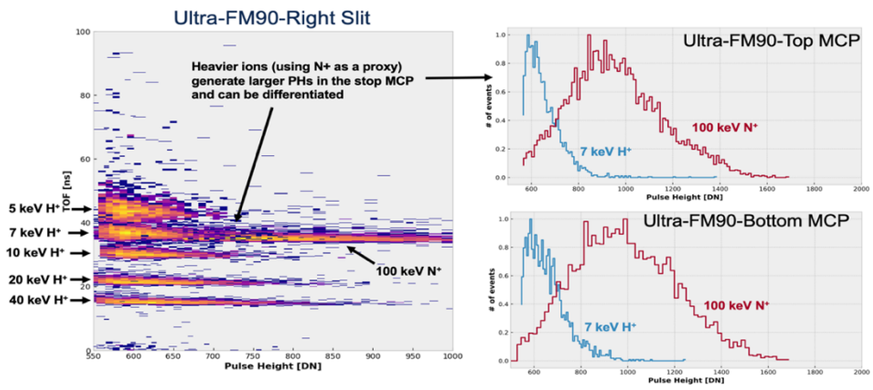


Figure 13: Pulse Height distributions for 7 keV H+ and 100 keV N+ for Ultra90; Ultra45 exhibits similar behaviour.

Ultra's MCP based mass resolution shall be able to differentiate between H (lights) from O (heavies). ***As it can be seen from Figure 13, Ultra can differentiate 7 keV H^+ from 100 keV N^+ ions (that is, lights from heavies with the same TOF) via MCP pulse height analysis (peaks of distributions are clearly separated) and therefore it meets requirements RULTRA-1046; -1052; -1058.*** In reality, the energetic ENA populations will be primarily Hydrogen ones, thus the majority of our PHs will be generated by light ions.

4.4 Ultra TOF x PH Angular Resolution

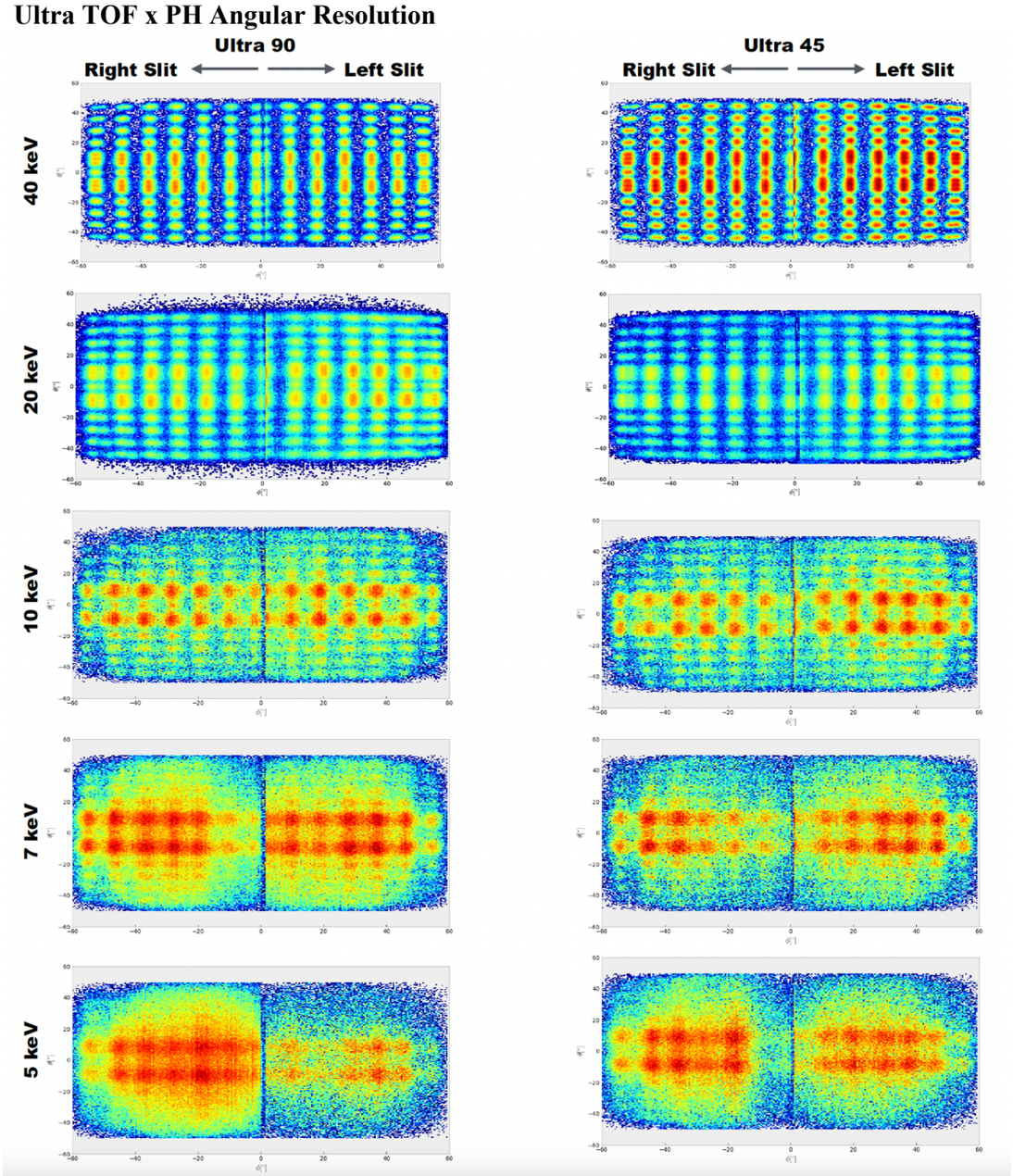


Figure 14: Counts on the Ultra45 and Ultra90 back planes in φ *vs* θ coordinate system for the theta-phi scans of 5, 7, 10, 20, and 40 keV H+

In order to satisfy IMAP mission L2 requirement of ***high angular resolution all-sky maps*** of Hydrogen energetic neutral atoms (MRD-L2-13) Ultra shall measure Hydrogen neutral atoms of 10 – 20 keV energies with an angular resolution of 6 x 6 degrees. Since the angular resolution worsens with decreasing energy, due to more scattering in the foil, the actual requirement is that Ultra satisfies 6x6 degree angular resolution at 10 keV. **Figure 14** shows counts on the Ultra45 and Ultra90 back planes in φ *vs* θ coordinate system for 5, 7, 10, 20, and 40 keV H+. We can see that as energy decreases the resolution worsens. Another effect worth noting is the "splitting" of the distributions at the edges of the FOV (high φ and θ angles), attributed to the charged component coming out of the start foil being deflected by the electrostatic potentials. Identifying those FOV regions during ground testing help us isolate them during our analysis while in flight. **Figure 15** shows φ-θ maps of the worst (highest) value between the FWHM values of the φ and θ distributions. ***This way, we can identify that, for 10 keV there is a limited FOV within which Ultra meets the requirement of FWHM ≤ 6º (blue color dots). At 20 keV the requirement is satisfied almost throughout the FOV of the instrument. Therefore, Ultra meets its angular resolution requirement RULTRA-1049; -1056; -1061.***

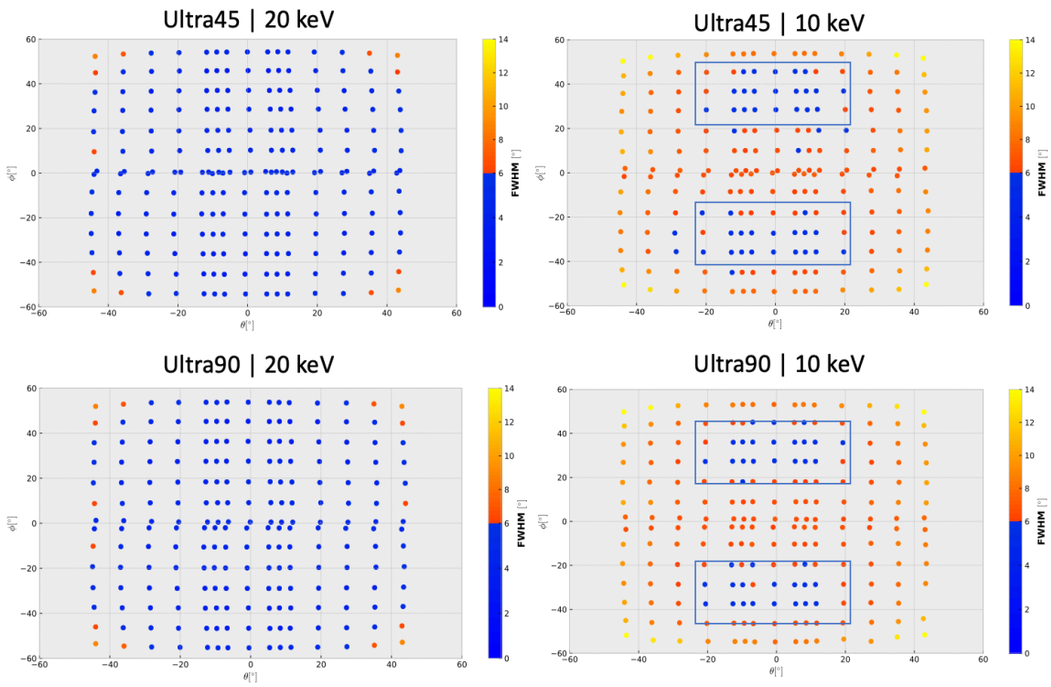


Figure 15: φ-θ maps of the worst (highest) value between the FWHM values of the φ and θ distributions. Blue color dots indicate locations in the instrument where the criterion of FWHM ≤ 6º is satisfied.

4.5 Ultra MCP Sensitivity within the FOV

Using shutter sources (Am-241 radioactive source; see Figure 5iii) we stimulate both the MCP and SSDs at the back plane. **Figure 16 (top)** shows counts on the back plane MCP in ϕ, θ coordinates illustrating the sensitivity of the MCP and its full FOV across: $-60° \leq \phi \leq +60°$ & $-45° \leq \theta \leq +45°$. **Figure 16 (bottom)** shows the response of the SSDs, which are arranged along the y-direction (see **Figure 2** for instrument coordinates).

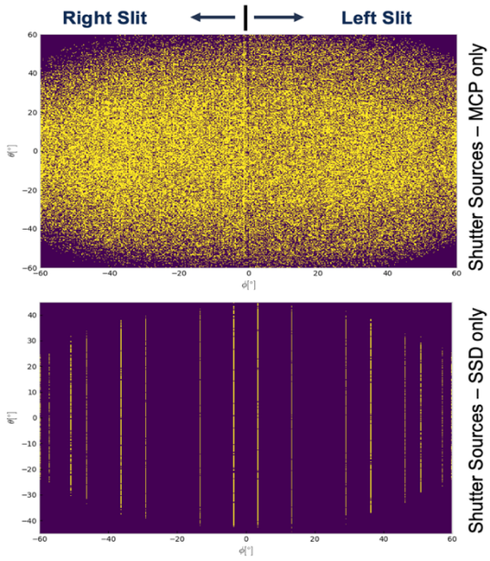


Figure 16 (top): counts on the back plane MCP in ϕ, θ coordinates; (bottom): counts on the backplane SSDs

4.6 Ultra UV Rejection Capability

UV testing supports the SNR requirement by measuring low intensity ion (our proxy for ENAs) signals in the presence of UV generated backgrounds. The test includes using a UV source that is mounted directly to the instrument's deflection system and positioned such that it illuminates one slit while radioactive sources or monoenergetic beams are illuminating the adjacent slit (see **Figure 6** for LED configuration).

Ultra EM testing with UV and alpha sources:

Ultra EM was tested without the deflection blades on. The top left panel of **Figure 17** shows the timeline of the UV test conducted. The LED UV source was attached to the right slit of the instrument. For the first 5 min of the test, the source arm was swept from 0 to 85º, i.e. filling the left slit of the instrument, while the LED UV sources were attached on the right slit.

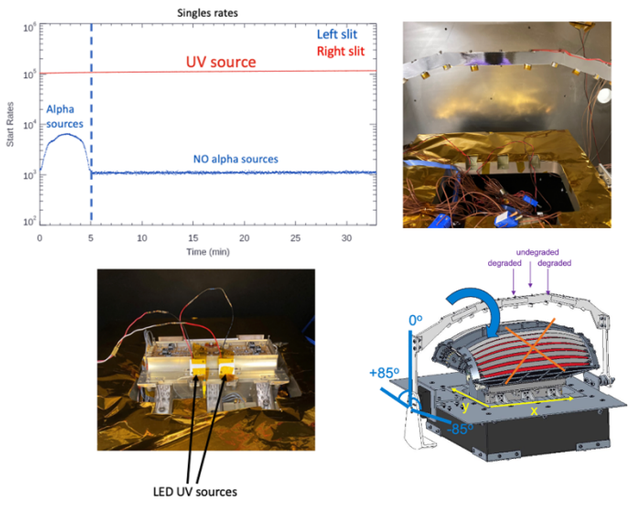


Figure 17: (top left) Test timeline: First five minutes of test both alpha and UV sources were used, for the rest 27 min only UV sources were used; (top right) source arm with alternating degraded and undegraded sources; (bottom left) LED UV sources attached on the right slit; (bottom right) Ultra with source arm attached schematic (note that in this test the deflection blade was not on).

For the next 27 min of the test, the source arm was outside the Ultra FOV, therefore Ultra was only measuring counts from the UV source. With this timeline we can check how many of the accidental counts i.e. UV background that would pass the FSW valid event criterion is due to "pure UV" accidentals, caused by start-stop-coincidence UV counts vs accidentals caused by UV triggered start matched with foreground (alpha particle in this case) stop-coincidence pair.

Figure 18 shows the results of our test. **Figure 18(A)** shows counts registered at the Ultra MCP backplane, in phi-theta coordinates, without FSW valid event criterion applied. **Figure 18(B)** shows counts registered (without valid event criterion being applied) in the (CoinXpos – Xstop) vs

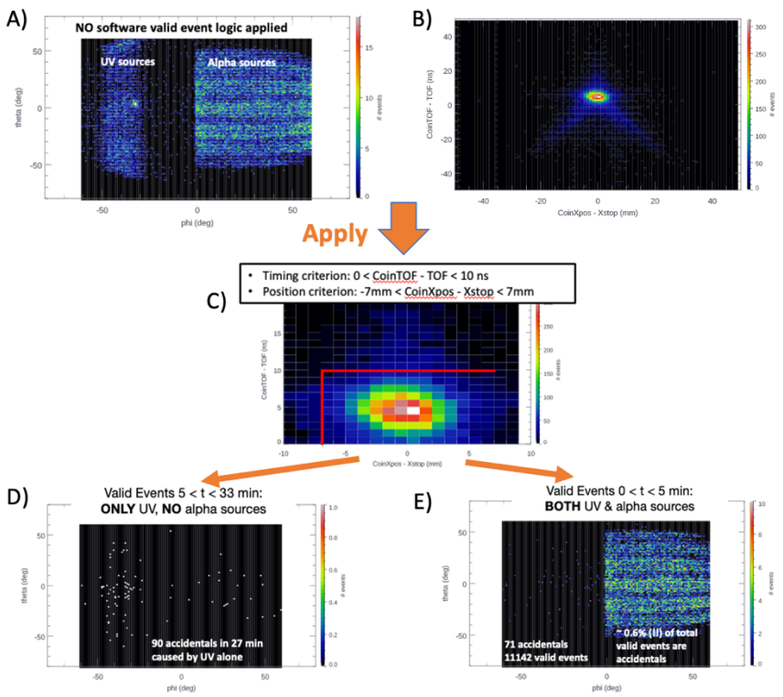


Figure 18 (A) Counts registered at the Ultra MCP backplane, in phi-theta coordinates, without FSW valid event criterion applied; (B) Counts registered in the CoinXpos – Xstop vs CoinTOF – TOF space; (C) Application of the Valid Event Criterion where the difference in x position between stop and coincidence (CoinXpos – Xstop) is between -7 and 7 mm, and the time it takes for an electron to fly from the stop MCP to the coincidence (CoinTOF – TOF) one is less than 10 ns; (D) Valid Events registered after the first 5 min of the test, when only UV was counts were present (all accidentals); (E) Counts registered at the Ultra MCP backplane, in phi-theta coordinates, after the FSW criterion was applied, for the first 5 min of the testing, when both UV and alpha sources were present.

(CoinTOF – TOF) space, where (CoinXpos – Xstop) is the difference between the stop x position and coincidence x position, and (CoinTOF – TOF) is the time it takes for an electron to fly from the stop MCP to the coincidence one. **Figure 18(C)** shows the limits of the valid event criterion, i.e. (CoinXpos – Xstop) is between -7 and 7 mm, and (CoinTOF – TOF) is less than 10 ns; **Figure**

18(D) Valid Events registered when we apply the valid event criterion after the first 5 min of the test, when only UV was counts were present, i.e. all of these counts are "pure UV" accidentals. And we get only 90 accidentals in 27 min. **Figure 18(E)** shows the counts registered at the Ultra MCP backplane, in phi-theta coordinates, after the FSW criterion was applied for the first 5 min of the testing, when both UV and alpha sources were present. In that case we see that out of 11142 valid events, 71 one of them were accidentals (we identify the accidentals as the ones that have a right slit start, since that's the slit that the LEDs were attached to), which is 0.6% of the total counts. Note that the amount of accidentals per minute the first 5 min of the test has increased compared to the interval when only UV source was present, because when both UV and alpha sources are present the accidentals are increasing with increased foreground (since the majority of them are caused by UV triggered start matched with foreground (alpha particle) stop-coincidence pair.

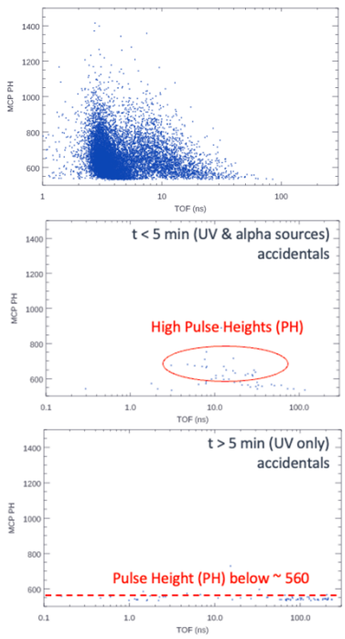


Figure 19: TOF vs MCP PH distribution of the valid events throughout the test (top panel), during the first 5 min (middle panel) and for t > 5 min (lower panel).

Figure 19 shows TOF vs Stop MCP PH distribution of the valid events throughout the test (top panel), during the first 5 min (middle panel) and for t > 5 min (lower panel). From the middle panel, it is evident that there are accidentals with high PH when both UV and alpha sources are present, indicating that Stop/Coincidence pair caused by an alpha particle is matched with a UV Start triggering the state machine a few ns earlier than the alpha Start. The number of accidentals of this type is proportional to the foreground. On the contrary, the number of accidentals created by random UV Starts, UV Stops, and UV Coincidences (those are the only ones occurring in the case when only UV source was present) have low PH, so setting higher PH threshold could further reduce them.

Finally, one of the concerns of high UV rates bombarding the start MCP is the dead time, which affects the valid events registered by the FPGA, and thus we need to apply R vs R corrections.

Figure 20 shows the R vs R correction of Ultra Source Rates for different UV start rates.

We have performed 4 different tests:

- Full sweep of alpha sources, NO LED
- Left sweep of alpha sources, WITH LED at 100K/s rate on the right slit.
- Source arm at 60º WITH LED at 100K/s.
- Source arm at 60º WITH LED at 400K/s.
- Source arm 60º WITH LED at 100K/s, after raising the CFD threshold to 16 (smaller pulses, created by UV, are rejected)

We found:

- Ratio of VEs from Sweep WITH LED @100K/s over Sweep WITHOUT LED: 1300/1650 ~ 79% (i.e. UV rates decrease the VE)
- Ratio of VEs from Source Arm at 60° WITH LED @100K/s over Source Arm at 60° WITHOUT LED: 600/750 ~ 80%; @400K/s LED, 400/750 ~ 53% (i.e. Higher UV rates decrease the VE even further)

Therefore, we need to apply the appropriate corrections to compensate for missed Starts due to State Machine dead time. At the 60° location the VE rate from the source arm sources is well below the peak, at about 750/sec. With the LED UV on, lower rates (blue trace) reflect reduced rates caused by Start-driven dead time. It should be noted that 400K/s is an over-estimate for UV rates. Maximum UV rates for the narrow (nominal) shutter slit is 100K/s. Nonetheless there are mitigation strategies in the case that UV background is too high (e.g. using shutter foil).

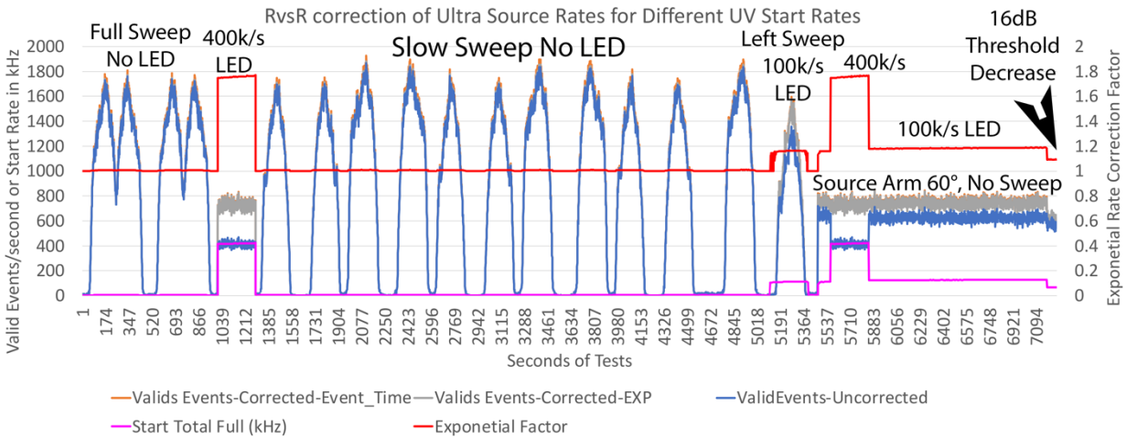


Figure 20: R vs R correction of Ultra Source Rates for Different UV start rates

Ultra FM testing with UV sources and 7 keV proton beam:

The Ultra FM was tested with the deflection blades on using both UV sources (at 100 kcps), attached to the right deflection blade assembly (see Figure 6) and 7 keV proton beam (at ~10 counts per sec) illuminating the left slit. Based on the EM testing we decided to "open up" the valid event criterion to allow for more foreground to be registered. **Figure 21** shows the results of our FM test. **Figure 21(A)** shows the counts registered at the Ultra MCP backplane, in phi-theta coordinates, without FSW valid event criterion applied. **Figure 21(B)** shows counts registered (without valid event criterion being applied) in the (CoinXpos – Xstop) vs (CoinTOF – TOF) space. **Figure 21(C)** is the same as **Figure 21(B)** after the new valid event criterion has been applied (see pseudocode below and FSW for more details), which, compared to the original one, has two negative spurs (see **Figure 22** for explanation of these negative spurs). **Figure 21(D)** shows the counts registered at the Ultra MCP backplane, in phi-theta coordinates, after the FSW criterion was applied. Note that the high density spot on the right slit is cause by ~ 2keV (65 ns) protons being knocked off a water molecule (when UV photo electrons are accelerated to the Start MCP), and subsequently being accelerated by the 2kV potential onto the Stop foil (at the edge of the straggling curve). For more details on how that distribution is formed see **Figure 23**. **Figure 21(E)** shows only the accidental counts in the xstop-ystop plane (the high density line distribution are the 2 keV protons mentioned

above). **Figure 21(F)** shows the accidentals in the xstop-ystop plane if the extra requirement of TOF < 65 ns is applied (in order to get rid of the 2 keV protons). In that case the total percentage of accidentals with respect to the foreground is 1.7%. Nonetheless, further investigation of the data showed that the "spurs" include a large number of "pure UV" accidentals, therefore while in-flight we'll have to investigate how to limit the valid event criterion on the ground, for different energies, in order to achieve the maximum foreground and minimum background, i.e. maximum signal-to-noise ratio (SNR).

if ImgParams.eTOFMin <= eTOF <= ImgParams.eTOFMax
*t1 = (eTOF - eTOFOff1) * eTOFSlope1/1024*
*t2 = (eTOF - eTOFOff2) * eTOFSlope2/1024*
if t1 <= (Xc - Xb) <= t2 or
-t2 <= (Xc - Xb) <= -t1
... continue event processing
else
reject event
else
reject event

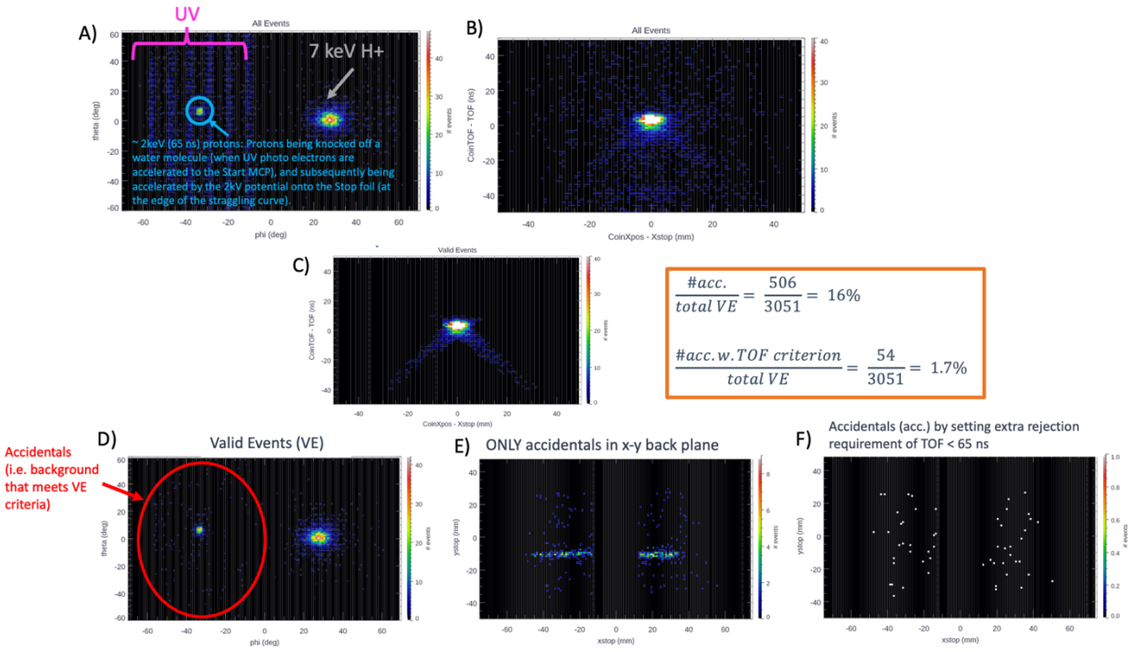


Figure 21: (A) counts registered at the Ultra MCP backplane, in phi-theta coordinates, without FSW valid event criterion applied; (B) counts registered (without valid event criterion being applied) in the (CoinXpos – Xstop) vs (CoinTOF – TOF) space; (C) is the same as (B) after the new valid event criterion has been applied; (D) counts registered at the Ultra MCP backplane, in phi-theta coordinates, after the FSW criterion was applied; (E) Only the accidental counts in the xstop-ystop plane; (F) accidentals in the xstop-ystop plane if the extra requirement of TOF < 65 ns is applied

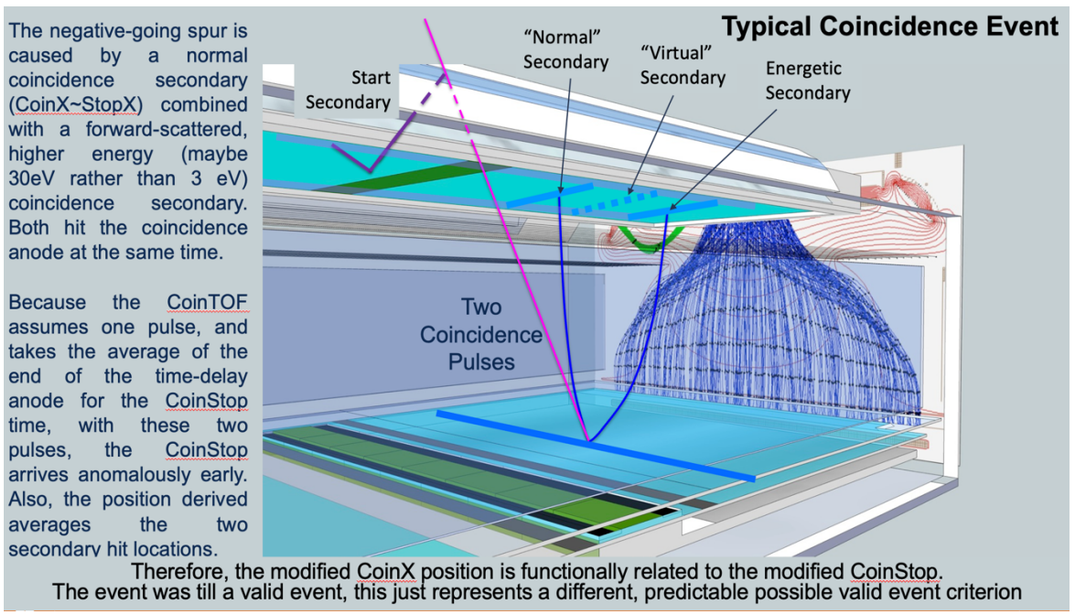
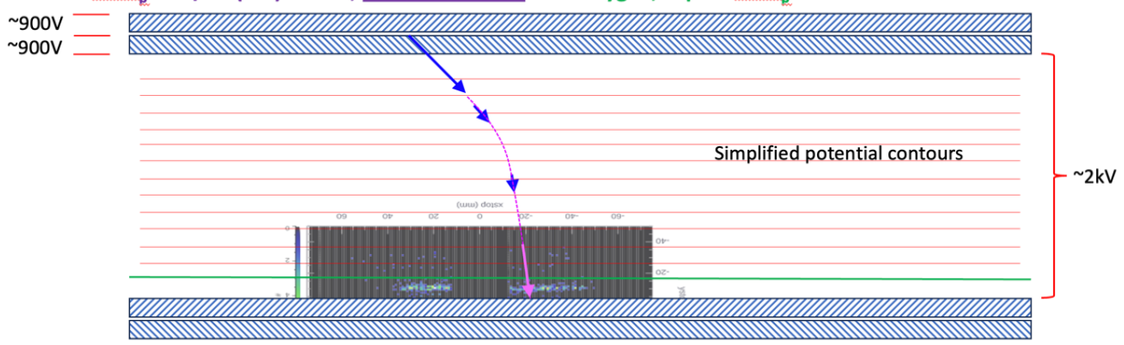


Figure 22: Graphic depicting how the "spurs" in the new valid event criterion definition include more foreground events.

- **Hypothesis:** "2"keV protons (and oxygen) exit Front MCP with ~1keV energy.
- The apparent measured theta angle would be the pore bias angle (13°), but because the acceleration by the electrostatic potentials is in the plane, the ending angle is ~8.5° (and they have ~3keV energy).
- Their out-of-plane energy is $1*\sin^2(13°) = 0.05$keV.
- Their average energy in flight would be $E_{avg} = 0.05/\sin^2(8.5°) = 2.3$keV, which probably makes sense.
- Distance traveled ~4cm, therefore TOF = 4/[438E5*sqrt(2.3)] = 60ns.
- **$cTOF_p$ = 60/cos(32°) = 70ns; Measured ~63ns. For Oxygen, expect $cTOF_p$ x 4 = 252. Measured = 225 to 250.**



Proton exits Start MCP pore with ~600 to 900V energy, at the pore bias angle. It is accelerated by the electron optics potentials, ending up at the Stop with >2keV energy. It's average energy over the path (determining TOF) is ~2keV. It is displaced (horizontally, which is the X dimension) by about 7 or 8 mm, due to its original bias exiting the pore.

Figure 23: Graphic depicting how the 2 keV proton accidentals are formed within the sensor.

5. Deriving Measurement Efficiencies from Calibrations

5.1 Formulism

Ultra measurement efficiencies can be derived by equating the ion flux measured at the absolute beam monitor (ABM) to the incident ion flux at Ultra's aperture. To do this we can write the following equation:

$$R(E) = \frac{N_{Ultra}(E,\theta,\phi)A(\theta)}{\epsilon(E,\theta,\phi) \times g_d(\theta,\phi)\Delta t}$$

The quantity on the left-hand side represents the normalized number of particles per time, where $R(E) = R_{ABM} \times \langle PY \rangle \times \Delta y$. The parameters R_{ABM}, $\langle PY \rangle$, Δy are explained in detail in the next section. The right-hand side of the equation represents number of particles per time measured by Ultra which are properly weighted by its instrument response dependences. $N_{Ultra}(E,\theta,\phi)$ represents the total number of valid events (i.e., events that meet coincidence logic), $A(\theta)$ is the projected area of Ultra's slit, Δt is the accumulation time, $g_d(\theta,\phi)$ is the simulated effective area of the instrument, and $\epsilon(E,\theta,\phi)$ is the measurement efficiency. Deriving the quantity $\epsilon(E,\theta,\phi)$ is one of the main purposes of these calibrations, therefore we will discuss in detail below how we derived the other quantities.

5.2 Determining R(E)

As discussed above, $R(E) = R_{ABM} \times \langle PY \rangle \times \Delta y$, where R_{ABM} is the average rate reported by the ABM over an approximate three-minute average. The rates are read out at ~1 Hz but are very stable over the accumulation period, so taking an average is very reasonable. Modest beam rate drift can and does occur over timescales of hours, but periodic measurements of R_{ABM} can correct for this known behavior. The ABM consists of two channel electron multipliers (CEMs) on either side of a thin foil used for secondary electron production. As the primary ion traverses this foil it can produce a forward and backward scattered electron that are steered to the CEMs. R_{ABM} is

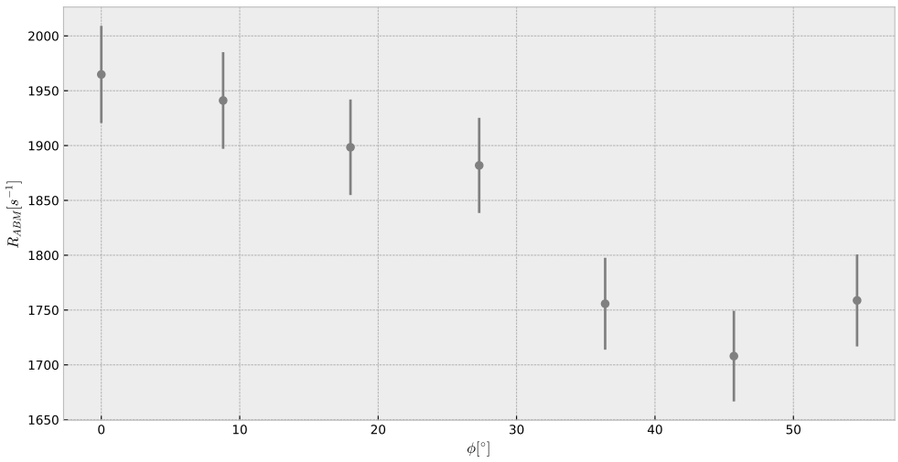


Figure 24: R_{ABM} as a function of instrument phi-angle. This represents a roughly eight hour testing period.

calculated by taking a ratio of the product of the individual CEM rates to the coincidence rate. The equation is: $R_{ABM} = R_{CEM1}R_{CEM2}/R_{CEM1,2}$. The benefit of this approach is that it divides out the detection efficiencies of the CEMs. **Figure 24** is a plot of R_{ABM} over a full angle-angle test. Error bars are calculated assuming Poisson statistics and the horizontal axis is effectively time, but it is remapped into Ultra's phi angle.

$\langle PY \rangle$ is the normalized counts per width, which is the is along $\hat{y}$ in Ultra's coordinate system. This quantity is calculated using a 2D microchannel plate beam imager that is located upstream from Ultra and is co-located with the ABM. The most critical dimension is the one along $\hat{y}$ since that intersects Ultra's slit in the dimension that is not being translated. To estimate the density we take the histogram counts along $\hat{y}$ and bin them in spatial coordinates along the MCP. Here 0.4 ns is approximately 2.675 mm. Then $\langle PY \rangle = (counts\ per\ bin / \sum counts\ per\ bin) \times (0.4ns / 2.675\,mm)$. **Figure 25** illustrates the measured MCP count distribution along $\hat{y}$ and the normalization in the right panel, with the shaded region highlighting the region that intersects Ultra's width. For this particular beam test, $\langle PY \rangle \cong 0.25$.

Finally, Δy is simply the width of Ultra's slit. Although Ultra has several slit configurations, we focused our calibrations on two: i) the narrow slit, which is 0.5 mm wide and ii) the wide slit, which is 2 mm.

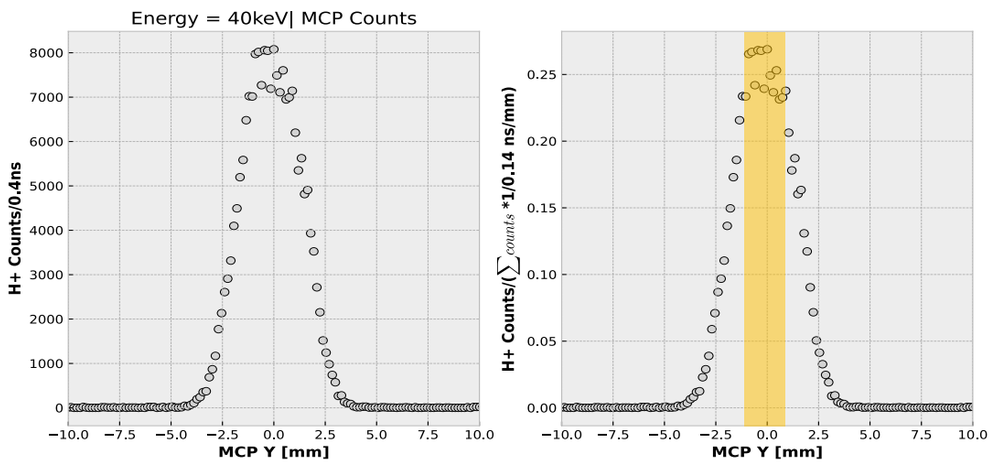


Figure 25: Distribution of counts measured on the imaging MCP as explain in text. The panel on the right shows the distribution normalized to the total number of counts with a shaded region representing +/- 1 mm.

5.3 Determining $A(\theta)$ and Δt

The projected area of the beam onto the slit at different θ angles (see Figure XX) can be calculated simply by the physical area of the slit (length × width, or $L_x \times \Delta y$ in the notation we use here) multiplied by the cos (θ). Therefore, $A(\theta) = L_x \Delta y cos(\theta)$. L_x is a constant 80 mm and Δy depends on the slit configuration used during the test. Δy for the narrow slit is 0.5 mm, and 2 mm for the wide slit. In general, the narrow slit is used for beam energies $\geq$ 10 keV and the wide slit is used for $<$ 10 keV due to the low intensities in the beam. When alternating between slits we ensured that the measured count rate differences between the two configurations were purely

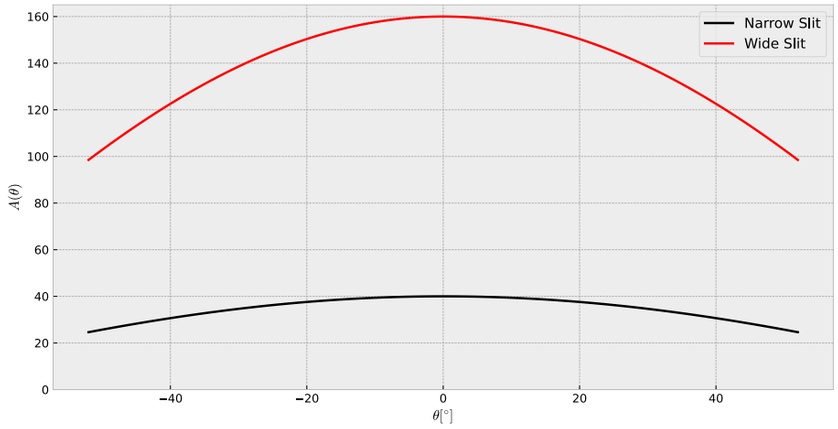


Figure 26: Projected area (A) as a function of θ for the narrow and wide slit configurations. θ range mimics the +/- 52° or the extremes of Ultra's FoV.

geometric (i.e., increased by a factor of four when going from thin to wide; see **Figure 26**). This was important to check because the wider slit could intersect a non-uniform portion of the beam and therefore bias our calibrations.

The accumulation time, Δt, is calculated based on the translation speed, $v_{translate}$, of Ultra's slit across the beam or $\Delta t = N \times (L_x / v_{translate})$, where N is the number of scans that were performed. For the majority of angle-angle tests N = 2—which represents the instruments slewing in one direction, stopping, and returning—was used. If the beam intensity was low, sometimes N = 4 and/or a slower $v_{translate}$ was used to increase the accumulation time and therefore the number of valid events. **Figure 27** depicts the $v_{translate}$ profile for a typical N = 2 case. The bottom panel in **Figure 27** zooms in on one leg of the motion to highlight the speed profile. The average $v_{translate} \cong 0.997$ mm/s with a standard deviation of ~1%.

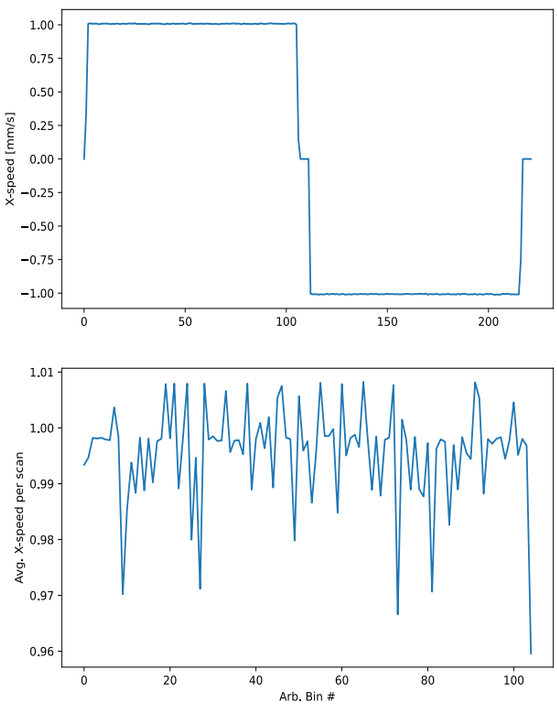


Figure 27: Velocity profile of the translation motion (parallel to the long dimension of the slit or $\hat{\mathbf{x}}$.

5.4 Determining $\mathbf{N_{Ultra}(E, \theta, \phi)}$

Valid particle events are represented by $\mathbf{N_{Ultra}(E, \theta, \phi)}$. The flight software document details the procedure for determining a valid event, but we will also briefly summarize here. The software computes the particle TOF based on the timing pulses from the start and stop anodes

as well as the time it takes for an electron, eTOF, to travel from the stop foil to the coincidence anode. A valid event must have consistent x-positions between the stop and coincidence anodes and reasonable eTOF values. Reasonable is not rigorously defined because the science team is still tweaking the values to optimize the signal-to-noise ratio. However, for the efficiencies reported below we used the following code (in Python) and values to compute valid events:

```
TDC_norm_DN = 0.2

TOFx=TDC_norm_DN/2.*(df['StopN_norm_TDC'][ve_result]+df['StopS_norm_TDC'][ve_resu
t])

TOFy=TDC_norm_DN/2.*(df['StopE_norm_TDC'][ve_result]
+df['StopW_norm_TDC'][ve_result])

Dtofyx = TOFy - TOFx

xstartminusxstop = df['Xstart'][ve_result]-df['Xstop'][ve_result]
coinxposminusxstop = df['coinxpos'][ve_result]-df['Xstop'][ve_result]
etof = df['coinTOf'][ve_result] - df['TOF'][ve_result]
eTOFOff1 = 10
eTOFOff2 = -5
eTOFSlope1 = 0.6667
eTOFSlope2 = 0.75
eTOFmax = 9
eTOFmin = -40
TOFDiffTpMin = 22.6
TOFDiffTpMax = 26.6
et1 = (etof - eTOFOff1) * eTOFSlope1
et2 = (etof - eTOFOff2) * eTOFSlope2

valid_events_result = np.where( (etof <= eTOFmax) & (etof >= eTOFmin) \
                        & (((coinxposminusxstop >= et1) & (coinxposminusxstop <= et2)) |
((coinxposminusxstop >= -1*et2) & (coinxposminusxstop <= -1*et1)))\
                          & ((df['StopType'][ve_result] ==1) | (df['StopType'][ve_result] ==
2))
                          & ((Dtofyx >= TOFDiffTpMin) & (Dtofyx <= TOFDiffTpMax)) \
                            & (df['ctof'][ve_result] >= 0))[0]
```

5.5 Determining $\mathbf{g_d(\theta, \phi)}$

$g_d(\theta, \phi)$ is the geometric function, which is essentially the solid angle weighted effective area at a given combination of polar angles. The units of $g_d(\theta, \phi)$ are cm^2 and it relates to the total geometric factor (cm^2 sr) by taking the integral over solid angle, i.e., $= \int \int g_d(\theta, \phi) d\theta \, d\phi$. The product of g_d and ϵ is usually referred to as the response function and together they map how to properly weight counts of a particular species, energy, and incident angle (in both θ, ϕ as defined in **Figure 2**) to a flux. In theory, g and ϵ, are easily separated, but this is nearly impossible to do experimentally. In short, the ultimate goal is to determine $\epsilon = \epsilon(E, \theta, \phi)$ by dividing out g_d (see

first assumption)—which does not depend on species and E—using incident flux measurements from the absolute beam monitor upstream of Ultra's aperture (section 5.2).

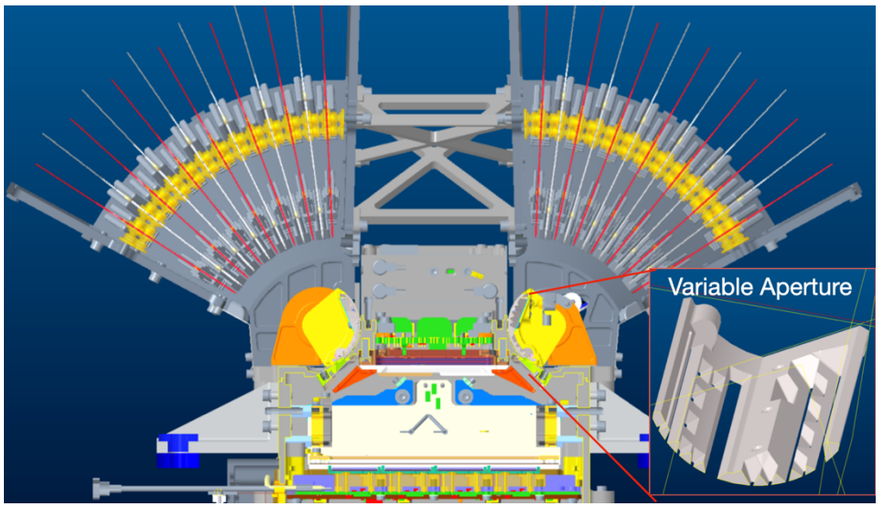


Figure 28: Ultra CAD model and variable aperture illustrating different configurations.

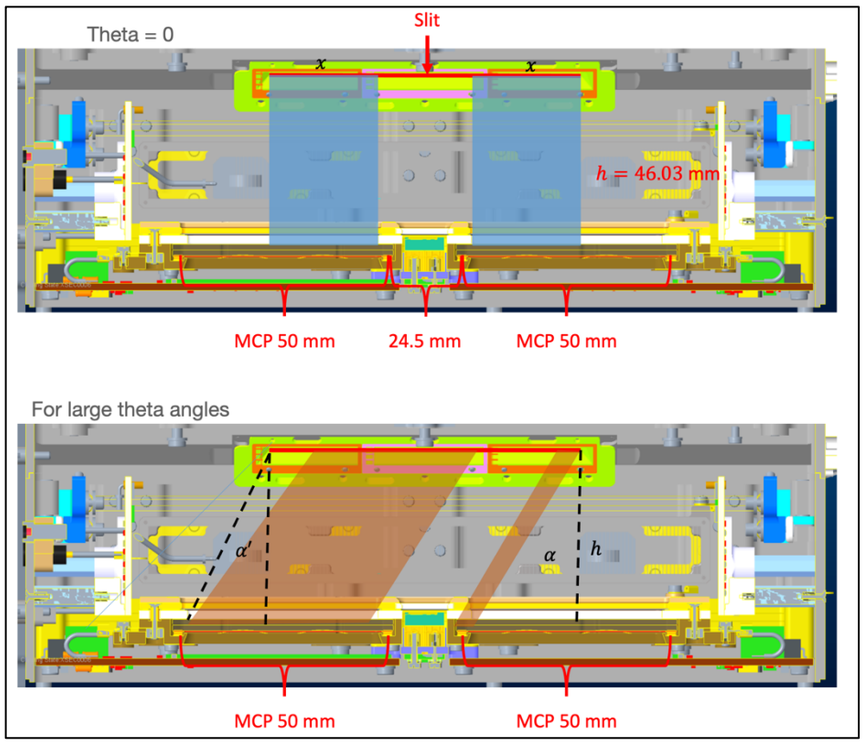


Figure 29: Area projections onto MCP back plane for varying theta angles

The geometric function was determined both analytically and from detailed particle tracing simulations. For the analytic model, the detailed CAD drawings (**Figure 28**) of Ultra make it possible to parameterize the solid angle subtended by the various slit configurations onto the MCP back plane as a function of incident direction in θ, ϕ coordinates (see **Figure 2** for angle definitions). First, we consider only the area projections of the slit and ignore shadowing effects from the mechanical structure (e.g., deflection blades, nubs, holders, etc.). **Figure 29** illustrates area projections for two different incident angles, α. A two-dimensional response is computed and the corresponding 2D integral provides the total GF (see **Figure 30**). Next, we consider the mechanical structure how that impacts G.

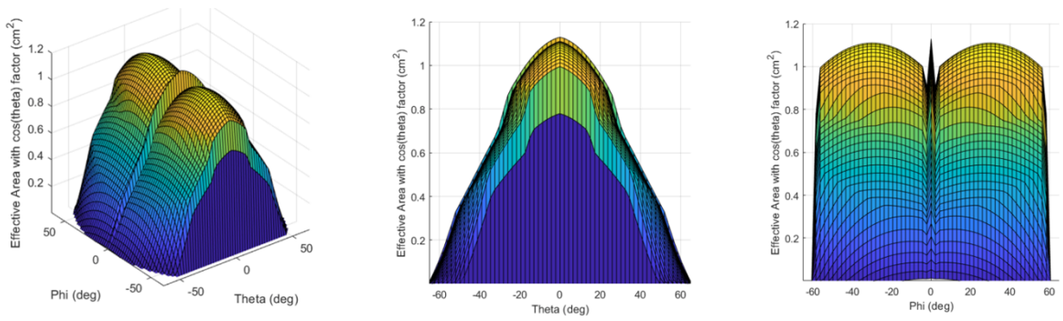


Figure 30: Effective areas derived from analytical model without mechanical obstructions.

Ultra's deflection blades effectively shadow the incoming particles since they act as physical blockages. The shadowing can be estimated based on the dimensions of the blade, which are 0.7 mm thick and spaced every 4.53°. Therefore, each blade blocks ~0.76°, which translates to a reduction in sensitivity of 16.8%. **Figure 31** illustrates the blockage of a single blade for the narrow slit as a function of ϕ (note there is no θ dependance) and s, where s is defined by the slit thickness divided by two. The modeled wide slit blockage is shown in **Figure 32**. Unlike the narrow slit, the wide slit is not full blocked by a given deflection blade. The effect on the solid angle and GF is shown in **Figure 33**, where drops in effective area along ϕ are due to the blades.

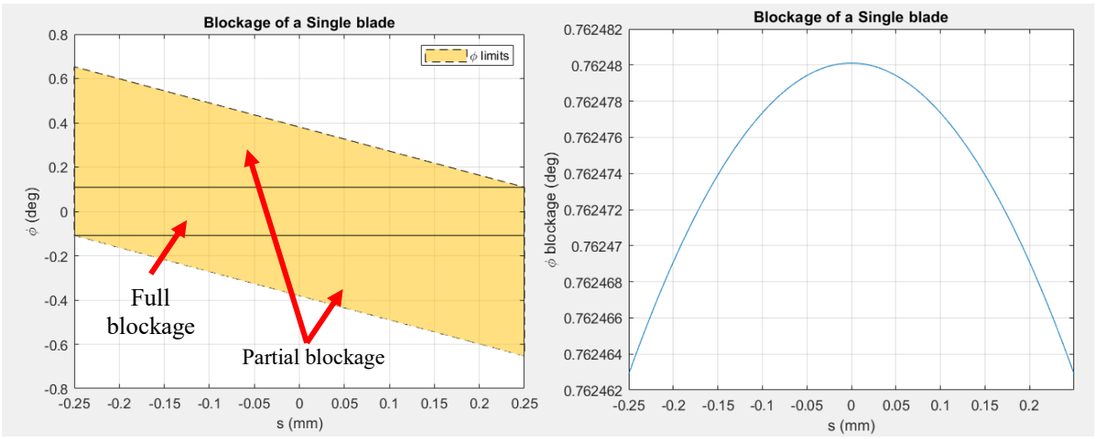


Figure 31: Blockage of a single blade for the narrow slit as a function of phi and slit half-width.

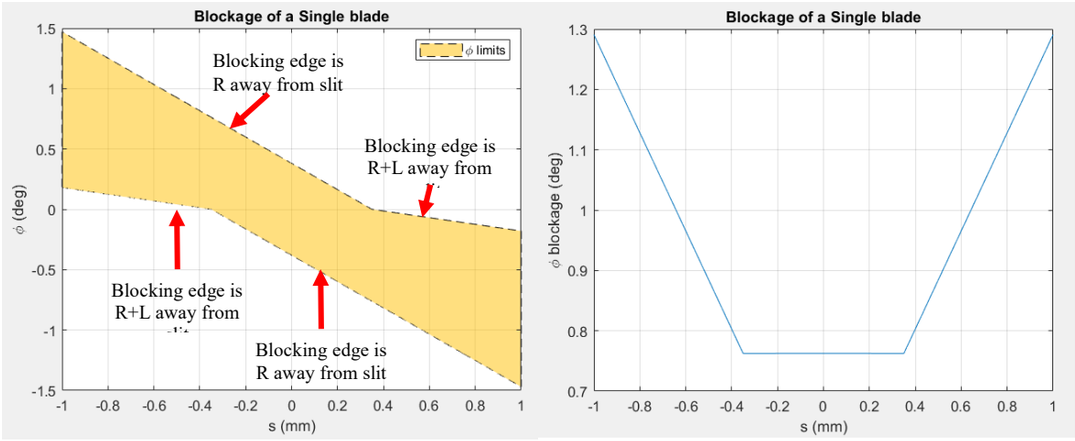


Figure 32: Blockage of a single blade for the wide slit as a function of phi and slit half-width.

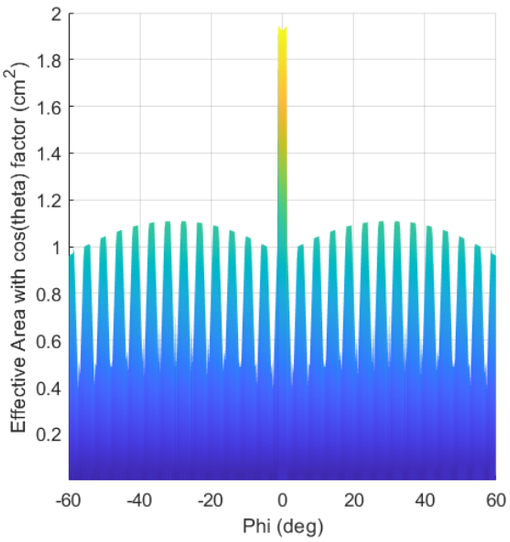


Figure 33: Effective area including blade shadowing.

Next, we consider the additional blockages due to: i) the four sets of nubs between pairs of deflection blades that are spaced out along the θ direction, ii) the aperture holder edges, and iii) the structure holding the deflection blades in place. See **Figures 34a, 34b, 34c**, respectively. By projecting the shadows of these structures onto the slit we can estimate how they reduce the G. Taking all these mechanical aspects into consideration, the analytical model suggests the total G is 0.493 cm^{2}sr for the narrow slit and 1.85 cm^{2}sr for the wide slit. Note these numbers differ from those in **Table 2** because we are not factoring in the grid transmissions (which we assume, over Ultra's required energy range, are purely geometric as well). We do this because we do not model grids in SIMION. Next, we perform particle tracing simulations to verify the analytical approach.

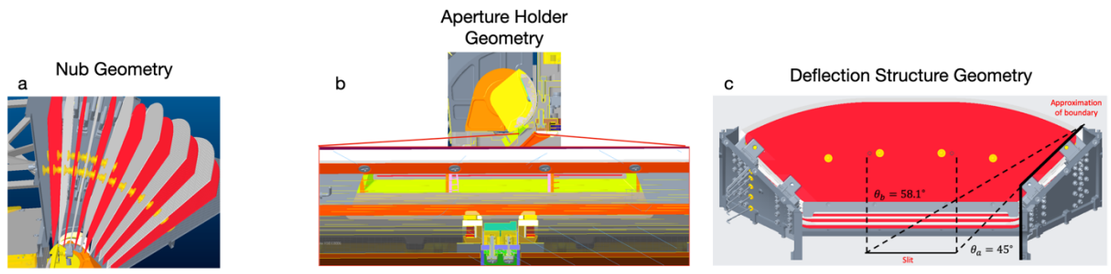


Figure 34: Geometries of nubs (panel a), aperture holder (b), and deflection structure (c)

Particle tracing simulations using SIMION. SIMION is a commonly used and experimentally validated software package used in simulating the response functions of particle instruments. The software also allows CAD models to be directly imported for simulations, therefore the simulation model includes all mechanical structures we modeled above for direct comparison (**Figure 35**). We used a two-step process to simulate the particle trajectories that would make it through the instrument unobstructed. First, we distribute particles along the full slit, carefully modeling their angular and positional distributions, and launch them in the direction of the MCP back plane and record their positions. Next, we take the particles that hit active areas of the MCP and fly them

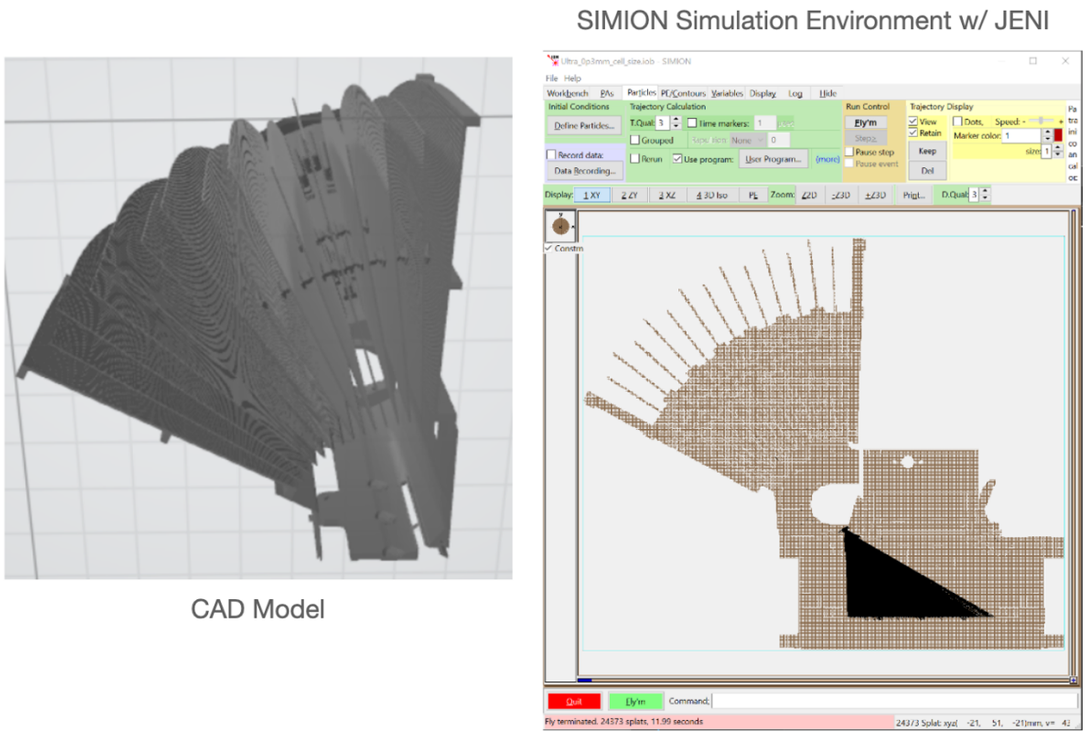


Figure 35: Cross-sectional view of Ultra's CAD model that was imported into the SIMION simulation software for modelling.

backwards tracking the ones that exit beyond the deflection blades. This subset of particles represents those that would define the active area and thus total G. The number of particles detected are binned in θ, ϕ and are normalized by the total number of particles flown in that angle-angle bin. The simulations are shown in **Figure 36** (wide slit) and **Figure 37** (narrow slit) and are compared to the analytical model. Agreement to within 1% was achieved, thus demonstrating the GF meets the measurement requirements.

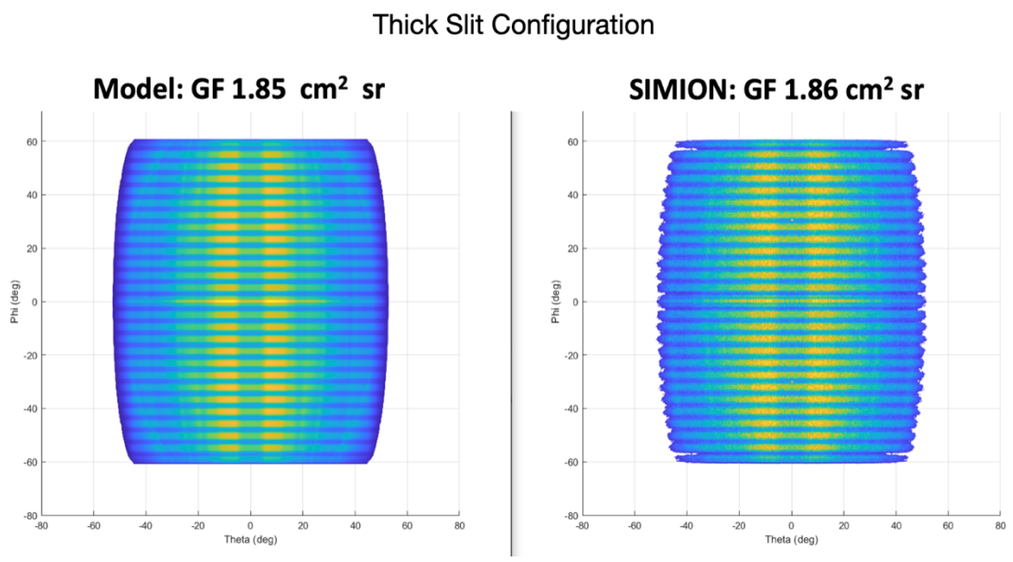


Figure 36: Comparisons of angle-angle response and total GF for model (left) and SIMION (right) for the wide slit.

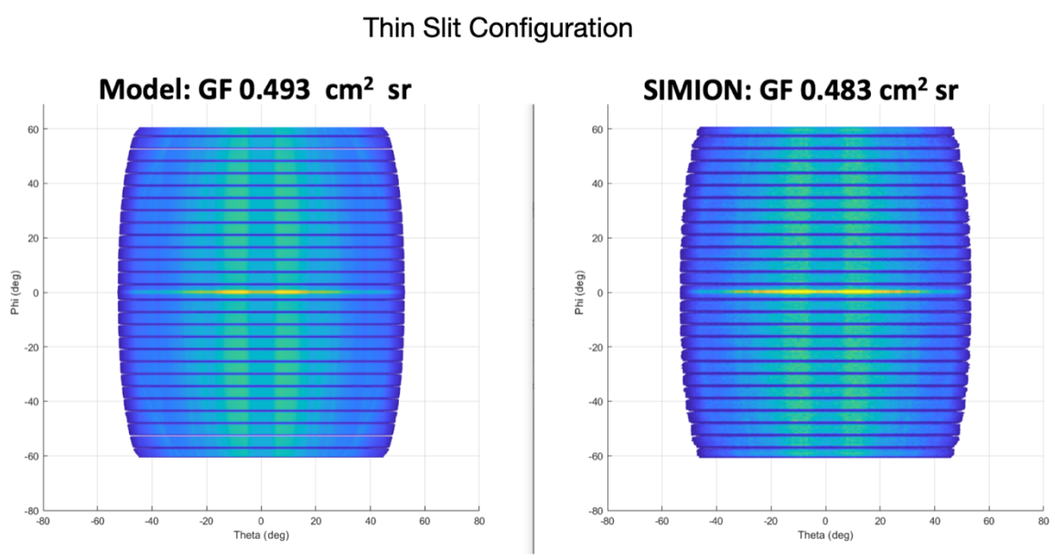


Figure 37: Same as Fig. 36, but for the narrow slit

SSD Geometric Factors. Similar methods as discussed above were used for determining the SSD GFs for different slit configurations. Ultra has 8 (6 mm × 7 mm) SSDs arranged between the two stop MCPs (along the x-coordinate). Analytical modeling of the SSDs (**Figure 38**) corresponding to a various aperture designs are captured in the **Table 2**. The table shows that the calculated GFs for SSDs meet the requirements.

Table 2: Derived SSD GF for various aperture configurations. Note that grid transmissions are not included here.

Aperture (mm)	SSD GF (cm^2sr)
1 × 3 (0.5 mm wide)	0.00193
3 × 3 (0.5 mm wide)	0.00376
7 × 4 (0.5 mm wide)	0.0119
1 × 80 (0.5 mm wide)	0.0327
1 × 80 (2.0 mm wide)	0.118

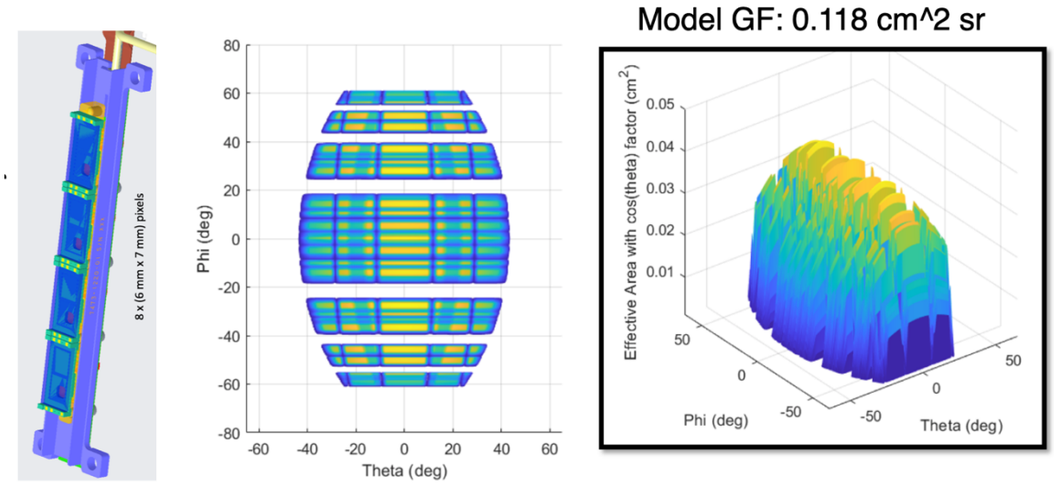


Figure 38: Ultra SSD CAD model (left), angle-angle response (middle), effective area and total GF (right).

5.6 Determining $\epsilon(E, \theta, \phi)$

Rearranging **equation X** for the efficiency, $\epsilon(E, \theta, \phi)$, and expanding the terms discussed in sections 5.1-5.5 provides us with (note that some terms divide out, which is not explicitly shown here):

$$\epsilon(E, \theta, \phi) = \frac{N_{Ultra}(E, \theta, \phi) \times cos(\theta) \times v_{translate}}{R_{ABM} \times \langle PY \rangle \times g_d(\theta, \phi) \times N \times 0.8}$$

The only new term in Eqn. X is the constant 0.8, which represents the ratio of the number particles, in the $\hat{y}$ direction, between a MCP located at the ABM and a MCP located at Ultra's slit. The 20% reduction in the number of particles per Δy bin is due to the beam divergence and remains nearly constant across the measured energies. Below we show the efficiencies as function of energy and angles. Note that the absolute values are still being tweaked, but expected relative changes are on

order ~10-20%. This is because the Ultra team is still refining small differences in the coincidence parameters to maximize the signal to noise ratio by rejecting accidentals due to UV.

Figure 39 shows the Ultra45 and Ultra90 efficiency profiles as a function of phi (different curve colors) and theta for three energies. It can be seen that the two sensors perform very similarly.

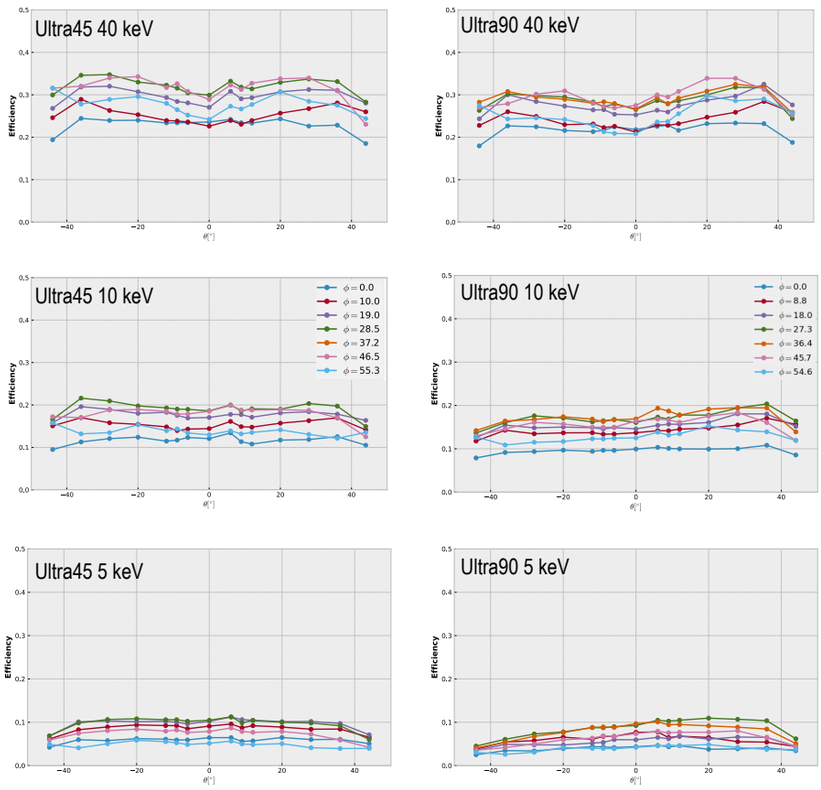


Figure 39: Ultra45 (left panels) and Ultra90 (right panels) efficiencies as a function of theta and phi angles for three energies: 40 keV (top row), 10 keV (middle row), and 5 keV (bottom row). The efficiencies were calculated based on methodology described in sections 5.1 – 5.6. The legends found associated with the 10 keV data represent the phi values used for each sensor. Note they are slightly different between Ultra45 and Ultra90.

Here we plot the efficiencies as a function of energy for combinations of theta/phi angles (**Figure 40).** Error bars represent the propagation of uncertainties associated with the various quantities discussed between sections 5.1 -5.4 (i.e., $\boldsymbol{\delta}\mathrm{N}_{\boldsymbol{U}\mathrm{ltra}}$, $\boldsymbol{\delta RABM}$, $\boldsymbol{\delta PY}$, $\boldsymbol{\delta vx}$, etc.). The magenta points depict measurements at additional energies that were only taken at $\phi = 28.5°$ and $\theta = 20°$. Those points were then scaled, based on their relative differences to adjacent energies, to the other angles. The blue curve represents an empirical fit with the functional form:

$$\varepsilon(E,\theta,\phi) = \frac{L(\theta,\phi)}{1 + e^{(-k(\theta,\phi)(E - x_o(\theta,\phi)))}}$$

where $k, x_o, and\ L$ are the free fitting parameters.

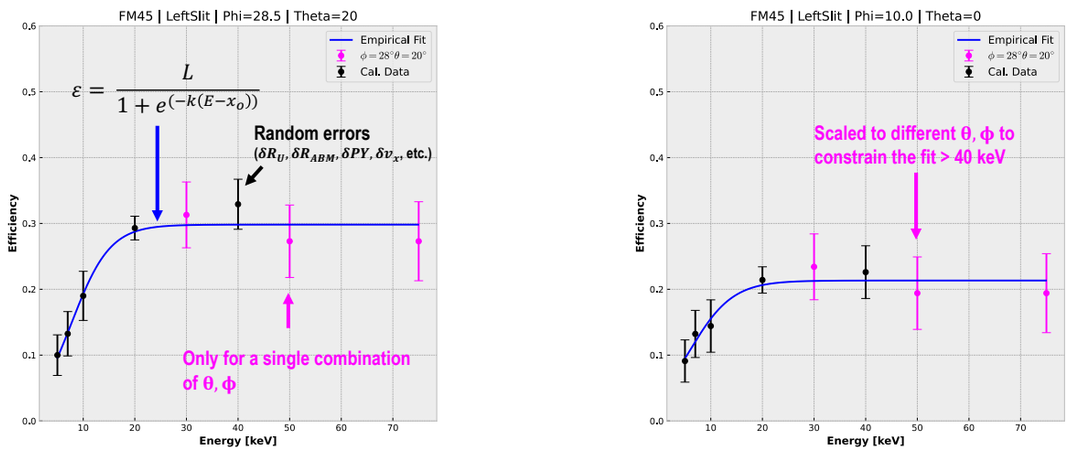


Figure 40: Efficiencies as a function of energy. These plots mainly illustrate the empirical fit that was applied to the data, therefore we just show Ultra45 at a couple different angles. The error bars represent propagation of errors associated with various measurements needed to determine an efficiency. The magenta points are discussed in the text and the solid blue curve represents the fit based on the equation shown in the left panel.

Figure 41 shows the ensemble of efficiency curves from FM45 and FM90 based on the empirical model and the derived free fitting parameters.

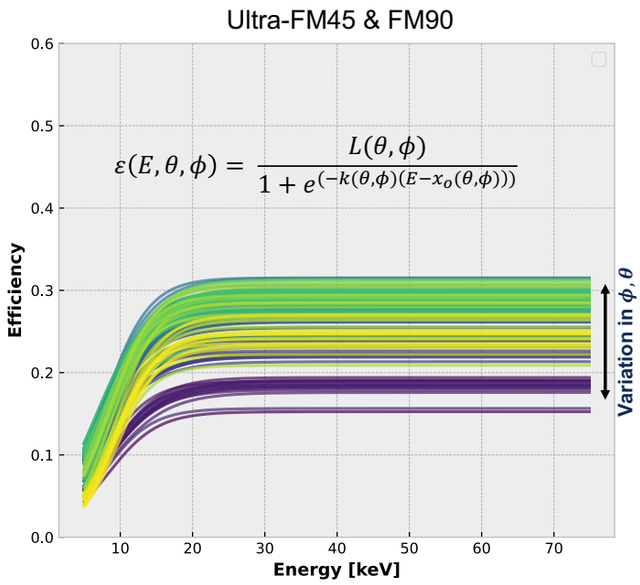


Figure 41: Ensemble of efficiency curves using the empirical fitting function and the derived fitting parameters for all angle/angle combinations.

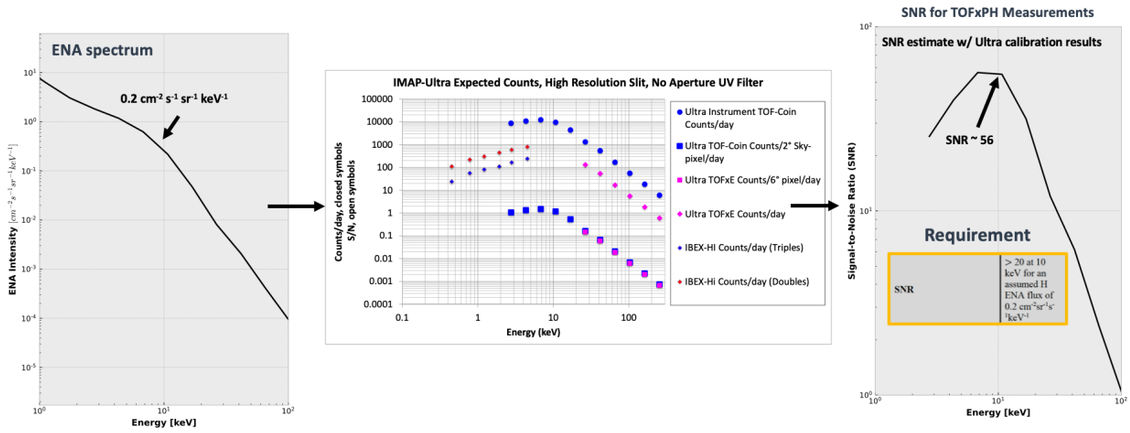
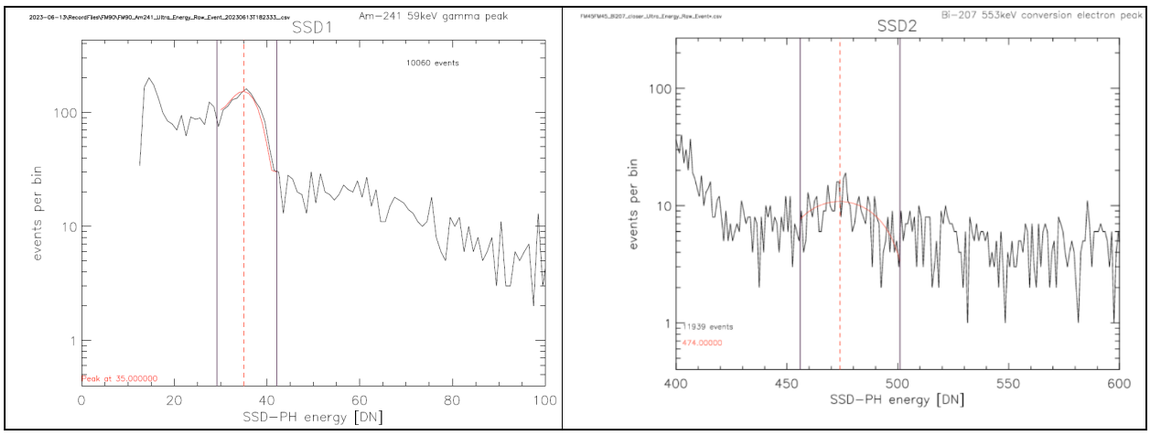


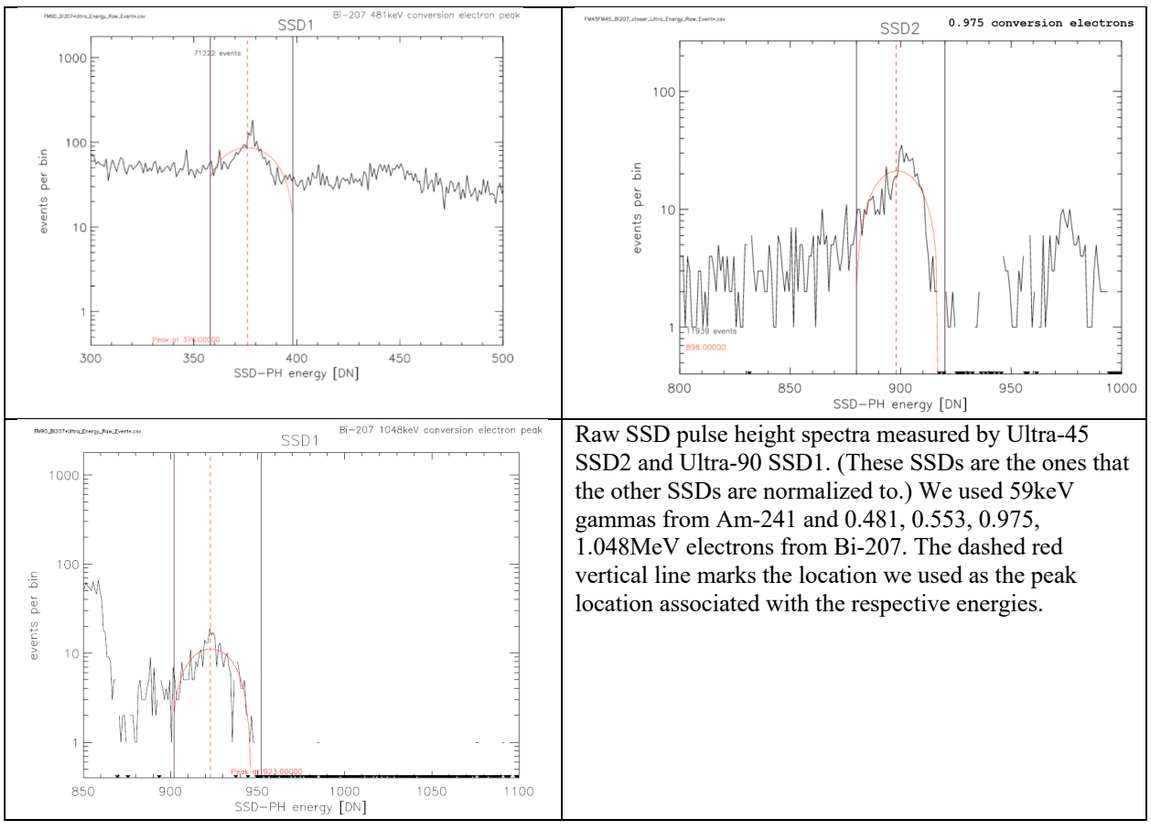
Figure 42: Updated SNR calculations using efficiencies derived from Ultra laboratory calibrations

Finally, **Figure 42** shows the updated SNR calculations, using the efficiencies derived from the Ultra Calibrations, and the ENA input spectrum showing on the left panel. ***According to the new calculations Ultra's SNR meets IMAP requirements because SNR > 20 (56) at E = 10keV for an input flux of 0.2 cm^{-2} s^{-1} sr^{-1} keV^{-1} therefore IMAP Ultra meets requirements RULTRA-1051 and RULTRA-1055.*** Ultra can also achieve favorable SNRs (≥ 6) for ENA energies out to 40 keV (required energy range).

6. SSD Calibration

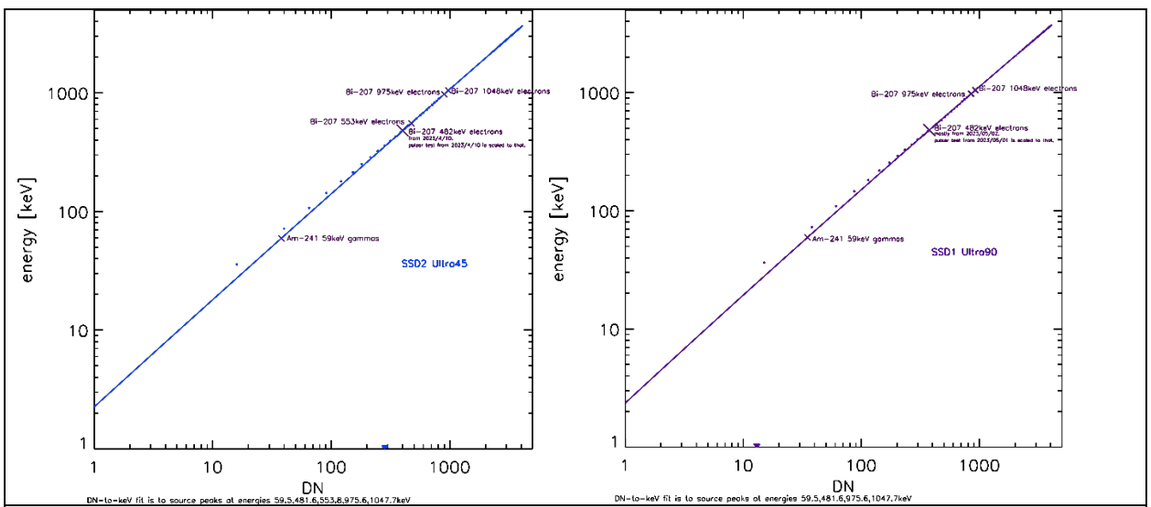
The Ultra SSD energy measurement is performed through measuring the SSD pulse height and pulse width after a particle deposits energy within one of the SSDs. The pulse information is initially provided as a raw "DN" number that through calibration needs to be associated with a physical energy. We used radioactive sources that produce particles with well-known energies to find the pulse height to energy association. Below are a few examples.





Raw SSD pulse height spectra measured by Ultra-45 SSD2 and Ultra-90 SSD1. (These SSDs are the ones that the other SSDs are normalized to.) We used 59keV gammas from Am-241 and 0.481, 0.553, 0.975, 1.048MeV electrons from Bi-207. The dashed red vertical line marks the location we used as the peak location associated with the respective energies.

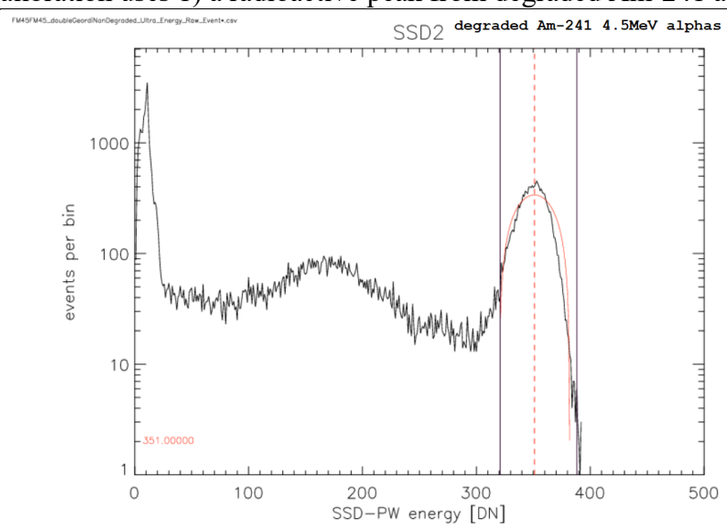
Besides radioactive sources, we also measured the Ultra-internal pulser. As the pulser is inaccurate at low energies, we ultimately did not use it.
Putting everything together yields the SSD-pulse-height to energy conversion shown below.



SSD pulse height to energy conversion for Ultra-45 SSD2 (left) and Ultra-90 SSD1 (right). Each labeled cross represents the location of a radioactive peak in DN (as shown above) on the horizontal axis, associated with the

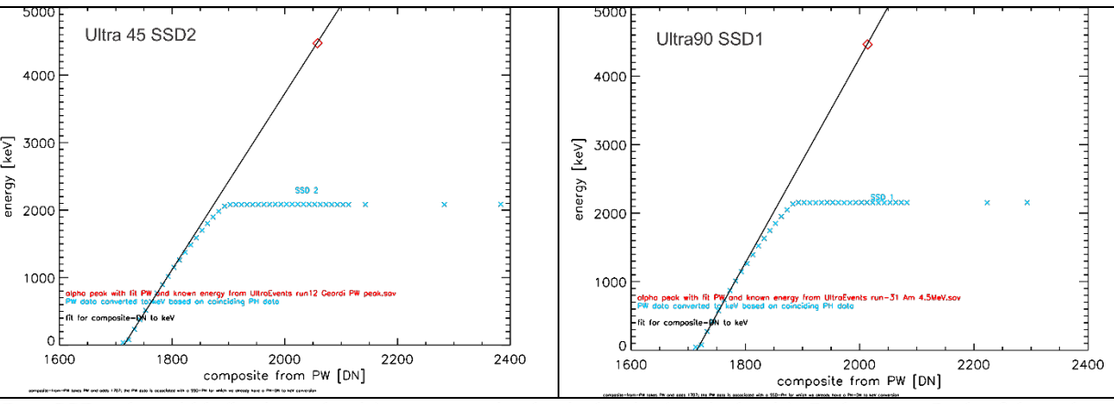
known energy of that peak on the vertical axis. Small symbols are pulser values, scaled to the 0.975MeV peak. The solid curve is the calibration fit.

The text above explained the calibration of the SSD pulse height. That pulse height saturates for particles around 2MeV, so that we need to use the SSD pulse width instead. The pulse width calibration uses 1) a radioactive peak from degraded Am-241 at the highest energies, see below.



Raw SSD pulse width spectrum measured by Ultra-45 SSD2. We used the 4.5MeV alphas of degraded Am-241. The dashed red vertical line marks the location we used as the peak location associated with the respective energy.

2) For the lower energies, we use the fact that degraded Am-241 also produces a broad distribution of lower energy alpha particles. At sufficiently low energies, both pulse height and width are valid. Because we know how to calibrate the pulse height, we automatically know how to calibrate the pulse width.
Putting 1) and 2) together yields the SSD pulse width to energy calibration shown below.



Raw SSD pulse width (horizontal axis) vs. energy in physical units (vertical axis). Red square: Peak of the pulse width distribution of degraded Am-241 vs. the known energy of that peak. Blue crosses: Calibrated pulse height (vertical axis) of degraded Am-241 alpha particles vs. their associated raw pulse width. It can be seen that the pulse height saturates at ~2MeV, from which point on the values become meaningless. Black curve: Calibration fit used for pulse width.

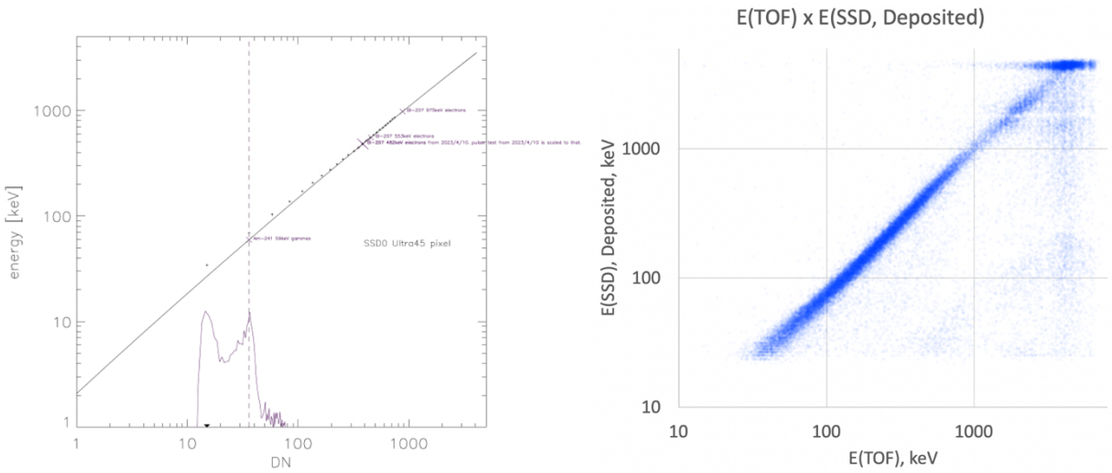


Figure 43: (Left) DN vs energy using energy peaks for Bi-207 0.975 MeV electrons, Bi-207 553 keV electrons, Bi-207 482 keV electrons, Am-241 59 keV gammas and pulser data. (Right) Deposited energy to SSD detector using degraded Am-241 sources vs energy calculated by the TOF.

7. Environmental Calibration Activities

Environmental testing consisted of a series of vibration and thermal cycling tests to ensure Ultra could survive launch and the thermal environment of space with no degradation to its performance. The vibration tests were conducted first and included sine and random frequency testing. Details regarding the specific profiles used can be found in other documents, but in short, the sine testing covered 27 g peak perpendicular, 18 g peak parallel, over a 5-100 Hz frequency range. Random testing was comprised of 14.1 grms GEVS and used force washers for response limiting. Thermal testing consisted of a thermal balance test used for instrument bakeout, heater power verification, and long duration thermal balances. Thermal cycling consisted of a long bakeout with six thermal cycles ranging from -45°C cold plateaus to +45°C hot plateaus. **Figure 44** depicts the test set up for vibration (left panel) and thermal (right panel). Anomalies were observed with both the vibration and thermal testing. These anomalies were documented in detail for the NASA review

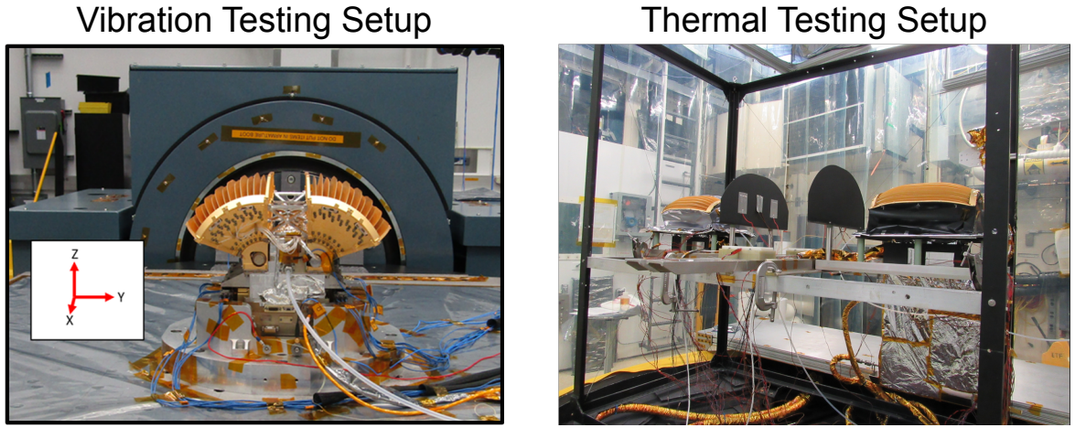


Figure 44: Pictures of Ultra's vibration test set up (left panel) and thermal test set up.

board, but we will provide a high-level summary here. First we will briefly discuss the acceleration grid failure realized during vibration testing then we will discuss observed temperature dependencies on the start distributions, which are key in determining the particles trajectory. Finally, in the later sections we will show comparisons of pre- and post-environmental testing as well our efforts in cross calibrating the two Ultra sensors.

7.1 FM90 vibration failure

The Ultra FM90 unit failed its vacuum function checkout post vibration testing. Specifically, it failed to reach high voltage indicating a short was present. Upon inspection of the FM90 sensor, it was realized that the acceleration grid, responsible for maintaining a 2 kV bias for steering start electrons, delaminated from its nickel frame and shorted (**Figure 45**). This failure necessitated additional component vibration tests of the original acceleration grid structure and a couple variants that included extra stiffening struts along the trapezoidal opening (see Figure 2) to reduce deformations in the frame that likely caused the failure. After analyzing the results of the standalone grid assembly testing and modeling the impact to the electron optics due to additional struts modifying the electric potentials, it was decided to go with the so-called two strut design. Figure 3 illustrates the difference between the baseline and final designs. The addition of the two struts were tucked away just at the edge of the grid opening and had virtually no impact to the electron optics.

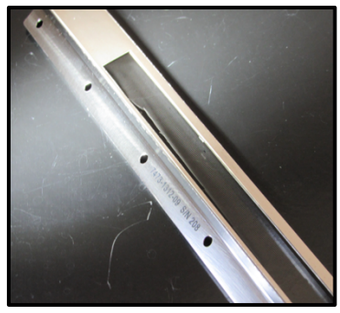


Figure 45: FM90 grid assembly illustrating separation along the edge of the frame.

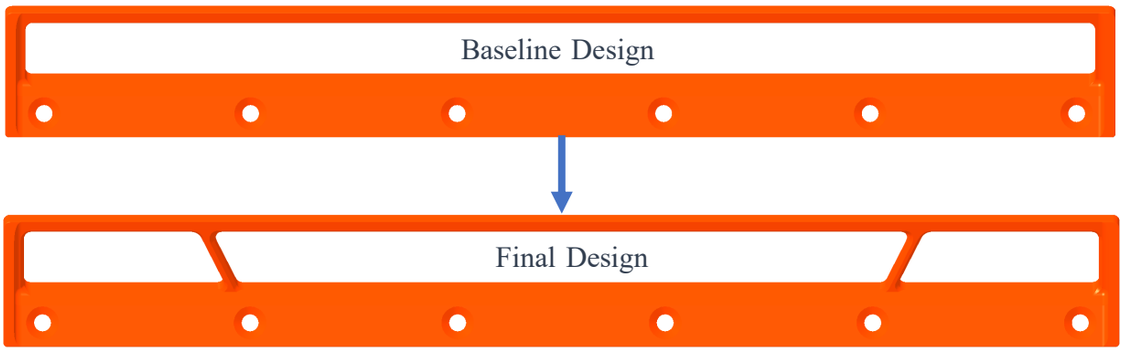


Figure 46: Cartoon showing the difference between the baseline and final grid assembly designs that were necessitated after a failure was realized from vibration testing.

7.2 Thermal testing anomaly

During thermal cycling, Ultra was occasionally fully powered and its aperture was configured in the radioactive source position. This allowed the performance of Ultra to be monitored as a function of temperature. It was observed that the start distributions (the locations of particle starts along the x-dimension of the slit determined from timing pulses) appeared to become skewed at the lower temperatures. **Figure 47** illustrates this effect. The bottom most panels in Fig. 4 highlight, with red boxes, the nominal start distributions which exhibit a fairly flat response with diminutions occurring at locations corresponding to physical structures in the foil holder. At the lower temperatures (for an extreme example look at the top panels), the diminutions are no longer

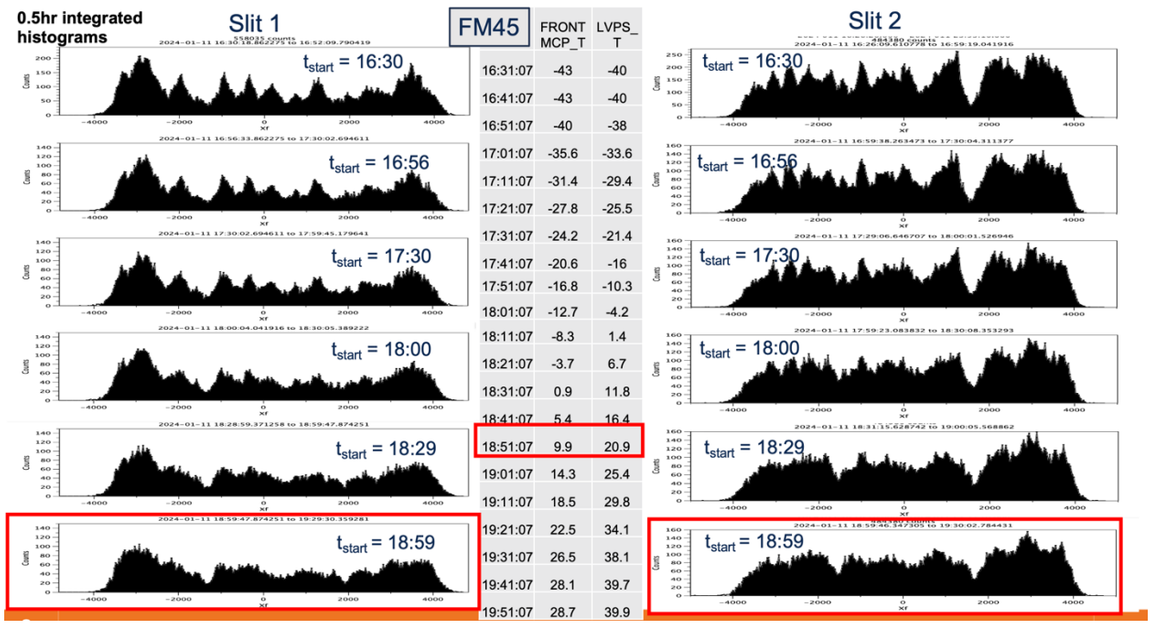


Figure 47: Ultra FM45 start distributions for slit 1 (left) and slit 2 (right) during thermal testing. The distributions were accumulated over ~30 min intervals. The red box around the bottom panels highlights nominal looking start distributions, but then progressively become more distorted as the temperatures decreased (going toward the top panel or decreasing start times). The data in the middle show the times and corresponding front MCP and LVPS temperatures at various times.

present and the relatively flat response now has a series of peaks and valleys that are likely forming due to the mismatch of real locations. Note that nothing else, except the temperature, has changed during this time period. Because the start positions are needed to calculate the theta angle, it was soon realized that this may have a negative impact to Ultra's angular resolution measurement requirements.

After environmental testing, Ultra was installed into the accelerator chamber for post-environmental checkout with an emphasis on exploring the start distribution anomaly. The chamber is outfitted with a thermal shroud that can cool the instrument ~ -10°C, which is ~35°C warmer than achievable in the

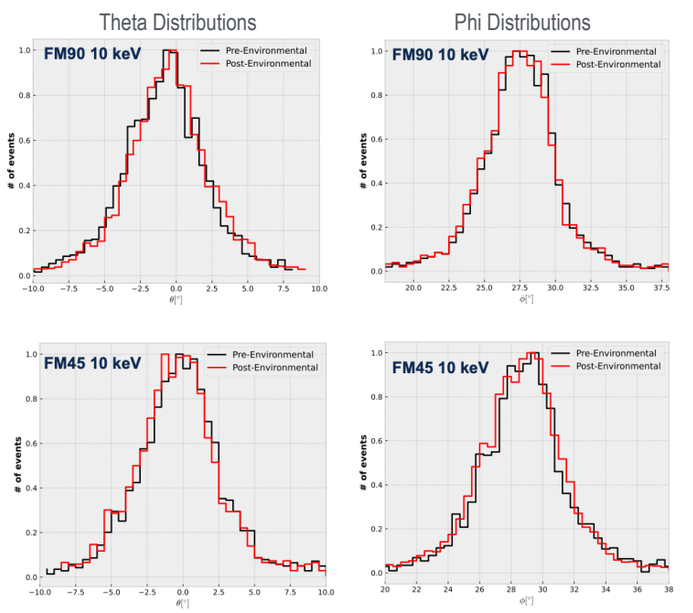


Figure 48: FM90 (top row) and FM45 (bottom row) theta and phi angular distributions at 10 keV. Black and red curves represent data taken before and after, respectively, environmental testing.

thermal chamber, but still cold enough to explore the effect. First it was important to establish that the anomaly was due to temperature and not due to a part failure or design flaw. The θ, ϕ angular distributions at room temperature compare extremely well between pre- and post-environmental, instilling confidence that the performance is unchanged (See **Figure 48).** Then we cooled Ultra and performed beam testing at a multiple temperatures, angles, and energies. The results are shown in **Figure 49**. As suspected, the FWHM of the theta distributions appear to degrade with decreasing temperature. And importantly, the extrapolation of angular resolution suggest that Ultra no longer meets its 10 keV angular requirements near (for Ultra45) and below (for Ultra90) -20°C. As currently planned the operational temperature of Ultra is near -20°C; however, a thermal analysis was performed and the results suggest that the survival heaters can be duty cycled to achieve a warm thermal balance resulting in no degradation of the angular resolution. The IMAP project has tentatively agreed to flight rule.

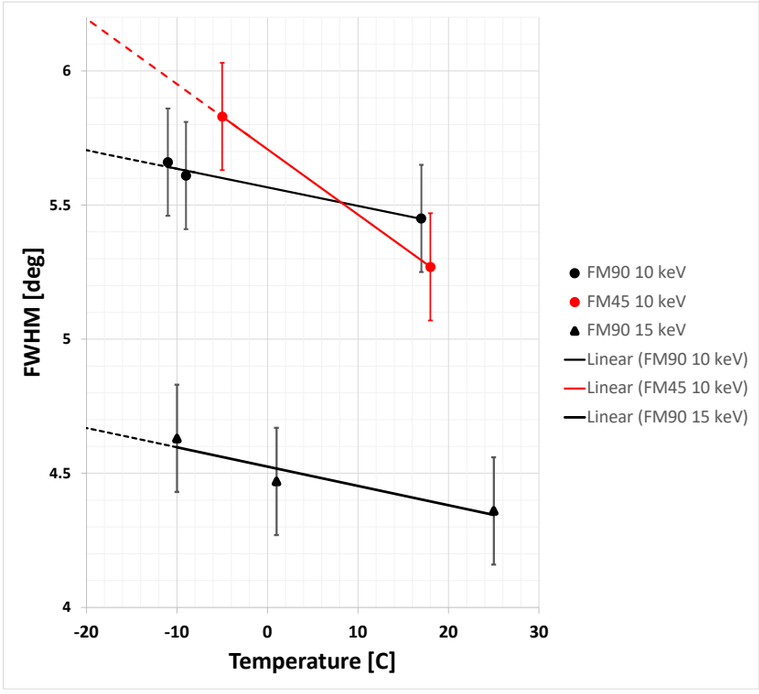


Figure 49: FWHMs of the theta distributions as a function of temperature for FM90 (black curves) and FM45 (red). Solid lines represent purely linear fits to the data with the dashed portions explicitly highlight the extrapolation region.

Figure 48 illustrated that the angular distributions before and after environmental testing remained unchanged a room temperature, but here we also show the time of flight (TOF) distributions and the measured efficiencies at different angles. Measured TOF distributions for a 10 keV proton beam are shown in **Figure 50** and it can be seen that the TOF system remained unchanged.

The pre- and post-environmental efficiencies are shown in **Figure 51**. The curves represent the angle-dependent efficiencies as discussed in section 5, and the red circles represent the post-environmental beam tests at the following θ-angles: -20°, 0°, and +20°. The absolute values compare extremely well. For these to agree requires a multiplicity of processes to remain unchanged, such as: the TOFxPH system, spatial and timing coincidence logic, losses due to mechanical obstructions and interactions with foils, etc.

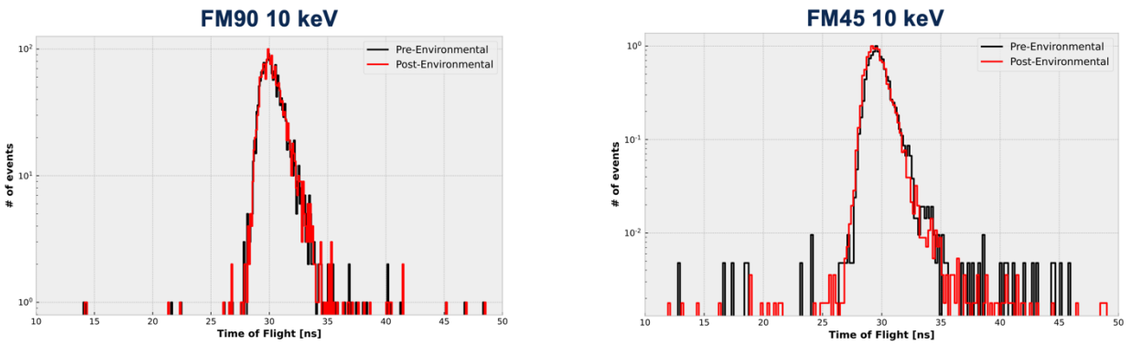


Figure 50: FM90 (left) and FM45 (right) measured time of flight distributions for a 10 keV proton beam. Black and red curves represent data taken before and after, respectively, environmental testing.

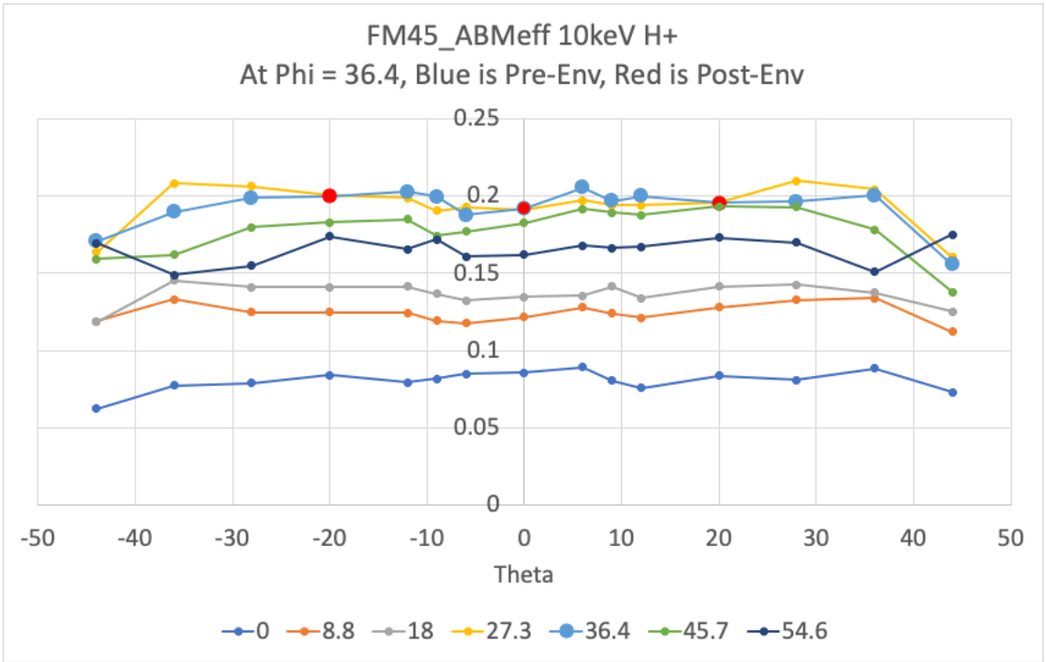


Figure 51: Efficiency comparisons before (solid curves) and after (red circles) environmental testing. Data represents FM45 measurements of a 10 keV proton beam.

8. Cross Calibration between Ultra-90 and Ultra-45

Although the two Ultra sensors were calibrated independently and the results suggest they compare very well, we wanted to perform a test at an uncharacterized energy and to see how well the two sensors estimated the incident beam flux. This test demonstrated the fidelity of the empirical fits in capturing the energy and angle dependent efficiencies. In this case, the proton energy was set to 15 keV. This energy was chosen because it is both within the measurement requirement range and happens to be where the response function is changing relatively rapidly and therefore, is a gauge of how well we can interpolate. **Figure 52 left panel** shows where on the efficiency curve 15 keV is located and the value picked based on the interpolation of our fitting function. **Figure 52 right panel** shows derived ABM rate (the ABM rate was calculated by inverting the efficiency equation in section 5). The black circles in Fig. 8 right panel represent the calculated rates and the red points are the rates from the actual ABM. ***Both sensors performed well and were able to come to within ~10% relative accuracy (between Ultra45 and 90) and absolute accuracy of each sensor with respect to the measured ABM rate within 25%. Therefore Ultra meets requirements RULTRA-1540; -1541.*** This test also served as a proof of concept for the cross-calibration tests that will happen between IMAP-Ultra and IMAP-Hi using a very similar technique, but at the Los Alamos National Laboratory facility.

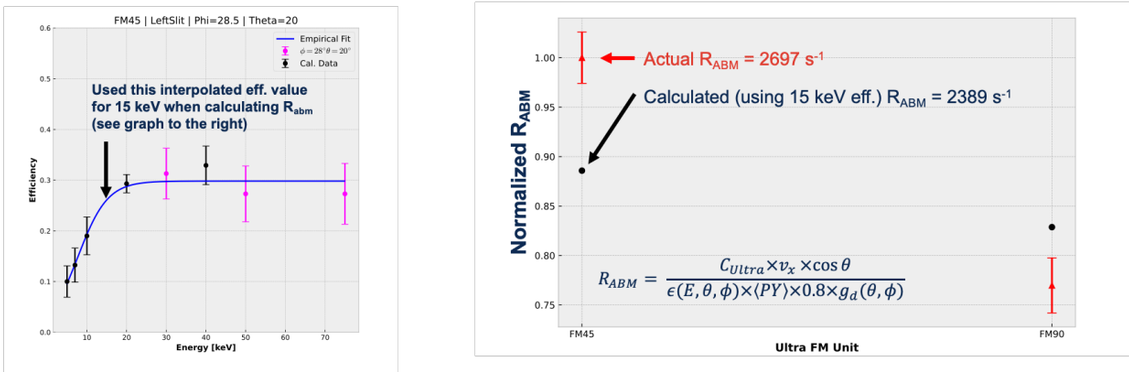


Figure 52: Results of the cross calibration test. The 15 keV efficiency point used based on interpolation (left panel) and the derived ABM rates from the Ultra sensors (right panel). The rates were normalized to 1 such that relative changes between the units and derived/measured rates can be easily interpreted.

9. Efficiency of Deflection Blade Assembly

Tests were performed with the Ultra EM in order to i) assess forward scattering of particles from the deflection blades and ii) assess the efficiency of the deflection blade assembly in deflecting the charged particles.

Test setup: We're shooting 100 keV beam (mix of ions and neutrals) on the blade using 0V on the HV plates. Gradually increase the voltage (rump up every 32 V) and see only the ions (bent by the field) registering hits into the sensor and then disappear again when the HV reaches high enough levels. Note that the VE at the beginning of the test are because part of them beam is getting into the sensor (not all of it is falling on the blades). That is not the case at the end of the run, when all the ions are falling onto the blade and no VE are observed, proving that there are no forward

scattered particles into the sensor. Nonetheless, we also conduct an experiment for longer time described below.

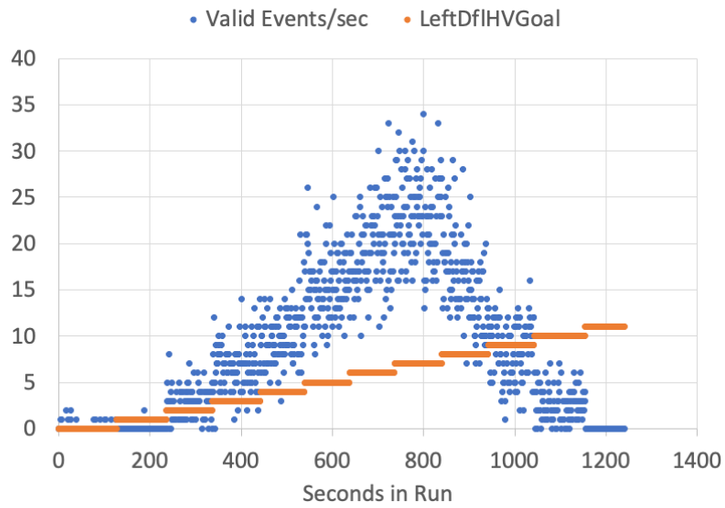


Figure 53: Valid events registering in the Ultra sensor while the HV on the Left Deflection Assembly is being increased.

Test setup: we're shoot 100 keV proton beam on the blade using 320V on the HV plates (way below the operational levels)

- set up a geometry for which the 100keV proton beam made it through into the slit at somewhat lower deflection voltages, and then hit the deflection blade near the bottom of the blade at somewhat higher deflection. This location and geometry was intended to produce a worst-case condition for generating forward scattered ions or neutrals off the blade serration points, and subsequent entry through the slit. The test was successful in that, for this "worst-case" geometry and rather low deflection voltage, we nevertheless saw almost no events.
- In flight, with much higher deflection voltages on the blades, we expect to get similar performance up to ~300keV/e.

The rate of about 190 valid events in a 14 second spin, so that is about 14 events/second. Shooting the beam on the blade for 1.5 hour, we got 2 valid events with positive TOFs (most of the 49 events recorded had negative TOFs, thus rejected by logic). Of those two events, one had a TOF that was about right for the 100keV protons, the other had a TOF that would be for a 37keV proton. So conceivably, we got two events in 5400 seconds, or 0.00037 events/second. So the ratio foreground/deflection is $0.00037/14 = 2.6*10^{-5}$.

10. IMAP-Ultra & -Hi Cross-Calibration Activity

IMAP-Ultra and -Hi instruments will be cross-calibrated at the Los Alamos National Lab facility using a neutral beam (see **Figure 54** for test setup CAD model). The measurements will occur over three overlapping energy channels, one common look direction and one particular entrance location. Hi has an energy of 0.5 – 10 keV with an energy resolution of 45%. Ultra's energy range spans 5 – 40 keV with an energy resolution requirement of less than 70%, but intrinsic energy resolution ranging from a few % up to ~25%. A cross calibration working group (led by IMAP

deputy project scientist Drew Turner) has developed the following requirements for the cross-calibration activity:

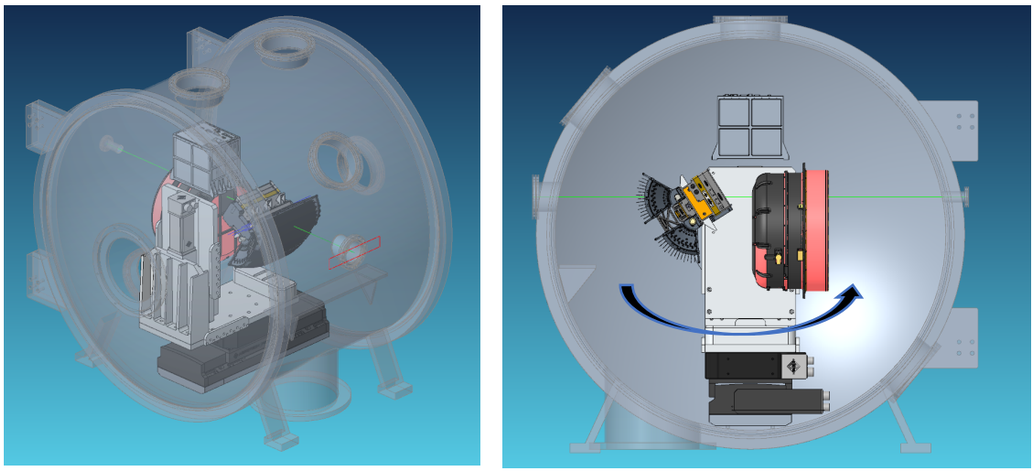


Figure 54: CAD model of IMAP-Ultra and -Hi cross-calibration test setup in the LANL vacuum chamber.

1. IMAP-Ultra shall be cross-calibrated with IMAP-Hi prior to spacecraft integration using a beam of neutral hydrogen at no less than three energies between 5 keV and 13 keV in the overlapping energy range between the instruments. Specifically, we will target the IMAP-Hi central passband energies of: 5.6 keV, 8.4 keV, and 12.7 keV. Tests will occur ~~over~~ at ~~least~~ the boresight look-direction for IMAP-Hi and a single corresponding look-direction for IMAP-Ultra.
2. IMAP instrument cross-calibrations for each pair of instruments (IMAP-Lo and -Hi and IMAP-Hi and -Ultra) shall be performed at approximately the same time (within the interval required for rotating each instrument into the beam), in the same facilities, with representatives from both respective instrument teams present for the calibration tests.
3. Relative accuracy requirement for IMAP X-Cal: Each pair of IMAP instruments with overlapping energy ranges shall have relative accuracy of ≤ 25% on a pre-determined set of overlapping energy channels for neutrals incident down the boresight, after calibration factors are applied
4. Absolute accuracy requirement for IMAP X-Cal: Each IMAP ENA instrument shall have absolute accuracy of ≤ 10%, after calibration factors are applied, compared to a laboratory calibration source consisting of a collimated beam of single-species, monoenergetic neutrals
5. Calibration beam requirement, species: The calibration beam shall consist of neutral hydrogen atoms
6. Calibration beam requirement, flux uncertainty: The flux of the calibration beam for IMAP X-Cal shall be monitored and known to an accuracy within ±10%
7. Calibration beam requirement, energy resolution: The calibration beam shall be monoenergetic to within ±TBD eV (several eV is just fine for Ultra) of any particular energy set point over the functional range used for testing

8. Calibration beam requirement, collimation: The calibration beam shall be collimated to within ~1° degrees spread in neutral incidence angle

Note: Discussions are ongoing and some details will change. Updates will be included here to guide the cross-calibration plan between IMAP-Ultra and -Hi.

11. Simulations of predicted Ultra Maps.

To estimate the quality of ENA flux and spatial resolution for regions of the sky, we have developed a forward simulation that incorporates predicted spacecraft ephemeris and attitude, Poisson distributed counts based on a given input flux, and modelled the instrument response for Ultra 90 and Ultra 45.

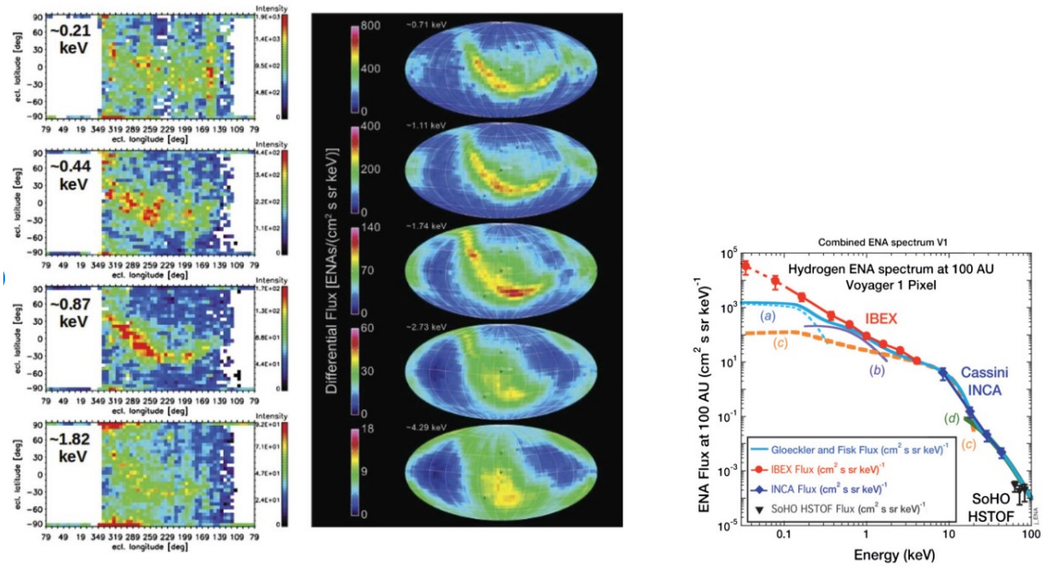


Figure 55: (left) IBEX-Lo and IBEX-Hi flux maps. (right) Power laws used to estimate energy dependent Fluxes. Ref: https://www.researchgate.net/publication/360794704_The_Heliosphere_and_Local_Interstellar_Medium_from_Neutral_Atom_Observations_at_Energies_Below_10_keV

A representative input flux was selected by examining historical IBEX flux maps and then scaling based on the combined observed IBEX and Cassini INCA power laws (see **Figure 55**). 3 data points were selected: J = 1000, 650, and 250 counts / (s cm2 sr keV) to represent a high, medium, and low flux value at approximately 0.71keV. The values selected were then placed in an IMAP logo heliospheric flux map (**Figure 56**) and the input flux scaled accordingly by energy assuming the power law as:

$$J = AE^{\gamma}$$

Slope (γ) values used were $\gamma_{IBEX} = -1.7, \gamma_{INCA} = -3.3$. The IMAP logo input allows for quick comparison of flux map reconstruction both spatially (map pixels in correct place) and numerically (predicted flux is the right value). The IMAP logo input flux pictured in Figure 56 shows the

scaled flux values at ~4.4 keV, which is within the energy range that IMAP-Hi covers. We can use the overlapping energy channels to assess performance of IMAP-Hi vs IMAP-Ultra.

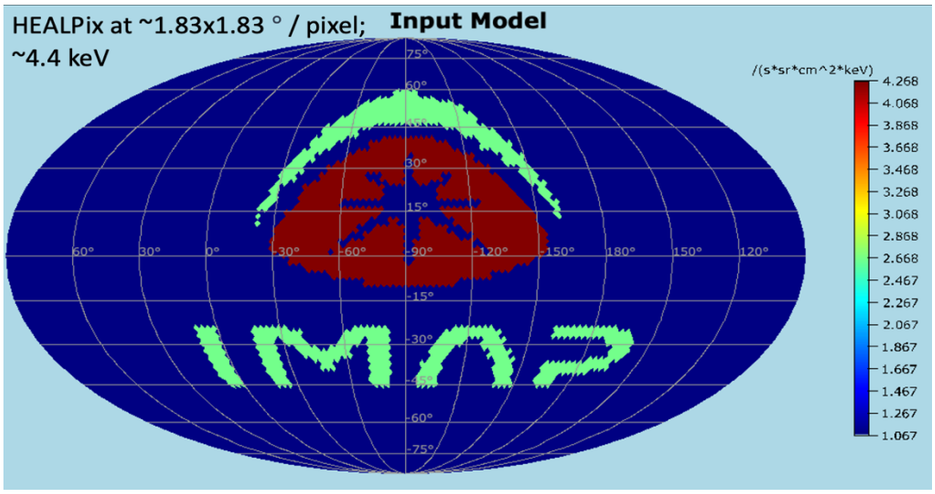


Figure 56. Input flux at 4.4 keV. Ecliptic Inertial J2000 reference frame with HEALPix Tessellation.

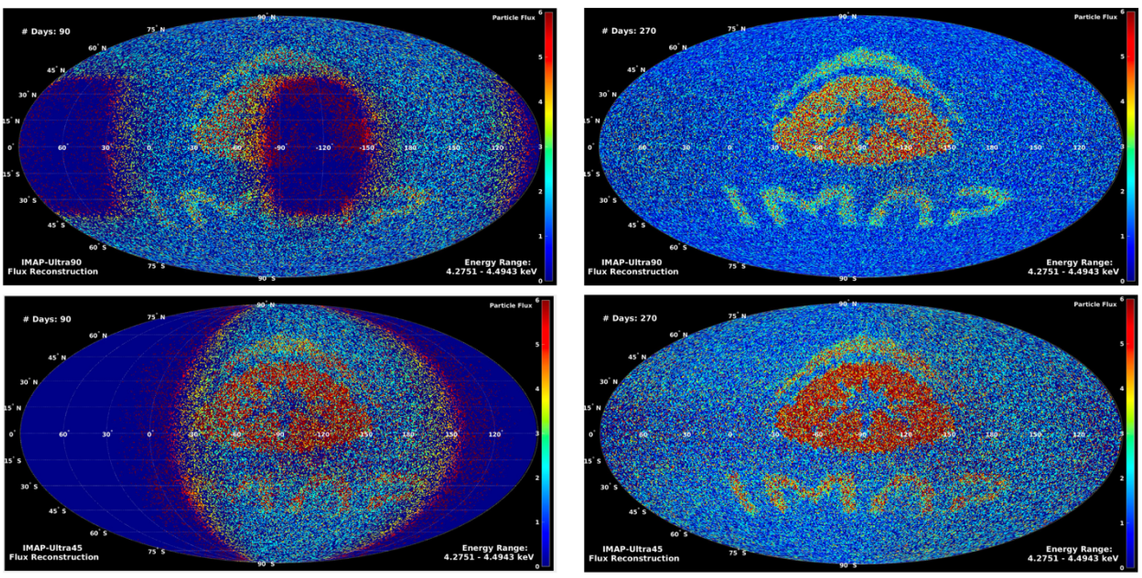


Figure 57: Flux reconstruction from simulated Ultra 90 and 45 maps for the first 90 and 270 days of the mission

In Figure 57 we show integrated maps over the 90 and 270 first days of the mission, and we see that Ultra meets its requirement to cover at least 25% of the sky every 90 days (RULTRA-1058) and having integrated observation time greater than or equal to 270 days over a 2 year period (RULTRA-1050; RULTRA-1057), since we can create a full map over 270 days within the first year. It should be noted that these maps did not include scattering due to the foils.

3.8.3 In-Flight Calibrations

IMAP-Ultra in-flight calibration report embedded below

Ultra Performance Review During Pre-Phase E Activities

HV ramp up: MCP detectors and deflection assemblies

Both U45 and U90 sensors performed nominally during their initial turn on and HV ramp up on the MCP and deflection assemblies. Figures 1 (U45) and 2 (U90) depict the HV ramp up profiles and start rates generated from UV striking the front foil and creating electrons that are measured by the front MCP.

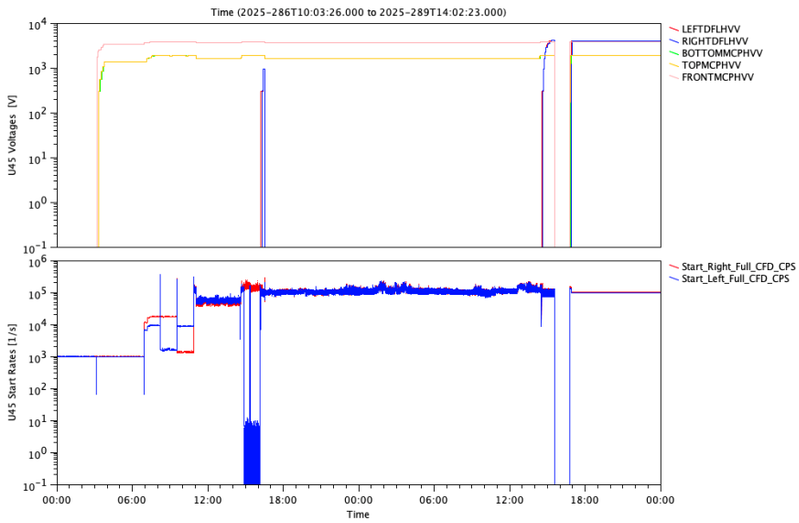


Figure 1: U45 MCP (i.e., bottom, top, right) and left/right deflection voltages during 0.003 and 0.006 activities. Voltages and rates due to UV starts are nominal.

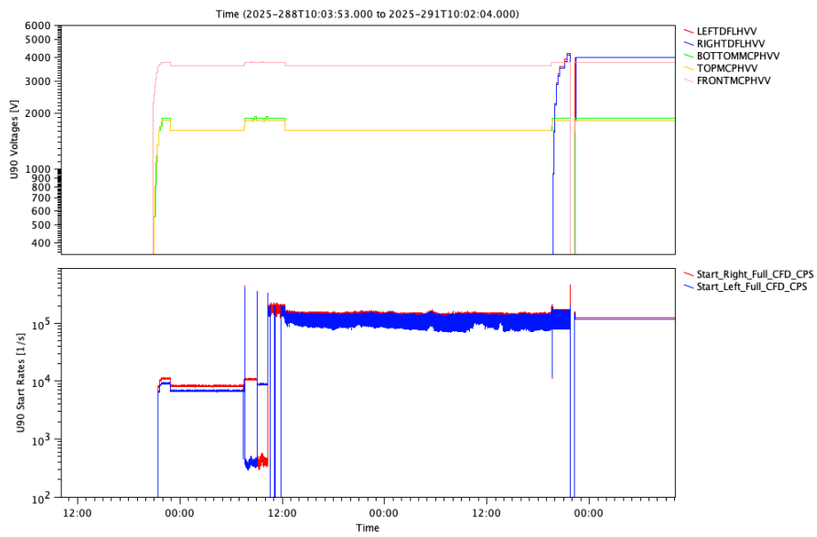


Figure 2: U90 MCP (i.e., bottom, top, right) and left/right deflection voltages during 0.003 and 0.006 activities. Voltages and rates due to UV starts are nominal.

Pre- and post-launch performance comparisons

Both the U45 and U90 sensors have their own internal calibration sources which is comprised of Am-241 radioactive material. During ground calibrations, measurements such as coincidence rates, time-of-flight (TOF) and positional distributions were acquired with the intention for diagnosing changes to in-flight performance. Below is a non-exhaustive showcasing of figures illustrating pre- and post-launch performances. Differences in total counts is because the integration times between the ground calibration test and in-flight data are different. In summary, both sensors compare remarkably well to ground calibrations that suggest the performance is unchanged during launch and commissioning.

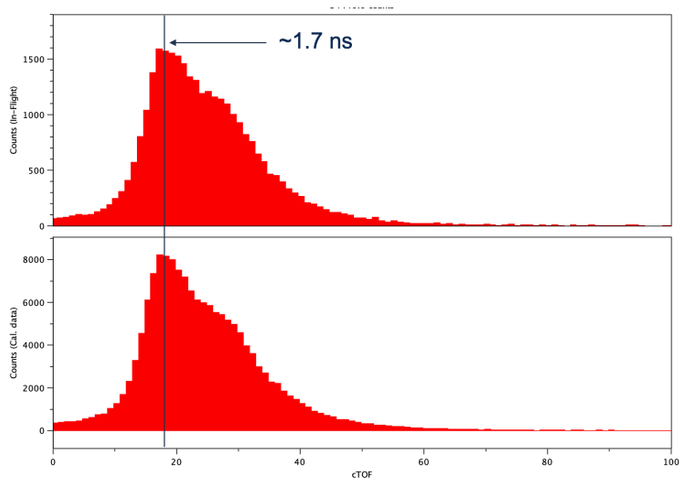


Figure 3: U45 TOF distributions of the calibration source. In-flight data in the top panel, ground calibration data in the bottom panel.

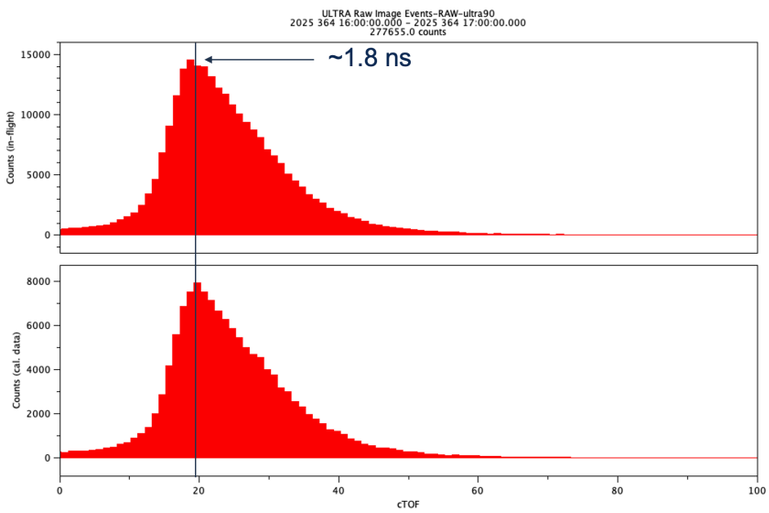


Figure 4: same format as Fig. 3 except for U90.

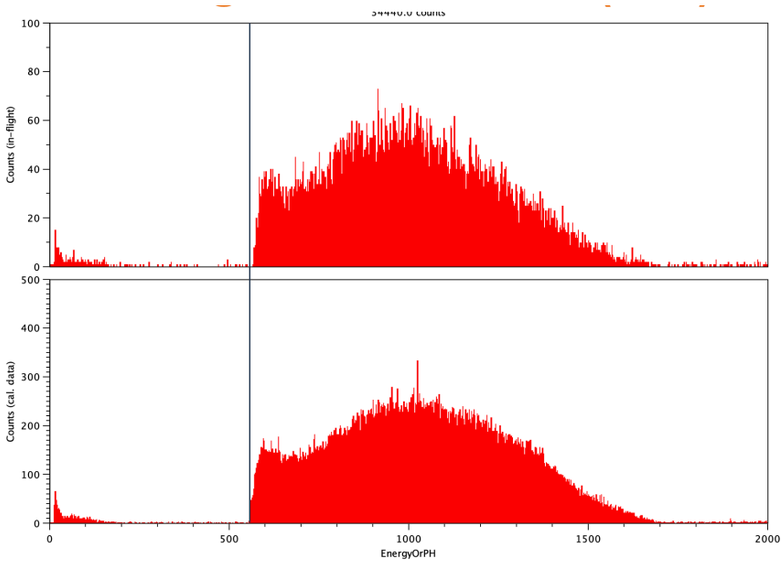


Figure 5: U45 MCP pulse height (PH) distributions of the Am-241 internal calibration source. In-flight data in top panel, ground calibration data in bottom panel. Vertical line is to guide the eye.

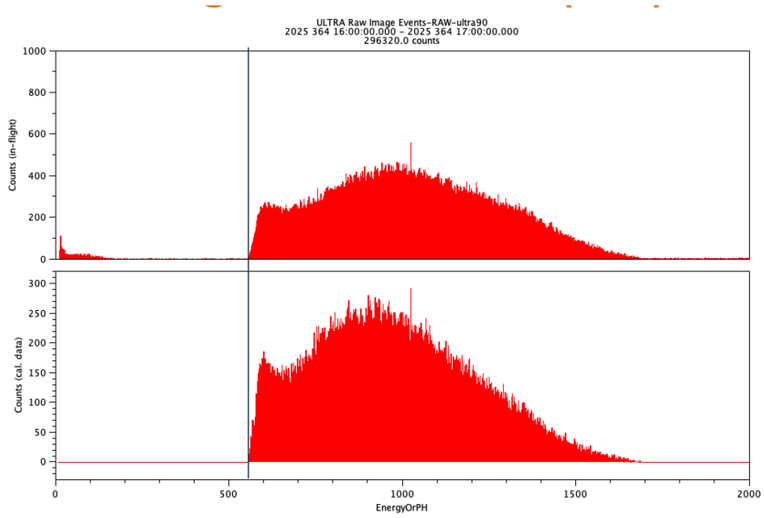


Figure 6: same format as Fig. 3 except for U90

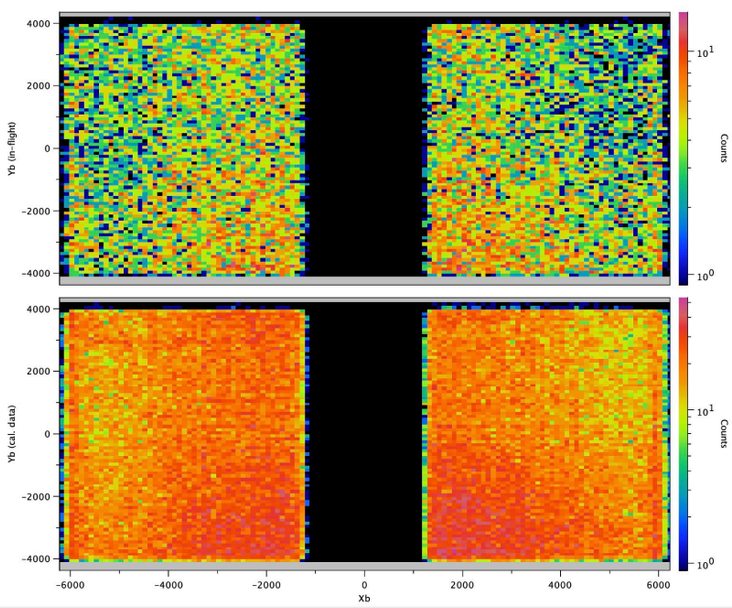


Figure 7: U45 MCP positional distributions (Y vs. X in instrument coordinates) stimulated by the internal calibration source. In-flight data on top, ground calibrations on bottom.

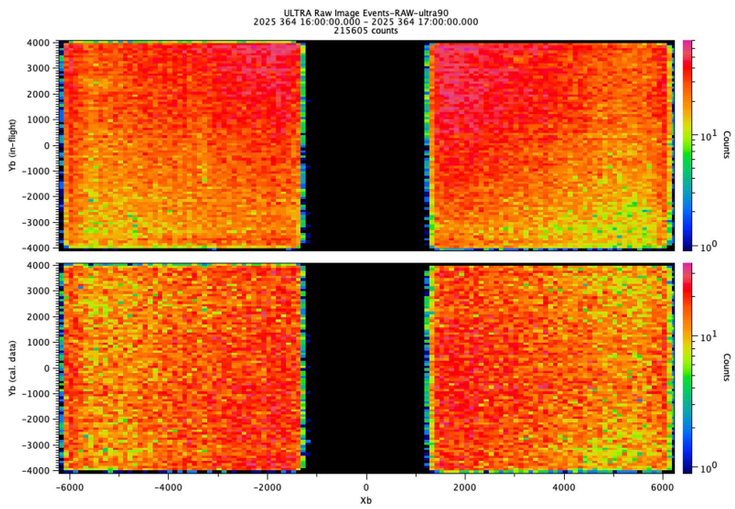


Figure 8: same format as Fig. 7 except for U90.

MCP performance during the commissioning period

Trends in the various rates on both U90 and U45 are shown in Figure 9. The start rates (on both left & right slits) show decreasing rates with increasing time. These rate decreases are consistent with gains changing on the MCP, which is expected and consistent with other ENA imagers flown by APL. Gain changes do impact the overall measurement efficiencies, so a gain test and raising of HV occurred on 12/30 with the macro 77. The new HVs were uploaded and went into effect after LOI on January 17, 2026.

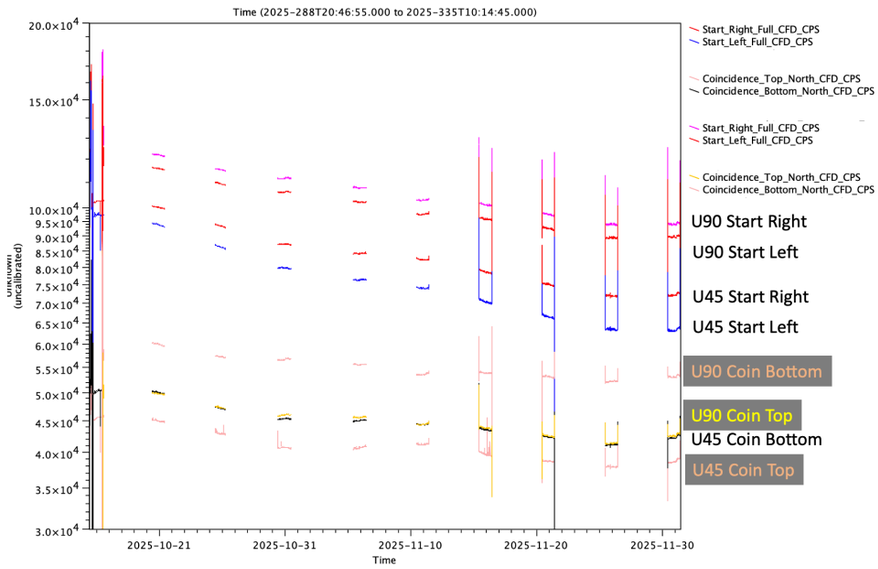


Figure 9: Rates as a function of time for U45 and U90.

Characterizing ion rejection performance and environmental factors that can contaminate ENA heliospheric maps

Inspecting the TOF distributions during deflection HV ramp up periods provided a great opportunity for understanding the ion rejection performance with in-flight conditions. Figure 10 spans a time range where U90's deflection blades went from off to ~4 kV. The TOF distributions in Fig. 10 top panel show a gradual decrease of the counts at higher TOFs (lower ion energies) ~20-30 ns at 0 V to only ions with TOFs below ~8 ns (~120 keV/q) when the HV is ~3.5 kV. This point is further illustrated in Figure 11 where it shows the TOFxE distributions with annotations converting TOFs to energy-per-nucleon for the different species.

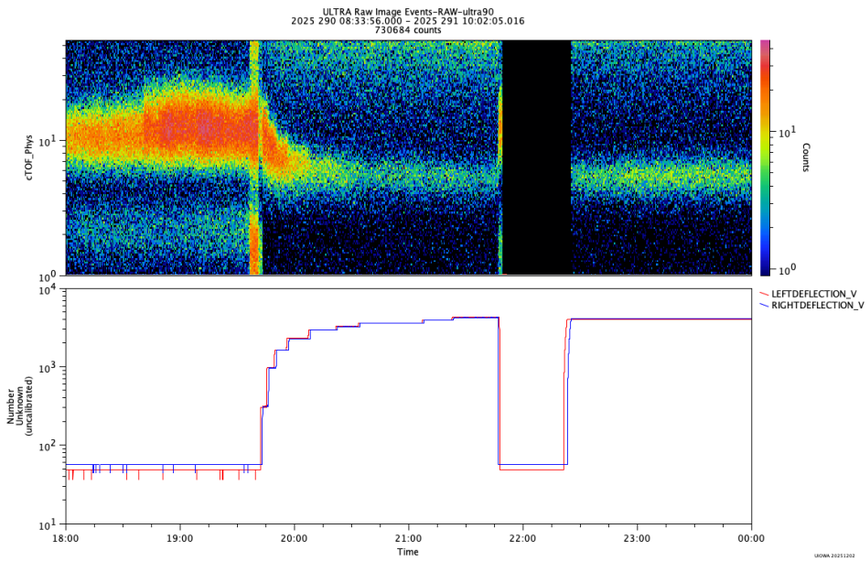


Figure 10: U90 TOF distributions (top) against HVs on the deflection assembly (Bottom).

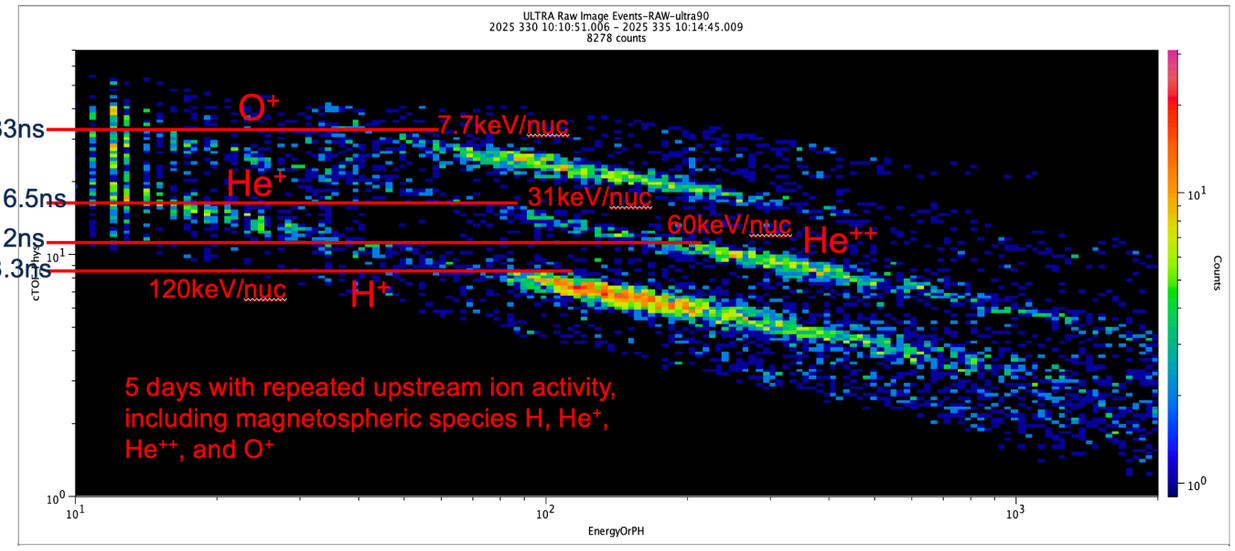


Figure 11: U90 TOFxE distributions of upstream ion events to illustrate ion rejection performance. Counts show a decrease at higher TOFs (lower energies) w.r.t to the red horizontal line for each species and then an increase. This behavior is expected because the local ions are being rejected and the longer TOF data corresponds to heliosphere ENAs.

One main objective of commissioning and the science demo period was to understand how to characterize the local environment and determine so-called good times, i.e., times when contamination of ENA signals were non-existent. Figure 12 illustrates a long period of time highlighting the various representative conditions Ultra observes in-flight. Specifically, periods of time where backgrounds, due to upstream ions or solar energetic particles (SEPs), are not detected (denoted as “good” in the plot) as well as time periods were there are enhanced backgrounds due to SEPs (denoted as “SEP”). Although more nuanced, time-periods that look like the “good” regions go into making heliospheric maps. Phase angle distributions (Fig. 12 top) are useful in ensuring all events are being telemetered. Since Ultra relies on raw event data, and not histogram data products, it is critical to collect all events. When ions dominate the events, they often exceed the software limitation of 90 events/sector and manifest as anisotropic phase angle distributions.

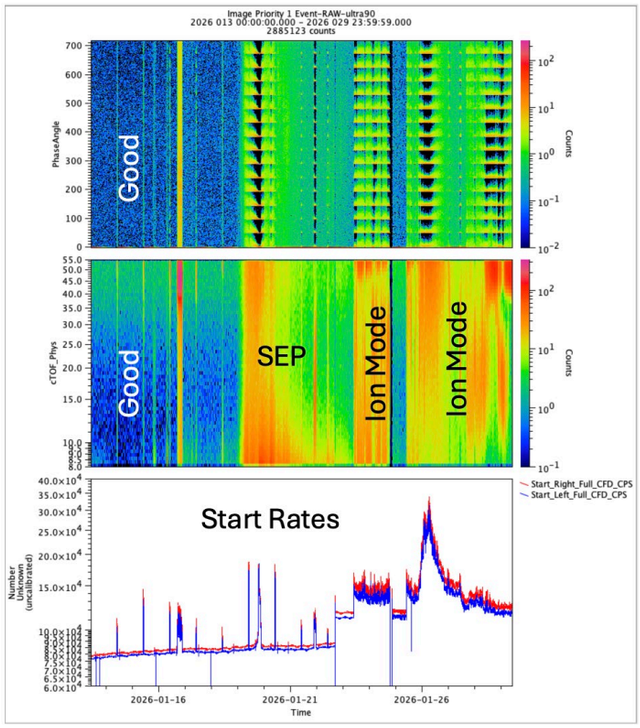


Figure 12: Phase angle, TOF, and start rates as a function of time for U90.

Preliminary maps based on hand selected good times

During times of "quiet" solar wind conditions—i.e., no upstream ion events, SEPs, strong SW densities, etc.—the TOF distributions show no time varying structures throughout a day with a clear count distribution that is consistent with a power law source (see Figure 13). Binning those counts into angular distributions as function of spin phase clearly shows some structure, which is attributed to heliospheric ENAs. The U45 and U90 intensity maps shown in Figure 14 are from a hand-selected list of good pointings. The maps clearly show known global features of the heliosphere and compare fairly well with both IBEX and IMAP-Hi (Figure 15). These maps indicate that Ultra is performing well and we have successfully determined a good operating configuration for Ultra (deflection duty cycling aside) to produce heliospheric ENA maps with little-to-negligible backgrounds.

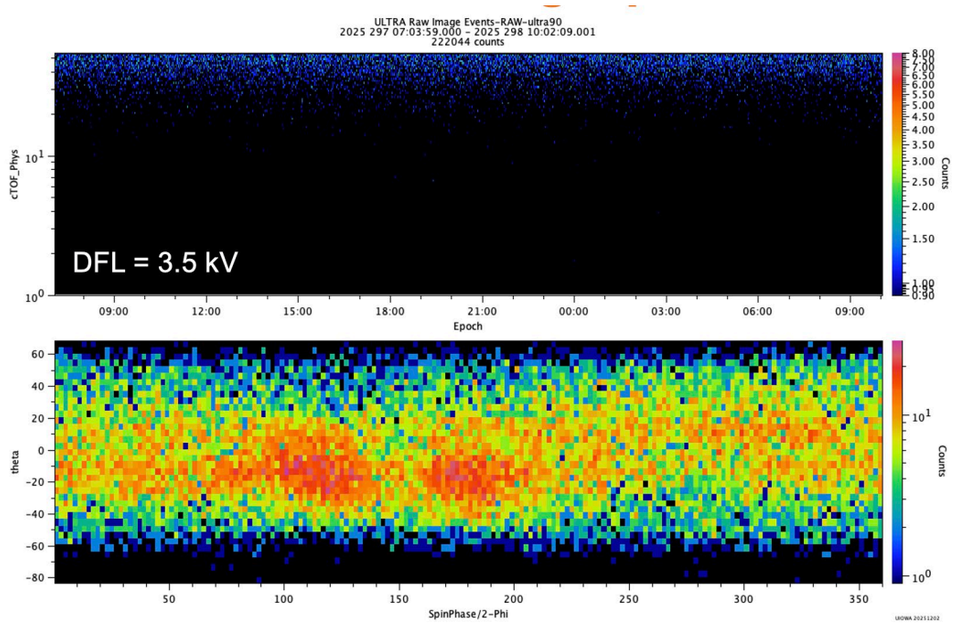


Figure 13: U90 TOF distributions (top) for a "good" pointing which clear heliospheric structure on the bottom.

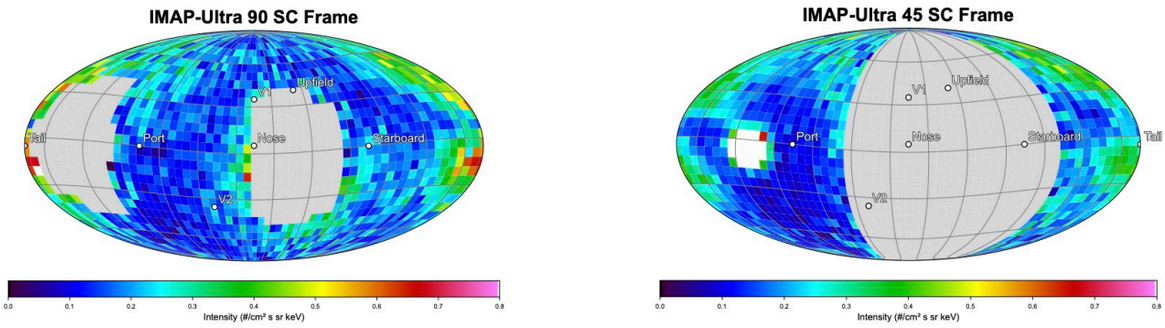


Figure 14: Heliospheric intensity maps centered on the nose direction obtained during the commissioning phase of IMAP.

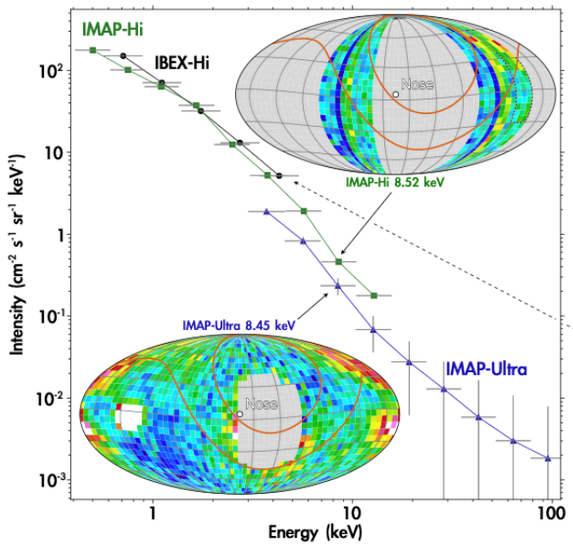


Figure 15: Energy spectra and ENA intensity map comparisons between IMAP-Hi and -Ultra. With no corrections, sensitive updates, etc., the intensities between Hi and Ultra are within a factor of 2, suggesting great agreement and the instruments are performing well.

3.9 IDEX

3.9.1 Strategy & Approach

IDEX was calibrated at the University of Colorado's Dust Accelerator Facility. At that facility, dust grains with a known charge, speed, and mass can be directed into the instrument, simulating measurements in the space environmental while offering calibrated laboratory conditions. With this facility, the following instrument characteristics and performance factors were calibrated:

- Composition mass spectrum, including time-of-flight characterization, mass range and resolution
- Target and ion grid signals and charge yield as a function of impact speed

3.9.2 Pre-Flight Instrument Calibration

IDEX calibration report embedded below

Contents

1 Instrument Description **2**

2 Instrument Performance and Calibration **4**

2.0.1 TOF Mass Spectrum 7

2.0.2 TOF Analysis 9

2.0.3 TOF Mass Resolution 12

2.0.4 Target and Ion Grid Signals 12

Chapter 1

Instrument Description

IDEX is an in situ impact ionization dust analyzer that measures the mass and composition of individual dust particles. It is an event-driven instrument that detects and measures particles that enter the aperture of the instrument and reach the target surface at the bottom. The measurement principle is based on impact ionization, a process in which the particle vaporizes and its components partially ionize upon high-velocity impact. The resulting transient impact plasma consists of electrons and ions.

The total impact charge Q depends on the particle's mass M, impact speed v, and the target material. The impact charge approximately follows a power-law relationship in the form of

$$Q \cong \alpha \, M \, v^{\beta}, \tag{1.1}$$

where values of the parameters α and β are a function of the target material and can be determined by laboratory measurements (Auer, 2001; Collette et al., 2014). The mass of the detected dust particle can be determined from the measured impact charge using Eq. 1.1, provided the impact velocity is known. This requires the assumption that the laboratory-derived calibration curve remains valid beyond the mass range accessible with a dust accelerator (chapter 2).

The operating principle is illustrated in Figure 1.1. Individual dust particles enter the instrument through an aperture and pass through a set of grid electrodes before impacting the target at the bottom of the instrument. The target is biased to a nominal voltage of $+2.5\ kV$ and positioned 33 mm behind a grounded acceleration grid. Upon impact, a transient plasma is generated and separated by the strong electric field, which extracts positively charged ions and molecules. These cations are accelerated and focused onto a centrally located ion detector for TOF analysis, whereas the negative charges are collected and measured on the target.

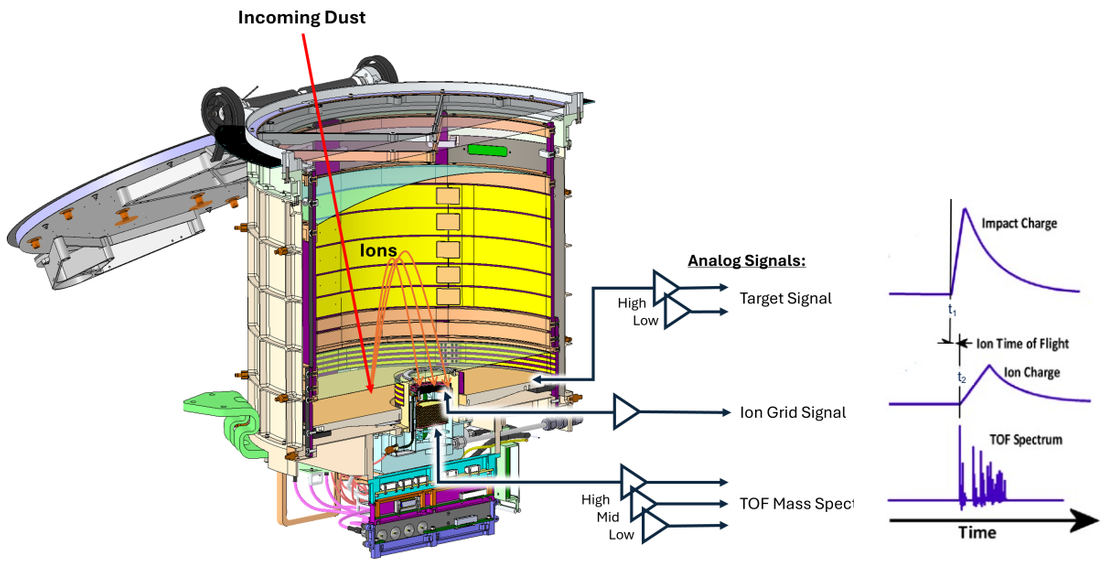


Figure 1.1: Cut-away schematic view of IDEX showing its principle of operation. Upon striking the positively biased target, an impacting dust particle generates a partially ionized plasma plume. The target collects electrons and anions from the plume, and the positively charged ions are accelerated and follow ballistic trajectories through an ion optics region, which focuses them onto a centrally located detector, producing compositional TOF mass spectra. Each IDEX dust impact event is recorded through six signal waveforms: the target impact charge measured on both high- and low-gain channels (QTH and QTL), the ion charge collected on a grid located above the detector (QI), and the TOF mass spectra acquired from the detector using low-, medium-, and high-gain channels ($TOFL; TOFM; TOFH$).

Chapter 2

Instrument Performance and Calibration

Both the engineering model (EM) and the flight model (FM) of IDEX were tested and calibrated at the Dust Accelerator Facility at the University of Colorado (https://impact.colorado.edu), where the charge, speed, and mass of impacting dust particles are known with uncertainties $\lesssim 1\%$ (Shu et al., 2012; James et al., 2020).

The Sensor Heads of the EM and FM units are functionally identical, including the manufacturing processes of the targets and the detectors used. The EM, however, lacks the full capabilities of the processor board and cannot run the FSW. Instead, analog signals from the CSA and detector boards were recorded using a high-speed (1 GHz bandwidth) digitizing oscilloscope with 12-bit resolution and a 1.25 GS/s sampling rate. The FM was operated using the FSW in conjunction with a spacecraft emulator, enabling command and telemetry exchange identical to in-flight operations.

Table 2.1 summarizes the test campaigns, while Figure 2.1 shows the mass–velocity distributions of particles impacting IDEX. The calibration measurements used iron, platinum-coated olivine, and aluminum particles. Iron was included for historical continuity, as it was also used to calibrate heritage instruments. Olivine, a common mineral in the Solar System, was coated with a thin layer of platinum to ensure compatibility with the accelerator (Hillier et al., 2009). Aluminum particles were used to assess the cleanliness of the FM target before shipping the instrument from LASP.

The accelerator overlaps with only a limited portion of the mass–velocity range that IDEX is expected to encounter in space. Consequently, the corresponding impact charge range achievable in the laboratory is significantly lower than the one anticipated in flight. An additional Ground Support Equipment (GSE) CSA board was developed and used in most calibration measurements to address this limitation. Apart from the higher gain (see Table 2.2), the GSE CSAs have similar characteristics to the flight CSAs regarding rise-time. A pulsed laser was used to simulate the generation of impact plasmas at the target, testing IDEX over the full expected range of impact charges. An Nd:YAG laser with a pulse duration ~ 8 ns operated at a wavelength of 532 nm was focused onto the target surface using a set of lenses mounted in front of the instrument aperture. The laser pulse energy varied over a wide range to generate an ablated charge in the range from 0.5 pC to over 32 nC. The testing was done with the instrument bias voltages set to nominal flight values. The functionality of the target and ion grid CSAs was verified. TOF mass spectra were also collected.

Figure 2.2 shows a representative set of the six waveforms recorded by IDEX from a single dust impact event. Table 2.2 lists the characteristics of IDEX's electronics and conversion factors from the instrument's internal units to the physical units of the various measurements.

Date	Instrument	Material	# Impacts
September 2022	EM	Iron	10,500
January 2025	EM	Iron	3,700
February 2025	EM	Olivine (Pt coat.)	7,400
November 2023	FM (Pre-Env)	Iron	1,200
December 2023	FM (Post-Env)	Olivine (Pt coat.)	1,100
December 2023	FM (Post-Env)	Aluminum	300

Table 2.1: IDEX EM and FM calibration campaigns before (Pre-Env) and after (Post-Env) environmental testing campaigns at the CU Boulder/IMPACT dust accelerator facility (Shu et al., 2012).

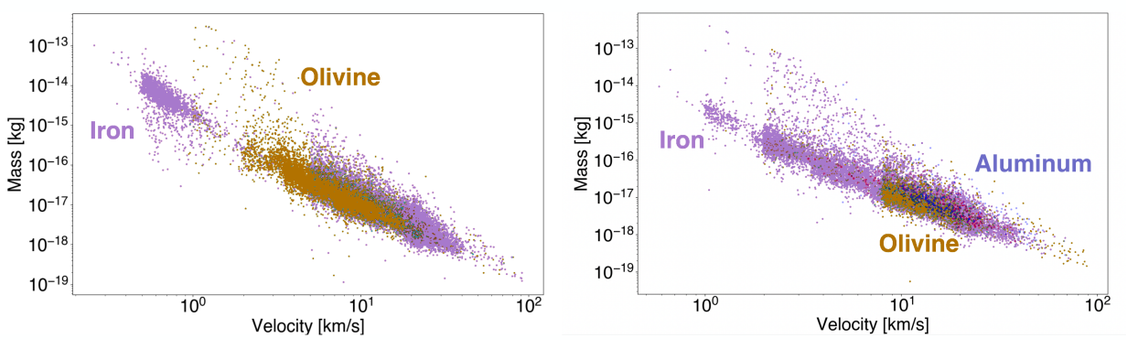


Figure 2.1: The mass-velocity distributions of the accelerated particles during the test and calibration campaigns using the IDEX EM (*left*) and FM (*right*) models. Most measurements were performed using iron and platinum-coated olivine particles, and aluminum particles were used in the last campaign before shipping out the FM for integration (Table 2.1). The characteristic distribution of the particles arises from the operating principles of the dust accelerator. (Shu et al., 2012).

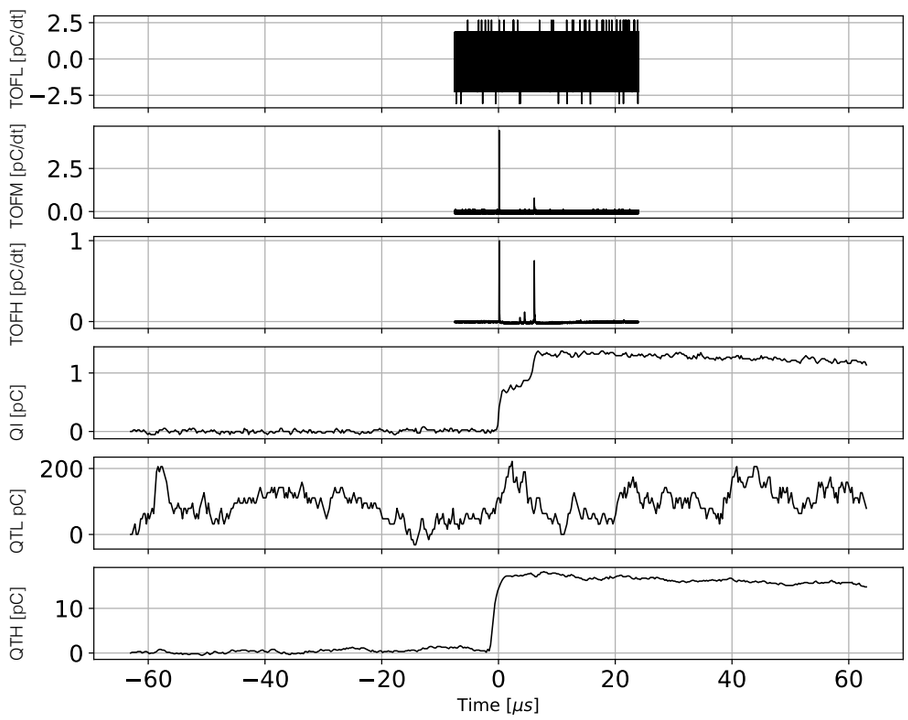


Figure 2.2: The six waveforms recorded by IDEX FM at the dust accelerator from an impact event of a platinum-coated olivine particle with mass $m = 3.2 \times 10^{-17}$ kg and speed $v = 4.92$ km/s (from top to bottom): $TOFL; TOFM; TOFH; QI; QTL$; and QTH. The waveform capture was triggered by exceeding a threshold of 580 DN, corresponding to 0.395 pC/Δt, where $\Delta t = 3.846$ ns, i.e., $\simeq 0.1$ mA on the $TOFH$ channel. The $TOFH$ waveform is saturated, reaching its maximum current (Table 2.2). The steps in QI represent a crude, integrated TOF spectrum. Channels $TOFL$ and QTL are mostly noise due to their lower gain.

Data	#	Rate	Res.	U.size	C.size	Conv.	Range
TOF		[MSps]	[bits]	[kB]	[kB]	[mA/DN]	[mA]
TOFL (low)	8,192	260	10	10.24	4.0	1.34×10^{-1}	68.31
TOFM (medium)	8,192	260	10	10.24	4.0	2.93×10^{-3}	1.49
TOFH (high)	8,192	260	10	10.24	4.0	7.50×10^{-5}	0.038
Charge						[pC/DN]	[pC]
QTL (target low)	512	4.0625	12	0.77	0.3	1.58×10^{1}	32,416
QTH (target high)	512	4.0625	12	0.77	0.3	1.63×10^{-1}	333.6
QIG (ion grid)	512	4.0625	12	0.77	0.3	7.46×10^{-4}	1.526
QTH*	-	-	-	-	-	1.36×10^{-3}	2.776
QIG*	-	-	-	-	-	2.61×10^{-4}	0.535

Table 2.2: Characteristics of the signal channels recorded by IDEX: the number of data points in the captured waveform per event, the sampling rate, resolution, uncompressed and compressed data volume, the conversion factors between instrument data numbers (DN) and the physical unit of the measurement, and the range of the measurement. *The characteristics of the GSE electronics used for laboratory tests are listed in the bottom two rows.

2.0.1 TOF Mass Spectrum

The $TOFL, TOFM$, and $TOFH$ channels measure the TOF spectrum with different signal gains, and the high dynamic range data product is obtained by combining the signals from all three channels as needed. Starting with the most sensitive channel ($TOFH$), any saturated segments are replaced with data from the next less sensitive channel, appropriately scaled to match (Table 2.2). A flag is raised if any segment remains saturated after this process.

TOF Mass Scale

The TOF spectrum captures the arrival times t_i of ions with masses m_i as related by

$$t_i = t_0 + a\sqrt{m_i}, \tag{2.1}$$

where t_0 represents the shift parameter (i.e., the time of the impact) and a denotes the stretch parameter (a characteristic of the ion optics design); both parameters are unknown. A fully automated algorithm to determine an initial t_0 and a involves a list of 22 of the most abundant elements in the Solar System that can show up in a TOF spectrum (McSween and Huss, 2022) with masses m_{Ai} that is turned into a synthetic TOF spectrum $S(t_{Ai})$ following Eq. 2.1. $S(t_{Ai})$ and the recorded TOF have the same length, the $S(t_{Ai})$ amplitudes are set to 1, and the line widths are three samples centered on t_{Ai}. The procedure steps through the range $1300 \leq a \leq 1600$ ns $\mathrm{u}^{-\frac{1}{2}}$, repeatedly finding the shift parameter that maximizes the cross-correlation coefficient between the TOF log amplitudes and $S(t_{Ai})$. The largest correlation coefficient identifies the best initial choice for t_0 and a, which can be refined by visual inspection if necessary. A quality factor monitors the success of the procedure, the average "distance" of each m_i from the closest integer atomic mass u value

$$\kappa = \frac{1}{N}\sum_{i=1}^{N} \left| m_i - \mathrm{int}(m_i) \right|, \tag{2.2}$$

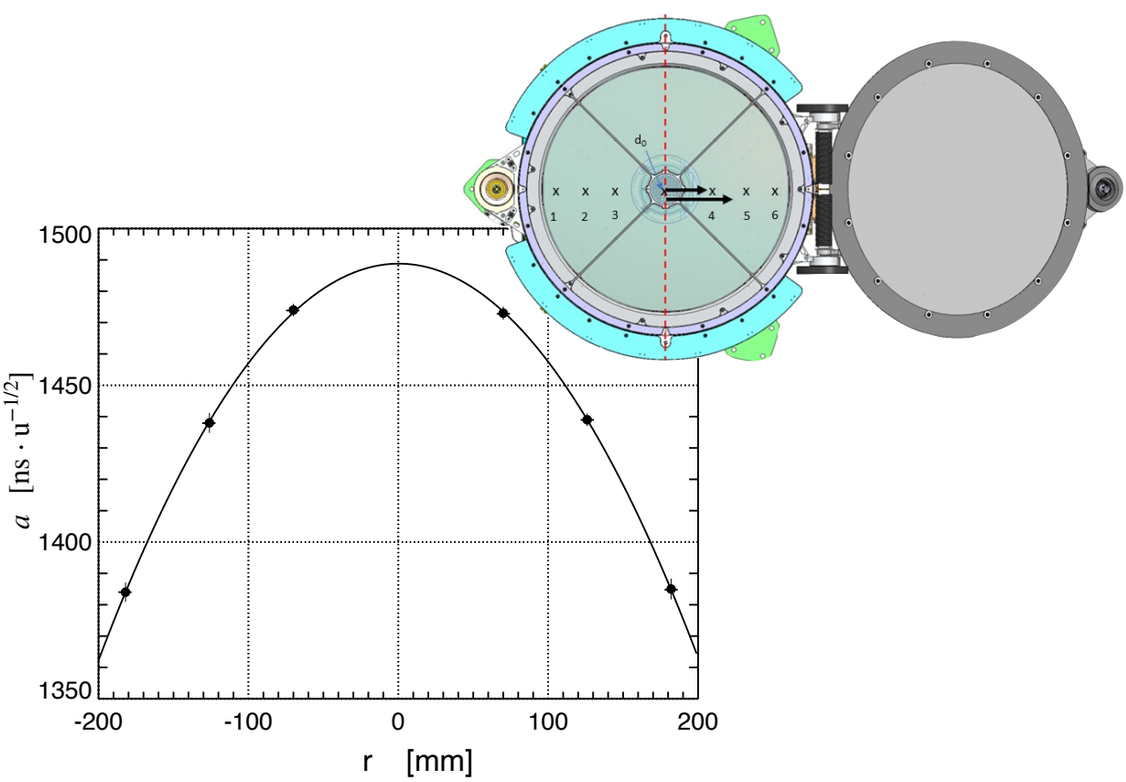


Figure 2.3: The stretch parameter a as a function of the impact location, identified in the top right insert, at distances $-182, -126, -70, +70, +126, +182$ mm from the center of the target. The vertical bars represent 1 σ error, the horizontal bars represent the characteristic width of $\simeq 1$ cm of the accelerator dust beam. The impact distance r [mm] from the center of the target as a function of a can be estimated as the positive solution of the quadratic equation: $0.0032 \cdot r^2 - 0.0022 \cdot r + (a - 1488) = 0$.

where N is the number of mass lines identified in the TOF with SNR ≥ 3. A value of $\kappa \geq 0.05$ indicates a poor fit.

The stretch parameter a is set by the geometry of IDEX's ion optics and the applied bias potentials. However, it also exhibits a slight dependence on the radial distance of the impact location on the target (Figure 2.3). The average flight time of an ion generated near the outer edge is shorter than that of an ion of the same mass originating near the center of the target. The stretch parameter is calculated for each mass spectrum, thereby providing information about the radial position of the impact on the target. Combined with the 4 rpm spin rate of the IMAP spacecraft, this effect can be used to improve the angular resolution of IDEX.

2.0.2 TOF Analysis

Figure 2.4 shows TOF mass spectra examples of low and high-speed iron, olivine, and aluminum particles recorded by the IDEX FM. The relative ion content of the mass lines is a function primarily of the dust composition and the impact speed. Applying the speed-dependent relative sensitivity factors, the true abundances of the various elements that are present in the TOF spectrum can be estimated to provide information on the possible mineral type of the impacting dust particle (Hillier et al., 2012; Fiege et al., 2014; Cohen et al., 2019; Eckart et al., 2023; Ayari et al., 2025). The TOF mass spectra are analyzed to calculate the relative abundances of the identified mass lines. The analysis is performed in the time domain, where the mass lines are traditionally fitted using exponentially modified Gaussian (EMG) functions (Kempf et al., 2025).

$$f(t; A, \mu, \sigma, \lambda) = A\frac{\lambda}{2}\exp\left[\frac{\lambda}{2}\left(2\mu + \lambda\sigma^2 - 2t\right)\right]\operatorname{erfc}\left(\frac{\mu + \lambda\sigma^2 - t}{\sqrt{2}\sigma}\right) \tag{2.3}$$

The fitting parameters are: A, μ and σ, the amplitude, mean and variance of the Gaussian component, and λ, the decay rate of the exponential component.

The analysis is performed iteratively 'from left to right', i.e., starting at the lowest mass present. The mass line is fitted to Eq. 2.3 using a four-parameter non-linear least-squares fitting routine (Markwardt, 2009). The ion abundance in the mass line is the integral under the curve. The fitted line is then subtracted from the data to remove any overlapping contribution to the subsequent mass lines. The fitting routine is then applied to the next identified mass line. Figure 2.5 demonstrates this procedure by calculating the isotope ratios of Mg, Si, and Fe (Table 2.3) from a single olivine particle impact.

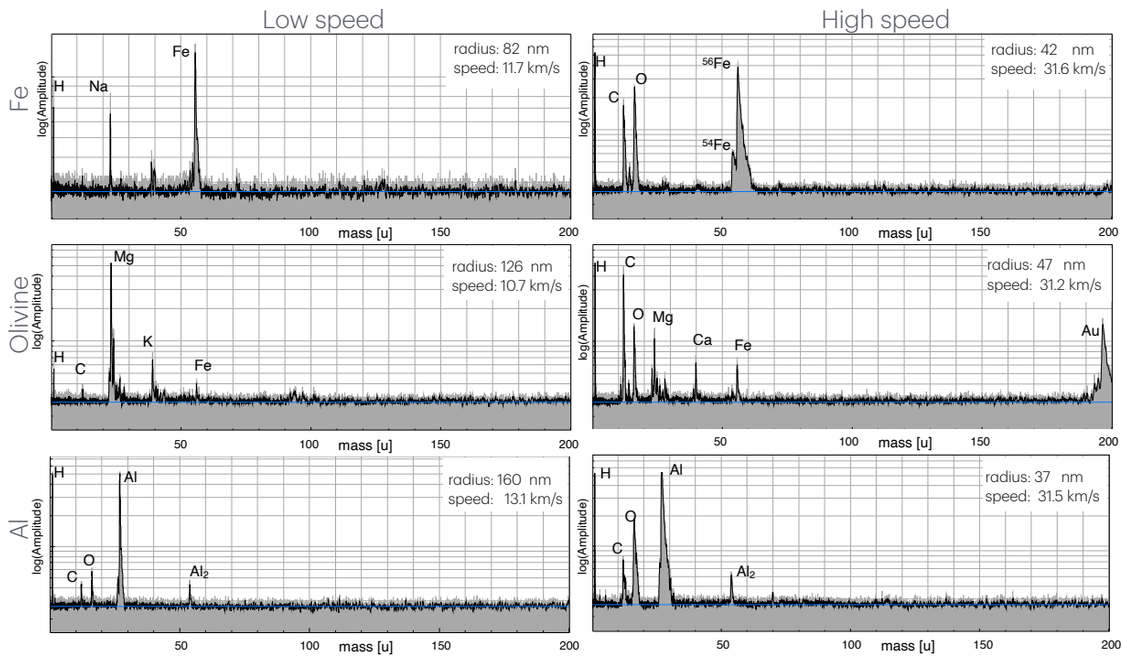


Figure 2.4: Mass spectra of Fe, olivine, and Al (top to bottom) recorded by the IDEX FM instrument at low ($\simeq$ 10 km/s) and high ($\simeq$ 30 km/s) impact speeds. The high-speed olivine impact example shows the mass line of gold (197 u) from IDEX's target.

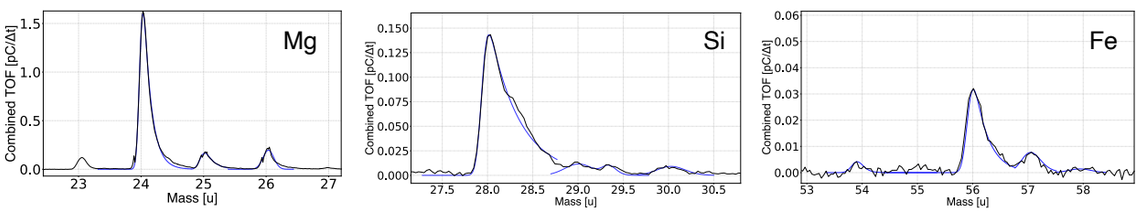


Figure 2.5: Segments of the TOF record of an olivine particle with mass of $7.93{\cdot}10^{-18}$ kg and impact speed 15.3 km/s, showing the isotopes of magnesium, silicon, and iron, recorded by the IDEX FM. The measured isotopic abundance ratios are listed in Table 2.3. The isotopes of Mg, Si, and Fe contributed to the total charge content of the TOF record ($QTOF$ = 22 pC), 71%, 10%, and 4%, respectively.

Isotope	Abundance [%]	Reference [%]
^{24,25,26}Mg	80±6; 10±2; 10±3	78.99; 10.00; 11.01
^{28,29,30}Si	89±4; 6±1; 5±2	92.23; 4.67; 3.10
^{54,56,57,58}Fe	4±2; 94±7; 2±1; 0.2±0.2	5.8; 91.75; 2.12; 0.28

Table 2.3: The abundances of Mg, Si, and Fe isotopes from the impact event in Figure 2.5 compared to their terrestrial reference values (Faure and Mensing, 2005) indicate that minor constituents that contribute at least 0.1% of the total charge content of a TOF spectrum can be reliably identified by IDEX.

2.0.3 TOF Mass Resolution

The resolution of an individual mass line is $m/\Delta m$, where Δm is its full width at half maximum (FWHM). The variation of mass resolution with ion mass is shown in Figure 2.6. The resolution is consistent across all impact locations on the target and asymptotically approaches a value of $R_0 = m/\Delta m \simeq 220$. The mass resolution is determined by the instrument's ion optics and by the initial energy and angular distributions of ions produced during the impact ionization process. In principle, the mass resolution of a TOF instrument is independent of ion mass; however, the decrease in resolution at low ion masses (Figure 2.6) is due to the finite pulse width of the electron multiplier. Using Eq. 2.1 and the relationship between mass and time resolution, $m/\Delta m = \frac{1}{2}t/\Delta t$, the mass resolution as a function of ion mass is

$$\frac{m}{\Delta m} = \frac{1}{2}\frac{a\sqrt{m}}{\sqrt{\Delta t_{det}^2 + \left(\frac{1}{2}\frac{a\sqrt{m}}{R_0}\right)^2}}, \tag{2.4}$$

where $\Delta t_{\rm det}$ is the single-ion pulse width of the detector, and R_0 is the asymptotic mass resolution determined by the instrument geometry and the expansion characteristics of the impact plasma cloud (e.g., its energy and angular distributions).

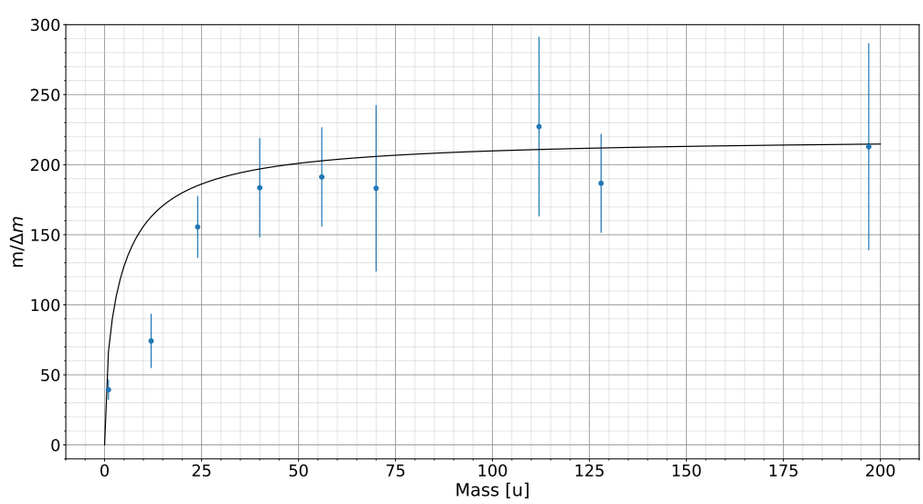


Figure 2.6: The mass resolution of the IDEX FM TOF measurements as a function of ion mass, derived from mass spectra of iron particle impacts. The black curve is based on Eq. 2.4, with $\Delta t_{\rm det}$= 10.3 ns, the characteristic stretch parameter (Figure 2.3) $a = 1440$ ns$\cdot u^{-1/2}$, and $R_0 = 220$.

2.0.4 Target and Ion Grid Signals

The two target channels (QTL, QTH) are combined, if needed, to correct saturated waveforms. For the analysis of the target (QT) and ion-grid (QI) signals, each waveform is fitted by an analytical function to consistently identify their characteristics (Horányi et al., 2014), using a seven-parameter non-linear least-squares fitting routine (Markwardt, 2009):

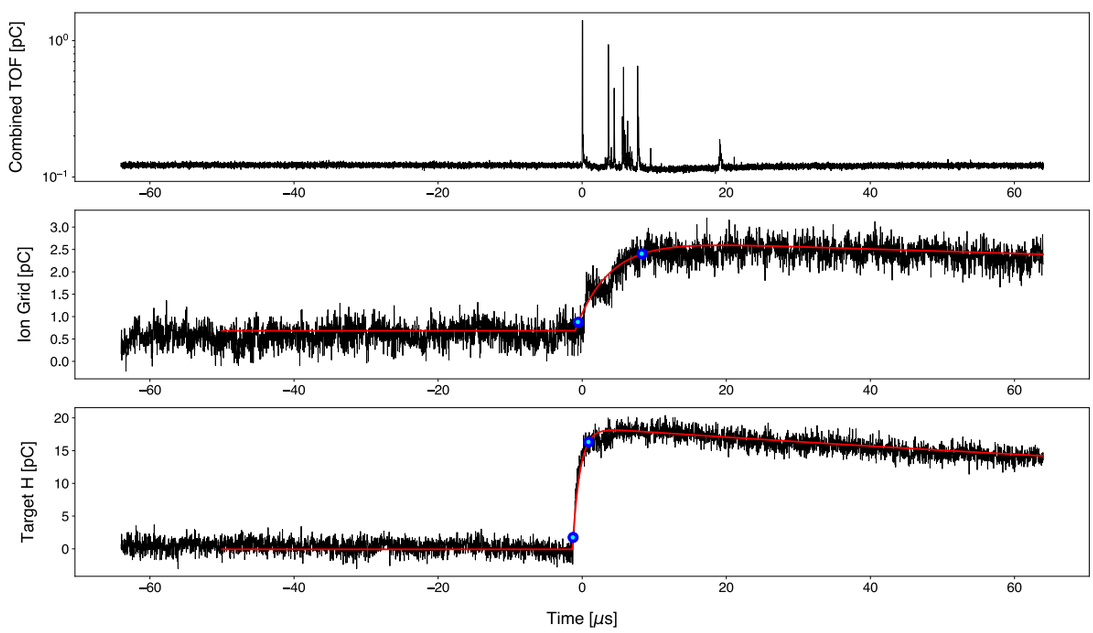


Figure 2.7: IDEX EM record of an olivine particle with impact speed v =22 km/s, mass $m = 5.3 * 10^{-15}$ kg (168 nm radius), showing the combined TOF, QI, and QT waveforms fitted using Eq. 2.5. The fit parameters for QI are: $t_0^{QI} = -0.93$ μs, $C_0^{QI} = 0.007$ pC, $C_2^{QI} = 2.6$ pC, $\tau_1^{QI} = 4.19$ μs, $\tau_2^{QI} = 33.32$ μs; and for QT: $t_0^{QT} = -1.4$ μs, $C_0^{QT} = 4.7$ pC, $C_2^{QT} = 18.05$ pC, $\tau_1^{QT} = 0.85$ μs, $\tau_2^{QT} = 41.1$ μs. τ_0 and C_1 remain undefined in the absence of an induced charge, and the second term in Eq. 2.5 is ignored. The data acquisition of this impact event was triggered on the first mass line in the TOF spectrum (H). The small blue dots mark the 10 and 90% value of QI and QT.

$$w[t; t_0, C_0, C_1, C_2, \tau_0, \tau_1, \tau_2] = C_0 - \underbrace{\mathrm{H}(\mathrm{t}_0 - \mathrm{t})\left[\mathrm{C}_1\left(\frac{\mathrm{t}-\mathrm{t}_0}{\tau_0}\right)\right]}_{\text{Induced Charge}} + \underbrace{\mathrm{H}(\mathrm{t}-\mathrm{t}_0)\left[\mathrm{C}_2\left(1-\mathrm{e}^{-\frac{\mathrm{t}-\mathrm{t}_0}{\tau_1}}\right)\mathrm{e}^{-\frac{\mathrm{t}-\mathrm{t}_0}{\tau_2}} - \mathrm{C}_1\right]}_{\text{Impact Charge}} \tag{2.5}$$

where H is the Heaviside step function, and the parameters represent the initial baseline C_0, the characteristic width of the induced charge signal τ_0, the start time of the signal following the induced charge record t_0, the characteristic rise and decay times τ_1 and τ_2, respectively. These analytic fits are used to identify the amplitude of the signals QT and QI, their rise & decay times τ_1^{QT}, τ_1^{QI} & τ_2^{QT}, and τ_2^{QI}, and the signal-to-noise ratios (SNR) of QT, QI, with the noise levels calculated from the first 50 points that establish the baseline for each waveform. Figure 2.7 shows an example of the fitting procedure.

The fitted target signals are used to generate IDEX's specific charge yield as a function of the impact speed, $Y(v) = QT/M$, shown in Figure 2.8. The calibration curve is fitted with a segmented power law distribution, similar to earlier impact ionization dust instruments (Auer, 2001; Göller and Grün, 1989; Srama, 2006; Horányi et al., 2014; Kempf et al., 2025)

$$Y(v; A, a_1, a_2, a_3, v_b, v_c, k) = A\, v^{a_1}\left[\left(1+\left(\frac{v}{v_b}\right)^k\right)^{\frac{a_2-a_1}{k}} \times \left(1+\left(\frac{v}{v_c}\right)^k\right)^{\frac{a_3-a_2}{k}}\right], \tag{2.6}$$

with A being a scale factor, a_1, a_2, and a_3 the power law exponents for the low, medium, and high-velocity segments, respectively, v_b and v_c the characteristic speeds where the slope transition happens, and k setting the sharpness of the transitions. The charge yield weakly depends on the composition of the impacting dust particles (Göller and Grün, 1989). Table 2.4 lists the parameters for Eq. 2.6 for the dust materials used in the IDEX calibration campaign.

The charge yield curve enables the mass, M, of the dust particle, to be estimated from the total charge it generates on the target: $M = QT/Y(v)$. The uncertainty of the mass estimate of impact ionization dust instruments is given with a unitless error factor, ΔM, such that there is a 68% probability to have the true value in the range $M/\Delta M$ and $M \cdot \Delta M$ (Grün et al., 1992b,a; Srama, 2006; Horányi et al., 2009; Kempf et al., 2025). Table 2.4 lists the error factors in the mass determination, assuming that the impact speed is known.

Similar to the Ulysses and Galileo dust instruments (Grün et al., 1992b,a), IDEX's speed estimates are derived from the rise time of the target signal QT_τ and the ratio QI/QT (Figure 2.9). The impact speed as a function of the rise time, $v(QT_\tau)$, is a fit to the calibration data using the same form as Eq. 2.6

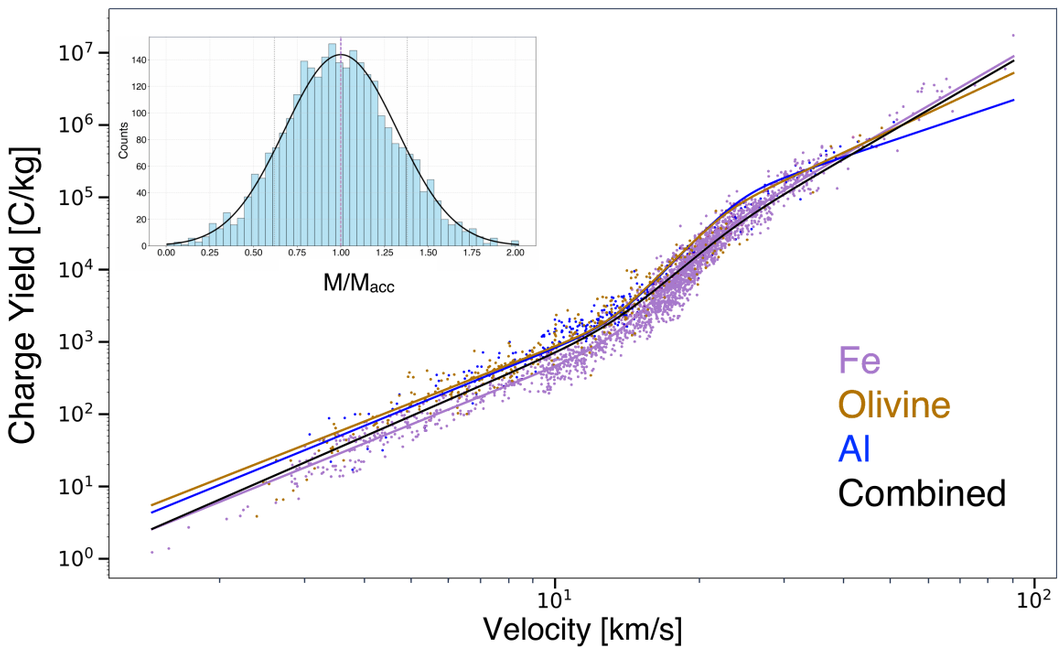


Figure 2.8: Charge yield for iron (red), aluminum (blue), and olivine (green dots) dust particles. The insert shows the distribution of the ratio of the dust particle's mass, as calculated from the fit (Eq. 2.6) for all materials combined, over the mass reported by the accelerator. The fit parameters, standard errors, and the error factors are listed in Table 2.4.

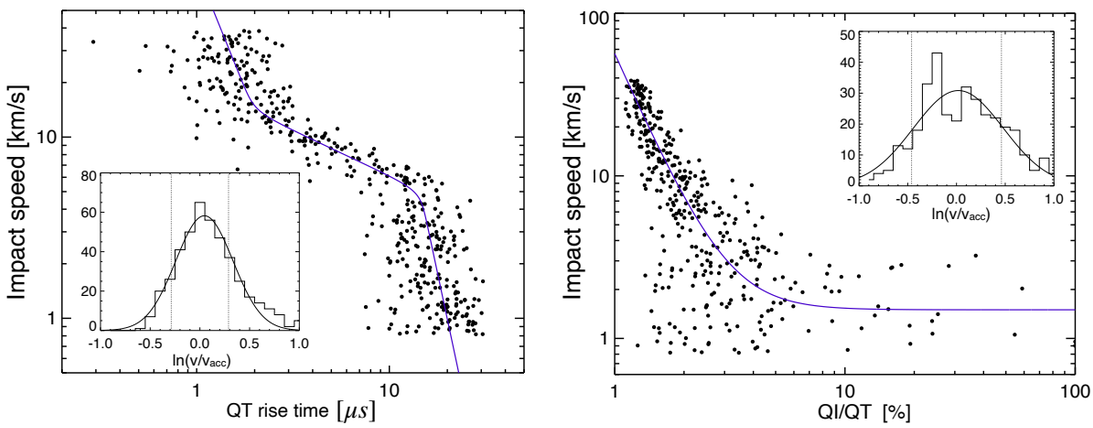


Figure 2.9: The impact speed of a dust particle as a function of the rise time of QT $(left)$ and the ratio QI/QT $(right)$. The inserts show the Gaussian fits to the log of the ratios of the fit over the data, with $\sigma_{QT} \simeq 0.28$ and $\sigma_{QI/QT} \simeq 0.46$, the error factors (e^{σ}) are $\Delta v_{QT} \simeq 1.33$ and $\Delta v_{QI/QT} \simeq 1.58$

				QT/M					
Material	log(A)	a_1	a_2	a_3	v_b [km/s]	v_c [km/s]	k	σ	ΔM_Y
Fe	-0.02	2.7	6.7	3.9	13.0	23.7	11.6	0.35	1.41
Olivine	0.32	2.6	6.7	3.1	13.0	22.8	13.9	0.32	1.37
Al	0.21	2.7	6.8	2.2	13.1	24.6	12.3	0.43	1.51
Combined	0.06	2.8	5.9	4.1	13.0	22.7	8.2	0.40	1.47
				v					
Material	log(A)	a_1	a_2	a_3	v_b [km/s]	v_c [km/s]	k	σ	ΔQT_c
Combined	1.27	-0.2	-2.1	-0.37	5.3	13.3	13.3	0.28	1.33

Table 2.4: The parameters of the fit of the charge yield as function of the impact speed $Y(v; A, a_1, a_2, a_3, v_b, v_c, k)$ (*top*) and the target signal rise time as a function of the velocity $QT_\tau(v; A, a_1, a_2, a_3, v_b, v_c, k)$ (*bottom*) using Eq. 2.7, the standard error σ of the Gaussian fitted to the ratio of the fit over the data, and the error factor of the fit $\Delta M_Y \simeq exp(\sqrt{\ln(1+\sigma^2)})$.

$$QT_\tau(v; A, a_1, a_2, a_3, v_b, v_c, k) = A\, v^{a_1} \left[\left(1 + \left(\frac{v}{v_b} \right)^k \right)^{\frac{a_2 - a_1}{k}} \times \left(1 + \left(\frac{v}{v_c} \right)^k \right)^{\frac{a_3 - a_2}{k}} \right], \tag{2.7}$$

and its parameters are listed in Table 2.4. The impact speed as a function of QI/QT fit is

$$v(QI/QT) = c \cdot (QI/QT)^p + v_0, \tag{2.8}$$

with parameters $c = 55$ [km/s], $p = -3.2$, and $v_0 = 1.5$ [km/s].

The error factors $\Delta v_{QT} \simeq 1.33$, and $\Delta v_{Qi/QT} \simeq 1.58$, result $\Delta v \simeq 1.28$, for the weighted average value of v. The error factor for mass determination $\Delta M = \Delta M_Y \cdot (\Delta v)^{a_2} \lesssim 8$, where $a_2 = 6.8$ the largest power exponent of v in the yield curve (Table 2.4), that allows the radius of the impacting particle to be estimated with an error factor of $\lesssim 2$, assuming that the corresponding TOF spectra can be used to estimate the density.

The fully functioning IDEX EM will be used at the dust accelerator facility to extend the types of minerals and organic particles that are candidates to be identified by IDEX in space, to extend our calibrations and iteratively improve our ability to determine the mass, speed, and composition of the recorded IDP and ISD particles.

Bibliography

Auer S (2001) Instrumentation. In: Grün E, Gustafson B, Dermott S, Fechtig H (eds) Interplanetary Dust, Springer, pp 387–438

Ayari E, Horányi M, Turner NJ, Corbett T, Fontanese J, Hillier J, Kempf S, Mikula R, Munsat T, Schmitt J, Sternovsky Z, Szalay JR, Trieloff M, Ulibarri Z, Westphal A (2025) Elemental and isotopic analysis of olivine with impact ionization dust instruments. Planetary and Space Sci (submitted)

Cohen BA, Szalay JR, Rivkin AS, Richardson JA, Klima RL, Ernst CM, Chabot NL, Sternovsky Z, HoráNyi M (2019) Using dust shed from asteroids as microsamples to link remote measurements with meteorite classes. Meteoritics and Planetary Science 54(9):2046–2066, DOI 10.1111/maps.13348, 1906.00876

Collette A, Grün E, Malaspina D, Sternovsky Z (2014) Micrometeoroid impact charge yield for common spacecraft materials. Journal of Geophysical Research (Space Physics) 119(8):6019–6026, DOI 10.1002/2014JA020042

Eckart LM, Hillier JK, Postberg F, Marchi S, Sternovsky Z (2023) Linking meteorites to their asteroid parent bodies: The capabilities of dust analyzer instruments during asteroid flybys. Meteoritics & Planetary Sci.58(10):1449–1468, DOI 10.1111/maps.14060

Faure G, Mensing TM (2005) Isotopes: Principles and Applications, 3rd edn. John Wiley & Sons

Fiege K, Trieloff M, Hillier JK, Guglielmino M, Postberg F, Srama R, Kempf S, Blum J (2014) Calibration of relative sensitivity factors for impact ionization detectors with high-velocity silicate microparticles. Icarus 241:336 – 345, DOI https://doi.org/10.1016/j.icarus.2014.07.015, URL http://www.sciencedirect.com/science/article/pii/S0019103514003819

Göller JR, Grün E (1989) Calibration of the Galileo/Ulysses dust detectors with different projectile materials and at varying impact angles. Planetary and Space Science 37:1197–1206, DOI 10.1016/0032-0633(89)90014-7

Grün E, Fechtig H, Hanner MS, Kissel J, Lindblad BA, Linkert D, Maas D, Morfill GE, Zook HA (1992a) The Galileo Dust Detector. Space Science Reviews 60:317–340

Grün E, Fechtig H, Kissel J, Linkert D, Maas D, McDonnell JAM, Morfill GE, Schwehm G, Zook HA, Giese RH (1992b) The Ulyssses dust experiment. A&AS92:411–423

Hillier JK, Sestak S, Green SF, Postberg F, Srama R, Trieloff M (2009) The production of platinum-coated silicate nanoparticle aggregates for use in hypervelocity impact experiments. Planetary and Space Science

Hillier JK, Postberg F, Sestak S, Srama R, Kempf S, Trieloff M, Sternovsky Z, Green SF (2012) Impact ionization mass spectra of anorthite cosmic dust analogue particles. J. Geophys. Res.117(E9):E09002

Horányi M, Sternovsky Z, Gruen E, Srama R, Lankton M, Gathright D (2009) The lunar dust experiment (LDEX) on the lunar atmosphere and dust environment explorer (LADEE) mission. In: Lunar and Planetary Institute Science Conference Abstracts, Lunar and Planetary Institute Science Conference Abstracts, vol 40, p 1741

Horányi M, Sternovsky Z, Lankton M, Dumont C, Gagnard S, Gathright D, Grün E, Hansen D, James D, Kempf S, Lamprecht B, Szalay JR, Srama R, Wright G (2014) The Lunar Dust Experiment (LDEX) onboard the Lunar Atmosphere and Dust Environment Explorer (LADEE) mission. Space Science Reviews 185:93 – 113, DOI 10.1007/978-3-319-18717-45

Horányi M, Tucker S, Sternovsky Z, Tyagi K, Knappmiller S, Ayari E, Mikula R, Szalay JR, Kempf S, Bollendonk C, Gurnee R, Fisher M, McCann D, Coakley L, Gurst S, Davis K, Bramer S, Miller M, Neher J, Newcomb G, Oberg S, Sayler J, Wade S, Deaton T, Doner A, Fontanese J, Grün E, Miller C, Wing R, Holguin L, Fowle M, Hellickson T, Rhode A, Brennan N, Hansen D, O'Connor D, Kostovny A, Shaver S, Looney K, Turner NJ, Hillier J, Postberg F, Srama R, Christian E, Gkioulidou M, McComas DJ, Schwadron NA (2025) Interstellar Dust Experiment (IDEX) Onboard NASA's Interstellar Mapping And Acceleration Probe (IMAP). Space Sci. Rev.221(8):102, DOI 10.1007/s11214-025-01230-1

James D, Fontanese J, Munsat T, Horányi M (2020) Calibration methods of charge sensitive amplifiers at the Colorado dust accelerator. Review of Scientific Instruments 91(11):113301, DOI 10.1063/5.0020018

Kempf S, Tucker S, Altobelli N, Briois C, Cable ML, Grün E, Gudipati MS, Henderson BL, Hsu HW, Hand K, Horanyi M, Postberg F, Schmidt J, Srama R, Sternovsky Z, Tobie G, Zolotov MY, Belting C, Bortfeldt S, Bouwman J, Brennan N, Bryant K, Cassidy T, Crotser D, Curtin A, DeVito E, Ebuen D, Faber N, Fisher M, Fontanese J, Fowle M, Frank W, Gurst S, Haselschwardt S, Hoxie V, Hubbell K, James D, Kien M, Knappmiller S, Kohnert R, Lampe A, Lankton M, Lev-Tov S, McGinn C, Miller M, Newcomb G, Oberg S, O'Brien L, Pilewskie K, Polson S, Scarffe-Barrett V, Summers D, Wade S, Ware A, Yehle A, Wuerthner C, Garcia Arteaga A, Oaida B, Eberl C, Fitton P, Goode W, Levin Z, Lowry G, Stanley J, Tracy A, Ulibarri Z, Williams E, Yoke C, Southworth BS, Hillier JK, Khawaja N, Klenner F, Napoleoni M, Simolka J, Sioeng J (2025) Suda: A surface dust analyser for compositional mapping of the galilean moon europa. Space Science Reviews 221(1):10, DOI 10.1007/s11214-025-01134-0, URL https://doi.org/10.1007/s11214-025-01134-0

Markwardt CB (2009) Non-linear Least-squares Fitting in IDL with MPFIT. In: Bohlender DA, Durand D, Dowler P (eds) Astronomical Data Analysis Software and Systems XVIII, Astronomical Society of the Pacific Conference Series, vol 411, p 251

McSween J Harry Y, Huss GR (2022) Cosmochemistry, 2nd edn. Cambridge University Press, Cambridge, UK

Shu A, Collette A, Drake K, Grün E, Horányi M, Kempf S, Mocker A, Munsat T, Northway P, Srama R, Sternovsky Z, Thomas E (2012) 3 MV hypervelocity dust accelerator at the Colorado Center for Lunar Dust and Atmospheric Studies. Review of Scientific Instruments 83(7):075108, DOI 10.1063/1.4732820

Srama R (2006) Calibration of the cassini dust detector cda, in prep.

Srama R (2006) Cda calibration report. Tech. rep., MPI-K

3.9.3 In-Flight Calibrations

IDEX in-flight calibration report to be included here.

3.10 GLOWS

3.10.1 Strategy & Approach

Calibration of IMAP's GLOWS instrument occurred at the Physikalisch-Technische Bundesanstalt's Metrology Light Source facility in Berlin, Germany. The calibrations followed a two-step process to determine 1) instrument sensitivity and performance validation; 2) in-flight tracking of sensitivity degradation. In-flight calibrations use measurements of known stars as "standard candles" to track performance of the instrument over time. Pre-flight, ground calibrations used a calibration light source to determined the following:

- Quantum efficiency and spectral response
- Point spread function
- Front-end electronics performance and characteristics
- Instrument sensitivity and signal-to-noise ratio

3.10.2 Pre-Flight Instrument Calibration

GLOWS calibration report embedded below width=!,height=!,pages=1-26

3.10.3 In-Flight Calibrations

GLOWS in-flight calibration report to be included here.

3.11 Cross-Calibration

3.11.1 SWAPI & CoDICE

SWAPI and CoDICE cross-calibration report embedded here

SWAPI and CoDICE Cross Calibration

To compare the instrument measurements in the overlapping energy range, we performed both ground and flight cross calibrations between the SWAPI and CoDICE instruments.

For the ground calibration, SWAPI and CoDICE were calibrated together in the same chamber using the same ion beams at the Princeton Space Physics Laboratory (see Rankin et al. 2025 for details on the facility). The cross-calibration effort focused on characterizing energy and angular response functions for 2 keV He^+ (solar wind; e.g., through SWAPI's sunglasses aperture) and 16 keV He^+ (suprathermal particles). To establish a common reference point with respect to the incident beam's flux, an absolute beam monitor (ABM) measurement was taken before and after each instrument test, and instrument data were normalized to the beam rate values inferred from the ABM.

Figure 1 shows the angular response functions for CoDICE and SWAPI, obtained by fixing the instruments at specific ESA voltages while sweeping through a fine range of elevation angles. Both instruments exhibit strong angular coverage when CoDICE is in the normal geometric factor (GF) mode, as denoted by the horizontal bars spanning each instrument's angular range; these values are derived from the full-width-at-half-maximum (FWHM) of the spline-fitted angular distribution. As expected, CoDICE's reduced GF mode no longer matches with SWAPI's angular range (see Livi et al. 2026 for more details). When considering the SWAPI data, it is worth noting that the difference in SWAPI's ABM normalized rates between 16keV and 2keV He^+ is consistent with the ~1000x attenuation through its sunglasses (Figure 1b).

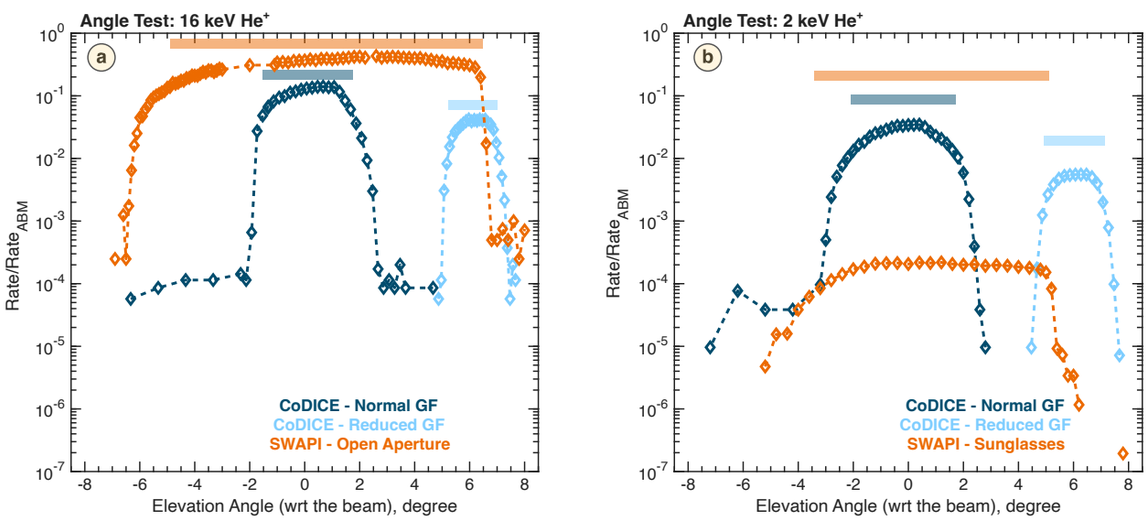


Figure 1. Cross characterization of angular response functions between CoDICE and SWAPI for (a) 16 keV He^+ and (b) 2keV He^+. SWAPI's result is represented in oranges, while result from CoDICE is shown in dark blue (normal geometric factor, GF) and light blue (reduced GF),

respectively. The angular range for SWAPI and CoDICE (normal GF and reduced GF) are indicated as orange, dark blue, and light blue horizontal bars, respectively.

Table 1 summarizes the derived centroid energies from the energy tests, where the instruments were parked at an elevation angle of 0 degree and swept across a wide range of ESA voltages. Derived energies were computed by multiplying the ESA voltages by each instrument's k-factor. The results show strong agreement in the derived centroid energy between CoDICE and SWAPI. Further calibration analysis is needed to integrate these angular and energy response function characterization with the flight calibration to assess the relative detection efficiency differences between the instruments.

Table 1. Summary of the centroid energy derived from the energy tests for SWAPI and CoDICE (in both normal and reduced GF mode).

	Centroid Energy (eV)	
Energy/Species	**2 keV He^+**	**16 keV He^+**
SWAPI	1,964.6	16,044
CoDICE – Normal GF	1,966.1	16,099
CoDICE – Reduced GF	1,945.7	16,020

3.11.2 CoDICE & HIT

CoDICE and HIT cross-calibration report embedded here

3.11.3 IMAP-Lo & IMAP-Hi

IMAP-Lo & IMAP-Hi cross-calibration report embedded here

This memo summarizes the analysis of IMAP-Hi data collected during cross-calibration of the IMAP-Hi90 sensor with IMAP-Ultra90 and the IMAP-Hi45 sensor with IMAP-Lo. Although differences were discovered in the IMAP-Hi45 sensor behaviour after its deintegration from the spacecraft compared to its behaviour prior to delivery, analysis of cross-calibration does not lead to modifications to the earlier calibration of IMAP-Hi45 and IMAP-Hi90.

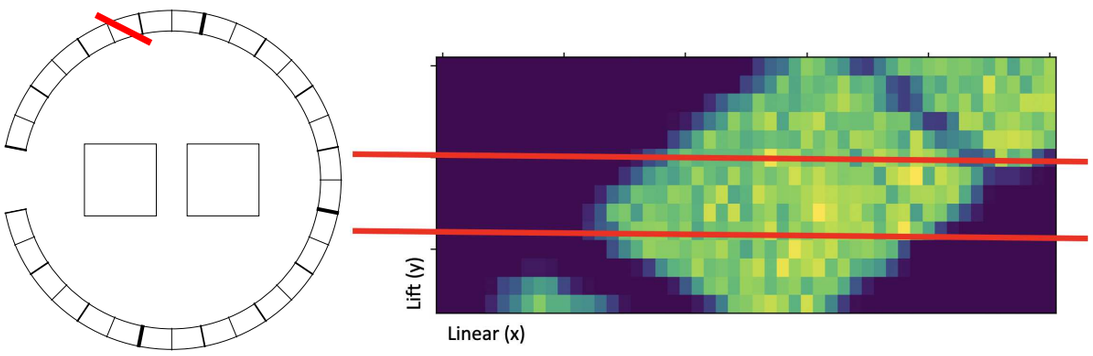
Hi-Ultra Cross Calibration

Hi90 was cross-calibrated with Ultra90 at the start of November 2024, in the LANL beam facility. A 4mm square aperture was used to define the beam, with the square sides aligned visually with horizontal and vertical. The species was always neutral hydrogen, oriented as normal as possible to the instrument aperture. A Quantar imaging MCP was used to verify beam shape and size, and Hi90's deflectors were used to confirm that the beam was neutral. The table of beam energies and settings is below.

Date	Energy (keV)	ESA setting	Specific clock range	ABM before and after(/s)
Nov 4	12.7	9	1730759484 1730759728	5364, 5476
Nov 4	8.5	7	1730764316 1730764554	10487, 10248
Nov 4	5.7	8	1730767221 1730767455	14092, 13926
Nov 4	3.75	6	1730774254 1730774489	15340, 15289
Nov 5	12.7	9	1730827224 1730827458	4817, 4792
Nov 5	8.5	8	1730829537 1730829766	9727, 9738

The cross-calibration mounting assembly allowed horizontal and vertical linear motion as well as azimuthal ("lazy Susan") motion to rotate either Hi (azimuth $\approx 180°$) or Ultra (azimuth $\approx 0°$) into the beam. The azimuthal stage also allowed fine alignment of the instruments' entrance apertures perpendicular to beam. Normal incidence was determined to be $+0.35°$ from azimuthal stage locations $0°$ and $180°$ for the two sensors, consistent with earlier calibration work. No adjustment in polar angle ("rotisserie") was possible for Hi (Ultra was mounted on a polar stage and could adjust this angle during cross-cal). Prior calibration work with a polar stage installed, and studies of the beam in summer 2024 using an imaging MCP on a linear stage moved along the beam direction, indicate an $\approx 0.4°$ beam angle in vertical.

The vertical and horizontal motion stage ranges allowed putting beam on any part of the Ultra slit, and on two of the conversion foils of Hi. For Ultra, the entire aperture was scanned by moving Ultra horizontally at a constant rate across the beam. For Hi, two horizontal scans at 0.5 mm/s, separated in vertical by 3.0 mm, were used. The foil used for cross calibration was the one at a rotation angle of 101.25 - 112.5° clockwise from the alignment mirror when looking at the entrance aperture of Hi. The portion of foil covered is shown in the figure below by the two lines. The data shown in the plot is from Lo/Hi cross-calibration and is intended simply to illustrate the foil scan location.



The crux of cross-calibration was exposing Ultra and Hi to exactly the same beam in the same facility, to avoid any potential issues with transfer standards. Enough of the sensor aperture needed to be exposed to

avoid large uncertainties in extrapolating sensor performance from the cross-cal measurements to the overall response of the sensor.

Absolute beam monitor (ABM) data (N_A, N_B, and N_{AB}) was collected at 1 s cadence before and after each measurement for at least 60 seconds. Over a minute, the statistical uncertainty of the inferred beam intensity was on the order of $< 0.3\%$, and typically smaller than beam drift over calibration intervals. Even if the absolute calibration of the ABM is not trusted – which is the premise behind putting the "same beam" on two sensors in cross-calibration – the ABM can still serve as a monitor of beam stability. The beam intensity numbers reported here are simply $N_A N_B / N_{AB}$ and do not include a correction for entrance grid transmission ($\approx 1/0.95$) or dark counts on the CEMs (negligible). The duration of a typical Ultra scan or Hi scan (between ABM measurements) was under ten minutes. It also took under ten minutes to rotate from one sensor in beam to the other. ABM data was collected during the azimuthal rotation between sensors.

Hi90 was calibrated in the same facility at these energies just a few days earlier, using COTS HVPS for all high voltages rather than the EBox power supplies, which have coarser voltage resolution (and considerably lesser current monitoring/controlling capabilities). Calibration at 5.7, 8.5, and 12.7 keV occurred during October 28-30, using a 2 mm circular aperture to define the neutral beam. Some issues with beam stability over this time period were resolved during cross cal with the identification of the partial failure of one of the SRS function generators used to raster and steer the ion beam prior to neutralization. The fix was replacing the SRS unit, which occurred after the 8.5 keV data was collected on November 4.

Hi90 performance during Hi-Ultra cross-cal was compared to prior calibrated performance by the following analysis:

1. Hi90 calibration data (not cross-calibration data) for the appropriate conversion foil was analyzed by position on the foil and normalized to ABM count rate linearly interpolated in time between the preceding and following ABM measurements to create a map of detection efficiency (detected events divided by incident beam intensity) over the area the foil. Calibration direct event data comes from the FEE "fast DE" connection, bypassing C&DH processing.

   Linear interpolation between ABM measurements captures much of the drift observed in the LANL beam, which is usually related to drifts over the day of temperature, humidity (affecting H available for the beam in room air), and pressure in the beamline after the bending magnet (affecting how much of the ion beam is neutralized).

   For 8.5 and 12.7 keV, the energies at which Hi-Ultra cross-calibration was intended, calibration data was collected over the foil observed in cross-calibration. However, at the additional energies observed during cross-cal in the spur of the moment, full phase 3 "snake" scans were performed on this foil at 3.75 keV (ESA 6) but not at 5.7 keV (ESA 7) due to time constraints.

2. Cross-calibration data was similarly created for the slice of foil observed, to create a linear plot of detection efficiency along the horizontal scan. Direct event data during cross-calibration comes from the RAW_DE packets generated by the C&DH in HVENG mode. During this cross-cal, these packets were generated every two seconds. Because the packets did not fill up entirely, they are expected to hold the record of every event observed, dropping none. RAW_DE packets, in contrast to SCI_DE packets, do not apply any qualification culling schemes to the events that they store. FSW version 4.1 was loaded at the very start of this cross-calibration.

3. The calibration map was used to create a linear plot of expected detection efficiency along the cross-calibration path, for a beam of approximately 4 mm across (an exact convolution is not necessary because Hi90 response does not depend sharply on where the beam enters, as long as the entire beam strikes the conversion foil).

4. The linear plots created at the two preceding steps were compared to confirm any general trends as a function of location (for example, a slight increase or decrease in detection efficiency related to distance from sensor's axis of symmetry).

5. The average rate away from the edges of the foil (where specifics of the convolution performed in step 3 could matter) was determined for the two linear plots, one from calibration and one from cross-calibration.

6. The vertical angle offset could not be determined in cross calibration as the alignment mirror was not visible in this configuration. Assuming a vertical angle consistent with previous measurements, a true-vertical mounting alignment during cross-calibration, and a collimator angular response on the order of 4° FWHM, this implies a collimator transmission function lowered by approximately 10% in cross-calibration compared to previous calibration, to within a few per cent. This correction factor was applied to the cross-calibration average detection efficiency.

7. The two average detection efficiency numbers were compared. In the cases of the two official measurements (12.7 and 8.5 keV), the measurements taken on consecutive days were used as a rough guide of the cross calibration uncertainty.

By this process, the idea is to determine to what degree the absolute detection efficiency of Hi90 changed between calibration and cross calibration over a fraction of the entrance aperture, and to use any factor found as an overall corrective scaling factor for calibration data. No differences in energy response and angular response are expected, or were tested for during cross-calibration: such changes would need to arise from a mechanical change in the sensor and not detector aging or contamination.

Success for the Hi-Ultra cross-calibration was defined as putting the same beam at one energy (of 12.7 and 8.5 keV) on both Hi and Ultra for long enough for each sensor to complete a scan at known (ideally, normal) incidence which gathered statistically useful information. The definition of the "same beam" was less than 10% variation in beam intensity as measured before and after with the ABM.

In all this analysis, it is necessary first to define a *calibration product*: in other words, what kind of signal from Hi90's detectors is required to register a "detected event"? Hi90 uses a three-detector, quadruple-coincidence scheme with time-of-flight (TOF) available to enforce qualification ranges for detected events. The entire ground processing chain, and the analysis of calibration and cross-calibration data, is designed to allow for redefining qualification schemes and for multiple differently designed calibration products. This is to allow for adjustments to work around backgrounds that may be observed on orbit.

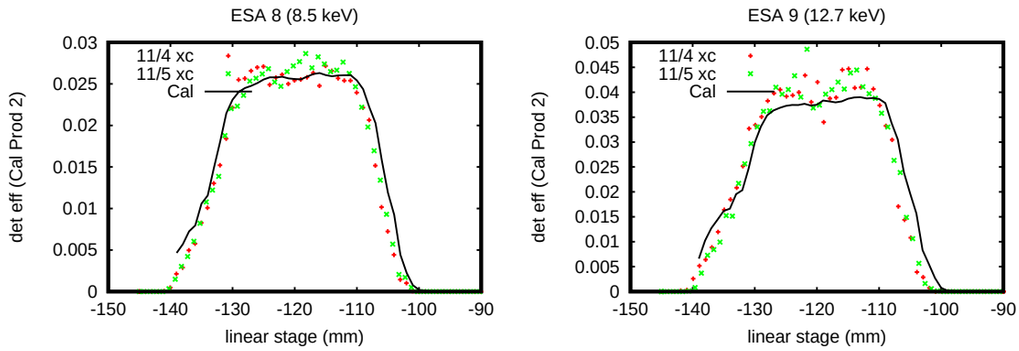
The following definitions were used for "detected event":

1. Matching the currently planned "Calibration Product 1", which is to be the lowest-background data product:

   - ABC1C2 quadruple coincidence, and ABC1 and AC1C2 triple coincidence (BC1C2 is excluded as it's less clean).
   - if A and B are present, $t_B - t_A$ must be in the range 15 to 80 ns.
   - if A and C1 are present, $t_C - t_A$ must be in the range -20 to 70 ns.
   - if B and C1 are present, $t_C - t_B$ must be in the range -50 to 20 ns.
   - if C1 and C2 are present, $t_{C2} - t_{C1}$ must be in the range 16/2 to 80/2 ns.

2. All double, triple, or quadruple coincidences except BC and BCC, with the same time ranges for AB, AC1, and BC1, but no time range required for C1 C2 (if C2 is present). This is based on the observation that C2 is the signal most susceptible to changes due to air exposure, and the observation that the BC coincidence is the one most susceptible to noise, because for both noise and signal, $t_B - t_C$ is expected to be nearly zero.

The comparison of calibration data to cross-calibration data for ESA 8 at 8.5 keV and ESA 9 at 12.7 keV, using Calibration Product 2, is plotted below, across the foil. As stated earlier, the exact behaviour at the edge of the foil is not the part to compare, as it is sensitive to specifics of the convolution in step 3. The part to compare is between linear stage locations of -130 and -110, when the 4 mm beam strikes entirely on the conversion foil. The total area under the curve in this range is the most statistically accurate comparison. The number of detected counts per cross calibration point plotted is on the order of 600, so the 1σ expected scatter from point to point is about $\pm 4\%$, similar to what is observed.



The summary of the information between calibration and cross-calibration is below. The numbers given in the three columns prior to the ratio is the detection efficiency of the sensor: what fraction of entering ENAs produce a valid signal consistent with the listed calibration product? The final column is a ratio of the detection efficiency seen in calibration to that seen in cross-calibration, with all discussed corrections applied (specifically, for polar angle). Ideally this ratio is unity.

		Orig cal	Nov 4 x cal	Nov 5 x cal	Ratio, cross-cal:cal
ESA 8	Cal Product 1	0.0186	0.0177	0.0184	0.967
	Cal Product 2	0.0461	0.0464	0.0472	1.015
ESA 9	Cal Product 1	0.0292	0.0287	0.0295	0.997
	Cal Product 2	0.0676	0.0717	0.0722	1.065

The chief uncertainties in this analysis are:

- uncertainty in the polar angle between the IMAP-Hi entrance aperture and the beam. In this analysis, the assumption was made of an approximately 0.4° offset from normal, consistent with beam characterization studies assuming perfect alignment of the assembly holding IMAP-Hi, corresponding to approximately a 10% reduction in beam intensity due to the collimator compared to normal incidence. However, this angle was not measured, and the estimate could easily be off by as much as $\pm 0.1°$ (1σ), which correlates to a $\pm 3\%$ systematic error in the comparison to calibration.
- uncertainty in exactly aligning the foil range being studied between the 2 mm circular beam in calibration and the 4 mm square beam in cross calibration. Slightly shifting the area being convolved with beam in the analysis indicated a typical uncertainty on the order of a couple per cent.
- ABM beam stability: although linear interpolation over time was used, beam drift may not be entirely linear. Before/after beam drift was as much as 2.3% in cross-cal and as much as 4.2% at ESA 9 when calibrating these particular conversion foils prior to cross-calibration. Additionally, during some of the earlier calibration there were further beam stability issues, as discussed above.

Adding these uncertainties in quadrature results in an overall uncertainty of slightly better than 5% (1σ) – well within the requirement of 10%. Within uncertainty, the performance of Hi90 in cross-calibration matches the earlier performance during calibration. The overall systematic uncertainty associated with a poorly known polar angle is large enough to preclude shifting calibration values as a result of cross-calibration, but small enough to declare agreement within uncertainties and within requirements.

Calibrating the ABM?

The preceding analysis of the Hi data from Hi-Ultra cross-cal linearly interpolates ABM data over time between ABM measurements, and is phrased in terms of determining the sensor's detection efficiency. Some prefer the data reported differently, in a manner more suited to an instrument going into a new facility: what beam count rate does the instrument claim it saw, using the previously determined calibration? This

number can then be compared to the ABM's average value during data collection (or at least the before/after ABM data average).

The inferred flux can be produced from the previous analysis by multiplying the ABM average value by the ratio produced in the final step of the analysis enumerated above. It's a fairly pointless way to make the comparison, but it's harmless enough. The table below contains these numbers, using Cal Product 1.

Measurement	ABM flux averaged before/after (/s)	Flux inferred from Hi90 (/s)
Nov 4, 8.5 keV	10368	9866
Nov 4, 12.7 keV	5420	5514
Nov 5, 8.5 keV	9733	9628
Nov 5, 12.7 keV	4805	4756

Lo-Hi Cross-Calibration

Hi45 was cross-calibrated with IMAP-Lo at the start of February 2025, in the LANL beam facility. A 2 mm circular aperture was used to define the beam. The species for cross-calibration was always neutral hydrogen (although during this cross-calibration campaign, Lo was calibrated with beams of other species as well), oriented as normal as possible to the instrument aperture. A Quantar imaging MCP was used to verify beam shape and size, and Hi45's deflectors were used to confirm that the beam was neutral. The table of beam energies and settings is below.

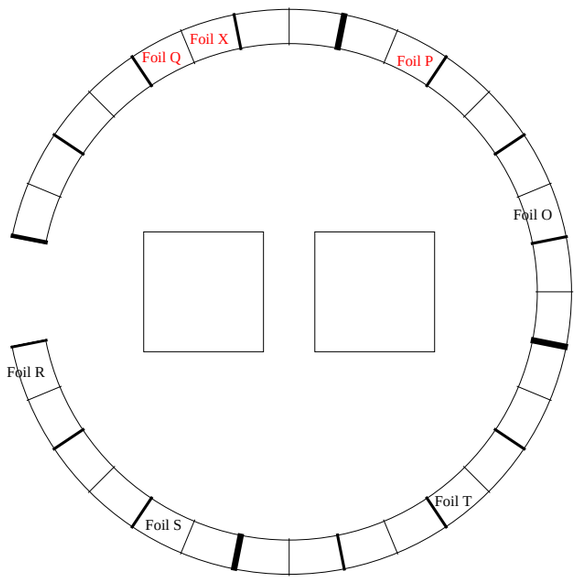
Date	Energy (eV)	ESA setting	Specific clock range	ABM before and after(/s)
Feb 7	930	3	1738956423 1738957351	40139, 40453
Feb 7	750	2	1738971781 1738972682	33882, 32662
Feb 7	500	1	1738974024 1738974908	27480, 26930

The mounting of Hi45 in this phase of cross-calibration was identical to that of Hi90 during Hi-Ultra cross-calibration, except that Hi45 faced the beam at an azimuth angle near 0° (Lo faced the beam at an azimuth near 180°). The same caveats concerning polar angle apply to the Lo-Hi cross-calibration as well. On Hi45, FSW4.1 was run during cross-calibration. FSW4.6 was loaded immediately after.

The crux of cross-calibration was exposing Lo and Hi to exactly the same beam in the same facility, to avoid any potential issues with transfer standards. Enough of the sensor aperture needed to be exposed to avoid large uncertainties in extrapolating sensor performance from the cross-cal measurements to the overall response of the sensor. Success for the Lo-Hi cross-calibration was defined as putting the same beam at two energies (of 500, 750, and 930 eV) on both Lo and Hi for long enough for each sensor to complete a scan at known (ideally, normal) incidence which gathered statistically useful information. The definition of the "same beam" was less than 10% variation in beam intensity as before and after with the ABM.

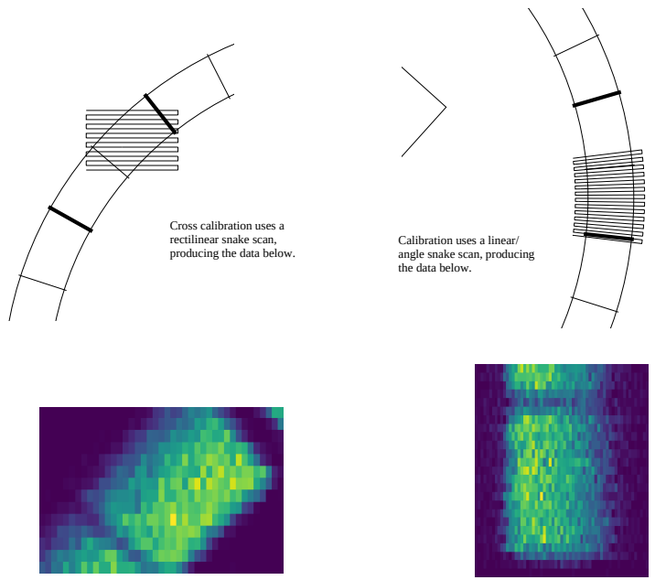
For Lo, most analysis was performed at specific spots on the entrance aperture with the assumption that performance there could be matched to performance over the entire entrance aperture using knowledge from calibration with Princeton's much larger beam; however, larger areas of the aperture were also scanned by moving Lo horizontally and vertically at a constant rate of 1 mm/s across the beam.

For Hi, full snake scans of one foil, at the usual 1 mm/s, were used. The portion of foil examined is shown in the figure below as Foil "X".



"Snake" scans during calibration were performed with IMAP-Hi positioned normal to the beam and vertically aligned so that the beam position on the sensor changed radially with horizontal linear stage motion. The linear stage motion began and ended with the beam entirely radially off the conversion foil, either radially inward or radially outward, and proceeded at 1 mm/s. Linear moves were alternated with steps in "FERRIS" of 0.555°, or a rotation of the instrument around its axis of symmetry, normal to the entrance aperture. These steps correspond approximately to shifting the beam 1.5 mm on the conversion foil.

In comparison, "snake" scans during cross-calibration were performed with the rotation replaced with a displacement in vertical ("LIFT"). The following diagrams make the difference clear.



Snake scans take about 12 minutes to run.

Due to time constraints, final calibration of Hi45 at 500, 750, and 908 eV did not put beam on the specific conversion foil pane tested in cross-cal – the one at a rotation angle of 101.25 - 112.5° clockwise from the

alignment mirror when looking at the entrance aperture (foil "X"). The closest foils tested were the one starting at 125.° (foil "Q") and the one ending at 67.5° (foil "P"), a few panes in either direction.

Hi45 performance during Lo-Hi cross-cal was compared to prior calibrated performance by the following analysis:

1. The average detection efficiency over foil panes "P", "Q", and "X" were determined from Phase 3 calibration data at central ESA energies for ESA settings 3, 4, and 5 (1.10, 1.65, and 2.50 keV). The behaviour of foil "X" compared to foils "P" and "Q" was established.

   As discussed in the Hi-Ultra cross-calibration, data was analyzed by position on the foil and normalized to ABM count rate linearly interpolated in time between the preceding and following ABM measurements to create a map of detection efficiency (detected events divided by incident beam intensity) over the area of the foil. Calibration direct event data comes from the FEE "fast DE" connection, bypassing C&DH processing.

   In averaging this type of snake scan (radial/rotational), one should weight the outer radial side of the calibration snake scans more heavily, as each data point collected there reflects the input of a larger area. Testing of algorithms revealed that, at least at the energies investigated in cross-calibration, the effect made no difference at the per cent level.

   Calibration across all panes at 1.1, 1.65, and 2.50 keV showed that detection efficiency for the data product being used here was the same to within $\approx 1\%$ for foils "X" and "Q", and consistently slightly lower for foil "X" than foil "P", by as much as 6% at higher energies.

2. The average detection efficiency over foil panes "P" and "Q" were determined from calibration data (as in the preceding step) at central ESA energies for ESA settings 1 and 2 (0.50 and 0.75 keV) and for calibration data taken at 0.908 keV. The average detection efficiency over foil "X" was inferred by comparison to foils "P" and "Q".

3. Phase 3 calibration data was taken at 908 eV and not at the 930 eV used in cross-calibration. Interpolating between energies in Phase 1 calibration, the geometric factor over the entire foil is expected to be 1.1106 times greater at 930 eV than at 908 eV. Thus, for the 930 eV cross-calibration, the 908 eV average detection efficiency over the foil was multiplied by this factor to facilitate comparison with 930 eV.

4. The vertical angle offset could not be determined in cross calibration because the alignment mirror was not visible in this configuration. Assuming a vertical angle consistent with previous measurements, a true-vertical mounting alignment during cross-calibration, and a collimator angular response on the order of 4° FWHM, this implies a collimator transmission function lowered by approximately 8% in cross-calibration compared to previous calibration, to within a few per cent. This correction factor was applied to the cross-calibration average detection efficiency.

5. The average detection efficiency over foil pane "X" during cross-calibration was determined at the three cross-calibration energies, using horizontal-vertical snake scan data normalized to ABM count rate linearly interpolated in time between the preceding and following ABM scans.

6. The two values for average detection efficiency over the foil – one from calibration, one from cross-calibration – were compared.

Lo-Hi cross-calibration occurred after Hi45 integration to and deintegration from the spacecraft. It was observed during cross calibration that a noise peak in the C1C2 TOF spectrum had shifted from outside the TOF range expected of ENAs to inside this range. As a result, the Hi45 "C2" signal became less useful as part of a qualification scheme. Therefore, the product used to compare Hi45 performance during cross-calibration with its performance earlier during calibration is calibration product 2, as defined in the Hi-Ultra cross-calibration. This product ignores both the timing and presence of C2 and thus is somewhat more robust against the difference in behaviour observed in Hi45 after its return from the spacecraft.

In the table below, the assumption is made of a similar polar angle misalignment as assumed for Hi-Ultra cross-calibration and observed in beam studies of approximately 0.35°. This factor is included in the

predicted efficiency of foil "X" to be compared to cross-cal. The uncertainty in this angle is the largest single contributor to the cross calibration uncertainty.

ESA	Energy (eV)	Cal eff, "P"	Cal eff, "Q"	Predicted Cal eff, "X"	Cross-cal eff, "X"	Ratio, xcal:cal
3	908/930	0.001721	0.001677	0.001727	0.001913	1.11
2	750	0.001655	0.001598	0.001481	0.001572	1.06
1	500	0.0005402	0.0005242	0.000488	0.000602	1.23

The difference between calibration efficiency and cross-calibration efficiency at this stage of analysis was unexpected.

Inasmuch as the C2 peak of the MCP detector clearly changed, the first follow-on analysis is to investigate the efficiency of each of the three detectors: CEMs A and B, and MCP C. In the calibration case of very low noise/background rates compared to bright signal rates from beam, the detector efficiencies can be reasonably constructed from "long" coincidences as follows:

$$\varepsilon_A = \frac{\text{All events with A, B, and C}}{\text{All events with B and C}} = \frac{l_{ABC} + l_{ABC1C2}}{l_{ABC} + l_{ABC1C2} + l_{BC} + l_{BC1C2}}$$

$$\varepsilon_B = \frac{\text{All events with A, B, and C}}{\text{All events with A and C}} = \frac{l_{ABC} + l_{ABC1C2}}{l_{ABC} + l_{ABC1C2} + l_{AC} + l_{AC1C2}}$$

$$\varepsilon_C = \frac{\text{All events with A, B, and C}}{\text{All events with A and B}} = \frac{l_{ABC} + l_{ABC1C2}}{l_{ABC} + l_{ABC1C2} + l_{AB}}$$

Efficiency data by detector is presented in the table below for calibration and cross-calibration. Calibration data is presented for foils "P" and "Q", and cross-calibration data for foil "X". Uncertainties based on Poisson statistics are not shown, as their effect is evident from the sub-percent jitter in efficiencies seen from energy to energy.

Energy	Detector efficiencies, cal	Detector efficiencies, cross-cal
908/930	$\varepsilon_A = 0.669, 0.638$ $\varepsilon_B = 0.712, 0.705$ $\varepsilon_C = 0.423, 0.429$	$\varepsilon_A = 0.657$ $\varepsilon_B = 0.719$ $\varepsilon_C = 0.510$
750	$\varepsilon_A = 0.661, 0.637$ $\varepsilon_B = 0.705, 0.696$ $\varepsilon_C = 0.414, 0.430$	$\varepsilon_A = 0.646$ $\varepsilon_B = 0.708$ $\varepsilon_C = 0.509$
500	$\varepsilon_A = 0.662, 0.615$ $\varepsilon_B = 0.704, 0.684$ $\varepsilon_C = 0.435, 0.426$	$\varepsilon_A = 0.647$ $\varepsilon_B = 0.708$ $\varepsilon_C = 0.513$

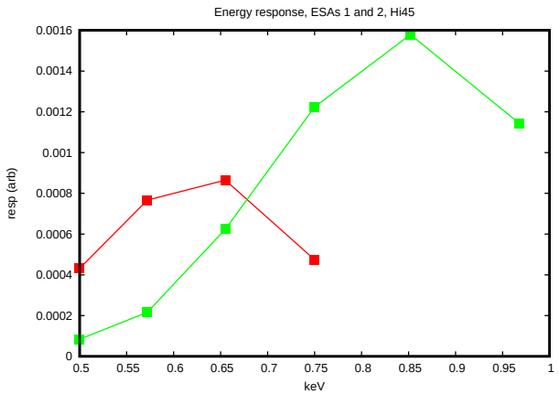
In short, the detection efficiency of the MCP appears to have increased by on the order of 20% since its original calibration (along with the noise peak shifting). Why the efficiency change occurred is not clear. MCP DQE is known to be affected by surface conditions, and likely the MCP was exposed to considerably more humidity just prior to the cross-calibration installation than during calibration in LANL (where there's a de facto permanent waiver on cleanroom humidity). Additionally, the amount of outgassing hardware in the chamber during cross-calibration was significantly higher than in calibration, and the pumpdown time was much shorter. Fortunately, MCP detection efficiency is a quantity that can be monitored and corrected for during the mission, as has been done for two of the three IBEX-Hi CEMs.

The calibration product used here is all double, triple, or quadruple coincidences including an "A": if we ignore the presence or absence of C2, the events are ABC + AC + AB, with overall detection efficiency $\varepsilon_A\varepsilon_B\varepsilon_C + \varepsilon_A(1-\varepsilon_B)\varepsilon_C + \varepsilon_A\varepsilon_B(1-\varepsilon_C) = \varepsilon_A(\varepsilon_B + \varepsilon_C - \varepsilon_B\varepsilon_C)$. Thus the detector section's expected detection efficiency during calibration is approximately 53.7% and during cross-calibration is approximately 55.8% (note that this is just one contributor to the overall sensor detection efficiency). The ratio of detector-section overall efficiency in cross-cal compared to calibration due to the enhanced detection efficiency of the MCP is 1.04. Thus, the MCP change alone is not enough on its own to explain the discrepancy between calibration and cross-calibration. However, this 4% correction brings the difference between calibration and cross-calibration to well inside the requirement of 10%, except for ESA 1.

The shift in ESA 1 is likely real and likely is associated with the relative ability of flight HVPS compared to COTS HVPS in maintaining the ESA voltages requested. The "central energy" E_c of the bandpass depends on the ESA voltages. As E_c decreases, the 10-20 V shift in supplied voltage compared to desired voltage makes a larger difference in actual ESA behaviour.

ESA Step (E_c)	Target V (Inner)	Target V (Outer)	Cal V (I)	Cal V (O)	Xcal V (I)	Xcal V (O)
1 (500 eV)	-472	+122	-474	+123	-466	+100
2 (750 eV)	-713	+164	-715	+165	-704	+143
3 (1.1 keV)	-1047	+213	-1049	+214	-1013	+190

E_c was generally specified at or below the actual peak response of an ESA step so as to be better representative of the typical ENA energy observed with a typical energy spectrum (*i.e.*, to minimize the "flux correction"). This may have been a lesson learned from IBEX. As a result, the lessening of ESA voltages by the flight HVPS compared to the intended voltages tends to lower the peak energy of the response and thus increase the detection efficiency at the nominal E_c, as is implied in the following plot of the energy response of Hi45 at ESA settings 1 and 2, as determined in "new phase 1" of calibration. In the plot, the lines are to guide the eye; data was taken only at the points. It is clear that E_c for both ESA 1 (500 eV) and ESA 2 (750 eV) is below the peak response in energy. Short of a SIMION campaign, it's worth noting for ESA setting 1 that the voltage difference between inner and outer analyzers is on order of E_c, and that shifting the ESA 1 energy response by $\approx$ 20 V, corresponding to the lessened voltage difference in the ESA, changes the response at 500 eV by about +20%, which is of the right magnitude to explain the discrepancy between cross-calibration and calibration.



The chief uncertainties in this analysis are:

- uncertainty in the polar angle between the IMAP-Hi entrance aperture and the beam. In this analysis, the assumption was made of an approximately 0.35° offset from normal, consistent with beam characterization studies assuming perfect alignment of the assembly holding IMAP-Hi, corresponding to approximately a 8% reduction in beam intensity due to the collimator compared to normal incidence. However, this angle was not measured, and the estimate could easily be off by as much as $\pm 0.1°$ (1σ), which correlates to a $\pm$3% systematic error in the comparison to calibration.

- uncertainty due to different voltages being applied to the ESAs by the flight HVPS compared to the COTS HVPS in calibration. This made a significant difference in ESA 1 (on the order of 20%) and likely a few per cent difference in ESAs 2 and 3. We assign a $\pm$5% uncertainty at 500 eV and a $\pm$2% uncertainty at 750 and 930 eV.

- uncertainty in the interpolation to 908 eV from calibration at 930 eV, particularly in light of the previous point. The uncertainty to apply here is unclear without exact knowledge of the energy response shape. Using a range of sensible energy response shapes for the inference, coupled with the uncertainties of the data itself, leads to an uncertainty of less than 5%.

- uncertainty in the efficiency correction determined from the long coincidence counts. This was a 4% correction that is good to better than 1%.
- ABM beam stability: although linear interpolation over time was used, beam drift may not be entirely linear, and was as much as 3.7% in cross-cal and as much as 3.7% at ESAs 1 and 3 when calibrating the neighbouring conversion foils prior to cross-calibration. Correlation of foil "X" compared to its neighbours introduced as much as a 1.5% uncertainty.

In total, adding in quadrature, the result is a 1σ uncertainty of about 7% at 500 and 930 eV and about 5% at 750 eV – all below the requirement of 10%. The final results are summarized in the table below.

ESA	Energy (eV)	Ratio, cross-cal efficiency to prior calibration efficiency
3	908/930	1.07 ± 0.07
2	750	1.02 ± 0.05
1	500	0.99 ± 0.07

The summary and takeaways from the Lo-Hi cross-calibration for IMAP-Hi are thus:

1. MCP efficiency was seen to change considerably since delivery. Tracking the efficiency of the three sections of the detector, which was planned, appears necessary. The shift in TOF of some background into the "valid ENA" range required a redefinition of TOF ranges; further redefinition may be required after launch, depending on backgrounds observed in space. The calibration analysis software has been set up to make this kind of reanalysis minimally painful.
2. The 10-20V offset in flight HVPS from requested voltages for the ESA has considerable effects in the lowest ESA step. ESA step 1 has always been the worst calibrated step in the sense that neutral ENAs with energies below $E_c = 500$ eV cannot be produced in meaningful quantities at the LANL calibration facility and thus no calibration data is collected over a significant fraction of this step's energy acceptance. Operation of the ESAs in flight at ESA voltages different from those in calibration appears to require further analysis (SIMION modelling) at ESA step 1 and possibly at ESA step 2. It is likely worth checking if increasing the commanded ESA voltages by a LSB would get closer to the intended operating voltage: it's likely that FSW truncates down and never rounds up.

   Additionally, the IMAP-Hi team should revisit what E_c values it would like to assert, now that calibration is complete.
3. Other than the two effects mentioned above, cross-calibration performance of Hi45 was well inside 10% of that determined in calibration, and no further adjustments to the calibration are warranted by cross calibration analysis.

Calibrating the ABM?

As with Hi-Ultra, one can take the various corrections and factors and end with a table of "predicted ABM count rate" compared to the actual. In the table that follows, a 0.35° polar angle offset has been estimated, and a scaling of 1.04 has been applied to account for the observed increased MCP detection efficiency. At 930 eV, a scaling factor of 1.11 has been used to adjust the calibration at 908 eV. At 500 eV, pending SIMION analysis, a correction of $\approx 20\%$ has been applied to account for the shifted ESA voltages.

Measurement	ABM flux averaged before/after (/s)	Flux inferred from Hi90 (/s)
930	40296	42919
750	33272	33958
500	27205	26891

Revision Log

April 4, 2025 Initial release

April 9, 2025 Very minor wording clarifications; addition of clear table of final Lo-Hi cross-cal:cal ratios and uncertainties.

3.11.4 IMAP-Hi & IMAP-Ultra

IMAP-Hi and IMAP-Ultra cross-calibration report embedded here

IMAP/CMAD 4

Data Processing Algorithms

4.1 Data Processing Background and Approach

The IMAP team processes, distributes, and archives Level 0 through Level 3 data to support IMAP operations and the science community. IMAP's Science Operations Center (SOC) is functionally divided into a Payload Operations Center (POC) for operations-related functions and a Science Data Center (SDC) for data production, management, and distribution functions. Figure 4.1 details the architecture of the SOC and how it is incorporated into IMAP's Mission Operations Center (MOC), antenna partners, and interfaces with the payload and greater community and archive centers. Backup and recovery mechanisms are employed at the SOC and include contingency plans for ensuring a full recovery from catastrophic damage or failure. This includes offline and offsite backup of all irreplaceable information, including software, calibration data, and other system dependencies.

The IMAP data pipeline team is responsible for IMAP science data management, distribution, and processing of selected data sets. In collaboration with the Instrument Teams, the pipeline team determines data storage and distribution mechanisms and ensures that data are processed and released to the public within the required time frames (indicated in the IMAP Mission Requirements Document).

The IMAP team uses the Common Data Format (CDF) standard for all publicly-available scientific data products. This will facilitate the use of IMAP data in multi-mission scientific studies and will allow the data to be used with existing tools. The Common Data Format (CDF) standard was chosen based on its proven capabilities, familiarity to the Instrument Teams and corresponding scientific communities, self-describing and/or multi-platform support, its use by other heliophysics missions (including SDO, Cluster, THEMIS, MMS, Van Allen Probes, and others), and as it is the default format at the final mission archive (NASA's Space Physics Data Facility).

Calibration data are parameters and other information used as input to the data processing software to facilitate generation of usable science products. In many cases, these calibration data are used for science data processing and are thus managed along with the associated science data products. Calibration data are produced and maintained by IMAP's Instrument Teams, whether they are produced during instrument development on the ground prior to launch or during routine calibration activities on-orbit, and will be delivered to the SPDF to become part of the IMAP archive at mission closeout.

Engineering and housekeeping (collectively, "ancillary" data) data are stored within the mission archive and will be provided to the SPDF for long-term archiving throughout the mission. Additionally, information about spacecraft events, ephemerides, and other ancillary data are also stored. A number of these products are actively served to the IMAP team for use in data processing and health/safety analyses.

IMAP uses the data level definitions defined in Table 4.1.

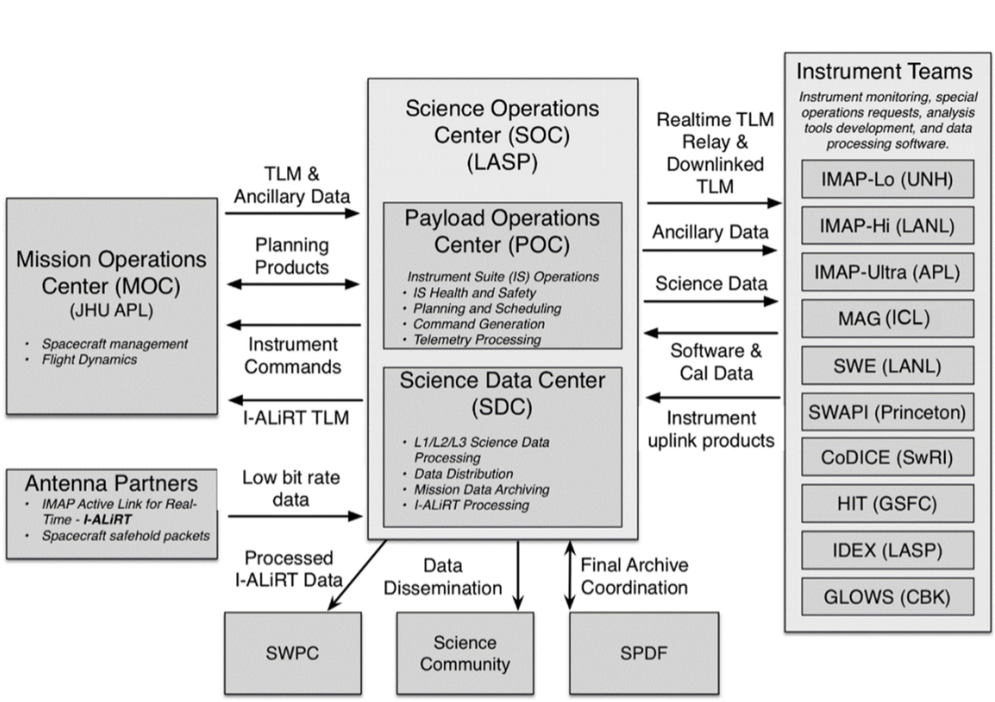


Figure 4.1: Overview of the IMAP ground system showing the key elements and linkages between them. Major functions for each element are also shown where appropriate.

IMAP Data Levels		
IMAP Data Level	**NASA PDS Data Level**	**Brief Description**
Raw	Raw	Raw telemetry data as received at the ground receiving station or ground test GSE, organized by contacts or ground test. Data sets may overlap and/or contain communication artifacts.
Level-0 (L0)	Partially Processed	Reconstructed, sequenced, gap-resolved, unprocessed instrument, payload, and spacecraft data; any and all communications artifacts, e.g., synchronization frames, communications headers, duplicate data are removed. These data will typically consist of binary CCSDS packets.
Level-1A (L1A)	Partially Processed	Fully decommutated but uncalibrated raw data at full resolution; time-referenced; "extracted telemetry items".
Level-1B (L1B)	Calibrated	Level-1A (extracted telemetry items) to which engineering (e.g. simple polynomial) calibrations have been applied; data have been annotated with ancillary information (e.g., ephemeris, attitude data) and initial instrument-level science calibrations have been applied.
Level-2 (L2)	Calibrated	Level-1 data that have been processed to physical units and/or derived geophysical parameters by combining calibration, ancillary, and other data. These data represent the lowest level of research grade scientific data and exist at the same time and/or spatial resolution as Level-1 data.
Level-3 (L3)	Derived	These data have been resampled spatially and/or temporally and may have been combined with measurements from other instruments to produce a merged data set.

Table 4.1: IMAP data level definitions.

Level-0 data are received by the IMAP data repository from the POC in the form of binary Consultative Committee for Space Data Systems (CCSDS) packets. These packets have been time-ordered with duplicates removed and contain the science data from each instrument. Further, any communication artifacts have been removed or corrected, including synchronization frames and communication headers. Level-0 data are not made publicly available but are archived along with all other mission data.

Level-1 data products take two different forms, a fully decommutated but uncalibrated data set at full resolution containing predominantly only "extracted telemetry items" and engineering data (Level-1A) and a calibrated data set that has instrument-level calibrations applied (Level-1B). Level-1A data are generally not of scientific use and therefore not made publicly available, whereas Level-1B data may be released as intermediate science data products to the community through standard data access interfaces at the

discretion of each instrument team. IMAP L1 data are described in Table 4.1.

IMAP Level-1 Products	
Instrument	**L1 Product Description**
SWAPI	H^+, He^+, He^{2+} combined counts binned by energy and spin sector
CoDICE	Ion count rates binned by mass, energy, azimuth, and spin sector
HIT	Energetic particle count rates binned by mass, energy, and spin sector
SWE	Electron counts binned by energy and spin sector
MAG	Vector magnetic fields in body centered coordinates
IMAP-Lo	Time-tagged coincident events, singles rates, and histograms
IMAP-Hi	Time-tagged coincident events, singles rates, and histograms
IMAP-Ultra	Time-tagged coincident events, singles rates, and histograms
IDEX	Time tagged coincident target and ion grid waveforms and TOF spectrum
GLOWS	Lyman-α counts binned by spin sector

Table 4.2: IMAP L1 product descriptions.

Level-2 data are Level-1 data that have been processed to physical units and/or derived physical parameters by combining calibration, ancillary, and other data. These data represent the lowest level of research grade scientific data and exist at the same time and/or spatial resolution as Level-1 data. All data products include data quality flags and uncertainties as appropriate to aid in accurate understanding of correct data use. IMAP L2 data are described in Table 4.1.

IMAP Level-2 Products	
Instrument	**L1 Product Description**
SWAPI	H^+, He^+, He^{2+} fluxes binned by energy and pitch angle
CoDICE	Ion fluxes binned by mass, energy, and pitch angle
HIT	Energetic particle fluxes binned by mass, energy, and pitch angle
SWE	Electron fluxes binned by energy and pitch angle
MAG	B-field vector in body centered and physical coordinates
IMAP-Lo	O, He, H ISN neutral rates; accumulated H ENA distribution vs energy and incident direction
IMAP-Hi	Accumulated H ENA distributions vs energy and incident direction
IMAP-Ultra	Accumulated H ENA distributions vs energy and incident direction
IDEX	Time-tagged validated impact and grid charge, TOF spectrum in physical units
GLOWS	Background subtracted Lyman-α counts vs time, ecliptic coordinates, and heliolatitude

Table 4.3: IMAP L2 product descriptions.

Include details of IMAP L3 data here and I-ALiRT data

Include details of I-ALiRT data here

Execution of science processing software commences daily using IT-provided algorithms, with Level-1B, Level-2, and Level-3 products being made available to the IMAP Science Team for review. Level-2 data are in physical units for all appropriate quantities, based on best current calibration factors and analysis routines. Reprocessing can occur throughout the operational mission if significant advances in instrument calibration and understanding warrant the production of a new data version. Version control systems are utilized in the data pipeline and by the Instrument Teams to ensure that changes in calibration and reprocessing are tracked and are transparent to the scientific user receiving data from the SDC.

In addition to raw telemetry and other ancillary data that are needed to support science processing by the Instrument Teams, there are a number of interdependencies between instrument processing algorithms. Data products that other teams depend on (e.g., magnetometer data) are provided via programmer-level interfaces once that data is available to be processed. For convenience, these interfaces work in much the same way as the interfaces that are used to access telemetry and ancillary data. Specific data processing needs and dependencies for each of the IMAP instruments are detailed in the sections below.

4.1.1 IMAP CDF Data File Contents

IMAP's Level-2 (L2) and Level-3 (L3) CDF data files contain the following contents:

Contents

1 imap_codice_l2_hi-direct-events 4

2 imap_codice_l2_hi-omni 7

3 imap_codice_l2_hi-sectored 10

4 imap_codice_l2_lo-direct-events 13

5 imap_codice_l2_lo-sw-species 18

6 imap_codice_l3a_hi-direct-events 27

7 imap_codice_l3a_lo-direct-events 31

8 imap_codice_l3a_lo-partial-densities 37

9 imap_codice_l3a_lo-sw-charge-state-distributions 40

10 imap_codice_l3a_lo-sw-ratios 41

11 imap_codice_l3b_hi-pitch-angle 42

12 imap_glows_l2_hist 45

13 imap_glows_l3a_hist 52

14 imap_glows_l3b_ion-rate-profile 56

15 imap_glows_l3c_sw-profile 58

16 imap_glows_l3d_solar-hist 60

17 imap_glows_l3e_survival-probability-hi-45 63

18 imap_glows_l3e_survival-probability-hi-90 65

19 imap_glows_l3e_survival-probability-lo 68

20 imap_glows_l3e_survival-probability-ul-hf 70

21 imap_glows_l3e_survival-probability-ul-sf 73

22 imap_hit_l2_standard-intensity 76

23 imap_hit_l2_summed-intensity 95

24 imap_idex_l2a_sci-10days 114

IMAP CDF summary

25 imap_mag_l2_burst-dsrf **123**

26 imap_mag_l2_burst-gse **125**

27 imap_mag_l2_burst-gsm **126**

28 imap_mag_l2_burst-rtn **128**

29 imap_mag_l2_burst-srf **130**

30 imap_mag_l2_norm-dsrf **131**

31 imap_mag_l2_norm-gse **133**

32 imap_mag_l2_norm-gsm **134**

33 imap_mag_l2_norm-rtn **136**

34 imap_mag_l2_norm-srf **138**

35 imap_swapi_l2_sci **139**

36 imap_swapi_l3a_alpha-sw **142**

37 imap_swapi_l3a_proton-sw **144**

38 imap_swapi_l3b_combined **146**

39 imap_swe_l2_sci **147**

40 imap_swe_l3_sci **150**

1 imap_codice_l2_hi-direct-events

CoDICE>Compact Dual Ion Composition Experiment
L2_hi-direct-events>Level-2 Hi Event Data
The Compact Dual Ion Composition Experiment (CoDICE) will measure the distributions and composition of interstellar pickup ions (PUIs), particles that make it through the heliosheath into the heliosphere. CoDICE also collects and characterizes solar wind ions including the mass and composition of highly energized particles (called suprathermal) from the Sun. CoDICE combines an electrostatic analyzer (ESA) with a Time-Of-Flight versus Energy (TOF / E) subsystem to simultaneously measure the velocity, arrival direction, ionic charge state, and mass of specific species of ions in the LISM. CoDICE also has a path for higher energy particles to skip the ESA but still get measured by the common TOF / E system. These measurements are critical in determining the Local Interstellar Medium (LISM) composition and flow properties, the origin of the enigmatic suprathermal tails on the solar wind distributions and advance understanding of the acceleration of particles in the heliosphere.
Users should acknowledge the sources of data used in all publications, presentations, and reports using an appropriate DOI. Appropriate acknowledgement to institutions, personnel, and funding agencies should be given, including acknowledging the IMAP Mission Principal Investigator, Prof. David J. McComas of Princeton University (Contract #80GSFC19C0027). IMAP Rules-of-the-Road for data usage can be found in the IMAP CMAD.

1.1 Data

1.1.1 Data Quality Flag

`data_quality`

Data Quality Flag per Priority (0=good, 1=suspect) (0=good)
`SPASE>Support>SupportQuantity:DataQuality`
Size: 6 time-varying
    Direct-event telemetry priority level (0-5) 0 – 5 (6 bins)
Quality flag propagated from the packet-level suspect bit for each direct-event priority bin. 0 = good packet group. 1 = suspect packet group. 65535 = fill when no direct-event data are present for the priority bin.

1.1.2 Elevation Angle

`elevation_angle`

(degrees)
`SPASE>Particle>ParticleType:Ion,ParticleQuantity:ArrivalDirection,Qualifier:DirectionAngle.Eleva`
Size: 6×10000 time-varying
    Direct-event telemetry priority level (0-5) 0 – 5 (6 bins)
    Event Number 0 – 9999 (10000 bins)

1.1.3 Energy per Nucleon

`energy_per_nuc`

(MeV/nuc)
`SPASE>Support>SupportQuantity:Other`
Size: 6×10000 time-varying
Direct-event telemetry priority level (0-5) 0 – 5 (6 bins)
Event Number 0 – 9999 (10000 bins)

1.1.4 Gain

`gain`

Gain Setting
`SPASE>Support>SupportQuantity:Other`
Size: 6×10000 time-varying
Direct-event telemetry priority level (0-5) 0 – 5 (6 bins)
Event Number 0 – 9999 (10000 bins)

1.1.5 Multi Flag

`multi_flag`

Multiple Event Flag
`SPASE>Support>SupportQuantity:DataQuality`
Size: 6×10000 time-varying
Direct-event telemetry priority level (0-5) 0 – 5 (6 bins)
Event Number 0 – 9999 (10000 bins)

1.1.6 Number of Events

`num_events`

Number of Events per Priority
`SPASE>Support>SupportQuantity:Other`
Size: 6 time-varying
Direct-event telemetry priority level (0-5) 0 – 5 (6 bins)

1.1.7 Spin Angle

`spin_angle`

(degrees)
SPASE>Particle>ParticleType:Ion,ParticleQuantity:ArrivalDirection,Qualifier:DirectionAngle.Azimu
Size: 6 × 10000 time-varying
Direct-event telemetry priority level (0-5) 0 – 5 (6 bins)
Event Number 0 – 9999 (10000 bins)

1.1.8 SSD Energy

ssd_energy

(keV)
SPASE>Particle>ParticleType:Ion,ParticleQuantity:Energy
Size: 6 × 10000 time-varying
Direct-event telemetry priority level (0-5) 0 – 5 (6 bins)
Event Number 0 – 9999 (10000 bins)

1.1.9 SSD ID

ssd_id

SSD Identifier
SPASE>Support>SupportQuantity:Other
Size: 6 × 10000 time-varying
Direct-event telemetry priority level (0-5) 0 – 5 (6 bins)
Event Number 0 – 9999 (10000 bins)

1.1.10 Time of Flight

tof

(ns)
SPASE>Particle>ParticleType:Ion,ParticleQuantity:TimeOfFlight
Size: 6 × 10000 time-varying
Direct-event telemetry priority level (0-5) 0 – 5 (6 bins)
Event Number 0 – 9999 (10000 bins)

1.1.11 PHA Type Code

type

PHA type code: 0=TCR, 1=DCR, 2=SSD-only
SPASE>Support>SupportQuantity:Other
Size: 6 × 10000 time-varying

Direct-event telemetry priority level (0-5) 0 – 5 (6 bins)
Event Number 0 – 9999 (10000 bins)
PHA type code for CoDICE-Hi direct events. 0 = TCR (Triple Coincidence Rate; ST+SP+APD), 1 = DCR (Double Coincidence Rate; ST+SP), 2 = SSD-only energy event (SSD only or ST+SSD only).

1.2 Support Data

1.2.1 Spin Number

`spin_number`

`SPASE>Support>SupportQuantity:Other`
Size: 6×10000 time-varying
Direct-event telemetry priority level (0-5) 0 – 5 (6 bins)
Event Number 0 – 9999 (10000 bins)

1.2.2 Spin Sector Index

`spin_sector`

`SPASE>Support>SupportQuantity:Positional`
Size: 6×10000 time-varying
Direct-event telemetry priority level (0-5) 0 – 5 (6 bins)
Event Number 0 – 9999 (10000 bins)

2 imap_codice_l2_hi-omni

CoDICE>Compact Dual Ion Composition Experiment
L2_hi-omni>Level-2 Hi Omnidirectional Species Intensities Data
The Compact Dual Ion Composition Experiment (CoDICE) will measure the distributions and composition of interstellar pickup ions (PUIs), particles that make it through the heliosheath into the heliosphere. CoDICE also collects and characterizes solar wind ions including the mass and composition of highly energized particles (called suprathermal) from the Sun. CoDICE combines an electrostatic analyzer (ESA) with a Time-Of-Flight versus Energy (TOF / E) subsystem to simultaneously measure the velocity, arrival direction, ionic charge state, and mass of specific species of ions in the LISM. CoDICE also has a path for higher energy particles to skip the ESA but still get measured by the common TOF / E system. These measurements are critical in determining the Local Interstellar Medium (LISM) composition and flow properties, the origin of the enigmatic suprathermal tails on the solar wind distributions and advance understanding of the acceleration of particles in the heliosphere.
Users should acknowledge the sources of data used in all publications, presentations, and reports using an appropriate DOI. Appropriate acknowledgement to institutions, personnel, and funding

agencies should be given, including acknowledging the IMAP Mission Principal Investigator, Prof. David J. McComas of Princeton University (Contract #80GSFC19C0027). IMAP Rules-of-the-Road for data usage can be found in the IMAP CMAD.

2.1 Data

2.1.1 Differential Intensity - C

`c`

Differential intensity for C at root-2-spaced energy-per-nucleon channels (# / cm2 s sr MeV/nuc)
`SPASE>Particle>ParticleType:Ion,ParticleQuantity:NumberFlux,Qualifier:Differential`
Size: 18 time-varying

Geometric mean energy per nucleon for C 0 – 9 MeV/nuc (18 bins)

2.1.2 Data Quality

`data_quality`

Data Quality (0=good, 1=suspect) (0=good)
`SPASE>Support>SupportQuantity:DataQuality`
time-varying
Quality flag propagated from the packet-level suspect bit. 0 = good data. 1 = suspect data. 255 = fill when no data are present.

2.1.3 Differential Intensity - Fe

`fe`

Differential intensity for Fe at root-2-spaced energy-per-nucleon channels (# / cm2 s sr MeV/nuc)
`SPASE>Particle>ParticleType:Ion,ParticleQuantity:NumberFlux,Qualifier:Differential`
Size: 18 time-varying

Geometric mean energy per nucleon for Fe 0 – 9 MeV/nuc (18 bins)

2.1.4 Differential Intensity - H

`h`

Differential intensity for H at root-2-spaced energy-per-nucleon channels (# / cm2 s sr MeV/nuc)
`SPASE>Particle>ParticleType:Ion,ParticleQuantity:NumberFlux,Qualifier:Differential`
Size: 15 time-varying

Geometric mean energy per nucleon for H 0 – 3 MeV/nuc (15 bins)

2.1.5 Differential Intensity - He3

`he3`

Differential intensity for He3 at root-2-spaced energy-per-nucleon channels (# / cm2 s sr MeV/nuc)
`SPASE>Particle>ParticleType:Ion,ParticleQuantity:NumberFlux,Qualifier:Differential`
Size: 15 time-varying
Geometric mean energy per nucleon for He3 0 – 3 MeV/nuc (15 bins)

2.1.6 Differential Intensity - He4

`he4`

Differential intensity for He4 at root-2-spaced energy-per-nucleon channels (# / cm2 s sr MeV/nuc)
`SPASE>Particle>ParticleType:Ion,ParticleQuantity:NumberFlux,Qualifier:Differential`
Size: 15 time-varying
Geometric mean energy per nucleon for He4 0 – 3 MeV/nuc (15 bins)

2.1.7 Differential Intensity - Junk

`junk`

Differential intensity for Junk (unclassified counts) at root-2-spaced energy-per-nucleon channels (# / cm2 s sr MeV/nuc)
`SPASE>Particle>ParticleType:Ion,ParticleQuantity:NumberFlux,Qualifier:Differential`
Size: 1 time-varying
Geometric mean energy per nucleon for Junk 0 – 0 MeV/nuc (1 bins)
Catch-all bin for counts that do not fall into any CoDICE Hi species classification bin.

2.1.8 Differential Intensity - Ne+Mg+Si

`ne_mg_si`

Differential intensity for Ne+Mg+Si at root-2-spaced energy-per-nucleon channels (# / cm2 s sr MeV/nuc)
`SPASE>Particle>ParticleType:Ion,ParticleQuantity:NumberFlux,Qualifier:Differential`
Size: 15 time-varying
Geometric mean energy per nucleon for Ne+Mg+Si 0 – 3 MeV/nuc (15 bins)

2.1.9 Differential Intensity - O

`o`

Differential intensity for O at root-2-spaced energy-per-nucleon channels (# / cm2 s sr MeV/nuc)
`SPASE>Particle>ParticleType:Ion,ParticleQuantity:NumberFlux,Qualifier:Differential`
Size: 18 time-varying
Geometric mean energy per nucleon for O 0 – 9 MeV/nuc (18 bins)

2.1.10 Differential Intensity - Ultra-Heavy

`uh`

Differential intensity for Ultra-Heavy ions at root-2-spaced energy-per-nucleon channels (# / cm2 s sr MeV/nuc)
`SPASE>Particle>ParticleType:Ion,ParticleQuantity:NumberFlux,Qualifier:Differential`
Size: 5 time-varying
Geometric mean energy per nucleon for Ultra-Heavy ions 0 – 0 MeV/nuc (5 bins)

3 imap_codice_l2_hi-sectored

CoDICE>Compact Dual Ion Composition Experiment
L2_hi-sectored>Level-2 Hi Sectored Species Intensities Data
The Compact Dual Ion Composition Experiment (CoDICE) will measure the distributions and composition of interstellar pickup ions (PUIs), particles that make it through the heliosheath into the heliosphere. CoDICE also collects and characterizes solar wind ions including the mass and composition of highly energized particles (called suprathermal) from the Sun. CoDICE combines an electrostatic analyzer (ESA) with a Time-Of-Flight versus Energy (TOF / E) subsystem to simultaneously measure the velocity, arrival direction, ionic charge state, and mass of specific species of ions in the LISM. CoDICE also has a path for higher energy particles to skip the ESA but still get measured by the common TOF / E system. These measurements are critical in determining the Local Interstellar Medium (LISM) composition and flow properties, the origin of the enigmatic suprathermal tails on the solar wind distributions and advance understanding of the acceleration of particles in the heliosphere.
Users should acknowledge the sources of data used in all publications, presentations, and reports using an appropriate DOI. Appropriate acknowledgement to institutions, personnel, and funding agencies should be given, including acknowledging the IMAP Mission Principal Investigator, Prof. David J. McComas of Princeton University (Contract #80GSFC19C0027). IMAP Rules-of-the-Road for data usage can be found in the IMAP CMAD.

3.1 Data

3.1.1 Differential Intensity - CNO

`cno`

Differential intensity for CNO by energy, spin sector, and elevation at x2-spaced energy-per-nucleon

channels (# / cm2 s sr MeV/nuc)
SPASE>Particle>ParticleType:Ion,ParticleQuantity:NumberFlux,Qualifier:Differential
Size: $8 \times 12 \times 12$ time-varying
Geometric mean energy per nucleon for CNO 0 – 4 MeV/nuc (8 bins)
Spin Sector Index 0 – 11 (12 bins)
Elevation Angle 30 – 150 degrees (12 bins)

3.1.2 Data Quality

data_quality

Data Quality (0=good, 1=suspect) (0=good)
SPASE>Support>SupportQuantity:DataQuality
time-varying
Quality flag propagated from the packet-level suspect bit. 0 = good data. 1 = suspect data. 255 = fill when no data are present.

3.1.3 Differential Intensity - Fe

fe

Differential intensity for Fe by energy, spin sector, and elevation at x2-spaced energy-per-nucleon channels (# / cm2 s sr MeV/nuc)
SPASE>Particle>ParticleType:Ion,ParticleQuantity:NumberFlux,Qualifier:Differential
Size: $8 \times 12 \times 12$ time-varying
Geometric mean energy per nucleon for Fe 0 – 4 MeV/nuc (8 bins)
Spin Sector Index 0 – 11 (12 bins)
Elevation Angle 30 – 150 degrees (12 bins)

3.1.4 Differential Intensity - H

h

Differential intensity for H by energy, spin sector, and elevation at x2-spaced energy-per-nucleon channels (# / cm2 s sr MeV/nuc)
SPASE>Particle>ParticleType:Ion,ParticleQuantity:NumberFlux,Qualifier:Differential
Size: $8 \times 12 \times 12$ time-varying
Geometric mean energy per nucleon for H 0 – 4 MeV/nuc (8 bins)
Spin Sector Index 0 – 11 (12 bins)
Elevation Angle 30 – 150 degrees (12 bins)

3.1.5 Differential Intensity - He3+He4

`he3he4`

Differential intensity for He3+He4 by energy, spin sector, and elevation at x2-spaced energy-per-nucleon channels (# / cm2 s sr MeV/nuc)
`SPASE>Particle>ParticleType:Ion,ParticleQuantity:NumberFlux,Qualifier:Differential`
Size: $8 \times 12 \times 12$ time-varying
Geometric mean energy per nucleon for He3+He4 0 – 4 MeV/nuc (8 bins)
Spin Sector Index 0 – 11 (12 bins)
Elevation Angle 30 – 150 degrees (12 bins)

3.1.6 Uncertainty - CNO

`unc_cno`

Uncertainty in differential intensity for CNO by energy, spin sector, and elevation at x2-spaced energy-per-nucleon channels (# / cm2 s sr MeV/nuc)
Size: $8 \times 12 \times 12$ time-varying
Geometric mean energy per nucleon for CNO 0 – 4 MeV/nuc (8 bins)
Spin Sector Index 0 – 11 (12 bins)
Elevation Angle 30 – 150 degrees (12 bins)

3.1.7 Uncertainty - Fe

`unc_fe`

Uncertainty in differential intensity for Fe by energy, spin sector, and elevation at x2-spaced energy-per-nucleon channels (# / cm2 s sr MeV/nuc)
Size: $8 \times 12 \times 12$ time-varying
Geometric mean energy per nucleon for Fe 0 – 4 MeV/nuc (8 bins)
Spin Sector Index 0 – 11 (12 bins)
Elevation Angle 30 – 150 degrees (12 bins)

3.1.8 Uncertainty - H

`unc_h`

Uncertainty in differential intensity for H by energy, spin sector, and elevation at x2-spaced energy-per-nucleon channels (# / cm2 s sr MeV/nuc)
Size: $8 \times 12 \times 12$ time-varying
Geometric mean energy per nucleon for H 0 – 4 MeV/nuc (8 bins)
Spin Sector Index 0 – 11 (12 bins)

Elevation Angle 30 – 150 degrees (12 bins)

3.1.9 Uncertainty - He3+He4

`unc_he3he4`

Uncertainty in differential intensity for He3+He4 by energy, spin sector, and elevation at x2-spaced energy-per-nucleon channels (# / cm2 s sr MeV/nuc)
Size: $8 \times 12 \times 12$ time-varying
Geometric mean energy per nucleon for He3+He4 0 – 4 MeV/nuc (8 bins)
Spin Sector Index 0 – 11 (12 bins)
Elevation Angle 30 – 150 degrees (12 bins)

3.2 Support Data

3.2.1 Spin Angle

`spin_angle`

(degrees)
`SPASE>Particle>ParticleType:Ion,ParticleQuantity:ArrivalDirection,Qualifier:DirectionAngle.Azimu`
Size: 12imes12 constant
Spin Sector Index 0 – 11 (12 bins)
Elevation Angle 30 – 150 degrees (12 bins)

4 imap_codice_l2_lo-direct-events

CoDICE>Compact Dual Ion Composition Experiment
L2_lo-direct-events>Level-2 Lo Event Data
The Compact Dual Ion Composition Experiment (CoDICE) will measure the distributions and composition of interstellar pickup ions (PUIs), particles that make it through the heliosheath into the heliosphere. CoDICE also collects and characterizes solar wind ions including the mass and composition of highly energized particles (called suprathermal) from the Sun. CoDICE combines an electrostatic analyzer (ESA) with a Time-Of-Flight versus Energy (TOF / E) subsystem to simultaneously measure the velocity, arrival direction, ionic charge state, and mass of specific species of ions in the LISM. CoDICE also has a path for higher energy particles to skip the ESA but still get measured by the common TOF / E system. These measurements are critical in determining the Local Interstellar Medium (LISM) composition and flow properties, the origin of the enigmatic suprathermal tails on the solar wind distributions and advance understanding of the acceleration of particles in the heliosphere.
Users should acknowledge the sources of data used in all publications, presentations, and reports using an appropriate DOI. Appropriate acknowledgement to institutions, personnel, and funding agencies should be given, including acknowledging the IMAP Mission Principal Investigator, Prof.

David J. McComas of Princeton University (Contract #80GSFC19C0027). IMAP Rules-of-the-Road for data usage can be found in the IMAP CMAD.

4.1 Data

4.1.1 APD Energy

`apd_energy`

(keV)
`SPASE>Particle>ParticleType:Ion,ParticleQuantity:Energy`
Size: 8×10000 time-varying
Direct-event telemetry priority level (0-7) 0 – 7 (8 bins)
Event Number 0 – 9999 (10000 bins)

4.1.2 APD ID

`apd_id`

APD Identifier
`SPASE>Support>SupportQuantity:Other`
Size: 8×10000 time-varying
Direct-event telemetry priority level (0-7) 0 – 7 (8 bins)
Event Number 0 – 9999 (10000 bins)

4.1.3 Data Quality Flag

`data_quality`

Data Quality Flag per Priority (0=good, 1=suspect) (0=good)
`SPASE>Support>SupportQuantity:DataQuality`
Size: 8 time-varying
Direct-event telemetry priority level (0-7) 0 – 7 (8 bins)
Quality flag propagated from the packet-level suspect bit for each direct-event priority bin. 0 = good packet group. 1 = suspect packet group. 65535 = fill when no direct-event data are present for the priority bin.

4.1.4 Elevation Angle

`elevation_angle`

(degrees)
`SPASE>Particle>ParticleType:Ion,ParticleQuantity:ArrivalDirection,Qualifier:DirectionAngle.Eleva`

Size: 8×10000 time-varying
Direct-event telemetry priority level (0-7) 0 – 7 (8 bins)
Event Number 0 – 9999 (10000 bins)

4.1.5 Energy per Charge

`energy_per_charge`

(keV/q)
`SPASE>Particle>ParticleType:Ion,ParticleQuantity:EnergyPerCharge`
Size: 8×10000 time-varying
Direct-event telemetry priority level (0-7) 0 – 7 (8 bins)
Event Number 0 – 9999 (10000 bins)

4.1.6 Energy Step

`energy_step`

Energy Step Index
`SPASE>Support>SupportQuantity:Other`
Size: 8×10000 time-varying
Direct-event telemetry priority level (0-7) 0 – 7 (8 bins)
Event Number 0 – 9999 (10000 bins)

4.1.7 Gain

`gain`

Gain Setting
`SPASE>Support>SupportQuantity:Other`
Size: 8×10000 time-varying
Direct-event telemetry priority level (0-7) 0 – 7 (8 bins)
Event Number 0 – 9999 (10000 bins)

4.1.8 Multi Flag

`multi_flag`

Multiple Event Flag
`SPASE>Support>SupportQuantity:DataQuality`
Size: 8×10000 time-varying
Direct-event telemetry priority level (0-7) 0 – 7 (8 bins)

Event Number 0 – 9999 (10000 bins)

4.1.9 NSO Energy Step

`nso_esa_step`

Energy Step When No Scan Operation (NSO) was activated (energy step)
time-varying
Indicates the energy step when No Scan Operation (NSO) was activated. In NSO, the ESA voltage is set to the first step in the scan and remains fixed until the next cycle boundary.

4.1.10 NSO Half Spin

`nso_half_spin`

When No Scan Operation (NSO) was activated (half spin number)
time-varying
Indicates the half spin when No Scan Operation (NSO) was activated. In NSO, the ESA voltage is set to the first step in the scan and remains fixed until the next cycle boundary.

4.1.11 NSO Spin Sector

`nso_spin_sector`

Spin Sector When No Scan Operation (NSO) was activated (spin sector)
time-varying
Indicates the spin sector when No Scan Operation (NSO) was activated. In NSO, the ESA voltage is set to the first step in the scan and remains fixed until the next cycle boundary.

4.1.12 Number of Events

`num_events`

Number of Events per Priority
`SPASE>Support>SupportQuantity:Other`
Size: 8 time-varying
Direct-event telemetry priority level (0-7) 0 – 7 (8 bins)

4.1.13 Position

`position`

IMAP CDF summary

Position Index
SPASE>Support>SupportQuantity:Other
Size: 8 × 10000 time-varying
Direct-event telemetry priority level (0-7) 0 – 7 (8 bins)
Event Number 0 – 9999 (10000 bins)

4.1.14 Spin Angle

spin_angle

(degrees)
SPASE>Particle>ParticleType:Ion,ParticleQuantity:ArrivalDirection,Qualifier:DirectionAngle.Azimu
Size: 8 × 10000 time-varying
Direct-event telemetry priority level (0-7) 0 – 7 (8 bins)
Event Number 0 – 9999 (10000 bins)

4.1.15 Time of Flight

tof

(ns)
SPASE>Particle>ParticleType:Ion,ParticleQuantity:TimeOfFlight
Size: 8 × 10000 time-varying
Direct-event telemetry priority level (0-7) 0 – 7 (8 bins)
Event Number 0 – 9999 (10000 bins)

4.1.16 PHA Type Code

type

PHA type code: 0=TCR, 1=DCR, 2=APD-only
SPASE>Support>SupportQuantity:Other
Size: 8 × 10000 time-varying
Direct-event telemetry priority level (0-7) 0 – 7 (8 bins)
Event Number 0 – 9999 (10000 bins)
PHA type code for CoDICE-Lo direct events. 0 = TCR (Triple Coincidence Rate; STA+STB+SP+APD), 1 = DCR (Double Coincidence Rate; STA+STB+SP), 2 = APD-only energy event (APD with only one or two of STA, STB, and SP).

4.2 Support Data

4.2.1 Spin Sector Index

`spin_sector`

`SPASE>Support>SupportQuantity:Positional`
Size: 8×10000 time-varying
Direct-event telemetry priority level (0-7) 0 – 7 (8 bins)
Event Number 0 – 9999 (10000 bins)

5 imap_codice_l2_lo-sw-species

CoDICE>Compact Dual Ion Composition Experiment
L2_lo-sw-species>Level-2 Lo Sunward Species Intensities Data
The Compact Dual Ion Composition Experiment (CoDICE) will measure the distributions and composition of interstellar pickup ions (PUIs), particles that make it through the heliosheath into the heliosphere. CoDICE also collects and characterizes solar wind ions including the mass and composition of highly energized particles (called suprathermal) from the Sun. CoDICE combines an electrostatic analyzer (ESA) with a Time-Of-Flight versus Energy (TOF / E) subsystem to simultaneously measure the velocity, arrival direction, ionic charge state, and mass of specific species of ions in the LISM. CoDICE also has a path for higher energy particles to skip the ESA but still get measured by the common TOF / E system. These measurements are critical in determining the Local Interstellar Medium (LISM) composition and flow properties, the origin of the enigmatic suprathermal tails on the solar wind distributions and advance understanding of the acceleration of particles in the heliosphere.
Users should acknowledge the sources of data used in all publications, presentations, and reports using an appropriate DOI. Appropriate acknowledgement to institutions, personnel, and funding agencies should be given, including acknowledging the IMAP Mission Principal Investigator, Prof. David J. McComas of Princeton University (Contract #80GSFC19C0027). IMAP Rules-of-the-Road for data usage can be found in the IMAP CMAD.

5.1 Data

5.1.1 Sunward - cnoplus

`cnoplus`

cnoplus Pickup Ion Sunward Species (#/(cm^2-s-sr-keV/q))
`SPASE>Particle>ParticleType:Ion,ParticleQuantity:NumberFlux,Qualifier:Differential`
Size: 128×1 time-varying
Energy per charge (E/q) sweeping step 0 – 127 (128 bins)
Spin sector indicating range of spin angles 0 – 0 (1 bins)

5.1.2 Sunward Differential Intensity - C4+

`cplus4`

Differential intensity from sunward-looking detectors measuring solar-wind C4+ (#/(cm^2-s-sr-keV/q))
`SPASE>Particle>ParticleType:Ion,ParticleQuantity:NumberFlux,Qualifier:Differential`
Size: 128 × 1 time-varying
- Energy per charge (E/q) sweeping step 0 – 127 (128 bins)
- Spin sector indicating range of spin angles 0 – 0 (1 bins)

5.1.3 Sunward Differential Intensity - C5+

`cplus5`

Differential intensity from sunward-looking detectors measuring solar-wind C5+ (#/(cm^2-s-sr-keV/q))
`SPASE>Particle>ParticleType:Ion,ParticleQuantity:NumberFlux,Qualifier:Differential`
Size: 128 × 1 time-varying
- Energy per charge (E/q) sweeping step 0 – 127 (128 bins)
- Spin sector indicating range of spin angles 0 – 0 (1 bins)

5.1.4 Sunward Differential Intensity - C6+

`cplus6`

Differential intensity from sunward-looking detectors measuring solar-wind C6+ (#/(cm^2-s-sr-keV/q))
`SPASE>Particle>ParticleType:Ion,ParticleQuantity:NumberFlux,Qualifier:Differential`
Size: 128 × 1 time-varying
- Energy per charge (E/q) sweeping step 0 – 127 (128 bins)
- Spin sector indicating range of spin angles 0 – 0 (1 bins)

5.1.5 Data Quality

`data_quality`

Indicates whether data quality is suspect (1).
time-varying

5.1.6 Sunward Differential Intensity - Fe HiQ

`fe_hiq`

Differential intensity from sunward-looking detectors measuring solar-wind Fe HiQ (#/(cm^2-s-sr-keV/q))
`SPASE>Particle>ParticleType:Ion,ParticleQuantity:NumberFlux,Qualifier:Differential`
Size: 128 × 1 time-varying
- Energy per charge (E/q) sweeping step 0 – 127 (128 bins)
- Spin sector indicating range of spin angles 0 – 0 (1 bins)

5.1.7 Sunward Differential Intensity - Fe LoQ

`fe_loq`

Differential intensity from sunward-looking detectors measuring solar-wind Fe LoQ (#/(cm^2-s-sr-keV/q))
`SPASE>Particle>ParticleType:Ion,ParticleQuantity:NumberFlux,Qualifier:Differential`
Size: 128 × 1 time-varying
- Energy per charge (E/q) sweeping step 0 – 127 (128 bins)
- Spin sector indicating range of spin angles 0 – 0 (1 bins)

5.1.8 Sunward - heplus

`heplus`

heplus Pickup Ion Sunward Species (#/(cm^2-s-sr-keV/q))
`SPASE>Particle>ParticleType:Ion,ParticleQuantity:NumberFlux,Qualifier:Differential`
Size: 128 × 1 time-varying
- Energy per charge (E/q) sweeping step 0 – 127 (128 bins)
- Spin sector indicating range of spin angles 0 – 0 (1 bins)

5.1.9 Sunward Differential Intensity - He++

`heplusplus`

Differential intensity from sunward-looking detectors measuring solar-wind He++ (#/(cm^2-s-sr-keV/q))
`SPASE>Particle>ParticleType:Ion,ParticleQuantity:NumberFlux,Qualifier:Differential`
Size: 128 × 1 time-varying
- Energy per charge (E/q) sweeping step 0 – 127 (128 bins)
- Spin sector indicating range of spin angles 0 – 0 (1 bins)

5.1.10 Sunward Differential Intensity - H+

`hplus`

Differential intensity from sunward-looking detectors measuring solar-wind H+ (#/(cm^2-s-sr-keV/q))
`SPASE>Particle>ParticleType:Ion,ParticleQuantity:NumberFlux,Qualifier:Differential`
Size: 128 × 1 time-varying
Energy per charge (E/q) sweeping step 0 – 127 (128 bins)
Spin sector indicating range of spin angles 0 – 0 (1 bins)

5.1.11 Sunward Differential Intensity - Mg

`mg`

Differential intensity from sunward-looking detectors measuring solar-wind Mg (#/(cm^2-s-sr-keV/q))
`SPASE>Particle>ParticleType:Ion,ParticleQuantity:NumberFlux,Qualifier:Differential`
Size: 128 × 1 time-varying
Energy per charge (E/q) sweeping step 0 – 127 (128 bins)
Spin sector indicating range of spin angles 0 – 0 (1 bins)

5.1.12 Sunward Differential Intensity - Ne

`ne`

Differential intensity from sunward-looking detectors measuring solar-wind Ne (#/(cm^2-s-sr-keV/q))
`SPASE>Particle>ParticleType:Ion,ParticleQuantity:NumberFlux,Qualifier:Differential`
Size: 128 × 1 time-varying
Energy per charge (E/q) sweeping step 0 – 127 (128 bins)
Spin sector indicating range of spin angles 0 – 0 (1 bins)

5.1.13 NSO Energy Step

`nso_esa_step`

Energy Step When No Scan Operation (NSO) was activated (energy step)
time-varying
Indicates the energy step when No Scan Operation (NSO) was activated. In NSO, the ESA voltage is set to the first step in the scan and remains fixed until the next cycle boundary.

5.1.14 NSO Spin Sector

`nso_spin_sector`

Spin Sector When No Scan Operation (NSO) was activated (spin sector)
time-varying
Indicates the spin sector when No Scan Operation (NSO) was activated. In NSO, the ESA voltage is set to the first step in the scan and remains fixed until the next cycle boundary.

5.1.15 Sunward Differential Intensity - O5+

`oplus5`

Differential intensity from sunward-looking detectors measuring solar-wind O5+ (#/(cm^2-s-sr-keV/q))
`SPASE>Particle>ParticleType:Ion,ParticleQuantity:NumberFlux,Qualifier:Differential`
Size: 128 × 1 time-varying
Energy per charge (E/q) sweeping step 0 – 127 (128 bins)
Spin sector indicating range of spin angles 0 – 0 (1 bins)

5.1.16 Sunward Differential Intensity - O6+

`oplus6`

Differential intensity from sunward-looking detectors measuring solar-wind O6+ (#/(cm^2-s-sr-keV/q))
`SPASE>Particle>ParticleType:Ion,ParticleQuantity:NumberFlux,Qualifier:Differential`
Size: 128 × 1 time-varying
Energy per charge (E/q) sweeping step 0 – 127 (128 bins)
Spin sector indicating range of spin angles 0 – 0 (1 bins)

5.1.17 Sunward Differential Intensity - O7+

`oplus7`

Differential intensity from sunward-looking detectors measuring solar-wind O7+ (#/(cm^2-s-sr-keV/q))
`SPASE>Particle>ParticleType:Ion,ParticleQuantity:NumberFlux,Qualifier:Differential`
Size: 128 × 1 time-varying
Energy per charge (E/q) sweeping step 0 – 127 (128 bins)
Spin sector indicating range of spin angles 0 – 0 (1 bins)

5.1.18 Sunward Differential Intensity - O8+

`oplus8`

Differential intensity from sunward-looking detectors measuring solar-wind O8+ (#/(cm^2-s-sr-keV/q))
SPASE>Particle>ParticleType:Ion,ParticleQuantity:NumberFlux,Qualifier:Differential
Size: 128 × 1 time-varying
Energy per charge (E/q) sweeping step 0 – 127 (128 bins)
Spin sector indicating range of spin angles 0 – 0 (1 bins)

5.1.19 Sunward Differential Intensity - Si

si

Differential intensity from sunward-looking detectors measuring solar-wind Si (#/(cm^2-s-sr-keV/q))
SPASE>Particle>ParticleType:Ion,ParticleQuantity:NumberFlux,Qualifier:Differential
Size: 128 × 1 time-varying
Energy per charge (E/q) sweeping step 0 – 127 (128 bins)
Spin sector indicating range of spin angles 0 – 0 (1 bins)

5.1.20 Sunward - unc_cnoplus

unc_cnoplus

unc_cnoplus Pickup Ion Sunward Species uncertainty (#/(cm^2-s-sr-keV/q))
SPASE>Particle>ParticleType:Ion,ParticleQuantity:NumberFlux,Qualifier:Uncertainty
Size: 128 × 1 time-varying
Energy per charge (E/q) sweeping step 0 – 127 (128 bins)
Spin sector indicating range of spin angles 0 – 0 (1 bins)

5.1.21 Sunward Uncertainty - C4+

unc_cplus4

Uncertainty in differential intensity from sunward-looking detectors measuring solar-wind C4+ (#/(cm^2-s-sr-keV/q))
SPASE>Particle>ParticleType:Ion,ParticleQuantity:NumberFlux,Qualifier:Uncertainty
Size: 128 × 1 time-varying
Energy per charge (E/q) sweeping step 0 – 127 (128 bins)
Spin sector indicating range of spin angles 0 – 0 (1 bins)

5.1.22 Sunward Uncertainty - C5+

unc_cplus5

Uncertainty in differential intensity from sunward-looking detectors measuring solar-wind C5+

(#/(cm^2-s-sr-keV/q))
SPASE>Particle>ParticleType:Ion,ParticleQuantity:NumberFlux,Qualifier:Uncertainty
Size: 128 × 1 time-varying
Energy per charge (E/q) sweeping step 0 – 127 (128 bins)
Spin sector indicating range of spin angles 0 – 0 (1 bins)

5.1.23 Sunward Uncertainty - C6+

unc_cplus6

Uncertainty in differential intensity from sunward-looking detectors measuring solar-wind C6+
(#/(cm^2-s-sr-keV/q))
SPASE>Particle>ParticleType:Ion,ParticleQuantity:NumberFlux,Qualifier:Uncertainty
Size: 128 × 1 time-varying
Energy per charge (E/q) sweeping step 0 – 127 (128 bins)
Spin sector indicating range of spin angles 0 – 0 (1 bins)

5.1.24 Sunward Uncertainty - Fe HiQ

unc_fe_hiq

Uncertainty in differential intensity from sunward-looking detectors measuring solar-wind Fe HiQ
(#/(cm^2-s-sr-keV/q))
SPASE>Particle>ParticleType:Ion,ParticleQuantity:NumberFlux,Qualifier:Uncertainty
Size: 128 × 1 time-varying
Energy per charge (E/q) sweeping step 0 – 127 (128 bins)
Spin sector indicating range of spin angles 0 – 0 (1 bins)

5.1.25 Sunward Uncertainty - Fe LoQ

unc_fe_loq

Uncertainty in differential intensity from sunward-looking detectors measuring solar-wind Fe LoQ
(#/(cm^2-s-sr-keV/q))
SPASE>Particle>ParticleType:Ion,ParticleQuantity:NumberFlux,Qualifier:Uncertainty
Size: 128 × 1 time-varying
Energy per charge (E/q) sweeping step 0 – 127 (128 bins)
Spin sector indicating range of spin angles 0 – 0 (1 bins)

5.1.26 Sunward - unc_heplus

unc_heplus

unc_heplus Pickup Ion Sunward Species uncertainty (#/(cm^2-s-sr-keV/q))
`SPASE>Particle>ParticleType:Ion,ParticleQuantity:NumberFlux,Qualifier:Uncertainty`
Size: 128 × 1 time-varying
Energy per charge (E/q) sweeping step 0 – 127 (128 bins)
Spin sector indicating range of spin angles 0 – 0 (1 bins)

5.1.27 Sunward Uncertainty - He++

`unc_heplusplus`

Uncertainty in differential intensity from sunward-looking detectors measuring solar-wind He++ (#/(cm^2-s-sr-keV/q))
`SPASE>Particle>ParticleType:Ion,ParticleQuantity:NumberFlux,Qualifier:Uncertainty`
Size: 128 × 1 time-varying
Energy per charge (E/q) sweeping step 0 – 127 (128 bins)
Spin sector indicating range of spin angles 0 – 0 (1 bins)

5.1.28 Sunward Uncertainty - H+

`unc_hplus`

Uncertainty in differential intensity from sunward-looking detectors measuring solar-wind H+ (#/(cm^2-s-sr-keV/q))
`SPASE>Particle>ParticleType:Ion,ParticleQuantity:NumberFlux,Qualifier:Uncertainty`
Size: 128 × 1 time-varying
Energy per charge (E/q) sweeping step 0 – 127 (128 bins)
Spin sector indicating range of spin angles 0 – 0 (1 bins)

5.1.29 Sunward Uncertainty - Mg

`unc_mg`

Uncertainty in differential intensity from sunward-looking detectors measuring solar-wind Mg (#/(cm^2-s-sr-keV/q))
`SPASE>Particle>ParticleType:Ion,ParticleQuantity:NumberFlux,Qualifier:Uncertainty`
Size: 128 × 1 time-varying
Energy per charge (E/q) sweeping step 0 – 127 (128 bins)
Spin sector indicating range of spin angles 0 – 0 (1 bins)

5.1.30 Sunward Uncertainty - Ne

`unc_ne`

Uncertainty in differential intensity from sunward-looking detectors measuring solar-wind Ne (#/(cm^2-s-sr-keV/q))
SPASE>Particle>ParticleType:Ion,ParticleQuantity:NumberFlux,Qualifier:Uncertainty
Size: 128 × 1 time-varying
Energy per charge (E/q) sweeping step 0 – 127 (128 bins)
Spin sector indicating range of spin angles 0 – 0 (1 bins)

5.1.31 Sunward Uncertainty - O5+

unc_oplus5

Uncertainty in differential intensity from sunward-looking detectors measuring solar-wind O5+ (#/(cm^2-s-sr-keV/q))
SPASE>Particle>ParticleType:Ion,ParticleQuantity:NumberFlux,Qualifier:Uncertainty
Size: 128 × 1 time-varying
Energy per charge (E/q) sweeping step 0 – 127 (128 bins)
Spin sector indicating range of spin angles 0 – 0 (1 bins)

5.1.32 Sunward Uncertainty - O6+

unc_oplus6

Uncertainty in differential intensity from sunward-looking detectors measuring solar-wind O6+ (#/(cm^2-s-sr-keV/q))
SPASE>Particle>ParticleType:Ion,ParticleQuantity:NumberFlux,Qualifier:Uncertainty
Size: 128 × 1 time-varying
Energy per charge (E/q) sweeping step 0 – 127 (128 bins)
Spin sector indicating range of spin angles 0 – 0 (1 bins)

5.1.33 Sunward Uncertainty - O7+

unc_oplus7

Uncertainty in differential intensity from sunward-looking detectors measuring solar-wind O7+ (#/(cm^2-s-sr-keV/q))
SPASE>Particle>ParticleType:Ion,ParticleQuantity:NumberFlux,Qualifier:Uncertainty
Size: 128 × 1 time-varying
Energy per charge (E/q) sweeping step 0 – 127 (128 bins)
Spin sector indicating range of spin angles 0 – 0 (1 bins)

5.1.34 Sunward Uncertainty - O8+

`unc_oplus8`

Uncertainty in differential intensity from sunward-looking detectors measuring solar-wind O8+ (#/(cm^2-s-sr-keV/q))
`SPASE>Particle>ParticleType:Ion,ParticleQuantity:NumberFlux,Qualifier:Uncertainty`
Size: 128 × 1 time-varying
Energy per charge (E/q) sweeping step 0 – 127 (128 bins)
Spin sector indicating range of spin angles 0 – 0 (1 bins)

5.1.35 Sunward Uncertainty - Si

`unc_si`

Uncertainty in differential intensity from sunward-looking detectors measuring solar-wind Si (#/(cm^2-s-sr-keV/q))
`SPASE>Particle>ParticleType:Ion,ParticleQuantity:NumberFlux,Qualifier:Uncertainty`
Size: 128 × 1 time-varying
Energy per charge (E/q) sweeping step 0 – 127 (128 bins)
Spin sector indicating range of spin angles 0 – 0 (1 bins)

5.2 Support Data

5.2.1 Energy per charge

`energy_per_charge`

(keV/e)
Size: 128 constant
Energy per charge (E/q) sweeping step 0 – 127 (128 bins)

6 imap_codice_l3a_hi-direct-events

CoDICE>Compact Dual Ion Composition Experiment
L3A_hi-direct-events>Level-3A direct events
Like its sister instrument Solar Wind and Pickup Ions (SWAPI), the CoDICE instrument collects and counts two types of particles: ones from the solar wind flowing from the Sun and particles called pick-up ions (PUIs) that entered the heliosphere from outside our solar neighborhood and traveled inwards where IMAP orbits about a million miles from the Earth. The solar wind particles CoDICE collects and sorts are highly energized particles, called suprathermal particles, which are moving faster (and therefore have higher energy) than the solar wind particles that SWAPI collects. CoDICE also simultaneously measures the velocity, direction of travel, energies, and types of specific species of PUIs from the local interstellar medium, the interstellar material surrounding our solar

system found directly outside of the heliosphere. Some of these are hydrogen and helium ions like SWAPI, but CoDICE is also able to collect and analyze heavier ions than SWAPI can.
Users should acknowledge the sources of data used in all publications, presentations, and reports using an appropriate DOI. Appropriate acknowledgement to institutions, personnel, and funding agencies should be given, including acknowledging the IMAP Mission Principal Investigator, Prof. David J. McComas of Princeton University (Contract #80GSFC19C0027). IMAP Rules-of-the-Road for data usage can be found in the IMAP CMAD.

6.1 Primary variables

6.1.1 Data Quality Flag

`data_quality`

Data quality flag (0=valid, 1=invalid) (0=valid 1=invalid)
Size: 6 time-varying
    Priority bin index 0 – 5 (6 bins)

6.1.2 Elevation Angle

`elevation_angle`

Elevation Angle of event in despun pointing set frame (degrees)
`SPASE>Particle>ParticleType:Ion,ParticleQuantity:ArrivalDirection,Qualifier:DirectionAngle.Eleva`
Size: 6×10000 time-varying
    Priority bin index 0 – 5 (6 bins)
    Event bin index 0 – 9999 (10000 bins)

6.1.3 Energy per nuc

`energy_per_nuc`

(MeV/nuc)
Size: 6×10000 time-varying
    Priority bin index 0 – 5 (6 bins)
    Event bin index 0 – 9999 (10000 bins)

6.1.4 Estimated Mass

`estimated_mass`

Estimated mass (amu)
Size: 6×10000 time-varying

Priority bin index 0 – 5 (6 bins)
Event bin index 0 – 9999 (10000 bins)

6.1.5 Multi Flag

`multi_flag`

Multiple detector flag (1=multiple SSDs triggered) (1=multiple SSDs triggered)
Size: 6×10000 time-varying
Priority bin index 0 – 5 (6 bins)
Event bin index 0 – 9999 (10000 bins)

6.1.6 Number of events

`num_events`

Size: 6 time-varying
Priority bin index 0 – 5 (6 bins)

6.1.7 Spin angle

`spin_angle`

Spin angle when event was observed in despun pointing set frame (degrees)
Size: 6×10000 time-varying
Priority bin index 0 – 5 (6 bins)
Event bin index 0 – 9999 (10000 bins)

6.1.8 Spin Number

`spin_number`

Spin number
Size: 6×10000 time-varying
Priority bin index 0 – 5 (6 bins)
Event bin index 0 – 9999 (10000 bins)

6.1.9 SSD Energy

`ssd_energy`

SSD energy (MeV)

Size: 6 × 10000 time-varying
Priority bin index 0 – 5 (6 bins)
Event bin index 0 – 9999 (10000 bins)

6.1.10 SSD ID

`ssd_id`

Solid State Detector identifier
Size: 6 × 10000 time-varying
Priority bin index 0 – 5 (6 bins)
Event bin index 0 – 9999 (10000 bins)

6.1.11 Event Time of Flight

`tof`

Time of Flight of Event (ns)
Size: 6 × 10000 time-varying
Priority bin index 0 – 5 (6 bins)
Event bin index 0 – 9999 (10000 bins)

6.1.12 PHA Type

`type`

Size: 6 × 10000 time-varying
Priority bin index 0 – 5 (6 bins)
Event bin index 0 – 9999 (10000 bins)

6.2 Other data

6.2.1 Gain

`gain`

Gain Setting
`SPASE>Support>SupportQuantity:Other`
Size: 6 × 10000 time-varying
Priority bin index 0 – 5 (6 bins)
Event bin index 0 – 9999 (10000 bins)

6.3 Support Data

6.3.1 Spin Sector Index

`spin_sector`

`SPASE>Support>SupportQuantity:Positional`
Size: 6×10000 time-varying
Priority bin index 0 – 5 (6 bins)
Event bin index 0 – 9999 (10000 bins)

7 imap_codice_l3a_lo-direct-events

CoDICE>Compact Dual Ion Composition Experiment
L3A_lo-direct-events>Level-3A direct events
Like its sister instrument Solar Wind and Pickup Ions (SWAPI), the CoDICE instrument collects and counts two types of particles: ones from the solar wind flowing from the Sun and particles called pick-up ions (PUIs) that entered the heliosphere from outside our solar neighborhood and traveled inwards where IMAP orbits about a million miles from the Earth. The solar wind particles CoDICE collects and sorts are highly energized particles, called suprathermal particles, which are moving faster (and therefore have higher energy) than the solar wind particles that SWAPI collects. CoDICE also simultaneously measures the velocity, direction of travel, energies, and types of specific species of PUIs from the local interstellar medium, the interstellar material surrounding our solar system found directly outside of the heliosphere. Some of these are hydrogen and helium ions like SWAPI, but CoDICE is also able to collect and analyze heavier ions than SWAPI can.
Users should acknowledge the sources of data used in all publications, presentations, and reports using an appropriate DOI. Appropriate acknowledgement to institutions, personnel, and funding agencies should be given, including acknowledging the IMAP Mission Principal Investigator, Prof. David J. McComas of Princeton University (Contract #80GSFC19C0027). IMAP Rules-of-the-Road for data usage can be found in the IMAP CMAD.

7.1 Primary variables

7.1.1 APD Energy

`apd_energy`

Deposited energy at APD (keV)
Size: 7×10000 time-varying
Priority number where particle is observed 0 – 6 (7 bins)
Index of event 0 – 9999 (10000 bins)

7.1.2 APD ID

`apd_id`

Size: 7×10000 time-varying
Priority number where particle is observed 0 – 6 (7 bins)
Index of event 0 – 9999 (10000 bins)

7.1.3 Data quality

`data_quality`

Data quality (0=good, 1=suspect) (0=good 1=suspect)
Size: 7 time-varying
Priority number where particle is observed 0 – 6 (7 bins)
Propagated from packet-level suspect bit via level 2. 0=good packet group. 1=suspect packet group.

7.1.4 Elevation

`elevation`

Elevation per event (degrees)
Size: 7×10000 time-varying
Priority number where particle is observed 0 – 6 (7 bins)
Index of event 0 – 9999 (10000 bins)

7.1.5 Energy per Charge

`energy_per_charge`

(keV/q)
Size: 7×10000 time-varying
Priority number where particle is observed 0 – 6 (7 bins)
Index of event 0 – 9999 (10000 bins)

7.1.6 Energy Step

`energy_step`

Energy Step Index
Size: 7×10000 time-varying
Priority number where particle is observed 0 – 6 (7 bins)

Index of event 0 – 9999 (10000 bins)

7.1.7 Gain

`gain`

Size: 7×10000 time-varying
Priority number where particle is observed 0 – 6 (7 bins)
Index of event 0 – 9999 (10000 bins)

7.1.8 Mass

`mass`

Mass of event (amu)
Size: 7×10000 time-varying
Priority number where particle is observed 0 – 6 (7 bins)
Index of event 0 – 9999 (10000 bins)

7.1.9 Mass per charge

`mass_per_charge`

Mass per charge of event (amu/q)
Size: 7×10000 time-varying
Priority number where particle is observed 0 – 6 (7 bins)
Index of event 0 – 9999 (10000 bins)

7.1.10 Multi flag

`multi_flag`

Multiple detector flag (1=multiple APDs triggered) (1=multiple APDs triggered)
Size: 7×10000 time-varying
Priority number where particle is observed 0 – 6 (7 bins)
Index of event 0 – 9999 (10000 bins)

7.1.11 Normalization factor

`normalization`

Size: $7 \times 128 \times 24$ time-varying

Priority number where particle is observed 0 – 6 (7 bins)
Energy bins 1 – 81 keV/e (128 bins)
Spin angle bins 8 – 352 degrees (24 bins)

7.1.12 Normalization factor

`normalization_per_event`

Normalization per event
Size: 7×10000 time-varying
Priority number where particle is observed 0 – 6 (7 bins)
Index of event 0 – 9999 (10000 bins)

7.1.13 Number of events

`num_events`

Size: 7 time-varying
Priority number where particle is observed 0 – 6 (7 bins)

7.1.14 Position index

`position`

Position index per event
Size: 7×10000 time-varying
Priority number where particle is observed 0 – 6 (7 bins)
Index of event 0 – 9999 (10000 bins)

7.1.15 Spin angle

`spin_angle`

Spin angle per event (degrees)
Size: 7×10000 time-varying
Priority number where particle is observed 0 – 6 (7 bins)
Index of event 0 – 9999 (10000 bins)

7.1.16 Spin sector

`spin_sector`

Spin sector per event
`SPASE>Support>SupportQuantity:Positional`
Size: 7×10000 time-varying
Priority number where particle is observed 0 – 6 (7 bins)
Index of event 0 – 9999 (10000 bins)

7.1.17 Time of flight

`tof`

(ns)
Size: 7×10000 time-varying
Priority number where particle is observed 0 – 6 (7 bins)
Index of event 0 – 9999 (10000 bins)

7.1.18 PHA Type

`type`

Event PHA Type: 0=TCR; 1=DCR, 2=APD only (0=TCR; 1=DCR, 2=APD only)
Size: 7×10000 time-varying
Priority number where particle is observed 0 – 6 (7 bins)
Index of event 0 – 9999 (10000 bins)
PHA type code. 0 = TCR (Triple Coincidence, STA + STB + SP + APD); 1 = DCR (Double Coincidence, STA + STB + SP); 2 = APD-only energy event (APD with one or two of STA, STB, SP).

7.2 Other data

7.2.1 NSO Energy Step

`nso_esa_step`

Energy Step When No Scan Operation (NSO) was activated
time-varying
Indicates the energy step when No Scan Operation (NSO) was activated. In NSO, the ESA voltage is set to the first step in the scan and remains fixed until the next cycle boundary.

7.2.2 NSO Half Spin

`nso_half_spin`

When No Scan Operation (NSO) was activated (half spin number)
time-varying

Indicates the half spin when No Scan Operation (NSO) was activated. In NSO, the ESA voltage is set to the first step in the scan and remains fixed until the next cycle boundary.

7.2.3 NSO Spin Sector

`nso_spin_sector`

Spin Sector When No Scan Operation (NSO) was activated
time-varying
Indicates the spin sector when No Scan Operation (NSO) was activated. In NSO, the ESA voltage is set to the first step in the scan and remains fixed until the next cycle boundary.

7.2.4 RGFO Energy Step

`rgfo_esa_step`

Energy Step When Reduced Gain Factor Operation (RGFO) was activated
time-varying
Indicates the energy step when Reduced Gain Factor Operation (RGFO) was activated. In RGFO, the Entrance ESA voltage is reduced in order to limit the number of ions that reach the detectors.

7.2.5 RGFO Half Spin

`rgfo_half_spin`

Half Spin When Reduced Gain Factor Operation (RGFO) was activated
time-varying
Indicates the half spin when Reduced Gain Factor Operation (RGFO) was activated. In RGFO, the Entrance ESA voltage is reduced in order to limit the number of ions that reach the detectors.

7.2.6 RGFO Spin Sector

`rgfo_spin_sector`

Spin Sector When Reduced Gain Factor Operation (RGFO) was activated
time-varying
Indicates the spin sector when Reduced Gain Factor Operation (RGFO) was activated. In RGFO, the Entrance ESA voltage is reduced in order to limit the number of ions that reach the detectors.

7.3 Support Data

7.3.1 Acquisition Time

`acquisition_time_per_esa_step`

Acquisition time for each step of energy (ms)
Size: 128 time-varying
Energy per charge (E/q) sweeping step 0 – 127 (128 bins)

7.3.2 Half Spin Number

`half_spin_per_esa_step`

Half spin number for each step of energy
Size: 128 time-varying
Energy per charge (E/q) sweeping step 0 – 127 (128 bins)

8 imap_codice_l3a_lo-partial-densities

CoDICE>Compact Dual Ion Composition Experiment
L3A_lo-partial-densities>Level-3A partial densities
Like its sister instrument Solar Wind and Pickup Ions (SWAPI), the CoDICE instrument collects and counts two types of particles: ones from the solar wind flowing from the Sun and particles called pick-up ions (PUIs) that entered the heliosphere from outside our solar neighborhood and traveled inwards where IMAP orbits about a million miles from the Earth. The solar wind particles CoDICE collects and sorts are highly energized particles, called suprathermal particles, which are moving faster (and therefore have higher energy) than the solar wind particles that SWAPI collects. CoDICE also simultaneously measures the velocity, direction of travel, energies, and types of specific species of PUIs from the local interstellar medium, the interstellar material surrounding our solar system found directly outside of the heliosphere. Some of these are hydrogen and helium ions like SWAPI, but CoDICE is also able to collect and analyze heavier ions than SWAPI can.
Users should acknowledge the sources of data used in all publications, presentations, and reports using an appropriate DOI. Appropriate acknowledgement to institutions, personnel, and funding agencies should be given, including acknowledging the IMAP Mission Principal Investigator, Prof. David J. McComas of Princeton University (Contract #80GSFC19C0027). IMAP Rules-of-the-Road for data usage can be found in the IMAP CMAD.

8.1 Primary variables

8.1.1 Partial density of C+4

`cplus4_partial_density`

(#/cm^3)
time-varying

8.1.2 Partial density of C+5

`cplus5_partial_density`

(#/cm^3)
time-varying

8.1.3 Partial density of C+6

`cplus6_partial_density`

(#/cm^3)
time-varying

8.1.4 Partial density of Fe (high Q)

`fe_hiq_partial_density`

(#/cm^3)
time-varying

8.1.5 Partial density of Fe (low Q)

`fe_loq_partial_density`

(#/cm^3)
time-varying

8.1.6 Partial density of He++

`heplusplus_partial_density`

(#/cm^3)
time-varying

8.1.7 Partial density of H+

`hplus_partial_density`

(#/cm^3)
time-varying

8.1.8 Partial density of Mg

`mg_partial_density`

(#/cm^3)
time-varying

8.1.9 Partial density of Ne

`ne_partial_density`

(#/cm^3)
time-varying

8.1.10 Partial density of O+5

`oplus5_partial_density`

(#/cm^3)
time-varying

8.1.11 Partial density of O+6

`oplus6_partial_density`

(#/cm^3)
time-varying

8.1.12 Partial density of O+7

`oplus7_partial_density`

(#/cm^3)
time-varying

8.1.13 Partial density of O+8

`oplus8_partial_density`

(#/cm^3)
time-varying

8.1.14 Partial density of Si

`si_partial_density`

(#/cm^3)
time-varying

9 imap_codice_l3a_lo-sw-charge-state-distributions

CoDICE>Compact Dual Ion Composition Experiment
L3A_lo-sw-charge-state-distributions>Level-3A charge state distributions
Like its sister instrument Solar Wind and Pickup Ions (SWAPI), the CoDICE instrument collects and counts two types of particles: ones from the solar wind flowing from the Sun and particles called pick-up ions (PUIs) that entered the heliosphere from outside our solar neighborhood and traveled inwards where IMAP orbits about a million miles from the Earth. The solar wind particles CoDICE collects and sorts are highly energized particles, called suprathermal particles, which are moving faster (and therefore have higher energy) than the solar wind particles that SWAPI collects. CoDICE also simultaneously measures the velocity, direction of travel, energies, and types of specific species of PUIs from the local interstellar medium, the interstellar material surrounding our solar system found directly outside of the heliosphere. Some of these are hydrogen and helium ions like SWAPI, but CoDICE is also able to collect and analyze heavier ions than SWAPI can.
Users should acknowledge the sources of data used in all publications, presentations, and reports using an appropriate DOI. Appropriate acknowledgement to institutions, personnel, and funding agencies should be given, including acknowledging the IMAP Mission Principal Investigator, Prof. David J. McComas of Princeton University (Contract #80GSFC19C0027). IMAP Rules-of-the-Road for data usage can be found in the IMAP CMAD.

9.1 Primary variables

9.1.1 C charge state abundances

`carbon_charge_state_distribution`

Carbon charge state relative abundances
Size: 3 time-varying
    Carbon charge state 4 – 6 (3 bins)

9.1.2 O charge state abundances

`oxygen_charge_state_distribution`

Oxygen charge state relative abundances
Size: 4 time-varying
    Oxygen charge state 5 – 8 (4 bins)

10 imap_codice_l3a_lo-sw-ratios

CoDICE>Compact Dual Ion Composition Experiment
L3A_lo-sw-ratios>Level-3A sw ratios
Like its sister instrument Solar Wind and Pickup Ions (SWAPI), the CoDICE instrument collects and counts two types of particles: ones from the solar wind flowing from the Sun and particles called pick-up ions (PUIs) that entered the heliosphere from outside our solar neighborhood and traveled inwards where IMAP orbits about a million miles from the Earth. The solar wind particles CoDICE collects and sorts are highly energized particles, called suprathermal particles, which are moving faster (and therefore have higher energy) than the solar wind particles that SWAPI collects. CoDICE also simultaneously measures the velocity, direction of travel, energies, and types of specific species of PUIs from the local interstellar medium, the interstellar material surrounding our solar system found directly outside of the heliosphere. Some of these are hydrogen and helium ions like SWAPI, but CoDICE is also able to collect and analyze heavier ions than SWAPI can.
Users should acknowledge the sources of data used in all publications, presentations, and reports using an appropriate DOI. Appropriate acknowledgement to institutions, personnel, and funding agencies should be given, including acknowledging the IMAP Mission Principal Investigator, Prof. David J. McComas of Princeton University (Contract #80GSFC19C0027). IMAP Rules-of-the-Road for data usage can be found in the IMAP CMAD.

10.1 Primary variables

10.1.1 Ratio C6 to C4

`c6_to_c4_ratio`

Charge State Ratio C6 to C4
time-varying

10.1.2 Ratio C6 to C5

`c6_to_c5_ratio`

Charge State Ratio C6 to C5
time-varying

10.1.3 Ratio C to O

`c_to_o_ratio`

Elemental Abundance Ratio C to O
time-varying

10.1.4 Ratio Fe to O

`fe_to_o_ratio`

Elemental Abundance Ratio Fe to O
time-varying

10.1.5 Ratio FeLo to FeHi

`felo_to_fehi_ratio`

Charge State Ratio Fe Low (+6 - +12) to Fe High (+13 - +17)
time-varying

10.1.6 Ratio Mg to O

`mg_to_o_ratio`

Elemental Abundance Ratio Mg to O
time-varying

10.1.7 Ratio O7 to O6

`o7_to_o6_ratio`

Charge State Ratio O7 to O6
time-varying

11 imap_codice_l3b_hi-pitch-angle

CoDICE>Compact Dual Ion Composition Experiment
L3B_hi-pitch-angle>Level-3b pitch angle
Like its sister instrument Solar Wind and Pickup Ions (SWAPI), the CoDICE instrument collects and counts two types of particles: ones from the solar wind flowing from the Sun and particles called pick-up ions (PUIs) that entered the heliosphere from outside our solar neighborhood and

traveled inwards where IMAP orbits about a million miles from the Earth. The solar wind particles CoDICE collects and sorts are highly energized particles, called suprathermal particles, which are moving faster (and therefore have higher energy) than the solar wind particles that SWAPI collects. CoDICE also simultaneously measures the velocity, direction of travel, energies, and types of specific species of PUIs from the local interstellar medium, the interstellar material surrounding our solar system found directly outside of the heliosphere. Some of these are hydrogen and helium ions like SWAPI, but CoDICE is also able to collect and analyze heavier ions than SWAPI can.
Users should acknowledge the sources of data used in all publications, presentations, and reports using an appropriate DOI. Appropriate acknowledgement to institutions, personnel, and funding agencies should be given, including acknowledging the IMAP Mission Principal Investigator, Prof. David J. McComas of Princeton University (Contract #80GSFC19C0027). IMAP Rules-of-the-Road for data usage can be found in the IMAP CMAD.

11.1 Primary variables

11.1.1 CNO Intensity

`cno_intensity_by_pitch_angle`

CNO intensity binned by pitch angle (1/(cm^2 s MeV/nuc sr))
Size: 8×6 time-varying
CNO energy bins 0 – 4 MeV/nuc (8 bins)
Pitch angle bins 15 – 165 degrees (6 bins)

11.1.2 CNO Intensity

`cno_intensity_by_pitch_angle_and_gyrophase`

CNO intensity binned by pitch angle and gyrophase (1/(cm^2 s MeV/nuc sr))
Size: $8 \times 6 \times 12$ time-varying
CNO energy bins 0 – 4 MeV/nuc (8 bins)
Pitch angle bins 15 – 165 degrees (6 bins)
Gyrophase bins 15 – 345 degrees (12 bins)

11.1.3 Fe Intensity

`fe_intensity_by_pitch_angle`

Fe intensity binned by pitch angle (1/(cm^2 s MeV/nuc sr))
Size: 8×6 time-varying
Fe energy bins 0 – 4 MeV/nuc (8 bins)
Pitch angle bins 15 – 165 degrees (6 bins)

11.1.4 Fe Intensity

`fe_intensity_by_pitch_angle_and_gyrophase`

Fe intensity binned by pitch angle and gyrophase (1/(cm^2 s MeV/nuc sr))
Size: $8 \times 6 \times 12$ time-varying
- Fe energy bins 0 – 4 MeV/nuc (8 bins)
- Pitch angle bins 15 – 165 degrees (6 bins)
- Gyrophase bins 15 – 345 degrees (12 bins)

11.1.5 H Intensity

`h_intensity_by_pitch_angle`

H intensity binned by pitch angle (1/(cm^2 s MeV/nuc sr))
Size: 8×6 time-varying
- H energy bins 0 – 4 MeV/nuc (8 bins)
- Pitch angle bins 15 – 165 degrees (6 bins)

11.1.6 H Intensity

`h_intensity_by_pitch_angle_and_gyrophase`

H intensity binned by pitch angle and gyrophase (1/(cm^2 s MeV/nuc sr))
Size: $8 \times 6 \times 12$ time-varying
- H energy bins 0 – 4 MeV/nuc (8 bins)
- Pitch angle bins 15 – 165 degrees (6 bins)
- Gyrophase bins 15 – 345 degrees (12 bins)

11.1.7 He3He4 Intensity

`he3he4_intensity_by_pitch_angle`

He3He4 intensity binned by pitch angle (1/(cm^2 s MeV/nuc sr))
Size: 8×6 time-varying
- He3He4 energy bins 0 – 4 MeV/nuc (8 bins)
- Pitch angle bins 15 – 165 degrees (6 bins)

11.1.8 He3He4 Intensity

`he3he4_intensity_by_pitch_angle_and_gyrophase`

He3He4 intensity binned by pitch angle and gyrophase (1/(cm^2 s MeV/nuc sr))

IMAP CDF summary

Size: $8 \times 6 \times 12$ time-varying
He3He4 energy bins 0 – 4 MeV/nuc (8 bins)
Pitch angle bins 15 – 165 degrees (6 bins)
Gyrophase bins 15 – 345 degrees (12 bins)

11.2 Other data

11.2.1 Quality flags for CoDICE Hi L3b

`codice_flags`

Quality flags for CoDICE Hi L3b (caution required if nonzero) (0: okay; nonzero: caution)
time-varying
Each bit corresponds to a specific potential concern. See release notes for details. Bit 2: preliminary MAG L1D used for magnetic field direction instead of the nominal MAG L2 product. Other bits are reserved.

12 imap_glows_l2_hist

GLOWS>GLObal Solar Wind Structure
L2_hist>Level-2 histogram
The GLObal Solar Wind Structure (GLOWS) is a non-imaging single-pixel Lyman-alpha photometer to investigate the global heliolatitudinal structure of the solar wind and its evolution during the solar cycle. Additionally, GLOWS investigates the distribution of interstellar neutral hydrogen (ISN H) and the solar radiation pressure acting on ISN H. The objectives of GLOWS are accomplished by observation of the modulation of heliospheric backscatter glow of ISN H (the helioglow) along a scanning circle in the sky. GLOWS design and assembly is led by the Space Research Center, Warsaw, Poland (CBK PAN). See https://imap.princeton.edu/spacecraft/instruments/global-solar-wind-structure-glows for more details.
Users should acknowledge the sources of data used in all publications, presentations, and reports using an appropriate DOI. Appropriate acknowledgement to institutions, personnel, and funding agencies should be given, including acknowledging the IMAP Mission Principal Investigator, Prof. David J. McComas of Princeton University (Contract #80GSFC19C0027). IMAP Rules-of-the-Road for data usage can be found in the IMAP CMAD.

12.1 Data

12.1.1 Occurrences of bad-time flags

`bad_time_flag_occurrences`

Numbers of occurences for each bad-time flag during observational day
`SPASE>Support>SupportQuantity:DataQuality`
Size: 17 time-varying

Flag index for daily-occurrence counters of L1B flags 0 – 16 (17 bins)

12.1.2 Exposure time per bin

`exposure_times`

Exposure times for histogram bins for observational day (s)
`SPASE>Support>SupportQuantity:Other`
Size: 3600 time-varying
Histogram bin number 0 – 3599 (3600 bins)

12.1.3 Bad-angle flags for histogram

`histogram_flag_array`

Bad-angle flags for histogram bins
`SPASE>Support>SupportQuantity:DataQuality`
Size: 3600 time-varying
Histogram bin number 0 – 3599 (3600 bins)

12.1.4 Pointing-averaged photon flux

`photon_flux`

Photon flux in scanning-circle bins averaged over observational day (Rayleigh)
`SPASE>Wave>WaveType:Electromagnetic,WaveQuantity:Intensity,Qualifier:Scalar`
Size: 3600 time-varying
Histogram bin number 0 – 3599 (3600 bins)

12.1.5 Histogram of counts

`raw_histograms`

Histogram of counts for observational day (#)
`SPASE>Support>SupportQuantity:Other`
Size: 3600 time-varying
Histogram bin number 0 – 3599 (3600 bins)

12.2 Support Data

12.2.1 Ecliptic latitudes of bins

`ecliptic_lat`

Ecliptic latitudes of bin centers (degrees)
`SPASE>Support>SupportQuantity:Positional`
Size: 3600 time-varying
Histogram bin number 0 – 3599 (3600 bins)

12.2.2 Ecliptic longitudes of bins

`ecliptic_lon`

Ecliptic longitudes of bin centers (degrees)
`SPASE>Support>SupportQuantity:Positional`
Size: 3600 time-varying
Histogram bin number 0 – 3599 (3600 bins)

12.2.3 Observation end time UTC

`end_time`

End time (UTC) of observational day (N/A)
`SPASE>Support>SupportQuantity:Temporal`
time-varying

12.2.4 Average filter temperature

`filter_temperature_average`

Filter temperature averaged over observational day (Celsius)
`SPASE>Support>SupportQuantity:Other`
time-varying

12.2.5 Std dev of filter temperature

`filter_temperature_std_dev`

Standard deviation of filter temperature (Celsius)
`SPASE>Support>SupportQuantity:Housekeeping`
time-varying

12.2.6 Average HV voltage

`hv_voltage_average`

CEM HV voltage averaged over observational day (V)
`SPASE>Support>SupportQuantity:Housekeeping`
time-varying

12.2.7 Std dev of HV voltage

`hv_voltage_std_dev`

Standard deviation of CEM HV voltage (V)
`SPASE>Support>SupportQuantity:Housekeeping`
time-varying

12.2.8 Spin-axis pointing number

`identifier`

Spin-axis pointing number to identify observational day
`SPASE>Support>SupportQuantity:Temporal`
time-varying

12.2.9 Number of bins in histogram

`number_of_bins`

`SPASE>Support>SupportQuantity:Other`
time-varying

12.2.10 Number of good L1B inputs

`number_of_good_l1b_inputs`

Number of good L1B inputs per observational day
`SPASE>Support>SupportQuantity:Other`
time-varying

12.2.11 Average position angle offset

`position_angle_offset_average`

Position angle offset averaged over observational day (degrees)
SPASE>Support>SupportQuantity:Positional
time-varying
Derived from SPICE Kernels

12.2.12 Std dev of position angle offset

position_angle_offset_std_dev

Standard deviation of position angle offset (degrees)
SPASE>Support>SupportQuantity:DataQuality
time-varying
Derived from SPICE Kernels

12.2.13 Average pulse length

pulse_length_average

Pulse length averaged over observational day (us)
SPASE>Support>SupportQuantity:Housekeeping
time-varying

12.2.14 Std dev of pulse length

pulse_length_std_dev

Standard deviation of pulse length (us)
SPASE>Support>SupportQuantity:Housekeeping
time-varying

12.2.15 Average spacecraft location

spacecraft_location_average

Spacecraft location averaged over observational day (ecliptic frame) (km)
SPASE>Support>SupportQuantity:Positional
Size: 3 time-varying
    Component index for cartesian ecliptic coordinates 0 – 2 (3 bins)
Derived from SPICE Kernels

12.2.16 Std dev of spacecraft location

`spacecraft_location_std_dev`

Standard deviation of spacecraft location (km)
`SPASE>Support>SupportQuantity:DataQuality`
Size: 3 time-varying
    Component index for cartesian ecliptic coordinates 0 – 2 (3 bins)
Derived from SPICE Kernels

12.2.17 Average spacecraft velocity

`spacecraft_velocity_average`

Spacecraft velocity averaged over observational day (ecliptic frame) (km/s)
`SPASE>Support>SupportQuantity:Velocity`
Size: 3 time-varying
    Component index for cartesian ecliptic coordinates 0 – 2 (3 bins)
Derived from SPICE Kernels

12.2.18 Std dev of spacecraft velocity

`spacecraft_velocity_std_dev`

Standard deviation of spacecraft velocity (km/s)
`SPASE>Support>SupportQuantity:DataQuality`
Size: 3 time-varying
    Component index for cartesian ecliptic coordinates 0 – 2 (3 bins)
Derived from SPICE Kernels

12.2.19 Spin angle for bin centers

`spin_angle`

Spin angle (measured from north) for bin centers (degrees)
`SPASE>Support>SupportQuantity:SpinPhase`
Size: 3600 time-varying
    Histogram bin number 0 – 3599 (3600 bins)

12.2.20 Average spin axis pointing

`spin_axis_orientation_average`

Spin axis pointing averaged over observational day (ecliptic lon and lat) (degrees)
SPASE>Support>SupportQuantity:SpinPhase
Size: 2 time-varying
Derived from SPICE Kernels

12.2.21 Std dev of spin axis pointing

spin_axis_orientation_std_dev

Standard deviation of spin axis pointing (degrees)
SPASE>Support>SupportQuantity:DataQuality
Size: 2 time-varying
Derived from SPICE Kernels

12.2.22 Average spin period

spin_period_average

Spin period averaged over observational day (s)
SPASE>Support>SupportQuantity:SpinPeriod
time-varying

12.2.23 Average spin period (ground)

spin_period_ground_average

Spin period (ground processing) averaged over observational day (s)
SPASE>Support>SupportQuantity:SpinPeriod
time-varying

12.2.24 Std dev of spin period (ground)

spin_period_ground_std_dev

Standard deviation of spin period (ground processing) (s)
SPASE>Support>SupportQuantity:DataQuality
time-varying

12.2.25 Std dev of spin period

spin_period_std_dev

Standard deviation of spin period (s)
SPASE>Support>SupportQuantity:DataQuality
time-varying

12.2.26 Observation start time UTC

start_time

Start time (UTC) of observational day (N/A)
SPASE>Support>SupportQuantity:Temporal
time-varying

12.2.27 Total number of L1B inputs

total_l1b_inputs

Total number of L1B inputs per observational day
SPASE>Support>SupportQuantity:Other
time-varying

13 imap_glows_l3a_hist

GLOWS>GLObal Solar Wind Structure
L3A_hist>Level-3A histogram
The GLObal Solar Wind Structure (GLOWS) is a non-imaging single-pixel Lyman-alpha photometer to investigate the global heliolatitudinal structure of the solar wind and its evolution during the solar cycle. Additionally, GLOWS investigates the distribution of interstellar neutral hydrogen (ISN H) and the solar radiation pressure acting on ISN H. The objectives of GLOWS are accomplished by observation of the modulation of heliospheric backscatter glow of ISN H (the helioglow) along a scanning circle in the sky. GLOWS design and assembly is led by the Space Research Center, Warsaw, Poland (CBK PAN). See https://imap.princeton.edu/spacecraft/instruments/global-solar-wind-structure-glows for more details.
Users should acknowledge the sources of data used in all publications, presentations, and reports using an appropriate DOI. Appropriate acknowledgement to institutions, personnel, and funding agencies should be given, including acknowledging the IMAP Mission Principal Investigator, Prof. David J. McComas of Princeton University (Contract #80GSFC19C0027). IMAP Rules-of-the-Road for data usage can be found in the IMAP CMAD.

13.1 Primary variables

13.1.1 Pointing-averaged Photon Flux

`photon_flux`

Photon flux in scanning-circle bins averaged over observational day (Rayleigh)
Size: 80 time-varying
Spin angle (measured from north) for bin centers 2 – 350 degrees (80 bins)

13.2 Other data

13.2.1 Exposure Time Per Bin

`exposure_times`

Exposure times for histogram bins for observational day (s)
Size: 80 time-varying
Spin angle (measured from north) for bin centers 2 – 350 degrees (80 bins)

13.2.2 Histogram Of Counts

`raw_histogram`

Histogram of counts for observational day (#)
Size: 80 time-varying
Spin angle (measured from north) for bin centers 2 – 350 degrees (80 bins)

13.3 Support Data

13.3.1 Ecliptic Latitudes Of Bins

`ecliptic_lat`

Ecliptic latitudes of bin centers (degrees)
Size: 80 time-varying
Spin angle (measured from north) for bin centers 2 – 350 degrees (80 bins)

13.3.2 Ecliptic Longitudes Of Bins

`ecliptic_lon`

Ecliptic longitudes of bin centers (degrees)
Size: 80 time-varying

Spin angle (measured from north) for bin centers 2 – 350 degrees (80 bins)

13.3.3 Observation End Time UTC

`end_time`

End time (UTC) of observational day
time-varying

13.3.4 Extra-heliospheric Background

`extra_heliospheric_bckgrd`

Extra-heliospheric background estimate (Rayleigh)
Size: 80 time-varying
Spin angle (measured from north) for bin centers 2 – 350 degrees (80 bins)

13.3.5 Average Filter Temperature

`filter_temperature_average`

Filter temperature averaged over observational day (Celsius)
time-varying

13.3.6 Average HV Voltage

`hv_voltage_average`

CEM HV voltage averaged over observational day (V)
time-varying

13.3.7 Spin-axis pointing number

`identifier`

Spin-axis pointing number to identify observational day
time-varying

13.3.8 Number Of Histogram Bins

`number_of_bins`

Number of histogram bins
time-varying

13.3.9 Average Position Angle Offset

`position_angle_offset_average`

Position angle offset averaged over observational day (degrees)
time-varying

13.3.10 Average Pulse Length

`pulse_length_average`

Pulse length averaged over observational day (us)
time-varying

13.3.11 Average Spacecraft Location

`spacecraft_location_average`

Spacecraft location averaged over observational day (ecliptic frame) (km)
Size: 3 time-varying
Component index for cartesian ecliptic coordinates 0 – 2 (3 bins)

13.3.12 Average Spacecraft Velocity

`spacecraft_velocity_average`

Spacecraft velocity averaged over observational day (ecliptic frame) (km/s)
Size: 3 time-varying
Component index for cartesian ecliptic coordinates 0 – 2 (3 bins)

13.3.13 Average Spin Axis Pointing

`spin_axis_orientation_average`

Spin axis pointing averaged over observational day (ecliptic lon and lat) (degrees)
Size: 2 time-varying
Component index for ecliptic longitude and latitude 0 – 1 (2 bins)

13.3.14 Average Spin Period

`spin_period_average`

Spin period averaged over observational day (s)
time-varying

13.3.15 Average Spin Period (Ground)

`spin_period_ground_average`

Spin period (ground processing) averaged over observational day (s)
time-varying

13.3.16 Observation Start Time UTC

`start_time`

Start time (UTC) of observational day
time-varying

13.3.17 Time-dependent Background

`time_dependent_bckgrd`

Time-dependent background estimate (Rayleigh)
Size: 80 time-varying
Spin angle (measured from north) for bin centers 2 – 350 degrees (80 bins)

14 imap_glows_l3b_ion-rate-profile

GLOWS>GLObal Solar Wind Structure
L3B_ion-rate-profile>Level-3B Ion Rate Profile
The GLObal Solar Wind Structure (GLOWS) is a non-imaging single-pixel Lyman-alpha photometer to investigate the global heliolatitudinal structure of the solar wind and its evolution during the solar cycle. Additionally, GLOWS investigates the distribution of interstellar neutral hydrogen (ISN H) and the solar radiation pressure acting on ISN H. The objectives of GLOWS are accomplished by observation of the modulation of heliospheric backscatter glow of ISN H (the helioglow) along a scanning circle in the sky. GLOWS design and assembly is led by the Space Research Center, Warsaw, Poland (CBK PAN). See https://imap.princeton.edu/spacecraft/instruments/global-solar-wind-structure-glows for more details.
Users should acknowledge the sources of data used in all publications, presentations, and reports using an appropriate DOI. Appropriate acknowledgement to institutions, personnel, and funding

agencies should be given, including acknowledging the IMAP Mission Principal Investigator, Prof. David J. McComas of Princeton University (Contract #80GSFC19C0027). IMAP Rules-of-the-Road for data usage can be found in the IMAP CMAD.

14.1 Primary variables

14.1.1 Charge Exchange Rate

`cx_rate`

Averaged charge exchange rate profile (stationary atom approximation) (s^-1)
Size: 19 time-varying
Latitudinal grid from -90 to 90 -90 – 90 degrees (19 bins)

14.1.2 Photoionization Rate

`ph_rate`

Averaged photoionization rate profile (s^-1)
Size: 19 time-varying
Latitudinal grid from -90 to 90 -90 – 90 degrees (19 bins)

14.1.3 Sum Rate

`sum_rate`

Averaged ionization rate profile obtained from lightcurve (s^-1)
Size: 19 time-varying
Latitudinal grid from -90 to 90 -90 – 90 degrees (19 bins)

14.2 Other data

14.2.1 Quality Flags for GLOWS L3b

`glows_flags`

Quality flags for GLOWS L3b (caution required if nonzero) (0: okay; nonzero: caution)
time-varying
Each bit corresponds to a specific potential concern. See release notes for details. All bits are reserved for future use.

14.3 Support Data

14.3.1 Carrington Rotation

`cr`

Carrington rotation number
time-varying

14.3.2 UV Anisotropy Factor

`uv_anisotropy_factor`

UV anisotropy factor
Size: 19 time-varying
Latitudinal grid from -90 to 90 -90 – 90 degrees (19 bins)

14.3.3 UV Anisotropy Source

`uv_anisotropy_flag`

Source flag for UV anisotropy
time-varying
Primarily for instrument team traceability. Details in release notes. Values: -1: Unspecified 10000: Constant model 20000: Pheomenological model 20010: Pheomenological model 1 20020: Pheomenological model 2

15 imap_glows_l3c_sw-profile

GLOWS>GLObal Solar Wind Structure
L3C_sw-profile>Level-3C Solar Wind Profile
The GLObal Solar Wind Structure (GLOWS) is a non-imaging single-pixel Lyman-alpha photometer to investigate the global heliolatitudinal structure of the solar wind and its evolution during the solar cycle. Additionally, GLOWS investigates the distribution of interstellar neutral hydrogen (ISN H) and the solar radiation pressure acting on ISN H. The objectives of GLOWS are accomplished by observation of the modulation of heliospheric backscatter glow of ISN H (the helioglow) along a scanning circle in the sky. GLOWS design and assembly is led by the Space Research Center, Warsaw, Poland (CBK PAN). See https://imap.princeton.edu/spacecraft/instruments/global-solar-wind-structure-glows for more details.
Users should acknowledge the sources of data used in all publications, presentations, and reports using an appropriate DOI. Appropriate acknowledgement to institutions, personnel, and funding agencies should be given, including acknowledging the IMAP Mission Principal Investigator, Prof. David J. McComas of Princeton University (Contract #80GSFC19C0027). IMAP Rules-of-the-

IMAP CDF summary

Road for data usage can be found in the IMAP CMAD.

15.1 Primary variables

15.1.1 Alpha Abundance

`alpha_abundance_ecliptic`

Averaged alpha-particles to protons ratio in the ecliptic plane
time-varying

15.1.2 Ecliptic Plasma Speed

`plasma_speed_ecliptic`

Averaged solar wind plasma speed in the ecliptic plane (km/s)
time-varying

15.1.3 Plasma Speed Profile

`plasma_speed_profile`

Averaged profile of solar wind plasma speed (km/s)
Size: 19 time-varying
    Latitudinal grid from -90 to 90 -90 – 90 degrees (19 bins)

15.1.4 Ecliptic Proton Density

`proton_density_ecliptic`

Averaged proton density in the ecliptic plane adjusted to 1 au (cm^-3)
time-varying

15.1.5 Proton Density Profile

`proton_density_profile`

Averaged profile of proton density adjusted to 1 au (cm^-3)
Size: 19 time-varying
    Latitudinal grid from -90 to 90 -90 – 90 degrees (19 bins)

15.2 Other data

15.2.1 Quality Flags for GLOWS L3c

`glows_flags`

Quality flags for GLOWS L3c (caution required if nonzero) (0: okay; nonzero: caution)
time-varying
Each bit corresponds to a specific potential concern. See release notes for details. Bit 2: Solar wind alpha/proton density ratio not available in OMNI data; used nominal value of 0.04 Other bits are reserved.

15.3 Support Data

15.3.1 Carrington Rotation

`cr`

Carrington rotation number
time-varying

16 imap_glows_l3d_solar-hist

GLOWS>GLObal Solar Wind Structure
L3D_solar-hist>Level-3D Solar History
The GLObal Solar Wind Structure (GLOWS) is a non-imaging single-pixel Lyman-alpha photometer to investigate the global heliolatitudinal structure of the solar wind and its evolution during the solar cycle. Additionally, GLOWS investigates the distribution of interstellar neutral hydrogen (ISN H) and the solar radiation pressure acting on ISN H. The objectives of GLOWS are accomplished by observation of the modulation of heliospheric backscatter glow of ISN H (the helioglow) along a scanning circle in the sky. GLOWS design and assembly is led by the Space Research Center, Warsaw, Poland (CBK PAN). See https://imap.princeton.edu/spacecraft/instruments/global-solar-wind-structure-glows for more details.
Users should acknowledge the sources of data used in all publications, presentations, and reports using an appropriate DOI. Appropriate acknowledgement to institutions, personnel, and funding agencies should be given, including acknowledging the IMAP Mission Principal Investigator, Prof. David J. McComas of Princeton University (Contract #80GSFC19C0027). IMAP Rules-of-the-Road for data usage can be found in the IMAP CMAD.

16.1 Primary variables

16.1.1 Electron Density

`electron_density`

Electron density (#/cm^3)
time-varying

16.1.2 Solar Lyman-alpha

`lyman_alpha`

Composite solar Lyman-alpha irradiance (#/cm^2/s)
time-varying

16.1.3 Photoionization Rate

`phion`

Photoionization rate in the ecliptic plane (#/s)
time-varying

16.1.4 Plasma Speed

`plasma_speed`

Solar wind plasma speed (km/s)
Size: 19 time-varying
Latitudes from -90 to 90 -90 – 90 degrees (19 bins)

16.1.5 Proton Density

`proton_density`

Solar wind proton density (#/cm^3)
Size: 19 time-varying
Latitudes from -90 to 90 -90 – 90 degrees (19 bins)

16.1.6 Solar UV Anisotropy

`uv_anisotropy`

Solar UV radiation anisotropy
Size: 19 time-varying
Latitudes from -90 to 90 -90 – 90 degrees (19 bins)

16.2 Other data

16.2.1 Quality Flags for GLOWS L3d

`glows_flags`

Quality flags for GLOWS L3d (caution required if nonzero) (0: okay; nonzero: caution)
time-varying
Each bit corresponds to a specific potential concern. See release notes for details. Bit 2: Solar wind alpha/proton density ratio not available in OMNI data; input GLOWS L3c file used nominal value of 0.04. Other bits are reserved.

16.3 Support Data

16.3.1 Carrington Rotation

`cr_grid`

Carrington rotation number
time-varying

16.3.2 Plasma Speed Source

`plasma_speed_flag`

Solar wind plasma speed source
time-varying
Primarily for instrument team traceability. Details in release notes. Values: -1: Unspecified 20000: Speed from GLOWS measurements and ancillary inputs 20001: Speed interpolated 88888: Value extrapolated by repeating previous measured value

16.3.3 Proton Density Source

`proton_density_flag`

Solar wind proton density source
time-varying
Primarily for instrument team traceability. Details in release notes. Values: -1: Unspecified 10000: Density from same source as speed data 10001: Density from source of speed data, interpolated 88888: Value extrapolated by repeating previous measured value

16.3.4 UV Anisotropy Source

`uv_anisotropy_flag`

Ultraviolet anisotropy source
time-varying
Primarily for instrument team traceability. Details in release notes. Values: -1: Unspecified 10000: Constant model 20000: Pheomenological model 20010: Pheomenological model 1 20020: Pheomenological model 2 30001: UV anisotropy interpolated 88888: Value extrapolated by repeating previous measured value

17 imap_glows_l3e_survival-probability-hi-45

GLOWS>GLObal Solar Wind Structure
L3E_survival-probability-hi-45>Level-3E Survival Probability Hi 45
The GLObal Solar Wind Structure (GLOWS) is a non-imaging single-pixel Lyman-alpha photometer to investigate the global heliolatitudinal structure of the solar wind and its evolution during the solar cycle. Additionally, GLOWS investigates the distribution of interstellar neutral hydrogen (ISN H) and the solar radiation pressure acting on ISN H. The objectives of GLOWS are accomplished by observation of the modulation of heliospheric backscatter glow of ISN H (the helioglow) along a scanning circle in the sky. GLOWS design and assembly is led by the Space Research Center, Warsaw, Poland (CBK PAN). See https://imap.princeton.edu/spacecraft/instruments/global-solar-wind-structure-glows for more details.
Users should acknowledge the sources of data used in all publications, presentations, and reports using an appropriate DOI. Appropriate acknowledgement to institutions, personnel, and funding agencies should be given, including acknowledging the IMAP Mission Principal Investigator, Prof. David J. McComas of Princeton University (Contract #80GSFC19C0027). IMAP Rules-of-the-Road for data usage can be found in the IMAP CMAD.

17.1 Primary variables

17.1.1 Probability Of Survival

`surv_prob`

Survival probabilities for IMAP-Hi
Size: 16×360 time-varying

Energies associated with the survival probabilities for IMAP-Hi 0 – 20 keV (16 bins)

Angle on the circle around axis rotation, with the radius elongation angle. The 0 spin_angle is the direction nearest north pole. 1 – 360 degrees (360 bins)

17.2 Other data

17.2.1 Quality Flags for GLOWS L3e Hi-45

`glows_flags`

Quality flags for GLOWS L3e Hi-45 (caution required if nonzero) (0: okay; nonzero: caution)
time-varying
Each bit corresponds to a specific potential concern. See release notes for details. Bit 2: Solar wind alpha/proton density ratio not available in OMNI data; input GLOWS L3c file used nominal value of 0.04. Other bits are reserved.

17.3 Support Data

17.3.1 Elongation

`elongation`

Position of Hi instrument (degree)
time-varying

17.3.2 Spacecraft Latitude

`spacecraft_latitude`

IMAP spacecraft latitude (degrees)
time-varying

17.3.3 Spacecraft Longitude

`spacecraft_longitude`

IMAP spacecraft longitude (degrees)
time-varying

17.3.4 Spacecraft Radius

`spacecraft_radius`

Distance from IMAP to sun (AU)
time-varying

17.3.5 Spacecraft Velocity X

`spacecraft_velocity_x`

IMAP spacecraft x velocity (km/s)
time-varying

17.3.6 Spacecraft Velocity Y

`spacecraft_velocity_y`

IMAP spacecraft y velocity (km/s)
time-varying

17.3.7 Spacecraft Velocity Z

`spacecraft_velocity_z`

IMAP spacecraft z velocity (km/s)
time-varying

17.3.8 Spin Axis Latitude

`spin_axis_latitude`

Latitude of spin axis (degrees)
time-varying

17.3.9 Spin Axis Longitude

`spin_axis_longitude`

Longitude of spin axis (degrees)
time-varying

18 imap_glows_l3e_survival-probability-hi-90

GLOWS>GLObal Solar Wind Structure
L3E_survival-probability-hi-90>Level-3E Survival Probability Hi 90
The GLObal Solar Wind Structure (GLOWS) is a non-imaging single-pixel Lyman-alpha photometer to investigate the global heliolatitudinal structure of the solar wind and its evolution during the solar cycle. Additionally, GLOWS investigates the distribution of interstellar neutral hydrogen (ISN

H) and the solar radiation pressure acting on ISN H. The objectives of GLOWS are accomplished by observation of the modulation of heliospheric backscatter glow of ISN H (the helioglow) along a scanning circle in the sky. GLOWS design and assembly is led by the Space Research Center, Warsaw, Poland (CBK PAN). See https://imap.princeton.edu/spacecraft/instruments/global-solar-wind-structure-glows for more details.
Users should acknowledge the sources of data used in all publications, presentations, and reports using an appropriate DOI. Appropriate acknowledgement to institutions, personnel, and funding agencies should be given, including acknowledging the IMAP Mission Principal Investigator, Prof. David J. McComas of Princeton University (Contract #80GSFC19C0027). IMAP Rules-of-the-Road for data usage can be found in the IMAP CMAD.

18.1 Primary variables

18.1.1 Probability Of Survival

`surv_prob`

Survival probabilities for IMAP-Hi
Size: 16×360 time-varying

Energies associated with the survival probabilities for IMAP-Hi 0 – 20 keV (16 bins)

Angle on the circle around axis rotation, with the radius elongation angle. The 0 spin_angle is the direction nearest north pole. 1 – 360 degrees (360 bins)

18.2 Other data

18.2.1 Quality Flags for GLOWS L3e Hi-90

`glows_flags`

Quality flags for GLOWS L3e Hi-90 (caution required if nonzero) (0: okay; nonzero: caution)
time-varying
Each bit corresponds to a specific potential concern. See release notes for details. Bit 2: Solar wind alpha/proton density ratio not available in OMNI data; input GLOWS L3c file used nominal value of 0.04. Other bits are reserved.

18.3 Support Data

18.3.1 Elongation

`elongation`

Position of Hi instrument (degree)
time-varying

18.3.2 Spacecraft Latitude

`spacecraft_latitude`

IMAP spacecraft latitude (degrees)
time-varying

18.3.3 Spacecraft Longitude

`spacecraft_longitude`

IMAP spacecraft longitude (degrees)
time-varying

18.3.4 Spacecraft Radius

`spacecraft_radius`

Distance from IMAP to sun (AU)
time-varying

18.3.5 Spacecraft Velocity X

`spacecraft_velocity_x`

IMAP spacecraft x velocity (km/s)
time-varying

18.3.6 Spacecraft Velocity Y

`spacecraft_velocity_y`

IMAP spacecraft y velocity (km/s)
time-varying

18.3.7 Spacecraft Velocity Z

`spacecraft_velocity_z`

IMAP spacecraft z velocity (km/s)
time-varying

18.3.8 Spin Axis Latitude

`spin_axis_latitude`

Latitude of spin axis (degrees)
time-varying

18.3.9 Spin Axis Longitude

`spin_axis_longitude`

Longitude of spin axis (degrees)
time-varying

19 imap_glows_l3e_survival-probability-lo

GLOWS>GLObal Solar Wind Structure
L3E_survival-probability-lo>Level-3E Survival Probability Lo
The GLObal Solar Wind Structure (GLOWS) is a non-imaging single-pixel Lyman-alpha photometer to investigate the global heliolatitudinal structure of the solar wind and its evolution during the solar cycle. Additionally, GLOWS investigates the distribution of interstellar neutral hydrogen (ISN H) and the solar radiation pressure acting on ISN H. The objectives of GLOWS are accomplished by observation of the modulation of heliospheric backscatter glow of ISN H (the helioglow) along a scanning circle in the sky. GLOWS design and assembly is led by the Space Research Center, Warsaw, Poland (CBK PAN). See https://imap.princeton.edu/spacecraft/instruments/global-solar-wind-structure-glows for more details.
Users should acknowledge the sources of data used in all publications, presentations, and reports using an appropriate DOI. Appropriate acknowledgement to institutions, personnel, and funding agencies should be given, including acknowledging the IMAP Mission Principal Investigator, Prof. David J. McComas of Princeton University (Contract #80GSFC19C0027). IMAP Rules-of-the-Road for data usage can be found in the IMAP CMAD.

19.1 Primary variables

19.1.1 Probability Of Survival

`surv_prob`

Survival probabilities for IMAP-Lo
Size: 24×360 time-varying

Energies associated with the survival probabilities for IMAP-Lo 0 – 4 keV (24 bins)

Angle on the circle around axis rotation, with the radius elongation angle. The 0 spin_angle is the direction nearest north pole. 1 – 360 degrees (360 bins)

19.2 Other data

19.2.1 Quality Flags for GLOWS L3e Lo

`glows_flags`

Quality flags for GLOWS L3e Lo (caution required if nonzero (0: okay; nonzero: caution)
time-varying
Each bit corresponds to a specific potential concern. See release notes for details. Bit 2: Solar wind alpha/proton density ratio not available in OMNI data; input GLOWS L3c file used nominal value of 0.04. Other bits are reserved.

19.3 Support Data

19.3.1 Elongation

`elongation`

Position of Lo instrument (degree)
time-varying

19.3.2 Spacecraft Latitude

`spacecraft_latitude`

IMAP spacecraft latitude (degrees)
time-varying

19.3.3 Spacecraft Longitude

`spacecraft_longitude`

IMAP spacecraft longitude (degrees)
time-varying

19.3.4 Spacecraft Radius

`spacecraft_radius`

Distance from IMAP to sun (AU)
time-varying

19.3.5 Spacecraft Velocity X

`spacecraft_velocity_x`

IMAP spacecraft x velocity (km/s)
time-varying

19.3.6 Spacecraft Velocity Y

`spacecraft_velocity_y`

IMAP spacecraft y velocity (km/s)
time-varying

19.3.7 Spacecraft Velocity Z

`spacecraft_velocity_z`

IMAP spacecraft z velocity (km/s)
time-varying

19.3.8 Spin Axis Latitude

`spin_axis_latitude`

Latitude of spin axis (degrees)
time-varying

19.3.9 Spin Axis Longitude

`spin_axis_longitude`

Longitude of spin axis (degrees)
time-varying

20 imap_glows_l3e_survival-probability-ul-hf

GLOWS>GLObal Solar Wind Structure
L3E_survival-probability-ul>Level-3E Survival Probability Ul HF
The GLObal Solar Wind Structure (GLOWS) is a non-imaging single-pixel Lyman-alpha photometer to investigate the global heliolatitudinal structure of the solar wind and its evolution during the solar cycle. Additionally, GLOWS investigates the distribution of interstellar neutral hydrogen (ISN

H) and the solar radiation pressure acting on ISN H. The objectives of GLOWS are accomplished by observation of the modulation of heliospheric backscatter glow of ISN H (the helioglow) along a scanning circle in the sky. GLOWS design and assembly is led by the Space Research Center, Warsaw, Poland (CBK PAN). See https://imap.princeton.edu/spacecraft/instruments/global-solar-wind-structure-glows for more details.
Users should acknowledge the sources of data used in all publications, presentations, and reports using an appropriate DOI. Appropriate acknowledgement to institutions, personnel, and funding agencies should be given, including acknowledging the IMAP Mission Principal Investigator, Prof. David J. McComas of Princeton University (Contract #80GSFC19C0027). IMAP Rules-of-the-Road for data usage can be found in the IMAP CMAD.

20.1 Primary variables

20.1.1 Probability Of Survival

`surv_prob`

Survival probabilities for IMAP-Ultra
Size: 20×3072 time-varying
Energies associated with the survival probabilities for IMAP-Ultra 2 – 356 keV (20 bins)
Heal pixel index 0 – 3071 (3072 bins)

20.2 Other data

20.2.1 Quality Flags for GLOWS L3e Ultra HF

`glows_flags`

Quality flags for GLOWS L3e Ultra HF (caution required if nonzero) (0: okay; nonzero: caution)
time-varying
Each bit corresponds to a specific potential concern. See release notes for details. Bit 2: Solar wind alpha/proton density ratio not available in OMNI data; input GLOWS L3c file used nominal value of 0.04. Other bits are reserved.

20.3 Support Data

20.3.1 Elongation Excluded

`elongation_excluded`

Region of excluded values from Ultra instrument (degree)
time-varying

20.3.2 HAE latitude

`pixel_latitude`

Pixel center latitude in HAE (ECLIPJ2000) (degrees)
Size: 3072 time-varying
    Heal pixel index 0 – 3071 (3072 bins)
Reference frames are defined according to IMAP mission SPICE kernels.

20.3.3 HAE longitude

`pixel_longitude`

Pixel center longitude in HAE (ECLIPJ2000) (degrees)
Size: 3072 time-varying
    Heal pixel index 0 – 3071 (3072 bins)
Reference frames are defined according to IMAP mission SPICE kernels.

20.3.4 Spacecraft Latitude

`spacecraft_latitude`

IMAP spacecraft latitude (degrees)
time-varying

20.3.5 Spacecraft Longitude

`spacecraft_longitude`

IMAP spacecraft longitude (degrees)
time-varying

20.3.6 Spacecraft Radius

`spacecraft_radius`

Distance from IMAP to sun (AU)
time-varying

20.3.7 Spacecraft Velocity X

`spacecraft_velocity_x`

IMAP spacecraft x velocity (km/s)
time-varying

20.3.8 Spacecraft Velocity Y

`spacecraft_velocity_y`

IMAP spacecraft y velocity (km/s)
time-varying

20.3.9 Spacecraft Velocity Z

`spacecraft_velocity_z`

IMAP spacecraft z velocity (km/s)
time-varying

20.3.10 Spin Axis Latitude

`spin_axis_latitude`

Latitude of spin axis (degrees)
time-varying

20.3.11 Spin Axis Longitude

`spin_axis_longitude`

Longitude of spin axis (degrees)
time-varying

21 imap_glows_l3e_survival-probability-ul-sf

GLOWS>GLObal Solar Wind Structure
L3E_survival-probability-ul>Level-3E Survival Probability Ul
The GLObal Solar Wind Structure (GLOWS) is a non-imaging single-pixel Lyman-alpha photometer to investigate the global heliolatitudinal structure of the solar wind and its evolution during the solar cycle. Additionally, GLOWS investigates the distribution of interstellar neutral hydrogen (ISN H) and the solar radiation pressure acting on ISN H. The objectives of GLOWS are accomplished by observation of the modulation of heliospheric backscatter glow of ISN H (the helioglow) along a scanning circle in the sky. GLOWS design and assembly is led by the Space Research Center,

Warsaw, Poland (CBK PAN). See https://imap.princeton.edu/spacecraft/instruments/global-solar-wind-structure-glows for more details.
Users should acknowledge the sources of data used in all publications, presentations, and reports using an appropriate DOI. Appropriate acknowledgement to institutions, personnel, and funding agencies should be given, including acknowledging the IMAP Mission Principal Investigator, Prof. David J. McComas of Princeton University (Contract #80GSFC19C0027). IMAP Rules-of-the-Road for data usage can be found in the IMAP CMAD.

21.1 Primary variables

21.1.1 Probability Of Survival

`surv_prob`

Survival probabilities for IMAP-Ultra
Size: 20×3072 time-varying
Energies associated with the survival probabilities for IMAP-Ultra 2 – 356 keV (20 bins)
Heal pixel index 0 – 3071 (3072 bins)

21.2 Other data

21.2.1 Quality Flags for GLOWS L3e Ultra SF

`glows_flags`

Quality flags for GLOWS L3e Ultra SF (caution required if nonzero) (0: okay; nonzero: caution)
time-varying
Each bit corresponds to a specific potential concern. See release notes for details. Bit 2: Solar wind alpha/proton density ratio not available in OMNI data; input GLOWS L3c file used nominal value of 0.04. Other bits are reserved.

21.3 Support Data

21.3.1 Elongation Excluded

`elongation_excluded`

Region of excluded values from Ultra instrument (degree)
time-varying

21.3.2 HAE latitude

`pixel_latitude`

Pixel center latitude in HAE (ECLIPJ2000) (degrees)
Size: 3072 time-varying
    Heal pixel index 0 – 3071 (3072 bins)
Reference frames are defined according to IMAP mission SPICE kernels.

21.3.3 HAE longitude

`pixel_longitude`

Pixel center longitude in HAE (ECLIPJ2000) (degrees)
Size: 3072 time-varying
    Heal pixel index 0 – 3071 (3072 bins)
Reference frames are defined according to IMAP mission SPICE kernels.

21.3.4 Spacecraft Latitude

`spacecraft_latitude`

IMAP spacecraft latitude (degrees)
time-varying

21.3.5 Spacecraft Longitude

`spacecraft_longitude`

IMAP spacecraft longitude (degrees)
time-varying

21.3.6 Spacecraft Radius

`spacecraft_radius`

Distance from IMAP to sun (AU)
time-varying

21.3.7 Spacecraft Velocity X

`spacecraft_velocity_x`

IMAP spacecraft x velocity (km/s)
time-varying

21.3.8 Spacecraft Velocity Y

`spacecraft_velocity_y`

IMAP spacecraft y velocity (km/s)
time-varying

21.3.9 Spacecraft Velocity Z

`spacecraft_velocity_z`

IMAP spacecraft z velocity (km/s)
time-varying

21.3.10 Spin Axis Latitude

`spin_axis_latitude`

Latitude of spin axis (degrees)
time-varying

21.3.11 Spin Axis Longitude

`spin_axis_longitude`

Longitude of spin axis (degrees)
time-varying

22 imap_hit_l2_standard-intensity

HIT>IMAP High-energy Ion Telescope
L2_standard-intensity>Level-2 Standard Intensity
The High-energy Ion Telescope (HIT) measures the elemental composition, energy spectra, angle distributions, and arrival times of high-energy ions. HIT delivers full-sky coverage from a wide instrument field-of-view (FOV) to enable a high resolution of ion measurements, such as observing shock-accelerated ions, determining the origin of the solar energetic particles (SEPs) spectra, and resolving particle transport in the heliosphere. See https://imap.princeton.edu/spacecraft/instruments/high-energy-ion-telescope-hit for more details.
Users should acknowledge the sources of data used in all publications, presentations, and reports using an appropriate DOI. Appropriate acknowledgement to institutions, personnel, and funding agencies should be given, including acknowledging the IMAP Mission Principal Investigator, Prof.

IMAP CDF summary

David J. McComas of Princeton University (Contract #80GSFC19C0027). IMAP Rules-of-the-Road for data usage can be found in the IMAP CMAD.

22.1 Data

22.1.1 Al Intensity Standard

`al_standard_intensity`

Al Standard Omnidirectional Intensity in 9 energy bins (1/(cm^2 s MeV/nuc sr))
`SPASE>Particle>ParticleType:Ion,ParticleQuantity:NumberFlux,Qualifier:Differential`
Size: 9 time-varying

Geometric mean energy per nucleon for Al 7 – 46 MeV/nuc (9 bins)

22.1.2 Ar Intensity Standard

`ar_standard_intensity`

Ar Standard Omnidirectional Intensity in 13 energy bins (1/(cm^2 s MeV/nuc sr))
`SPASE>Particle>ParticleType:Ion,ParticleQuantity:NumberFlux,Qualifier:Differential`
Size: 13 time-varying

Geometric mean energy per nucleon for Ar 4 – 46 MeV/nuc (13 bins)

22.1.3 C Intensity Standard

`c_standard_intensity`

C Standard Omnidirectional Intensity in 12 energy bins (1/(cm^2 s MeV/nuc sr))
`SPASE>Particle>ParticleType:Ion,ParticleQuantity:NumberFlux,Qualifier:Differential`
Size: 12 time-varying

Geometric mean energy per nucleon for C 3 – 30 MeV/nuc (12 bins)

22.1.4 Ca Intensity Standard

`ca_standard_intensity`

Ca Standard Omnidirectional Intensity in 13 energy bins (1/(cm^2 s MeV/nuc sr))
`SPASE>Particle>ParticleType:Ion,ParticleQuantity:NumberFlux,Qualifier:Differential`
Size: 13 time-varying

Geometric mean energy per nucleon for Ca 4 – 46 MeV/nuc (13 bins)

22.1.5 Dynamic threshold state

`dynamic_threshold_state`

Raw dynamic threshold state per integration
`SPASE>Support>SupportQuantity:InstrumentMode`
time-varying

22.1.6 Fe Intensity Standard

`fe_standard_intensity`

Fe Standard Omnidirectional Intensity in 16 energy bins (1/(cm^2 s MeV/nuc sr))
`SPASE>Particle>ParticleType:Ion,ParticleQuantity:NumberFlux,Qualifier:Differential`
Size: 16 time-varying

Geometric mean energy per nucleon for Fe 3 – 61 MeV/nuc (16 bins)

22.1.7 H Intensity Standard

`h_standard_intensity`

H Standard Omnidirectional Intensity in 12 energy bins (1/(cm^2 s MeV/nuc sr))
`SPASE>Particle>ParticleType:Ion,ParticleQuantity:NumberFlux,Qualifier:Differential`
Size: 12 time-varying

Geometric mean energy per nucleon for H 2 – 14 MeV/nuc (12 bins)

22.1.8 He3 Intensity Standard

`he3_standard_intensity`

He3 Standard Omnidirectional Intensity in 11 energy bins (1/(cm^2 s MeV/nuc sr))
`SPASE>Particle>ParticleType:Ion,ParticleQuantity:NumberFlux,Qualifier:Differential`
Size: 11 time-varying

Geometric mean energy per nucleon for He3 2 – 14 MeV/nuc (11 bins)

22.1.9 He4 Intensity Standard

`he4_standard_intensity`

He4 Standard Omnidirectional Intensity in 12 energy bins (1/(cm^2 s MeV/nuc sr))
`SPASE>Particle>ParticleType:Ion,ParticleQuantity:NumberFlux,Qualifier:Differential`
Size: 12 time-varying

Geometric mean energy per nucleon for He4 2 – 14 MeV/nuc (12 bins)

22.1.10 He Intensity Standard

`he_standard_intensity`

He (total) Standard Omnidirectional Intensity in 11 energy bins (1/(cm^2 s MeV/nuc sr))
`SPASE>Particle>ParticleType:Ion,ParticleQuantity:NumberFlux,Qualifier:Differential`
Size: 11 time-varying

Geometric mean energy per nucleon for He 2 – 14 MeV/nuc (11 bins)

22.1.11 Mg Intensity Standard

`mg_standard_intensity`

Mg Standard Omnidirectional Intensity in 14 energy bins (1/(cm^2 s MeV/nuc sr))
`SPASE>Particle>ParticleType:Ion,ParticleQuantity:NumberFlux,Qualifier:Differential`
Size: 14 time-varying

Geometric mean energy per nucleon for Mg 3 – 46 MeV/nuc (14 bins)

22.1.12 N Intensity Standard

`n_standard_intensity`

N Standard Omnidirectional Intensity in 12 energy bins (1/(cm^2 s MeV/nuc sr))
`SPASE>Particle>ParticleType:Ion,ParticleQuantity:NumberFlux,Qualifier:Differential`
Size: 12 time-varying

Geometric mean energy per nucleon for N 3 – 30 MeV/nuc (12 bins)

22.1.13 Na Intensity Standard

`na_standard_intensity`

Na Standard Omnidirectional Intensity in 8 energy bins (1/(cm^2 s MeV/nuc sr))
`SPASE>Particle>ParticleType:Ion,ParticleQuantity:NumberFlux,Qualifier:Differential`
Size: 8 time-varying

Geometric mean energy per nucleon for Na 7 – 36 MeV/nuc (8 bins)

22.1.14 Ne Intensity Standard

`ne_standard_intensity`

Ne Standard Omnidirectional Intensity in 13 energy bins (1/(cm^2 s MeV/nuc sr))
`SPASE>Particle>ParticleType:Ion,ParticleQuantity:NumberFlux,Qualifier:Differential`
Size: 13 time-varying
Geometric mean energy per nucleon for Ne 3 – 36 MeV/nuc (13 bins)

22.1.15 Ni Intensity Standard

`ni_standard_intensity`

Ni Standard Omnidirectional Intensity in 9 energy bins (1/(cm^2 s MeV/nuc sr))
`SPASE>Particle>ParticleType:Ion,ParticleQuantity:NumberFlux,Qualifier:Differential`
Size: 9 time-varying
Geometric mean energy per nucleon for Ni 9 – 61 MeV/nuc (9 bins)

22.1.16 O Intensity Standard

`o_standard_intensity`

O Standard Omnidirectional Intensity in 12 energy bins (1/(cm^2 s MeV/nuc sr))
`SPASE>Particle>ParticleType:Ion,ParticleQuantity:NumberFlux,Qualifier:Differential`
Size: 12 time-varying
Geometric mean energy per nucleon for O 3 – 30 MeV/nuc (12 bins)

22.1.17 S Intensity Standard

`s_standard_intensity`

S Standard Omnidirectional Intensity in 13 energy bins (1/(cm^2 s MeV/nuc sr))
`SPASE>Particle>ParticleType:Ion,ParticleQuantity:NumberFlux,Qualifier:Differential`
Size: 13 time-varying
Geometric mean energy per nucleon for S 4 – 46 MeV/nuc (13 bins)

22.1.18 Si Intensity Standard

`si_standard_intensity`

Si Standard Omnidirectional Intensity in 14 energy bins (1/(cm^2 s MeV/nuc sr))
`SPASE>Particle>ParticleType:Ion,ParticleQuantity:NumberFlux,Qualifier:Differential`
Size: 14 time-varying
Geometric mean energy per nucleon for Si 3 – 46 MeV/nuc (14 bins)

22.2 Support Data

22.2.1 Al minus statistical uncertainty

`al_stat_uncert_minus`

Minus statistical uncertainty for Al (1/(cm^2 s MeV/nuc sr))
`SPASE>Particle>ParticleType:Ion,ParticleQuantity:NumberFlux,Qualifier:Differential_Uncertainty`
Size: 9 time-varying
Geometric mean energy per nucleon for Al 7 – 46 MeV/nuc (9 bins)

22.2.2 Al plus statistical uncertainty

`al_stat_uncert_plus`

Plus statistical uncertainty for Al (1/(cm^2 s MeV/nuc sr))
`SPASE>Particle>ParticleType:Ion,ParticleQuantity:NumberFlux,Qualifier:Differential_Uncertainty`
Size: 9 time-varying
Geometric mean energy per nucleon for Al 7 – 46 MeV/nuc (9 bins)

22.2.3 Al minus systematic uncertainty

`al_sys_err_minus`

Minus systematic uncertainty for Al (1/(cm^2 s MeV/nuc sr))
`SPASE>Particle>ParticleType:Ion,ParticleQuantity:NumberFlux,Qualifier:Differential_Uncertainty`
Size: 9 time-varying
Geometric mean energy per nucleon for Al 7 – 46 MeV/nuc (9 bins)

22.2.4 Al Plus Systematic Uncertainty

`al_sys_err_plus`

Plus systematic uncertainty for Al (1/(cm^2 s MeV/nuc sr))
`SPASE>Particle>ParticleType:Ion,ParticleQuantity:NumberFlux,Qualifier:Differential_Uncertainty`
Size: 9 time-varying
Geometric mean energy per nucleon for Al 7 – 46 MeV/nuc (9 bins)

22.2.5 Ar minus statistical uncertainty

`ar_stat_uncert_minus`

Minus statistical uncertainty for Ar (1/(cm^2 s MeV/nuc sr))
`SPASE>Particle>ParticleType:Ion,ParticleQuantity:NumberFlux,Qualifier:Differential_Uncertainty`

Size: 13 time-varying
Geometric mean energy per nucleon for Ar 4 – 46 MeV/nuc (13 bins)

22.2.6 Ar plus statistical uncertainty

`ar_stat_uncert_plus`

Plus statistical uncertainty for Ar (1/(cm^2 s MeV/nuc sr))
`SPASE>Particle>ParticleType:Ion,ParticleQuantity:NumberFlux,Qualifier:Differential_Uncertainty`
Size: 13 time-varying
Geometric mean energy per nucleon for Ar 4 – 46 MeV/nuc (13 bins)

22.2.7 Ar minus systematic uncertainty

`ar_sys_err_minus`

Minus systematic uncertainty for Ar (1/(cm^2 s MeV/nuc sr))
`SPASE>Particle>ParticleType:Ion,ParticleQuantity:NumberFlux,Qualifier:Differential_Uncertainty`
Size: 13 time-varying
Geometric mean energy per nucleon for Ar 4 – 46 MeV/nuc (13 bins)

22.2.8 Ar Plus Systematic Uncertainty

`ar_sys_err_plus`

Plus systematic uncertainty for Ar (1/(cm^2 s MeV/nuc sr))
`SPASE>Particle>ParticleType:Ion,ParticleQuantity:NumberFlux,Qualifier:Differential_Uncertainty`
Size: 13 time-varying
Geometric mean energy per nucleon for Ar 4 – 46 MeV/nuc (13 bins)

22.2.9 C minus statistical uncertainty

`c_stat_uncert_minus`

Minus statistical uncertainty for C (1/(cm^2 s MeV/nuc sr))
`SPASE>Particle>ParticleType:Ion,ParticleQuantity:NumberFlux,Qualifier:Differential_Uncertainty`
Size: 12 time-varying
Geometric mean energy per nucleon for C 3 – 30 MeV/nuc (12 bins)

22.2.10 C plus statistical uncertainty

`c_stat_uncert_plus`

Plus statistical uncertainty for C (1/(cm^2 s MeV/nuc sr))
`SPASE>Particle>ParticleType:Ion,ParticleQuantity:NumberFlux,Qualifier:Differential_Uncertainty`
Size: 12 time-varying
Geometric mean energy per nucleon for C 3 – 30 MeV/nuc (12 bins)

22.2.11 C minus systematic uncertainty

`c_sys_err_minus`

Minus systematic uncertainty for C (1/(cm^2 s MeV/nuc sr))
`SPASE>Particle>ParticleType:Ion,ParticleQuantity:NumberFlux,Qualifier:Differential_Uncertainty`
Size: 12 time-varying
Geometric mean energy per nucleon for C 3 – 30 MeV/nuc (12 bins)

22.2.12 C Plus Systematic Uncertainty

`c_sys_err_plus`

Plus systematic uncertainty for C (1/(cm^2 s MeV/nuc sr))
`SPASE>Particle>ParticleType:Ion,ParticleQuantity:NumberFlux,Qualifier:Differential_Uncertainty`
Size: 12 time-varying
Geometric mean energy per nucleon for C 3 – 30 MeV/nuc (12 bins)

22.2.13 Ca minus statistical uncertainty

`ca_stat_uncert_minus`

Minus statistical uncertainty for Ca (1/(cm^2 s MeV/nuc sr))
`SPASE>Particle>ParticleType:Ion,ParticleQuantity:NumberFlux,Qualifier:Differential_Uncertainty`
Size: 13 time-varying
Geometric mean energy per nucleon for Ca 4 – 46 MeV/nuc (13 bins)

22.2.14 Ca plus statistical uncertainty

`ca_stat_uncert_plus`

Plus statistical uncertainty for Ca (1/(cm^2 s MeV/nuc sr))
`SPASE>Particle>ParticleType:Ion,ParticleQuantity:NumberFlux,Qualifier:Differential_Uncertainty`
Size: 13 time-varying

Geometric mean energy per nucleon for Ca 4 – 46 MeV/nuc (13 bins)

22.2.15 Ca minus systematic uncertainty

`ca_sys_err_minus`

Minus systematic uncertainty for Ca (1/(cm^2 s MeV/nuc sr))
`SPASE>Particle>ParticleType:Ion,ParticleQuantity:NumberFlux,Qualifier:Differential_Uncertainty`
Size: 13 time-varying

Geometric mean energy per nucleon for Ca 4 – 46 MeV/nuc (13 bins)

22.2.16 Ca Plus Systematic Uncertainty

`ca_sys_err_plus`

Plus systematic uncertainty for Ca (1/(cm^2 s MeV/nuc sr))
`SPASE>Particle>ParticleType:Ion,ParticleQuantity:NumberFlux,Qualifier:Differential_Uncertainty`
Size: 13 time-varying

Geometric mean energy per nucleon for Ca 4 – 46 MeV/nuc (13 bins)

22.2.17 Fe minus statistical uncertainty

`fe_stat_uncert_minus`

Minus statistical uncertainty for Fe (1/(cm^2 s MeV/nuc sr))
`SPASE>Particle>ParticleType:Ion,ParticleQuantity:NumberFlux,Qualifier:Differential_Uncertainty`
Size: 16 time-varying

Geometric mean energy per nucleon for Fe 3 – 61 MeV/nuc (16 bins)

22.2.18 Fe plus statistical uncertainty

`fe_stat_uncert_plus`

Plus statistical uncertainty for Fe (1/(cm^2 s MeV/nuc sr))
`SPASE>Particle>ParticleType:Ion,ParticleQuantity:NumberFlux,Qualifier:Differential_Uncertainty`
Size: 16 time-varying

Geometric mean energy per nucleon for Fe 3 – 61 MeV/nuc (16 bins)

22.2.19 Fe minus systematic uncertainty

`fe_sys_err_minus`

Minus systematic uncertainty for Fe (1/(cm^2 s MeV/nuc sr))
SPASE>Particle>ParticleType:Ion,ParticleQuantity:NumberFlux,Qualifier:Differential_Uncertainty
Size: 16 time-varying
Geometric mean energy per nucleon for Fe 3 – 61 MeV/nuc (16 bins)

22.2.20 Fe Plus Systematic Uncertainty

fe_sys_err_plus

Plus systematic uncertainty for Fe (1/(cm^2 s MeV/nuc sr))
SPASE>Particle>ParticleType:Ion,ParticleQuantity:NumberFlux,Qualifier:Differential_Uncertainty
Size: 16 time-varying
Geometric mean energy per nucleon for Fe 3 – 61 MeV/nuc (16 bins)

22.2.21 H minus statistical uncertainty

h_stat_uncert_minus

Minus statistical uncertainty for H (1/(cm^2 s MeV/nuc sr))
SPASE>Particle>ParticleType:Ion,ParticleQuantity:NumberFlux,Qualifier:Differential_Uncertainty
Size: 12 time-varying
Geometric mean energy per nucleon for H 2 – 14 MeV/nuc (12 bins)

22.2.22 H plus statistical uncertainty

h_stat_uncert_plus

Plus statistical uncertainty for H (1/(cm^2 s MeV/nuc sr))
SPASE>Particle>ParticleType:Ion,ParticleQuantity:NumberFlux,Qualifier:Differential_Uncertainty
Size: 12 time-varying
Geometric mean energy per nucleon for H 2 – 14 MeV/nuc (12 bins)

22.2.23 H minus systematic uncertainty

h_sys_err_minus

Minus systematic uncertainty for H (1/(cm^2 s MeV/nuc sr))
SPASE>Particle>ParticleType:Ion,ParticleQuantity:NumberFlux,Qualifier:Differential_Uncertainty
Size: 12 time-varying
Geometric mean energy per nucleon for H 2 – 14 MeV/nuc (12 bins)

22.2.24 H Plus Systematic Uncertainty

`h_sys_err_plus`

Plus Systematic uncertainty for H (1/(cm^2 s MeV/nuc sr))
`SPASE>Particle>ParticleType:Ion,ParticleQuantity:NumberFlux,Qualifier:Differential_Uncertainty`
Size: 12 time-varying
Geometric mean energy per nucleon for H 2 – 14 MeV/nuc (12 bins)

22.2.25 He3 minus statistical uncertainty

`he3_stat_uncert_minus`

Minus statistical uncertainty for He3 (1/(cm^2 s MeV/nuc sr))
`SPASE>Particle>ParticleType:Ion,ParticleQuantity:NumberFlux,Qualifier:Differential_Uncertainty`
Size: 11 time-varying
Geometric mean energy per nucleon for He3 2 – 14 MeV/nuc (11 bins)

22.2.26 He3 plus statistical uncertainty

`he3_stat_uncert_plus`

Plus statistical uncertainty for He3 (1/(cm^2 s MeV/nuc sr))
`SPASE>Particle>ParticleType:Ion,ParticleQuantity:NumberFlux,Qualifier:Differential_Uncertainty`
Size: 11 time-varying
Geometric mean energy per nucleon for He3 2 – 14 MeV/nuc (11 bins)

22.2.27 He3 minus systematic uncertainty

`he3_sys_err_minus`

Minus systematic uncertainty for He3 (1/(cm^2 s MeV/nuc sr))
`SPASE>Particle>ParticleType:Ion,ParticleQuantity:NumberFlux,Qualifier:Differential_Uncertainty`
Size: 11 time-varying
Geometric mean energy per nucleon for He3 2 – 14 MeV/nuc (11 bins)

22.2.28 He3 Plus Systematic Uncertainty

`he3_sys_err_plus`

Plus systematic uncertainty for He3 (1/(cm^2 s MeV/nuc sr))
`SPASE>Particle>ParticleType:Ion,ParticleQuantity:NumberFlux,Qualifier:Differential_Uncertainty`
Size: 11 time-varying

Geometric mean energy per nucleon for He3 2 – 14 MeV/nuc (11 bins)

22.2.29 He4 minus statistical uncertainty

`he4_stat_uncert_minus`

Minus statistical uncertainty for He4 (1/(cm^2 s MeV/nuc sr))
`SPASE>Particle>ParticleType:Ion,ParticleQuantity:NumberFlux,Qualifier:Differential_Uncertainty`
Size: 12 time-varying

Geometric mean energy per nucleon for He4 2 – 14 MeV/nuc (12 bins)

22.2.30 He4 plus statistical uncertainty

`he4_stat_uncert_plus`

Plus statistical uncertainty for He4 (1/(cm^2 s MeV/nuc sr))
`SPASE>Particle>ParticleType:Ion,ParticleQuantity:NumberFlux,Qualifier:Differential_Uncertainty`
Size: 12 time-varying

Geometric mean energy per nucleon for He4 2 – 14 MeV/nuc (12 bins)

22.2.31 He4 minus systematic uncertainty

`he4_sys_err_minus`

Minus systematic uncertainty for He4 (1/(cm^2 s MeV/nuc sr))
`SPASE>Particle>ParticleType:Ion,ParticleQuantity:NumberFlux,Qualifier:Differential_Uncertainty`
Size: 12 time-varying

Geometric mean energy per nucleon for He4 2 – 14 MeV/nuc (12 bins)

22.2.32 He4 Plus Systematic Uncertainty

`he4_sys_err_plus`

Plus systematic uncertainty for He4 (1/(cm^2 s MeV/nuc sr))
`SPASE>Particle>ParticleType:Ion,ParticleQuantity:NumberFlux,Qualifier:Differential_Uncertainty`
Size: 12 time-varying

Geometric mean energy per nucleon for He4 2 – 14 MeV/nuc (12 bins)

22.2.33 He minus statistical uncertainty

`he_stat_uncert_minus`

Minus statistical uncertainty for He (1/(cm^2 s MeV/nuc sr))
SPASE>Particle>ParticleType:Ion,ParticleQuantity:NumberFlux,Qualifier:Differential_Uncertainty
Size: 11 time-varying
Geometric mean energy per nucleon for He 2 – 14 MeV/nuc (11 bins)

22.2.34 He plus statistical uncertainty

he_stat_uncert_plus

Plus statistical uncertainty for He (1/(cm^2 s MeV/nuc sr))
SPASE>Particle>ParticleType:Ion,ParticleQuantity:NumberFlux,Qualifier:Differential_Uncertainty
Size: 11 time-varying
Geometric mean energy per nucleon for He 2 – 14 MeV/nuc (11 bins)

22.2.35 He minus systematic uncertainty

he_sys_err_minus

Minus systematic uncertainty for He (1/(cm^2 s MeV/nuc sr))
SPASE>Particle>ParticleType:Ion,ParticleQuantity:NumberFlux,Qualifier:Differential_Uncertainty
Size: 11 time-varying
Geometric mean energy per nucleon for He 2 – 14 MeV/nuc (11 bins)

22.2.36 He plus systematic uncertainty

he_sys_err_plus

Plus systematic uncertainty for He (1/(cm^2 s MeV/nuc sr))
SPASE>Particle>ParticleType:Ion,ParticleQuantity:NumberFlux,Qualifier:Differential_Uncertainty
Size: 11 time-varying
Geometric mean energy per nucleon for He 2 – 14 MeV/nuc (11 bins)

22.2.37 Mg minus statistical uncertainty

mg_stat_uncert_minus

Minus statistical uncertainty for Mg (1/(cm^2 s MeV/nuc sr))
SPASE>Particle>ParticleType:Ion,ParticleQuantity:NumberFlux,Qualifier:Differential_Uncertainty
Size: 14 time-varying
Geometric mean energy per nucleon for Mg 3 – 46 MeV/nuc (14 bins)

22.2.38 Mg plus statistical uncertainty

`mg_stat_uncert_plus`

Plus statistical uncertainty for Mg (1/(cm^2 s MeV/nuc sr))
`SPASE>Particle>ParticleType:Ion,ParticleQuantity:NumberFlux,Qualifier:Differential_Uncertainty`
Size: 14 time-varying
Geometric mean energy per nucleon for Mg 3 – 46 MeV/nuc (14 bins)

22.2.39 Mg minus systematic uncertainty

`mg_sys_err_minus`

Minus systematic uncertainty for Mg (1/(cm^2 s MeV/nuc sr))
`SPASE>Particle>ParticleType:Ion,ParticleQuantity:NumberFlux,Qualifier:Differential_Uncertainty`
Size: 14 time-varying
Geometric mean energy per nucleon for Mg 3 – 46 MeV/nuc (14 bins)

22.2.40 Mg Plus Systematic Uncertainty

`mg_sys_err_plus`

Plus systematic uncertainty for Mg (1/(cm^2 s MeV/nuc sr))
`SPASE>Particle>ParticleType:Ion,ParticleQuantity:NumberFlux,Qualifier:Differential_Uncertainty`
Size: 14 time-varying
Geometric mean energy per nucleon for Mg 3 – 46 MeV/nuc (14 bins)

22.2.41 N minus statistical uncertainty

`n_stat_uncert_minus`

Minus statistical uncertainty for N (1/(cm^2 s MeV/nuc sr))
`SPASE>Particle>ParticleType:Ion,ParticleQuantity:NumberFlux,Qualifier:Differential_Uncertainty`
Size: 12 time-varying
Geometric mean energy per nucleon for N 3 – 30 MeV/nuc (12 bins)

22.2.42 N plus statistical uncertainty

`n_stat_uncert_plus`

Plus statistical uncertainty for N (1/(cm^2 s MeV/nuc sr))
`SPASE>Particle>ParticleType:Ion,ParticleQuantity:NumberFlux,Qualifier:Differential_Uncertainty`
Size: 12 time-varying

Geometric mean energy per nucleon for N 3 – 30 MeV/nuc (12 bins)

22.2.43 N minus systematic uncertainty

`n_sys_err_minus`

Minus systematic uncertainty for N (1/(cm^2 s MeV/nuc sr))
`SPASE>Particle>ParticleType:Ion,ParticleQuantity:NumberFlux,Qualifier:Differential_Uncertainty`
Size: 12 time-varying

Geometric mean energy per nucleon for N 3 – 30 MeV/nuc (12 bins)

22.2.44 N Plus Systematic Uncertainty

`n_sys_err_plus`

Plus systematic uncertainty for N (1/(cm^2 s MeV/nuc sr))
`SPASE>Particle>ParticleType:Ion,ParticleQuantity:NumberFlux,Qualifier:Differential_Uncertainty`
Size: 12 time-varying

Geometric mean energy per nucleon for N 3 – 30 MeV/nuc (12 bins)

22.2.45 Na minus statistical uncertainty

`na_stat_uncert_minus`

Minus statistical uncertainty for Na (1/(cm^2 s MeV/nuc sr))
`SPASE>Particle>ParticleType:Ion,ParticleQuantity:NumberFlux,Qualifier:Differential_Uncertainty`
Size: 8 time-varying

Geometric mean energy per nucleon for Na 7 – 36 MeV/nuc (8 bins)

22.2.46 Na plus statistical uncertainty

`na_stat_uncert_plus`

Plus statistical uncertainty for Na (1/(cm^2 s MeV/nuc sr))
`SPASE>Particle>ParticleType:Ion,ParticleQuantity:NumberFlux,Qualifier:Differential_Uncertainty`
Size: 8 time-varying

Geometric mean energy per nucleon for Na 7 – 36 MeV/nuc (8 bins)

22.2.47 Na minus systematic uncertainty

`na_sys_err_minus`

Minus systematic uncertainty for Na (1/(cm^2 s MeV/nuc sr))
SPASE>Particle>ParticleType:Ion,ParticleQuantity:NumberFlux,Qualifier:Differential_Uncertainty
Size: 8 time-varying
Geometric mean energy per nucleon for Na 7 – 36 MeV/nuc (8 bins)

22.2.48 Na Plus Systematic Uncertainty

na_sys_err_plus

Plus systematic uncertainty for Na (1/(cm^2 s MeV/nuc sr))
SPASE>Particle>ParticleType:Ion,ParticleQuantity:NumberFlux,Qualifier:Differential_Uncertainty
Size: 8 time-varying
Geometric mean energy per nucleon for Na 7 – 36 MeV/nuc (8 bins)

22.2.49 Ne minus statistical uncertainty

ne_stat_uncert_minus

Minus statistical uncertainty for Ne (1/(cm^2 s MeV/nuc sr))
SPASE>Particle>ParticleType:Ion,ParticleQuantity:NumberFlux,Qualifier:Differential_Uncertainty
Size: 13 time-varying
Geometric mean energy per nucleon for Ne 3 – 36 MeV/nuc (13 bins)

22.2.50 Ne plus statistical uncertainty

ne_stat_uncert_plus

Plus statistical uncertainty for Ne (1/(cm^2 s MeV/nuc sr))
SPASE>Particle>ParticleType:Ion,ParticleQuantity:NumberFlux,Qualifier:Differential_Uncertainty
Size: 13 time-varying
Geometric mean energy per nucleon for Ne 3 – 36 MeV/nuc (13 bins)

22.2.51 Ne minus systematic uncertainty

ne_sys_err_minus

Minus systematic uncertainty for Ne (1/(cm^2 s MeV/nuc sr))
SPASE>Particle>ParticleType:Ion,ParticleQuantity:NumberFlux,Qualifier:Differential_Uncertainty
Size: 13 time-varying
Geometric mean energy per nucleon for Ne 3 – 36 MeV/nuc (13 bins)

22.2.52 Ne Plus Systematic Uncertainty

`ne_sys_err_plus`

Plus systematic uncertainty for Ne (1/(cm^2 s MeV/nuc sr))
`SPASE>Particle>ParticleType:Ion,ParticleQuantity:NumberFlux,Qualifier:Differential_Uncertainty`
Size: 13 time-varying

Geometric mean energy per nucleon for Ne 3 – 36 MeV/nuc (13 bins)

22.2.53 Ni minus statistical uncertainty

`ni_stat_uncert_minus`

Minus statistical uncertainty for Ni (1/(cm^2 s MeV/nuc sr))
`SPASE>Particle>ParticleType:Ion,ParticleQuantity:NumberFlux,Qualifier:Differential_Uncertainty`
Size: 9 time-varying

Geometric mean energy per nucleon for Ni 9 – 61 MeV/nuc (9 bins)

22.2.54 Ni plus statistical uncertainty

`ni_stat_uncert_plus`

Plus statistical uncertainty for Ni (1/(cm^2 s MeV/nuc sr))
`SPASE>Particle>ParticleType:Ion,ParticleQuantity:NumberFlux,Qualifier:Differential_Uncertainty`
Size: 9 time-varying

Geometric mean energy per nucleon for Ni 9 – 61 MeV/nuc (9 bins)

22.2.55 Ni minus systematic uncertainty

`ni_sys_err_minus`

Minus systematic uncertainty for Ni (1/(cm^2 s MeV/nuc sr))
`SPASE>Particle>ParticleType:Ion,ParticleQuantity:NumberFlux,Qualifier:Differential_Uncertainty`
Size: 9 time-varying

Geometric mean energy per nucleon for Ni 9 – 61 MeV/nuc (9 bins)

22.2.56 Ni Plus Systematic Uncertainty

`ni_sys_err_plus`

Plus systematic uncertainty for Ni (1/(cm^2 s MeV/nuc sr))
`SPASE>Particle>ParticleType:Ion,ParticleQuantity:NumberFlux,Qualifier:Differential_Uncertainty`
Size: 9 time-varying

Geometric mean energy per nucleon for Ni 9 – 61 MeV/nuc (9 bins)

22.2.57 O minus statistical uncertainty

`o_stat_uncert_minus`

Minus statistical uncertainty for O (1/(cm^2 s MeV/nuc sr))
`SPASE>Particle>ParticleType:Ion,ParticleQuantity:NumberFlux,Qualifier:Differential_Uncertainty`
Size: 12 time-varying

Geometric mean energy per nucleon for O 3 – 30 MeV/nuc (12 bins)

22.2.58 O plus statistical uncertainty

`o_stat_uncert_plus`

Plus statistical uncertainty for O (1/(cm^2 s MeV/nuc sr))
`SPASE>Particle>ParticleType:Ion,ParticleQuantity:NumberFlux,Qualifier:Differential_Uncertainty`
Size: 12 time-varying

Geometric mean energy per nucleon for O 3 – 30 MeV/nuc (12 bins)

22.2.59 O minus systematic uncertainty

`o_sys_err_minus`

Minus systematic uncertainty for O (1/(cm^2 s MeV/nuc sr))
`SPASE>Particle>ParticleType:Ion,ParticleQuantity:NumberFlux,Qualifier:Differential_Uncertainty`
Size: 12 time-varying

Geometric mean energy per nucleon for O 3 – 30 MeV/nuc (12 bins)

22.2.60 O Plus Systematic Uncertainty

`o_sys_err_plus`

Plus systematic uncertainty for O (1/(cm^2 s MeV/nuc sr))
`SPASE>Particle>ParticleType:Ion,ParticleQuantity:NumberFlux,Qualifier:Differential_Uncertainty`
Size: 12 time-varying

Geometric mean energy per nucleon for O 3 – 30 MeV/nuc (12 bins)

22.2.61 S minus statistical uncertainty

`s_stat_uncert_minus`

Minus statistical uncertainty for S (1/(cm^2 s MeV/nuc sr))
SPASE>Particle>ParticleType:Ion,ParticleQuantity:NumberFlux,Qualifier:Differential_Uncertainty
Size: 13 time-varying
Geometric mean energy per nucleon for S 4 – 46 MeV/nuc (13 bins)

22.2.62 S plus statistical uncertainty

s_stat_uncert_plus

Plus statistical uncertainty for S (1/(cm^2 s MeV/nuc sr))
SPASE>Particle>ParticleType:Ion,ParticleQuantity:NumberFlux,Qualifier:Differential_Uncertainty
Size: 13 time-varying
Geometric mean energy per nucleon for S 4 – 46 MeV/nuc (13 bins)

22.2.63 S minus systematic uncertainty

s_sys_err_minus

Minus systematic uncertainty for S (1/(cm^2 s MeV/nuc sr))
SPASE>Particle>ParticleType:Ion,ParticleQuantity:NumberFlux,Qualifier:Differential_Uncertainty
Size: 13 time-varying
Geometric mean energy per nucleon for S 4 – 46 MeV/nuc (13 bins)

22.2.64 S Plus Systematic Uncertainty

s_sys_err_plus

Plus systematic uncertainty for S (1/(cm^2 s MeV/nuc sr))
SPASE>Particle>ParticleType:Ion,ParticleQuantity:NumberFlux,Qualifier:Differential_Uncertainty
Size: 13 time-varying
Geometric mean energy per nucleon for S 4 – 46 MeV/nuc (13 bins)

22.2.65 Si minus statistical uncertainty

si_stat_uncert_minus

Minus statistical uncertainty for Si (1/(cm^2 s MeV/nuc sr))
SPASE>Particle>ParticleType:Ion,ParticleQuantity:NumberFlux,Qualifier:Differential_Uncertainty
Size: 14 time-varying
Geometric mean energy per nucleon for Si 3 – 46 MeV/nuc (14 bins)

22.2.66 Si plus statistical uncertainty

`si_stat_uncert_plus`

Plus statistical uncertainty for Si (1/(cm^2 s MeV/nuc sr))
`SPASE>Particle>ParticleType:Ion,ParticleQuantity:NumberFlux,Qualifier:Differential_Uncertainty`
Size: 14 time-varying
Geometric mean energy per nucleon for Si 3 – 46 MeV/nuc (14 bins)

22.2.67 Si minus systematic uncertainty

`si_sys_err_minus`

Minus systematic uncertainty for Si (1/(cm^2 s MeV/nuc sr))
`SPASE>Particle>ParticleType:Ion,ParticleQuantity:NumberFlux,Qualifier:Differential_Uncertainty`
Size: 14 time-varying
Geometric mean energy per nucleon for Si 3 – 46 MeV/nuc (14 bins)

22.2.68 Si Plus Systematic Uncertainty

`si_sys_err_plus`

Plus systematic uncertainty for Si (1/(cm^2 s MeV/nuc sr))
`SPASE>Particle>ParticleType:Ion,ParticleQuantity:NumberFlux,Qualifier:Differential_Uncertainty`
Size: 14 time-varying
Geometric mean energy per nucleon for Si 3 – 46 MeV/nuc (14 bins)

23 imap_hit_l2_summed-intensity

HIT>IMAP High-energy Ion Telescope
L2_summed-intensity>Level-2 Summed Intensity
The High-energy Ion Telescope (HIT) measures the elemental composition, energy spectra, angle distributions, and arrival times of high-energy ions. HIT delivers full-sky coverage from a wide instrument field-of-view (FOV) to enable a high resolution of ion measurements, such as observing shock-accelerated ions, determining the origin of the solar energetic particles (SEPs) spectra, and resolving particle transport in the heliosphere. See https://imap.princeton.edu/spacecraft/instruments/high-energy-ion-telescope-hit for more details.
Users should acknowledge the sources of data used in all publications, presentations, and reports using an appropriate DOI. Appropriate acknowledgement to institutions, personnel, and funding agencies should be given, including acknowledging the IMAP Mission Principal Investigator, Prof. David J. McComas of Princeton University (Contract #80GSFC19C0027). IMAP Rules-of-the-Road for data usage can be found in the IMAP CMAD.

23.1 Data

23.1.1 Al intensity summed

`al_summed_intensity`

Al Summed Omnidirectional Intensity in 3 energy bins (useful for quiet times) (1/(cm^2 s MeV/nuc sr))
`SPASE>Particle>ParticleType:Ion,ParticleQuantity:NumberFlux,Qualifier:Differential`
Size: 3 time-varying

Geometric mean energy per nucleon for Al 8 – 21 MeV/nuc (3 bins)

23.1.2 Ar intensity summed

`ar_summed_intensity`

Ar Summed Omnidirectional Intensity in 5 energy bins (useful for quiet times) (1/(cm^2 s MeV/nuc sr))
`SPASE>Particle>ParticleType:Ion,ParticleQuantity:NumberFlux,Qualifier:Differential`
Size: 5 time-varying

Geometric mean energy per nucleon for Ar 5 – 34 MeV/nuc (5 bins)

23.1.3 C intensity summed

`c_summed_intensity`

C Summed Omnidirectional Intensity in 4 energy bins (useful for quiet times) (1/(cm^2 s MeV/nuc sr))
`SPASE>Particle>ParticleType:Ion,ParticleQuantity:NumberFlux,Qualifier:Differential`
Size: 4 time-varying

Geometric mean energy per nucleon for C 5 – 21 MeV/nuc (4 bins)

23.1.4 Ca intensity summed

`ca_summed_intensity`

Ca Summed Omnidirectional Intensity in 5 energy bins (useful for quiet times) (1/(cm^2 s MeV/nuc sr))
`SPASE>Particle>ParticleType:Ion,ParticleQuantity:NumberFlux,Qualifier:Differential`
Size: 5 time-varying

Geometric mean energy per nucleon for Ca 5 – 34 MeV/nuc (5 bins)

23.1.5 Dynamic threshold state

`dynamic_threshold_state`

Raw dynamic threshold state per integration
`SPASE>Support>SupportQuantity:InstrumentMode`
time-varying

23.1.6 Fe intensity summed

`fe_summed_intensity`

Fe Summed Omnidirectional Intensity in 5 energy bins (useful for quiet times) (1/(cm^2 s MeV/nuc sr))
`SPASE>Particle>ParticleType:Ion,ParticleQuantity:NumberFlux,Qualifier:Differential`
Size: 5 time-varying
Geometric mean energy per nucleon for Fe 5 – 34 MeV/nuc (5 bins)

23.1.7 H intensity summed

`h_summed_intensity`

H Summed Omnidirectional Intensity in 4 energy bins (useful for quiet times) (1/(cm^2 s MeV/nuc sr))
`SPASE>Particle>ParticleType:Ion,ParticleQuantity:NumberFlux,Qualifier:Differential`
Size: 4 time-varying
Geometric mean energy per nucleon for H 3 – 12 MeV/nuc (4 bins)

23.1.8 He3 intensity summed

`he3_summed_intensity`

He3 Summed Omnidirectional Intensity in 3 energy bins (useful for quiet times) (1/(cm^2 s MeV/nuc sr))
`SPASE>Particle>ParticleType:Ion,ParticleQuantity:NumberFlux,Qualifier:Differential`
Size: 3 time-varying
Geometric mean energy per nucleon for He3 5 – 12 MeV/nuc (3 bins)

23.1.9 He4 intensity summed

`he4_summed_intensity`

He4 Summed Omnidirectional Intensity in 4 energy bins (useful for quiet times) (1/(cm^2 s MeV/nuc

sr))
SPASE>Particle>ParticleType:Ion,ParticleQuantity:NumberFlux,Qualifier:Differential
Size: 4 time-varying
Geometric mean energy per nucleon for He4 3 – 12 MeV/nuc (4 bins)

23.1.10 He intensity summed

`he_summed_intensity`

He (total) Summed Omnidirectional Intensity in 3 energy bins (useful for quiet times) (1/(cm^2 s MeV/nuc sr))
SPASE>Particle>ParticleType:Ion,ParticleQuantity:NumberFlux,Qualifier:Differential
Size: 3 time-varying
Geometric mean energy per nucleon for He 5 – 12 MeV/nuc (3 bins)

23.1.11 Mg intensity summed

`mg_summed_intensity`

Mg Summed Omnidirectional Intensity in 4 energy bins (useful for quiet times) (1/(cm^2 s MeV/nuc sr))
SPASE>Particle>ParticleType:Ion,ParticleQuantity:NumberFlux,Qualifier:Differential
Size: 4 time-varying
Geometric mean energy per nucleon for Mg 5 – 21 MeV/nuc (4 bins)

23.1.12 N intensity summed

`n_summed_intensity`

N Summed Omnidirectional Intensity in 4 energy bins (useful for quiet times) (1/(cm^2 s MeV/nuc sr))
SPASE>Particle>ParticleType:Ion,ParticleQuantity:NumberFlux,Qualifier:Differential
Size: 4 time-varying
Geometric mean energy per nucleon for N 5 – 21 MeV/nuc (4 bins)

23.1.13 Na intensity summed

`na_summed_intensity`

Na Summed Omnidirectional Intensity in 2 energy bins (useful for quiet times) (1/(cm^2 s MeV/nuc sr))
SPASE>Particle>ParticleType:Ion,ParticleQuantity:NumberFlux,Qualifier:Differential
Size: 2 time-varying

Geometric mean energy per nucleon for Na 12 – 21 MeV/nuc (2 bins)

23.1.14 Ne intensity summed

`ne_summed_intensity`

Ne Summed Omnidirectional Intensity in 4 energy bins (useful for quiet times) (1/(cm^2 s MeV/nuc sr))
`SPASE>Particle>ParticleType:Ion,ParticleQuantity:NumberFlux,Qualifier:Differential`
Size: 4 time-varying

Geometric mean energy per nucleon for Ne 5 – 21 MeV/nuc (4 bins)

23.1.15 Ni intensity summed

`ni_summed_intensity`

Ni Summed Omnidirectional Intensity in 3 energy bins (useful for quiet times) (1/(cm^2 s MeV/nuc sr))
`SPASE>Particle>ParticleType:Ion,ParticleQuantity:NumberFlux,Qualifier:Differential`
Size: 3 time-varying

Geometric mean energy per nucleon for Ni 12 – 34 MeV/nuc (3 bins)

23.1.16 O intensity summed

`o_summed_intensity`

O Summed Omnidirectional Intensity in 4 energy bins (useful for quiet times) (1/(cm^2 s MeV/nuc sr))
`SPASE>Particle>ParticleType:Ion,ParticleQuantity:NumberFlux,Qualifier:Differential`
Size: 4 time-varying

Geometric mean energy per nucleon for O 5 – 21 MeV/nuc (4 bins)

23.1.17 S intensity summed

`s_summed_intensity`

S Summed Omnidirectional Intensity in 5 energy bins (useful for quiet times) (1/(cm^2 s MeV/nuc sr))
`SPASE>Particle>ParticleType:Ion,ParticleQuantity:NumberFlux,Qualifier:Differential`
Size: 5 time-varying

Geometric mean energy per nucleon for S 5 – 34 MeV/nuc (5 bins)

23.1.18 Si intensity summed

`si_summed_intensity`

Si Summed Omnidirectional Intensity in 5 energy bins (useful for quiet times) (1/(cm^2 s MeV/nuc sr))
`SPASE>Particle>ParticleType:Ion,ParticleQuantity:NumberFlux,Qualifier:Differential`
Size: 5 time-varying

Geometric mean energy per nucleon for Si 5 – 34 MeV/nuc (5 bins)

23.2 Support Data

23.2.1 Al minus statistical uncertainty

`al_stat_uncert_minus`

Minus statistical uncertainty for Al (1/(cm^2 s MeV/nuc sr))
`SPASE>Particle>ParticleType:Ion,ParticleQuantity:NumberFlux,Qualifier:Differential_Uncertainty`
Size: 3 time-varying

Geometric mean energy per nucleon for Al 8 – 21 MeV/nuc (3 bins)

23.2.2 Al plus statistical uncertainty

`al_stat_uncert_plus`

Plus statistical uncertainty for Al (1/(cm^2 s MeV/nuc sr))
`SPASE>Particle>ParticleType:Ion,ParticleQuantity:NumberFlux,Qualifier:Differential_Uncertainty`
Size: 3 time-varying

Geometric mean energy per nucleon for Al 8 – 21 MeV/nuc (3 bins)

23.2.3 Al minus systematic uncertainty

`al_sys_err_minus`

Minus systematic uncertainty for Al (1/(cm^2 s MeV/nuc sr))
`SPASE>Particle>ParticleType:Ion,ParticleQuantity:NumberFlux,Qualifier:Differential_Uncertainty`
Size: 3 time-varying

Geometric mean energy per nucleon for Al 8 – 21 MeV/nuc (3 bins)

23.2.4 Al Plus Systematic Uncertainty

`al_sys_err_plus`

Plus systematic uncertainty for Al (1/(cm^2 s MeV/nuc sr))

SPASE>Particle>ParticleType:Ion,ParticleQuantity:NumberFlux,Qualifier:Differential_Uncertainty
Size: 3 time-varying
Geometric mean energy per nucleon for Al 8 – 21 MeV/nuc (3 bins)

23.2.5 Ar minus statistical uncertainty

ar_stat_uncert_minus

Minus statistical uncertainty for Ar (1/(cm^2 s MeV/nuc sr))
SPASE>Particle>ParticleType:Ion,ParticleQuantity:NumberFlux,Qualifier:Differential_Uncertainty
Size: 5 time-varying
Geometric mean energy per nucleon for Ar 5 – 34 MeV/nuc (5 bins)

23.2.6 Ar plus statistical uncertainty

ar_stat_uncert_plus

Plus statistical uncertainty for Ar (1/(cm^2 s MeV/nuc sr))
SPASE>Particle>ParticleType:Ion,ParticleQuantity:NumberFlux,Qualifier:Differential_Uncertainty
Size: 5 time-varying
Geometric mean energy per nucleon for Ar 5 – 34 MeV/nuc (5 bins)

23.2.7 Ar minus systematic uncertainty

ar_sys_err_minus

Minus systematic uncertainty for Ar (1/(cm^2 s MeV/nuc sr))
SPASE>Particle>ParticleType:Ion,ParticleQuantity:NumberFlux,Qualifier:Differential_Uncertainty
Size: 5 time-varying
Geometric mean energy per nucleon for Ar 5 – 34 MeV/nuc (5 bins)

23.2.8 Ar Plus Systematic Uncertainty

ar_sys_err_plus

Plus systematic uncertainty for Ar (1/(cm^2 s MeV/nuc sr))
SPASE>Particle>ParticleType:Ion,ParticleQuantity:NumberFlux,Qualifier:Differential_Uncertainty
Size: 5 time-varying
Geometric mean energy per nucleon for Ar 5 – 34 MeV/nuc (5 bins)

23.2.9 C minus statistical uncertainty

`c_stat_uncert_minus`

Minus statistical uncertainty for C (1/(cm^2 s MeV/nuc sr))
`SPASE>Particle>ParticleType:Ion,ParticleQuantity:NumberFlux,Qualifier:Differential_Uncertainty`
Size: 4 time-varying
Geometric mean energy per nucleon for C 5 – 21 MeV/nuc (4 bins)

23.2.10 C plus statistical uncertainty

`c_stat_uncert_plus`

Plus statistical uncertainty for C (1/(cm^2 s MeV/nuc sr))
`SPASE>Particle>ParticleType:Ion,ParticleQuantity:NumberFlux,Qualifier:Differential_Uncertainty`
Size: 4 time-varying
Geometric mean energy per nucleon for C 5 – 21 MeV/nuc (4 bins)

23.2.11 C minus systematic uncertainty

`c_sys_err_minus`

Minus systematic uncertainty for C (1/(cm^2 s MeV/nuc sr))
`SPASE>Particle>ParticleType:Ion,ParticleQuantity:NumberFlux,Qualifier:Differential_Uncertainty`
Size: 4 time-varying
Geometric mean energy per nucleon for C 5 – 21 MeV/nuc (4 bins)

23.2.12 C Plus Systematic Uncertainty

`c_sys_err_plus`

Plus systematic uncertainty for C (1/(cm^2 s MeV/nuc sr))
`SPASE>Particle>ParticleType:Ion,ParticleQuantity:NumberFlux,Qualifier:Differential_Uncertainty`
Size: 4 time-varying
Geometric mean energy per nucleon for C 5 – 21 MeV/nuc (4 bins)

23.2.13 Ca minus statistical uncertainty

`ca_stat_uncert_minus`

Minus statistical uncertainty for Ca (1/(cm^2 s MeV/nuc sr))
`SPASE>Particle>ParticleType:Ion,ParticleQuantity:NumberFlux,Qualifier:Differential_Uncertainty`
Size: 5 time-varying

Geometric mean energy per nucleon for Ca 5 – 34 MeV/nuc (5 bins)

23.2.14 Ca plus statistical uncertainty

`ca_stat_uncert_plus`

Plus statistical uncertainty for Ca (1/(cm^2 s MeV/nuc sr))
`SPASE>Particle>ParticleType:Ion,ParticleQuantity:NumberFlux,Qualifier:Differential_Uncertainty`
Size: 5 time-varying

Geometric mean energy per nucleon for Ca 5 – 34 MeV/nuc (5 bins)

23.2.15 Ca minus systematic uncertainty

`ca_sys_err_minus`

Minus systematic uncertainty for Ca (1/(cm^2 s MeV/nuc sr))
`SPASE>Particle>ParticleType:Ion,ParticleQuantity:NumberFlux,Qualifier:Differential_Uncertainty`
Size: 5 time-varying

Geometric mean energy per nucleon for Ca 5 – 34 MeV/nuc (5 bins)

23.2.16 Ca Plus Systematic Uncertainty

`ca_sys_err_plus`

Plus systematic uncertainty for Ca (1/(cm^2 s MeV/nuc sr))
`SPASE>Particle>ParticleType:Ion,ParticleQuantity:NumberFlux,Qualifier:Differential_Uncertainty`
Size: 5 time-varying

Geometric mean energy per nucleon for Ca 5 – 34 MeV/nuc (5 bins)

23.2.17 Fe minus statistical uncertainty

`fe_stat_uncert_minus`

Minus statistical uncertainty for Fe (1/(cm^2 s MeV/nuc sr))
`SPASE>Particle>ParticleType:Ion,ParticleQuantity:NumberFlux,Qualifier:Differential_Uncertainty`
Size: 5 time-varying

Geometric mean energy per nucleon for Fe 5 – 34 MeV/nuc (5 bins)

23.2.18 Fe plus statistical uncertainty

`fe_stat_uncert_plus`

Plus statistical uncertainty for Fe (1/(cm^2 s MeV/nuc sr))
SPASE>Particle>ParticleType:Ion,ParticleQuantity:NumberFlux,Qualifier:Differential_Uncertainty
Size: 5 time-varying
Geometric mean energy per nucleon for Fe 5 – 34 MeV/nuc (5 bins)

23.2.19 Fe minus systematic uncertainty

`fe_sys_err_minus`

Minus systematic uncertainty for Fe (1/(cm^2 s MeV/nuc sr))
SPASE>Particle>ParticleType:Ion,ParticleQuantity:NumberFlux,Qualifier:Differential_Uncertainty
Size: 5 time-varying
Geometric mean energy per nucleon for Fe 5 – 34 MeV/nuc (5 bins)

23.2.20 Fe Plus Systematic Uncertainty

`fe_sys_err_plus`

Plus systematic uncertainty for Fe (1/(cm^2 s MeV/nuc sr))
SPASE>Particle>ParticleType:Ion,ParticleQuantity:NumberFlux,Qualifier:Differential_Uncertainty
Size: 5 time-varying
Geometric mean energy per nucleon for Fe 5 – 34 MeV/nuc (5 bins)

23.2.21 H minus statistical uncertainty

`h_stat_uncert_minus`

Minus statistical uncertainty for H (1/(cm^2 s MeV/nuc sr))
SPASE>Particle>ParticleType:Ion,ParticleQuantity:NumberFlux,Qualifier:Differential_Uncertainty
Size: 4 time-varying
Geometric mean energy per nucleon for H 3 – 12 MeV/nuc (4 bins)

23.2.22 H plus statistical uncertainty

`h_stat_uncert_plus`

Plus statistical uncertainty for H (1/(cm^2 s MeV/nuc sr))
SPASE>Particle>ParticleType:Ion,ParticleQuantity:NumberFlux,Qualifier:Differential_Uncertainty
Size: 4 time-varying
Geometric mean energy per nucleon for H 3 – 12 MeV/nuc (4 bins)

23.2.23 H minus systematic uncertainty

`h_sys_err_minus`

Minus systematic uncertainty for H (1/(cm^2 s MeV/nuc sr))
`SPASE>Particle>ParticleType:Ion,ParticleQuantity:NumberFlux,Qualifier:Differential_Uncertainty`
Size: 4 time-varying
Geometric mean energy per nucleon for H 3 – 12 MeV/nuc (4 bins)

23.2.24 H Plus Systematic Uncertainty

`h_sys_err_plus`

Plus Systematic uncertainty for H (1/(cm^2 s MeV/nuc sr))
`SPASE>Particle>ParticleType:Ion,ParticleQuantity:NumberFlux,Qualifier:Differential_Uncertainty`
Size: 4 time-varying
Geometric mean energy per nucleon for H 3 – 12 MeV/nuc (4 bins)

23.2.25 He3 minus statistical uncertainty

`he3_stat_uncert_minus`

Minus statistical uncertainty for He3 (1/(cm^2 s MeV/nuc sr))
`SPASE>Particle>ParticleType:Ion,ParticleQuantity:NumberFlux,Qualifier:Differential_Uncertainty`
Size: 3 time-varying
Geometric mean energy per nucleon for He3 5 – 12 MeV/nuc (3 bins)

23.2.26 He3 plus statistical uncertainty

`he3_stat_uncert_plus`

Plus statistical uncertainty for He3 (1/(cm^2 s MeV/nuc sr))
`SPASE>Particle>ParticleType:Ion,ParticleQuantity:NumberFlux,Qualifier:Differential_Uncertainty`
Size: 3 time-varying
Geometric mean energy per nucleon for He3 5 – 12 MeV/nuc (3 bins)

23.2.27 He3 minus systematic uncertainty

`he3_sys_err_minus`

Minus systematic uncertainty for He3 (1/(cm^2 s MeV/nuc sr))
`SPASE>Particle>ParticleType:Ion,ParticleQuantity:NumberFlux,Qualifier:Differential_Uncertainty`
Size: 3 time-varying

Geometric mean energy per nucleon for He3 5 – 12 MeV/nuc (3 bins)

23.2.28 He3 Plus Systematic Uncertainty

`he3_sys_err_plus`

Plus systematic uncertainty for He3 (1/(cm^2 s MeV/nuc sr))
`SPASE>Particle>ParticleType:Ion,ParticleQuantity:NumberFlux,Qualifier:Differential_Uncertainty`
Size: 3 time-varying

Geometric mean energy per nucleon for He3 5 – 12 MeV/nuc (3 bins)

23.2.29 He4 minus statistical uncertainty

`he4_stat_uncert_minus`

Minus statistical uncertainty for He4 (1/(cm^2 s MeV/nuc sr))
`SPASE>Particle>ParticleType:Ion,ParticleQuantity:NumberFlux,Qualifier:Differential_Uncertainty`
Size: 4 time-varying

Geometric mean energy per nucleon for He4 3 – 12 MeV/nuc (4 bins)

23.2.30 He4 plus statistical uncertainty

`he4_stat_uncert_plus`

Plus statistical uncertainty for He4 (1/(cm^2 s MeV/nuc sr))
`SPASE>Particle>ParticleType:Ion,ParticleQuantity:NumberFlux,Qualifier:Differential_Uncertainty`
Size: 4 time-varying

Geometric mean energy per nucleon for He4 3 – 12 MeV/nuc (4 bins)

23.2.31 He4 minus systematic uncertainty

`he4_sys_err_minus`

Minus systematic uncertainty for He4 (1/(cm^2 s MeV/nuc sr))
`SPASE>Particle>ParticleType:Ion,ParticleQuantity:NumberFlux,Qualifier:Differential_Uncertainty`
Size: 4 time-varying

Geometric mean energy per nucleon for He4 3 – 12 MeV/nuc (4 bins)

23.2.32 He4 Plus Systematic Uncertainty

`he4_sys_err_plus`

Plus systematic uncertainty for He4 (1/(cm^2 s MeV/nuc sr))
SPASE>Particle>ParticleType:Ion,ParticleQuantity:NumberFlux,Qualifier:Differential_Uncertainty
Size: 4 time-varying
Geometric mean energy per nucleon for He4 3 – 12 MeV/nuc (4 bins)

23.2.33 He minus statistical uncertainty

he_stat_uncert_minus

Minus statistical uncertainty for He (1/(cm^2 s MeV/nuc sr))
SPASE>Particle>ParticleType:Ion,ParticleQuantity:NumberFlux,Qualifier:Differential_Uncertainty
Size: 3 time-varying
Geometric mean energy per nucleon for He 5 – 12 MeV/nuc (3 bins)

23.2.34 He plus statistical uncertainty

he_stat_uncert_plus

Plus statistical uncertainty for He (1/(cm^2 s MeV/nuc sr))
SPASE>Particle>ParticleType:Ion,ParticleQuantity:NumberFlux,Qualifier:Differential_Uncertainty
Size: 3 time-varying
Geometric mean energy per nucleon for He 5 – 12 MeV/nuc (3 bins)

23.2.35 He minus systematic uncertainty

he_sys_err_minus

Minus systematic uncertainty for He (1/(cm^2 s MeV/nuc sr))
SPASE>Particle>ParticleType:Ion,ParticleQuantity:NumberFlux,Qualifier:Differential_Uncertainty
Size: 3 time-varying
Geometric mean energy per nucleon for He 5 – 12 MeV/nuc (3 bins)

23.2.36 He plus systematic uncertainty

he_sys_err_plus

Plus systematic uncertainty for He (1/(cm^2 s MeV/nuc sr))
SPASE>Particle>ParticleType:Ion,ParticleQuantity:NumberFlux,Qualifier:Differential_Uncertainty
Size: 3 time-varying
Geometric mean energy per nucleon for He 5 – 12 MeV/nuc (3 bins)

23.2.37 Mg minus statistical uncertainty

`mg_stat_uncert_minus`

Minus statistical uncertainty for Mg (1/(cm^2 s MeV/nuc sr))
`SPASE>Particle>ParticleType:Ion,ParticleQuantity:NumberFlux,Qualifier:Differential_Uncertainty`
Size: 4 time-varying
Geometric mean energy per nucleon for Mg 5 – 21 MeV/nuc (4 bins)

23.2.38 Mg plus statistical uncertainty

`mg_stat_uncert_plus`

Plus statistical uncertainty for Mg (1/(cm^2 s MeV/nuc sr))
`SPASE>Particle>ParticleType:Ion,ParticleQuantity:NumberFlux,Qualifier:Differential_Uncertainty`
Size: 4 time-varying
Geometric mean energy per nucleon for Mg 5 – 21 MeV/nuc (4 bins)

23.2.39 Mg minus systematic uncertainty

`mg_sys_err_minus`

Minus systematic uncertainty for Mg (1/(cm^2 s MeV/nuc sr))
`SPASE>Particle>ParticleType:Ion,ParticleQuantity:NumberFlux,Qualifier:Differential_Uncertainty`
Size: 4 time-varying
Geometric mean energy per nucleon for Mg 5 – 21 MeV/nuc (4 bins)

23.2.40 Mg Plus Systematic Uncertainty

`mg_sys_err_plus`

Plus systematic uncertainty for Mg (1/(cm^2 s MeV/nuc sr))
`SPASE>Particle>ParticleType:Ion,ParticleQuantity:NumberFlux,Qualifier:Differential_Uncertainty`
Size: 4 time-varying
Geometric mean energy per nucleon for Mg 5 – 21 MeV/nuc (4 bins)

23.2.41 N minus statistical uncertainty

`n_stat_uncert_minus`

Minus statistical uncertainty for N (1/(cm^2 s MeV/nuc sr))
`SPASE>Particle>ParticleType:Ion,ParticleQuantity:NumberFlux,Qualifier:Differential_Uncertainty`
Size: 4 time-varying

Geometric mean energy per nucleon for N 5 – 21 MeV/nuc (4 bins)

23.2.42 N plus statistical uncertainty

`n_stat_uncert_plus`

Plus statistical uncertainty for N (1/(cm^2 s MeV/nuc sr))
`SPASE>Particle>ParticleType:Ion,ParticleQuantity:NumberFlux,Qualifier:Differential_Uncertainty`
Size: 4 time-varying

Geometric mean energy per nucleon for N 5 – 21 MeV/nuc (4 bins)

23.2.43 N minus systematic uncertainty

`n_sys_err_minus`

Minus systematic uncertainty for N (1/(cm^2 s MeV/nuc sr))
`SPASE>Particle>ParticleType:Ion,ParticleQuantity:NumberFlux,Qualifier:Differential_Uncertainty`
Size: 4 time-varying

Geometric mean energy per nucleon for N 5 – 21 MeV/nuc (4 bins)

23.2.44 N Plus Systematic Uncertainty

`n_sys_err_plus`

Plus systematic uncertainty for N (1/(cm^2 s MeV/nuc sr))
`SPASE>Particle>ParticleType:Ion,ParticleQuantity:NumberFlux,Qualifier:Differential_Uncertainty`
Size: 4 time-varying

Geometric mean energy per nucleon for N 5 – 21 MeV/nuc (4 bins)

23.2.45 Na minus statistical uncertainty

`na_stat_uncert_minus`

Minus statistical uncertainty for Na (1/(cm^2 s MeV/nuc sr))
`SPASE>Particle>ParticleType:Ion,ParticleQuantity:NumberFlux,Qualifier:Differential_Uncertainty`
Size: 2 time-varying

Geometric mean energy per nucleon for Na 12 – 21 MeV/nuc (2 bins)

23.2.46 Na plus statistical uncertainty

`na_stat_uncert_plus`

Plus statistical uncertainty for Na (1/(cm^2 s MeV/nuc sr))
SPASE>Particle>ParticleType:Ion,ParticleQuantity:NumberFlux,Qualifier:Differential_Uncertainty
Size: 2 time-varying
Geometric mean energy per nucleon for Na 12 – 21 MeV/nuc (2 bins)

23.2.47 Na minus systematic uncertainty

na_sys_err_minus

Minus systematic uncertainty for Na (1/(cm^2 s MeV/nuc sr))
SPASE>Particle>ParticleType:Ion,ParticleQuantity:NumberFlux,Qualifier:Differential_Uncertainty
Size: 2 time-varying
Geometric mean energy per nucleon for Na 12 – 21 MeV/nuc (2 bins)

23.2.48 Na Plus Systematic Uncertainty

na_sys_err_plus

Plus systematic uncertainty for Na (1/(cm^2 s MeV/nuc sr))
SPASE>Particle>ParticleType:Ion,ParticleQuantity:NumberFlux,Qualifier:Differential_Uncertainty
Size: 2 time-varying
Geometric mean energy per nucleon for Na 12 – 21 MeV/nuc (2 bins)

23.2.49 Ne minus statistical uncertainty

ne_stat_uncert_minus

Minus statistical uncertainty for Ne (1/(cm^2 s MeV/nuc sr))
SPASE>Particle>ParticleType:Ion,ParticleQuantity:NumberFlux,Qualifier:Differential_Uncertainty
Size: 4 time-varying
Geometric mean energy per nucleon for Ne 5 – 21 MeV/nuc (4 bins)

23.2.50 Ne plus statistical uncertainty

ne_stat_uncert_plus

Plus statistical uncertainty for Ne (1/(cm^2 s MeV/nuc sr))
SPASE>Particle>ParticleType:Ion,ParticleQuantity:NumberFlux,Qualifier:Differential_Uncertainty
Size: 4 time-varying
Geometric mean energy per nucleon for Ne 5 – 21 MeV/nuc (4 bins)

23.2.51 Ne minus systematic uncertainty

`ne_sys_err_minus`

Minus systematic uncertainty for Ne (1/(cm^2 s MeV/nuc sr))
`SPASE>Particle>ParticleType:Ion,ParticleQuantity:NumberFlux,Qualifier:Differential_Uncertainty`
Size: 4 time-varying
Geometric mean energy per nucleon for Ne 5 – 21 MeV/nuc (4 bins)

23.2.52 Ne Plus Systematic Uncertainty

`ne_sys_err_plus`

Plus systematic uncertainty for Ne (1/(cm^2 s MeV/nuc sr))
`SPASE>Particle>ParticleType:Ion,ParticleQuantity:NumberFlux,Qualifier:Differential_Uncertainty`
Size: 4 time-varying
Geometric mean energy per nucleon for Ne 5 – 21 MeV/nuc (4 bins)

23.2.53 Ni minus statistical uncertainty

`ni_stat_uncert_minus`

Minus statistical uncertainty for Ni (1/(cm^2 s MeV/nuc sr))
`SPASE>Particle>ParticleType:Ion,ParticleQuantity:NumberFlux,Qualifier:Differential_Uncertainty`
Size: 3 time-varying
Geometric mean energy per nucleon for Ni 12 – 34 MeV/nuc (3 bins)

23.2.54 Ni plus statistical uncertainty

`ni_stat_uncert_plus`

Plus statistical uncertainty for Ni (1/(cm^2 s MeV/nuc sr))
`SPASE>Particle>ParticleType:Ion,ParticleQuantity:NumberFlux,Qualifier:Differential_Uncertainty`
Size: 3 time-varying
Geometric mean energy per nucleon for Ni 12 – 34 MeV/nuc (3 bins)

23.2.55 Ni minus systematic uncertainty

`ni_sys_err_minus`

Minus systematic uncertainty for Ni (1/(cm^2 s MeV/nuc sr))
`SPASE>Particle>ParticleType:Ion,ParticleQuantity:NumberFlux,Qualifier:Differential_Uncertainty`
Size: 3 time-varying

Geometric mean energy per nucleon for Ni 12 – 34 MeV/nuc (3 bins)

23.2.56 Ni Plus Systematic Uncertainty

`ni_sys_err_plus`

Plus systematic uncertainty for Ni (1/(cm^2 s MeV/nuc sr))
`SPASE>Particle>ParticleType:Ion,ParticleQuantity:NumberFlux,Qualifier:Differential_Uncertainty`
Size: 3 time-varying

Geometric mean energy per nucleon for Ni 12 – 34 MeV/nuc (3 bins)

23.2.57 O minus statistical uncertainty

`o_stat_uncert_minus`

Minus statistical uncertainty for O (1/(cm^2 s MeV/nuc sr))
`SPASE>Particle>ParticleType:Ion,ParticleQuantity:NumberFlux,Qualifier:Differential_Uncertainty`
Size: 4 time-varying

Geometric mean energy per nucleon for O 5 – 21 MeV/nuc (4 bins)

23.2.58 O plus statistical uncertainty

`o_stat_uncert_plus`

Plus statistical uncertainty for O (1/(cm^2 s MeV/nuc sr))
`SPASE>Particle>ParticleType:Ion,ParticleQuantity:NumberFlux,Qualifier:Differential_Uncertainty`
Size: 4 time-varying

Geometric mean energy per nucleon for O 5 – 21 MeV/nuc (4 bins)

23.2.59 O minus systematic uncertainty

`o_sys_err_minus`

Minus systematic uncertainty for O (1/(cm^2 s MeV/nuc sr))
`SPASE>Particle>ParticleType:Ion,ParticleQuantity:NumberFlux,Qualifier:Differential_Uncertainty`
Size: 4 time-varying

Geometric mean energy per nucleon for O 5 – 21 MeV/nuc (4 bins)

23.2.60 O Plus Systematic Uncertainty

`o_sys_err_plus`

Plus systematic uncertainty for O (1/(cm^2 s MeV/nuc sr))
SPASE>Particle>ParticleType:Ion,ParticleQuantity:NumberFlux,Qualifier:Differential_Uncertainty
Size: 4 time-varying
Geometric mean energy per nucleon for O 5 – 21 MeV/nuc (4 bins)

23.2.61 S minus statistical uncertainty

s_stat_uncert_minus

Minus statistical uncertainty for S (1/(cm^2 s MeV/nuc sr))
SPASE>Particle>ParticleType:Ion,ParticleQuantity:NumberFlux,Qualifier:Differential_Uncertainty
Size: 5 time-varying
Geometric mean energy per nucleon for S 5 – 34 MeV/nuc (5 bins)

23.2.62 S plus statistical uncertainty

s_stat_uncert_plus

Plus statistical uncertainty for S (1/(cm^2 s MeV/nuc sr))
SPASE>Particle>ParticleType:Ion,ParticleQuantity:NumberFlux,Qualifier:Differential_Uncertainty
Size: 5 time-varying
Geometric mean energy per nucleon for S 5 – 34 MeV/nuc (5 bins)

23.2.63 S minus systematic uncertainty

s_sys_err_minus

Minus systematic uncertainty for S (1/(cm^2 s MeV/nuc sr))
SPASE>Particle>ParticleType:Ion,ParticleQuantity:NumberFlux,Qualifier:Differential_Uncertainty
Size: 5 time-varying
Geometric mean energy per nucleon for S 5 – 34 MeV/nuc (5 bins)

23.2.64 S Plus Systematic Uncertainty

s_sys_err_plus

Plus systematic uncertainty for S (1/(cm^2 s MeV/nuc sr))
SPASE>Particle>ParticleType:Ion,ParticleQuantity:NumberFlux,Qualifier:Differential_Uncertainty
Size: 5 time-varying
Geometric mean energy per nucleon for S 5 – 34 MeV/nuc (5 bins)

23.2.65 Si minus statistical uncertainty

`si_stat_uncert_minus`

Minus statistical uncertainty for Si (1/(cm^2 s MeV/nuc sr))
`SPASE>Particle>ParticleType:Ion,ParticleQuantity:NumberFlux,Qualifier:Differential_Uncertainty`
Size: 5 time-varying
Geometric mean energy per nucleon for Si 5 – 34 MeV/nuc (5 bins)

23.2.66 Si plus statistical uncertainty

`si_stat_uncert_plus`

Plus statistical uncertainty for Si (1/(cm^2 s MeV/nuc sr))
`SPASE>Particle>ParticleType:Ion,ParticleQuantity:NumberFlux,Qualifier:Differential_Uncertainty`
Size: 5 time-varying
Geometric mean energy per nucleon for Si 5 – 34 MeV/nuc (5 bins)

23.2.67 Si minus systematic uncertainty

`si_sys_err_minus`

Minus systematic uncertainty for Si (1/(cm^2 s MeV/nuc sr))
`SPASE>Particle>ParticleType:Ion,ParticleQuantity:NumberFlux,Qualifier:Differential_Uncertainty`
Size: 5 time-varying
Geometric mean energy per nucleon for Si 5 – 34 MeV/nuc (5 bins)

23.2.68 Si Plus Systematic Uncertainty

`si_sys_err_plus`

Plus systematic uncertainty for Si (1/(cm^2 s MeV/nuc sr))
`SPASE>Particle>ParticleType:Ion,ParticleQuantity:NumberFlux,Qualifier:Differential_Uncertainty`
Size: 5 time-varying
Geometric mean energy per nucleon for Si 5 – 34 MeV/nuc (5 bins)

24 imap_idex_l2a_sci-10days

IDEX>Interstellar Dust Experiment
L2A_SCI-10DAYS>Level-2A Science 10-Day Data
The Interstellar Dust Experiment (IDEX) is a time-of-flight (TOF) dust impact ionization mass spectrometer on the IMAP mission that provides the elemental composition, speed, and mass distributions of interstellar dust and interplanetary dust particles. Each record contains the data

from a single dust impact. See https://imap.princeton.edu/spacecraft/instruments/interstellar-dust-experiment-idex for more details.
Users should acknowledge the sources of data used in all publications, presentations, and reports using an appropriate DOI. Appropriate acknowledgement to institutions, personnel, and funding agencies should be given, including acknowledging the IMAP Mission Principal Investigator, Prof. David J. McComas of Princeton University (Contract #80GSFC19C0027). IMAP Rules-of-the-Road for data usage can be found in the IMAP CMAD.

24.1 Data

24.1.1 Position X

`ephemeris_position_x`

Cartesian coord X positions for the IMAP spacecraft in the ECLIPJ2000 frame. (km)
`SPASE>Support>SupportQuantity:Positional`
time-varying

24.1.2 Position Y

`ephemeris_position_y`

Cartesian coord Y positions for the IMAP spacecraft in the ECLIPJ2000 frame. (km)
`SPASE>Support>SupportQuantity:Positional`
time-varying

24.1.3 Position Z

`ephemeris_position_z`

Cartesian coord Z positions for the IMAP spacecraft in the ECLIPJ2000 frame. (km)
`SPASE>Support>SupportQuantity:Positional`
time-varying

24.1.4 Velocity X

`ephemeris_velocity_x`

Velocity X positions for the IMAP spacecraft in the ECLIPJ2000 frame. (km/s)
`SPASE>Support>SupportQuantity:Velocity`
time-varying

24.1.5 Velocity Y

`ephemeris_velocity_y`

Velocity Y positions for the IMAP spacecraft in the ECLIPJ2000 frame. (km/s)
`SPASE>Support>SupportQuantity:Velocity`
time-varying

24.1.6 Velocity Z

`ephemeris_velocity_z`

Velocity Z positions for the IMAP spacecraft in the ECLIPJ2000 frame. (km/s)
`SPASE>Support>SupportQuantity:Velocity`
time-varying

24.1.7 Chi Square (Ion Grid)

`ion_grid_chi_squared`

Chi squared value for the Ion Grid signal fit.
`SPASE>Support>SupportQuantity:DataQuality`
time-varying

24.1.8 Estimated Dust Mass (Ion Grid)

`ion_grid_dust_mass_estimate`

Estimated dust mass from Ion Grid signal based on impact charge. (Kg)
`SPASE>Particle>ParticleType:Dust>ParticleQuantity:Mass>Qualifier:Derived`
time-varying

24.1.9 Ion Grid Fit Parameters

`ion_grid_fit_parameters`

Fitted parameters for Ion Grid impact signal.
`SPASE>Particle>ParticleType:Dust>ParticleQuantity:Current>Qualifier:Fit`
Size: 5 time-varying
    Target fit parameter index 0 – 4 (5 bins)
Parameters include time of impact, constant offset, amplitude, rise time, discharge time.

24.1.10 Ion Grid Fit Results

`ion_grid_fit_results`

Values of Ion Grid signal fit evaluated at each time point. (pC)
`SPASE>Particle>ParticleType:Dust>ParticleQuantity:Current>Qualifier:Derived`
Size: 512 time-varying
    Low sampling rate time index 0 – 511 (512 bins)

24.1.11 Ion Grid Impact Charge

`ion_grid_impact_charge`

Charge from the dust impact on Ion Grid (IG) channel derived from the fitted curve. (pC)
`SPASE>Particle>ParticleType:Dust>ParticleQuantity:Current>Qualifier:Derived`
time-varying

24.1.12 Reduced Chi Square (Ion Grid)

`ion_grid_reduced_chi_squared`

Reduced chi squared value for the Ion Grid signal fit.
`SPASE>Support>SupportQuantity:DataQuality`
time-varying

24.1.13 Estimated Velocity (Ion Grid)

`ion_grid_velocity_estimate`

Estimated particle velocity from Ion Grid signal based on impact charge. (km/s)
`SPASE>Particle>ParticleType:Dust>ParticleQuantity:Velocity>Qualifier:Derived`
time-varying

24.1.14 Latitude

`latitude`

Latitude of the dust event as observed from Earth in the ECLIPJ2000 frame. (Degrees)
`SPASE>Support>SupportQuantity:Latitude`
time-varying

24.1.15 Longitude

`longitude`

Longitude of the dust event as observed from Earth in the ECLIPJ2000 frame. (Degrees)
`SPASE>Support>SupportQuantity:Longitude`
time-varying

24.1.16 Mass Scale

`mass_scale`

Preliminary time-to-mass scale for the TOF waveform. (amu)
`SPASE>Support>SupportQuantity:Temporal`
Size: 8189 time-varying
    High sampling rate time index 0 – 8188 (8189 bins)

24.1.17 Solar Longitude

`solar_longitude`

Solar Longitude of the IMAP spacecraft (Degrees)
`SPASE>Support>SupportQuantity:Longitude`
time-varying

24.1.18 Spin Phase

`spin_phase`

IMAP Spin Phase (Degrees)
`SPASE>Support>SupportQuantity:SpinPhase`
time-varying

24.1.19 Chi Square (Target High)

`target_high_chi_squared`

Chi squared value for the Target High signal fit.
`SPASE>Support>SupportQuantity:DataQuality`
time-varying

24.1.20 Estimated Dust Mass (Target High)

`target_high_dust_mass_estimate`

Estimated dust mass from Target High signal based on impact charge. (Kg)
`SPASE>Particle>ParticleType:Dust>ParticleQuantity:Mass>Qualifier:Derived`
time-varying

24.1.21 Target High Fit Parameters

`target_high_fit_parameters`

Fitted parameters for Target High impact signal.
`SPASE>Particle>ParticleType:Dust>ParticleQuantity:Current>Qualifier:Fit`
Size: 5 time-varying
    Target fit parameter index 0 – 4 (5 bins)
Parameters include time of impact, constant offset, amplitude, rise time, discharge time.

24.1.22 Target High Fit Results

`target_high_fit_results`

Values of Target High signal fit evaluated at each time point. (pC)
`SPASE>Particle>ParticleType:Dust>ParticleQuantity:Current>Qualifier:Derived`
Size: 512 time-varying
    Low sampling rate time index 0 – 511 (512 bins)

24.1.23 Target High Impact Charge

`target_high_impact_charge`

Charge from the dust impact on Target High (TH) derived from the fitted curve. (pC)
`SPASE>Particle>ParticleType:Dust>ParticleQuantity:Current>Qualifier:Derived`
time-varying

24.1.24 Reduced Chi Square (Target High)

`target_high_reduced_chi_squared`

Reduced chi-square value for the Target High waveform fit.
`SPASE>Support>SupportQuantity:DataQuality`
time-varying

24.1.25 Estimated Velocity (Target High)

`target_high_velocity_estimate`

Estimated particle velocity from Target High signal based on impact charge. (km/s)
`SPASE>Particle>ParticleType:Dust>ParticleQuantity:Velocity>Qualifier:Derived`
time-varying

24.1.26 Chi Square (Target Low)

`target_low_chi_squared`

Chi squared value for the Target Low signal fit.
`SPASE>Support>SupportQuantity:DataQuality`
time-varying

24.1.27 Estimated Dust Mass (Target Low)

`target_low_dust_mass_estimate`

Estimated dust mass from Target Low signal based on impact charge. (Kg)
`SPASE>Particle>ParticleType:Dust>ParticleQuantity:Mass>Qualifier:Derived`
time-varying

24.1.28 Target Low Fit Parameters

`target_low_fit_parameters`

Fitted parameters for Target Low impact signal.
`SPASE>Particle>ParticleType:Dust>ParticleQuantity:Current>Qualifier:Fit`
Size: 5 time-varying
    Target fit parameter index 0 – 4 (5 bins)
Parameters include time of impact, constant offset, amplitude, rise time, discharge time.

24.1.29 Target Low Fit results

`target_low_fit_results`

Values of Target Low signal fit evaluated at each time point. (pC)
`SPASE>Particle>ParticleType:Dust>ParticleQuantity:Current>Qualifier:Derived`
Size: 512 time-varying
    Low sampling rate time index 0 – 511 (512 bins)

24.1.30 Target Low Impact Charge

`target_low_impact_charge`

Total charge from the dust impact on Target Low (TL) channel derived from the fitted curve. (pC)
`SPASE>Particle>ParticleType:Dust>ParticleQuantity:Current>Qualifier:Derived`
time-varying

24.1.31 Reduced Chi Square (Target Low)

`target_low_reduced_chi_squared`

Reduced chi squared value for the Target Low signal fit.
`SPASE>Support>SupportQuantity:DataQuality`
time-varying

24.1.32 Estimated Velocity (Target Low)

`target_low_velocity_estimate`

Estimated particle velocity from Target Low signal based on impact charge. (km/s)
`SPASE>Particle>ParticleType:Dust>ParticleQuantity:Velocity>Qualifier:Derived`
time-varying

24.1.33 High Sample Rate Time

`time_high_sample_rate`

High sample rate time steps for a dust event. (microseconds)
`SPASE>Support>SupportQuantity:Temporal`
Size: 8189 time-varying
    High sampling rate time index 0 – 8188 (8189 bins)
The high sample rate in microseconds. Steps are approximately 1/260 microseconds in duration. Used by the TOF_High, TOF_Mid, and TOF_Low variables.

24.1.34 Low Sample Rate Time

`time_low_sample_rate`

Low sample rate time steps for a dust event. (microseconds)
`SPASE>Support>SupportQuantity:Temporal`
Size: 512 time-varying

Low sampling rate time index 0 – 511 (512 bins)
The low sample rate is 4.0625 MHz, so adjacent samples are separated by approximately 1/4.0625 microseconds.

24.1.35 TOF Peak Area

`tof_peak_area_under_fit`

Area under the EMG curve for each mass peak.
`SPASE>Particle>ParticleType:Ion>ParticleQuantity:Current>Qualifier:Integral`
Size: 500 time-varying
Index variable for mass-resolved TOF peak-fit products. 0 – 499 (500 bins)

24.1.36 Chi Square (TOF peak fits)

`tof_peak_chi_square`

Chi squared value for the TOF peak emg fits.
`SPASE>Support>SupportQuantity:DataQuality`
Size: 500 time-varying
Index variable for mass-resolved TOF peak-fit products. 0 – 499 (500 bins)

24.1.37 TOF Peak Kappa

`tof_peak_kappa`

Mass-scale alignment metric for the TOF peak solution.
`SPASE>Support>SupportQuantity:DataQuality`
time-varying
Kappa measures how closely detected TOF peaks align with integer mass positions on the preliminary mass scale.

24.1.38 Reduced Chi Square (TOF peak fits)

`tof_peak_reduced_chi_square`

Reduced chi squared value for the TOF peak emg fits.
`SPASE>Support>SupportQuantity:DataQuality`
Size: 500 time-varying
Index variable for mass-resolved TOF peak-fit products. 0 – 499 (500 bins)

24.1.39 TOF Signal to Noise Ratio

`tof_snr`

Signal-to-noise ratio of the TOF High waveform.
`SPASE>Support>SupportQuantity:DataQuality`
time-varying
Computed relative to a pre-impact baseline window.

24.2 Support Data

24.2.1 Mass Scale Alias

`mass`

Mass-scale output retained for compatibility with the L2A product structure. (amu)
`SPASE>Support>SupportQuantity:Other`
Size: 8189 time-varying
    High sampling rate time index 0 – 8188 (8189 bins)
Mass-scale output retained for compatibility with the current L2A product structure. This variable is not intended to be the primary science-facing mass-scale output.

24.2.2 TOF Peak Fit Parameters

`tof_peak_fit_parameters`

EMG fit parameters (mu, sigma, lambda) for TOF High peaks.
`SPASE>Particle>ParticleType:Ion>ParticleQuantity:Current>Qualifier:Fit`
Size: 500×3 time-varying
    Index variable for mass-resolved TOF peak-fit products. 0 – 499 (500 bins)
    Peak fit parameter index 0 – 2 (3 bins)

25 imap_mag_l2_burst-dsrf

MAG>Magnetometer
L2_burst-dsrf>Level 2 burst rate data in DSRF
The IMAP magnetometer MAG consists of two vector magnetic field sensors which measure the magnetic field in the vicinity of the spacecraft. MAG will contribute to our understanding of the acceleration and transport of charged particles in the heliosphere, the dynamics of interplanetary shocks, and provide real time space weather measurements via the I-AliRT service. MAG design, assembly, operations, and calibration are led by Imperial College London. See https://imap.princeton.edu/spacecraft/instruments/magnetometer-mag for more details.
Users should acknowledge the sources of data used in all publications, presentations, and reports using an appropriate DOI. Appropriate acknowledgement to institutions, personnel, and funding

agencies should be given, including acknowledging the IMAP Mission Principal Investigator, Prof. David J. McComas of Princeton University (Contract #80GSFC19C0027). IMAP Rules-of-the-Road for data usage can be found in the IMAP CMAD.

25.1 Data

25.1.1 Magnetic Field DSRF

`b_dsrf`

Magnetic field in the Despun Spacecraft Reference Frame (DSRF) (nT)
`SPASE>Field>FieldQuantity:Magnetic,Qualifier:Vector,CoordinateSystemName:DSRF,CoordinateRepresen`
Size: 3 time-varying
Magnetic field vector 0 – 2 counts (3 bins)

25.1.2 Magnetic Field Magnitude

`magnitude`

Magnitude of the magnetic field (nT)
`SPASE>Field>FieldQuantity:Magnetic,Qualifier:Scalar`
time-varying

25.1.3 Quality Flag

`quality_flags`

Data quality flag. 0: Good data, 1: Bad data. (0=good)
`SPASE>Support>SupportQuantity:DataQuality`
time-varying
The quality flag indicates the overall quality of the data at each timestamp. More detail on the data quality can be found in the quality bitmask. - 0: Good data - 1: Bad quality data not suitable for science

25.2 Support Data

25.2.1 Quality Bitmask

`quality_bitmask`

Bitmask indicating when spacecraft related activities influenced the measurement.
`SPASE>Support>SupportQuantity:DataQuality`
time-varying
The bitmask is an 8-bit integer where each bit represents a different quality flag. The bits are

defined as follows: - Bit 0: Data is sourced from secondary sensor - Bit 1: Thruster firing signals have been removed - Bit 2: Spacecraft interference impacts this data - Bit 3: Instrument signals have been removed - Bits 4-7: Reserved for in flight calibration

25.2.2 Sensor Range

`range`

Range of the magnetometer sensor
`SPASE>Support>SupportQuantity:InstrumentMode`
time-varying

26 imap_mag_l2_burst-gse

MAG>Magnetometer
L2_burst-gse>Level 2 burst rate data in GSE
The IMAP magnetometer MAG consists of two vector magnetic field sensors which measure the magnetic field in the vicinity of the spacecraft. MAG will contribute to our understanding of the acceleration and transport of charged particles in the heliosphere, the dynamics of interplanetary shocks, and provide real time space weather measurements via the I-AliRT service. MAG design, assembly, operations, and calibration are led by Imperial College London. See https://imap.princeton.edu/spacecraft/instruments/magnetometer-mag for more details.
Users should acknowledge the sources of data used in all publications, presentations, and reports using an appropriate DOI. Appropriate acknowledgement to institutions, personnel, and funding agencies should be given, including acknowledging the IMAP Mission Principal Investigator, Prof. David J. McComas of Princeton University (Contract #80GSFC19C0027). IMAP Rules-of-the-Road for data usage can be found in the IMAP CMAD.

26.1 Data

26.1.1 Magnetic Field GSE

`b_gse`

Magnetic field in GSE coordinates (nT)
`SPASE>Field>FieldQuantity:Magnetic,Qualifier:Vector,CoordinateSystemName:GSE,CoordinateRepresent`
Size: 3 time-varying
Magnetic field vector 0 – 2 counts (3 bins)

26.1.2 Magnetic Field Magnitude

`magnitude`

Magnitude of the magnetic field (nT)
SPASE>Field>FieldQuantity:Magnetic,Qualifier:Scalar
time-varying

26.1.3 Quality Flag

quality_flags

Data quality flag. 0: Good data, 1: Bad data. (0=good)
SPASE>Support>SupportQuantity:DataQuality
time-varying
The quality flag indicates the overall quality of the data at each timestamp. More detail on the data quality can be found in the quality bitmask. - 0: Good data - 1: Bad quality data not suitable for science

26.2 Support Data

26.2.1 Quality Bitmask

quality_bitmask

Bitmask indicating when spacecraft related activities influenced the measurement.
SPASE>Support>SupportQuantity:DataQuality
time-varying
The bitmask is an 8-bit integer where each bit represents a different quality flag. The bits are defined as follows: - Bit 0: Data is sourced from secondary sensor - Bit 1: Thruster firing signals have been removed - Bit 2: Spacecraft interference impacts this data - Bit 3: Instrument signals have been removed - Bits 4-7: Reserved for in flight calibration

26.2.2 Sensor Range

range

Range of the magnetometer sensor
SPASE>Support>SupportQuantity:InstrumentMode
time-varying

27 imap_mag_l2_burst-gsm

MAG>Magnetometer
L2_burst-gsm>Level 2 burst rate data in GSM
The IMAP magnetometer MAG consists of two vector magnetic field sensors which measure the magnetic field in the vicinity of the spacecraft. MAG will contribute to our understanding of

the acceleration and transport of charged particles in the heliosphere, the dynamics of interplanetary shocks, and provide real time space weather measurements via the I-AliRT service. MAG design, assembly, operations, and calibration are led by Imperial College London. See https://imap.princeton.edu/spacecraft/instruments/magnetometer-mag for more details.
Users should acknowledge the sources of data used in all publications, presentations, and reports using an appropriate DOI. Appropriate acknowledgement to institutions, personnel, and funding agencies should be given, including acknowledging the IMAP Mission Principal Investigator, Prof. David J. McComas of Princeton University (Contract #80GSFC19C0027). IMAP Rules-of-the-Road for data usage can be found in the IMAP CMAD.

27.1 Data

27.1.1 Magnetic Field GSM

`b_gsm`

Magnetic field in GSM coordinates (nT)
`SPASE>Field>FieldQuantity:Magnetic,Qualifier:Vector,CoordinateSystemName:GSM,CoordinateRepresent`
Size: 3 time-varying
Magnetic field vector 0 – 2 counts (3 bins)

27.1.2 Magnetic Field Magnitude

`magnitude`

Magnitude of the magnetic field (nT)
`SPASE>Field>FieldQuantity:Magnetic,Qualifier:Scalar`
time-varying

27.1.3 Quality Flag

`quality_flags`

Data quality flag. 0: Good data, 1: Bad data. (0=good)
`SPASE>Support>SupportQuantity:DataQuality`
time-varying
The quality flag indicates the overall quality of the data at each timestamp. More detail on the data quality can be found in the quality bitmask. - 0: Good data - 1: Bad quality data not suitable for science

27.2 Support Data

27.2.1 Quality Bitmask

`quality_bitmask`

Bitmask indicating when spacecraft related activities influenced the measurement.
`SPASE>Support>SupportQuantity:DataQuality`
time-varying
The bitmask is an 8-bit integer where each bit represents a different quality flag. The bits are defined as follows: - Bit 0: Data is sourced from secondary sensor - Bit 1: Thruster firing signals have been removed - Bit 2: Spacecraft interference impacts this data - Bit 3: Instrument signals have been removed - Bits 4-7: Reserved for in flight calibration

27.2.2 Sensor Range

`range`

Range of the magnetometer sensor
`SPASE>Support>SupportQuantity:InstrumentMode`
time-varying

28 imap_mag_l2_burst-rtn

MAG>Magnetometer
L2_burst-rtn>Level 2 burst rate data in RTN
The IMAP magnetometer MAG consists of two vector magnetic field sensors which measure the magnetic field in the vicinity of the spacecraft. MAG will contribute to our understanding of the acceleration and transport of charged particles in the heliosphere, the dynamics of interplanetary shocks, and provide real time space weather measurements via the I-AliRT service. MAG design, assembly, operations, and calibration are led by Imperial College London. See https://imap.princeton.edu/spacecraft/instruments/magnetometer-mag for more details.
Users should acknowledge the sources of data used in all publications, presentations, and reports using an appropriate DOI. Appropriate acknowledgement to institutions, personnel, and funding agencies should be given, including acknowledging the IMAP Mission Principal Investigator, Prof. David J. McComas of Princeton University (Contract #80GSFC19C0027). IMAP Rules-of-the-Road for data usage can be found in the IMAP CMAD.

28.1 Data

28.1.1 Magnetic Field RTN

`b_rtn`

Magnetic field in RTN coordinates (nT)
SPASE>Field>FieldQuantity:Magnetic,Qualifier:Vector,CoordinateSystemName:RTN,CoordinateRepresent
Size: 3 time-varying
Magnetic field vector 0 – 2 counts (3 bins)

28.1.2 Magnetic Field Magnitude

magnitude

Magnitude of the magnetic field (nT)
SPASE>Field>FieldQuantity:Magnetic,Qualifier:Scalar
time-varying

28.1.3 Quality Flag

quality_flags

Data quality flag. 0: Good data, 1: Bad data. (0=good)
SPASE>Support>SupportQuantity:DataQuality
time-varying
The quality flag indicates the overall quality of the data at each timestamp. More detail on the data quality can be found in the quality bitmask. - 0: Good data - 1: Bad quality data not suitable for science

28.2 Support Data

28.2.1 Quality Bitmask

quality_bitmask

Bitmask indicating when spacecraft related activities influenced the measurement.
SPASE>Support>SupportQuantity:DataQuality
time-varying
The bitmask is an 8-bit integer where each bit represents a different quality flag. The bits are defined as follows: - Bit 0: Data is sourced from secondary sensor - Bit 1: Thruster firing signals have been removed - Bit 2: Spacecraft interference impacts this data - Bit 3: Instrument signals have been removed - Bits 4-7: Reserved for in flight calibration

28.2.2 Sensor Range

range

Range of the magnetometer sensor

SPASE>Support>SupportQuantity:InstrumentMode
time-varying

29 imap_mag_l2_burst-srf

MAG>Magnetometer
L2_burst-srf>Level 2 burst rate data in SRF
The IMAP magnetometer MAG consists of two vector magnetic field sensors which measure the magnetic field in the vicinity of the spacecraft. MAG will contribute to our understanding of the acceleration and transport of charged particles in the heliosphere, the dynamics of interplanetary shocks, and provide real time space weather measurements via the I-AliRT service. MAG design, assembly, operations, and calibration are led by Imperial College London. See https://imap.princeton.edu/spacecraft/instruments/magnetometer-mag for more details.
Users should acknowledge the sources of data used in all publications, presentations, and reports using an appropriate DOI. Appropriate acknowledgement to institutions, personnel, and funding agencies should be given, including acknowledging the IMAP Mission Principal Investigator, Prof. David J. McComas of Princeton University (Contract #80GSFC19C0027). IMAP Rules-of-the-Road for data usage can be found in the IMAP CMAD.

29.1 Data

29.1.1 Magnetic Field SRF

b_srf

Magnetic field in the Spacecraft Reference Frame (SRF) (nT)
SPASE>Field>FieldQuantity:Magnetic,Qualifier:Vector,CoordinateSystemName:SRF,CoordinateRepresent
Size: 3 time-varying
Magnetic field vector 0 – 2 counts (3 bins)

29.1.2 Magnetic Field Magnitude

magnitude

Magnitude of the magnetic field (nT)
SPASE>Field>FieldQuantity:Magnetic,Qualifier:Scalar
time-varying

29.1.3 Quality Flag

quality_flags

Data quality flag. 0: Good data, 1: Bad data. (0=good)

SPASE>Support>SupportQuantity:DataQuality
time-varying
The quality flag indicates the overall quality of the data at each timestamp. More detail on the data quality can be found in the quality bitmask. - 0: Good data - 1: Bad quality data not suitable for science

29.2 Support Data

29.2.1 Quality Bitmask

quality_bitmask

Bitmask indicating when spacecraft related activities influenced the measurement.
SPASE>Support>SupportQuantity:DataQuality
time-varying
The bitmask is an 8-bit integer where each bit represents a different quality flag. The bits are defined as follows: - Bit 0: Data is sourced from secondary sensor - Bit 1: Thruster firing signals have been removed - Bit 2: Spacecraft interference impacts this data - Bit 3: Instrument signals have been removed - Bits 4-7: Reserved for in flight calibration

29.2.2 Sensor Range

range

Range of the magnetometer sensor
SPASE>Support>SupportQuantity:InstrumentMode
time-varying

30 imap_mag_l2_norm-dsrf

MAG>Magnetometer
L2_norm-dsrf>Level 2 normal rate data in DSRF
The IMAP magnetometer MAG consists of two vector magnetic field sensors which measure the magnetic field in the vicinity of the spacecraft. MAG will contribute to our understanding of the acceleration and transport of charged particles in the heliosphere, the dynamics of interplanetary shocks, and provide real time space weather measurements via the I-AliRT service. MAG design, assembly, operations, and calibration are led by Imperial College London. See https://imap.princeton.edu/spacecraft/instruments/magnetometer-mag for more details.
Users should acknowledge the sources of data used in all publications, presentations, and reports using an appropriate DOI. Appropriate acknowledgement to institutions, personnel, and funding agencies should be given, including acknowledging the IMAP Mission Principal Investigator, Prof. David J. McComas of Princeton University (Contract #80GSFC19C0027). IMAP Rules-of-the-Road for data usage can be found in the IMAP CMAD.

30.1 Data

30.1.1 Magnetic Field DSRF

`b_dsrf`

Magnetic field in the Despun Spacecraft Reference Frame (DSRF) (nT)
`SPASE>Field>FieldQuantity:Magnetic,Qualifier:Vector,CoordinateSystemName:DSRF,CoordinateRepresen`
Size: 3 time-varying
Magnetic field vector 0 – 2 counts (3 bins)

30.1.2 Magnetic Field Magnitude

`magnitude`

Magnitude of the magnetic field (nT)
`SPASE>Field>FieldQuantity:Magnetic,Qualifier:Scalar`
time-varying

30.1.3 Quality Flag

`quality_flags`

Data quality flag. 0: Good data, 1: Bad data. (0=good)
`SPASE>Support>SupportQuantity:DataQuality`
time-varying
The quality flag indicates the overall quality of the data at each timestamp. More detail on the data quality can be found in the quality bitmask. - 0: Good data - 1: Bad quality data not suitable for science

30.2 Support Data

30.2.1 Quality Bitmask

`quality_bitmask`

Bitmask indicating when spacecraft related activities influenced the measurement.
`SPASE>Support>SupportQuantity:DataQuality`
time-varying
The bitmask is an 8-bit integer where each bit represents a different quality flag. The bits are defined as follows: - Bit 0: Data is sourced from secondary sensor - Bit 1: Thruster firing signals have been removed - Bit 2: Spacecraft interference impacts this data - Bit 3: Instrument signals

have been removed - Bits 4-7: Reserved for in flight calibration

30.2.2 Sensor Range

`range`

Range of the magnetometer sensor
`SPASE>Support>SupportQuantity:InstrumentMode`
time-varying

31 imap_mag_l2_norm-gse

MAG>Magnetometer
L2_norm-gse>Level 2 normal rate data in GSE
The IMAP magnetometer MAG consists of two vector magnetic field sensors which measure the magnetic field in the vicinity of the spacecraft. MAG will contribute to our understanding of the acceleration and transport of charged particles in the heliosphere, the dynamics of interplanetary shocks, and provide real time space weather measurements via the I-AliRT service. MAG design, assembly, operations, and calibration are led by Imperial College London. See https://imap.princeton.edu/spacecraft/instruments/magnetometer-mag for more details.
Users should acknowledge the sources of data used in all publications, presentations, and reports using an appropriate DOI. Appropriate acknowledgement to institutions, personnel, and funding agencies should be given, including acknowledging the IMAP Mission Principal Investigator, Prof. David J. McComas of Princeton University (Contract #80GSFC19C0027). IMAP Rules-of-the-Road for data usage can be found in the IMAP CMAD.

31.1 Data

31.1.1 Magnetic Field GSE

`b_gse`

Magnetic field in GSE coordinates (nT)
`SPASE>Field>FieldQuantity:Magnetic,Qualifier:Vector,CoordinateSystemName:GSE,CoordinateRepresent`
Size: 3 time-varying
Magnetic field vector 0 – 2 counts (3 bins)

31.1.2 Magnetic Field Magnitude

`magnitude`

Magnitude of the magnetic field (nT)
`SPASE>Field>FieldQuantity:Magnetic,Qualifier:Scalar`

time-varying

31.1.3 Quality Flag

`quality_flags`

Data quality flag. 0: Good data, 1: Bad data. (0=good)
`SPASE>Support>SupportQuantity:DataQuality`
time-varying
The quality flag indicates the overall quality of the data at each timestamp. More detail on the data quality can be found in the quality bitmask. - 0: Good data - 1: Bad quality data not suitable for science

31.2 Support Data

31.2.1 Quality Bitmask

`quality_bitmask`

Bitmask indicating when spacecraft related activities influenced the measurement.
`SPASE>Support>SupportQuantity:DataQuality`
time-varying
The bitmask is an 8-bit integer where each bit represents a different quality flag. The bits are defined as follows: - Bit 0: Data is sourced from secondary sensor - Bit 1: Thruster firing signals have been removed - Bit 2: Spacecraft interference impacts this data - Bit 3: Instrument signals have been removed - Bits 4-7: Reserved for in flight calibration

31.2.2 Sensor Range

`range`

Range of the magnetometer sensor
`SPASE>Support>SupportQuantity:InstrumentMode`
time-varying

32 imap_mag_l2_norm-gsm

MAG>Magnetometer
L2_norm-gsm>Level 2 normal rate data in GSM
The IMAP magnetometer MAG consists of two vector magnetic field sensors which measure the magnetic field in the vicinity of the spacecraft. MAG will contribute to our understanding of the acceleration and transport of charged particles in the heliosphere, the dynamics of interplanetary shocks, and provide real time space weather measurements via the I-AliRT service.

IMAP CDF summary

MAG design, assembly, operations, and calibration are led by Imperial College London. See https://imap.princeton.edu/spacecraft/instruments/magnetometer-mag for more details.
Users should acknowledge the sources of data used in all publications, presentations, and reports using an appropriate DOI. Appropriate acknowledgement to institutions, personnel, and funding agencies should be given, including acknowledging the IMAP Mission Principal Investigator, Prof. David J. McComas of Princeton University (Contract #80GSFC19C0027). IMAP Rules-of-the-Road for data usage can be found in the IMAP CMAD.

32.1 Data

32.1.1 Magnetic Field GSM

`b_gsm`

Magnetic field in GSM coordinates (nT)
`SPASE>Field>FieldQuantity:Magnetic,Qualifier:Vector,CoordinateSystemName:GSM,CoordinateRepresent`
Size: 3 time-varying
Magnetic field vector 0 – 2 counts (3 bins)

32.1.2 Magnetic Field Magnitude

`magnitude`

Magnitude of the magnetic field (nT)
`SPASE>Field>FieldQuantity:Magnetic,Qualifier:Scalar`
time-varying

32.1.3 Quality Flag

`quality_flags`

Data quality flag. 0: Good data, 1: Bad data. (0=good)
`SPASE>Support>SupportQuantity:DataQuality`
time-varying
The quality flag indicates the overall quality of the data at each timestamp. More detail on the data quality can be found in the quality bitmask. - 0: Good data - 1: Bad quality data not suitable for science

32.2 Support Data

32.2.1 Quality Bitmask

`quality_bitmask`

Bitmask indicating when spacecraft related activities influenced the measurement.
SPASE>Support>SupportQuantity:DataQuality
time-varying
The bitmask is an 8-bit integer where each bit represents a different quality flag. The bits are defined as follows: - Bit 0: Data is sourced from secondary sensor - Bit 1: Thruster firing signals have been removed - Bit 2: Spacecraft interference impacts this data - Bit 3: Instrument signals have been removed - Bits 4-7: Reserved for in flight calibration

32.2.2 Sensor Range

range

Range of the magnetometer sensor
SPASE>Support>SupportQuantity:InstrumentMode
time-varying

33 imap_mag_l2_norm-rtn

MAG>Magnetometer
L2_norm-rtn>Level 2 normal rate data in RTN
The IMAP magnetometer MAG consists of two vector magnetic field sensors which measure the magnetic field in the vicinity of the spacecraft. MAG will contribute to our understanding of the acceleration and transport of charged particles in the heliosphere, the dynamics of interplanetary shocks, and provide real time space weather measurements via the I-AliRT service. MAG design, assembly, operations, and calibration are led by Imperial College London. See https://imap.princeton.edu/spacecraft/instruments/magnetometer-mag for more details.
Users should acknowledge the sources of data used in all publications, presentations, and reports using an appropriate DOI. Appropriate acknowledgement to institutions, personnel, and funding agencies should be given, including acknowledging the IMAP Mission Principal Investigator, Prof. David J. McComas of Princeton University (Contract #80GSFC19C0027). IMAP Rules-of-the-Road for data usage can be found in the IMAP CMAD.

33.1 Data

33.1.1 Magnetic Field RTN

b_rtn

Magnetic field in RTN coordinates (nT)
SPASE>Field>FieldQuantity:Magnetic,Qualifier:Vector,CoordinateSystemName:RTN,CoordinateRepresent
Size: 3 time-varying
    Magnetic field vector 0 – 2 counts (3 bins)

33.1.2 Magnetic Field Magnitude

`magnitude`

Magnitude of the magnetic field (nT)
`SPASE>Field>FieldQuantity:Magnetic,Qualifier:Scalar`
time-varying

33.1.3 Quality Flag

`quality_flags`

Data quality flag. 0: Good data, 1: Bad data. (0=good)
`SPASE>Support>SupportQuantity:DataQuality`
time-varying
The quality flag indicates the overall quality of the data at each timestamp. More detail on the data quality can be found in the quality bitmask. - 0: Good data - 1: Bad quality data not suitable for science

33.2 Support Data

33.2.1 Quality Bitmask

`quality_bitmask`

Bitmask indicating when spacecraft related activities influenced the measurement.
`SPASE>Support>SupportQuantity:DataQuality`
time-varying
The bitmask is an 8-bit integer where each bit represents a different quality flag. The bits are defined as follows: - Bit 0: Data is sourced from secondary sensor - Bit 1: Thruster firing signals have been removed - Bit 2: Spacecraft interference impacts this data - Bit 3: Instrument signals have been removed - Bits 4-7: Reserved for in flight calibration

33.2.2 Sensor Range

`range`

Range of the magnetometer sensor
`SPASE>Support>SupportQuantity:InstrumentMode`
time-varying

34 imap_mag_l2_norm-srf

MAG>Magnetometer
L2_norm-srf>Level 2 normal rate data in SRF
The IMAP magnetometer MAG consists of two vector magnetic field sensors which measure the magnetic field in the vicinity of the spacecraft. MAG will contribute to our understanding of the acceleration and transport of charged particles in the heliosphere, the dynamics of interplanetary shocks, and provide real time space weather measurements via the I-AliRT service. MAG design, assembly, operations, and calibration are led by Imperial College London. See https://imap.princeton.edu/spacecraft/instruments/magnetometer-mag for more details.
Users should acknowledge the sources of data used in all publications, presentations, and reports using an appropriate DOI. Appropriate acknowledgement to institutions, personnel, and funding agencies should be given, including acknowledging the IMAP Mission Principal Investigator, Prof. David J. McComas of Princeton University (Contract #80GSFC19C0027). IMAP Rules-of-the-Road for data usage can be found in the IMAP CMAD.

34.1 Data

34.1.1 Magnetic Field SRF

`b_srf`

Magnetic field in the Spacecraft Reference Frame (SRF) (nT)
`SPASE>Field>FieldQuantity:Magnetic,Qualifier:Vector,CoordinateSystemName:SRF,CoordinateRepresent`
Size: 3 time-varying
Magnetic field vector 0 – 2 counts (3 bins)

34.1.2 Magnetic Field Magnitude

`magnitude`

Magnitude of the magnetic field (nT)
`SPASE>Field>FieldQuantity:Magnetic,Qualifier:Scalar`
time-varying

34.1.3 Quality Flag

`quality_flags`

Data quality flag. 0: Good data, 1: Bad data. (0=good)
`SPASE>Support>SupportQuantity:DataQuality`
time-varying
The quality flag indicates the overall quality of the data at each timestamp. More detail on the data quality can be found in the quality bitmask. - 0: Good data - 1: Bad quality data not suitable

for science

34.2 Support Data

34.2.1 Quality Bitmask

`quality_bitmask`

Bitmask indicating when spacecraft related activities influenced the measurement.
`SPASE>Support>SupportQuantity:DataQuality`
time-varying
The bitmask is an 8-bit integer where each bit represents a different quality flag. The bits are defined as follows: - Bit 0: Data is sourced from secondary sensor - Bit 1: Thruster firing signals have been removed - Bit 2: Spacecraft interference impacts this data - Bit 3: Instrument signals have been removed - Bits 4-7: Reserved for in flight calibration

34.2.2 Sensor Range

`range`

Range of the magnetometer sensor
`SPASE>Support>SupportQuantity:InstrumentMode`
time-varying

35 imap_swapi_l2_sci

SWAPI>Solar Wind and Pickup Ion
L2_SCI>Level-2 Science data
The Solar Wind and Pickup Ion (SWAPI) instrument onboard Interstellar Mapping and Acceleration Probe (IMAP) is a top-hat electrostatic analyzer designed to measure energy-per-charge distributions of solar wind protons (H+), alpha particles (He++), and interstellar He+ pickup ions (PUIs), across a range of 0.1 to 20 keV/q. See https://imap.princeton.edu/spacecraft/instruments/solar-wind-and-pickup-ions-swapi for more details. SWAPI's Level 1 data contains primary, secondary, and coincidence counts per ESA voltage step and time. Level 2 data converts these counts into count rates using a constant livetime of 145ms and includes the ESA energy associated with each voltage step.
Users should acknowledge the sources of data used in all publications, presentations, and reports using an appropriate DOI. Appropriate acknowledgement to institutions, personnel, and funding agencies should be given, including acknowledging the IMAP Mission Principal Investigator, Prof. David J. McComas of Princeton University (Contract #80GSFC19C0027). IMAP Rules-of-the-Road for data usage can be found in the IMAP CMAD.

IMAP CDF summary

35.1 Data

35.1.1 ESA Energy

`esa_energy`

ESA energy in eV/q corresponding to each step id for each sweep (eV / q)
`SPASE>Particle>ParticleType:Ion,ParticleQuantity:EnergyPerCharge`
Size: 72 time-varying
Energy step id in lookup table; corresponding energy in eV/q is provided by esa_energy 0 – 71 (72 bins)

35.1.2 Coincidence Rates

`swp_coin_rate`

(counts/s)
`SPASE>Particle>ParticleType:Ion,ParticleQuantity:CountRate,Qualifier:Average`
Size: 72 time-varying
Energy step id in lookup table; corresponding energy in eV/q is provided by esa_energy 0 – 71 (72 bins)

35.1.3 Quality Flag

`swp_l1a_flags`

Bitwise science and housekeeping quality flags. See VAR_NOTES for bit definitions.
`SPASE>Support>SupportQuantity:EncodedParameter`
Size: 72 time-varying
Energy step id in lookup table; corresponding energy in eV/q is provided by esa_energy 0 – 71 (72 bins)
Flags are stored as a 15-bit bitmask with VALIDMAX=32767 when bits 0-14 are all set. The implemented flags are: bit 0 (value 1) INF, bit 1 (value 2) NEG, bit 2 (value 4) SWP_PCEM_COMP, bit 3 (value 8) SWP_SCEM_COMP, bit 4 (value 16) SWP_COIN_COMP, bit 5 (value 32) OVR_T_ST, bit 6 (value 64) UND_T_ST, bit 7 (value 128) PCEM_CNT_ST, bit 8 (value 256) SCEM_CNT_ST, bit 9 (value 512) PCEM_V_ST, bit 10 (value 1024) PCEM_I_ST, bit 11 (value 2048) PCEM_INT_ST, bit 12 (value 4096) SCEM_V_ST, bit 13 (value 8192) SCEM_I_ST, and bit 14 (value 16384) SCEM_INT_ST.

35.1.4 Primary CEM Rates

`swp_pcem_rate`

Primary Channel Electron Multiplier (CEM) Rates (counts/s)

SPASE>Particle>ParticleType:Ion,ParticleQuantity:CountRate,Qualifier:Average
Size: 72 time-varying

Energy step id in lookup table; corresponding energy in eV/q is provided by esa_energy 0 – 71 (72 bins)

35.1.5 Secondary CEM Rates

swp_scem_rate

Secondary Channel Electron Multiplier (CEM) Rates (counts/s)
SPASE>Particle>ParticleType:Ion,ParticleQuantity:CountRate,Qualifier:Average
Size: 72 time-varying

Energy step id in lookup table; corresponding energy in eV/q is provided by esa_energy 0 – 71 (72 bins)

35.2 Support Data

35.2.1 ESA LVL5

esa_lvl5

ESA LVL5 ID.
SPASE>Support>SupportQuantity:Other
time-varying

35.2.2 FPGA Revision

fpga_rev

Revision number of the FPGA.
SPASE>Support>SupportQuantity:Other
time-varying

35.2.3 FPGA Type

fpga_type

Type number of the FPGA.
SPASE>Support>SupportQuantity:Other
time-varying

35.2.4 LUT Choice

`lut_choice`

Which LUT is in use.
`SPASE>Support>SupportQuantity:Other`
time-varying

35.2.5 Plan ID

`plan_id`

Plan ID.
`SPASE>Support>SupportQuantity:Other`
time-varying

35.2.6 Science Start time

`sci_start_time`

Start time of sweep in UTC
`SPASE>Support>SupportQantity:Temporal`
time-varying

35.2.7 Sweep Table

`sweep_table`

Sweep table ID.
`SPASE>Support>SupportQuantity:Other`
time-varying

36 imap_swapi_l3a_alpha-sw

SWAPI>The Solar Wind and Pickup Ion
L3a_ALPHA-SW>Level-3a Alpha Solar Wind
The Solar Wind and Pickup Ion (SWAPI) instrument onboard the Interstellar Mapping and Acceleration Probe (IMAP) is a top-hat electrostatic analyzer designed to measure energy-per-charge distributions of solar wind protons (H+), alpha particles (He++), and interstellar pickup ions (PUIs; combined H+ and He+) across a range of 0.1 to 20 keV/q. See https://imap.princeton.edu/spacecraft/instruments/solar wind-and-pickup-ions-swapi for more details.
The alpha parameters are obtained after obtaining the proton parameters by fitting the sum of the proton+alpha Maxwellian distributions to the measured coincidence rates using forward modeling,

fully accounting for the 3D instrument response and spacecraft spin. The alpha-proton differential flow is constrained to be aligned with the magnetic field.
Users should acknowledge the sources of data used in all publications, presentations, and reports using an appropriate DOI. Appropriate acknowledgement to institutions, personnel, and funding agencies should be given, including acknowledging the IMAP Mission Principal Investigator, Prof. David J. McComas of Princeton University (Contract #80GSFC19C0027). IMAP Rules-of-the-Road for data usage can be found in the IMAP CMAD.

36.1 Primary variables

36.1.1 Alpha Solar Wind Density

`alpha_sw_density`

Number density of the solar wind alpha-particle population (cm^-3)
time-varying

36.1.2 Alpha Solar Wind Speed

`alpha_sw_speed`

Magnitude of the bulk velocity vector of the solar wind alpha-particle population (spacecraft frame) (km/s)
time-varying

36.1.3 Alpha Solar Wind Speed (Sun Frame)

`alpha_sw_speed_sun`

Magnitude of the bulk velocity vector of the solar wind alpha-particle population (Sun frame) (km/s)
time-varying

36.1.4 Alpha Solar Wind Temperature

`alpha_sw_temperature`

Scalar temperature of the solar wind alpha-particle population (K)
time-varying

36.1.5 Alpha Solar Wind Velocity (RTN)

`alpha_sw_velocity_rtn`

Solar wind alpha-particle bulk velocity vector in RTN coordinates (spacecraft frame) (km/s)
Size: 3 time-varying

36.1.6 Alpha Solar Wind Velocity (RTN, Sun Frame)

`alpha_sw_velocity_rtn_sun`

Solar wind alpha-particle bulk velocity vector in RTN coordinates (Sun frame) (km/s)
Size: 3 time-varying

36.2 Other data

36.2.1 Quality Flags for SWAPI L3a

`swp_flags`

Quality flags for SWAPI L3a (caution required if nonzero) (0: okay; nonzero: caution)
time-varying
Each bit corresponds to a specific potential concern. See release notes for details. Bit 2: Bad fit: fitting resulted in invalid values or large residuals. Bit 3: Fit error: fit failed to complete. Bit 4: preliminary MAG L1D was used for acquiring the magnetic field direction instead of the nominal MAG L2 product. All other bits are reserved.

36.3 Support Data

36.3.1 Alpha Solar Wind Velocity Covariance (RTN)

`alpha_sw_velocity_rtn_covariance`

Covariance matrix in RTN coordinates (frame-independent), with standard errors given by the square root of the diagonal (kmˆ2/sˆ2)
Size: 3×3 time-varying

37 imap_swapi_l3a_proton-sw

SWAPI>The Solar Wind and Pickup Ion
L3a_PROTON-SW>Level-3a Proton Solar Wind
The Solar Wind and Pickup Ion (SWAPI) instrument onboard the Interstellar Mapping and Acceleration Probe (IMAP) is a top-hat electrostatic analyzer designed to measure energy-per-charge distributions of solar wind protons (H+), alpha particles (He++), and interstellar pickup ions (PUIs; com-

bined H+ and He+) across a range of 0.1 to 20 keV/q. See https://imap.princeton.edu/spacecraft/instruments/solar wind-and-pickup-ions-swapi for more details.
The proton parameters are obtained by fitting a Maxwellian distribution to the measured coincidence rates using forward modeling, fully accounting for the 3D instrument response and spacecraft spin.
Users should acknowledge the sources of data used in all publications, presentations, and reports using an appropriate DOI. Appropriate acknowledgement to institutions, personnel, and funding agencies should be given, including acknowledging the IMAP Mission Principal Investigator, Prof. David J. McComas of Princeton University (Contract #80GSFC19C0027). IMAP Rules-of-the-Road for data usage can be found in the IMAP CMAD.

37.1 Primary variables

37.1.1 Proton Solar Wind Density

`proton_sw_density`

Number density of the solar wind proton population (cm^-3)
time-varying

37.1.2 Proton Solar Wind Speed

`proton_sw_speed`

Magnitude of the bulk velocity vector of the solar wind proton population (spacecraft frame) (km/s)
time-varying

37.1.3 Proton Solar Wind Speed (Sun Frame)

`proton_sw_speed_sun`

Magnitude of the bulk velocity vector of the solar wind proton population (Sun frame) (km/s)
time-varying

37.1.4 Proton Solar Wind Temperature

`proton_sw_temperature`

Scalar temperature of the solar wind proton population (K)
time-varying

37.1.5 Proton Solar Wind Velocity (RTN)

`proton_sw_velocity_rtn`

Solar wind proton bulk velocity vector in RTN coordinates (spacecraft frame) (km/s)
Size: 3 time-varying

37.1.6 Proton Solar Wind Velocity (RTN, Sun Frame)

`proton_sw_velocity_rtn_sun`

Solar wind proton bulk velocity vector in RTN coordinates (Sun frame) (km/s)
Size: 3 time-varying

37.2 Other data

37.2.1 Quality Flags for SWAPI L3a

`swp_flags`

Quality flags for SWAPI L3a (caution required if nonzero) (0: okay; nonzero: caution)
time-varying
Each bit corresponds to a specific potential concern. See release notes for details. Bit 2: Bad fit: fitting resulted in invalid values or large residuals. Bit 3: Fit error: fit failed to complete. Bit 4: preliminary MAG L1D was used for acquiring the magnetic field direction instead of the nominal MAG L2 product. All other bits are reserved.

37.3 Support Data

37.3.1 Proton Solar Wind Velocity Covariance (RTN)

`proton_sw_velocity_rtn_covariance`

Covariance matrix in RTN coordinates (frame-independent), with standard errors given by the square root of the diagonal (kmˆ2/sˆ2)
Size: 3×3 time-varying

38 imap_swapi_l3b_combined

SWAPI>The Solar Wind and Pickup Ion
L3B_COMBINED>Level-3 Science data
The Solar Wind and Pickup Ion (SWAPI) instrument onboard the Interstellar Mapping and Acceleration Probe (IMAP) is a top-hat electrostatic analyzer designed to measure energy-per-charge distributions of solar wind protons (H+), alpha particles (He++), and interstellar pickup ions (PUIs; com-

bined H+ and He+) across a range of 0.1 to 20 keV/q. See https://imap.princeton.edu/spacecraft/instruments/solar
wind-and-pickup-ions-swapi for more details.
Users should acknowledge the sources of data used in all publications, presentations, and reports using an appropriate DOI. Appropriate acknowledgement to institutions, personnel, and funding agencies should be given, including acknowledging the IMAP Mission Principal Investigator, Prof. David J. McComas of Princeton University (Contract #80GSFC19C0027). IMAP Rules-of-the-Road for data usage can be found in the IMAP CMAD.

38.1 Primary variables

38.1.1 Combined Differential Flux

`combined_differential_flux`

Combined differential flux (cm^-2 s^-1 sr^-1 (eV/q)^-1)
Size: 62 time-varying
Combined solar wind energy 100 – 19763 eV/q (62 bins)

39 imap_swe_l2_sci

SWE>Solar Wind Electron
L2_SCI>Level-2 Science data
The IMAP Solar Wind Electron (SWE) instrument measures the solar wind electrons in the heliosphere. SWE will contribute to our understanding of the acceleration and transport of charged particles in the heliosphere. SWE design and assembly is led by Los Alamos National Laboratory. See https://imap.princeton.edu/spacecraft/instruments/solar-wind-electron-swe for more details.
Users should acknowledge the sources of data used in all publications, presentations, and reports using an appropriate DOI. Appropriate acknowledgement to institutions, personnel, and funding agencies should be given, including acknowledging the IMAP Mission Principal Investigator, Prof. David J. McComas of Princeton University (Contract #80GSFC19C0027). IMAP Rules-of-the-Road for data usage can be found in the IMAP CMAD.

39.1 Data

39.1.1 Flux

`flux`

Number flux organized by energy (eV), spin angle, CEM angle (1 / (eV * cm^2 * s * ster))
`SPASE>Particle>ParticleType:Electron,ParticleQuantity:NumberFlux,Qualifier:Array`
Size: $24 \times 30 \times 7$ time-varying
Energy of the particle in eV 3 – 5266 eV (24 bins)
Spin angle in despun spacecraft coordinates. Angle resolution is 12 degree, with bin centers 6 - 354 degree (30 bins) 6 – 354 Degree (30 bins)

Polar angle of each CEM detector relative to spin axis. Angle resolution is 21 degree, with bin centers -63 - 63 degree (7 bins) -63 – 63 Degree (7 bins)

39.1.2 Flux Spin Sector

`flux_spin_sector`

Number flux organized by ESA step and spin sector and CEM (1 / (eV * cm^2 * s * ster))
`SPASE>Particle>ParticleType:Electron,ParticleQuantity:NumberFlux,Qualifier:Array`
Size: $24 \times 30 \times 7$ time-varying
Energy step id in lookup table 0 – 23 (24 bins)
Spin sector. 30 measurements nominally 0 – 29 (30 bins)
CEM detector number 0 – 6 (7 bins)

39.1.3 Spin Angle Spin Sector

`inst_az_spin_sector`

Spin angle in despun spacecraft coordinates organized by ESA step and spin sector (Degree)
`SPASE>Support>SupportQuantity:SpinPhase,Qualifier:Array,CoordinateSystemName:SC,CoordinateRepres`
Size: 24×30 time-varying
Energy step id in lookup table 0 – 23 (24 bins)
Spin sector. 30 measurements nominally 0 – 29 (30 bins)

39.1.4 Phase Space Density

`phase_space_density`

Phase space density organized by energy (eV), spin angle, CEM angle (s^3 / cm^6)
`SPASE>Particle>ParticleType:Electron,ParticleQuantity:PhaseSpaceDensity,Qualifier:Array`
Size: $24 \times 30 \times 7$ time-varying
Energy of the particle in eV 3 – 5266 eV (24 bins)
Spin angle in despun spacecraft coordinates. Angle resolution is 12 degree, with bin centers 6 - 354 degree (30 bins) 6 – 354 Degree (30 bins)
Polar angle of each CEM detector relative to spin axis. Angle resolution is 21 degree, with bin centers -63 - 63 degree (7 bins) -63 – 63 Degree (7 bins)

39.1.5 Phase Space Density Spin Sector

`phase_space_density_spin_sector`

Phase space density organized by ESA step and spin sector and CEM (s^3 / cm^6)
`SPASE>Particle>ParticleType:Electron,ParticleQuantity:PhaseSpaceDensity,Qualifier:Array`

Size: $24 \times 30 \times 7$ time-varying
Energy step id in lookup table 0 – 23 (24 bins)
Spin sector. 30 measurements nominally 0 – 29 (30 bins)
CEM detector number 0 – 6 (7 bins)

39.2 Support Data

39.2.1 Acquisition Duration

`acq_duration`

Acquisition duration (microseconds)
`SPASE>Support>SupportQuantity:Temporal,Qualifier:Array`
Size: 24×30 time-varying
Energy step id in lookup table 0 – 23 (24 bins)
Spin sector. 30 measurements nominally 0 – 29 (30 bins)

39.2.2 Acquisition time by ESA step and spin sector

`acquisition_time`

Acquisition time organized by ESA step and spin sector (sec)
`SPASE>Support>SupportQuantity:Temporal,Qualifier:Array`
Size: 24×30 time-varying
Energy step id in lookup table 0 – 23 (24 bins)
Spin sector. 30 measurements nominally 0 – 29 (30 bins)
This stores the acquisition times of each measurement. This time is calculated by combining ACQ_START_COARSE, ACQ_START_FINE, acquisition duration and settle duration. It is center time of each science measurement (each energy and angle step).

39.2.3 SWE data quality flags

`data_quality`

In-flight calibration quality flags. Bit 2 (LAST_CAL_INTERVAL): set if any acquisition time in this cycle was extrapolated using the last two entries in the calibration table.
`SPASE>Support>SupportQuantity:DataQuality`
time-varying
There is 1 flag currently in use. Stored as a bitwise flag. Bit 2 (LAST_CAL_INTERVAL, value 4): counter values were extrapolated using the last two calibration table entries. All other bits are reserved.

40 imap_swe_l3_sci

SWE>Solar Wind Electron
L3_SCI>Level-3 Science data
The IMAP Solar Wind Electron (SWE) instrument measures the solar wind electrons in the heliosphere. SWE will contribute to our understanding of the acceleration and transport of charged particles in the heliosphere. SWE design and assembly is led by the Los Alamos National Laboratory. See https://imap.princeton.edu/spacecraft/instruments/solar-wind-electron-swe for more details.
Users should acknowledge the sources of data used in all publications, presentations, and reports using an appropriate DOI. Appropriate acknowledgement to institutions, personnel, and funding agencies should be given, including acknowledging the IMAP Mission Principal Investigator, Prof. David J. McComas of Princeton University (Contract #80GSFC19C0027). IMAP Rules-of-the-Road for data usage can be found in the IMAP CMAD.

40.1 Primary variables

40.1.1 Core Chi-square

`core_chisq`

Chi square error for core moment fitting
time-varying

40.1.2 Core Density Fit

`core_density_fit`

Density of core electrons found through Maxwellian fitting (#/cm^3)
time-varying
Analytically calculated from Bi-Maxellian fit

40.1.3 Core Density Integrated

`core_density_integrated`

Density of core electrons found through numerical integration (#/cm^3)
time-varying
Numerically integrated

40.1.4 Core/Halo Breakpoint

`core_halo_breakpoint`

SW electron core/halo breakpoint (eV)
time-varying

40.1.5 Core Heat Flux Magnitude Integrated

`core_heat_flux_magnitude_integrated`

Core heat flux magnitude integrated (uW / m^2)
time-varying
Calculated by integration over the measured phase space distribution

40.1.6 Core Heat Flux Phi Integrated

`core_heat_flux_phi_integrated`

Core heat flux phi integrated (degrees)
time-varying
Calculated by integration over the measured phase space distribution. In RTN coordinates, phi is the angle in the R-T plane.

40.1.7 Core Heat Flux Theta Integrated

`core_heat_flux_theta_integrated`

Core heat flux theta integrated (degrees)
time-varying
Calculated by integration over the measured phase space distribution. In RTN coordinates, theta is the angle relative to the N axis.

40.1.8 Core Speed Fit

`core_speed_fit`

Core speed fit (km/s)
time-varying
Analytically calculated from Bi-Maxellian fit. Recommend using SWAPI ion measurements for solar wind speed/velocity.

40.1.9 Core Speed Integrated

`core_speed_integrated`

Core speed integrated (km/s)
time-varying
Calculated by integration over the measured phase space distribution. Recommend using SWAPI ion measurements for solar wind speed/velocity.

40.1.10 Core T Parallel Fit

`core_t_parallel_fit`

Core t_parallel fit (K)
time-varying
Analytically calculated from Bi-Maxellian fit

40.1.11 Core T Parallel Integrated

`core_t_parallel_integrated`

Core t_parallel integrated
time-varying
Calculated by integration over the measured phase space distribution

40.1.12 Core T Perpendicular Fit

`core_t_perpendicular_fit`

Core t_perpendicular fit (K)
time-varying
Analytically calculated from Bi-Maxellian fit

40.1.13 Core T Perpendicular Integrated

`core_t_perpendicular_integrated`

Average of two perpendicular core temperature eigenvalues (K)
time-varying
Calculated by integration over the measured phase space distribution

40.1.14 Core T Ratio Perpendicular Integrated

`core_t_ratio_perpendicular_integrated`

Ratio of perpendicular core temperature eigenvalues

time-varying
Calculated by integration over the measured phase space distribution

40.1.15 Core T Integrated Parallel To Mag

`core_temperature_parallel_to_mag`

Core temperature parallel to mag (K)
time-varying
Calculated by integration over the measured phase space distribution, rotated to the measured magnetic field direction

40.1.16 Core T Integrated Perpendicular To Mag

`core_temperature_perpendicular_to_mag`

Average of two core temperature eigenvalues perpendicular to mag (K)
time-varying
Calculated by integration over the measured phase space distribution, rotated to the measured magnetic field direction

40.1.17 Core Temperature Phi RTN Fit

`core_temperature_phi_rtn_fit`

Core temperature fit, rotated to RTN coordinates, phi (degrees)
time-varying
Analytically calculated from Bi-Maxellian fit. In RTN coordinates, phi is the angle in the R-T plane.

40.1.18 Core Temperature Phi RTN Integrated

`core_temperature_phi_rtn_integrated`

Core temperature integrated, rotated to RTN coordinates, phi (degrees)
time-varying
Calculated by integration over the measured phase space distribution. In RTN coordinates, phi is the angle in the R-T plane.

40.1.19 Core Integrated T Ratio Perpendicular To Mag

`core_temperature_ratio_perpendicular_to_mag`

Ratio of core two temperature eigenvalues perpendicular to mag
time-varying
Calculated by integration over the measured phase space distribution, rotated to the measured magnetic field direction

40.1.20 Core Temperature Tensor Integrated

`core_temperature_tensor_integrated`

Core temperature tensor integrated (10^4 K)
Size: 6 time-varying
    Tensor id 1 – 6 (6 bins)
Calculated by integration over the measured phase space distribution

40.1.21 Core Temperature Theta RTN Fit

`core_temperature_theta_rtn_fit`

Core temperature fit, rotated to RTN coordinates, theta (degrees)
time-varying
Analytically calculated from Bi-Maxellian fit. In RTN coordinates, theta is the angle relative to the N axis.

40.1.22 Core Temperature Theta RTN Integrated

`core_temperature_theta_rtn_integrated`

Core temperature theta RTN integrated (degrees)
time-varying
Calculated by integration over the measured phase space distribution

40.1.23 Core Velocity Vector RTN Fit

`core_velocity_vector_rtn_fit`

Core velocity vector RTN fit (km/s)
Size: 3 time-varying
Analytically calculated from Bi-Maxellian fit. Recommend using SWAPI ion measurements for solar wind speed/velocity.

40.1.24 Core Velocity Vector RTN Integrated

`core_velocity_vector_rtn_integrated`

Core velocity vector RTN integrated (km/s)
Size: 3 time-varying
Calculated by integration over the measured phase space distribution. Recommend using SWAPI ion measurements for solar wind speed/velocity.

40.1.25 Halo Chi-square

`halo_chisq`

Chi square error for halo moment fitting
time-varying

40.1.26 Halo Density Fit

`halo_density_fit`

Density of halo electrons found through Maxwellian fitting (#/cm^3)
time-varying
Analytically calculated from Bi-Maxellian fit

40.1.27 Halo Density Integrated

`halo_density_integrated`

Halo density integrated (#/cm^3)
time-varying
Calculated by integration over the measured phase space distribution

40.1.28 Halo Heat Flux Magnitude Integrated

`halo_heat_flux_magnitude_integrated`

Halo heat flux magnitude integrated (uW / m^2)
time-varying
Calculated by integration over the measured phase space distribution

40.1.29 Halo Heat Flux Phi Integrated

`halo_heat_flux_phi_integrated`

Halo heat flux integrated, rotated to RTN coordinates, phi (degrees)
time-varying
Calculated by integration over the measured phase space distribution. In RTN coordinates, phi is the angle in the R-T plane.

40.1.30 Halo Heat Flux Theta Integrated

`halo_heat_flux_theta_integrated`

Halo heat flux integrated, rotated to RTN coordinates, theta (degrees)
time-varying
Calculated by integration over the measured phase space distribution. In RTN coordinates, theta is the angle relative to the N axis.

40.1.31 Halo Speed Fit

`halo_speed_fit`

Halo speed fit (km/s)
time-varying
Analytically calculated from Bi-Maxellian fit. Recommend using SWAPI ion measurements for solar wind speed/velocity.

40.1.32 Halo Speed Integrated

`halo_speed_integrated`

Halo speed integrated (km/s)
time-varying
Calculated by integration over the measured phase space distribution. Recommend using SWAPI ion measurements for solar wind speed/velocity.

40.1.33 Halo T Parallel Fit

`halo_t_parallel_fit`

Halo t_parallel fit (K)
time-varying

Analytically calculated from Bi-Maxellian fit

40.1.34 Halo T Parallel Integrated

`halo_t_parallel_integrated`

Halo t_parallel integrated
time-varying
Calculated by integration over the measured phase space distribution

40.1.35 Halo T Perpendicular Fit

`halo_t_perpendicular_fit`

Halo t_perpendicular fit (K)
time-varying
Analytically calculated from Bi-Maxellian fit

40.1.36 Halo T Perpendicular Integrated

`halo_t_perpendicular_integrated`

Average of two perpendicular halo temperature eigenvalues (K)
time-varying
Calculated by integration over the measured phase space distribution

40.1.37 Halo T Ratio Perpendicular Integrated

`halo_t_ratio_perpendicular_integrated`

Ratio of two perpendicular halo temperature eigenvalues
time-varying
Calculated by integration over the measured phase space distribution

40.1.38 Halo T Integrated Parallel To Mag

`halo_temperature_parallel_to_mag`

Halo temperature parallel to mag (K)
time-varying
Calculated by integration over the measured phase space distribution, rotated to the measured

magnetic field direction

40.1.39 Halo T Integrated Perpendicular To Mag

`halo_temperature_perpendicular_to_mag`

Halo temperature perpendicular to mag (K)
time-varying
Calculated by integration over the measured phase space distribution, rotated to the measured magnetic field direction

40.1.40 Halo Temperature Phi RTN Fit

`halo_temperature_phi_rtn_fit`

Halo temperature fit, rotated to RTN coordinates, phi (degrees)
time-varying
Analytically calculated from Bi-Maxellian fit. In RTN coordinates, phi is the angle in the R-T plane.

40.1.41 Halo Temperature Phi Rtn Integrated

`halo_temperature_phi_rtn_integrated`

Halo temperature integrated, rotated to RTN coordinates, phi (degrees)
time-varying
Calculated by integration over the measured phase space distribution, rotated to the measured magnetic field direction. In RTN coordinates, phi is the angle in the R-T plane.

40.1.42 Halo Integrated T Ratio Perpendicular To Mag

`halo_temperature_ratio_perpendicular_to_mag`

Ratio of two halo temperatures perpendicular to mag
time-varying
Calculated by integration over the measured phase space distribution, rotated to the measured magnetic field direction

40.1.43 Halo Temperature Tensor Integrated

`halo_temperature_tensor_integrated`

Halo temperature tensor integrated (10^4 K)

IMAP CDF summary

Size: 6 time-varying
Tensor id 1 – 6 (6 bins)
Calculated by integration over the measured phase space distribution

40.1.44 Halo Temperature Theta RTN Fit

`halo_temperature_theta_rtn_fit`

Halo temperature fit, rotated to RTN coordinates, theta (degrees)
time-varying
Analytically calculated from Bi-Maxellian fit. In RTN coordinates, theta is the angle relative to the N axis.

40.1.45 Halo Temperature Theta RTN Integrated

`halo_temperature_theta_rtn_integrated`

Halo temperature integrated, rotated to RTN coordinates, theta (degrees)
time-varying
Calculated by integration over the measured phase space distribution. In RTN coordinates, theta is the angle relative to the N axis.

40.1.46 Halo Velocity Vector RTN Fit

`halo_velocity_vector_rtn_fit`

Halo velocity vector RTN fit (km/s)
Size: 3 time-varying
Analytically calculated from Bi-Maxellian fit. Recommend using SWAPI ion measurements for solar wind speed/velocity.

40.1.47 Halo Velocity Vector RTN Integrated

`halo_velocity_vector_rtn_integrated`

Halo velocity vector RTN integrated (km/s)
Size: 3 time-varying
Calculated by integration over the measured phase space distribution. Recommend using SWAPI ion measurements for solar wind speed/velocity.

40.1.48 Electron Intensity

`intensity_by_pitch_angle`

Intensity by pitch angle (cm^-2 sr^-1 s^-1 eV^-1)
Size: 24 × 20 time-varying
- Bin center energy 3 – 5266 eV (24 bins)
- Pitch angle 4 – 176 degrees (20 bins)

40.1.49 Electron Intensity

`intensity_by_pitch_angle_and_gyrophase`

Intensity by pitch angle and gyrophase (cm^-2 sr^-1 s^-1 eV^-1)
Size: 24 × 20 × 24 time-varying
- Bin center energy 3 – 5266 eV (24 bins)
- Pitch angle 4 – 176 degrees (20 bins)
- Gyrophase 8 – 352 degrees (24 bins)

Sparsely sampled: there are more pitch/gyro angle bins than actual measurement directions.

40.1.50 Electron Phase Space Density

`phase_space_density_1d`

Electron phase space density (1d) (s^3 cm^-6)
Size: 24 time-varying
- Bin center energy 3 – 5266 eV (24 bins)

40.1.51 Electron Phase Space Density

`phase_space_density_by_pitch_angle`

Phase space density by pitch angle (s^3 cm^-6)
Size: 24 × 20 time-varying
- Bin center energy 3 – 5266 eV (24 bins)
- Pitch angle 4 – 176 degrees (20 bins)

40.1.52 Electron Phase Space Density

`phase_space_density_by_pitch_angle_and_gyrophase`

Phase space density by pitch angle and gyrophase (s^3 cm^-6)
Size: 24 × 20 × 24 time-varying

Bin center energy 3 – 5266 eV (24 bins)
Pitch angle 4 – 176 degrees (20 bins)
Gyrophase 8 – 352 degrees (24 bins)
Sparsely sampled: there are more pitch/gyro angle bins than actual measurement directions.

40.1.53 Electron Phase Space Density Inward

`phase_space_density_inward`

Electron phase space density (inward) (s^3 cm^-6)
Size: 24 time-varying
Bin center energy 3 – 5266 eV (24 bins)
Inward/outward are each integrated over half the pitch angle distribution (0-90 or 90-180 degree pitch angle), with outward being the larger and inward the smaller of these two.

40.1.54 Electron Phase Space Density Outward

`phase_space_density_outward`

Electron phase space density (outward) (s^3 cm^-6)
Size: 24 time-varying
Bin center energy 3 – 5266 eV (24 bins)
Inward/outward are each integrated over half the pitch angle distribution (0-90 or 90-180 degree pitch angle), with outward being the larger and inward the smaller of these two.

40.1.55 Spacecraft Potential At SWE

`spacecraft_potential`

IMAP spacecraft potential calculated at SWE (V)
time-varying

40.1.56 Total Density Integrated

`total_density_integrated`

Total density integrated (#/cm^3)
time-varying
Calculated by integration over the measured phase space distribution

40.1.57 Total Heat Flux Magnitude Integrated

`total_heat_flux_magnitude_integrated`

Total heat flux magnitude integrated (uW / m^2)
time-varying
Calculated by integration over the measured phase space distribution

40.1.58 Total Heat Flux Phi Integrated

`total_heat_flux_phi_integrated`

Total heat flux integrated, rotated to RTN coordinates, phi (degrees)
time-varying
Calculated by integration over the measured phase space distribution. In RTN coordinates, phi is the angle in the R-T plane.

40.1.59 Total Heat Flux Theta Integrated

`total_heat_flux_theta_integrated`

Total heat flux integrated, rotated to RTN coordinates, theta (degrees)
time-varying
Calculated by integration over the measured phase space distribution. In RTN coordinates, theta is the angle relative to the N axis.

40.1.60 Total Speed Integrated

`total_speed_integrated`

Total speed integrated
time-varying
Calculated by integration over the measured phase space distribution. Recommend using SWAPI ion measurements for solar wind speed/velocity.

40.1.61 Total T Parallel Integrated

`total_t_parallel_integrated`

Total t_parallel integrated
time-varying
Calculated by integration over the measured phase space distribution

40.1.62 Total T Perpendicular Integrated

`total_t_perpendicular_integrated`

Average of perpendicular total temperature eigenvalues (K)
time-varying
Calculated by integration over the measured phase space distribution

40.1.63 Total T Ratio Perpendicular Integrated

`total_t_ratio_perpendicular_integrated`

Ratio of perpendicular total temperature eigenvalues
time-varying
Calculated by integration over the measured phase space distribution

40.1.64 Total T Integrated Parallel To Mag

`total_temperature_parallel_to_mag`

Total temperature parallel to mag (K)
time-varying
Calculated by integration over the measured phase space distribution

40.1.65 Total T Integrated Perpendicular To Mag

`total_temperature_perpendicular_to_mag`

Total temperature perpendicular to mag (K)
time-varying
Calculated by integration over the measured phase space distribution, rotated to the measured magnetic field direction

40.1.66 Total Temperature Phi RTN Integrated

`total_temperature_phi_rtn_integrated`

Total temperature integrated, rotated to RTN coordinates, phi (degrees)
time-varying
Calculated by integration over the measured phase space distribution. In RTN coordinates, phi is the angle in the R-T plane.

40.1.67 Total Integrated T Ratio Perpendicular To Mag

`total_temperature_ratio_perpendicular_to_mag`

Ratio of total two temperature eigenvalues perpendicular to mag
time-varying
Calculated by integration over the measured phase space distribution, rotated to the measured magnetic field direction

40.1.68 Total Temperature Tensor Integrated

`total_temperature_tensor_integrated`

Total temperature tensor integrated (10^4 K)
Size: 6 time-varying
    Tensor id 1 – 6 (6 bins)
Calculated by integration over the measured phase space distribution

40.1.69 Total Temperature Theta RTN Integrated

`total_temperature_theta_rtn_integrated`

Total temperature integrated, rotated to RTN coordinates, theta (degrees)
time-varying
Calculated by integration over the measured phase space distribution. In RTN coordinates, theta is the angle relative to the N axis.

40.1.70 Total Velocity Vector RTN Integrated

`total_velocity_vector_rtn_integrated`

Total velocity vector RTN integrated (km/s)
Size: 3 time-varying
Calculated by integration over the measured phase space distribution. Recommend using SWAPI ion measurements for solar wind speed/velocity.

40.2 Other data

40.2.1 Quality Flags for SWE L3

`swe_flags`

Quality flags for SWE L3 (caution required if nonzero) (0: okay; nonzero: caution)
time-varying

Each bit corresponds to a specific potential concern. See release notes for details. Bit 2: first 4 points of the PSD 1D Rebinned are linear in log PSD - log energy space; spacecraft_potential is set to 2.5 V Bit 3: breakpoint finding algortithm fell back to a spline method, which failed Bit 4: fit to resolve the photo-core breakpoint fell back to spline method Bit 5: fit to resolve the core-halo breakpoint fell back to spline method Bit 6: Unimplemented. Reserved to indicate any of IMAP Ultra deflectors are turned off. (Nominal is when IMAP Ultra deflectors are turned on) Bit 7: any temperature product yielded a value found to be an extreme statistical outlier, similar to a spike removal routine. Bit 8: preliminary MAG L1D was used for acquiring the magnetic field direction instead of the nominal MAG L2 product. Bit 9: solar wind vector is unresolved, but measured speed is used from SWAPI L3A Bit 10: any density or temperature moment is negative (unphysical) Bit 11: any PSD value is unphysically large (>1e-19). Bit 12: passthrough of LAST_CAL_INTERVAL from L2 Quality Flags: calibration was extrapolated using the last two entries in the calibration table. Bit 13: Unimplemented. Reserved to indicate predictive ephemeris was used instead of reconstructed ephemeris.

40.3 Support Data

40.3.1

`core_fit_num_points`

Number of energies used on core fit
time-varying

40.3.2 Raw 1D PSD

`raw_1d_psd_rebinned`

Raw 1D PSD from rebinned data
Size: 24 time-varying
Bin center energy 3 – 5266 eV (24 bins)

40.3.3 Raw PSD by phi

`raw_psd_by_phi_rebinned`

Raw PSD by spin angle phi from rebinned data
Size: 24×30 time-varying
Bin center energy 3 – 5266 eV (24 bins)
Spin angle in instrument frame. Angle resolution is 12 degree nominally 6 – 354 Degree (30 bins)

40.3.4 Raw PSD by theta

`raw_psd_by_theta_rebinned`

Raw PSD by polar angle theta from rebinned data
Size: 24×7 time-varying
Bin center energy 3 – 5266 eV (24 bins)
Angle of each CEM detector -63 – 63 Degree (7 bins)

4.2 Particle Data

4.2.1 SWAPI

SWAPI data product definitions and processing algorithms are embedded below

Contents

1. SCOPE 5
2. APPLICABLE DOCUMENTS 7
3. ABBREVIATIONS 8
4. INSTRUMENT DESCRIPTION 9
5. DEFINITIONS OF TERMS 13
6. ALGORITHMS OVERVIEW 14
6.1. Data Volume 14
6.2. Data Product Definitions 14
6.3. L0 Data Content & Format 15
6.4. L1, L2, and L3 Data Product Grouping 16
6.5. Processing Flow 16
7. HERITAGE INSTRUMENT (NEW HORIZONS' SWAP) 18
7.1. Heritage Instrument Processing Reuse 20
7.1.1.Heritage Instrument Processing Overview: Pickup Ions 20
8. EXTERNAL DEPENDENCIES 23
9. CALIBRATION DATA 24
9.1. Ground Calibration: End-to-End Model 24
9.1.1. SIMION Module Results 26
9.2. Ground Calibration: Princeton Lab 28
9.3. Ground Calibration: Cross-Calibration with CoDICE 28
9.4. On-Orbit Calibration Data 28
9.5. Instrument Response Function 29
9.5.1. Central Effective Area and Azimuthal Transmission: 30
9.5.2. Energy-Angle Passbands: 31
10. ALGORITHMS DETAILED PROCESSING 33
10.1 L0-L1 Data Processing 34
10.1.1 Data management 34
10.1.2 Marking data not qualified for L0-L1 processing 35

10.1.3 CDF L1 data product file conten 36
10.2 L1-L2 Data Processing 39
10.3 ESA Unit Conversion Ancillary Data Product (ADP) 40
10.4 L2-L3a Data Processing 42
10.4.1 Solar Wind Proton (H^+) Parameters 43
10.4.2 Solar Wind Alpha (He^{2+}) Parameters 55
10.4.3 Pickup Helium (He^+) Parameters 58
10.5 L2-L3b Data Processing 68
10.6 Summary of SWAPI Data Products 68
11 MAINTENANCE OF SWAPI GROUND DATA PROCESSING 72
12 RECOMMENDED TESTING APPROACHES 73
13 CODE DELIVERY 74
14 I-ALIRT PRODUCTS 75
15 QUICK LOOK PRODUCTS 78
16 REFERENCES 80

1. SCOPE

The Solar Wind and Pickup Ion (SWAPI) instrument is being built by the Space Physics Group in the Department of Astrophysical Sciences at Princeton University. It is one of ten instruments on board the Interstellar Mapping and Acceleration Probe (IMAP) mission. IMAP is scheduled for launch in February 2025.



FIGURE 1. THE SOLAR WIND AND PICKUP ION INSTRUMENT IS DESIGNED TO MEASURE DISTRIBUTIONS OF COMBINED HELIUM AND HYDROGEN PICKUP IONS, WHICH ENTER THROUGH THE INSTRUMENT'S OPEN APERTURE (LEFT; PUIS), AS WELL AS SOLAR WIND PROTONS AND ALPHAS WHICH ENTER ATTENUATED THROUGH ITS APERTURE GRID ASSEMBLY (AKA "SUNGLASSES"; RIGHT; SW).

This document is a SWAPI Algorithms Document intended for use by members of the IMAP Science Data Center (SDC) to implement, test, and validate executable software that will routinely produce designated data products during the science mission.
The following information will be included:

- procedural descriptions
- flow diagrams
- programmable equations
- associated pseudocode

This information will be complete and detailed enough such that a third party can generate executable code that correctly implements the algorithms with a reasonable amount of collaborative assistance.

2. APPLICABLE DOCUMENTS

LASP 167441 IMAP - IMAP Payload Operations Center (POC) - Instrument Team (IT) ICD

LASP 167442 IMAP Science Data Center (SDC) to Instrument Team (IT) ICD

3. ABBREVIATIONS

ADP	Ancillary Data Product
CCSDS	Consultative Committee for Space Data Systems standard protocol
CEM	Channel Electron Multiplier
CoDICE	The Compact Dual Ion Composition Experiment
COIN	Coincidence Rate
ESA	Electrostatic Analyzer
FSW	Flight Software
GI ICD	General Instrument to Spacecraft Interface Control Document (ICD)
HV	High Voltage
HVPS	High Voltage Power Supply
IMAP	Interstellar Mapping and Acceleration Probe
ICD	Interface Control Document
I-ALiRT	IMAP Active Link for Real-Time
ITF	Interface Transfer Frame
JHU/APL	Johns Hopkins University/Applied Physics Laboratory
LASP	Laboratory for Atmospheric and Space Physics, University of Colorado, Boulder
LSB	Least Significant Bit
LUT	Lookup Table
MOC	Mission Operations Center
PCEM	Primary Channel Electron Multiplier
PFTs	Packet Filter Tables
POC	Payload Operations Center
PUIs	Pickup Ions
S/C	Spacecraft
SCEM	Secondary Channel Electron Multiplier
SCI	Science
SDC	Science Data Center
SOC	Science Operation Center
SW	Solar Wind
SWAP	Solar Wind Around Pluto instrument
SWAPI	Solar Wind and Pickup Ion instrument
SwRI	Southwest Research Institute

4. INSTRUMENT DESCRIPTION

The SWAPI instrument will measure solar wind protons (H^+) and helium ions (He^{2+}) together with Interstellar He^+ and H^+ pickup ions (PUIs).

A block diagram of the SWAPI instrument is shown in Figure 2.

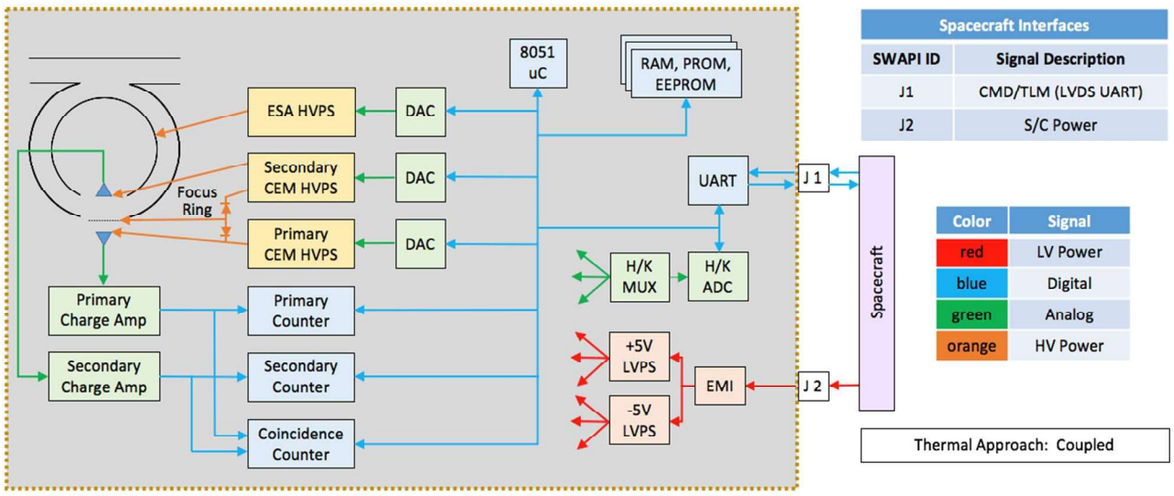


FIGURE 2. SWAPI INSTRUMENT BLOCK DIAGRAM

SWAPI is a modified version of New Horizons Solar Wind Around Pluto (SWAP) instrument. The instrument electro-optics section comprises:

- a 0.1% transmissive grounded grid that attenuates particles entering the instrument from the solar wind direction, without attenuating pickup ions from all other open aperture directions
- an Electrostatic Analyzer (ESA) with energy-per-charge (E/q) selection
- a field-free flight path
- a coincidence detector section

These elements select the energies and attenuation factors for the measured solar wind and PUIs. Transmitted ions are post-accelerated into the detector section that employs an ultrathin carbon foil and two Channel Electron Multipliers (CEMs): (1) a primary CEM (PCEM), which measures ions that pass through the carbon foil, and (2) a secondary CEM (SCEM), which attracts secondary electrons liberated from the carbon foil. Events that are measured by both the PCEM and SCEM within 100 nanoseconds are recorded as coincidence (COIN) events.

A cross-section of the electro-optics is shown in Figure 3.

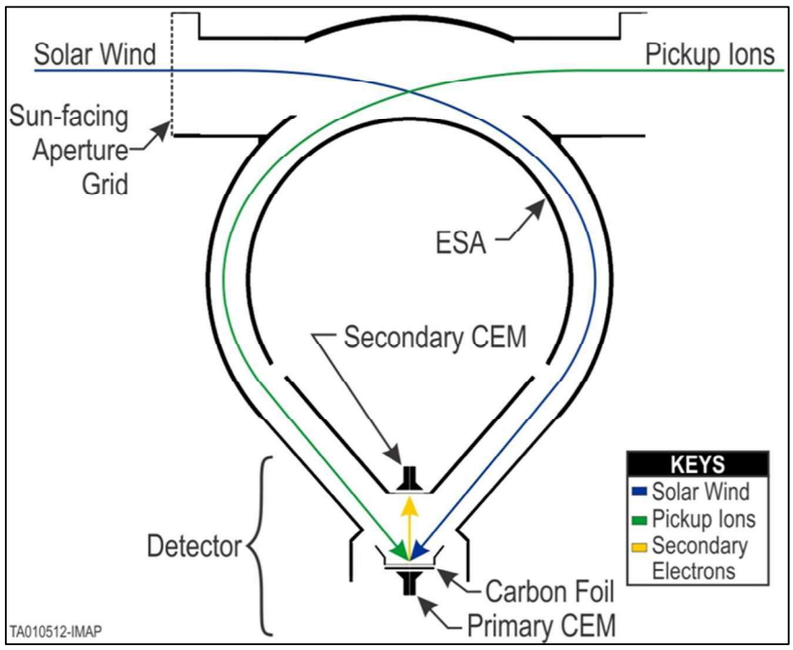


FIGURE 3. SWAPI ELECTRO-OPTICS CROSS-SECTION

SWAPI has a High Voltage Power Supply (HVPS), Low Voltage Power Supply (LVPS) and Processing Board (PB). The ESA, primary CEM (PCEM) and secondary CEM (SCEM) are tied to three separate HVPSs controlled by an 8051 microcontroller. The ESA HV steps up to 10.2 kV while the CEM HVs are maintained at a steady value of up to 4 kV.

Primary and secondary pulses are received from charge amplifiers and accumulated in counters. If both occur within a 100 ns window, a coincidence (COIN) is also registered.

The SWAPI instrument, shown in Figure 2, is a single integrated mechanical assembly consisting of two sensor sections and an electronics enclosure. The instrument is mounted on a spacecraft-provided bracket, which in turn is mounted to the underside of the top deck of the spacecraft in Bay D.

The electrical interface with the spacecraft is via a single D-type pin power connector and a single subminiature D-type data socket connector. The data connector also incorporates connections to the spacecraft Arm and Test Panel for instrument Disable/Safe/Arm selection using the appropriate spacecraft-provided connectors.

5. DEFINITIONS OF TERMS

The following terms are used in this document to describe the SWAPI algorithms.

Term	**Definition**	**Unit**
Bulk velocity	Measure of the peak of solar wind distribution	km/s
Count	Number of particles recorded on the instrument	#
Count rate	Number of Counts per unit time	#/s
Density	Number of particles per unit volume, i.e., number density	#/cm^3
Efficiency	correction factor applied in L1-L2 processing to correct for particle detection which may change over time	dimensionless
Flux	Particle count rate per unit area per unit solid angle per unit energy/charge	#/ [cm^2 s sr eV/q]
Geometric factor	Energy width per Energy multiplied by effective area ($A_{eff} * \frac{\Delta E}{E}$)	cm^2 sr eV/eV
Temperature	Measure of the broadness of the distribution	K

6. ALGORITHMS OVERVIEW

6.1. Data Volume

The SWAPI team anticipates 4.786560 MB/day raw data, and 22 MB/day processed data (including L1, L2, L3 data products). The filename structure is defined in the IMAP SDC-Instruments ICD. For SWAPI the following filenames will be defined:

imap_swapi_<data_level>_<descriptor>_<start_date>-<repointing>_<version>.<extension>

Possible contents of SWAPI filenames are as follows (more info on SDC site):

Field	Optional or required?	SWAPI options
dataLevel	Required	l1 l2 l3a l3b
descriptor	Optional	12s (L1 or L2 data, default) 1m-sw-p (L3a data) 1m-sw-a (L3a data) 10m-pui-he (L3a data) 10m-combined (L3b data)
extension	Required	cdf

6.2. Data Product Definitions

The following definitions are provided in the IMAP SOC Documentation:

- Level 0: Reconstructed, unprocessed instrument, payload, and spacecraft data; any and all communications artifacts have been removed. These data will consist of binary CCSDS packets.
- Level 1: Fully decommutated but uncalibrated raw data at full resolution; time-referenced; ‘extracted telemetry items’
- Level 2: Level 1 data that have been processed to physical units by combining calibration, ancillary, and other data. These data represent the lowest grade of research-grade scientific data and exist at the same time and/or spatial resolution as Level 1 data.

- Level 3: These data have been resampled spatially and/or temporally and may have been combined with measurements from other instruments to produce a merged data set. Ex: density of a distribution

6.3. L0 Data Content & Format

SWAPI simultaneously observes solar wind and PUIs. There are seven types of SWAPI science and engineering data.

Telemetry name	**Data type**	**Description**
SWP_HK– Housekeeping	Engineering data	Instrument status, counters, ADC values, etc.
SWP_MG – Event Messages	Engineering data	Asynchronous event packets
SWP_SCI – Science	Science data	PCEM, SCEM, and Coincidence Counts for each of 6 samples acquired in a 1-second period Reports the ESA Level for a single sample; other levels can be determined from the lookup table
SWP_LGSCI – "Large" Science	Science data	Used for testing; same as SCI packet, but includes all 6 ESA Levels
SWP_IAL – IALiRT	Science data	Subset of Science packet (only has Coincidence Counts)
SWP_AUT – Autonomy	Engineering data	Minimum required per ICD (power off/cycle flags)
SWP_MD – Memory Dump	Engineering data	Fixed-size (128-byte payload)

The raw science data consists of primary, secondary, and coincidence counts packaged in CCSDS packets. The CCSDS telemetry packets have variable (even) length, up to 4096 bytes, including headers, per GI ICD. All SWAPI SCI packets are fixed-size (54 bytes/432 bits) with 1 second of data (6 ESA steps) per packet. All the packet types have a CHKSUM parameter. This parameter is calculated onboard and is also calculated on the ground to check the data.

The SDC receives Level 0 science and housekeeping data, ancillary data, mission events, and SPICE kernels from the MOC/POC and makes them available to the Instrument Teams.

The L0 data product contains packetized instrument telemetry in CCSDS format. Per the IMAP SDC-Instruments ICD, The SDC will create Level 0 data and add version numbers to the Level 0 filenames such that the Level 0 filenames become

imap_l0_sci_<instrument>_YYYYMMDD_vNN.pkts

6.4. L1, L2, and L3 Data Product Grouping

Counts at L1 and L2 are grouped by sweeps; the L1 and L2 data product contains one sweep. Each sweep is 12 seconds in duration and includes 72 steps in energy. Packet generation is synchronized with sweeps such that the first step of any sweep marks the creation of a new packet. A full 72-step sweep is therefore telemetered in 12 1-second packets. For the L1 and L2 science product, the 72 steps consist of

- 1 step to ramp up to full ESA voltage
- 62 fixed steps (E/q) with energy range: 0.1-20 keV/q
- 9 variable steps with usage defined according to a sweep plan
  - Since February 1, 2026, Sweep Plan 4 has been the default for nominal operations
    - 3 fine steps for low-energy background (ESA voltages: 35, 20, and 5 V)
    - 6 fine steps above and below the peak E/q bin
  - Sweep Plan 5 has been used for electron hoovering background tests
    - 9 fine steps with ESA voltages of 40, 35, 30, 25, 20, 15, 10, 4, and 0 V

The L3 data product may be delivered at a variety of cadences (e.g., daily, hourly) that combine multiple sweeps together. One- and ten-minute cadences are baselined.

6.5. Processing Flow

The flow diagram of the IMAP SWAPI data processing from Level 0 to Level 3 is shown in Figure 4.

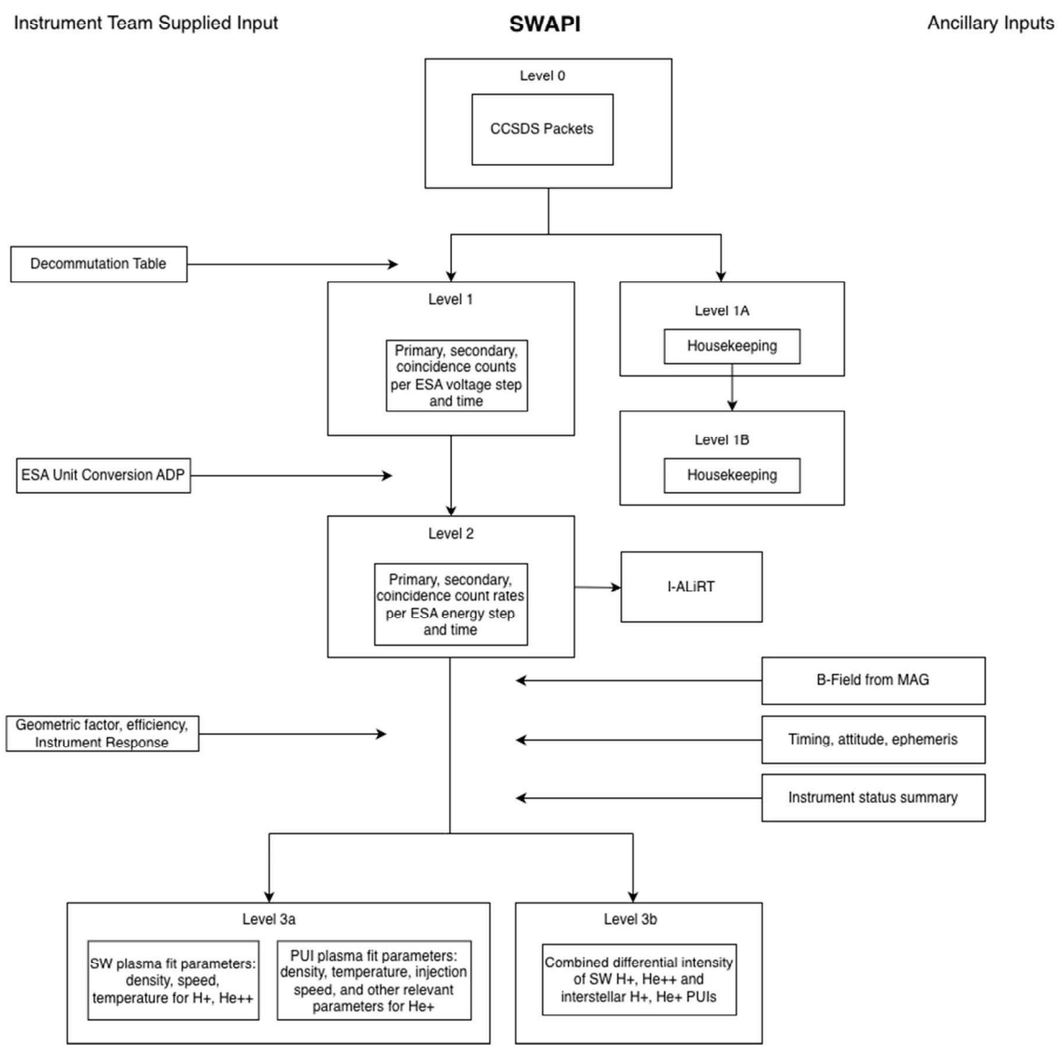


FIGURE 4. IMAP SWAPI DATA PIPELINE FLOW DIAGRAM.

7. HERITAGE INSTRUMENT (NEW HORIZONS' SWAP)

The Solar Wind Around Pluto (SWAP) instrument (McComas et al. 2008) was designed to measure the solar wind at large distances from the Sun and its interaction with Pluto, including Pluto-generated pickup ions (PUIs). Because of the great heliocentric distances and the large range of viewing directions, SWAP was designed to have extremely high sensitivity, a very large field of view, and very low backgrounds. These attributes allowed SWAP to make unprecedented measurements of Pluto's interaction with the solar wind (McComas et al. 2016), as well as unique measurements of the Jovian magnetotail to >2500 R_J (McComas et al. 2007) and fundamental observations of interstellar PUIs (McComas et al. (2021), and references therein). SWAP continues to make excellent observations of the solar wind and interstellar PUIs, now out past 53 au (McComas et al. 2022).

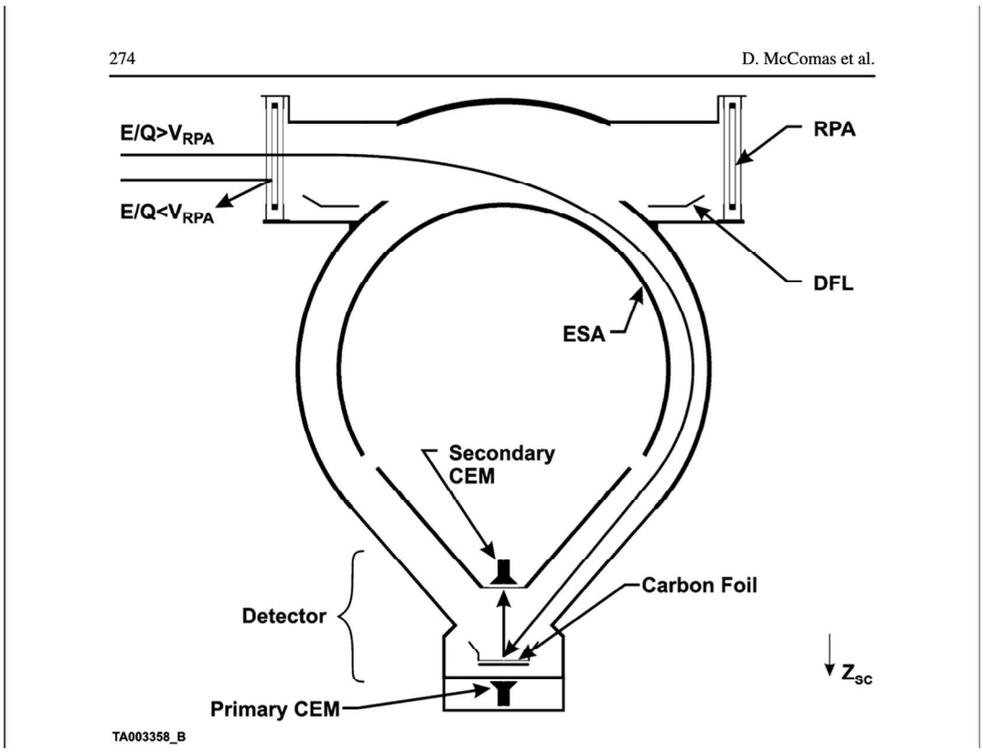


FIGURE 5. SCHEMATIC DIAGRAM OF THE SWAP'S ELECTRO-OPTICS INCLUDING RPA, DEFLECTOR, AND DETECTOR ASSEMBLY. TAKEN FROM MCCOMAS ET AL. (2008).

Figure 5 schematically depicts the SWAP principle electro-optics, which consists of (1) a retarding potential analyzer (RPA), (2) a deflector (DFL), and (3) an electrostatic analyzer (ESA).

Collectively, these elements select the angles and energies of the solar wind and PUIs to be measured. Ions having energy per charge (E/q) greater than the RPA voltage enter through the RPA. The RPA was used to protect SWAP from the very high solar wind fluxes in the inner heliosphere; beyond Jupiter, the RPA was generally left off. The ESA provides energy selection and rejects ions outside the selected E/q range. It also protects the detectors from UV light and neutral particles. Ions selected by the ESA are registered with a coincidence detector system. The voltage on the ESA is varied from 0 to -4000 V which enables it to select particles from 35 eV/q to 7.5 keV/q with a ΔE/E of 8.5% FWHM.

Figure 6 shows the comparison of the energy-angle response function of the SWAP instrument for a 1 keV proton beam in lab (left panel) and with a SIMION model (right panel). The energy and angle binning in the SIMION model were set to the same values as in the instrument for a better comparison. Clearly, there is an excellent agreement between the modeling and the calibration measurements with the ion beam.

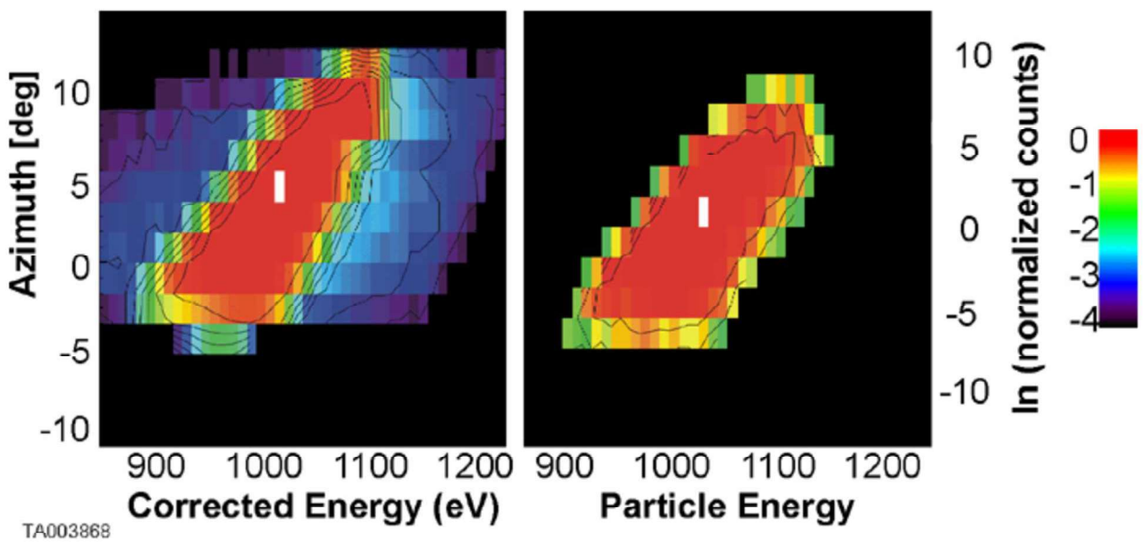


FIGURE 6. COMPARISON BETWEEN THE ENERGY-ANGLE RESPONSE FUNCTION OF THE SWAP INSTRUMENT FOR 1-KEV PROTON BEAM IN THE LAB (LEFT) AND WITH THE SIMION MODEL (RIGHT). TAKEN FROM MCCOMAS ET AL. (2008).

On February 19, 2021, the SWAP team performed a simple flight software upgrade by redefining the internal formatting of a large daily histogram into 47 sequential (~30 minutes) histograms with normal 64-step energy resolution and started producing the high-cadence data product. This allowed measuring individual solar wind and PUI distributions nearly 50 times faster

than the one-day distributions previously collected. This time resolution is able to resolve interplanetary shock structures and quantify the particle heating across the shocks (see McComas et al. (2022) for details and for the current configuration and capabilities of SWAP).

7.1. Heritage Instrument Processing Reuse

Heritage NH-SWAP code will not be reused for SWAPI for L0-L2 data processing (note that NH-SWAP data processing ends at L2, not L3); however, the processing steps were adapted for SWAPI, drawing on the SWAP team's experience over decades of operations. The SWAP PUI code is reused and modified for SWAPI at L3.

7.1.1. Heritage Instrument Processing Overview: Pickup Ions

The L2 data processing code for H^+ PUIs observed by New Horizons' SWAP instrument includes an iterative fitting of the generalized Vasyliunas & Siscoe model (Chen et al. (2014) model) for the pickup H^+ to their observed count rates:

$$f(\boldsymbol{r}, w) = \frac{\alpha S(\boldsymbol{r}, w)}{4\pi} \frac{\beta_0 r_0^2}{r u_{\mathrm{sw}} v_{\mathrm{b}}^3} w^{\alpha-3}\, n_{\mathrm{H,HTS}} \exp\left(-\frac{\lambda}{r}\frac{\theta}{\sin\theta} w^{-\alpha}\right) \Theta(1-w), \quad (1)$$

where the survival probability of PUIs from their pickup distance to the point of observation is $S(\boldsymbol{r},w)$, $w = v/v_{\mathrm{b}}$, β_0 is the ionization rate normalized to $r_0 = 1$ au, u_{sw} is the solar wind bulk speed in the solar inertial frame, θ is the angle between radial and the interstellar hydrogen inflow direction, $n_{H,HTS}$ is the density of the interstellar neutral hydrogen at the upwind heliospheric termination shock, λ is the hydrogen ionization cavity size, where the interstellar neutral atom density decreases by a factor of $1/e$, and Θ is the Heaviside step function.

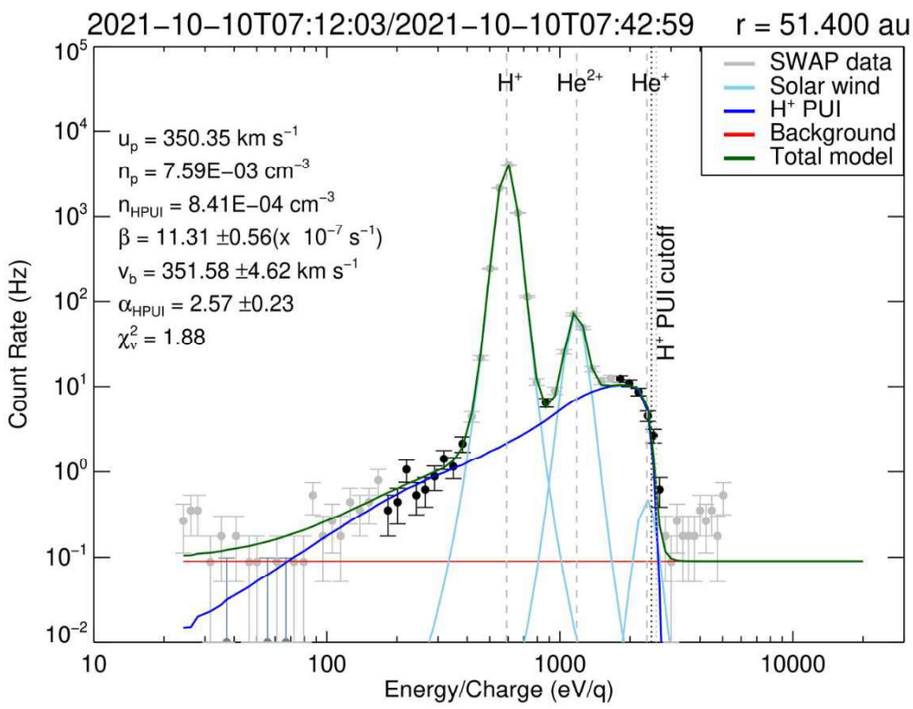


FIGURE 7. EXAMPLE OF A HIGH-CADENCE, ION DISTRIBUTION (GREY AND BLACK DOTS) TAKEN AT 51.4 AU ON OCTOBER 10, 2021, FROM 7:12:03 TO 7:42:59 UTC. FITS TO THE SOLAR WIND PROTON (H^+), ALPHA PARTICLE (He^{2+}), AND He^+ PEAKS ARE SHOWN IN LIGHT BLUE WITH CENTROIDS INDICATED BY VERTICAL DASHED LINES. INTERSTELLAR H^+ PICKUP IONS (DARK BLUE) ARE FIT TO THE BLACK SUBSET OF POINTS USING EQUATION 1. THE SOLAR WIND PROTON SPEED AND DENSITY, PUI H^+ DENSITY, IONIZATION RATE, INJECTION SPEED, COOLING INDEX, AND REDUCED X^2 FOR THE PUI FIT ARE ALL LISTED ON THE LEFT. THIS FIGURE IS TAKEN FROM MCCOMAS ET AL. (2022).

The free parameters used for the fitting equation (1) are ionization rate (β), injection speed (v_b), and PUI cooling index (α). There is only one bulk speed used in the fitting – the PUI bulk speed is assumed to be the same as the solar wind bulk speed. The process of iteratively fitting the E/q spectra at ~30 mins resolution (McComas et al. 2022) is fundamentally the same as the process of fitting 24 hr SWAP spectra (Swaczyna et al. 2020; McComas et al. 2021), the only difference is the energy bin selections. The energy bins (black data points in Figure 7) selection criteria for ~30 mins resolution data are as follows:

a) Below the solar wind proton peak energy, all energy bins down to 30% of the solar wind proton peak energy bin value are included unless the SWAP count rate in bins is less than 2 times the modeled solar wind proton count rate.
b) Between the solar wind proton and alpha peaks, a single data point for most of the distributions, including the one shown in Figure 7 was included. The bin with the lowest count rate between solar wind proton peak and He^{2+} peak is included unless the SWAP count rate in that bin is less than 2 times the sum of modeled count rate due to solar wind protons and alpha particles.
c) Above the solar wind alpha peak, the five energy bins just below the calculated H^{+} PUI cutoff energy were included. One energy bin just above this calculated cutoff and any additional consecutive energy bins above the cutoff were always included if their count rate is at least 10% of the maximum count rate between the alpha particle peak and the cutoff.

Application of this fitting procedure to SWAPI He^{+} PUI measurements is described in Section 10.4.3.

8. EXTERNAL DEPENDENCIES

The SWAPI ground processing depends on the following external dependencies:

- S/C thruster data. SWAPI data will be flagged in the L1 data product and beyond if obtained during **spacecraft thruster activity** for data quality reasons. SWAPI will be off for at least 25 minutes prior to, during, and for 1 hour after delta-V and stationkeeping maneuvers but will be fully operational for the daily repointing maneuvers. SC thruster firing history comes from the MOC.

- MAG Level 2 data. The magnetic field data (highest is Level 2 for MAG data) is used during SWAPI L3 processing to constrain the flow solar wind alpha flow vector. Whenever, MAG Level 2 data is not available, L1D data is used for processing the solar wind alpha data products, which is then reprocessed once Level 2 data is available. Only the data processed with the L2 data will be released to the public.

- Timing, attitude, ephemeris – The Level 3 calculation of the solar wind flow deflection angle using ~1 min resolution data requires the knowledge of the IMAP/SWAPI **spin phases** for each ESA energy bins of the individual sweep and pointing of the spacecraft in a standard coordinate system. IMAP SPICE kernels are used for this purpose.

9. CALIBRATION DATA

SWAPI's ground calibration will consist of: (1) simulations from the SWAPI End-to-End model, (2) calibration measurements performed in the Princeton Space Physics Lab, and (3) results from the cross-calibration of SWAPI with CoDICE. Data from in-the-lab calibrations will be integrated into an End-to-End model of the instrument to generate lookup tables (LUTs). As described in the next Section, these LUTs are at the core of the algorithms used to process SWAPI's in-flight data.

SWAPI's in-flight calibration data will consist of: (1) periodic gain curves that will be performed every ~3 to 6 months in order to optimize voltage settings for the PCEM and SCEM detectors and (2) in-flight comparisons with CoDICE.

9.1. Ground Calibration: End-to-End Model

The SWAPI team is working on a complete end-to-end model of the instrument to test algorithms, inform calibration, and validate models used to generate the LUTs for SWAPI data processing. The general idea is to use parameters from real observations at 1 AU (ACE and Wind measurements from the OMNI database) as inputs to a simulated instrument, perform realistic data processing, and compare the outputs to the original inputs. The end-to-end model consists of several modules, including: (1) SW OMNI observations, (2) SW and PUI distribution function model, (3) coordinate system transformation matrices, (4) a SIMION-based electro-optical model, and (5) a module to convert the simulated data to expected instrument telemetry formats.

A summary of the end-to-end model is given in the diagram in Figure 8. The left-hand branch of the "V" represents a complete simulation of the instrument and its environment, while the right-hand branch describes the processing to be done with simulated SWAPI telemetry. The in-flight data processing is very similar to the right-hand branch, with a few minor notes: the "telemetry output" (orange) will reflect the raw (L0) in-flight data, the "in-the-lab calibrations" (blue) is supplemented with in-flight calibrations, and the "distribution function fitting analysis" is performed by algorithms. The parameters generated by each module are summarized in Figure 9.

A table describing the LUT format and contents is added in the L3 code.

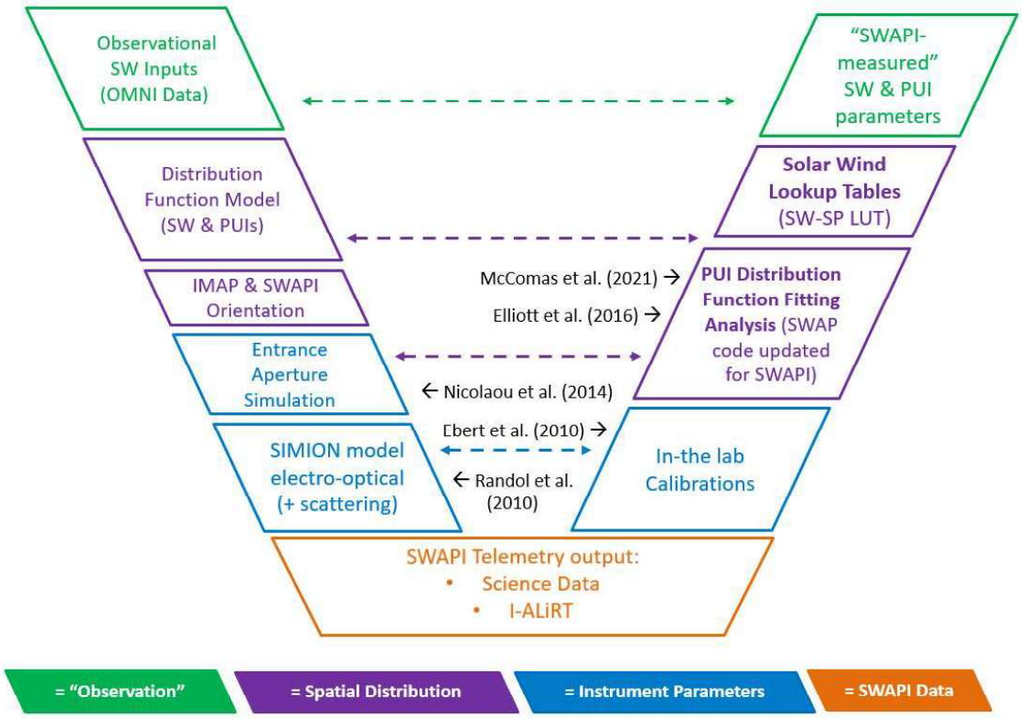


FIGURE 8. SUMMARY OF THE SWAPI END-TO-END MODEL.

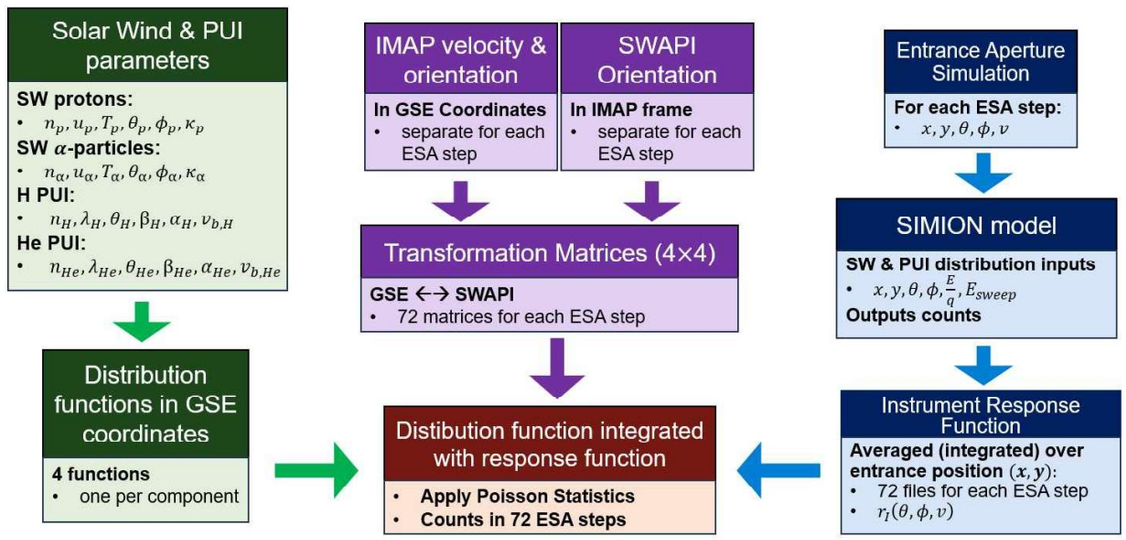


FIGURE 9. FLOW DIAGRAM AND SUMMARY OF PARAMETERS GENERATED BY VARIOUS MODULES OF THE SWAPI END-TO-END MODEL.

9.1.1. SIMION Module Results

We used SIMION to determine how SWAPI responds to different inputs. For each ESA voltage, we simulated ions entering the instrument over a range of energies, entry locations, and angles. Figure 10 shows an example of the ions flying through SWAPI. We recorded whether an ion entering the instrument with a specific entry location, direction, and energy would reach the detector or not. This allowed us to develop a response function for SWAPI as a function of the incoming ion properties for each ESA voltage. We then integrated this function assuming a uniform beam of ions enters SWAPI. The result is a lookup table containing the ion energies, entry angles, and the relative intensities observed by SWAPI at each ESA voltage. The results are shown in Figure 11.

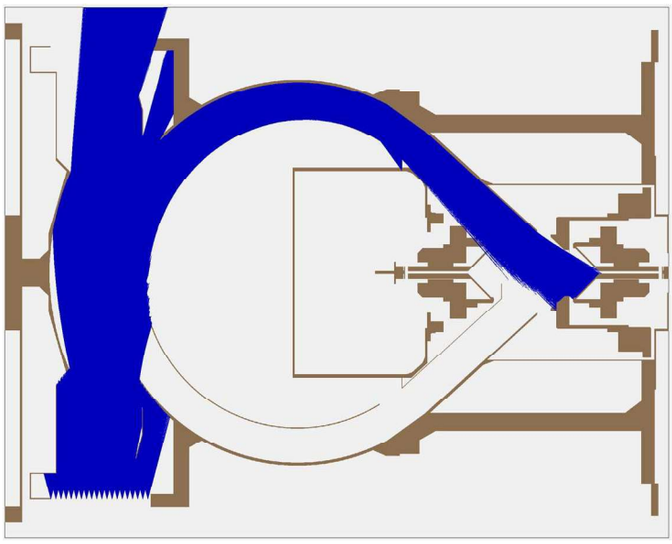


Figure 10. Example of ions flying through SWAPI in SIMION. The ions (in blue) start at the entrance with a range of starting locations, directions, and energies.

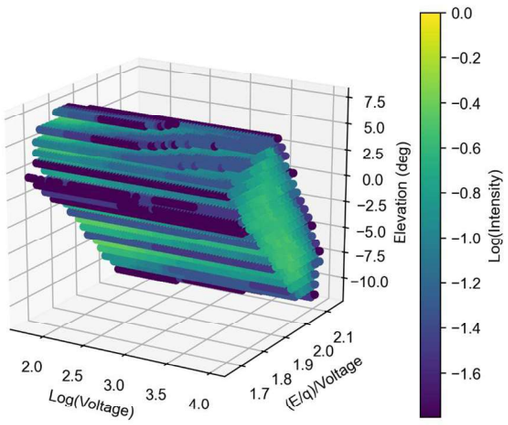


Figure 11. Results of the simulations assuming uniform ion beams. The logarithm of the relative intensity is shown as a function of the logarithm of the ESA voltage (in volts), the ions' entry angle, and the ratio of the ion energy per charge to ESA voltage.

9.2. Ground Calibration: Princeton Lab

In-the-lab calibrations focus on measuring instrument response over: (i) a full range of energies (0.4 to 18 keV/q required; 0.1 to 20 keV/q tested), (ii) a broad range of angles, (iii) over each optical element (e.g., through the SW attenuation grid as well as the open aperture), and (iv) for multiple species (H and He required). The instrument's energy-angle response is reflected in passband measurements, which are achieved by positioning SWAPI at various angles with respect to an incident beam (azimuthal angle). The instrument response over its entire entrance aperture was calibrated via elevation-angle rolls. The responses are key for determining the instrument's geometric factor.

Other aspects of SWAPI that were tested during calibration include: (i) voltage settings of the CEMs (via high-voltage gain curves), (ii) absolute detection efficiency, (iii) active area of the ultra-thin carbon foil, (iv) transmission and scattering, (v) UV suppression, and (iv) rate dependence and backgrounds.

Details of the Calibration and its key results can be found in Rankin et al. (2025).

9.3. Ground Calibration: Cross-Calibration with CoDICE

Cross-calibration between SWAPI and CoDICE was conducted at Princeton with both instruments in the same chamber at the same time, rotating in and out of the beam. An absolute beam monitor was used to estimate the incoming flux and beam uniformity was regularly monitored. Testing was done primarily with 2 keV/q and 16 keV/q protons and Helium for a variety of parameters, including fixed ESA voltages, ESAs sweep over full instrument energy ranges, at several elevation angles, and at fixed azimuths of 0° (e.g., through SWAPI sunglasses) and 90° (e.g., through SWAPI's open aperture) to target the solar wind and pickup ion viewing sectors, respectively. Further details can be found in the SWAPI and CoDICE instrument papers: Rankin et al. (2025), Livi et al. (2025).

9.4. On-Orbit Calibration Data

SWAPI's on-orbit calibrations consist of high-voltage gain curves and in-flight comparison with the CoDICE instrument. When the instrument is first turned on, results from ground calibrations in the lab is used to inform PCEM and SCEM target voltage settings. Once nominal operations are

achieved, on-orbit gain curve tests are performed every ~3 to 6 months in order to determine the best voltages to use for the PCEM and SCEM detectors.

SWAPI's detector arrangement enables a calculation of absolute efficiency. This calculation represents the measurements in a way that is independent of performance and variability of its detectors as they age (Funsten et al. 2005). The equations used for the calculation is as follows:

$$\varepsilon = COIN^2/(PRM \times SEC)$$

For primary (PCEM), secondary (SEC), and coincidence (COIN) count rates. The CEM gain is set so that the secondary electrons generated by the ions incident on SWAPI's ultra-thin carbon foil yield a pulse magnitude that is larger than the lower level discriminator setting of the amplifier electronics. The optimal level is determined by stepping voltages until the count rate "flattens out". After some detector bias voltage, the rates become constant and independent of further increases and so this voltage setting is used. However, CEM gain decreases as a rate that depends on the total charge that is output over its lifetime. This gain decrease can be compensated by increasing the detector voltage, and so on-orbit gain curve tests are needed to determine new voltage settings as the CEMs age over the course of the mission.

In-flight comparisons with CoDICE will be performed once data from each instrument has been validated and processed on the ground using overlapping species and energy ranges.

9.5. Instrument Response Function

The coincidence count rate for ESA voltage setting V is modeled as

$$C(V) = \sum_s \int d^3v\, v\, f^s(\boldsymbol{v})\, \mathcal{A}^s(\boldsymbol{v}, V),$$

where f^s is the VDF of species s and $\mathcal{A}^s$ is the effective area function.

In instrument coordinates (speed v, elevation angle θ, azimuth angle ϕ; Rankin et al. (2025)_), $\mathcal{A}^s$ is decomposed as

$$\mathcal{A}^s(v, \theta, \phi, V) = \mathcal{A}_0^s(V) \cdot P_{\text{region}(\phi)}\left(\frac{v}{v_0^s}, \theta, V\right) \cdot T(\phi),$$

where $v_0^s = \sqrt{2k^* q^s |V|/m^s}$ is the central speed; $\mathcal{A}_0^s$ is the central effective area; region(ϕ) is SG for $|\phi| \leq 20°$, OA otherwise; P_r is the region-specific energy-angle passband; T is the azimuthal transmission factor.

These three functions are stored in CSV files. The production code loads them from ancillary files. The normalizations of $\mathcal{A}_0^s$ and P_r are aligned in terms of the value at $\theta = 0°$ and $k^* \equiv 1.89$ eV/V/e, the peak $(E/q)/|V|$ at $\theta = 0°$ based on high-resolution SIMION simulations. k^* differs from $k_{L2} = 1.93$ eV/V/e, which is the k-factor estimated pre-launch from lab measurements (Rankin et al. 2025) and used to convert from ESA energy in the L2 CDF files to the actual ESA voltage of the instrument. The difference between k^* and k_{L2} is likely because of inaccuracies in the beam energy and orientation in the lab measurements. The exact cause of this discrepancy is still under investigation, but for now (as of the initial IMAP data release), we use the k* value derived from the SIMION simulations.

9.5.1. Central Effective Area and Azimuthal Transmission:

$T(\phi)$ is tabulated as a function of $|\phi|$ from 0° to 180° at 0.1° spacing. Missing transmission entries are treated as zero, and the interpolator uses $|\phi|$ after wrapping azimuth into $[-180°, 180°)$. The flat portions of the azimuth response are explicitly included in the interpolator for performance: $T = 10^{-3}$ for the central sunglass region ($|\phi| \leq 9°$), and $T = 1$ across the main open aperture range ($31° \leq |\phi| \leq 115°$).

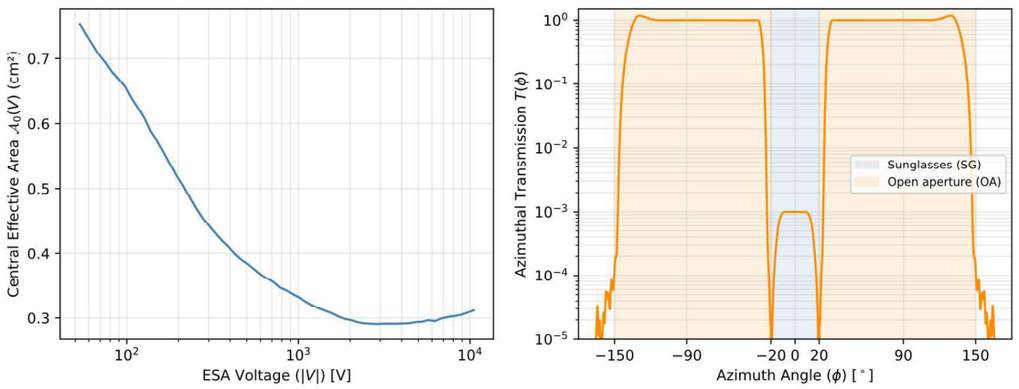


FIGURE 12. CENTRAL EFFECTIVE AREA AND AZIMUTHAL TRANSMISSION

$\mathcal{A}_{0,(\mathrm{lab})}^{\mathrm{H}^+}(V)$ describes the central effective area for protons at the beginning of the mission. The detector efficiency degrades with time and is species-dependent. Therefore, an efficiency calibration table is used to scale the central effective area.

The efficiency calibration table has two columns: ε_{H} for hydrogen and $\varepsilon_{\mathrm{He}}$ for helium. They are used as follows:

Protons (H^{+}):

$$\mathcal{A}_0^{\mathrm{H}^+}(V) = \mathcal{A}_{0,(\mathrm{lab})}^{\mathrm{H}^+}(V)\frac{\varepsilon_{\mathrm{H}}(t)}{\varepsilon_{\mathrm{H}}(t_{\mathrm{lab}})},$$

where $\varepsilon_{\mathrm{H}}(t_{\mathrm{lab}})$ is the first proton entry in the table on or after 2025-11-01 and $\varepsilon_{\mathrm{H}}(t)$ is the most recent entry whose timestamp precedes t.

Alphas (He^{2+}) & PUIs (He^{+}):

$$\mathcal{A}_0^{\mathrm{He}^{++}}(V) = \mathcal{A}_0^{\mathrm{He}^{+}}(V) = \mathcal{A}_{0,(\mathrm{lab})}^{\mathrm{H}^+}(V)\frac{\varepsilon_{\mathrm{He}}(t)}{\varepsilon_{\mathrm{H}}(t_{\mathrm{lab}})}$$

Only the relative values are used here, so this is agnostic to whether the values in the table are scaled to an absolute efficiency in the future.

Initially, the hydrogen column is set to 1, and the helium column is set to 1.05. The ratio of 1.05 for helium comes from the high-energy limit observed in the lab for He^{+} versus H^{+}. Above a few keV per charge, the ratio was observed to be consistently 1.05. Since both solar wind alphas and pickup ions tend to be above that threshold, the increase of the ratio at low energies has not been accounted for. It has also been assumed that He^{+} and He^{++} have the same efficiency based on theoretical expectations and preliminary analyses of SWAPI's measurements in space.

9.5.2. Energy-Angle Passbands:

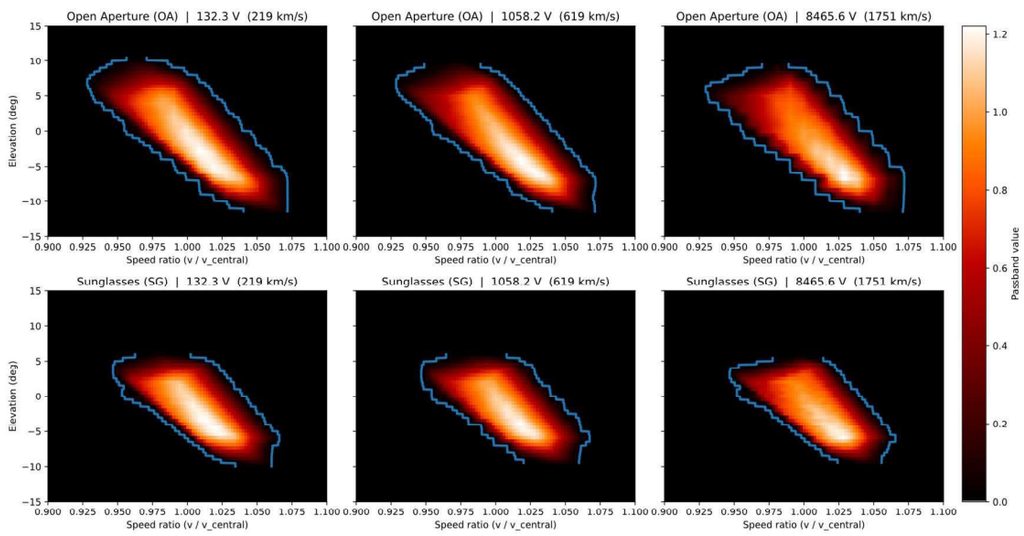


FIGURE 13. EXAMPLES OF INTERPOLATED PASSBANDS WITH INTEGRATION LIMITS.

10. ALGORITHMS DETAILED PROCESSING

SWAP and SWAPI have largely different Level 0, 1, 2, and 3 data products and data processing steps due to their different mission structures. The SWAP instrument produced six types of data: real-time science, summary, histogram, housekeeping, messages, and memory dump. During the cruise phase of the New Horizons mission, SWAP saved memory space by producing summary and histogram data instead of recording and transmitting the full distribution of count rates as a function of energy (speed). Notably, SWAPI does not produce summary or histogram data, but does produce large science, I-ALiRT, and Autonomy data.

TABLE 1. SCIENCE OPERATIONS COMPARISON FOR NH/SWAP AND IMAP/SWAPI

Item / Function	NH / SWAP	IMAP / SWAPI
Mission Destination	Pluto and Kuiper Belt (30 to 50 AU) and Outer Heliosphere (50 AU and beyond)	Sun-Earth Lagrange point (L1; 1 AU)
Science Measurements	Solar Wind protons (H^+) and alphas (He^{2+}); Pluto Pickup Ions; Pickup Ion protons (H^+)	Solar Wind protons (H+) and alphas (He^{++}); Proton (H^+) and Helium (He^+) Pickup Ions (Helium dominated)
Instrument Cycle		
Duration	64 seconds	12 seconds
ESA steps	2 per second i.e., 128 steps per cycle	6 per second i.e., 72 steps per cycle
ESA step duration	0.5 second	0.167 second
Stepping regime	64 coarse steps over full energy range followed by 64 fine steps over the Solar wind peak.	One step for large voltage transition. 62 coarse steps across full energy range followed by 9 small steps defined according to one of 16 sweep plans; nominal operations uses Sweep Plan 4 which distributes 6 fine steps across Solar wind peak and dedicates 3 for low-energy backgrounds.

10.1 L0-L1 Data Processing

L0-L1 data processing decommutates the L0 CCSDS packets and solves for primary, secondary, and coincidence counts. Only science telemetry (SWP_SCI) is processed into a L1 data product, though other telemetry groups are referenced to create the L1 data product. L0 Housekeeping data is stored after applying equations and coefficients for Temperature Conversions and equations and coefficients for engineering conversions.

10.1.1 Data management

The contents of the L1.sci CDF file are described in this section. The steps for creating the attributes of the L1.sci data product are as follows:

1. Apply Decommutation Table to CCSDS packets; save decommutated packets
2. Check all packets received that haven't been successfully processed yet
    a. Packets that are successfully processed should be relocated from the processing directory or have metadata marking their "processed" status. Packets for which earlier processing failed are candidates for reprocessing each time the pipeline runs.
3. Group packets received that meet specified criteria
    a. Checksum is correct
        i. Checksum is an 8-bit xor or all packet bytes (including the CCSDS header), except for the checksum byte.
    b. Twelve consecutive seconds of science data correspond to a single sweep, which is the unit of L1 data and downstream products
        i. SCI data packets are produced at 1Hz, so 12 packets = 1 sweep
            1. Note: One sweep takes 12 seconds in duration and includes 72 steps in energy. 5 sweeps take 60 seconds (4 spacecraft spins).
        ii. Find 12 packets spanning 12 seconds (look at SWP_SCI.SHCOARSE) with matching SWP_SCI.PLAN_ID (The PLAN ID used for the current science sweeping mode if any) and SWP_SCI.SWEEP_TABLE (Sweep table ID within the PLAN ID that is being used for the current science sweeping mode) to group packets by sweep
        iii. Beginning of a sweep is marked by SWP_SCI.SEQ_NUMBER=0 (this telemetry point is the Sequence counter of a set of 6 steps in energy sweep – SEQ_NUMBER=0 indicates the packet contains the first 6 ESA voltage steps, SEQ_NUMBER=1 indicates the next 6 steps, and the entire sweep is marked by SEQ_NUMBER 0-11. The end of a sweep is marked by SWP_SCI.SEQ_NUMBER=11; all packets must be present to process a sweep
        iv. Only process complete sweeps (72 steps)

1. 1 step to ramp up to full ESA voltage
2. 62 fixed steps (E/q) with energy range: 0.1-20 (TBC) keV/q
3. 9 variable steps centered on peak E/q bin

4. Process packet groups corresponding to sweeps by timestamp, starting with the earliest data
    a. Define empty arrays for the column data (PCEM counts, SCEM counts, COIN counts, etc.)
    b. Save PCEM, SCEM, and COIN counts stored in SWP_SCI.PCEM_CNT0 through SWP_SCI.PCEM_CNT5, SWP_SCI.SCEM_CNT0 through SWP_SCI.SCEM_CNT5, and SWP_SCI.COIN_CNT0 through SWP_SCI.COIN_CNT5, respectively as 1x72 arrays to include the counts during the 1st, 2nd, 3rd, 4th, 5th, and 6th 1/6-second time interval of each of the 12 consecutive packets. Decipher PCEM, SCEM, and COIN counts using SWP_SCI.PCEM_RNG_ST0 through SWP_SCI.PCEM_RNG_ST5, SWP_SCI.SCEM_RNG_ST0 through SWP_SCI.SCEM_RNG_ST5, and SWP_SCI.COIN_RNG_ST0 through SWP_SCI.COIN_RNG_ST5 as indicators of compressed count ranges that should be converted to raw format.
        i. Note: There are 3 compression regions: 1) 0 <= value <=65535 2) 65536 <= value <= 1,048,575 3) 1,048,576 <= value. For regions (2) and (3), the corresponding RNG_ST bit will be set to 1. Compression is simply a divide-by-16, so to unroll it, something like:

```
if XXX_RNG_ST0 == 0:            # Uncompressed
    actual_value = XXX_CNT0
elif (XXX_RNG_ST0==1 && XXX_CNT0==0xFFFF):    # Overflow
    actual_value = <some constant that indicates overflow>
elif (XXX_RNG_ST0==1 && XXX_CNT0!=0xFFFF):
    actual_value = XXX_CNT0 * 16
```

    c. Other columns to populate from SWP_SCI are shown in Table 2.
    d. Metadata marker for saturation at L1, gets n processed by L1. L2/L3 will not process if there is a saturation flag
    e. Combine columns into a table and write it to a CDF file
    f. Mark the CCSDS packets “processed” so they will not be reprocessed during any future loops

10.1.2 Marking data not qualified for L0-L1 processing

Level 0 data will be marked as Not a Number (NaN) at L0-L2 processing and potentially rejected for L3 data processing for any of the following reasons:

- SWP_HK.CHKSUM is wrong
- SWAPI mode (SWP_SCI.MODE) is not HVSCI
- Check for saturation. If count rates exceed 4.0 MHz using SWP_SCI.PCEM_CNT0 through SWP_SCI.PCEM_CNT5 or SWP_SCI.SCEM_CNT0 through SWP_SCI.SCEM_CNT5 the sweep may later be discarded.
- SWP_HK.PCEM_RATE_ST = 1 at any point during the sweep. The count rate threshold for the PCEM counter has been exceeded once and has continued to be exceeded despite measures by FSW
- SWP_HK.SCEM_RATE_ST = 1 at any point during the sweep. The count rate threshold for the SCEM counter has been exceeded once and has continued to be exceeded despite measures by FSW

Note: The FSW automatically transitions to SAFE if:

- PCEM current or voltage, SCEM current or voltage, or temperature, current, or voltage sensors experience two consecutive samples out-of-limit
- PCEM count rate or SCEM count rate experience six or more consecutive samples out-of-limit (note: count rate limit is 4.0 MHz for PCEM and SCEM).

10.1.3 CDF L1 data product file contents

The contents of the L1.sci CDF file are listed in the following table.

TABLE 2. LEVEL 1 DATA PRODUCT CONTENTS.

Field	Description	Format
Instrument	Instrument or source identifier	String (“swapi”)
dataLevel	An indicator of the data level of the data product	String (“l1”)
startTime	Conversion of SWP_SCI.SHCOARSE (CCSDS Packet Time (SCLK) at which C&DH software created packet) to UTC observation time basis	yyyymmddthhmmss
orbnum	Orbit number in which observation began, generated by MOC and stored at SDC	int

mode	An optional field used to indicate the mode in which an instrument is configured	State (HVSCI)
dataProductDescriptor	An optional field that may be used to further describe the data contained within the file	String (“-1m”)
predict/reconstruct	“p” or “r” depending on whether file is generated with predicted or reconstructed ephemeris.	String (“p” or “r”)
versionInfo	Format: vNN-NN	String (“vNN-NN”)
filetype	An extension indicating the type/format of the data product, e.g. “cdf”	String (“cdf”)
SWP_HK.LUT_CHOICE	Which LUT is in use	String
SWP_HK.FPGA_TYPE	Type number of the FPGA	State
SWP_HK.FPGA_REV	Revision number of the FPGA	String
SWP_SCI.SWEEP_TABLE	Sweep Table ID	Hex
SWP_SCI.PLAN_ID	Plan ID	Hex
SWP_L1_FLAGS	Array of flags for data quality	Bitwise flag (16-bit int)
ESA_LVL5	ESA LVL 5 ID	16-bit int
SWP_PCEM_COUNTS	PCEM counts for full sweep	1x72 int array
SWP_SCEM_COUNTS	SCEM counts for full sweep	1x72 int array
SWP_COIN_COUNTS	Coincidence counts	1x72 int array
SWP_PCEM_COUNTS_ERR_PLUS	Upper uncertainty in PCEM counts	1x72 fp array
SWP_PCEM_COUNTS_ERR_MINUS	Lower uncertainty in PCEM counts	1x72 fp array
SWP_SCEM_COUNTS_ERR_PLUS	Upper uncertainty in SCEM counts	1x72 fp array
SWP_SCEM_COUNTS_ERR_MINUS	Lower uncertainty in SCEM counts	1x72 fp array
SWP_COIN_COUNTS_ERR_PLUS	Upper uncertainty in COIN counts	1x72 fp array
SWP_COIN_COUNTS_ERR_MINUS	Lower uncertainty in COIN counts	1x72 fp array

Flags will be set in the SWP_L1_FLAGS array based on the following conditions occurring at any time during a sweep:

TABLE 3. LEVEL 1 FLAG ARRAY CONTENTS.

Attribute	Description	Format
SWP_HK.OVR_T_ST	The upper temperature limit of any one of the thermistors has been exceeded.	0 or 1
SWP_HK.UND_T_ST	The lower temperature limit of any one of the thermistors has been exceeded.	0 or 1
SWP_HK.PCEM_CNT_ST	The PCEM count rate was tripped but handled by SWAPIFW	0 or 1
SWP_HK.SCEM_CNT_ST	The SCEM count rate was tripped but handled by SWAPIFW	0 or 1
SWP_PCEM_RNG_ST# COMP	Compressed count range (pull from SWP_SCI.PCEM_RNG_ST0)	0 or 1
SWP_SCEM_COMP	Compressed count ranges appeared in any of SWP_SCI.SCEM_RNG_ST0 through SWP_SCI.SCEM_RNG_ST5	0 or 1
SWP_COIN_COMP	Compressed count ranges appeared in any of SWP_SCI.COIN_RNG_ST0 through SWP_SCI.COIN_RNG_ST5	0 or 1
SWP_HK.PCEM_V_ST = 1	voltage tolerance for the PCEM for its current setting has been exceeded	0 or 1
SWP_HK.PCEM_I_ST = 1	current threshold for the PCEM has been exceeded once and has continued to be exceeded despite measures by FSW	0 or 1
SWP_HK.PCEM_INT_ST = 1	PCEM current interrupt was tripped but handled by FSW	0 or 1
SWP_HK.SCEM_V_ST = 1	voltage tolerance for the SCEM for its current setting has been exceeded	0 or 1
SWP_HK.SCEM_I_ST = 1	current threshold for the SCEM has been exceeded once and has continued to be exceeded despite measures by FSW	0 or 1
SWP_HK.SCEM_INT_ST = 1	SCEM current interrupt was tripped but handled by FSW	0 or 1

Uncertainty is quantified for the PCEM, SCEM, and COIN counts. The Poisson contribution is

$$\Delta n = \sqrt{n}$$

The upper (_COUNTS_ERR_PLUS) and lower (_COUNTS_ERR_MINUS) uncertainties for the counts will be the same, except if we modify them to be asymmetric uncertainties in the future. The compression of counts also contributes to the uncertainty. This uncertainty is estimated in an empirical way for which we first generate some count rate numbers that spans the range of higher count rates to cover. Then we compress and un-compress these count rates and compare the

difference between the two cases. These differences are then used to construct an empirical expression to estimate the error.

10.2 L1-L2 Data Processing

L1-L2 data processing divides counts by time to produce count rates and updates the uncertainty. Tables 2-3 describe the L2 data product except SWP_PCEM_COUNTS, SWP_SCEM_COUNTS, SWP_COIN_COUNTS, SWP_PCEM_COUNTS_ERR_PLUS, SWP_PCEM_COUNTS_ERR_MINUS, SWP_SCEM_COUNTS_ERR_PLUS, SWP_SCEM_COUNTS_ERR_MINUS, and SWP_COIN_COUNTS_ERR_PLUS, SWP_COIN_COUNTS_ERR_MINUS are updated as follows.

$$\text{SWP_PCEM_RATE} = \frac{\text{SWP_PCEM_COUNTS}}{t_{live}}$$

We calculate SWP_PCEM_RATE_ERR_PLUS value using SWP_PCEM_COUNTS_ERR_PLUS data from level one and divide by t_{live} = 0.145 s. Then update SWP_PCEM_COUNTS_ERR_PLUS with the newly calculated uncertainty value SWP_PCEM_RATE_ERR_PLUS. Repeat for SWP_SCEM_COUNTS_ERR_PLUS, SWP_COIN_COUNTS_ERR_PLUS, and so on.

$$\text{SWP_PCEM_RATE_ERR_PLUS} = \frac{\text{SWP_PCEM_COUNTS_ERR_PLUS}}{t_{live}}$$

Then we update SWP_PCEM_COUNTS_ERR_PLUS with the newly calculated uncertainty value (SWP_PCEM_RATE_ERR_PLUS). Repeat the same procedure for SCEM and COIN. No additional rejection, culling, or flagging of suspect/bad data is performed during L1-L2 processing. However, an additional flag is added in SWP_L1_FLAGS to indicate data taken during SC thruster activity, namely, daily repointing maneuvers.

Attribute	Description	Format
SWP_SC_THRUSTER	The spacecraft thrusters were on during data acquisition.	0 or 1

The uncertainty in the count rate is obtained by using the Poisson statistics, i.e., $\Delta C = \frac{\sqrt{N}}{t_{bin}}$ where N is the number of counts per energy bin, t_{bin} is the exposure time per energy bin, and ΔC is the uncertainty in the count rate. The exposure time per energy bin is obtained by dividing the time for one complete sweep (12 s, coarse + fine sweep) by the total energy steps (72), i.e., $t_{live} = 0.145$ s (see Table 1). Note that the actual time spent for acquiring counts (live time) per energy bin is less than 0.167 s because some fraction of this time is spent to set up the HVPS (settling

time). The upper (_RATE_ERR_PLUS) and lower (_RATE_ERR_MINUS) uncertainties for the count rates will be the same, except if we modify them to be asymmetric uncertainties in the future.

10.3 ESA Unit Conversion Ancillary Data Product (ADP)

The SWAPI ground processing from L1 to L2 data includes the conversion of ESA Step Number (from 0 to 71) to Energy (keV). The SWAPI Instrument Team provides ADP updates as needed. Table 3 shows the first and last rows of the ESA Unit Conversion ADP.

TABLE 3. START AND END OF ESA UNIT CONVERSION ADP.

timestamp	ESA Step #	K factor	Voltage	Energy	Sweep #	ESA Index Number	LUT version number
2/11/2025 0:00	0	1.88	619	1,163	0	544	4
2/11/2025 0:00	1	1.88	619	1,163	0	544	4
2/11/2025 0:00	2	1.88	619	1,163	0	544	4
2/11/2025 0:00	3	1.88	619	1,163	0	544	4
			:				
			:				
2/11/2025 0:00	60	1.88	69	129	0	960	4
2/11/2025 0:00	61	1.88	64	120	0	976	4
2/11/2025 0:00	62	1.88	57	107	0	992	4
2/11/2025 0:00	63	1.88	Solve	Solve	0	-16	4

2/11/2025 0:00	64	1.88	Solve	Solve	0	-12	4
2/11/2025 0:00	65	1.88	Solve	Solve	0	-8	4
2/11/2025 0:00	66	1.88	Solve	Solve	0	-4	4
2/11/2025 0:00	67	1.88	Solve	Solve	0	0	4
2/11/2025 0:00	68	1.88	Solve	Solve	0	4	4
2/11/2025 0:00	69	1.88	Solve	Solve	0	8	4
2/11/2025 0:00	70	1.88	Solve	Solve	0	12	4
2/11/2025 0:00	71	1.88	Solve	Solve	0	16	4

TO CONVERT THE ESA STEP NUMBER TO AN ENERGY FOR A SINGLE 72-STEP ESA SWEEP:

- For ESA Step Numbers 0-62, simply use the corresponding Energy in the ADP.
- For ESA Step Numbers 63-71 (Voltage and Energy columns say "Solve" in the ADP):
    a. Find v_p16=SWP_SCI ESA_LVL5 at SWP_SCI SEQ_NUMBER=11 in this sweep
    b. On LUT_Notes_vx tab of ADP (corresponding to the LUT version number column in the ADP), find r_p16 row number of voltage in Column B (ESA Voltage)
    c. Energy for ESA Step Number 71 is Column C (Energy) on row r_p16
    d. Energy for ESA Step Number 70 is Column C (Energy) on row r_p16-4
        - "Row r_p16-4" terminology means the row 4 rows prior to row r_p16
    e. Energy for ESA Step Number 69 is Column C (Energy) on row r_p16-8
    f. Energy for ESA Step Number 68 is Column C (Energy) on row r_p16-12
    g. Energy for ESA Step Number 67 is Column C (Energy) on row r_p16-16
    h. Energy for ESA Step Number 66 is Column C (Energy) on row r_p16-20

i. Energy for ESA Step Number 65 is Column C (Energy) on row r_p16-24
j. Energy for ESA Step Number 64 is Column C (Energy) on row r_p16-28
k. Energy for ESA Step Number 63 is Column C (Energy) on row r_p16-32

The ADP file naming convention is defined by IMAP as follows:

imap_<instrument>_<description>_<start_date>_<end_date>_<version>.<extension>

The ESA Unit Conversion ADP filename is:

imap_swapi_esa-unit-conversion_<start_date>_<end_date>_<version>.xlsx

For example, the initial ADP delivery during ground test is called:

imap_swapi_esa-unit-conversion_20250211_v00.xlsx

10.4 L2-L3a Data Processing

The L3a data processing includes the estimation of parameters of the core solar wind protons (H^+), solar wind alpha particles (He^{2+}), and the helium PUIs (He^+) from the count rates in the L2 product. To estimate these parameters, we model the SWAPI coarse scan histograms by using the SWAPI instrument response function and geometric factor obtained from the SIMION model, Geant4 model, and lab calibration results to create a LUT. The instrument response function depends on the ESA energy, and azimuthal and elevation angle of the solar wind flow direction with respect to the SWAPI instrument axis. The LUT is used to derive solar wind proton and alpha particle parameters (Sections 10.3.1-10.3.2). Deriving L3a parameters for He^+ PUIs uses a forward model fitting similar to the NH SWAP methodology (Section 10.3.3).

10.4.1 Solar Wind Proton (H^+) Parameters

IMAP, and hence SWAPI, rotate around the Sun pointing axis with a rotation rate of 4 rpm (15 s per rotation). The SWAPI instrument is designed to make a complete sweep over its entire energy range in 12 s. The 12 s sweep includes 1 coarse sweep from ~19 keV to ~100 eV and 1 fine sweep around the solar wind proton peak (up to 9 steps, but variable according to sweep plans of the time of this writing, SWAPI's nominal plan is plan 4 which retains~6 energy bins around the peak and 3 fine-sweep bins to sample backgrounds at low energies). There are 62 energy bins from the highest to the lowest ESA energy bin, 9 energy bins for the fine sweep, and one extra step to go from the lower to the higher ESA energy. Therefore, there are altogether 72 steps (62 coarse + 9 fine + 1 dead time) for each 12 s sweep. To calculate the solar wind proton (H^+) parameters, we use the 1 min cadence data. Here, we demonstrate how we can use 1 min cadence data to estimate core solar wind proton parameters. The 1 min cadence SWAPI data includes 5 coarse sweeps and 5 fine sweeps. We use both coarse and fine steps to fit the solar wind protons. Depending on the sweep plan, one or more fine steps can be set to low ESA voltages to measure the background count rates, and these energy bins are excluded from the fit. The background count rate at the Sun-Earth Lagrange point (L1) can change over time based on a variety of factors, including variability in solar-UV output (see, e.g., Bzowski et al. 2013; Sokol et al. 2013), as well as changing galactic and anomalous cosmic ray intensity levels (see, e.g., review by Leske et al. 2013). The 12-second sweeps are grouped into non-overlapping five-sweep chunks, resulting in a one-minute cadence for the final output. Five sweeps are used because that corresponds to the least common multiple of the spin rate (approximately 15 seconds) and the sweep cadence (12 seconds). This chunking approach is used to ensure the use of S/C spin phase variation to determine the solar wind bulk velocity.

The solar wind velocity distribution function (VDF) is modeled as a drifting Maxwellian

$$f^p(\boldsymbol{v};\boldsymbol{x}) = \frac{n}{(\sqrt{2\pi}\,v_{\mathrm{th}})^3}\exp\left(-\frac{|\boldsymbol{v}-\boldsymbol{v}_b|^2}{2v_{\mathrm{th}}^2}\right) = \frac{n}{(\sqrt{2\pi}\,v_{\mathrm{th}})^3}\exp\left(-\frac{v^2 - 2\,v\,(\hat{\boldsymbol{d}}\cdot\boldsymbol{v}_b) + v_b^2}{2v_{\mathrm{th}}^2}\right),$$

with density n, $v_{\mathrm{th}} = \sqrt{k_B T/m_p}$ (T being temperature), and bulk velocity $\boldsymbol{v}_b = (v_R, v_T, v_N)^{\mathsf{T}}$ in the spacecraft RTN frame. The flow direction in RTN coordinates, $\hat{\boldsymbol{d}}(\theta,\phi)$, is obtained by applying the measurement-specific rotation matrix to

$$\hat{\mathbf{d}}\ (\theta,\phi)\ \equiv \frac{\mathbf{v}}{\|\ \mathbf{v}\ \|} = (-\cos\theta\sin\phi, -\cos\theta\cos\phi, -\sin\theta)^{\mathsf{T}}.$$

Substituting the VDF into the coincidence rate integral:

$$C(V; n, v_{\text{th}}, \mathbf{v}_b) = \frac{n\mathcal{A}_0(V)}{\left(\sqrt{2\pi}v_{\text{th}}\right)^3} \sum_{\text{region}} \int \mathrm{d}\theta \cos\theta \int \mathrm{d}\phi T(\phi) \int \mathrm{d}v v^3 P\left(\frac{v}{v_0(V)}, \theta\right) \exp\left(-\frac{v^2 - 2v(\hat{\mathbf{d}}(\theta,\phi)\cdot\mathbf{v}_b) + v_b^2}{2v_{\text{th}}^2}\right).$$

The region sum includes the sunglasses (SG, $|\phi| \le 20°$) and the two sides of the open aperture (OA, $20° \le |\phi| \le 150°$).

Each region is integrated using nested Gauss-Legendre quadrature with fixed numbers of integration points:

$$(N_\theta, N_\phi, N_v) = (21, 21, 15).$$

Integral limits:

- **Speed limits:** The speed integral is limited to the overlap between the passband's speed width and the VDF-driven interval

  $$[v_b - \Delta v_{\text{VDF}},\ v_b + \Delta v_{\text{VDF}}], \qquad \Delta v_{\text{VDF}} = 6v_{\text{th}},$$

  where $v_b = |\boldsymbol{v}_b|$ and v_{th} is the thermal speed.

  The integral is skipped early if there is no overlap with the conservative range $[0.9v_0,\ 1.1v_0]$. Otherwise, using the passband's integration contour, denoted

  $$[r_{\text{min}}(\theta)v_0,\ r_{\text{max}}(\theta)v_0],$$

  the speed limits at a given elevation are given by

  $$v_{\text{lo}}(\theta) = \max(v_b - \Delta v_{\text{VDF}},\ r_{\text{min}}(\theta)v_0),$$

  $$v_{\text{hi}}(\theta) = \min(v_b + \Delta v_{\text{VDF}},\ r_{\text{max}}(\theta)v_0).$$

  Any θ where $v_{\text{hi}}(\theta) \le v_{\text{lo}}(\theta)$ is skipped.

Angular Limits:

The angular extent of the VDF within a factor of $\varepsilon = 10^{-6}$ is given by

$$\Delta\alpha = \arccos\left(\text{clamp}\left(\frac{v_{\text{th}}^2 \ln\varepsilon}{v_0 v_b} + 1;\ -1,\ 1\right)\right),$$

The window is centered on the bulk-flow direction in the instrument frame. For measurement i, this direction is computed from $\boldsymbol{v}_{b,i}^{\mathrm{XYZ}} = R_i^{\top}\boldsymbol{v}_b$ (Rankin et al. 2025):

$$\phi_{b,i} = \arctan2(-v_{b,i,x}^{\mathrm{XYZ}}, -v_{b,i,y}^{\mathrm{XYZ}}), \qquad \theta_{b,i} = \arcsin\left(-\frac{v_{b,i,z}^{\mathrm{XYZ}}}{v_b}\right).$$

These angles define only the integration limits; the Maxwellian exponent still uses the RTN-frame dot product $\widehat{\boldsymbol{d}}_i \cdot \boldsymbol{v}_b$ directly. For each measurement, they give the rectangular window

$$[\theta_{b,i} - \Delta\alpha,\ \theta_{b,i} + \Delta\alpha] \times [\phi_{b,i} - \Delta\alpha,\ \phi_{b,i} + \Delta\alpha],$$

which is then clamped to the passband elevation range and azimuth range for the region. The azimuthal region is skipped if the window is clamped to zero.

For OA, the azimuth window is further reduced with a 64-point scan of the azimuth-only integrand, approximated as

$$h(\phi) = T(\phi)\exp\left[-\frac{v_0^2 + v_b^2 - 2v_0 v_b \cos\alpha(\theta_b', \phi)}{2v_{\mathrm{th}}^2}\right],$$

where $v = v_0$, θ_b' is the bulk elevation clamped into the OA passband's elevation range, and $\alpha(\theta_b', \phi)$ is the angle with respect to the bulk flow direction. The reduced window includes the range where $h(\phi) > 10^{-6}\max h$ padded by one sample on each side. The OA integral is skipped if the heuristic estimate of its contribution to the total integral

$$\frac{n\,\mathcal{A}_0(V)}{(\sqrt{2\pi}\,v_{\mathrm{th}})^3}\,v_0^3\,\Delta\theta\,\Delta v\int_{\phi_{\mathrm{lo}}}^{\phi_{\mathrm{hi}}} h\,(\phi)\,\mathrm{d}\phi,$$

is below $\max(0.1\ \mathrm{Hz},\ 10^{-3}C_{\mathrm{SG}})$. Here $\Delta\theta$ is the clamped OA elevation width (in units of radians) and $\Delta v = (r_{\max}(0) - r_{\min}(0))v_0$ is the passband width at $\theta = 0$.

Deadtime Correction:

The detector deadtime is $\tau = 183.7$ ns. Following Tsoulfanidis (1995), p. 74, the true count rate n and measured rate g are related by $n = g/(1 - g\tau)$. Rearranged for the forward model, the true model rate C^{model} is mapped to the predicted observed rate before computing residuals:

$$C_i^{\mathrm{observed}} = \frac{C_i^{\mathrm{model}}}{1 + \tau\,C_i^{\mathrm{model}}} = C_i^{\mathrm{model}} \cdot \mathcal{D}_i, \qquad \mathcal{D}_i \equiv \frac{1}{1 + \tau\,C_i^{\mathrm{model}}}.$$

This deadtime correction is often non-negligible. It reaches 5% at $C \approx 2.7 \times 10^5$ Hz, a routine value for high-flux solar wind.

Optimized Integral Validation:

The optimized integrator is validated against a high-resolution fixed-limit reference integrator with a much denser grid and no dynamic integration limits. The figure below compares the two integrators for a sample of solar wind configurations.

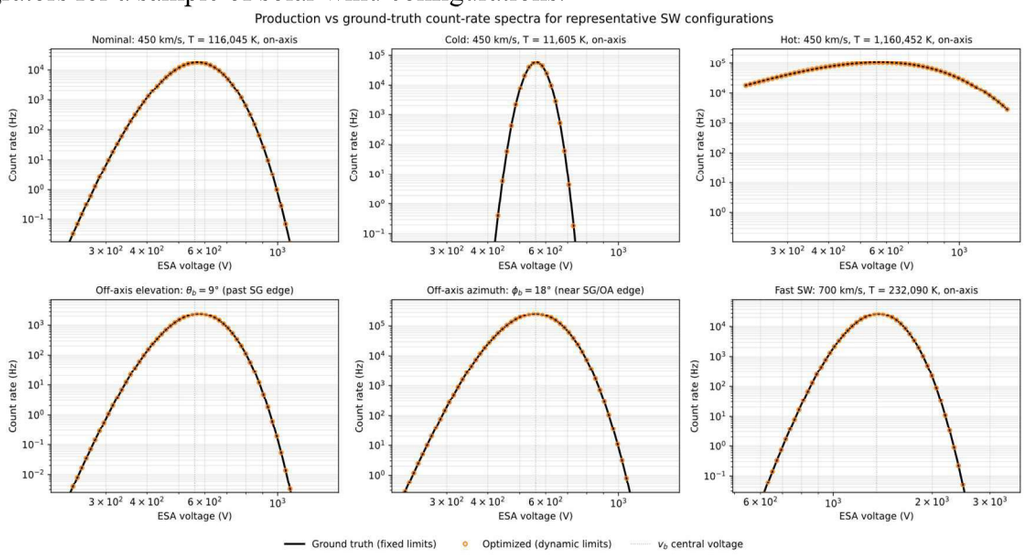


FIGURE 14. PRODUCTION VS GROUND-TRUTH SPECTRA FOR SIX REPRESENTATIVE SW CONFIGURATIONS.

For a thorough validation experiment, the optimized integrator is compared with the fixed-grid reference across 10,000 solar wind cases drawn from WIND/SWE 2-min data in 2025. The integrals are calculated at V where $v_0(V) = v_b$, which is approximately the location of the peak coincidence rate. For the vast majority of the time, the relative error is less than 1%. And under all situations where the solar wind is in the field of view, the error is less than 5%.

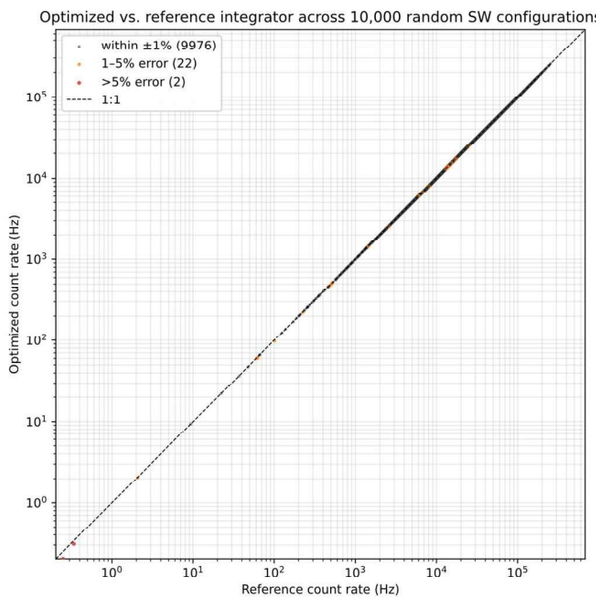


Figure 15. Optimized vs reference count rate across 10,000 WIND-derived SW configurations, with the 1:1 line and points colored by relative error bucket.

Analytic Jacobian:

Since $C(V)$ is linear in $f^p(\boldsymbol{v};\boldsymbol{x})$ and $\mathcal{A}(\boldsymbol{v},V)$ is independent of $\boldsymbol{x}$,

$$\frac{\partial C(V)}{\partial x_j} = \frac{\partial}{\partial x_j}\int \mathrm{d}^3v\, v\, f^p(\boldsymbol{v};\boldsymbol{x})\,\mathcal{A}(\boldsymbol{v},V) = \int \mathrm{d}^3v\, v\, \frac{\partial f^p}{\partial x_j}(\boldsymbol{v};\boldsymbol{x})\,\mathcal{A}(\boldsymbol{v},V).$$

Thus, the same integral used for C can evaluate all five columns of the Jacobian in one pass.

To evaluate $\partial f^p / \partial x_j$ for each component of $\boldsymbol{x}$, it is useful to have the logarithm of the VDF, which is

$$\ln f^p = \ln n - 3/2\,\ln v_{\mathrm{th}}^2 - \frac{|\boldsymbol{v}-\boldsymbol{v}_b|^2}{2\,v_{\mathrm{th}}^2} + \text{const.}$$

Expanding the squared offset, $|\boldsymbol{v}-\boldsymbol{v}_b|^2 = v^2 - 2\,v\,(\hat{\boldsymbol{d}}\cdot\boldsymbol{v}_b) + v_b^2$, where $\hat{\boldsymbol{d}}$ is the look direction in RTN.

Log Density:

$$\frac{\partial f^p}{\partial n} = \frac{f^p}{n}.$$

Converting to log-space via $\partial f^p / \partial \ln n = n\ \partial f^p / \partial n$,

$$\frac{\partial f^p}{\partial \ln n} = f^p.$$

Log Temperature:

$$\frac{\partial \ln f^p}{\partial v_{\text{th}}^2} = -\frac{3}{2\,v_{\text{th}}^2} + \frac{|\boldsymbol{v} - \boldsymbol{v}_b|^2}{2\,v_{\text{th}}^4}.$$

The remaining steps are three applications of the same change-of-variables identity,

$$\frac{\partial g}{\partial y} = \frac{\partial g}{\partial x} \cdot \frac{\partial x}{\partial y},$$

in the sequence $v_{\text{th}}^2 \to T$ ($v_{\text{th}}^2 = k_B T/m$), $\ln f^p \to f^p$, and $T \to \ln T$.

First:

$$\frac{\partial \ln f^p}{\partial T} = \frac{\partial v_{\text{th}}^2}{\partial T} \cdot \frac{\partial \ln f^p}{\partial v_{\text{th}}^2} = \frac{v_{\text{th}}^2}{T} \frac{\partial \ln f^p}{\partial v_{\text{th}}^2} = \frac{1}{T} \cdot \left(\frac{|\boldsymbol{v} - \boldsymbol{v}_b|^2}{2\,v_{\text{th}}^2} - 3/2 \right).$$

Then:

$$\frac{\partial f^p}{\partial T} = \frac{f^p}{T} \cdot \left(\frac{|\boldsymbol{v} - \boldsymbol{v}_b|^2}{2\,v_{\text{th}}^2} - 3/2 \right).$$

Finally:

$$\frac{\partial f^p}{\partial \ln T} = f^p \cdot \left(\frac{|\boldsymbol{v} - \boldsymbol{v}_b|^2}{2\,v_{\text{th}}^2} - 3/2 \right).$$

Note that the sign reverses across $|\boldsymbol{v} - \boldsymbol{v}_b|^2 = 3\,v_{\text{th}}^2$: increasing T decreases f^p for $v \approx v_b$ and increases it for $v \gg v_b$.

Bulk Velocity Components:

$$\nabla_{v_b} \ln f^p = -\frac{1}{v_{\text{th}}^2}\, \nabla_{v_b} [1/2\, |\boldsymbol{v} - \boldsymbol{v}_b|^2] = \frac{1}{v_{\text{th}}^2}\, (\boldsymbol{v} - \boldsymbol{v}_b).$$

Multiplying by f^p,

$$\nabla_{\boldsymbol{v}_b} f^p = \frac{f^p}{v_{\text{th}}^2}\,(\boldsymbol{v} - \boldsymbol{v}_b).$$

So, the three components are

$$\frac{\partial f^p}{\partial v_R} = \frac{f^p}{v_{\text{th}}^2}\,(\boldsymbol{v} - \boldsymbol{v}_b)_R, \qquad \frac{\partial f^p}{\partial v_T} = \frac{f^p}{v_{\text{th}}^2}\,(\boldsymbol{v} - \boldsymbol{v}_b)_T, \qquad \frac{\partial f^p}{\partial v_N} = \frac{f^p}{v_{\text{th}}^2}\,(\boldsymbol{v} - \boldsymbol{v}_b)_N.$$

Because deadtime depends on C^{model}, it propagates into the residual Jacobian by the chain rule. Differentiating $C^{\text{observed}} = C^{\text{model}}/(1 + \tau\, C^{\text{model}})$ with respect to C^{model} via the quotient rule,

$$\frac{\partial C^{\text{observed}}}{\partial C^{\text{model}}} = \frac{(1 + \tau\, C^{\text{model}}) - C^{\text{model}} \cdot \tau}{(1 + \tau\, C^{\text{model}})^2} = \frac{1}{(1 + \tau\, C^{\text{model}})^2} = \mathcal{D}^2.$$

Thus, the Jacobian columns $\partial C_i^{\text{model}} / \partial x_j$ are scaled by $\mathcal{D}_i^2$ to obtain:

$$\frac{\partial C_i^{\text{observed}}}{\partial x_j} = \frac{\partial C_i^{\text{observed}}}{\partial C_i^{\text{model}}} \cdot \frac{\partial C_i^{\text{model}}}{\partial x_j} = \mathcal{D}_i^2 \cdot \frac{\partial C_i^{\text{model}}}{\partial x_j}.$$

A representative SWAPI solar wind proton fit is shown below:

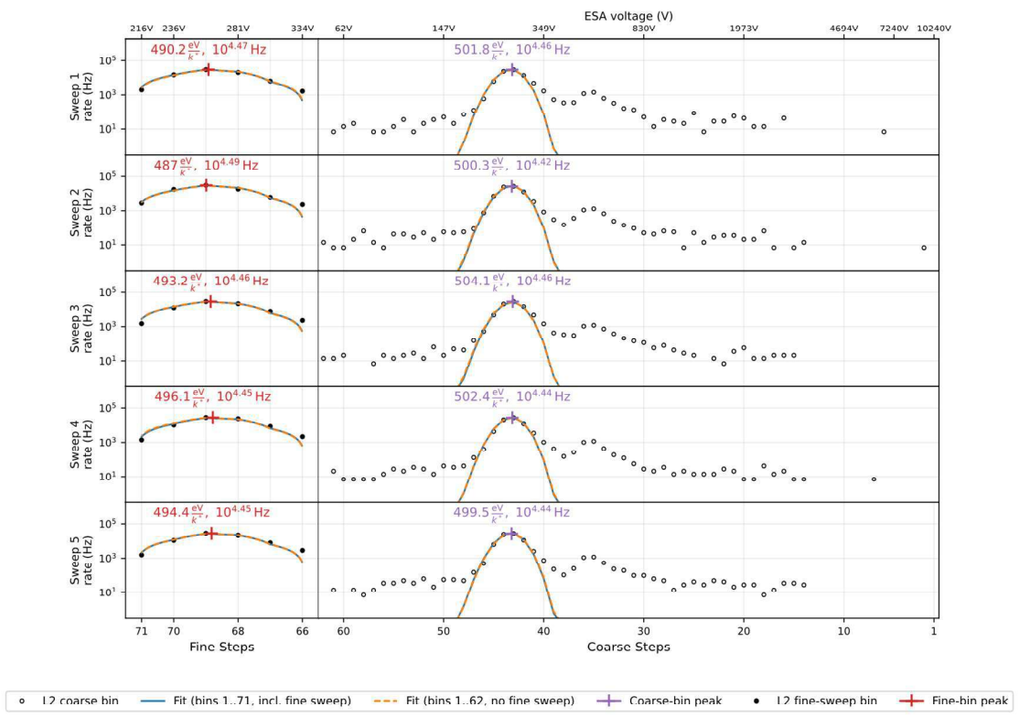


FIGURE 17. SWAPI PROTON FIT ON L2 FIGHT DATA: 5 INDIVIDUALS COARSE (RIGHT PANELS) AND FINE (LEFT PANELS) SWEEPS WITH THE PRODUCTION FIT OVERLAID ON THE MEASURED COINCIDENCE COUNT RATE.

The fitted moments and their 1-σ uncertainties are listed blow in Table 4. The reported uncertainties come from an approximate covariance matrix that accounts for heteroscedasticity. The bootstrap σ column provides a nonparametric estimate of the uncertainty. WIND/SWE measurements at around the same time are included for comparison. The RTN velocity components for WIND are computed from the GSE components via $v_R \approx -V_{x,\mathrm{GSE}}$, $v_T \approx -V_{y,\mathrm{GSE}}$, $v_N \approx V_{z,\mathrm{GSE}}$. Differences between the spacecraft measurements may include systematic effects such as spatial separation and temporal variation of the solar wind.

TABLE 4. SWAPI SOLAR WIND PROTON FITTED PARAMETERS WITH THEIR 1-σ UNCERTAINTIES. FITTED VALUES USING COARSE + FINE STEPS AND ONLY THE COARSE STEPS ARE SHOWN FOR COMPARISON.

Quantity	SWAPI all ESA steps	bootstrap σ	coarse steps only	WIND/SWE 2-min @ 22:49:48 UT
Density n (cm^{-3})	5.122 ± 0.094	± 0.099	5.091 ± 0.134	5.710 ± 0.053
Temperature T (K)	$(1.741 \pm 0.069) \times 10^4$	$\pm 0.074 \times 10^4$	$(1.757 \pm 0.101) \times 10^4$	$(2.096 \pm 0.41) \times 10^4$
Speed $\lvert v \rvert$ (km/s, inertial)	307.1 ± 0.26	± 0.28	307.3 ± 0.34	333.6 ± 6.40
v_R (km/s, inertial RTN)	307.06 ± 0.26	± 0.27	307.18 ± 0.41	+333.30 ± 6.40
v_T (km/s, inertial RTN)	+3.71 ± 1.30	± 1.32	+6.07 ± 2.20	+12.70 ± 1.00
v_N (km/s, inertial RTN)	-2.81 ± 1.37	± 1.39	-3.79 ± 1.81	-0.30 ± 1.00

The start time for each sweep is denoted t_{start}. For ESA step i (0-indexed, although recall that step 0 is skipped), the measurement time is:

$$t_i = t_{\text{start}} + i \cdot 12/72 \text{ s} = t_{\text{start}} + (i+1) \cdot 0.16 - \left(\frac{0.145}{2}\right) \text{s}.$$

The SWAPI-to-RTN rotation matrices are obtained from the SPICE kernels for each ESA step based on the time of measurement. These are used directly in the forward modeling processing. If the rotation matrices are unavailable, the chunk is skipped and assigned fill values.
The spacecraft velocity in the Sun's inertial frame is also obtained for the center of each chunk, which is used to transform the final bulk velocity vector. If unavailable, the fit is still performed, but the Sun-frame outputs cannot be computed.

The proton model parameters are represented by the vector

$$\boldsymbol{x} = (\ln n, \ln T, v_R, v_T, v_N).$$

$\ln n$, $\ln T$ represent the density and temperature in log space (so that the density and temperature are always positive). v_R, v_T, v_N represent the bulk velocity vector in the spacecraft's frame of reference, denoted $\boldsymbol{v}_b^{\mathrm{SC}}$. The optimal parameters are found by solving the minimization problem

$$\hat{\boldsymbol{x}} = \underset{\boldsymbol{x}}{\operatorname{argmin}} \sum_j \left[C_j^{\mathrm{observed}}(\boldsymbol{x}) - C_j \right]^2,$$

where C_j is the coincidence rate for measurement j and $C_j^{\mathrm{observed}}(\boldsymbol{x})$ is the model coincidence rate. Note that measurement j represents all 5 sweeps, including coarse and fine sweeps.

The residuals are intentionally left unweighted. Because Poisson variance is proportional to count rate, inverse-variance weighting would give extra weight to low-count points away from the peak. That is a problem because other populations (e.g., the proton shoulder, pickup ions, and alpha particles) contribute significantly to the total count rate away from the peak. For SWAPI, this is a particularly noticeable effect because the sunglasses attenuate the cold, core solar wind population and thus magnify the relative contribution of high-temperature secondary proton populations.

The initial guess of fit parameters is as follows:

The bulk speed is first set to $v_b^{(0)}$, the speed corresponding to the peak coincidence rate.

The temperature is first set to:

$$T^{(0)} = \max\left(1\,\mathrm{eV}/k_B, 60{,}000\,\mathrm{K} \cdot \left(\frac{v_b^{(0)}}{400\,\mathrm{km/s}}\right)^2\right).$$

$v_b^{(0)}$ and $T^{(0)}$ are then refined by fitting an arbitrarily normalized Gaussian curve:

$$C(V) \propto \exp\left(-\frac{(v_0(V) - \mu_v)^2}{2\sigma_v^2}\right)$$

after which

$$v_b^{(0)} = \mu_v,$$

$$T^{(0)} = \max(1\,\mathrm{eV}, m\sigma_v^2/k_B),$$

and:

$$\boldsymbol{v}_b^{\mathrm{SC},(0)} = -v_b\,\hat{\boldsymbol{y}}^{\mathrm{RTN}}.$$

where $\hat{\boldsymbol{y}}^{\mathrm{RTN}}$ is the normalized mean y-axis basis vector in RTN coordinates (taken from the rotation matrices). By design, the solar wind bulk velocity direction is close to $-\hat{\boldsymbol{y}}^{\mathrm{RTN}}$ on average.

The density's initial guess is

$$n^{(0)} = \underset{n}{\operatorname{argmin}} \sum_i [\, n\, m_i\, \mathcal{D}(n\, m_i) - C_i\,]^2\,, \qquad m_i = C_i^{\mathrm{model}}(n = 1; T^{(0)}, \boldsymbol{v}_b^{\mathrm{SC},(0)}).$$

The mean squared error function often has a local minimum with bulk velocity flipped about the spin axis $\hat{\boldsymbol{s}}^{\mathrm{RTN}}$. Fortunately, the local minimum has a much larger mean squared error (MSE) than the global minimum. After obtaining the parameters and MSE from the first minimum ($\boldsymbol{v}_b$, n, T, and MSE), the following procedure is repeated up to six times:

1. **Flip the bulk velocity, rescale the density.**

$$\mathbf{v}_b^{\boldsymbol{flip}} = \mathbf{2}\hat{\boldsymbol{s}}\,(\hat{\boldsymbol{s}}.\boldsymbol{v_b}) - \mathbf{v}_b,$$

$$\mathbf{n}^{\boldsymbol{flip}} = \arg\,\min_n \sum_i [\mathbf{n}\,\mathbf{m}_i \mathbf{D}(\boldsymbol{n}\,\boldsymbol{m}_i) - \mathbf{C}_i]^2\,, \mathbf{m}_i = \mathbf{C}_i^{model}(\mathbf{n} = \mathbf{1}; \mathbf{T}, \mathbf{v}_b^{SC,(k)})$$

2. **Check the threshold.** If $\sqrt{\mathrm{MSE}^{\mathrm{flip}}} \geq 10\sqrt{\mathrm{MSE}}$, stop iterating.

3. **Fit again if within the threshold.** Now the starting point for the fit is $(\boldsymbol{v}_b^{\mathrm{flip}}, n^{\mathrm{flip}}, T)$.

4. **Compare the two fits.** If the MSE at the new local minimum is no worse than it was at the previous local minimum, accept the new solution and continue iterating.

To validate that the algorithm finds the correct solution (global minimum) under realistic conditions, the following experiment was performed:

1. Sample 10,000 solar wind parameters from WIND/SWE's nonlinear Maxwellian fits in 2025.
2. Simulate realistic input data for each: 5 sweeps, 62 ESA steps each (coarse sweep only; if the fine sweeps were included too, it would improve the result slightly); rotation matrices with realistic spacecraft spin; and forward-modeled coincidence rates using the same model used for fitting, but with Poisson noise added.
3. Apply the minimization algorithm to the simulated coincidence rates, yielding estimates for the solar wind proton parameters.

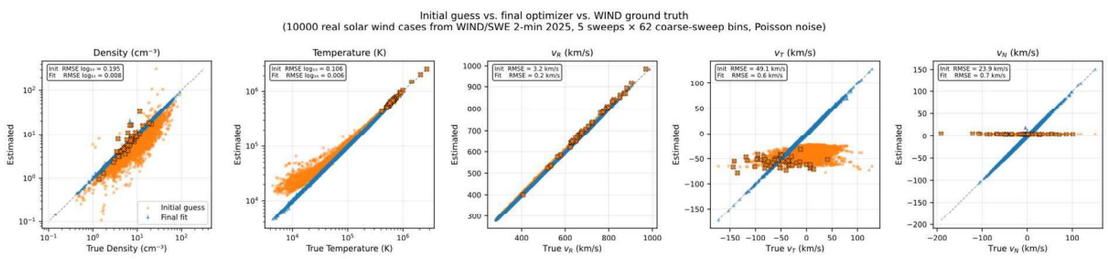


FIGURE 18. INITIAL-GUESS VS. FINAL-FIT ACCURACY FOR 10000 REAL WIND/SWE SOLAR WIND CONDITIONS AS INPUTS.

Uncertainty Quantification: Unweighted residuals are used to avoid biasing the fit by not giving too much weight to off-peak points with significant contributions from populations besides the solar wind proton core distribution. Even when the true variance of the residuals is not uniform (heteroscedasticity), unweighted least squares—which is optimal under homoscedastic, normally distributed errors—is still unbiased, albeit not maximally efficient. But although the fit itself is unbiased, the Jacobian-based covariance matrix $\Sigma_{\boldsymbol{x}} = (\sum_i r_i^2 / (N - \mathrm{DOF})) \cdot (J^\top J)^+$ that is often used is inaccurate in the presence of heteroscedastic errors. Instead, the heteroscedasticity-consistent HC3 method is used (MacKinnon & White 1985; Long & Ervin 2000; Hayes & Cai 2007) to estimate the covariance matrix:

$$\Sigma_{\boldsymbol{x}} = (J^\top J)^+ J^\top \mathrm{diag}(r_i^2/(1-h_{ii})^2)\, J\, (J^\top J)^+,$$

where $r_i = \mathrm{pred}_i - \mathrm{obs}_i$ is the residual for measurement i, $h_{ii} = J_i\,(J^\top J)^+ J_i^\top$, and $^+$ represents the Moore–Penrose pseudoinverse (used instead of a true inverse for numerical stability).

The results shown in Figure 21 validate the uncertainty estimate empirically. The ground truth is ($n = 5\,\mathrm{cm}^{-3}$, $T = 10^5\,\mathrm{K}$, $\boldsymbol{v}_{\mathrm{RTN}} = (450{,}5{,}-3)\,\mathrm{km/s}$), so there is one true coincidence rate spectrum. 1000 synthetic 5-sweep chunks are generated by adding Poisson noise, 1% log-normal noise, and an energy-independent, Poisson-distributed 10 Hz background. Note that the uncertainties primarily represent statistical error and do not necessarily take systematic error into account. For example, density relies on the central effective area calibration, which has an uncertainty of up to 20%. This introduces a systematic error that applies equally to all density measurements.

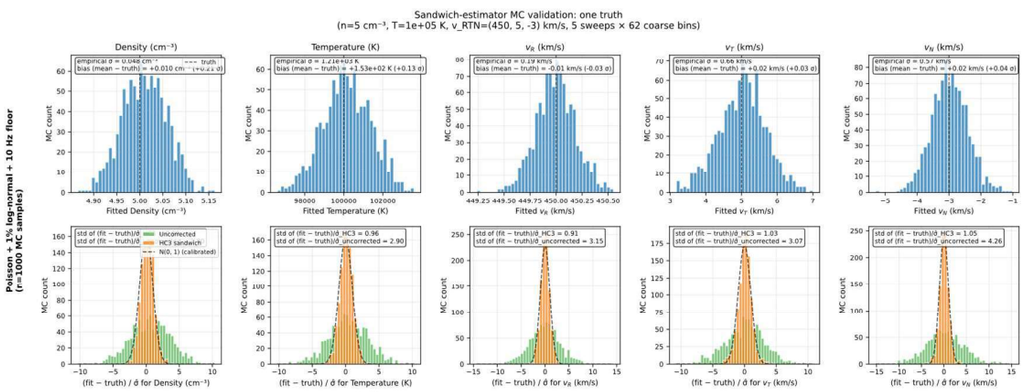


FIGURE 19. VALIDATION OF UNCERTAINTY ESTIMATION.

Flagging of data:

- If the optimizer reports success=False, or any error occurs, the flag FIT_ERROR is set, and fill values are reported for fit parameters.
- If $R^2 < 0.9$ or $T > 5 \times 10^5$ K, the flag BAD_FIT is set, and fill values are reported.

R^2 is computed using only the measurements ***within ±4 points of the peak after averaging the spectrum across the five sweeps (retaining only the coarse-sweep bins, since the fine sweeps have a different energy in each sweep)***. The coincidence rates are averaged across sweeps before computing R^2 because individual sweeps have lower R^2 due to the solar wind's variability on short timescales. The R^2 check is intended to confirm that the model, which assumes that the distribution is unchanging over the one-minute chunk, is a reasonable representation of the one-minute average distribution, rather than testing whether it captures all the temporal variation.

WHENEVER THE FIT FAILS AND FILL VALUES ARE REPORTED, PROTON_SW_SPEED IS STILL POPULATED BASED ON THE PEAK OF THE SWEEP-AVERAGED COINCIDENCE RATES. THE PEAK IS IDENTIFIED BY USING A COINCIDENCE RATE-WEIGHTED AVERAGE (COARSE SWEEP ONLY?).

10.4.2 Solar Wind Alpha (He^{2+}) Parameters

The solar wind alpha (He^{2+}) parameters will be determined by using count rates for 5 coarse sweeps (1 min cadence). These parameters include the flow vector, density, and temperature of the solar wind alpha distribution.

After fitting the solar wind proton parameters on a five-sweep chunk, the proton parameters are held fixed, and three parameters of the solar wind alpha population are estimated: density $n^{\mathrm{He}^{2+}}$, temperature $T^{\mathrm{He}^{2+}}$, and a field-aligned drift speed $\Delta v^{\mathrm{He}^{2+}}$. The alpha bulk velocity is modeled as

$$\boldsymbol{v}^{\mathrm{He}^{2+}} = \boldsymbol{v}^{\mathrm{He}^{2+}} + \Delta v^{\mathrm{He}^{2+}}\,\widehat{\boldsymbol{B}},$$

where $\boldsymbol{v}^{p}$ is the proton bulk velocity and $\widehat{\boldsymbol{B}}$ is the direction of the chunk-averaged magnetic field. The solution vector used for optimization is

$$\boldsymbol{x}^{\mathrm{He}^{2+}} = (\log n^{\mathrm{He}^{2+}},\ \log T^{\mathrm{He}^{2+}},\ \Delta v^{\mathrm{He}^{2+}}).$$

The inputs that are used for fitting protons are also used for fitting alphas except that only the coarse steps are used for alphas.

The solar wind alpha data product has an additional magnetic field dependency because the model constrains the alpha-proton drift to lie along $\widehat{\boldsymbol{B}}$. For the magnetic field direction, MAG L2 data is used, but when it is not yet available, L1D is used and the PRELIMINARY_MAG flag is set. For each five-sweep alpha chunk, the magnetic field in RTN components is averaged over the one-minute interval. The mean vector is then normalized, providing $\widehat{\boldsymbol{B}}^{\mathrm{RTN}}$. When the window has no non-fill values in the magnetic field, it is skipped and fill values are reported in the alpha products.

For alphas, the coincidence rate is modeled as the sum of the proton and alpha contributions with deadtime correction applied after the summation:

$$C(V) = [C^{p}(V) + C^{\alpha}(V;\,\boldsymbol{x}^{\alpha})] \cdot \mathcal{D}(C^{p}(V) + C^{\alpha}(V;\,\boldsymbol{x}^{\alpha})),$$

where C^{p}/ C^{α} is the coincidence rate contribution from protons / alphas evaluated using the solar wind forward model.

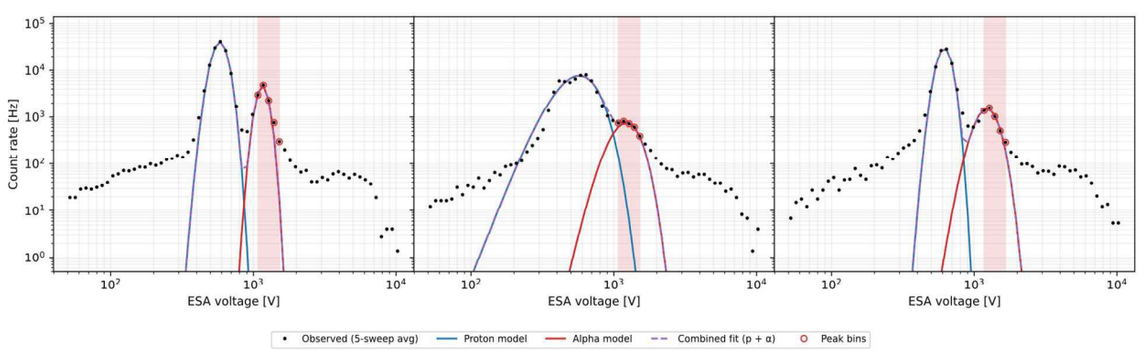


FIGURE 160. EXAMPLE SWAPI HISTOGRAMS OBTAINED BY STATISTICALLY COMBINING THE COUNT RATES OF 5 COARSE SWEEPS (1 MIN CADENCE). THE SHADED RED REGION AROUND THE SOLAR WIND ALPHA PEAK REPRESENTS THE SOLAR WIND ALPHA (HE^{2+}) REGION.

ALPHA PEAK-FINDING ON L2 FLIGHT SPECTRA:

Before fitting the alpha distribution, the points to include in the fit is identified. For this, first, the proton-subtracted residuals are calculated:

$$R_i = C_i - 2C_i^p.$$

The alpha peak is identified as the maximum between the first increase in R_i between 1.5 and 4 times the energy per charge of the proton peak. **The factor of two in the residual is so that errors in the proton model on the order of a few percent are not mistaken for the alpha peak.** Once the peak is identified, one point at lower energy and three points at higher energies—in addition to the peak itself, for a total of five points—are used to fit the alpha parameters. The fit fails if the selected five points do not fall within the selected range of 1.5 to 4 times the proton peak.

After that, the alpha parameters are initialized with $T^{\mathrm{He}^{2+}} = T^p$ and $\Delta v^{\mathrm{He}^{2+}} = 0$ then optimized using scipy.optimize.least_squares with method='lm' to solve

$$\widehat{\boldsymbol{x}}^{\mathrm{He}^{2+}} = \arg\min_{\boldsymbol{x}^{\mathrm{He}^{2+}}} \sum_s \sum_i \left[C_{i,s}^{\text{observed}}(\boldsymbol{x}^{\mathrm{He}^{2+}}) - C_{i,s} \right]^2, \quad i \in \text{alpha peak window}, \quad s \in \{1, \ldots, 5\},$$

where $C_{i,s}$ is the measured coincidence rate for ESA step i of sweep s and $C_{i,s}^{\text{observed}}(\boldsymbol{x}^{\mathrm{He}^{2+}})$ is the model coincidence rate. The Jacobian is the same as for protons except for the differential flow:

$$\frac{\partial C^{\mathrm{He}^{2+}}}{\partial(\Delta v^{\mathrm{He}^{2+}})} = \nabla_{\boldsymbol{v}^{\mathrm{He}^{2+}}} C^{\mathrm{He}^{2+}} \cdot \widehat{\boldsymbol{B}} = \sum_{c \in \{R,T,N\}} \frac{\partial C^{\mathrm{He}^{2+}}}{\partial v_{\mathrm{He}^{2+},c}} \widehat{B}_c.$$

With the deadtime correction included, the Jacobian is thus:

$$J^{\mathrm{He}^{2+}} = \mathcal{D}^2(C^p + C^{\mathrm{He}^{2+}}) \left[\frac{\partial C^{\mathrm{He}^{2+}}}{\partial \log n^{\mathrm{He}^{2+}}} \quad \frac{\partial C^{\mathrm{He}^{2+}}}{\partial \log T^{\mathrm{He}^{2+}}} \quad \nabla_{\boldsymbol{v}^{\mathrm{He}^{2+}}} C^{\mathrm{He}^{2+}} \cdot \widehat{\boldsymbol{B}} \right].$$

Notes on error handling:

- If the proton fit fails, fill values are reported and the proton quality flag is propagated.
- If the alpha fit fails at any point, fill values are reported and FIT_ERROR is set.
- If the alpha fit converges but $R^2 < 0.9$, fill values are reported and BAD_FIT is set. Note that R^2 is computed using the sweep-averaged coincidence rate for the points used in the alpha fit.

10.4.3 Pickup Helium (He^+) Parameters

For the He^+ PUI parameters, we use statistically combined count rates for 50 coarse sweeps (10 min cadence). The He^+ PUI fit region includes energy bins in between the theoretical H^+ PUI cutoff and the theoretical He^+ PUI cutoff. We use a forward model fit (e.g., Chen et al. model used for SWAP data processing) with fit parameters such as cutoff speed, ionization rate, cooling index, and background rate. The forward model fit is then used to derive the PUI density, temperature, and other relevant parameters.

The generalized Vasyliunas & Siscoe model (Chen et al. (2014) model) for the pickup He^+ can be written as:

$$f(r,w,\psi) = \frac{\alpha}{4\pi}\frac{\beta_E r_E^2}{r u_{\mathrm{sw}} v_{\mathrm{b}}^3} w^{\alpha-3}\, n_{\mathrm{He}}(r w^{\alpha},\psi)\, \Theta(1-w), \tag{7}$$

where α is the non-adiabatic cooling index, $w = v/v_b$, v is the PUI speed in the SW frame, v_b is the local cutoff speed of He^+ PUI in the SW frame given by $v_b = |\boldsymbol{u}_{SW} - \boldsymbol{u}|$, $\boldsymbol{u}$ is the bulk velocity of interstellar helium at position (r,ψ) in the *solar inertial frame,* $\boldsymbol{u}_{SW}$ is the solar wind bulk velocity in the solar inertial frame, β_E is the ionization rate at $r_E = 1$ au, ψ is the angle between radial direction and the interstellar helium inflow direction, $n_{He}(rw^{\alpha},\psi)$ is the density of the interstellar neutral helium at (r' (= rw^{α}), ψ), and Θ is the Heaviside step function. The interstellar helium inflow comes from (255.7°, 5.1°) with a speed of 25.4 km s^{-1} in *ecliptic J2000* coordinates (McComas et al. 2015). The fitting of the PUI distributions to the SWAPI count rates involves the following steps:

- The density of the interstellar neutral helium is calculated using the *hot model* (Thomas 1978) for interstellar neutrals propagating into the heliosphere. We precompute this density as a function of ψ and distance r'. For a particular angle ψ, we calculate the density over the distance range $r\frac{v_{min}}{v_b} \le r' \le r\frac{v_{max}}{v_b}$. Here, v_{min} and v_{max} represent speeds corresponding to the minimum energy of the first ESA passband and maximum energy of the last ESA passband, respectively. The precomputed neutral helium density is used as a LUT. The *hot model* calculation may not be accurate enough, and future improvements may be made to model the propagation of interstellar neutrals through the heliosphere (e.g., global magnetohydrodynamic models of the SW-LISM interaction).
- Then we calculate the model count rate by integrating the distribution function over the instrument's energy and angle widths. The model count rate at ESA energy E_e is given by (Elliott et al. 2016)

$$C_{PUI}(V) = \int \mathrm{d}^3v\, v\, f_{\mathrm{PUI}}(\boldsymbol{v})\mathcal{A}^s(\boldsymbol{v}, V), \qquad (9)$$

The modeled count rates are then converted to the model counts by multiplying them by the ESA bin exposure time for 50 sweeps, i.e., $M_C(V) = 50 * t_{bin} * C_{PUI}(V)$.

- **Fitting energy range:** We use all energy bins over the range: $1.25 * E_{b,H^+} < E_e < 1.2 * E_{b,He^+}$ (~0.1 Hz, see Figure 20). The H^+ PUI cutoff energy in the SWAPI frame is given by $E_{b,H^+} \approx \frac{1}{2} m_{H^+} \left(2v'_{b,H^+}\right)^2$, where $v'_{b,H^+} = |\boldsymbol{u}_{SW} - \boldsymbol{u}_H - \boldsymbol{u}_{IMAP}|$. Here $\boldsymbol{u}_{IMAP}$ is the IMAP spacecraft's velocity in the solar inertial frame (from SPICE kernel) and $\boldsymbol{u}_H$ is the bulk velocity of interstellar hydrogen, which is 22 km s^{-1} (Lallement et al. 2005) coming from (252.2°, 9.0°) in *ecliptic J2000* coordinates. We consider the following free parameters for the fitting:
  - Cooling index (α)
  - Ionization rate (β_E)
  - Cutoff speed (v_b)
  - Background count rate (CR_{bkg}). We assume a constant background count rate at all energy ranges considered for the fitting, supported by NH SWAP observations.
- The best-fit model is obtained by minimizing the *Poisson likelihood chi-square* between the modeled and observed counts (e.g., using the MPFIT library). The *Poisson likelihood chi-square* (Cash 1979, Baker & Cousins 1984, Xi 2020) is given by

$$\chi^2_{\lambda,p} = 2 \sum_e \left(M_C(E_e) - C(E_e) + C(E_e) \ln\left(\frac{C(E_e)}{M_C(E_e)}\right)\right), \qquad (10)$$

where $C(E_e)$ and $M_C(E_e)$ are the observed and modeled counts at energy $E_{e,}$ respectively. Note that the model counts in Equation (10) also include the background counts (i.e., sum of C_{bkg} and model counts obtained from Equation (9)).
- The best-fit distribution obtained from the *Poisson likelihood chi-square* minimization is then integrated numerically (e.g., using the QUADPACK library) to get the density and temperature of He^+ PUI.
  - Density:

$$n_{He^+\,PUI} = \iiint_{0\,0\,0}^{v_b\ \pi\ 2\pi} f(v)\, v^2 dv \sin\theta\, d\theta\, d\phi = 4\pi \int_0^{v_b} f(v)\, v^2\, dv \quad (11)$$

  - Temperature:

$$T_{He^+\,PUI} = \frac{m_{He^+}}{3k_B}\frac{\int_0^{v_b} f(v)\, v^4\, dv}{\int_0^{v_b} f(v)\, v^2\, dv} \quad (12)$$

The uncertainties in density and temperature of He^+ PUI are obtained by manually propagating the 1-sigma uncertainty of the fit parameters given by

$$\sigma_{n_{He^+PUI}} = \sqrt{\Sigma_{j=1}^{4}\left(n_{He^+PUI} - (n_{He^+PUI})_{j+\sigma_j}\right)^2}$$

$$\sigma_{T_{He^+PUI}} = \sqrt{\Sigma_{j=1}^{4}\left(T_{He^+PUI} - (T_{He^+PUI})_{j+\sigma_j}\right)^2},$$

where density and temperature at '$j+\sigma_j$' are obtained by adding 1-sigma uncertainty to the best-fit value of the fit parameter 'j' in Equations (11) and (12). Note that the calculations of density and temperature involve numerical integrations, and we cannot use simple error propagation formulas to get their uncertainties.

Simplified Count rate integral: f_{PUI} is isotropic in the solar wind's comoving frame (where $\boldsymbol{v}_{\mathrm{sw}} = 0$). Thus, one can change variables $\boldsymbol{u} \equiv \boldsymbol{v} - \boldsymbol{v}_{\mathrm{sw}}$ ($\mathrm{d}^3v = \mathrm{d}^3u$, $v' = |\boldsymbol{u}|$), using $\mathrm{d}^3u = v'^{\,2}\,\mathrm{d}v'\,\mathrm{d}\omega_u$ ($\int \mathrm{d}\omega_u = 4\pi$), resulting in the 1D integral

$$\mathrm{C}_{PUI}(V) = \int_0^{\infty} v'^{\,2}\,\mathrm{d}v'\; f_{\mathrm{PUI}}(v')\, H(v', V; \boldsymbol{v}_{\mathrm{sw}}),$$

where

$$H(v', V; \boldsymbol{v}_{\mathrm{sw}}) \;\equiv\; \int \mathrm{d}\omega_u\; |\boldsymbol{v}|\, \mathcal{A}(\boldsymbol{v}, V)$$

is the angular integral of $|\boldsymbol{v}|\,\mathcal{A}$ on the spherical shell defined by $|\boldsymbol{v} - \boldsymbol{v}_{\mathrm{sw}}| = v'$, with dimensions of volume per time. We can convert the angular integral to a velocity integral as follows:

$$H(v', V; \boldsymbol{v}_{\mathrm{sw}}) = \int \mathrm{d}^3v\; \frac{\delta(v' - \|\,\boldsymbol{v} - \boldsymbol{v}_{\mathrm{sw}}\,\|)}{v'^2}\; |\boldsymbol{v}|\, \mathcal{A}(\boldsymbol{v}, V)$$

In spherical instrument coordinates:

$$H(v', V; \boldsymbol{v}_{\mathrm{sw}}) = \int \mathrm{d}v\, \mathrm{d}\theta\, \mathrm{d}\phi\; v^3 \cos\theta\; \frac{\delta(v' - \|\,\boldsymbol{v} - \boldsymbol{v}_{\mathrm{sw}}\,\|)}{v'^2}\; \mathcal{A}(\boldsymbol{v}, V)$$

To make this integral easier to calculate, we can fix v' and integrate over two coordinates from (θ, ϕ, v). We choose to integrate over (θ, v) so that we only need to interpolate the passband once for each region.

The term inside the delta function is satisfied when:

$$v'^2 = v^2 + v_{\text{sw}}^2 - 2vv_{\text{sw}}\cos\alpha,$$

where α denotes the angle between $\boldsymbol{v}$ and $\boldsymbol{v}_{\text{sw}}$, given by:

$$\cos\alpha = \frac{v^2 + v_{\text{sw}}^2 - v'^2}{2vv_{\text{sw}}} = \sin\theta\sin\theta_b + \cos\theta\cos\theta_b\cos(\phi - \phi_b).$$

Solving for the ϕ term:

$$\cos(\phi - \phi_b) = \frac{\cos\alpha - \sin\theta\sin\theta_b}{\cos\theta\cos\theta_b},$$

which has zero or two solutions (depending on whether the right-hand side lies in $[-1,1]$):

$$\phi_\pm = \phi_b \pm \arccos\left(\frac{\cos\alpha - \sin\theta\sin\theta_b}{\cos\theta\cos\theta_b}\right)$$

(The boundary case where the argument equals ± 1 yields a single (degenerate) root $\phi_+ = \phi_-$ but can be ignored for integration purposes.)

Define $R(\phi) \equiv \| \boldsymbol{v} - \boldsymbol{v}_{\text{sw}} \|$ at fixed (v, θ). Using $\delta(v' - R(\phi)) = \sum_\pm \delta(\phi - \phi_\pm)/|R'(\phi_\pm)|$, the integral is reduced to:

$$H(v', V; \boldsymbol{v}_{\text{sw}}) = \int \mathrm{d}v \int \mathrm{d}\theta \; \frac{v^3\cos\theta}{v'^2} \sum_\pm \frac{\mathcal{A}(v, \theta, \phi_\pm, V)}{|R'(\phi_\pm)|}.$$

Differentiating $R^2(\phi) = v^2 + v_{\text{sw}}^2 - 2vv_{\text{sw}}\cos\alpha(\phi)$ with respect to ϕ gives

$$2R(\phi)\,R'(\phi) = 2\,v\,v_{\text{sw}}\cos\theta\cos\theta_b\sin(\phi - \phi_b),$$

and $R(\phi_\pm) = v'$,

$$|R'(\phi_\pm)| = \frac{v\,v_{\text{sw}}\cos\theta\cos\theta_b\,|\sin(\phi_\pm - \phi_b)|}{v'}.$$

Substituting $|R'(\phi_\pm)|$ into the integral:

$$H(v', V; \boldsymbol{v}_{\text{sw}}) = \int \mathrm{d}v \int \mathrm{d}\theta \; \frac{v^2}{v_{\text{sw}}\,v'\cos\theta_b} \sum_\pm \frac{\mathcal{A}(v, \theta, \phi_\pm, V)}{|\sin(\phi_\pm - \phi_b)|},$$

Below, we compare this optimized calculation of H to a direct shell quadrature integral.

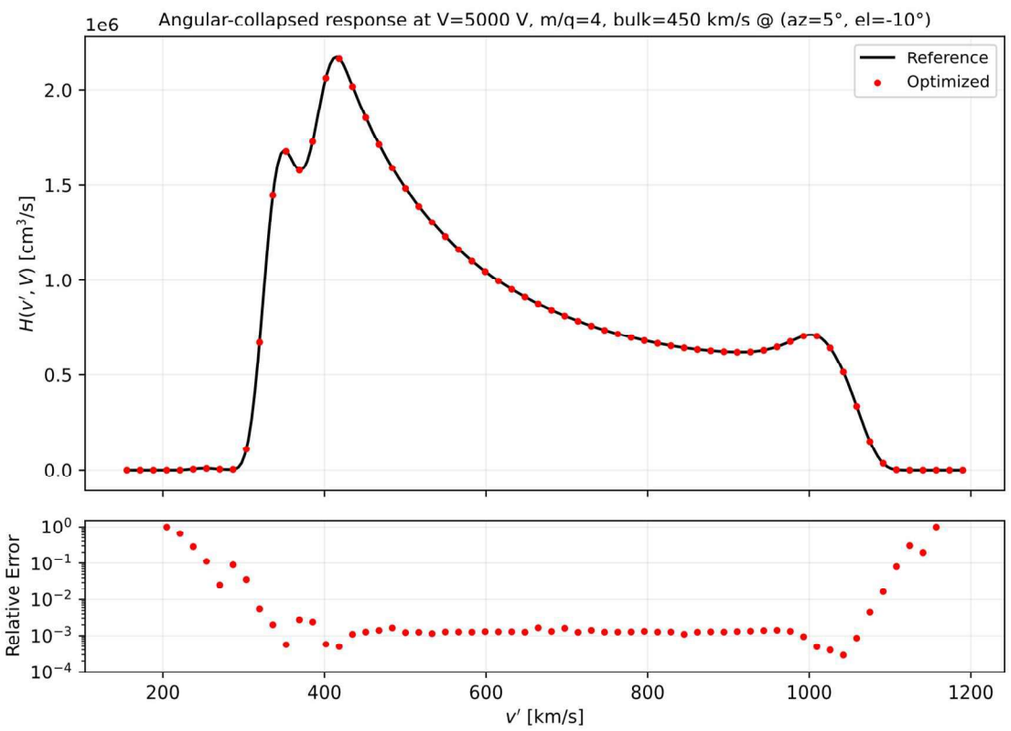


FIGURE 171. CLOSED-FORM Φ-INVERSION RESULT COMPARED WITH A NUMERICAL SHELL-INTEGRAL REFERENCE FOR H(V', V) AT V=5000 V, M/Q=4, BULK=450 KM/S AT (AZ=5°, EL=−10°).

Numerical Integration:

The integration weight tensor W_{ijk}

$$W_{ijk} = \Delta v' \cdot {v'_k}^2 \cdot H(v'_k, V_j; \boldsymbol{v}_{\mathrm{sw,ij}}).$$

is precomputed on a uniform grid $v'_k \in [v'_{\min}, v'_{\max}]$ with spacing $\Delta v'$, defined by

$$v'_{\min} = \max\left(1\ \mathrm{km/s},\ 0.8\, v_{\mathrm{sw}}\, \frac{r_{\min}}{r}\right),$$

$$v'_{\max} = 1.2 v_{\mathrm{sw}},$$

where $r_{\min}$ is the minimum r in the $n(r,\psi)$ lookup table. The boundaries are chosen based on the minimum and maximum cutoff speed in the fitting bounds.

Using W_{ijk}, the model coincidence rate is given by

$$C_{ij}^{(\text{model})}(\boldsymbol{x}) = C_{\text{bg}} + \sum_k W_{ijk}\, f_{\text{PUI}}(v'_k; \boldsymbol{x}),$$

a single tensor operation after evaluating $f_{\text{PUI}}(v'_k; \boldsymbol{x})$ on the grid only one time for all sweeps and steps.

It is essential to ensure continuity in derivatives with respect to the cutoff speed v_b despite the discrete grid so that uncertainties can be estimated. The numerical integration setup is equivalent to a midpoint rule, so v'_j represents the bin center. Instead of evaluating the Heaviside step function when calculating f_{PUI} based on $\Theta(v'_j - v_b)$ alone, it is applied based on the fraction of the cutoff bin that is within the cutoff. The exact index of the bin containing the cutoff point is

$$j_{\text{cutoff}} = \text{round}\left(\frac{v_b - v'_0}{\Delta v'}\right).$$

The fraction of this bin that is below the cutoff is

$$\frac{v_b - \left(v'_{j=j_{\text{cutoff}}} - \frac{\Delta v'}{2}\right)}{\Delta v'}.$$

THEREFORE, WE SIMPLY SCALE f_{PUI} IN THE CUTOFF BIN BY THAT FACTOR AND SET BINS ABOVE THE CUTOFF TO ZERO. THE PLOT BELOW CONFIRMS THAT THIS APPROACH ACCURATELY CORRECTS THE CUTOFF DISCRETIZATION EVEN AT AN ESA VOLTAGE THAT IS STRONGLY AFFECTED BY THE CUTOFF.

Below, the optimized 1D integral is validated by comparing it to a reference 3D integral with automatic handling of units via `pint` and dimensionality using `xarray`.

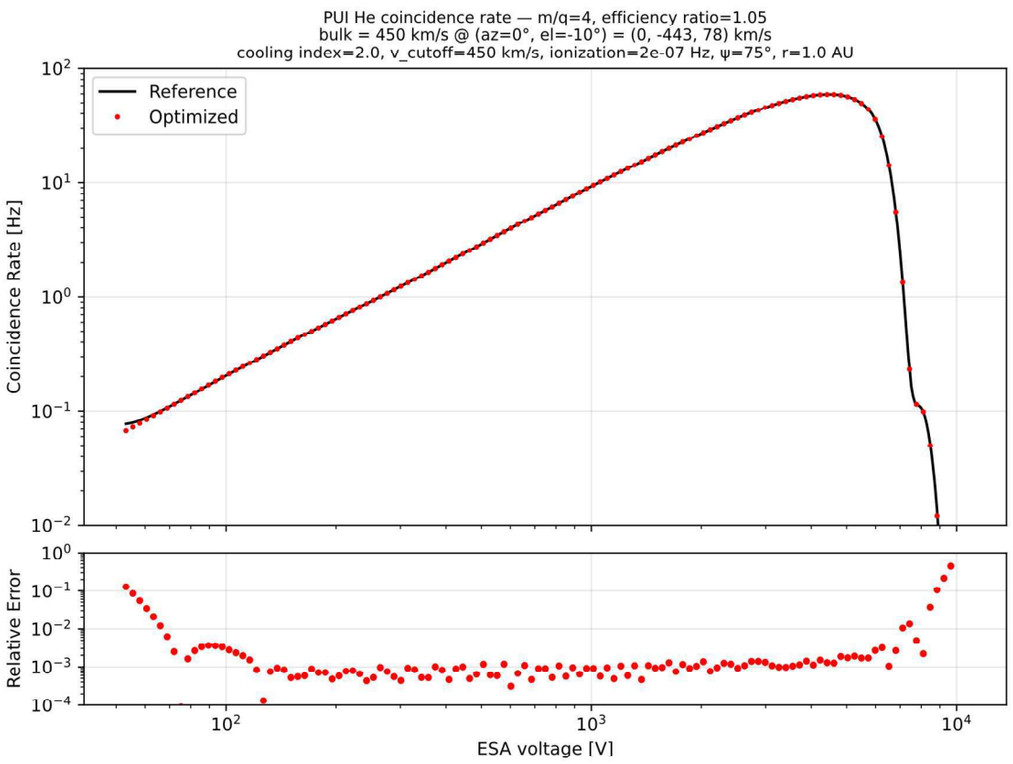


FIGURE 18. XARRAY + PINT REFERENCE: TOTAL COINCIDENCE-RATE SPECTRUM ACROSS THE ESA VOLTAGE TABLE, USING PARAMETERS SPECIFIED IN THE REFERENCE SCRIPT.

Optimization Strategy:

The PUI parameters to be determined are $\boldsymbol{x} = (\alpha_{\mathrm{PUI}}, \beta_E, v_b, C_{\mathrm{bg}})$. To enable the application of physical constraints on the parameters, the constrained optimization problem in $\boldsymbol{x}$ is posed as an unconstrained problem in $\tilde{x}$, given by

$$\tilde{\boldsymbol{x}} = \arcsin\left(\frac{2(\boldsymbol{x} - \boldsymbol{x}_{\min})}{\boldsymbol{x}_{\max} - \boldsymbol{x}_{\min}} - 1\right),$$

with bounds defined in the table below.

TABLE 5. FITTING PARAMETER BOUNDS AND INITIAL VALUES FOR HE+ PUIS.

Parameter	x_{min}	x_{max}	Initial
α_{PUI}	1.0	5.0	1.5
β_E	0.6×10^{-9} s^{-1}	8×10^{-7} s^{-1}	10^{-7} s^{-1}
v_b	0.8 v_{sw}	1.2 v_{sw}	v_{sw}
C_{bg}	0	10 Hz	0.1 Hz

The Nelder-Mead method is used for optimization, with a heuristic five-vertex simplex specified explicitly .
The optimal parameters are estimated by maximizing the Poisson likelihood—yielding optimal parameters $\hat{\boldsymbol{x}}$—through minimization of

$$\hat{\boldsymbol{x}} = \underset{\boldsymbol{x}}{\operatorname{argmin}} \sum_{i,j} C_{ij}^{(\mathrm{model})}(\boldsymbol{x}) - C_{ij} \ln C_{ij}^{(\mathrm{model})}(\boldsymbol{x}).$$

The covariance matrix of $\hat{\tilde{\boldsymbol{x}}}$ is estimated using the inverse of the Hessian of the negative log likelihood function,

$$\Sigma_{\tilde{\boldsymbol{x}}} = [\nabla^2 \mathcal{L}(\hat{\tilde{\boldsymbol{x}}})]^{-1},$$

and then the covariance matrix for the PUI parameters $\boldsymbol{x}$ is given by

$$\Sigma_{\boldsymbol{x}} = \mathrm{J}\, \Sigma_{\tilde{\boldsymbol{x}}}\, \mathrm{J}^{\mathrm{T}},$$

where $J = \partial \boldsymbol{x} / \partial \tilde{\boldsymbol{x}}$.

Failure Cases:

When C_{bkg} is higher than 1 Hz, a fill value is reported for C_{bkg} because of the probable influence of suprathermal populations, but the other parameters are kept.

If the uncertainty estimation fails (suggesting that the solution is not a minimum), or the coefficient of determination R^2 is less than 0.9 for the sweep-averaged coincidence rates in the fitting window, then the BAD_FIT flag is set and fill values are reported.

Numerical Test:

Shown below is an experiment validating that the fitting algorithm recovers the ground truth parameters and accurately estimates the uncertainty given an ideal model with Poisson noise added.

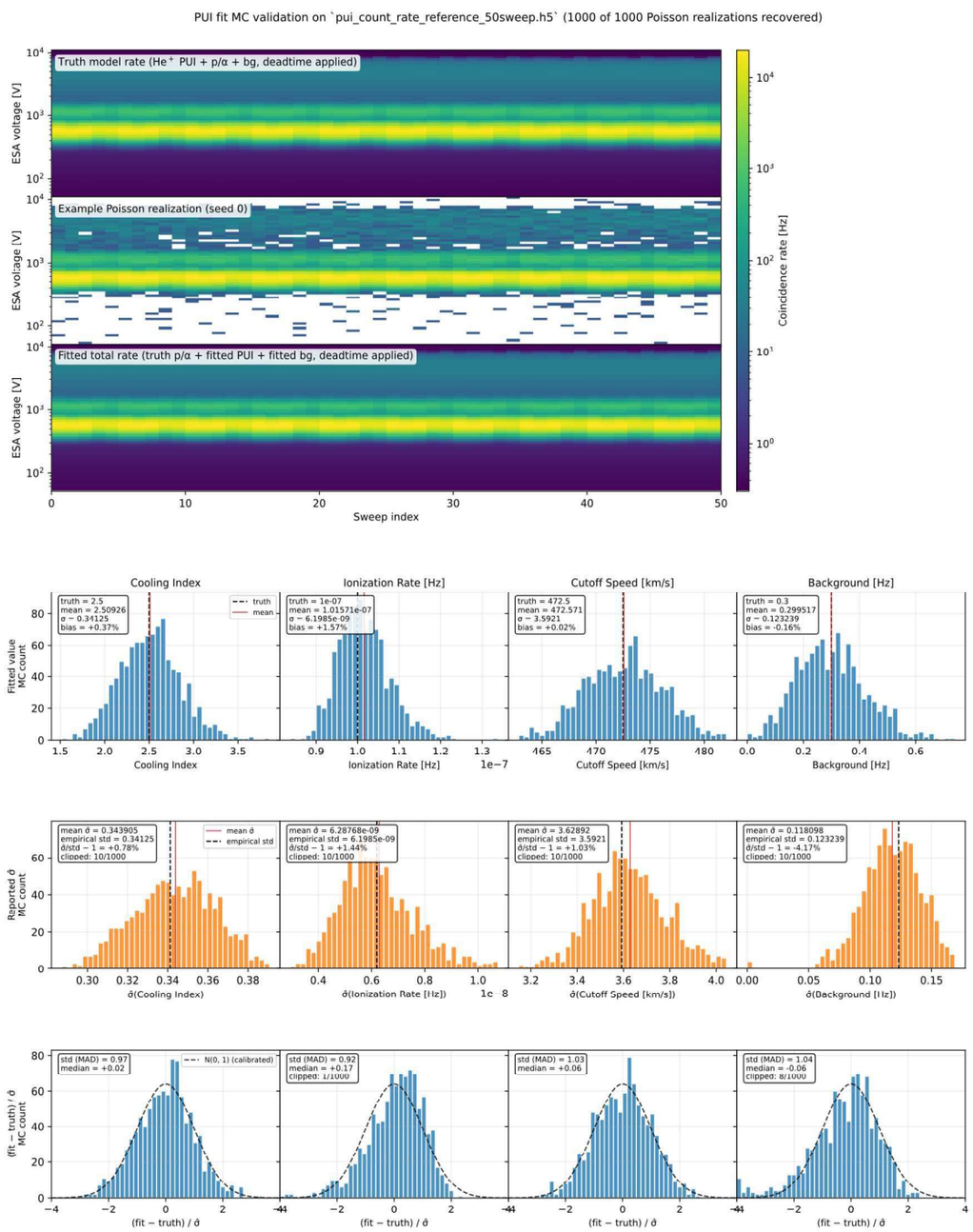


FIGURE 193. VALIDATION OF THE FITTING ALGORITHM

10.5 L2-L3b Data Processing

L2-L3b data processing uses geometric factor and the efficiency of the SWAPI instrument to produce: the combined differential intensity of SW protons (H^+), solar wind alpha particles (He^{2+}), and interstellar PUIs (H^+ and He^+). The conversion of the count rate to the differential flux is performed by using the following equation

$$J\left(\frac{E}{q}\right) = \frac{C(E/q)}{\frac{E}{q} * G(E/q) * \varepsilon}, \qquad (13)$$

where $J(\frac{E}{q})$ is the differential flux in units of #/ [cm^2 s sr eV/q], $C(E/q)$ is the count rate, $G(E/q)$ is the geometric factor, and ε is the efficiency of the instrument which varies over time. The efficiency of the instrument will be updated after each gain test performed in the space and will be provided in a LUT. This calculation assumes the same efficiency of the instrument for both hydrogen and helium (i.e., efficiency is assumed independent of the mass and used H efficiency). Note that the combined differential flux data product is useful to compare the solar wind proton flux.

The uncertainty in the combined differential flux is obtained by propagating the uncertainty in the observed count rate as

$$\Delta J = J\sqrt{\left(\frac{\Delta C}{C}\right)^2 + \left(\frac{\Delta(E/q)}{(E/q)}\right)^2} \qquad (14)$$

Here, the uncertainty in the count rate, ΔC, and energy, $\Delta(E/q)$ contributes to the uncertainty of the combined differential flux.

10.6 Summary of SWAPI Data Products

L1 Data Products

- **Counts and Count Uncertainties:**
  - **Time resolution:** 12 s (72 values per sweep, coarse + fine sweep)
  - **Components:** primary, secondary, coincidence
  - **Inputs Required:** L0 CCSDS packets
  - **Ancillary files:** Decommutation Table

L2 Data products

- **Count Rates and Count Rate Uncertainties:**
  - **Time resolution:** 12 s
  - **Components:** primary, secondary, coincidence
  - **Inputs Required:** L1 counts and count uncertainties as a function of 72 ESA voltage steps (per sweep)
  - **Ancillary files:** ESA unit conversion table, accumulation time per ESA step (TBC)

L3a Data Products

1. Solar Wind Proton (H^+) Products:

- **Velocity (km s^{-1})**
  - **Time resolution:** 1 min
  - **Components:** (v_R, v_T, v_N), IMAP de-spun frame and solar inertial frame
  - **Inputs Required:** L2 count rates and count rate uncertainties as a function of E/q for 62 coarse energy bins (5 sweeps)
  - **Ancillary files:** IMAP spin phase (SPICE kernels), Frame kernel for coordinate transformation (SPICE), LUT for efficiency (instrument team updates after each gain test in space), LUT for the instrument response function (instrument team)
- **Density (cm^{-3})**
  - **Time resolution:** 1 min
  - **Components:** n_{SW}
  - **Inputs Required:** L2 count rates and count rate uncertainties as a function of E/q for 62 coarse energy bins (5 sweeps)
  - **Ancillary files:** same as for velocity
- **Temperature (K)**
  - **Time resolution:** 1 min
  - **Components:** T_{SW} (isotropic)
  - **Inputs Required:** L2 count rates and count rate uncertainties as a function of E/q for 62 coarse energy bins (5 sweeps)
  - **Ancillary files:** same as for velocity

2. Solar Wind Alpha (He^{2+}) Products:

- **Velocity (km s^{-1})**
  - **Time resolution:** 1 min
  - **Components:** (v_R, v_T, v_N), IMAP de-spun frame and solar inertial frame
  - **Inputs Required:** L2 count rates and count rate uncertainties as a function of E/q for 62 coarse energy bins (5 sweeps)
  - **Ancillary files:** IMAP spin phase (SPICE kernels), Frame kernel for coordinate transformation (SPICE), LUT for the efficiency (instrument team updates after each gain test in space), LUT for the instrument response function (instrument team), magnetic field vector (L2 data, L1d is used if L2 not available)
- **Density (cm^{-3})**
  - **Time resolution:** 1 min
  - **Components:** $n_{He^{2+}}$
  - **Inputs Required:** L2 count rates and count rate uncertainties as a function of E/q for 62 coarse energy bins (5 sweeps)
  - **Ancillary files:** same as for velocity
- **Temperature (K)**
  - **Time resolution:** 1 min
  - **Components:** $T_{He^{2+}}$ (isotropic)
  - **Inputs Required:** L2 count rates and count rate uncertainties as a function of E/q for 62 coarse energy bins (5 sweeps)
  - **Ancillary files:** same as for velocity

3. Pickup Helium (He^{+}) Products:

- **Fit Parameters:** Cooling index, Cutoff speed (km s^{-1}), Ionization Rate (s^{-1}), Background Rate (Hz)
  - **Time resolution:** 10 min
  - **Components:** α, v_b, β_E, C_{bkg}
  - **Inputs Required:** L2 count rates and count rate uncertainties as a function of E/q for 62 coarse energy bins (50 sweeps)
  - **Ancillary files:** IMAP spin phase (SPICE), Frame kernel from coordinate transformation (SPICE), LUT for the efficiency (instrument team updates after each gain test in space), LUT for the instrument response function (instrument team), LUT for the interstellar neutral He density (instrument team), LUT for interstellar neutral H and He flow vector
- **Density (cm^{-3})**

- **Time resolution:** 10 min
- **Components:** n_{He^+}
- **Inputs Required:** L2 count rates and count rate uncertainties as a function of E/q for 62 coarse energy bins (50 sweeps)
- **Ancillary files:** Same as for fit parameters

- **Temperature (K)**
  - **Time resolution:** 10 min
  - **Components:** T_{He^+} (isotropic)
  - **Inputs Required:** L2 count rates and count rate uncertainties as a function of E/q for 62 coarse energy bins (50 sweeps)
  - **Ancillary files:** Same as for fit parameters

L3b Data Products

- **Combined differential flux**
  - **Time resolution:** 10 min
  - **Components:** $J(E/q)$
  - **Inputs Required:** L2 count rates and count rate uncertainties as a function of E/q for 62 coarse energy bins (50 sweeps)
  - **Ancillary files:** $\frac{\Delta E}{E}$, energy-dependent geometric factor ($G(E/q)$), efficiency (ϵ) – instrument team

11 MAINTENANCE OF SWAPI GROUND DATA PROCESSING

The only regular maintenance of the SWAPI ground data processing is updating the PCEM and SCEM voltages periodically. The gain test is SWAPI's only calibration activity during routine operations and will occur multiple times during commissioning, but only every ~3 months during the mission operational phase. The PCEM and SCEM voltage updates will be provided in a LUT that reflects the results of the gain curve analysis. LUT improvements will be made asynchronously with SWAPI data production. The 1x2 LUT format is provided in
Table 6. The ground processing will also need to incorporate the resulting efficiency changes acquired after gain curve tests.

TABLE 6. 1X2 LUT CONTAINING PCEM AND SCEM VOLTAGE SETTINGS DERIVED FROM GAIN TEST ANALYSIS.

PCEM setting (V)	SCEM level (V)

12 RECOMMENDED TESTING APPROACHES

SWAPI processing code was tested by the SDC working with the SWAPI data team. The SWAPI team ran the ETE model and provided inputs and outputs to the SDC to allow the SDC to verify the implementation of the SWAPI ground processing code.

13 CODE DELIVERY

SWAPI delivers the SWAPI L3 processing code using a Docker container via AWS.

14 I-ALIRT PRODUCTS

The I-ALiRT cadence for instruments is required to be 15 seconds. A single SWAPI sweep is 12 seconds. SWAPI's I-ALiRT contents consist of coincidence counts only, reported as a single coarse sweep, delivered at a cadence of 12 seconds. The I-ALiRT algorithms use coincidence count rates and count rate uncertainties (see Section 0) for each coarse sweep and calculate the pseudo-moments of solar wind H^+. The SWAPI I-ALiRT data products are summarized below:

- **Data products:** pseudo speed, density, and temperature of H^+ solar wind
- **Time resolution:** 12 s
- **Components:** u_p, n_p, T_p (isotropic)
- **Inputs required:** coincidence count rates and count rate uncertainties as a function of E/q for 62 coarse energy bins (1 sweep)
- **Ancillary files:** Effective area (A_{eff}), FWHM of energy width ($\frac{\Delta E}{E}$)

The I-ALiRT algorithms for SWAPI use an analytical model for solar wind measurements, originally developed for SWAP (Elliott et al. 2016), to determine the pseudo speed, density, and temperature of solar wind H^+. The analytical model uses instrument effective area (A_{eff}), azimuthal width of the field of view ($\Delta\phi$), and energy passband (E_e) and does not require any angular response functions. The SWAPI's count rate ($C(E_e)$) for each ESA energy passband (E_e) is given by

$$C(E_e) = \left(nA_{\text{eff}} \left(\frac{\beta}{\pi}\right)^{\frac{3}{2}} e^{-\beta(v_e^2+u^2-2v_e u)} \right) \sqrt{\frac{\pi}{\beta u v_e}}\, \text{erf}\left(\sqrt{\beta u v_e}\left(\frac{\Delta\phi}{2}\right)\right)\left(v_e^4 \frac{\Delta v}{v_e} \sin^{-1}(v_{\text{th}}/v_e)\right),$$

where n is the solar wind density, u is the bulk solar wind flow speed, v_e is the center speed of the energy passband E_e ($v_e = \sqrt{2E_e/m}$), Δv is the speed width of the energy passband, v_{th} is the thermal velocity of solar wind ions ($v_{\text{th}} = \sqrt{2k_B T/m}$), $\beta = 1/v_{\text{th}}^2$, and 'erf' is the error function ($\text{erf}(z) = \frac{2}{\sqrt{\pi}}\int_0^z e^{-t^2} dt$). The speed width of the energy passband is obtained from the FWHM of energy width as

$$\frac{\Delta v}{v} = \frac{1}{2}\left(\frac{\Delta E}{E}\right),$$

where $\Delta E/E$ (=0.085) is the SWAPI's energy resolution for solar wind protons. The effective area of the SWAPI is $A_{\text{eff}} = 1.633 \times 10^{-4}$ cm^2. The azimuthal width of the FOV for solar wind is given by

$$\Delta\phi = 30°.$$

The pseudo speed (u_p), density (n_p), and temperature (T_p) of the solar wind H^+ are found by minimizing the sum of weighted (inverse variance weighted) squares of the difference between modeled and observed count rates using the non-linear least square minimization algorithm (e.g., Levenberg-Marquardt algorithm). A simulation of SWAPI's coarse sweep for the solar wind speed of 550 km s^{-1}, density 5.27 cm^{-3}, and temperature 1×10^5 K generated using the full instrument response function is shown in Figure24 (black data points with error bar). The energy range (red dots) considered for the analytical model fit are three energy bins on the left and two on the right of the E_{peak}, where E_{peak} is the energy corresponding to the ESA bin with the highest count rates. The pseudo density, speed, and temperature of the core SW protons with their 1-σ uncertainties obtained from the analytical model fit (blue curve) are depicted in the top right corner of Figure24. As one can see, the results of the analytical fit yield reasonable results compared to the actual input conditions. The pseudo speed is close to the expected value, and the density and temperature are within acceptable ranges of the input conditions to create the I-ALiRT product at a cadence well within the requirements. Future improvements may be made to correct the values of pseudo speed, density, and temperature based on the pre-computed LUT for a range of input parameters.

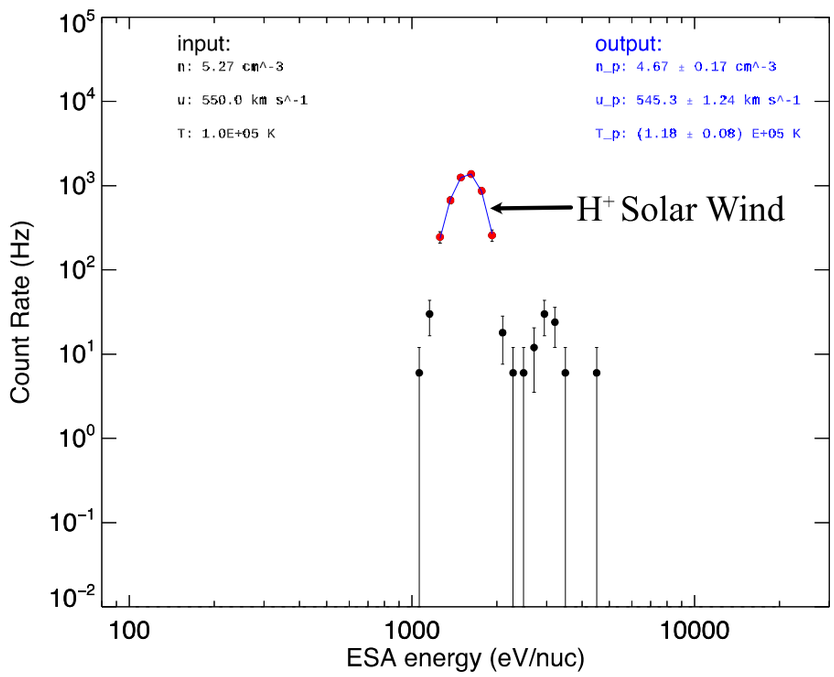


FIGURE24. SWAPI'S MODEL COUNT RATE AS A FUNCTION OF ENERGY/CHARGE FOR A 12-SECOND COARSE SWEEP. THE ANALYTICAL MODEL FIT TO THE ENERGY BINS NEAR THE PEAK COUNT RATE (RED DOTS) IS SHOWN IN BLUE.

Processing update for flight data:

- The solar wind proton parameters appear to show significant change within 5 sweeps due to S/C spin phase variation. A simple correction using 5 sweeps averaged (2 sweeps before, 2 sweeps after, and 1 current sweep) values is provided.
- The count rates in the space appear to be much higher compared to those shown in Figure 24, which made the pseudo density much higher compared to a realistic value. This systematic offset is accounted for by correcting the pseudo density by scaling it to $\frac{1}{e}$ times the 5-sweep-averaged fitted density.

15 QUICK LOOK PRODUCTS

The Quick Look products for SWAPI include

- Color-coded spectrograms of count rate as a function of energy/charge vs time. An example is provided in Figure 25.

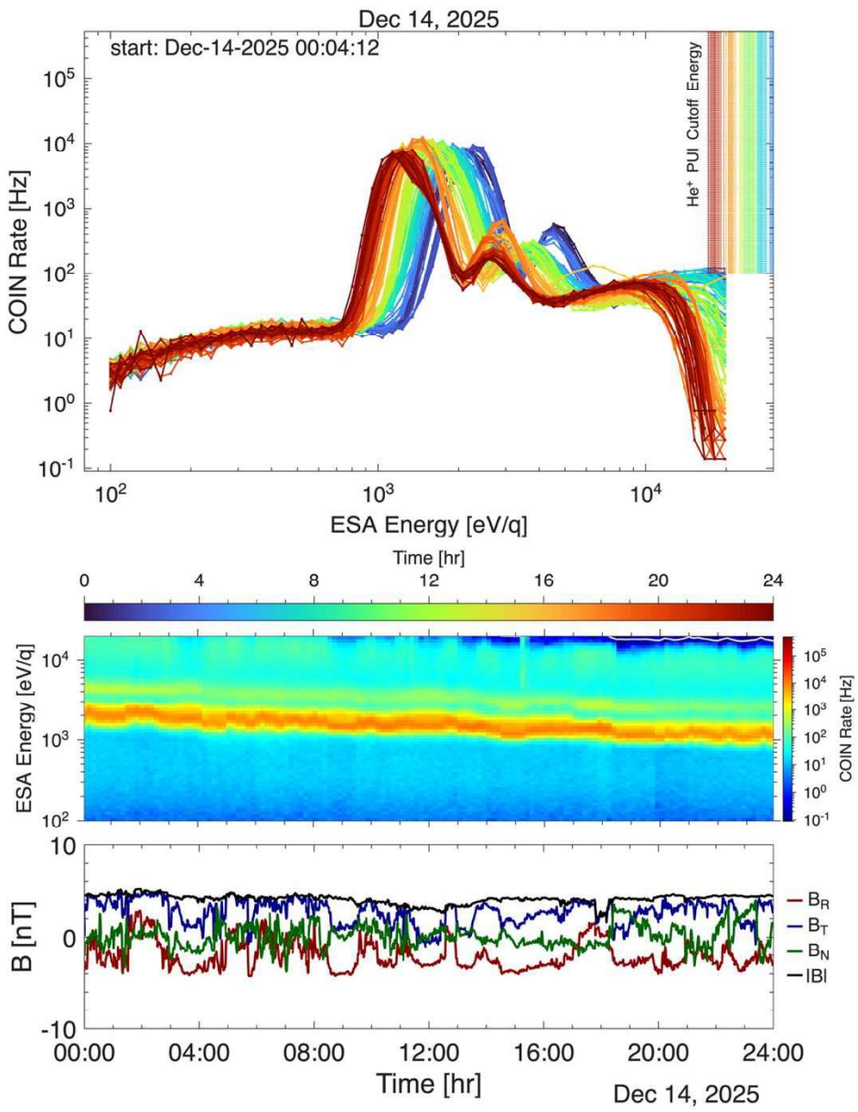


FIGURE 25. SWAPI DAILY QUICK LOOK PLOT SHOWING COINCIDENCE RATE AS A FUNCTION OF ENERGY PER CHARGE (TOP PANEL), COLOR-CODED SPECTROGRAM (MIDDLE PANEL), AND MAG L1D DATA (BOTTOM PANEL).

16 REFERENCES

Bzowski, M., Sokół, J. M., Tokumaru, M., et al. 2013, Vol. 13

Chen, J. H., Bochsler, P., Möbius, E., & Gloeckler, G. 2014, JGR, 119, 7142

Elliott, H. A., McComas, D. J., Valek, P., et al. 2016, ApJ, 223, 19

Hayes, A. F., & Cai, L. 2007, Behavior Research Methods, 39, 709

Leske, R. A., Cummings, A. C., Mewaldt, R. A., & Stone, E. C. 2013, SSRv, 176, 253

Livi, S. A., Desai, M. I., Ogasawara, K., et al. 2025, SSRv, 222, 1

Long, J. S., & Ervin, L. H. 2000, The American Statistician, 54 (Taylor & Francis), 217

MacKinnon, J. G., & White, H. 1985, Journal of Econometrics, 29, 305

McComas, D., Allegrini, F., Bagenal, F., et al. 2008, SSRv, 140, 261

McComas, D. J., Allegrini, F., Bagenal, F., et al. 2007, Sci, 318, 217

McComas, D. J., Elliott, H. A., Weidner, S., et al. 2016, JGR, 121, 4232

McComas, D. J., Shrestha, B. L., Swaczyna, P., et al. 2022, ApJ, 934, 147

McComas, D. J., Swaczyna, P., Szalay, J. R., et al. 2021, ApJS, 254, 19

Rankin, J. S., McComas, D. J., Alimaganbetov, M., et al. 2025, SSRv, 221, 108

Sokół, J. M., Bzowski, M., Tokumaru, M., Fujiki, K., & McComas, D. J. 2013, SoPh, 285, 167

Swaczyna, P., McComas, D. J., Zirnstein, E. J., et al. 2020, ApJ, 903, 48

4.2.2 CoDICE

CoDICE data product definitions and processing algorithms are embedded below

TABLE OF CONTENTS

1. INTRODUCTION 1
2. PRODUCT OVERVIEW 1
2.1 Product Description 1
2.2 Product Requirements 1
2.3 Satellite Instrument Description 2
3. BACKGROUND ON HERITAGE INSTRUMENTS 3
4. THEORETICAL DESCRIPTION 4
4.1 Physical Description 4
4.2 Angular Mappings in Sensor Coordinates 4
5. DATA PROCESSING 10
5.1 Algorithm Description 10
5.2 Processing Pipeline 11
5.3 Data Validation 11
6. DATA PRODUCTS OVERVIEW 12
7. COMMON PROCESSING ALGORITHMS/FUNCTIONS 15
8. EXAMPLE OF UNPACKING 22
9. INSTRUMENT OPERATION TIMELINE, CHANGES, AND DATA CAVEATS 22
9.1 Instrument Operation Timeline and Changes 22
9.2 Data Caveats 24
10. DATA LEVEL 1A 25
10.1 CoDICE – Common 25
10.1.1 L1A – Housekeeping Data 25
10.2 CoDICE-Hi 25
10.2.1 L1A – Hi Instrument Counters 25
10.2.2 L1A – Hi Direct Event Data 27
10.2.3 L1A – Hi Omni-Directional Species Counts 29
10.2.4 L1A – Hi Sectored Species Counts 30
10.2.5 L1A – Hi Priority Counts 31
10.3 CoDICE-Lo 32
10.3.1 L1A – Lo Instrument Counters 32
10.3.2 L1A – Lo Direct Event Data 34
10.3.3 L1A – Lo Species Counts 34
10.3.4 L1A – Lo Angular Counts 35
10.3.5 L1A – Lo Priority Counts 39
10.4 I-ALiRT 41
10.4.1 CoDICE Lo I-ALiRT 41
10.4.2 CoDICE Hi I-ALiRT 42
11. DATA LEVEL 1B 43
11.1 CoDICE-Hi 43
11.1.1 L1B – Hi Instrument Rates 43
11.1.2 L1B – Hi Omni-Directional Species Rates 43

11.1.3 L1B – Hi Sectored Species Rates ... *43*
11.1.4 L1B – Hi Priority Rates ... *44*
11.2 CoDICE-Lo ... 44
11.2.1 L1B – Lo Instrument Rates ... *44*
11.2.2 L1B – Lo Species Rates ... *45*
11.2.3 L1B – Lo Angular Rates ... *45*
11.2.4 L1B – Lo Priority Rates ... *46*
11.3 Comments ... 46

12. DATA LEVEL 2 ... 46

12.1 CoDICE-Hi ... 46
12.1.1 L2 – Hi Direct Event Data ... *46*
12.1.2 L2 – Hi Sectored Intensities ... *47*
12.1.3 L2 – Hi Omni-directional Intensities ... *48*
12.2 CoDICE-Lo ... 49
12.2.1 L2 – Lo Direct Event Data ... *49*
12.2.2 L2 – Lo Angular Intensities ... *50*
12.2.3 L2 – Lo Species Intensities ... *53*

13. DATA LEVEL 3 ... 55

13.1 CoDICE-Hi ... 55
13.1.1 L3a – Direct Event Data ... *55*
13.1.2 L3b – Pitch Angle Distributions ... *56*
13.2 CoDICE-Lo ... 56
13.2.1 L3a – Partial densities of solar wind species ... *56*
13.2.2 L3a – Elemental abundance ratios ... *58*
13.2.3 L3a – Ionization charge state ratios ... *58*
13.2.4 L3a – Ionization charge state distributions ... *58*
13.2.5 L3a – Direct Event Data ... *59*
13.2.6 L3b – 3-D Instrument Frame distributions from Event Data ... *61*
13.3 Combined Data Products ... 65
13.3.1 L3c – Combined Energy Time Spectrogram ... *65*
13.3.2 L3c – Combined Pitch Angle Distributions ... *68*

14. I-ALIRT DATA ... 71

14.1 CoDICE-Hi ... 71
14.2 CoDICE-Lo ... 72
14.2.1 Intermediate Products ... *73*
14.2.2 Forming the public data products ... *74*

15. OPERATION MODES ... 75

Appendix A Acronyms / Abbreviations ... A-1
Appendix B – CoDICE-Hi: Derivation of True Omni-directional Intensity ... B-1
Appendix C – Calculations of Spin Sector Acquisition Times ... C-1

REVISION NOTICE

Version Identifier	Date of Issue	Summary of Changes
Rev 0 Chg 0	January 2023	Initial Release
Rev 1 Chg 0	June 2025	Refined and provide additional details throughout
Rev 2 Chg 0	October 2025	**All L2 and i-ALiRT products**: Uncertainty calculation added to **Hi L2 and iAliRT products:** Value of Hi G-factor (G_k) has been updated **Lo L2 and L3b products:** Geometric factors have been updated for SW and NSW directions. **Lo L2 Angular Intensity:** An additional step in the position to elevation angle transformation has been added **L3a Hi Pitch Angles:** unit vector equations have been corrected **Added L3c Combined Energy Time spectrogram section** **Added L3c Combined Pitch Angle Distributions section** **Removed Despinning from L0 L1A Priority Counts** **Re-ordered indexing** throughout document from (inst_az x spin) to (spin x inst_az) to be consistent with Project conventions **Lo L1B products:** added conversion from voltage_table to energy_table at L1b, which provides ESA energy-per-charge **L3b Lo 3D VDFS:** updated algorithm to form normalized count array
Rev 3 Chg 0	May 2026	**i-ALiRT**: Updated acquisition time computation for conversion to rates **Lo L3a Partial Densities:** Updated equation to include proper unit conversion factor **Corrected Fe (low Q) and Fe (high Q) m/q values in L3 and i-ALiRT sections** **Section 5 & 4:** Re-organized sections **Section 9** - Added a new section to describe and track instrument operation modes, changes, and data caveats **Section 10.3.4 -** Added new ESA sweep table **Lo L1a Angular & Species Counts –** Added algorithms for assigning NaN to data based on NSO status **Lo L2 Angular & Species Intensity –** Added algorithms to determine appropriate G-factor based on RGFO status **Lo L3a Direct Events:** Updated the computation of the normalization factor **L3b Lo 3D VDFS:** updated algorithm based on new normalization matrix provided in L3a and to use APD_ID for angular binning **Spin Angle Computations –** Updated to compute spin angles relative to the $+X_{Co}$ axis during spacecraft spin phase 0. This affects all products with spin angle information (hi-sectored, hi-direct-events, hi-ialirt, lo-direct-events, lo-3D-vdfs). Updated SC-instrument coordinate offset from 316 to 46 deg.
Rev 3 Chg 1	June 2026	Removed EAR statement from cover page.

TBDs AND TBRs

This document contains information that is as complete as possible. Items that are best estimates due to a lack of final numerical values or specification references are noted **TBR** (To Be Reviewed). Items that are not yet defined are noted **TBD** (To Be Determined). The following table summarizes the TBD/TBR items in this revision of the document, and supplements the revision notice above.

Section	Title
4.4 – 4.8	Several TBDs in these work-in-progress sections

1. INTRODUCTION

The Compact Dual Ion Composition Experiment (CoDICE) combines an ElectroStatic Analyzer (ESA) with a common Time-Of-Flight (TOF) versus energy (E) subsystem (TOF-E) to simultaneously measure (1) the 3D velocity distribution functions (VDFs) and ionic charge state and mass composition of ~0.5–80 keV/q ions in CoDICE-Lo and (2) the mass composition and arrival direction of ~0.03–5 MeV / nuc ions in CoDICE-Hi (Desai et al. 2015, 2016b, 2017). These measurements are required to (1) determine the Local InterStellar Medium (LISM) composition and flow properties and (2) discover the origin of the enigmatic suprathermal tails and advance understanding of the acceleration of particles in the heliosphere. This document describes the process in going from the CoDICE raw telemetry to fully calibrated science products.

2. PRODUCT OVERVIEW

2.1 Product Description

The final data products for CoDICE cover (1) Solar Wind heavy ions, (2) Pickup Ions, and (3) suprathermal particles. The solar wind ions include 1D and 3D Velocity Distribution Functions (VDFs) for multiple species, as well as elemental composition and abundance ratios. For Pickup ions, CoDICE measures 1D and 3D VDFs of He, C, N, O, Ne, from which abundance ratios can be determined. Such ions include interstellar and inner source Pickup ions. The suprathermal particles include angular distributions and energy spectra for major species. Standard data-level definitions are used: Level 0–the raw CCSDS packets, Level 1a: Raw data decommunated into formatted variables; Level 1b –Decommutated data with counts converted to rates; Level 2–Validated science products; Level 3–Higher level science results. CoDICE Level 1 and 2 products are detailed in this document. In addition, the CoDICE instrument generates the <5 min latency product for the real-time I-ALiRT data stream.

2.2 Product Requirements

The Science Data Center (SDC) accesses data packets after each spacecraft (SC) contact along with ancillary data needed for processing and calibration. Science data are produced centrally by the SDC using algorithms, software, and calibration data provided and managed by each instrument team. The SDC maintains a version-controlled but flexible, shareable software library, and higher-level science data products are produced in the machine-independent self-describing Common Data Format (CDFs). The CoDICE products are standard CDF files usable by any standard CDF plotting software such as Autoplot, SDDAS, pySPEDAS, etc. or CAVA. The NASA Space Physics Data Facility (SPDF) is the final archive for CoDICE data along with other IMAP instruments, with the SDC being responsible for archiving, and levels of data products are transferred to the SPDF regularly and made available through their Coordinated Data Analysis Web (CDAWeb) site with final versions archived at mission closeout. The CoDICE team provides records of processed data with all relevant information on calibration and instrument properties to the NASA archive. This archive includes all raw data, calibration/conversion software, final heliospheric images, VDFs of SW ions and PUIs, validated measurements of ST ions, key parameters for selected events, and model results, along with appropriate headers and documentation.

2.3 Satellite Instrument Description

Figure 1 shows the cross section of the CoDICE 3D electro-optics model. CoDICE is comprised of two major subsystems (1) ElectroStatic Analyzer (ESA) subsystem, and (2) a shared TOF-E subsystem, with two isolated apertures for lower-energy ions (CoDICE-Lo) and higher energy ions (CoDICE-Hi).
CoDICE-Lo measures ions between ~0.5 and 80 keV/q that enter the collimated aperture (blue trajectories in Fig. 18) and are selected and focused according to their E/q onto a carbon foil at the entrance to the TOF-E subsystem. The ESA voltages step through 128 steps over 16 spacecraft spins (~4 minutes), each step selecting a particular energy per charge. The carbon foil subassembly, biased at −15 kV, accelerates the incoming ions before they strike the thin carbon foil (~1 μg/cm^2) at the entrance of the TOF-E subsystem. This interaction produces secondary electrons that are guided to the outer annulus of the Start MicroChannel Plate (MCP). Then the mostly neutralized ions traverse a flight path and strike one of 24 Avalanche PhotoDiodes (APDs; Ogasawara et al. 2016) where they generate secondary electrons that are guided to the center of the Stop MCP. The TOF between the Start and Stop MCP signals yields the ion velocity. The residual energy (E) of the neutralized ion is measured by one of the 24 azimuthally distributed APDs. The combined measurements, (E/q, TOF, and E), determine the mass (M), charge state (q), and M/q.

CoDICE-Hi measures ions between ~0.03 and 5 MeV/nuc that enter the common TOF-E subsystem through 12 separate 12° × 7° FOV collimators and total 150 nm Al-Polyimide foils (100 nm and 50 nm double foil construction) that attenuate UV light to < 0.1% and stop low-energy (< 10 keV) protons. Start and Stop MCP signals are generated by secondary electrons produced as the incident ions traverse a thin ~ 1 μg/cm^2 C foil located at the TOF-E entrance and strike one of 12 Solid State Detectors (SSDs) distributed over 360° azimuth, respectively. Each SSD, 700 μm thick with an active area of 15 × 15 mm^2, determines the ion's energy (E)). This, along with the TOF, yields the ion velocity and provides the ion mass. The secondary electrons are detected by the same MCPs shared with CoDICE-Lo, but in separate areas on the MCPs; Hi-Start electrons are guided toward the center portion of Start MCP, and Hi-Stop electrons are guided toward the outer annulus of Stop MCP. Electrons > 20 keV are identified by deposited energy and < 2 ns TOFs. CoDICE-Hi covers 1.8π sr in each spacecraft spin.

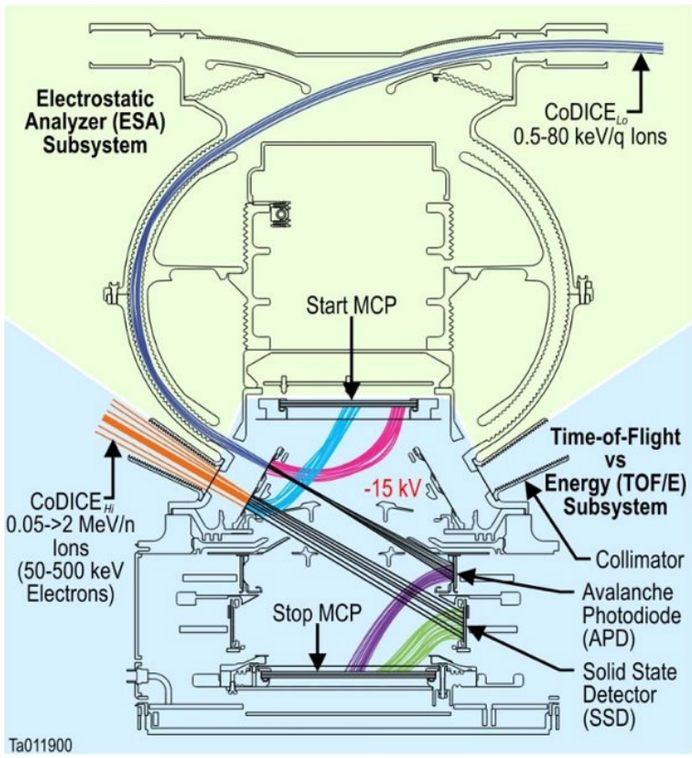


Figure 1: Principle of operation of the CoDICE. The CoDICE uses a novel compact design to measure plasma and pickup ions (CoDICE-Lo) and energetic ions (CoDICE-Hi) with a common TOF subsystem.

3. BACKGROUND ON HERITAGE INSTRUMENTS

CoDICE is a unique instrument; however, the type of data collected is similar to other missions. Therefore, portions of the CoDICE analysis are based on previous experience with Advanced Composition (ACE), Wind, Ulysses, Solar Orbiter, and Solar Terrestrial Relations Observatory (STEREO). The observables for CoDICE-Lo are like the ACE/Solar Wind Composition Spectrometer (SWICS), Ulysses/SWICS, Solar Orbiter/Heavy Ion Sensor (HIS), and STEREO/Plasma and Suprathermal Ion Composition (PLASTIC), while those for CoDICE-Hi is similar to Wind/Suprathermal through Energetic Particle Telescope (STEP) and STEREO/Suprathermal Ion Telescope (SIT).

4. THEORETICAL DESCRIPTION

4.1 Physical Description

One of the azimuth sectors for CoDICE-Lo points to the sun-direction all the time, and the sensor field-of-view rotates around the vector pointing the sun. Therefore, one sector measures the solar wind continuously, while other sectors rotate to cover the whole sky particle distributions. Thus 24 CoDICE-Lo angular sectors continuously measure 0° and 180°, ±15°, ±30°, ±45°, ±60°, ±75°, ±90°, ±105°, ±120°, ±135°, ±150°, ±165° from the sunward direction. In the formulation below, we use subscript k for these sectors and φ to represent the corresponding azimuthal angle. Channel-1 (Ch-1) denotes the sun direction, and the other channels are identified clockwise in the sensor coordinate (Ch 2 to 24 looking from the ESA side to the TOF/E; $\varphi_1 = 0°$, $\varphi_2 = 15°$,… etc.). The CoDICE-Hi has a cone shaped FOV centered 30° above the CoDICE-Lo FOV plane. Thus ±~20° from the sun direction and anti-sun direction will not be covered by the instrument. All apertures are numbered from Ch-1 to Ch-12, in terms of the angle from the Sun with the same coordinate as CoDICE-Lo: Ch-1 (180°), Ch-2 (-150°), Ch-3 (-120°), Ch-4 (-90°), Ch-5 (-60°), Ch-6 (-30°), Ch-7 (0°), Ch-8 (30°), Ch-9 (60°), Ch-10 (90°), Ch-11 (120°), Ch-12 (150°). CoDICE-Lo uses the delay-line anode measuring the signal from the Start MCP to identify the particle arrival directions in addition to the identification numbers for energy detectors, while CoDICE-Hi uses the detector ID to determine particles' arrival directions. These azimuthal IDs covers different directions in the spacecraft frame due to the spacecraft spin. The spin angle (θ) is identified with 15° resolution for CoDICE-Lo, and 30° resolution for CoDICE-Hi. These spin sectors are identified by the subscript n (i.e., θ_n).

The CoDICE-Lo ESA has typical transmission characteristics for dimensions in elevation angle and energy, while keeping an excellent azimuth angle focusing at the carbon foil locations. CoDICE-Lo relies on this focusing effect to determine the azimuthal arrival directions of particles. Based on the transmission characteristics, the energy per charge of the incident particles is selected by altering the voltage applied to the ESA. The ESA steps are identified by the subscript *l*, with each ESA step corresponding to a particular energy per charge. The entrance ESA and main ESA operate with the same voltage for the normal mode, while the entrance ESA voltage is reduced by a configurable factor (nominal is 70%) for the reduced geometric factor mode (this mode is identified as the subscript m).
Finally, the species (subscript j) are identified by the measured total energy (E_{SSD}) and the time-of-flight (τ) for CoDICE-Hi and by the measured total energy (E_{APD}), the time-of-flight (τ) and the Energy per Charge based on the ESA voltage, as detailed in this document.

4.2 Angular Mappings in Sensor Coordinates

CoDICE Instrument Frame:
In the CoDICE sensor coordinate system, the +Z axis points towards the Sun and the +X axis points from the instrument towards the spacecraft. The +Y axis completes the right-hand rule. In these coordinates, the azimuth angle (φ) is measured clockwise from the +Z axis when viewing the Y-Z plane from the +X direction (i.e., when looking towards the instrument from the spacecraft). Note that this angle is measured in the Y-Z plane, i.e. in the plane of the APD FOVs.

IMAP Spacecraft (SC) Frame:
In the de-spun SC frame, the +Z axis is the average spin vector of the spacecraft, the +X axis is the North Ecliptic Pole, and +Y completes the right hand rule.

Look Direction Unit Vectors

The tables below provide the look direction unit vectors for each APD or SSD in the CoDICE instrument frame.

Hi look direction unit vectors in Instrument Frame			
SSD ID	$\mathbf{n_x}$	$\mathbf{n_y}$	$\mathbf{n_z}$
0	-0.5	0	-0.866025
1	-0.5	0.433013	-0.75
3	-0.5	0.75	-0.433013
4	-0.5	0.866025	0
5	-0.5	0.75	0.433013
7	-0.5	0.433013	0.75
8	-0.5	0	0.866025
9	-0.5	-0.433013	0.75
11	-0.5	-0.75	0.433013
12	-0.5	-0.866025	0
13	-0.5	-0.75	-0.433013
15	-0.5	-0.433013	-0.75

Lo look direction unit vectors in Instrument Frame			
APD ID	$\mathbf{n_x}$	$\mathbf{n_y}$	$\mathbf{n_z}$
1	0	0	1
2	0	-0.258819	0.965926
3	0	-0.5	0.866025
4	0	-0.707107	0.707107
5	0	-0.866025	0.5
6	0	-0.965926	0.258819
7	0	-1	0
8	0	-0.965926	-0.258819
9	0	-0.866025	-0.5
10	0	-0.707107	-0.707107
11	0	-0.5	-0.866025
12	0	-0.258819	-0.965926
13	0	0	-1
14	0	0.258819	-0.965926
15	0	0.5	-0.866025

16	0	0.707107	-0.707107
17	0	0.866025	-0.5
18	0	0.965926	-0.258819
19	0	1	0
20	0	0.965926	0.258819
21	0	0.866025	0.5
22	0	0.707107	0.707107
23	0	0.5	0.866025
24	0	0.258819	0.965926

Azimuth Angles

The tables below provide the mapping between the position (for CoDICE-Lo) and SSD IDs (for CoDICE-Hi) and the azimuthal angles in the instrument coordinate system. The values correspond to the center of each angular bin.

Lo Azimuth Angle Mapping	
POSITION	**Azimuth Angle (φ°)**
1	0
2	15
3	30
4	45
5	60
6	75
7	90
8	105
9	120
10	135
11	150
12	165
13	180
14	195
15	210
16	225
17	240
18	255
19	270
20	285
21	300

22	315
23	330
24	345

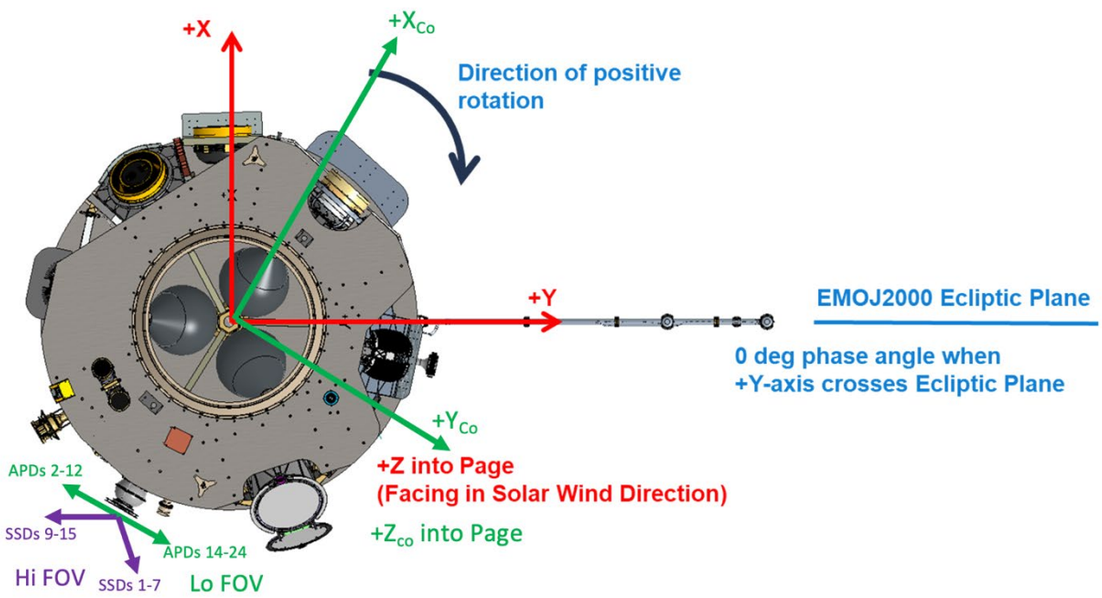
Hi Azimuth Angle Mapping	
SSD ID	**Azimuth Angle (φ_k°)**
0	180
1	210
3	240
4	270
5	300
7	330
8	0
9	30
11	60
12	90
13	120
15	150

Spin Angles

*The spin angles for the CoDICE instrument **SHOULD** be calculated using the look direction unit vectors provided above and the SPICE software with the appropriate instrument kernel. SPICE can then transform the spin angles into different desired frames, such as the spacecraft frame.*

The schematic below shows the relation between the spacecraft coordinates and CoDICE coordinates (with subscripts 'Co'). The spacecraft spin phase angle 0° is defined as the moment when the $+Y_{SC}$ axis crosses the ecliptic plane. The spin angle in the spacecraft frame is then defined as the angle from the $+X_{SC}$ axis (aligned with the north ecliptic pole) to the central look direction of the relevant detector.

Since the CoDICE instrument coordinate system rotates as the spacecraft spins, the spin angle in instrument coordinates is computed relative to a fixed reference direction defined as the direction of the $+X_{Co}$ axis at spacecraft spin phase angle 0°. The offset angle between $+X_{SC}$ and $+X_{Co}$ at spacecraft spin phase angle 0° is ~46.0°. With these definitions, the spin angle in CoDICE coordinates for both Lo and Hi are computed below. The CoDICE L1 angular data for both Hi and Lo are binned into spin angle bins, identified by a spin sector index (n) ranging from 0 to 11 for Hi (30° bins) and 0 to 23 for Lo (15° bins).



Lo:
The FOV of APDs 1 and 13 is perpendicular to the X-Y plane and thus, spin angle for these APDs is meaningless. With this in mind, the physical spin angles for Lo in sensor coordinates can be calculated from the spin sector index as follows:

$$\theta_{Lo,n} = n * 15° + 277.5°, \qquad \text{APD} = 1 - 24$$

Here, $\theta_{Lo,n}$ is the physical spin angle corresponding to the center of the angular bin in sensor coordinates. ***Note, this equation assumes that the data has been 'de-spun' and that the spin angle index corresponds to the physical angle measured spanning 360° (see Section 10.3.4 for de-spinning algorithm).***

Hi:
For CoDICE-Hi the calculation is more involved due to the 30° inclination of the SSD FOVs relative to the FOV plane of the Lo APDs. For a given Hi spin sector index (n) the physical spin angle measured is different for each SSD, and depends on the SSD azimuthal angle φ_k. The Hi spin angles for each SSD can be calculated by first computing the spin angles for spin index 0 and then incrementing by 30°.

For the Hi spin sector index $n = 0$ and SSD k, the spin angles are calculated as:

$$\theta_{Hi,0,k} = 180° + tan^{-1}\left(\frac{n_{y,k}}{n_{x,k}}\right) + 15°$$

Here, $n_{y,k}$ and $n_{x,k}$ are the y and x components of the Hi look direction unit vectors in instrument coordinates for SSD k (see table above). These values correspond to the center of the spin angle bin. The spin angles for the remaining spin sectors are calculated by incrementing the sector $n = 0$ values by 30° for each SSD. The table below provides the calculated spin angles for Hi SSD. The values correspond to the center of each angular bin.

Hi Spin Angles (deg) in the Instrument Frame												
	Spin Sector Index (30 degree bins)											
SSD ID	**0**	**1**	**2**	**3**	**4**	**5**	**6**	**7**	**8**	**9**	**10**	**11**
0	195.00	225.00	255.00	285.00	315.00	345.00	15.00	45.00	75.00	105.00	135.00	165.00
1	154.11	184.11	214.11	244.11	274.11	304.11	334.11	4.11	34.11	64.11	94.11	124.11
3	138.69	168.69	198.69	228.69	258.69	288.69	318.69	348.69	18.69	48.69	78.69	108.69
4	135.00	165.00	195.00	225.00	255.00	285.00	315.00	345.00	15.00	45.00	75.00	105.00
5	138.69	168.69	198.69	228.69	258.69	288.69	318.69	348.69	18.69	48.69	78.69	108.69
7	154.11	184.11	214.11	244.11	274.11	304.11	334.11	4.11	34.11	64.11	94.11	124.11
8	195.00	225.00	255.00	285.00	315.00	345.00	15.00	45.00	75.00	105.00	135.00	165.00
9	235.89	265.89	295.89	325.89	355.89	25.89	55.89	85.89	115.89	145.89	175.89	205.89
11	251.31	281.31	311.31	341.31	11.31	41.31	71.31	101.31	131.31	161.31	191.31	221.31
12	255.00	285.00	315.00	345.00	15.00	45.00	75.00	105.00	135.00	165.00	195.00	225.00
13	251.31	281.31	311.31	341.31	11.31	41.31	71.31	101.31	131.31	161.31	191.31	221.31
15	235.89	265.89	295.89	325.89	355.89	25.89	55.89	85.89	115.89	145.89	175.89	205.89

Spin Angle in SC Coordinates:

At spacecraft spin phase angle 0°, the $+X_{Co}$ axis is is offset by ~46.0° relative to the $+X_{SC}$ axis. Thus, the conversion of spin angle from the instrument coordinates to SC coordinates is given by:

$$\theta_{SC} = (\theta_{inst} + 46°)\ mod\ 360°$$

Here, mod is the modular arithmetic function. This applies to spin angles for both Hi SSDs and Lo APDs.

Note, the elevation angle in the instrument frame is equivalent to elevation angle in the SC frame.

5. DATA PROCESSING

5.1 Algorithm Description

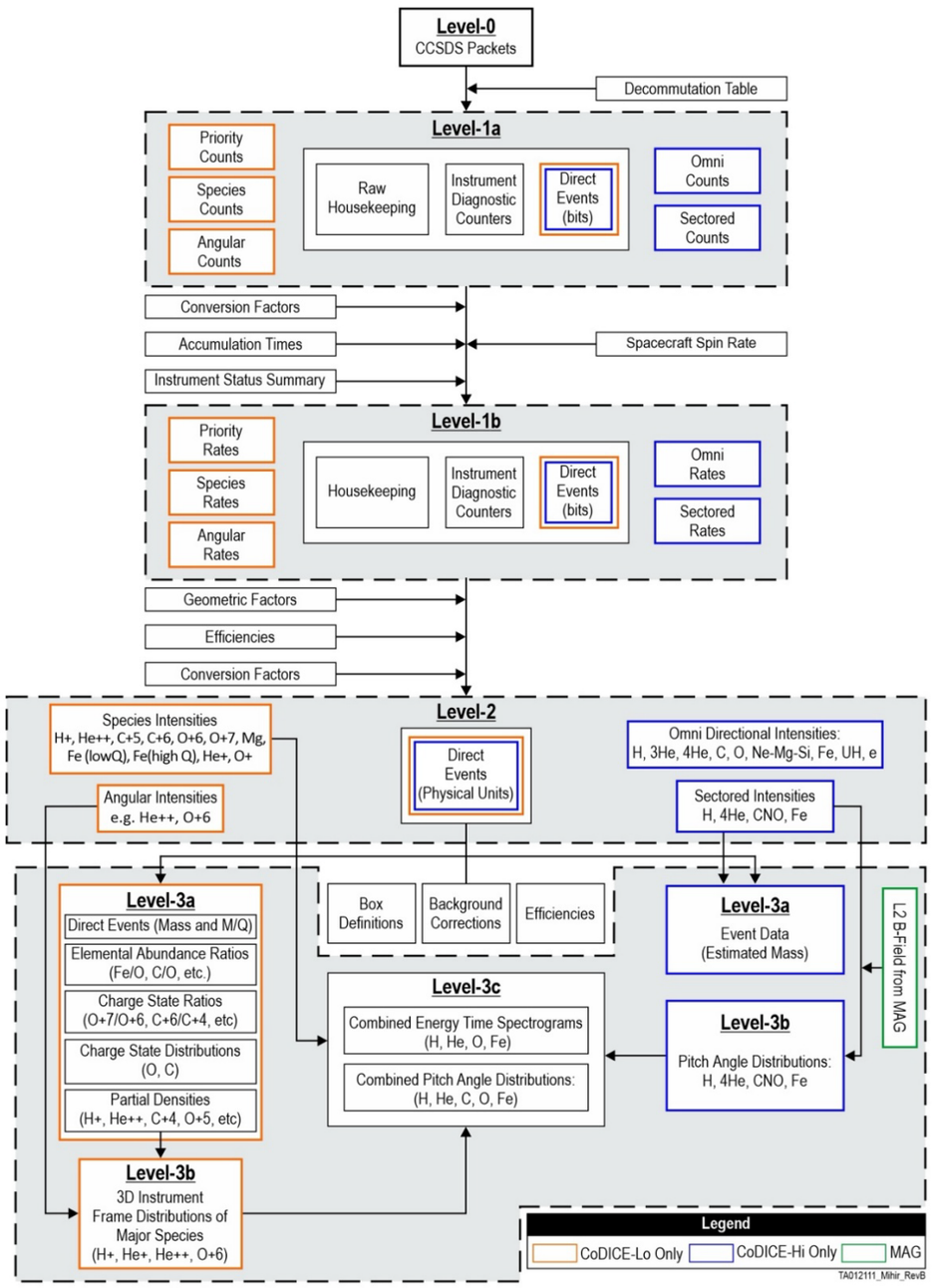


Figure 2: Processing Outline

Due to the complexity of the instrument, a spreadsheet is **required** to decode the packets on the ground. Every data packet has four identification (ID) fields (Table_ID, Plan_ID, Plan_Step, View_ID) that must be used in tandem to determine how the data is collapsed onboard the spacecraft. Each event that CoDICE-Hi and CoDICE-Lo observes will be processed through a set of lookup tables (LUT) which are contained in excel spreadsheets along with the corresponding bins that are used to determine the outputs of each LUT.

5.2 Processing Pipeline

Raw telemetry data (L0) is converted from its native CCSDS packets to various levels of science data. The level 1A (L1A) data is the decommutated version of the L0 data and stored in CDF files and are used as the basis for all further levels. Level 1 data are separated into housekeeping/engineering and science data. To create level 1B (L1B) data, conversion factors are applied to the housekeeping/engineering data, and accumulation times and spacecraft spin rates are applied to the science data to produce rates. Geometric factors, efficiencies, and other conversion factors are applied to L1B data to convert it to physical units to produce the L2 data. Within the L2 data, specific species are identified and separated into different CDF variables. L2 is considered the lowest level usable for science analysis. Level 3 (L3) products use Event data to create additional species products and combine Hi and Lo variables to produce distribution functions. Box definitions, background corrections, and efficiencies are applied where needed.

5.3 Data Validation

Before launch, each data product and processing algorithm was validated independently and in multiple stages using synthetic data. First, data products were developed internally at SwRI and validated through an independent set of codes by comparing each data variable point-by-point to ensure exact matches. Once internally validated, the IMAP Science Data Center used this algorithm document to produce each product on their own. These products were once again compared point-by-point to the internally validated products from SwRI.

After the IMAP launch, the data pipeline was re-validated using flight data both internally at SwRI and between files produced at SwRI and the SDC.

6. DATA PRODUCTS OVERVIEW

Table 1: CoDICE L1 Data Products – for L1a, the data is in raw counts and for L1B products, the data is in rates (Hz (TBR)).

IMAP Level-1 Products			
Sensor(s)	**Product**	**Description**	**File Prefix**
CoDICE	Housekeeping	Instrument Voltages, Currents and Digital Settings.	imap_codice_l1[ab]_hskp_
CoDICE-Lo	Instrument Counters	Engineering Rates (e.g. start rate, stop rate, coincidence rates).	imap_codice_l1[ab]_lo-counters-aggregated_ imap_codice_l1[ab]_lo-counters-singles_
CoDICE-Lo	Direct Events	Full information (e.g. Energy, time-of flight) on individual events.	imap_codice_l1[ab]_lo-direct-events_
CoDICE-Lo	Species Counts/Rates	Counts/Rates for key species. There will be a separate file for sunward (sw) and non-sunward (nsw) facing data.	imap_codice_l1[ab]_lo-[n]sw-species_
CoDICE-Lo	Priority Counts/Rates	Number of events within defined ranges. Used for normalizing the direct events. There will be a separate file for sunward (sw) and non-sunward (nsw) facing data.	imap_codice_l1[ab]_lo-[n]sw-priority_
CoDICE-Lo	Angular Counts/Rates	Counts/Rates for key species binned by spin angle and position. There will be a separate file for sunward (sw) and non-sunward (nsw) facing data.	imap_codice_l1[ab]_lo-[n]sw-angular_
CoDICE-Hi	Instrument Counters	Engineering Rates (e.g. start rate, stop rate, coincidence rates).	imap_codice_l1[ab]_hi-counters-aggregated_ imap_codice_l1[ab]_hi-counters-singles_
CoDICE-Hi	Direct Events	Full information (e.g. Energy, time-of flight) on individual events.	imap_codice_l1[ab]_hi-direct-events_
CoDICE-Hi	Priority Counts	Number of events within defined ranges. Used for normalizing the direct events.	imap_codice_l1[ab]_hi-priority_
CoDICE-Hi	Omni-Directional Counts/Rates	Omni-Directional Counts/Rates for key species.	imap_codice_l1[ab]_hi-omni_
CoDICE-Hi	Sectored Counts/Rates	Counts/Rates for key species. Contains both sectored rates and omni-directional rates.	imap_codice_l1[ab]_hi-sectored_

Table 2: CoDICE L2 Data Products - primary science products for public consumption.

IMAP Level-2 Products			
Sensor(s)	**Product**	**Description**	**File Prefix**
CoDICE-Lo	Species Intensities	Differential Intensity for H+, He+, He++. C+5, C+6, O+, O+6+ O+7, Mg, Fe.	imap_codice_l2_lo-[n]sw-species_
CoDICE-Lo	Angular Intensities	Differential Intensity for key species binned by spin angle and instrument azimuth. Species are He++, O+6, C+5, Fe+10, and PUI He+.	imap_codice_l2_lo-[n]sw-angular_
CoDICE-Lo	Direct Events	Full information (e.g. Energy, time-of flight) on individual events in physical units.	imap_codice_l2_lo-direct-events_
CoDICE-Hi	Omni-directional Intensities	Omni-directional Intensities for H, 3He, 4He, C, O, Ne-Mg-Si, Fe, UH.	imap_codice_l2_hi-omni_
CoDICE-Hi	Sectored Intensities	Intensities for H, 4He, CNO, Fe.	imap_codice_l2_hi-sectored_
CoDICE-Hi	Direct Events	Full information (e.g. Energy, time-of flight) on individual events in physical units.	imap_codice_l2_hi-direct-events_

Table 3: CoDICE L3 Data Products

IMAP Level-3 Science Products			
Sensor(s)	**Product**	**Description**	**File Prefix**
CoDICE-Lo	Direct Events	Full information (e.g. Energy, time-of flight) on individual events, along with mass-per-charge and mass of each event estimated using calibration data.	imap_codice_l3a_lo-direct-events_
CoDICE-Lo	SW 3D Instrument Frame Distributions	Intensity as a function of azimuthal sector, spin sector, and energy in the instrument frame computed from Direct Event data.	imap_codice_l3a_lo-<species>-3d-distribution_
CoDICE-Lo	SW Elemental Abundance ratios	Key SW elemental abundance ratios computed from partial density product (C/O, Mg/O, Fe/O).	imap_codice_l3a_lo-sw-ratios_
CoDICE-Lo	SW Charge state ratios	Key SW charge state ratios computed from partial density product (O^{+7}/O^{+6}, C^{+6}/C^{+4}, C^{+6}/C^{+5}, Fe^{low}/Fe^{high}).	imap_codice_l3a_lo-partial-densities_
CoDICE-Lo	SW Charge state distributions	Relative abundances of the charge states for SW Oxygen and Carbon computed from partial density product.	imap_codice_l3a_lo-sw-charge-state-distributions_
CoDICE-Hi	Pitch Angle Distributions	Intensity as a function of pitch angle and energy for H, ^{4}He, O, and Fe	imap_codice_l3_hi-pitch-angle_
CoDICE-Hi	Direct Events	Full information (e.g. Energy, time-of flight) on individual events, along with E/n and mass of each event estimated using calibration data.	imap_codice_l3_hi-direct-events_
CoDICE-Lo CoDICE-Hi	Combined Energy Time Spectrograms	Intensity as a function of energy and time for H, He, O, and Fe	

Table 4: CoDICE iALiRT Data Products

IMAP iALiRT Data			
Sensor(s)	**Product**	**Description**	**File Prefix**
CoDICE-Hi	Omni directional species rates	H at 1 minute resolution.	imap_ialirt_l1_realtime
CoDICE-Lo	SW Matrix Rates	Abundance ratios of SW species products C/O, Mg/O, Fe/O, c6+/c5+, O7+,/O6+, Fe_loq/Fe_hiq	imap_ialirt_l1_realtime

7. COMMON PROCESSING ALGORITHMS/FUNCTIONS

All L0 data is written with a CCSDS header that looks like the following:

Mnemonic	Start Byte	Start Bit in Byte	Start Bit	Length In Bits	Description
PHVERNO	0	0	0	3	CCSDS Packet Version Number (always 0)
PHTYPE	0	3	3	1	CCSDS Packet Type Indicator (0=telemetry)
PHSHF	0	4	4	1	CCSDS Packet Secondary Header Flag (always 1)
PHAPID	0	5	5	11	CCSDS Packet Application Process ID
PHGROUPF	2	0	16	2	CCSDS Packet Grouping Flags (3=not part of group)
PHSEQCNT	2	2	18	14	CCSDS Packet Sequence Count (increments with each new packet)
PHDLEN	4	0	32	16	CCSDS Packet Length (number of bytes after Packet length minus 1)
SHCOARSE	6	0	48	32	S/C Time [seconds] Whole-seconds part of SCLK

Every subsequent byte is different depending on what product is being read. For the actual definitions, one must use the spreadsheet that describes the packet. What is listed in this document are the mnemonic needed to define the product, the maximum length in bits, and a description of the field.

CoDICE science products are packed using an extremely flexible packing algorithm that can be decided post launch. Table_ID is meant to capture different configurations so if we make changes to the table (e.g. update a View configuration to change compression settings), the Table_ID would be increased. This ID is reported in all the science telemetry packets so one will know which version of the spreadsheet to refer to when processing the data.

Additionally, the decoding algorithm is based upon an initial plan id that is further subdivided into various plan steps. For CoDICE-Lo, the sweep table defines the voltage steps that are used to cover the full energy per charge range. The stepping table defines how many voltage steps and which steps are used during each spacecraft spin. A full cycle takes 16 spins. The *plans* define which sweep table, and which stepping table was used. These are extremely important when computing the timing information for each step.

To reduce the required telemetry, many of the science data products do not use the full angular resolution. Some combine all angles (omni-directional), some combine adjacent angles, and some only use a subset of the angles. This is called "collapsing" the science products. To determine how the science products are collapsed on board the spacecraft, one must use the *views* to determine how to unpack the data blobs.

Although the collapsing can be configured post-launch, all collapsed regions must be "rectangular". This means that regions that are collapsed must be adjacent to one another in the collapse table and not randomly distributed. Furthermore, it is agreed that if the array size of the regions to be collapsed are changed, a new data product will be created.

CoDICE Direct Event Data packets are organized as follows:

Mnemonic	Description
Packet_Version	Packet version. Incremented each time the format of the packet changes.
Spin_Period	Spin period reported by the Spacecraft in the Time and Status message. Reported period is the period that was active when the 16-spin acquisition cycle started.
Acq_Start_Seconds	Full-seconds portion of the time at which the 16-spin cycle started
Acq_Start_Subseconds	Sub-seconds portion of the time at which the 16-spin cycle started
Spare_1	Strictly for alignment.
ST_Bias_Gain_Mode_Flag	Indicates whether FSW is tracking the Suprathermal High-Gain bias curve or the Low-Gain bias curve. (Not used for CoDICE-Hi)
SW_Bias_Gain_Mode_Flag	Indicates whether FSW is tracking the Solarwind High-Gain bias curve or the Low-Gain bias curve. (Not used for CoDICE-Hi)
Priority	The priority included in this packet.
Num_Events	Number of events selected for downlink (i.e. number of events in the Event_Data array)
Compressed	Whether the event data is compressed. If this value is a 1, then the Event_Data array is compressed using the Rice compression algorithm.
Byte_Count	Number of bytes in the Event_Data array. If compressed, this value represents the length of the compressed data.
Event_Data	Optionally compressed array of Event Data - Full events have a lot of redundant data (e.g. will have many events with the same priority/spin/spin phase information). How well does compression to deal with the redundancy? - Could include mini-headers for each (priority, spin, spin-phase) group and strip the redundant data from the events

Mnemonic	Description
RGFO_Half_Spin*	Indicates the point when Reduced Gain Factor Operation (RGFO) was activated. In RGFO, the Entrance ESA voltage is reduced in order to limit the number of ions that reach the detectors. (Not used for CoDICE-Hi)
RGFO_esa_step*	Indicates the ESA step at which RGFO limit is exceeded. RGFO mode is activated for all ESA steps after this value.
RGFO_spin_sector*	Indicates the spin sector at which RGFO limit is exceeded. RGFO mode is activated for spin sectors after this value.
NSO_Half_Spin*	Indicates the point when No-Scan Operation (NSO) was activated. In NSO, the ESA voltage is set to the first step in the scan and remains fixed until the next cycle boundary. (Not used for CoDICE-Hi)
NSO_esa_step*	Indicates the ESA step at which NSO limit is exceeded. NSO mode is activated after this ESA step.
NSO_ spin_sector*	Indicates the spin sector at which NSO limit is exceeded. NSO mode is activated for all spin sectors after this value.

* These variables were added after the FSW update that occurred on 01/29/2026

All other CoDICE science packets (except for direct events) have the following organization:

Mnemonic	Description
Packet_Version	Packet version. Incremented each time the format of the packet changes.
Spin_Period	Spin period reported by the Spacecraft in the Time and Status message. Reported period is the period that was active when the 16-spin acquisition cycle started.
Acq_Start_Seconds	Full-seconds portion of the time at which the 16-spin cycle started
Acq_Start_Subseconds	Sub-seconds portion of the time at which the 16-spin cycle started
Spare	
ST_Bias_Gain_Mode_Flag	Indicates whether FSW is tracking the Suprathermal High-Gain bias curve or the Low-Gain bias curve. (Not used for CoDICE-Hi)
SW_Bias_Gain_Mode_Flag	Indicates whether FSW is tracking the Solarwind High-Gain bias curve or the Low-Gain bias curve. (Not used for CoDICE-Hi)
Table_ID	Unique ID assigned to a specific table configuration. This field is used to link the overall acquisition and processing settings to a specific table configuration.
Plan_ID	Plan table that was in use
Plan_Step	Plan step that was active when this data was acquired and processed.

Mnemonic	Description
View_ID	View ID provides information about how data was collapsed and/or compressed.
RGFO_Half_Spin	Indicates the point when Reduced Gain Factor Operation (RGFO) was activated. In RGFO, the Entrance ESA voltage is reduced in order to limit the number of ions that reach the detectors. (Not used for CoDICE-Hi)
NSO_Half_Spin	Indicates the point when No-Scan Operation (NSO) was activated. In NSO, the ESA voltage is set to the first step in the scan and remains fixed until the next cycle boundary. (Not used for CoDICE-Hi)
Spare	
Data_Quality_Flag	Indicates that there was some error detected during acquisition or processing of the data. Errors could include corrupted acquisition memory (i.e., EDAC errors), timing violations, or other events that interrupted or otherwise affected data collection.
Compression_Flag	How the data array is compressed: 0 – No Compression 1 – Lossy A Compression 2 – Lossy B Compression 3 – Lossless (LZMA) Compression 4 – Lossy A + Lossless Compression 5 – Lossy B + Lossless Compression
Byte_Count	Number of bytes in the data array. If compressed, this value represents the length of the compressed data.
RGFO_esa_step*	Indicates the ESA step at which RGFO limit is exceeded. RGFO mode is activated for all ESA steps after this value.
RGFO_spin_sector*	Indicates the spin sector at which RGFO limit is exceeded. RGFO mode is activated for spin sectors after this value.
NSO_esa_step*	Indicates the ESA step at which NSO limit is exceeded. NSO mode is activated after this ESA step.
NSO_ spin_sector*	Indicates the spin sector at which NSO limit is exceeded. NSO mode is activated for all spin sectors after this value.

* These variables were added after the FSW update that occurred on 01/29/2026

For items with a *Byte_Count* field, this represents the length of the variable data array. If the data array is compressed, it contains the compressed length, and the uncompressed length is up to the maximum length in bits defined below.

Data format is a series of spin-angle x position x spin number data cubes collapsed per the SCI_LUT Collapse Table selected by the View_ID. Which counters are included is determined by using the Plan_ID and Plan_Step to index into the SCI_LUT Data Products Hi/Lo tables to find all the counters that are associated with the View_ID.

The collapsed data cubes are also optionally compressed using Lossy and/or Lossless Compression. Lossy compression is a table-based 24->8-bit compression applied to each counter value. Lossless compression uses the LZMA compression algorithm and is applied to the full Data field as a single unit.

Field will additionally be padded in order to meet the requirement of packets being a multiple of 16 bits and any pad bits will be accounted for in the CCSDS header Length field, but will *not* be included in the Byte_Count field

When this array is too large for a single CCSDS packet, CoDICE will utilize the CCSDS Grouping flags to provide the full data packet over several CCSDS packets.

When written to a CDF file, an Epoch variable is written in CDF_TT2000 format which is the start time of the acquisition. This is the combination of Acq_Start_Seconds and Acq_Start_Subseconds. For variables with an accumulation period, a DELTA_EPOCH_PLUS is written with the units of seconds.

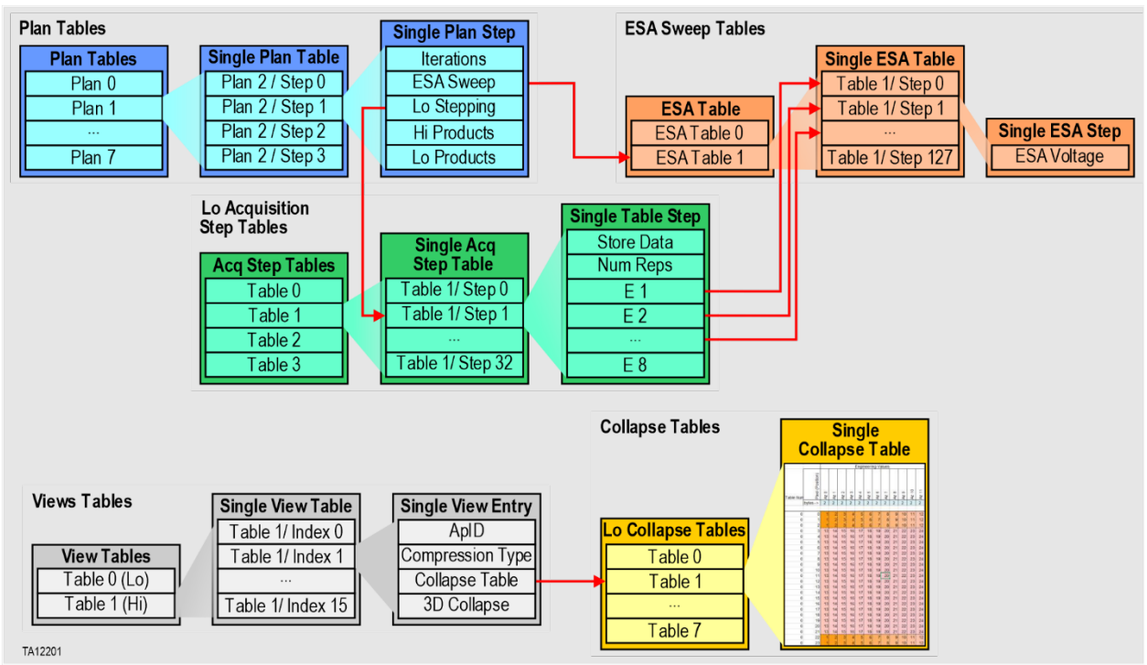


Figure 3 - Flow diagram for unpacking the science data

The following algorithm can be used to decommutate and unpack the science data. This is dependent on the SCI_LUT spreadsheet to interpret:

1) Given "Plan ID" and "Plan Step" from the telemetry packet, look up the appropriate entry in the plan table:

   PlanTables [plan ID][plan_step]

This gives a single-row record consisting of the following values:

Iterations	Number of times the step is repeated; don't care for ground processing
ESA Sweep	Which ESA Sweep table was used (0 or 1) (index into ESA Sweep table). For nominal operations, we will only use sweep table 0, descending in energy.
Lo Stepping	Which Lo Stepping table was used (0 through 4) (index into Lo Stepping table)
Hi Products	Which Data Products – Hi table is used. For nominal operations, this will be 0, but can be changed.
Lo Products	Which Data Products – Lo table is used. For nominal operations, this will be 0, but can be changed.

2) For energies acquired at each step:

Use the "ESA Sweep" index from the Plan Step entry to select the appropriate table from the ESA Sweep table. Table consists of 128 entries, where each entry is the voltage that corresponds to an energy step. These voltages can be mapped to energies by multiplying by the k-factor and dividing by 1000 to go into keV/e units. **The k-factor is currently 5.76.**

3) For acquisition time of each step:

Use the "Lo Stepping" index from the Plan Step entry to select the "Lo Stepping" table.

To look up the timing for a given energy step, find the row of the step table that includes the step number, and index across to the "Acq Time (including Sector Margin)" column. The value in this column is the acquisition time, in milliseconds, for the energy step.

4) To unpack science data blobs:

From the "View ID" from the telemetry packet, one must use the “Data Products – Lo” or “Data Products – Hi” and search for the View ID in the Engineering Values portion. If the number appears in any row of four columns, a packet of that type is in the data. From here. look up the appropriate row in the "Views" table. This will give you a record with the following fields:

1) APID - Expected APID of the packet (could use as a sanity check, but otherwise not important for ground processing)
2) Compression
   - None
   - Lossy A/B Only (table-based log compression)
   - Lossless Only
   - Lossless + Lossy
3) Collapse Table - Index into the "Collapse_Hi" or "Collapse_Lo" tables

4) Uncompress the data:
    a. If lossless compressed, apply LZMA decompression.
    b. If lossy compressed, apply table-based decompression (reverse-compression based on center of compression regions)
    c. If both, do the lossless decompression first, and then undo the lossy compression.
5) Extract the data:
    a. Lo (APIDs: 0x480-0x48F)
        i. Data blobs consist of 128 frames, representing the 128 energy steps.
        ii. Frames started as matrices of [12 (spin angle) x 24 (position)].
        iii. Use the "Collapse Table" entry from the View Table entry to index into the Collapse_Lo table.
    b. Hi (APIDs: 0x490-0x49F)
        i. Data blobs consist of 192 frames, representing the 192 counters.
        ii. Each frame is a matrix of [*n* spins x 24 spin angles x 16 azimuths]
        iii. Use the "Collapse Table" entry from the View Table entry to index into the Collapse_Hi table.
        iv. Use the “3D Collapse” to know how many spins went into the matrix.
6) Based on the Collapse Table ID, the index into Collapse_Lo or Collapse_Hi will determine what data product in being extracted and how it will be written into the CDF file. For the L1A data, no transformations will be done with the data, except to write the Electrons as the subtraction of the Flashed – Unflashed data.

5) Timing Information for each Energy Step:

Number of populated eV entries in a single row of the acquisition step table determines how many ESA steps (num_acq_steps) are taken during a half-spin while the row is active.

Given the following parameters, the acquisition time can be computed:

- Number of Steps (unitless)
- Number of Spin Sectors (unitless)
- Spin Period (microseconds)
- Sector margin (milliseconds)
- Dwell Fraction (percentage)
- Minimum HV Settle Time (milliseconds)
- Maximum HV Settle Time (milliseconds)

```
sector_time_us = spin_period_us / num_sectors
total_non_acquire_time_us = sector_time_us * (100 - dwell_fraction_pct) / 100
total_hv_settle_time_us = total_non_acquire_time_us - sector_margin_us
hv_settle_time_per_step_us = total_hv_settle_time_us / num_acq_steps
hv_settle_time_per_step_us = min (hv_settle_time_per_step_us, max_hv_settle_us)
acq_time_per_step_us = (((sector_time_us - sector_margin_us) / num_acq_steps) –
                                        hv_settle_time_per_step_us)
```

8. EXAMPLE OF UNPACKING

Table_ID is 1, Plan_ID is 0, Plan_Step is 0, and View_ID is 3:

With Table_ID of 1, we use version 1 which is 26850.03-SCI-LUT-01.xls.
With Plan_ID of 0, we will look at Plan tab and see Plan 0 is on rows 7-10. With Plan_Step of 0, we will use row 7 meaning Iterations is 1, ESA Sweep 0, Lo Stepping of 0, and Hi/Lo products of 0.
With an ESA Sweep of 0, we will use the ESA Sweep Table 0, which has 128 energies decreasing in voltage in the ESA Sweep tab.
For a sweep step of 74, and a Lo Stepping of 0, we will use row 28 of the Lo Stepping tab. This gives us an acquisition time of 118.75 ms.

To unpack the science data, we will go to the Views tab and for Lo data, go to row 10 based on a View_ID of 3. This means the data is both lossy and lossless compressed and uses collapse table of 3.

We must first uncompress the data and then from the Collapse_Lo tab, use the SW Angular Counts table which is table number 3. This shows that we will write 128 E/q steps x 12 spin sectors x 5 positions in the imap_codice_l1a_lo-angular CDF with the variable “SunwardAngularCounts”.

9. INSTRUMENT OPERATION TIMELINE, CHANGES, AND DATA CAVEATS

This section describes the nominal operation of the instrument and provides a timeline for changes to the operation that took place throughout commissioning.

9.1 Instrument Operation Timeline and Changes

RGFO Mode: In the reduced geometric factor operation (RGFO) mode, the ratio of voltages applied to the upper and lower portion of the CoDICE ESA is reduced (normally the ratio is 1). This reduces the number of ions that are able to pass through the ESA section, thereby reducing the count rate on the Lo MCPs. In the launch-configuration operation of the instrument, the flight software (FSW) monitors the total counts measured by the START-A and START-B MCP over the course of a half-spin of the spaceraft (~7.5 s). If these total counts surpass a limit (tunable via onboard LUTs), then the instrument enters RGFO mode on the next half-spin and remains in RGFO until either NSO mode is triggered or the end of the current 32 half-spin cycle. Changes to the RGFO implementation that occurred throughout commissioning are described in the table below.

NSO Mode: In the no-scan operation (NSO) mode, the ESA voltage is set to the highest value (esa step 0) and remains at that value until the end of the current 32 half-spin cycle. In the launch configuration operation of the instrument, NSO can only be triggered while the instrument is in RGFO mode. To trigger NSO, the FSW monitors the total counts measured by the START-A and START-B MCP over the course of a half-spin. If these total counts surpass a limit (tunable via onboard LUTs), then the instrument enters NSO mode on the next half-spin and remains in NSO mode until the end of the current 32 half-spin cycle. Changes to the NSO implementation that occurred throughout commissioning are described in the table below.

Period Number	Date Range	Description of Instrument Operation
P0	Launch - 11/24/2025	- RGFO triggers on total counts accumulated over half spin. If limit is surpassed, instrument enters RGFO mode on next half spin - When in RGFO mode, NSO triggers on total counts accumulated over half spin. If limit is surpassed, instrument enters NSO mode on next half spin
P1	11/24/2025 – 12/18/2025	- RGFO limit is reduced so that RGFO always triggers on half spin 0. However, ESA voltage ratio remains 1 so that the instrument does not actually operate with reduced G-factor. - NSO mode still triggers on half spin boundaries.
P2	12/18/2025 – 01/29/2026	- ESA sweep table is updated so that only 3 ESA steps are sampled per half-spin starting at ESA step 80 (576 V, 3.3 keV/e) - RGFO and NSO implementation is the same as during P1
P3	01/29/2026 – 04/03/2026	FSW Update: - RGFO and NSO now trigger based on count rates measured during a single ESA step and spin sector. Trigger is based on count rate rather than total counts. Count rates are monitored at each ESA step and spin sector pair and mode switch is implemented during the following ESA step spin sector pair o Additional fields added to all COUNTS and PHA science packets: ▪ RGFO half-spin (already in COUNTS packets, only added to PHA) ▪ RGFO spin-sector ▪ RGFO e-step ▪ NSO half-spin (already in COUNTS packets, only added to PHA) ▪ NSO spin-sector ▪ NSO e-step - HI/LO Priority Counts packets are no longer lossy-compressed (lossless only) - Swapped Fe highQ/lowQ labels o Affects: ▪ View 0: Lo – IALiRT (label swap) ▪ View 5: Lo – SW Species Counts (label swap) ▪ View 7: Lo – SW Angular Counts (changed selected species) • Data prior to the v1.5 FSW load were sending Species 13 (SW – Fe highQ, but was labeled as Fe lowQ) • Data after the v1.5 FSW load will send Species 14 (SW – Fe lowQ) - Enabled 2 additional species for Lo Angular Counts: o SW – He+ (View 7, ApID 0x486) o NSW – He+ (View 8, ApID 0x487)

		- Increased PHA allocation o Lo: 5,760 -> 11,520 events per cycle o Hi: 5,000 -> 10,000 events per cycle - Updated Hi Priority Scheme o P5 = Heavies, P4 = Helium, P3 = Protons.
P4	04/03/2026 – Current*	- Lo SCI_LUT update o Fixed indexing issue that resulted in species rates being assigned to the wrong rate box. - Lo onboard species classification LUT update o Refined mass boundaries for key species o Binned H+ data now consists of TCRs only (was DCRs during P0 – P3) - Hi onboard species classification LUT update o Corrected bug that was sending low tof events to low priority

*Current in reference to the date of this document publication. Check with instrument team for real-time updates.

9.2 Data Caveats

Due to issues identified post-launch, the following CoDICE-Lo data products are not currently being produced at all levels (L1a – L2): *lo-nsw-species, lo-sw-angular, lo-nsw-angular*.

The table below summarizes known caveats that should be considered when using CoDICE L2 data products. **This table applies to all data included in the first official IMAP data release in Summer 2026**. Note, that most of these issues will be fixed or mitigated in future data releases.

CoDICE L2 Products	Description of Caveat	Effects on Data
l2_lo-sw-species	Counts are binned into SW/NSW products using delay-line position instead of APD ID	Lower counts than expected --> lower intensity values
	Species classification boxes need to be fine tuned	Charge state species are not well separated/identified
l2_lo-direct-events	Delay-line position is not an accurate identifier of particle direction	Position should only be used to support APD ID
	Automatic tof correction based on position	Larger uncertainty in tof measurement
l2_hi-omni	Detection threshold depends on SSD ID	Increased noise at lower energies
	ASIC baseline fluctuates based on countrate, resulting in pseudo-TCRs for low energy data	Increased noise/false counts at lower energies
	Onboard mass computation needs correction	Mass tracks trend downward at low energy-per-nuc

	MG and LG energy channels not well calibrated	Higher energy portion of MG channel is usable. Lower energy portion of MG channel is not currently usable. LG channel is currently not usable.
l2_hi-sectored	Detection threshold depends on SSD ID	Increased noise at lower energies
	ASIC baseline fluctuates based on countrate, resulting in pseudo-TCRs for low energy data	Increased noise/false counts at lower energies
	Onboard mass computation needs correction	Mass tracks trend downward at low energy-per-nuc
	MG and LG energy channels not well calibrated	Higher energy portion of MG channel is usable. Lower energy portion of MG channel is not currently usable. LG channel is currently not usable.
l2_hi-direct-events	MG and LG energy channels not well calibrated	Higher energy portion of MG channel is usable. Lower energy portion of MG channel is not currently usable. LG channel is currently not usable.

10. DATA LEVEL 1A

10.1 CoDICE – Common

10.1.1 L1A – Housekeeping Data

Housekeeping data is broken up into two packets: one for relatively static definitions that are needed when the instrument is powered on, and a second for nominal housekeeping which has the standard housekeeping data such as voltages and currents.

These are written as raw values directly from the L0 packets from the P_COD_NHK packet.

10.2 CoDICE-Hi

10.2.1 L1A – Hi Instrument Counters

There are two instrument counters packets for CoDICE-Hi: singles and aggregated. They are packed identically but decoded differently. For the aggregated packet, all spin sectors for all SSDs are summed into a single value for the double coincidence rates (DCR), start only (STO), stop only (SPO), multi-start (MST), and ASIC 1 and 2 invalid flag events. For the singles packet, the triple coincidence rates (TCR), SSD only (SSDO), and start plus SSD (STSSD) events are summed for every spin sector but stored per SSD ID (array of 12). The final counter data packets are summed over 16 spins.

Mnemonic		Max Length in Bits	Description
Data	2949120	Counter Data Variable Length - Maximum (based on uncollapsed, uncompressed data, and assuming all counters included): 16 spins x 16 positions x 24 spin-sectors x 32 bits x 15 counters = 2,949,120 bits (368,640 bytes) Nominal (based on current plan for counter selection, collapsing, and compression): 840 bits (106 bytes)	

The data is then unpacked into the following variables:

Rate Type	Rate #	Instrument Rate
0	0:15	Event A – Triple Coincidence Rate (TCR)
1	0	Event B – Double Coincidence Rate (DCR)
2	0	Event C – Start Only (STO)
3	0	Event D – Stop Only (SPO)
4	0:15	Event E – SSD Only (SSDO)
5	N/A	Reserved
6	0:15	Event G – Start + SSD (STSSD)
7	0	Event H – Multi Start (MST)
8:11	N/A	Reserved
12	0	Low TOF Cutoff
13:14	N/A	Reserved
15	0:1	ASIC [1:2] Flag Invalid Count
	2:3	ASIC [1:2] Channel Invalid Count

These are written as raw values directly from the L0 packets from the P_COD_HI_INST_COUNTERS_AGGREGATED and P_COD_HI_INST_COUNTS_SINGLES packets. This packet may change to include additional counters to account for efficiencies. The event type letters correspond to different possible event detections (e.g. DCR, TCR, etc.). Where the Rate # is listed as 0:15, these are stored in the singles packet ordered by SSD id. The others are stored in the aggregated packet.

10.2.2 L1A – Hi Direct Event Data

The event data will be based on what is defined in the P_COD_HI_PHA packet. The Hi direct events are in the Event_Data subsection and are defined as follows:

Number of Bits	Description
11	SSD Energy
10	TOF
4	SSD ID
2	Energy Range
1	Multi-Flag
2	PHA Type
5	Spin Sector (0-23)
4	Spin Number
3	Priority
22	Spare

Note, although there are only 12 SSDs, the SSD ID values range from 0 – 15. In the original instrument design, four of the 12 SSDs were planned to be dual-pixel to measure electrons, hence there were 16 SSD IDs. This was not implemented in the flight instrument, but the software still reflects these 16 SSD ID values. The valid SSD IDs are: 0, 1, 3, 4, 5, 7, 8, 9, 11, 12, 13, 15. The remaining four values are not valid.

The energy range bit defines which gain mode the event was detected in. The table below provides the mapping.

Energy Range Bit Value	Gain Mode
0	No energy
1	Low Gain
2	Mid Gain
3	High Gain

The event data packet will have all six priorities (0-5) and will share a single epoch. Based on the priority, they will each be written to separate CDF variables with its corresponding timestamp. Each of these can have up to 10000 events per packet and this is determined on board the spacecraft. The variables are named <variable name>. The variables are stored as UINT1, except for SSD Energy and TOF which are stored as UINT2. Additionally, the number of events from the Num_Events field and data quality from the Suspect field should be written to the CDF per priority number.

Each ion that triggers a START in CoDICE-Hi and is followed by a single STOP signal within 512 nanoseconds is counted as a "VALID STOP" event. Each "VALID STOP" event that is accompanied by a coincidence with the solid-state detector amplifier is a VALID TCR EVENT is counted and analyzed by the system. Each VALID STOP event that is **not** accompanied by a coincidence with the solid-state detector amplifier is a VALID DCR EVENT. Finally, an event for which there is a small TOF is measured in coincidence with the solid-state detector amplifier is a VALID SSD EVENT.

Each valid event is formatted into a Pulse-Height-Analysis (PHA) event whose contents are shown in the tables below. There are three types of PHA events:

1) TCR: START + STOP + SSD
2) DCR: START + STOP + no SSD
3) SSD: SSD only

TCR EVENT (A)	TOF	Energy	E Range	Spin Sector	SSD-ID	spin count	PHA type
bins (resolution)	1024	2048	3	12	16	16	3
bits	10	11	2	4	4	4	2

DCR EVENT (B)	TOF	Energy	E Range	Spin Sector	SSD-ID	spin count	PHA type
bins (resolution)	1024	1	1	12	1	4	3
bits	10	0	0	4	0	2	2

SSD EVENT (E)	TOF	Energy	E Range	Spin Sector	SSD-ID	spin count	PHA type
bins (resolution)	1	2048	3	12	16	4	3
bits	0	11	2	4	4	2	2

10.2.3 L1A – Hi Omni-Directional Species Counts

The table below provides a description of the raw un-collapsed *L1A Omni Counts* data packet.

Mnemonic	Max Length in Bits	Description
Data	28704768	Counter Data Variable Length - Maximum (based on uncollapsed, uncompressed data, and assuming all 146 sqrt(2) species counters included): 16 spins x 16 positions x 24 spin-sectors x 32 bits x 146 counters = 28,704,768 bits (3,588,096 bytes) Nominal (based on current plan for counter selection, collapsing, and compression): 42,240 bits (5,281 bytes)

The counts will be stored in a single CDF file as a different variable for every species and will be based on what is defined in the P_COD_HI_OMNI_SPECIES_COUNTS packet.

For the nominal case, the species being stored will be: H, He3, He4, C, O, Ne/Mg/Si, Fe, UH, and unknown. The CDF will need to contain the energy table for each of these species with the centers and their plus/minus delta.

The final *L1A Omni Counts* data product for each species is formed from the raw data packet by summing the counts over all spin sectors and SSD IDs. The total counts are provided as a function of energy-per-nuc in bins with logarithmic spacing of sqrt(2). In the nominal configuration, the counts are summed over every 4 spins and provided at a cadence of 1 min. Since the number of spins for a full sweep is 16, there are 4 values stored per species in the raw data packet. The dimensions of the *L1A Omni Counts* for species (j) is:

$$\mathrm{C_j}(i) - \text{ (rt2 spaced energy-per-nuc bins)} \quad \text{[counts]}$$

Here, the subscript j corresponds to ion species and i is the energy bin index. Note, the number of energy-per-nuc bins varies between species.

The uncertainty in counts is also provided as a separate variable. These are computed as:

$$\sigma_{\mathrm{j}}(i) = \sqrt{\mathrm{C_j}(i)}$$

In the CDF for this product the geometric center of each energy-per-nuc bin along with the delta between the center and upper/lower values of each energy bin are provided in units MeV/n. Thus, the passband of each energy-per-nuc bin (E_i) is given by:

$$\Delta \mathrm{E}_i = E_{i,minus} + E_{i,plus}$$

Here $E_{i,plus}$ and $E_{i,minus}$ have cdf variable names:

energy_<species>_delta_plus and *energy_<species>_delta_minus*

10.2.4 L1A – Hi Sectored Species Counts

The table below provides a description of the raw un-collapsed *L1A Sectored Counts* data packet.

Mnemonic	Max Length in Bits	Description
Data	9043968	Counter Data Variable Length - Maximum (based on uncollapsed, uncompressed data, and assuming all x2 species counters included): 16 spins x 16 positions x 24 spin-sectors x 32 bits x 46 counters = 9,043,968 bits (1,130,496 bytes) Nominal (based on current plan for counter selection, collapsing, and compression): 4672 bits (584 bytes)

The counts will be stored in a CDF file with each species being a different CDF variable organized by energy, SSD position, and spin sector. The data will be based on what is defined in the P_COD_HI_SECTORED_COUNTS packet.

For the nominal case, the species being stored will be: H, He3He4, CNO, and Fe. The CDF will need to contain the energy table for each of these species with the centers and their plus/minus delta.

The raw L0 Sectored Counts are accumulated into 12 spin sector bins (30° spin angle resolution) and summed over every 16 spins (4 min cadence). The *L1A Sectored Counts* data product for each species is provided as a function of energy-per-nuc with logarithmic bin spacing of 2. The dimensions of the *L1A Sectored Counts* for species (j) is:

$\mathrm{C_j}(i,n,k)$ – (*x2*-spaced energy-per-nuc bins, 12 spin sectors, 12 SSD IDs) [counts]

Here, the subscript j corresponds to ion species, i is the energy bin index, k is the SSD ID index, and n is spin sector index.

The uncertainty in counts is also provided as a separate variable. These are computed as:

$$\sigma_{\mathrm{j}}(i,k,n) = \sqrt{\mathrm{C_j}(i,n,k)}$$

In the CDF for this product the geometric center of each energy-per-nuc bin along with the plus/minus delta values of each energy bin are provided in units MeV/n. Thus, the passband of each energy-per-nuc bin (E_i) is given by:

$$\Delta \mathrm{E}_i = E_{i,minus} + E_{i,plus}$$

Here $E_{i,plus}$ and $E_{i,minus}$ have cdf variable names:

energy_<species>_delta_plus and *energy_<species>_delta_minus*

10.2.5 L1A – Hi Priority Counts

Mnemonic	Max Length in Bits	Description
Data	9437184	Counter Data Variable Length Nominal (based on current plan for counter selection, collapsing, and compression): 840 bits (105 bytes) Data format is a series of (spin-angle * position * spin number) data cubes collapsed per the SCI_LUT collapse table selected by the view ID. Which counters are included is determined by using the plan ID and plan step to index into the SCI_LUT data products Hi/Lo table to find all the counters that are associated with the view ID. In the nominal case, data is summed across all the spin angles and there are 6 priorities.

In the nominal case, when writing to CDF, the data will be written as a single value per time step with each priority (0-7) being its own variable.

This data is taken from a P_COD_HI_PRIORITY_COUNTS packet.

10.3 CoDICE-Lo

10.3.1 L1A – Lo Instrument Counters

Mnemonic	Max Length In Bits	Description
Data	1179648	Counter Data Variable Length - Maximum (based on uncollapsed, uncompressed data, and assuming all 24 rates are included): 128 ESA-steps x 24 rates x 12 spin sectors x 24 bits = 884,736 bits (110,592 bytes) In the current configuration, this product combines adjacent spin-angles, so there are only 6 spin sectors in the final product. When this array is too large for a single CCSDS packet, CoDICE will utilize the CCSDS Grouping flags to provide the full data packet over several CCSDS packets.

There are two types of CoDICE-Lo counters packets: COD_LO_INST_COUNTS_AGGREGATED and COD_LO_INST_COUNTS_SINGLES. The AGGREGATED includes a variety of different rates, as shown below. The SINGLES packet contains the rates from the 24 APD detectors.

For the aggregated counts, the data is unpacked identically to other CoDICE-Lo packets, but then the data is then unpacked into **a selection** of the following variables:

Rate Type	Instrument Rate
0	Event A – Triple Coincidence Rate (TCR)
1	Event B – Double Coincidence Rate (DCR)
2	Event C – TOF + APD
3	Event D – TOF Only
4	Event E – Position + APD
5	Event F – Position Only
6	Event G – STA or STB + APD
7	Event H – STA or STB Only
8	Reserved
9	Reserved
10	Event K – SP Only
11	Event L – APD Only
12	Low TOF Cutoff

13	Singles – Start-A (STA)
14	Singles – Start-B (STB)
15	Singles – Stop (SP)
16	Singles – APD [1:24]
17	Singles – Total Position Count
18	Singles – Invalid Position Count
19	Reserved
20	ASIC 1 Flag Invalid Count
21	ASIC 2 Channel Invalid Count
22	ASIC 1 Flag Invalid Count
23	ASIC 2 Channel Invalid Count
24	TEC-4 Timeout Count – TOF, No Position
25	TEC-4 Timeout Count – Position, No TOF
26	TEC-4 Timeout Count – No Position or TOF
27	TEC-5 Timeout Count – TOF, No Position
28	TEC-5 Timeout Count – Position, No TOF
29	TEC-5 Timeout Count – No Position or TOF

To know which of the rates were written, the SCI_LUT spreadsheet must be used and the Collapse_Lo table #1 will have a non-zero value in the table. The non-zero value in the table refers to where in the array the value is written. Since this is configurable, the CDF file which contains this information must have all the variables defined, but only the returned values will be filled. For whatever rate is returned, the 180° of spin angles will be divided up into 30° bins (6 spin-sector pairs) with the full 128 energies returned.

For nominal configuration, there are 6 rates returned in the AGGREGATED packet. They are:

Rate Type	Instrument Rate
0	Event A – Triple Coincidence Rate (TCR)
1	Event B – Double Coincidence Rate (DCR)
13	Singles – Start-A (STA)
14	Singles – Start-B (STB)
15	Singles – Stop (SP)
16	Singles – Total Position Count

Thus, the dimensions of the nominal AGGREGATED packets are 128 ESA-steps x 6 rates x 6 spin-sectors.

For the singles counters packet, the data is unpacked identically to other CoDICE-Lo packets, but the data will have the rates from the 24 APD detectors. Thus, the dimensions of the nominal SINGLES packet are 128 ESA-steps x 24 rates x 6 spin-sectors.

10.3.2 L1A – Lo Direct Event Data

The event data will be based on what is defined in the P_COD_LO_PHA packet. The Lo direct events are in the Event_Data subsection and are defined as follows:

Number of Bits	Description
1	APD Gain
5	APD ID
5	Position
9	APD Energy
10	TOF
1	Multi-Flag
2	PHA Type
5	Spin Sector
7	ESA Step
3	Priority
16	Spare

The packet will have all eight priorities (0-7) and will share a single epoch. Based on the priority, they will each be written to separate CDF variables with its corresponding timestamp. Each of these can have up to 10000 events per packet and this is determined on board the spacecraft. The variables are stored as UINT1, except for APD Energy and TOF which are stored as UINT2. Additionally, the number of events from the Num_Events field and data quality from the Suspect field should be written to the CDF per priority number.

10.3.3 L1A – Lo Species Counts

Mnemonic	Max Length in Bits	Description
Data	1179648	Counter Data Variable Length; Maximum (based on uncollapsed, uncompressed data, and assuming all 32 species-counters included): 128 ESA-steps x 24 positions x 12 spin sectors x 32 bits x 32 counters = 37,748,736 bits (4,718,592 bytes) Realistically, data is aggressively collapsed and compressed, and only a subset of the 32 species counters will be included, so this data field will be much smaller than the maximum.

The data is collapsed over spin sectors and instrument azimuthal angle (positions) onboard the spacecraft resulting in two values for each energy. Five of the azimuth angles (apd_id = 1, 2, 3, 23, 24) are collapsed together for a sunward product and the remaining 19 angles are collapsed together for a non-sunward product. Since the spacecraft spin axis is sun-facing, these angle assignments remain constant and are separated onboard the spacecraft and telemetered down as separate products.

For each species id, two different 128 ESA-steps x 1 position CDF variables are written; one for sunward, one for non-sunward and the data is from the P_COD_LO_SW_SPECIES_COUNTS and P_COD_LO_NSW_SPECIES_COUNTS packets for sunward and non-sunward products respectively.

There are 16 sunward species correspond to H+, He++, O+5, O+6, O+7, O+8, C+4, C+5, C+6, Ne, Mg, Si, Fe(low Q) and Fe(high Q), He+ and the combined group of C+, N+ and O+.
There are 8 non-sunward species, corresponding to H+, He++, O5-8, C4-6, Ne+Mg+Si, Fe, He+ and CNO+.

NSO Implementation: These rules dictate what data should be assigned fill values due to NSO mode.
Launch – 11/24/2025:
The NSO_Half_Spin variable identifies the half-spin number (0-31) during which the NSO threshold limit was triggered. The instrument enters NSO mode on the following half-spin. Thus, the data for all ESA steps, spin sectors, and positions measured during half-spin numbers greater than the NSO_Half_Spin value should be set to NaN.
11/24/2025 – 01/29/2026:
The NSO_Half_Spin variable identifies the half-spin number (0-31) during which the NSO threshold limit was triggered. The instrument enters NSO mode on the following half-spin. Thus, the data for all ESA steps, spin sectors, and positions measured during half-spin numbers greater than the NSO_Half_Spin value should be set to NaN.
01/29/2026 – Current:
The Lo L1A product now contains variables that indicate the esa step and spin sector during which the RGFO or NSO limits are triggered. Since the NSO mode activates at a specific ESA step and spin sector within a given half-spin the summed counts are not representative of the true ion population being measured. Thus, we assign NaN's to all data acquired during half-spins greater than or equal to NSO_half_spin.

i.e., For half_spin >= NSO_half_spin → set all data to NaN

The uncertainty in counts for both SW and NSW products is provided as separate variables and computed by taking the square root of the counts, e.g.,

$$\sigma_j(l) = \sqrt{\mathrm{C_j}(l)}$$

10.3.4 L1A – Lo Angular Counts

Mnemonic	Max Length in Bits	Description
Data	37748736	Counter Data Variable Length; Maximum (based on uncollapsed, uncompressed data, and assuming all 32 species-counters included):

Mnemonic	Max Length in Bits	Description
		128 ESA-steps x 24 positions x 12 spin-sectors x 32 bits x 32 counters = 37,748,736 bits (4,718,592 bytes) Realistically, data is aggressively collapsed and compressed, and only a subset of the 32 species counters will be included, so this data field will be much smaller than the maximum.

Data is written as a 3-D data cube with energy moving the slowest. The spin angle is written first and then moving up in instrument angle. For each of these 2D matrices (spin angle x instrument angle), one is written for every energy. The data is arranged on board the spacecraft using the mechanism shown in Figure 1. This can be changed on board; this means the correct table ID must be referenced to analyze the measurements.

Sunward and non-sunward products are separated onboard the spacecraft and telemetered down as different products. Furthermore, not all species have a sunward and non-sunward product.

The un-packed Angular Counts data arrays for species j, esa step l, position k, and spin angle index n, have dimenions of:

SW: – (128 ESA-steps x 12 spin sector x 5 positions)
NSW – (128 ESA-steps x 12 spin sector x 19 positions)

NSO Implementation: These rules dictate what data should be assigned fill values due to NSO mode.
Launch – 11/24/2025:
The NSO_Half_Spin variable identifies the half-spin number (0-31) during which the NSO threshold limit was triggered. The instrument enters NSO mode on the following half-spin. Thus, the data for all ESA steps, spin sectors, and positions measured during half-spin numbers greater than the NSO_Half_Spin value should be set to NaN.
11/24/2025 – 01/29/2026:
The NSO_Half_Spin variable identifies the half-spin number (0-31) during which the NSO threshold limit was triggered. The instrument enters NSO mode on the following half-spin. Thus, the data for all ESA steps, spin sectors, and positions measured during half-spin numbers greater than the NSO_Half_Spin value should be set to NaN.
01/29/2026 – Current:
The Lo L1A product now contains variables that indicate the esa step and spin sector during which the RGFO or NSO limits are triggered. The data spin_sector variable ranges from 0-11 and is the instrument reported spin sector. Note that the rgfo_spin_sector and nso_spin_sector variables correspond to a full spin (rather than half spin) and range from 0 – 23. Thus, when comparing the spin_sector variable to the nso_spin_sector variable, the nso_spin_sector should be mod 12. The following algorithm defines when to assign NaN to the angular data product due to NSO operation:

1. For half_spin > NSO_half_spin → set all data to NaN
2. For half_spin = NSO_half_spin
    a. For spin_sector > NSO_spin_sector → set all data to NaN

b. For spin_sector = NSO_spin_sector
    i. For esa_step > NSO_esa_step → set all data to NaN

ESA Stepping Scheme and Spin Sectors vs Spin Angles

Since the CoDICE-Lo FOV covers the full sky over the course of a single half-spin of the spacecraft, the data is accumulated onboard at this half-spin cadence for a total of 32 half-spins. With each half-spin, different ESA voltage steps are sampled. The tables below provides the ESA steps that are sampled during each half-spin for different time periods throughout the mission. The pixel orientation refers to the orientation of the APD FOVs relative to the beginning of a full spin. So, the spin angles measured for a given APD are offset by 180° between orientation A and B. Since the data is accumulated at the half-spin cadence, spin sector values of 0 – 11 are always reported regardless of pixel orientation. This must be accounted for when forming the angular rate arrays. From here on, Lo spin sectors shall correspond to the spin index bin relative to each half-spin (ranging from 0 – 11). Spin angle shall correspond to the physical spin angle that is measured (ranging from 0° - 360° or 0 – 23 indices).

CoDICE-Lo ESA stepping scheme: Launch – 12/18/2025							
Half Spin Number	**Pixel Orientation**	**ESA Step**					
0	A	0	-	-	-	-	-
1	B	1	-	-	-	-	-
2	A	2	-	-	-	-	-
3	B	3	-	-	-	-	-
4	A	4	5	-	-	-	-
5	B	6	7	-	-	-	-
6	A	8	9	-	-	-	-
7	B	10	11	-	-	-	-
8	A	12	13	14	-	-	-
9	B	15	16	17	-	-	-
10	A	18	19	20	-	-	-
11	B	21	22	23	-	-	-
12	A	24	25	26	27	-	-
13	B	28	29	30	31	-	-
14	A	32	33	34	35	-	-
15	B	36	37	38	39	-	-
16	A	40	41	42	43	44	-
17	B	45	46	47	48	49	-
18	A	50	51	52	53	54	-
19	B	55	56	57	58	59	-
20	A	60	61	62	63	64	-
21	B	65	66	67	68	69	-
22	A	70	71	72	73	74	-
23	B	75	76	77	78	79	-
24	A	80	81	82	83	84	85
25	B	86	87	88	89	90	91
26	A	92	93	94	95	96	97
27	B	98	99	100	101	102	103
28	A	104	105	106	107	108	109
29	B	110	111	112	113	114	115

30	A	116	117	118	119	120	121
31	B	122	123	124	125	126	127

CoDICE-Lo ESA stepping scheme: 12/18/2025 - Current							
Half Spin Number	**Pixel Orientation**	**ESA Step**					
0	A	0	-	-	-	-	-
1	B	1	-	-	-	-	-
2	A	2	-	-	-	-	-
3	B	3	-	-	-	-	-
4	A	4	5	-	-	-	-
5	B	6	7	-	-	-	-
6	A	8	9	-	-	-	-
7	B	10	11	-	-	-	-
8	A	12	13	14	-	-	-
9	B	15	16	17	-	-	-
10	A	18	19	20	-	-	-
11	B	21	22	23	-	-	-
12	A	24	25	26	27	-	-
13	B	28	29	30	31	-	-
14	A	32	33	34	35	-	-
15	B	36	37	38	39	-	-
16	A	40	41	42	43	44	-
17	B	45	46	47	48	49	-
18	A	50	51	52	53	54	-
19	B	55	56	57	58	59	-
20	A	60	61	62	63	64	-
21	B	65	66	67	68	69	-
22	A	70	71	72	73	74	-
23	B	75	76	77	78	79	-
24	A	80	81	82	-	-	-
25	B	83	84	85	-	-	-
26	A	86	87	88	-	-	-
27	B	89	90	91	-	-	-
28	A	92	93	94	-	-	-
29	B	95	96	97	-	-	-
30	A	98	99	100	-	-	-
31	B	101	102	103	-	-	-

De-spinning Algorithm

Once unpacked, the L0 data arrays consist of counts as a function of 128 ESA Steps x 5/19 positions x 12 spin sectors. Note that the 5/19 positions correspond to the sunward or non-sunward packets. The 5 positions in the SW array correspond to positions 1, 2, 3, 23 and 24. The 19 positions in the NSW array correspond to positions 4 through 22. Each data array corresponds to a 4-min accumulation over the course of 32 half-spins. This data needs to be reformatted into the final angular counts array which consists of counts as a function of 128 ESA Steps x 24 spin angles x 5/19 positions. The table below provide the mapping from spin sector index in the L0 product to spin angle index in the L1A product.

Half Spin Parity (even/odd)	Pixel Orientation	Positions	L0 Spin Sector IDs	L1A Spin Angle IDs	SW Position Index	NSW Position Index
Even	A	1 - 12	0-11	0-11	0-2	0-9
Even	A	13 - 24	0-11	12 - 23	3-4	10-18
Odd	B	1 - 12	0-11	12 - 23	0-2	0-9
Odd	B	13 - 24	0-11	0-11	3-4	10-18

Once the data has been de-spun into the 128 ESA Steps x 24 spin angle indices x 5/19 positions array, the spin angle indices now correspond to the physical spin angle measured which covers the full 360°.

The final L1A Angular Counts data arrays, $C_j(l,n,k)$, for species j, esa step l, position k, and spin angle index n, have dimenions of:

SW: – (128 ESA-steps x 24 spin angle x 5 positions)
NSW – (128 ESA-steps x 24 spin angle x 19 positions)

The uncertainty in counts is provided as a separate variable, computed as:

$$\sigma_j(l,k,n) = \sqrt{\mathrm{C_j}(l,k,n)}$$

All data is from the P_COD_LO_SW_ANGULAR_COUNTS and P_COD_LO_NSW_ANGULAR_COUNTS packets for sunward and non-sunward products respectively.

10.3.5 L1A – Lo Priority Counts

Mnemonic	Max Length in Bits	Description
Data	9437184	Counter Data Variable Length; Maximum (based on uncollapsed, uncompressed data, and assuming all 8 priority-counters included): 128 ESA-steps x 24 positions x 12 spin-sectors x 32 bits x 8 counters = 9,437,184 bits (1,179,648 bytes) Realistically, data is aggressively collapsed and compressed, and only a subset of the 32 species counters will be included, so this data field will be much smaller than the maximum.

Data is written as a 3D data cube as shown in Figure 4 with energy moving the slowest. The spin sector is written first and then moving up in instrument angle. One 2D matrix (spin sector x instrument angle) is written for every E/q step. Some angles are summed together on board the spacecraft using the mechanism shown in Figure 2. The collapsing method can be changed on board so the correct table ID must be referenced.

The final L1A Priority Counts are summed over all positions and the final data arrays have dimenions of:

SW & NSW – (128 ESA-steps x 12 spin-sectors)

When writing to CDF, the data will be written as a 128 ESA- step x 12 spin sector array with each priority (0-7) being its own variable.

This data is taken from a P_COD_LO_PRIORITY_COUNTS packet.

NSO Implementation: These rules dictate what data should be assigned fill values due to NSO mode.
Launch – 11/24/2025:
The NSO_Half_Spin variable identifies the half-spin number (0-31) during which the NSO threshold limit was triggered. The instrument enters NSO mode on the following half-spin. Thus, the data for all ESA steps, spin sectors, and positions measured during half-spin numbers greater than the NSO_Half_Spin value should be set to NaN.
11/24/2025 – 01/29/2026:
The NSO_Half_Spin variable identifies the half-spin number (0-31) during which the NSO threshold limit was triggered. The instrument enters NSO mode on the following half-spin. Thus, the data for all ESA steps, spin sectors, and positions measured during half-spin numbers greater than the NSO_Half_Spin value should be set to NaN.
01/29/2026 – Current:
The Lo L1A product now contains variables that indicate the esa step and spin sector during which the RGFO or NSO limits are triggered. The data spin_sector variable ranges from 0-11 and is the instrument reported spin sector. Note that the rgfo_spin_sector and nso_spin_sector variables correspond to a full spin (rather than half spin) and range from 0 – 23. Thus, when comparing the spin_sector variable to the nso_spin_sector variable, the nso_spin_sector should be mod 12. The following algorithm defines when to assign NaN to the angular data product due to NSO operation:

3. For half_spin > NSO_half_spin → set all data to NaN
4. For half_spin = NSO_half_spin
    a. For spin_sector > NSO_spin_sector → set all data to NaN
    b. For spin_sector = NSO_spin_sector
        i. For esa_step > NSO_esa_step → set all data to NaN

10.4 I-ALiRT

The I-ALiRT data is packed identically to the regular science data except that it is transmitted differently. An I-ALiRT packets for both Lo and Hi will have the same CCSDS header and then the following:

Mnemonic	Max Length in Bits	Description
SHCOARSE	32	Spacecraft time in seconds
ACQUISITION_TIME	32	Spacecraft time at the end of the acquisition cycle. All packets for a given cycle will have the same acquisition time.
STATUS	8	Data Quality / Status
COUNTER	8	Counter to indicate which block of data is included in this packet. Values 0 – 231 indicate valid data. Values of 231 – 239 indicate fill data (0xFF).

10.4.1 CoDICE Lo I-ALiRT

After the COUNTER, the packet will have the following fields:

Mnemonic	Max Length in Bits	Description
DATA_00	8	Data byte
DATA_01	8	Data byte
DATA_02	8	Data byte
DATA_03	8	Data byte
DATA_04	8	Data byte
DATA_05	8	Data byte
DATA_06	8	Data byte
DATA_07	8	Data byte
DATA_08	8	Data byte
DATA_09	8	Data byte
DATA_10	8	Data byte
DATA_11	8	Data byte
DATA_12	8	Data byte
DATA_13	8	Data byte
DATA_14	8	Data byte
SPARE_0	8	Spare for alignment
CHECKSUM	16	Checksum

We assume the Plan ID, Plan Step, and View ID are all 0, so from the views tab of the SCI_LUT, all I-ALiRT packets for Lo will be Lossy A + Lossless compressed.
Onboard the spacecraft, all the data from all spin sectors and five positions are summed into a single value. The data will be organized by species (not ESA-step) and will be in the following order:

The fifteen bytes must be packaged together to make a COD_LO_SW_SPECIES_COUNTS product. When an entire 0-231 inclusive set of data has been received, it will then be processed identically to the SW_SPECIES_COUNTS product with a single spin sector and single azimuth (position) and 128 energies.

The other difference between the I-ALiRT packet and the SW_SPECIES_COUNTS product are the number of species written to telemetry. Although configurable, the nominal species will be He++, C+5, C+6, O+6, O+7, O+8, Mg, Fe lowQ, and Fe hiQ.

The uncertainty in i-ALiRT counts is provided as a separate variable and computed as the square root of the counts, e.g.,

$$\sigma_j(l) = \sqrt{\mathrm{C_j}(l)}$$

10.4.2 CoDICE Hi I-ALiRT

After the COUNTER, the packet will have the following fields:

Mnemonic	Max Length in Bits	Description
DATA_00	8	Data byte
DATA_01	8	Data byte
DATA_02	8	Data byte
DATA_03	8	Data byte
DATA_04	8	Data byte
SPARE_0	8	Spare for alignment
CHECKSUM	16	Checksum

We assume the Plan ID, Plan Step, and View ID are all 0, so from the views tab of the SCI_LUT, all I-ALiRT packets for Hi will be Lossy A + Lossless compressed.

Onboard the spacecraft, H counts are binned into 4 spin sector bins (summing over every 6 spin sectors), 4 azimuthal look directions (corresponding to 3 SSD IDs), and 15 energy-per-nuc bins with logarithmic spacing of sqrt(2). This data product is accumulated over 4 spins and provided at 1 min time resolution.

The five bytes must be packaged together to make a COD_HI_SECT_SPECIES_COUNTS product. When an entire 0-239 inclusive set of data has been received, it will then be processed identically to the COD_HI_SECT_SPECIES_COUNTS product with just Hydrogen and 15 energies.

The other difference between the I-ALiRT packet and the COD_HI_SECT_SPECIES_COUNTS product are the species written to telemetry. Although configurable, the nominal species will just be H.

The uncertainty in i-ALiRT counts is provided as a separate variable and computed as the square root of the counts, e.g.,

$$\sigma_j(i,k,n) = \sqrt{\mathrm{C_j}(i,n,k)}$$

11. DATA LEVEL 1B

11.1 CoDICE-Hi

To convert data products from L1A to L1B, counts are divided by the flight software acquisition time, $\tau_{\mathrm{FSW}}(n_{sector}, n_{spin})$, corresponding to the total acquisition time over which each data product is accumulated. For CoDICE-Hi, the nominal time spent acquiring data during a single 15° spin sector is $t_{acquire} = 0.59916$ [s]. This value is configurable, and a detailed calculation is described in Appendix B.

The flight software acquisition time for each data product is then calculated as:

$$\tau_{FSW}(n_{sector}, n_{spin}) = t_{acquire} * n_{sector} * n_{spin}$$

n_{sector} is the number of spin sectors that the counts are summed over.

n_{spin} is the number of spins over which the data is summed.

11.1.1 L1B – Hi Instrument Rates

Both the singles and aggregated instrument counter data is summed over all spin angles, so $n_{sector} = 24$. The data is provided at a cadence of 4 min (corresponding to 16 spins) and so $n_{spin} = 16$. With these values, the *L1B Instrument Rates* are computed by dividing the *L1A Instrument Counters* by $\tau_{FSW}(24{,}16) = 24 * 16 * t_{acquire}$.

11.1.2 L1B – Hi Omni-Directional Species Rates

CoDICE-Hi Species Counts are summed over $n_{sector} = 24$ spin sectors and $n_{spin} = 4$ spins. So, the conversion to count rate is given by:

$$\mathrm{R_j}(i) = \frac{\mathrm{C_j}(i)}{(24*4*\mathrm{t_{acquire}})} \quad \text{[counts/s]}$$

Note, the flight software acquisition time is configurable via LUTs.

The uncertainties in counts are converted to rates in the same way.

11.1.3 L1B – Hi Sectored Species Rates

CoDICE-Hi Sectored Counts are summed over $n_{sector} = 2$ spin sectors and $n_{spin} = 16$ spins. So the conversion to count rate is given by:

$$\mathrm{R_j}(i,n,k) = \frac{\mathrm{C_j}(i,n,k)}{(2*16*\mathrm{t_{acquire}})} \quad \text{[counts/s]}$$

Note, the flight software acquisition time is configurable via LUTs.

The uncertainties in counts are converted to rates in the same way.

11.1.4 L1B – Hi Priority Rates

Priority Counts are summed over all spin angles, so $n_{sector} = 24$. The data is provided at a cadence of 4 min (corresponding to 16 spins) and so $n_{spin} = 16$. With these values, the *L1B Priority Rates* are computed by dividing the *L1A Priority Counts* by $\tau_{FSW}(24{,}16) = 24 * 16 * t_{acquire}$.

11.2 CoDICE-Lo

For CoDICE-Lo, the full energy per charge range is collected over 16 spins. Each spin is divided into 24 spin sectors, and the sectors in each half-spin sample several ESA-steps varying from 1 step to 6 steps per sector. The details of the parameters needed to determine the accumulation time are given in Appendix B. The algorithms from appendix B are used to calculate

$t_{acquire}$, which is the time, in microseconds, spent acquiring data for one ESA step in one 15° sector. Different data products are accumulated over different numbers of spin sectors, n_{sector}, so for each product, the accumulation time over the accumulated number of sectors is

$t_{accum} = t_{acquire} * 10^{-3} * n_{sector}$, which gives the time in seconds (s).

In the esa-step sequence from high energies to low energies, if the rate exceeds a programmed value, the sequence stops, the esa voltages is set to the values for step 0, and there is no further accumulation until the start of the next cycle. The half spin where this occurs is set in the variable NSO_Half_Spin. The data in all data arrays for esa-steps that are in half-spins after NSO_Half_Spin should be set to NaN (Not a number). This application should be done in L1A data.

11.2.1 L1B – Lo Instrument Rates

The L1A final data array for Instrument Rate Type *j* will be:
$C_j(l, n)$, where j is the Rate Type, n is the 30° spin sector (0-5) (having summed 2 15° sectors) and *l* is the ESA-step (0-127).

CoDICE-Lo Instrument rates are collected over $n_{sector} = 2$. So to convert to a rate,

$$\mathrm{R_j}(l, n) = \frac{\mathrm{C_j}(l,n)}{(t_{acquire} * 10^{-3} * 2)} \quad \text{[counts/s]}$$

The energy_table for L1A provides the energy-per-charge values corresponding to each ESA step. This variable is computed as follows:

$$\text{energy_table}(l) = voltage_table(l) * k_factor * 10^{-3} \quad \text{[keV/e]}$$

Here, $voltage_table$ and k_factor are variables provided in the L1A data product.

11.2.2 L1B – Lo Species Rates

The L1A final data array for Species Counts for species j will be:
$C_j(l)$, where j is the Rate Type and l is the ESA-step (0-127).

Due to the ESA stepping scheme, the last spin sector of at ESA step 127 is used as a flyback step and so counts are not accumultated. Thus, the n_{sector} value is as follows:

$$n_{sector} = 12 \text{ for ESA steps } 0 – 126$$

$$n_{sector} = 11 \text{ for ESA steps } 127$$

So to convert to a rate,

$$\mathrm{R_j}(l) = \frac{\mathrm{C_j}(l)}{(t_{acquire} * 10^{-3} * n_{sector})} \quad \text{[counts/s]}$$

The uncertainties in counts are converted to rates in the same way.

The energy_table for L1A provides the energy-per-charge values corresponding to each ESA step. This variable is computed as follows:

$$\text{energy_table}(l) = voltage_table(l) * k_factor * 10^{-3} \quad \text{[keV/e]}$$

Here, $voltage_table$ and k_factor are variables provided in the L1A data product.

11.2.3 L1B – Lo Angular Rates

The L1A final data array for Angular Counts for species j will be:
$C_j(l, n, k)$, where j is the species, k is the azimuthal sector(1-24), n is the spin angle index (0-23) and l is the ESA step (0-127).

CoDICE-Lo Angular Counts are collected over $n_{sector} = 1$ spin sectors. So to convert to a rate,

$$\mathrm{R_j}(l, n, k) = \frac{C_j(l,n,k)}{(t_{acquire} * 10^{-3} * 1)} \quad \text{[counts/s]}$$

The uncertainties in counts are converted to rates in the same way.

The energy_table for L1A provides the energy-per-charge values corresponding to each ESA step. This variable is computed as follows:

$$\text{energy_table}(l) = voltage_table(l) * k_factor * 10^{-3} \quad \text{[keV/e]}$$

Here, $voltage_table$ and k_factor are variables provided in the L1A data product.

11.2.4 L1B – Lo Priority Rates

The L1A final data array for Priority Counts for Priority *j* will be:
$C_j(n, l)$, where j is the priority, *n* is the spin sector (0-11) and *l* is the ESA-step (0-127).

CoDICE-Lo Priority Counts are collected over $n_{sector} = 1$ spin sectors. So to convert to a rate,

$$\mathrm{R_j}(l) = \frac{\mathrm{C_j}(l)}{(t_{acquire} * 10^{-3} * 1)} \quad \text{[counts/s]}$$

The energy_table for L1A provides the energy-per-charge values corresponding to each ESA step. This variable is computed as follows:

$$\text{energy_table}(l) = voltage_table(l) * k_factor * 10^{-3} \quad \text{[keV/e]}$$

Here, $voltage_table$ and k_factor are variables provided in the L1A data product.

11.3 Comments

To convert all CoDICE L1A housekeeping products to the L1B counterpart, all voltages and currents are converted to physical units.

12. DATA LEVEL 2

12.1 CoDICE-Hi

12.1.1 L2 – Hi Direct Event Data

Parameters in the L1A event data will be converted to Physical Units as described in the table below. The Hi direct events are in the Event_Data subsection and are defined as follows per priority number:

Description	Conversion
SSD Energy	Converted to MeV using calibration data for each SSD and the recorded gain setting for each event
TOF	Converted to ns
Elevation Angle	Converted SSD ID to elevation angle in degrees relative to spacecraft spin axis
Gain	No Change
Multi-Flag	No Change
PHA Type	No Change
Spin Angle	Converted to angle in degrees from spin sector
Spin Number	No Change
Energy per Nuc	Computed from TOF channel using calibration data. Provided in MeV/nuc.

Hi Direct Event Spin and Elevation Angle Computations

Spin Angle:

The Direct Events are provided as a function of 24 spin angles covering an entire spin. Thus, for Direct Events, the spin sector corresponds to 15 degree bins and ranges from 0 – 23. The spin angles are thus calculated using the following formula:

$$\theta_{n,k} = \left(\theta_{0,k} + 15° * n\right) mod\ 360°\,, \qquad \text{for } n = 0, 1, \ldots, 23$$

Where $\theta_{0,k}$ is the center of the angular bin for spin sector index 0 for the Direct Events, provided in the table below. Note that SSD Index corresponds to the location in the data array, whereas SSD ID is the identification number for SSD.

Hi Direct Event Spin Angles (deg) in the Instrument Frame												
SSD Index	**0**	**1**	**2**	**3**	**4**	**5**	**6**	**7**	**8**	**9**	**10**	**11**
SSD ID	**0**	**1**	**3**	**4**	**5**	**7**	**8**	**9**	**11**	**12**	**13**	**15**
$\boldsymbol{\theta_{0,k}}$	187.50	146.61	131.19	127.50	131.19	146.61	187.50	228.39	243.81	247.50	243.81	228.39

Elevation Angle:

SSD Index	SSD ID (k)	Elevation Angle
0	0	150.0°
1	1	138.6°
2	3	115.7°
3	4	90.0°
4	5	64.3°
5	7	41.4°
6	8	30.0°
7	9	41.4°
8	11	64.3°
9	12	90.0°
10	13	115.7°
11	15	138.6°

For each SSD ID the elevation angle is the angle between the spacecraft spin axis and the center of the SSD FOV. These angles are reported in the L2 Event Data products and provided in the table to the below. These angles correspond to the centers of the angular bins.

12.1.2 L2 – Hi Sectored Intensities

CoDICE-Hi L2 sectored intensities are produced for each species (j) as a function of energy bin (i), SSD ID (k), and spin sector (n). To produce the CoDICE-Hi L2 sectored intensities, the sectored count rates are converted to sectored intensities by the following equation:

$$I_j(i,n,k) = \frac{R_j(i,n,k)}{G_k \cdot \epsilon_{jik} \cdot \Delta E_{ji}} \qquad [\#/(\text{cm}^2\text{-sr-s-MeV/nuc})]$$

G_k is the physical geometric factor for a single SSD determined from a Simion instrument model.

ϵ_{jik} is the efficiency for species j, energy bin i, and position k. This factor also depends on the particle priority scheme.
ΔE_{ji} is the energy pass band, corresponding to the incident energy of energy bin i and species j. It is computed from the plus/minus energy-per-nuc bin values contained in the cdf files as: $\Delta E_{ji} = E_{i,minus} + E_{i,plus}$.
$R_j(i,n,k)$ are the Level-1b Sectored Rates for species j, energy bin i, spin sector n, and position k

The uncertainty in intensity is computed from the rates uncertainties using the same conversions above.

Hi Sectored Intensity Spin and Elevation Angle

Spin Angle:

Since the sectored intensities are summed over every two spin sectors onboard, they are provided as a function of 12 spin angles covering an entire spin. Thus, for Sectored Intensities, the spin sector corresponds to 30 degree bins and ranges from 0 – 11. The spin angles are thus calculated using the following formula:

$$\theta_{k,n} = \left(\theta_{k,0} + 30° * n\right) mod\ 360°, \qquad \text{for } n = 0, 1, \dots, 11$$

Where $\theta_{k,0}$ is the center of the angular bin for spin sector index 0 for the Sectored Intensity, provided in the table below. Note that SSD Index corresponds to the location in the data array, whereas SSD ID is the identification number for SSD.

Hi Sectored Intensity Spin Angles (deg) in the Instrument Frame												
SSD Index	**0**	**1**	**2**	**3**	**4**	**5**	**6**	**7**	**8**	**9**	**10**	**11**
SSD ID	**0**	**1**	**3**	**4**	**5**	**7**	**8**	**9**	**11**	**12**	**13**	**15**
$\boldsymbol{\theta_{k,0}}$	195.00	154.11	138.69	135.00	138.69	154.11	195.00	235.89	251.31	255.00	251.31	235.89

Elevation Angle:
The elevation angles reported in this product are computed as described above in Section 11.1.1 (Hi L2 Direct Events).

12.1.3 L2 – Hi Omni-directional Intensities

The calculation of Level-2 Omni-directional Intensities assumes isotropy over the full-sky.

For each species the omni-directional intensity is calculated from the species rates as follows:

$$I_j(i) = \frac{R_j(i)}{(\sum_k G_k)\cdot \epsilon_{ji} \cdot \Delta E_{ji}} \quad [\#/(\text{cm}^2\text{-sr-s-MeV/nuc})]$$

$R_j(i)$ are the Level-1b Species Rates for species j and energy bin i
G_k is the physical geometric factor for a single SSD determined from a Simion instrument model.
ϵ_{ji} is the efficiency for species j, energy bin i and averaged over all SSDs. This factor also depends on the particle priority scheme.

ΔE_{ji} is the energy pass band, corresponding to the incident energy of energy bin i and species j. It is computed from the plus/minus energy-per-nuc bin values contained in the cdf files as: $\Delta E_{ji} = E_{i,minus} + E_{i,plus}$.

The uncertainty in intensity is computed from the rates uncertainties using the same conversions above.

Note, over the course of a spin, each Hi-SSD observes a different amount of solid angle that depends on the azimuth angle (position) of the SSD. However, since the species rates are summed over all angles onboard the SC, these differences in solid angle observed by each SSD over the course of a spin cannot be accounted for using the species rates. Thus, the omni-directional intensities described above should be thought of as a pseudo-omni-directional intensity. A derivation of the true omni-directional intensities using the Level-1b Sectored Intensities and including solid angle correction factors is described in Appendix ##.

12.2 CoDICE-Lo

12.2.1 L2 – Lo Direct Event Data

Parameters in the L1A event data will be converted to Physical Units as described in the table below. The Lo direct events are in the Event_Data subsection and are defined as follows per priority:

Description	Conversion
APD Gain	No Change
APD ID	No Change
Position	No Change
Elevation Angle	Converted from position to elevation angle in degrees relative to the spacecraft spin axis
APD Energy	Converted to keV using calibration data for each APD (based on APD ID and APD Gain and ST/SW Bias Gain Mode Flag)
TOF	Converted to ns using calibration data
Multi-Flag	No Change
PHA Type	No Change
Spin Angle	Spin sector converted to Angle in degrees
ESA Step	Converted to keV/e using voltage table and analyzer constant

Spin Angle

The reported spin sector index in the L1A direct event data is relative to an entire spin and ranges from 0 – 23, corresponding to 15 degree spin angle bins. This spin sector is ‘de-spun’ at L2 to account for APDs 2-12 and 14-24 viewing opposite directions. Thus, the spin angle is computed as:

$$\theta_{Lo,n} = n * 15° + 277.5°, \qquad \text{k} = 1 – 24$$

Elevation Angle

Since multiple positions sample the same physical elevation angle, but for different spin phases, the final data arrays provided in products that retain angular information will be reformed to remove this redundancy. We are transforming from an instrument-frame coordinate system where the positions correspond to the "azimuth" angle over the 360 degree FOV of the instrument to a coordinate system aligned with the spin axis, where the positions correspond to the elevation angle relative to the spin axis and the spin angle gives the 360 degree azimuthal angle around the X-Y plane.

The table below provides the mapping from position to elevation angle. The colors indicate SW and NSW variables which is relevant to the Angular Rates product. These values correspond to the centers of the angular bins.

Lo Position to Elevation Angle Mapping		
Positions to be sorted	**Product**	**Elevation Angle (°)**
1	SW	0
2, 24	SW	15
3, 23	SW	30
4, 22	NSW	45
5, 21	NSW	60
6, 20	NSW	75
7, 19	NSW	90
8, 18	NSW	105
9, 17	NSW	120
10, 16	NSW	135
11, 15	NSW	150
12, 14	NSW	165
13	NSW	180

12.2.2 L2 – Lo Angular Intensities

RGFO Implementation for G_m Determination: These rules apply to both SW/NSW Angular products.

Launch – 11/24/2025:

The mode is determined by checking whether the half-spin number for the ESA step *l* is less than or equal to the half-spin number specified by the parameter RGFO_Half_Spin. The RGFO_Half_Spin value indicates the half spin number at which the RGFO count threshold was reached. When this happens, the instrument enters RGFO mode in the following half spin. If the half-spin is less than or equal to RGFO_Half_Spin, then the "Full" geometric factor is used. If it is greater than RGFO_Half_Spin, then the reduced geometric factor is used.

11/24/2025 – 01/29/2026:

The RGFO threshold was lowered so that it is triggered immediately on half-spin 0. However, the ESA voltage ratio remains 1. Thus, the RGFO_half_spin should be ignored and the Full G_m should be used.

01/29/2026 – Current:
The Lo L1B product now contains variables that indicate the esa step and spin sector during which the RGFO limit is triggered. The spin_sector variable in the angular data product ranges from 0-24 and has been 'de-spun' at L1a. The rgfo_spin_sector variable ranges from 0-23. In the following algorithm, spin_angle refers to the L1B angular bin (0 – 23) which is despun and spin_sector refers to the non-despun spin sector reported from the instrument (0-11). The correct G_m is selected as follows:

1. For half_spin > rgfo_half_spin → use 'Reduced' G_m
2. For half_spin < rgfo _half_ spin → use 'Full G_m
3. For half_spin = rgfo_half_spin
    a. Define spin_angle_full bins to use 'Full' G_m as all spin_angle bins that are less than (rgfo_spin_sector *mod* 12). Extend this list by also adding 12 to each of these values:
        i. **For all esa steps and all spin_angle_full values use 'Full' G_m**
        ii. Ex: if (rgfo_spin_sector *mod* 12) = 3 then spin_angle_full = [0,1,2,12,13,14]
    b. Define spin_angle_red bins that use 'Reduced' G_m as all spin_angle bins that are greater than rgfo_spin_sector. Extend this list by also adding 12 to each of these values:
        i. **For all esa steps and all spin_angle_red values use 'Reduced' G_m**
        ii. Ex: if rgfo_spin_sector = 3 then spin_angle_red = [4,5,6,7,8,9,10,11,16,17,18,19,20,21,22,23]
    c. For spin_angle = (rgfo_spin_sector *mod* 12) and (spin_angle *mod* 12) = (rgfo_spin_sector *mod* 12):
        i. Use Full G_m for esa_step <= rgfo_esa_step
        ii. Use Reduced G_m for esa_step > rgfo_esa_step
        iii. Ex: Let rgfo_half_spin = 10, rgfo_spin_sector = 3, and rgfo_esa_step = 19. (ESA steps = [18,19,20] sampled during half spin 10).
            1. Full G_m for spin_angle = [3, 15] and esa_step = [18,19]
            2. Reduced G_m for spin_angle = [3, 15] and esa_step = [20]

SW/NSW Angular intensities
The CoDICE-Lo angular intensities are arrays of differential intensity for a set of species sorted by energy per charge, azimuthal and spin angle. To produce the CoDICE-Lo Angular Intensities, L1B Angular rates (counts/seconds) are converted to differential intensity.

$$J_j(l,n,k) = \frac{\mathrm{R_j}(l,n,k)}{G_m \cdot \varepsilon_{jlk} \cdot \left(\frac{E}{q}\right)_l}$$

J is the differential intensity [particles / (cm^2 s sr keV/q)]
$\mathrm{R_j}(l,n,k)$ is the angular rate in counts/second for species j, k is the position (1 – 24), n is the spin angle index (0-23) and l is the ESA-step (0-127).
ε_{jlk} is the efficiency for species, j, position k, and ESA-step l.

$\left(\frac{E}{q}\right)_l$ is the energy per charge for ESA-step l.
G_m is the geometric factor (cm^2 str eV/eV) for one angular bin for mode m, which is either "Full" or "Reduced". G_m is provided for each APD ID and ESA step and so can be represented as an array with dimensions (128 ESA steps x 24 APD IDs). This array is provided as part of the calibration data.

The uncertainty in intensity is computed from the rates uncertainties using the same conversions above.

Position to Elevation
After the intensities are computed, the data array is then transformed into coordinates corresponding to the physical elevation angles measured rather than the instrument-frame position angles. This process is the same as described in the section above except with an additional step to account for positions 1 and 13. The table mapping position to elevation angle is reproduced here for clarity.

Lo Position to Elevation Angle Mapping			
Positions to be sorted	**Product**	**Elevation Angle (°)**	**SW/NSW Array index**
1	SW	0	0
2, 24	SW	15	1
3, 23	SW	30	2
4, 22	NSW	45	0
5, 21	NSW	60	1
6, 20	NSW	75	2
7, 19	NSW	90	3
8, 18	NSW	105	4
9, 17	NSW	120	5
10, 16	NSW	135	6
11, 15	NSW	150	7
12, 14	NSW	165	8
13	NSW	180	9

Positions 1 and 13 only observe half of the total 24 spin angles for each esa step. To account for this, we replicate the counts observed in position 1 and 13 for each esa step to either spin angles 0-11 or 12-23, depending on the pixel orientation (A/B).

SW Position 1
$J_j(l_A, 12{:}\,23, 0) = J_j(l_A, 0{:}\,11, 0)$ $\quad$ $J_j(l_B, 0{:}\,11, 0) = J_j(l_B, 12{:}\,23, 0)$

NSW Position 13
$J_j(l_A, 0{:}\,11, 9) = J_j(l_A, 12{:}\,23, 9)$ $\quad$ $J_j(l_B, 12{:}\,23, 9) = J_j(l_B, 0{:}\,11, 9)$

Here l_A and l_B are esa steps for configuration A and B, respectively. Note that the array indices are used in the above mappings for position 1 and 13.

This transformation is applied to the intensities and their uncertainties, resulting in the final data arrays for the SW and NSW products which have dimensions:

SW: $J_j(l,n,k)$ ~ (128 E/q x 24 spin angles x 3 elevation angles)
NSW: $J_j(l,n,k)$ ~ (128 E/q x 24 spin angles x 10 elevation angles)

Spin Angle:

Since the angular product has been 'de-spun' at L1a, with spin sector 0 corresponding to the directions of APDs 2-12, the physical spin angle in instrument coordinates can be computed as follows:

$$\theta_{Lo,n} = n * 15° + 7.5° + 270°$$

Here, $\theta_{Lo,n}$ is the center of the physical spin angle bin corresponding to spin angle index n, which ranges from 0 – 23. The $270°$ accounts for spin angle of APDs 2-12 at spin sector 0 in instrument coordinates.
Note, this assumes that the data has been 'de-spun' as described in the L1A Lo Angular Counts section. See section 4.2 for more details on the Instrument and SC coordinate systems, as well as look direction vectors.

12.2.3 L2 – Lo Species Intensities

The species intensities are summed on-board into two broad angular ranges, a "sunward" range that covers a 75 degree cone centered on the spacecraft spin axis, and the "non-sunward" range that covers all other angles.
Within the sunward range there are two types of populations that have different expected angular distributions. The "solar wind species" come in a narrow beam distribution, while the pick-up ion distribution is spread over a wide range of angles. Thus different assumptions are made in calculating the particle differential flux.

RGFO Implementation for G_m Determination: These rules apply to both SW/NSW Species products.
Launch – 11/24/2025:
The mode is determined by checking whether the half-spin number for the ESA step *l* is less than or equal to the half-spin number specified by the parameter RGFO_Half_Spin. The RGFO_Half_Spin value indicates the half spin number at which the RGFO count threshold was reached. When this happens, the instrument enters RGFO mode in the following half spin. If the half-spin is less than or equal to RGFO_Half_Spin, then the "Full" geometric factor is used. If it is greater than RGFO_Half_Spin, then the reduced geometric factor is used.
11/24/2025 – 01/29/2026:
The RGFO threshold was lowered so that it is triggered immediately on half-spin 0. However, the ESA voltage ratio remains 1. Thus, the RGFO_half_spin should be ignored and the Full G_m should be used.
01/29/2026 – Current:
Since the RGFO mode is implemented within a half-spin at a given esa step and spin sector and since the species data is summed over all spin sectors, the data during this half spin cannot be de-convolved. Thus, the intensity during the half_spin = RGFO_half_spin should be set to fill values.
Thus, the data is treated as follows:

1. For half_spin = rgfo_half_spin → data is set to fill values
2. For half_spin > rgfo_half_spin → use 'Reduced' G_m

3. For half_spin < rgfo _half_ spin → use 'Full G_m

SW Solar Wind Species:

For the beam-like solar wind species we calculate the flux assuming that they come in a distribution that always lands on azimuthal position 1, the position viewing along the spin axis. From L1B we have the rate: $R(l)$, where j is the species and l is the ESA-step (0-127).
With the assumption that the flux all lands on one position, we just use the Geometric Factor for one azimuthal sector, G_m

$$J_j(l) = \frac{\mathrm{R_j}(l)}{G_m \cdot \varepsilon_{jl1} \cdot (E/q)_l}$$

J is the differential number flux [particles / (cm^2 s sr keV/q)]
$\mathrm{R_j}$ is the species rate in counts/second, for energy step, l.
G_m is the SW geometric factor (cm^2 str eV/eV) for position 1 and mode m, which is either "Full" or "Reduced", as explained above
ε_{jl1} is the efficiency depending on the ESA step, l, and species, j, for position 1.
$(E/q)_l$ is the energy per charge for ESA step l, in keV/e

The uncertainty in intensity is computed from the rates uncertainties using the same conversions above.

The solar wind species are H+, He++, O+5, O+6, O+7, O+8, C+4, C+5, C+6, Ne, Mg, Si, Fe(low Q) and Fe(highQ).

SW Pick-up Ion Species:

For pick-up ion species rates, the flux in the sunward sector will be calculated assuming that the flux is isotropic over the sunward range, which includes 5 azimuthal bins. In this case

$$J_j(l) = \frac{\mathrm{R_j}(l)}{5 * G_m \cdot \varepsilon_{jl} \cdot (\frac{E}{q})_l}$$

J is the differential intensity [particles / (cm^2 s sr keV/e)]
$\mathrm{R_j}$ is the species rate in counts/second.
G_m is the SW geometric factor (cm^2 str eV/eV) for position 1 for mode m, which is either "Full" or "Reduced", as explained above. The factor of 5 is because there are 5 angular bins summed for this rate.
ε_{jl} is the efficiency depending on the ESA step, l, species, j. The average efficiency over the 5 positions is used.
$(E/q)_l$ is the energy per charge for ESA-step l, in keV/q
The uncertainty in intensity is computed from the rates uncertainties using the same conversions above.

The pick-up ion species are He+ and the group of CNO+.

NSW Species:

The flux in the non-sunward sector will be calculated assuming that the flux is isotropic over the non-sunward range. In this case:

$$J_j(l) = \frac{\mathrm{R_j}(l)}{19 * G_m \cdot \varepsilon_{jl} \cdot \left(\frac{E}{q}\right)_l}$$

J is the differential intensity [particles / (cm^2 s sr eV/e)]
$\mathrm{R_j}$ is the species rate in counts/second.
$\mathrm{G_m}$ is the NSW geometric factor (cm^2 str eV/eV) averaged over the 19 NSW positions for mode m, which is either "Full" or "Reduced", as explained above. The factor of 19 is because there are 19 positions summed for this rate.
ε_{jl} is the efficiency depending on the ESA step, l, species, j. And average efficiency over the 19 positions is used.
$\left(\frac{E}{q}\right)_l$ is the energy per charge for ESA step *l,* in keV/q

The uncertainty in intensity is computed from the rates uncertainties using the same conversions above.

The non-sunward species are H+, He++ O5-8, C4-6, Ne+Mg+Si, Fe, He+ and CNO+.

13. DATA LEVEL 3

13.1 CoDICE-Hi

13.1.1 L3a – Direct Event Data

This product includes all of the information from the L2 direct event data (time of detection, TOF, SSD Energy, SSD ID, Energy Range, type, spin sector, spin number, and priority). In addition, this product includes the energy-per-nuc (E_n) and estimated mass (u) of the particle. The E_n is calculated using a lookup table that converts the measured TOF channel directly to incident E_n in MeV/n based on calibration data. The mass (u) of each event is calculated as:

$$u = \frac{E_{ssd}}{E_n} * \epsilon \qquad \text{[amu]}$$

E_{SSD} is the SSD Energy provided by the L2 direct event packet in units [MeV].

E_n is the energy-per-nuc determined from the TOF via a calibration lookup table.

ϵ is a correction factor accounting for energy loss through the foils and dead layer of the SSD.

13.1.2 L3b – Pitch Angle Distributions

Level 3 pitch angle distributions will be provided for H, He3He4, CNO, and Fe ion species at a cadence of 4 min. These are computed from the L2 Hi Sectored Intensities, which are provided as a function of energy (i), spin angle (n), and elevation angle (k) in the instrument frame of reference.

To compute the look direction unit vector of each SSD in the spacecraft frame, we first convert the spin angles from the CoDICE instrument frame to the SC frame using the following equation:

$$\theta_{SC} = (\theta_{inst} + 46°)\ mod\ 360°$$

Here, θ is the spin angle in the SC or instrument (inst) frame and mod is the modular arithmetic function.
The elevation angle (ϕ) is the same in both frames and so $\phi_{SC} = \phi_{inst}$.
The look direction unit vector $\hat{n}_{SC} = [n_x, n_y, n_z]$ in the SC frame is given by:

$$n_x = \cos(\theta_{SC})\sin(\phi_{SC})$$
$$n_y = \sin(\theta_{SC})\sin(\phi_{SC})$$
$$n_z = \cos(\phi_{SC})$$

Note, to compute the unit vectors, the spin and elevation angle inputs should be in radian units. These look directions defines the direction that particles are measured from. Thus, the direction of travel of particles is given by the negative of this vector (i.e., $-1 * \hat{n}_{SC}$). The pitch angle corresponding to each (i, n, k) bin is computed by:

$$\alpha(i,n,k) = \cos^{-1}\left(-\hat{n}_{SC} \circ \frac{\vec{B}_{SC}}{|\overrightarrow{B_{SC}}|}\right) * \frac{180}{\pi}$$

Here, $\vec{B}_{SC}$ is the magnetic field vector averaged over the 1 min accumulation period in the spacecraft frame. The operation inside of the parenthesis represents the dot product between the two vectors.

For each energy passband, the L2 Sectored Intensities are then averaged and binned into 30° pitch angle bins ranging from $0° - 180°$ based on the derived values of $\alpha(i,n,k)$. The final data product is a 2-D array with dimensions (Energy × Pitch Angle) and containing the average intensity in each bin.

13.2 CoDICE-Lo

13.2.1 L3a – Partial densities of solar wind species

From the CoDICE-Lo L2 Species Intensities, Solar Wind, Sunward product, partial densities of the solar wind species are calculated. The following table gives the species index, j, and the average mass per charge for each of the species included in this product. The index j refers to the species index of the Species Intensities. Species 1-14 (out of 16 sunward species) are solar wind species.

Index, j	Species	m/q (AMU/e)
1	H+	1.0
2	He++	2.0
3	C+4	3.0
4	C+5	2.4
5	C+6	2.0
6	O+5	3.2
7	O+6	2.7
8	O+7	2.28
9	O+8	2.0
10	Ne	3.6
11	Mg	3.5
12	Si	4.0
13	Fe (high Q)	3.85
14	Fe (low Q)	7.25

We start with the L2 Species Intensity, $J_j(l)$, where j is the species index and l is the ESA step.

We then apply the weighting factors needed to determine the density contribution for each ESA step.

$$d_N_j(l) = C \cdot \Delta\vartheta \cdot \Delta\varphi \cdot \frac{\Delta E}{E} \cdot \mathrm{J_j}(l) \cdot \sqrt{\left(\frac{E}{q}\right)_l} \cdot \sqrt{(m/q)_j}$$

where $\Delta\vartheta$, $\Delta\varphi$, and $\frac{\Delta E}{E}$ are constants representing the angular and energy step sizes. $C = 2.283x10^{-8}$ is a conversion factor to convert the partial density to physical units of [cm^{-3}].

For each species, we then calculate a weighted sum over the ESA-steps to get the number density (N).

The densities are then given by the following:

$$N_j = \sum_{l=0}^{128} d_N_j(l)$$

We note that for H+ and He++ the densities likely to not contain the peak of the solar wind. We will decide when seeing the data which species should be released as final products. The ratio products, below, may be released before these density products are released.

13.2.2 L3a – Elemental abundance ratios

These ratios can be created from the partial densities product (13.2.1),

Elemental Abundances

$$\frac{\boldsymbol{C}}{\boldsymbol{O}} = \frac{N_3 + N_4 + N_5}{N_6 + N_7 + N_8 + N_9}$$

$$\frac{\boldsymbol{Mg}}{\boldsymbol{O}} = \frac{N_{10}}{N_6 + N_7 + N_8 + N_9}$$

$$\frac{\boldsymbol{Fe}}{\boldsymbol{O}} = \frac{N_{13} + N_{14}}{N_6 + N_7 + N_8 + N_9}$$

This should be created at 12 minute cadence.

13.2.3 L3a – Ionization charge state ratios

This data product is also created using the partial densities product (13.2.1)

Charge State Ratios

$$\frac{\boldsymbol{C^{+6}}}{\boldsymbol{C^{+5}}} = \frac{N_5}{N_4}$$

$$\frac{\boldsymbol{C^{+6}}}{\boldsymbol{C^{+4}}} = \frac{N_5}{N_3}$$

$$\frac{\boldsymbol{O^{+7}}}{\boldsymbol{O^{+6}}} = \frac{N_8}{N_7}$$

$$\frac{\boldsymbol{Fe^{low}}}{\boldsymbol{Fe^{high}}} = \frac{N_{14}}{N_{13}}$$

This will be created at 12 minute cadence.

13.2.4 L3a – Ionization charge state distributions

This product is also created from the partial densities product (13.2.1)

For Oxygen, create a 4 element array that represents the relative abundance of charge states 5-8.

Oxygen_charge(0) = $\frac{N_6}{N_6+N_7+N_8+N_9}$; gives relative abundance of charge state 5

Oxygen_charge(1) = $\frac{N_7}{N_6+N_7+N_8+N_9}$; gives relative abundance of charge state 6

Oxygen_charge(2) = $\frac{N_8}{N_6+N_7+N_8+N_9}$; gives relative abundance of charge state 7

Oxygen_charge(3) = $\frac{N_9}{N_6+N_7+N_8+N_9}$; gives relative abundance of charge state 8

For Carbon, create a 3 element array that represents the relative abundance of charge states 4-6.

Carbon_charge(0) = $\frac{N_3}{N_3+N_4+N_5}$; gives relative abundance of charge state 4

Carbon_charge(1) = $\frac{N_4}{N_3+N_4+N_5}$; gives relative abundance of charge state 5

Carbon_charge(2) = $\frac{N_5}{N_3+N_4+N_5}$; gives relative abundance of charge state 6

13.2.5 L3a – Direct Event Data

The **mass** algorithm is determined using an empirical formula. The low direct event data should include all information in the L2 Lo event data (12.2.2) (TOF, Energy, Anode Position, APD ID, APD Gain bit, energy per charge step, and spin angle, the priority and then the calculated energy and time-of-flight, plus an estimate of the mass per charge and the mass.

We will also add a calculated mass for each event and a calculated mass per charge.

The **mass per charge** algorithm is given by the following:

$$M/Q = 2 * \left(E/Q + PAC - \alpha\right) * \left(\tau/d\right)^2 = \left(E/Q + PAC - \alpha\right) * \tau^2 * \mathrm{K}$$

Where:
E/Q is the energy per charge, based on the ESA step (in keV/e)
PAC is the post-acceleration voltage (default 15 kV, constant)
α is an approximation for the energy lost in the carbon foil (default 0, for now)
τ is the time-of-flight, in nano-seconds
d is the pathlength (10.64 cm) (used in K)
K is the conversion constant to put the result in AMU/Q

$$K = 2 * \frac{1.602x10^{-16}J}{keV} * \frac{1AMU}{1.673x10^{-27}kg} * \left(\frac{1}{10.64cm}\right)^2 * \left(\frac{100cm}{m}\right)^2 * \left(\frac{1s}{10^9ns}\right)^2$$
$$= 1.692x10^{-5}\ \frac{AMU}{keV * ns^2}$$

If the time of flight, τ, is in channel number, not in ns, the conversion is:

$$\tau_{ns} = 0.6217 * \tau_{ch} - 7.4437$$

based on the measured energy, **E**, in keV, and the time-of-flight, **τ**, in ns.

X=ln(E)
Y=ln(τ)
Z=A[0] +A[1]*X + A[2]*Y+A[3]*X*Y+A[4]*X^2 + A[5]*Y^3
$Mass = e^Z$ (This gives the Mass in AMU)
The coefficients are found by a fit. Preliminary values for the fit are:

A[0] = -0.85674
A[1] = -0.363739
A[2] = -1.36612
A[3] = 0.30347
A[4] = 0.0290419
A[5] = 0.0557362

Normalization Factor

Inputs: L2 Lo Event data, and L1A priority counts.

We will also include the "normalization_per_event" variable which provides the normalized count value for each direct event determined from the ratio of the total number of events (from the priority counts) for this priority $P(p,l,n)$ to the total number of events with this priority for this energy per charge step and spin sector ($CP(p,l,n)$) contained in the direct events. Here, p is the priority, l is the energy per charge step, and n is the spin sector.

To account for the spin sector in the L1a priority counts which ranges from 0-11, while the spin sector in the L2 Direct Events range from 0-23 and have been 'de-spun', we apply the following algorithm:

1. Create an array of priority counts using the sw and nsw L1a priority counts variables. The array has shape: P = [epoch, 7 priority, 128 esa step, 12 spin sector]

2. Replicate the array over the spin sector dimension. This creates a new array with shape: Pnew = [epoch, 7 priority, 128 esa step, **24 spin sector**].

3. Fill new array as:

   Pnew[*,*,*,0:11] = P and Pnew[*,*,*,12:23] = P.

4. Initialize an array with shape CP = [epoch, 7 priority, 128 esa step, **24 spin sector**]

5. Use the direct events to fill the CP array (spin sectors 0 -11 only). For a given epoch (ep_id), priority (p), esa step (l) and spin sector (n), fill the CP array as follows:

   CP[ep_id, p, l, n] = C[ep_id, p, l, n] + C[ep_id, p, l, n +12]

   Here, the C[ep_id, p p, l, n] is the number of direct events with [ep_id, p p, l, n] coordinates and n ranges from 0 – 11.

6. Fill the second half of the CP matrix as follows

   CP[*,*,*,12:23] = CP[*,*,*,0:11]

7. Compute normalization factor as:

$$\text{normalization}(epoch, p, l, n) = \frac{Pnew(ep_id, p, l, n)}{CP(ep_id, p, l, n)}$$

8. Initialize the *normalization_per_event* array with shape: [epoch, 7 priority, 10000]. Use the *spin_sector* and *esa_step* from L2 direct events product to fill in the *normalization_per_event* array using the computed *normalization* array from step 7 as follows:

   normalization_per_event $[ep_id, p, ev_id] = normalization\ (ep_id, p, l_0, n_0)$

   $l_0 = esa_step[ep_id, p, ev_id]$
   $n_0 = spin_sector[ep_id, p, ev_id]$
   ep_id is the epoch index
   p is the priority index (0 – 6)
   ev_id is the event index (0 – 10000)

Both the *normalization_per_event* and *normalization* arrays are provided in the L3a Direct Events product.

13.2.6 L3b – 3-D Instrument Frame distributions from Event Data

In order to get full energy- spin-phase – azimuth angle distributions for a variety of species, the L3a Direct Events are used which includes a mass and mass-per-charge determination. If this does not exist, this would need to be calculated here.

3D VDF Algorithm

We first create an array of normalized counts using the L3a Direct Event data. Note that the *spin_sector* variable in the L3a product has been de-spun to be consistent with the *spin_angle* values. Furthermore, the L3a product contains a *normalization_per_event* which contains the normalized count value for each direct event measured.

1) For a given species, define a range of mass and mass per charge.
2) In each cycle, create an array of normalized counts, $C_j(p,l,n,k)$, where j is the species, k is the APD ID (1-24), n is the spin sector index (0-23), l is the ESA step (0-127), and p is the priority.
   a. For a given (p,l,n,k) tuple use the *esa_step, spin_sector,* and *position* variables (each with dimensions [epoch, 7 priority, 10000 events]) to identify all direct event indices corresponding to the tuple (p,l,n,k)
   b. Sum the values from the *normalization_per_event* variable over the identified indices to get the total normalized count value corresponding to the tuple (p,l,n,k)
   c. Fill $C_j(p,l,n,k)$ with the total normalized count value
3) Sum the contributions from the different priorities

$$C_j(l,n,k) = \sum_p C_j(p,l,n,k)$$

4) Convert to a rate using the *acquisition_time_per_esa_step* variable

$$\mathrm{R_j}(l,n,k) = \frac{C_j(l,n,k)}{(t_{acquire}(l)*1)} \quad \text{[counts/s]}$$

5) Convert to Intensity

$$J_j(l,n,k) = \frac{\mathrm{R_j}(l,n,k)}{G_m \cdot \varepsilon_{jkl} \cdot \left(\frac{E}{q}\right)_l}$$

Here, ε_{jkl} is the efficiency for species j and esa step l and position k, provided in calibration LUTs. G_m is provided for each APD ID (position, k) and ESA step and so can be represented as an array with dimensions (128 ESA steps x 24 APD IDs). Refer to the section below to determine which G_m to use (Full or Reduced).

6) Reduce intensity array position dimension to elevation angle by summing counts over the positions to be sorted in the table below. For this mapping from position to elevation refer to the table below.

Lo Position to Elevation Angle Mapping		
Positions to be sorted	**Product**	**Elevation Angle (°)**
1	SW	0
2, 24	SW	15
3, 23	SW	30
4, 22	NSW	45
5, 21	NSW	60
6, 20	NSW	75
7, 19	NSW	90
8, 18	NSW	105
9, 17	NSW	120
10, 16	NSW	135
11, 15	NSW	150
12, 14	NSW	165
13	NSW	180

Positions 1 and 13 only observe half of the total 24 spin angles for each esa step. To account for this, we replicate the counts observed in position 1 and 13 for each esa step to either spin angles 0-11 or 12-23, depending on the pixel orientation (A/B).

Position 1

$J_j(l_A, 12{:}23, 0) = J_j(l_A, 0{:}11, 0)$ $\quad\quad$ $J_j(l_B, 0{:}11, 0) = J_j(l_B, 12{:}23, 0)$

Position 13

$J_j(l_A, 12{:}23, 12) = J_j(l_A, 0{:}11, 12)$ $\quad\quad$ $J_j(l_B, 0{:}11, 12) = J_j(l_B, 12{:}23, 12)$

Here l_A and l_B are esa steps for configuration A and B, respectively. Note that the array indices are used in the above mappings for position 1 and 13.

The final array of intensities should have the shape:

$J_j(l, n, k)$ =(128 energy-per-charge, 24 spin angles, 13 elevation angles)

The elevation angles are provided in the table above.

Since spin_sector in the L3a direct event product is 'de-spun', the physical spin angle in instrument coordinates can be computed as follows:

$$\theta_{Lo,n} = (n * 15° + 7.5° + 270°)\ mod\ 360$$

Here, $\theta_{Lo,n}$ is the center of the physical spin angle bin corresponding to spin angle index n, which ranges from 0 – 23. The $270°$ accounts for spin angle of APDs 2-12 at spin sector 0 in instrument coordinates.
See section 4.2 for more details on the Instrument and SC coordinate systems, as well as look direction vectors

.

RGFO Implementation for G_m Determination

Launch – 11/24/2025:

The mode is determined by checking whether the half-spin number for the ESA step *l* is less than or equal to the half-spin number specified by the parameter RGFO_Half_Spin. The RGFO_Half_Spin value indicates the half spin number at which the RGFO count threshold was reached. When this happens, the instrument enters RGFO mode in the following half spin. If the half-spin is less than or equal to RGFO_Half_Spin, then the "Full" geometric factor is used. If it is greater than RGFO_Half_Spin, then the reduced geometric factor is used.

11/24/2025 – 01/29/2026:

The RGFO threshold was lowered so that it is triggered immediately on half-spin 0. However, the ESA voltage ratio remains 1. Thus, the RGFO_half_spin should be ignored and the Full G_m should be used.

01/29/2026 – Current:

The Lo product now contains variables that indicate the esa step and spin sector during which the RGFO limit is triggered. The spin_sector variable in the angular data product ranges from 0-24 and has been 'de-spun' at L1a. The rgfo_spin_sector variable ranges from 0-23. In the following algorithm, spin_angle refers to (0 – 23) which is despun and spin_sector refers to the non-despun spin sector reported from the instrument (0-11). The correct G_m is selected as follows:

1. For half_spin > rgfo_half_spin → use 'Reduced' G_m
2. For half_spin < rgfo _half_ spin → use 'Full G_m
3. For half_spin = rgfo_half_spin
    a. Define spin_angle_full bins to use 'Full' G_m as all spin_angle bins that are less than (rgfo_spin_sector *mod* 12). Extend this list by also adding 12 to each of these values:
        i. **For all esa steps and all spin_angle_full values use 'Full' G_m**
        ii. Ex: if (rgfo_spin_sector *mod* 12) = 3 then spin_angle_full = [0,1,2,12,13,14]
    b. Define spin_angle_red bins that use 'Reduced' G_m as all spin_angle bins that are greater than rgfo_spin_sector. Extend this list by also adding 12 to each of these values:
        i. **For all esa steps and all spin_angle_red values use 'Reduced' G_m**
        ii. Ex: if rgfo_spin_sector = 3 then spin_angle_red = [4,5,6,7,8,9,10,11,16,17,18,19,20,21,22,23]
    c. For spin_angle = (rgfo_spin_sector *mod* 12) and (spin_angle *mod* 12) = (rgfo_spin_sector *mod* 12):
        i. Use Full G_m for esa_step <= rgfo_esa_step
        ii. Use Reduced G_m for esa_step > rgfo_esa_step
        iii. Ex: Let rgfo_half_spin = 10, rgfo_spin_sector = 3, and rgfo_esa_step = 19. (ESA steps = [18,19,20] sampled during half spin 10).
            1. Full G_m for spin_angle = [3, 15] and esa_step = [18,19]
            2. Reduced G_m for spin_angle = [3, 15] and esa_step = [20]
            3.

13.3 Combined Data Products

13.3.1 L3c – Combined Energy Time Spectrogram

This product consists of H, He, O, and Fe intensities covering the full range of the CoDICE-Lo and Hi instrument. Level 2 data products are used to produce a single combined energy-time spectrogram for each species. The first step is to produce energy-time spectrograms from Lo and Hi for each species in a common format.

Step 1: CoDICE-Lo Convert Distributions to E/n

We use SW and NSW data from the L2 Species Intensities product. For each species, j, the intensities ($J_j(l)$) are provided as a function of 128 energy-per-charge values (indexed by l). Since the L2 data is provided as a function of energy-per-charge, we perform the following steps for each species to convert the units to energy-per-nuc in units of MeV/amu. The final Lo intensities and energy bins are referred to as $\tilde{J}_j(l)$ and $\tilde{E}_H$.

Hydrogen: The charge of H is $Q_H = 1$ and the mass is m = 1 amu, thus the converted Lo H product is computed as:

$$\tilde{J}_H(l) = \frac{\left(J_{H,SW}(l) + J_{H,NSW}(l)\right)}{Q_H} * m * 1000 \qquad \text{[particles / (cm}^2\text{ s sr MeV/n)]}$$

$$\tilde{E}_H = \frac{E_H}{m*1000} \qquad \text{[MeV/n]}$$

Here, $\tilde{E}_H$ is the 128 energy-per-nuc bins corresponding to $\tilde{J}_H(l)$, and E_H is the 128 energy-per-charge bins corresponding to the L2 data. $J_{H,SW}(l)$ and $J_{H,NSW}(l)$ are the SW and NSW H intensities from the L2 Species product.

Helium: We use He^{++} intensities with charge $Q_{He} = 2$ and mass m=4. The converted Lo He product is computed as:

$$\tilde{J}_{He}(l) = \frac{\left(J_{He2+,SW}(l) + J_{He2+,NSW}(l)\right)}{Q_{He}} * m * 1000 \qquad \text{[particles / (cm}^2\text{ s sr MeV/n)]}$$

$$\tilde{E}_{He} = \frac{E_{He} * q}{m*1000} \qquad \text{[MeV/n]}$$

Here, $\tilde{E}_{He}$ is the 128 energy-per-nuc bins corresponding to $\tilde{J}_{He}(l)$, and E_{He} is the 128 energy-per-charge bins corresponding to the L2 data. $J_{He,SW}(l)$ and $J_{He,NSW}(l)$ are the SW and NSW H intensities from the L2 Species product.

Oxygen: Since the NSW O intensities are minimal compared to the SW O intensities and they are not split into a different charge state products, we only use the SW O intensities, provided for four different charge states (i.e., $5^+, 6^+, 7^+, and\ 8^+$). We convert each of the individual charge state distribution to common units by:

$$\tilde{J}_{O,q}(l) = \frac{J_{q,SW}(l)}{q} * m * 1000 \quad \text{[particles / (cm}^2\text{ s sr MeV/n)]}$$

$$\tilde{E}_{O,q} = \frac{E_O * q}{m * 1000} \quad \text{[MeV/n]}$$

Here, $J_{q,SW}(l)$ is the SW Oxygen intensities for charge state q from the Lo *L2 Species* product. q is the charge of each individual species which takes values of $q = 5, 6, 7, 8$. The mass is m = 16 and E_O is the 128 energy-per-charge values corresponding to the Lo *L2 Species Intensities* product.

Iron: Similar to the computation for Oxygen, we only use the SW Fe intensities. For the SW low and high charge state products, we assume a charge state of $Q_{Fe,low} = 9$ and $Q_{Fe,low} = 15$ with a mass of m=56. The converted Fe intensities are given by:

$$\tilde{J}_{Fe,low}(l) = \frac{\left(J_{low,SW}(l)\right)}{Q_{Fe,low}} * m * 1000 \quad \text{[particles / (cm}^2\text{ s sr MeV/n)]}$$

$$\tilde{J}_{Fe,high}(l) = \frac{\left(J_{high,SW}(l)\right)}{Q_{Fe,high}} * m * 1000 \quad \text{[particles / (cm}^2\text{ s sr MeV/n)]}$$

$$\tilde{E}_{Fe,high} = \frac{E_{Fe} * Q_{Fe,high}}{m * 1000} \quad \text{[MeV/n]}$$

$$\tilde{E}_{Fe,low} = \frac{E_{Fe} * Q_{Fe,low}}{m * 1000} \quad \text{[MeV/n]}$$

Here, $J_{low,SW}(l)$ and $J_{high,SW}(l)$ are the SW low and high charge state Fe intensities from the Lo *L2 Species* product.

Step 2: CoDICE-Lo Energy Re-binning

Each species data is re-binned into common energy-per-nuc bins with logarithmic spacing of sqrt(2) defined as follows:

1. Compute the upper and lower energy-per-nuc bin values as:

$$E_{l,i} = E_{min} * 2^{i/2}, \quad \text{for } i = 0, 1, \ldots, 19$$

$$E_{u,i} = E_{min} * 2^{(i+1)/2}, \quad \text{for } i = 0, 1, \ldots, 19$$

2. The center of each energy bin is then given by:

$$E_i = \sqrt{E_{u,i} * E_{l,i}} \quad \text{for } i = 0, 1, \ldots, 19$$

Here, $E_{min} = 0.0001$ and $E_{max} = 0.1$ MeV/n.

The re-binned intensities are computed by integrating the intensities produced in Step 1 over each of these new energy-per-nuc bins. For O and Fe species, this re-binning is done for each individual charge state distribution. For example:

$$\tilde{J}_{O,q}(i) = \frac{\left(\sum_{E_{l,i} \le \tilde{E}_{O,q}(l) < E_{u,i}} \tilde{J}_{O,q}(l) * \Delta E\right)}{\sum \Delta E} \quad \text{for } i = 0, 1, \ldots, 19 \text{ and } q = 5, 6, 7, 8$$

Here, ΔE is the spacing of the CoDICE Lo energy bins that fall within the range $E_{l,i} - E_{u,i}$.

This step results in a set of 20 intensities and energy-per-nuc bins for each species.

For the O and Fe products, we next sum the re-binned individual charge state distributions resulting in the final O and Fe intensities for Lo as:

$$\tilde{J}_O(i) = \sum_{q=5,6,7,8} \tilde{J}_{O,q}(i)$$

And

$$\tilde{J}_{Fe}(i) = \tilde{J}_{Fe,low}(i) + \tilde{J}_{Fe,high}(i)$$

Step 3: Hi Intensities

The Hi L2 intensities are provided as a function of energy-per-nuc bins at a cadence of 1-min.

First, to avoid overlap between the Hi and Lo distributions, we restrict the energy-per-nuc range of the Hi data based on the table below.

L3c Hi Energy Ranges		
Species	E_{min}	E_{max}
H	0.08	5.0
He	0.04	5.0
O	0.03	5.0
Fe	0.02	5.0

Note that the He3 and He4 species products from the L2 Hi Omni Intensities are summed together for the He product.

Next, we time-average the Hi intensity over each 4-min time period corresponding to the Lo intensities in step 2. This effectively averages every 4 omni-directional intensity distributions from the Hi L2 product.

Step 4: Combine the Hi and Lo intensities

The Lo intensities from Step 2 are combined with the Hi intensities from Step 3 to form the final L3c product. The final data array provides intensities as a function of energy-per-nuc bins. The Lo and Hi intensity and energy-per-nuc arrays are concatenated to form single data and energy-per-nuc bin arrays. These are then provided as the *L3c Combined Energy Time Spectrograms*.

13.3.2 L3c – Combined Pitch Angle Distributions

This product consists of He and O intensities binned by pitch angle and covering the full range of the CoDICE-Lo and Hi instrument. Level 2 data products are used to produce a single combined pitch angle distribution for each species. The first step is to produce pitch angle distributions from Lo and Hi for each species in a common format. The pitch angle distribution for CoDICE-Hi is already computed at L3a. For CoDICE-Lo, we use the L2 Angular Intensities.

Step 1: Combine and Convert Angular Intensities to [MeV/n] units

We use data from the L2 Angular Intensities products. For each species, j, the intensities $J_j(l,n,k)$ are provided as a function of 128 energy-per-charge values (indexed by l), 3/10 elevation angles for the SW/NSW product (indexed by k), and 24 spin angles (indexed by n) at a 4-min cadence.

Helium:

First, we combine the SW and NSW He^{++} intensity y arrays into a single intensity array with dimensions (128 energy, 24 spin, 13 elevation).
We then convert the full distribution and corresponding energy-per-charge values to units of MeV/n:

$$\tilde{J}_j(l,n,k) = \frac{J_j(l,n,k)}{Q_{He}} * m_{He} * 1000 \qquad \text{[particles / (cm}^2\text{ s sr MeV/n)]}$$

$$\tilde{E}_j = \frac{E_j * Q_{He}}{m_{He} * 1000} \qquad \text{[MeV/n]}$$

Here, $m_{He} = 4$ and $Q_{He} = 2$.
E_j are the 128 energy-per-charge values corresponding to the L2 data.

Oxygen:

Since the NSW product does not contain data for O6+ and the vast majority of counts from O6+ are expected in the SW direction, we use the SW O6+ data only. The SW distribution and corresponding energy-per-charge values are converted to units of MeV/n:

$$\tilde{J}_O(l,n,k) = \frac{J_O(l,n,k)}{Q_O} * m_O * 1000 \qquad \text{[particles / (cm}^2\text{ s sr MeV/n)]}$$

$$\tilde{E}_j = \frac{E_j * Q_O}{m_O * 1000} \qquad \text{[MeV/n]}$$

Here, $m_O = 16$ and $Q_O = 6$.
E_j are the 128 energy-per-charge values corresponding to the L2 data.
Note, for the Oxygen product, the elevation angle index ranges from 0 – 2.

Step 2: Compute CoDICE-Lo Pitch Angle Distributions

To compute the look direction unit vector of each SSD in the spacecraft frame, we first convert the spin angles from the CoDICE instrument frame to the SC frame using the following equation:

$$\theta_{SC} = (\theta_{inst} + 46°)\ mod\ 360°$$

Here, θ is the spin angle in the SC or instrument (inst) frame and mod is the modular arithmetic function.
The elevation angle (ϕ) is the same in both frames and so $\phi_{SC} = \phi_{inst}$.

The look direction unit vector $\hat{n}_{SC} = [n_x, n_y, n_z]$ in the SC frame is given by:

$$n_x = \cos(\theta_{SC})\sin(\phi_{SC})$$
$$n_y = \sin(\theta_{SC})\sin(\phi_{SC})$$
$$n_z = \cos(\phi_{SC})$$

Note, to compute the unit vectors, the spin and elevation angle inputs should be in radian units. These look directions define the direction that particles are measured from. Thus, the direction of travel of particles is given by the negative of this vector (i.e, $-1 * \hat{n}_{SC}$). The pitch angle corresponding to each (l, n, k) bin is computed by:

$$\alpha(l,n,k) = \cos^{-1}\left(-\hat{n}_{SC} \circ \frac{\vec{B}_{SC}}{|\overrightarrow{B_{SC}}|}\right) * \frac{180}{\pi}$$

Here, $\vec{B}_{SC}$ is the magnetic field vector averaged over the 4 min accumulation period in the spacecraft frame. The operation inside of the parenthesis represents the dot product between the two vectors.

For each energy-per-nuc value, $\tilde{J}_j(l,n,k)$ is averaged and binned into 30° pitch angle bins ranging from $0° - 180°$ based on the derived values of $\alpha(l,n,k)$. The final data product is a 2-D array with dimensions (Energy × Pitch Angle) and containing the average intensity in each bin. This array is referred to as $J_j(l,\alpha)$, where l is the energy-per-nuc index and α is the pitch angle bin index.

Step 3: CoDICE-Lo Energy Re-binning

The pitch angle distributions computed in Step2 are provided in 128 energy-per-nuc bins. We next re-bin the distributions in the energy dimension as follows.

We first define an energy-per-nuc range for each species which we use to define a new set of energy-per-nuc bins. Each set will contain 20 logarithmic-spaced bins defined as follows:

1. Compute dE in log space by:

$$dE = \frac{(\log_{10}(E_{max}) - \log_{10} E_{min})}{20}$$

2. Compute the upper and lower energy-per-nuc bin values as:

$$E_{l,i} = 10^{(\log_{10}(E_{min}) + i * dE)}, \qquad \text{for } i = 0, 1, \ldots, 19$$

$$E_{u,i} = 10^{(\log_{10}(E_{l,i}) + dE)}, \qquad \text{for } i = 0, 1, \ldots, 19$$

3. The center of each energy bin is then given by:

$$E_i = \sqrt{E_{u,i} * E_{l,i}} \qquad \text{for } i = 0, 1, \ldots, 19$$

Here, E_{min} and E_{max} are the lower and upper energy-per-nuc values for each species provided in the table below. The values are computed from the min/max energy-per-charge values and assuming average charge states of 2 and 6 for He and O, respectively.

L3c Lo Energy Ranges in MeV/n		
Species	E_{min}	E_{max}
He	0.00025	0.040
O	0.0002	0.030

The re-binned pitch angle intensities are computed by averaging the intensity in each pitch angle bin over each of the newly defined energy ranges. For example:

$$\tilde{J}_j(l, \alpha) = \frac{\left(\sum_{E_{l,i} \le \tilde{E}_j(l) < E_{u,i}} J_j(l, \alpha)\right)}{N_i} \quad \text{for } i = 0, 1, \ldots, 19$$

Here, N_i is the number of $\tilde{E}_j$ values that fall within the range $E_{l,i} - E_{u,i}$. This computation happens for each pitch angle bin individually.

Step 4: Prepare Hi Pitch Angle Distributions

The Hi 3b Pitch Angle Distributions are provided as a function of energy-per-nuc bins and pitch angle at a cadence of 4-min.

To avoid overlap between the Hi and Lo distributions, we restrict the energy-per-nuc range of the Hi data based on the table below.

L3c Hi Energy Ranges		
Species	E_{min}	E_{max}
He	0.04	5.0
O	0.03	5.0

Step 5: Combine Hi and Lo pitch angle distributions

The Lo pitch angle distributions from Step 3 are combined with the Hi pitch angle distributions from Step 4 to form the final L3c product. The Lo and Hi intensity and energy-per-nuc arrays are concatenated to form single data and energy-per-nuc bin arrays. The final data array provides intensities as a function of energy-per-nuc and pitch angle at 4-min cadence for He and O. These are then provided as the *L3c Combined Pitch Angle Distributions*.

14. I-ALIRT DATA

14.1 CoDICE-Hi

The Hi I-ALiRT L1A Counts are summed over $n_{sector} = 6$, 15° spin sectors and $n_{spin} = 4$ spins, so the conversion to rates is given by:

$$\mathrm{R}(i,n,g) = \frac{\mathrm{C}(i,n,g)}{6*4*t_{acquire}*10^{-3}} \quad \text{[counts/s]}$$

$\mathrm{C}(i,n,g)$ are the L1A Hi I-ALiRT counts. $t_{acquire}$ is the acquisition time per SSD and spin sector determined from parameters reported from the spacecraft.

$i = 0, \ldots, 14$ corresponds to the energy-per-nuc bins

$n = 0, 1, 2, 3$ corresponds to the spin sector bin index

$g = 0, 1, 2, 3$ corresponds to each of the four groups of 3 SSDs over which the counts are summed. The table below provides the SSD IDs included in each group.

Group (g)	**SSD IDs (k)**	**Elevation Angle (°)**
0	0, 1, 3	132.8
1	4, 5, 7	65.7
2	8, 9, 11	47.1
3	12, 13, 15	114.3

Note, $\mathrm{R}(i,n,g)$ is the equivalent of L1B iALiRT rates.

The final I-ALiRT product for CoDICE Hi provides H intensities in 15 energy-per-nuc passbands, which is computed as follows:

$$\mathrm{I}(i,n,g) = \frac{\mathrm{R}(i,n,g)}{\mathrm{G_g}\cdot\epsilon_{ig}\cdot(\Delta E_i)} \quad \text{[\#/(cm}^2\text{-sr-s-MeV/nuc)]}$$

$R_j(i)$ are the Level-1b Species Rates for species j and energy bin i

G_g is the sum of the physical geometric factors (G_k) over the three SSDs in group g (identified in the table above).

ϵ_{ig} is the average of the H efficiencies for SSDs in group g and energy bin i (i.e., $\epsilon_{ig} = \frac{\sum_{k(g)} \epsilon_{Hik}}{3}$), where $k(g)$ correspond to the SSD IDs in group$g$ from the table above. These efficiency values are provided in LUTs.

ΔE_i is the energy pass band for bin i. It is computed from the plus/minus energy-per-nuc bin values contained in the cdf files as: $\Delta E_i = E_{i,minus} + E_{i,plus}$.

The uncertainty in intensity is computed from the rates uncertainties using the same conversions above.

Hi iALiRT - Spin Angles

The spin angles for the Hi iALiRT product correspond to the midpoint value for each group of SSD IDs over each set of spin sectors that the counts were summed over. They are calculated as:

$$\theta_{g,n} = \left(\theta_{g,0} + 90° * n\right) mod\ 360°, \qquad \text{for } n = 0, 1, 2, 3$$

Where $\theta_{g,0}$ is the reference spin angle for the first iALiRT spin angle bin 0 and SSD group, g. These values are provided in the table below and correspond to the middle of the angular bin.

Hi iALiRT spin angles (deg) in the Instrument Frame for spin angle bin = 0				
	SSD Group (g)			
	0	**1**	**2**	**3**
$\boldsymbol{\theta_{g,0}}$	196.85	174.55	253.16	275.44

14.2 CoDICE-Lo

The CoDICE-Lo I-ALiRT telemetered data consists of a subset of the CoDICE-Lo Species Counts. The species included are all solar wind species from the Sunward sector. The species are He++, C+5, C+6, O+6, O+7, O+8, Mg, Fe (low Q), and Fe (high Q) at all 128 ESA-steps. The following table gives the species index, j, and the mass per charge for each of the species.

Index, j	Species	m/q (AMU/e)
0	He++	2.0
1	C+5	2.4
2	C+6	2.0
3	O+6	2.7
4	O+7	2.28
5	O+8	2.0
6	Mg	3.5
7	Fe (high Q)	3.85
8	Fe (low Q)	7.25

To create the final products, which consist of elemental abundance and charge state ratios, we first create intermediate products that are used by the team to validate data going into the final products. These intermediate products are then used to construct the final public data.

14.2.1 Intermediate Products

Similar to the Level 1A, we first calculate the rates for each of the species:

$$\mathrm{R_j}(l) = \frac{\mathrm{C_j}(l)}{(t_{acquire} * 10^{-3} * n_{sector})} \quad \text{[counts/s]}$$

Where:

$$n_{sector} = 12 \text{ for ESA steps } 0 - 126$$

$$n_{sector} = 11 \text{ for ESA steps } 127$$

$\mathrm{C_j}(l)$ is the telemetered counts for species j at ESA-step l.

$t_{acquire}$ is the accumulation time for 1 spin sector, as determined using the algorithms in Appendix B. This quantity will be a constant for each ESA-step once the instrument is operational and so can be read from a table.

We then calculate the differential intensity for each energy step, which is the same as calculating the level 2 product. This takes into account the efficiencies and geometric factors.

$$J_j(l) = \frac{\mathrm{R_j}(l)}{G_m \cdot \varepsilon_{jl1} \cdot (E/q)_l}$$

J is the differential number flux [particles / (cm^2 s sr keV/q)]
$\mathrm{R_j}$ is the species rate in counts/second, for energy step, l.
$\mathrm{G_m}$ is the SW geometric factor (cm^2 str eV/eV) for position 1 and mode m, which is either "Full" or "Reduced", as explained below.
ε_{jl1} is the efficiency depending on the ESA step, l, and species, j, for position 1.
$(E/q)_l$ is the energy per charge for ESA step l, in keV/q

The intensity uncertainty is also provided as a separate variable and computed from the L1A counts as:

$$U_j(l) = \frac{\sqrt{\mathrm{C_j}(l)}}{G_m \cdot \varepsilon_{jl1} \cdot \left(\frac{E}{q}\right)_l * (t_{acquire} * 10^{-3} * 12)}$$

For $\mathrm{G_m}$, the mode is determined by checking whether the half-spin number for the ESA step l is less than or equal to the half-spin number specified by the parameter RGFO_Half_Spin. If the half-spin is less than or equal to RGFO_Half_Spin, then the "Full" geometric factor is used (m=0). If it is greater than RGFO_Half_Spin, then the reduced geometric factor is used (m=1).

We then apply the weighting factors needed to determine the pseudo-density (and uncertainties), but don't sum yet. We note that because our final public products are ratios, we have neglected several constant factors that would be needed to calculate the density because they cancel out when the ratios are taken.

$$d_psN_j(l) = \mathrm{J_j}(l) \cdot \sqrt{\left(\frac{E}{q}\right)_l} \cdot \sqrt{(m/q)_j}$$

$$d_psU_j(l) = \mathrm{U_j}(l) \cdot \sqrt{\left(\frac{E}{q}\right)_l} \cdot \sqrt{(m/q)_j}$$

For each species, we then calculate a weighted sum over the ESA-steps to get the pseudo-number density (psN).

The pseudo-densities and uncertainties are then given by the following:

$$psN_j = \sum_{l=0}^{128} d_psN_j(l)$$

$$psU_j = \sqrt{\sum_{l=0}^{128} \left(d_psU_j(l)\right)^2}$$

14.2.2 Forming the public data products

Once the pseudo-densities are calculated, the public data products can be determined

Elemental Abundances

$$\frac{\boldsymbol{C}}{\boldsymbol{O}} = \frac{psN_1 + psN_2}{psN_3 + psN_4 + psN_5}$$

$$\frac{\boldsymbol{Mg}}{\boldsymbol{O}} = \frac{psN_6}{psN_3 + psN_4 + psN_5}$$

$$\frac{\boldsymbol{Fe}}{\boldsymbol{O}} = \frac{psN_7 + psN_8}{psN_3 + psN_4 + psN_5}$$

Charge State Ratios

$$\frac{\boldsymbol{C^{+6}}}{\boldsymbol{C^{+5}}} = \frac{psN_2}{psN_1}$$

$$\frac{\boldsymbol{O^{+7}}}{\boldsymbol{O^{+6}}} = \frac{psN_4}{psN_3}$$

$$\frac{\boldsymbol{Fe^{low}}}{\boldsymbol{Fe^{high}}} = \frac{psN_8}{psN_7}$$

The uncertainties in each of the abundance and charge state ratio products (referred to here as R) are computed by the following steps:

1. Sum the relevant uncertainties in the numerator in quadrature
$$\boldsymbol{\Delta R_{top}} = \sqrt{\sum_{i \in \boldsymbol{numerator}} (psU_i)^2}$$
2. Sum the relevant uncertainties in the denominator in quadrature
$$\boldsymbol{\Delta R_{bot}} = \sqrt{\sum_{i \in \boldsymbol{denominator}} (psU_i)^2}$$
3. Compute final error using propagation of uncertainty formula:
$$\boldsymbol{\Delta R} = \frac{\boldsymbol{R_{top}}}{\boldsymbol{R_{bot}}} * \sqrt{\left(\frac{\boldsymbol{\Delta R_{top}}}{\boldsymbol{R_{top}}}\right)^2 + \left(\frac{\boldsymbol{\Delta R_{bot}}}{\boldsymbol{R_{bot}}}\right)^2}$$

Here, R_{top} and R_{bot} are the summed numerator and denominators for the relevant ratio.

15. OPERATION MODES

The CoDICE instrument has 4 operational modes: SAFE, LVENV (Low-Voltage Engineering), HVENG (High-Voltage Engineering), and Science. All the data described in this document is only available for Science mode. During Science mode, the instruments are routinely measuring data and processing it through the on-board look-up tables to generate the products that we see in the L0 data.

In the normal operation of the CoDICE-Lo instrument, it uses two “Geometric Factor Modes” as referred to in section 11.2.2, called “Full” and “Reduced”. The geometric factor is changed electrostatically by using a different combination of voltages on the electrostatic analyzer plates. The CoDICE-Lo entrance system steps through energy-per-charge steps from high values to low values. The energy per charge steps sampled change every half spin. The counts in each energy per charge step during a half-spin are monitored. When the count rate exceeds a threshold value, the geometric factor switches to “Reduced” on the next half spin. That Reduced value is maintained to the end of the sequence, unless the threshold is exceeded a second time. If the threshold is exceeded, the stepping sequence is stopped, and no data is taken in the lower energy steps. The sequence starts again at the highest energy per charge at the beginning of the next cycle. As described in section 11.2.2, the variables that contain the information about the switch are RGFO_Half_Spin, which gives the first half-spin number when the Reduced Geometric Factor is used. The variable NSO_Half_Spin indicates the half-spin when the stepping sequence stops.

Appendix A Acronyms / Abbreviations

Acronym	Definition
ESA	Electrostatic analyzer
TOF	Time-of-flight
CoDICE	Compact Dual Ion Composition Experiment
CCSDS	Consultative Committee for Space Data Systems
APD	Avalanche photodiode
EPQ	Energy per charge step
PHA	Pulse Height Analysis
LISM	Local interstellar medium
VDF	Velocity Distribution Function
MCP	Microchannel Plate
FOV	Field-Of-View

Appendix B – CoDICE-Hi: Derivation of True Omni-directional Intensity

Over the course of a spin, each Hi-SSD observes a solid angle that depends on the azimuth angle (position) of the SSD. The solid angle for a given position is constant over spin sector, thus, the solid angle covered by a single position over the course of a single spin sector ($\Omega_{N,k}$) is equal to the spin-integrated solid angle of that position divided by the number of spin sectors plus the instantaneous FOV of each SSD:

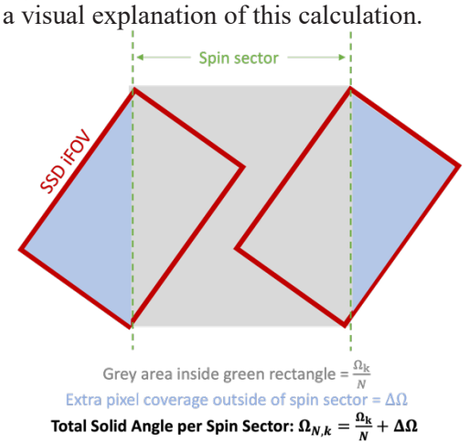
$$\Omega_{N,k} = \frac{\Omega_k}{N} + \Delta\Omega$$

N is the number of spin sectors per spin (nominally N = 12)

$\Delta\Omega = (7° * 12°) * \left(\frac{\pi}{180°}\right)^2 = 0.0256$ sr is the instantaneous FOV of an SSD.

Ω_k is the spin-integrated solid angle observed by SSD k (described in the next subsection).

The schematic below provides a visual explanation of this calculation.



Angular Bounds for Spin-Integrated Solid Angle Calculation

Over the course of a spin, the FOV of a single CoDICE-Hi observes a portion of the sky defined by $\varphi'_{k,l} < \varphi' < \varphi'_{k,u}$. Here, $\varphi'_{k,l}$ and $\varphi'_{k,u}$ are the minimum and maximum angles relative to the spacecraft spin axis that the CoDICE-Hi rectangular pixel covers. In the remainder of this section, a primed angle indicates an angle relative to the spacecraft spin axis of a point that is inclined to the CoDICE-Lo FOV plane. Since the CoDICE-Hi FOV is inclined by $\theta_{inc} = 30°$ to the CoDICE-Lo FOV plane, the angle relative to the spin axis of the center of a CoDICE-Hi pixel (φ'_k) is not equal to the corresponding angle in the CoDICE-Lo FOV plane (φ_k). The relation between φ'_k and $\varphi_k$is given by:

$$\varphi'_k = \cos^{-1}(\cos(\theta_{inc}) \cdot \cos(\varphi_k))$$

Due to the 30° inclination and the rectangular shape of each CoDICE-Hi pixel, $\varphi'_{k,l}$ and $\varphi'_{k,u}$ are different for each SSD. In general, for an inclination angle of θ above the CoDICE-Lo FOV plane, a non-primed angle (φ) is related to the corresponding primed angle (φ_k) by:

$$\varphi' = \cos^{-1}(\cos(\theta) \cdot \cos(\varphi))$$

Since the Hi pixels are rectangular, the values of $\varphi'_{k,l}$ and $\varphi'_{k,u}$ mostly correspond to one of the corners of the pixels (for Pixel 1 and Pixel 7 one of these angles corresponds to the midpoints of the side of the pixel closest to and farthest from the spin axis, respectively). In the following text we calculate $\varphi'_{k,l}$ and $\varphi'_{k,u}$ for CoDICE-Hi pixel 1, 2, 3, and 4 individually. The remaining values are then given by symmetry relations at the end of this section. In these calculations, $\alpha = 7°$ refers to the angular width of a pixel in the spin-direction (elevation) and $\beta = 12°$ refers to the angular width of a pixel in the azimuthal direction.

Angular Bounds: Pixel 1 - $(\boldsymbol{k = 1})$
For this pixel, $\varphi_1 = 0°$ and $\varphi'_1 = 30°$ which is the angle relative to the spin axis of the center of the pixel. The angle $\varphi'_{1,l}$ corresponds to the midpoint of the Hi pixel closest to the spin axis, and the angle $\varphi'_{1,u}$ corresponds to one of the two corners of the pixel that are farthest from the spin axis. To calculate these angles in the primed system, we follow the following process: Starting with φ_1, we add/subtract an amount of $\pm\frac{\beta}{2}$ to that angle, which represents a rotation in the CoDICE-Lo FOV plane by $\frac{\beta}{2}$. This gives the value of φ for the four corners (for the midpoint, we do not add/subtract anything). The inclination angle for the corners and midpoint is then given by $\theta = \theta_{inc} \pm \frac{\alpha}{2}$. This results in the following:

$$\varphi'_{1,l} = \cos^{-1}\left(\cos\left(\theta_{inc} - \frac{\alpha}{2}\right) \cdot \cos(\varphi_1)\right)$$

$$\varphi'_{1,u} = \cos^{-1}\left(\cos\left(\theta_{inc} + \frac{\alpha}{2}\right) \cdot \cos\left(\varphi_1 \pm \frac{\beta}{2}\right)\right)$$

Note, in the $\pm$ sign in the second cos term of $\varphi'_{1,u}$ is irrelevant since $\varphi_1 = 0$ and $\cos\left(\frac{\beta}{2}\right) = \cos\left(-\frac{\beta}{2}\right)$.

Angular Bounds: Pixels 2, 3 and 4 $(\boldsymbol{k = 2, 3, 4})$
The calculations for these three pixels are similar to that for Pixel 1. Here, the largest and smallest primed angle for each pixel corresponds to one of the corners of each pixel. Similar to the calculation above, the corners of these pixels have primed angles given by:

$$\varphi'_{l1,k} = \cos^{-1}\left(\cos\left(\theta_{inc} - \frac{\alpha}{2}\right) \cdot \cos\left(\varphi_k - \frac{\beta}{2}\right)\right)$$

$$\varphi'_{l2,k} = \cos^{-1}\left(\cos\left(\theta_{inc} + \frac{\alpha}{2}\right) \cdot \cos\left(\varphi_k - \frac{\beta}{2}\right)\right)$$

$$\varphi'_{u1,k} = \cos^{-1}\left(\cos\left(\theta_{inc} + \frac{\alpha}{2}\right) \cdot \cos\left(\varphi_k + \frac{\beta}{2}\right)\right)$$

$$\varphi'_{u2,k} = \cos^{-1}\left(\cos\left(\theta_{inc} - \frac{\alpha}{2}\right) \cdot \cos\left(\varphi_k + \frac{\beta}{2}\right)\right)$$

Note the difference in the signs of the $\frac{\alpha}{2}$ and $\frac{\beta}{2}$ terms. With these definitions, $\varphi'_{k,u}$ and $\varphi'_{k,l}$ are:

$$\varphi'_{k,u} = \max\{\varphi'_{l2,k},\ \varphi'_{l1,k},\ \varphi'_{u2,k},\ \varphi'_{u1,k}\}$$

$$\varphi'_{k,l} = \min\{\varphi'_{l2,k},\ \varphi'_{l1,k},\ \varphi'_{u2,k},\ \varphi'_{u1,k}\}$$

for k = 2, 3, 4.

Spin-Integrated Solid Angle Calculation

Using the calculations of $\varphi'_{k,l}$, and $\varphi'_{k,u}$, the spin-integrated solid angle (Ω_k) for each pixel is computed as the surface area of a unit sphere bounded by polar angles $[\varphi'_{k,l},\ \varphi'_{k,u}]$. This is given by the following equation:

$$\Omega_k = 2\pi\left(\cos\left(\varphi'_{k,l}\right) - \cos\left(\varphi'_{k,u}\right)\right)$$

This calculation is performed for ion Pixels 1, 2, 3, and 4 using the values described above. The remaining solid angles are given by the following symmetry relations:

$$\Omega_1 = \Omega_7$$
$$\Omega_4 = \Omega_{10}$$
$$\Omega_2 = \Omega_6 = \Omega_8 = \Omega_{12}$$
$$\Omega_3 = \Omega_5 = \Omega_9 = \Omega_{11}$$

The final computed values of $\Omega_k$for pixels are shown in table ##. This table also provides the solid angle covered by each pixel per spin sector (i.e., $\Omega_{12,k} = \frac{\Omega_k}{12} + \Delta\Omega$). Figure ## shows the sky coverage of each CoDICE-Hi pixel over the course of a full spin, the total over all pixels being 1.956 sr.

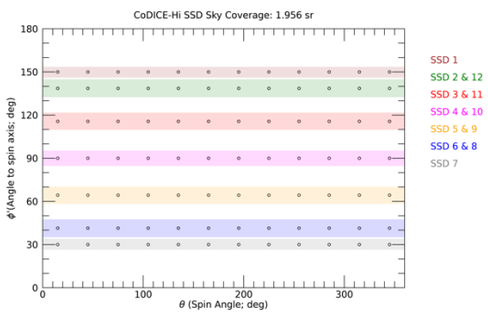


Figure ##. Sky coverage map of the CoDICE-Hi SSDs over the course of a single spin.

Table ##: CoDICE-Hi –Spin-integrated Solid Angle

Location (k)	SSD ID (ID)	φ (deg)	φ' (deg)	Ω_k (sr)	$\Omega_{12,k}$ (sr)
1	0	180	150.0	0.412282	0.05994
2	2	-150	138.6	0.89809	0.10042
3	3	-120	115.6	1.17406	0.12342
4	4	-90	90.0	1.17554	0.12354
5	6	-60	63.3	1.17406	0.12342

Location (k)	SSD ID (ID)	φ (deg)	φ' (deg)	Ω_k (sr)	$\Omega_{12,k}$ (sr)
6	7	-30	41.4	0.89809	0.10042
7	8	0	30.0	0.412282	0.05994
8	10	30	41.4	0.89809	0.10042
9	11	60	64.3	1.17406	0.12342
10	12	90	90.0	1.17554	0.12354
11	14	120	115.7	1.17406	0.12342
12	15	150	138.6	0.89809	0.10042

Solid-Angle-Corrected Omni-directional Intensity

The omni-directional intensity for species (j) is calculated by integrating the sectored intensities over spin sector and SSD ID and normalizing by the total sky coverage of . This integration is performed over solid angle space, and is approximated as a summation by:

$$\tilde{I}_j(i) = \frac{\sum_k \Omega_{12,k} * (\sum_n I_j(i,n,k))}{\Omega_T} \quad [\#/(\text{cm}^2\text{-sr-s-MeV/nuc})]$$

Here, $\Omega_T = 1.956\ [sr]$ is the total portion of the sky that the CoDICE-Hi observes over a full spin.

Appendix C – Calculations of Spin Sector Acquisition Times

This section describes the calculations of the time spent acquiring data during a single spin sector for CoDICE-Hi and CoDICE-Lo. Table B-1 provides a set of equations which are common to both CoDICE-Hi and CoDICE-Lo calculations.

Table B-1. Values common to CoDICE-Lo and CoDICE-HI

Equation[1]	*Notes*
$t_{sectorTime} = int\left(\frac{P_{spinPeriod} * 320}{NumSectors}\right)$	• $t_{sectorTime}$ is the total time, in microseconds, for a single spin sector • $NumSectors$ is 24; this is technically configurable but should not change. • $P_{spinPeriod}$ ranges from 45687 – 48031 [spin ticks]. It is initially set to 45687 spin ticks. One spin tick is equal to 320 μs, which gives a total acquisition time for a single spin of $P_{spinPeriod} * 320 * 10^{-6} = 14.62\ [s]$, which guarantees it is shorter than the actual spin. This value may can be set closer to the actual spin period once it stabilizes. This parameter is set in units of 'spin ticks' (320 μs per tick) in the LUT and is scaled to microseconds by the FSW • The spin period range yields a $t_{sectorTime}$ between 0.609 and 0.640 seconds; the baseline 15-second spin period yields a sector time of 0.625 seconds.
$t_{sectorMargin} = P_{sectorMargin} * 1000$	• $t_{sectorMargin}$ is the dead time, in microseconds, at the end of each spin sector for FSW to process data and prepare for the next sector. • Nominal value is 5000 μs (0.005 seconds) • $P_{sectorMargin}$ is specified in the LUT in milliseconds (nominal value is 5), and is scaled to microseconds by the FSW
$t_{minHvSettle} = P_{minHvSettle} * 1000$	• $t_{minHvSettle}$ is the minimum time, in microseconds, that can be used for HV settling. If the computed time is less than this value, it will be increased to comply. • Nominal value is 5,000 μs (0.005 seconds) • $P_{minHvSettle}$ is specified in the LUT in milliseconds (nominal value is 5), and is scaled to microseconds by the FSW
$t_{maxHvSettle} = P_{maxHvSettle} * 1000$	• $t_{maxHvSettle}$ is the maximum time, in microseconds, that can be used for HV settling. If the computed time is more than this value, it will be reduced to comply. • Nominal value is 100,000 μs (0.1 seconds) • $P_{maxHvSettle}$ is specified in the LUT in milliseconds (nominal value is 100), and is scaled to microseconds by the FSW

(a) [1] t_{xxx} values are times, in microseconds; P_{xxx} values are tunable LUT Parameters

B.1 CoDICE-Hi Acquisition Time

For CoDICE-Hi, the time spent acquiring data during a single spin sector is given by:

$$\boldsymbol{t_{acquire} = \left(t_{sectorTime} - t_{sectorMargin} - t_{minHvSettle}\right) * 10^{-6} = 0.59916} \quad [s]$$

Here, $\boldsymbol{t_{sectorTime}}$, $\boldsymbol{t_{sectorMargin}}$, and $\boldsymbol{t_{minHvSettle}}$ are from Table B-1. Note that CoDICE-Hi doesn't actually need HV Settling time, but the same collection algorithm is used for both sensors, and this gives the FSW a bit of time to get things set up at the beginning of each sector.

B.2 CoDICE-Lo Acquisition Time

The ESA voltage stepping scheme for CoDICE-Lo further complicates the calculation of the acquisition time for each sector. Table B-2 provides variables that are specific towards the CoDICE-Lo calculation. Using these variables, the time spent acquiring data for each ESA step in a given sector is:

$$\boldsymbol{t_{acquire} = \left(\frac{\left(t_{sectorTime} - t_{sectorMargin}\right)}{NumAcqSteps} - t_{hvSettlePerStep}\right) * 10^{-3}} \quad [ms]$$

Table B-2. CoDICE-Lo Acquisition Timing Variables

Equation	*Notes*
$t_{nonAcquire} = int\left(t_{sectorTime} * \frac{100 - P_{dwellFraction}}{100}\right)$	• $t_{nonAcquire}$ is the total time spent *not* acquiring data during the spin sector. This is based on a 'Dwell Fraction' parameter (nominally set to 95% to meet the L3 requirement to be collecting 95% of the time) • $P_{dwellFraction}$ is the percentage of time spent acquiring data; it is nominally set to 95 (so acquiring 95% of the time; remaining time is consumed by HV settling, sector margin, and spin sync)
$t_{totalHvSettle} = t_{nonAcquire} - t_{sectorMargin}$	• $t_{totalHvSettle}$ is the total time spent during the sector waiting for HV settling between acquisitions.
$t'_{hvSettlePerStep} = int\left(\frac{t_{totalHvSettle}}{NumAcqSteps}\right)$ $t_{hvSettlePerStep} = \max\left(t_{minHvSettle}, min\left(t'_{hvSettlePerStep}, t_{maxHvSettle}\right)\right)$	• $t_{hvSettlePerStep}$ is the HV settling time before each individual acquisition • *NumAcqSteps* is the number of ESA steps that will be scanned during the sector (lookup from the SCI LUT Lo Stepping table). This varies from 1 to 6 over the course of a full scan.

4.2.3 HIT

HIT data product definitions and processing algorithms are embedded below



Contents

1 Introduction **8**
- 1.1 Document Purpose . . . 8
- 1.2 Acronyms . . . 8
- 1.3 Scope . . . 9

2 HIT Instrument Description **9**
- 2.1 Instrument Overview . . . 9
- 2.2 Sensor Head . . . 9
- 2.3 Boresight . . . 11
- 2.4 HIT Electronics . . . 12
- 2.5 Differences From Heritage Instrument . . . 14
  - 2.5.1 I-ALiRT Apertures . . . 14
  - 2.5.2 L1 and L4 Position . . . 14
  - 2.5.3 I-ALiRT Data Products . . . 14
  - 2.5.4 Spinning Spacecraft . . . 14
  - 2.5.5 FPGA . . . 15
  - 2.5.6 State Machine . . . 15
  - 2.5.7 ADCs . . . 15
  - 2.5.8 Software . . . 15

3 Operating Modes **15**
- 3.1 Nominal Science Mode . . . 15
  - 3.1.1 Dynamic Thresholds . . . 15
- 3.2 Safe Mode . . . 16
- 3.3 Boot Mode . . . 16

4 Data Products **18**
- 4.1 Data Product Level Definitions . . . 18
  - 4.1.1 Telemetry . . . 18
  - 4.1.2 Level 0 - Raw Data . . . 18
  - 4.1.3 Level 1a - Reformatted Data . . . 18
  - 4.1.4 Level 1b - Partially Processed Data . . . 18
  - 4.1.5 Level 2 - Calibrated Data . . . 19
  - 4.1.6 Level 3 - Derived Science Products . . . 19
  - 4.1.7 Data Flow Diagram . . . 19
- 4.2 Science Data . . . 20
  - 4.2.1 Science Rates (Species Counts and Rate Counters) . . . 20
  - 4.2.2 Sector Rates . . . 21
  - 4.2.3 Singles and Coincident Rates . . . 22

Draft

4.2.4 Livetimes, Event Processing Counters, and Priority Buffer Counters . . . 22
4.2.5 Event Buffer - Event Record Format . . . 25
4.2.6 Extended Header Block . . . 29
4.2.7 Event Buffer - STIM Events . . . 30
4.2.8 PHA Word . . . 31
4.2.9 Theoretical Description of Primary Science Products . . . 33
4.2.10 Science Data Types . . . 34
4.3 Uncertainties . . . 35
4.3.1 Statistical Uncertainties . . . 35
4.3.2 Systematic Uncertainties . . . 35
4.3.2.1 Chance Coincidences . . . 35
4.3.2.2 Live-time Effects . . . 36
4.4 I-ALiRT Data . . . 36

5 Level 0 to Level 1a Processing 37
5.1 Rates Compression/Decompression Algorithm . . . 37
5.2 APID and Packet Number . . . 39
5.3 HIT Science Frame Header . . . 39
5.4 HIT Science Frame Format Summary . . . 41
5.5 Lev1A Uncertainty . . . 77

6 Level 1a to Level 1b Processing 77
6.1 Energy Bins . . . 78
6.2 Livetime Corrected Standard and Sectored Rates . . . 78
6.3 Summed Rates . . . 80
6.4 Sector Rates . . . 88
6.5 Housekeeping . . . 88

7 Level 1b to Level 2 Processing 97
7.1 Conversion to Intensity . . . 97
7.1.1 Standard Rates . . . 97
7.2 Sectored Rates . . . 137
7.3 Summed Rates . . . 141

8 I-ALiRT Algorithms 144
8.1 Level 0 Processing . . . 144
8.2 Level 1 I-ALiRT Data . . . 147

9 Lev3 Algorithms 149
9.1 PHA Products . . . 149
9.1.1 Incident Ion Energy Calculation . . . 152

Draft

9.1.2 ADC-MeV Conversion 153
9.1.3 Cosine Correction 154
9.1.4 Charge Calculation 155
9.2 Lev3 Sectored Products 161
9.3 Lev3 Electron Science Products 163

Draft



1 Introduction

1.1 Document Purpose

This document provides a description of the algorithms used to produce science data and I-ALiRT products from the IMAP High-energy Ion Telescope (HIT) instrument measurements on the Interstellar Mapping and Acceleration Probe (IMAP).

1.2 Acronyms

ACR Anomalous Cosmic Rays

ADC Analog-to-Digital Converter

EPI-Hi High-Energy Energetic Particle Instrument

FEE Front-End Electronics

FoV Field of View

FPGA Field Programmable Gate Array

FSW Flight Software

GCR Galactic Cosmic Rays

HIT High-energy Ion Telescope

HVPS High Voltage Power Supply

I-ALiRT IMAP Active Link for Real-Time

IC Integrated Circuit

IDPU Instrument Data Processing Unit

IMAP Interstellar Mapping and Acceleration Probe

LET Low Energy Telescope

LVPS Low Voltage Power Supply

MISC Minimal Instruction Set Computer

PHA Pulse Height Analysis

PHASIC Pulse Height Analysis System Integrated Circuit

Draft

SDC Science Data Center

SSD Solid-State Detector

STEREO Solar Terrestrial Relations Observatory

1.3 Scope

The purpose of the information contained in this document is to provide the necessary information for the IMAP Science Data Center (SDC) to develop and test software that will produce the science data products required by the instrument and mission.

2 HIT Instrument Description

2.1 Instrument Overview

HIT is one of five in-situ instruments included in the IMAP science payload. HIT measures ∼2-40 MeV/nucleon ion (H to Ni) compositions, energy spectra, angular distribution, and temporal distributions. The combination of SWAPI, CoDICE, and HIT provide continuous measurements of ions from 0.1 keV - 40 MeV/nucleon. The HIT design draws significant heritage from the Low Energy Telescope (LET) on board the Solar Terrestrial Relations Observatory (STEREO) and from the high-energy Energetic Particle Instrument (EPI-Hi) on Parker Solar Probe. The full HIT instrument (Fig. 1) consists of a sensor head, as shown in the far right of Fig. 2 and an electronics box separated by a long support tube which provides the sensor head with an unimpeded field of view (FoV).

2.2 Sensor Head

The HIT sensor subsystem consists of 14 solid-state detectors (SSD) broken up into individual detector segments whose signals are individually analyzed by custom built Pulse Height Analysis System Integrated Circuits (PHASICs deriving heritage from STEREO/LET, STEREO/HET and Parker Solar Probe/EPI-Hi. HIT utilizes a standard "dE/dx vs. residual E" measurement technique in which the combination of the energy deposit in the detector in which a particle stopped and the energy deposit in the detector through which the particle passed immediately before the stopping layer allows the identification of the incident ion species and energy. This measurement technique has

Draft

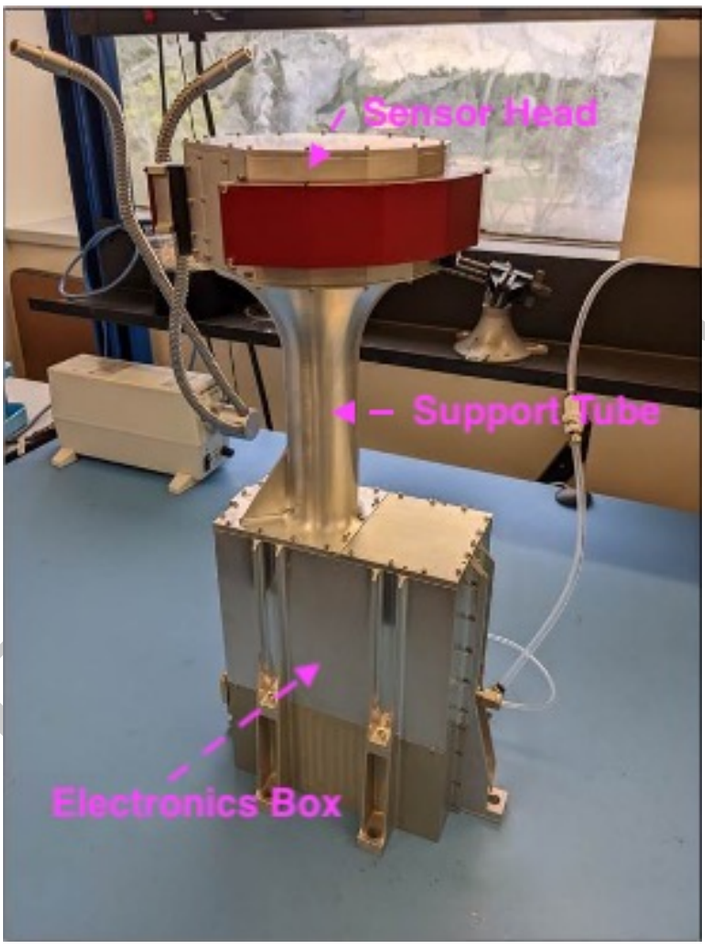


Figure 1: Annotated photograph of HIT engineering model.

extensive spaceflight heritage (e.g. ACE/SIS, Voyager/CRS, Voyager/LECP, STEREO/LET, STEREO/HET, Parker Solar Probe/EPI-Hi).

An exploded view of the HET sensor head is shown in Fig. 3. The HIT sensor head has 10 entrance apertures, 8 of which are identical "science apertures" and 2 are identical "I-ALiRT apertures." The apertures are divided into two groups of five which are arranged along the arc of a circle adjacent to one another. The outer region of all 10 apertures are occupied by the 24 μm thick L1 detectors. Each L1 detector has an active area of 2 cm^2 subdivided into 3 segments. The two "I-ALiRT" apertures also include a 1500 μm thick L4 detector, subdivided into two active areas, optimized for the measurement of energetic electrons. In the center of the sensor head are 4 large, rectangular SSDs, L2 and L3. The two L2 detectors are 50 μm thick with an active area of 10.2 cm^2 divided into 10 segments. The two L3 detectors are 1000 μm thick with an active area of 15.6 cm^2 divided into three segments. The identification of the individual L1, L2, and L3 segments triggered along with the triggered L1 detector determines the direction of the incident ion.

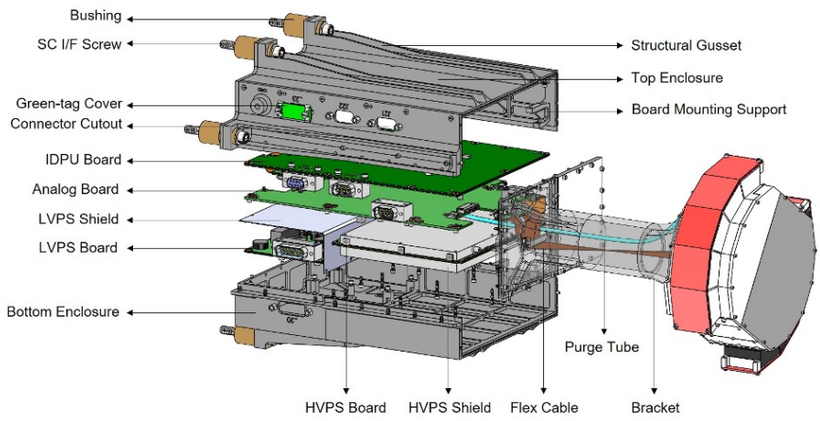


Figure 2: Exploded view of the full HIT instrument.

2.3 Boresight

The instrument boresight location is shown in Fig. 4 in the spacecraft frame. HIT is rotated 30° counterclockwise from the spacecraft $\hat{Y}$ axis. The instrument boresight will be taken to be along the spacecraft $\hat{Z}$ axis (i.e., along the sun-spacecraft line) between the L0B and L1B apertures. The rotation matrix to convert between the instrument frame and the spacecraft frame is shown in Fig. 5. Thus, the HIT instrument vector is -0.5 $\hat{X}$ 0.866025 $\hat{Y}$ 0 $\hat{Z}$ with respect to the spacecraft frame. The inverse (transpose) must be used to convert from the spacecraft from to the instrument frame.

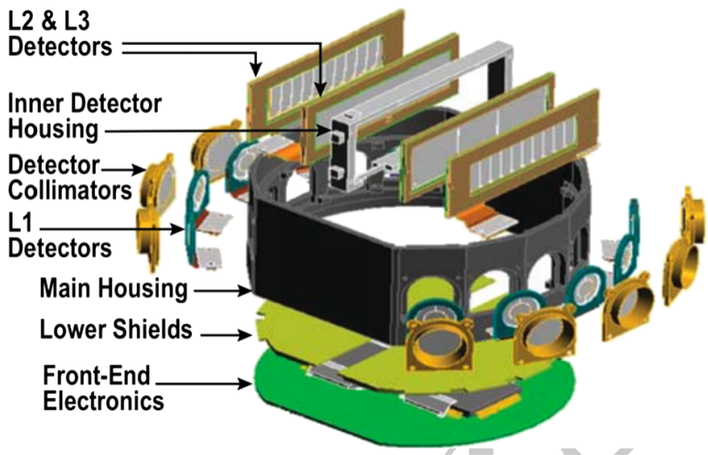


Figure 3: Exploded, annotated model of the HIT sensor head.

2.4 HIT Electronics

A block diagram of the HIT front-end electronics (FEE) is shown in Fig. 6. The HIT SSD signals are readout by the custom PHASICs (four in total). Each PHASIC has 16 identical readout channels of pulse height analysis (PHA) circuitry as well as internal pulsers to monitor SSD gains and offsets. The PHASICs achieve a wide dynamic range through the use of a dual gain approach.

Event pulse heights calculated by the PHASICs are passed to an FPGA section (RTAX-2000) which performs on-board particle species identification, energy binning, and data packetization. The FPGA also serves to configure the PHASICs and collect certain housekeeping data.

In addition to the FEE data-processing electronics, the HIT electronics also include the following boards:

High Voltage Power Supply (HVPS) Provides bias voltages to the HIT SSDs.

Low Voltage Power Supply (LVPS) Provides regulated low voltages to electronics boards.

Instrument Data Processing Unit (IDPU) Passes science data and Command and Telemetry between the instrument and the spacecraft.

Analog Board Interface between the FEE and the HVPS and LVPS. Also handles temperature monitoring.

Draft

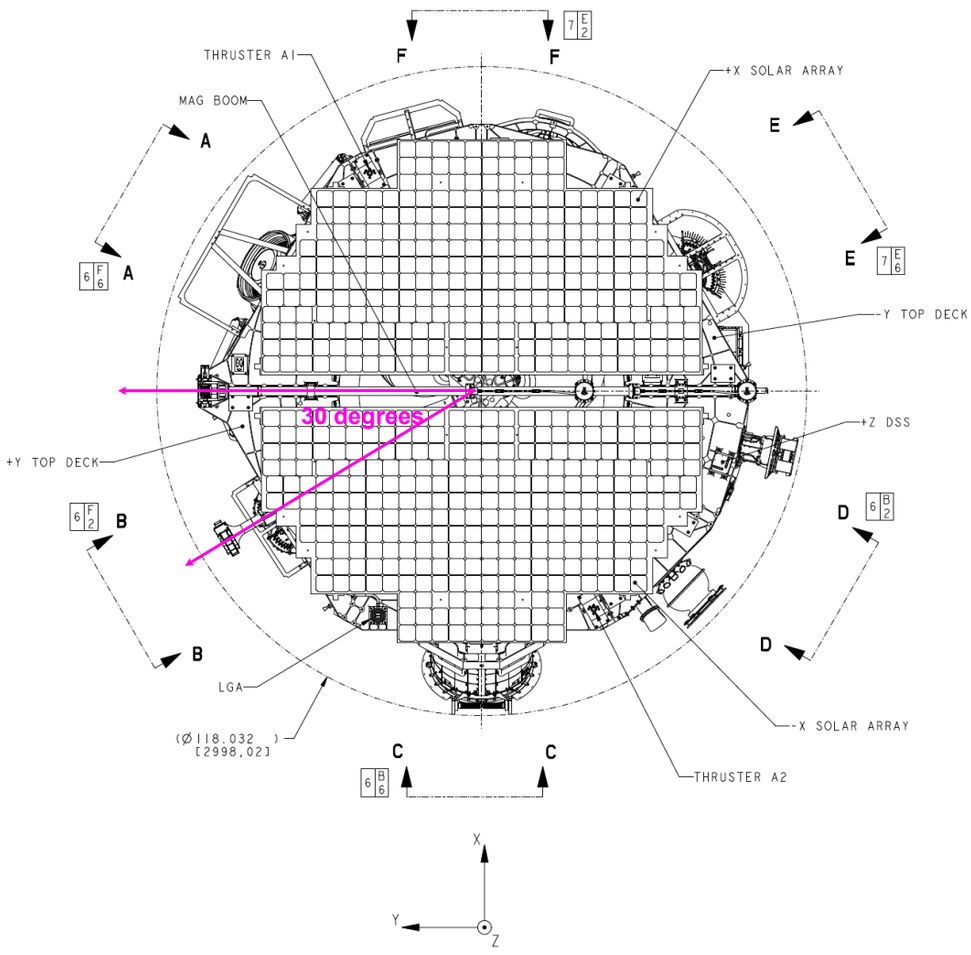


Figure 4: Graphical depiction of HIT instrument boresight frame in relation to spacecraft coordinate axes.

HIT (BAY B)	0.866025 0.500000 0.000000	-0.500000 0.866025 0.000000	0.000000 0.000000 1.000000	-18.407 [-467,53] 31.881 [809,78] 40.063 [1017,60]	30°	0°

Figure 5: Rotation matrix to transform from instrument frame to spacecraft frame.

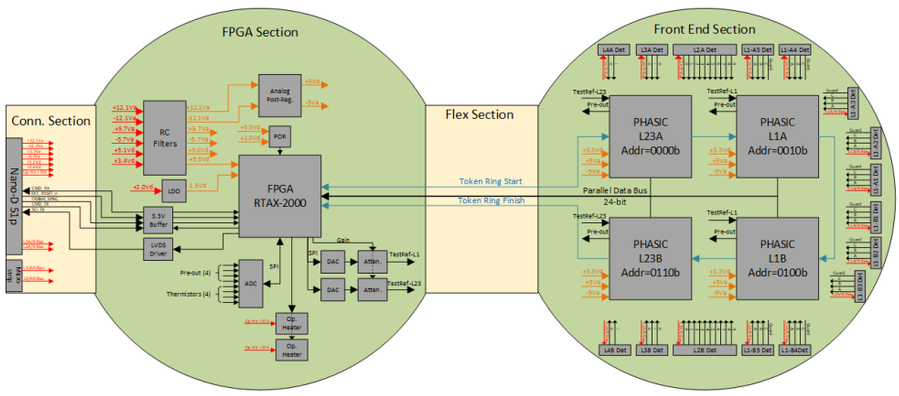


Figure 6: HIT FEE block diagram.

2.5 Differences From Heritage Instrument

This section lists the high-level differences between IMAP/HIT and its primary heritage instrument, STEREO/LET.

2.5.1 I-ALiRT Apertures

As discussed above, 2 of the 10 entrance apertures have a second, thicker detector (L4) located behind the outer L1 detectors. Energetic electrons are measured with L1 and the outer annulus of L4 in anticoincidence with the central region of L4 (to distinguish between incident electrons and protons) to aid in real-time space weather monitoring.

2.5.2 L1 and L4 Position

L1 and L4 detectors in the entrance apertures have been moved outward to fit the thicker L4 detector.

2.5.3 I-ALiRT Data Products

HIT will provide real-time electron and proton data from the I-ALiRT apertures on a 4 second cadence to satisfy the space weather monitoring required by the IMAP mission.

2.5.4 Spinning Spacecraft

The IMAP spacecraft spins at a rate of 4 rpm in contrast to the STEREO spacecrafts which are 3-axis stabilized. As such, the actual look direction of each aperture will change continuously and need to be tracked to calculate anisotropy and pitch angle distributions.

Draft



2.5.5 FPGA

The RTAX-2000 was chosen based on the HIT-SYS-TRD-0004 FPGA trade study in order to maximize resource utilization.

2.5.6 State Machine

The Minimal Instruction Set Computer (MISC) used on STEREO/LET has been replaced with a state machine built into the FPGA.

2.5.7 ADCs

The custom/discreet ADCs used on STEREO/LET have been replaced with monolithic integrated circuits (ICs)

2.5.8 Software

Flight software will be written in the C++ programming language replacing the Forth code used on STEREO/LET.

3 Operating Modes

3.1 Nominal Science Mode

The HIT operating principle is "turn us on and leave us on." This means that HIT can remain on through spacecraft operations including thruster firings. In Science Mode, the high voltage bias to the SSDs is on.

3.1.1 Dynamic Thresholds

When a large SEP event, with high intensities of energetic ions and electrons, is incident on an energetic particle detector, the instrument can saturate, resulting in an increase in dead-time and a reduction of data quality. Accidentally coincidence events involving more than one particle are also significantly more likely during these periods of high particle intensity (this source of systematic error is described in further detail below). To mitigate these issues, HIT includes an automatic "dynamic threshold" in which the geometry factor of the instrument is reduced by increasing the effective energy threshold on certain detector segments. This effective threshold increase is accomplished by disabling the high-gain PHA channels on certain detector segments, which primarily reduces the effective geometry factor for light ions (H and He) with minimal effect on the heavy ions ($Z \geq 6$) as these particles trigger the low-gain channels. The instrument automatically changes dynamic threshold level according to a

Draft



(commandable) level of the single-detector count rate. As the energetic particle intensity, and as a result the measured single-detector count rate, decreases, the instrument returns to lower dynamic threshold modes. This transition typically happens when the count rate is roughly half of the rate required to step up in dynamic threshold mode (also commandable). An example of the effects of dynamic thresholds on the count rates of various species and instrumental rates are shown in Fig. 7 in the case of the STEREO/LET data from the July 14, 2000 (Bastille Day) SEP event. As the Monitor rate increases, the instrument automatically places itself in higher dynamic threshold levels (visible as the times when the Monitor and H & He count rates sharply drop), thereby preserving livetime to maintain the ability to measure Z$\geq$ ions.

In the nominal dynamic threshold state (DT0), all high-gains are functioning. Above DT0 are 3 higher dynamic threshold levels in which the geometry factor is progressively reduced in response to high count rates. These dynamic threshold states only effect the "science apertures" leaving the I-ALiRT apertures in their nominal configuration. The 3 higher dynamic threshold levels are summarized below.

DT1 High-gain PHA is disabled on the outer regions all 16 L1 segments in the science apertures (i.e., the I-ALiRT apertures are unaffected). This effectively raises the threshold required to trigger the detectors, making them insensitive to H and He. The geometry factor is thus reduced to only that produced by the inner L1 detectors.

DT2 High-gain PHA is disabled on all L1 detectors in the science aperture (i.e., the I-ALiRT apertures are unaffected) apart from the two center L1 detectors (L1A2 and L1B2).

DT3 High-gain PHA is disabled on all L2 detectors apart from the 2 center detectors on both the A and B side (i.e., L2A4, L2A5, L2B4, L2B5 remain active). High-gain PHA is also disabled on outer L3 detectors.

Draft

3.2 Safe Mode

If the instrument is put into safe (or standby) mode, the high voltage bias to the SSDs is shut off. Issues such as high SSD current can cause the instrument to automatically put itself into Safe Mode.

3.3 Boot Mode

When the instrument is in boot mode, the following steps are performed:

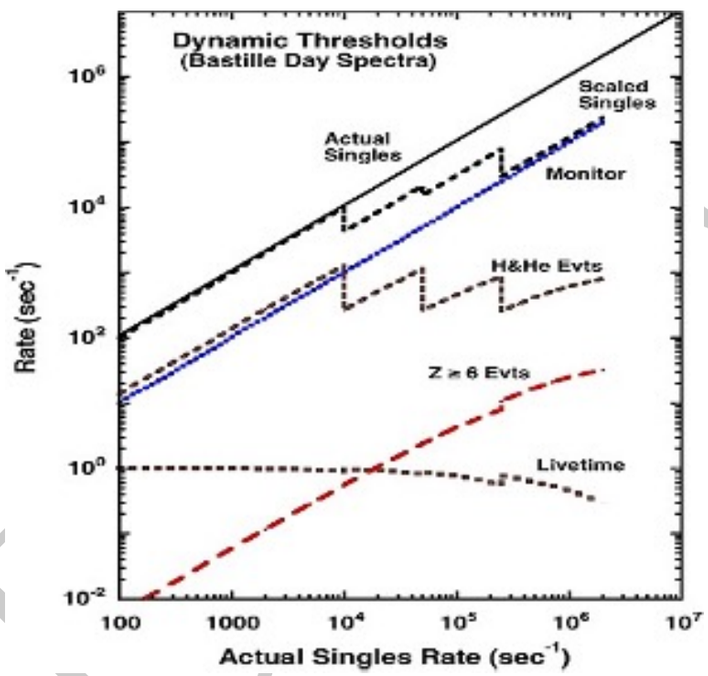


Figure 7: Example of the effect of dynamic thresholds in the case of the STEREO/LET data from the July 14, 2000 (Bastille Day) SEP event.

- Upload flight software (FSW) tables and images
- If command is received within 10 seconds, HIT stays in BOOT mode and data is upload to SRAM
- Command then sent to write data into MRAM
- FSW then sends "Maintenance Status" packet confirmation data
- HIT transitions to Safe mode

4 Data Products

The IMAP Science Team uses version 4 of the NASA Planetary Data System (PDS4) specification for Processing Levels of Science Data Sets. Below are descriptions of the IMAP/HIT data levels using the PSD4 nomenclature.

4.1 Data Product Level Definitions

4.1.1 Telemetry

An encoded byte stream used to transfer data from one or more instruments to temporary storage where the raw instrument data will be extracted.

4.1.2 Level 0 - Raw Data

Original data from an instrument. If compression, reformatting, packetization, or other translation has been applied to facilitate data transmission or storage, those processes will be reversed so that the archived data are in a PDS approved archive format.

4.1.3 Level 1a - Reformatted Data

Data that have been processed beyond the raw level but which have not yet reached calibrated status. In the case of HIT, this will be raw particle counts organized by species, energy, and look direction.

4.1.4 Level 1b - Partially Processed Data

Data that have been processed beyond the raw level but which have not yet reached calibrated status. In the case of HIT, this will be particle count rates organized by species, energy, and look direction. This utilizes information regarding the instrument livetime.

Draft

4.1.5 Level 2 - Calibrated Data

Data converted to physical units, which makes values independent of the instrument. In the case of HIT, this will be particle intensityes converted from count rate data using pre-determined geometry factors and efficiencies.

4.1.6 Level 3 - Derived Science Products

Results that have been distilled from one or more calibrated data products (e.g., particle pitch angles utilizing B data from IMAP/MAG, combined spectrograms with CoDICE, etc.). Supplementary data, such as calibration tables or tables of viewing geometry, used to interpret observational data should also be classified as 'derived' data if not easily matched to one of the other categories.

4.1.7 Data Flow Diagram

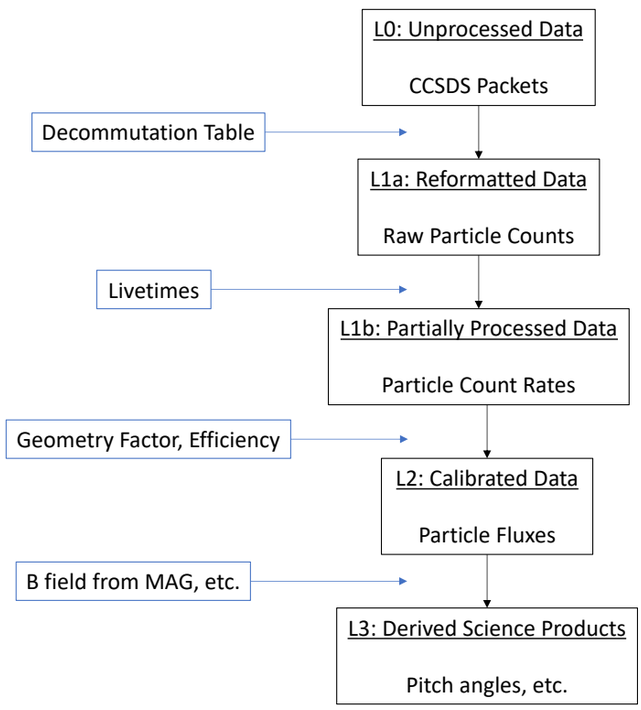


Figure 8: IMAP/HIT Data Flow Diagram



4.2 Science Data

4.2.1 Science Rates (Species Counts and Rate Counters)

For the science rates coming with each frame, counts for H and He (He-3 and He-4), 13 heavy elements (C, N, O, Ne, Na, Mg, Al, Si, S, Ar, Ca, Fe, and Ni), and various "background" counts (including charge ranges) will be transmitted. Science Rates will be organized top–down in order of penetration range, then species, then energy for the eight ion apertures (A1-4 and B1-4). After those rates are ions that go through the I-ALiRT apertures (A0 and B0), but still trigger the ion requirements (L1L2). The extra energy loss in the L4 detectors moves the ions to higher energy. Science rates included in the HIT Science Frame are summarized in Tables 17 - 22 and their locations in the HIT Science Frame are detailed in the same tables.

Particles which pass certain onboard processing cuts are sorted into matrices according to their penetration range in the instrument and by ΔE vs. E' measurements. Each matrix represents a penetration range — into the L2 detectors (RNG2, or L1L2), into one L3 detector (RNG3, or L2L3), or into two L3 detectors and possibly beyond (RNG4, PEN, or L3AL3B). These rates exactly match the ones on STEREO/IMPACT/LET. In addition, there are new HIT ranges RNG2I (L1L4L2), RNG3I (L1L4L2L3), and RNG4I (L1L4L2L3L3) Within each penetration range, the associated matrix covers a ΔE vs. E' space that spans particles from Z=1 (H) to Z≥40 (Zr). The matrices are used by onboard processing to identify particles by range in the instrument and charge, and further onboard processing is used to determine particle kinetic energy. The matrices span 128 bins in the x–axis and 400 bins in the y–axis, and they are shown graphically in Appendix C.

Particles that are sorted through the matrices are counted in arrays in the HIT onboard memory, sorted by penetration range, species (element, charge, charge range, or background), and energy (for elements). Particle counting rates with defined element and energy are termed "foreground rates" (FGRATES), following the curved tracks bounding elements in the figures in Appendix C. Foreground rates include elements (and helium isotopes) such as H, He-3, He-4, C, N, O, Ne, Na, Mg, Al, Si, Ar, Ca, Fe, and Ni. Particles counted by the FGRATES are assigned Particle IDs which equal their index values in the FGRATES arrays associated with each penetration range (L1L2=L2FGRATES, L2L3=L3FGRATES, L3AL3B=PENFGRATES, (L1+L4)L2=L2IFGRATES, (L1+L4)L2L3=L3IFGRATES, (L1+L4)L2L3AL3B =PENIFGRATES). These Particle IDs are also used to identify particles in the Event Record Headers The Particle IDs are given in Tables 17, 19, and 21. Particles not located in the FGRATES regions of the matrices, or particles which are otherwise unclassified by the matrices, are assigned a Particle ID of 255. Note that some elements are

Draft



classified by the Range 3 matrix but not in the other matrices. These particles are also assigned a Particle ID of 255 when located in the Range 2 or Range 4 matrices, e.g. Na in RNG 2 and RNG 4.

Particle IDs may be duplicated between different ranges. While it may be convenient for science analysis for particles having the same charge and energy range in two different matrices to have the same Particle ID, it would add additional load to limited onboard computing resources. It will be less strain on computing resources to account for different Particle IDs during analysis on the ground.

Particles in the matrices which do not fall along element or isotope tracks are termed "background rates" (BGRATES). Background rates are counts from broad regions of ΔE vs E' space in the matrices such as the Li, Be, and B region between He and C, or the "backward moving particles" region to the lower right corner of ΔE vs. E' plots. The background rates also include regions covering STIM events, described elsewhere. All background rate events are assigned Particle ID 255. The background rates are summarized in Tables 18, 20, and 22.

Finally, science rate counters are stored in onboard memory in 24 bit counters, but in the Science Frame, these rates are compressed to 16 bits. The compression algorithm will be a 16 bit modified biased exponent hidden one algorithm, as detailed in Section 5.

Thus, there are currently 371 Science Rates in the HIT Science Data Frame, for a total of 742 bytes.

4.2.2 Sector Rates

The eight ion apertures (A1-4 and B1-4) and the spinning of the spacecraft are used to separate the 4π sky into 120 sectors, with eight 22.5° bins perpendicular to the spin axis (declination) and fifteen 24° bins in the spin direction (inclination). The I-ALiRT apertures (A0 and B0) are not included in the sector rates. Because of the large number of sectors, and the corresponding reduction in statistics, the sector rates are accumulated for 10 minutes and are transmitted over the next 10 minutes (120 sector rates/minute). Thus, in processing, the livetimes from the previous 10 minute block (n-1) must be used to correct a given 10 minute block (n). Each look direction rate will be encoded in 16 bit compressed rates, using the same format and compression/decompression algorithm as the science rates. Thus, we send a total of 240 bytes of look direction rates per HIT Science Frame.

0° in declination is defined as the spin axis in the sunward direction (which is a few degrees away from true sunward) and the eight 22.5° bins are labeled 0 – 7 and cover the entire 180° of declination. 0° in inclination is the zero spin phase that the spacecraft includes in the Time and Status message every

Draft

second. The 15 inclination 24° bins (labeled 0-14) are determined from timing (incrementing every second), with the assumption that the spin rate is the nominal 4 rpm. Deviation of the spin rate from 4 rpm will change the angular width of the fifteenth bin (smaller than 24° for spin $\leq$ 4 rpm, and larger for spin $\geq$ 4 rpm). This needs to be corrected on the ground. No onboard correction is planned. A new spin phase zero resets the inclination bin index.

The combination of the L1 sector and the L2 sector triggered are used to determine the correct declination bin (see Table 2). In addition to look directions, or sectors, these rates are divided into 10 energy bins and element or element ranges: H, He–3, He-4, CNO, NeMgSi, and Fe (see Table 24).

As described above and in the HIT-FSW-DESC-004 document, every minute SECTORRATES includes 120 look directions (eight 22.5 degree declination [j = 0-7] times fifteen 24 degree inclination [k = 0-14] for one of ten of the selected species/energies (see below table).

4.2.3 Singles and Coincident Rates

There are 58 ADCs in HIT, and each ADC will be measured for singles rates at low and high gain thresholds. These rates will be compressed to 16 bits, using the same compression/decompression algorithm employed for science and look direction rates. Thus, there will be a total of 116 singles rates in the HIT Science Frame, for a total of 232 bytes. The singles rates are given in order of detector address number, which is used by the HIT onboard software for detector addressing. The ordering of singles rates in the HIT Science Format is top–down by detector number, then by high gain and low gain. Thus, the first four bytes in the Singles Rates block are L2A0 (detector address 0), with the first two bytes being L2A0 high gain singles rate, and the second two bytes being L2A0 low gain singles rate. (Furthermore, given the byte ordering described in Section 2.1, the first byte of the L2A0 high gain singles rate is the high byte, and the second byte is the low byte.) See Section 5, Table 13 for a summary of the singles rates and their location in the HIT Science Frame.

Coincidence rates are listed in Section 4, Table 15. These rates count coincident hits for detector groups for the minute spanned by the Science Frame. Space in the HIT Science Frame is allocated for 20 coincidence rates, compressed to 16 bits as with other rates.

4.2.4 Livetimes, Event Processing Counters, and Priority Buffer Counters

Space is allocated in the HIT Science Frame for livetime counters, event processing counters, and priority buffer counters. These counters are event or processing counts used or otherwise maintained by the HIT onboard software.

Draft



	L2B0	L2B1	L2B2	L2B3	L2B4	L2B5	L2B6	L2B7	L2B8	L2B9
L1B1a	1	1	0	0	0	0	0	0	0	0
L1B1b	1	1	1	0	0	0	0	0	0	0
L1B1c	1	1	1	0	0	0	0	0	0	0
L1B2a	2	2	1	1	1	1	0	0	0	0
L1B2b	2	2	2	1	1	1	1	0	0	0
L1B2c	2	2	2	2	1	1	1	1	0	0
L1B3a	3	3	2	2	2	2	2	1	1	1
L1B3b	3	3	3	2	2	2	2	1	1	1
L1B3c	3	3	3	3	2	2	2	2	1	1
L1B4a	4	3	3	3	3	3	3	3	2	2
L1B4b	4	4	3	3	3	3	3	3	2	2
L1B4c	4	4	4	3	3	3	3	3	3	2
	L2A0	L2A1	L2A2	L2A3	L2A4	L2A5	L2A6	L2A7	L2A8	L2A9
L1A1a	6	6	7	7	7	7	7	7	7	7
L1A1b	6	6	6	7	7	7	7	7	7	7
L1A1c	6	6	6	7	7	7	7	7	7	7
L1A2a	5	5	6	6	6	6	7	7	7	7
L1A2b	5	5	5	6	6	6	6	7	7	7
L1A2c	5	5	5	5	6	6	6	6	7	7
L1A3a	4	4	5	5	5	5	5	6	6	6
L1A3b	4	4	4	5	5	5	5	6	6	6
L1A3c	4	4	4	4	5	5	5	5	6	6
L1A4a	3	4	4	4	4	4	4	5	5	5
L1A4b	3	3	4	4	4	4	4	4	5	5
L1A4c	3	3	3	4	4	4	4	4	4	5

Table 2: Sector Directions (Declination)

Draft

i	0	1	2	3	4	5	6	7	8	9
Species/	H	H	H	4He	4He	CNO	CNO	NeMgSi	NeMgSi	Fe
Energy Bin	1.8-3.6 MeV	4-6 MeV	6-10 MeV	4-6 MeV/n	6-12 MeV/n	4-6 MeV/n	6-12 MeV/n	4-6 MeV/n	6-12 MeV/n	4-12 MeV/n

Table 3: Species/energy bins for Sector Rates

HIT Livetimes, event processing counters, and priority buffer counters are listed in Section 5, Tables 12, 14, and 16, respectively. All of the counters are stored as 24 bit numbers in the HIT onboard memory, and in the HIT Science Format, they are compressed to 16 bits using the same compression algorithm as is used with the science rates. The one exception is the Front End Electronics livetime counter (bytes 8–7 in the HIT Science Frame), which is scaled from 24 bits to 16 bits.

Notes on Table 12: The NUMTRIG, NUMREJECT, etc. counters are hardware counters, with counters for events taken under hazard (.HAZ) conditions. NUMTRIG is the number of trigger events detected by the hardware during every even numbered second during the minute of accumulation time for the science frame. NUMREJECT is the number of trigger events rejected for further analysis, as determined by hardware conditions described elsewhere. NUMACCPHA is the number of trigger events accepted for further analysis with PHA data, as determined by the hardware. NUMACCNPHA is the number of trigger events accepted for further analysis without PHA data; however, since all accepted events currently include PHA data, this number is always zero. Under the current definitions, the sum of NUMREJECT and NUMACCPHA should equal NUMTRIG. Because these counters are accumulated only during even numbered seconds, they represent only half the total number of triggers, etc. which could be detected during the entire minute.

The equivalent .HAZ counts are those counted under hazard conditions, and these are accumulated during odd numbered seconds during the minute. A trigger event is flagged as a .HAZ event if it comes within 18/6.4 (2.8) microseconds after the previous trigger. The .HAZ condition is an added condition to the trigger logic; it is not exclusive. Therefore, if NUMTRIG and NUMTRIG.HAZ events were counted simultaneously, the NUMTRIG.HAZ events would count a subset of the NUMTRIG events. The NUMREJECT.HAZ and NUMACCPHA.HAZ events are defined as NUMREJECT and NUMACCPHA events, only with the .HAZ condition added. As with non-.HAZ events, the .HAZ events represent only half the total number of .HAZ events which could occur during a given minute, since they are accumulated only during odd numbered seconds.

Currently, all .HAZ events are rejected for analysis, though this rejection

Draft



can be commanded on or off. The livetime counter is not incremented during .HAZ events, when such events are rejected for analysis.

4.2.5 Event Buffer - Event Record Format

With the fixed format data described in previous sections for the HIT Science Frame, there remain 2733 bytes, all of which will be pulse height data in an Event Buffer. Events (pulse heights) are sampled by the HIT MISC from priority buffers listed in Section 5, Table 16, and the sampled pulse heights are packaged into Event Records in the Event Buffer. The telemetered events will not exceed the Event Buffer length.

At the top of the event buffer will be a header containing the number of events saved to the buffer. If the minimum event length of 2 ADC hits is 72 bits (9 bytes – see below), then the event buffer can contain up to XXX events, with one 3 byte event buffer header. Unused buffer space will be filled with 0x00's, and empty packets will not be transmitted.

Within the buffer, each event should be collected in a defined event record, composed of an Event Record Header (ERH) followed by a variable number of ADC fields. The 32 bit Event Record Header is defined as follows:

The particle ID identifies the particle by species and energy, based on how it was sorted through the HIT Matrices. If the particle is not a "foreground" event (i.e. if it is not identified as a selected element or helium isotope for a given matrix) and is instead a "background" event, or if the particle is not sorted by the HIT matrices, it is assigned a Particle ID of 255. For the identifiable elements targeted by the HIT instrument, the Particle ID is sufficient to identify element and energy.

Additional information is provided by the priority buffer number (bits 8–12). This number identifies the priority buffer from which the Event is taken. Although all events in the Event Buffer are taken from the Priority Buffers, not all events are sorted by the HIT Matrices. Not all particles which trigger the HIT instrument enter the Priority Buffers. Instead, a sample of trigger events is sent to the Priority Buffers, which are defined and weighted to target particle types according to the goals of the HIT instrument. Priority Buffers (listed in Table 16 and described in detail elsewhere — TBD) are defined to identify classes of particles by penetration range, by charge or charge range, or by other characteristic (e.g. STIM events). There is some overlap in information between Particle ID and Priority Buffer number. The Priority Buffer definitions and the filling and extracting methods are described elsewhere (TBD). See Section 5, Table 16 for a list of Priority Buffer numbers.

The Time Tag (Latency) Bits duplicate the four least significant bits of the minutes field of an onboard clock (HIT internal minute counter), as an indicator of event latency. When events are packaged and placed in priority buffers,

Draft



Data	Bit	Note
Particle ID	0–7	= particle ID if the particles are sorted by the HIT Matrices as "foreground" particles. (=255 if the particles are not sorted by the matrices or are identified as background particles). Allows matrices to ID particles by range (matrix), species, and energy. See Section 5, Tables 17–22 for lists of Particle IDs. See also SEP HIT and Central MISC Processors Flight Software Requirements (STEREO-CIT-CIT-002.F).
Priority Buffer Number	8–12	See Section 5, Table 16 for a list of Priority Buffer Numbers and their descriptions.
STIM Tag	13	Flags a STIM event.
HAZ Tag	14	Hazard flag.
Time Tag (Latency Bits)	15–18	Duplicates the 4 least significant bits of the HIT onboard minutes counter (Section 5, and Table 11); used to identify event latency
A/B Event Tag	19	A=0, B=1
Unread ADCs	20	=1 if any ADCs not included in the event record
Long Event Flag	21	=1 if extra event data is included. Long events will also include extra stim data if the STIM tag is set.
Culling Flag	22	=1 if number of ADCs culled from this event is nonzero.
Spare	23	

Table 4: Event Record Header (ERH)

these minutes bits are copied onto the ERH Latency Bits. Later, when the full Science Frame is packaged into CCSDS packets, the time of the assembly of the Science Frame is copied onto time fields in the CCSDS packet headers and

Draft



onto the Minutes counter of MISCBITS (Table 11). Because the time that an event is popped off its priority buffer and placed into the Science Frame may be delayed by more than one minute after the event is first pushed onto the priority buffer, the Latency Bits for a given event may not correspond to the time that the event's Science Frame is assembled. It is up to the user of the data to determine what value of the latency bits precisely corresponds to times associated with given Science Frames.

For some classes of events, large numbers of detectors or ADCs in the HIT instrument may be triggered and result in signals. The HIT Data Format (Event Record Format) described herein is capable of returning events with the maximum of 54 ADC hits. Most of these events are unlikely to be sorted by the HIT Matrices, but some fraction of them will be sent to the Event Buffer. For events with sufficiently large numbers of hit ADCs, not all ADCs will be included in the Event Record. The onboard software will determine the maximum number of ADC signals transmitted for each event (8 TBR). Bits 25–27 will count the number of ADCs in the event which are not included in the Event Record, with a saturation value of 7.

A separate number counting the ADCs included in the Event Record is not included in the Event Record Header. Instead, an End of Record (EOR) bit is employed in the ADC Field, described later in this section. Furthermore, HIT has a VERBOSE mode in which both low gain and high gain signals from a given ADC may be transmitted. By relying on the EOR bit in the ADC Fields, the format allows for transmission of low and high gain signals for any given ADC, and the EOR bit itself is sufficient to mark the length of an Event Record.

An Extended Header flag (bit 29) marks the addition 2 bytes of header information. A STIM block flag (bit 30) marks the addition 2 bytes of STIM block information to the header, described in Section 2.10. A final ADC culling flag (bit 31) marks the condition that one or more ADCs were culled by onboard software for the event. If culling mode is off, this bit is always zero.

The L1A through L3B in the long event trigger tags identify which detector groups were involved in the trigger conditions, and the A/B tag identifies which side of the detector provided the trigger. The HAZ flag marks a hazard condition TBD. The STIM flag marks a calibration event, where the stim pulser for one or more PHASIC channels has been fired, generating an artificial PHA value. STIM events follow a special format

Following the header are a number of ADC fields. Each ADC field will contain the following:

Thus, each ADC signal and identifier is encoded in 20 bits. Note that the End of Record (EOR) bit is 0 except when set to 1 for the last ADC Field in an event record. The detector ID is the same as the detector address, a list

Draft



Data	# Bits	Note
ADC Signal	12	11 bits signal, 1 bit overflow
ADC/Detector ID	6	54 detectors maximum
Low/High gain	1	0 = high gain, 1 = low gain
Last hit flag (End of Record, EOR)	1	Set to 1 for the last ADC in an event, 0 for all other ADCs

Table 5: ADC Field — Minimum Bit Allocations

of which can be found with the singles rates table, Section 5, Table 13. The format of the ADC Field is given in Figure 9:

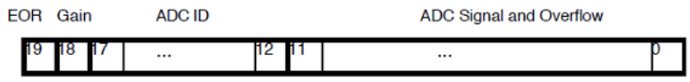


Figure 9: Event Record ADC Field. End of Record (EOR) and Gain bits are defined in Table 4.2.5

The smallest event record (one event record header plus 2 ADC Fields) would be 72 bits long. A 3 ADC event would be 92 bits long. The event records will be padded by 4 bits for each event record with odd numbers of ADC Fields, allowing all event records to be aligned to byte boundaries. Table 6 and Figures 10–11 show some examples, with the figures diagramming Event Records as 3 bytes wide for illustration only.

# ADC Fields	# bits without padding	Padding bits	# bytes with padding
2	72	0	9
3	92	4	12
4	112	0	14
5	132	4	17
6	152	0	19
7	172	4	22

Table 6: Bit padding of Event Records.

Draft

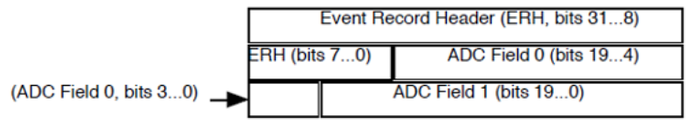


Figure 10: Event Record with 2 ADC Fields. Left to right is MSB to LSB, spanning 3 bytes.

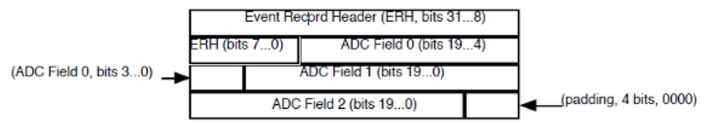


Figure 11: Event Record with 3 ADC Fields. Left to right is MSB to LSB, spanning 3 bytes.

Note: In the event of a bit error, particularly in the End of Record (EOR) bit in the ADC field, it is possible that all subsequent events in the Event Buffer will be unreconstructible or, at the very least, very difficult to reconstruct. Such bit errors are expected to be extremely rare. Possible remedies in the Event Record format may include enforcing MISC word boundaries for the ADC Field, and forcing bit 23 (EOR bit) in such ADC Fields to be 0 except at EOR. The disadvantage of this approach is an increase in the length in bytes of some events. The increasing number of unused bits in each event record will reduce the number of events possible in an Event Buffer.

4.2.6 Extended Header Block

If bit 21 of the Event Record Header is set, an additional three-byte Extended Header Block (or Extended Information Block) is appended after the ERH and ADC fields and before an optional STIM Information Block (Section 2.10). This Extended Header Block contains additional information useful for diagnosing onboard software function and performance.

The first byte contains flags for the groups of detectors that generated the trigger.

The Extended Header Block also contains DEINDEX (9 bits) and EPINDEX (7 bits). DEINDEX is the delta-E axis matrix index generated by the onboard software to map the given event to a HIT Matrix Map (see Appendix C). It has a value in the range 0-399. EPINDEX is the residual energy axis matrix index (E-prime) generated by the onboard software to map the given event to a HIT Matrix Map, and it has a value in the range 0-127.

Draft

Data	Bit	Note
L1A Tag	0	Indicates an L1A detector contributed to the coincidence trigger
L2A Tag	1	Indicates an L2A detector contributed to the coincidence trigger
L3A Tag	2	Indicates an L3A detector contributed to the coincidence trigger
L1B Tag	3	Indicates an L1B detector contributed to the coincidence trigger
L2B Tag	4	Indicates an L2B detector contributed to the coincidence trigger
L3B Tag	5	Indicates an L3B detector contributed to the coincidence trigger
L4A Tag	6	Indicates an L4A detector contributed to the coincidence trigger
L4B Tag	7	Indicates an L4B detector contributed to the coincidence trigger

Table 7: Detector Group Flags

4.2.7 Event Buffer - STIM Events

Bit 13 of the Event Record Header identifies calibration, or STIM, events. These events include livetime STIM events and ADC STIM events. Both of these types of STIM events will be included in the Event Buffer, with different priorities and different (or unassigned) particle IDs. However, because they represent a different class of event than regular particles, it is anticipated that additional information may be needed for calibration and identification. Therefore, if the STIM Flag (bit 13) AND the Long Event Flag (bit 21) are set, an additional 3-byte STIM Information Block is appended to the Event Record for STIM events, after the ADC fields and optional Extended Header block.

A two ADC STIM event is shown in Figure 12.

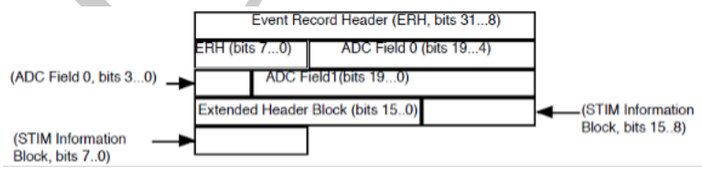


Figure 12: Event Record with 2 ADC Fields. Left to right is MSB to LSB, spanning 3 bytes. Optional Extended Header Block is also attached.

STIM events will be padded to fill out bytes in the same way that regular events are padded, at the end of the event record.

The STIM information block contains a "seconds" counter, the DACLEVEL, and the DACCONFIGURATION. The seconds counter contains the second

Draft

number within the accumulation minute of the HIT Science Frame during which the STIM event was taken. For example, during normal mode operation, livetime STIM events are accumulated during the 0-8 second, 10-18 second, 20-28 second, etc. time intervals, while ADC STIM events are accumulated at the 9 second, 19 second, 29 second, etc. points. The DACLEVEL (0-31) and DACCONFIGURATION (0-14) indicate via tables in the HIT onboard software what the DAC settings are for the STIM events and which ADCs are stimulated, respectively.

4.2.8 PHA Word

Following the headers, there are one or more compressed PHA words. Each PHA word is 20 bits long (2.5 bytes). If there is an odd number of PHA words, there are 4 bits added to the end of the event, so each event occupies an integral number of bytes. The last PHA in the event has its most-significant bit (bit 19) set to 1.

The order of detector addresses are shown in Table 8. The gain bit in the PHA word indicates whether the data comes from the high gain (1) or low gain channel of a particular detector..

Detector Name	Detector Address
L1A0a	16
L1A0b	17
L1A0c	18
L1A1a	19
L1A1b	20
L1A1c	21
L1A2a	22
L1A2b	23
L1A2c	24
L1A3a	25
L1A3b	26
L1A3c	27
L1A4a	28

Draft

L1A4b	29
L1A4c	30
L2A0	9
L2A1	8
L2A2	7
L2A3	6
L2A4	5
L2A5	4
L2A6	3
L2A7	2
L2A8	1
L2A9	0
L3Ao	15
L3Ai	14
L4Ao	31
L4Ai	13
L1B0a	32
L1B0b	33
L1B0c	34
L1B1a	35
L1B1b	36
L1B1c	37
L1B2a	38
L1B2b	39
L1B2c	40
L1B3a	41
L1B3b	42
L1B3c	43

Draft

L1B4a	44
L1B4b	45
L1B4c	46
L2B0	57
L2B1	56
L2B2	55
L2B3	54
L2B4	53
L2B5	52
L2B6	51
L2B7	50
L2B8	49
L2B9	48
L3Bo	63
L3Bi	62
L4Bo	47
L4Bi	61

Table 8: Detector Addresses

4.2.9 Theoretical Description of Primary Science Products

The primary HIT science data products come in the form of energetic ion intensities ($cm^{-2}s^{-1}sr^{-1}MeV/nuc^{-1}$) for 16 species in ∼12 energy bins. The particle intensity data is derived from the raw counts (Lev1a) and the count rates (Lev1b - these factor in instrument livetime) organized by species, energy, and look direction. A visualization of the energy bins for each ion species is shown in Fig. 13. The particle intensity is calculated according to

$$j_i(N,X) = \frac{1}{\Delta t \Delta E_i} \frac{\sum_{j=2}^{4} q_{ij}(N,X) - b_{ij}(N,X)}{\sum_{j=2}^{4} \sigma_{ij}(N,X)\lambda_{ij}(N,X)} \tag{1}$$

with the following symbol definitions:

Draft

N ion species

M energy bin

X look direction

q particle counts from telemetry (function of N, M, X)

Δt livetime from telemetry (units of s)

ΔE energy bin width (units of MeV)

σ geometry factor (units of $cm^{-2}sr$)

λ detection efficiency

b background counts

The geometry factor (σ)and detection efficiency (λ) are nominally energy-dependent and dependent on the dynamic threshold state of the instrument at a given time. Until determined otherwise, λ is assumed to be 1. The intensity (j) may also be affected a relatively steady background (primarily due to galactic cosmic rays (GCR) and anomalous cosmic rays (ACR)) that can be subtracted once a value is determined in flight.

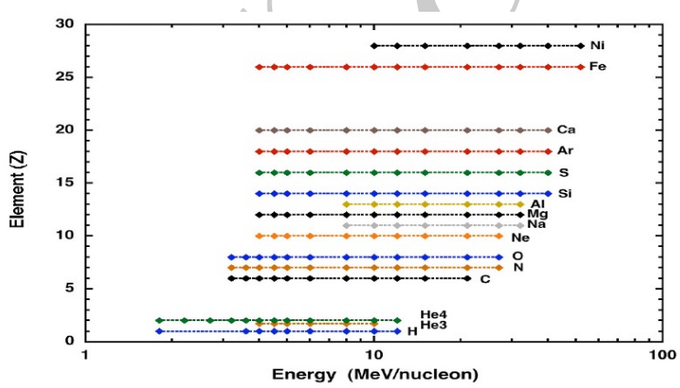


Figure 13: Visualization of energy bins for all ion species measured by HIT

4.2.10 Science Data Types

The L1 and L2 science data are made available in several different types that differ in their energy bin width, number of summed detector segments, and integration time. These are:



Standard The standard data includes rates for all species and energies shown in Fig. 13. The standard data is provided on a full-instrument basis (i.e. not broken up by specific look-directions) on a 1-minute time cadence.

Summed The summed data product combines the standard energy bins into wider bins to increase the statistics for a given species. These data are particularly useful during "quiet times" without SEP events.

Sectored In order to provide anisotropy information, HIT will provide a sectored data product with 15 separate sectors in the spin phase and 8 perpendicular sectors. The sectored data will be provided with a lower time-resolution (10 minutes) and over a limited number of species with wider energy bins. The available sectored rates are summarized below.

H 1.8 - 3.6 MeV, 4.0 - 6.0 MeV, 6.0 - 10 MeV

^{4}He 4.0 - 6.0 MeV, 6.0 - 12.0 MeV

CNO 4.0 - 6.0 MeV, 6.0 - 12.0 MeV

NeMgSi 4.0 - 6.0 MeV, 6.0 - 12.0 MeV

Fe 4.0 - 12.0 MeV

In addition to the primary science data, HIT will also provide a variety of supplementary rates (e.g., singles rates, trigger rates, etc.). These will be kept as Level 1a (counts) products and primarily used for timing and evaluation of background.

4.3 Uncertainties

4.3.1 Statistical Uncertainties

The primary non-systematic uncertainties are a result of the limitations of counting statistics. The Level 1a data includes the raw instrumental counts for each integration time allowing the calculation of statistical uncertainties.

4.3.2 Systematic Uncertainties

4.3.2.1 Chance Coincidences Chance coincidences (i.e., two or more particles interacting with the HIT detectors with timing and energy-deposit such that they appear to the flight software as multiple hits by a single particle) are another source of potential systematic uncertainties. Segmenting the detectors helps to mitigate this effect as multiple hits in the same detector can be removed if they hit separate segments. Further consistency checks will be employed during ground processing to minimize the effect of chance coincidences.

Draft



4.3.2.2 Live-time Effects Extremely high count rates can produce errors in the live-time reported by the flight software. The live-time counter records the time interval during which the instrument is waiting for a trigger. Once the instrument triggers, it enters a coincidence window to determine if any other detectors trigger within that window. An independent event could trigger a detector during the coincidence window despite the fact that the instrument is not technically "live" to accept an independent event during the coincidence window. In order to correct for this effect, the live-time must be corrected to include the addition of the length of the coincidence window for every trigger. Thus, a correction can be made using the formula

$$\text{Live-time}_{\text{corrected}} = \text{Live-time} + (\Delta t \times N_{trig}) \tag{2}$$

where Δt is the length of the time per trigger to add and N_{trig} is the number of triggers. Δt can be determined using the "livestim" data provided by the onboard pulsers which give an independent measure of the live-time. The factor of Δt will be explored using high intensity runs at the accelerators during HIT calibrations.

4.4 I-ALiRT Data

The primary I-ALiRT data products provided by HIT are those of low-, medium-, and high-energy protons and ~0.5 - 1 MeV electrons divided into sunward and anti-sunward propagating groups. Thus, HIT provides 8 total primary I-ALiRT rates. These primary rates have a 1 minute cadence to allow real time monitoring. These primary (public) data products are derived from supplemental (non-public) rates, at first using simplified algorithms (TBD). However, a number of rates have been included in the I-ALiRT data that should allow improvement in the algorithms, especially with regard to background subtraction. Supplemental HIT I-ALiRT rates are described below.

- 26 singles and trigger rates (13 in each direction) at a 60 second cadence.
- 5 engineering rates at a 60 second cadence.
- 3 species identified proton rates at a 60 second cadence.
- 2 species identified helium rates at a 60 second cadence.
- 12 rates (6 in each direction) of 1d cuts on L4i (inner segment of L4) energy deposit at a 60 second cadence. These, and raw events, help distinguish between electron and proton measurements due to the difference in energy loss of the two populations.

Draft



- 8 rates (4 in each direction) of events that trigger L4i and the corresponding L3 but not L3 on the opposite side.

5 Level 0 to Level 1a Processing

Conversion of Lev0 data to Lev1a data requires unpacking of the CCSDS files into CDFs. This requires all science packets to be retrieved for a given day plus an additional buffer of 5 minutes at the beginning of the day (i.e., starting at 11:55 of the previous day) and 15 minutes end of the request interval (i.e. 00:15 of the following day) in order to handle any potential issues due to the fact that data can span multiple files. The 10 minute buffer ensures that HIT will have complete frames of Sectored data.

The full HIT Science Frame Format is shown in Section 5.4. The Lev1a data that will be released to the public will consist of raw count data (i.e. number of counts in each bin for each integration time) and raw housekeeping. The internal Lev1a data will include pulse height event data, autonomy, derived, memory dump, and message log. It is expected that the Lev1A data will consist of arrays of values for each data product as a function of time. For example, a single L2FGRATES 1.0-1.8 MeV/nuc H data (Particle ID 0 in Table 17) array over the course of one day would include an array of 1,440 integer values corresponding to the number of counts in that bin over each minute in one day.

- Input: CCSDS packets
- Processing Requirement(s): deconvolution table
- Output: Lev1a CDF files

Arrays will be separated by section.

5.1 Rates Compression/Decompression Algorithm

The following algorithms were suggested in an e-mail from Don Reames and used on STEREO/LET, for compressing 32 bits to 16 bits. This finalized algorithm is a modified biased exponent, hidden one algorithm with a 12 bit mantissa and a 4 bit exponent. Numbers up to 2^{12} are uncompressed, and numbers up to 2^{13} decompress with no "error".

```
/* Rewrite to allow flexible arrangements of bits. AWL 030909 */
unsigned int num_bits=16, num_mantissa_bits=12, num_exponent_bits=4;
unsigned long output_mask=0xffff; /* 0xffff 16 bit, 0x0fff 12 bit */
```

Draft



```
/* 32-bit -> 16-bit compression for SW and HW rates     */
/* useage:  rateout=pack_rate(ratein);                  */

unsigned int pack_rate(ratein)
long ratein;
{
 unsigned int rateout, power=0;
 unsigned long mask;

 mask = (0xffffffff<<(num_mantissa_bits+1));
 while (ratein&mask)
 {
  power += (0x0001<<num_mantissa_bits);
  ratein>>=1;
 }
 rateout=ratein;
 if (power)
 {
  rateout = power + (0x0001<<num_mantissa_bits)
  | (rateout & (output_mask>>num_exponent_bits));
 }

 rateout = (rateout & output_mask);

 return rateout;
}

/* Unpacking (not required in flight code) */
/* switched from long to unsigned long -- AWL 011107 */
unsigned long long_rate(packed) /* Unpack to long */
unsigned long packed;   /* was just long.  AWL 030908 */
{
 unsigned long power;  /* was just long.  AWL 030908 */
 unsigned long out;  /* was just long.  AWL 030908 */

 power = packed>>num_mantissa_bits;
 if (power>1)
 {
  out = ( (packed & (output_mask>>num_exponent_bits))
  | (0x0001<<num_mantissa_bits) );
  out = out<<(power-1);
```

Draft

```
 }
 else
 out = packed;
 return out;
}

double dbl_rate(packed) /* Unpack to double */
unsigned packed;
{
 int power;
 double out;

 power = packed>>num_mantissa_bits;
 if (power>1)
 {
  out = ( (packed & (output_mask>>num_exponent_bits))
  | (0x0001<<num_mantissa_bits) );
  out = out * pow(2.,(double)(power-1));
 }
 else
 out = packed;
 return out;
}
```

5.2 APID and Packet Number

The ApID value of 580 is assigned to every HIT Science Frame Packet, and this value is stored in the CCSDS packet header (not part of the HIT Science Frame itself). In order to identify individual packets within the HIT Science Frame, bits 0–4 of the subseconds field of the CCSDS packet header are replaced by a packet number.

The ApID will be assigned by the HIT MISC and entered into each CCSDS packet header. The HIT Science Data Frame does not make direct use of the source sequence counter in each CCSDS packet header.

5.3 HIT Science Frame Header

Some header information is included in the CCSDS packet headers (secondary headers). However, because CCSDS packet formatting may be removed during ground-based analysis in order to extract full HIT Science data from each set of

Draft

APID (Decimal)	APID (Hex)	Description	Date Length (Bytes)	Cadence
1250	0x4e2	Autonomy/Aliveness	2	1 / sec.
1251	0x4e3	Housekeeping	140	1 / min.
1252	0x4e4	Science	262	20 / min.
1253	0x4e5	I-ALiRT	54	1 / sec.
1254	0x4e6	Message Log	0-360	As needed
1255	0x4e7	Memory Dump	360	On command

Table 9: ApIDs designating the 6 types of HIT CCSDS packets.

Draft

Packet #	Packet Description
0-4	Science Frame Header, Counters and Rates
5	Counters and Rates, Start of Event Buffer
6-19	Event Buffer Frames

Table 10: HIT Science Packet Numbers

HIT CCSDS packets, it will be useful to include a HIT Science Frame Header.

The HIT Science Frame Header is allocated as 5 bytes at the top of the HIT Science Frame. Byte 0 is the spacecraft ID (SCID) and frame version number (SFVER). The two most significant bits are the spacecraft ID — 00 for the EM unit (no spacecraft), 01 for FM1 (flight version). The remaining bits are a HIT Science Frame Version number; the current version number is 11. Should the version number ever exceed 128, the version number in these bits will be calculated modulo 128.

Bytes 1 and 2 (high byte and low byte) contain the number of valid bytes (SFLEN) in the complete HIT Science Frame (not including CCSDS header and checksum). "Valid" bytes include all the bytes from the frame header to the last byte of the last event in the event buffer, and this counter does not include CCSDS packet headers or checksums. Because 6 CCSDS packets containing fixed format data are always present, this number is never less than 1418. This number never exceeds 4160. The three most significant bits of byte 1 are unused.

The last two bytes (bytes 3-4) of the HIT Science Frame Header are defined as a checksum (SFCHECK), to verify the integrity of the HIT Science Frame Data. The checksum algorithm is TBD. It is proposed that the two bytes be set such that the sum of all bytes or MISC words modulo 216 equal zero. Individual bytes are summed, with the checksum allowed to grow to 16 bits. This checksum is independent of the CCSDS packet checksums and is calculated by the HIT MISC prior to the calculation of CCSDS packet checksums by SEP Central.

5.4 HIT Science Frame Format Summary

Tables 11–27 summarize the HIT Science Data Frame Format, viewing the HIT Data Frame as a stream of numbered bytes (0-4159). These tables provide the byte locations of data elements in the HIT Science Frame as serve as decommutation tables to transform Lev0 data into Lev1a.

Draft



Frame Byte # (First)	**Frame Byte #** (Last)	**Description**
0	0	Bits 6-7 = 00 (EM1unit), 01 (EM2), 10 (FM) Bits 0-5 = frame version number
1	1	Bit 7 = CodeOK Bits 3-6 = HeaterDutyCycle Bit 2 = LeakConv Bits 0-1 = DyThState
2	2	Minute (HIT internal minute counter)
3	5	Three Spare Bytes

Table 11: Miscellaneous Bits, MISCBITS

Frame Byte # (First)	**Frame Byte #** (Last)	**Description**
6	7	Livetime counter, Front End Electronics (LIVE_TIME)
8	9	# Triggers (NUMTRIG)
10	11	# Rejected Events (NUMREJECT)
12	13	# Accepted Events with PHA data (NUMACCPHA)
14	15	# Accepted Events without PHA data (NUMACCNPHA)
16	17	NUMTRIG.HAZ
18	19	NUMREJECT.HAZ
20	21	NUMACCPHA.HAZ
22	23	NUMACCNPHA.HAZ

Table 12: Livetime Counters, ERATES

Draft



Frame Byte # (First)	Frame Byte # (Last)	# Bytes	Description
24	25	2	L2A9, High Gain
26	27	2	L2A9, Low Gain
28	29	2	L2A8, High Gain
30	31	2	L2A8, Low Gain
32	33	2	L2A7, High Gain
34	35	2	L2A7, Low Gain
36	37	2	L2A6, High Gain
38	39	2	L2A6, Low Gain
40	41	2	L2A5, High Gain
42	43	2	L2A5, Low Gain
44	45	2	L2A4, High Gain
46	47	2	L2A4, Low Gain
48	49	2	L2A3, High Gain
50	51	2	L2A3, Low Gain
52	53	2	L2A2, High Gain
54	55	2	L2A2, Low Gain
56	57	2	L2A1, High Gain
58	59	2	L2A1, Low Gain
60	61	2	L2A0, High Gain
62	63	2	L2A0, Low Gain
64	65	2	L4Ai, High Gain
66	67	2	L4Ai, Low Gain
68	69	2	L3Ai, High Gain
70	71	2	L3Ai, Low Gain

Draft

72	73	2	L3Ao, High Gain
74	75	2	L3Ao, Low Gain
76	77	2	L1A0a, High Gain
78	79	2	L1A0a, Low Gain
80	81	2	L1A0b, High Gain
82	83	2	L1A0b, Low Gain
84	85	2	L1A0c, High Gain
86	87	2	L1A0c, Low Gain
88	89	2	L1A1a, High Gain
90	91	2	L1A1a, Low Gain
92	93	2	L1A1b, High Gain
94	95	2	L1A1b, Low Gain
96	97	2	L1A1c, High Gain
98	99	2	L1A1c, Low Gain
100	101	2	L1A2a, High Gain
102	103	2	L1A2a, Low Gain
104	105	2	L1A2b, High Gain
106	107	2	L1A2b, Low Gain
108	109	2	L1A2c, High Gain
110	111	2	L1A2c, Low Gain
112	113	2	L1A3a, High Gain
114	115	2	L1A3a, Low Gain
116	117	2	L1A3b, High Gain
118	119	2	L1A3b, Low Gain
120	121	2	L1A3c, High Gain
122	123	2	L1A3c, Low Gain
124	125	2	L1A4a, High Gain
126	127	2	L1A4a, Low Gain

Draft

128	129	2	L1A4b, High Gain
130	131	2	L1A4b, Low Gain
132	133	2	L1A4c, High Gain
134	135	2	L1A4c, Low Gain
136	137	2	L4Ao, High Gain
138	139	2	L4Ao, Low Gain
140	141	2	L1B0a, High Gain
142	143	2	L1B0a, Low Gain
144	145	2	L1B0b, High Gain
146	147	2	L1B0b, Low Gain
148	149	2	L1B0c, High Gain
150	151	2	L1B0c, Low Gain
152	153	2	L1B1a, High Gain
154	155	2	L1B1a, Low Gain
156	157	2	L1B1b, High Gain
158	159	2	L1B1b, Low Gain
160	161	2	L1B1c, High Gain
162	163	2	L1B1c, Low Gain
164	165	2	L1B2a, High Gain
166	167	2	L1B2a, Low Gain
168	169	2	L1B2b, High Gain
170	171	2	L1B2b, Low Gain
172	173	2	L1B2c, High Gain
174	175	2	L1B2c, Low Gain
176	177	2	L1B3a, High Gain
178	179	2	L1B3a, Low Gain
180	181	2	L1B3b, High Gain
182	183	2	L1B3b, Low Gain

Draft

184	185	2	L1B3c, High Gain
186	187	2	L1B3c, Low Gain
188	189	2	L1B4a, High Gain
190	191	2	L1B4a, Low Gain
192	193	2	L1B4b, High Gain
194	195	2	L1B4b, Low Gain
196	197	2	L1B4c, High Gain
198	199	2	L1B4c, Low Gain
200	201	2	L4Bo, High Gain
202	203	2	L4Bo, Low Gain
204	205	2	L2B9, High Gain
206	207	2	L2B9, Low Gain
208	209	2	L2B8, High Gain
210	211	2	L2B8, Low Gain
212	213	2	L2B7, High Gain
214	215	2	L2B7, Low Gain
216	217	2	L2B6, High Gain
218	219	2	L2B6, Low Gain
220	221	2	L2B5, High Gain
222	223	2	L2B5, Low Gain
224	225	2	L2B4, High Gain
226	227	2	L2B4, Low Gain
228	229	2	L2B3, High Gain
230	231	2	L2B3, Low Gain
232	233	2	L2B2, High Gain
234	235	2	L2B2, Low Gain
236	237	2	L2B1, High Gain
238	239	2	L2B1, Low Gain

Draft



240	241	2	L2B0, High Gain
242	243	2	L2B0, Low Gain
244	245	2	L4Bi, High Gain
246	247	2	L4Bi, Low Gain
248	249	2	L3Bi, High Gain
250	251	2	L3Bi, Low Gain
252	253	2	L3Bo, High Gain
254	255	2	L3Bo, Low Gain

Table 13: Singles Rates, SNGRATES

Draft



Frame Byte # (First)	**Frame Byte #** (Last)	**Description**
256	257	NREAD (events read from event FIFO)
258	259	NHAZ (events rejected for Hazard condition)
260	261	NADCSTIM (ADC-calibration STIM events)
262	263	NODD (odd events)
264	265	NODDFIX (fixed odd events)
266	267	NMULTI (events with multiple hits in relevant layers)
268	269	NMULTIFIX (fixed multi events)
270	271	NBADTRAJ (events rejected for inconsistent/bad trajectory)
272	273	NL2 (events sorted into L12 event category)
274	275	NL3 (events sorted into L123 event category)
276	277	NL4 (events sorted into L1423 event category)
278	279	NPEN (events sorted into PEN event category)
280	281	NFORMAT (events handled by the telemetry event formatter)
282	283	NASIDE (events the software assumed were Aside events)
284	285	NBSIDE (events the software assumed were Bside events)
286	287	NERROR (events that caused a processing error - should never happen)
288	289	NBADTAGS (events with bad tags from onboard event-processing)

Table 14: Event Processing Rates, EVPRATES

Draft



Frame Byte # (First)	Frame Byte # (Last)	# Bytes	Description
290	291	2	L12A
292	293	2	L123A
294	295	2	L12B
296	297	2	L123B
298	299	2	2TEL
300	301	2	PENA
302	303	2	PENA?
304	305	2	PENB
306	307	2	PENB?
308	309	2	ILA
310	311	2	IHA
312	313	2	ILB
314	315	2	IHB
316	317	2	L142A
318	319	2	L1423A
320	321	2	L142B
322	323	2	L1423B
324	325	2	PEN4A
326	327	2	PEN4B
328	329	2	ERROR
330	331	2	L1A (incl L1A0)
332	333	2	L2A
334	335	2	L3A
336	337	2	L1B (incl L1B0)
338	339	2	L2B
340	341	2	L3B

Table 15: Coincidence Rates, COINRATES

Draft



Frame Byte # (First)	**Frame Byte #** (Last)	**Description**
342	343	PB #0 ADC-cal events
344	345	PB #1 Range 2, 3, or 4 events that fall into Z>=40 matrix box
346	347	PB #2 Range 2, 3, or 4 events that fall into 31<=Z<=39 matrix box
348	349	PB #3 Range 3 events that fall into 9<=Z<=30 matrix box, or any foreground box that is painted over it.
350	351	PB #4 Range 2 events that fall into 9<=Z<=30 matrix box, or any foreground box that is painted over it.
352	353	PB #5 Range 3 events that fall into the LiBeB, CNO, C, N, or O matrix boxes
354	355	PB #6 Range 2 events that fall into the LiBeB, CNO, C, N, or O matrix boxes
356	357	PB #7 Range 4 events that fall into the LiBeB, CNO, or 9<=Z<=30 matrix boxes, or any foreground matrix box from C thru Ni.
358	359	PB #8 Range 4 events that fall into the PEN_Z>30 matrix box ("penetrating" or "Range 5" events)
360	361	PB #9 Matrix-sort Reject events, with L3 signal, Z>=3
362	363	PB #10 Matrix-sort Reject events, with NO L3 signal, Z>=3
364	365	PB #11 Range 3 events that fall into 3He matrix box
366	367	PB #12 Range 2 events that fall into 3He matrix box
368	369	PB #13 I-ALiRT High Energy Events (trigger L4 and L3)
370	371	PB #14 I-ALiRT Low Energy Events (trigger L4 and not L3)
372	373	PB #15 Any L14 that stop in L2 (don't trigger L3)

Draft

374	375	PB #16 Range 4 events that fall into the PEN_3<=Z<=30 matrix box ("penetrating" or "Range 5" events)
376	377	PB 212 #17 Any L14 events that stop in first L3 (trigger L2 & L3, not second L3)
378	379	PB #18 Range 3 events that fall into the He background or 4He foreground matrix box
380	381	PB #19 Range 4 events that fall into any He matrix box
382	383	PB #20 Range 2 events that fall into the He background or 4He foreground matrix box
384	385	PB #21 Any L14 events that trigger both L3s
386	387	PB #22 Range 3 events that fall into any H matrix box
388	389	PB #23 Range 4 events that fall into any H matrix box
390	391	PB #24 Range 2 events that fall into any H matrix box
392	393	PB #25 Matrix-sort Reject events, with L3 signal, Z<3
394	395	PB #26 Matrix-sort Reject events, with NO L3 signal, Z<3
396	397	PB #27 Range 4 events that fall into the PEN_H_He matrix box ("penetrating" or "Range 5" events)
398	399	PB #28 Range 2, 3, or 4 events that fall into the "Backward" matrix box
400	401	PB #29 "Clean" Livetime STIM events (stim events that fall into a STIM matrix box)
402	403	PB #30 "Poor" Livetime STIM events (stim events that either fall outside a STIM matrix box, or are rejected because of multiple hits in a layer, etc.)
404	405	PB #31 ERROR - Onboard processing of the event was aborted due to an error. Occurs if the tag-bits of the event are invalid. Can also occur if the onboard processing reaches a point that it should never reach.

Table 16: Priority Buffer Rates, PBUFRATES

Draft



Frame Byte # (First)	Frame Byte # (Last)	Description	Particle ID
406	407	H (1.0-1.8 MeV/nuc)	0
408	409	H (1.8-2.2 MeV/nuc)	1
410	411	H (2.2-2.7 MeV/nuc)	2
412	413	H (2.7-3.2 MeV/nuc)	3
414	415	H (3.2-3.6 MeV/nuc)	4
416	417	H (3.6-4.0 MeV/nuc)	5
418	419	H (4.0-4.5 MeV/nuc)	6
420	421	H (4.5-5.0 MeV/nuc)	7
422	423	H (5.0-70.0 MeV/nuc)	8
424	425	He-3 (1.0-2.2 MeV/nuc)	9
426	427	He-3 (2.2-2.7 MeV/nuc)	10
428	429	He-3 (2.7-3.2 MeV/nuc)	11
430	431	He-3 (3.2-3.6 MeV/nuc)	12
432	433	He-3 (3.6-4.0 MeV/nuc)	13
434	435	He-3 (4.0-4.5 MeV/nuc)	14
436	437	He-3 (4.5-5.0 MeV/nuc)	15
438	439	He-3 (5.0-6.0 MeV/nuc)	16
440	441	He-3 (6.0-70.0 MeV/nuc)	17
442	443	He-4 (1.0-1.8 MeV/nuc)	18
444	445	He-4 (1.8-2.2 MeV/nuc)	19
446	447	He-4 (2.2-2.7 MeV/nuc)	20
448	449	He-4 (2.7-3.2 MeV/nuc)	21
450	451	He-4 (3.2-3.6 MeV/nuc)	22
452	453	He-4 (3.6-4.0 MeV/nuc)	23
454	455	He-4 (4.0-4.5 MeV/nuc)	24

Draft

456	457	He-4 (4.5-5.0 MeV/nuc)	25
458	459	He-4 (5.0-70.0 MeV/nuc)	26
460	461	C (1.0-3.2 MeV/nuc)	27
462	463	C (3.2-3.6 MeV/nuc)	28
464	465	C (3.6-4.0 MeV/nuc)	29
466	467	C (4.0-4.5 MeV/nuc)	30
468	469	C (4.5-5.0 MeV/nuc)	31
470	471	C (5.0-6.0 MeV/nuc)	32
472	473	C (6.0-8.0 MeV/nuc)	33
474	475	C (8.0-10.0 MeV/nuc)	34
476	477	C (10.0-70.0 MeV/nuc)	35
478	479	N (1.0-3.2 MeV/nuc)	36
480	481	N (3.2-3.6 MeV/nuc)	37
482	483	N (3.6-4.0 MeV/nuc)	38
484	485	N (4.0-4.5 MeV/nuc)	39
486	487	N (4.5-5.0 MeV/nuc)	40
488	489	N (5.0-6.0 MeV/nuc)	41
490	491	N (6.0-8.0 MeV/nuc)	42
492	493	N (8.0-10.0 MeV/nuc)	43
494	495	N (10.0-70.0 MeV/nuc)	44
496	497	O (1.0-3.2 MeV/nuc)	45
498	499	O (3.2-3.6 MeV/nuc)	46
500	501	O (3.6-4.0 MeV/nuc)	47
502	503	O (4.0-4.5 MeV/nuc)	48
504	505	O (4.5-5.0 MeV/nuc)	49
506	507	O (5.0-6.0 MeV/nuc)	50
508	509	O (6.0-8.0 MeV/nuc)	51
510	511	O (8.0-10.0 MeV/nuc)	52

Draft

512	513	O (10.0-70.0 MeV/nuc)	53
514	515	Ne (1.0-3.2 MeV/nuc)	54
516	517	Ne (3.2-3.6 MeV/nuc)	55
518	519	Ne (3.6-4.0 MeV/nuc)	56
520	521	Ne (4.0-4.5 MeV/nuc)	57
522	523	Ne (4.5-5.0 MeV/nuc)	58
524	525	Ne (5.0-6.0 MeV/nuc)	59
526	527	Ne (6.0-8.0 MeV/nuc)	60
528	529	Ne (8.0-10.0 MeV/nuc)	61
530	531	Ne (10.0-12.0 MeV/nuc)	62
532	533	Ne (12.0-70.0 MeV/nuc)	63
534	535	Mg (1.0-3.2 MeV/nuc)	64
536	537	Mg (3.2-3.6 MeV/nuc)	65
538	539	Mg (3.6-4.0 MeV/nuc)	66
540	541	Mg (4.0-4.5 MeV/nuc)	67
542	543	Mg (4.5-5.0 MeV/nuc)	68
544	545	Mg (5.0-6.0 MeV/nuc)	69
546	547	Mg (6.0-8.0 MeV/nuc)	70
548	549	Mg (8.0-10.0 MeV/nuc)	71
550	551	Mg (10.0-12.0 MeV/nuc)	72
552	553	Mg (12.0-15.0 MeV/nuc)	73
554	555	Mg (15.0-70.0 MeV/nuc)	74
556	557	Si (1.0-3.2 MeV/nuc)	75
558	559	Si (3.2-3.6 MeV/nuc)	76
560	561	Si (3.6-4.0 MeV/nuc)	77
562	563	Si (4.0-4.5 MeV/nuc)	78
564	565	Si (4.5-5.0 MeV/nuc)	79
566	567	Si (5.0-6.0 MeV/nuc)	80

Draft

568	569	Si (6.0-8.0 MeV/nuc)	81
570	571	Si (8.0-10.0 MeV/nuc)	82
572	573	Si (10.0-12.0 MeV/nuc)	83
574	575	Si (12.0-15.0 MeV/nuc)	84
576	577	Si (15.0-70.0 MeV/nuc)	85
578	579	S (1.0-3.6 MeV/nuc)	86
580	581	S (3.6-4.0 MeV/nuc)	87
582	583	S (4.0-4.5 MeV/nuc)	88
584	585	S (4.5-5.0 MeV/nuc)	89
586	587	S (5.0-6.0 MeV/nuc)	90
588	589	S (6.0-8.0 MeV/nuc)	91
590	591	S (8.0-10.0 MeV/nuc)	92
592	593	S (10.0-12.0 MeV/nuc)	93
594	595	S (12.0-15.0 MeV/nuc)	94
596	597	S (15.0-70.0 MeV/nuc)	95
598	599	Ar (1.0-3.6 MeV/nuc)	96
600	601	Ar (3.6-4.0 MeV/nuc)	97
602	603	Ar (4.0-4.5 MeV/nuc)	98
604	605	Ar (4.5-5.0 MeV/nuc)	99
606	607	Ar (5.0-6.0 MeV/nuc)	100
608	609	Ar (6.0-8.0 MeV/nuc)	101
610	611	Ar (8.0-10.0 MeV/nuc)	102
612	613	Ar (10.0-12.0 MeV/nuc)	103
614	615	Ar (12.0-15.0 MeV/nuc)	104
616	617	Ar (15.0-21.0 MeV/nuc)	105
618	619	Ar (21.0-70.0 MeV/nuc)	106
620	621	Ca (1.0-3.6 MeV/nuc)	107
622	623	Ca (3.6-4.0 MeV/nuc)	108

Draft

624	625	Ca (4.0-4.5 MeV/nuc)	109
626	627	Ca (4.5-5.0 MeV/nuc)	110
628	629	Ca (5.0-6.0 MeV/nuc)	111
630	631	Ca (6.0-8.0 MeV/nuc)	112
632	633	Ca (8.0-10.0 MeV/nuc)	113
634	635	Ca (10.0-12.0 MeV/nuc)	114
636	637	Ca (12.0-15.0 MeV/nuc)	115
638	639	Ca (15.0-21.0 MeV/nuc)	116
640	641	Ca (21.0-70.0 MeV/nuc)	117
642	643	Fe (1.0-2.7 MeV/nuc)	118
644	645	Fe (2.7-3.2 MeV/nuc)	119
646	647	Fe (3.2-3.6 MeV/nuc)	120
648	649	Fe (3.6-4.0 MeV/nuc)	121
650	651	Fe (4.0-4.5 MeV/nuc)	122
652	653	Fe (4.5-5.0 MeV/nuc)	123
654	655	Fe (5.0-6.0 MeV/nuc)	124
656	657	Fe (6.0-8.0 MeV/nuc)	125
658	659	Fe (8.0-10.0 MeV/nuc)	126
660	661	Fe (10.0-12.0 MeV/nuc)	127
662	663	Fe (12.0-15.0 MeV/nuc)	128
664	665	Fe (15.0-21.0 MeV/nuc)	129
666	667	Fe (21.0-70.0 MeV/nuc)	130
668	669	Na, Al, Ni, unidentified	255

Table 17: HIT Sciene Data Frame, Range 2 (L1L2) Science/Foreground Rates, L2FGRATES

Draft

Frame Byte # (First)	**Frame Byte #** (Last)	**Description**	**Particle ID**
670	671	H Background	255
672	673	He Background	255
674	675	LiBeB Background	255
676	677	CNO Background	255
678	679	Z=9-30 Background	255
680	681	Z=30-40 Background	255
682	683	Z>=40 Background	255
684	685	Backward Background	255
686	687	H, He STIM	255
688	689	CNO STIM	255
690	691	Fe STIM	255
692	693	STIM error	255

Table 18: HIT Science Data Frame, Range 2 (L1L2) Science/Background Rates, L2BGRATES

Draft



Frame Byte # (First)	Frame Byte # (Last)	Description	Particle ID
694	695	H (1.0-3.2 MeV/nuc)	0
696	697	H (3.2-3.6 MeV/nuc)	1
698	699	H (3.6-4.0 MeV/nuc)	2
700	701	H (4.0-4.5 MeV/nuc)	3
702	703	H (4.5-5.0 MeV/nuc)	4
704	705	H (5.0-6.0 MeV/nuc)	5
706	707	H (6.0-8.0 MeV/nuc)	6
708	709	H (8.0-10.0 MeV/nuc)	7
710	711	H (10.0-12.0 MeV/nuc)	8
712	713	H (12.0-15.0 MeV/nuc)	9
714	715	H (15.0-70.0 MeV/nuc)	10
716	717	He-3 (1.0-4.0 MeV/nuc)	11
718	719	He-3 (4.0-4.5 MeV/nuc)	12
720	721	He-3 (4.5-5.0 MeV/nuc)	13
722	723	He-3 (5.0-6.0 MeV/nuc)	14
724	725	He-3 (6.0-8.0 MeV/nuc)	15
726	727	He-3 (8.0-10.0 MeV/nuc)	16
728	729	He-3 (10.0-12.0 MeV/nuc)	17
730	731	He-3 (12.0-15.0 MeV/nuc)	18
732	733	He-3 (15.0-70.0 MeV/nuc)	19
734	735	He-4 (1.0-3.2 MeV/nuc)	20
736	737	He-4 (3.2-3.6 MeV/nuc)	21
738	739	He-4 (3.6-4.0 MeV/nuc)	22
740	741	He-4 (4.0-4.5 MeV/nuc)	23
742	743	He-4 (4.5-5.0 MeV/nuc)	24

Draft

744	745	He-4 (5.0-6.0 MeV/nuc)	25
746	747	He-4 (6.0-8.0 MeV/nuc)	26
748	749	He-4 (8.0-10.0 MeV/nuc)	27
750	751	He-4 (10.0-12.0 MeV/nuc)	28
752	753	He-4 (12.0-15.0 MeV/nuc)	29
754	755	He-4 (15.0-70.0 MeV/nuc)	30
756	757	C (1.0-4.5 MeV/nuc)	31
758	759	C (4.5-5.0 MeV/nuc)	32
760	761	C (5.0-6.0 MeV/nuc)	33
762	763	C (6.0-8.0 MeV/nuc)	34
764	765	C (8.0-10.0 MeV/nuc)	35
766	767	C (10.0-12.0 MeV/nuc)	36
768	769	C (12.0-15.0 MeV/nuc)	37
770	771	C (15.0-21.0 MeV/nuc)	38
772	773	C (21.0-27.0 MeV/nuc)	39
774	775	C (27.0-33.0 MeV/nuc)	40
776	777	C (33.0-70.0 MeV/nuc)	41
778	779	N (1.0-5.0 MeV/nuc)	42
780	781	N (5.0-6.0 MeV/nuc)	43
782	783	N (6.0-8.0 MeV/nuc)	44
784	785	N (8.0-10.0 MeV/nuc)	45
786	787	N (10.0-12.0 MeV/nuc)	46
788	789	N (12.0-15.0 MeV/nuc)	47
790	791	N (15.0-21.0 MeV/nuc)	48
792	793	N (21.0-27.0 MeV/nuc)	49
794	795	N (27.0-33.0 MeV/nuc)	50
796	797	N (33.0-70.0 MeV/nuc)	51
798	799	O (1.0-5.0 MeV/nuc)	52

Draft

800	801	O (5.0-6.0 MeV/nuc)	53
802	803	O (6.0-8.0 MeV/nuc)	54
804	805	O (8.0-10.0 MeV/nuc)	55
806	807	O (10.0-12.0 MeV/nuc)	56
808	809	O (12.0-15.0 MeV/nuc)	57
810	811	O (15.0-21.0 MeV/nuc)	58
812	813	O (21.0-27.0 MeV/nuc)	59
814	815	O (27.0-33.0 MeV/nuc)	60
816	817	O (33.0-70.0 MeV/nuc)	61
818	819	Ne (1.0-6.0 MeV/nuc)	62
820	821	Ne (6.0-8.0 MeV/nuc)	63
822	823	Ne (8.0-10.0 MeV/nuc)	64
824	825	Ne (10.0-12.0 MeV/nuc)	65
826	827	Ne (12.0-15.0 MeV/nuc)	66
828	829	Ne (15.0-21.0 MeV/nuc)	67
830	831	Ne (21.0-27.0 MeV/nuc)	68
832	833	Ne (27.0-33.0 MeV/nuc)	69
834	835	Ne (33.0-40.0 MeV/nuc)	70
836	837	Ne (40.0-70.0 MeV/nuc)	71
838	839	Na (1.0-6.0 MeV/nuc)	72
840	841	Na (6.0-8.0 MeV/nuc)	73
842	843	Na (8.0-10.0 MeV/nuc)	74
844	845	Na (10.0-12.0 MeV/nuc)	75
846	847	Na (12.0-15.0 MeV/nuc)	76
848	849	Na (15.0-21.0 MeV/nuc)	77
850	851	Na (21.0-27.0 MeV/nuc)	78
852	853	Na (27.0-33.0 MeV/nuc)	79
854	855	Na (33.0-40.0 MeV/nuc)	80

Draft

856	857	Na (40.0-70.0 MeV/nuc)	81
858	859	Mg (1.0-6.0 MeV/nuc)	82
860	861	Mg (6.0-8.0 MeV/nuc)	83
862	863	Mg (8.0-10.0 MeV/nuc)	84
864	865	Mg (10.0-12.0 MeV/nuc)	85
866	867	Mg (12.0-15.0 MeV/nuc)	86
868	869	Mg (15.0-21.0 MeV/nuc)	87
870	871	Mg (21.0-27.0 MeV/nuc)	88
872	873	Mg (27.0-33.0 MeV/nuc)	89
874	875	Mg (33.0-40.0 MeV/nuc)	90
876	877	Mg (40.0-52.0 MeV/nuc)	91
878	879	Mg (52.0-70.0 MeV/nuc)	92
880	881	Al (1.0-6.0 MeV/nuc)	93
882	883	Al (6.0-8.0 MeV/nuc)	94
884	885	Al (8.0-10.0 MeV/nuc)	95
886	887	Al (10.0-12.0 MeV/nuc)	96
888	889	Al (12.0-15.0 MeV/nuc)	97
890	891	Al (15.0-21.0 MeV/nuc)	98
892	893	Al (21.0-27.0 MeV/nuc)	99
894	895	Al (27.0-33.0 MeV/nuc)	100
896	897	Al (33.0-40.0 MeV/nuc)	101
898	899	Al (40.0-52.0 MeV/nuc)	102
900	901	Al (52.0-70.0 MeV/nuc)	103
902	903	Si (1.0-6.0 MeV/nuc)	104
904	905	Si (6.0-8.0 MeV/nuc)	105
906	907	Si (8.0-10.0 MeV/nuc)	106
908	909	Si (10.0-12.0 MeV/nuc)	107
910	911	Si (12.0-15.0 MeV/nuc)	108

Draft

912	913	Si (15.0-21.0 MeV/nuc)	109
914	915	Si (21.0-27.0 MeV/nuc)	110
916	917	Si (27.0-33.0 MeV/nuc)	111
918	919	Si (33.0-40.0 MeV/nuc)	112
920	921	Si (40.0-52.0 MeV/nuc)	113
922	923	Si (52.0-70.0 MeV/nuc)	114
924	925	S (1.0-6.0 MeV/nuc)	115
926	927	S (6.0-8.0 MeV/nuc)	116
928	929	S (8.0-10.0 MeV/nuc)	117
930	931	S (10.0-12.0 MeV/nuc)	118
932	933	S (12.0-15.0 MeV/nuc)	119
934	935	S (15.0-21.0 MeV/nuc)	120
936	937	S (21.0-27.0 MeV/nuc)	121
938	939	S (27.0-33.0 MeV/nuc)	122
940	941	S (33.0-40.0 MeV/nuc)	123
942	943	S (40.0-52.0 MeV/nuc)	124
944	945	S (52.0-70.0 MeV/nuc)	125
946	947	Ar (1.0-6.0 MeV/nuc)	126
948	949	Ar (6.0-8.0 MeV/nuc)	127
950	951	Ar (8.0-10.0 MeV/nuc)	128
952	953	Ar (10.0-12.0 MeV/nuc)	129
954	955	Ar (12.0-15.0 MeV/nuc)	130
956	957	Ar (15.0-21.0 MeV/nuc)	131
958	959	Ar (21.0-27.0 MeV/nuc)	132
960	961	Ar (27.0-33.0 MeV/nuc)	133
962	963	Ar (33.0-40.0 MeV/nuc)	134
964	965	Ar (40.0-52.0 MeV/nuc)	135
966	967	Ar (52.0-70.0 MeV/nuc)	136

Draft

968	969	Ca (1.0-8.0 MeV/nuc)	137
970	971	Ca (8.0-10.0 MeV/nuc)	138
972	973	Ca (10.0-12.0 MeV/nuc)	139
974	975	Ca (12.0-15.0 MeV/nuc)	140
976	977	Ca (15.0-21.0 MeV/nuc)	141
978	979	Ca (21.0-27.0 MeV/nuc)	142
980	981	Ca (27.0-33.0 MeV/nuc)	143
982	983	Ca (33.0-40.0 MeV/nuc)	144
984	985	Ca (40.0-52.0 MeV/nuc)	145
986	987	Ca (52.0-70.0 MeV/nuc)	146
988	989	Fe (1.0-8.0 MeV/nuc)	147
990	991	Fe (8.0-10.0 MeV/nuc)	148
992	993	Fe (10.0-12.0 MeV/nuc)	149
994	995	Fe (12.0-15.0 MeV/nuc)	150
996	997	Fe (15.0-21.0 MeV/nuc)	151
998	999	Fe (21.0-27.0 MeV/nuc)	152
1000	1001	Fe (27.0-33.0 MeV/nuc)	153
1002	1003	Fe (33.0-40.0 MeV/nuc)	154
1004	1005	Fe (40.0-52.0 MeV/nuc)	155
1006	1007	Fe (52.0-70.0 MeV/nuc)	156
1008	1009	Ni (1.0-8.0 MeV/nuc)	157
1010	1011	Ni (8.0-10.0 MeV/nuc)	158
1012	1013	Ni (10.0-12.0 MeV/nuc)	159
1014	1015	Ni (12.0-15.0 MeV/nuc)	160
1016	1017	Ni (15.0-21.0 MeV/nuc)	161
1018	1019	Ni (21.0-27.0 MeV/nuc)	162
1020	1021	Ni (27.0-33.0 MeV/nuc)	163
1022	1023	Ni (33.0-40.0 MeV/nuc)	164

Draft



1024	1025	Ni (40.0-52.0 MeV/nuc)	165
1026	1027	Ni (52.0-70.0 MeV/nuc)	166

Table 19: HIT Sciene Data Frame, Range 3 (L2L3) Science/Foreground Rates, L3FGRATES

Frame Byte # (First)	**Frame Byte #** (Last)	**Description**	**Particle ID**
1028	1029	H Background	255
1030	1031	He Background	255
1032	1033	LiBeB Background	255
1034	1035	CNO Background	255
1036	1037	Z=9-30 Background	255
1038	1039	Z=30-40 Background	255
1040	1041	Z>=40 Background	255
1042	1043	Backward Background	255
1044	1045	H, He STIM	255
1046	1047	CNO STIM	255
1048	1049	Fe STIM	255
1050	1051	STIM error	255

Table 20: HIT Science Data Frame, Range 3 (L2L3) Science/Background Rates, L3BGRATES

Draft



Frame Byte # (First)	Frame Byte # (Last)	Description	Particle ID
1052	1053	H (1.0-12.0 MeV/nuc)	0
1054	1055	H (12.0-15.0 MeV/nuc)	1
1056	1057	H (15.0-70.0 MeV/nuc)	2
1058	1059	He-4 (1.0-12.0 MeV/nuc)	3
1060	1061	He-4 (12.0-15.0 MeV/nuc)	4
1062	1063	He-4 (15.0-70.0 MeV/nuc)	5
1064	1065	C (1.0-21.0 MeV/nuc)	6
1066	1067	C (21.0-27.0 MeV/nuc)	7
1068	1069	C (27.0-33.0 MeV/nuc)	8
1070	1071	C (33.0-70.0 MeV/nuc)	9
1072	1073	N (1.0-21.0 MeV/nuc)	10
1074	1075	N (21.0-27.0 MeV/nuc)	11
1076	1077	N (27.0-33.0 MeV/nuc)	12
1078	1079	N (33.0-70.0 MeV/nuc)	13
1080	1081	O (1.0-27.0 MeV/nuc)	14
1082	1083	O (27.0-33.0 MeV/nuc)	15
1084	1085	O (33.0-70.0 MeV/nuc)	16
1086	1087	Ne (1.0-27.0 MeV/nuc)	17
1088	1089	Ne (27.0-33.0 MeV/nuc)	18
1090	1091	Ne (33.0-40.0 MeV/nuc)	19
1092	1093	Ne (40.0-70.0 MeV/nuc)	20
1094	1095	Mg (1.0-33.0 MeV/nuc)	21
1096	1097	Mg (33.0-40.0 MeV/nuc)	22
1098	1099	Mg (40.0-52.0 MeV/nuc)	23
1100	1101	Mg (52.0-70.0 MeV/nuc)	24

Draft



1102	1103	Si (1.0-33.0 MeV/nuc)	25
1104	1105	Si (33.0-40.0 MeV/nuc)	26
1106	1107	Si (40.0-52.0 MeV/nuc)	27
1108	1109	Si (52.0-70.0 MeV/nuc)	28
1110	1111	Fe (1.0-40.0 MeV/nuc)	29
1112	1113	Fe (40.0-52.0 MeV/nuc)	30
1114	1115	Fe (52.0-70.0 MeV/nuc)	31
1116	1117	He-3, Na, Al, S, Ar, Ca, Ni, Unidentified	255

Table 21: HIT Science Data Frame, Range 4 (L3AL3B) Science/Foreground Rates, PENFGRATES

Draft

Frame Byte # (First)	**Frame Byte #** (Last)	**Description**	**Particle ID**
1118	1119	H Background	255
1120	1121	He Background	255
1122	1123	LiBeB Background	255
1124	1125	CNO Background	255
1126	1127	Z=9-30 Background	255
1128	1129	Z=30-40 Background	255
1130	1131	Z>=40 Background	255
1132	1133	Backward Background	255
1134	1135	H, He PEN	255
1136	1137	Z=3-30 PEN	255
1138	1139	Z>30 PEN	255
1140	1141	H, He STIM	255
1142	1143	CNO STIM	255
1144	1145	Fe STIM	255
1146	1147	STIM error	255

Table 22: HIT Science Data Frame, Range 4 (L3AL3B) Science/Background Rates, PENBGRATES

Draft



Frame Byte # (First)	**Frame Byte #** (Last)	**Description**
1148	1149	L4Ai deltaE bin 0
1150	1151	L4Ai deltaE bin 1
1152	1153	L4Ai deltaE bin 2
1154	1155	L4Ai deltaE bin 3
1156	1157	L4Ai deltaE bin 4
1158	1159	L4Ai deltaE bin 5
1160	1161	L4Ai vs L3A bin 0
1162	1163	L4Ai vs L3A bin 1
1164	1165	L4Ai vs L3A bin 2
1166	1167	L4Ai vs L3A bin 3
1168	1169	L4Bi deltaE bin 0
1170	1171	L4Bi deltaE bin 1
1172	1173	L4Bi deltaE bin 2
1174	1175	L4Bi deltaE bin 3
1176	1177	L4Bi deltaE bin 4
1178	1179	L4Bi deltaE bin 5
1180	1181	L4Bi vs L3B bin 0
1182	1183	L4Bi vs L3B bin 1
1184	1185	L4Bi vs L3B bin 2
1186	1187	L4Bi vs L3B bin 3

Table 23: HIT Science Data Frame, IALIRTRATES

Draft

Frame Byte # (First)	Frame Byte # (Last)	Description
1188	1189	Species/Energy[i] SectorRate[0,0]
1190	1191	Species/Energy[i] SectorRate[0,1]
1192	1193	Species/Energy[i] SectorRate[0,2]
1194	1195	Species/Energy[i] SectorRate[0,3]
1196	1197	Species/Energy[i] SectorRate[0,4]
1198	1199	Species/Energy[i] SectorRate[0,5]
1200	1201	Species/Energy[i] SectorRate[0,6]
1202	1203	Species/Energy[i] SectorRate[0,7]
1204	1205	Species/Energy[i] SectorRate[0,8]
1206	1207	Species/Energy[i] SectorRate[0,9]
1208	1209	Species/Energy[i] SectorRate[0,10]
1210	1211	Species/Energy[i] SectorRate[0,11]
1212	1213	Species/Energy[i] SectorRate[0,12]
1214	1215	Species/Energy[i] SectorRate[0,13]
1216	1217	Species/Energy[i] SectorRate[0,14]
1218	1219	Species/Energy[i] SectorRate[1,0]
1220	1221	Species/Energy[i] SectorRate[1,1]
1222	1223	Species/Energy[i] SectorRate[1,2]
1224	1225	Species/Energy[i] SectorRate[1,3]
1226	1227	Species/Energy[i] SectorRate[1,4]
1228	1229	Species/Energy[i] SectorRate[1,5]
1230	1231	Species/Energy[i] SectorRate[1,6]
1232	1233	Species/Energy[i] SectorRate[1,7]
1234	1235	Species/Energy[i] SectorRate[1,8]
1236	1237	Species/Energy[i] SectorRate[1,9]

Draft

1238	1239	Species/Energy[i] SectorRate[1,10]
1240	1241	Species/Energy[i] SectorRate[1,11]
1242	1243	Species/Energy[i] SectorRate[1,12]
1244	1245	Species/Energy[i] SectorRate[1,13]
1246	1247	Species/Energy[i] SectorRate[1,14]
1248	1249	Species/Energy[i] SectorRate[2,0]
1250	1251	Species/Energy[i] SectorRate[2,1]
1252	1253	Species/Energy[i] SectorRate[2,2]
1254	1255	Species/Energy[i] SectorRate[2,3]
1256	1257	Species/Energy[i] SectorRate[2,4]
1258	1259	Species/Energy[i] SectorRate[2,5]
1260	1261	Species/Energy[i] SectorRate[2,6]
1262	1263	Species/Energy[i] SectorRate[2,7]
1264	1265	Species/Energy[i] SectorRate[2,8]
1266	1267	Species/Energy[i] SectorRate[2,9]
1268	1269	Species/Energy[i] SectorRate[2,10]
1270	1271	Species/Energy[i] SectorRate[2,11]
1272	1273	Species/Energy[i] SectorRate[2,12]
1274	1275	Species/Energy[i] SectorRate[2,13]
1276	1277	Species/Energy[i] SectorRate[2,14]
1278	1279	Species/Energy[i] SectorRate[3,0]
1280	1281	Species/Energy[i] SectorRate[3,1]
1282	1283	Species/Energy[i] SectorRate[3,2]
1284	1285	Species/Energy[i] SectorRate[3,3]
1286	1287	Species/Energy[i] SectorRate[3,4]
1288	1289	Species/Energy[i] SectorRate[3,5]
1290	1291	Species/Energy[i] SectorRate[3,6]
1292	1293	Species/Energy[i] SectorRate[3,7]

Draft

1294	1295	Species/Energy[i] SectorRate[3,8]
1296	1297	Species/Energy[i] SectorRate[3,9]
1298	1299	Species/Energy[i] SectorRate[3,10]
1300	1301	Species/Energy[i] SectorRate[3,11]
1302	1303	Species/Energy[i] SectorRate[3,12]
1304	1305	Species/Energy[i] SectorRate[3,13]
1306	1307	Species/Energy[i] SectorRate[3,14]
1308	1309	Species/Energy[i] SectorRate[4,0]
1310	1311	Species/Energy[i] SectorRate[4,1]
1312	1313	Species/Energy[i] SectorRate[4,2]
1314	1315	Species/Energy[i] SectorRate[4,3]
1316	1317	Species/Energy[i] SectorRate[4,4]
1318	1319	Species/Energy[i] SectorRate[4,5]
1320	1321	Species/Energy[i] SectorRate[4,6]
1322	1323	Species/Energy[i] SectorRate[4,7]
1324	1325	Species/Energy[i] SectorRate[4,8]
1326	1327	Species/Energy[i] SectorRate[4,9]
1328	1329	Species/Energy[i] SectorRate[4,10]
1330	1331	Species/Energy[i] SectorRate[4,11]
1332	1333	Species/Energy[i] SectorRate[4,12]
1334	1335	Species/Energy[i] SectorRate[4,13]
1336	1337	Species/Energy[i] SectorRate[4,14]
1338	1339	Species/Energy[i] SectorRate[5,0]
1340	1341	Species/Energy[i] SectorRate[5,1]
1342	1343	Species/Energy[i] SectorRate[5,2]
1344	1345	Species/Energy[i] SectorRate[5,3]
1346	1347	Species/Energy[i] SectorRate[5,4]
1348	1349	Species/Energy[i] SectorRate[5,5]

Draft

1350	1351	Species/Energy[i] SectorRate[5,6]
1352	1353	Species/Energy[i] SectorRate[5,7]
1354	1355	Species/Energy[i] SectorRate[5,8]
1356	1357	Species/Energy[i] SectorRate[5,9]
1358	1359	Species/Energy[i] SectorRate[5,10]
1360	1361	Species/Energy[i] SectorRate[5,11]
1362	1363	Species/Energy[i] SectorRate[5,12]
1364	1365	Species/Energy[i] SectorRate[5,13]
1366	1367	Species/Energy[i] SectorRate[5,14]
1368	1369	Species/Energy[i] SectorRate[6,0]
1370	1371	Species/Energy[i] SectorRate[6,1]
1372	1373	Species/Energy[i] SectorRate[6,2]
1374	1375	Species/Energy[i] SectorRate[6,3]
1376	1377	Species/Energy[i] SectorRate[6,4]
1378	1379	Species/Energy[i] SectorRate[6,5]
1380	1381	Species/Energy[i] SectorRate[6,6]
1382	1383	Species/Energy[i] SectorRate[6,7]
1384	1385	Species/Energy[i] SectorRate[6,8]
1386	1387	Species/Energy[i] SectorRate[6,9]
1388	1389	Species/Energy[i] SectorRate[6,10]
1390	1391	Species/Energy[i] SectorRate[6,11]
1392	1393	Species/Energy[i] SectorRate[6,12]
1394	1395	Species/Energy[i] SectorRate[6,13]
1396	1397	Species/Energy[i] SectorRate[6,14]
1398	1399	Species/Energy[i] SectorRate[7,0]
1400	1401	Species/Energy[i] SectorRate[7,1]
1402	1403	Species/Energy[i] SectorRate[7,2]
1404	1405	Species/Energy[i] SectorRate[7,3]

Draft

1406	1407	Species/Energy[i] SectorRate[7,4]
1408	1409	Species/Energy[i] SectorRate[7,5]
1410	1411	Species/Energy[i] SectorRate[7,6]
1412	1413	Species/Energy[i] SectorRate[7,7]
1414	1415	Species/Energy[i] SectorRate[7,8]
1416	1417	Species/Energy[i] SectorRate[7,9]
1418	1419	Species/Energy[i] SectorRate[7,10]
1420	1421	Species/Energy[i] SectorRate[7,11]
1422	1423	Species/Energy[i] SectorRate[7,12]
1424	1425	Species/Energy[i] SectorRate[7,13]
1426	1427	Species/Energy[i] SectorRate[7,14]

Table 24: HIT Science Data Frame, Look Direction/Sectored Rates, SECTORRATES

Frame Byte # (First)	**Frame Byte #** (Last)	**Description**	**Particle ID**
1428	1429	H, Range L1L4L2	0
1430	1431	H, Range L1L4L2L3	1
1432	1433	H, Range L1L4L2L3L3	2
1434	1435	He3, Range L1L4L2	3
1436	1437	He3, Range L1L4L2L3	4
1438	1439	He3, Range L1L4L2L3L3	5
1440	1441	He4, Range L1L4L2	6
1442	1443	He4, Range L1L4L2L3	7
1444	1445	He4, Range L1L4L2L3L3	8
1446	1447	C, Range L1L4L2	9
1448	1449	C, Range L1L4L2L3	10

Draft

1450	1451	C, Range L1L4L2L3L3	11
1452	1453	N, Range L1L4L2	12
1454	1455	N, Range L1L4L2L3	13
1456	1457	N, Range L1L4L2L3L3	14
1458	1459	O, Range L1L4L2	15
1460	1461	O, Range L1L4L2L3	16
1462	1463	O, Range L1L4L2L3L3	17
1464	1465	Ne, Range L1L4L2	18
1466	1467	Ne, Range L1L4L2L3	19
1468	1469	Ne, Range L1L4L2L3L3	20
1470	1471	Na, Range L1L4L2	21
1472	1473	Na, Range L1L4L2L3	22
1474	1475	Na, Range L1L4L2L3L3	23
1476	1477	Mg, Range L1L4L2	24
1478	1479	Mg, Range L1L4L2L3	25
1480	1481	Mg, Range L1L4L2L3L3	26
1482	1483	Al, Range L1L4L2	27
1484	1485	Al, Range L1L4L2L3	28
1486	1487	Al, Range L1L4L2L3L3	29
1488	1489	Si, Range L1L4L2	30
1490	1491	Si, Range L1L4L2L3	31
1492	1493	Si, Range L1L4L2L3L3	32
1494	1495	S, Range L1L4L2	33
1496	1497	S, Range L1L4L2L3	34
1498	1499	S, Range L1L4L2L3L3	35
1500	1501	Ar, Range L1L4L2	36
1502	1503	Ar, Range L1L4L2L3	37
1504	1505	Ar, Range L1L4L2L3L3	38

Draft



1506	1507	Ca, Range L1L4L2	39
1508	1509	Ca, Range L1L4L2L3	40
1510	1511	Ca, Range L1L4L2L3L3	41
1512	1513	Fe, Range L1L4L2	42
1514	1515	Fe, Range L1L4L2L3	43
1516	1517	Fe, Range L1L4L2L3L3	44
1518	1519	Ni, Range L1L4L2	45
1520	1521	Ni, Range L1L4L2L3	46
1522	1523	Ni, Range L1L4L2L3L3	47

Table 25: HIT Science Data Frame, including L4 Science/Foreground Rates, L4FGRATES

Frame Byte # (First)	**Frame Byte #** (Last)	**Description**	**Particle ID**
1524	1525	H BG, Range L1L4L2	255
1526	1527	H BG, Range L1L4L2L3	255
1528	1529	H BG, Range L1L4L2L3L3	255
1530	1531	He BG, Range L1L4L2	255
1532	1533	He BG, Range L1L4L2L3	255
1534	1535	He BG, Range L1L4L2L3L3	255
1536	1537	LiBeB BG, Range L1L4L2	255
1538	1539	LiBeB BG, Range L1L4L2L3	255
1540	1541	LiBeB BG, Range L1L4L2L3L3	255
1542	1543	CNO BG, Range L1L4L2	255
1544	1545	CNO BG, Range L1L4L2L3	255
1546	1547	CNO BG, Range L1L4L2L3L3	255
1548	1549	Z>9 BG, Range L1L4L2	255

Draft

1550	1551	Z>9 BG, Range L1L4L2L3	255
1552	1553	Z>9 BG, Range L1L4L2L3L3	255
1554	1555	Backward BG, Range L1L4L2	255
1556	1557	Backward BG, Range L1L4L2L3	255
1558	1559	Backward BG, Range L1L4L2L3L3	255
1560	1561	H, He PEN BG, Range L1L4L2	255
1562	1563	H, He PEN BG, Range L1L4L2L3	255
1564	1565	H, He PEN BG, Range L1L4L2L3L3	255
1566	1567	Z>2 PEN BG, Range L1L4L2	255
1568	1569	Z>2 BG, Range L1L4L2L3	255
1570	1571	Z>2 BG, Range L1L4L2L3L3	255

Table 26: HIT Science Data Frame, including L4 Science/Background Rates, L4BGRATES

Frame Byte # (First)	**Frame Byte #** (Last)	**Description**
1572	1573	Event Buffer Header (# Event Records)
1574	5239	Event Records (Filled As Needed)

Table 27: HIT Science Data Frame, Event Buffer

Draft



5.5 Lev1A Uncertainty

The uncertainty for the raw Lev1A HIT data will be calculated as asymmetric Poisson uncertainty as prescribed in Gehrels 1986 (DOI: 10.1086/164079). Specifically, HIT will use standard 1σ (0.8413) confidence limits. For upper limits, we use Eq. 10 from Gehrels 1986 with $S = 1$

$$\lambda_u = n + \sqrt{n+1} + 1 \tag{3}$$

where n is the number of raw counts in a particular variable/integration time. Thus, the upper uncertainty is:

$$\delta_u = \sqrt{n+1} + 1 \tag{4}$$

For the lower confidence limit, we use Eq. 13 from Gehrels 1986 with $S = 1$

$$\lambda_l = n - \sqrt{n} \tag{5}$$

And thus, the lower uncertainty is:

$$\delta_l = \sqrt{n} \tag{6}$$

The DELTA PLUS and DELTA MINUS variables in the CDFs will be populated with δ_u and δ_l.

The uncertainty (both DELTA PLUS and DELTA MINUS) for any fill values should also be automatically set as a fill value.

6 Level 1a to Level 1b Processing

Conversion of Level 1a instrumental counts in each integration time to live-time corrected count rates is the primary processing required to generate Level 1b data. Within this step, select energy bins are combined on a species-by-species basis to form the Summed Rates.

- Input: Level 1a CDF files
- Processing Requirement(s): instrument livetime, conversion tables for housekeeping
- Output: Level 1b CDF files

Draft

6.1 Energy Bins

In all data levels higher than Level 1a, energy bins for a given species will be identified by their geometric mean and their bin edges. The geometric mean of two values, a and b, is defined as:

$$\sqrt{a \cdot b} \tag{7}$$

it should be noted that, due to the varying spectral features of SEP events, the true mean of the particles measured in a given energy bin is variable (even over the course of a single event). Thus, the geometric mean is provided only as a "characteristic energy" to identify the bin. The bin limits are the fundamental values that are not variable. For each energy bin, delta_plus and delta_minus values will be reported such that

delta_plus = bin maximum energy - geometric mean
delta_minus = geometric mean - bin minimum energy

6.2 Livetime Corrected Standard and Sectored Rates

The instrument livetime counter is found as part of the ERATES in Table 12. The livetime gives the fraction of time during which the instrument was available to collect data during each integration time. The HIT livetime is derived from the number of clock cycles in which the front-end electronics wait for a trigger in a given minute. The FPGA clock rate is 16 MHz, corresponding to 960,000,000 clock cycles per minute. As with other rates, the LIVE_TIME field is compressed to a 16 bit float (see Sec. 5.1). The count for nominal 60 second science frames with live time of 14% or greater exceeds what the 16 bit floating-point compression can hold, resulting in a rollover of the field's value. The decompressed LIVE_TIME value can still be converted to a fractional live time using the below 3 segment linear function, which is valid from ~0.002% to 110% live time. Note that the conversion will be incorrect for values of live time below 0.001667% (count 16,000). This situation should be detectable via other mnemonics, such as NUMTRIG (Table 12) or STIM event counts (PBUFRATES #29 and #30, Table 16).

$$\text{Livetime Fraction} = \begin{cases} \text{LIVE_TIME} \times (1.04 \times 10^{-9}) & \text{LIVE_TIME} > 16000 \\ \text{LIVE_TIME} \times (3.41 \times 10^{-5}) + 0.14 & 0 \leq \text{LIVE_TIME} \leq 4101 \\ \text{LIVE_TIME} \times (6.827 \times 10^{-5}) & 4101 \leq \text{LIVE_TIME} \leq 16000 \end{cases} \tag{8}$$

Draft

Thus, the conversion from counts in each integration time to livetime-corrected counts has the form

$$\text{Count Rates} = \frac{\text{Counts}}{\text{Livetime Fraction}} \tag{9}$$

This conversion should be done for all Science Rates (i.e., Tables 13, and 15-24). The units in each of the species/energy bins after conversion will remain counts, however, these rates will no longer be restricted to integer values. A full list of all of the data products expected to be livetime corrected is given in document HIT_L1A_L1B_Table_JGM_2_6_24.

The Level 1B Sectored Rates using the livetime counter from the previous 10 minutes of data according to Fig. 14. Thus, for the sectored rates, the livetimes must be calculated and summed from the ten minutes preceding the data in question.

$$\text{Livetime}_{sector} = \sum_{0}^{9} \text{Livetime Fraction} \tag{10}$$

In which the Livetime Fraction for a given minute is given by Eq. 8. The raw counts must also be divided by a factor of 15 to account for the fact that a single spacecraft rotation is split into 15 inclination ranges to find the count rate for the sectored data.

$$\text{Count Rates}_{sector} = \frac{\text{Raw Counts}}{15 \times \text{Livetime}} \tag{11}$$

To ensure that complete 10 minute Sectored blocks are included in each day's worth of data, a 5 minute buffer from the previous day's (n-1) data is included with the current (n) day's data. Thus, if the 11th packet of the 6th minute of a given Sectored block is within the current day, then the full livetime from the previous block will be included. Additionally, a 15 minute buffer of the following day (n+1) is included in the current day's (n) data to ensure that if a Sectored block stretches into the following day, the full block will be maintained.

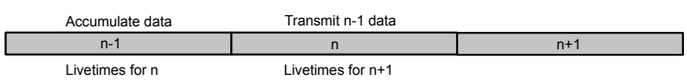


Figure 14: Schmatic of the livetimes corresponding to a given 10 minute block of Sectored data. Each grey shaded box represents a 10 minute Sectored data block.

The Lev1B uncertainties will be calculated by dividing the Lev1A uncertainties by the livetime.

Draft

6.3 Summed Rates

Particular Standard Rates energy bins will be summed to produce Lev1b rates with higher counting statistics. These rates are formed by combining the Standard Rates for a particular species in each of the above energy bins regardless of their penetration range. These Summed Rates also include the summing of different species in a particular energy bins to form element "groups" including the CNO group annd NeMgSi. Explicit lists of each Lev1a product that is utilized to make an Lev1b product is given in the below table. After summing the appropriate Lev1a rates, the sum is divded by the fractional livetime as in Eq. 11 to form summed livetime-corrected counts.

The Lev1B Summed Rate uncertainties are calculated by summing the upper and lower uncertainties from Lev1A and dividing by the livetime, just as is done in calculating the Lev1B science variables.

H 1.8-3.6 MeV/nuc Count Rate	H 1.8-2.2 MeV/nuc Counts R2, H 2.2-2.7 MeV/nuc Counts R2, H 2.7-3.2 MeV/nuc Counts R2, H 3.2-3.6 MeV/nuc Counts R2, H 1.0-3.2 MeV/nuc Counts R3, H 3.2-3.6 MeV/nuc Counts R3, Livetime Counter (ERATES[0])
H 4.0-6.0 MeV/nuc Count Rate	H 4.0-4.5 MeV/nuc Counts R2, H 4.5-5.0 MeV/nuc Counts R2, H 4.0-4.5 MeV/nuc Counts R3, H 4.5-5.0 MeV/nuc Counts R3, H 5.0-6.0 MeV/nuc Counts R3, Livetime Counter (ERATES[0])
H 6.0-10.0 MeV/nuc Count Rate	H 6.0-8.0 MeV/nuc Counts R3, H 8.0-10.0 MeV/nuc Counts R3, Livetime Counter (ERATES[0])
H 10.0-15.0 MeV Count Rate	H 10.0-12.0 MeV/nuc Counts R3, H 12.0-15.0 MeV/nuc Counts R3, H 12.0-15.0 MeV/nuc Counts R4, Livetime Counter (ERATES[0])
He3 4.0-6.0 MeV/nuc Count Rate	He3 4.0-4.5 MeV/nuc Counts R2, He3 4.5-5.0 MeV/nuc Counts R2, He3 5.0-6.0 MeV/nuc Counts R2, He3 4.0-4.5MeV/nuc Counts R3, He3 4.5-5.0 MeV/nuc Counts R3, He3 5.0-6.0 MeV/nuc Counts R3, Livetime Counter (ERATES[0])
He3 6.0-10.0 MeV/nuc Count Rate	He3 6.0-8.0 MeV/nuc Counts R3, He3 8.0-10.0 MeV/nuc Counts R3, Livetime Counter (ERATES[0])

Draft

He3 10.0-15.0 MeV/nuc Count Rate	He3 10.0-12.0 MeV/nuc Counts R3, He3 12.0-15.0 MeV/nuc Counts R3, Livetime Counter (ERATES[0])
He4 1.8-3.6 MeV/nuc Count Rate	He4 1.8-2.2 MeV/nuc Counts R2, He4 2.2-2.7 MeV/nuc Counts R2, He4 2.7-3.2 MeV/nuc Counts R2, He4 3.2-3.6 MeV/nuc Counts R2, He4 3.2-3.6 MeV/nuc Counts R3, Livetime Counter (ERATES[0])
He4 4.0-6.0 MeV/nuc Count Rate	He4 4.0-4.5 MeV/nuc Counts R2, He4 4.5-5.0 MeV/nuc Counts R2, He4 4.0-4.5 MeV/nuc Counts R3, He4 4.5-5.0 MeV/nuc Counts R3, He4 5.0-6.0 MeV/nuc Counts R3, Livetime Counter (ERATES[0])
He4 6.0-10.0 MeV/nuc Count Rate	He4 6.0-8.0 MeV/nuc Counts R3, He4 8.0-10.0 MeV/nuc Counts R3, Livetime Counter (ERATES[0])
He4 10.0-15.0 MeV/nuc Count Rate	He4 10.0-12.0 MeV/nuc Counts R3, He4 12.0-15.0 MeV/nuc Counts R3, He4 12.0-15.0 MeV/nuc Counts R4, Livetime Counter (ERATES[0])
He 4.0-6.0 MeV/nuc Count Rate	He3 4.0-4.5 MeV/nuc Counts R2, He3 4.5-5.0 MeV/nuc Counts R2, He3 5.0-6.0 MeV/nuc Counts R2, He3 4.0-4.5MeV/nuc Counts R3, He3 4.5-5.0 MeV/nuc Counts R3, He3 5.0-6.0 MeV/nuc Counts R3, He4 4.0-4.5 MeV/nuc Counts R2, He4 4.5-5.0 MeV/nuc Counts R2, He4 4.0-4.5 MeV/nuc Counts R3, He4 4.5-5.0 MeV/nuc Counts R3, He4 5.0-6.0 MeV/nuc Counts R3, Livetime Counter (ERATES[0])
He 6.0-10.0 MeV/nuc Count Rate	He3 6.0-8.0 MeV/nuc Counts R3, He3 8.0-10.0 MeV/nuc Counts R3, He4 6.0-8.0 MeV/nuc Counts R3, He4 8.0-10.0 MeV/nuc Counts R3, Livetime Counter (ERATES[0])
He 10.0-15.0 MeV/nuc Count Rate	He3 10.0-12.0 MeV/nuc Counts R3, He3 12.0-15.0 MeV/nuc Counts R3, He4 10.0-12.0 MeV/nuc Counts R3, He4 12.0-15.0 MeV/nuc Counts R3, He4 12.0-15.0 MeV/nuc Counts R4, Livetime Counter (ERATES[0])

Draft

C 4.0-6.0 MeV/nuc Count Rate	C 4.0-4.5 MeV/nuc Counts R2, C 4.5-5.0 MeV/nuc Counts R2, C 5.0-6.0 MeV/nuc Counts R2, C 4.5-5.0 MeV/nuc Counts R3, C 5.0-6.0 MeV/nuc Counts R3, Livetime Counter (ERATES[0])
C 6.0-10.0 MeV/nuc Count Rate	C 6.0-8.0 MeV/nuc Counts R2, C 8.0-10.0 MeV/nuc Counts R2, C 6.0-8.0 MeV/nuc Counts R3, C 8.0-10.0 MeV/nuc Counts R3, Livetime Counter (ERATES[0])
C 10.0-15.0 MeV/nuc Count Rate	C 10.0-12.0 MeV/nuc Counts R3, C 12.0-15.0 MeV/nuc Counts R3, Livetime Counter (ERATES[0])
C 15.0-27.0 MeV/nuc Count Rate	C 15.0-21.0 MeV/nuc Counts R3, C 21.0-27.0 MeV/nuc Counts R3, C 21.0-27.0 MeV/nuc Counts R4, Livetime Counter (ERATES[0])
N 4.0-6.0 MeV/nuc Count Rate	N 4.0-4.5 MeV/nuc Counts R2, N 4.5-5.0 MeV/nuc Counts R2, N 5.0-6.0 MeV/nuc Counts R2, N 5.0-6.0 MeV/nuc Counts R3, Livetime Counter (ERATES[0])
N 6.0-10.0 MeV/nuc Count Rate	N 6.0-8.0 MeV/nuc Counts R2, N 8.0-10.0 MeV/nuc Counts R2, N 6.0-8.0 MeV/nuc Counts R3, N 8.0-10.0 MeV/nuc Counts R3, Livetime Counter (ERATES[0])
N 10.0-15.0 MeV/nuc Count Rate	N 10.0-12.0 MeV/nuc Counts R3, N 12.0-15.0 MeV/nuc Counts R3, Livetime Counter (ERATES[0])
N 15.0-27.0 MeV/nuc Count Rate	N 15.0-21.0 MeV/nuc Counts R3, N 21.0-27.0 MeV/nuc Counts R3, N 21.0-27.0 MeV/nuc Counts R4, Livetime Counter (ERATES[0])
O 4.0-6.0 MeV/nuc Count Rate	O 4.0-4.5 MeV/nuc Counts R2, O 4.5-5.0 MeV/nuc Counts R2, O 5.0-6.0 MeV/nuc Counts R2, O 5.0-6.0 MeV/nuc Counts R3, , Livetime Counter (ERATES[0])

Draft

O 6.0-10.0 MeV/nuc Count Rate	O 6.0-8.0 MeV/nuc Counts R2, O 8.0-10.0 MeV/nuc Counts R2, O 6.0-8.0 MeV/nuc Counts R3, O 8.0-10.0 MeV/nuc Counts R3, Livetime Counter (ERATES[0])
O 10.0-15.0 MeV/nuc Count Rate	O 10.0-12.0 MeV/nuc Counts R3, O 12.0-15.0 MeV/nuc Counts R3, Livetime Counter (ERATES[0])
O 15.0-27.0 MeV/nuc Count Rate	O 15.0-21.0 MeV/nuc Counts R3, O 21.0-27.0 MeV/nuc Counts R3, Livetime Counter (ERATES[0])
Ne 4.0-6.0 MeV/nuc Count Rate	Ne 4.0-4.5 MeV/nuc Counts R2, Ne 4.5-5.0 MeV/nuc Counts R2, Ne 5.0-6.0 MeV/nuc Counts R2
Ne 6.0-10.0 MeV/nuc Count Rate	Ne 6.0-8.0 MeV/nuc Counts R2, Ne 8.0-10.0 MeV/nuc Counts R2, Ne 6.0-8.0 MeV/nuc Counts R3, Ne 8.0-10.0 MeV/nuc Counts R3, Ne 6.0-8.0 MeV/nuc Counts R3, N 8.0-10.0 MeV/nuc Counts R3 , Livetime Counter (ERATES[0])
Ne 10.0-15.0 MeV/nuc Count Rate	Ne 10.0-12.0 MeV/nuc Counts R2, Ne 10.0-12.0 MeV/nuc Counts R3, Ne 12.0-15.0 MeV/nuc Counts R3, Ne 10.0-12.0 MeV/nuc Counts R3, Ne 12.0-15.0 MeV/nuc Counts R3 , Livetime Counter (ERATES[0])
Ne 15.0-27.0 MeV/nuc Count Rate	Ne 15.0-21.0 MeV/nuc Counts R3, Ne 21.0-27.0 MeV/nuc Counts R3, Livetime Counter (ERATES[0])
Na 10.0-15.0 MeV/nuc Count Rate	Na 10.0-12.0 MeV/nuc Counts R3, Na 12.0-15.0 MeV/nuc Counts R3, Livetime Counter (ERATES[0])

Draft

Na 15.0-27.0 MeV/nuc Count Rate	Na 15.0-21.0 MeV/nuc Counts R3, Na 21.0-27.0 MeV/nuc Counts R3, Livetime Counter (ERATES[0])
Mg 4.0-6.0 MeV/nuc Count Rate	Mg 4.0-4.5 MeV/nuc Counts R2, Mg 4.5-5.0 MeV/nuc Counts R2, Mg 5.0-6.0 MeV/nuc Counts R2
Mg 6.0-10.0 MeV/nuc Count Rate	Mg 6.0-8.0 MeV/nuc Counts R2, Mg 8.0-10.0 MeV/nuc Counts R2, Mg 6.0-8.0 MeV/nuc Counts R3, Mg 8.0-10.0 MeV/nuc Counts R3, Livetime Counter (ERATES[0])
Mg 10.0-15.0 MeV/nuc Count Rate	Mg 10.0-12.0 MeV/nuc Counts R2, Mg 12.0-15.0 MeV/nuc Counts R2, Mg 10.0-12.0 MeV/nuc Counts R3, Mg 12.0-15.0 MeV/nuc Counts R3, Livetime Counter (ERATES[0])
Mg 15.0-27.0 MeV/nuc Count Rate	Mg 15.0-21.0 MeV/nuc Counts R3, Mg 21.0-27.0 MeV/nuc Counts R3, Livetime Counter (ERATES[0])
Al 6.0-10.0 MeV/nuc Count Rate	Al 6.0-8.0 MeV/nuc Counts R3, Al 8.0-10.0 MeV/nuc Counts R3, Livetime Counter (ERATES[0])
Al 10.0-15.0 MeV/nuc Count Rate	Al 10.0-12.0 MeV/nuc Counts R3, Al 12.0-15.0 MeV/nuc Counts R3, Livetime Counter (ERATES[0])
Al 15.0-27.0 MeV/nuc Count Rate	Al 15.0-21.0 MeV/nuc Counts R3, Al 21.0-27.0 MeV/nuc Counts R3, Livetime Counter (ERATES[0])

Draft

Si 4.0-6.0 MeV/nuc Count Rate	Si 4.0-4.5 MeV/nuc Counts R2, Si 4.5-5.0 MeV/nuc Counts R2, Si 5.0-6.0 MeV/nuc Counts R2, Livetime Counter (ERATES[0])
Si 6.0-10.0 MeV/nuc Count Rate	Si 6.0-8.0 MeV/nuc Counts R2, Si 8.0-10.0 MeV/nuc Counts R2, Si 6.0-8.0 MeV/nuc Counts R3, Si 8.0-10.0 MeV/nuc Counts R3, Livetime Counter (ERATES[0])
Si 10.0-15.0 MeV/nuc Count Rate	Si 10.0-12.0 MeV/nuc Counts R2, Si 12.0-15.0 MeV/nuc Counts R2, Si 10.0-12.0 MeV/nuc Counts R3, Si 12.0-15.0 MeV/nuc Counts R3, Livetime Counter (ERATES[0])
Si 15.0-27.0 MeV/nuc Count Rate	Si 15.0-21.0 MeV/nuc Counts R3, Si 21.0-27.0 MeV/nuc Counts R3, Livetime Counter (ERATES[0])
Si 27.0-40.0 MeV/nuc Count Rate	Si 27.0-33.0 MeV/nuc Counts R3, Si 33.0-40.0 MeV/nuc Counts R3, Si 33.0-40.0 MeV/nuc Counts R4, Livetime Counter (ERATES[0])
S 4.0-6.0 MeV/nuc Count Rate	S 4.0-4.5 MeV/nuc Counts R2, S 4.5-5.0 MeV/nuc Counts R2, S 5.0-6.0 MeV/nuc Counts R2, Livetime Counter (ERATES[0])
S 6.0-10.0 MeV/nuc Count Rate	S 6.0-8.0 MeV/nuc Counts R2, S 8.0-10.0 MeV/nuc Counts R2, S 6.0-8.0 MeV/nuc Counts R3, S 8.0-10.0 MeV/nuc Counts R3, Livetime Counter (ERATES[0])
S 10.0-15.0 MeV/nuc Count Rate	S 10.0-12.0 MeV/nuc Counts R2, S 12.0-15.0 MeV/nuc Counts R2, S 10.0-12.0 MeV/nuc Counts R3, S 12.0-15.0 MeV/nuc Counts R3, Livetime Counter (ERATES[0])
S 15.0–27.0 MeV/nuc Count Rate	Si 15.0-21.0 MeV/nuc Counts R3, Si 21.0-27.0 MeV/nuc Counts R3, Livetime Counter (ERATES[0])

Draft

S 27.0-40.0 MeV/nuc Count Rate	Si 27.0-33.0 MeV/nuc Counts R3, Si 33.0-40.0 MeV/nuc Counts R3, Livetime Counter (ERATES[0])
Ar 4.0-6.0 MeV/nuc Count Rate	Ar 4.0-4.5 MeV/nuc Counts R2, Ar 4.5-5.0 MeV/nuc Counts R2, Ar 5.0-6.0 MeV/nuc Counts R2, Livetime Counter (ERATES[0])
Ar 6.0-10.0 MeV/nuc Count Rate	Ar 6.0-8.0 MeV/nuc Counts R2, Ar 8.0-10.0 MeV/nuc Counts R2, Ar 6.0-8.0 MeV/nuc Counts R3, Ar 8.0-10.0 MeV/nuc Counts R3, Livetime Counter (ERATES[0])
Ar 10.0-15.0 MeV/nuc Count Rate	Ar 10.0-12.0 MeV/nuc Counts R2, Ar 12.0-15.0 MeV/nuc Counts R2, Ar 10.0-12.0 MeV/nuc Counts R3, Ar 12.0-15.0 MeV/nuc Counts R3, Livetime Counter (ERATES[0])
Ar 15.0-27.0 MeV/nuc Count Rate	Ar 15.0-21.0 MeV/nuc Counts R2, Ar 15.0-21.0 MeV/nuc Counts R3, Ar 21.0-27.0 MeV/nuc Counts R3, Livetime Counter (ERATES[0])
Ar 27.0-40.0 MeV/nuc Count Rate	Ar 27.0-33.0 MeV/nuc Counts R3, Ar 33.0-40.0 MeV/nuc Counts R3, Livetime Counter (ERATES[0])
Ca 4.0-6.0 MeV/nuc Count Rate	Ca 4.0-4.5 MeV/nuc Counts R2, Ca 4.5-5.0 MeV/nuc Counts R2, Ca 5.0-6.0 MeV/nuc Counts R2, Livetime Counter (ERATES[0])
Ca 6.0-10.0 MeV/nuc Count Rate	Ca 6.0-8.0 MeV/nuc Counts R2, Ca 8.0-10.0 MeV/nuc Counts R2, Ca 8.0-10.0 MeV/nuc Counts R3, Livetime Counter (ERATES[0])

Draft

Ca 10.0-15.0 MeV/nuc Count Rate	Ca 10.0-12.0 MeV/nuc Counts R2, Ca 12.0-15.0 MeV/nuc Counts R2, Ca 10.0-12.0 MeV/nuc Counts R3, Ca 12.0-15.0 MeV/nuc Counts R3, Livetime Counter (ERATES[0])
Ca 15.0-27.0 MeV/nuc Count Rate	Ca 15.0-21.0 MeV/nuc Counts R2, Ca 15.0-21.0 MeV/nuc Counts R3, Ca 21.0-27.0 MeV/nuc Counts R3, Livetime Counter (ERATES[0])
Ca 27.0-40.0 MeV/nuc Count Rate	Ca 27.0-33.0 MeV/nuc Counts R3, Ca 33.0-40.0 MeV/nuc Counts R3, Livetime Counter (ERATES[0])
Fe 4.0-6.0 MeV/nuc Count Rate	Fe 4.0-4.5 MeV/nuc Counts R2, Fe 4.5-5.0 MeV/nuc Counts R2, Fe 5.0-6.0 MeV/nuc Counts R2
Fe 6.0-10.0 MeV/nuc Count Rate	Fe 6.0-8.0 MeV/nuc Counts R2, Fe 8.0-10.0 MeV/nuc Counts R2, Fe 8.0-10.0 MeV/nuc Counts R3, Livetime Counter (ERATES[0])
Fe 10.0-15.0 MeV/nuc Count Rate	Fe 10.0-12.0 MeV/nuc Counts R2, Fe 12.0-15.0 MeV/nuc Counts R2, Fe 10.0-12.0 MeV/nuc Counts R3, Fe 12.0-15.0 MeV/nuc Counts R3, Livetime Counter (ERATES[0])
Fe 15.0-27.0 MeV/nuc Count Rate	Fe 15.0-21.0 MeV/nuc Counts R2, Fe 15.0-21.0 MeV/nuc Counts R3, Fe 21.0-27.0 MeV/nuc Counts R3, Livetime Counter (ERATES[0])
Fe 27.0-40.0 MeV/nuc Count Rate	Fe 27.0-33.0 MeV/nuc Counts R3, Fe 33.0-40.0 MeV/nuc Counts R3, Livetime Counter (ERATES[0])

Draft

Ni 10.0-15.0 MeV/nuc Count Rate	Ni 10.0-12.0 MeV/nuc Counts R3, Ni 12.0-15.0 MeV/nuc Counts R3, Livetime Counter (ERATES[0])
Ni 15.0-27.0 MeV/nuc Count Rate	Ni 15.0-21.0 MeV/nuc Counts R3, Ni 21.0-27.0 MeV/nuc Counts R3, Livetime Counter (ERATES[0])
Ni 27.0-40.0 MeV/nuc Count Rate	Ni 27.0-33.0 MeV/nuc Counts R3, Ni 33.0-40.0 MeV/nuc Counts R3, Livetime Counter (ERATES[0])

Table 28: Full table of summed Lev1b rates

6.4 Sector Rates

See livetime correction described by Eq. 11 and surrounding discussion.

6.5 Housekeeping

The raw housekeeping values are translated from their digital values to voltages and temperatures according to the following table:

Lev1b Data Product	**Lev1a Data Products used**	**Equation**
Preamp L234A Voltage	Digital L234A Preamp	V = 0.00121 * Digital L234A Preamp
Preamp L1A Voltage	Digital L1A Preamp	V = 0.00121 * Digital L234A Preamp

Draft



Preamp L1B Voltage	Digital L1B Preamp	V = 0.00121 * Digital L234A Preamp
Preamp L234B Voltage	Digital L234B Preamp	V = 0.00121 * Digital L234A Preamp
Temperature 0	Temperature 0 Digital	FEE Board Connversion from HIT-ELEC-HDBK-0008 (copied to the right)
Temperature 1	Temperature 1 Digital	FEE Board Connversion from HIT-ELEC-HDBK-0008 (copied to the right)
Temperature 2	Temperature 2 Digital	FEE Board Connversion from HIT-ELEC-HDBK-0008 (copied to the right)
Temperature 3	Temperature 3 Digital	FEE Board Connversion from HIT-ELEC-HDBK-0008 (copied to the right)
Analog Temperature	Analog Temperature Digital	Analog Board Conversion from HIT-ELEC-HDBK-0008 (copied to the right)
HVPS Temperature	HVPS Temperature Digital	Analog Board Conversion from HIT-ELEC-HDBK-0008 (copied to the right)
IDPU Temperature	IDPU Temperature Digital	Analog Board Conversion from HIT-ELEC-HDBK-0008 (copied to the right)
LVPS Temperature	LVPS Temperature Digital	Analog Board Conversion from HIT-ELEC-HDBK-0008 (copied to the right)
3.4VD Ebox	3.4VD Ebox Digital	V = 0.001242 * (3.4VD Ebox Digital)
5.1VD Ebox	5.1VD Ebox Digital	V = 0.00151 * (5.1VD Ebox Digital)
+12VA Ebox	+12VA Ebox Digital	V = 0.004007 * (+12Va Ebox Digital)
-12VA Ebox	-12VA Ebox Digital	V = (0.004680 * (-12VA Ebox Digital)) - 13.95
+5.7VA Ebox	+5.7VA Ebox Digital	V = 0.001835 * (+5.7VA Ebox Digital)

Draft



-5.7VA Ebox	-5.7VA Ebox Digital	V = (0.003028 * (-5.7VA Ebox Digital)) - 7.274
+5Vref	+5Vref Digital	V = 0.001526 * (+5Vref Digital)
L1A/B Bias	L1A/B Bias Digital	V = (0.005490 * (L1A/B Bias Digital)) - 0.013
L2A/B Bias	L2A/B Bias Digital	V = (0.005467 * (L2A/B Bias Digital)) + 0.018
L3/4A Bias	L3/4A Bias Digital	V = (0.06712 * L3/4A Bias Digital)) - 2.77
L3/4B Bias	L3/4B Bias Digital	V = (0.06686 * (L3/4B Bias Digital)) - 2.28
+2.0VD Ebox	+2.0VD Ebox Digital	V = 0.001225 * (+2.0VD Ebox Digital)

Table 29: Lev1a to LevB Housekeeping conversion factors

The thermistor conversion values required for conversion of Temperature Digital values to true temperatures are provided in the below table

Temp.	**Res.**	**Analog (V)**	**Analog (Digital)**	**FEE (V)**	**FEE (Digital)**
-40	884600	4.582469954	3753	4.492179565	3679
-39	830900	4.55787164	3733	4.46288538	3655
-38	780800	4.532156954	3712	4.432334242	3630
-37	733900	4.505217925	3690	4.400407723	3604
-36	690200	4.47716658	3667	4.367248798	3577
-35	649300	4.447869571	3643	4.33271053	3548
-34	611000	4.417293233	3618	4.29676512	3519
-33	575200	4.385483379	3592	4.259478673	3489
-32	541700	4.352402378	3565	4.220819698	3457
-31	510400	4.318104907	3537	4.180865007	3424
-30	481000	4.282407407	3507	4.139414802	3390
-29	453500	4.245459652	3477	4.096657633	3355

Draft



-28	427700	4.207161125	3446	4.052491946	3319
-27	403500	4.16752737	3413	4.006951341	3282
-26	380900	4.126760563	3380	3.960282803	3243
-25	359600	4.084507042	3345	3.912097476	3204
-24	339600	4.040932889	3310	3.862602366	3163
-23	320900	3.99626401	3273	3.812069375	3122
-22	303300	3.95024746	3235	3.760228118	3080
-21	286700	3.902804247	3196	3.707008017	3036
-20	271200	3.854462763	3157	3.653017241	2992
-19	256500	3.804509048	3116	3.597475456	2946
-18	242800	3.753865182	3074	3.541423571	2900
-17	229800	3.701675258	3032	3.483929654	2853
-16	217600	3.648558015	2988	3.425692695	2806
-15	206200	3.594839609	2944	3.36708034	2758
-14	195400	3.539855072	2899	3.307379824	2709
-13	185200	3.483822423	2853	3.24684432	2659
-12	175600	3.427010148	2807	3.185776488	2609
-11	166600	3.3697411	2760	3.124531133	2559
-10	158000	3.310980721	2712	3.062015504	2508
-9	150000	3.252385082	2664	3	2457
-8	142400	3.192825112	2615	2.937293729	2406
-7	135200	3.13253012	2566	2.87414966	2354
-6	128500	3.072692492	2517	2.811816193	2303
-5	122100	3.011840158	2467	2.748761819	2251
-4	116000	2.950152594	2416	2.685185185	2199
-3	110300	2.888947093	2366	2.622444127	2148
-2	104900	2.827493261	2316	2.559785261	2096
-1	99800	2.766075388	2265	2.497497497	2045

Draft



0	94980	2.704749972	2215	2.435634424	1995
1	90410	2.643412666	2165	2.374087495	1944
2	86090	2.582338473	2115	2.313128056	1894
3	81990	2.521372778	2065	2.252596296	1845
4	78110	2.460777519	2015	2.192746056	1796
5	74440	2.400670795	1966	2.133684935	1747
6	70960	2.340987068	1917	2.075339261	1700
7	67660	2.281802239	1869	2.017774067	1653
8	64530	2.223179219	1821	1.96104054	1606
9	61560	2.16516601	1773	1.905174548	1560
10	58750	2.108001435	1726	1.850393701	1515
11	56070	2.051291432	1680	1.796309348	1471
12	53540	1.995676159	1634	1.743519604	1428
13	51130	1.940712063	1589	1.691590022	1385
14	48840	1.886588381	1545	1.640687987	1344
15	46670	1.833503575	1502	1.590986568	1303
16	44600	1.78115016	1459	1.542185339	1263
17	42640	1.729957806	1417	1.494671901	1224
18	40770	1.679574854	1376	1.448106841	1186
19	38990	1.630153023	1335	1.402618893	1149
20	38990	1.630153023	1335	1.402618893	1149
21	35700	1.534823732	1257	1.315401621	1077
22	34170	1.488629433	1219	1.273384512	1043
23	32710	1.443385403	1182	1.232386406	1009
24	31320	1.399213724	1146	1.192506853	977
25	30000	1.356238698	1111	1.153846154	945
26	28740	1.314249131	1076	1.1162032	914
27	27540	1.273349362	1043	1.079661283	884

Draft

28	26400	1.23364486	1010	1.044303797	855
29	25310	1.194882447	979	1.009895459	827
30	24270	1.157146944	948	0.976502776	800
31	23280	1.120523681	918	0.944192083	773
32	22330	1.084717769	888	0.912695169	747
33	21430	1.050181319	860	0.882401384	723
34	20570	1.016605713	833	0.853031434	699
35	19740	0.983655571	806	0.824285953	675
36	18960	0.952189634	780	0.796906523	653
37	18210	0.921465439	755	0.770239404	631
38	17490	0.891528188	730	0.744318665	610
39	16800	0.862422998	706	0.719178082	589
40	16150	0.834625323	684	0.695221696	569
41	15520	0.807324178	661	0.671745152	550
42	14920	0.780988275	640	0.649147233	532
43	14350	0.755660874	619	0.627459554	514
44	13800	0.730932203	599	0.606326889	497
45	13280	0.707285897	579	0.586158192	480
46	12770	0.683838492	560	0.566196684	464
47	12290	0.661535149	542	0.547243744	448
48	11830	0.639943741	524	0.528927837	433
49	11390	0.619089031	507	0.511266721	419
50	10970	0.598995304	491	0.494277733	405
51	10570	0.5796863	475	0.477977752	391
52	10180	0.560696189	459	0.46197132	378
53	9807	0.542380568	444	0.44655623	366
54	9450	0.524708495	430	0.431703974	354
55	9109	0.50769711	416	0.41742661	342

Draft

56	8781	0.491211779	402	0.403609086	331
57	8467	0.475316335	389	0.390303041	320
58	8166	0.459973413	377	0.377475362	309
59	7876	0.445092454	365	0.36504876	299
60	7599	0.430787197	353	0.353116665	289
61	7332	0.416913069	341	0.341557038	280
62	7076	0.403531183	330	0.330419515	271
63	6830	0.390598193	320	0.31966676	262
64	6594	0.378122348	310	0.309304464	253
65	6367	0.36605839	300	0.299293954	245
66	6149	0.354413307	290	0.289640034	237
67	5940	0.343193899	281	0.280347366	230
68	5738	0.33229864	272	0.271331026	222
69	5545	0.321841082	264	0.262684163	215
70	5359	0.311718377	255	0.254320941	208
71	5180	0.301935183	247	0.246244533	202
72	5007	0.292441039	240	0.238412677	195
73	4842	0.283350109	232	0.230918907	189
74	4682	0.274501067	225	0.223629659	183
75	4529	0.266008058	218	0.216638445	177
76	4381	0.2577635	211	0.2098562	172
77	4239	0.249826141	205	0.203330807	167
78	4102	0.242143043	198	0.197018309	161
79	3970	0.234716803	192	0.190920458	156
80	3843	0.227549945	186	0.185038953	152
81	3720	0.220588235	181	0.179328963	147
82	3602	0.213890406	175	0.173838343	142
83	3489	0.207458764	170	0.16856864	138

Draft

84	3379	0.201181248	165	0.163427775	134
85	3273	0.195116426	160	0.15846349	130
86	3172	0.189323402	155	0.153723879	126
87	3073	0.183631518	150	0.149069106	122
88	2979	0.178214623	146	0.14464114	118
89	2887	0.17290117	142	0.140299552	115
90	2799	0.167807767	137	0.136139457	111
91	2714	0.162877788	133	0.132114415	108
92	2632	0.158112265	129	0.128225115	105
93	2552	0.153453916	126	0.124424682	102
94	2476	0.149020174	122	0.120808775	99
95	2402	0.144695309	119	0.117282866	96
96	2331	0.14053852	115	0.113895105	93
97	2262	0.136491999	112	0.110598267	91
98	2195	0.132556314	109	0.10739273	88
99	2131	0.128790901	105	0.104326796	85
100	2069	0.125137597	102	0.101353006	83
101	2009	0.12159692	100	0.098471703	81
102	1950	0.118110236	97	0.095635115	78
103	1894	0.114796228	94	0.092939722	76
104	1840	0.111596312	91	0.090337785	74
105	1788	0.108510948	89	0.087829607	72
106	1737	0.105481132	86	0.085367172	70
107	1688	0.102566595	84	0.082998977	68
108	1640	0.099708171	82	0.080676899	66
109	1594	0.096965715	79	0.078449515	64
110	1550	0.094339623	77	0.076317085	63
111	1507	0.091770495	75	0.074231334	61

Draft

112	1465	0.089258515	73	0.072192382	59
113	1425	0.086863761	71	0.070248952	58
114	1386	0.084526626	69	0.068352633	56
115	1348	0.082247279	67	0.066503532	54
116	1311	0.080025882	66	0.06470176	53
117	1276	0.077922712	64	0.062996169	52
118	1241	0.075817744	62	0.061289399	50
119	1208	0.07383141	60	0.059679077	49
120	1176	0.071903737	59	0.058116549	48
121	1145	0.070034865	57	0.056601908	46
122	1114	0.068164574	56	0.055086338	45
123	1085	0.066413662	54	0.053667705	44
124	1057	0.064721947	53	0.052297218	43
125	1029	0.063029071	52	0.050925972	42
126	1002	0.061395554	50	0.049602978	41
127	976.3	0.059839684	49	0.048343027	40
128	951.1	0.058313131	48	0.047106966	39
129	926.7	0.056834141	47	0.045909556	38
130	903	0.055396734	45	0.044745944	37
131	880	0.054000982	44	0.043616178	36
132	857.7	0.052646957	43	0.042520303	35
133	836.1	0.051334727	42	0.041458367	34
134	815	0.050052202	41	0.040420572	33
135	794.6	0.048811592	40	0.039416794	32
136	774.8	0.047606876	39	0.03844215	31
137	755.6	0.046438106	38	0.037496675	31
138	736.9	0.045299243	37	0.036575475	30
139	718.8	0.044196422	36	0.035683507	29

Draft



140	701.2	0.043123595	35	0.034815871	29
141	684.1	0.042080801	34	0.033972593	28
142	667.5	0.041068078	34	0.033153699	27
143	651.3	0.040079359	33	0.032354277	26
144	635.6	0.03912078	32	0.031579282	26
145	620.3	0.038186266	31	0.0308238	25
146	605.5	0.037281958	31	0.030092788	25
147	591.1	0.036401773	30	0.029381327	24
148	577.1	0.035545739	29	0.028689433	23
149	563.5	0.03471388	28	0.028017124	23
150	550.2	0.033900101	28	0.027359468	22

Table 30: Thermistor conversion factors

All other Lev1a housekeeping values are passed directly to Lev1b with no further processing.

7 Level 1b to Level 2 Processing

The processing from Lev1b to Lev2 data converts the live-time corrected counts (in units of counts per integration time) to physical intensity units.

- Input: Lev1b CDF files
- Processing Requirement(s): geometry factors, energy bin widths, efficiencies, dynamic threshold state, instrument status table, instrument status summary, spin pulse
- Output: Lev2 CDF files

7.1 Conversion to Intensity

7.1.1 Standard Rates

The conversion of the Lev1b livetime-corrected count data to physical units requires the species- and energy-dependent geometry factors, energy bin widths, and efficiencies. The calculation is performed as in Eq. 12 (using the same

Draft

symbols as defined in Eq. **??**) the ion intensith in the ith energy bin can be calculated as:

$$j_i(N,X) = \frac{1}{60\Delta t \Delta E_i} \frac{\sum_{j=2}^{4} q_{ij}(N,X) - b_{ij}(N,X)}{\sum_{j=2}^{4} \sigma_{ij}(N,X)\lambda_{ij}(N,X)} \tag{12}$$

where j denotes the range (j = 2, 3, 4). The factor of 60 in the denominator converts from the count rate in Lev1B that is in units of counts per integration time to counts per second. Specific bins from each of the Standard Rates ranges are combined to produce Level 2 data that are not broken out by range. These combinations are shown in Table 31. The first step to producing the Level 2 data products is to sum the data from particular Level 1b products from different ranges. These combinations are shown below in Table 31. To process these data according to Eq. **??**, the dynamic threshold state for the time period in question must be determined using the dynamic threshold bit. The base state is dynamic threshold level 0. The geometry factors and efficiencies can be different for the different dynamic threshold states. These are listed in the tables below.

The Lev2 statistical uncertainty is calculated by Eq. 12 replacing q_{ij} with $\delta_{u/l,ij}$ Lev1b uncertainties. All fill values should have uncertainties that are also fill values. All Lev2 HIT data will have associated systematic uncertainty data products. At launch, the values for all systematic uncertainties will be 0. This will be updated post-launch if/when systematic uncertainties are identified. The full uncertainty should be calculated as the combination of the statistical and systematic uncertainties by adding both quantities in quadrature, i.e.,:

$$\delta_{full} = \sqrt{\delta_{stat}^2 + \delta_{sys}^2} \tag{13}$$

Level 2 Product	**Range(s)**	**Species/Energy**
H (1.8-2.2 MeV/nuc) Intensity	2	H (1.8-2.2 MeV/nuc) Count Rate
H (2.2-2.7 MeV/nuc) Intensity	2	H (2.2-2.7 MeV/nuc) Count Rate
H (2.7-3.2 MeV/nuc) Intensity	2	H (2.7-3.2 MeV/nuc) Count Rate
H (3.2-3.6 MeV/nuc) Intensity	2, 3	H (3.2-3.6 MeV/nuc) Count Rate
H (3.6-4.0 MeV/nuc) Intensity	2, 3	H (3.6-4.0 MeV/nuc) Count Rate
H (4.0-4.5 MeV/nuc) Intensity	2, 3	H (4.0-4.5 MeV/nuc) Count Rate
H (4.5-5.0 MeV/nuc) Intensity	2, 3	H (4.5-5.0 MeV/nuc) Count Rate
H (5.0-6.0 MeV/nuc) Intensity	3	H (5.0-6.0 MeV/nuc) Count Rate

Draft

H (6.0-8.0 MeV/nuc) Intensity	3	H (6.0-8.0 MeV/nuc) Count Rate
H (8.0-10.0 MeV/nuc) Intensity	3	H (8.0-10.0 MeV/nuc) Count Rate
H (10.0-12.0 MeV/nuc) Intensity	3	H (10.0-12.0 MeV/nuc) Count Rate
H (12.0-15.0 MeV/nuc) Intensity	3, 4	H (12.0-15.0 MeV/nuc) Count Rate
He3 (2.2-2.7 MeV/nuc) Intensity	2	He3 (2.2-2.7 MeV/nuc) Count Rate
He3 (2.7-3.2 MeV/nuc) Intensity	2	He3 (2.7-3.2 MeV/nuc) Count Rate
He3 (3.2-3.6 MeV/nuc) Intensity	2	He3 (3.2-3.6 MeV/nuc) Count Rate
He3 (3.6-4.0 MeV/nuc) Intensity	2	He3 (3.6-4.0 MeV/nuc) Count Rate
He3 (4.0-4.5 MeV/nuc) Intensity	2, 3	He3 (4.0-4.5 MeV/nuc) Count Rate
He3 (4.5-5.0 MeV/nuc) Intensity	2, 3	He3 (4.5-5.0 MeV/nuc) Count Rate
He3 (5.0-6.0 MeV/nuc) Intensity	2, 3	He3 (5.0-6.0 MeV/nuc) Count Rate
He3 (6.0-8.0 MeV/nuc) Intensity	3	He3 (6.0-8.0 MeV/nuc) Count Rate
He3 (8.0-10.0 MeV/nuc) Intensity	3	He3 (8.0-10.0 MeV/nuc) Count Rate
He3 (10.0-12.0 MeV/nuc) Intensity	3	He3 (10.0-12.0 MeV/nuc) Count Rate
He3 (12.0-15.0 MeV/nuc) Intensity	3	He3 (12.0-15.0 MeV/nuc) Count Rate
He4 (1.8-2.2 MeV/nuc) Intensity	2	He4 (1.8-2.2 MeV/nuc) Count Rate
He4 (2.2-2.7 MeV/nuc) Intensity	2	He4 (2.2-2.7 MeV/nuc) Count Rate
He4 (2.7-3.2 MeV/nuc) Intensity	2	He4 (2.7-3.2 MeV/nuc) Count Rate
He4 (3.2-3.6 MeV/nuc) Intensity	2, 3	He4 (3.2-3.6 MeV/nuc) Count Rate
He4 (3.6-4.0 MeV/nuc) Intensity	2, 3	He4 (3.6-4.0 MeV/nuc) Count Rate
He4 (4.0-4.5 MeV/nuc) Intensity	2, 3	He4 (4.0-4.5 MeV/nuc) Count Rate
He4 (4.5-5.0 MeV/nuc) Intensity	2, 3	He4 (4.5-5.0 MeV/nuc) Count Rate
He4 (5.0-6.0 MeV/nuc) Intensity	3	He4 (5.0-6.0 MeV/nuc) Count Rate
He4 (6.0-8.0 MeV/nuc) Intensity	3	He4 (6.0-8.0 MeV/nuc) Count Rate
He4 (8.0-10.0 MeV/nuc) Intensity	3	He4 (8.0-10.0 MeV/nuc) Count Rate
He4 (10.0-12.0 MeV/nuc) Intensity	3	He4 (10.0-12.0 MeV/nuc) Count Rate
He4 (12.0-15.0 MeV/nuc) Intensity	3, 4	He4 (12.0-15.0 MeV/nuc) Count Rate

Draft

He (2.2-2.7 MeV/nuc) Intensity	2	He4 (2.2-2.7 MeV/nuc) Count Rate
		He3 (2.2-2.7 MeV/nuc) Count Rate
He (2.7-3.2 MeV/nuc) Intensity	2	He4 (2.7-3.2 MeV/nuc) Count Rate
		He3 (2.7-3.2 MeV/nuc) Count Rate
He (3.2-3.6 MeV/nuc) Intensity	2, 3	He4 (3.2-3.6 MeV/nuc) Count Rate
He (3.6-4.0 MeV/nuc) Intensity	2, 3	He4 (3.6-4.0 MeV/nuc) Count Rate
He (4.0-4.5 MeV/nuc) Intensity	2, 3	He4 (4.0-4.5 MeV/nuc) Count Rate
		He3 (4.0-4.5 MeV/nuc) Count Rate
He (4.5-5.0 MeV/nuc) Intensity	2, 3	He4 (4.5-5.0 MeV/nuc) Count Rate
		He3 (4.5-5.0 MeV/nuc) Count Rate
He (5.0-6.0 MeV/nuc) Intensity	3	He4 (5.0-6.0 MeV/nuc) Count Rate
		He3 (5.0-6.0 MeV/nuc) Count Rate
He (6.0-8.0 MeV/nuc) Intensity	3	He4 (6.0-8.0MeV/nuc) Count Rate
		He3 (6.0-8.0 MeV/nuc) Count Rate
He (8.0-10.0 MeV/nuc) Intensity	3	He4 (8.0-10.0 MeV/nuc) Count Rate
		He3 (8.0-10.0 MeV/nuc) Count Rate
He (10.0-12.0 MeV/nuc) Intensity	3	He4 (10.0-12.0 MeV/nuc) Count Rate
		He3 (10.0-12.0 MeV/nuc) Count Rate
He (12.0-15.0 MeV/nuc) Intensity	3, 4	He4 (12.0-15.0 MeV/nuc) Count Rate
C (3.2-3.6 MeV/nuc) Intensity	2	C (3.2-3.6 MeV/nuc) Count Rate
C (3.6-4.0 MeV/nuc) Intensity	2	C (3.6-4.0 MeV/nuc) Count Rate
C (4.0-4.5 MeV/nuc) Intensity	2	C (4.0-4.5 MeV/nuc) Count Rate
C (4.5-5.0 MeV/nuc) Intensity	2, 3	C (4.5-5.0 MeV/nuc) Count Rate
C (5.0-6.0 MeV/nuc) Intensity	2, 3	C (5.0-6.0 MeV/nuc) Count Rate
C (6.0-8.0 MeV/nuc) Intensity	2, 3	C (6.0-8.0 MeV/nuc) Count Rate
C (8.0-10.0 MeV/nuc) Intensity	2, 3	C (8.0-10.0 MeV/nuc) Count Rate
C (10.0-12.0 MeV/nuc) Intensity	3	C (10.0-12.0 MeV/nuc) Count Rate
C (12.0-15.0 MeV/nuc) Intensity	3	C (12.0-15.0 MeV/nuc) Count Rate

Draft

C (15.0-21.0 MeV/nuc) Intensity	3	C (15.0-21.0 MeV/nuc) Count Rate
C (21.0-27.0 MeV/nuc) Intensity	3, 4	C (21.0-27.0 MeV/nuc) Count Rate
C (27.0-33.0 MeV/nuc) Intensity	3, 4	C (27.0-33.0 MeV/nuc) Count Rate
N (3.2-3.6 MeV/nuc) Intensity	2	N (3.2-3.6 MeV/nuc) Count Rate
N (3.6-4.0 MeV/nuc) Intensity	2	N (3.6-4.0 MeV/nuc) Count Rate
N (4.0-4.5 MeV/nuc) Intensity	2	N (4.0-4.5 MeV/nuc) Count Rate
N (4.5-5.0 MeV/nuc) Intensity	2	N (4.5-5.0 MeV/nuc) Count Rate
N (5.0-6.0 MeV/nuc) Intensity	2, 3	N (5.0-6.0 MeV/nuc) Count Rate
N (6.0-8.0 MeV/nuc) Intensity	2, 3	N (6.0-8.0 MeV/nuc) Count Rate
N (8.0-10.0 MeV/nuc) Intensity	2, 3	N (8.0-10.0 MeV/nuc) Count Rate
N (10.0-12.0 MeV/nuc) Intensity	3	N (10.0-12.0 MeV/nuc) Count Rate
N (12.0-15.0 MeV/nuc) Intensity	3	N (12.0-15.0 MeV/nuc) Count Rate
N (15.0-21.0 MeV/nuc) Intensity	3	N (15.0-21.0 MeV/nuc) Count Rate
N (21.0-27.0 MeV/nuc) Intensity	3, 4	N (21.0-27.0 MeV/nuc) Count Rate
N (27.0-33.0 MeV/nuc) Intensity	3, 4	N (27.0-33.0 MeV/nuc) Count Rate
O (3.2-3.6 MeV/nuc) Intensity	2	O (3.2-3.6 MeV/nuc) Count Rate
O (3.6-4.0 MeV/nuc) Intensity	2	O (3.6-4.0 MeV/nuc) Count Rate
O (4.0-4.5 MeV/nuc) Intensity	2	O (4.0-4.5 MeV/nuc) Count Rate
O (4.5-5.0 MeV/nuc) Intensity	2	O (4.5-5.0 MeV/nuc) Count Rate
O (5.0-6.0 MeV/nuc) Intensity	2, 3	O (5.0-6.0 MeV/nuc) Count Rate
O (6.0-8.0 MeV/nuc) Intensity	2, 3	O (6.0-8.0 MeV/nuc) Count Rate
O (8.0-10.0 MeV/nuc) Intensity	2, 3	O (8.0-10.0 MeV/nuc) Count Rate
O (10.0-12.0 MeV/nuc) Intensity	3	O (10.0-12.0 MeV/nuc) Count Rate
O (12.0-15.0 MeV/nuc) Intensity	3	O (12.0-15.0 MeV/nuc) Count Rate
O (15.0-21.0 MeV/nuc) Intensity	3	O (15.0-21.0 MeV/nuc) Count Rate
O (21.0-27.0 MeV/nuc) Intensity	3	O (21.0-27.0 MeV/nuc) Count Rate
O (27.0-33.0 MeV/nuc) Intensity	3, 4	O (27.0-33.0 MeV/nuc) Count Rate
Ne (3.2-3.6 MeV/nuc) Intensity	2	Ne (3.2-3.6 MeV/nuc) Count Rate

Draft

Ne (3.6-4.0 MeV/nuc) Intensity	2	Ne (3.6-4.0 MeV/nuc) Count Rate
Ne (4.0-4.5 MeV/nuc) Intensity	2	Ne (4.0-4.5 MeV/nuc) Count Rate
Ne (4.5-5.0 MeV/nuc) Intensity	2	Ne (4.5-5.0 MeV/nuc) Count Rate
Ne (5.0-6.0 MeV/nuc) Intensity	2	Ne (5.0-6.0 MeV/nuc) Count Rate
Ne (6.0-8.0 MeV/nuc) Intensity	2, 3	Ne (6.0-8.0 MeV/nuc) Count Rate
Ne (8.0-10.0 MeV/nuc) Intensity	2, 3	Ne (8.0-10.0 MeV/nuc) Count Rate
Ne (10.0-12.0 MeV/nuc) Intensity	2, 3	Ne (10.0-12.0 MeV/nuc) Count Rate
Ne (12.0-15.0 MeV/nuc) Intensity	3	Ne (12.0-15.0 MeV/nuc) Count Rate
Ne (15.0-21.0 MeV/nuc) Intensity	3	Ne (15.0-21.0 MeV/nuc) Count Rate
Ne (21.0-27.0 MeV/nuc) Intensity	3	Ne (21.0-27.0 MeV/nuc) Count Rate
Ne (27.0-33.0 MeV/nuc) Intensity	3, 4	Ne (27.0-33.0 MeV/nuc) Count Rate
Ne (33.0-40.0 MeV/nuc) Intensity	3, 4	Ne (33.0-40.0 MeV/nuc) Count Rate
Na (6.0-8.0 MeV/nuc) Intensity	3	Na (6.0-8.0 MeV/nuc) Count Rate
Na (8.0-10.0 MeV/nuc) Intensity	3	Na (8.0-10.0 MeV/nuc) Count Rate
Na (10.0-12.0 MeV/nuc) Intensity	3	Na (10.0-12.0 MeV/nuc) Count Rate
Na (12.0-15.0 MeV/nuc) Intensity	3	Na (12.0-15.0 MeV/nuc) Count Rate
Na (15.0-21.0 MeV/nuc) Intensity	3	Na (15.0-21.0 MeV/nuc) Count Rate
Na (21.0-27.0 MeV/nuc) Intensity	3	Na (21.0-27.0 MeV/nuc) Count Rate
Na (27.0-33.0 MeV/nuc) Intensity	3	Na (27.0-33.0 MeV/nuc) Count Rate
Na (33.0-40.0 MeV/nuc) Intensity	3	Na (33.0-40.0 MeV/nuc) Count Rate
Mg (3.2-3.6 MeV/nuc) Intensity	2	Mg (3.2-3.6 MeV/nuc) Count Rate
Mg (3.6-4.0 MeV/nuc) Intensity	2	Mg (3.6-4.0 MeV/nuc) Count Rate
Mg (4.0-4.5 MeV/nuc) Intensity	2	Mg (4.0-4.5 MeV/nuc) Count Rate
Mg (4.5-5.0 MeV/nuc) Intensity	2	Mg (4.5-5.0 MeV/nuc) Count Rate
Mg (5.0-6.0 MeV/nuc) Intensity	2	Mg (5.0-6.0 MeV/nuc) Count Rate
Mg (6.0-8.0 MeV/nuc) Intensity	2, 3	Mg (6.0-8.0 MeV/nuc) Count Rate
Mg (8.0-10.0 MeV/nuc) Intensity	2, 3	Mg (8.0-10.0 MeV/nuc) Count Rate
Mg (10.0-12.0 MeV/nuc) Intensity	2, 3	Mg (10.0-12.0 MeV/nuc) Count Rate

Draft

Mg (12.0-15.0 MeV/nuc) Intensity	2, 3	Mg (12.0-15.0 MeV/nuc) Count Rate
Mg (15.0-21.0 MeV/nuc) Intensity	3	Mg (15.0-21.0 MeV/nuc) Count Rate
Mg (21.0-27.0 MeV/nuc) Intensity	3	Mg (21.0-27.0 MeV/nuc) Count Rate
Mg (27.0-33.0 MeV/nuc) Intensity	3	Mg (27.0-33.0 MeV/nuc) Count Rate
Mg (33.0-40.0 MeV/nuc) Intensity	3, 4	Mg (33.0-40.0 MeV/nuc) Count Rate
Mg (40.0-52.0 MeV/nuc) Intensity	3, 4	Mg (40.0-52.0 MeV/nuc) Count Rate
Al (6.0-8.0 MeV/nuc) Intensity	3	Al (6.0-8.0 MeV/nuc) Count Rate
Al (8.0-10.0 MeV/nuc) Intensity	3	Al (8.0-10.0 MeV/nuc) Count Rate
Al (10.0-12.0 MeV/nuc) Intensity	3	Al (10.0-12.0 MeV/nuc) Count Rate
Al (12.0-15.0 MeV/nuc) Intensity	3	Al (12.0-15.0 MeV/nuc) Count Rate
Al (15.0-21.0 MeV/nuc) Intensity	3	Al (15.0-21.0 MeV/nuc) Count Rate
Al (21.0-27.0 MeV/nuc) Intensity	3	Al (21.0-27.0 MeV/nuc) Count Rate
Al (27.0-33.0 MeV/nuc) Intensity	3	Al (27.0-33.0 MeV/nuc) Count Rate
Al (33.0-40.0 MeV/nuc) Intensity	3	Al (33.0-40.0 MeV/nuc) Count Rate
Al (40.0-52.0 MeV/nuc) Intensity	3	Al (40.0-52.0 MeV/nuc) Count Rate
Si (3.2-3.6 MeV/nuc) Intensity	2	Si (3.2-3.6 MeV/nuc) Count Rate
Si (3.6-4.0 MeV/nuc) Intensity	2	Si (3.6-4.0 MeV/nuc) Count Rate
Si (4.0-4.5 MeV/nuc) Intensity	2	Si (4.0-4.5 MeV/nuc) Count Rate
Si (4.5-5.0 MeV/nuc) Intensity	2	Si (4.5-5.0 MeV/nuc) Count Rate
Si (5.0-6.0 MeV/nuc) Intensity	2	Si (5.0-6.0 MeV/nuc) Count Rate
Si (6.0-8.0 MeV/nuc) Intensity	2, 3	Si (6.0-8.0 MeV/nuc) Count Rate
Si (8.0-10.0 MeV/nuc) Intensity	2, 3	Si (8.0-10.0 MeV/nuc) Count Rate
Si (10.0-12.0 MeV/nuc) Intensity	2, 3	Si (10.0-12.0 MeV/nuc) Count Rate
Si (12.0-15.0 MeV/nuc) Intensity	2, 3	Si (12.0-15.0 MeV/nuc) Count Rate
Si (15.0-21.0 MeV/nuc) Intensity	3	Si (15.0-21.0 MeV/nuc) Count Rate
Si (21.0-27.0 MeV/nuc) Intensity	3	Si (21.0-27.0 MeV/nuc) Count Rate
Si (27.0-33.0 MeV/nuc) Intensity	3	Si (27.0-33.0 MeV/nuc) Count Rate
Si (33.0-40.0 MeV/nuc) Intensity	3, 4	Si (33.0-40.0 MeV/nuc) Count Rate

Draft

Si (40.0-52.0 MeV/nuc) Intensity	3, 4	Si (40.0-52.0 MeV/nuc) Count Rate
S (3.6-4.0 MeV/nuc) Intensity	2	S (3.6-4.0 MeV/nuc) Count Rate
S (4.0-4.5 MeV/nuc) Intensity	2	S (4.0-4.5 MeV/nuc) Count Rate
S (4.5-5.0 MeV/nuc) Intensity	2	S (4.5-5.0 MeV/nuc) Count Rate
S (5.0-6.0 MeV/nuc) Intensity	2	S (5.0-6.0 MeV/nuc) Count Rate
S (6.0-8.0 MeV/nuc) Intensity	2, 3	S (6.0-8.0 MeV/nuc) Count Rate
S (8.0-10.0 MeV/nuc) Intensity	2, 3	S (8.0-10.0 MeV/nuc) Count Rate
S (10.0-12.0 MeV/nuc) Intensity	2, 3	S (10.0-12.0 MeV/nuc) Count Rate
S (12.0-15.0 MeV/nuc) Intensity	2, 3	S (12.0-15.0 MeV/nuc) Count Rate
S (15.0-21.0 MeV/nuc) Intensity	3	S (15.0-21.0 MeV/nuc) Count Rate
S (21.0-27.0 MeV/nuc) Intensity	3	S (21.0-27.0 MeV/nuc) Count Rate
S (27.0-33.0 MeV/nuc) Intensity	3	S (27.0-33.0 MeV/nuc) Count Rate
S (33.0-40.0 MeV/nuc) Intensity	3	S (33.0-40.0 MeV/nuc) Count Rate
S (40.0-52.0 MeV/nuc) Intensity	3	S (40.0-52.0 MeV/nuc) Count Rate
Ar (3.6-4.0 MeV/nuc) Intensity	2	Ar (3.6-4.0 MeV/nuc) Count Rate
Ar (4.0-4.5 MeV/nuc) Intensity	2	Ar (4.0-4.5 MeV/nuc) Count Rate
Ar (4.5-5.0 MeV/nuc) Intensity	2	Ar (4.5-5.0 MeV/nuc) Count Rate
Ar (5.0-6.0 MeV/nuc) Intensity	2	Ar (5.0-6.0 MeV/nuc) Count Rate
Ar (6.0-8.0 MeV/nuc) Intensity	2, 3	Ar (6.0-8.0 MeV/nuc) Count Rate
Ar (8.0-10.0 MeV/nuc) Intensity	2, 3	Ar (8.0-10.0 MeV/nuc) Count Rate
Ar (10.0-12.0 MeV/nuc) Intensity	2, 3	Ar (10.0-12.0 MeV/nuc) Count Rate
Ar (12.0-15.0 MeV/nuc) Intensity	2, 3	Ar (12.0-15.0 MeV/nuc) Count Rate
Ar (15.0-21.0 MeV/nuc) Intensity	2, 3	Ar (15.0-21.0 MeV/nuc) Count Rate
Ar (21.0-27.0 MeV/nuc) Intensity	3	Ar (21.0-27.0 MeV/nuc) Count Rate
Ar (27.0-33.0 MeV/nuc) Intensity	3	Ar (27.0-33.0 MeV/nuc) Count Rate
Ar (33.0-40.0 MeV/nuc) Intensity	3	Ar (33.0-40.0 MeV/nuc) Count Rate
Ar (40.0-52.0 MeV/nuc) Intensity	3	Ar (40.0-52.0 MeV/nuc) Count Rate
Ca (3.6-4.0 MeV/nuc) Intensity	2	Ca (3.6-4.0 MeV/nuc) Count Rate

Draft

Ca (4.0-4.5 MeV/nuc) Intensity	2	Ca (4.0-4.5 MeV/nuc) Count Rate
Ca (4.5-5.0 MeV/nuc) Intensity	2	Ca (4.5-5.0 MeV/nuc) Count Rate
Ca (5.0-6.0 MeV/nuc) Intensity	2	Ca (5.0-6.0 MeV/nuc) Count Rate
Ca (6.0-8.0 MeV/nuc) Intensity	2	Ca (6.0-8.0 MeV/nuc) Count Rate
Ca (8.0-10.0 MeV/nuc) Intensity	2, 3	Ca (8.0-10.0 MeV/nuc) Count Rate
Ca (10.0-12.0 MeV/nuc) Intensity	2, 3	Ca (10.0-12.0 MeV/nuc) Count Rate
Ca (12.0-15.0 MeV/nuc) Intensity	2, 3	Ca (12.0-15.0 MeV/nuc) Count Rate
Ca (15.0-21.0 MeV/nuc) Intensity	2, 3	Ca (15.0-21.0 MeV/nuc) Count Rate
Ca (21.0-27.0 MeV/nuc) Intensity	3	Ca (21.0-27.0 MeV/nuc) Count Rate
Ca (27.0-33.0 MeV/nuc) Intensity	3	Ca (27.0-33.0 MeV/nuc) Count Rate
Ca (33.0-40.0 MeV/nuc) Intensity	3	Ca (33.0-40.0 MeV/nuc) Count Rate
Ca (40.0-52.0 MeV/nuc) Intensity	3	Ca (40.0-52.0 MeV/nuc) Count Rate
Fe (2.7-3.2 MeV/nuc) Intensity	2	Fe (2.7-3.2 MeV/nuc) Count Rate
Fe (3.2-3.6 MeV/nuc) Intensity	2	Fe (3.2-3.6 MeV/nuc) Count Rate
Fe (3.6-4.0 MeV/nuc) Intensity	2	Fe (3.6-4.0 MeV/nuc) Count Rate
Fe (4.0-4.5 MeV/nuc) Intensity	2	Fe (4.0-4.5 MeV/nuc) Count Rate
Fe (4.5-5.0 MeV/nuc) Intensity	2	Fe (4.5-5.0 MeV/nuc) Count Rate
Fe (5.0-6.0 MeV/nuc) Intensity	2	Fe (5.0-6.0 MeV/nuc) Count Rate
Fe (6.0-8.0 MeV/nuc) Intensity	2	Fe (6.0-8.0 MeV/nuc) Count Rate
Fe (8.0-10.0 MeV/nuc) Intensity	2, 3	Fe (8.0-10.0 MeV/nuc) Count Rate
Fe (10.0-12.0 MeV/nuc) Intensity	2, 3	Fe (10.0-12.0 MeV/nuc) Count Rate
Fe (12.0-15.0 MeV/nuc) Intensity	2, 3	Fe (12.0-15.0 MeV/nuc) Count Rate
Fe (15.0-21.0 MeV/nuc) Intensity	2, 3	Fe (15.0-21.0 MeV/nuc) Count Rate
Fe (21.0-27.0 MeV/nuc) Intensity	3	Fe (21.0-27.0 MeV/nuc) Count Rate
Fe (27.0-33.0 MeV/nuc) Intensity	3	Fe (27.0-33.0 MeV/nuc) Count Rate
Fe (33.0-40.0 MeV/nuc) Intensity	3	Fe (33.0-40.0 MeV/nuc) Count Rate
Fe (40.0-52.0 MeV/nuc) Intensity	3, 4	Fe (40.0-52.0 MeV/nuc) Count Rate
Fe (52.0-70.0 MeV/nuc) Intensity	3, 4	Fe (52.0-70.0 MeV/nuc) Count Rate

Draft

Ni (8.0-10.0 MeV/nuc) Intensity	3	Ni (8.0-10.0 MeV/nuc) Count Rate
Ni (10.0-12.0 MeV/nuc) Intensity	3	Ni (10.0-12.0 MeV/nuc) Count Rate
Ni (12.0-15.0 MeV/nuc) Intensity	3	Ni (12.0-15.0 MeV/nuc) Count Rate
Ni (15.0-21.0 MeV/nuc) Intensity	3	Ni (15.0-21.0 MeV/nuc) Count Rate
Ni (21.0-27.0 MeV/nuc) Intensity	3	Ni (21.0-27.0 MeV/nuc) Count Rate
Ni (27.0-33.0 MeV/nuc) Intensity	3	Ni (27.0-33.0 MeV/nuc) Count Rate
Ni (33.0-40.0 MeV/nuc) Intensity	3	Ni (33.0-40.0 MeV/nuc) Count Rate
Ni (40.0-52.0 MeV/nuc) Intensity	3	Ni (40.0-52.0 MeV/nuc) Count Rate
Ni (52.0-70.0 MeV/nuc) Intensity	3	Ni (52.0-70.0 MeV/nuc) Count Rate

Table 31: HIT Level 2 Standard Rate products

Table 32 lists the energy bin width, geometry factor, and efficiency for each of the Level 2 Standard Rates listed in Table 31 for dynamic threshold state 0.

Species	**Lower En. (MeV/n)**	**Upper En. (MeV/n)**	**ΔE (MeV/n)**	**Geo. Fact. (cm^2 sr)**	**Eff.**
H	1.8	2.2	0.4	3.415	1
H	2.2	2.7	0.5	3.441	1
H	2.7	3.2	0.5	3.448	1
H	3.2	3.6	0.4	3.450	1
H	3.6	4	0.4	3.460	1
H	4	4.5	0.5	3.457	1
H	4.5	5	0.5	3.467	1
H	5	6	1	3.471	1
H	6	8	2	3.469	1
H	8	10	2	2.819	1
H	10	12	2	1.101	1
H	12	15	3	0.200	1
He3	2.2	2.7	0.5	3.413	1

Draft



He3	2.7	3.2	0.5	3.452	1
He3	3.2	3.6	0.4	3.457	1
He3	3.6	4	0.4	3.460	1
He3	4	4.5	0.5	3.457	1
He3	4.5	5	0.5	3.460	1
He3	5	6	1	3.466	1
He3	6	8	2	3.482	1
He3	8	10	2	3.500	1
He3	10	12	2	3.520	1
He3	12	15	3	3.528	1
He4	1.8	2.2	0.4	3.447	1
He4	2.2	2.7	0.5	3.456	1
He4	2.7	3.2	0.5	3.462	1
He4	3.2	3.6	0.4	3.453	1
He4	3.6	4	0.4	3.462	1
He4	4	4.5	0.5	3.472	1
He4	4.5	5	0.5	3.469	1
He4	5	6	1	3.476	1
He4	6	8	2	3.488	1
He4	8	10	2	3.508	1
He4	10	12	2	3.525	1
He4	12	15	3	3.535	1
He	2.2	2.7	0.5	3.455	1
He	2.7	3.2	0.5	3.462	1
He	3.2	3.6	0.4	3.454	1
He	3.6	4	0.4	3.462	1
He	4	4.5	0.5	3.472	1

Draft



He	4.5	5	0.5	3.469	1
He	5	6	1	3.476	1
He	6	8	2	3.488	1
He	8	10	2	3.508	1
He	10	12	2	3.525	1
He	12	15	3	3.535	1
C	3.2	3.6	0.4	3.418	1
C	3.6	4	0.4	3.435	1
C	4	4.5	0.5	3.447	1
C	4.5	5	0.5	3.468	1
C	5	6	1	3.461	1
C	6	8	2	3.465	1
C	8	10	2	3.480	1
C	10	12	2	3.474	1
C	12	15	3	3.509	1
C	15	21	6	3.527	1
C	21	27	6	3.552	1
C	27	33	6	3.872	1
N	3.2	3.6	0.4	2.874	1
N	3.6	4	0.4	3.438	1
N	4	4.5	0.5	3.447	1
N	4.5	5	0.5	3.453	1
N	5	6	1	3.457	1
N	6	8	2	3.466	1
N	8	10	2	3.475	1
N	10	12	2	3.488	1
N	12	15	3	3.505	1

Draft



N	15	21	6	3.532	1
N	21	27	6	3.556	1
N	27	33	6	3.655	1
O	3.2	3.6	0.4	1.324	1
O	3.6	4	0.4	3.408	1
O	4	4.5	0.5	3.450	1
O	4.5	5	0.5	3.451	1
O	5	6	1	3.455	1
O	6	8	2	3.465	1
O	8	10	2	3.473	1
O	10	12	2	3.476	1
O	12	15	3	3.500	1
O	15	21	6	3.524	1
O	21	27	6	3.563	1
O	27	33	6	3.592	1
Ne	3.2	3.6	0.4	0.002	1
Ne	3.6	4	0.4	1.846	1
Ne	4	4.5	0.5	3.425	1
Ne	4.5	5	0.5	3.439	1
Ne	5	6	1	3.446	1
Ne	6	8	2	3.463	1
Ne	8	10	2	3.476	1
Ne	10	12	2	3.475	1
Ne	12	15	3	3.492	1
Ne	15	21	6	3.515	1
Ne	21	27	6	3.559	1
Ne	27	33	6	3.590	1

Draft



Ne	33	40	7	3.704	1
Na	6	8	2	3.459	1
Na	8	10	2	3.465	1
Na	10	12	2	3.476	1
Na	12	15	3	3.493	1
Na	15	21	6	3.515	1
Na	21	27	6	3.557	1
Na	27	33	6	3.597	1
Na	33	40	7	3.711	1
Mg	3.2	3.6	0.4	0.001	1
Mg	3.6	4	0.4	0.011	1
Mg	4	4.5	0.5	2.657	1
Mg	4.5	5	0.5	3.446	1
Mg	5	6	1	3.449	1
Mg	6	8	2	3.459	1
Mg	8	10	2	3.465	1
Mg	10	12	2	3.486	1
Mg	12	15	3	3.490	1
Mg	15	21	6	3.512	1
Mg	21	27	6	3.557	1
Mg	27	33	6	3.590	1
Mg	33	40	7	3.629	1
Mg	40	52	12	4.058	1
Al	6	8	2	3.453	1
Al	8	10	2	3.463	1
Al	10	12	2	3.472	1
Al	12	15	3	3.486	1

Draft



Al	15	21	6	3.511	1
Al	21	27	6	3.553	1
Al	27	33	6	3.588	1
Al	33	40	7	3.634	1
Al	40	52	12	4.054	1
Si	3.2	3.6	0.4	0.001	1
Si	3.6	4	0.4	0.002	1
Si	4	4.5	0.5	1.163	1
Si	4.5	5	0.5	3.390	1
Si	5	6	1	3.450	1
Si	6	8	2	3.452	1
Si	8	10	2	3.462	1
Si	10	12	2	3.466	1
Si	12	15	3	3.480	1
Si	15	21	6	3.512	1
Si	21	27	6	3.549	1
Si	27	33	6	3.593	1
Si	33	40	7	3.641	1
Si	40	52	12	3.928	1
S	3.6	4	0.4	0.001	1
S	4	4.5	0.5	0.134	1
S	4.5	5	0.5	3.031	1
S	5	6	1	3.446	1
S	6	8	2	3.453	1
S	8	10	2	3.465	1
S	10	12	2	3.479	1
S	12	15	3	3.483	1

Draft

S	15	21	6	3.507	1
S	21	27	6	3.544	1
S	27	33	6	3.588	1
S	33	40	7	3.632	1
S	40	52	12	3.787	1
Ar	3.6	4	0.4	0.002	1
Ar	4	4.5	0.5	1.031	1
Ar	4.5	5	0.5	3.349	1
Ar	5	6	1	3.449	1
Ar	6	8	2	3.461	1
Ar	8	10	2	3.470	1
Ar	10	12	2	3.479	1
Ar	12	15	3	3.487	1
Ar	15	21	6	3.508	1
Ar	21	27	6	3.550	1
Ar	27	33	6	3.590	1
Ar	33	40	7	3.631	1
Ar	40	52	12	3.783	1
Ca	3.6	4	0.4	0.001	1
Ca	4	4.5	0.5	0.002	1
Ca	4.5	5	0.5	0.962	1
Ca	5	6	1	3.362	1
Ca	6	8	2	3.451	1
Ca	8	10	2	3.460	1
Ca	10	12	2	3.470	1
Ca	12	15	3	3.479	1
Ca	15	21	6	3.504	1

Draft

Ca	21	27	6	3.540	1
Ca	27	33	6	3.585	1
Ca	33	40	7	3.623	1
Ca	40	52	12	3.678	1
Fe	2.7	3.2	0.5	0.000	1
Fe	3.2	3.6	0.4	0.000	1
Fe	3.6	4	0.4	0.001	1
Fe	4	4.5	0.5	0.002	1
Fe	4.5	5	0.5	0.390	1
Fe	5	6	1	3.265	1
Fe	6	8	2	3.453	1
Fe	8	10	2	3.455	1
Fe	10	12	2	3.471	1
Fe	12	15	3	3.474	1
Fe	15	21	6	3.496	1
Fe	21	27	6	3.529	1
Fe	27	33	6	3.556	1
Fe	33	40	7	3.598	1
Fe	40	52	12	3.645	1
Fe	52	70	18	3.964	1
Ni	8	10	2	3.458	1
Ni	10	12	2	3.470	1
Ni	12	15	3	3.478	1
Ni	15	21	6	3.498	1
Ni	21	27	6	3.528	1
Ni	27	33	6	3.560	1
Ni	33	40	7	3.599	1

Draft

Ni	40	52	12	3.643	1
Ni	52	70	18	3.878	1

Table 32: Geometry factors, energy bin widths, and efficiencies for Level 2 Standard Rates for dynamic threshold state 0.

Table 33 lists the energy bin width, geometry factor, and efficiency for each of the Level 2 Standard Rates listed in Table 31 for dynamic threshold state 1.

Species	**Lower En. (MeV/n)**	**Upper En. (MeV/n)**	**ΔE (MeV/n)**	**Geo. Fact. (cm^2 sr)**	**Eff.**
H	1.8	2.2	0.4	0.683	1
H	2.2	2.7	0.5	0.688	1
H	2.7	3.2	0.5	0.690	1
H	3.2	3.6	0.4	0.690	1
H	3.6	4	0.4	0.692	1
H	4	4.5	0.5	0.691	1
H	4.5	5	0.5	0.693	1
H	5	6	1	0.694	1
H	6	8	2	0.694	1
H	8	10	2	0.564	1
H	10	12	2	0.220	1
H	12	15	3	0.040	1
He3	2.2	2.7	0.5	0.683	1
He3	2.7	3.2	0.5	0.690	1
He3	3.2	3.6	0.4	0.691	1
He3	3.6	4	0.4	0.692	1
He3	4	4.5	0.5	0.691	1
He3	4.5	5	0.5	0.692	1

Draft



He3	5	6	1	0.693	1
He3	6	8	2	0.696	1
He3	8	10	2	0.700	1
He3	10	12	2	0.704	1
He3	12	15	3	0.706	1
He4	1.8	2.2	0.4	0.689	1
He4	2.2	2.7	0.5	0.691	1
He4	2.7	3.2	0.5	0.692	1
He4	3.2	3.6	0.4	0.691	1
He4	3.6	4	0.4	0.692	1
He4	4	4.5	0.5	0.694	1
He4	4.5	5	0.5	0.694	1
He4	5	6	1	0.695	1
He4	6	8	2	0.698	1
He4	8	10	2	0.702	1
He4	10	12	2	0.705	1
He4	12	15	3	0.707	1
He	2.2	2.7	0.5	0.691	1
He	2.7	3.2	0.5	0.692	1
He	3.2	3.6	0.4	0.691	1
He	3.6	4	0.4	0.692	1
He	4	4.5	0.5	0.694	1
He	4.5	5	0.5	0.694	1
He	5	6	1	0.695	1
He	6	8	2	0.698	1
He	8	10	2	0.702	1
He	10	12	2	0.705	1

Draft



He	12	15	3	0.707	1
C	3.2	3.6	0.4	0.684	1
C	3.6	4	0.4	0.687	1
C	4	4.5	0.5	0.689	1
C	4.5	5	0.5	0.694	1
C	5	6	1	0.692	1
C	6	8	2	0.693	1
C	8	10	2	0.696	1
C	10	12	2	0.695	1
C	12	15	3	0.702	1
C	15	21	6	0.705	1
C	21	27	6	0.710	1
C	27	33	6	0.774	1
N	3.2	3.6	0.4	0.575	1
N	3.6	4	0.4	0.688	1
N	4	4.5	0.5	0.689	1
N	4.5	5	0.5	0.691	1
N	5	6	1	0.691	1
N	6	8	2	0.693	1
N	8	10	2	0.695	1
N	10	12	2	0.698	1
N	12	15	3	0.701	1
N	15	21	6	0.706	1
N	21	27	6	0.711	1
N	27	33	6	0.731	1
O	3.2	3.6	0.4	0.265	1
O	3.6	4	0.4	0.682	1

Draft

O	4	4.5	0.5	0.690	1
O	4.5	5	0.5	0.690	1
O	5	6	1	0.691	1
O	6	8	2	0.693	1
O	8	10	2	0.695	1
O	10	12	2	0.695	1
O	12	15	3	0.700	1
O	15	21	6	0.705	1
O	21	27	6	0.713	1
O	27	33	6	0.718	1
Ne	3.2	3.6	0.4	0.000	1
Ne	3.6	4	0.4	0.369	1
Ne	4	4.5	0.5	0.685	1
Ne	4.5	5	0.5	0.688	1
Ne	5	6	1	0.689	1
Ne	6	8	2	0.693	1
Ne	8	10	2	0.695	1
Ne	10	12	2	0.695	1
Ne	12	15	3	0.698	1
Ne	15	21	6	0.703	1
Ne	21	27	6	0.712	1
Ne	27	33	6	0.718	1
Ne	33	40	7	0.741	1
Na	6	8	2	0.692	1
Na	8	10	2	0.693	1
Na	10	12	2	0.695	1
Na	12	15	3	0.699	1

Draft

Na	15	21	6	0.703	1
Na	21	27	6	0.711	1
Na	27	33	6	0.719	1
Na	33	40	7	0.742	1
Mg	3.2	3.6	0.4	0.000	1
Mg	3.6	4	0.4	0.002	1
Mg	4	4.5	0.5	0.531	1
Mg	4.5	5	0.5	0.689	1
Mg	5	6	1	0.690	1
Mg	6	8	2	0.692	1
Mg	8	10	2	0.693	1
Mg	10	12	2	0.697	1
Mg	12	15	3	0.698	1
Mg	15	21	6	0.702	1
Mg	21	27	6	0.711	1
Mg	27	33	6	0.718	1
Mg	33	40	7	0.726	1
Mg	40	52	12	0.812	1
Al	6	8	2	0.691	1
Al	8	10	2	0.693	1
Al	10	12	2	0.694	1
Al	12	15	3	0.697	1
Al	15	21	6	0.702	1
Al	21	27	6	0.711	1
Al	27	33	6	0.718	1
Al	33	40	7	0.727	1
Al	40	52	12	0.811	1

Draft

Si	3.2	3.6	0.4	0.000	1
Si	3.6	4	0.4	0.000	1
Si	4	4.5	0.5	0.233	1
Si	4.5	5	0.5	0.678	1
Si	5	6	1	0.690	1
Si	6	8	2	0.690	1
Si	8	10	2	0.692	1
Si	10	12	2	0.693	1
Si	12	15	3	0.696	1
Si	15	21	6	0.702	1
Si	21	27	6	0.710	1
Si	27	33	6	0.719	1
Si	33	40	7	0.728	1
Si	40	52	12	0.786	1
S	3.6	4	0.4	0.000	1
S	4	4.5	0.5	0.027	1
S	4.5	5	0.5	0.606	1
S	5	6	1	0.689	1
S	6	8	2	0.691	1
S	8	10	2	0.693	1
S	10	12	2	0.696	1
S	12	15	3	0.697	1
S	15	21	6	0.701	1
S	21	27	6	0.709	1
S	27	33	6	0.718	1
S	33	40	7	0.726	1
S	40	52	12	0.757	1

Draft



Ar	3.6	4	0.4	0.000	1
Ar	4	4.5	0.5	0.206	1
Ar	4.5	5	0.5	0.670	1
Ar	5	6	1	0.690	1
Ar	6	8	2	0.692	1
Ar	8	10	2	0.694	1
Ar	10	12	2	0.696	1
Ar	12	15	3	0.697	1
Ar	15	21	6	0.702	1
Ar	21	27	6	0.710	1
Ar	27	33	6	0.718	1
Ar	33	40	7	0.726	1
Ar	40	52	12	0.757	1
Ca	3.6	4	0.4	0.000	1
Ca	4	4.5	0.5	0.000	1
Ca	4.5	5	0.5	0.192	1
Ca	5	6	1	0.672	1
Ca	6	8	2	0.690	1
Ca	8	10	2	0.692	1
Ca	10	12	2	0.694	1
Ca	12	15	3	0.696	1
Ca	15	21	6	0.701	1
Ca	21	27	6	0.708	1
Ca	27	33	6	0.717	1
Ca	33	40	7	0.725	1
Ca	40	52	12	0.736	1
Fe	2.7	3.2	0.5	0.000	1

Draft



Fe	3.2	3.6	0.4	0.000	1
Fe	3.6	4	0.4	0.000	1
Fe	4	4.5	0.5	0.000	1
Fe	4.5	5	0.5	0.078	1
Fe	5	6	1	0.653	1
Fe	6	8	2	0.691	1
Fe	8	10	2	0.691	1
Fe	10	12	2	0.694	1
Fe	12	15	3	0.695	1
Fe	15	21	6	0.699	1
Fe	21	27	6	0.706	1
Fe	27	33	6	0.711	1
Fe	33	40	7	0.720	1
Fe	40	52	12	0.729	1
Fe	52	70	18	0.793	1
Ni	8	10	2	0.692	1
Ni	10	12	2	0.694	1
Ni	12	15	3	0.696	1
Ni	15	21	6	0.700	1
Ni	21	27	6	0.706	1
Ni	27	33	6	0.712	1
Ni	33	40	7	0.720	1
Ni	40	52	12	0.729	1
Ni	52	70	18	0.776	1

Table 33: Geometry factors, energy bin widths, and efficiencies for Level 2 Standard Rates for dynamic threshold state 1.

Draft



Table 34 lists the energy bin width, geometry factor, and efficiency for each of the Level 2 Standard Rates listed in Table 31 for dynamic threshold state 2.

Species	**Lower En.** (MeV/n)	**Upper En.** (MeV/n)	**ΔE** (MeV/n)	**Geo. Fact.** (cm^2 sr)	**Eff.**
H	1.8	2.2	0.4	0.136584	1
H	2.2	2.7	0.5	0.1376568	1
H	2.7	3.2	0.5	0.1379136	1
H	3.2	3.6	0.4	0.1379864	1
H	3.6	4	0.4	0.138384	1
H	4	4.5	0.5	0.1382672	1
H	4.5	5	0.5	0.1386696	1
H	5	6	1	0.1388304	1
H	6	8	2	0.1387504	1
H	8	10	2	0.1127616	1
H	10	12	2	0.0440536	1
H	12	15	3	0.0080144	1
He3	2.2	2.7	0.5	0.1365328	1
He3	2.7	3.2	0.5	0.1380856	1
He3	3.2	3.6	0.4	0.1382648	1
He3	3.6	4	0.4	0.138412	1
He3	4	4.5	0.5	0.13828	1
He3	4.5	5	0.5	0.1384112	1
He3	5	6	1	0.1386416	1
He3	6	8	2	0.1392688	1
He3	8	10	2	0.1399864	1
He3	10	12	2	0.1408096	1
He3	12	15	3	0.1411328	1
He4	1.8	2.2	0.4	0.1378976	1

Draft



He4	2.2	2.7	0.5	0.1382288	1
He4	2.7	3.2	0.5	0.1384736	1
He4	3.2	3.6	0.4	0.1381376	1
He4	3.6	4	0.4	0.1384728	1
He4	4	4.5	0.5	0.1388864	1
He4	4.5	5	0.5	0.1387632	1
He4	5	6	1	0.1390288	1
He4	6	8	2	0.1395312	1
He4	8	10	2	0.1403072	1
He4	10	12	2	0.1410032	1
He4	12	15	3	0.1414104	1
He	2.2	2.7	0.5	0.1382112	1
He	2.7	3.2	0.5	0.1384688	1
He	3.2	3.6	0.4	0.13814	1
He	3.6	4	0.4	0.138472	1
He	4	4.5	0.5	0.13888	1
He	4.5	5	0.5	0.1387592	1
He	5	6	1	0.1390264	1
He	6	8	2	0.1395296	1
He	8	10	2	0.1403032	1
He	10	12	2	0.141	1
He	12	15	3	0.1414072	1
C	3.2	3.6	0.4	3.41806	1
C	3.6	4	0.4	3.43468	1
C	4	4.5	0.5	3.4472	1
C	4.5	5	0.5	3.4677	1
C	5	6	1	3.46138	1

Draft

C	6	8	2	3.46458	1
C	8	10	2	3.47978	1
C	10	12	2	3.474	1
C	12	15	3	3.50882	1
C	15	21	6	3.52714	1
C	21	27	6	3.55204	1
C	27	33	6	3.87152	1
N	3.2	3.6	0.4	2.8743	1
N	3.6	4	0.4	3.4377	1
N	4	4.5	0.5	3.44746	1
N	4.5	5	0.5	3.45346	1
N	5	6	1	3.45678	1
N	6	8	2	3.46598	1
N	8	10	2	3.47534	1
N	10	12	2	3.48836	1
N	12	15	3	3.50548	1
N	15	21	6	3.53182	1
N	21	27	6	3.55572	1
N	27	33	6	3.65516	1
O	3.2	3.6	0.4	1.32412	1
O	3.6	4	0.4	3.40832	1
O	4	4.5	0.5	3.44954	1
O	4.5	5	0.5	3.45086	1
O	5	6	1	3.45518	1
O	6	8	2	3.46514	1
O	8	10	2	3.47316	1
O	10	12	2	3.47588	1

Draft

O	12	15	3	3.49978	1
O	15	21	6	3.52392	1
O	21	27	6	3.56288	1
O	27	33	6	3.59158	1
Ne	3.2	3.6	0.4	0.00184	1
Ne	3.6	4	0.4	1.8455	1
Ne	4	4.5	0.5	3.425	1
Ne	4.5	5	0.5	3.43902	1
Ne	5	6	1	3.44606	1
Ne	6	8	2	3.4629	1
Ne	8	10	2	3.47594	1
Ne	10	12	2	3.47526	1
Ne	12	15	3	3.49242	1
Ne	15	21	6	3.51476	1
Ne	21	27	6	3.55948	1
Ne	27	33	6	3.59022	1
Ne	33	40	7	3.70364	1
Na	6	8	2	3.45928	1
Na	8	10	2	3.46536	1
Na	10	12	2	3.47552	1
Na	12	15	3	3.4934	1
Na	15	21	6	3.51534	1
Na	21	27	6	3.55662	1
Na	27	33	6	3.59688	1
Na	33	40	7	3.71056	1
Mg	3.2	3.6	0.4	0.00056	1
Mg	3.6	4	0.4	0.01146	1

Draft

Mg	4	4.5	0.5	2.6573	1
Mg	4.5	5	0.5	3.44594	1
Mg	5	6	1	3.44902	1
Mg	6	8	2	3.45872	1
Mg	8	10	2	3.46468	1
Mg	10	12	2	3.48568	1
Mg	12	15	3	3.49012	1
Mg	15	21	6	3.51206	1
Mg	21	27	6	3.55654	1
Mg	27	33	6	3.5903	1
Mg	33	40	7	3.6286	1
Mg	40	52	12	4.05832	1
Al	6	8	2	3.45308	1
Al	8	10	2	3.46306	1
Al	10	12	2	3.47248	1
Al	12	15	3	3.486	1
Al	15	21	6	3.51144	1
Al	21	27	6	3.55256	1
Al	27	33	6	3.58784	1
Al	33	40	7	3.63428	1
Al	40	52	12	4.05398	1
Si	3.2	3.6	0.4	0.00058	1
Si	3.6	4	0.4	0.00166	1
Si	4	4.5	0.5	1.16254	1
Si	4.5	5	0.5	3.38976	1
Si	5	6	1	3.44992	1
Si	6	8	2	3.45184	1

Draft



Si	8	10	2	3.46212	1
Si	10	12	2	3.4661	1
Si	12	15	3	3.48014	1
Si	15	21	6	3.51188	1
Si	21	27	6	3.54904	1
Si	27	33	6	3.59342	1
Si	33	40	7	3.64074	1
Si	40	52	12	3.92812	1
S	3.6	4	0.4	0.00148	1
S	4	4.5	0.5	0.13366	1
S	4.5	5	0.5	3.03138	1
S	5	6	1	3.44574	1
S	6	8	2	3.4527	1
S	8	10	2	3.46542	1
S	10	12	2	3.47918	1
S	12	15	3	3.48282	1
S	15	21	6	3.50736	1
S	21	27	6	3.54404	1
S	27	33	6	3.58826	1
S	33	40	7	3.63246	1
S	40	52	12	3.78708	1
Ar	3.6	4	0.4	0.0024	1
Ar	4	4.5	0.5	1.03066	1
Ar	4.5	5	0.5	3.34924	1
Ar	5	6	1	3.44938	1
Ar	6	8	2	3.46096	1
Ar	8	10	2	3.46986	1

Draft



Ar	10	12	2	3.4794	1
Ar	12	15	3	3.48722	1
Ar	15	21	6	3.50784	1
Ar	21	27	6	3.54998	1
Ar	27	33	6	3.59038	1
Ar	33	40	7	3.63132	1
Ar	40	52	12	3.78276	1
Ca	3.6	4	0.4	0.00084	1
Ca	4	4.5	0.5	0.00246	1
Ca	4.5	5	0.5	0.96168	1
Ca	5	6	1	3.3616	1
Ca	6	8	2	3.45146	1
Ca	8	10	2	3.46034	1
Ca	10	12	2	3.47002	1
Ca	12	15	3	3.47898	1
Ca	15	21	6	3.5036	1
Ca	21	27	6	3.53976	1
Ca	27	33	6	3.58474	1
Ca	33	40	7	3.62258	1
Ca	40	52	12	3.67846	1
Fe	2.7	3.2	0.5	0.00018	1
Fe	3.2	3.6	0.4	0.00024	1
Fe	3.6	4	0.4	0.00096	1
Fe	4	4.5	0.5	0.00246	1
Fe	4.5	5	0.5	0.3899	1
Fe	5	6	1	3.26502	1
Fe	6	8	2	3.45292	1

Draft



Fe	8	10	2	3.45522	1
Fe	10	12	2	3.47062	1
Fe	12	15	3	3.47424	1
Fe	15	21	6	3.4955	1
Fe	21	27	6	3.52856	1
Fe	27	33	6	3.5562	1
Fe	33	40	7	3.5978	1
Fe	40	52	12	3.64532	1
Fe	52	70	18	3.96388	1
Ni	8	10	2	3.45838	1
Ni	10	12	2	3.47046	1
Ni	12	15	3	3.47826	1
Ni	15	21	6	3.49778	1
Ni	21	27	6	3.52796	1
Ni	27	33	6	3.56026	1
Ni	33	40	7	3.59852	1
Ni	40	52	12	3.64296	1
Ni	52	70	18	3.87798	1

Table 34: Geometry factors, energy bin widths, and efficiencies for Level 2 Standard Rates for dynamic threshold state 2.

Draft

Table 35 lists the energy bin width, geometry factor, and efficiency for each of the Level 2 Standard Rates listed in Table 31 for dynamic threshold state 2.

Species	**Lower En. (MeV/n)**	**Upper En. (MeV/n)**	**ΔE (MeV/n)**	**Geo. Fact. (cm^2 sr)**	**Eff.**
H	1.8	2.2	0.4	0.0273168	1
H	2.2	2.7	0.5	0.02753136	1



H	2.7	3.2	0.5	0.02758272	1
H	3.2	3.6	0.4	0.02759728	1
H	3.6	4	0.4	0.0276768	1
H	4	4.5	0.5	0.02765344	1
H	4.5	5	0.5	0.02773392	1
H	5	6	1	0.02776608	1
H	6	8	2	0.02775008	1
H	8	10	2	0.02255232	1
H	10	12	2	0.00881072	1
H	12	15	3	0.00160288	1
He3	2.2	2.7	0.5	0.02730656	1
He3	2.7	3.2	0.5	0.02761712	1
He3	3.2	3.6	0.4	0.02765296	1
He3	3.6	4	0.4	0.0276824	1
He3	4	4.5	0.5	0.027656	1
He3	4.5	5	0.5	0.02768224	1
He3	5	6	1	0.02772832	1
He3	6	8	2	0.02785376	1
He3	8	10	2	0.02799728	1
He3	10	12	2	0.02816192	1
He3	12	15	3	0.02822656	1
He4	1.8	2.2	0.4	0.02757952	1
He4	2.2	2.7	0.5	0.02764576	1
He4	2.7	3.2	0.5	0.02769472	1
He4	3.2	3.6	0.4	0.02762752	1
He4	3.6	4	0.4	0.02769456	1
He4	4	4.5	0.5	0.02777728	1

Draft

He4	4.5	5	0.5	0.02775264	1
He4	5	6	1	0.02780576	1
He4	6	8	2	0.02790624	1
He4	8	10	2	0.02806144	1
He4	10	12	2	0.02820064	1
He4	12	15	3	0.02828208	1
He	2.2	2.7	0.5	0.02764224	1
He	2.7	3.2	0.5	0.02769376	1
He	3.2	3.6	0.4	0.027628	1
He	3.6	4	0.4	0.0276944	1
He	4	4.5	0.5	0.027776	1
He	4.5	5	0.5	0.02775184	1
He	5	6	1	0.02780528	1
He	6	8	2	0.02790592	1
He	8	10	2	0.02806064	1
He	10	12	2	0.0282	1
He	12	15	3	0.02828144	1
C	3.2	3.6	0.4	3.41806	1
C	3.6	4	0.4	3.43468	1
C	4	4.5	0.5	3.4472	1
C	4.5	5	0.5	3.4677	1
C	5	6	1	3.46138	1
C	6	8	2	3.46458	1
C	8	10	2	3.47978	1
C	10	12	2	3.474	1
C	12	15	3	3.50882	1
C	15	21	6	3.52714	1

Draft

C	21	27	6	3.55204	1
C	27	33	6	3.87152	1
N	3.2	3.6	0.4	2.8743	1
N	3.6	4	0.4	3.4377	1
N	4	4.5	0.5	3.44746	1
N	4.5	5	0.5	3.45346	1
N	5	6	1	3.45678	1
N	6	8	2	3.46598	1
N	8	10	2	3.47534	1
N	10	12	2	3.48836	1
N	12	15	3	3.50548	1
N	15	21	6	3.53182	1
N	21	27	6	3.55572	1
N	27	33	6	3.65516	1
O	3.2	3.6	0.4	1.32412	1
O	3.6	4	0.4	3.40832	1
O	4	4.5	0.5	3.44954	1
O	4.5	5	0.5	3.45086	1
O	5	6	1	3.45518	1
O	6	8	2	3.46514	1
O	8	10	2	3.47316	1
O	10	12	2	3.47588	1
O	12	15	3	3.49978	1
O	15	21	6	3.52392	1
O	21	27	6	3.56288	1
O	27	33	6	3.59158	1
Ne	3.2	3.6	0.4	0.00184	1

Draft



Ne	3.6	4	0.4	1.8455	1
Ne	4	4.5	0.5	3.425	1
Ne	4.5	5	0.5	3.43902	1
Ne	5	6	1	3.44606	1
Ne	6	8	2	3.4629	1
Ne	8	10	2	3.47594	1
Ne	10	12	2	3.47526	1
Ne	12	15	3	3.49242	1
Ne	15	21	6	3.51476	1
Ne	21	27	6	3.55948	1
Ne	27	33	6	3.59022	1
Ne	33	40	7	3.70364	1
Na	6	8	2	3.45928	1
Na	8	10	2	3.46536	1
Na	10	12	2	3.47552	1
Na	12	15	3	3.4934	1
Na	15	21	6	3.51534	1
Na	21	27	6	3.55662	1
Na	27	33	6	3.59688	1
Na	33	40	7	3.71056	1
Mg	3.2	3.6	0.4	0.00056	1
Mg	3.6	4	0.4	0.01146	1
Mg	4	4.5	0.5	2.6573	1
Mg	4.5	5	0.5	3.44594	1
Mg	5	6	1	3.44902	1
Mg	6	8	2	3.45872	1
Mg	8	10	2	3.46468	1

Draft



Mg	10	12	2	3.48568	1
Mg	12	15	3	3.49012	1
Mg	15	21	6	3.51206	1
Mg	21	27	6	3.55654	1
Mg	27	33	6	3.5903	1
Mg	33	40	7	3.6286	1
Mg	40	52	12	4.05832	1
Al	6	8	2	3.45308	1
Al	8	10	2	3.46306	1
Al	10	12	2	3.47248	1
Al	12	15	3	3.486	1
Al	15	21	6	3.51144	1
Al	21	27	6	3.55256	1
Al	27	33	6	3.58784	1
Al	33	40	7	3.63428	1
Al	40	52	12	4.05398	1
Si	3.2	3.6	0.4	0.00058	1
Si	3.6	4	0.4	0.00166	1
Si	4	4.5	0.5	1.16254	1
Si	4.5	5	0.5	3.38976	1
Si	5	6	1	3.44992	1
Si	6	8	2	3.45184	1
Si	8	10	2	3.46212	1
Si	10	12	2	3.4661	1
Si	12	15	3	3.48014	1
Si	15	21	6	3.51188	1
Si	21	27	6	3.54904	1

Draft

Si	27	33	6	3.59342	1
Si	33	40	7	3.64074	1
Si	40	52	12	3.92812	1
S	3.6	4	0.4	0.00148	1
S	4	4.5	0.5	0.13366	1
S	4.5	5	0.5	3.03138	1
S	5	6	1	3.44574	1
S	6	8	2	3.4527	1
S	8	10	2	3.46542	1
S	10	12	2	3.47918	1
S	12	15	3	3.48282	1
S	15	21	6	3.50736	1
S	21	27	6	3.54404	1
S	27	33	6	3.58826	1
S	33	40	7	3.63246	1
S	40	52	12	3.78708	1
Ar	3.6	4	0.4	0.0024	1
Ar	4	4.5	0.5	1.03066	1
Ar	4.5	5	0.5	3.34924	1
Ar	5	6	1	3.44938	1
Ar	6	8	2	3.46096	1
Ar	8	10	2	3.46986	1
Ar	10	12	2	3.4794	1
Ar	12	15	3	3.48722	1
Ar	15	21	6	3.50784	1
Ar	21	27	6	3.54998	1
Ar	27	33	6	3.59038	1

Draft

Ar	33	40	7	3.63132	1
Ar	40	52	12	3.78276	1
Ca	3.6	4	0.4	0.00084	1
Ca	4	4.5	0.5	0.00246	1
Ca	4.5	5	0.5	0.96168	1
Ca	5	6	1	3.3616	1
Ca	6	8	2	3.45146	1
Ca	8	10	2	3.46034	1
Ca	10	12	2	3.47002	1
Ca	12	15	3	3.47898	1
Ca	15	21	6	3.5036	1
Ca	21	27	6	3.53976	1
Ca	27	33	6	3.58474	1
Ca	33	40	7	3.62258	1
Ca	40	52	12	3.67846	1
Fe	2.7	3.2	0.5	0.00018	1
Fe	3.2	3.6	0.4	0.00024	1
Fe	3.6	4	0.4	0.00096	1
Fe	4	4.5	0.5	0.00246	1
Fe	4.5	5	0.5	0.3899	1
Fe	5	6	1	3.26502	1
Fe	6	8	2	3.45292	1
Fe	8	10	2	3.45522	1
Fe	10	12	2	3.47062	1
Fe	12	15	3	3.47424	1
Fe	15	21	6	3.4955	1
Fe	21	27	6	3.52856	1

Draft

Fe	27	33	6	3.5562	1
Fe	33	40	7	3.5978	1
Fe	40	52	12	3.64532	1
Fe	52	70	18	3.96388	1
Ni	8	10	2	3.45838	1
Ni	10	12	2	3.47046	1
Ni	12	15	3	3.47826	1
Ni	15	21	6	3.49778	1
Ni	21	27	6	3.52796	1
Ni	27	33	6	3.56026	1
Ni	33	40	7	3.59852	1
Ni	40	52	12	3.64296	1
Ni	52	70	18	3.87798	1

Table 35: Geometry factors, energy bin widths, and efficiencies for Level 2 Standard Rates for dynamic threshold state 3.

7.2 Sectored Rates

The conversion from count rates to intensities for the sectored rates uses the same algorithm as the standard rates (i.e., Eq 12) apart from requiring a factor of 10 in the denominator as the integration time for the sectored rates is 10 minutes. Thus the equation is:

$$j_i(N,X) = \frac{1}{600\Delta t \Delta E_i} \frac{\sum_{j=2}^{4} q_{ij}(N,X) - b_{ij}(N,X)}{\sum_{j=2}^{4} \sigma_{ij}(N,X)\lambda_{ij}(N,X)} \tag{14}$$

The table of geometry factors, efficiencies, and energy bin widths is shown in Table 36 below.

The Lev2 uncertainty is calculated by Eq. 14 replacing q_{ij} with $\delta_{u/l,ij}$ Lev1b uncertainties. Any fill values should have uncertainties that are also fill values. The Lev2 systematic uncertainty will be 0 at launch and updated if/when systematic uncertainties in the data are identified. The full uncertainty should

Draft



be calculated as the combination of the statistical and systematic uncertainties by adding both quantities in quadrature, i.e.,:

$$\delta_{full} = \sqrt{\delta_{stat}^2 + \delta_{sys}^2} \tag{15}$$

Species	**Sector**	**Lower En. (MeV/n)**	**Upper En. (MeV/n)**	**ΔE (MeV/n)**	**Geo. Fact. (cm^2 sr)**	**Eff.**
H	0	1.8	4	2.2	0.41686	1
H	1	1.8	4	2.2	0.49253	1
H	2	1.8	4	2.2	0.45156	1
H	3	1.8	4	2.2	0.35599	1
H	4	1.8	4	2.2	0.33312	1
H	5	1.8	4	2.2	0.47444	1
H	6	1.8	4	2.2	0.49253	1
H	7	1.8	4	2.2	0.41686	1
H	0	4	6	2	0.42008	1
H	1	4	6	2	0.49746	1
H	2	4	6	2	0.45515	1
H	3	4	6	2	0.35921	1
H	4	4	6	2	0.33619	1
H	5	4	6	2	0.47817	1
H	6	4	6	2	0.49746	1
H	7	4	6	2	0.42008	1
H	0	6	10	4	0.39177	1
H	1	6	10	4	0.47095	1
H	2	6	10	4	0.42764	1
H	3	6	10	4	0.33171	1
H	4	6	10	4	0.31091	1
H	5	6	10	4	0.44844	1

Draft



H	6	6	10	4	0.47095	1
H	7	6	10	4	0.39177	1
4He	0	4	6	2	0.41995	1
4He	1	4	6	2	0.49964	1
4He	2	4	6	2	0.45649	1
4He	3	4	6	2	0.3584	1
4He	4	4	6	2	0.33563	1
4He	5	4	6	2	0.47925	1
4He	6	4	6	2	0.49964	1
4He	7	4	6	2	0.41995	1
4He	0	6	12	6	0.42404	1
4He	1	6	12	6	0.5045	1
4He	2	6	12	6	0.45897	1
4He	3	6	12	6	0.36098	1
4He	4	6	12	6	0.33793	1
4He	5	6	12	6	0.48202	1
4He	6	6	12	6	0.5045	1
4He	7	6	12	6	0.42404	1
CNO	0	4	6	2	0.41976	1
CNO	1	4	6	2	0.49594	1
CNO	2	4	6	2	0.45356	1
CNO	3	4	6	2	0.35698	1
CNO	4	4	6	2	0.33409	1
CNO	5	4	6	2	0.47645	1
CNO	6	4	6	2	0.49594	1
CNO	7	4	6	2	0.41976	1
CNO	0	6	12	6	0.42026	1

Draft



CNO	1	6	12	6	0.49871	1
CNO	2	6	12	6	0.45567	1
CNO	3	6	12	6	0.35809	1
CNO	4	6	12	6	0.3351	1
CNO	5	6	12	6	0.47866	1
CNO	6	6	12	6	0.49871	1
CNO	7	6	12	6	0.42026	1
NeMgSi	0	4	6	2	0.37544	1
NeMgSi	1	4	6	2	0.43535	1
NeMgSi	2	4	6	2	0.40251	1
NeMgSi	3	4	6	2	0.32308	1
NeMgSi	4	4	6	2	0.30221	1
NeMgSi	5	4	6	2	0.42339	1
NeMgSi	6	4	6	2	0.43535	1
NeMgSi	7	4	6	2	0.37544	1
NeMgSi	0	6	12	6	0.42046	1
NeMgSi	1	6	12	6	0.49714	1
NeMgSi	2	6	12	6	0.45432	1
NeMgSi	3	6	12	6	0.35764	1
NeMgSi	4	6	12	6	0.33475	1
NeMgSi	5	6	12	6	0.47721	1
NeMgSi	6	6	12	6	0.49714	1
NeMgSi	7	6	12	6	0.42046	1
Fe	0	4	12	8	0.2752	1
Fe	1	4	12	8	0.31996	1
Fe	2	4	12	8	0.29577	1
Fe	3	4	12	8	0.23669	1

Draft

Fe	4	4	12	8	0.2213	1
Fe	5	4	12	8	0.31118	1
Fe	6	4	12	8	0.31996	1
Fe	7	4	12	8	0.2752	1

Table 36: Geometry factors, energy bin widths, and efficiencies for Level 2 Sectored Rates for the 8 sectors.

7.3 Summed Rates

The geometry factors, energy bin widths and efficiencies to convert the summed count rates into intensityes with physical units are shown in Table 37. Similar to Eq. 12, the ion intensity of the kth summed energy bin can be calculated as:

$$j_i(N,X) = \frac{1}{60\Delta t \Delta E_i} \frac{\sum_{i\to k}\sum_{j=2}^{4} q_{ij}(N,X) - b_{ij}(N,X)}{\sum_{j=2}^{4}\sigma_{ij}(N,X)\lambda_{ij}(N,X)} \tag{16}$$

The Lev2 statistical uncertainty is calculated by Eq. 16 replacing q_{ij} with $\delta_{u/l,ij}$ Lev1b uncertainties. The Lev2 systematic uncertainty will be 0 at launch and then be updated if/when systematic uncertainties are identified in the data. The full uncertainty should be calculated as the combination of the statistical and systematic uncertainties by adding both quantities in quadrature, i.e.,:

$$\delta_{full} = \sqrt{\delta_{stat}^2 + \delta_{sys}^2} \tag{17}$$

Species	**Lower En. (MeV/n)**	**Upper En. (MeV/n)**	**ΔE (MeV/n)**	**Geo. Fact. (cm^2 sr)**	**Eff.**
H	1.8	4	2.2	3.435	1
H	4	6	2	3.465	1
H	6	10	4	3.244	1
H	10	15	5	0.673	1
He3	4	6	2	3.461	1
He3	6	10	4	3.488	1
He3	10	15	5	3.524	1

Draft



He4	1.8	4	2.2	3.454	1
He4	4	6	2	3.473	1
He4	6	10	4	3.495	1
He4	10	15	5	3.530	1
He	4	6	2	3.473	1
He	6	10	4	3.495	1
He	10	15	5	3.530	1
C	4	6	2	3.458	1
C	6	10	4	3.470	1
C	10	15	5	3.491	1
C	15	27	12	3.535	1
N	4	6	2	3.453	1
N	6	10	4	3.469	1
N	10	15	5	3.497	1
N	15	27	12	3.540	1
O	4	6	2	3.452	1
O	6	10	4	3.468	1
O	10	15	5	3.487	1
O	15	27	12	3.537	1
Ne	4	6	2	3.437	1
Ne	6	10	4	3.467	1
Ne	10	15	5	3.483	1
Ne	15	27	12	3.529	1
Na	10	15	5	3.484	1
Na	15	27	12	3.529	1
Mg	4	6	2	3.167	1
Mg	6	10	4	3.461	1

Draft



Mg	10	15	5	3.488	1
Mg	15	27	12	3.526	1
Al	6	10	4	3.457	1
Al	10	15	5	3.479	1
Al	15	27	12	3.525	1
Si	4	6	2	2.621	1
Si	6	10	4	3.455	1
Si	10	15	5	3.473	1
Si	15	27	12	3.524	1
Si	27	40	13	3.613	1
S	4	6	2	2.157	1
S	6	10	4	3.457	1
S	10	15	5	3.481	1
S	15	27	12	3.519	1
S	27	40	13	3.607	1
Ar	4	6	2	2.563	1
Ar	6	10	4	3.464	1
Ar	10	15	5	3.483	1
Ar	15	27	12	3.521	1
Ar	27	40	13	3.607	1
Ca	4	6	2	1.522	1
Ca	6	10	4	3.455	1
Ca	10	15	5	3.474	1
Ca	15	27	12	3.515	1
Ca	27	40	13	3.601	1
Fe	4	6	2	1.333	1
Fe	6	10	4	3.454	1

Draft

Fe	10	15	5	3.472	1
Fe	15	27	12	3.506	1
Fe	27	40	13	3.574	1
Ni	10	15	5	3.474	1
Ni	15	27	12	3.508	1
Ni	27	40	13	3.576	1

Table 37: Geometry factors, energy bin widths, and efficiencies for Level 2 Summed Rates

8 I-ALiRT Algorithms

All I-ALiRT data is derived directly from the I-ALiRT packets.

8.1 Level 0 Processing

Each second, 6 I-ALiRT bytes are sent down of which 2 bytes include rates from *Fast Rate 1*, 2 bytes include rates from *Fast Rate 2*, and 2 bytes include rates from *Slow Rate*. The bytes sent down each second are shown in Table 38.

Subcom Counter	**Fast Rate 1**	**Fast Rate 2**	**Slow Rate**
0	L1A Trigger	L1B Trigger	L1A
1	IAevent Trigger	IBevent Trigger	L2A
2	NFORMAT	Aevent Trigger	L3A
3	L3A Trigger	L3B Trigger	L1a0AHG
4	L1A Trigger	L1B Trigger	L1b0AHG
5	IAevent Trigger	Ibevent Trigger	L1c0AHG
6	NFORMAT	Aevent Trigger	L4iAHG
7	L3A Trigger	L3B Trigger	L4oAHG
8	L1A Trigger	L1B Trigger	L1B

Draft

9	IAevent Trigger	Ibevent Trigger	L2B
10	NFORMAT	Aevent Trigger	L3B
11	L3A Trigger	L3B Trigger	L1a0BHG
12	L1A Trigger	L1B Trigger	L1b0BHG
13	IAevent Trigger	Ibevent Trigger	L1c0BHG
14	NFORMAT	Aevent Trigger	L4iBHG
15	L3A Trigger	L3B Trigger	L4oBHG
16	L1A Trigger	L1B Trigger	I-ALiRT Rate 1
17	IAevent Trigger	Ibevent Trigger	I-ALiRT Rate 2
18	NFORMAT	Aevent Trigger	I-ALiRT Rate 3
19	L3A Trigger	L3B Trigger	I-ALiRT Rate 4
20	L1A Trigger	L1B Trigger	I-ALiRT Rate 5
21	IAevent Trigger	Ibevent Trigger	I-ALiRT Rate 6
22	NFORMAT	Aevent Trigger	I-ALiRT Rate 7
23	L3A Trigger	L3B Trigger	I-ALiRT Rate 8
24	L1A Trigger	L1B Trigger	I-ALiRT Rate 9
25	IAevent Trigger	Ibevent Trigger	I-ALiRT Rate 10
26	NFORMAT	Aevent Trigger	I-ALiRT Rate 11
27	L3A Trigger	L3B Trigger	I-ALiRT Rate 12
28	L1A Trigger	L1B Trigger	I-ALiRT Rate 13
29	IAevent Trigger	Ibevent Trigger	I-ALiRT Rate 14
30	NFORMAT	Aevent Trigger	I-ALiRT Rate 15
31	L3A Trigger	L3B Trigger	I-ALiRT Rate 16
32	L1A Trigger	L1B Trigger	I-ALiRT Rate 17
33	IAevent Trigger	Ibevent Trigger	I-ALiRT Rate 18
34	NFORMAT	Aevent Trigger	I-ALiRT Rate 19
35	L3A Trigger	L3B Trigger	I-ALiRT Rate 20

Draft



36	L1A Trigger	L1B Trigger	IAevent Trigger
37	IAevent Trigger	Ibevent Trigger	IBevent Trigger
38	NFORMAT	Aevent Trigger	NFORMAT
39	L3A Trigger	L3B Trigger	NASIDE
40	L1A Trigger	L1B Trigger	Erate 1 (Livetime)
41	IAevent Trigger	Ibevent Trigger	Erate 2 (NUMTRIG)
42	NFORMAT	Aevent Trigger	Erate 3 (NUMREJECT)
43	L3A Trigger	L3B Trigger	Erate 4 (NUMACCPHA)
44	L1A Trigger	L1B Trigger	Erate 5 (NUMACCNPHA)
45	IAevent Trigger	Ibevent Trigger	L12A
46	NFORMAT	Aevent Trigger	L123A
47	L3A Trigger	L3B Trigger	L12B
48	L1A Trigger	L1B Trigger	2TEL
49	IAevent Trigger	Ibevent Trigger	PENA
50	NFORMAT	Aevent Trigger	PENA?
51	L3A Trigger	L3B Trigger	L12B
52	L1A Trigger	L1B Trigger	2TEL
53	IAevent Trigger	Ibevent Trigger	PENA
54	NFORMAT	Aevent Trigger	PENA?
55	L3A Trigger	L3B Trigger	H (6.0-8.0 MeV/nuc) L23FG
56	L1A Trigger	L1B Trigger	H (12.0-15.0 MeV/nuc) L23FG
57	IAevent Trigger	Ibevent Trigger	H (15.0-70.0 MeV/nuc) L23FG
58	NFORMAT	Aevent Trigger	He-4 (6.0-8.0 MeV/nuc) L23FG
59	L3A Trigger	L3B Trigger	He-4 (15.0-70.0 MeV/nuc) L23FG

Table 38: Description of I-ALiRT rates each second.

Each of the 60 sets of rates should be decommutated and made into a major frame. A set of the 60 groups of 3 rates consistutes a full I-ALiRT set.

Draft



8.2 Level 1 I-ALiRT Data

The public I-ALiRT data are derived from the 20 I-ALiRT rates sent down as "Slow Rates" and the 5 rates corresponding to H and He L23FG data (duplicate from those rates in the science data). Descriptions of the 20 I-ALiRT rates listed in Table 38 are shown in Table 39.

Slow Rate	**Description**
I-ALiRT Rate 1	L4Ai ΔE bin
I-ALiRT Rate 2	L4Ai ΔE bin
I-ALiRT Rate 3	L4Ai ΔE bin
I-ALiRT Rate 4	L4Ai ΔE bin
I-ALiRT Rate 5	L4Ai ΔE bin
I-ALiRT Rate 6	L4Ai ΔE bin
I-ALiRT Rate 7	L4Ai vs L3A bin
I-ALiRT Rate 8	L4Ai vs L3A bin
I-ALiRT Rate 9	L4Ai vs L3A bin
I-ALiRT Rate 10	L4Ai vs L3A bin
I-ALiRT Rate 11	L4Bi ΔE bin
I-ALiRT Rate 12	L4BiΔE bin
I-ALiRT Rate 13	L4Bi ΔE bin
I-ALiRT Rate 14	L4Bi ΔE bin
I-ALiRT Rate 15	L4Bi ΔE bin
I-ALiRT Rate 16	L4Bi ΔE bin
I-ALiRT Rate 17	L4Bi vs L3B bin
I-ALiRT Rate 18	L4Bi vs L3B bin
I-ALiRT Rate 19	L4Bi vs L3B bin
I-ALiRT Rate 20	L4Bi vs L3B bin

Table 39: Description of I-ALiRT rates utilized for higher level data products.

Draft

The six rates labeled "L4Ai ΔE bin" in Table 39 correspond to horizontal slices of mean measured energy in the L4 detectors as shown in Fig. 15. The first two rates (I-ALiRT Rate 1 and I-ALiRT Rate 2 as labeled in the above tables) correspond to two low energy measurements below the minimum ionizing particle peak (i.e., less than ∼270 keV). The next two correspond to bands within the minimum ionizing particle peak (i.e., ∼270 keV - 1 MeV). The final two correspond to high energies above the minimum ionizing particle peak (i.e., greater than ∼1 MeV)

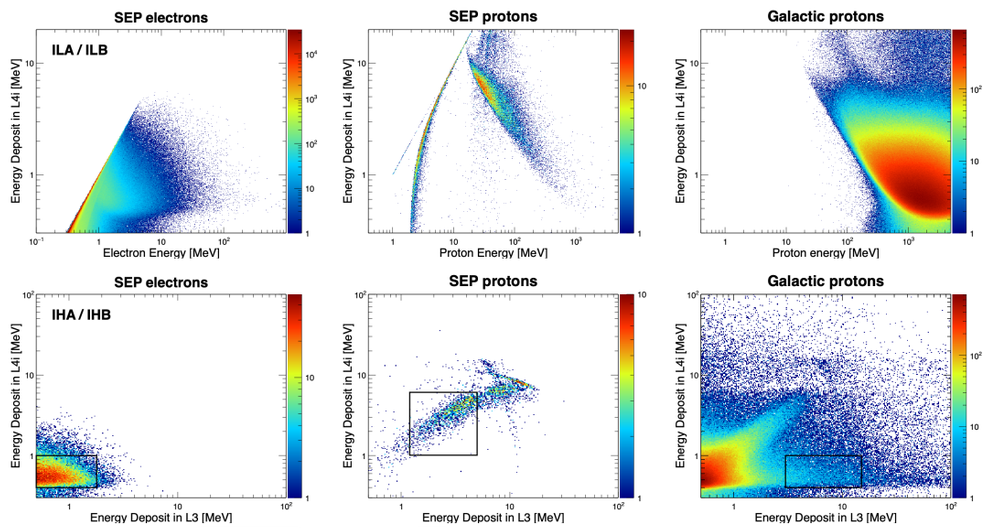


Figure 15: Top panels: simulated energy loss in an L4 detector as a function of incident energy (acquired by the low-energy trigger), for SEP electrons (left) and protons (middle), and galactic protons (right). Bottom: corresponding L4 vs. L3 energy loss distributions (high-energy trigger). The three boxes indicate the ranges used for the the I-ALiRT Rates.

The I-ALiRT rates labeled "L4Ai vs L3A bin" correspond to the three boxes shown in the bottom panels of Fig. 15 and a fourth box capturing any particles that did not fall into the other boxes. In order of increasing energy deposit in L3, the boxes correspond to 1) ∼1-10 MeV solar electrons, 2) ∼30-200 solar protons, 3) ≳500 MeV galactic protons. These 3 boxes and the background box correspond to the order of the I-ALiRT Rates shown in Table 39.

After launch, the algorithms will be updated to use the high energy SEP proton box as a background subtraction for the high energy electrons. There will be 6 HIT I-ALiRT electron products with the following algorithms

- HIT low energy e- A side = I-ALiRT Rate 1 + I-ALiRT Rate 2
- HIT medium energy e- A side = I-ALiRT Rate 5 + I-ALiRT Rate 6



- HIT high energy e- A side = I-ALiRT Rate 7
- HIT low energy e- B side = I-ALiRT Rate 11 + I-ALiRT Rate 12
- HIT medium energy e- B side = I-ALiRT Rate 15 + I-ALiRT Rate 16
- HIT high energy e- B side = I-ALiRT Rate 17

There will be 4 HIT I-ALiRT proton products with the below algorithms.

- HIT low energy H omni = H (6.0 - 8.0 MeV/nuc) L23FG
- HIT medium energy H omni = H (12.0-15.0 MeV/nuc) L23FG
- HIT high energy H A side = I-ALiRT Rate 8
- HIT high energy H B side = I-ALiRT Rate 18

There will be 2 HIT I-ALiRT Helium-4 products with the below algorithms

- HIT low energy He omni = He-4 (6.0-8.0 MeV/nuc) L23FG
- HIT high energy He omni = He-4 (15.0-70.0 MeV/nuc) L23FG

9 Lev3 Algorithms

HIT L3 data include pitch angle distributions derived from the L2 Sector data and IMAP/MAG data, science quality electron data derived from data produced by the I-ALiRT apertures, and calculations of ion charge using the raw Pulse Height Analysis event data from Lev1A. Below are descriptions of the products, the required inputs, the ancillary files required, and the algorithms required to produce these products.

9.1 PHA Products

HIT telemeters a portion of the raw PHA "event" data which will be unaltered from Lev1A data. The event data are raw PHA values in engineering units corresponding to the energy deposited in a given detector. These data provide more detailed information than the "rates" data. For each detected particle, Lev3 data should include:

- time of detection
- calculated ion energy (MeV/nuc)
- calculated charge (Z)

Draft



The inputs required for these data include:

- HIT Lev1A raw event data

The ancillary files required for these calculations include:

- Conversion factors provided by the HIT team to calculate deposited energy in a given detector from ADC units. These conversion relations will be provided based on detector "type" (i.e., L1, L2, etc.) so there will be 4 in total.
- Lookup tables provided by the HIT team to find Z for a given combination of ΔE and E'. These will be provided on a Range-by-Range basis, thus there will be 3 in total.

The class of event and range of a given event is determined according to Table 40. In Table 40, the first twelve columns correspond to the largest signal on each "layer". This is determined by comparing all high gain values across a single layer as well as any non-zero low gain values multiplied by 20. L1A14 means any of the 3 signals (abc) on any of L1A1, L1A2, L1A3, L1A4. L1A0 is any of the 3 signals on L1A0. L2A is any of the 10 signals on L2A, etc. The L4 columns are just single signals. 0 requires a signal to not be present in that particle detector and 1 requires a signal to be present in that detector. A "*" means the signal could either be there or not.

L1A14	L1A0	L2A	L3A	L3B	L2B	L1B0	L1B14	L4iA	L4oA	L4iB	L4oB	Class	Range
1	0	1	0	*	0	0	*	0	0	0	*	L12A	2A
1	0	1	0	*	1	0	0	0	0	0	*	L12A	2A
1	0	1	1	0	0	0	*	0	0	0	*	L123A	3A
1	0	1	1	0	1	0	0	0	0	0	*	L123A	3A
*	0	0	*	0	1	0	1	0	*	0	0	L12B	2B
0	0	1	*	0	1	0	1	0	*	0	0	L12B	2B
*	0	0	0	1	1	0	1	0	*	0	0	L123B	3B
0	0	1	0	1	1	0	1	0	*	0	0	L123B	3B
1	0	1	0	0	1	0	1	0	0	0	0	2TEL	NOCALC
1	0	1	1	0	1	0	1	0	0	0	0	2TEL	NOCALC

Draft

1	0	1	0	1	1	0	1	0	0	0	0	2TEL	NOCALC
1	0	1	1	1	1	0	1	0	0	0	0	2TEL	NOCALC
1	0	1	1	1	0	0	*	0	0	0	*	PENA	4A
1	0	1	1	1	1	0	0	0	0	0	*	PENA?	4A
*	0	0	1	1	1	0	1	0	*	0	0	PENB	4B
0	0	1	1	1	1	0	1	0	*	0	0	PENB?	4B
0	0	0	0	0	0	0	*	1	0	0	*	ILA	NOCALC
0	0	*	1	*	0	0	*	1	0	0	*	IHA	NOCALC
*	0	0	0	0	0	0	0	0	*	1	0	ILB	NOCALC
*	0	0	*	1	*	0	0	0	*	1	0	IHB	NOCALC
0	1	1	0	*	0	*	0	1	0	0	*	L142A	NOCALC
0	1	1	0	*	0	*	0	0	1	0	*	L142A	NOCALC
0	1	1	0	*	1	0	0	1	0	0	*	L142A	NOCALC
0	1	1	0	*	1	0	0	0	1	0	*	L142A	NOCALC
0	1	1	1	0	0	*	0	1	0	0	*	L1423A	NOCALC
0	1	1	1	0	0	*	0	0	1	0	*	L1423A	NOCALC
0	1	1	1	0	1	0	0	1	0	0	*	L1423A	NOCALC
0	1	1	1	0	1	0	0	0	1	0	*	L1423A	NOCALC
0	*	0	*	0	1	1	0	0	*	1	0	L142B	NOCALC
0	*	0	*	0	1	1	0	0	*	0	1	L142B	NOCALC
0	0	1	*	0	1	1	0	0	*	1	0	L142B	NOCALC
0	0	1	*	0	1	1	0	0	*	0	1	L142B	NOCALC
0	*	0	0	1	1	1	0	0	*	1	0	L1423B	NOCALC
0	*	0	0	1	1	1	0	0	*	0	1	L1423B	NOCALC
0	0	1	0	1	1	1	0	0	*	1	0	L1423B	NOCALC
0	0	1	0	1	1	1	0	0	*	0	1	L1423B	NOCALC
0	1	1	1	1	0	*	0	1	0	0	0	PEN4A	NOCALC

Draft

0	1	1	1	1	0	*	0	0	1	0	0	PEN4A	NOCALC
0	*	0	1	1	1	1	0	0	0	1	0	PEN4B	NOCALC
0	*	0	1	1	1	1	0	0	0	0	1	PEN4B	NOCALC

Table 40: Event classification and range table

9.1.1 Incident Ion Energy Calculation

The incident energy of a given particle will be found as the sum of all the energy deposit values for all detectors in which the particle interacted. The energy for each individual detector should also be provided as output.

```
int far WINCORR2[] = {
256, 256, 256, 256, 256, 256, 256, 256, 256, 256, 256, 256, 256, 256, 256, 256,
405, 405, 405, 389, 389, 389, 389, 389, 389, 389, 389, 389, 389, 389, 389, 256,
405, 405, 405, 389, 389, 389, 389, 389, 389, 389, 389, 389, 389, 389, 389, 256,
256, 256, 256, 256, 256, 256, 256, 256, 256, 256, 256, 256, 256, 256, 256, 256
};
int far WINCORR3[] = {
256, 256, 256, 256, 256, 256, 256, 256, 256, 256, 256, 256, 256, 256, 256, 256,
425, 425, 425, 417, 417, 417, 417, 417, 417, 417, 417, 417, 417, 417, 417, 256,
425, 425, 425, 417, 417, 417, 417, 417, 417, 417, 417, 417, 417, 417, 417, 256,
256, 256, 256, 256, 256, 256, 256, 256, 256, 256, 256, 256, 256, 256, 256, 256
};
```

Table 41: Array Definition for WINCORR2 and WINCORR3.

To compensate for energy degradation within the dual protective Kapton foils shielding each aperture, a multiplicative correction factor is applied to the L1 sensor signals. In the I-ALiRT apertures, the inner foils are localized between the L1 and L4 detector planes. The outer foils incorporate a CCAg+ITO coating on the exterior face and vapor-deposited aluminum (VDA) on the interior surface, whereas the inner foils feature VDA coatings on both sides. Collectively, these foil layers provide an effective mass thickness of approximately 14.8 μm Silicon equivalent. Relative to this baseline reference, the simulated

Draft

	a [MeV/ADC]	b [MeV]
L1 LG	5.159319e-01	-2.396621e+01
L2 LG	1.028532e+00	-4.554092e+01
L3 LG	1.931152e+00	-8.533005e+01
L1 HG	1.241479e-02	-1.170833e-01
L2 HG	2.442080e-02	-7.905500e-01
L3 HG	4.472975e-02	-1.716000e+00

Table 42: Average coefficients used for the ADC-to-MeV conversion (via Equation 18), for both low- and high-gain channels.

energy loss is lower in Range 2 and elevated in both Range 3/Range 4 and the A0/B0 apertures. This behavior is anticipated due to the inherent deviations between the stopping-power characteristics of the composite foil materials and elemental silicon. Consequently, the flight software executes two independent correction arrays: `WINCORR2` for Range 2 and `WINCORR3` for Range 3/Range 4 (Table 41). Each array entry is stored as a fixed-point integer scaled by a factor of 256, defined by $\lfloor 256 \times \mathrm{corr} \rfloor$, where the correction factor $corr \geq 1$ is derived from Geant4 simulations averaged across all incident ion species.

9.1.2 ADC-MeV Conversion

The conversion is based on the ADC calibration data run by the FSW and derived by J. Dumonthier (GSFC-672), version 05/23/2024. The resulting MeV values come from the DAC settings and the selected injection capacitance and, for each of the 64 channels, they are obtained by a linear fit of the data (calibration curves):

$$E[MeV] = a * PHA[ADC] + b, \tag{18}$$

with the (a, b) parameters having some variation from PHASIC to PHASIC and channel to channel. However, such differences are relatively small (see Figure 16), and results can be averaged in order to obtain six sets of coefficients for the L1, L2 and L3 sensors (three for low-gain and three for high-gain mode). The numerical values are reported in Table 42.

On 2026-05-14, all L1A/B14 low-gain offsets were dropped down by 8 due to updates to the low-gain thresholds as raising the threshold requires lowering the magnitude of the offset subtracted.

Draft

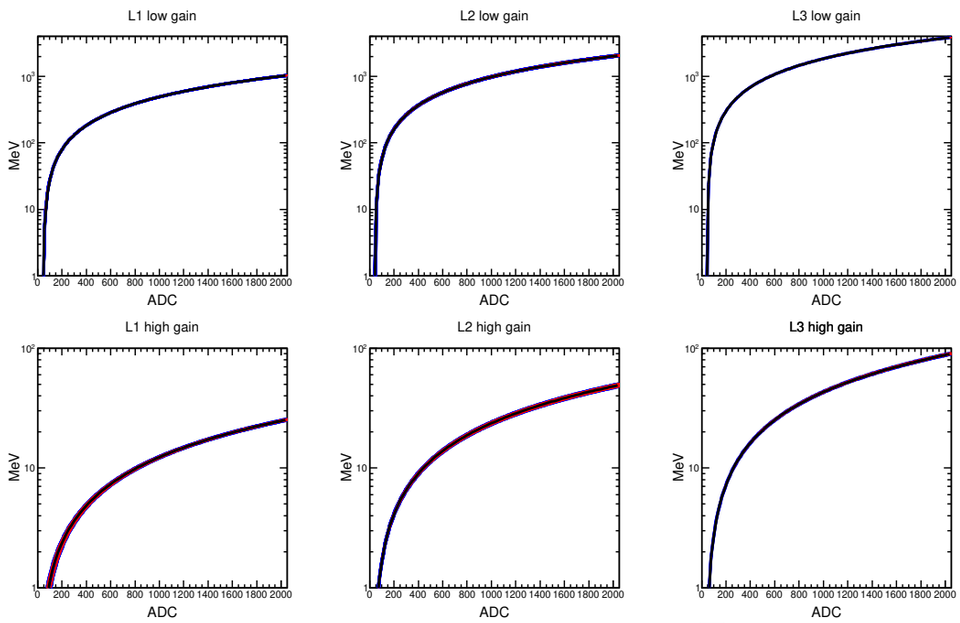


Figure 16: Calibration curves (see Equation 18) for both low- (top) and high-gain (bottom) channels.

9.1.3 Cosine Correction

Particles which pass certain onboard processing cuts are sorted into matrices according to their penetration *Range* in the instrument and by ΔE vs. E' measurements, where ΔE is the energy deposit in the detector that the particle fully penetrates and $E^{'}$ the energy deposited in a following detector in which the particle is absorbed. For instance, in the case of *Range*3, ΔE and $E^{'}$ correspond to the energy loss in the L2 and L3, respectively (see Figure 19).

In order to improve the energy resolution and the resulting selection efficiency, the recorded signals can be corrected by accounting for the proportionality between the deposited energy and the cosine of the inclination angle $\cos\theta$, which can be expressed by the ratio $L_\theta = L_0/L$ of the nominal detector thickness to the actual thickness penetrated. For *Range*2, these quantities refer to the L1 detector segment traversed by the particle, while for *Range*3 and *Range*4 the L2 sensors are used.

Particle simulations were employed to compute the L_θ associated with each particle trajectory inside the FoV by evaluating the total path L in each sensor; the resulting distributions were used to calculate the mean inclination angle $\overline{L}_\theta$ associated with each of the 150 L1 vs. L2 segment combinations, for each energy *Range*. Results are reported in Tables 43, 44 and 45. Then, the desired

Draft

transformation is accomplished by multiplying both ΔE and E' by $K_\theta = \overline{L}_\theta^{1/a}$ where the a power-law index was obtained with the following iterative procedure, optimized for providing the highest ^{3}He/^{4}He discrimination (see Figure 18). Specifically, $a = 1.61$ for *Range*2, $a = 1.68$ for *Range*3 and $a = 1.82$ for *Range*4. The same method has been applied to the I-ALiRT apertures (A0/B0), with the following results: $a = 2.36$ for *Range*2, $a = 1.73$ for *Range*3 and $a = 1.76$ for *Range*4.

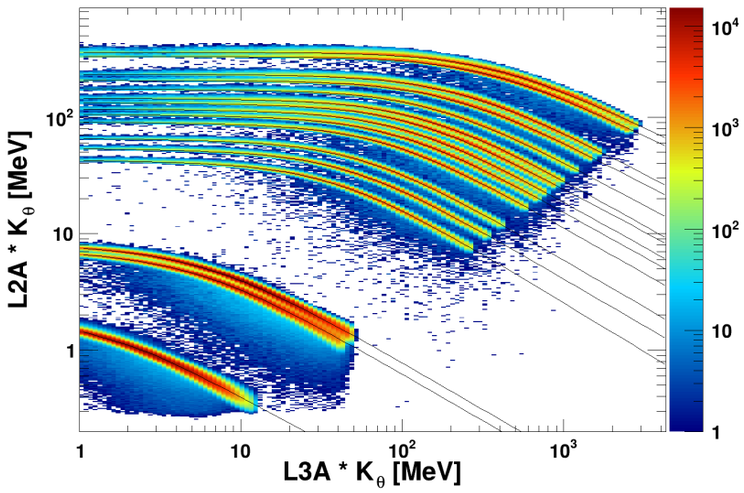


Figure 17: Ion tracks for *Range*3. The black lines show the double-power-law fit of each track.

The bounds of the energies for each range are

9.1.4 Charge Calculation

Particles which pass certain onboard processing cuts are sorted into matrices according to their penetration *Range* in the instrument and by ΔE vs. E' measurements, where ΔE is the energy deposit in the detector that the particle fully penetrates and E' the energy deposited in a following detector in which the particle is absorbed. For instance, in the case of *Range*3, ΔE and E' correspond to the energy loss in the L2 and L3, respectively (see Figure 19). Both ΔE and E' are corrected by a factor accounting for the particle trajectory inclination angle ($\cos\theta$ correction, $\overline{K}_\theta$).

For each energy *Range* (*Range*2, *Range*3, *Range*4), there is a set of 75 numerical values, representing the 5 parameters (a_1, a_2, b_1, b_2, γ) of the power-law function fitting the ion tracks, for each of the 15 ion species measured by HIT (H, ^{4}He, C, N, O, Ne, Na, Mg, Al, Si, S, Ar, Ca, Fe and Ni; the ^{3}He

Draft

	L1A0a	L1A0b	L1A0c	L1A1a	L1A1b	L1A1c	L1A2a	L1A2b	L1A2c	L1A3a	L1A3b	L1A3c	L1A4a	L1A4b	L1A4c
L2A0	0.9881	0.9854	0.9809	0.9643	0.9550	0.9439	0.9506	0.9378	0.9233	0.9474	0.9322	0.9144	0.9640	0.9482	0.9286
L2A1	0.9910	0.9891	0.9854	0.9766	0.9686	0.9583	0.9696	0.9596	0.9468	0.9712	0.9599	0.9453	0.9826	0.9733	0.9585
L2A2	0.9939	0.9919	0.9884	0.9862	0.9801	0.9710	0.9841	0.9770	0.9664	0.9864	0.9797	0.9685	0.9919	0.9879	0.9781
L2A3	0.9954	0.9942	0.9911	0.9929	0.9895	0.9822	0.9929	0.9893	0.9816	0.9941	0.9917	0.9844	0.9950	0.9949	0.9894
L2A4	0.9963	0.9963	0.9940	0.9956	0.9952	0.9904	0.9954	0.9958	0.9915	0.9949	0.9964	0.9932	0.9940	0.9968	0.9947
L2A5	0.9959	0.9969	0.9954	0.9932	0.9965	0.9950	0.9915	0.9957	0.9954	0.9904	0.9952	0.9956	0.9903	0.9952	0.9960
L2A6	0.9933	0.9959	0.9959	0.9844	0.9916	0.9941	0.9816	0.9894	0.9929	0.9821	0.9893	0.9929	0.9853	0.9915	0.9943
L2A7	0.9882	0.9930	0.9947	0.9685	0.9797	0.9865	0.9663	0.9771	0.9841	0.9710	0.9801	0.9862	0.9795	0.9866	0.9909
L2A8	0.9804	0.9866	0.9907	0.9451	0.9599	0.9712	0.9467	0.9595	0.9697	0.9583	0.9686	0.9765	0.9733	0.9809	0.9864
L2A9	0.9679	0.9765	0.9823	0.9146	0.9322	0.9474	0.9232	0.9379	0.9503	0.9436	0.9547	0.9642	0.9663	0.9746	0.9807

Table 43: Cosine corrections K_θ for *Range*2.

Draft

L2A0	0.7029	0.6823	0.6585	0.8447	0.8241	0.8021	0.9532	0.9414	0.9272	0.9955	0.9959	0.9917	0.9257	0.9489	0.9630
L2A1	0.7304	0.7073	0.6821	0.8718	0.8518	0.8300	0.9715	0.9617	0.9492	0.9915	0.9963	0.9958	0.8884	0.9164	0.9359
L2A2	0.7554	0.7313	0.7057	0.8988	0.8798	0.8585	0.9853	0.9785	0.9681	0.9802	0.9894	0.9930	0.8494	0.8804	0.9039
L2A3	0.7812	0.7570	0.7310	0.9246	0.9075	0.8870	0.9937	0.9905	0.9829	0.9627	0.9758	0.9835	0.8104	0.8431	0.8700
L2A4	0.8081	0.7841	0.7575	0.9482	0.9334	0.9146	0.9962	0.9967	0.9924	0.9404	0.9567	0.9682	0.7730	0.8064	0.8353
L2A5	0.8360	0.8125	0.7861	0.9682	0.9567	0.9403	0.9925	0.9967	0.9962	0.9147	0.9334	0.9481	0.7383	0.7716	0.8014
L2A6	0.8642	0.8420	0.8159	0.9835	0.9758	0.9627	0.9829	0.9904	0.9938	0.8871	0.9076	0.9247	0.7059	0.7385	0.7687
L2A7	0.8922	0.8722	0.8470	0.9930	0.9894	0.9803	0.9681	0.9786	0.9853	0.8585	0.8800	0.8987	0.6760	0.7078	0.7379
L2A8	0.9193	0.9019	0.8787	0.9958	0.9963	0.9915	0.9491	0.9618	0.9714	0.8300	0.8519	0.8718	0.6485	0.6795	0.7093
L2A9	0.9444	0.9304	0.9117	0.9917	0.9959	0.9955	0.9273	0.9414	0.9532	0.8021	0.8242	0.8449	0.6237	0.6529	0.6817

Table 44: Cosine corrections K_θ for *Range*3.

Draft

	L1A0a	L1A0b	L1A0c	L1A1a	L1A1b	L1A1c	L1A2a	L1A2b	L1A2c	L1A3a	L1A3b	L1A3c	L1A4a	L1A4b	L1A4c
L2A0	0.7183	0.6968	0.6783	0.8565	0.8369	0.8174	0.9568	0.9455	0.9323	0.9959	0.9963	0.9922	0.9313	0.9528	0.9661
L2A1	0.7346	0.7115	0.6870	0.8813	0.8625	0.8418	0.9736	0.9645	0.9528	0.9922	0.9967	0.9961	0.8969	0.9227	0.9410
L2A2	0.7591	0.7348	0.7106	0.9062	0.8886	0.8683	0.9864	0.9803	0.9705	0.9818	0.9902	0.9935	0.8600	0.8891	0.9113
L2A3	0.7846	0.7605	0.7349	0.9303	0.9143	0.8950	0.9942	0.9913	0.9842	0.9655	0.9777	0.9849	0.8237	0.8546	0.8799
L2A4	0.8112	0.7872	0.7617	0.9521	0.9384	0.9210	0.9965	0.9970	0.9930	0.9448	0.9600	0.9707	0.7889	0.8205	0.8470
L2A5	0.8385	0.8150	0.7892	0.9708	0.9600	0.9447	0.9931	0.9969	0.9965	0.9211	0.9382	0.9522	0.7556	0.7870	0.8156
L2A6	0.8660	0.8445	0.8189	0.9849	0.9777	0.9655	0.9842	0.9912	0.9942	0.8953	0.9143	0.9304	0.7251	0.7558	0.7851
L2A7	0.8944	0.8746	0.8497	0.9936	0.9903	0.9818	0.9704	0.9802	0.9864	0.8682	0.8885	0.9061	0.6961	0.7269	0.7556
L2A8	0.9210	0.9035	0.8809	0.9961	0.9966	0.9923	0.9528	0.9647	0.9736	0.8418	0.8623	0.8811	0.6709	0.6997	0.7283
L2A9	0.9454	0.9314	0.9132	0.9923	0.9963	0.9958	0.9322	0.9456	0.9567	0.8174	0.8374	0.8561	0.6691	0.6893	0.7136

Table 45: Cosine corrections K_θ for *Range4*.

Draft

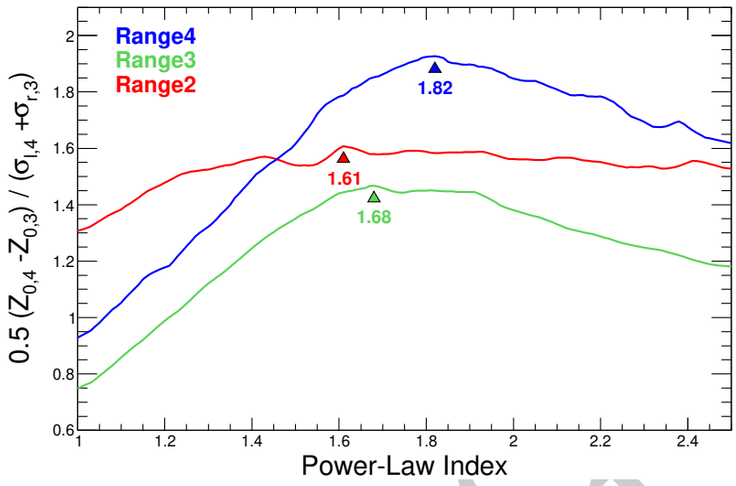


Figure 18: Dependence of charge resolution factor on the power-law index a. The three values providing the best ^{3}He/^{4}He discrimination are marked for each *Range*.

Range	ΔE_{min} **(MeV)**	ΔE_{max} **(MeV)**	E'_{min} **(MeV)**	E'_{max} **(MeV)**
2	0.1	430	0.2	860
3	0.2	860	1	4300
4	1	4300	1	4300

Table 46: Ranges of possible values of E' and ΔE for each range.

isotope is excluded). The double-power-law function is given by:

$$f_t(E') = \left[\left(a_1 E'^{b_1}\right)^{\gamma} + \left(a_2 E'^{b_2}\right)^{\gamma}\right]^{\frac{1}{\gamma}} \tag{19}$$

where $a_1 E'^{b_1}$ and $a_2 E'^{b_2}$ are power-law functions describing the energy regions below and above the interval around the ion track turnover, respectively; the additional free parameter γ describes the transition between the two power laws. The fit results for *Range*3 are displayed in Figure 19, while the parameters for all three *ranges* are reported in Tables 47, 48 and 49. The same methodology was applied to the I-ALiRT apertures (A0/B0), with corresponding parameters listed in Tables 50, 51 and 52. In particular, for the *Range*2, the data are described by a single power law, so only the a_1 and b_1 fit parameters are used (Table 50).

Draft

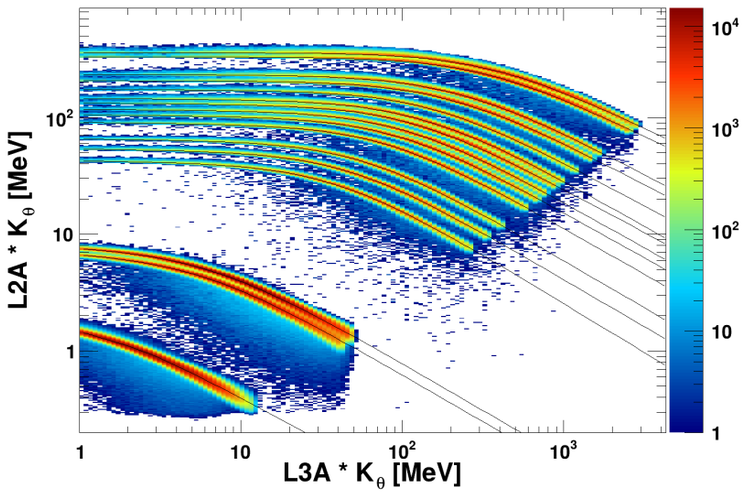


Figure 19: Ion tracks for *Range*3. The black lines show the double-power-law fit of each track.

Algorithm Application

1. For a given ($E^{'}$, ΔE) measurement, a graph is built by associating the $f_t(E^{'})$ relative to each of the 15 tracks (evaluated at $E^{'}$ via Equation 19) with the corresponding (integer) nuclear charge Z_t. An example is reported in Figure 20.

2. The resulting (non-integer) charge Z is obtained by interpolating the Z_t vs. $f_t(E^{'})$ graph at ΔE, under the power-law assumption. Specifically, if $f_t(E_1^{'})$ and $f_t(E_2^{'})$ correspond to the closest pair of ions (with charge $Z_{t,1}$ and $Z_{t,2}$) so that $f_t(E_1^{'}) < \Delta E < f_t(E_2^{'})$, then

$$Z(\Delta E) = A\,(\Delta E)^B, \tag{20}$$

where

$$B = \log[\,Z_{t,2}\,/\,Z_{t,1}\,]\;/\;\log[\,f_t(E_2^{'})\,/\,f_t(E_1^{'})\,] \tag{21}$$

and

$$A = Z_{t,1}\;/\;[\,f_t(E_1^{'})\,]^B. \tag{22}$$

3. In the case ΔE is higher than the nickel peak value $f_{Ni}(E^{'})$, the charge is extrapolated by using the iron and nickel pair; similarly, the H and ^{4}He pair is used when ΔE is lower than the hydrogen peak value $f_H(E^{'})$.

4. The energy-integrated charge histogram associated with each range matrix is obtained by summing up all the particle entries with Z estimated according to Equation 20.

Draft



Z_t	a_1	b_1	a_2	a_b	γ
1	1.479963e+00	8.209081e-02	1.056083e+00	-6.688255e-01	-1.759770e+00
2	4.964089e+00	-2.347052e-02	1.119467e+01	-6.892635e-01	-2.222412e+00
6	2.587211e+01	1.218594e-02	4.106214e+03	-1.256034e+00	-8.434640e-01
7	3.208165e+01	7.707944e-03	2.944465e+03	-1.113833e+00	-1.038501e+00
8	3.863437e+01	9.539366e-03	8.653277e+03	-1.227574e+00	-9.272040e-01
10	5.128670e+01	1.664116e-02	4.316894e+03	-9.913076e-01	-1.239285e+00
11	5.800006e+01	1.720292e-02	4.251641e+03	-9.382665e-01	-1.389592e+00
12	6.463724e+01	1.945454e-02	6.811090e+03	-9.786677e-01	-1.283539e+00
13	7.101556e+01	2.499757e-02	5.451054e+03	-9.004415e-01	-1.434989e+00
14	3.307547e+02	-1.016750e-01	2.434280e+04	-3.028693e-09	-2.299653e-01
16	9.348524e+01	4.418190e-03	7.976853e+02	-4.986653e-01	-4.782615e+00
18	1.085192e+02	7.100202e-03	9.061990e+02	-4.675327e-01	-5.881363e+00
20	1.212440e+02	1.199842e-02	9.543358e+02	-4.481641e-01	-5.864268e+00
26	1.634267e+02	1.807242e-02	1.057107e+03	-3.715106e-01	-1.066283e+01
28	1.779868e+02	1.780692e-02	1.133637e+03	-3.632466e-01	-1.176421e+01

Table 47: Double-power-law fit results (see Equation 19) for *Range2* (A14/B14 apertures).

Draft

Results are displayed in Figure 21 for *Range3*. This method is used, e.g., to estimate the decimal charge Z associated with ^{3}He isotope measurements (see right panel in Figure 21), by interpolating between the H and the ^{4}He tracks; the resulting value is $\sim$1.9.

9.2 Lev3 Sectored Products

A full description of the Sectored rate data is provided in Sec. 4.2.2. The sectored rates are collected on a 10 minute cadence with a different species/energy sent down each minute according to Table 3.

The Lev2 Sectored data will consist of intensities for the 10 species/energy bins in physical units binned by declination and inclination angles. In total there are 120 look directions consisting of eight 22.5° declination bins and fifteen 24° inclination bins. A drawing to illustrate this is shown in Fig. 22.

Z_t	a_1	b_1	a_2	a_b	γ
1	1.453953e+00	-3.433355e-01	2.174537e+00	-7.499576e-01	-6.333077e+00
2	7.645239e+00	-5.772561e-02	2.961728e+01	-7.905325e-01	-1.967359e+00
6	4.251565e+01	-8.075919e-03	8.445316e+02	-8.396609e-01	-1.579686e+00
7	5.331862e+01	-3.690031e-03	1.454459e+03	-8.563961e-01	-1.484515e+00
8	6.532380e+01	-1.759982e-02	1.506928e+03	-8.017355e-01	-1.839473e+00
10	8.841751e+01	-4.672032e-03	2.680709e+03	-7.942925e-01	-1.802791e+00
11	1.022556e+02	3.122387e-03	5.270435e+03	-8.482708e-01	-1.466593e+00
12	1.138565e+02	1.648505e-03	5.199846e+03	-8.158559e-01	-1.603033e+00
13	1.267025e+02	1.216113e-02	6.798835e+03	-8.160702e-01	-1.497994e+00
14	1.394042e+02	7.434322e-03	8.372908e+03	-8.202076e-01	-1.495869e+00
16	1.666386e+02	4.861300e-03	8.498519e+03	-7.709579e-01	-1.683556e+00
18	2.004655e+02	1.796604e-03	9.676462e+03	-7.350743e-01	-1.893294e+00
20	2.204714e+02	6.721033e-03	9.789824e+03	-7.082093e-01	-1.971441e+00
26	3.133529e+02	6.018827e-03	1.434066e+04	-6.626533e-01	-2.181724e+00
28	3.368751e+02	1.208747e-02	1.826999e+04	-6.730212e-01	-2.002748e+00

Table 48: Double-power-law fit results (see Equation 19) for *Range3* (A14/B14 apertures).

The Lev3 data will combine the

- HIT Lev2 Sectored Intensity data
- MAG Lev1D magnetic field vector in despun frame

to produce species/energy-dependent intensity data products in physical units in angular bins with relation to the magnetic field vector. The magnetic field data will be averaged over the 10 minute collection time of the HIT Sectored data. The angle between the particle acceptance direction (for a given combination of inclination and declination) and the magnetic field vector will be calculated. An illustration showing the concept of the pitch angle is shown in Fig. 23. An array of pitch angles corresponding to the HIT Sectored bins will be produced.

Another product with both pitch angle and gyrophase will be constructed using the same data (see Fig. 23 for illustration of gyrophase).

Draft



Z_t	a_1	b_1	a_2	a_b	γ
1	1.154340e+01	-7.114543e-02	1.011661e+02	-1.052054e+00	-1.717067e+00
2	4.811216e+01	-1.103459e-02	6.323176e+02	-7.755388e-01	-1.607142e+00
6	2.676431e+02	-4.494929e-04	1.493469e+04	-7.874666e-01	-1.444953e+00
7	3.437643e+02	-6.705931e-03	1.568531e+04	-7.352394e-01	-1.666771e+00
8	4.254100e+02	-1.157973e-02	7.921619e+03	-5.849140e-01	-2.449569e+00
10	5.902855e+02	-1.705847e-03	1.939047e+04	-6.267098e-01	-1.954604e+00
11	6.974519e+02	-2.227489e-03	3.906509e+04	-6.850924e-01	-1.737538e+00
12	7.861641e+02	-4.283877e-03	2.107218e+04	-5.731322e-01	-2.201842e+00
13	8.908970e+02	2.216163e-03	8.528126e+04	-7.245672e-01	-1.523295e+00
14	9.850535e+02	-1.797150e-03	7.608972e+04	-6.950917e-01	-1.738658e+00
16	1.232022e+03	-7.479155e-03	3.545218e+04	-5.505602e-01	-2.394372e+00
18	1.500582e+03	2.210960e-03	1.567151e+05	-6.830830e-01	-1.572172e+00
20	1.717848e+03	-5.895197e-03	1.173455e+05	-6.349220e-01	-1.998707e+00
26	2.592495e+03	-5.837627e-04	4.148593e+05	-6.875006e-01	-1.597780e+00
28	2.864045e+03	-3.316593e-03	1.538460e+05	-5.585982e-01	-2.167948e+00

Table 49: Double-power-law fit results (see Equation 19) for *Range4* (A14/B14 apertures).

Draft

2D "skymap" data will be output using the input 22.5°x24° bins and the pitch angle as input. The output bins will be 22.5° in pitch angle and 24° in gyrophase

There are no ancillary files that will be required to produce this data product.

9.3 Lev3 Electron Science Products

We plan to utilize the I-ALiRT data to generate science-quality electron Intensities in several energy bins. There are 6 HIT I-ALiRT electron products, 3 from the A-side and 3 from the B-side (see Sec. 8.2). The low energy and medium e- data are single-parameter measurements utilizing only energy deposit in the L4 SSD. The high energy e- data utilize energy deposit in L4 and L3. For the science quality electron products, modeling will be required to calculate

Z_t	a_1	b_1	a_2	a_b	γ
1	1.325101e-01	-1.259808e-02	0.0	0.0	1.0
2	5.370965e-01	2.047460e-03	0.0	0.0	1.0
6	3.052834e+00	6.483596e-03	0.0	0.0	1.0
7	3.959032e+00	-2.883245e-03	0.0	0.0	1.0
8	4.862085e+00	-1.150285e-03	0.0	0.0	1.0
10	7.224655e+00	-1.309652e-02	0.0	0.0	1.0
11	8.322483e+00	-7.165193e-03	0.0	0.0	1.0
12	9.437984e+00	-9.049199e-03	0.0	0.0	1.0
13	1.099386e+01	-1.323460e-02	0.0	0.0	1.0
14	1.193748e+01	-7.226051e-03	0.0	0.0	1.0
16	1.468762e+01	-4.396047e-03	0.0	0.0	1.0
18	1.839030e+01	-3.284405e-03	0.0	0.0	1.0
20	2.040375e+01	-2.160571e-03	0.0	0.0	1.0
26	3.179083e+01	-1.762030e-03	0.0	0.0	1.0
28	3.486592e+01	-1.608827e-03	0.0	0.0	1.0

Table 50: Double-power-law fit results (see Equation 19) for *Range2* (A0/B0 apertures).

Draft

a response function for the different I-ALiRT products to determine the incident energy corresponding to measured energy in each of those data products. The ion contamination will also need to be determined to subtract out that background and produce a clean, science quality electron measurement. The required inputs for these data are:

- 6 I-ALiRT electron data products
- High energy proton measurements (TBD range/bin) to subtract out background

Early in the mission, we will also likely need to utilize the PHA data to examine energy deposit in L4 and L3 to get a sense of the ion contamination to the electrons. The ancillary files that will be required likely include



Z_t	a_1	b_1	a_2	a_b	γ
1	1.461753e+00	-3.763489e-01	1.986990e+00	-7.060189e-01	-1.148860e+01
2	2.150123e+01	5.618652e-01	9.974164e+01	-1.019735e+00	-4.000465e-01
6	4.476987e+01	-3.756624e-02	7.236927e+02	-8.138707e-01	-1.880098e+00
7	5.437193e+01	1.473079e-03	1.568607e+03	-8.683268e-01	-1.429238e+00
8	6.476354e+01	2.943513e-02	1.843986e+03	-8.276303e-01	-1.364661e+00
10	9.109171e+01	2.242113e-03	3.151333e+03	-8.173360e-01	-1.600867e+00
11	1.016141e+02	4.588678e-02	6.574376e+03	-8.745927e-01	-1.145520e+00
12	1.225553e+02	-2.415002e-02	3.612749e+03	-7.633395e-01	-2.084295e+00
13	1.331190e+02	2.937245e-02	1.726559e+04	-9.380498e-01	-1.021453e+00
14	1.446913e+02	1.415987e-02	6.520513e+03	-7.814509e-01	-1.544396e+00
16	1.761002e+02	4.393547e-03	8.657145e+03	-7.702114e-01	-1.654499e+00
18	1.970318e+02	3.184437e-02	1.581287e+04	-7.960034e-01	-1.384478e+00
20	2.432598e+02	-4.725174e-03	1.216708e+04	-7.342470e-01	-1.764839e+00
26	3.273470e+02	2.122526e-02	4.063510e+04	-7.882034e-01	-1.356335e+00
28	3.713219e+02	-4.161703e-05	1.482567e+04	-6.441385e-01	-2.280535e+00

Table 51: Double-power-law fit results (see Equation 19) for *Range*3 (A0/B0 apertures).

- Electron response matrices for the L4-only data and for the L3 vs. L4 data

Draft

Z_t	a_1	b_1	a_2	a_b	γ
1	1.141516e+01	-1.003283e-01	1.831367e+01	-4.435884e-01	-8.630497e+00
2	4.782043e+01	-6.075567e-03	3.918498e+02	-6.812506e-01	-1.956810e+00
6	2.665183e+02	9.671847e-04	1.522629e+04	-7.937632e-01	-1.454821e+00
7	3.495769e+02	-1.663598e-02	9.192679e+03	-6.626882e-01	-2.184069e+00
8	4.208862e+02	7.458882e-04	4.465959e+04	-8.215504e-01	-1.294397e+00
10	5.884850e+02	6.804680e-03	8.180725e+04	-8.163633e-01	-1.254637e+00
11	7.084569e+02	-5.487147e-03	7.048009e+04	-7.686574e-01	-1.560483e+00
12	8.179122e+02	-1.684424e-02	1.859367e+04	-5.671695e-01	-2.729415e+00
13	9.285631e+02	-1.194766e-02	2.331319e+05	-8.667603e-01	-1.417516e+00
14	9.847908e+02	5.312153e-03	1.295641e+05	-7.546234e-01	-1.392755e+00
16	1.230445e+03	-4.391514e-03	1.046576e+05	-6.925557e-01	-1.796468e+00
18	1.458808e+03	9.266277e-03	1.668667e+05	-7.004060e-01	-1.632794e+00
20	1.767014e+03	-1.228790e-02	3.860805e+05	-7.818811e-01	-1.660001e+00
26	2.589173e+03	2.850223e-03	7.344096e+05	-7.554010e-01	-1.454490e+00
28	3.016836e+03	-1.285369e-02	5.115148e+05	-7.023136e-01	-1.821810e+00

Table 52: Double-power-law fit results (see Equation 19) for *Range*4 (A0/B0 apertures).

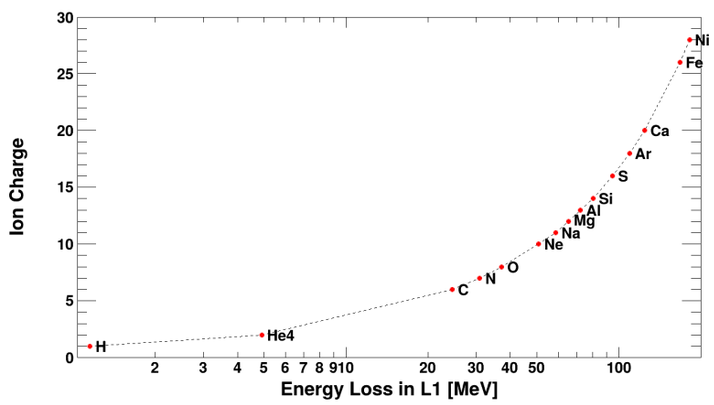


Figure 20: Z_t vs. $f_t(E')$ graph at sample E' energy loss in L2 for *Range*2.

Draft

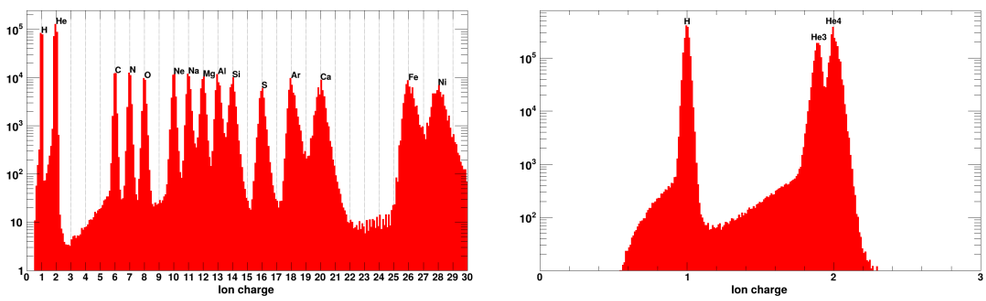


Figure 21: Left: energy-integrated charge distribution obtained for *Range*3. Right: detail of the $Z < 3$ region.

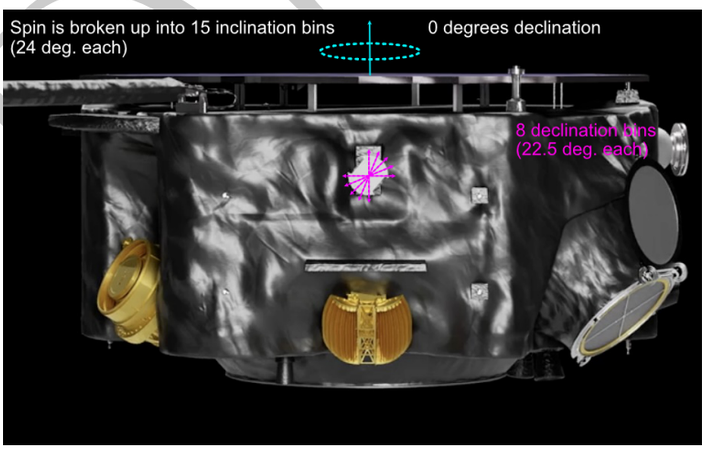


Figure 22: Drawing to illustrate how the Sectored rates are determined.

Draft

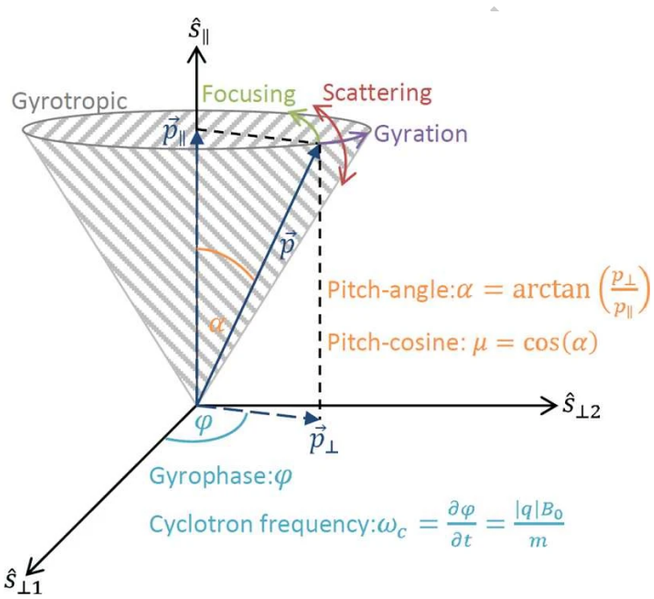


Figure 23: Definition of particle pitch angle and gyrophase (from van den Berg et al. 2020)

4.2.4 SWE

SWE data product definitions and processing algorithms are embedded below

Table of Contents

1 Introduction 4

1.1 Document Purpose 4

1.2 Scope 4

2 SWE Instrument Description 5

2.1 Overview 5

2.2 Sensor Head 6

2.3 Electronics 7

3 Nominal Operation 8

3.1 Operating Modes 8

3.1.1 Spacecraft Time Interface 9

3.2 Nominal Science Operations 9

3.3 Data Products 11

3.3.1 Science Data 12

3.3.2 Housekeeping Data 12

3.3.3 Engineering Mode Data 12

3.3.4 In-Flight Calibration Data 13

3.3.5 i-ALiRT Data 13

3.4 Data processing 16

3.4.1 Heritage data processing 16

3.4.2 Level 0 to Level 1a Processing 16

3.4.3 Level 1a to Level 1b Processing 19

3.4.4 Level 1b to Level 2 Processing 21

3.4.5 i-ALiRT Processing 25

3.4.6 Level 2 to Level 3 Processing 29

Appendix A: Telemetry packet conversions 33

Appendix B: Telemetry Packet Definitions 35

1 Introduction

1.1 Document Purpose

This document provides a description of the algorithms used to produce science data products from the IMAP Solar Wind Electron (SWE) instrument measurements. The data products are documented in the IMAP Science Data Management Plan (SDMP). This document includes a description of the data collection and data products, as well as details of the processing flow, algorithms, and data processing tasks.

1.2 Scope

The intended purpose of this information is to enable members of the IMAP Science Data Center (SDC) to implement, test, and validate executable software that will routinely produce designated data products during the science mission. For IMAP, Science Algorithm Documentation consists of the combination of documentation, instructions, specifications, and any available reference/prototype computer code needed to produce a science data product.

2 SWE Instrument Description

2.1 Overview

SWE is a heritage-design instrument, based on the design flown as the NASA Ulysses/SWOOPS, ACE/SWEPAM, and Genesis/GEM solar wind electron instruments. SWE (*Figure 1*) consists of a Sensor Head (SH) and associated Front End Electronics (FEE), located on top of an Electronics Box (EBOX). The EBOX includes the low voltage power supply (LVPS), the high voltage power supply (HVPS), and command & data handling (CDH) boards together with a backplane circuit board.

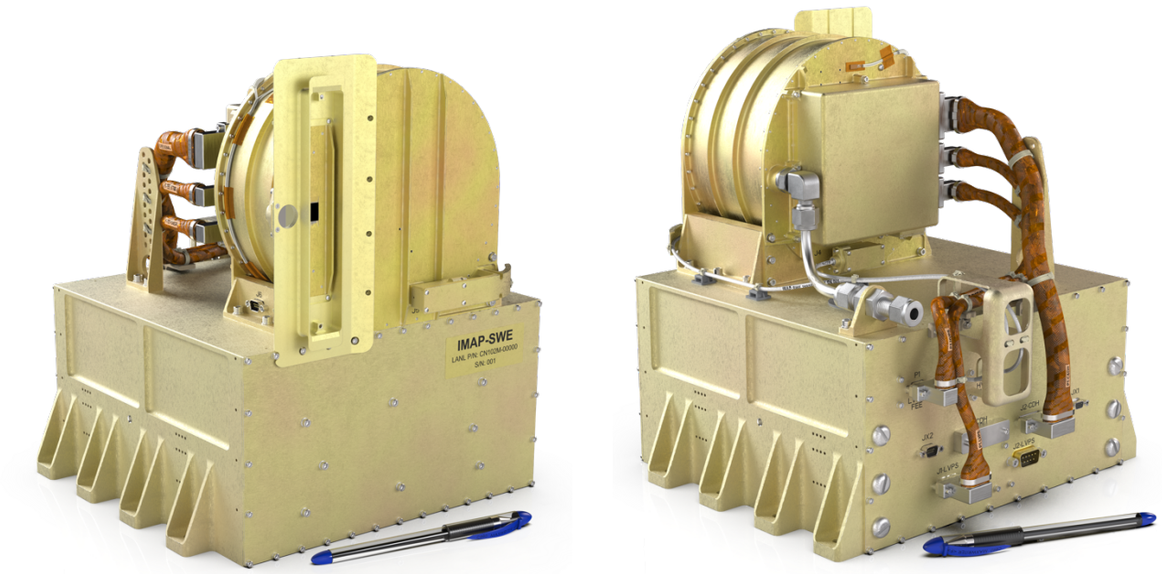


Figure 1: Front and Back views of the SWE Instrument model, showing the Sensor Head (cylinder) and Front End Electronics (box at back of SH) on top of the EBOX.

2.2 Sensor Head

The IMAP Solar Wind Electron (SWE) instrument measures the 3D distribution of solar wind thermal and suprathermal electrons from 1 eV to 5 keV. The SWE Sensor Head (*Figure 2*) consists of a spherical section electrostatic analyzer (ESA) followed by seven channel electron multiplier (CEM) detectors. Electrons enter the instrument through an aperture oriented normal to the spacecraft spin axis. A positive high voltage on the inner ESA plate biases the analyzer such that only electrons within a narrow range of energies and azimuthal angles pass through and are detected by the CEMs. Stepping this voltage provides coverage of the full energy range. Electrons entering the instrument at different angles relative to the aperture normal are detected in different CEMs, yielding 21° polar angle resolution within the fan-shaped field of view (FOV). As the IMAP spacecraft spins, the FOV sweeps out >95% of 4π steradians, missing only small conical holes centered parallel and antiparallel to the spin axis. Front end electronics (FEE) are co-located within the sensor head.

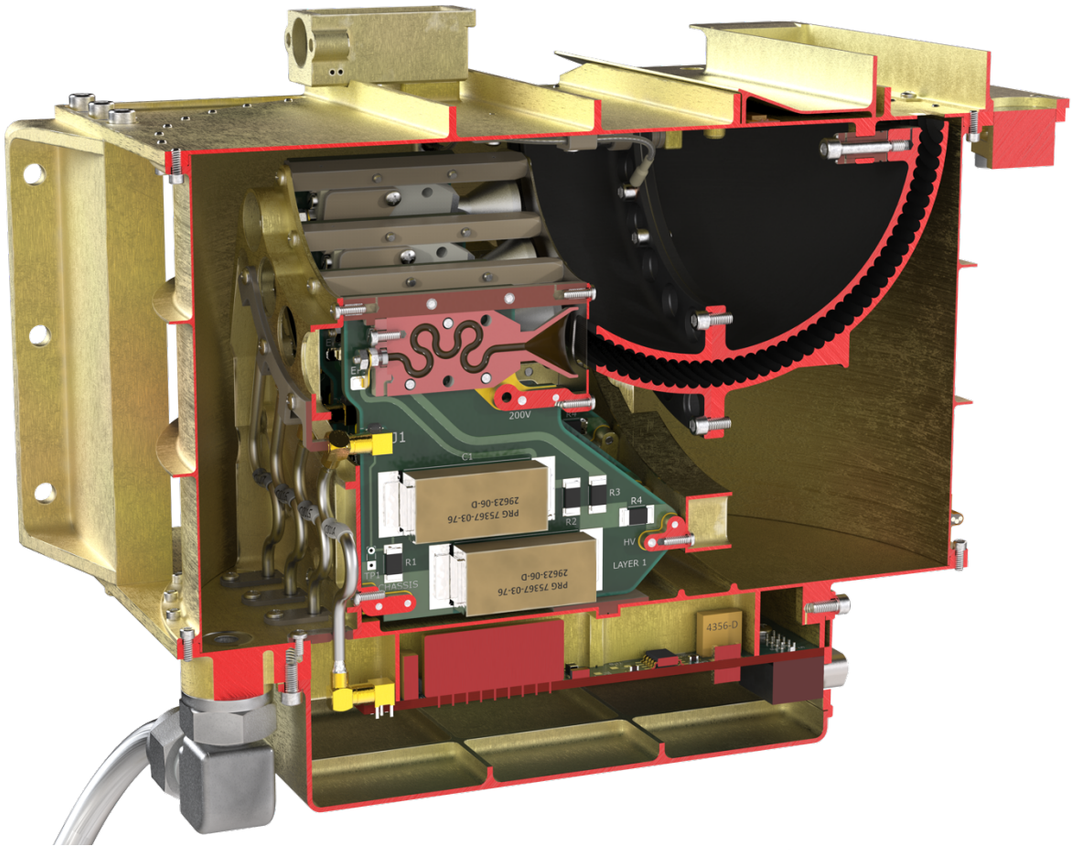


Figure 2: SWE Instrument Cross Section, showing the spherical section ESA plates followed by the CEM detectors (gold cones). The front end electronics (FEE) is located at the bottom, the EBOX is not shown in this picture.

2.3 Electronics

Electronics in the SWE sensor head include supporting electronics for the CEM detectors, and the front end electronics. The majority of SWE electronics are located in the EBOX. SWE uses the IMAP Common Electronics (ICE) EBOX structure, LVPS, CDH, and backplane boards. The SWE HVPS is also located in the EBOX. *Figure 3* shows a block diagram of the SWE electronics, including spacecraft connections (orange), Sensor electronics (yellow), FEE (green), and EBOX (blue).

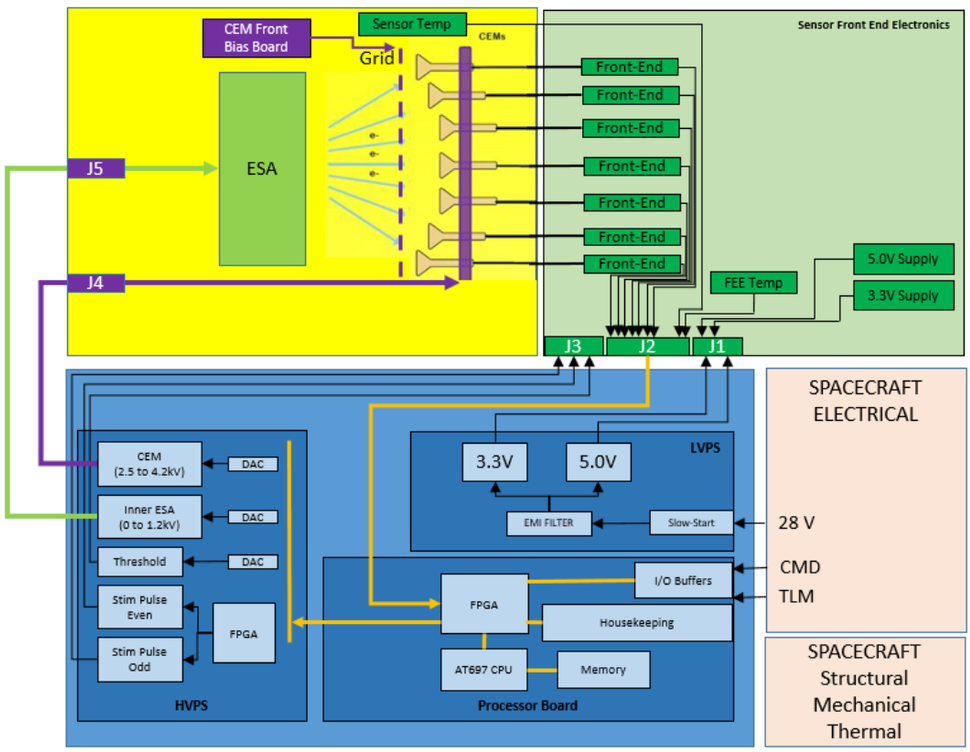


Figure 3: SWE Block Diagram, including the sensor head detector section (yellow), FEE (green), and EBOX (blue).

The Low Voltage Power Supply (LVPS) board converts primary spacecraft power to the necessary secondary voltages (+3.3 V, +/-5 V, +/-12 V) using three DC-DC converters. The board include voltage and current monitoring on all rails.

The High Voltage Power Supply (HVPS) board includes two independent supplies to produce the high voltages required for the ESA (+1200 V) and the CEM detectors (up to +4200 V). The CEM voltage output is commandable, with a nominal voltage of +2800 V at the beginning of the mission. The ESA stepping supply is a dual-range supply; the voltage will be stepped every ~83.333 ms to provide measurements over the full SWE energy range at each measurement angle. The HVPS board also includes circuitry to provide a threshold for the FEE preamplifier circuit, and LVDS pulser signals to the preamplifiers.

The Command and Data Handling (CDH) board handles data processing for SWE measurements, including collection of science data into memory, HVPS control, processing of analog monitor signals, generation of telemetry packets to the spacecraft, and implementation of commands received from the ground.

The Backplane board makes connections to the spacecraft (spin, PPS, Command & Telemetry), and provides interconnections between the LVPS, HVPS, CDH board, and the sensor electronics.

CEM board electronics are used to bias the CEM detectors. The CEM front voltage of +200 V is derived via a voltage divider circuit from the CEM rear bias. The CEM board includes connections to the high voltage bias for the front and rear of the CEM detectors, low pass filtering of the HV, and connections to extract the signal from the CEM detectors into the FEE.

The FEE electronics board uses A121 preamplifiers to amplify and shape the pulses received from each of the CEM detectors, a logic level translator to isolate analog and digital signals, and an LVDS driver to send signals to the CDH board for further processing.

3 Nominal Operation

3.1 Operating Modes

Table 4 shows the SWE flight software (FSW) operational modes. SWE has a total of six operating modes. Two of these are used for booting the instrument and starting the SWE App FSW, and the other four are used by the SWE App FSW, which handles the bulk of the SWE operations. These modes are shown in Figure 4. Transitions between modes only take place as shown in the Figure 4 diagram.

Following Boot mode, the instrument always transitions into low voltage engineering (LVENG) mode. In this mode, low-voltage monitors and engineering housekeeping data are collected and telemetered, and memory upload, dump, and diagnostic commands are allowed. Instrument safing from any mode will bring the instrument to LVENG mode.

Low voltage science (LVSCI) mode is used to test end-to-end science data acquisition based on stim pulse input to the FEE.

In high voltage engineering (HVENG) mode, high voltages are set to fixed levels by ground command. This mode is used extensively for ground testing, and is also used during commissioning to bring up the high voltages during slow ramp-ups before the start of science operations.

High voltage science (HVSCI) mode is used for science data collection during nominal operations. In this mode, ESA voltages are stepped by the FSW, with CEM counter data collected at each voltage step. Transitions out of HVSCI mode shall take place after a nominal 15-second measurement quarter cycle has been completed.

An Equal Opportunity Employer / Managed by Triad National Security, LLC for the U.S. Department of Energy's NNSA.

National Nuclear Security Administration

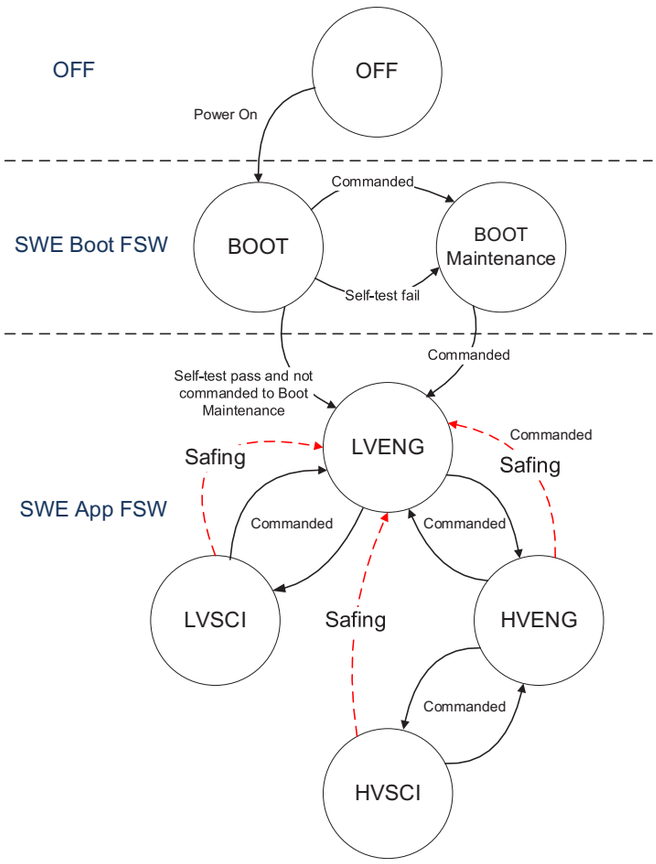


Figure 4: SWE Operating modes, with two modes for Boot FSW and 4 modes for App FSW.

3.1.1 Spacecraft Time Interface

SWE's FPGA consists of two timers used for tracking time. The 32-bit MET coarse counter contains the whole seconds of Mission Elapsed Time and the 20-bit MET fine counter contains microseconds within the second. A time-and-status packet is delivered from the spacecraft every second containing the Spacecraft Clock (SCLK) of the next 1PPS. SWE FPGA sets its MET coarse counter to this value when the next 1PPS occurs; the MET fine counter is zeroed. If the time-and-status packet fails to arrive, the time counters continue to update on their own. Both the whole second and microsecond counters are used to tag science telemetry. The 1PPS signal is used to control the pacing of FSW operations, such as telemetry generation.

3.2 Nominal Science Operations

Nominal SWE science operations take place in HVSCI mode, as described above. Figure 5 shows the nominal 1-minute science data acquisition cycle. A full cycle consists of four nominal 15-second quarter cycles, each consisting of a set of ESA voltage levels. The ESA level is nominally updated every 83.333 milliseconds, corresponding to 2 degrees of spin. Assuming a nominal 15 second spacecraft spin period,

measurements over 0.5 seconds, including 6 different ESA levels and 12 degrees of spacecraft spin, are considered to come from a given spin-angle bin. A full data set over four quarter cycles includes data at 24 energies in 30 12-degree wide spin-angle bins. The cycle shown in Figure 5 assumes a nominal 15 second spacecraft spin period.

However, we note that SWE measurements are not synced to the spacecraft spin, but will instead be time-based measurements with the exact timing based on the 1PPS signal dependent on the actual spacecraft spin period. The IMAP spin rate is planned to be between 3.9 – 4.1 Hz, giving a nominal spin period between 14.6 – 15.4 seconds. The SWE quarter cycle length is configurable in the FSW, and will be set to be slightly longer than a spacecraft spin period, to ensure full measurement over all spin angles for each energy step.

A SWE measurement cycle includes measurements at 24 energies (corresponding to 24 ESA voltage levels) at each of 30 spin angles. Measurements are made at a subset of these energy-angle bins in each quarter cycle. As illustrated in Figure 5, in each quarter cycle measurements are made at 6 different ESA voltage levels for each spin angle, with one set of 6 ESA levels in the odd-numbered spin angles and a different set of 6 ESA levels in the even-numbered spin angles. For each ESA step, that is for each energy-angle measurement, counter values are accumulated for each of the 7 CEM detectors, giving measurements as a function of energy, spin angle, and polar angle (CEM). Over the course of a full cycle, all ESA voltage steps are used at all spin angles. Several 24-element ESA tables are stored in the CDH MRAM, with one selected before acquisition. The 720 ESA steps used in each full cycle are precomputed

before acquisition begins. Every quarter cycle (nominally 15 seconds), the FSW transmits the science data product, the counter values as a function of energy, spin angle, and polar angle, to the spacecraft.

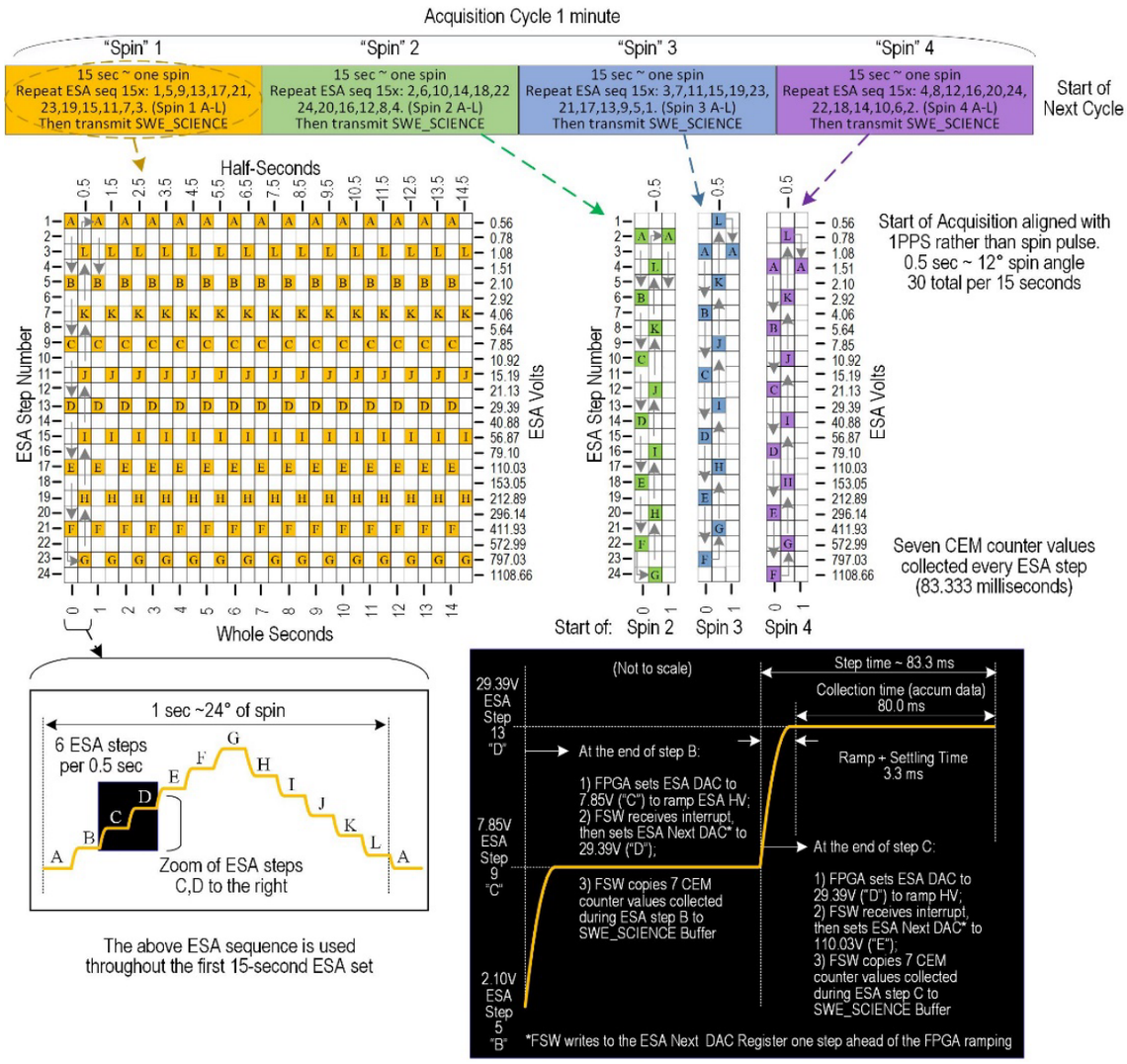


Figure 5: SWE science data acquisition timing and flow.

3.3 Data Products

SWE data products vary by operating mode, with science data collected only in HVSCI mode. The science data, consisting of electron counts as a function of detector, spin sector, ESA voltage, and time are the focus of this document. Additional data products include housekeeping data such as voltage and current monitors, and occasional diagnostic data such as flight software reports and memory dump data.

3.3.1 Science Data

As described in Figure 5, SWE science data are measured over 4 quarter-cycles, each nominally covering one 15-sec spacecraft spin, and in practice covering slightly more than one spin. A full SWE data product covering the full range of energies and angles is formed by combining data from four quarter-cycles. Figure 6 shows the SWE data processing pipeline, as defined in the IMAP Science Data Management Plan. The SWE Level-1A product consists of these raw counts as a function of voltage step and spin angle sector. Level-1B data are generated by converting from counts to count rate based on the data acquisition period from the housekeeping data.

Generation of Level 2 data involves incorporation of the instrument geometric factors to convert count rates to physically meaningful intensity or phase space distribution functions. In addition, instrument calibrations are used to convert ESA voltages to particle energies, and spacecraft ephemeris information is used to convert spin sectors to spacecraft spin angles in a physically meaningful coordinate system.

Level 3 data products incorporate magnetic field observations from the MAG instrument to calculate the pitch angle (particle travel direction relative to the magnetic field) for each individual SWE measurement. Data are then binned by pitch angle to obtain the 3D particle distribution as a function of energy, pitch angle, and phase angle. In addition, the ion plasma velocity calculated from the SWAPI instrument is used to transform the SWE measurements into the solar wind reference frame. SWAPI moments (N, V, T) are also used together with SWE measurements for understanding of the spacecraft potential, and in the calculation of electron moments from the SWE measurements.

3.3.2 Housekeeping Data

SWE housekeeping data include

- Operation mode
- CDH monitors
- Low voltage monitors
- High voltage monitors
- High voltage settings (enable/disable, limit plug status, range)
- Temperature sensors
- FEE thresholds
- Stim pulse status

Processing of housekeeping data is done as part of Level 1 processing, and includes decommutation of the CCSDS packets, expansion of each housekeeping parameter to the appropriate length in bytes, and conversion from raw units to engineering units.

3.3.3 Engineering Mode Data

In engineering mode (HVENG or LVENG), SWE counts from each of the 7 CEM detectors are recorded every 1 second (SWE_CEM_RAW data). As noted above, these data are primarily used for ground testing and during on-orbit commissioning. Engineering data from flight require only basic Level 1 processing, in particular decommutation of the CCSDS packets.

3.3.4 In-Flight Calibration Data

In flight, SWE will periodically be commanded via a macro to run a calibration sequence. This calibration consists of setting the ESA to a fixed voltage, then stepping the CEM voltage around the nominal voltage to steps of Vnom - 200 V, Vnom - 100 V, Vnom + 100 V, Vnom + 200 V. These data are then examined on the ground to determine whether the CEM detectors are still operating in saturation, or whether the CEM bias voltage needs to be increased. The calibration sequence is nominally run once per week, although a slower frequency may also be acceptable if required. The telemetry data format for calibration mode data is the same as that for science mode data, so Level 0 and Level 1 processing is the same as for science mode data.

The in-flight calibration data should not be included in the Level 2 or higher science products, but will instead be handled separately. A SWE science team member will be required to examine data on the ground and determine if a CEM bias voltage increase is required. Such increases are expected infrequently, on a time scale of several months to years.

In flight calibration parameters are stored in calibration files with file names of the format: imap_swe_l1b-in-flight-cal_YYYYMMDD_vXXX.csv. For these file names, YYYYMMDD represent the date on which the file should first be used for processing. The version number XXX is nominally 001, but may be increased later in the mission if reprocessing is required. Each file consists of one row of data for each in-flight calibration point, where each row includes the time stamp for the calibration measurement, followed by calibration factors for each of the 7 CEM detectors. All factors are set to 1.0 for times prior to initial SWE instrument commissioning, and at times after commissioning are set to the values determined from the in-flight calibration measurements.

As discussed below, in section 3.4.3, calibrations are applied to the data at each time step, based on linear interpolation of the calibration factors from the two gain sweep tests surrounding the time of each measurement. Thus when a new calibration measurement is added, the filename date is set to the date of the previous in-flight calibration, as a linear interpolation is time is now possible back to the time of the previous calibration measurement. At the time of this writing, to provide quick-look data, the calibration files also include a last line with a time stamp set far in the future and factors which are the same as those from the last measurement. This allows initial L1B and higher processing using the most recent calibration factors, while the calibration filename dates are used to ensure reprocessing will occur once new calibration measurements are available.

The calibration factors are multiplicative factors, by which counts measurements from each CEM are multiplied to account for gain degradation over time. As discussed below (sections 3.4.3 and 3.4.5), these factors are applied during L1A -> L1B processing, and are also applied to i-ALiRT counts prior to combining data from the 7 CEM detectors. We note that i-ALiRT processing necessarily uses the most recent in-flight calibration factors available, as interpolation between data points is of course not possible for real time analysis.

3.3.5 i-ALiRT Data

SWE is part of the IMAP Active Link for Real-Time (i-ALiRT) real time data system. SWE i-ALiRT telemetry products include electron counts from all 7 CEM detectors at all spin angles for a subset of 8 of the 24

energy channels. These channels are selected to cover the suprathermal electron energy range, from 100 – 1000 eV. Processing of the SWE i-ALiRT measurements on the ground will include combination of measurements from four quarter-cycles, followed by identification of peaks in the angular distribution at each energy step. A primary data product will be to identify the presence of unidirectional or counterstreaming strahl beams along the magnetic field direction and characterization of these electron beams. This processing algorithm will be based on a similar algorithm run onboard by the Genesis/GEM instrument. A second data product will consist simply of counts as a function of time at each energy step.

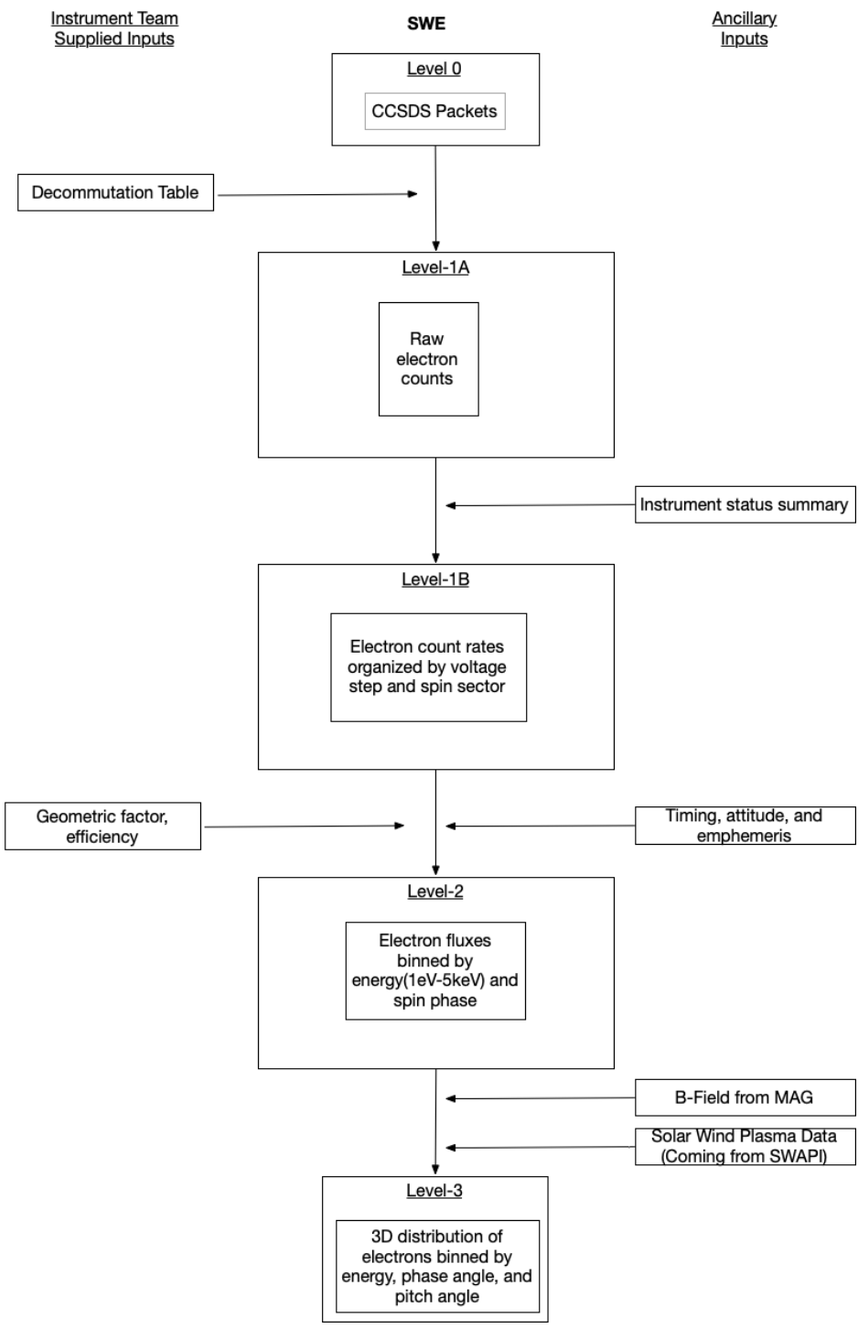


Figure 6: SWE data processing pipeline.

3.4 Data processing

3.4.1 Heritage data processing

Data processing for IMAP/SWE will be heavily based on processing codes from the heritage Ulysses/SWOOPS, ACE/SWEPAM, and Genesis/GEM instruments. The Ulysses/SWOOPS processing codes were written in Fortran. These codes were updated to C for ACE/SWEPAM, with similar codes applied to the Genesis/GEM processing. As the SWEPAM instrument is the only one of these heritage instruments that is still operational, the SWEPAM codes are the most up-to-date and will be used as the basis for the IMAP/SWE processing algorithms.

Like the heritage instruments, SWE makes measurements at 7 polar angles using 7 CEM detectors. However, the number of energy steps has been modified for SWE (increased from 20 to 24), and the energy stepping scheme has also been modified. Like SWE, each of the heritage instruments required several spins to build up a full measurement covering all energy steps. However, the heritage instruments made measurements at contiguous energies in each spin (lowest *n* energies in the first spin, second lowest *n* energies in the second spin, etc.), while SWE covers the full energy range in each spin, with reduced energy and angle resolution. These modifications mean that the SWEPAM code used to combine data from different energies and angles to build up a full measurement will need to be modified for use with SWE data; however the algorithms used to process data from a full measurement can be taken directly from the heritage codes. We note that, while not the baseline plan, SWE flight software does include the ability to select from 8 onboard look up tables to define different energy stepping schemes (including something like the heritage stepping scheme described above), as well as the ability to upload new look up tables if necessary. Data processing described below discusses only the nominal SWE ESA stepping scheme. If another scheme is used, processing code modifications would consist of minor adjustments in sorting the measurements by angle and energy step; these will not be addressed unless deemed necessary later in the mission.

3.4.2 Level 0 to Level 1a Processing

3.4.2.1 Science Data

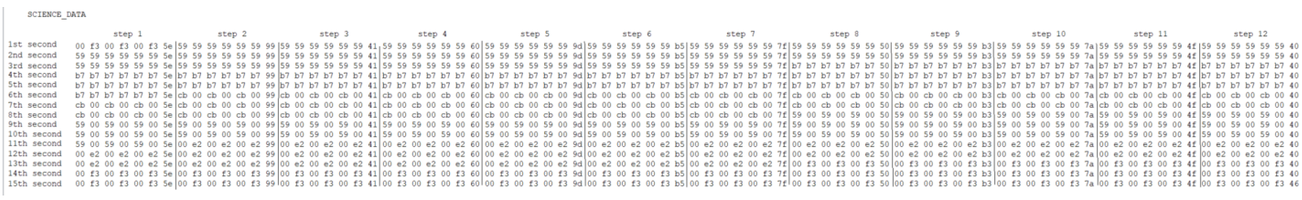
The “SCIENCE_DATA” field of the SWE_SCIENCE telemetry packet holds the science data. It is a 1260-byte exact field that starts on the 32th byte, 0 bit of the packet. It is also the last field before the checksum.

You can think of the 1260 bytes as a 3-dimensional array of:

7 (CEM_COUNTS) * 12 (STEPS_EACH_SECOND) * 15 (SECONDS)

More specifically, the first 7 bytes will correspond to readings of CEM 1 to CEM 7 of the first ESA step of the first second of the quarter cycle. The next 7 bytes will be the 7 CEM readings for the 2nd ESA step of the first second. This repeats until you reach the 12th step of the first second (two spin angles). Then the next 7 bytes will be for the first step of the 2nd second (next two spin angles).

Below is a visual representation of the science data in GSEOS.



This data is compressed data. App FSW applied the compression method used by the SWEPAM instrument of the ACE mission to convert a 16 bit value to 8 bit. This, unfortunately, will lose some of the fidelity of the data.

To decompress the data, please follow these steps with the table below:

1. Represent the 8 bit number in binary. The value represented by the upper 4 bits will be called index, and the value represented by the lower 4 bits will be called multi.

   Bits: | 7 6 5 4 | 3 2 1 0 |

   index | multi

2. Using the index, find the corresponding base and step_size values in the table.
3. Calculate the 16 bit value using the following formula:

   N = base [index] + multi * step_size[index] + (step_size[index] – 1) / 2

   Note: for step_size[index] – 1 divide by 2, we only keep the whole number part of the quotient.

index	base	step_size
0	0	1
1	16	1
2	32	2
3	64	4
4	128	8
5	256	16
6	512	16
7	768	16
8	1024	32
9	1536	32
10	2048	64
11	3072	128
12	5120	256
13	9216	512
14	17408	1024
15	33792	2048

Here is an example:

You have a 8 bit value of 230, which is 11100110 in binary. The upper 4 bits is 1110, which is 14 in decimal, so index is 14. The lower 4 bits is 0110, which is 6 in decimal. So multi is 6.

(You can also represent 230 in Hex format, which is E6. That means index is E (14), and multi is 6.)

So your decompressed 16 bit value will be:

17408 + 6 * 1024 + (1024 – 1) / 2 = 24063

(Note: When we compress, over a thousand numbers can compress down to 230, from 23552 to 24575. Our decompression arrives at the middle of the range).

Decompression of counts data could be done here, or could be part of L1a to L1b processing. Note that for RBSP/HOPE, the decompression was part of L0 to L1 processing.

3.4.2.2 i-ALiRT data

SWE_IALIRT telemetry packet is structured quite differently from the SWE_SCIENCE packet. Here instead of putting all science data in one field, each 8-bit data point has its own field, with its unique field name. So starting from byte 18, bit 0, there are 28 fields representing one second of science data from 4 ESA steps and 7 CEMs. More specifically, the first 4 fields are for the 4 ESA steps of CEM1, and the next 4 fields are for the 4 ESA steps for CEM2, and it goes on until all 7 CEMs are covered.

This data is compressed data. The compression method is exactly the same as used for Science packet. Please refer to the science data section on how to decompress the data.

3.4.2.3 Housekeeping data

The SWE_APP_HK telemetry packet has many data points and each in its own field.

Some of the values need to be converted from raw units to engineering units. Please refer to Appendix A for details on how to convert the values.

Please note for HVPS_ESA_DAC, there will be two different conversion based on whether we are in high range or low range of the ESA voltage.

3.4.2.4 CEM raw data

The SWE_CEM_RAW telemetry packet is fairly simple. Starting from byte 14, bit 0, there are 7 consecutive fields each 4 bytes long representing the counts from CEM1 to CEM7.

There is no data compression.

3.4.2.5 Other data

Other telemetry packets such as those for autonomy, static housekeeping, event messages, and memory dump should also be decommutated at this level and they may also aid in the production of higher level science products.

3.4.3 Level 1a to Level 1b Processing

Level 1a to Level 1b processing for SWE consists of organizing the counts by voltage step and spin sector. As the counts have already been decompressed as part of Level 1a processing, the steps incorporate ground calibration measurement of the electronics deadtime, conversion from counts to counts rate (Hz) based on the data acquisition period, and, when appropriate, incorporation of inflight calibration.

Deadtime correction: L1a to L1b processing will also include deadtime correction of the counts. The deadtime algorithm is given below, as a function in C code. Note that this model assumes a non-paralyzable model of the detector, with a dead time for this instrument of 1.5e-6 seconds. The dead time for SWE will be based on the SWE electronics, with the actual value defined during instrument calibration. In this algorithm, *tsampl* is the sampling time for each measurement.

```
int deadtime_e(double c[N_ENERGIES][N_CEMS][N_PHI],double
ccounts[N_ENERGIES][N_CEMS][N_PHI],double tsampl)
{
/* Correct counts for dead time
*
*  Non-paralyzable model: n = m/(1-mt)
*   c[N_ENERGIES][N_CEMS][32] = array of raw counts (counts/sampling interval)
*   ccounts[N_ENERGIES][N_CEMS][32] = array of corrected counts (counts/sampling interval)
*   dead time = XXXXX sec
*
*/

int i,j,k;
double correct;
double r,s,t;

for (i=0; i<N_ENERGIES; i++){
  for (j=0; j<N_CEMS; j++){
    for (k=0; k<N_PHI; k++){
      correct = 1.0 - ((1.5e-6)*c[i][j][k]/tsampl);
      /* arbitrary x10 cutoff */
      correct = (correct < 0.1) ? 0.1 : correct;
      ccounts[i][j][k] = c[i][j][k]/correct;
    }
  }
}
}
```

Conversion from Counts to Count Rate (counts/second): At this point, counts can be converted from counts to count rate, simply by dividing the corrected counts by the accumulation time for each measurement (*tsampl*, in the above code fragment). For SWE the nominal accumulation time is 80 milliseconds (see Figure 5); this value will be set in flight based on the actual spacecraft spin period, and will be available in the SWE science packet data (variable ACQ_DURATION, in units of microseconds),

and will be part of the “Instrument Status Summary” data. The accumulation time can be changed in flight, but changes are expected to be infrequent, with changes made only as required in response to changes in the spacecraft spin rate.

Apply calibrations based on in-flight calibration: L1a to L1b processing will include incorporation of time-dependent calibrations based on in-flight calibrations. The in-flight calibrations consist of varying the bias voltage to the CEM detectors to determine if the nominal bias voltage is still appropriate, or if the bias voltage needs to be increased. Between voltage increases, data from these gain sweeps are used to determine the CEM gain at the operating bias voltage relative to the gain at the optimal voltage. These factors are applied to the flight data to given consistent calibration over time.

The electron_cal() function reads in the file of calibration factors over time, and performs a linear interpolation between calibration points to determine the appropriate factor to apply for measurements at each time step.

```
_/*
   ** APPLY ELECTRON CALIBRATION FACTORS
   **
   ** These factors are used to account for changes in gain with time.
   **
   ** They are derived from the weekly electron calibration data.
   ** The procedure is to compare the counts obtained at the operating CEM
   ** level (step 2 of the cal run) to the counts are the next higher CEM
   ** level (step 3 of the cal run).  We assume that the next higher
   ** level is correct, and use this ratio to scale the counts.
   **
   */

   cal_factor = electron_cal(mystruct.sct);

   for (i=0; i<N_ENERGIES; i++){
    for (j=0; j<N_CEMS; j++){
          for (k=0; k<N_PHI; k++){
             counts[i][j][k] = ccounts[i][j][k] * cal_factor[j];
          }
    }
   }

/*****************\
** electron_cal  **  given an S/C time, return interpolated electron cals
\*****************/
float *
electron_cal(uint32 sct)
{
  int i;
  static int last_i;                    /* value of i at previous iteration */
```

```
 static float factor[7];

 /*
 ** First time through?  Read in the calibration data
 */
 if (cal == NULL) init_electron_cal();

 /*
 ** Iterate over all points, until we find ourselves within this range.
 **
 ** When we do, return a linear interpolation of the factors at the
 ** two measured points.
 **
 ** NOTE: since the cal data file is in sequential order, and the only
 ** code that invokes us also does so in sequence, we can optimize a
 ** step by preserving last_i and assuming we will never be invoked for
 ** a time prior to the last one.
 */
 for (i=last_i; i < npoints-1; i++){
   if (cal[i].sct <= sct  &&  sct < cal[i+1].sct) {
     int j;
     int run = cal[i+1].sct - cal[i].sct;
     int tdif= sct         - cal[i].sct;

     last_i = i;

     for (j=0; j<7; j++) {
           float slope = (cal[i+1].factor[j] - cal[i].factor[j]) / run;

           factor[j] = cal[i].factor[j] + slope * tdif;
     }
     return factor;
   }
 }

 printf("cannot extrapolate beyond last cal\n");
 exit(1);
}
```

3.4.4 Level 1b to Level 2 Processing

SWE Level 1b to Level 2 processing consists of converting the counts values to physical phase space distribution or intensity units, and organizing the data by energy step, polar angle, and spin phase.

Calculation of particle energy: The particle energy measured at each step is determined from the voltage applied to the electrostatic analyzer (ESA) plates. The ratio of measured energy to applied

voltage is referred to as the analyzer constant k = E/V, and is determined from ground calibration. This value will be stored in a calibration data file, where it can be read by the processing code. The particle energies are required for calculation of the intensity or phase space density.

Calculation of polar angle: As each CEM detector is oriented at a given angle relative to the spacecraft spin axis, the polar angle is the same for all measurements by a given detector. The central detector points outward perpendicular to the spacecraft spin axis. The other detectors point at nominally +/-21°, +/-42°, and +/-63° relative to this detector.

Conversion from counts to phase space density (fv): This step involves application of the instrument geometric factors, as determined from ground calibrations. The geometric factors are constant over time, with time variations in the detector gains applied in Level 1b processing, as described above. In this heritage code, the geometric factors are hard-coded into the routine; geometric factors can also be stored in a calibration data file to be read by the processing routine. The geometric factors below are the nominal SWE geometric factors for the 7 CEM detectors (1-7) as of October 2025, and may be refined by further analysis.

```
/* Nominal SWE geometric factors
g = {424.4e-6, 564.5e-6, 763.8e-6, 916.9e-6, 792.0e-6, 667.7e-6, 425.2e-6};

int fspace(double ccounts[N_ENERGIES][N_CEMS][N_PHI],double
energy[N_ENERGIES][N_CEMS][N_PHI],double fv[N_ENERGIES][N_CEMS][N_PHI],double tsampl,double
g[N_CEMS])
{

/*  Calculate phase space density fv in units of s^3/cm^6
*
*   fv(v,theta,phi) = 2*C(E,theta,phi)/(G*v^4*tau)
*
*    C = corrected counts
*    E = electron energy, in eV
*    v = electron speed, computed from energy, in cm/s
*    tau = sampling time, in s
*    G = geometric factor, in (cm^2 * ster)
*/

int i,j,k;
double vto4;
double gg[N_CEMS];

/* Ace geometric factors
g = {255.6e-6, 511.0e-6, 633.4e-6, 659.5e-6, 733.5e-6, 540.3e-6, 272.9e-6};
*/
 gg[0] = 255.6e-6;
 gg[1] = 511.0e-6;
```

```
  gg[2] = 633.4e-6;
  gg[3] = 659.5e-6;
  gg[4] = 733.5e-6;
  gg[5] = 540.3e-6;
  gg[6] = 272.9e-6;
for (i=0; i<N_ENERGIES; i++){
  for (j=0; j<N_CEMS; j++){
    for (k=0; k<N_PHI; k++){
      if (ccounts[i][j][k] < 0) {
        fv[i][j][k] = 0.0;
      }
      else {
        vto4 = 1.237e31*energy[i][j][k]*energy[i][j][k];
        fv[i][j][k] = 2*ccounts[i][j][k]/(gg[j]*tsampl*vto4);
      }
    }
  }
}
for (i=0; i<N_ENERGIES; i++){
  for (k=0; k<N_PHI; k++){
    if (k % 2 == 0) {
      fv[i][0][k] = 0.5*fv[i][0][k+1];
      fv[i][6][k] = 0.5*fv[i][6][k+1];
    }
    else {
      fv[i][0][k] = 0.5*fv[i][0][k];
      fv[i][6][k] = 0.5*fv[i][6][k];
    }
  }
}
}
```

Calculation of Electron Intensity In the heritage code, electron distributions are always saved in units of phase space distribution rather than intensity. We note that distribution function f (units s^3 cm^{-6}) can easily be converted to differential intensity (units $1/(cm^2$ s ster eV)). Intensity j (equivalent to number flux, not to energy flux) has units of $1/(cm^2$ s eV ster), and is calculated by: j = C/(G * E * tau), where C is the measured counts, E is the particle energy in eV, G is the geometric factor with units of (cm^2 ster eV/eV), and tau is the measurement interval in seconds. Combining this equation with the definition of phase space distribution fv, above, gives the conversation from fv to j:

$$j(v, \theta, \phi) = fv(v, \theta, \phi) * v^4 / (2.0 * E),$$

where v is the particle velocity in cm/s and E is the particle energy in eV. Since particle velocity and energy are related by $E = 0.5 * m * v^2$, where m is the particle mass (9.10938×10^{-31} kg for electrons), conversion from fv in units of (cm^3 cm^{-6}) to j in units of $1/(cm^2$ s eV ster) becomes:

$$j(v, \theta,\phi) = 6.187 \times 10^{30} * fv(v, \theta, \phi) * E$$

where E is the electron energy in units of eV.

Calculation of spin phase: As described above, SWE measurements are made at 30 spin angles in each quarter-cycle measurement. Because the SWE measurements are not synced to the spacecraft spin, the physical angles for each measurement will vary over time. In Level 1 SWE data products, the data are organized by the spin sector of each measurement, which is simply an index from 1-15. As part of Level 2 processing, the spin sectors are converted to spin angles of the spacecraft by combining SWE timing information with knowledge of the spacecraft spin from spacecraft ephemeris data.

As noted above, the SWE ESA voltage is nominally stepped every 83.333 ms. This value is setable in flight, and includes a high voltage settling time (SETTLE_DURATION, nominally 3.333 ms) combined with a data acquisition period (ACQ_DURATION, nominally 80.0 ms). We note that in the SWE L1 data files these parameters are both given in units of microseconds. The start time of the first data collection interval of a SWE quarter-cycle is given by the MET counters described above, the coarse time ACQ_START_COARSE giving the seconds in mission elapsed time of the acquisition start time (in units of seconds) and the fine time ACQ_START_FINE giving the microseconds within that second (in units of microseconds). This start time represents the beginning of the first data acquisition period, after the first settling time. Determination of the start times of the subsequent 179 measurements within the quarter cycle is thus given by:

sci_step_acquisition_time_sec = ACQ_START_COARSE + ACQ_START_FINE / 1000000 +
(step * (ACQ_DURATION + SETTLE_DURATION) / 1000000)

To obtain the middle of each acquisition period then simply requires adding an additional half of a data acquisition period:

sci_step_acquisition_middle_ time_sec = ACQ_START_COARSE + ACQ_START_FINE / 1000000 +
(step * (ACQ_DURATION + SETTLE_DURATION) / 1000000) +
(ACQ_DURATION / 1000000) / 2

To facilitate comparison with other IMAP instruments, required for Level 3 processing, the spin phase angles will be calculated in despun spacecraft coordinates.

Organization of SWE data by Energy and Spin Phase: The last step of SWE Level 2 processing is to sort the calculated phase space densities or intensities by energy and spin phase. As described in Figure 5, measurement in energy and spin angle is complex, with a full measurement built up over multiple spacecraft spins. To simplify analysis of the data, the SWE data at this stage are sorted by energy and spin angle, so that the resulting distribution is organized in order of monotonically increasing energy and angle. As the SWE data acquisition is not synced to the spacecraft spin, measurements in each SWE quarter-cycle are obtained at different spin angles. Combining the four quarter-cycles thus requires binning the data into spin angle bins. For Level 2, these bins will be defined to be 12 degrees wide, in despun spacecraft coordinates. Binning will be determined by the central spin phase angle of each spin bin. Data will remain sorted by ESA voltage step and CEM detector, with Level 2 data including the energies corresponding to the 24 ESA voltage steps and the polar angles corresponding to each CEM detector. The primary Level 2 data product is a matrix every full SWE cycle (nominally 1 minute) of electron phase space distribution with size (7 CEMs x 24 energy steps x 30 spin phase bins), and the same matrix with units of electron intensity.

In addition, to facilitate Level 2 to Level 3 processing, the SWE Level 2 data set will also include phase space distribution and intensity matrices for the original measurements (7 CEM detectors x 180

energy/spin phase bins per quarter-cycle), together with the time stamps and spin phase angles for each individual measurement. These data will allow calculation of the electron pitch angle for each individual measurement, leading to the most accurate pitch angle distributions.

3.4.5 i-ALiRT Processing

A main SWE i-ALiRT product is the identification of bidirectional electron streaming, based on the algorithms developed for onboard identification during the Genesis mission [Neugebauer et al., 2003]. The i-ALiRT parameter BDE will consist of a single value at each time step, with a value of 1 indicating counterstreaming electrons and a value of 0 indicating nominal unidirectional electron flow. These bidirectional or counterstreaming electrons are typically a signature of a coronal mass ejection, in which the interplanetary magnetic field is connected to the Sun at both ends. We note that on occasion counterstreaming electrons can also result from connection of the interplanetary magnetic field to the Earth's bow shock; thus counterstreaming is not a definitive CEM signature but must be considered in the context of other measurements.

As noted, above, the SWE i-ALiRT data consist of electron counts in 8 energy channels from all 7 CEM detectors at all spin angles. These data are a subset of the SWE Science data discussed above, including energies between 100 – 1000 eV, in the suprathermal electron range where we expect particle distributions to be driven by the interplanetary magnetic field topology. Specifically, for the nominal stepping table shown in Figure 5, the SWE i-ALiRT packet includes ESA steps 12-19, indicated by the

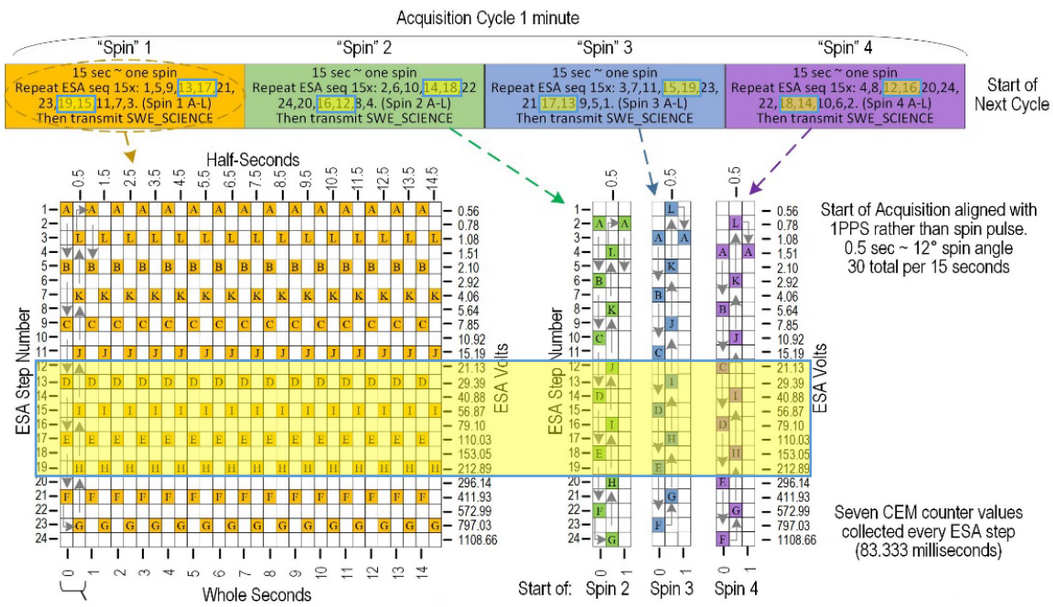


Figure 7: SWE science data acquisition (from Figure 5), with i-ALiRT data indicated by the yellow box.

yellow box in Figure 7. Each (nominal) 1 second i-ALiRT packet contains 28 measurements, including data from all 7 CEMs at 4 ESA steps (4 energies) with 2 energies measured in a first spin angle bin, e. g. for CEM 0: SWE_IALIRT.ELECTRON_COUNTS_SPIN_I_POL_0_E_0J and

SWE_IALIRT.ELECTRON_COUNTS_SPIN_I_POL_0_E_1J, and the other 2 in a second spin angle bin (e. g. for CEM 0: SWE_IALIRT.ELECTRON_COUNTS_SPIN_I_POL_0_E_2J and SWE_IALIRT.ELECTRON_COUNTS_SPIN_I_POL_0_E_3J). A full i-ALiRT data set is obtained over nominally 1 minute, including data from 4 SWE quarter-cycles; this timing is the same as for the SWE Science data.

As SWE i-ALiRT data are simply a subset of the Science data set, processing of i-ALiRT data begins with the same steps defined above for Level 0 to Level 1 processing of the SWE Science data. Following data decommutation, the i-ALiRT data (the 28 measurements) must first be decompressed from 8 bit to 16 bit values, as defined in Section 3.4.2.1. Next, the deadtime correction must be applied, as defined in Section 3.4.3.

For i-ALiRT calculations, we do not need to convert counts to phase space distribution or intensity, but do need to normalize the counts based on the geometric factors for each CEM detector. The geometric factors are determined from calibration measurements combined with SIMION modeling of SWE, and do not change over time. However, as the instruments age results from in-flight calibrations will need to be incorporated into the analysis in the same way as for the Science data, as discussed in Section 3.4.3. The in-flight calibration factors will be the same for i-ALiRT and Science data analysis, but as noted above the i-ALiRT analysis will necessarily use the most recent calibration factors as interpolation between two in-flight calibrations is not possible in real time. In practice, this simply adds an additional factor (*cal_factor* in the code fragment below) to the analysis. At launch, *cal_factor* = 1 for all 7 CEMs. We note that for a full nominal 1-minute i-ALiRT data set, N_ENERGIES=8 and N_PHI = 30. Again, single (1 second) i-ALiRT packet includes data from 4 energies each in one of two spin angle bins. The geometric factors below are the nominal SWE geometric factors for the 7 CEM detectors (1-7) as of October 2025, and may be refined by further analysis.

```
/* Nominal SWE geometric factors
g = {424.4e-6, 564.5e-6, 763.8e-6, 916.9e-6, 792.0e-6, 667.7e-6, 425.2e-6};
*/
  gg[0] = 435.0e-6;
  gg[1] = 599.0e-6;
  gg[2] = 808.0e-6;
  gg[3] = 781.0e-6;
  gg[4] = 876.0e-6;
  gg[5] = 548.0e-6;
  gg[6] = 432.0e-6;
for (i=0; i<N_ENERGIES; i++){
   for (j=0; j<N_CEMS; j++){
      for (k=0; k<N_PHI; k++){
        if (ccounts[i][j][k] < 0) {
          fv[i][j][k] = 0.0;
        }
        else {
          norm_counts[i][j][k] = ccounts[i][j][k] * cal_factor[j] / (gg[j]
        }
      }
```

```
  }
}
```

Because SWE measurements are not synced to the spacecraft spin, SWE spin angle bins (numbered 1-30) view different physical angles in each SWE quarter-cycle. As the spacecraft ephemeris data required to convert SWE spin angle bins to physical angles is not available for i-ALiRT processing, SWE i-ALiRT processing will be performed separately for each quarter-cycle. While the intent is that a SWE quarter-cycle be very close to a spacecraft spin period, we cannot count on these two times being sufficiently close to each other than the angular different can be ignored. Processing by quarter-cycle will provide consistent results, regardless of the relative durations of a spacecraft spin period and a SWE quarter-cycle. We note that if a SWE quarter-cycle is sufficiently longer than a spacecraft spin, it may be necessary to leave out the last azimuthal step of each quarter cycle in the analysis described below. However, the intent is that a SWE quarter-cycle be very close to a spacecraft spin, so assessment of the need for modified analysis will depend on the length and stability of the spacecraft spin period as observed in flight.

From Figure 7, it can be seen that 2 quarter-cycles are required for i-ALiRT measurements at all 8 energy steps. Since one criterion for defining the SWE i-ALiRT bidirectional electron parameter (see below) will be the identification of counterstreaming electrons over a range of energies, this means that the appropriate time cadence for SWE i-ALiRT data will be 30 seconds.

The first step in searching for counterstreaming electrons looks for an asymmetry in the counts as a function of spin angle (code fragment below this paragraph). For this search, the normalized counts are summed over all CEMs, as below, giving counts from each packet as a function of energy and azimuthal angle (*pol_summed_counts*). At each of the 4 energies in a quarter-cycle, we then look for the azimuthal angle with the maximum counts, A_{peak}. This direction is assumed to be the magnetic field direction, and we then look 90° (A_{90}) and 180° (A_{180}) away from this angle. The expectation is that for unidirectional flow counts at A_{90} and A_{180} will be lower than at A_{peak}, while for bidirectional flow counts at both A_{peak} and A_{180} will be larger than at A_{90}.

```
for (i=0; i<N_ENERGIES; i++){
  for (j=0; j<N_CEMS; j++){
    for (k=0; k<N_PHI; k++){
        pol_summed_counts[i][k] =pol_ summed_ccounts[i][k] + norm_counts[i][j][k]
    }
  }
}
```

Data are next analyzed separately for each of the 4 energies (ESA steps) in the quarter-cycle. Within a given quarter-cycle, data for a given ESA step will be measured in either odd-numbered or even-numbered spin angle bins. At each ESA step, we first identify the azimuthal angle A_{peak} with the maximum number of counts C_{peak}. C_{180} is then identified as the counts in the azimuthal bin A_{180} at an angle 180 degrees away from A_{peak}, that is, 15 bins away. C_{90} is the counts in the azimuthal bin 90 degrees away from A_{peak}, that is, the average of bins X and Y. So, for example, if peak counts are

observed in azimuthal bin A_{peak} = 5 (of 1-30, green), A_{180} would be the average of azimuthal bins 19 and 21 (blue), and A_{90} (purple) would be the average of azimuthal bins (11 and 13) and (27 and 29), as shown in the line below.

1 3 5 7 9 11 13 15 17 19 21 23 25 27 29

For a quarter-cycle in which even-numbered bins are measured, an example is given below. In this example, peak counts are observed in azimuthal bin A_{peak} = 10 (green). A_{180} is thus the average of azimuthal bins 24 and 26 (blue), and A_{90} (purple) would be the average of azimuthal bins (16, 18) and (2, 4).

2 4 6 8 10 12 14 16 18 20 21 24 26 28 30

In general, then, if A_{peak} = N, A_{180} is the average of N+14 and N+16, and A_{90} is the average of N+6, N+8, N+22, and N+24 (all mod 30). The minimum counts C_{min} is then defined as the minimum of C_{180} and C_{90}. Bidirectional electron streaming at a given ESA step is identified if both C_{peak}/C_{min} and C_{180}/C_{min} exceed a threshold level. The threshold level will be refined based on flight observations, but the initial value (based on Genesis experience) is a threshold of 1.75.

Depending on the direction of the interplanetary magnetic field, it is possible that counterstreaming electrons could be observed in the polar angle direction rather than the azimuthal angle direction. Thus if counterstreaming is not observed in the above analysis, a second search will be done in the other dimension. This analysis again begins with the *norm_counts* variable calculated above, however this time counts are summed over azimuthal angle rather than CEM, giving *az_summed_counts* that are a function of energy and CEM.

```
for (i=0; i<N_ENERGIES; i++){
  for (j=0; j<N_CEMS; j++){
    for (k=0; k<N_PHI; k++){
        az_ summed_counts[i][j] = az_summed_ccounts[i][j] + norm_counts[i][j][k]
    }
  }
}
```

At each energy, C_{min} is then defined as the average of the counts in CEMs 3, 4, and 5. Bidirectional electron streaming at a given ESA step is identified if both C_{CEM1}/C_{min} and C_{CEM7}/C_{min} exceed a threshold level. Again, the initial threshold value is 1.75 and this parameters will be refined based on flight observations.

This procedure will be performed for two SWE quarter-cycles (30 seconds of i-ALiRT data) to give results at all 8 SWE i-ALiRT energy steps. The bidirectional electron parameter BDE will then be set to 1 if bidirectional electrons are identified in at least a minimum number of ESA steps, and set to 0 if the threshold conditions are not met for a sufficient number of ESA steps. The number of ESA steps will be refined based on flight observations, with an initial value of 3 of the 8 ESA steps.

A second SWE i-ALiRT data product is simply the normalized counts as a function of time. For this parameter counts at each ESA step will be summed over both azimuthal and polar angles, giving counts as each ESA step as a function of time (*summed_counts*). For consistency with the bidirectional electron parameter, this data product will have a 30 second cadence, including data from 2 SWE quarter-cycles. These counts allow estimation of the time variability of the suprathermal electrons and of the energy distribution of these electrons.

```
for (i=0; i<N_ENERGIES; i++){
  for (j=0; j<N_CEMS; j++){
    for (k=0; k<N_PHI; k++){
       summed_counts[i] = summed_ccounts[i] + norm_counts[i][j][k]
    }
  }
}
```

3.4.6 Level 2 to Level 3 Processing

SWE Level 2 to Level 3 processing consists of combining the SWE measurements with magnetometer measurements from the MAG instrument to calculate the electron pitch angle of each measurement, and then binning the data to obtain the distribution of electrons as a function of pitch angle and phase angle. Ion velocities obtained from the SWAPI instrument are used to transform the SWE electron distributions into the solar wind reference frame. Pitch angle calculations require that the SWE and MAG data be in the same reference frame. Here we will use despun spacecraft coordinates for the calculations.

Moments of the electron distribution (density, velocity, temperature) are also calculated at this level. However, because charging of the spacecraft makes it difficult to accurately measure very low energy electrons, we will ultimately assume that the bulk electron velocity is equal to the proton velocity, and that the electron density is equal to the ion density, both obtained from SWAPI calculations, and use the SWE moments analysis only to provide electron temperatures and heat flux.

Level 3 processing starts from the SWE Level 2 data files. In particular, Level 3 processing will use Level 2 variables which contain the electron phase space distributions as a function of energy, polar angle (CEM) and spin angle (SWE azimuthal angle bin) in despun spacecraft coordinates for each individual nominal 80 millisecond measurement (7 CEM detectors x 24 ESA voltage x 30 spin angle bins per SWE full cycle). The Level 2 files also include the energy corresponding to each ESA voltage step, and the polar angle corresponding to each CEM detector. For pitch angle calculations, starting from this full data set will allow calculation of pitch angle using the magnetic field vector measurement from MAG during each nominal 80 millisecond SWE data acquisition period.

Determination of spacecraft potential and core/halo break point: The first step in the SWE Level 3 processing is to determine the spacecraft potential. This is done by twice fitting two Maxwellian distributions to the 1D (averaged over both angles) phase space distribution as a function of energy. First, a 2-Maxwellian fit at energies below 30 eV to determine the spacecraft potential, and then a 2-Maxwellian fit at energies from 30 – 400 eV to identify the break between the thermal (core) and

suprathermal (halo) electrons. (In contrast, the code used for the heritage ACE/SWEPAM instrument performs a nonlinear least-squares fit of 3 Maxwellians to determine the two break points.) Steps include:

- Calculate weights for fit
- Calculate 2D energy spectrum (log(fv) vs E) for fits
- Perform fits to calculate spacecraft potential and core-halo break
  - Fits are performed using phase space distributions averaged over 7 full SWE measurements (~7 minute running average)
  - If no potential break is observed (spacecraft potential below the minimum SWE energy), set the potential to 2.5 V
  - Refine fits based on phase space distributions adjacent to the fitted break point
  - If either fit fails, fall back to a smoothed-spline technique using maximum curvature to determine breaks
- Use spacecraft potential to correct energies (see below)

We note that the break point finding algorithm has been optimized for times when the Ultra deflector voltage is at the nominal 3500 V level. The algorithm may fail at times when the Ultra deflectors are turned off, and a flag is added to the L3 data to indicate these times. In addition, the algorithm can fail at times when the spacecraft potential drops below the minimum SWE energy of ~3 eV. Further development will be required to determine a break point finding method for these times; any improvements will be incorporated in later data releases as appropriate.

Pitch Angle Calculation: The next step in the SWE Level 3 processing is to calculate the pitch angle distribution, including calculation of both the pitch angle and the gyrophase angle. This calculation requires knowledge of the spacecraft potential (above) of the magnetic field vector from the MAG instrument in the same coordinates as the SWE measurements, and of the solar wind velocity from the SWAPI instrument in the same coordinates. Calculations will be performed in the despun spacecraft coordinate frame, as both SWE and MAG data will be available in this frame. Steps in the pitch angle calculation include:

- Correct energies based on spacecraft potential
- Calculate velocity vector and energy in the solar wind reference frame for each individual measurement
- Calculate pitch angle and gyrophase angle for each individual measurement
- Define energy and pitch angle bins
  - The algorithm uses 20 9-degree wide pitch angle bins
  - The distribution is determined at the 24 nominal SWE measured energies.
  - Although not part of the heritage code, also define gyrophase angle bins here. As of this writing, data are binned into 24 15-degree-wide bins.
- Fit distribution as a function of energy for each pitch angle bin; use fit parameters to determine distribution at selected energies (nominal measurement energies)
  - If also sorting by gyrophase, fit for each pitch angle / gyrophase angle bin combination. Note that, as this calculation was not part of the heritage code, there may not be

sufficient data for this calculation as a full SWE measurement consists of 7 * 30 = 210 measurements at each energy step and we are binning into 240 pitch angle / gyrophase bins. It may be necessary to combine measurements over a longer time interval (say for example 5-10 full SWE cycles, roughly 5-10 minutes) to provide sufficient data for gyrophase binning. Again, the details will be investigated for a future data release.

- Integrate pitch angle distribution to obtain the 1D (energy) spectrum
- Also integrate the two halves of the distribution separately (pitch angles 0-90 and pitch angles 90-180 degrees). Use these to identify distributions “in” and “out” from the Sun, where “out” is defined as the direction with the maximum phase space distribution.

Moments Calculation: The final step in the SWE Level 3 processing is the calculation of moments of the distribution, including electron density, velocity, temperature, and heat flux. In the heritage ACE/SWEPAM code, the moments are calculated in two different ways, first by fitting a Bi-Maxwellian distribution to the measured electron distribution, and second by integration of the measured distribution. Moments are calculated separately for the thermal (“core”) and suprathermal (“halo”) components of the distribution, as well as over the full measured electron energy range (“total”). We note that since SWE measurements are made in discrete energy bands, the measurement is unlikely to extend down to zero energy, which would be required for accurate calculation of the electron density. To address this limitation, the moments integrals, which are likely more accurate as they do not assume a spectral form, are corrected using the fitted moments to fill in the lowest energy end of the electron distributions. Steps in the moments calculation include:

- Find S/C potential and Core/Halo break
  - For SWE, this was done previously as part of the pitch angle calculations
- Correct energies based on S/C potential
  - For SWE, this was done previously as part of the pitch angle calculations. Note that measurements are not transformed to the solar wind reference frame at this stage.
- Core moments Bi-Maxwellian fits (N, V, T, Q)
  - Setup
  - Linear regression fit
  - Calculate moments
  - Repeat with one fewer points if results bad
  - Convert to RTN coordinates
- Halo moments Bi-Maxwellian fits (N, V, T, Q)
  - Setup
  - Linear regression fit
  - Calculate moments
  - Repeat with one fewer points if results bad
  - Convert to RTN coordinates
- Core moments integrals (N, V, T, Q , correct based on fits)
  - Perform integration
  - Scale density based on fits
  - Rotate V to RTN coordinates

  - Calculate Core T eigenvalues & eigenvectors and select primary
  - Rotate temperature to RTN
  - Rotate temperature to magnetic field coordinates, calculate Tpar & Tperp
- Halo moments integrals (N, V, T, Q , correct based on fits)
  - Perform integration
  - Scale density based on fits
  - Rotate V to RTN coordinates
  - Calculate T eigenvalues & eigenvectors and select primary
  - Rotate temperature to RTN
  - Rotate temperature to magnetic field coordinates, calculate Tpar & Tperp
- Total moments integrals (N, V, T, Q)
  - Perform integration
  - Rotate V to RTN coordinates
  - Calculate T eigenvalues & eigenvectors and select primary
  - Rotate temperature to RTN
  - Rotate temperature to magnetic field coordinates, calculate Tpar & Tperp
- As noted in the above bullets, for all moments the results are converted to RTN coordinates, the primary temperature components are determined, and the integrated temperature components parallel/perpendicular to the magnetic field B are determined using the B field from MAG
- Calculate 1D (energy) distribution, summed over all angles

Appendix A: Telemetry packet conversions

We use algebraic expressions to calculate values in engineering unit based on raw units.

x represent the value in raw unit. * is muliplication

x**2 means x to the 2nd power, and x**3 means x to the third power, etc.

Science packet

SPIN_PHASE	(0.005493 * x)
SPIN_PERIOD	(0.00032 * x)
THRESHOLD_DAC	(0.001221 * x)

App Housekeeping packet

HVPS_CEM_DAC	(1.025641 * x)
THRESHHOLD	(0.001221 * x)
HVPS_VBULK	(0.51282 * x)
HVPS_VCEM	(1.34616 * x)
HVPS_VESA	(0.38462 * x)
HVPS_VESA_LOW_RANGE	(0.0078526 * x)
HVPS_ICEM	(0.064103 * x)
FEE_TEMP	(-450.33825359217) + (2.192767900136 * x) + (-0.00446557629080586 * x**2) + (4.89958700689258E-06 * x**3) + (-2.96758414518E-09 * x**4) + (9.3586789E-13 * x**5) + (-1.1994E-16 * x**6)
	(-450.33825359217) + (2.192767900136 * x) + (-0.00446557629080586 * x**2) + (4.89958700689258E-06 * x**3) + (-2.96758414518E-09 * x**4) + (9.3586789E-13 * x**5) + (-1.1994E-16 * x**6)
	(-450.33825359217) + (2.192767900136 * x) + (-0.00446557629080586 * x**2) + (4.89958700689258E-06 * x**3) + (-2.96758414518E-09 * x**4) + (9.3586789E-13 * x**5) + (-1.1994E-16 * x**6)
	(-450.33825359217) + (2.192767900136 * x) + (-0.00446557629080586 * x**2) + (4.89958700689258E-06 * x**3) + (-2.96758414518E-09 * x**4) + (9.3586789E-13 * x**5) + (-1.1994E-16 * x**6)
	(-450.33825359217) + (2.192767900136 * x) + (-0.00446557629080586 * x**2) + (4.89958700689258E-06 * x**3) + (-2.96758414518E-09 * x**4) + (9.3586789E-13 * x**5) + (-1.1994E-16 * x**6)
	(-450.33825359217) + (2.192767900136 * x) + (-0.00446557629080586 * x**2) + (4.89958700689258E-06 * x**3) + (-2.96758414518E-09 * x**4) + (9.3586789E-13 * x**5) + (-1.1994E-16 * x**6)
SENSOR_TEMP	(-284.312946045691) + (1.11090916107209 * x) + (-0.00169650877947062 * x**2) + (1.32892474174192E-06 * x**3) + (-5.1112837166E-10 * x**4) + (7.676107E-14 * x**5)
HVPS_TEMP	(-284.312946045691) + (1.11090916107209 * x) + (-0.00169650877947062 * x**2) + (1.32892474174192E-06 * x**3) + (-5.1112837166E-10 * x**4) + (7.676107E-14 * x**5)
CDH_PROCESSOR_TEMP	(-284.312946045691) + (1.11090916107209 * x) + (-0.00169650877947062 * x**2) + (1.32892474174192E-06 * x**3) + (-5.1112837166E-10 * x**4) + (7.676107E-14 * x**5)
CDH_1_8V_LDO_TEMP	(-284.312946045691) + (1.11090916107209 * x) + (-0.00169650877947062 * x**2) + (1.32892474174192E-06 * x**3) + (-5.1112837166E-10 * x**4) + (7.676107E-14 * x**5)

CDH_1_5V_LDO_TEMP	(-284.312946045691) + (1.11090916107209 * x) + (-0.00169650877947062 * x**2) + (1.32892474174192E-06 * x**3) + (-5.1112837166E-10 * x**4) + (7.676107E-14 * x**5)
CDH_SDRAM_TEMP	(-284.312946045691) + (1.11090916107209 * x) + (-0.00169650877947062 * x**2) + (1.32892474174192E-06 * x**3) + (-5.1112837166E-10 * x**4) + (7.676107E-14 * x**5)
LVPS_BACK_BOARD_TEMP	(-273.2) + (0.1444619083 * x)
LVPS_FRONT_BOARD_TEMP	(-273.2) + (0.1444619083 * x)
LVPS_MID_BOARD_TEMP	(-273.2) + (0.1444619083 * x)
LVPS_3_3V_VMON	(0.001611 * x)
LVPS_5V_P_VMON	(0.002441 * x)
LVPS_5V_N_VMON	(-0.002441 * x)
LVPS_12V_P_VMON	(0.005859 * x)
LVPS_12V_N_VMON	(-0.005859 * x)
LVPS_3_3V_IMON	(0.000916 * x)
LVPS_5V_P_IMON	(0.000461 * x)
LVPS_5V_N_IMON	(-0.000461 * x)
LVPS_12V_P_IMON	(0.000704 * x)
LVPS_12V_N_IMON	(-0.000704 * x)
CDH_1_5V_VMON	(0.001221 * x)
CDH_1_8V_VMON	(0.001221 * x)
CDH_3_3V_VMON	(0.001221 * x)
CDH_12V_P_VMON	(0.005897 * x)
CDH_12V_N_VMON	(-0.005841 * x)
CDH_5V_VMON	(0.002441 * x)
CDH_Analog_Ref_VMON	(0.002441 * x)
The following is a special case. Depending on if ESA is in low or high range, different conversion is used.	
HVPS_ESA_DAC in low range	(0.007852613 * x)
HVPS_ESA_DAC in high range	(0.384617788 * x)

Appendix B: Telemetry Packet Definitions

Some examples of packet definitions.
Note: packet definitions continue to change as the instrument development progresses.

Science packet

Mnemonic			Start Byte	Start Bit	Data Size
SWE_SCIENCE.PHVERNO			0	0	3
SWE_SCIENCE.PHTYPE			0	3	1
SWE_SCIENCE.PHSHF			0	4	1
SWE_SCIENCE.PHAPID			0	5	11
SWE_SCIENCE.PHGROUPF			2	0	2
SWE_SCIENCE.PHSEQCNT			2	2	14
SWE_SCIENCE.PHDLEN			4	0	16
SWE_SCIENCE.SHCOARSE			6	0	32
SWE_SCIENCE.ACQ_START_COARSE			10	0	32
SWE_SCIENCE.ACQ_START_FINE			14	0	20
SWE_SCIENCE.CEM_NOMINAL_ONLY			16	4	1
SWE_SCIENCE.SPIN_PERIOD_VALIDITY			16	5	1
SWE_SCIENCE.SPIN_PHASE_VALIDITY			16	6	1
SWE_SCIENCE.SPIN_PERIOD_SOURCE			16	7	1
SWE_SCIENCE.SETTLE_DURATION			17	0	15
SWE_SCIENCE.ACQ_DURATION			18	7	17
SWE_SCIENCE.SPIN_PHASE			21	0	16
SWE_SCIENCE.SPIN_PERIOD			23	0	16
SWE_SCIENCE.THRUSTER_FIRING			25	0	1
SWE_SCIENCE.HIGH_COUNT			25	1	1
SWE_SCIENCE.ESA_STEPS			25	2	6
SWE_SCIENCE.ESA_TABLE_NUM			26	0	8
SWE_SCIENCE.ESA_ACQ_CFG			27	0	8
SWE_SCIENCE.THRESHOLD_DAC			28	0	16
SWE_SCIENCE.STIM_CFG_REG			30	0	16
SWE_SCIENCE.SCIENCE_DATA			32	0	10080
SWE_SCIENCE.CKSUM			1292	0	16

App Housekeeping packet

SWE_APP_HK.PHVERNO			0	0	3
SWE_APP_HK.PHTYPE			0	3	1
SWE_APP_HK.PHSHF			0	4	1
SWE_APP_HK.PHAPID			0	5	11
SWE_APP_HK.PHGROUPF			2	0	2
SWE_APP_HK.PHSEQCNT			2	2	14
SWE_APP_HK.PHDLEN			4	0	16
SWE_APP_HK.SHCOARSE			6	0	32
SWE_APP_HK.APP_MODE			10	0	8
SWE_APP_HK.CMD_ACC_COUNT			11	0	8

 An Equal Opportunity Employer / Managed by Triad National Security, LLC for the U.S. Department of Energy's NNSA.

SWE_APP_HK.CMD_REJ_COUNT			12	0	8
SWE_APP_HK.LAST_OPCODE			13	0	16
SWE_APP_HK.HV_DISABLE_PLUG			15	0	1
SWE_APP_HK.HV_LIMIT_PLUG			15	1	1
SWE_APP_HK.HVPS_ENABLE			15	2	1
SWE_APP_HK.HVPS_CEM_ENABLE			15	3	1
SWE_APP_HK.HVPS_ESA_ENABLE			15	4	1
SWE_APP_HK.HVPS_LOW_RANGE_ENABLE			15	5	1
SWE_APP_HK.HVPS_BULK_ENABLE			15	6	1
SWE_APP_HK.SENSOR_P12A_N12A_CTRL			15	7	1
SWE_APP_HK.SENSOR_P5A_N5A_CTRL			16	0	1
SWE_APP_HK.SENSOR_P3p3D_P5D_CTRL			16	1	1
SWE_APP_HK.HVPS_ERROR_COUNT			16	2	6
SWE_APP_HK.HVPS_CEM_DAC			17	0	16
SWE_APP_HK.HVPS_ESA_DAC			19	0	16
SWE_APP_HK.THRESHHOLD			21	0	16
SWE_APP_HK.STIM_ENABLE			23	0	1
SWE_APP_HK.STIM_CONFIGURATION			23	1	15
SWE_APP_HK.HVPS_VBULK			25	0	12
SWE_APP_HK.HVPS_VCEM			26	4	12
SWE_APP_HK.HVPS_VESA			28	0	12
SWE_APP_HK.HVPS_VESA_LOW_RANGE			29	4	12
SWE_APP_HK.HVPS_ICEM			31	0	12
SWE_APP_HK.FEE_TEMP			32	4	12
SWE_APP_HK.SENSOR_TEMP			34	0	12
SWE_APP_HK.HVPS_TEMP			35	4	12
SWE_APP_HK.LVPS_BACK_BOARD_TEMP			37	0	12
SWE_APP_HK.LVPS_FRONT_BOARD_TEMP			38	4	12
SWE_APP_HK.LVPS_MID_BOARD_TEMP			40	0	12
SWE_APP_HK.LVPS_3_3V_VMON			41	4	12
SWE_APP_HK.LVPS_5V_P_VMON			43	0	12
SWE_APP_HK.LVPS_5V_N_VMON			44	4	12
SWE_APP_HK.LVPS_12V_P_VMON			46	0	12
SWE_APP_HK.LVPS_12V_N_VMON			47	4	12
SWE_APP_HK.LVPS_3_3V_IMON			49	0	12
SWE_APP_HK.LVPS_5V_P_IMON			50	4	12
SWE_APP_HK.LVPS_5V_N_IMON			52	0	12
SWE_APP_HK.LVPS_12V_P_IMON			53	4	12
SWE_APP_HK.LVPS_12V_N_IMON			55	0	12
SWE_APP_HK.CDH_PROCESSOR_TEMP			56	4	12
SWE_APP_HK.CDH_1_8V_LDO_TEMP			58	0	12
SWE_APP_HK.CDH_1_5V_LDO_TEMP			59	4	12
SWE_APP_HK.CDH_SDRAM_TEMP			61	0	12
SWE_APP_HK.CDH_1_5V_VMON			62	4	12
SWE_APP_HK.CDH_1_8V_VMON			64	0	12
SWE_APP_HK.CDH_3_3V_VMON			65	4	12
SWE_APP_HK.CDH_12V_P_VMON			67	0	12
SWE_APP_HK.CDH_12V_N_VMON			68	4	12
SWE_APP_HK.CDH_5V_VMON			70	0	12
SWE_APP_HK.CDH_Analog_Ref_VMON			71	4	12
SWE_APP_HK.TM_MARKER			73	0	32
SWE_APP_HK.spare			77	0	8
SWE_APP_HK.CKSUM			78	0	16

CEM_RAW packet

Mnemonic			Start Byte	Start Bit	Data Size
SWE_CEM_RAW.PHVERNO			0	0	3
SWE_CEM_RAW.PHTYPE			0	3	1
SWE_CEM_RAW.PHSHF			0	4	1
SWE_CEM_RAW.PHAPID			0	5	11
SWE_CEM_RAW.PHGROUPF			2	0	2
SWE_CEM_RAW.PHSEQCNT			2	2	14
SWE_CEM_RAW.PHDLEN			4	0	16
SWE_CEM_RAW.SHCOARSE			6	0	32
SWE_CEM_RAW.THRESHOLD_DAC			10	0	16
SWE_CEM_RAW.STIM_CFG_REG			12	0	16
SWE_CEM_RAW.CEM1_COUNTS			14	0	32
SWE_CEM_RAW.CEM2_COUNTS			18	0	32
SWE_CEM_RAW.CEM3_COUNTS			22	0	32
SWE_CEM_RAW.CEM4_COUNTS			26	0	32
SWE_CEM_RAW.CEM5_COUNTS			30	0	32
SWE_CEM_RAW.CEM6_COUNTS			34	0	32
SWE_CEM_RAW.CEM7_COUNTS			38	0	32
SWE_CEM_RAW.CKSUM			42	0	16

I-ALiRT packet

Mnemonic			Start Byte	Start Bit	Data Size
SWE_IALIRT.PHVERNO			0	0	3
SWE_IALIRT.PHTYPE			0	3	1
SWE_IALIRT.PHSHF			0	4	1
SWE_IALIRT.PHAPID			0	5	11
SWE_IALIRT.PHGROUPF			2	0	2
SWE_IALIRT.PHSEQCNT			2	2	14
SWE_IALIRT.PHDLEN			4	0	16
SWE_IALIRT.SHCOARSE			6	0	32
SWE_IALIRT.ACQUISITION_TIME			10	0	32
SWE_IALIRT.ACQUISITION_TIME_SUBSECOND			14	0	24
SWE_IALIRT.INSTRUMENT_NOMINAL_FLAG			17	0	1
SWE_IALIRT.SCIENCE_OPERATION_FLAG			17	1	1
SWE_IALIRT.SEQUENCE_NUMBER			17	2	6
SWE_IALIRT.ELECTRON_COUNTS_SPIN_I_POL_0_E_0J			18	0	8
SWE_IALIRT.ELECTRON_COUNTS_SPIN_I_POL_0_E_1J			19	0	8
SWE_IALIRT.ELECTRON_COUNTS_SPIN_I_POL_0_E_2J			20	0	8
SWE_IALIRT.ELECTRON_COUNTS_SPIN_I_POL_0_E_3J			21	0	8
SWE_IALIRT.ELECTRON_COUNTS_SPIN_I_POL_1_E_0J			22	0	8
SWE_IALIRT.ELECTRON_COUNTS_SPIN_I_POL_1_E_1J			23	0	8
SWE_IALIRT.ELECTRON_COUNTS_SPIN_I_POL_1_E_2J			24	0	8
SWE_IALIRT.ELECTRON_COUNTS_SPIN_I_POL_1_E_3J			25	0	8
SWE_IALIRT.ELECTRON_COUNTS_SPIN_I_POL_2_E_0J			26	0	8
SWE_IALIRT.ELECTRON_COUNTS_SPIN_I_POL_2_E_1J			27	0	8

SWE_IALIRT.ELECTRON_COUNTS_SPIN_I_POL_2_E_2J			28	0	8
SWE_IALIRT.ELECTRON_COUNTS_SPIN_I_POL_2_E_3J			29	0	8
SWE_IALIRT.ELECTRON_COUNTS_SPIN_I_POL_3_E_0J			30	0	8
SWE_IALIRT.ELECTRON_COUNTS_SPIN_I_POL_3_E_1J			31	0	8
SWE_IALIRT.ELECTRON_COUNTS_SPIN_I_POL_3_E_2J			32	0	8
SWE_IALIRT.ELECTRON_COUNTS_SPIN_I_POL_3_E_3J			33	0	8
SWE_IALIRT.ELECTRON_COUNTS_SPIN_I_POL_4_E_0J			34	0	8
SWE_IALIRT.ELECTRON_COUNTS_SPIN_I_POL_4_E_1J			35	0	8
SWE_IALIRT.ELECTRON_COUNTS_SPIN_I_POL_4_E_2J			36	0	8
SWE_IALIRT.ELECTRON_COUNTS_SPIN_I_POL_4_E_3J			37	0	8
SWE_IALIRT.ELECTRON_COUNTS_SPIN_I_POL_5_E_0J			38	0	8
SWE_IALIRT.ELECTRON_COUNTS_SPIN_I_POL_5_E_1J			39	0	8
SWE_IALIRT.ELECTRON_COUNTS_SPIN_I_POL_5_E_2J			40	0	8
SWE_IALIRT.ELECTRON_COUNTS_SPIN_I_POL_5_E_3J			41	0	8
SWE_IALIRT.ELECTRON_COUNTS_SPIN_I_POL_6_E_0J			42	0	8
SWE_IALIRT.ELECTRON_COUNTS_SPIN_I_POL_6_E_1J			43	0	8
SWE_IALIRT.ELECTRON_COUNTS_SPIN_I_POL_6_E_2J			44	0	8
SWE_IALIRT.ELECTRON_COUNTS_SPIN_I_POL_6_E_3J			45	0	8
SWE_IALIRT.CKSUM			46	0	16

4.3 Magnetic Fields

MAG data product definitions and processing algorithms are embedded below

IMAP PROJECT

IMAP MAG DATA CLEANING PROCESSES

MAG
MAGNETOMETER INSTRUMENT

project	IMAP
instrument	Magnetometer Instrument
code	MAG
organisation	Imperial College London
document title	IMAP MAG Data Cleaning Processes
prepared by	Mhairi Finlayson
approved by	Helen O'Brien
reference	IMAP-OPS-TN-ICL-013
issue	4
revision	0
date of issue	4 June 2026

CHANGE LOG

Date	Issue	Revision	Reason for change
12 Jan 2026	1	0	First release
29 May 2026	2	0	Updated for code v2.2.0 and data released in August 2026
4 June 2026	3	0	Focused version to be used as input for CMAD which includes descriptions of future improvements
4 June 2026	4	0	Removal of non-relevant sections for CMAD

Note: List of changes since first release.

CHANGE RECORD

Section(s)	Reason for change
3.1	Removal of IMAP-Lo Pivot platform Potential Improvements
3.3	Removal of Thruster Potential Improvements
4.2	Removal of gradiometer correlation overview
4.2	Added description of residual pivot platform movement to section 4

Note: Detailed changes are listed for this issue only. For previous changes, see earlier issues.

TABLE OF CONTENTS

Change Log 2
Change Record 2
Table Of Contents 2
1 Scope 3
2 Processing Flow 3
3 Features cleaned from IMAP MAG data 4
3.1 IMAP Lo Pivot Platform 4
3.1.1 Signal Characterisation 4
3.1.1 Cleaning Process 6
3.1.2 Results 8
3.2 H90 / H45/ ULTRA Decon heaters 8
3.2.1 Super-posed Epoch Analysis 8
3.3 Thrusters and pre-thruster signal removal 11
3.3.1 Signal Characterisation 11
3.3.2 Process 13
3.3.3 Results 15
3.3.4 Bug related to Burst Mode Thruster Cleaning 16
4 Features noted but not yet cleaned from IMAP MAG data 16

4.1 TCM Related Signals 16
4.2 Pivot Platform Movement 17

1 Scope

This document describes the cleaning processes for features identified in the IMAP MAG data. The cleaning processes are applied to all L2 data.

This document is valid for MAG calibration code **V2.2.0 and the inputs used for the August 2026 data release covering 1-Jan to 29-Apr 2026.**

Release v2.2.0 · ImperialCollegeLondon/IMAP_MAG_Calibration

2 Processing Flow

Version: V2.2.0
The calibration flow is defined by the wrapper script calibrate_L2_offsets.m. This script loads the required HK and configuration settings, calls the subroutines for cleaning of specific data features and generates the final offsets, which are applied to L1C (normal mode) and L1B (burst mode) to generate the L2 data products.

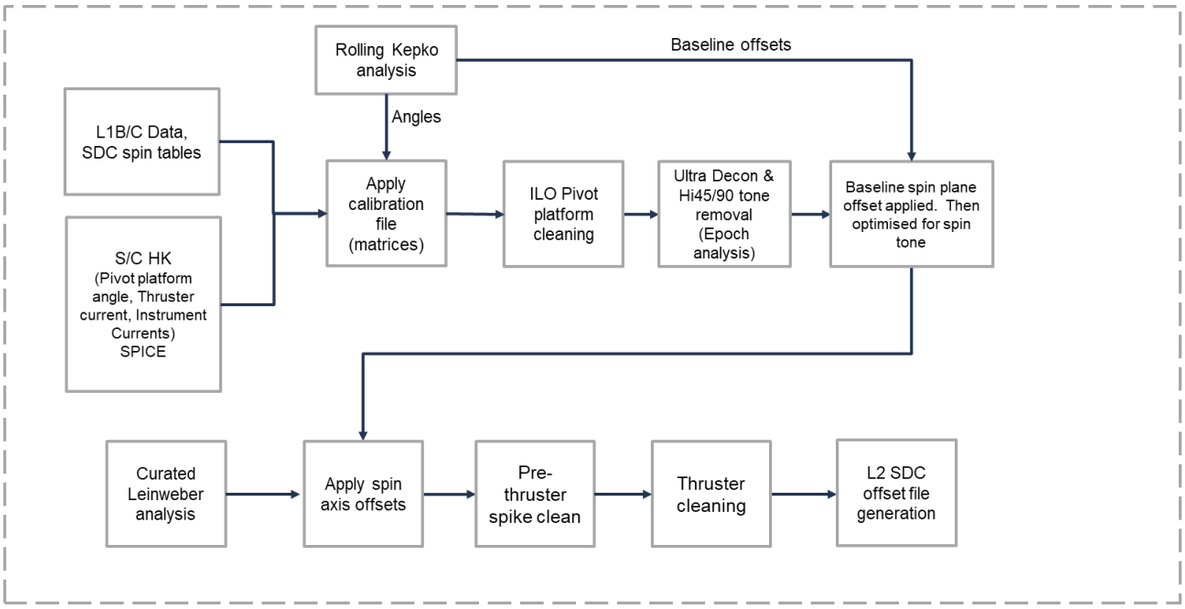


Figure 1: Calibration chain V2.2.0 flow

The flow incorporates the following blocks:

1. Apply Calibration File (matrices): for discussion of how angles are determined see IMAP-OPS-TN-ICL-017 for further details.

2. ILO pivot platform is cleaned (see Section 3.1)

3. Ultra Decontamination Heater and HI45/90 signal removal (see Section 3.2)

4. Apply Spin plane offset correction (combines a baseline and spin-tone reducing optimised offset: see IMAP-OPS-TN-ICL-017 for further details)

5. Apply spin axis offset correction (calculated using solar wind techniques see IMAP-OPS-TN-ICL-017 for further details)

6. Thruster and pre-thruster cleaning (see Section 3.3)

7. The output is a file with an offset for each vector in the input L1C (normal mode) or L1B (burst mode) file. This is used by SDC to produce the final L2 products.

3 Features cleaned from IMAP MAG data

3.1 IMAP Lo Pivot Platform

The Pivot Platform (PP) was highlighted before launch as being a known magnetic contamination source. Dedicated code has been put in place to clean this signal.

3.1.1 SIGNAL CHARACTERISATION

The IMAP-Lo Pivot Platform is a component of the IMAP-Lo instrument – it moves through up to 180 degrees of motion. For the period Sep-25 to Apr-26, it had three set points and moved up to once a day. Set points are at 75 degrees, 90 degrees, and 105 degrees.

These three positions of the pivot platform each result in a different magnetic signal at MAGo (and MAGi). The difference is large, and visible in rolling spin plane offsets as well as in gradiometry. Other more complex signatures are seen during the movement itself.

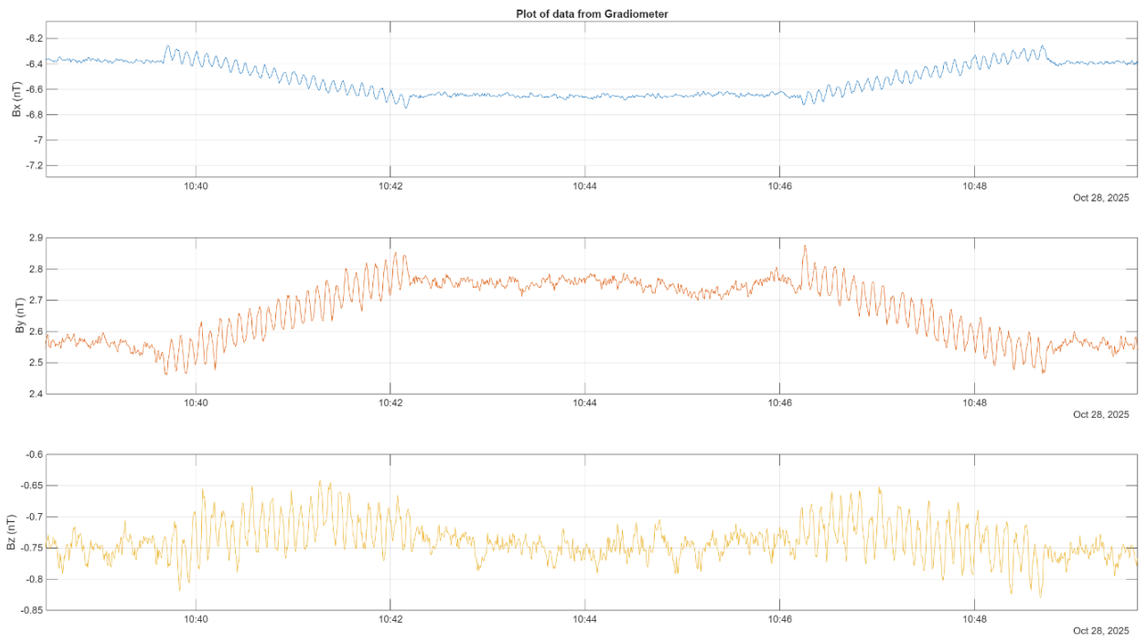


Figure 2 - ILO pivot platform movement seen in the MAG data. Figure shows the gradiometer at the time of a movement (difference between the measured field at MAGo compared to MAGi). Step change before and after movement plus more complex field signature during movement are clearly seen.

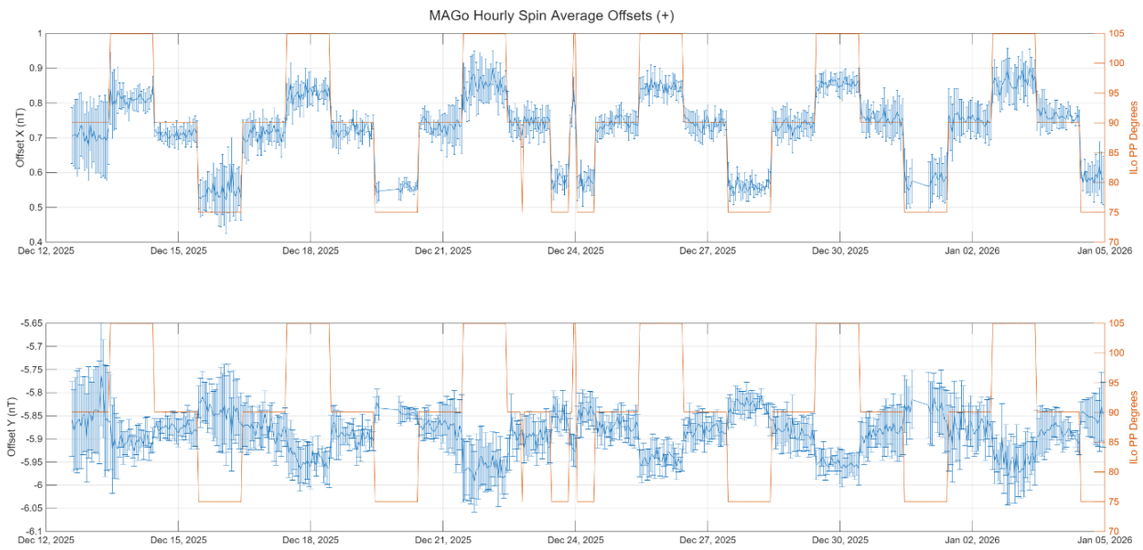


Figure 3: Rolling spin averaged MAGo spin plane offsets compared to coarse degrees of the IMAP-Lo pivot platform – shows repeating step changes associated with the pivot platform

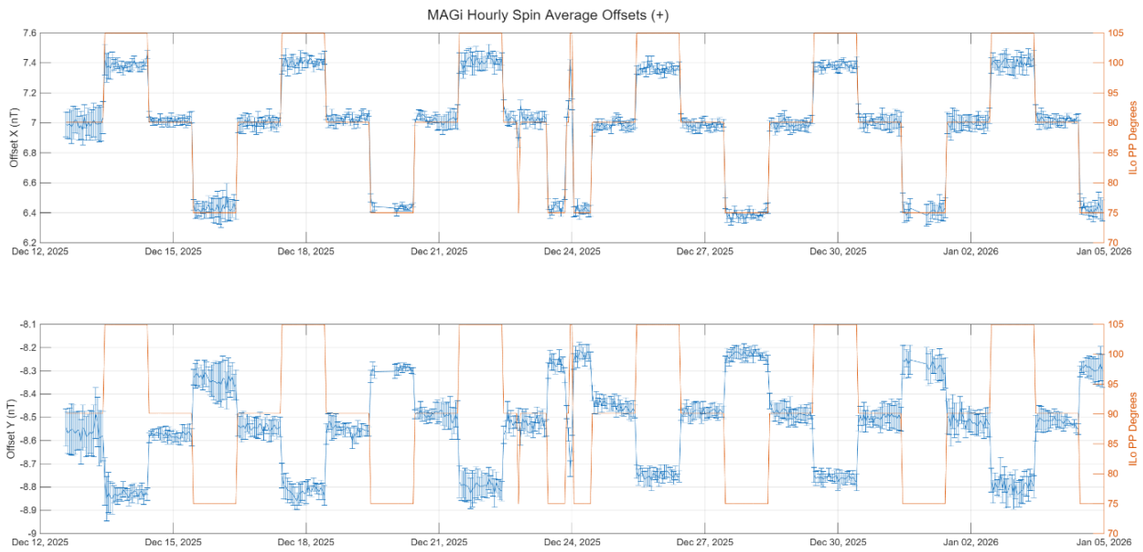


Figure 4: Rolling spin averaged MAGi spin plane offsets compared to coarse degrees of the IMAP-Lo pivot platform. The signal is larger in MAGi, consistent with MAGi being closer to the source

3.1.1 CLEANING PROCESS

Offsets from the 90 degree position have been calculated using movement data from March – April 2026 of the Pivot Platform. These offsets are pre-applied based on the housekeeping parameter ILOGLOBAL.PPM_NHK_POT_PRI which gives the degrees of position of the pivot platform. During platform movement, the offset is interpolated linearly between the start and stop positions.

Deltas are for each axis in this format: [75 degree delta, 90 degree delta=0 by design, 105 degree delta]. The deltas used are:


```
{
  "ilo_deltas":{
    "mago":
    {
      "x":[-0.1595,0.0000,0.1197],
      "y":[0.0747 ,0.0000,-0.0671],
      "z":[0.2459,0.0000,-0.0381]
    },
    "magi":
    {
      "x":[-0.5946,0.0000,0.3760],
      "y":[0.2647 ,0.0000,-0.2889],
      "z":[0.4930,0.0000,-0.0122]
    }
  }
}
```

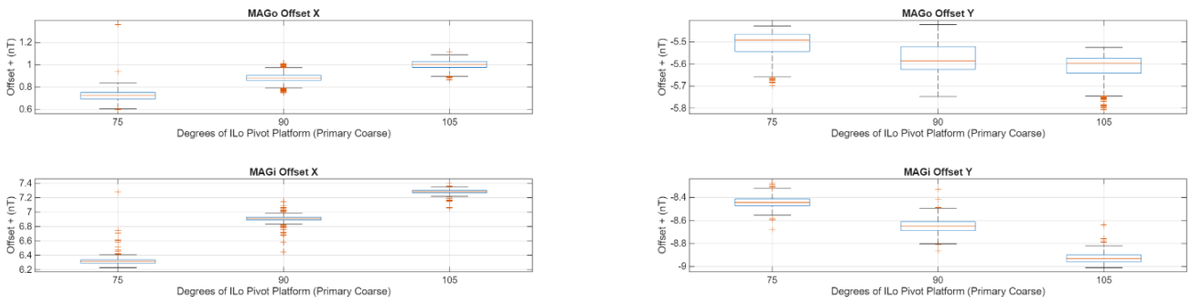


Figure 5: Deltas were determined by calculating the offset in spin plane for MAGo and MAGi at the 3 PP positions. The difference between these points is the delta used.

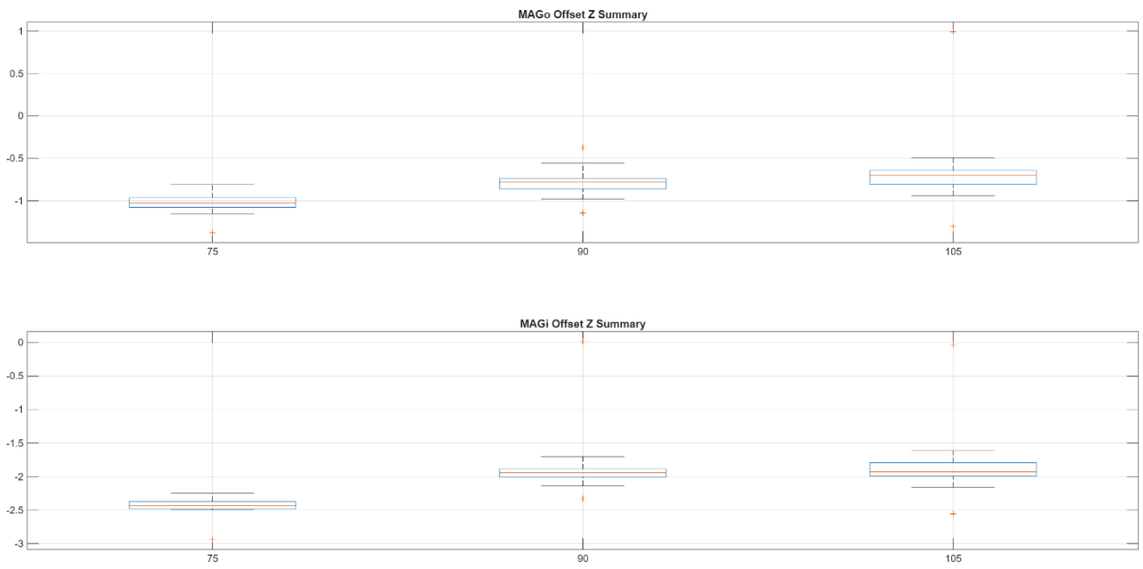


Figure 6: Offset in spin axis for MAGo and MAGi at the different PP positions

3.1.2 RESULTS

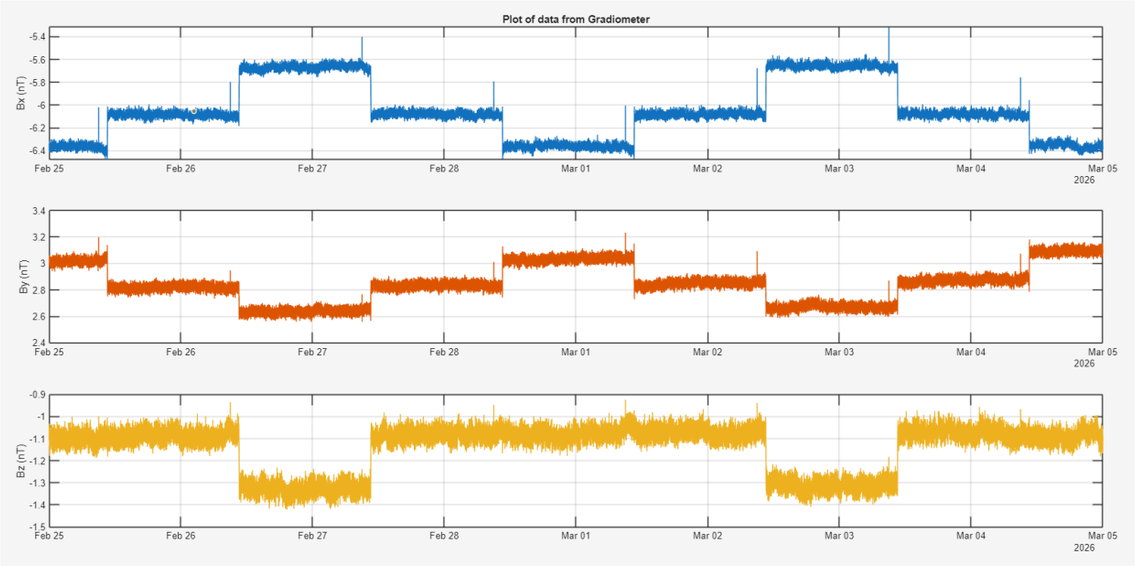


Figure 7: Gradiometer pre-PP removal, shows clear steps associated with the 3 PP positions

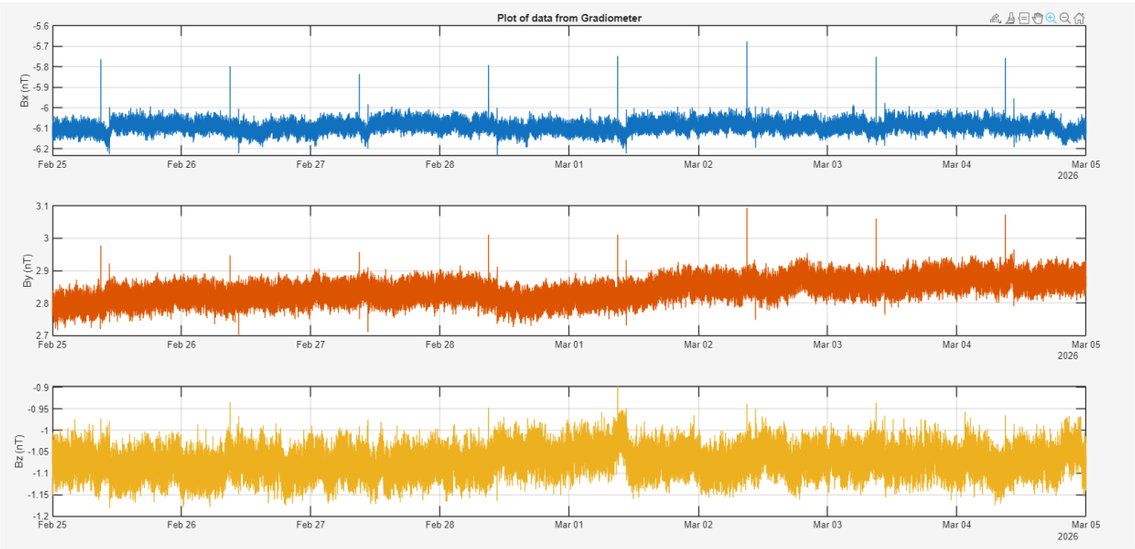


Figure 8: Gradiometer post PP removal showing steps are removed - (note spikes are from pre-thrusters and are not related to the PP)

3.2 H90 / H45/ ULTRA Decon heaters

3.2.1 SUPER-POSED EPOCH ANALYSIS

Introduced from code version 2.1.0, the superposed epoch analysis models the profile in gradiometer of the Hi45/Hi90 signal and the U45/U90 decontamination heater signal, then

removes a proportion of that from the MAGo data, triggered by housekeeping data from the instruments.

One month of data was used for the analysis, from 1-Nov to 30-Nov. For the decontamination heater signal, sharp changes in U45_DECON_HTR_CURR and U90_DECON_HTR_CURR were used to identify all instances of the decontamination heaters turning on, which occurs every 10 minutes.

The gradiometer time series across all instances were averaged together, to build a profile of the impact of the decontamination heaters.

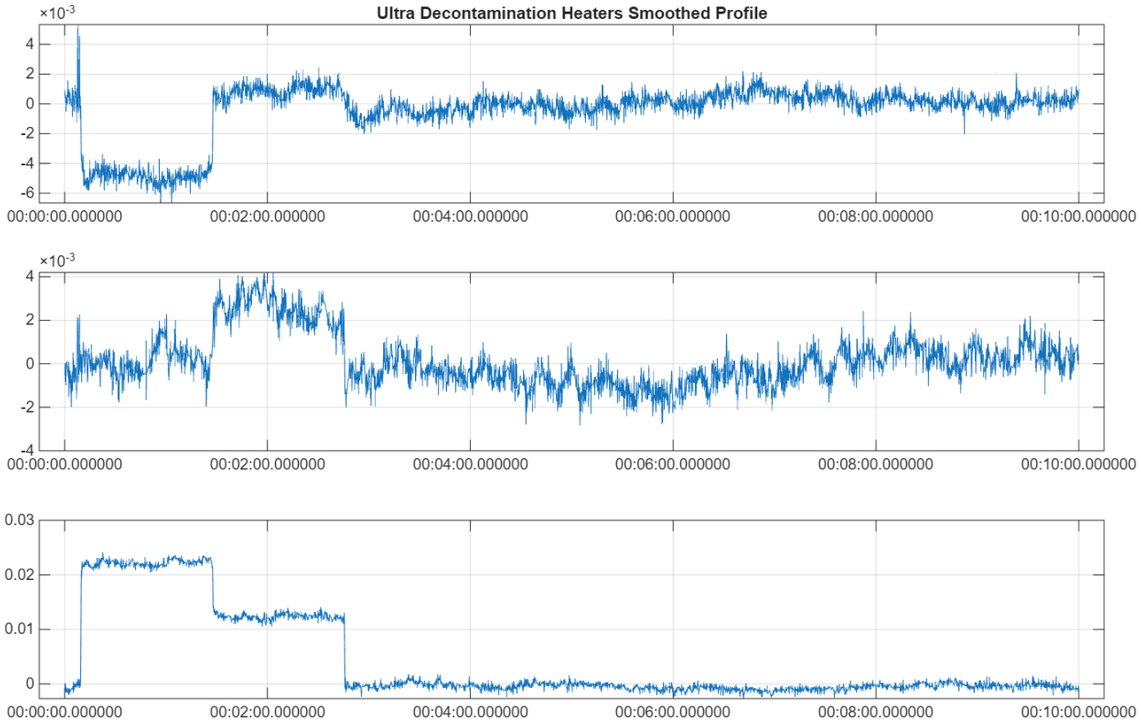


Figure 9: Ultra Decontamination Heater Profile in Gradiometer for x, y and z axes

A similar analysis was performed for the Hi-45/Hi-90 sourced signal, using H45_CURR and H90_CURR as the trigger currents to identify the feature.

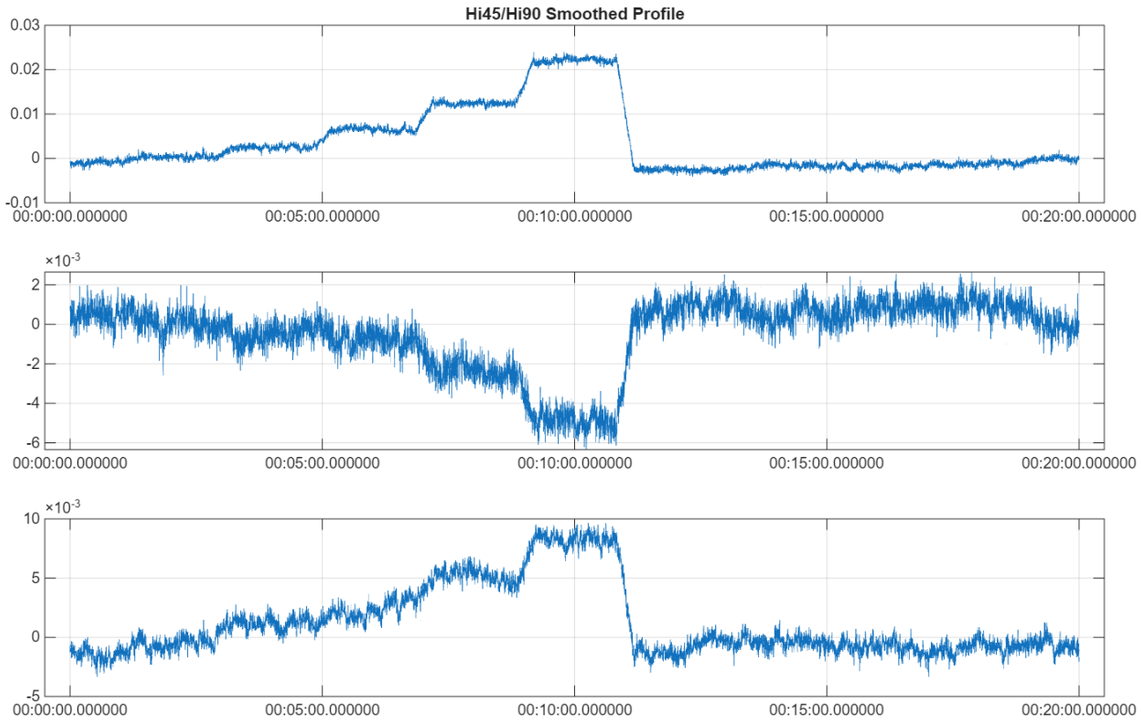


Figure 10: Hi45/Hi90 Profile in Gradiometer for x, y and z axes

A gradiometer factor was determined for removal of these signals from the original data. For the decontamination heaters, the large signal existing in the spin axis made it possible to perform a separate MAGo/MAGi epoch analysis, and calculate a gradiometer factor of 0.65 in MAGo.

The Hi45/90 interference predominately impacts the spin plane, which introduces significant complexity to performing a separate superposed epoch analysis. Instead, a gradiometer factor was calculated based on minimising spin tone in the spin plane, yielding a factor of 1.5 for MAGo.

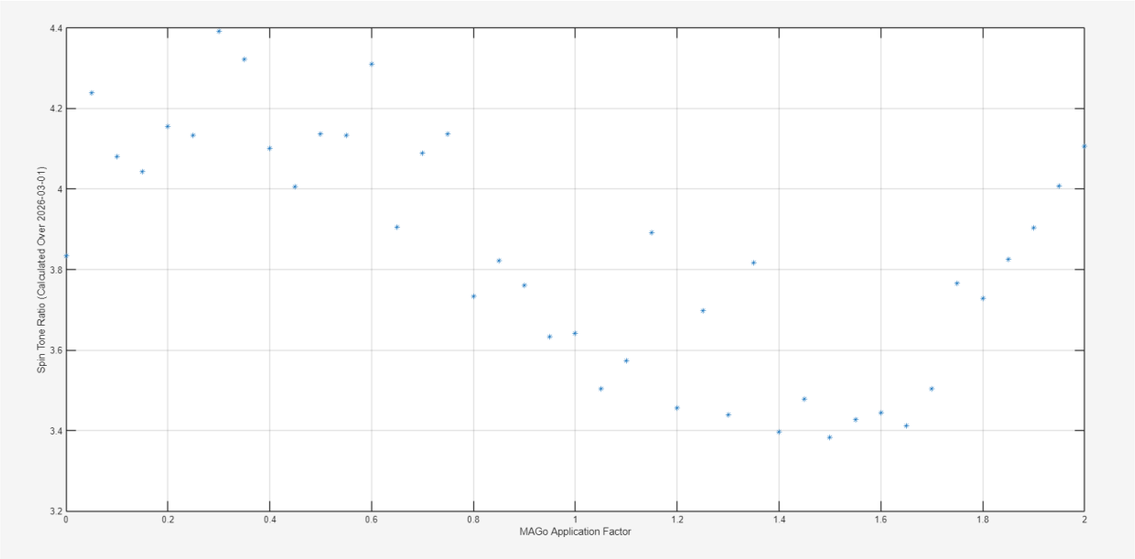


Figure 11: MAGo gradiometer factor minimisation – used for HI. A MAGo Application factor of 1.5 aligns with a minimum in the spin tone ratio

3.3 Thrusters and pre-thruster signal removal

3.3.1 SIGNAL CHARACTERISATION

The thrusters generate a series of spikes in the MAG data when they fire. In addition, a signal (called the pre-thruster signal) is generated approximately an hour before the thrusters fire. Both signals are cleaned from the data using a gradiometer technique.

One hour prior to the thrusters turning on, several activities occur. One of these activities causes a noticeable short DC signal in the gradiometer. The exact source has not been located – but it is designated a pre-thruster signal for MAG cleaning purposes.

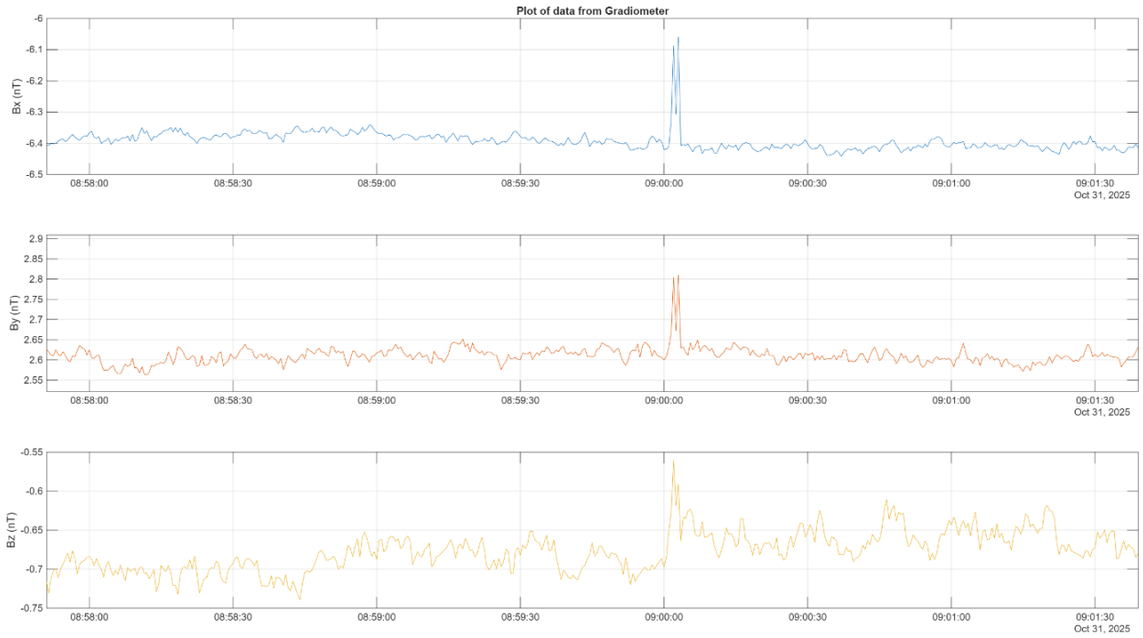


Figure 12: Pre-thruster activities seen in MAG data

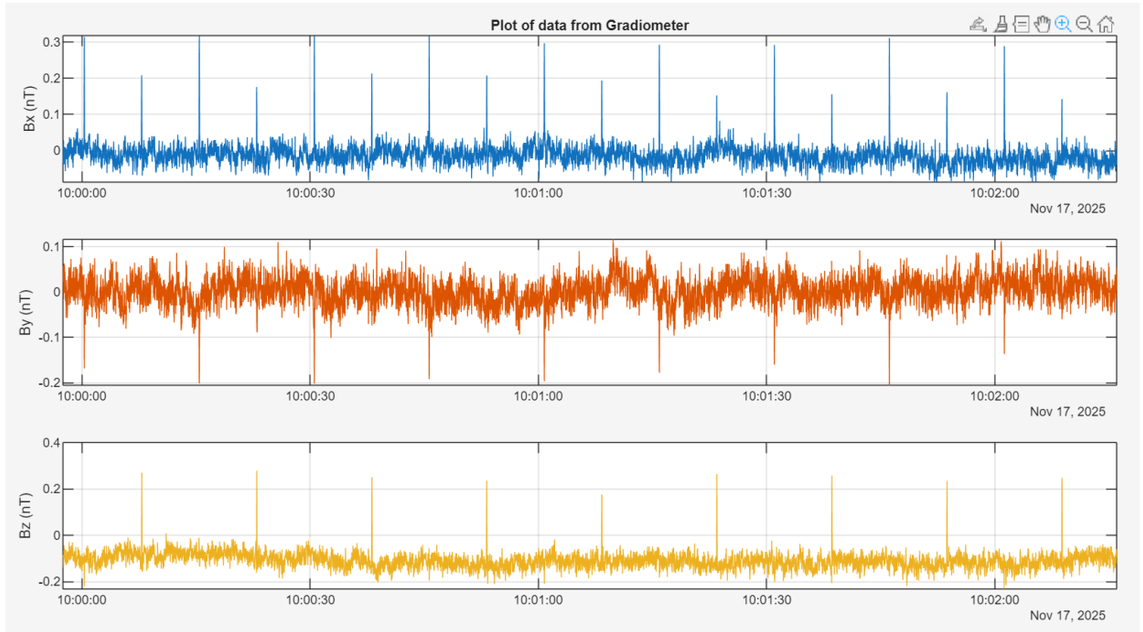


Figure 13: Thrusters firing visible in the delta between MAGi and MAGo. Seen as a series of spikes, occurs an hour after increase in THRUST_BUS_CURR

3.3.2 PROCESS

Gradiometer is used to clean the thruster and pre-thruster signals from the data. The thruster signals correlate with spacecraft housekeeping. The pre-thruster signals (that generally occur around 09:00 each day) occur within a minute of a spike in TAC_THRUST_BUS_GRP_1_CURR, or TAC_THRUST_BUS_GRP_2_CURR in the X285 packet. While the exact source of the pre-thruster signal is unknown, it always occurs in concert with a number of pre-thruster activities that occur an hour before the thrusters fire. Since the increase in the thruster BUS current is one of them, it is a reliable indicator that the signal is about to occur.

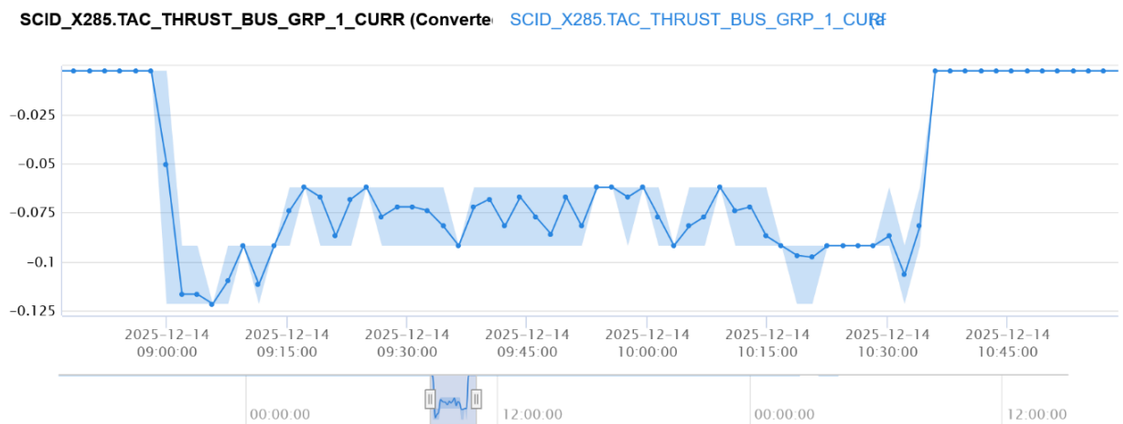


Figure 14: TAC_THRUST_BUS_CURR increases over the thruster firing period

Similarly, the increase always occurs an hour before the thrusters fire, so can also be used to identify when the thrusters will fire.

The data has initial offsets applied so that the delta between MAGi and MAGo is approximately zero. For both signals, the current increase is used to select a small segment of data, when the difference between two consecutive current measurements exceeds 0.05mA. For the pre-thruster signal, an approximately two-minute segment is selected. The segment is then transformed into a despun reference frame for the gradiometer process to be applied.

A despun reference frame is used for the gradiometer process as during the gradiometer process MAGi measurements are interpolated onto the MAGo timeline. In a spinning reference frame, additional complexity exists in attempting to interpolate along a sine wave. Whereas in a despun reference frame the data is approximately constant over short time frames, and a linear interpolation is more accurate.

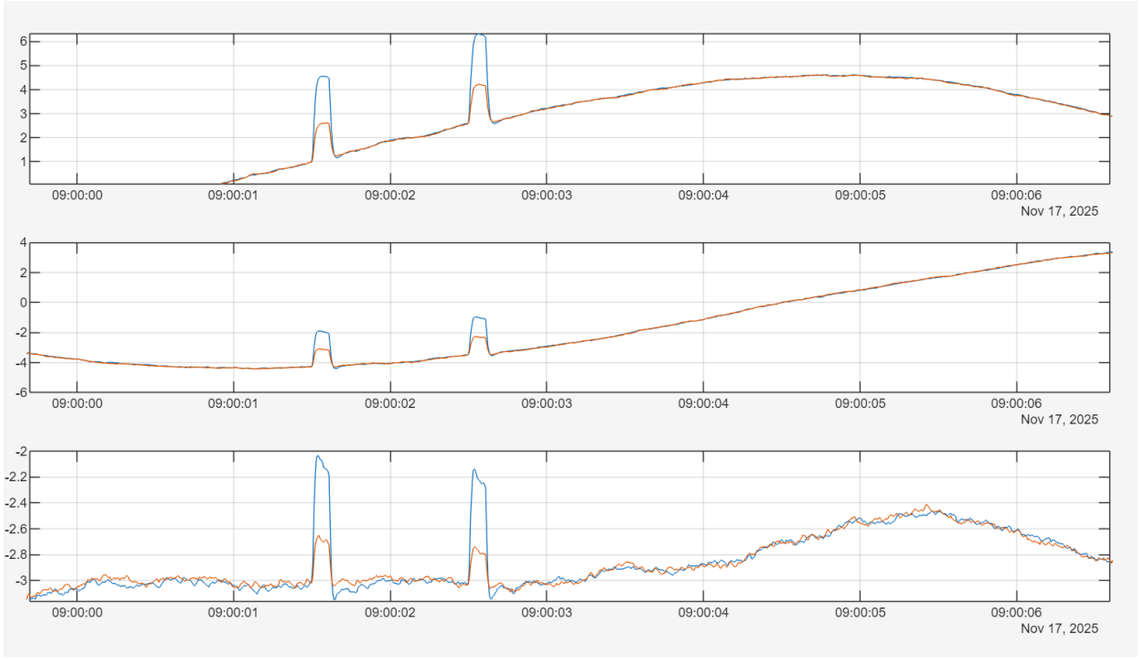


Figure 15: MAGo (red) and MAGi (blue) in the MAG frame – the ratio between the feature size is used to determine kappa value

A gradiometer factor, known as kappa, is identified for both the pre-thruster signal and the thruster signal. This was determined manually for both signals as the signals are large and visible in both MAGi and MAGo. Therefore, the ratio between the signal at MAGo, and the MAGi-MAGo delta can be measured and calculated. Each signal has its own individual gradiometer factor, and the signals were also measured separately in all three axes to construct a kappa value that alters each axis individually. The gradiometer factor was also determined in the orthogonal MAG frame – after the application of the calibration matrices but before transformation into the despun frame. The assessed values are as follows:

$$K_pre_thruster_signal = \begin{bmatrix} 0.71812 & 0 & 0 \\ 0 & 0.96282 & 0 \\ 0 & 0 & 0.455 \end{bmatrix}$$

$$K_thruster_signal = \begin{bmatrix} 0.965 & 0 & 0 \\ 0 & 0.8449 & 0 \\ 0 & 0 & 0.965 \end{bmatrix}$$

The gradiometer factors are then applied to the earlier identified despun segment. The gradiometer factors themselves must be transformed into the chosen despun frame, as they are non-constant in any despun frame. Then, for any vectors where the delta between MAGi and MAGo exceeds 0.1nT in any single axes, the appropriate gradiometer factor is applied to the delta, and then subtracted from the MAGo value. Additionally, vectors spanning

approximately two seconds around that threshold also have gradiometry applied to avoid edge effects where 0.09nT spikes remained.

3.3.3 RESULTS

Pre and post cleaning data is shown in Figure 16 and Figure 17 for the thruster and pre-thruster signals.

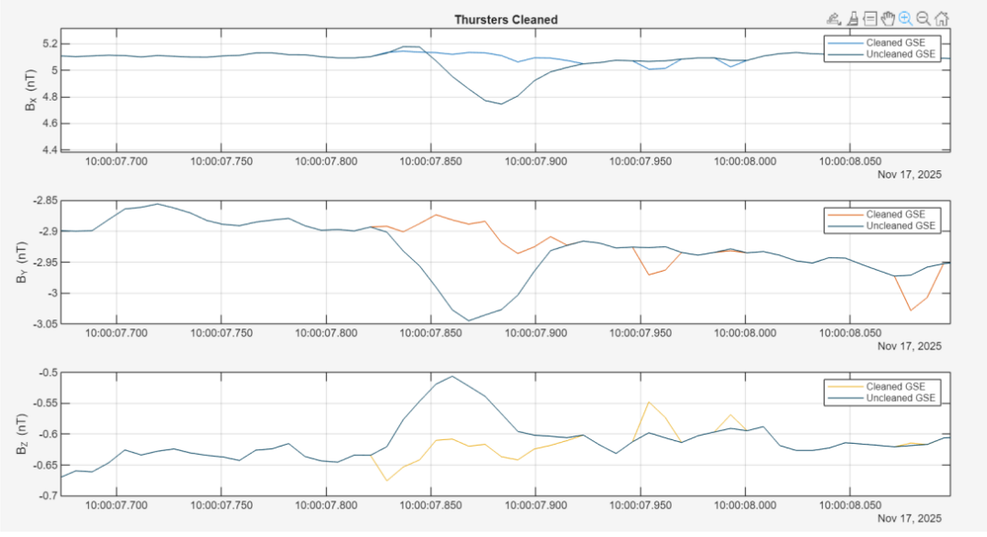


Figure 16: Thruster signal cleaned from burst data

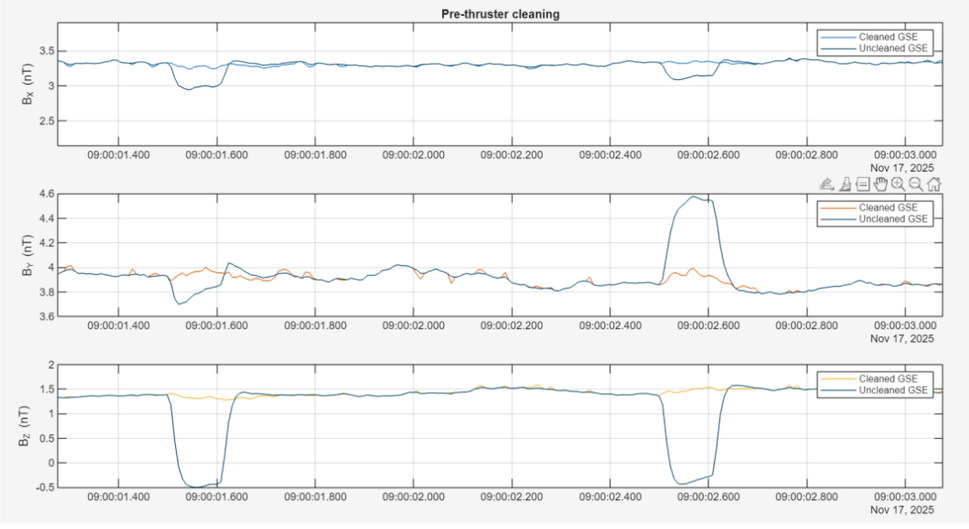


Figure 17: Pre-Thruster Signal cleaned from burst data

3.3.4 BUG RELATED TO BURST MODE THRUSTER CLEANING

The burst mode thruster cleaning introduces some NaN points (missing data points of a few s, distributed within max 2 minutes around thruster firings which normally occur at 10am UTC). These are represented by $-1e^{31}$ in the cdf files corresponding to the FILLVAL. Correcting this is a target for future code updates.

The burst mode thruster cleaning is also imperfect, and frequently leaves residual thruster signals in the data. Improving this is again a target for future updates to the cleaning process. The quality flags indicate when the thrusters are firing, and should be consulted before using data surrounding thruster firings.

Note: the period around the pre-thruster and thruster firings is flagged (quality flag set to 1=bad data).

4 Features noted but not yet cleaned from IMAP MAG data

4.1 TCM Related Signals

TCMs are rare manoeuvres which currently occur approximately once a month. The example shown here is TCM-3, which occurred on 19-Oct 2025, and caused significant signals in the gradiometer between MAGo and MAGi as seen in Figure 18. The trajectory correction manoeuvre occurred around 13:00, however the signal at 12:44 might also correspond to pre-TCM activities.

Note: the period around the TCMs is flagged (quality flag set to 1=bad data).

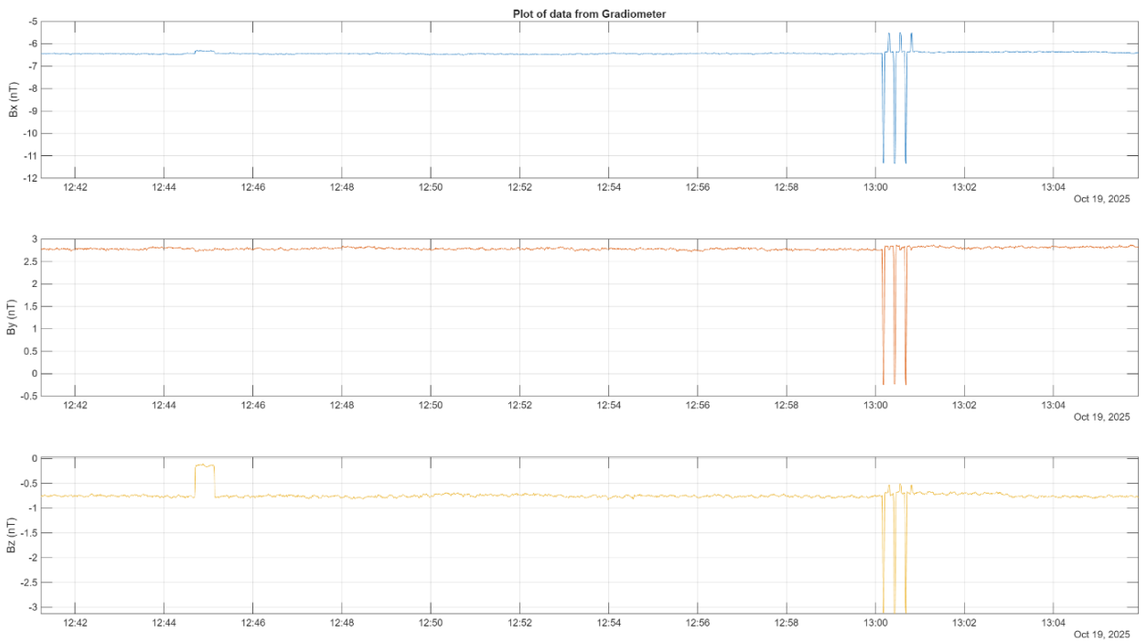


Figure 18 - TCM -3 signals

4.2 Pivot Platform Movement

During movement of the IMAP-Lo Pivot Platform, oscillations are seen in the MAG data.

Note: the period around the pivot platform movement is flagged (quality flag set to 1=bad data).

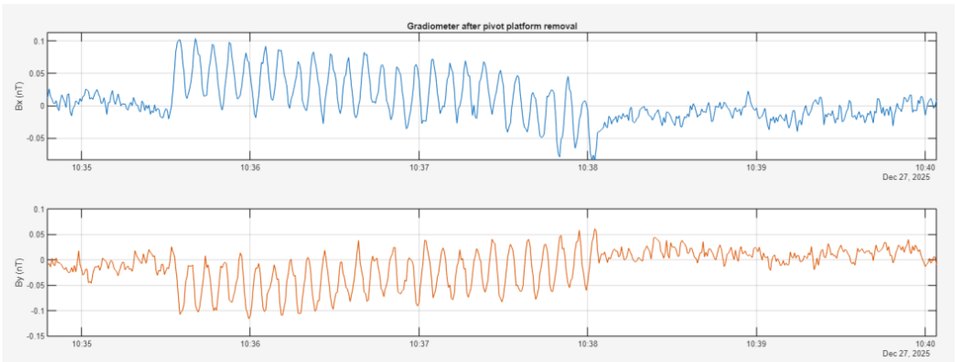


Figure 19 - Oscillation seen during movement of the PP – this is not currently cleaned from the data

[END OF DOCUMENT]

4.3.1 Validation

4.4 Energetic Neutral Atoms

4.4.1 IMAP-Lo

IMAP-Lo data product definitions and processing algorithms are embedded below

Draft version May 12, 2026
Typeset using LaTeX **modern** style in AASTeX631

Appendix A. The IMAP-Lo Mapping Algorithms (V8a)

N. A. Schwadron,[1,2] F. Rahmanifard,[1] E. Möbius,[1] A. Galli,[3] K. Fairchild,[1] H. Islam,[1] J. Bower,[1] M. Shen,[2] and D. R. Reisenfeld[4]

[1] *University of New Hampshire, Durham, NH, 03824, USA*
[2] *Department of Astrophysical Sciences, Princeton University, Princeton, NJ, 08544, USA*
[3] *University of Bern, Bern Switzerland*
[4] *Los Alamos National Laboratory, NM, USA*

Submitted to ApJ

1. AN OVERVIEW OF MAPPING ALGORITHMS

The IMAP-Lo mapping algorithms represent generalized approaches to creating ENA flux maps and rate maps based on the pointing sets created for level 2 data products. Products presented here include both level 2 maps and level 3 survival-probability corrected maps. The generalizations described here provide us with a way to use pointing sets to generate maps in a various coordinate frames, with a variety of different corrections for sputtering, and maps in the heliospheric inertial and spacecraft (S/C) reference frames.

IMAP-Lo will observe both ENAs and ISN by measuring two main observables: H- counts and O- counts. In general, the Hydrogen ENAs and ISN He and H will produce mostly H^- by direct charge exchange or surface sputtering whereas ISN O and Ne (and to a lesser extent ISN He) produce predominantly O^-. This document describes how maps are calculated, and describes the corrections that are applied. There are generally two types of maps considered: ENA maps formed from H atoms, and ISN maps formed from ISN H, He, O and Ne. The bulk of the material in this document applies to H ENA maps. The last section (§8) describes ISN map creation.

For ENAs, the sources are:

- Energetic Hydrogen Atoms (EHAs). EHAs enter the instrument, undergo charge-exchange on the conversion surface to create H^-, pass through the electrostatic analyzer (ESA) that defines the energy bandpass, and into the time-of-flight (TOF) section. A fundamental goal of IMAP is the mapping of EHAs.
- Oxygen Atoms. On the IBEX mission, oxygen maps provide an important input component. These oxygen atoms are predominantly interstellar in origin, although additional sources of O cannot be ruled out. Since O has a similar

first-ionization-potential as H, there is significant conversion on IMAP-Lo's conversion surface that generates O^- from incident O atoms. As with H^-, the O^- atoms then pass through the ESA that defines the bandpass and into the TOF section of the instrument.

It is notable that for each source of neutral atoms, there is also a background. Based on results from IBEX, the dominant background in the instrument emanates from surfaces (such as the P10 electrode). While the team has eliminated or reduced these sources of background, it is likely that some nlow-level background will be observed. However, because the background results from particles that pass through the ESA, it is important to treat the background as a separate source of particles. Therefore, differential fluxes are computed without subtracting background. The background fluxes are calculated separately.

Interstellar Neutral Atoms (ISN) are mapped, characterized and analyzed as rates since they often include contributions from multiple specifies. There are only two fundamental rate products delivered:

- Light Atom maps associated predominantly with ISN H and He
- Heavy Atom maps associated predominantly with ISN O and Ne

The ENAs are computed as maps, in various coordinate projections. All IMAP-Lo maps are in the ram hemisphere (look directions with a component in ram direction). The associated products include the following:

- **Maps in the S/C frame with no corrections**. The lowest level map or slice of data that is useful for science includes differential fluxes of H atoms in the S/C reference frame without any corrections applied.
- **Maps in the S/C frame with sputter and bootstrap corrections**. The next level map or slice of data that is useful for science includes differential fluxes of H atoms in the S/C reference frame with corrections for sputtering by O and Ne, and the bootstrap correction for sputtering by higher energy ENAs.
- **Flux corrected S/C frame maps.** The resulting maps go through a final flux correction that accounts for and corrects the energy bandpass integration.
- **Maps in the inertial frame**. These products are not considered high priority and placed on the list of "nice-to-haves". The third level map or slice of data that is useful for science includes differential fluxes of H atoms in the heliospheric reference frame with sputtering and the bootstrap corrections. These products are placed in the heliospheric reference via a kinematic transformation but the energy of ENAs in this reference frame varies over the map. High-latitudes experience little energy change relative to the S/C frame, and low latitudues have shifts in energy that decrease the energy in the inertial frame relative to the S/C frame.

- **Compton-Getting Maps in the inertial frame** . The fourth level map or slice of data that is useful for science includes differential fluxes of H atoms in the heliospheric reference frame with sputtering and bootstrap corrections, and Compton-Getting (CG) transform. These products are placed in the heliospheric reference with the CG transformation applied, and the energy of ENAs in this reference frame are constant over the map. The CG correction interpolates the energy of ENAs in the S/C frame so that the ENA energy is constant in the inertial reference frame. The CG correction can be applied reliably at ESA levels 4 - 7. At energy steps below this level, the ENA energy shift between frames is larger than the ESA bandpass ΔE, and larger than the difference between the next higher ESA level and the ESA level analyzed. At this point, the approximation associated with the CG correction breaks down fully. The CG correction is also only applied to products taken in high-resolution mode since high-throughput mode opens the energy acceptance making the transformation to a fixed energy in the heliospheric frame highly non-linear.

- **Survival Probability corrected maps**. These products represent the various ENA maps divided by the survival probability.

Maps can be at 6° or 4° resolution, although both resolutions are below the 9° field-of-view (FOV) of IMAP-Lo. Additionally, for IMAP-Lo, we mainly use 6° data products. Each of the maps can be corrected for survival probability.

The process of making a map or a slice of sky involves choosing a set of pointing sets, and then making the products of choice in a chosen coordinate system. Data products associated with maps or slices of sky are denoted:

- $J_k[\text{frame}, \text{corr}, \text{SP}, \text{res}, \text{mode}]$, δJ_k, and σJ_k for differential fluxes, statistical and systematic uncertainties in flux at energy level k.

- $J_k^B[\text{frame}, \text{corr}, \text{SP}, \text{res}, \text{mode}]$, δJ_i^B, and σJ_i^B for background differential fluxes, statistical and systematic uncertainties in background at energy level k.

- $E_k[\text{frame}, \text{corr}, \text{mode}]$ represents the energy of ENAs in a given frame. Note that the energy becomes a map or slice of sky for the heliospheric inertial frame with no CG correction.

The following definitions apply:

- **Frame**: either **s** (S/C frame), **h** (heliospheric inertial), or **g** (heliospheric inertial with CG transform).

- **Correction**: either **n** (no correction applied), **c** (sputtering correction only), **b** (sputtering and bootstrap correction), of **a** (all: sputtering, bootstrap and flux correction).

- **SP**: Survival Probability corrections are denoted **S** and if no correction is applied, this field is denoted **A** for 1 au map.

- **Resolution**: The res is **6**° or **4**°
- **Mode**: either **r** (for high energy resolution, $\Delta E/E \sim 0.7$) or **t** (for high throughput , $\Delta E/E \sim 1$).

As an example, the following map-type

$$J_6[gaS6r] \tag{1}$$

denotes the ESA level 6 in the heliospheric frame with the CG correction, sputtering/bootstrap/flux corrections applied, 6° binning, Survival-Probability corrections, and high-resolution mode. Another important example would be

$$J_6[saS6r] \tag{2}$$

denotes the ESA level 6 in the spaceccraft frame, sputtering/bootstrap/flux corrections applied, 6° binning, Survival-Probability corrections, and high-resolution mode.

Since the process of making maps is automated at some level, we will generate several files that aid in the map-making process:

- **Pointings File.** This file runs through indices for the maps. Each map index corresponds to a list of pointing sets that will be used. This convention will allow us to utilize data from an array of pointings on the pivot platform, and an array of bandpass throughput modes.

The algorithms apply to the entire data set. However, we may limit releases to include data at only 200 eV and above since lower energy steps may be dominated by background. Internally, the IMAP team needs to be able to evaluate all available maps at each energy step.

Regardless of science mode, data products and telemetry from IMAP-Lo are the same. Table 1 shows the data products that are accumulated at various levels. At level 1B, IMAP-Lo data are accumulated over 28 spins (about 7 min), whereas star sensor data are accumulated in 720 bins for each spin.

Pointing sets represent the basis for all IMAP-Lo maps. These data are composed of DEs and exposure time accumulated in 3600 × 40 arrays. Each element represents a 0.1° × 0.1° binned direction on the sky in the S/C frame. Within each pointing (roughly 1 day of science operations) an average spin direction is defined. The azimuthal angle is the horizontal angle about the spin direction, and is binned in 3600 azimuthal angle elements. The central elevation angle of the pointing set is the average angle between the instrument boresight and the nominal spin direction. Off-angles (or deviation angles) in elevation are defined relative to the central elevation angle. These elevation angles are binned within 40 elevation angle elements, allowing for variation of the boresight up to 2° either toward or away from the central elevation angle. The elevation angle binning allows for coning, nutation, and other

Table 1. IMAP-Lo Data Products

Product	Level	Comments
Star Sensor Data	1B	Processed star sensor data
Annotated DEs	1B	
Histograms & Monitor Rates	1B	
Pointing Sets	1C	
S/C Sputter & Bootstrap Corr. Maps	2	
S/C Frame Flux Maps	2	
Helio Frame Kin. Maps	2	
Helio Frame CG Maps	2	
H, O Rate Maps	2	
Surv. Prob. Corrected Maps	3	Fluxes projected to 80 au

angular variations that inevitably effect the instantaneous pointing of the instrument. For example, on IBEX-Lo, pointing variations are typically observed within 0.2°.

There is a subtle point concerning ram maps. An important reduction of background results by only including maps in the ram direction. However, for heliospheric frame maps (both Kinematically corrected, and CG corrected) The ram directions extend over some portion of the anti-ram hemisphere in the S/C frame. Therefore, it is essential that pointing sets extend over the entire spin phase and the full ±2° range on off-angles (elevation angle relative to nominal boresight pointing).

The IMAP-Lo datasets includes lower energy portions that have not been previously published. Over these lower energy ranges, it is inevitable that background rates will be substantial and may even exceed signal in some portions of the maps. Since backgrounds can be quite large, the simple operation of subtracting background can result in some fluxes becoming negative. This occurs because background is estimated and cannot be explicitly measured in most cases. When negative fluxes are computed, the simplest choice is to zero the flux. However, that operation is non-linear mathematically when considering the statistical operations performed. In other words, subtracting background at lower energies in the maps will lead to statistical biases and other irregularities in the data.

A better choice, which we adopt for IMAP-Lo, is to calculate the signal including the background. We do not explicitly subtract the background fluxes. Instead the maps are computed (with signal plus background) and a separate background map is computed. The background maps may then be subtracted from the map as an operation performed at the last step, or other operations can be performed to determine the signal-to-noise ratio. The background maps represent a product carried along with the maps that include both signal and background.

Maps are transformed so that they can be shown in various reference frames (e.g., the S/C frame, or the heliospheric frame). Since backgrounds are computed as a separate product, the background is projected into the frame of choice. This means that the background map is a *projection of background* into the chosen reference

frame. This does not mean that the background is produced in the chosen reference frame. The natural reference frame of the background is in the instrument in the nominal S/C reference frame.

After maps are formed, they may be survival probability corrected. This involves estimating a survival probability corrected map and dividing this from the map products. These survival probability corrections are formed at the very end of the map-making process and are included for level 3 products on IMAP-Lo.

Below we detail the methodology associated with each of the corrections, and transformations applied.

2. S/C FRAME MAPS WITH NO CORRECTIONS

The most basic level of map ($J_k[snA6r]$, $J_k[snA4r]$, $J_k[snA6t]$, $J_k[snA4t]$) is that in the S/C reference frame with no corrections applied. The level 2 ENA pointing sets include counts C, efficiency factors ϵ, rates R, differential fluxes J, uncertainties, δJ, σJ, background fluxes J^B, uncertainties δJ^B, σJ^B and exposure times τ in 0.1° bins. The convention adopted here and throughout this document is that statistical uncertainties δY and systematic uncertainties σY are tied to a given mean quantity Y. Typically mean values are formed from inverse variance weighted averages. The formation of a map or a slice of sky involves finding the set of elements i from the pointing sets that fall into a given map pixel. The differential flux within the map pixel represents an exposure time average over the set:

$$\langle J\rangle_{\rm pxl} = \frac{\sum_i C_i/\epsilon_i}{GE\sum_i \tau_i} \tag{3}$$

$$\langle (\delta J)^2\rangle_{\rm pxl} = \frac{\sum_i C_i/\epsilon_i^2}{[GE\sum_i \tau_i]^2} \tag{4}$$

$$\langle \sigma J\rangle_{\rm pxl} = \frac{\sigma G}{G}\langle J\rangle_{\rm pxl} \tag{5}$$

$$\langle J^B\rangle_{\rm pxl} = \frac{\sum_i J_i^B\tau_i}{\sum_i \tau_i} \tag{6}$$

$$\langle (\delta J^B)^2\rangle_{\rm pxl} = \frac{\sum_i \delta J_i^2\tau_i^2}{[\sum_i \tau_i]^2} \tag{7}$$

$$\langle \sigma J^B\rangle_{\rm pxl} = \frac{\sigma G}{G}\langle J^B\rangle_{\rm pxl} \tag{8}$$

where E is the corresponding bin energy, G is the geometric factor with units of cm^2 sr eV/eV, and σG is the uncertainty in the geometric factor.

3. S/C FRAME MAPS WITH SPUTTERING CORRECTIONS

The sputtering corrections are included in maps ($J_k[scA6r]$, $J_k[scA4r]$, $J_k[scA6t]$, $J_k[scA4t]$) in the S/C reference frame. Neutral Oxygen particles may produce sputtered products (H, C and O) within the instrument at energies lower than the parent.

We therefore must apply an Oxygen sputtering correction in ESA levels 5 and 6 for 90° maps.

The level 2 ENA pointing sets are used to derive the O differential flux J_k^O and the associated background J_k^{OB} using the same methodology as detailed in equations (3) - (8):

$$\langle J_k^{O\prime}\rangle_{\rm pxl} = \langle J_k^O\rangle_{\rm pxl} - \langle J_k^{OB}\rangle_{\rm pxl} \tag{9}$$

$$\langle (\delta J_k^{O\prime})^2\rangle_{\rm pxl} = \langle (\delta J_k^O)^2\rangle_{\rm pxl} + \langle (\delta J_k^{OB})^2\rangle_{\rm pxl} \tag{10}$$

where $k = 5, 6$. If the flux in a pixel is less than 0, then it is set equal to 0.

The corrected O flux is then used to subtract out the sputtered products:

$$\langle J_k^c\rangle_{\rm pxl} = \langle J_k\rangle_{\rm pxl} - \langle J_k^{O\prime}\rangle_{\rm pxl} f_k^O \tag{11}$$

$$\langle (\delta J_k^c)^2\rangle_{\rm pxl} = \langle (\delta J_k)^2\rangle_{\rm pxl} + \langle (\delta J_k^{O\prime})^2\rangle_{\rm pxl} (f_k^O)^2 \tag{12}$$

$$\langle \sigma J_k^c\rangle_{\rm pxl} = \frac{\langle J_k^c\rangle_{\rm pxl}}{\langle J_k\rangle_{\rm pxl}} \langle \sigma J_k\rangle_{\rm pxl} \tag{13}$$

where $k = 5, 6$ and f_k^O is the ratio of sputter H to O. The quantity $\langle J_k^c\rangle_{\rm pxl}$ corresponds to sputter corrected differential flux. Estimates of f_k^O are provided in Table 2. These parameters will be re-evaluated early in the mission to derive improved estimates.

NOTE: These are for 90° maps. We need to evaluate these terms in flight, and terms at steps 3 and 4 will also need to be evaluated if we want to use maps at pivot angles other than 90°.

4. S/C FRAME MAPS WITH BOOTSTRAP & SPUTTERING CORRECTIONS

The bootstrap corrections are included in maps ($J_k[sbA6r]$, $J_k[sbA4r]$, $J_k[sbA6t]$, $J_k[sbA4t]$) in the S/C reference frame is detailed in Appendix E of McComas et al. (2014). The background fluxes are first subtracted from the fluxes within each pixel (and zeroing any negative values)

$$\langle J_k^{c\prime}\rangle_{\rm pxl} = \langle J_k^c\rangle_{\rm pxl} - \langle J_k^B\rangle_{\rm pxl} \tag{14}$$

$$\langle (\delta J_k^{c\prime})^2\rangle_{\rm pxl} = \langle (\delta J_k^c)^2\rangle_{\rm pxl} \tag{15}$$

$$\langle \sigma J_k^{c\prime}\rangle_{\rm pxl} = \left(\frac{\langle J_k^{c\prime}\rangle_{\rm pxl}}{\langle J_k^c\rangle_{\rm pxl}}\right) \langle \sigma J_k^c\rangle_{\rm pxl} \tag{16}$$

Table 2. Sputtering correction terms $h_{i,k}$.

Energy Level	f_k^O
5	0.15 ± 0.05
6	0.01 ± 0.008

These background corrected differential fluxes are used in the bootstrap algorithm

$$J_7^b = J_7^{c\prime} - h_{78} J_8^b \tag{17}$$

$$J_6^b = J_6^{c\prime} - \left(\sum_{k=7}^{8} h_{6k} J_k^b \right) \tag{18}$$

$$J_5^b = J_5^{c\prime} - \left(\sum_{k=6}^{8} h_{5k} J_k^b \right) \tag{19}$$

$$J_4^b = J_4^{c\prime} - \left(\sum_{k=5}^{8} h_{4k} J_k^b \right) \tag{20}$$

$$J_3^b = J_3^{c\prime} - \left(\sum_{k=4}^{8} h_{3k} J_k^b \right) \tag{21}$$

$$J_2^b = J_2^{c\prime} - \left(\sum_{k=3}^{8} h_{2k} J_k^b \right) \tag{22}$$

$$J_1^b = J_1^{c\prime} - \left(\sum_{k=2}^{8} h_{1k} J_k^b \right) \tag{23}$$

where $J_8^b = J_7^{c\prime}(E_8/E_7)^\gamma$, $\gamma = \ln(J_6^{c\prime}/J_7^{c\prime})/\ln(E_6/E_7)$, and again we zero any bootstrap fluxes that are negative. Here E_i are the respective S/C energy levels in HiThru or HiRes modes. $E_8 = 2.1E_7$ is a virtual energy channel. The associated uncertainties

$$(\delta J_7^b)^2 = (\delta J_7^{c\prime})^2 \tag{24}$$

$$(\delta J_6^b)^2 = (\delta J_6^{c\prime})^2 + h_{67}^2 (\delta J_7^b)^2 \tag{25}$$

$$(\delta J_5^b)^2 = (\delta J_5^{c\prime})^2 + \left(\sum_{k=6}^{7} h_{5k}^2 (\delta J_k^b)^2 \right) \tag{26}$$

$$(\delta J_4^b)^2 = (\delta J_4^{c\prime})^2 + \left(\sum_{k=5}^{7} h_{4k}^2 (\delta J_k^b)^2 \right) \tag{27}$$

$$(\delta J_3^b)^2 = (\delta J_3^{c\prime})^2 + \left(\sum_{k=4}^{7} h_{3k}^2 (\delta J_k^b)^2 \right) \tag{28}$$

$$(\delta J_2^b)^2 = (\delta J_2^{c\prime})^2 + \left(\sum_{k=3}^{7} h_{2k}^2 (\delta J_k^b)^2 \right) \tag{29}$$

$$(\delta J_1^b)^2 = (\delta J_1^{c\prime})^2 + \left(\sum_{k=2}^{7} h_{1k}^2 (\delta J_k^b)^2 \right). \tag{30}$$

While we have dropped the notation for averages per pixel ($\langle \ldots \rangle_{\mathrm{pxl}}$) these quantities are still evaluated based on pixel averages. For each of the bootstrap corrected fluxes, the systematic uncertainties scale with the corrected fluxes:

$$\sigma J_k^b = \left(\frac{J_k^b}{J_k^{c\prime}} \right) \sigma J_k^{c\prime} \tag{31}$$

The bootstrap correction has dropped subtraction of higher energy terms that is typically evaluated based on IMAP-Hi fluxes. The bootstrap corrections from higher energy fluxes are typically very small. The dependence is dropped so that maps can be evaluated for IMAP-Lo in any configuration of the pivot platform, without dependence on IMAP-Hi.

The final expression for bootstrap fluxes include the estimated backgrounds.

$$\Delta J_k^b = J_k^{c\prime} - J_k^b \tag{32}$$

$$\langle J_k^{bc} \rangle_{\rm pxl} = \langle J_k^c \rangle_{\rm pxl} - \langle \Delta J_k^b \rangle_{\rm pxl} \tag{33}$$

$$\langle (\delta J_k^{bc})^2 \rangle_{\rm pxl} = \langle (\delta J_k^b)^2 \rangle_{\rm pxl} \tag{34}$$

$$\langle \sigma J_k^{bc} \rangle_{\rm pxl} = \left(\frac{\langle J_k^{bc} \rangle_{\rm pxl}}{\langle J_k^b \rangle_{\rm pxl}} \right) \langle \sigma J_k^b \rangle_{\rm pxl} \tag{35}$$

5. S/C FRAME MAPS WITH FLUX CORRECTIONS

The flux correction takes into account the integration over the energy bandpass, and is applied to determine the fluxes coming into the instrument. The flux correction is applied to the observed fluxes in the S/C frame after the sputtering and bootstrap corrections have been applied. The S/C fluxes with the flux correction applied represent the sum of background fluxes and incident fluxes. Therefore the background fluxes in the S/C frame are also flux corrected.

We need to know the power-law slopes to determine the flux correction. For Lo, the differential fluxes and background fluxes in the S/C frame are denoted $(J_k^s, \delta J_k^s, \sigma J_k^s, J_k^{Bs}, \delta J_k^{Bs}, \sigma J_k^{Bs})$. Note that the quantity J_k^s includes the backgrounds. The energy at step k is denoted E_k^s. For Hi, on the other hand, subtract backgrounds first; apply ESA flux correction to signal only; then propagate the corresponding statistical and systematic uncertainties.

Table 3. Bootstrap terms $h_{i,k}$.

obs-i inc-k	1	2	3	4	5	6	7	8
1	0	0.03	0.01	0	0	0	0	0
2	0	0	0.05	0.02	0.01	0	0	0
3	0	0	0	0.09	0.03	0.016	0.01	0
4	0	0	0	0	0.16	0.068	0.016	0.01
5	0	0	0	0	0	0.29	0.068	0.016
6	0	0	0	0	0	0	0.52	0.061
7	0	0	0	0	0	0	0	0.75

For each flux, we first estimate the power-law slope,

$$\gamma_k = \ln\left(J^s_{\mathrm{k+1}}/J^s_{k-1}\right) / \ln(E^s_{\mathrm{k+1}}/E^s_{\mathrm{k-1}}) \tag{36}$$

$$\delta\gamma_k = [\gamma_k / \ln\left(J^s_{\mathrm{k+1}}/J^s_{k-1}\right)] \left[(\delta J^s_{k-1}/J^s_{k-1})^2 + (\delta J^s_{k+1}/J^s_{k+1})^2\right]^{1/2} \tag{37}$$

The only power-laws that cannot be specified are at the end-states (k=1, k=7) since there is no step below or above this, respectively. Therefore, we use the conditions:

$$\gamma_1 = \ln\left(J^s_2/J^s_1\right) / \ln(E^s_2/E^s_1) \tag{38}$$

$$\delta\gamma_1 = [\gamma_1 / \ln\left(J^s_2/J^s_1\right)] \left[(\delta J^s_1/J^s_1)^2 + (\delta J^s_2/J^s_2)^2\right]^{1/2} \tag{39}$$

and

$$\gamma_7 = \ln\left(J^s_7/J^s_6\right) / \ln(E^s_7/E^s_6) \tag{40}$$

$$\delta\gamma_7 = [\gamma_7 / \ln\left(J^s_7/J^s_6\right)] \left[(\delta J^s_7/J^s_7)^2 + (\delta J^s_6/J^s_6)^2\right]^{1/2} \tag{41}$$

The observed power-laws represent ESA transmission integrations over the source fluxes including the background (for Lo only). Therefore, the source flux (including background) at each energy level k is

$$J^{\mathrm{s,src}}_k = J^s_k / \eta_{\mathrm{esa,k}}(\gamma) \tag{42}$$

$$\delta J^{\mathrm{s,src}}_k = \delta J^s_k / \eta_{\mathrm{esa,k}}(\gamma) \tag{43}$$

The ESA transmission scale factors $\eta_{\mathrm{esa,k}}$ represent the bias of the response function to power-law distribution. The steeper the power-law, the larger the bias to lower-energies. These tend to enhance the observed flux after integration through the ESA for negative power-laws (see Figure 1). We have used the response functions of the instrument to develop fits to $\eta_{\mathrm{esa,k}}(\gamma)$ as indicated in Table 4. The fit for $\eta_{\mathrm{esa,k}}(\gamma) = M_0 + M_1\gamma + M_2\gamma^2 + M_3\gamma^3 + M_4\gamma^4 + M_5\gamma^5$

A short iterative process is used to get accurate approximations to derive power-law slopes and estimates of the source fluxes and the background source fluxes:

Table 4. Fit factors for $\eta_{\mathrm{esa,k}}(\gamma)$.

ENERGY LEVEL	1	2	3	4	5	6	7
M_0	1.0152	1.0142	1.013	1.0109	1.0145	1.0116	1.0156
M_1	-0.047723	-0.045778	-0.045334	-0.043671	-0.045219	-0.043433	-0.048728
M_2	0.0304	0.030061	0.030649	0.029741	0.029705	0.030755	0.029868
M_3	-0.001817	-0.0020424	-0.0021426	-0.0014197	-0.0021726	-0.0020747	-0.0016762
M_4	0.0023649	0.0021796	0.0021755	0.0016756	0.0020739	0.001899	0.0022885
M_5	-0.00032519	-0.00029036	-0.0002869	-0.0002298	-0.0002652	-0.0002476	-0.0003183

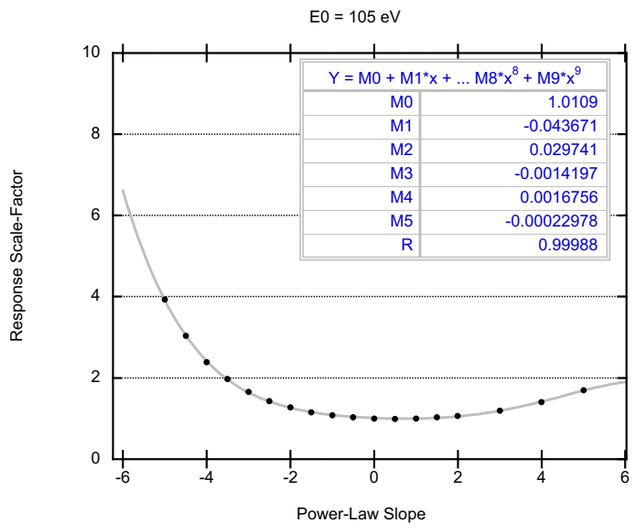


Figure 1. The ESA transmission function scale-factor $\eta_{\mathrm{esa,k}}(\gamma)$.

- For Lo, at each energy level k, we apply the flux correction after sputtering and bootstrap, using the total S/C fluxes J_k^s that include backgrounds (backgrounds are not subtracted at this stage). We apply the same ESA correction to the background fluxes J_k^{Bs} so that signal and background remain consistent throughout the pipeline. We use these fluxes to estimate power-laws γ at each level. For Hi, we use background-subtracted fluxes.
- We then use the fit factors in Table 4 to develop estimates for $\eta_{\mathrm{esa,k}}$ and $\eta^{\mathrm{bkg}}_{\mathrm{esa,k}}$ (for Lo only) for the source fluxes and background fluxes, respectively.
- Equation (42) is used to estimate the source fluxes and background source fluxes (for Lo only).
- These source fluxes and background source fluxes (for Lo only) are used to get improved estimates of the power-laws via predictor-corrector scheme (see Appendix A and the corresponding versions of Equations 38 & 40 for the end members),

$$\gamma_k = \ln(J^{\mathrm{s,src}}_{\mathrm{k+1}}/J^{\mathrm{s,src}}_{k-1})/\ln(E^s_{\mathrm{k+1}}/E^s_{\mathrm{k-1}}) \tag{44}$$

- The improved power-laws provide improved estimates for the transmission factors $\eta_{\mathrm{esa,k}}$ and $\eta^{\mathrm{bkg}}_{\mathrm{esa,k}}$ for the source fluxes and background fluxes (for Lo only), respectively.
- Equation (42) is used to estimate a final approximation for the source flux and background source flux (for Lo only) at each energy level.

The iterative scheme should track the total % of convergence at each iteration, and either end iteration once convergence is achieved to within average RMS $\sim$ 0.5%

or the iterations reach 20. Extremely rugged distributions were shown to converge within at most 16 iterations. Using the estimate for the power-laws γ_k and $\gamma_k^{\rm bkg}$, the source fluxes $J_k^{\rm s,src}$ and background source fluxes $J_k^{\rm s,bkg,src}$. The process outlined above is used to estimate fluxes and background fluxes in the S/C frame from the pointing sets.

Survival probabilities are also developed for the S/C reference frame. These survival probabilities are binned in the S/C frame map and divide the fluxes in the S/C frame to correct for survival probability. Similarly, the square of the survival probability divides the variance of the flux to estimate the SP-corrected variance. These operations are also performed on the background fluxes when the SP-correction is estimated.

6. S/C FRAME MAPS WITH SURVIVAL PROBABILITY CORRECTIONS

The survival probability corrections are included in flux maps ($J_k[snS6r]$, $J_k[snS4r]$, $J_k[snS6t]$, $J_k[snS4t]$), and bootstrap/sputter-corrected maps ($J_k[sbS6r]$, $J_k[sbS4r]$, $J_k[sbS6t]$, $J_k[sbS4t]$, $J_k[sbS6r]$) in the S/C reference frame. IMAP-Lo products include survival probability maps that are applied in the S/C frame $P^s_{\rm sp,k}$ and inertial frame $P^h_{\rm sp,k}$ for each of energy levels. The S/C frame fluxes $J^{sA}_{\rm k}$ that divide by the pointing set survival probabilities yield the survival probability corrected pointing set fluxes,

$$J_k^{sS} = \frac{J_k^{sA}}{P^s_{\rm sp,k}}. \tag{45}$$

Similarly, the flux statistical uncertainties, systematic uncertainties, the background fluxes, background flux statistical uncertainties and background systematic uncertainties are each divided by the survival probabilities to yield the survival probability-corrected differential fluxes.

Once the survival probability corrected fluxes, backgrounds and uncertainties are survival probability-corrected, the steps identified in previous sections (§2), (§3), and (§4) are taken to solve for the survival probability corrected maps.

7. KINEMATIC HELIOSPHERIC INERTIAL FRAME TRANSFORMATION

This product has been deprecated in priority. The product is on the list of "nice-to-haves".

The heliospheric inertial frame transformation is included in flux maps and energy maps ($J_k[hbA6r]$, $J_k[hbA4r]$, $J_k[sbA6t]$, $J_k[sbA4t]$) and ($J_k[hbS6r]$, $J_k[hbS4r]$, $J_k[sbS6t]$, $J_k[sbS4t]$) for energy levels $k = 1 - 7$. The heliospheric inertial frame transformation is also included in flux maps and energy maps without bootstrap corrections ($J_k[hnA6r]$, $J_k[hnA4r]$, $J_k[snA6t]$, $J_k[snA4t]$) and ($J_k[hnS6r]$, $J_k[hnS4r]$, $J_k[snS6t]$, $J_k[snS4t]$) for all energy levels.

We always bin counts and exposure times, not fluxes. For each pointing-set pixel i, we accumulate counts C_i, exposure time τ_i, and efficiency ϵ_i into the destination map

pixel. Flux and its uncertainties are computed after binning using Equations 49 - 51 (and the corresponding background Equations 57 - 59 for Lo).

Figure 2 shows the frame transformation from the S/C reference frame to the heliospheric inertial reference frame. The ENA velocity in the heliospheric inertial reference frame is denoted $\mathbf{v}^h$ and is related to the S/C frame velocity $\mathbf{v}^s$ by adding the S/C motion $\mathbf{u}$:

$$\mathbf{v}^h = \mathbf{v}^s + \mathbf{u} \tag{46}$$

While the geometry in Figure 2 is oriented for the case of the IMAP-Lo boresight with 90° elongation, equation(46) is general and applies to any pointing associated with the IMAP-Lo instrument.

The S/C velocity $u \approx 30$ km s^{-1} in the ram direction and the speed $v^s = \sqrt{2E^s/m}$ are known. The direction in the S/C frame are each specified by the 0.1° in the pointing set. Therefore, the heliospheric inertial velocity $\mathbf{v}^h$ is defined for every bin in the pointing set.

It is helpful to view the ENA velocity using the pivot-angle θ and spin-angle ϕ as shown in Figure 3. However, note that each pointing set direction is characterized by a unit vector ($\hat{e}_s = \mathbf{v}^s/v^s$) which is opposite the boresight direction in the S/C frame. α is the angle between $\hat{e}_s$ and $\hat{u}$ the S/C velocity unit vector:

$$\cos\alpha = \hat{\mathbf{e}}_\mathbf{s}(\theta,\phi).\hat{\mathbf{u}} \tag{47}$$

Use SPICE to find $\hat{e}_s$ and $\hat{u}$ for each day.

The particle energy using these angles is:

$$E^h = E^s + E_u - 2\sqrt{E^s E_u}\cos(\alpha) \tag{48}$$

where $E_u = mu^2/2 = 4.7$ eV and α is the angle between the boresight and the S/C ram direction. The energy of the ENA in the inertial plane also varies over the inertial map.

To solve for the ENA fluxes in the inertial frame, we loop over each pixel j in the selected pointing set. We use equations (46) to convert the velocity in the S/C frame v_j^s associated with the pointing pixel into the heliospheric inertial velocity v_j^h. Next, we find the pixel in the inertial map corresponding to v_j^h. We add the counts and the exposure time from the pointing set pixel to the accumulated counts and exposure time in the corresponding inertial map pixel.

After the counts and exposure times have been aggregated into each inertial frame pixel, we form the projected S/C frame differential energy flux:

$$\langle J_s\rangle = \frac{\sum_i C_i/\epsilon_i}{GE\sum_i \tau_i} \tag{49}$$

$$\langle(\delta J_s)^2\rangle = \frac{\sum_i C_i/\epsilon_i^2}{[GE\sum_i \tau_i]^2} \tag{50}$$

$$\langle\sigma J_s\rangle = \frac{\sigma G}{G}\langle J_s\rangle \tag{51}$$

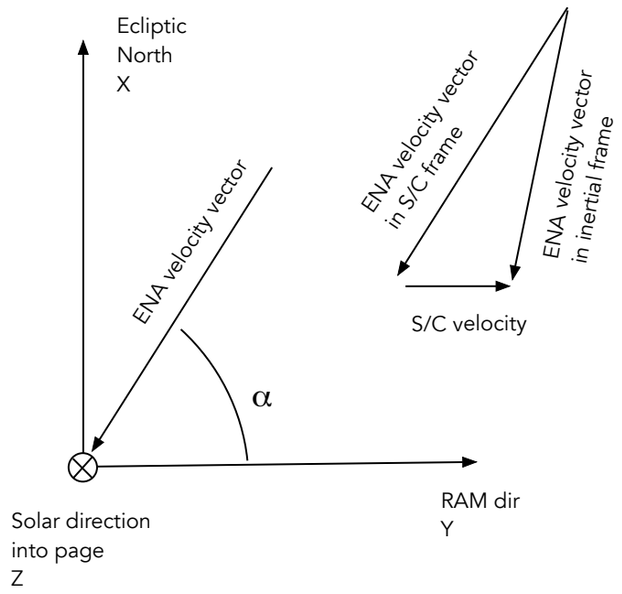


Figure 2. Basic geometry associated with viewing ENAs on IMAP-Lo. The frame transform from the S/C frame to the inertial reference frame involves adding the S/C velocity to the incident ENA velocity.

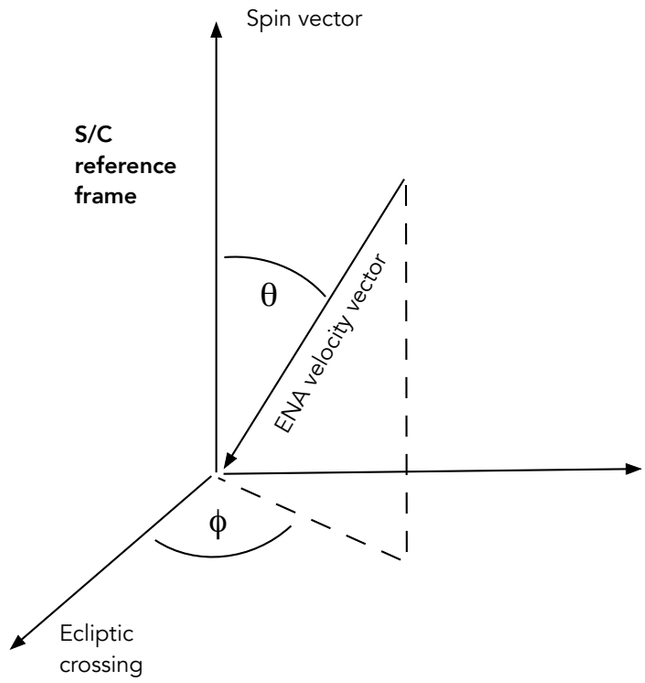


Figure 3. Velocity angles, the elongation θ and spin ϕ, that define the incident velocity.

where G and E are the geometric factor and energy in the S/C frame, C_i represents the counts from the aggregated set (i is the aggregation index), ϵ_i is the efficiency factor in the aggregated list, and τ_i is the exposure time in the aggregated list. The differential flux in the heliospheric frame that contributes to the heliospheric map pixel is obtained from Liouville theorem:

$$J_j^h = \langle J_s \rangle \left(\frac{E_j^h}{E_j^s} \right) \tag{52}$$

where $E_j^h = m(v^h)^2/2$ and $E_j^s = m(v^s)^2/2$. Note that each pointing set pixel will have a slightly different heliospheric frame energy,

$$\langle E^h \rangle_{\text{pxl}} = \frac{\sum_i E_i^h \tau_i}{\sum_i \tau_i} \tag{53}$$

for each HF pixel, also keep the exposure-weighted mean of the S/C energy that maps to the chosen HF energy E_k:

$$\langle E^s \rangle_{\text{pxl}} = \frac{\sum_i E_i^s \tau_i}{\sum_i \tau_i} \tag{54}$$

This corresponds to what the code returns in `energy_sc_average()`

So the final inertial frame energy represents an exposure-time weighted average of the inertial frame energies that map into a given pixel. Similarly, the variance that contributes to the inertial map pixel is

$$(\delta J_j^h)^2 = (\delta J_s)^2 \left(\frac{E_j^h}{E_j^s} \right)^2 \tag{55}$$

$$\sigma J_j^h = \sigma J^s \left(\frac{E_j^h}{E_j^s} \right) \tag{56}$$

The same transformations apply to the background flux that contributes to the pixel,

$$J_j^{Bh} = J^{Bs} \left(\frac{E_j^h}{E_j^s} \right) \tag{57}$$

$$(\delta J_j^{Bh})^2 = (\delta J^{Bs})^2 \left(\frac{E_j^h}{E_j^s} \right)^2 \tag{58}$$

$$\sigma J_j^{Bh} = \sigma J^{Bs} \left(\frac{E_j^h}{E_j^s} \right) \tag{59}$$

The resulting inertial map pixel contains the average differential flux in the heliospheric frame, the uncertainty, the background flux and uncertainty, and the average heliospheric energy in the pixel.

8. COMPTON-GETTING HELIOSPHERIC INERTIAL FRAME TRANSFORMATION

The Compton-Getting (CG) Heliospheric Inertial Frame inertial frame transformation is included in flux maps ($J_k[gbA6r]$, $J_k[gbA4r]$) and ($J_k[gbS6r]$, $J_k[gbS4r]$) for energy levels $k = 1 - 7$ (for Lo) and $k = 1 - 9$ (for Hi). We always bin counts and exposure times, not fluxes. For each pointing-set pixel i, we accumulate counts C_i, exposure time τ_i, and efficiency ϵ_i into the destination map pixel. Flux and its uncertainties are computed after binning using Equations 49 - 51 (and the corresponding background Equations 57 - 59 for Lo).

The CG transform cannot be applied to fluxes from Hi-throughput mode. Note that while we apply the transformation at all energy levels, the maps below IMAP-Lo ESA step 4 will need to be examined carefully, and may not be released if dominated by background.

The CG correction scheme steps through each of the directions in the pointing set (0.1° resolution). Each pointing set direction is characterized by a unit vector,

$$\hat{e}_s = \mathbf{v}^s / v^s. \tag{60}$$

which is opposite the boresight direction in the S/C frame. α is the angle between $\hat{e}_s$ and $\hat{u}$ and the S/C velocity vector:

$$\cos\alpha = \hat{\mathbf{e}}_\mathbf{s}(\theta, \phi).\hat{\mathbf{u}}$$

where ϕ denotes the spin angle and θ is fixed at $\sim 90°$ for Lo ENA days and Hi90. In contrast, $\theta \sim 135°$ for Hi45 and non-90° for Lo ISN days, which can complicate the determination of α. In addition, the spin axis is offset by about 4° from the Sun direction, and daily repointing can shift this by up to ±3°. Nevertheless, using SPICE to obtain $\hat{e}_s$ and $\hat{u}$ for each day ensures that the calculation remains straightforward.

Performing the CG correction requires finding the energy E^s in the S/C frame for a given pointing direction $\hat{e}_s$ (which specifies α) that corresponds to energy E^h in the inertial frame. Using equation (48), the energy relation implies

$$y^2 = x^2 - 2x\cos(\alpha) + 1 \tag{61}$$

where $y = \sqrt{E^h/E_u}$, $x = \sqrt{E^s/E_u}$. The solution for x is

$$x = \cos(\alpha) + \sqrt{y^2 - \sin^2(\alpha)} \tag{62}$$

With $E^s = x^2 E_u$, we are in the position to solve for the CG correction.

The procedure for the solving the CG transform follows the following steps:

1. For a given E^h (E^h is the heliospheric frame (HF) energy at which we create CG-corrected maps), we step through each point in the pointing set associated with a specific value of α to determine the energy in the S/C frame E^s and speed $v^s = \sqrt{2E^s/m}$. Note that E^s is not an ESA central energy: rather it is the α-dependent S/C energy that maps to the chosen HF energy E^h.

2. With the direction and speed in the S/C frame, we find the velocity vector $\mathbf{v}^s$. Equation (46) allows us to solve for the velocity in the heliospheric frame, $\mathbf{v}^h$, which provides the direction for binning in the heliospheric map(v_y^h/v_x^h provides the spin angle in the HF, Column V in the excel). The fluxes (J_k^s, δJ_k^s, σJ_k^s) and background fluxes (J_k^{Bs}, δJ_k^{Bs}, σJ_k^{Bs}) **are binned and exposure-time averaged within each** 4° **or** 6° **heliospheric map pixel**, as specified in Equations 49 - 51 and 57 - 59. **However, notes that they are spacecraft frame fluxes (hence, the superscrip s), because they are obtained by dividing rates accumulated in HF pixels by the Geometric Factor and center energy** E_k^{ESA} **associated with each step** k**. Excel: V/AS/AT define HF angular pixels; AV accumulates exposure.**

3. Each pset bin in a given HF pixel is associated with a potentially different S/C frame energy E^s. Therefore, for each HF pixel, keep the exposure-weighted mean of the S/C energy that maps to the chosen HF energy E^h:

$$\langle E_k^s \rangle_{\text{pxl}} = \frac{\sum_i E_i^s \, \tau_{i,k}}{\sum_i \tau_i} \tag{63}$$

This corresponds to what the code returns in `energy_sc_average()`.

Note. The target spacecraft-frame energy $E^s(E^h, \alpha)$ is set by the geometry in Equations 61 – 62 and is independent of ESA step. However, the subscript k in $\langle E_k^s \rangle$ only records that the pixel average used step-k exposure weights $\tau_{i,k}$. Consequently, the $\langle E_k^s \rangle$ values should agree across k up to small differences from the weighting.

4. At this point, we have associated each pixel of the HF map with exposure-time averages of $(J_k^s, \delta J_k^s, \sigma J_k^s, J_k^{Bs}, \delta J_k^{Bs}, \sigma J_k^{Bs}, E_k^s)$ at energy levels 1 - 7 (for Lo) and 1 - 9 (for Hi). For each flux, we estimate the power-law slope

$$\gamma_k = \ln\left(J_{\text{k+1}}^s / J_{\text{k-1}}^s\right) / \ln(E_{\text{k+1}}^{ESA} / E_{\text{k-1}}^{ESA}) \tag{64}$$

$$\delta\gamma_k = \left[\gamma_k / \ln\left(J_{\text{k+1}}^s / J_{\text{k-1}}^s\right)\right] \left[(\delta J_{k-1}^s / J_{k-1}^s)^2 + (\delta J_{k+1}^s / J_{k+1}^s)^2\right]^{1/2} \tag{65}$$

The only power-law that cannot be specified is at the end-states at k=1, and K=7 (for Lo) or 9 (for Hi) since there is no step below or above this. Therefore,

$$\gamma_1 = \ln\left(J_2^s / J_1^s\right) / \ln(E_2^{ESA} / E_1^{ESA}) \tag{66}$$

$$\delta\gamma_1 = \left[\gamma_1 / \ln\left(J_2^s / J_1^s\right)\right] \left[(\delta J_1^s / J_1^s)^2 + (\delta J_2^s / J_2^s)^2\right]^{1/2} \tag{67}$$

and

$$\gamma_K = \ln\left(J_{\text{K}}^s / J_{K-1}^s\right) / \ln(E_{\text{K}}^{ESA} / E_{\text{K-1}}^{ESA}) \tag{68}$$

$$\delta\gamma_K = \left[\gamma_K / \ln\left(J_{\text{K}} / J_{K-1}\right)\right] \left[(\delta J_K / J_K)^2 + (\delta J_{K-1} / J_{K-1})^2\right]^{1/2} \tag{69}$$

The observed power-laws represent ESA transmission integrations over the source fluxes in the background. Therefore, the source flux at each energy level k is

$$J_k^{\rm src} = J_k^s / \eta_{\rm esa,k}(\gamma) \tag{70}$$

The ESA transmission scale factors ($\eta_{\rm esa,k}$) represent the bias of the response function to power-law distribution. The steeper the power-law, the larger the bias to lower-energies. These tend to enhance the observed flux after integration through the ESA for negative power-laws (see Figure 1). We have used the response functions of the instrument to develop fits to $\eta_{\rm esa,k}(\gamma)$ as indicated in Table 4 (for Lo) and Table 5 (for Hi) [need the table here]. The fit for $\eta_{\rm esa,k}(\gamma) = M_0 + M_1\gamma + M_2\gamma^2 + M_3\gamma^3 + M_4\gamma^4 + M_5\gamma^5$.

5. A short iterative process is used to get accurate approximations to derive power-law slopes and estimates of the source fluxes and the background source fluxes:

   (a) at a given energy E^h in the HF, we find fluxes J_k^s (in the S/C frame), but binned according to HF frame. We use Equations 64 - 69 to estimated the power-law slope and uncertainty.

   Note. For Lo, backgrounds are not subtracted at this stage. Therefore, the total S/C fluxes J_k^s include backgrounds. We further apply the same scheme to estimate power-laws γ to the background fluxes so that signal and background remain consistent throughout the pipeline. For Hi, we use background-subtracted fluxes.

   (b) We then use the fit factors in Table 4 (Table 5 for Hi) to develop estimates for $\eta_{\rm esa,k}$ and $\eta_{\rm esa,k}^{\rm bkg}$ for the source fluxes and background fluxes (for Lo only), respectively.

   (c) Equation (42) is used to estimate the source fluxes and background source fluxes (for Lo only).

   (d) These source fluxes and background source fluxes (for Lo only) are used to get improved estimates of the power-laws via predictor-corrector scheme (see Appendix A),

$$\gamma_k = \ln(J_{\rm k+1}^{\rm src}/J_{k-1}^{\rm src}) / \ln(E_{\rm k+1}^{ESA}/E_{\rm k-1}^{ESA}) \tag{71}$$

   (e) The improved power-laws provide improved estimates for the transmission factors $\eta_{\rm esa,k}$ and $\eta_{\rm esa,k}^{\rm bkg}$ for the source fluxes and background fluxes (for Lo only), respectively.

   (f) Equation (70) is used to estimate a final approximation for the source flux and background source flux (for Lo only) at each energy level.

   Note. While in equation 71, we keep using newest estimates for the source flux J_k^{SRC} to improve our estimates of γ_k and $\eta_{esa,k}$, in Equation 70 to find a better estimation of J_k^{SRC}, we always go back to J_k^s.

The iterative scheme should track the total % of convergence at each iteration, and either end iteration once convergence is achieved to within average RMS $\sim 0.5\%$ or the iterations reach 20. Extremely rugged distributions were shown to converge within at most 16 iterations.

Note. In Steps 3–5 we computed and stored, for each ESA step $k = 1, \ldots, K$, the per-step quantities $\{J^s_k, \delta J^s_k, \sigma^s_{J_k}, J^s_{B,k}, \ldots\}$ on the HF grid. For the given E^h, Equations 61 – 62 give a *step-independent* spacecraft-frame energy $E^s(E^h, \alpha)$ per direction. Equation 63 then defines an exposure time-weighted pixel mean $\langle E^s_k \rangle$ for each k, (which we don't expect to be significantly different across k values). We then find the ESA interval that brackets this pixel mean energy, $E^{\rm ESA}_{k-1} < \langle E^s_k \rangle \leq E^{\rm ESA}_k$. We then set $k_{\rm ref} = k - 1$. For end members, if $\langle E^s \rangle \leq E^{\rm ESA}_1$, we use $k_{\rm ref} = 1$ and if $\langle E^s \rangle > E^{\rm ESA}_K$, we use $k_{\rm ref} = K$.

6. Using the estimate for the power-laws $\gamma_{k_{\rm ref}}$ and $\gamma^{\rm bkg}_{k_{\rm ref}}$, the source fluxes $J^{\rm src}_{k_{\rm ref}}$ and background source fluxes $J^{\rm bkg,src}_{k_{\rm ref}}$, we then estimate the differential flux in the inertial frame in two steps:

   (a) interpolate source flux from ESA center $E^{ESA}_{k_{\rm ref}}$ to $\left\langle E^s_{k_{\rm ref}} \right\rangle$ using the final slope $\gamma_{k_{\rm ref}}$ found at the end of iterations:

$$J^{src}_{k_{\rm ref}}(\left\langle E^s_{k_{\rm ref}} \right\rangle) = J^{\rm src}_{k_{\rm ref}}(\left\langle E^s_{k_{\rm ref}} \right\rangle / E^{\rm ESA}_{k_{\rm ref}})^{\gamma_{k_{\rm ref}}} \tag{72}$$

   This gives us source fluxes, binned in heliospheric coordinates, and projected to $\left\langle E^s_{k_{\rm ref}} \right\rangle$ energy.

   (b) We then apply Liouville theorem (Equation 52) to scale fluxes into the HF:

$$J^g = J^{\rm src}_{k_{\rm ref}}(\left\langle E^s_{k_{\rm ref}} \right\rangle)(E^h / \left\langle E^s_{k_{\rm ref}} \right\rangle) \tag{73}$$

$$J^g = J^{\rm src}_{k_{\rm ref}}(\left\langle E^s_{k_{\rm ref}} \right\rangle / E^{ESA}_{k_{\rm ref}})^{\gamma_{k_{\rm ref}}}(E^h / \left\langle E^s_{k_{\rm ref}} \right\rangle) \tag{74}$$

   The statistical uncertainty is

$$\delta J^g = J^g \left[\left(\frac{\delta J^{\rm src}_{k_{\rm ref}}}{J^{\rm src}_{k_{\rm ref}}} \right)^2 + \left(\frac{\ln(\left\langle E^s_{k_{\rm ref}} \right\rangle / E^{\rm ESA}_{k_{\rm ref}})}{\ln(E^{\rm ESA}_{k_{\rm ref}+1} / E^{\rm ESA}_{k_{\rm ref}})} \right)^2 \left\{ \left(\frac{\delta J^{\rm src}_{k_{\rm ref}}}{J^{\rm src}_{k_{\rm ref}}} \right)^2 + \left(\frac{\delta J^{\rm src}_{k_{\rm ref}+1}}{J^{\rm src}_{k_{\rm ref}+1}} \right)^2 \right\} \right]^{1/2} \tag{75}$$

   The systematic uncertainty is

$$\sigma J^g = \sigma J^{\rm src}_{k_{\rm ref}}(\left\langle E^s_{k_{\rm ref}} \right\rangle / E^{ESA}_{k_{\rm ref}})^{\gamma_{k_{\rm ref}}}(E^h / \left\langle E^s_{k_{\rm ref}} \right\rangle) \tag{76}$$

The process outlined above is used to estimate fluxes and background fluxes in the inertial frame from the pointing sets.

Note. While we typically make n HF maps at $E^h = E_k^{\rm ESA}$ (Lo: 1–7; Hi: 1–9), the CG procedure works for arbitrary E^h. Only the per-direction $E^s(\alpha)$ and the spectral interpolation target change; binning and geometry do not.

Survival probabilities are also developed for the inertial reference frame. These survival probabilities are binned in the inertial frame map and divide the fluxes in the inertial frame to correct for survival probability. Similarly, the square of the survival probability divides the variance of the flux to estimate the SP-corrected variance. These operations are also performed on the background fluxes when the SP-correction is estimated.

9. ISN RATE MAPS

The most basic level of rate map is computed in the S/C reference frame with no corrections applied. For interstellar neutrals, light atom and heavy atom rate maps will be prepared. The level 2 ISN pointing set light and heavy ion rates R, uncertainties, δR, σR, background rates R^B, uncertainties δR^B and σR^B and exposure times τ in 0.1° bins. The formation of a map or a slice of sky involves finding the set of elements i from the pointing sets that fall into a given map pixel. While the rates do not include the geometric factor, rates are formed from counts and average efficiency factors ϵ_i associated with the MCP tracks of IMAP-Lo. There are systematic errors associated with these efficiency factors. The rate within the map pixel represents an exposure time average over the set:

$$\langle R\rangle_{\rm pxl} = \frac{\sum_i C_i/\epsilon_i}{\sum_i \tau_i} \tag{77}$$

$$\langle (\delta R)^2\rangle_{\rm pxl} = \frac{\sum_i C_i/\epsilon_i^2}{[\sum_i \tau_i]^2} \tag{78}$$

$$\langle \sigma R\rangle_{\rm pxl} = \frac{\sum_i \sigma\epsilon_i\tau_i}{\sum_i \epsilon_i\ \tau_i}\langle R\rangle_{\rm pxl} \tag{79}$$

$$\langle R^B\rangle_{\rm pxl} = \frac{\sum_i R_i^B\tau_i}{\sum_i \tau_i} \tag{80}$$

$$\langle (\delta R^B)^2\rangle_{\rm pxl} = \frac{\sum_i \delta R_i^2\tau_i^2}{[\sum_i \tau_i]^2} \tag{81}$$

$$\langle \sigma R^B\rangle_{\rm pxl} = \frac{\sum_i \sigma R_i^B\tau_i}{\sum_i \tau_i} \tag{82}$$

$$\tag{83}$$

10. SURVIVAL PROBABILITY CORRECTED MAPS

For each type of IMAP-Lo map made, there is a survival probability map in the chosen frame and projection. That survival probability map divides the flux map to create the survival probability map.

Note that each map represents and sum of flux and background flux projected into the chosen reference frame. The survival probability map must also divide the

background flux map to maintain consistency between the map and the projected background flux.

APPENDIX

A. PREDICTOR-CORRECTOR SCHEME FOR SOURCE POWER LAWS

In the process of estimating power-laws for fluxes, a second-order scheme is used to greatly improve convergence to a final and accurate answer. The predictor-corrector scheme begins with the observed flux J_k in each energy step E_k, in the S/C frame. Note that here and throughout this appendix, the scheme applies to both the observed fluxes and estimated background fluxes. We also begin with an estimate of the source flux based on an initial estimate for the power-laws $\gamma_k^{n=0}$, where the power-laws are derived from observed fluxes themselves,

$$\gamma_k^{n=0} = \ln(J_{k+1}/J_{k-1})/\ln(E_{k+1}/E_{k-1}) \tag{A1}$$

The power-law at step $k = 1$ and $k = 7$ are

$$\gamma_1^{n=0} = \ln(J_2/J_1)/\ln(E_2/E_1) \tag{A2}$$

$$\gamma_7^{n=0} = \ln(J_7/J_6)/\ln(E_7/E_6) \tag{A3}$$

which applies throughout the appendix. This initial guess for power-laws, then feeds into the initial guess for the transmission factor $\eta_{\rm esa,k}(\gamma_k^{n=0})$ and the initial guess for the source function,

$$J_k^{\rm src,n=0} = J_k/\eta_{\rm esa,k}(\gamma_k^{\rm n=0}) \tag{A4}$$

In the first prediction step, we estimate power-laws from the source fluxes,

$$\gamma_k^{\rm n=0,p} = \ln(J_{k+1}^{\rm src,n=0}/J_{k-1}^{\rm src,n=0})/\ln(E_{k+1}/E_{k-1}) \tag{A5}$$

The predictor estimate for the power-law is

$$\gamma_k^{\rm n=0.5} = (1/2)(\gamma_k^{\rm n=0} + \gamma_k^{\rm n=0,p}) \tag{A6}$$

This predictor is then used to estimate the source fluxes

$$J_k^{\rm src,n=0.5} = J_k/\eta_{\rm esa,k}(\gamma_k^{\rm n=0.5}) \tag{A7}$$

In the first correction step, we re-estimate the power-laws from the source fluxes,

$$\gamma_k^{\rm n=0.5,c} = \ln(J_{k+1}^{\rm src,n=0.5}/J_{k-1}^{\rm src,n=0.5})/\ln(E_{k+1}/E_{k-1}) \tag{A8}$$

The corrector estimate for the power-law is

$$\gamma_k^{n=1} = (1/2)(\gamma_k^{n=0,p} + \gamma_k^{n=0.5,c}) \tag{A9}$$

This corrector is then used to estimate the source fluxes

$$J_k^{\mathrm{src,n=1}} = J_k / \eta_{\mathrm{esa,k}}(\gamma_k^{n=1}) \tag{A10}$$

The scheme then proceeds to the next iteration $n+1$ using first the predictor power-law from step n, then the corrector power-law from step n, based on the observed fluxes J_k and the source fluxes $J_k^{\mathrm{src,n}}$. At each step, we use a mean RMS deviation to estimate convergence,

$$\chi_n = \sqrt{\left(\sum_{k=1}^{7} \left[J_k^{\mathrm{src,n}} / J_k^{\mathrm{src,n-1}}\right]^2\right) / N_{\mathrm{esa}}} - 1 \tag{A11}$$

Here the summation extends over only the active reswept ESA steps, with N_{esa} independent values. Even for very rugged distributions the scheme converges. We recommend using a convergence criterion of $\chi_n < 0.5\%$, and terminating the iteration cycle either when the convergence criterion is reached or when the maximum number of iterations of $n = 20$ is reached.

REFERENCES

McComas, D. J., Allegrini, F., Bzowski, M., Dayeh, M. A., DeMajistre, R., Funsten, H. O., Fuselier, S. A., Gruntman, M., Janzen, P. H., Kubiak, M. A., Kucharek, H., Möbius, E., Reisenfeld, D. B., Schwadron, N. A., Sokół, J. M., & Tokumaru, M. 2014, Astrophys. J. Suppl., 213, 20

Validation

4.4.2 IMAP-Hi

Validation

4.4.3 IMAP-Ultra

IMAP-Ultra data product definitions and processing algorithms are embedded below

1.0 IMAP-Ultra Algorithms Introduction

This document describes the algorithms and processes required for transforming raw telemetered packets (level 0) to reconstructed flux map (level 2) data products for IMAP-Ultra. The following sections give more detail about each step and further describe the algorithms involved. Figure 2 provides a high-level flow diagram of this process and includes ancillary product names.

2.0 IMAP-Ultra Definitions

The **Geometric Function**, $G(\theta, \phi)$ [cm^2] is the effective sensitive area within the Field of View. This term includes grid factors, which are independent of energy, and does not include any energy dependent efficiency terms.

The **Geometric Factor**, GF [cm^2 sr] is the integral of the Geometric Function over the solid angles that define the FOV of the instrument.

The **Response Function** $S(\theta, \phi, E)$ [cm^2] is a function of the sensitive area for the given direction in the FOV, with energy dependence. The Response Function includes the Geometric Factor, and energy dependent transmission efficiencies. Also known as the Sensitivity.

The **Field of Regard** is defined as all directions that the start slit is exposed to at a given instant.

The **Field of View** is defined as all directions that the stop plates (MCP) can see given all geometric obstructions within the instrument. The Field of View (FOV) is a subset of the Field of Regard (FOR).

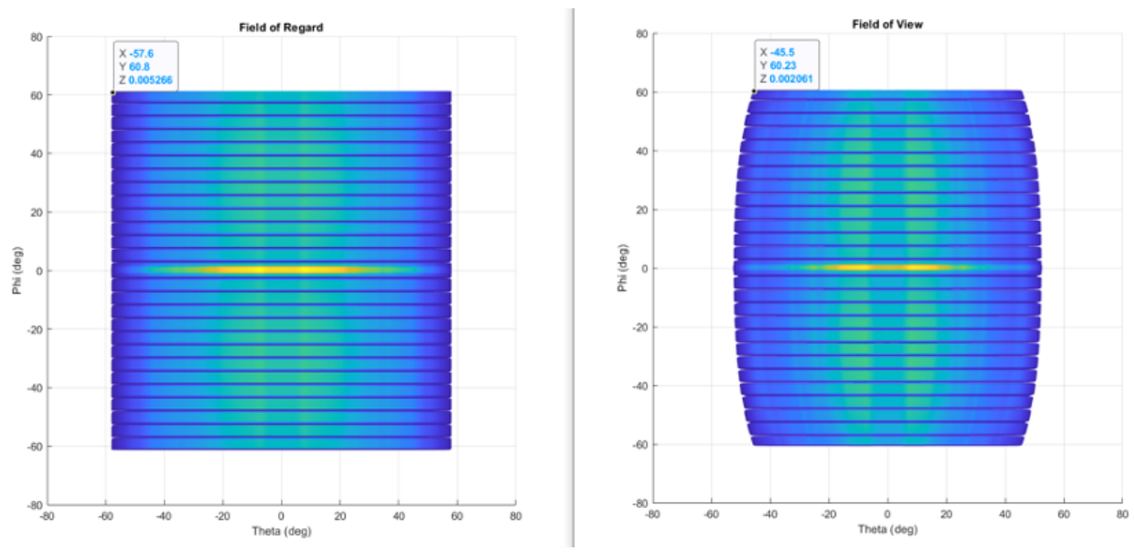


Figure 1. FOR and FOV including Geometric Function Sensitivity Dependence

Note: θ and ϕ in this section reference angles in the IMAP-Ultra instrument frame and are not to be confused with θ_p and ϕ_p described later in the Despun Pointing Set Coordinate System.

3.0 Algorithm Descriptions

IMAP-Ultra data product level descriptions are defined in [2] & Section 6.0, but are summarized in the following subsections for clarity and completeness. Each following subsection describes the algorithms required to develop each relevant data product within the data pipeline at the given level.

3.1 Level 0

Level 0 data products are packets downlinked from the spacecraft defined by the CCSDS space packet protocol standard.

3.1.1 Data Compression and Decompression Algorithms

IMAP-Ultra compresses large values using lossy logarithmic algorithms. Some values may be further losslessly compressed using a "Fast" algorithm. In addition, there is also an image specific compression that uses 8-bit log and fast compressed values.

Log Compression:

For energy spectra, IMAP-Ultra flight software employs 32-bit to 10-bit log compression. The 10-bit log compressed format for the exponent e, and mantissa m are 5-bit unsigned integers and e is always less than 28.

10-bit log decompression:

```
% for 10-bit log decompression
if e == 0
    result = m;
else
    result = bitshift((32+m),(e-1));
end
```

For rates, IMAP-Ultra flight software employs 27-bit to 16-bit log compression (0x371/0x3b1). The exponent e, and mantissa, m are 4-bit and 12-bit unsigned integers respectively. The largest value that can be represented with this code is 134,217,727. Larger values will be clamped.

16-bit log decompression:

```
% for 16-bit log decompression
if e == 0
    result = m;
else
    result = bitshift((4096+m), (e-1));
end
```

Some arrays within IMAP-Ultra data are compressed using a lossless Fast compression algorithm. Each array value is 10 bits after log compression. The values are organized into blocks of 16 values. Each block is compressed as a unit; if the length of the array is not a multiple of 16, the final unit will have fewer values. The max value determines how many bits are needed for each value. Each block is sent with a width field and 16 or possibly fewer in the last block, bit-packed values.

16-bit values can also be "Fast" compressed. The encoding format is similar to the 10-bit one, except that the length of the width fields increases from 4 to 5 (set widthBit = 5 in pseudocode below).

```
% read(n) is a function that reads the next n bits; read(0) returns 0;
widthBit = 4;
for b = 1:numel(blocks)
    width = read(widthBit);
    % block has 16 values, 1-16 in the last
    for k = 1:size(block(b))
        value(k) = read(width);
    end
end
```

For reference, the encoding format is specified in Tables 1 and 2 below.

Table 1: 10-Bit Fast Encoding Format

Name	Length (bits)	Value	Description
Width 1	4	0 - 10	Block 1 with width (W1) and 16 bit-packed values
Values 1	16 * W1	Unsigned Integers	
Width 2	4	0 - 10	Block 2 with width (W2) and 16 bit-packed values
Values 2	16 * W2	Unsigned Integers	
...			
Width N	4	0 - 10	Block N with width (WN) and up to 16 bit-packed values
Values N	1-16 * WN	Unsigned Integers	

Table 2: 16-Bit Fast Encoding Format

Name	Length (bits)	Value	Description
Width 1	5	0 - 16	Block 1 with width (W1) and 16 bit-packed values
Values 1	16 * W1	Unsigned Integers	
Width 2	5	0 - 16	Block 2 with width (W2) and 16 bit-packed values
Values 2	16 * W2	Unsigned Integers	
...			
Width N	5	0 - 16	Block N with width (WN) and up to 16 bit-packed values
Values N	1-16 * WN	Unsigned Integers	

For Image telemetry (e.g. TOF images: 0x373/0x3b3, 0x374/0x3b5, … 0x378/0x3b8) a window of N rows x M columns from the larger accumulated IMAP-Ultra image is telemetered. The telemetered window comprises 108° of elevation, covering the entire FOV and the full 360° of spin. Images with the highest (2°) angular resolution use windows of 54x180 pixels out of the full 90x180 pixel image. Which rows are telemetered differ between Ultra-90 and Ultra-45. For Ultra-90, the telemetered window is centered on the spin plane and the base row of the window is 54° down within the image. For Ultra-45 the base row of the window is at the bottom of the image. The window is compressed before being telemetered. The pixels are compressed in two steps: lossy compression and lossless entropy coding. First, the pixels are compressed using 16-bit to 8-bit log compression. Both exponent e and mantissa m are 4-bit unsigned integers; e is always less than 13. Decompression can be done as follows:

```
% for 8-bit log decompression
if e == 0
    result = m;
else
    result = bitshift((16+m), (e-1));
end
```

Next, the differences between adjacent pixels are computed. This results in an NxM block of differences. In general, each difference is computed by subtracting the pixel from its leftmost neighbor. In the case of pixels along the left edge of the window, each difference is computed by subtracting the pixel from the pixel below it. In the case of the lower left pixel, its difference is computed as the pixel subtracted from itself (0). These differences are encoded as unsigned 8-bit values such that a probability distribution function peaks at 0 and decreases with increasing values.

Each row of encoded differences is entropy coded using “Fast” compression as discussed above. The values are organized into blocks of 15. Each block is compressed as a unit. The max value in each block determines how many bits are needed for the values in the block. Each block is sent with a width field and 15 bit-packed values.

Table 3. Image Fast Encoding Format

Name	Length (bits)	Value	Description
Width 1	4	0 - 8	Block 1 with width (W1) and 15 bit-packed values
Values 1	15 * W1	Unsigned Integers	
Width 2	4	0 - 8	Block 2 with width (W2) and 15 bit-packed values
Values 2	15 * W2	Unsigned Integers	
...			
Width N	4	0 - 8	Block N with width (WN) and 15 bit-packed values
Values N	15 * WN	Unsigned Integers	

Decompression of fast-encoded image data is done using the following pseudo-C algorithm. This would be followed by log decompression as mentioned above.

```
pp = read(8 bits)                          // first pixel
for each row in window
        for each code block in row
                w = read(4 bits)
                for each value in block
                        Δcode = read(w bits)
                        Δf = (Δcode & 0x01) ? ~(Δcode>>1) : (Δcode>>1)
                        p[i,j] = (pp - Δf) & 0xff
                        pp = p[i,j]
        pp = p[i,0]
Where read(n) is a function that reads next n bits
Note: read(0) returns 0.
```

To summarize, the required decompression algorithms needed are described in Table 4.

Table 4: Decompression Algorithms by Packet Type

Packet Name	APID (45/90)	Decompression Algorithm	Notes
Single Events	0x380, 0x3c0	N/A	No decompression required
Auxiliary Data	0x370, 0x3b0	N/A	No decompression required
Image Rates	0x371, 0x3b1	16-bit log and fast-compressed values	Variable length packet, counts are the specific packet data that is 16-bit log and fast-compressed.
TOF Images	0x373, 0x3b3	8-bit log and fast-compressed values	APIDs are specifically for ENA PHxTOF High-Angular Res Image

3.2 Level 1A

Level 0 data is decompressed and properly unpacked into separate CDF files by APID. This cumulative data set is referred to as Level 1A data. Level 1A consists of Direct Events which are the raw unpacked data from the Image Single Events Packets [1, p. 179-181; Table 54], Auxiliary Packet Data [1, p. 186-188; Table 59], Image Rates [1, p. 182; Table 55], and TOF Images. Algorithm relevant information is summarized in Table 5 and includes information from both Single Event packets and Auxiliary packets. Image Rates and TOF images will be used for diagnostic purposes such as estimating backgrounds, creating a "bad times" list, and for culling. Further details are described in [2] and [3].

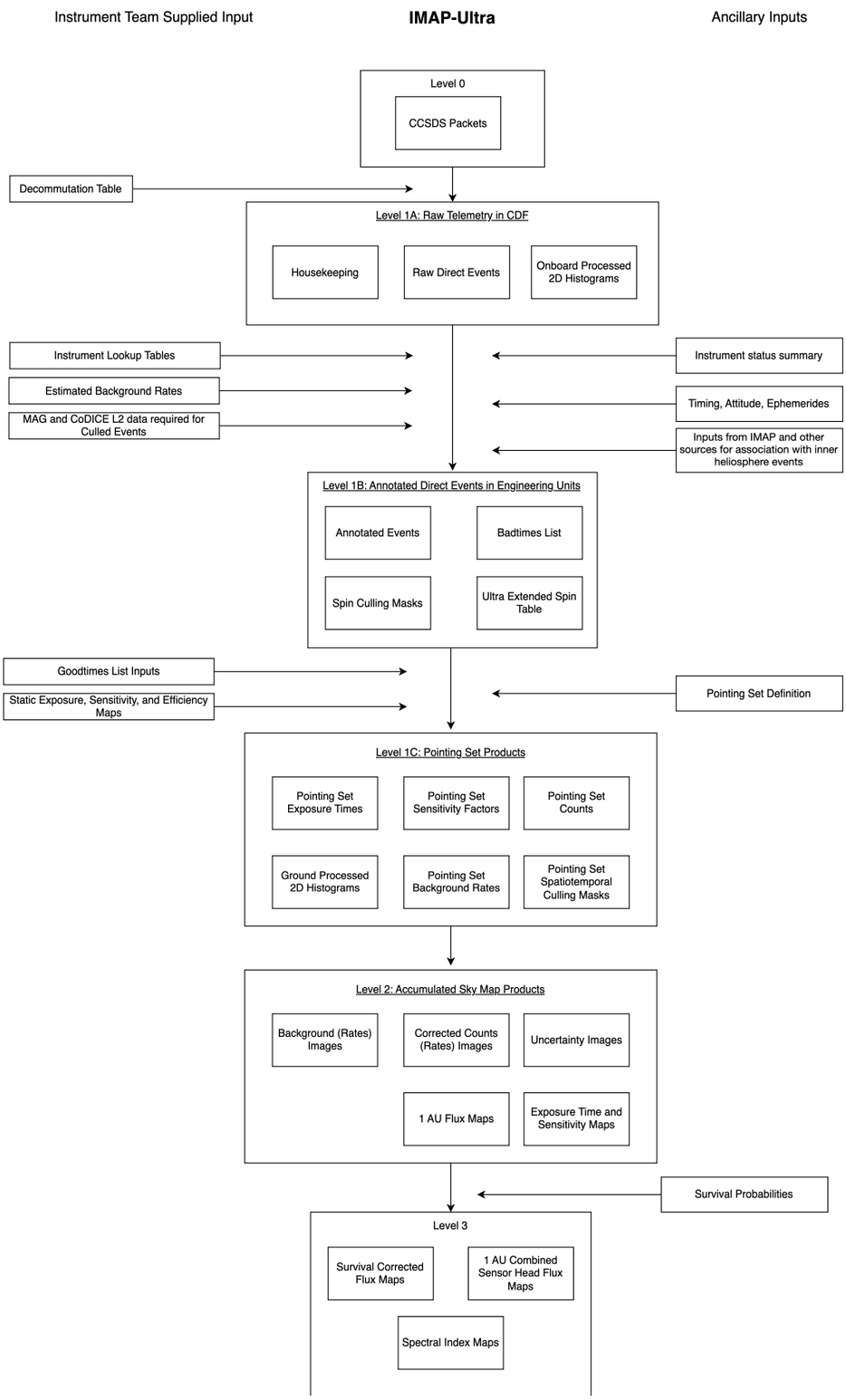


Figure 2: IMAP-Ultra Data Pipeline Diagram

Table 5: Direct Event Items Needed for Algorithms

Name	Symbol	Length (bits)	Value	Description
Secondary Header		32	Unsigned Integer	Time tag (SCLK)
Count		8	0 – 100	# events, N
Event Type N		8	Varies	Start type, stop type, and coin type (i.e. left right, top bottom, discrete, etc). confirm triple event
Start Position N	*StP*	11	0 - 2047	Valid if top/bottom type
Stop North N	*SpN*	11	0 - 2047	Valid if top/bottom type
Stop East N	*SpE*	11	0 - 2047	Valid if top/bottom type
Stop South N	*SpS*	11	0 - 2047	Valid if top/bottom type
Stop West N	*SpW*	11	0 - 2047	Valid if top/bottom type
Coin North N		11	0 - 2047	Valid if top/bottom type
Coin South N		11	0 - 2047	Valid if top/bottom type
Coin Discrete N		11	0 – 2047	Valid if discrete type
Energy / PH	*PH*	12	0-2047 (MCP) 0-4095 (SSD)	PH measurements
Bin N	*bin*			Aids determination of species & energy
Phase Angle N	θ_{event}	10	0 - 719	0.5° resolution
Spin Start Seconds	$\boldsymbol{t}_{spin\ start}$	32	Unsigned Integer	Start of spin in seconds. *Aux packet*
Spin Start Subseconds	$t_{start\ sub}$	16	0-999	Spin Start in milliseconds. *Aux packet*
Spin Number		32	Unsigned Integer	Confirm sequence in aux/event packet. *Aux packet*
Spin Duration	$t_{spin\ duration}$	16	Unsigned Integer	Spin period in milliseconds. *Aux packet*

3.3 Level 1B

Level 1B data uses the information from level 1A to begin the construction of Direct Events and Annotated Events, as well as a Bad Times list.

The Direct Events contain information about the detected events as seen by Ultra, before adding any spacecraft attitude or ephemeris information into the calculations. Table 6 provides an overview of the items in the Direct Events table and the following subsections describe the items further.

Table 6. Direct Events Table Items

Quantity	Description	Type	Note
$\boldsymbol{\varepsilon}$	Event ID, unique for each recorded event	64 bit integer	Hash generation or sequential
$\boldsymbol{t_\varepsilon}$	Event time	Double	Generated from packet time and spin phase in telemetry in IMAP standard time representation (eqn 1)
Raw Event	Raw event information from telemetry	bit field packed into 3 64 bit integers	[1, p. 179-181; Table 54] – from row 14 (event type) through 30 (phase angle)
$\vec{\boldsymbol{P}}^{\boldsymbol{f}}$	Event position (Xf,Yf) on front foil	2 element real vector	Position that the particle entered in instrument coordinates [1, p. 31]
$\vec{\boldsymbol{P}}^{\boldsymbol{b}}$	Event position (Xb,Yb) on back foil	2 element real vector	Position that the particle encountered backplane in instrument coordinates [1, p. 33]
$\vec{\boldsymbol{P}}^{\boldsymbol{c}}$	Event position (Xc,Yc) on coincidence	2 element real vector	Position that the particle encountered coincidence in instrument coordinates [1, p. 33]
$\boldsymbol{\tau^{ss}}$	TOF from start to stop	Real	[1, p. 34] TOF
$\boldsymbol{\tau^{sc}}$	TOF from stop to coin	Real	[1, p. 36] eTOF
$\boldsymbol{\tau^{c}}$	Corrected TOF	Real	[Eqn 7] cTOF
Event type	Event classification	8 bit bitfield	[1, Table 4] See Table 5.
$\vec{\boldsymbol{r}}^{\boldsymbol{U}}$	Particle position vector in Ultra Frame	3 element real vector	(2). Particle direction as measured from Ultra origin.
$\vec{\boldsymbol{v}}^{\boldsymbol{U}}$	Particle velocity in Ultra Frame	3 element real vector	(3). Particle velocity as measured from front to back foil.
Ɛ	SSD/PH #s	Real	[1, p. 41-45]
$\boldsymbol{\Sigma}$	Species confirmed from bin #		[1, p. 41-45]

The Annotated Events table is an extension of the Direct Events table with more geometric information from the events calculated using the IMAP attitude, ephemeris, and calibration information. This table will be carried through at various processing stages from Level 1B – Level 2 (with more information appended to it in other data levels). The Annotated Events table will initially include particle trajectory information (ENA velocity vectors) in various frames, spacecraft attitude information, species type, and energy estimates, among other items.

The following subsections describe basic calculations required to create the Direct Events and Annotated Event items. Table 7 describes the initial items that should be included in the Annotated Events.

Table 7: Annotated Event Items

Quantity	Description	Type	Note
$\boldsymbol{\varepsilon}$	Event ID, unique for each recorded event	64 bit integer	Hash generation or sequential
…	Direct Event Table Items	…	…
$\boldsymbol{\epsilon}$	Estimated event efficiency for particles path through the instrument	Real	$\epsilon = \epsilon(\theta_{inst}, \phi_{inst}, E^{\Delta}, \Sigma)$
$\boldsymbol{\theta_{FWHM}/\phi_{FWHM}}$	Full Width Half Max cal data for each event	Real	$\theta_{FWHM} = \theta_{FWHM}(\theta_{inst}, \phi_{inst}, E^{\Delta}, \Sigma)$
G	Geometric Function	Real	$G(\theta_{inst}, \phi_{inst})$
$\vec{\boldsymbol{v}}^{\boldsymbol{S}}$	Velocity vector in IMAP Spacecraft/Body Frame	3 element real vector	$\vec{v}^{S} = \boldsymbol{R_{SU}}\vec{v}^{U}$
$\vec{\boldsymbol{v}}^{\Delta}$	Velocity vector in Pointing Frame at rest wrt spacecraft	3 element real vector	$\vec{v}^{\Delta} = \boldsymbol{R}_{\Delta S}\,(t_{\epsilon})\vec{v}^{S}$
$\vec{\boldsymbol{v}}^{\boldsymbol{D}}$	Velocity vector in Pointing frame at rest wrt heliosphere	3 element real vector	$\vec{v}^{D} = \vec{V}^{D}_{IMAP} + \vec{v}^{\Delta}$
$\boldsymbol{E}^{\Delta}$	Energy at rest wrt to spacecraft	Real	$E^{\Delta} = m_{\Sigma}(\vec{v}^{\Delta} \cdot \vec{v}^{\Delta})/2$
$\boldsymbol{E}^{\boldsymbol{D}}$	Energy at rest wrt to heliosphere	Real	$E^{D} = m_{\Sigma}(\vec{v}^{\boldsymbol{D}} \cdot \vec{v}^{\boldsymbol{D}})/2$

The estimated event efficiency (ϵ) is the probability that an event of this description (i.e., with the θ_{inst}, ϕ_{inst} , $\vec{v}^{\boldsymbol{U}}$, Σ) results in this coincidence type (triples), normalized to the event efficiencies averaged over the range of measurable θ_{inst}, ϕ_{inst} and $\vec{v}^{\boldsymbol{U}}$ for the given Σ. The species, Σ, can initially be regarded as hydrogen only. It's listed here for completeness in the case we do obtain some statistically significant number of heavier elements. This information will be provided as a lookup table (see section 3.3.3)

θ_{FWHM} is a measure of the spread or scattering of an individual event and is a function of θ and ϕ in the instrument frame as well as energy and species. This information will be provided as input calibration tables to the SOC and should be used as a lookup table and applied as a field in the annotated events for each event. This information will later be used to build uncertainty maps due to scattering positional uncertainty at L1C and L2. These maps are built in the same manner as counts, but the values are averaged rather than summed.

Frame transform matrices ($\boldsymbol{R_{SU}}$, $\boldsymbol{R_{\Delta S}}$) are assumed to be supplied by the project/ISOC. $\boldsymbol{R_{SU}}$ is the rotation from the Ultra frame (U) to the spacecraft/body frame (S) and $\boldsymbol{R_{\Delta S}}$ is the rotation from the spacecraft to the DPS (Despun Pointing Set) or Pointing frame. Both the S (spacecraft) and Δ are considered to be at rest WRT the spacecraft. These values can be easily computed using NAIF SPICE frame kernels. Typically one would use SPICE calls to *PXFORM()* to query SPICE for the appropriate rotation matrix. With the provided frame kernel:

$\boldsymbol{R_{SU}}$ = *CSPICE_PXFORM*('IMAP_ULTRA_90', 'IMAP_SPACECRAFT', 0), and
$\boldsymbol{R_{\Delta S}}$ = *CSPICE_PXFORM*('IMAP_SPACECRAFT', 'IMAP_DPS', et)

The corrected velocity vector $\vec{v}^{\boldsymbol{D}}$ is the velocity vector for an observer at rest WRT to the heliosphere (the D frame is the Pointing frame at rest WRT the heliosphere rather then the Δ frame moving with the spacecraft). The equation is derived from the Galilean velocity transform $\vec{v}^{\Delta} = \vec{v}^{\boldsymbol{D}} - \vec{V}^{D}_{IMAP}$, where $\vec{V}^{D}_{IMAP}$ is the velocity of the IMAP spacecraft in the Pointing frame at rest with respect to the Heliosphere. $\vec{V}^{D}_{IMAP}$ can be determined with a SPICE call using the method SPKEZR.

3.3.1 Event Time Calculation

Calculation of event time requires single event packets as well as auxiliary packets. Auxiliary packets contain the Spin Duration, $t_{spin\ duration}$ (the measured spin period in milliseconds), the Spin Start Time, $t_{spin\ start}$ (seconds), and Spin Start Subseconds, $t_{start\ sub}$ (milliseconds). The Phase Angle, θ_{event} (integer from 0-719) from the event packet is used to provide the event time offset from the start of the spin. The event time can be calculated as follows (see Table 5).

$$t_{\varepsilon} = t_{spin\ start} + \frac{t_{start\ sub}}{1000} + \frac{t_{spin\ duration}}{1000}\frac{\theta_{event}}{720} \quad (1)$$

This event time will later be used for grouping events into the appropriate pointing sets, can aid in the determination of spatiotemporal noise and the creation of a bad times list.

3.3.2 ENA Instrument Frame Trajectories, Energy, and Species Determination

Given Direct Event information from Level 1A, we must first use instrument calibrated lookup tables and other scaling factors to calculate the particles trajectory in the instrument frame. These calibration tables will be provided to SDC. Each event will contain Start X Position, 4 measurements from the back MCP, in addition to coincidence measurements, See Table 5. The 4 Stop measurements use a calibration lookup table depending on the MCP (top or bottom) to determine the actual X and Y stop positions within the instrument.

Instrument frame estimated particle trajectory and TOF equations are provided in [1, p. 30-41; Sec. 3.3.1.1]. [1, p. 41-45; Sec 3.3.1.2] further describes how to determine the species of detected particles.

The remainder of this section is a summary of the algorithms described in the flight software specification. The general geometry of the instrument is shown in Figure 3.

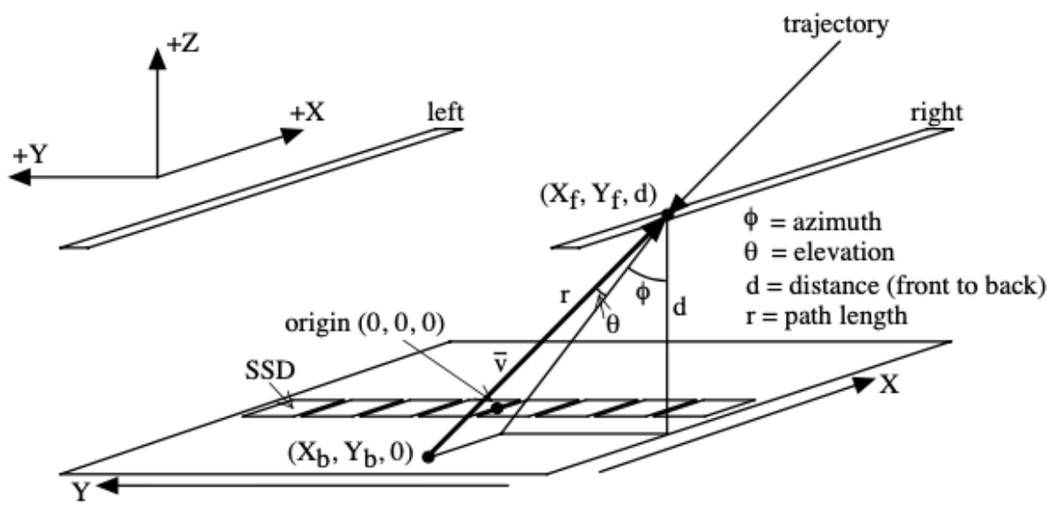


Figure 3: IMAP-Ultra Sensor Geometry [1, p. 38; Fig 21]

When the particle enters the front slit, the instrument measures its Xf and Yf positions as:

```
% Front Position Xf and Yf
if start_type == 'LEFT'
    % x start position (hundredths of a millimeter)
    Xf = ImgParams.XFtSc*-StP/1024 + ImgParams.XFtLtOff;
    Yf = 40.0; % mm
else
    % x start position (hundredths of a millimeter)
    Xf = ImgParams.XFtSc*-StP/1024 + ImgParams.XFtRtOff;
    Yf = -40.0; % mm
end
```

The items contained in the ImgParams structure XFtSc, XFtLtOff, and XFtRtOff are the X Front Scaling factor, the X Front-Left Offset, and the X Front Right Offset respectively. These values will be provided to SDC.

Each Back Anode (Top and Bottom) has 4 readout values, North, South, East, and West (Figure 4). The measured pulses must use calibration lookup tables to determine the corrected X and Y Stop positions (Xb and Yb).

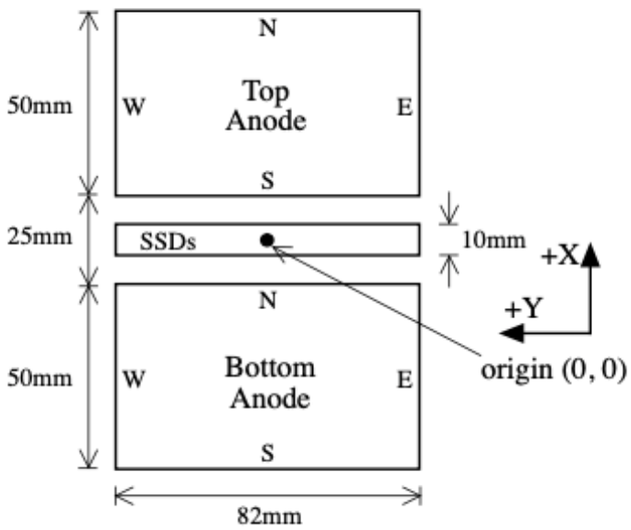


Figure 4: IMAP-Ultra Back Anodes [1, p. 32; Fig 16]

```
% Back Position Xb and Yb
if stop_type == 'TOP'

    % Corrected / Normalized North, South, East, West pulse positions
    SpNNorm = TpSpNNorm(SpN);
    SpSNorm = TpSpSNorm(SpS);
    SpENorm = TpSpENorm(SpE);
    SpWNorm = TpSpWNorm(SpW);

    % Stop positions Xb and Yb in hundredths of a millimeter
    Xb = XBkTp(SpSNorm - SpNNorm + 2047);
    Yb = YBkTp(SpENorm - SpWNorm + 2047);

else

    % Corrected / Normalized North, South, East, West pulse positions
    SpNNorm = BtSpNNorm(SpN);
    SpSNorm = BtSpSNorm(SpS);
    SpENorm = BtSpENorm(SpE);
    SpWNorm = BtSpWNorm(SpW);

    % Stop positions Xb and Yb in hundredths of a millimeter
    Xb = XBkBt(SpSNorm - SpNNorm + 2047);
    Yb = YBkBt(SpENorm - SpWNorm + 2047);

end
```

The N,S,E,W Top and Bottom calibration tables as well as X and Y Top and Bottom Back anode calibration tables will be provided to SDC.

The Time of Flight (TOF) calculation is then provided by example with the following pseudocode. Using the default scale and offsets per stop top or bottom anodes gives TOF in tenths of nanoseconds.

```
% Time of Flight
TOFx = SpNNorm + SpSNorm;
TOFy = SPENorm + SPWNorm;

% t1 is the average of the two TOFs measured in the X and Y directions.
% Division by 2 is already incorporated into the scale.
t1 = TOFx + TOFy;
% apply scaling factors and offsets
if stop_type == 'TOP'
    t2 = ImgParams.TOFSc * t1/1024 + ImgParams.TOFTpOff;
else
    t2 = ImgParams.TOFSc * t1/1024 + ImgParams.TOFBtOff;
end
% Apply the correction for the propagation delay of the start anode and
% some other effects.
% Final units of TOF are tenths of nanoseconds
TOF = t2 + Xf * ImgParams.XFtTOF/32768;
```

In this document, we do not list the calculations required to create particle trajectories in the instrument frame for events that impact the SSDs. The calculations are similar to the back MCPs but with lower position accuracy. For the SSD calculations see [1, p. 35-41; Sec. 3.3.1.1].

Before the particle trajectory can be computed, adjustments must be made to account for the displacement between the front slit and the start foil. The closest distance from the front slit to the front foil is $d_f = 3.39\ mm$, and the foil is tilted 45° with respect to the slit as shown in Figure 5. The vertical distance from the back MCP to the slit is $d_s = 46.19\ mm$.

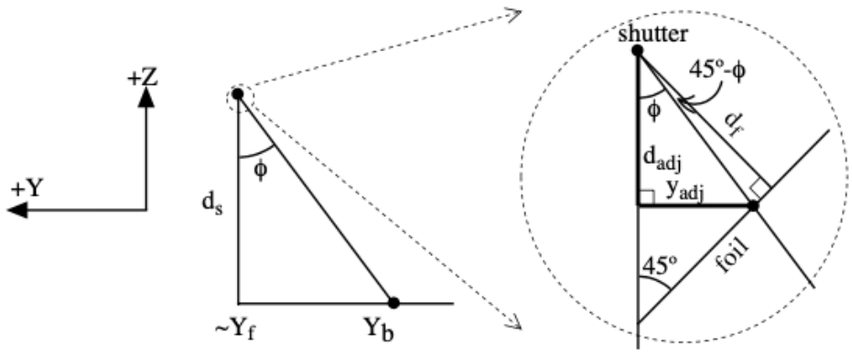


Figure 5: IMAP-Ultra Foil, Left Shutter Diagram [1, p. 39; Fig 22]

Using the Y adjustment look up table, along with the constants mentioned above, we can compute the corrected Y and Z (d) values for the trajectory.

```
% Adjustment Y and Z from the slit to the start foil
if start_type == 'LEFT'
    Yf = 40.0; %mm
    % there are 256 elements in the lookup table, and 81.92 is the valid
    % length of the back MCP in the Y direction in mm
    dYlut = (Yf - Yb)*256/81.92;
    % get the corrected y adjustment value
    yadj = YAdjustLUT(dYlut);
    % apply the offset and assign the Yf value to be the foil Y value
    Yf = Yf - yadj;
else
    Yf = -40.0; % mm
    dYlut = (Yb - Yf)*256/81.92;
    yadj = YAdjustLUT(dYlut);
    Yf = Yf + yadj;
end
% df is the closest distance from the slit to the foil in mm
df = 3.39;
% ds is the vertical distance from the back MCP to the slit in mm
ds = 46.19;
% dadj is the vertical distance from the slit to the vertical impact point
% on the foil in mm
dadj = sqrt(2)*df - yadj;
% Finally, d is the corrected vertical distance from the back MCP to the
% impact point on the foil (mm)
d = ds - dadj;
```

Once the Cartesian X, Y, and Z positions are in the same / appropriate units, the measured particle direction and the velocity vector in the Ultra instrument coordinate system can be computed as:

$$\vec{r}^{U} = \left(X_f - X_b, Y_f - Y_b, d\right) = (\Delta X, \Delta Y, d) \tag{2}$$

$$\vec{v}^{U} = -\frac{\vec{r}^{U}}{TOF}, \|\vec{v}^{U}\| = \frac{d_{min}}{cTOF} \tag{3}$$

Where d_{min} is the fixed distance between the front and back detectors, approximately 40.096 mm. The cTOF and the corrected pulse height are used in conjunction with another lookup table to determine the bin number (See Table 5). This bin number is then used to determine the species of the particle.

The corrected time of flight cTOF is the particles TOF as if it were traveling parallel with the boresight vector.

$$cTOF = TOF\,\frac{d_{min}}{r} \tag{4}$$

The magnitude of the particle position vector, r, is defined in equation 7.

There are known corrections that can be added to account for the energy loss with ENA foil impact. These algorithms are not currently included as an initial assessment suggests the loss is negligible.

Ultra instrument frame event azimuth and elevation can be determined from:

$$\phi = \tan^{-1}\left(\frac{\Delta Y}{d}\right) \tag{5}$$

$$\theta = \sin^{-1}\left(\frac{\Delta X}{r}\right) \tag{6}$$

$$r = \sqrt{\Delta X^2 + \Delta Y^2 + d^2} \tag{7}$$

The particle's pulse height is measured by the stop microchannel plate (MCP) for MCP stop events and measured by the SSD (referred to as energy in the FSW document) for SSD events. Particle species is determined via PHxTOF tables for MCP events and ExTOF tables for SSD events. These tables are used to obtain a bin number given the measured PH and cTOF values. The bin number is used to identify the particle species. For a complete description of these tables refer to the FSW document *3.3.1.2 Energy and Species Determination*.

We plan to only process MCP events for map making, which is the primary focus of this document. The pseudo code directly below shows how to correct the PH for MCP events before being used in the bin look-up table. For SSD events, please refer to the FSW document.

```
% Particle pulse height correction
if stop_type == 'TOP'
    Xlut = (Xb - 25/2) * 20/50;
    Ylut = (Yb + 82/2) * 32/82;
    Corrected PH = (PH - ImgParams.SpTpPHOffset) * SpTpPHCorr(Xlut, Ylut) /
1024;
else
    Xlut = (Xb + 50 + 25/2) * 20/50;
    Ylut = (Yb + 82/2) * 32/82;
    Corrected PH = (PH - ImgParams.SpBtPHOffset) * SpBtPHCorr(Xlut, Ylut) /
1024;
end
```

Once the particle bin number / species is determined via the bin to species lookup table, we wish to only include hydrogen particles. If the particle has an invalid bin number (255) or is not hydrogen, flag the particle and exclude it from further processing. We recommend using the velocity and mass of the species to compute the energy (eqn 8) for MCP events. Subsequent processing will only be built from MCP, triple coincidence events. The mass of hydrogen $m_H = 1.6735575 \times 10^{-27} kg$ and the conversion factor $\frac{Joules}{keV} = 1.602176634 \times 10^{-16}$ will be useful for equation 8.

The particle energy in the instrument frame is calculated as:

$$E = \frac{1}{2} m {v_U}^2 \quad (8)$$

At lower energies, there is a non-zero chance that scattering can cause the projected ENA θ_{inst} and ϕ_{inst} to fall outside of the nominal field of view of the instrument. If this occurs, flag the event with a logical filter. We will not include these particles in the counts maps as it could cause a divide by zero issue when converting to rates. Realistically, the corresponding spin duration P^S for this spin should subtract out the TOF + eTOF times; i.e. $P(E)^S = P^S - (\mathrm{TOF} + \mathrm{eTOF})$ for each event that scatters outside of the FOV. However, we expect the numbers of these events to be small and thus this exposure time correction unnecessary. Note applying this change would force the spin duration to be energy dependent. The nominal FOV and how to compute whether the particle falls within it is described in section 3.4.3.

3.3.3 Scattering and Efficiency Lookup Tables

Angular profiles representing the FWHM scattering in both the θ_{inst} and ϕ_{inst} directions were taken and tabulated at energies: 5, 7, 10, 20, and 40 keV. The Ultra instrument team will provide the SOC pre interpolated scattering matrices at fine energy resolutions (0.5 keV steps), such that a linear interpolation approximation to the ENA energies is sufficient. Four calibration data sets total will be provided to the SOC related to scattering: two for Ultra-90 left and right slit and two for Ultra-45 left and right slit entrance. Each of these files contain tabulated values for θ_{FWHM} and ϕ_{FWHM}.

For each ENA energy computed from equation 8, direction, and confirmed Hydrogen, the y_f value should be assessed to determine which entrance slit (positive LEFT) the ENA entered. Once the relevant data set is selected (left / right, U90/U45), two 3D linear interpolations should be performed for the event as a function of ENA energy, θ_{inst} and ϕ_{inst}. The first 3D interpolation is used to solve for θ_{FWHM} and the second for ϕ_{FWHM} scattering values. Store these as an annotated event item (Table 7) for the direct event. They'll later be reported as a quality metric for the positional uncertainty per map pixel. Figure 6 shows a representative full sensor scattering profile for hydrogen at 10 keV.

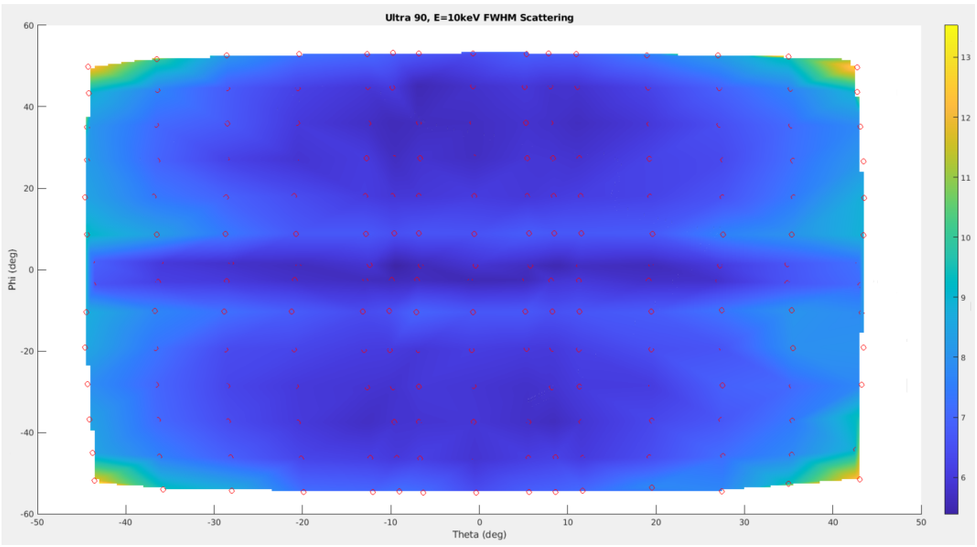


Figure 6. Combined Left and Right Slit FWHM values at 10 keV, grid interpolated for Ultra-90. Red dots correspond to $(\theta_{inst}, \phi_{inst})$ pairs from calibration. Color represents the FWHM in deg.

Angular profiles representing the instrument's efficiency in producing a triple coincidence measurement for hydrogen will be produced in a similar manner. However, there is only one 3D interpolation required per instrument – slit combo for a given ENA. This efficiency calibration product is not to be confused with the spun efficiencies provided for L1C processing, which will be discussed in section 3.4.4, as these efficiencies are directly in the instrument frame and not the Pointing frame. As with the scattering FWHM values, add the interpolated efficiency for each ENA to the annotated event items as described in Table 7.

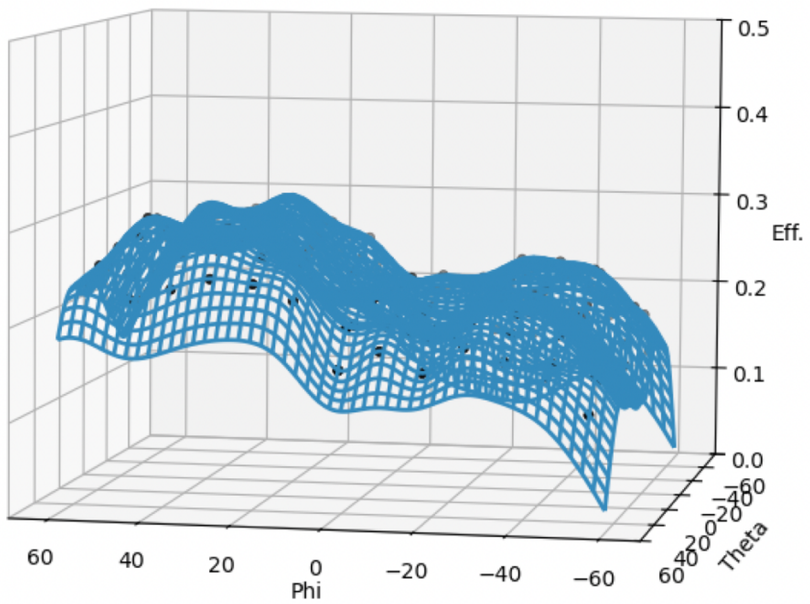


Figure 7. Ultra-45 Combined (Left and Right Slit) efficiencies

3.3.4 Ultra Event Rates Culling

At pre-launch, we recommend algorithms be put in place such that spins be excluded from processing if exceeding a threshold of 6σ from the mean or 3 counts per spin per Pointing (whichever is the largest). These thresholds should be computed per energy channel but do not hard code 6σ or 3 counts per spin. This will be an energy dependent spin culling and the bit flag should be included in the spin table (3.3.5), $\boldsymbol{\mathcal{F}_P}$. The generic algorithm is as follows:

- For each spin and energy bin, track the number of counts as the # counts/spin
- For the "not bad times" during each Pointing, take the mean value and sample standard deviation (σ) of counts per spin for each energy bin
- For spins where the # counts/spin exceed the 6σ (or 3 counts per spin) threshold, flag them in $\boldsymbol{\mathcal{F}_P}$ as spins to cull
    - Do not include counts during these spins, do not include those spins in the exposure time, or sensitivity map calculations.
    - Spins with 0 counts should be included in the calculations as long as the instrument was "listening" for particles.

This algorithm should be included as an optional culling in the processing pipeline (i.e. allow the Ultra event rates culling algorithm to be turned on or off in the pipeline).

3.3.5 Bad Times List

At this stage (Level 1B), the Bad Times list should mostly contain time periods when attitude information is poor, or when an unexpectedly high number of non-Triple / low confidence events occur. This exact number of unexpectedly high non-Triple events for the threshold is to be determined, but should be considered as a placeholder value for the SOC pipeline.

The Bad Times list will eventually be derived from the Spin Table. The Spin Table is a proposed, project-maintained data set which represents binary filters, on/off, switches that represent the non-nominal / nominal conditions that warrant a bad spin. Rates ρ_i, are constructed from image rate packets and may be useful for background calculations. We propose a minimum set of filter conditions:

- Ultra in a state not suitable for ENA imaging (e.g., voltages not appropriate)
- Ultra telemetry errors (e.g., checksum failures, bad packets)
- Ultra event rates beyond threshold (see section 3.3.4 *Ultra Event Rates Culling*)
- Attitude system not suitable for Ultra processing (e.g. spin rates out of bounds, repointing in progress, nutation > 0.25 deg)
- Excessive solar wind near Ultra's FOV
- Abundant Energetic ion / electron flux

Table 8 provides a summary of the proposed Spin Table Items. See also section 3.4.1 Culled Events and [3].

Table 8. Spin Table Proposed Items

Quantity	Description	Type	Note
S	Unique spin number	32 bit int	Project assigned
T_0	Spin start time	Double	Project assigned
P	Spin period	Double	Spin time (sec)
ρ_{start}	Total start pulses / spin	Double	# Start pulses for the spin
ρ_{stop}	Total stop pulses / spin	Double	# Stop pulses for the spin
ρ_{coin}	Total Coincidence / spin	Double	# Coincidences for the spin
ρ_{event}	Total processed events / spin	Double	Total # valid events for the spin telemetered from Ultra
ρ_{reject}	Total rejected events / spin	Double	Total # rejected events based on ground cal for spin; This will include tighter restriction for cal items (e.g. on coincidence logic)
$\mathcal{F}_U$	Spin filter from Ultra engineering / HK data	Bit field	See Bad Times section
$\mathcal{F}_A$	Spin filter derived from IMAP attitude	Bit field	See Bad Times section
$\mathcal{F}_I$	Spin filter derived from other IMAP instruments	Bit fields	See Bad Times section
$\mathcal{F}_P$	Spin filter from event rates beyond threshold	Bit fields	Energy dependent bit field(s) designating if spin should be included based on rate threshold

3.4 Level 1C

The IMAP pointing set definition will consist of an averaged IMAP Spin vector, $\hat{Z}$ and North Polar Ecliptic vector, $\widehat{N}$. Ideally these vectors will be built for each Pointing interval and will define the basis for a common grid in which multiple particle instruments aboard IMAP will use. For the duration of valid Pointing Grid(s), SDC will generate IMAP-Ultra Pointing Set: Counts, Exposure Times, Background Rates, Sensitivity Factors, Corrected Counts, Ground Processed 2D Histograms for comparison with those produced onboard the spacecraft, Culled Events lists and maps. These products are produced on a per Pointing basis.

At level 1C (L1C), two grid options / tessellations should be available for these products. HEALPix (default) tessellated pixels and rectangular pixel grids. The following subsections for L1C are written directly for the methods used for square pixels as they are slightly more complex. When using HEALPix, the same principles apply, but there may be nuanced differences between the two. We address these issues where important.

3.4.1 Pointing Grid and Binning ENA Counts

There will be two sets of grids per tessellation (HEALPix or square pixels), one for items with respect to the spacecraft rest frame Δ and another with respect to a heliocentric rest frame D.

Recall that the ENA trajectories are already computed in the instrument frame, and the Pointing frames from the annotated events (Table 7). We can now bin them in the Pointing frame given the Pointing Grid definition. The Pointing coordinate system is defined in SPICE, and so can be queried directly with "IMAP_DPS" and an ephemeris time. $\hat{Z}$ is the averaged spin direction per pointing vector and $\widehat{N}$ is the North Polar Ecliptic for the grid, each ENA event can be binned as follows, assuming 0.5° x 0.5° 2D angular bin sizes or an equivalent HEALPix map size of NSide = 64 (default), which corresponds to approximately 0.92 deg mean spacing per HEALPix pixel.

The grid should be initialized to zero counts, and each event added to the given bin. It is expected this grid will be sparse at daily cadence. The Pointing Set Counts grid, $C_{ije\Sigma}$ will be 4 dimensional, with the 3rd dimension representing the valid energy range for the given count and 4th dimension the species type (H, O). The integer subindices on the Pointing grid (i, j, e) refer to the range of ϕ_p, θ_p, and energy in which the event(s) took place, as shown in Figure 8. Bins in the figure may not be consistent with the final Pointing grid structure and the Figure should be used as a notional representation of the grid.

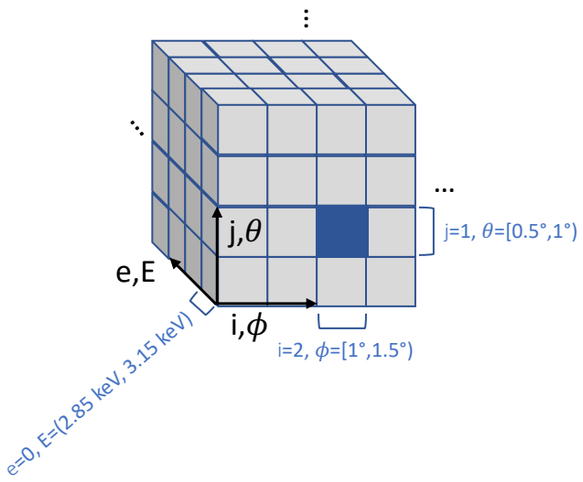


Figure 8. Example 3D Data Structure Representing the Pointing Grid (4D when including Species)

The energy bins will be subject to change once data is on the ground, but initially we assume bin spacings consistent with $\frac{\Delta E}{E} = \frac{E_2 - E_1}{\sqrt{E_1 E_2}} = \alpha$. Such that $E_{i+1} = E_i(1 + \frac{\alpha}{2})/(1 - \frac{\alpha}{2})$. For example, given a value of $\alpha = 0.2$, there are 23 energy bins required between 3.385 and 300 keV. We suggest initially, adjusting α to overlap energy channels with that of IMAP-Hi, for calibration purposes. The energy bin ranges should be allowed to be configured directly as requested, or computed with the equations above.

Each event can then be put into the Pointing frame and binned onto the Pointing Grid as follows:

For each event or set of events that has not been culled (determined by Spin table), and for each frame reference (Δ, or D), compute the unit vector for the valid event's direction on the Pointing grid

$$\hat{r}_{DPS} = \begin{bmatrix} x_{DPS} \\ y_{DPS} \\ z_{DPS} \end{bmatrix} \tag{9}$$

$$\theta_p = \tan^{-1} \frac{z_{DPS}}{\sqrt{x^2{}_{DPS} + y^2{}_{DPS}}}, \left[-\frac{\pi}{2}, \frac{\pi}{2}\right] \tag{10}$$

$$\phi_p = \tan^{-1} \frac{y_{DPS}}{x_{DPS}}, [0, 2\pi] \tag{11}$$

$$j = \theta_{bin} = FLOOR\left(\left(\frac{1}{2} - \frac{\theta_p}{\pi}\right)\left(\frac{180}{0.5}\right)\right) \tag{12}$$

$$i = \phi_{bin} = FLOOR\left(\left(\frac{\phi_p}{2\pi}\right)\left(\frac{360}{0.5}\right)\right) \tag{13}$$

For HEALPix maps, the geometric bin index can be determined simply by a call to the API with the *vec2pix()* method. Ensure all vectors for each map are in the proper reference frame.

For the event, the energy bin *e*, is determined such that the calculated energy (will be different for Δ and D frames) falls within the bin width for the given bin. Each HEALPix map will represent a map for the specified energy bin, just as with square pixels we represent it as the 3rd dimension.

For square pixels, the azimuth, elevation (ϕ_p, θ_p) reference bin is at the north-westerly most corner $\left(0, \frac{\pi}{2}\right)$ or $(0°, 90°)$. Since the bin widths and heights are 0.5°, then the center of the north-westerly most pixel represents $(0.25°, 89.75°)$. For each valid event, the bin (i,j,e,Σ) on the grid is incremented by 1 count.

The corresponding count uncertainties for each pixel and energy range is then simply

$$\sigma_{c_{\mathrm{ije\Sigma}}} = \sqrt{C_{\mathrm{ije\Sigma}}} \tag{14}$$

Corresponding count rate uncertainties are then

$$\sigma_{cr_{\mathrm{ije\Sigma}}} = \frac{\sigma_{c_{\mathrm{ije\Sigma}}}}{\tilde{\tau}_{ij}} \tag{15}$$

Where $\tilde{\tau}_{ij}$ is the total exposure time which passes the culling criteria for the Pointing. These uncertainties should also be kept as ancillary gridded products to track uncertainties in the final L2 flux estimates, and will eventually be used in L3 for the spectral indices residual weighting criteria.

3.4.2 Culled Events

Culled events are registered, valid events that should not be included in the Pointing Set Counts. Direct Events are to be culled when any of the following situations occur:

1) Events fall within the Bad Times List
2) High background count rates determined by other instrument data
3) Foreground obstruction, foreign or non-heliosphere ENA source has been determined to be present in Ultra's FOV (ex: Earth / Moon / Magnetosphere in Ultra-45 FOV)
4) Solar Energetic Particle event or rapid increase in counts is detected
5) ENA event falls outside of the nominal instrument FOV

Culled events will be tracked as an independent data set and added as a flag to the Annotated Events. We propose using the Spin Table as defined in section 3.3.5 to aide in certain types of Culling. This naturally leads to throwing entire spins out rather than single events – which makes the culling process straight forward.

For Ultra the process of spin culling consists of determining which spins should be included in the pointing sets. This will be done through bitwise operations on the spin filters, $\mathcal{F}_j$ (where j is the filter type, i.e., U, A, I), in the Spin table (see table 8). For each filter type we define a mask m_j that allows us to select the bits of $\mathcal{F}_j$ to be applied for culling. Initially all these bits will set on (excluded in processing), but experience will be needed to set these masks correctly. The masks will be used to construct the final applied filter $\widetilde{\mathcal{F}_j} = \mathcal{F}_j$ and m_j.

Subsequently all the bits of all the $\widetilde{\mathcal{F}_j}$ should be OR-ed together to create the final culling mask $\mathcal{C}_S$, which is a Boolean value associated with each spin. If $\mathcal{C}_S$is off for a spin, the data from that spin will be included in subsequent processing.

In order to take into account for spatially varying, long duration sources of contamination, we implement a spatial culling scheme as part of the pointing set generation process. For quasi-isotropic, short duration contamination, we will use the Spin Culling Mask $\mathcal{C}_S$ to eliminate contaminated spins from the subsequent processing. There may, however, be long duration (large fractions of a pointing), spatially concentrated sources of contamination (e.g., upstream ion events, energetic particle events) that we can address with a spatial mask. We assume that the sources of contamination can be represented at rest within the Pointing frame.

The spatial contamination will be identified by either the Low Res. Rate Images assembled from the TOF images accumulated on board OR level 2 data from other IMAP instruments. Each contaminated bin, β_Δ, will be accumulated in a table where the spins that are contaminated for that bin are listed. Events that fall into β_Δ during these spins will be subsequently removed from processing and the exposure time corrected accordingly.

Earth's magnetosphere will always be in the Ultra-45 FOV. Since we're building sky maps of ENA sources coming from the outer heliosphere, we want to exclude any ENA sources that may come from this region. This mask will be a per pointing mask that will be used to remove exposure times, counts, and sensitivities from being included in the sky maps. We can use the following algorithm to cull those ENAs and other TBD spatial culls as necessary.

1. User specifies a keep out radius for the magnetosphere $R_{keepout}$
    a. To keep this algorithm generic, we recommend not hard-coding values as we may eventually want to cull additional / multiple objects (e.g. Moon, Jupiter)
    b. Use $R_{keepout} = 30R_e$ (30 * 6378.137 km) as an initial size (and notionally 4*R_{moon}, 100*$R_{jupiter}$)
2. Compute the IMAP to EARTH (or other body) position in the Pointing frame (D_{body}) in time steps that can appropriately represent the bodies velocity in the Pointing frame through the pointing.
    a. You can use the *SPKPOS()* SPICE routine
    b. Recommend 30-minute steps for Earth
3. Compute an angular mask dimension (deg) as $\theta_{mask} = \tan^{-1}\left(\frac{R_{keepout}}{D_{body}}\right)$ at each time step throughout the pointing
4. The number of radial pixels from the body location is then $\frac{\theta_{mask}}{\Delta_{dpp}} = N_{pixels}$
    a. Δdpp is the grid spacing (0.5° for square pixels or ~0.92° for the default HEALPix)
5. The separation angle, θ_{sep_ij}, from the body is computed from each location on the Pointing Grid at each time step
    a. You can use the VSEP() SPICE routine to compute the angle between the body position and the given pixel on the grid
6. The pixels on the grid are then masked when θ_{sep_ij} <= θ_{mask}
    a. This accounts for variations over the course of the pointing set in body position
7. This mask will be used to cull regions of the exposure time, sensitivity, and counts maps for a given Pointing and so should be saved for future use.

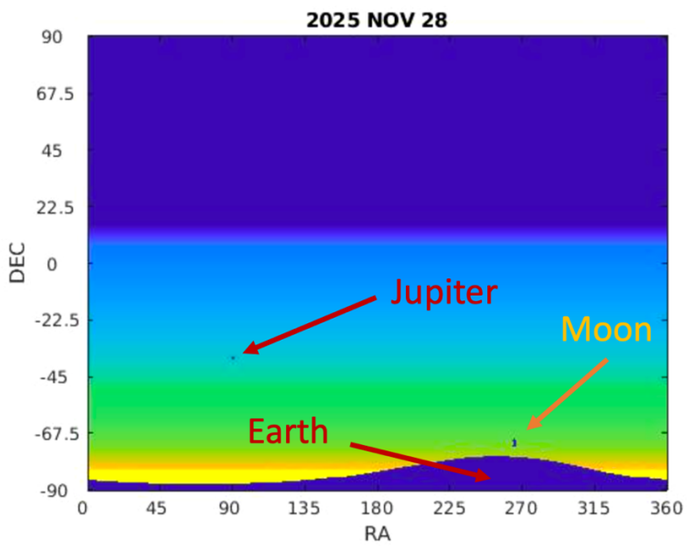


Figure 9. Representative Spatial Culling Masks of 3 Bodies for a single Pointing. Background color represents Ultra-45 exposure time in the Pointing Frame (yellow is high, blue is low)

3.4.3 Exposure Time Calculation

The exposure time is defined as the amount of time a given pixel in the sky (Pointing bin pixel at L1C) falls within the instruments Field of View. The calculation of exposure time for a full Pointing and all pixels which fall within the Instruments field of view is computationally expensive. We propose the following solution. For each pointing set frame definition, the exposure time will be approximately the same on a per spin basis assuming no major attitude instabilities. We precompute and tabulate a static exposure time τ_{ij}^{n} for each pixel in the sky in the Pointing frame and correct the total exposure time by the number of valid spins. The indices *i* and *j* represent spatial indices of the Pointing grid as described in the previous section.
The total exposure time for the Pointing can then be calculated as

$$\tilde{\tau}_{ij} = \sum_{spins} \tau_{ij}^{n} \frac{P^{s}}{P^{n}} \tag{16}$$

Where τ_{ij}^{n} is the nominal exposure time in a pixel per spin, P^{s} is the period of the current spin being summed over. Recall from section 3.3.2 that P^{s} may need adjusting due to scattered ENAs that fell outside of the FOV if the number of these is significant. P^{n} is the nominal spin period (i.e. 15 seconds). Figure 10 shows the nominal exposure time for a single spin on the Pointing grid. Each pixel of figure 10 is a representation of τ_{ij}^{n}. Figures and data were numerically computed using SPICE with calls to *GFRFOV()*.

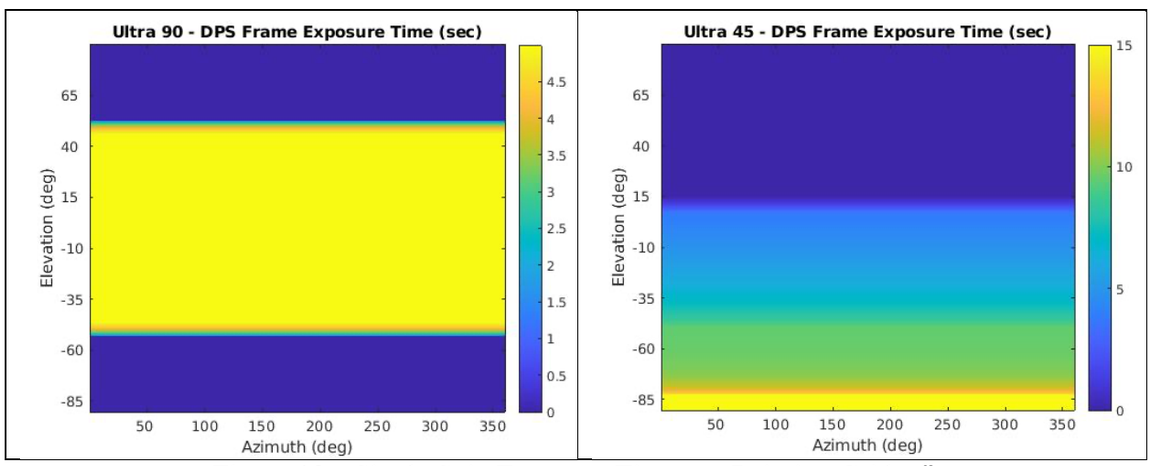


Figure 10a. Single Spin Exposure Times on Pointing Grid, τ_{ij}^{n}

A reduction in exposure time (duty cycle) is caused by the flight hardware listening for coincidence events that never occur, due to singles starts predominantly from UV radiation. The static exposure time for a given Pointing should be reduced by this spatially dependent exposure time reduction factor (the dead time). As the spacecraft spins, at each sector (nominally 1 second or every 24 degrees of rotation), the Image Rates packets provide a Start Right Full CFD and Start Left Full CFD pulses that should be summed and then divided by the sector integration

time, T_{int} , to convert to Hz to get the total Start Rates (*StartFullCFD*). T_{int} can be computed by taking the spin duration and dividing by the number of sectors (15).

IMAP-Ultra will produce image mode rates packets in sector mode 3 times per day (per Pointing) for 20 minutes each time. There will be a macro (macro-47) from the MOC that puts the packet data into sectored rates mode vs once per spin mode and these command times will be delivered to the SOC in a parameter packet each time this mode changes. Sectored mode is defined in the parameters packet with integer 3.

Use the packet data in sectored mode spins to build a function of Dead Time Ratio vs Spin Phase. For a given Pointing, take the computed values of dead-time ratio vs spin-phase and median the data at each spin phase. Then use a Piecewise Cubic Hermit Interpolation (PCHIP) approach to fit and fill the function, starting at spin-phase = 0, and incrementing in fine steps (1 ms).

The correction factor is to be computed at each sector as:

$$CF = \frac{e^{\left(5E^{-7}(StartFullCFD)\right)} e^{\left(8E^{-7}(CoinStopND)\right)} T_{int}}{(T_{int} - (EventActiveTime + 2\ StartPosTDCVE)\ 1E^{-7})} \quad (17)$$

Where CoinStopND is defined as:

$$CoinStopND = CoinTopNorthCFD + CoinBottomNorthCFD - StopTopNorthCFD - StopBottomNorthCFD$$

The majority of these terms come from the Hardware Event Counters (See Table 7 in the FSW document). Once the correction factor is computed, the dead time ratio (DTR) is the inverse of the correction factor.

$$DTR = \frac{1}{CF} \quad (18)$$

Use the nominal spin duration (15 sec / spin) starting at spacecraft spin-phase = 0°. In fine time steps (default to 1 ms), spin the spacecraft in the Pointing frame. This can be accomplished using SPICE and the DPS frame attitude kernel(s). At each iterative step, query the dead-time ratio function previously built for the given spin phase. Add the nominal exposure time increment (the time step) to every pixel in the Field of Regard (FOR) multiplied by the dead time ratio. The FOR four corners defined wrt the instrument frame are:

FOR Boundary Definition		
X	**Y**	**Z**
0.795473480854896	0.524801349028798	0.302994200132856
0.795473480854896	-0.524801349028798	0.302994200132856
-0.795473480854896	-0.524801349028798	0.302994200132856
-0.795473480854896	0.524801349028798	0.302994200132856

At each step, use the theta/phi dependence that defines the nominal Field of View (FOV) as the selection criteria in which to accumulate time into that pixel or not.

The nominal FOV boundary is defined as follows:

$$\theta_{nom}(\phi) = \text{atan}\left(\frac{5.0\cos\phi}{1+2.80\cos\phi}\right) - 0.0^{\circ} \quad (19)$$

The subtraction by 0.0° term is a placeholder in the future if IMAP-Ultra shows poor response near extreme theta values. We don't want to cull any detections from the instrument initially if it can be helped. With maximum and minimum values of theta (no buffer) as:

$$\theta(\phi = 0°) = 52.765°$$
$$\theta(\phi = 60°) = 46.169°$$

See examples of the dead-time ratio vs spin-phase and dead-time corrected Ultra-90 Exposure time in the figures below.

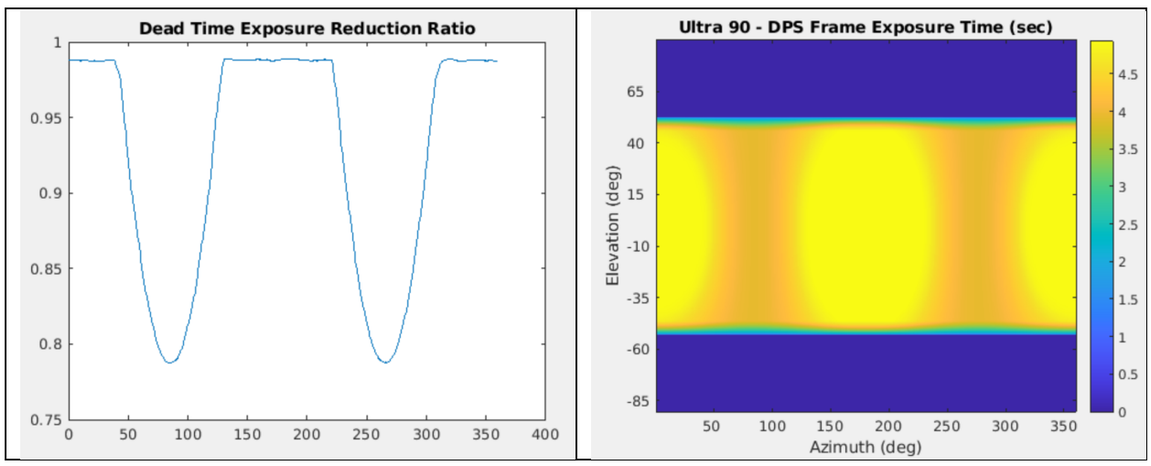


Figure 10b. Dead-Time Ratio vs Spin Phase and Corrected Single Spin Exposure Time

3.4.4 Sensitivity Factors

Instrument sensitivity factors can be created by multiplying the provided spun Geometric Function and spun energy dependent efficiencies (provided as input) to create the Response Function or Sensitivity, $S(\phi, \theta, E)$ on the Pointing set grid, S_{ije}. The Sensitivity includes energy dependence from instrument measured efficiencies and is static on a per nominal spin basis. S_{ije} is a static 3-dimensional product representing the averaged sensitivity over a single, nominal spin in the Pointing frame with the 3rd dimension representing the response for each energy at the geometric mean of the energy bin: $\sqrt{E_1 E_2}$.

The efficiencies will be pre-interpolated at fine steps in energy and provided to the SOC in the Pointing frame. To compute the efficiencies valid for the given energy bin, linearly interpolate the efficiency between the closest two energies provided from the calibration data for each pixel. Figures 11a and 11b show a representation of S_{ij} in the unit Pointing frame with energy dependence removed. See also Figures 14 and 15.

The spun sensitivity is mostly invariant from spin to spin. It may vary slightly due to attitude nutation, but the variation will be small compared to the differences in neighboring Pointing grid sensitivities across the small pixel size at L1C.

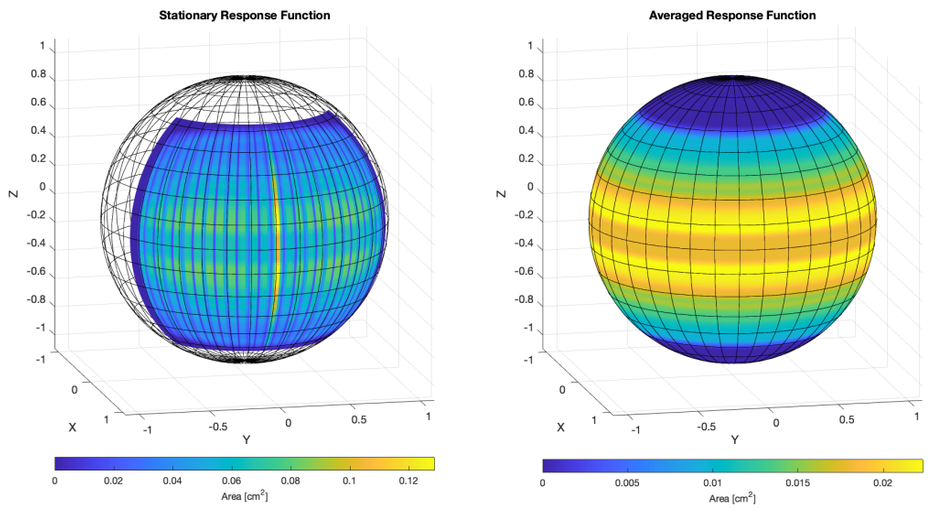


Figure 11a. IMAP-Ultra 90 Stationary and Averaged Sensitivity

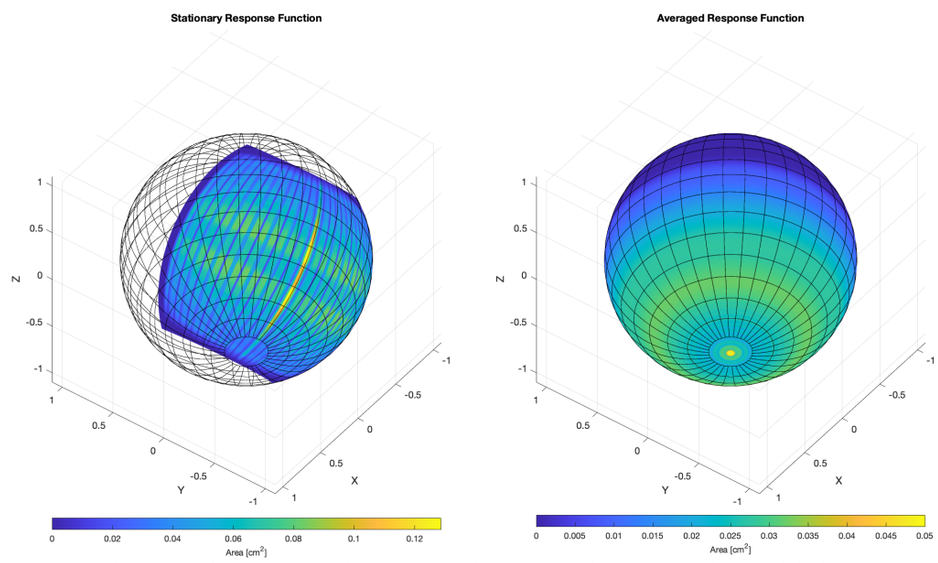


Figure 11b. IMAP-Ultra 45 Stationary and Averaged Sensitivity

3.4.5 Pointing Set Background Rates

We initially request that no backgrounds be subtracted without the IMAP-Ultra instrument teams looking at it first, however a method for computing background rates based on the singles rates (start, stop, coincidence) is discussed below. This algorithm should be implemented and the backgrounds stored on a per Pointing basis as a 3D grid with 3rd dimension representing energy. There should not be two versions of this product for the different reference frames (spacecraft and heliocentric) as the dominant cause of backgrounds we expect are caused by UV.

Singles rates should be computed from the hardware event counters as was done in section 3.4.3 (Exposure Time Calculation) for the RvsR correction. However, a simpler, spin-averaged approximation can be used initially to get a rough estimate of the backgrounds using the spin table start, stop, and coincidence rates per spin.

Let the energy dependent, average background rate per Pointing be computed as:

$$\rho_{bg}(E) = \frac{\Delta cTOF(E)\, \Delta eTOF\, \rho_{start}\, \rho_{stop}\, \rho_{coin}}{30} \tag{20}$$

Where:

- $\Delta cTOF(E)$ is the corrected TOF listening window range for the given energy bin (combine equations 3 and 8)
- $\Delta eTOF$ is the listening window for stops-coincidence. Default is 10 ns, but is also listed in the parameters file and should be computed as the difference in the maximum eTOF – minimum eTOF
- ρ_{start} is the mean pulse rate of starts computed during good-times over the Pointing
- ρ_{stop} is the mean pulse rate of stops computed during the good-times over the Pointing
- ρ_{coin} is the mean pulse rate of coincidence events computed during the good-times over the Pointing
- The '30' term in the denominator is the length of the coincidence MCP in the X dimension over the resolution of the coincidence measurement in X. The measurement is limited primarily by the secondary electoral spatial dispersion along X.

This energy dependent background rate should be added to every pixel in the Pointing Frame spun field of view. Realistically, the background will likely be spatially dependent – but we expect them to be so small that we will not subtract them from the count rates initially.

3.4.6 Ground Processed 2D Histograms

Ground Processed 2D Histograms are primarily used for diagnostic purposes and will not be used in Level 2, or Level 3 products. The ground processed histograms should be binned using the same spin-referenced coordinate system as the onboard histograms. For reference, see [1, p. 45-51; Sec. 3.3.1.3].

3.5 Level 2

The primary data products for Level 2 are intensity maps in the HAEJ2000 frame, both spacecraft and heliocentric (i.e. 1 AU flux maps). Mapping products described in this section are to be produced for periods of time where we have sufficient counting statistics. Initially, we request that all Ultra level 2 maps are capable of being built at the cadence summarized by Figure 12. In general, the pipeline should be setup such that any desired map can be generated over any requested cadence. Figure 12 is the requested map cadence that the maps are available, not necessarily what is delivered to SPDF.

Intensity maps and all other ancillary products are to be released as three-month, six-month, and twelve-month maps. Three-month maps are staggard and do not overlap per release. In the first 18 months of the mission, there should be 6, three-month map releases. Six-month maps are released after accumulating 6 months of data. Six-month maps, with three months of overlap should be available to the science team. In the first 18 months of the mission, there should be 5 full six-month maps available. Twelve-month maps are released after accumulating 12 months of data. There will be 9 months of overlap of accumulated data for each map available to the science team. In the first 18 months of the mission, there should be 3 full year maps available.

The previous paragraph describes map release cadences; however, we request the software be written in a flexible manner such that maps could be built over any duration (for example 2 week or 1-month maps). These would be built at the request of the scientists using the IMAP-Ultra data either via command-line or web interface (or by request of the SOC).

All level 2 products described in the pipeline flow diagram (Figure 2) will be produced by default in HAEJ2000, however it is requested that the software be written flexibly to allow maps built in alternative coordinate frames.

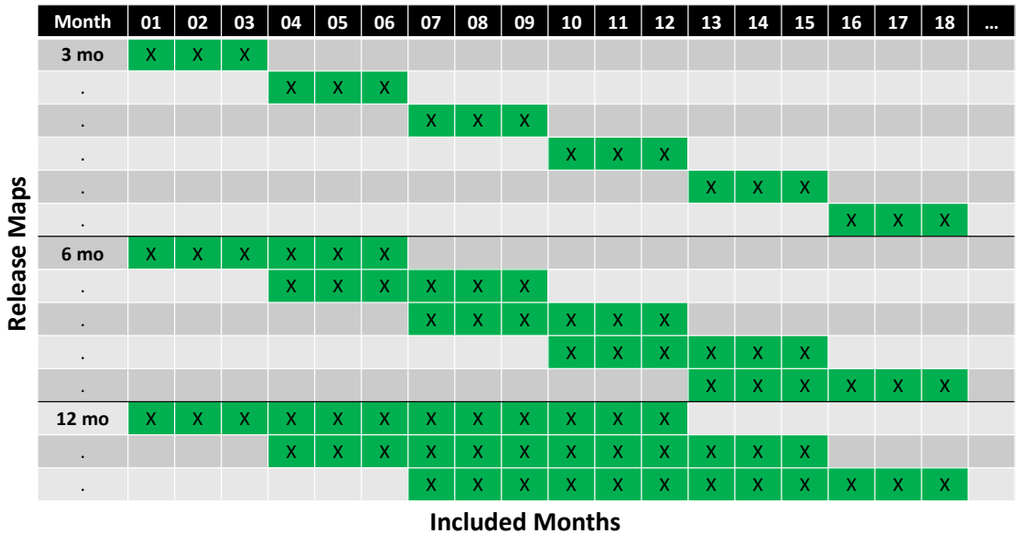


Figure 12. IMAP-Ultra Requested Map Cadence

3.5.1 Reprojecting the binned Pointing frame to Ecliptic Inertial Space

We can represent the ecliptic inertial frame (HAEJ2000 aka ECLIPJ2000 or just HAE) in a similar manner to that of the Pointing grid. Each bin in the grid corresponds to a right ascension and declination at the center of each pixel. Discretizing these grids in right ascension and declination $\left(\phi_{b_{ij}}, \theta_{b_{ij}}\right)$, we can represent each bin in the ecliptic inertial frame with a spherical to cartesian conversion.

$$\hat{r}_b = \begin{bmatrix} x_b \\ y_b \\ z_b \end{bmatrix} = \begin{bmatrix} \cos\left(\theta_{b_{ij}}\right)\cos\left(\phi_{b_{ij}}\right) \\ \cos\left(\theta_{b_{ij}}\right)\sin\left(\phi_{b_{ij}}\right) \\ \sin\left(\theta_{b_{ij}}\right) \end{bmatrix} \tag{21}$$

For each pointing, there will an associated Pointing frame definition that is built from averaging attitude quaternion data and placed into an attitude kernel for direct use with the NAIF SPICE API. For every bin in this new ecliptic inertial reference square-pixel grid, we want to pull items from the associated Pointing bin.

$$\hat{r}_{DPS} = \boldsymbol{R}_{pb}\hat{r}_b \tag{22}$$

$\boldsymbol{R}_{pb}$ is the rotation matrix from the ecliptic inertial frame (IMAP_HAE) to the Pointing frame and can be computed with the SPICE call: *CSPICE_PXFORM*('IMAP_HAE', 'IMAP_DPS', et), provided IMAP_HAE and IMAP_DPS are defined. This rotation matrix is unique for each Pointing. Equations (9) – (13) can then be used to determine the Pointing frame bin to pull from and assign to the ecliptic inertial grid.

Note that for continuous quantities such as exposure time and sensitivity factors, the process is exactly as described. With discrete quantities however, such as counts and count rates, care must be taken not to over or under represent the quantities assigned in each pixel due to different solid angles between bins in the "from" and "to" projections. These grids are on equally spaced parallels and meridians representing latitude and longitude in a simple cylindrical projection. The solid angles at the poles are smaller than those at the equator in both frames. When adding / binning counts or count rates, the added quantity should be weighted by the ratio of "TO" / "FROM" solid angle; i.e. for counts

$$C_{b_{\mathrm{ije\Sigma}}} = C_{b_{\mathrm{ije\Sigma}}} + C_{p_{\mathrm{ije\Sigma}}}\frac{\Omega_{b_{\mathrm{ije\Sigma}}}}{\Omega_{p_{\mathrm{ije\Sigma}}}} \tag{23}$$

Where subscripts *b* represents the ecliptic inertial bin, and *p* represents the Pointing frame bin that corresponds to the ecliptic inertial bin *b* in question. Ω is the solid angle for that given bin.

$$\Omega_{pixel} = \int_{\phi_i}^{\phi_{i+1}} d\phi \int_{\theta_j}^{\theta_{j+1}} \cos\theta \, d\theta = \Delta\left|\sin(\theta) - \sin(\theta \pm \Delta)\right| \tag{24}$$

Where Δ is the step size of the grid (radians), and θ is the latitude of the boundary of the given pixel or angular bin that defines the grid, not the pixel center coordinate.

It is recommended to initially use a much finer grid for the counts "TO" frame in order to ensure sufficient sampling of the "FROM" frame at L1C going into the final L2 map. Finer such that the largest solid angle for the L2 grid (i.e. those at the L2 equator) is smaller than that of the smallest solid angle of the L1C Pointing grid (i.e. those at the L1C poles). Set:

$$\Omega_{eq}^{L2} < \Omega_{pole}^{L1C}.$$

Once all counts are pulled for the map, then the L2 grid can be summed and resampled to the desired resolution grid that is consistent with the other data products. This ensures the minimal amount of loss in total counts when pulling pixels.

This method of pulling pixels into the final L2 map for discrete quantities will result in non-integer valued counts. This is done in an attempt to not alias the level 2 maps, which happens more so at the poles. If desired, a discrete counts map can be built from the inverse process just described by placing each Pointing count into the L2 map directly (pushing pixels), however it should not be used when building fluxes with square-pixel maps – otherwise there is the potential for fluxes of 0 in any coordinate frame near the poles.

When using a HEALPix tessellated map for binning, pushing pixels is acceptable for counts and maintains their discrete nature. When moving between coordinate frames like the Pointing frame to HAE, there's no guarantee that every pixel will have a 1-to-1 mapping. This is okay however as the primary purpose for using HEALPix is to ensure a consistent solid angle within a single map – which necessarily mitigates the pole issues previously discussed.

Other non-discrete quantities such as the exposure times, sensitivities, and FWHM scattering values should use the pull approach.

3.5.2 Accumulating multiple Pointing Grids into an Ecliptic Inertial Frame

We ultimately wish to accumulate each data product (counts, exposure times, etc.) onto a single ecliptic inertial frame using many Pointing grids. In order to do this, we initialize a 3-Dimensional angular grid which represents the ecliptic inertial space and energy in the same manner we did for the Pointing grid. For each Pointing Set definition, convert each non-zero data product's location in the Pointing frame to the Ecliptic Inertial frame as described in section 3.5.1 and accumulate each data product onto the grid. There will be many of these 3D grids in the ecliptic inertial frame which represent the different data products mentioned in Figure 2.

The general process is described with the following pseudocode:

Set tex[b]=0,cnt[b]=0,s[b]= 0,bk[b]=0,E[b]=0, f[b]=0, n in all sky elements
For each pointing p in $\mathbb{D}$
    For each β in p not eliminated by cull
        Find sky element b for pointing bin β
        cnt[b]= cnt[b] + C_β ; C_b
        tex[b]= tex[b] + $\tilde{\tau}_\beta$; $\tilde{\tau}_b$
        s[b]= s[b] + S_β $\tilde{\tau}_\beta$
        bk[b]= bk[b] + B_β $\tilde{\tau}_\beta$
        f[b]=f[b] + F_β $\tilde{\tau}_\beta$
        n[b]= n[b] +1
For each sky element b
    s[b]= s[b]/tex[b] ; $\bar{S}_b$
    bk[b]= bk[b]/tex[b] ; $\bar{B}_b$
    f[b] = f[b]/tex[b] $\bar{F}_b$

On the skymap / ecliptic inertial frame:

- "*tex*" is the total exposure time grid
- "*cnt*" is the counts grid
- "*s*" is the sensitivity grid
- "*bk*" is the background rate grid
- "*f*" is the FWHM scattering grid
- β represents elements on the Pointing grid, and *b* represents the ecliptic inertial indices.

This pseudocode is generic for both square-pixels and HEALPix tessellated maps and assumes that the map dimensions are of the same size between the Pointing frame and the L2 skymap frame. If the dimensions of the L1C map and the L2 map differ, then the calculations for "s", "bk", and "f" should further be weighted by the solid angle of the Pointing frame pixel when building the intermediate maps, then divided out by the solid angle of the skymap pixel to achieve the final weighted mean quantities in the skymap frame.

3.5.3 Total Exposure Time

In Figure 13 below, we use the process described in sections 3.5.1 – 3.5.2 to build a 180-day exposure time for Ultra-90 and Ultra-45. The single spin exposure times (Figure 10) in the Pointing frame were used with a nominal attitude & spin assumption with no culling (4 rpm, no nutation, and N = 5760 Spins per day or Pointing) and re-binned into the ecliptic inertial frame.

The non-uniform equatorial region from the Ultra-90 total exposure time is due to the fact that there are ~365.25 days in a year, and we've only covered 180 days in the map. With an extra ~3 days of coverage, the maps would be approximately symmetric.

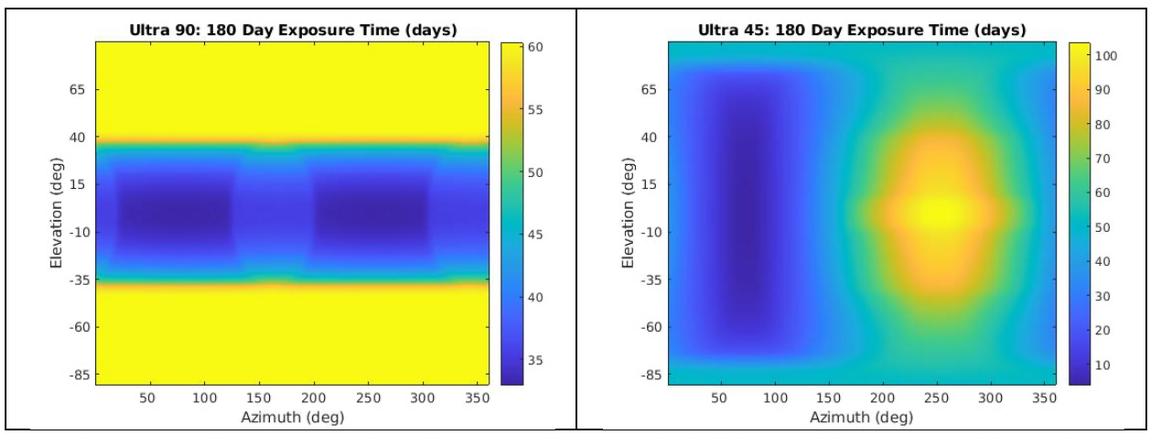


Figure 13. Example 180 Day Exposure Times in ECLIPJ2000, Ultra-90 and Ultra-45

3.5.4 Mean Sensitivity Factor

The mean sensitivity factor on the ecliptic inertial grid is constructed from the Pointing grids in a similar manner to the exposure time. As shown in the pseudocode in section 3.5.2, we bin both the spun sensitivity and the exposure time for each bin, then divide by the total exposure time on the ecliptic grid at the end – ultimately creating an exposure time weighted mean for the sensitivities. Figure 14 shows similar sensitivity factors as those in 3.4.4, except with energy dependence included (3.5 keV – i.e. the first midpoint of the first energy bin) and on the cylindrical Pointing grid. Figure 15 shows an example of what the 180-day averaged sensitivity factor products look like on the ecliptic inertial grid.

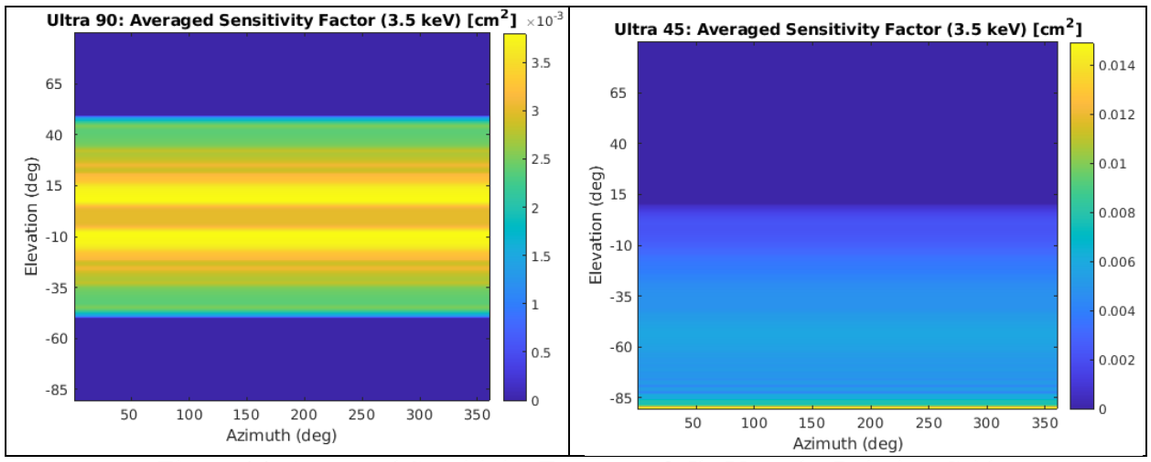


Figure 14. Averaged Sensitivity Factors at 3.5keV on the Pointing Grid

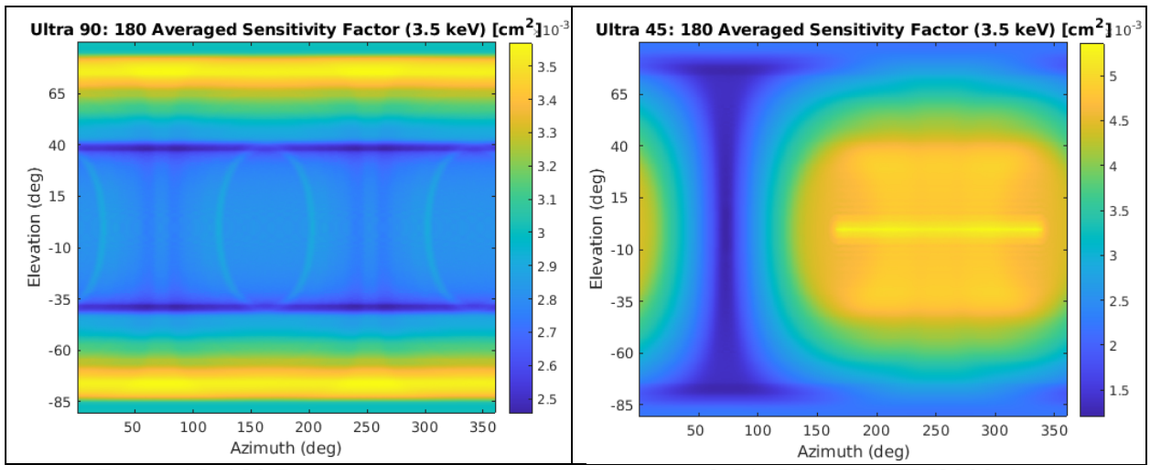


Figure 15. 180 Day Averaged Sensitivity Factors at 3.5 keV on ECLIPJ2000 Grid

3.5.5 Background Rate Images

Background Rate Images are the Pointing Set Background Rates from Level 1C (section 3.4.5), reprojected into an ecliptic inertial coordinate frame for each energy range as described in sections 3.5.1 - 3.5.2. Once the background rates are accumulated into the appropriate ecliptic inertial frame bins, the average is taken for each pixel and assigned in the final background rate image. We refer to this image as $\bar{B}_b$.

3.5.6 Corrected Rate Images

The corrected rate images are the count rates with background rate images subtracted in the ecliptic inertial grid.

$$\rho_{c_b} = \frac{C_b}{\bar{\tau}_b} - \bar{B}_b \tag{25}$$

ρ_{c_b} is the corrected rate image and should have units of counts per second. $\frac{C_b}{\bar{\tau}_b}$ are the ground accumulated rate images, and $\bar{B}_b$ is the mean background rate image. Each of these grids is 4 dimensional when considering species type. Sections 3.4.5 and 3.5.1 – 3.5.2 describe how to create these products.

3.5.7 Ancillary Images

Ancillary images are diagnostic products that will likely evolve over time as we learn from the measurements during the mission. Ancillary images we foresee being useful are:

- Averaged ENA velocity for a given pixel in the sky.
    - These images can be generated from the Annotated Events following the coordinate transformation procedures previously described in the document (sections 3.4.1 & 3.5.1 - 3.5.2).
- Mean Date, and Standard Deviation of Date maps
    - A useful product for understanding when each pixel in the final map is valid
    - This is basically a date-tagged pixel map. Building meta-data that makes this possible would be very useful. Whether it comes from the SOC or another mapping tool.
    - Mean and STD values can be computed on datetimes offsetting from the time of initial exposure for a given pixel and converting back to date and days (Pointings)
- Spatial Uncertainty maps
    - See sections 3.3.3 and 3.5.2. Spatial uncertainty maps are created from carrying through and averaging each spun FWHM scattering value onto the final L2 maps. Final results should be reported as Gaussian uncertainty in degrees. (i.e. approximately average FWHM / 2.355)

Uncertainties are similarly carried through the calculation and stored on their own grids that are associated with the Ground Accumulated Rate Images; See equations (14) (15)(25).

3.5.8 Level 2 Intensities

Level 2 products consist of intensity maps in different forms. The following subsections describe each level 2 intensity product.

The number of counts within a given energy range in a pixel is given by

$$C = \bar{\tau}\,\Omega_{pixel} \int S(\theta, \phi, E)\, J(E) dE \tag{26}$$

The response function is known, but in order to simplify the calculation we must remove it from the integral. Corrected count rates ρ_{c_b}, were computed in (25). We can approximate the intensity as

$$J_b = \frac{\rho_{c_b}}{\bar{S}_b \Omega_b \Delta E} \tag{27}$$

in units of counts/(cm^2 * sec * sr * keV). This product will be 4 dimensional as before if considering species. ΔE is the energy bin width for the given energy range bin in question. Recall that the 3rd dimension of C_b represents the energy range that the given count falls into, whereas the 3rd dimension of $\bar{S}_b$ is associated with a pre-defined energy from calibration or at the midpoint of the bin. Each $\bar{S}_b$ should be linearly interpolated with the measured ENA energy determined from $\vec{v}^U$ (8), which we get from the Annotated Events. If $\bar{S}_b$ is calibrated or interpolated to the midpoint of the energy bin for the grid, then we can use this directly without interpolation to the particles measured energy as an approximation as described in section 3.4.4. ΔE and the count rates will drive the flux estimate for different types of flux maps produced.

Estimated intensity uncertainty for bin b is given as:

$$\sigma_{Jb} = \frac{\sqrt{C_b}}{\bar{\tau}_b \bar{S}_b \Omega_b \Delta E} \tag{28}$$

At level 2, we assume all grids are produced initially using 0.5 degree spaced lat/lon grids or on HEALPix, NSide=64 as described in the document. Final products / flux maps can be re-binned to lower resolution grids as necessary. In addition, other binning approaches may be used such as Abrate at any stage beyond L1B, including initializing the common Pointing grid definition (level 1C) all the way through level 3.

Figure 16 shows a representative flux grid calculated at a low energy, binned on 0.5 x 0.5 degree bin spacing on a Mollweide projection.

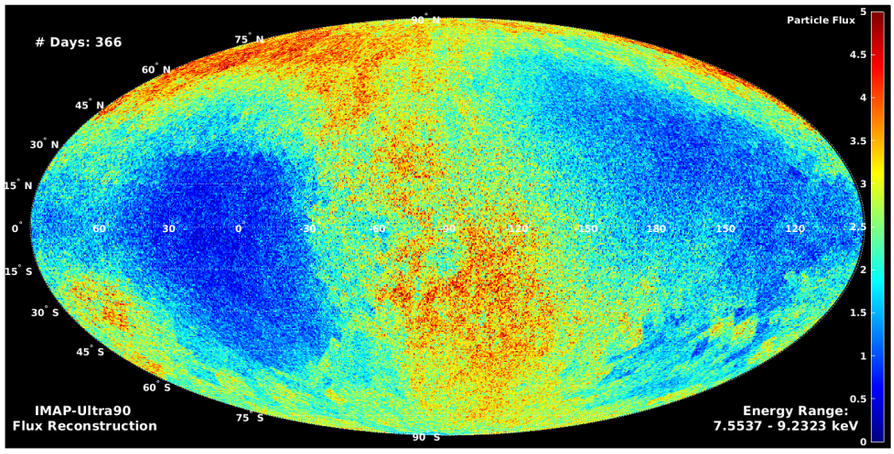


Figure 16. Representative Reconstructed Flux. HAE. Mollweide Projection

3.5.8.1 1 AU Intensities

1 AU Intensities collectively refer to fluxes built at the spacecraft origin (no Compton-getting) and heliocentric fluxes (with Compton-getting).

For heliocentric (aka sun-centered) inertial frames, Compton-getting will alter the particles energy estimates, especially at lower measured energies. We will likely see differences in binned counts for energy bins of those in a spacecraft-centered frame.

3.5.8.2 Conversion from HEALPix to Square Pixel Intensities

The proper way to convert from HEALPix tessellated maps to square pixels is to compute the surface integrals of the overlapping boundaries of the two tessellation types and assign the interior intensity value for each of those pixels. Unfortunately, this approach is very computationally expensive. We present an alternative approximation that is faster and that has the added benefit of being able to report an accuracy metric of the conversion for each pixel.

1. Setup the desired square pixel grid (i.e. 2°x2°, 4°x4°, etc.)
2. For each square pixel in the grid:
    a. Check if all 4 corners of the square pixel fall within a single HEALPix pixel
    b. If so:
        i. Assign the value of the HEALPix pixel to the square grid pixel and move to the next one
    c. Else:
        i. Successively chunk the square grid pixel up into smaller subpixels (i.e. 1 pixel turns into 4x4 = 16 subpixels that fall within the large pixel). Steps of subpixels are done successively in 4^n, where n is the iteration number.
        ii. Calculate the assigned intensity to the original / larger square pixel as:
            1. $J_{sq} = \frac{1}{\Omega_{sq}} \sum_i J_i \Omega_i$
            2. Where 'i' is the index of the subpixel, J_i is the intensity of the HEALPix pixel that the subpixel center point corresponds to, Ω_i is the solid angle of the subpixel and $\Omega_{sq}$is solid angle of the larger (map) square pixel
        iii. Check on each iteration of successively smaller subpixels if the intensity has changed to within a specified tolerance (i.e. $\left|\frac{\Delta J_{sq}}{J_{sq_{n-1}}}\right| \leq 10^{-6}$). It would be useful to set a maximum and minimum number of iterations
        iv. If the intensity change is within tolerance, assign the previously calculated flux value to the square pixel and move to the next square pixel
    d. The accuracy of the conversion for each pixel is then a function of the number of subpixels used, which that then either be quoted as a % of the size of the pixel dimension, or as the largest solid angle of the final sub-pixels used

3.6 Level 3

There are 3 primary level 3 products described in the following subsections.

3.6.1 1 AU Combined Sensor ENA Intensity Maps

1 AU combined flux maps are flux maps that are built from combining data from both instrument heads (Ultra90 and Ultra45). Since each instrument head is already properly calibrated as level 2 intensity map products, we can simply combine them together by using an exposure time weighted mean. The combined intensity for both instrument heads for each pixel is then:

$$J_{90+45} = \frac{\tau_{90} J_{90} + \tau_{45} J_{45}}{\tau_{90} + \tau_{45}} \tag{29}$$

Where τ_{inst} is the level 2 (energy dependent) exposure time for each pixel in the map. The corresponding uncertainties for the combined map would be given as follows:

$$\sigma^2_{J_{90+45}} = \frac{\tau^2_{90}\sigma^2_{90} + \tau^2_{45}\sigma^2_{45}}{(\tau_{90} + \tau_{45})^2} \tag{30}$$

With the variance σ^2_{inst} described by equation 23. Using this approach, combined intensity maps can simply be combined for each pixel and energy channel by an algebraic relation with the intensity, exposure times, and the uncertainty computed at level 2 for each instrument.

1AU combined sensor flux maps are to be computed in a heliocentric frame (i.e. Compton getting corrected).

3.6.2 Survival Corrected Intensity Maps

The survival corrected flux maps, also referred to as termination shock flux maps, 80 AU maps, or survival probability corrected maps, are produced in a very similar manner to level 2, 1 AU flux maps. These survival probabilities correct for the amount of particles lost in transit from the termination shock region to the IMAP spacecraft.

Hydrogen survival probabilities as a function of energy and Pointing, $P_{SH}(E, \theta, \phi, t)$, are provided from the IMAP-GLOWS instrument as level 2 maps in the ECLIPJ2000 reference frame on a HEALPix tessellated grid. The default number of pixels is 3072, but the dimensions are easily changeable according to the GLOWS team.

Per Pointing, survival probability maps will be taken at each provided hydrogen energy level, and interpolated to the energy bins that IMAP-Ultra uses in processing onto a L1C / Pointing grid. At L1C processing, for each Pointing, the HEALPix survival probability maps will be bicubically interpolated onto a 0.5°x0.5°x energy grid in the Pointing frame for square pixels, or HEALPix tessellated grids of NSide matching those of the L1C data products.

The equations for mapping flux are the same as described in 3.5.8, with the modified probability sky map in the denominator.

$$J = \frac{C_{Ultra}(E,\theta,\phi)}{P_{SH}(E,\theta,\phi,t)\epsilon_i(E,\theta,\phi)g_d(\theta,\phi)\ \Delta T\ \Delta E} \tag{31}$$

Figure 17, shows a representative sky map of the survival probabilities at lower energies for hydrogen.

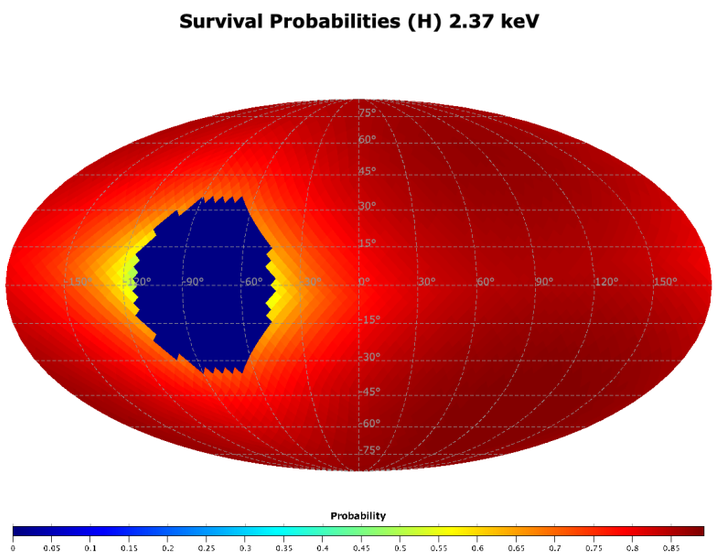


Figure 17. Representative Survival Probabilities at 2.37 keV for Single Pointing; HEALPix Tessellated, Mollweide Projection

3.6.3 Spectral Index Maps

Spectral index maps are to be built assuming a Power law flux of the form:

$$J = AE^{-\gamma} \tag{32}$$

E is the geometric midpoint for each energy channel, J is the intensity of each pixel produced from an L2 or L3 map, A (interpreted as the radiance) is a constant for each pixel across the energy spectra under consideration, and γ is the spectral index under consideration.

By default, the spectral index maps should be fit across the lowest IMAP-Ultra energy bin up to 15 keV in order to compare with IMAP-Hi and another spectral index map should be generated for all energies > 15 keV. These maps should use the L3 survival corrected fluxes and uncertainties discussed in section 3.6.2, but in general the algorithm should apply to any maps available at L2 or above and be customizable over any range of energies.

In order to determine γ and A, we can use a non-linear least squares regression algorithm known as Levenberg-Marguardt (LM). The cost function should be created such that the uncertainties are included as weights in the residual calculation.

Python pseudocode using the mpfit routine recommended by the project (https://github.com/segasai/astrolibpy/tree/master/mpfit) is as follows. This should be done for each pixel.

```
# Generate synthetic data (not proper statistics or energies for what we
# care about but this is just an example for how to use mpfit)
np.random.seed(42)
E = np.linspace(3.5, 15, 8)
true_A = 3.0
true_gamma = 1.7

J = true_A * np.power(E,-true_gamma)  # True Power Law
J_noise = J + 0.02 * np.random.normal(size=E.size)  # Add noise
J_sigma = np.std(J_noise)


# Define a Power law model
def power_law(params, E):
    A, gamma = params
    return A * np.power(E,-gamma)

# Define the residuals function
def residuals(params, data, E, err, fjac=True):
    model = power_law(params, E)
    return [0, (data - model)/err]

# Initial guess for parameters [A, gamma]
initial_guess = [2.5, 1.0]

# setup the fit
args = {'E': E, 'data': J_noise, 'err': J_sigma}

# Perform the Levenberg-Marquardt fit using mpfit
fit_result = mpfit.mpfit(residuals, initial_guess, functkw=args)

# Extract the best-fit parameters
best_params = fit_result.params
best_a, best_gamma = best_params
```

```
# Plot the data and the best-fit model
plt.figure(figsize=(8, 6))
plt.plot(E, J_noise, 'b.', label="Noisy Data")
plt.plot(E, power_law(best_params, E), 'r-', label="Power Law Fit")
plt.xlabel("Energy")
plt.ylabel("Intensity")
plt.legend()
plt.title(f"Single Pixel Power Law Fit: A={best_a:.2f},
Gamma={best_gamma:.2f}")
plt.show()
```

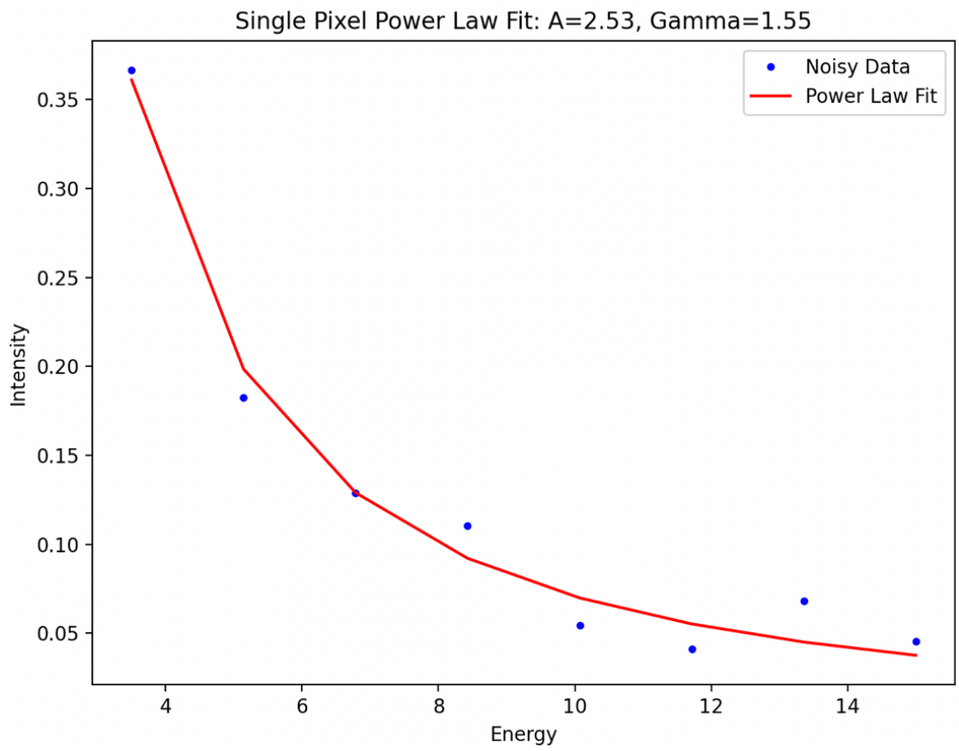


Figure 18. Spectral Index fit for a single Skymap pixel

4.0 References

1. IMAP-Ultra Flight Software Specification
2. IMAP Mapping Instruments Data Processing Plan
3. IMAP ENA and Neutral Backgrounds

5.0 List of Data Products for SDC

5.1 L1A

1. Pulse Height (PH) x TOF Lookup Table
2. Energy x TOF for SSD backplane events Lookup Table
3. Instrument Constants needed for Calculations
4. Instrument MCP Lookup Tables for position and TOF calculations

5.2 L1B Instrument Frame Calibration Products

Instrument Frame products are tabulated in spreadsheets with first two columns of θ_{inst} and ϕ_{inst} and subsequent columns representing the values at each energy (for all but Geometric Function).

1. Geometric Function (cm^2) – Figure 1.
2. Instrument Foil Scattering FWHM Values (degrees) – Figure 6.
    a. Ultra-90
    b. Ultra-45
3. Efficiency Values – Figure 7.
    a. Ultra-90
    b. Ultra-45

5.3 L1C Pointing Frame Calibration Products

Pointing Frame products are provided on HEALPix pixels with NSide 64 (~0.916° mean spacing) in spacecraft origin. SOC will build heliocentric equivalents for relevant items.

1. Geometric Function (cm^2)
    a. Ultra-90
    b. Ultra-45
2. Efficiency Values
    a. Ultra-90
    b. Ultra-45
3. Nominal Single Spin Exposure Time τ_{ij} with mean duty-cycle correction (seconds). Note: intent is for SOC to eventually compute this (see section 3.4.3) using the actual dead-time corrections.
    a. Ultra-90
    b. Ultra-45
4. (new) Nominal FWHM Scattering values
    a. Ultra-90
    b. Ultra-45

6.0 Data Level Description Summary

Table 9. IMAP-Ultra data products by processing level.

Level	Product	Description
L0 (Unprocessed)	CCSDS Packets	Reconstructed, unprocessed instrument data in the form of CCSDS packets, duplicate data are removed.
L1A (Processed from CCSDS packets to CDF)	Housekeeping	Instrument temperatures, voltages and currents, detector rates, readouts of set limits and levels, modes, etc. These are not scientific data, but may be required for some of the downstream data processing algorithms.
	Raw Event Data	Events detected by the instrument, either as 'Raw Events' or 'Onboard Processed Events' as described below (the format will depend on how the DPU reports the data). Each event will be described in enough detail (by the DPU) for subsequent processing.
	Onboard Processed Images	Events binned on board into images in a spin referenced coordinate system.
L1B (Ground Partially Processed)	Culled and Annotated Events	Processed Raw event data filtered for times/areas that are not contaminated by local backgrounds. Annotated/corrected with information required for further processing.
	Badtimes List	List of times with obvious problems such as incorrect spinning/pointing information. This information can likely be corrected downstream and thus recovery of this data for science is likely (similar across all ENA imagers).
	Ultra Extended Spin Table	A project maintained table with definitive spin information such as unique spin ID, spin start time, spin duration, flags associated with good / bad times, event flags from other instruments, etc.
L1C (Pointing Sets)	Ground accumulated counts and exposure time	Ground events binned by estimated energy, direction in the sky (and possibly other quantities, e.g. data quality or PHA qualifications), as well as exposure time on the Pointing set grid
	Ground Accumulated Rate Images	Background subtracted event rates with associated uncertainties derived from ground accumulated images.

	Ground accumulated Sensitivity Factors	Spun instrument sensitivities on the Pointing Grid. These are built from a nominal single spin sensitivity and represent the instrument response over the entire Pointing. The sensitivity includes the Geometric Factor and energy dependent transmission efficiencies
	Ancillary Data Images	Information on the same grid as the rate images that will be used for subsequent processing. Including but not limited to average velocity vector for each pixel (for CG correction)
	Spatiotemporal Culling Masks	Culling Masks for spatiotemporal issues on the Pointing set grids. Ultra-45 will need to cull out Earth's magnetosphere to include on ENAs from the heliosphere (see algorithm description in Ultra algorithm doc)
	Background Estimates	Estimated background rates on the same grids as the accumulated rates; For Ultra this will likely need to be accumulated over multiple Pointings due to anticipation of low particle counts per Pointing
Calibrated L2	Estimated fluxes	Estimated fluxes on a fixed inertial grid
	Estimated fluxes in frame at rest with the Sun	Compton-Getting corrected fluxes
	Ancillary images used in further processing	Accumulation exposure times used, per pixel velocity vectors, etc.
	Corrected Counts and Count Rates Images	Corrected counts and count rates (signal – background) on the fixed inertial grids used to produce the flux maps
	Background and Background Rate Images	Background and background rate images used to create the corrected counts and count rates maps
	Uncertainty Images	Uncertainties in flux, counts, and spatial uncertainty on the fixed inertial grids.
	1 AU flux maps	Fluxes determined from accumulating data over the period of ~6 months at rest with respect to the sun and the spacecraft
Derived L3	Survival Corrected Flux maps	Fluxes estimated at specified distance near termination shock
	Combined Ultra 90 and Ultra 45 Fluxes	Combined fluxes using both Ultra heads
	Spectra in selected directions	In the direction of the nose, sections of the ribbon/belt, the Voyagers, the basins, etc.

7.0 Catalog of Symbols

Quantity	Description	Type	Note
$\boldsymbol{\varepsilon}$	Event ID, unique for each recorded event	64 bit integer	Hash generation or unique ID
$\boldsymbol{t_\varepsilon}$	Event time	Double	Generated from packet time and spin phase in telemetry in IMAP standard time representation (1)
$\vec{\boldsymbol{P}}^{\boldsymbol{f}}$	Event position (Xf,Yf) on front foil	2 element real vector	Position that the particle entered in instrument coordinates [1, p. 31]
$\vec{\boldsymbol{P}}^{\boldsymbol{b}}$	Event position (Xb,Yb) on back foil	2 element real vector	Position that the particle encountered backplane in instrument coordinates [1, p. 33]
$\vec{\boldsymbol{P}}^{\boldsymbol{c}}$	Event position (Xc,Yc) on coincidence	2 element real vector	Position that the particle encountered coincidence in instrument coordinates [1, p. 33]
$\boldsymbol{\tau^{ss}}$	TOF from start to stop	Real	[1, p. 34] TOF
$\boldsymbol{\tau^{sc}}$	TOF from stop to coin	Real	[1, p. 36] eTOF
$\vec{\boldsymbol{v}}^{\boldsymbol{U}}$	Particle velocity in Ultra Frame	3 element real vector	(2). Particle velocity as measured from front to back foil.
Ɛ	Energy determined by SSD/PH	Real	[1, p. 41-45]
$\boldsymbol{\Sigma}$	Species determined from τ^{ss} and Ɛ		[1, p. 41-45]
$\boldsymbol{\epsilon}$	Estimated event efficiency for particles path through the instrument	Real	$\epsilon = \epsilon(\vec{P}^f, \vec{P}^b, E^\Delta, \Sigma)$
$\vec{\boldsymbol{v}}^{\boldsymbol{S}}$	Velocity vector in IMAP Spacecraft/Body Frame	3 element real vector	$\vec{v}^S = \boldsymbol{R_{SU}}\vec{v}^U$
$\vec{v}^\Delta$	Velocity vector in Pointing Frame at rest wrt spacecraft	3 element real vector	$\vec{v}^\Delta = \boldsymbol{R_{\Delta S}}\,(t_\epsilon)\vec{v}^S$
$\vec{\boldsymbol{v}}^{\boldsymbol{D}}$	Velocity vector in Pointing frame at rest wrt heliosphere	3 element real vector	$\vec{v}^D = \vec{V}^D_{IMAP} + \vec{v}^\Delta$
$\boldsymbol{E^\Delta}$	Energy at rest wrt to spacecraft	Real	$E^\Delta = m_\Sigma(\vec{v}^\Delta \cdot \vec{v}^\Delta)/2$

E^D	Energy at rest wrt to heliosphere	Real	$E^D = m_\Sigma(\vec{v}^D \cdot \vec{v}^D)/2$
S	Unique spin number	32 bit int	
T_0	Spin start time	Double	
P	Average spin period	Double	
ρ_{start}	Start pulses rate (/s)	Double	# Start pulses for the spin
ρ_{stop}	Stop pulses rate (/s)	Double	# Stop pulses for the spin
ρ_{coin}	Coincidence rates (/s)	Double	# Coincidences for the spin
ρ_{event}	Rate of processed events (/s)	Double	Total # valid events for the spin telemetered from Ultra
ρ_{reject}	Rate of rejected events (/s)	Double	Total # rejected events based on ground cal for spin; This will include tighter restriction for cal items (e.g. on coincidence logic)
$\mathcal{F}_U$	Spin filter from Ultra engineering / HK data	Bit field	See Bad Times section
$\mathcal{F}_A$	Spin filter derived from IMAP attitude	Bit field	See Bad Times section
$\mathcal{F}_I$	Spin filter derived from other IMAP instruments	Bit fields	See Bad Times section
$\mathcal{F}_P$	Spin filter from event rates beyond threshold	Bit fields	Energy dependent bit field(s) designating if spin should be included based on rate threshold

8.0 Revision History

Date	Author	Notes
November 1, 2022	Nick Dutton	1. Initial Draft level 0 – 2 algorithms
May 30, 2023	Nick Dutton	2. Included more level 0 – 1B algorithms with example code
March 26, 2024	Nick Dutton	3. Revised flow chart definition details 4. Included Ultra-45 spatiotemporal culling algorithm ~~5. more detailed background estimation algorithm~~
May 2, 2024	Nick Dutton	6. New numbering scheme; updated references to sections 7. Added algorithms for Events based culling (L1B) 8. Added new filters and annotated event items (FWHM) 9. Removed notional frame kernel sections (FK and IK)
Oct - Dec, 2024	Nick Dutton	10. Added Level 3 algorithms 11. Update processing diagram 12. Added new sections for new calibration data 13. Added additional ancillary product definitions
Jan, 2025	Nick Dutton	14. Added duty cycle approximation to exposure times
Jun, 2025	Nick Dutton	15. Updated L3 algorithms 16. Added corrected duty cycle adjustment for R-vs-R 17. Expanded deliverables section 18. Added revised info to L2 algorithms for HEALPix and square-pixels

Validation

4.4.4 All-Sky Maps

Mapping data product definitions and processing algorithms are embedded below

Validation

Remember to include the mapping tool here too

4.5 Interstellar Neutrals

Include details from IMAP-Lo here

4.5.1 Validation

4.6 Interplanetary and Interstellar Dust

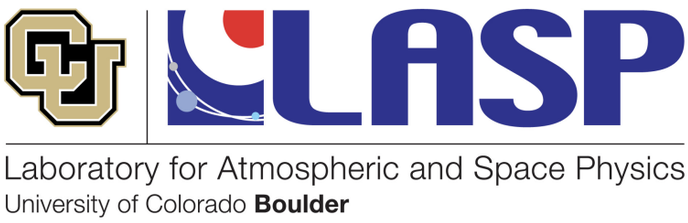
IDEX data product definitions and processing algorithms are embedded below

IDEX Algorithms Document

September 17, 2026

Ethan Ayari
Alex Doner
Jamey Szalay
Scott Knappmiller
Mihály Horányi

This document reflects the current state of the IDEX data processing pipeline. It will be updated, as needed, to capture future changes.





Contents

0 Nomenclature **3**
- 0.1 Acronyms . . . 3
- 0.2 Definitions . . . 4

1 Introduction **5**
- 1.1 Document Purpose . . . 5
- 1.2 Scope . . . 5
- 1.3 Document Organization . . . 5

2 IDEX Instrument Description **6**
- 2.1 Overview . . . 6
- 2.2 Sensor Head . . . 7
- 2.3 Electronics . . . 8

3 IDEX Measurement and Telemetry Structure **9**
- 3.1 Operating Modes . . . 9
  - 3.1.1 Science Mode . . . 10
  - 3.1.2 Transmit Mode . . . 11
- 3.2 Measurement Approach . . . 12
- 3.3 Relationship Between Events, Packets, and Data Products . . . 12
- 3.4 Science Telemetry Packets . . . 13
  - 3.4.1 Science Packet Types . . . 13
  - 3.4.2 Event Time Reconstruction . . . 13
  - 3.4.3 Waveform Fragment Assembly . . . 14
- 3.5 Event-Message Telemetry . . . 14
- 3.6 XTCE Packet Definitions . . . 15

4 Data Processing **16**
- 4.1 Overview . . . 16
- 4.2 Data Processing Structure . . . 18
- 4.3 Dependencies and Ancillary Inputs . . . 18
  - 4.3.1 Product-Window and Metadata Dependencies . . . 18
  - 4.3.2 L0 Dependencies . . . 19
  - 4.3.3 L1A Dependencies . . . 19
  - 4.3.4 L1B Dependencies . . . 19
  - 4.3.5 L2A Dependencies . . . 19
  - 4.3.6 L2B Dependencies . . . 20

4.4 Data Volume Expectancy . . . 20
4.5 CCSDS to Level 0: `idex_l0.py` . . . 21
4.5.1 Packet Decommutation . . . 21
4.5.2 Science and Housekeeping Separation . . . 21
4.6 Level 0 to Level 1A Processing: `idex_l1a.py` . . . 22
4.6.1 Ten-Day Product Assembly . . . 22
4.6.2 L1A Product Types . . . 22
4.6.3 Science Packet Classification and Event Grouping . . . 22
4.6.4 Event Time Reconstruction . . . 23
4.6.5 Trigger Delay and Time-Array Construction . . . 23
4.6.6 Waveform Fragment Assembly and Duplicate Handling . . . 23
4.6.7 Metadata Preservation and AID Correction . . . 24
4.6.8 Incomplete Event Filtering . . . 24
4.6.9 L1A Event Classification and Dust-Hit Detection . . . 24
4.6.10 Event Message Processing . . . 26
4.7 Level 1A to Level 1B Processing: `idex_l1b.py` . . . 27
4.7.1 L1B Science Processing . . . 27
4.7.2 L1B Event-Message Processing . . . 30
4.8 Level 1B to Level 2A Processing: `idex_l2a.py` . . . 31
4.8.1 Calibration Inputs . . . 31
4.8.2 Target and Ion Grid Signal Fits . . . 32
4.8.3 Velocity and Mass Estimates from Target Fits . . . 33
4.8.4 Ion Grid Mass and Velocity Estimation . . . 34
4.8.5 TOF Mass-Scale and Peak-Fit Products . . . 34
4.8.6 Current NaN Placeholder Block . . . 35
4.8.7 Future Work: Combined Target Waveform Fits . . . 36
4.8.8 Future Work: Combined TOF Waveform Fits . . . 36
4.8.9 L2A Output Summary . . . 36
4.9 Level 2A to Level 2B and Level 2C Processing: `idex_l2b.py` . . . 37
4.9.1 Spin-Phase Assignment . . . 37
4.9.2 Rectangular Spatial Mapping and Binned Products . . . 37
4.9.3 Science On-Time and Rate Calculation . . . 38
4.10 Calibration and Maintenance . . . 38
4.11 Data Validation and Testing . . . 39

A LASP Packets **40**

B IDEX Science Packet Definition **41**

Chapter 0

Nomenclature

0.1 Acronyms

- AID: Application Identifier
- APID: Application Process Identifier
- CDF: Common Data Format
- CCSDS: Consultative Committee for Space Data Systems
- CDRL: Contract Data Requirements List
- CSA: Charge-Sensitive Amplifier
- DAB: Decontamination Actuator Board
- DN: Digital Number
- EU: Engineering Unit
- FPGA: Field-Programmable Gate Array
- FSW: Flight Software
- HG: High Gain
- HK: Housekeeping
- HS: High Sample Rate
- IDP: Interplanetary Dust Particle
- IDEX: Interstellar Dust Experiment
- IMAP: Interstellar Mapping and Acceleration Probe
- ISD: Interstellar Dust
- L0: Level 0
- L1A: Level 1A
- L1B: Level 1B
- L2A: Level 2A
- L2B: Level 2B
- L2C: Level 2C
- LG: Low Gain
- LS: Low Sample Rate
- MET: Mission Elapsed Time
- MG: Mid Gain
- MSPS: Mega samples per second
- PUI: Pickup ions
- S/C: Spacecraft
- SDC: Science Data Center
- SDMP: Science Data Management Plan
- SOC: Science Operations Center
- SPICE: Spacecraft, Planet, Instrument, C-matrix, Events
- TOF: Time of Flight
- TTJ2000: Terrestrial Time J2000
- XTCE: XML Telemetric and Command Exchange

0.2 Definitions

Algorithm: A finite sequence of well-defined, computer-implementable instructions used to generate one or more data products from lower-level data, calibration files, and ancillary information.

Ancillary input: A supporting file or data source required by the pipeline but not produced directly from the preceding IDEX data level. Examples include calibration files, XTCE packet definitions, SPICE kernels, spin data, and processing-window tables.

CDF epoch: The time coordinate used in IMAP CDF products. For IDEX event-level products, the epoch represents the reconstructed event or message time and is stored in TTJ2000 nanoseconds.

Code: Computer-executable instructions in a common programming language that may be compiled or interpreted to perform designated computations.

Data level: A processing stage in the IMAP data pipeline. For IDEX, L0 contains packetized telemetry, L1A contains event-level science and message products, L1B contains engineering-unit and geometry-enhanced products, and L2 products contain calibrated or aggregated science quantities.

Engineering unit: A calibrated physical or instrument unit derived from a raw digital number using conversion coefficients or calibration tables.

Event-message product: A timestamped product derived from IDEX housekeeping/event-message telemetry. It contains rendered message strings and selected instrument-state information such as science and pulser state.

FPGA metadata header: The first science packet associated with a dust event. It is defined in the science XTCE file and contains event timing, event number, trigger information, block-count fields, and other metadata used to assemble and interpret waveform packets.

L0 packet file: The Level 0 packetized telemetry file read by the IDEX L1A parser. The L0 file preserves CCSDS packet data before event-level science and message products are assembled.

Pseudocode: Simplified code used to describe algorithm logic without requiring exact implementation syntax.

Science-event product: An event-level product derived from IDEX science telemetry. It contains reconstructed impact-event timing, metadata, waveform arrays, and later calibrated science quantities.

XTCE packet definition: An XML packet-definition file that defines the telemetry field names, bit widths, encodings, enumerated values, aliases, and packet/container structure used during packet decommutation.

Chapter 1

Introduction

1.1 Document Purpose

This document provides a description of the algorithms used to produce science data products from the IMAP Interstellar Dust Experiment (IDEX) instrument measurements. The data products are documented in the IMAP Science Data Management Plan (SDMP). This document includes a description of the data collection and data products, as well as details of the processing flow, algorithms, and data processing tasks.

1.2 Scope

The intended purpose of this information is to enable members of the IMAP Science Data Center (SDC) to implement, test, and validate executable software that will routinely produce designated data products during the science mission. For IMAP, Science Algorithm Documentation consists of the combination of documentation, instructions, specifications, and any available reference/prototype computer code needed to produce a science data product.

1.3 Document Organization

This document is organized to move from instrument context to telemetry structure and finally to the processing algorithms. Chapter 2 provides a high-level description of the IDEX instrument, its measurement concept, and expected performance. Chapter 3 describes how IDEX measurements are collected and represented in telemetry, including the instrument operating modes, science-event packet structure, event-message telemetry, and the relationship between packets and data products. Chapter 4 describes the processing pipeline used to convert IDEX telemetry through the successive data levels, including the major inputs, dependencies, calibration files, and processing steps for each product level. Supporting packet-definition details, software references, and extended metadata tables are provided in the appendices where appropriate.

Chapter 2

IDEX Instrument Description

2.1 Overview

The Interstellar Dust Experiment (IDEX) is a high-resolution impact ionization time-of-flight (TOF) mass spectrometer that provides the elemental composition and mass distributions of ISD and IDP particles. IDEX links the interstellar gas phase composition, as obtained with IMAP-Lo and through PUIs with CoDICE and SWAPI, with the makeup of ISD and IDP particles.

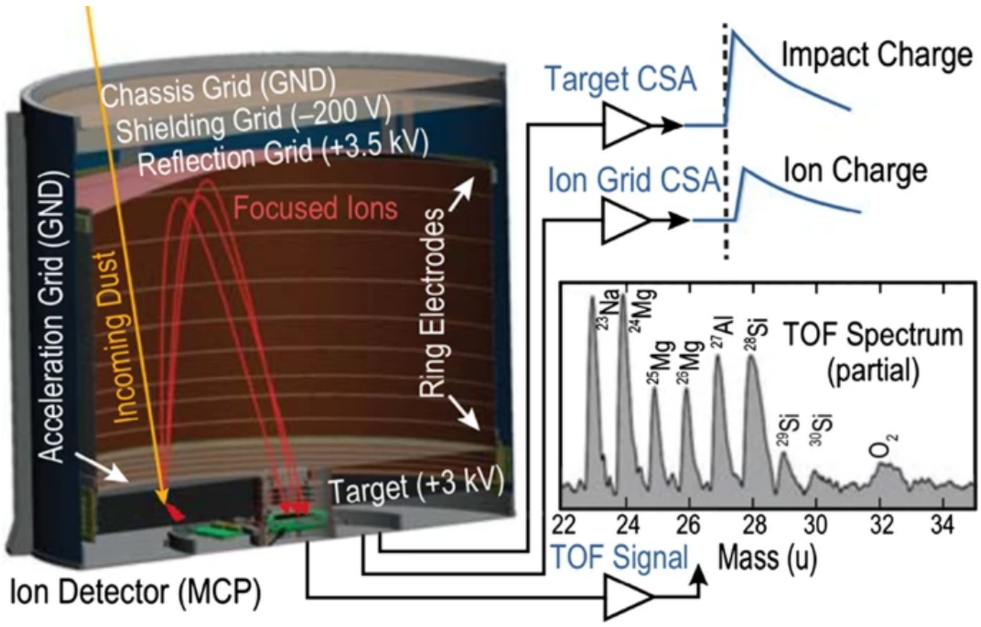


Figure 2.1: An outline of the IDEX instrument and principle of operation. The three types of signals produced (ion grid, target and time-of-flight) are labeled and depicted by their corresponding hardware.

IDEX is based on the heritage of past flight and laboratory instruments. Its operation principle

is based on the impact ionization process.

IDEX has two components, an electronics enclosure and a sensor head with a large effective target area (600 cm^2). The IDEX mechanical design consists of a simple Al shell structure that provides support for the biased electrodes of the TOF ion mass analyzer and the grids over its aperture. The centrally-located ion detector and the front-end charge sensitive amplifier are integrated into the bottom of the instrument.

Individual dust particles entering the instrument pass through a set of grid electrodes and impact the target (Figure 2.1). The target is biased at +2.5 kV to provide positive ion acceleration and the reflectron-type ion optics are used to generate TOF compositional mass spectra. The impact-generated negative charges are collected on the target. An electrostatic field, shaped by a set of biased rings and a curved grid electrode, provides spatial and temporal focusing of the accelerated ions onto the central detector.

Target cleanliness is of high importance to be maintained throughout the fabrication, integration and operation of IDEX. The primary concern is the condensation of volatiles on the target. The mitigate this risk, IDEX has a one-time deployable door and its in-flight operation allows for the regular (once per months) use of heaters to raise the target temperature to 120 C over 8 hours in order to release any possible condensible contaminants.

2.2 Sensor Head

An overview of the sensor head is shown in Figure 2.2.

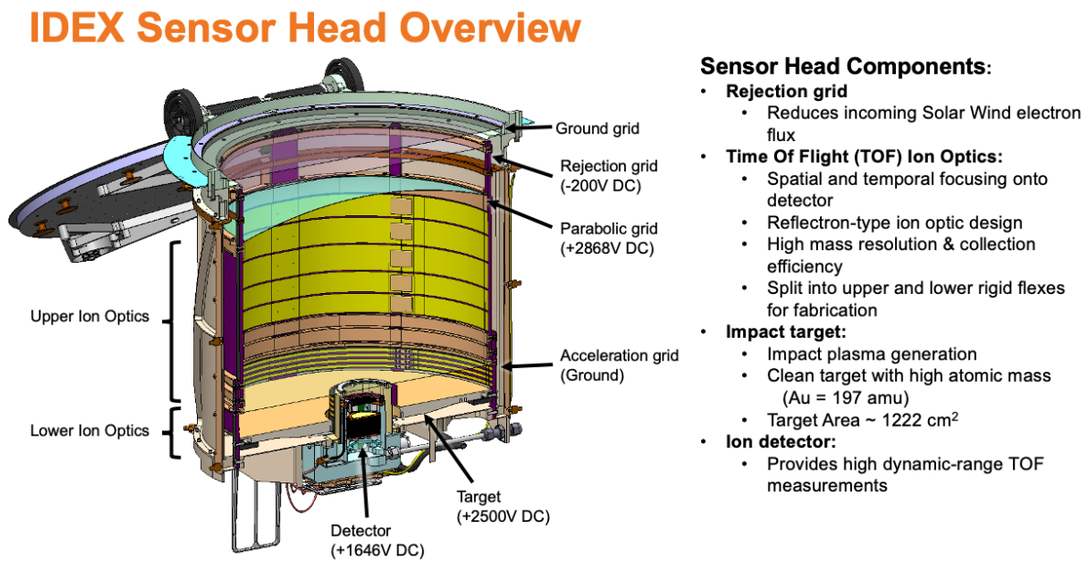


Figure 2.2: An outline of the IDEX instrument sensor head.

2.3 Electronics

The IDEX electronics leverage SUDA flight designs. The Decon/Actuator Board (DAB) is a new design that was added to control the door and decontamination heater. The amplifier boards (CSA, Detector Buffer) were re-designed from the SUDA heritage instrument to meet the IDEX requirements for charge detection ranges. An overview of the IDEX electronics is depicted in Figure 2.3.

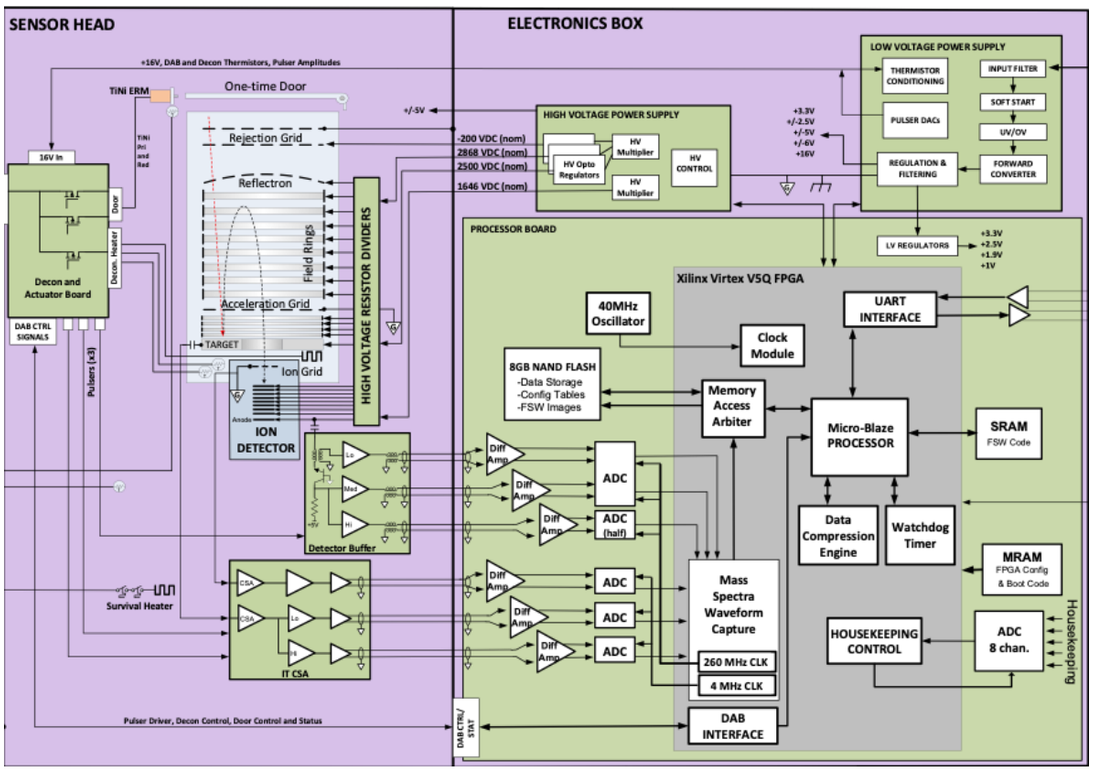


Figure 2.3: An outline of the IDEX instrument electronics system.

The 3 Time-of-Flight (TOF) gain stages, 2 Target CSA and 1 Ion grid CSA waveforms are the signals which the science data products are derived from. These constitute the packetized data accumulated in an 8 GB NAND flash and form the IDEX level 0 data product.

Chapter 3

IDEX Measurement and Telemetry Structure

This chapter describes how an IDEX dust measurement becomes telemetry and how that telemetry is organized before pipeline processing, focusing on the connection between the instrument measurement, science-event packetization, event-message telemetry, and the packet-definition files used by the data pipeline. The detailed L0 through L2 processing algorithms are described in Chapter 4.

The IDEX telemetry description is intentionally limited to the packet structures that affect science-event reconstruction and message interpretation. The full packet definitions are maintained in the IDEX XTCE XML files and should be treated as the authoritative source for field names, bit widths, data encodings, aliases, and enumerated values. This chapter does not reproduce the XML files field-by-field. Instead, it identifies the subset of telemetry fields needed to understand how science events and message products are constructed.

3.1 Operating Modes

IDEX has several instrument operating modes that control when the instrument is powered, waiting for commands, collecting science data, or transmitting stored event data. For the purposes of the science data pipeline, the most important modes are **science mode** and **transmit mode**. Science mode defines how impact events are detected and stored onboard, while transmit mode defines how stored event data are packetized and returned in telemetry.

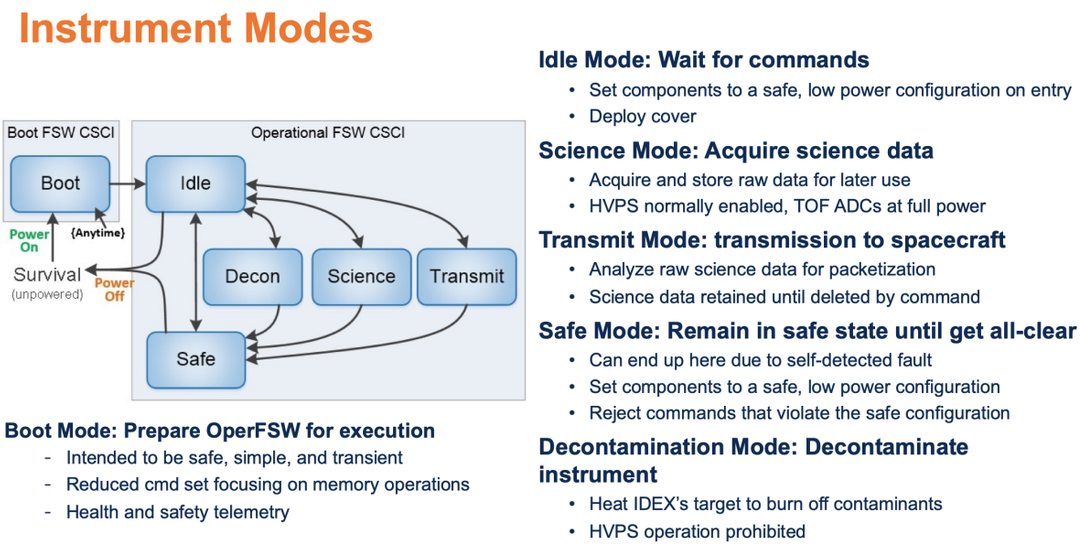


Figure 3.1: Outline of the IDEX instrument operating modes.

When the instrument is powered on, it enters a boot sequence in which flight software performs memory and initialization operations and reports health-and-safety telemetry. After boot, the instrument enters an idle state and waits for commands. From idle, the instrument can transition into the operational modes needed for science collection and telemetry transmission.

3.1.1 Science Mode

In science mode, IDEX continuously samples the charge-sensitive amplifier channels and maintains buffered waveform data for the six science signals. Because IDEX is an event-driven instrument, these buffered data are not treated as science events until an impact-like trigger occurs. When a trigger is detected, the instrument preserves the relevant pre-trigger and post-trigger waveform samples and stores the event data in onboard memory.

The science-event record contains the FPGA metadata header and waveform data from the time-of-flight, ion-grid, and target channels. The time-of-flight channels are sampled at the high-rate cadence, while the target and ion-grid channels are sampled at the low-rate cadence. These two sampling cadences determine the waveform time axes reconstructed later by the L1A pipeline.

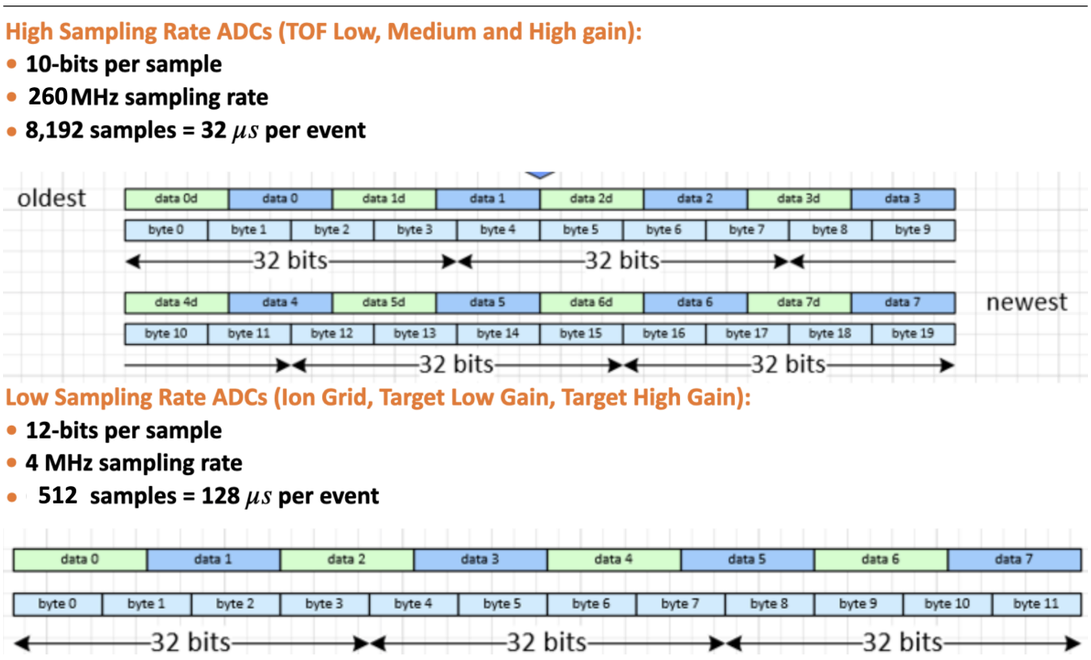


Figure 3.2: Conceptual packing of high-rate and low-rate waveform data for an IDEX science event.

3.1.2 Transmit Mode

After an event has been captured and stored, the instrument can transmit the corresponding event data as CCSDS telemetry packets. The transmitted science telemetry includes a metadata/header packet followed by waveform packet fragments. Those fragments are later associated with the correct event, ordered, decoded, and assembled into the L1A science product.

The trigger does not immediately return the instrument to an identical pre-trigger state. After the required post-trigger sampling is completed, the instrument observes a configured dead-time interval before it can accept another event. The value of this dead time is encoded in the FPGA metadata header and is reconstructed in the L1B pipeline. This interval is important for later rate interpretation because it defines time during which another dust impact may not be recordable by the instrument.

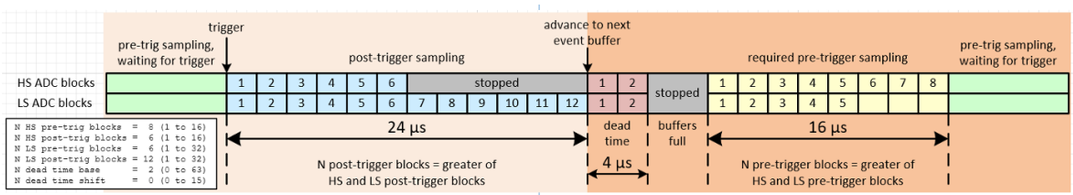


Figure 3.3: Conceptual instrument timeline for high-rate and low-rate ADC data around an event trigger.

Instrument mode transitions are commanded by the spacecraft and are also reflected in event-

message telemetry. These messages provide operational context for the science data, including state changes and pulser activity, and are processed separately from the waveform science events.

3.2 Measurement Approach

IDEX is an event-driven dust impact instrument. During nominal science operation, the instrument monitors charge-sensitive amplifier channels associated with the time-of-flight, target, and ion-grid measurement system. When the instrument detects an impact-like trigger, the flight electronics preserve buffered waveform data surrounding the trigger and package the event into telemetry.

A single dust event is therefore not transmitted as one simple data value. Instead, the event is represented by a science-event metadata header and a set of waveform packet fragments. The metadata header contains the event time, event number, trigger information, block counts, sample-delay information, and other instrument-state fields needed to reconstruct the event. The waveform fragments contain the digitized samples for the six waveform channels:

`TOF_High`, `TOF_Mid`, `TOF_Low`, `Target_High`, `Target_Low`, `Ion_Grid`.

The time-of-flight channels are sampled at the high-rate cadence,

$$\Delta t_{\mathrm{HS}} = \frac{1}{260}\ \mu\mathrm{s} \approx 3.846\ \mathrm{ns}, \tag{3.1}$$

while the target and ion-grid channels are sampled at the low-rate cadence,

$$\Delta t_{\mathrm{LS}} = \frac{1}{4.0625}\ \mu\mathrm{s} \approx 246.15\ \mathrm{ns}. \tag{3.2}$$

These waveform sample times are reconstructed in the L1A pipeline relative to the event trigger time.

3.3 Relationship Between Events, Packets, and Data Products

The telemetry structure separates an impact event into packet-level components, while the science products are organized at the event level. The processing pipeline therefore has to bridge two different views of the same measurement. At the telemetry level, the instrument produces CCSDS packets that are decommutated using the IDEX XTCE packet definitions. At the L1A product level, those packets are reassembled into event-level science and message products.

For science telemetry, the first packet associated with a dust event is the FPGA metadata header. Subsequent science packets contain waveform data fragments. The L1A science product is created by associating these waveform fragments with the correct metadata header, decoding or decompressing the waveform bits, and constructing one event-level record per dust impact. Each L1A science record contains the event time, instrument metadata, six waveform arrays, and corresponding high- and low-rate time arrays.

In parallel, IDEX event-message telemetry provides timestamped instrument log entries. These messages are not waveform science events, but they provide operational context such as state changes, pulser activity, command responses, and other instrument events. The L1A message product stores the message epoch, selected raw timing fields, and a rendered message string. The L1B message product further reduces those messages into state-change variables used for later processing.

3.4 Science Telemetry Packets

The IDEX science packet definition is contained in the science XTCE XML file. This file defines the packet fields used to decommutate science telemetry, including CCSDS header fields, packet creation time fields, science packet routing fields, FPGA metadata-header fields, waveform payload fields, synchronization fields, and CRC fields.

The packet creation time is encoded in the CCSDS secondary header using the coarse and fine time fields:

$$\texttt{SHCOARSE}, \qquad \texttt{SHFINE}.$$

These fields describe when the packet was generated. They are distinct from the dust-impact event time, which is reconstructed from the FPGA metadata header.

3.4.1 Science Packet Types

Science packets are routed using the `IDX__SCI0TYPE` field. In the current L1A implementation, this field identifies whether the packet is the FPGA metadata header or one of the waveform packet types. The science packet type values used by the pipeline are summarized in Table 3.1.

Table 3.1: Science packet types used during L1A event assembly.

Value	Pipeline label	Role
0x01	FIRST_PACKET	FPGA metadata header
0x02	TOF_HIGH	TOF high-gain waveform data
0x04	TOF_LOW	TOF low-gain waveform data
0x08	TOF_MID	TOF mid-gain waveform data
0x10	TARGET_LOW	Target low-gain waveform data
0x20	TARGET_HIGH	Target high-gain waveform data
0x40	ION_GRID	Ion-grid waveform data

The FPGA metadata header is therefore part of the science telemetry, not the housekeeping telemetry. In the science XTCE file, the corresponding metadata-header fields appear with the `IDX__TXHDR` prefix. These fields include the event trigger time, trigger identifier, event number, block-count information, trigger-control words, sample-delay information, instrument state, and related metadata used to interpret the waveform fragments.

3.4.2 Event Time Reconstruction

The dust-impact event time is reconstructed from FPGA metadata-header fields that represent the trigger event time, which is distinctly different from the packet creation time. The seconds counter is split across two 16-bit fields:

$$t_{\mathrm{sec}} = 2^{16}\,\texttt{IDX__TXHDRTIMESEC1} + \texttt{IDX__TXHDRTIMESEC2}. \tag{3.3}$$

The subsecond field is stored in units of 20 μs:

$$t_{\mathrm{sub}} = 20 \times 10^{-6}\,\texttt{IDX__TXHDRTIMESUBS}. \tag{3.4}$$

The event time used by the product is then

$$t_{\text{event}} = t_{\text{sec}} + t_{\text{sub}}. \tag{3.5}$$

During L1A processing, this event time is converted into the CDF `epoch` coordinate, expressed as TTJ2000 nanoseconds. UTC is a human-readable representation that can be derived from this epoch value, but UTC is not the native time basis stored in the L1A science product.

3.4.3 Waveform Fragment Assembly

The waveform packets following the FPGA metadata header are associated with the correct event using the event number and the active event header. Within each waveform type, packet fragments are ordered using the fragment-offset information. The payload bits are then assembled into complete waveform bit strings before decoding.

The L1A processing path handles duplicate or retransmitted fragments defensively. Exact duplicate science fragments are ignored. If a longer retransmitted fragment replaces a shorter copy, the longer copy is retained. If two fragments conflict in a way that cannot be resolved, the affected event may be skipped rather than producing an inconsistent waveform product. This behavior allows the pipeline to preserve complete, internally consistent events while rejecting events whose packet fragments cannot be reliably assembled.

Some science waveform payloads may be compressed. In that case, the waveform bit stream is decompressed before being converted into waveform samples. After decoding, high-rate waveform channels are assigned to the `time_high_sample_rate` coordinate, and low-rate waveform channels are assigned to the `time_low_sample_rate` coordinate.

3.5 Event-Message Telemetry

In addition to science waveform telemetry, IDEX produces event-message telemetry contained in the event-message packet. These messages are separate from dust-event waveform packets. They provide timestamped log information used to identify instrument state changes, pulser activity, command responses, and other operational events relevant to interpreting the science data.

The event-message time is reconstructed from the event-message fields:

$$t_{\text{msg}} = \texttt{ELSEC_EVTPKT} + 20 \times 10^{-6}\,\texttt{ELSSEC_EVTPKT}. \tag{3.6}$$

The message type is identified by

$$\texttt{ELID_EVTPKT},$$

and the four event-message parameter bytes are

$$\texttt{EL1PAR_EVTPKT}, \quad \texttt{EL2PAR_EVTPKT}, \quad \texttt{EL3PAR_EVTPKT}, \quad \texttt{EL4PAR_EVTPKT}.$$

The L1A message pipeline combines these fields with message-rendering dictionaries to create a human-readable message string. If a template or dictionary lookup is unavailable, the raw event identifier and parameter bytes can still be preserved in the output message text.

The L1A message product is a timestamped message-log product. The L1B message product reduces selected message strings into state variables such as `science_on` and `pulser_on`. This keeps operational state information available to downstream processing without treating the event-message packets as waveform science events.

3.6 XTCE Packet Definitions

The IDEX packet definitions are maintained in XTCE XML files. These files are the authoritative source for the raw telemetry layout. The science XML file defines the science packet structure, including the FPGA metadata header and waveform packet payloads. The housekeeping XML file defines housekeeping and event-message telemetry, including the event-message timestamp, event identifier, and parameter-byte fields.

Table 3.2 lists representative fields used by the pipeline. The table is intentionally limited to fields that help explain the measurement-to-product relationship. The complete field list, bit sizes, encodings, aliases, and enumerated values remain in the XTCE XML files.

Table 3.2: Representative XTCE-defined fields used by the IDEX pipeline.

Field	Defined in	Pipeline role
SHCOARSE	Science XML	Packet creation coarse time
SHFINE	Science XML	Packet creation fine time
IDX__SCI0TYPE	Science XML	Identifies header or waveform packet type
IDX__SCI0FRAGOFF	Science XML	Orders waveform fragments during event assembly
IDX__SCI0RAW	Science XML	Raw waveform payload for non-header science packets
IDX__TXHDRTIMESEC1/2	Science XML	Reconstructs event trigger seconds from FPGA metadata
IDX__TXHDRTIMESUBS	Science XML	Provides 20 μs event-time resolution
IDX__TXHDRTRIGID	Science XML	Identifies trigger-origin information
IDX__TXHDRBLOCKS	Science XML	Provides waveform block-count information
IDX__TXHDRSAMPDELAY	Science XML	Provides sample-delay information for waveform timing
ELSEC_EVTPKT	Housekeeping XML	Event-message coarse time
ELSSEC_EVTPKT	Housekeeping XML	Event-message fine time
ELID_EVTPKT	Housekeeping XML	Identifies event-message type
EL1PAR_EVTPKT–EL4PAR_EVTPKT	Housekeeping XML	Parameter bytes used for message rendering

This document avoids reproducing the full XML tables because doing so would duplicate information already maintained by the packet-definition files. If a packet field changes, the XML definition is the source that must be updated; this chapter should only need revision if the measurement concept or pipeline use of the packet fields changes.

Chapter 4

Data Processing

This chapter describes the necessary steps to convert data between each of the levels described in the processing flowchart.

4.1 Overview

The IDEX data processing pipeline converts raw packet telemetry into progressively higher-level science products. The pipeline begins with CCSDS packet files and the IDEX XTCE packet definitions described in Chapter 3.6. These XTCE files define the packet structure used during decommutation, while later processing stages apply calibration constants, ancillary calibration curves, spacecraft pointing information, spin-phase data, and ephemeris products to produce event-level science data. Figure **??** summarizes the overall flow of input products, intermediate data levels, and output products.

At a high level, the pipeline follows the standard IMAP processing structure. Raw packet files are first decommutated into decoded packet-level telemetry at L0. The L1A stage assembles packet fragments into event-level waveform and message products. The L1A science product algorithmically distinguishes science events, noise captures, and pulser-like events, identifies dust-like TOF waveform patterns, and records saturation in each waveform channel. The L1B science product propagates these flags for use by downstream processing, then converts selected quantities into engineering units, adds trigger and dead-time information, and attaches SPICE-derived event context. The L2A stage applies instrument calibration and waveform-fitting routines to estimate dust impact quantities such as charge, velocity, mass, and preliminary time-of-flight mass-spectrum products. Higher-level L2B and L2C products then aggregate individual impact events into rate products and mapped science products.

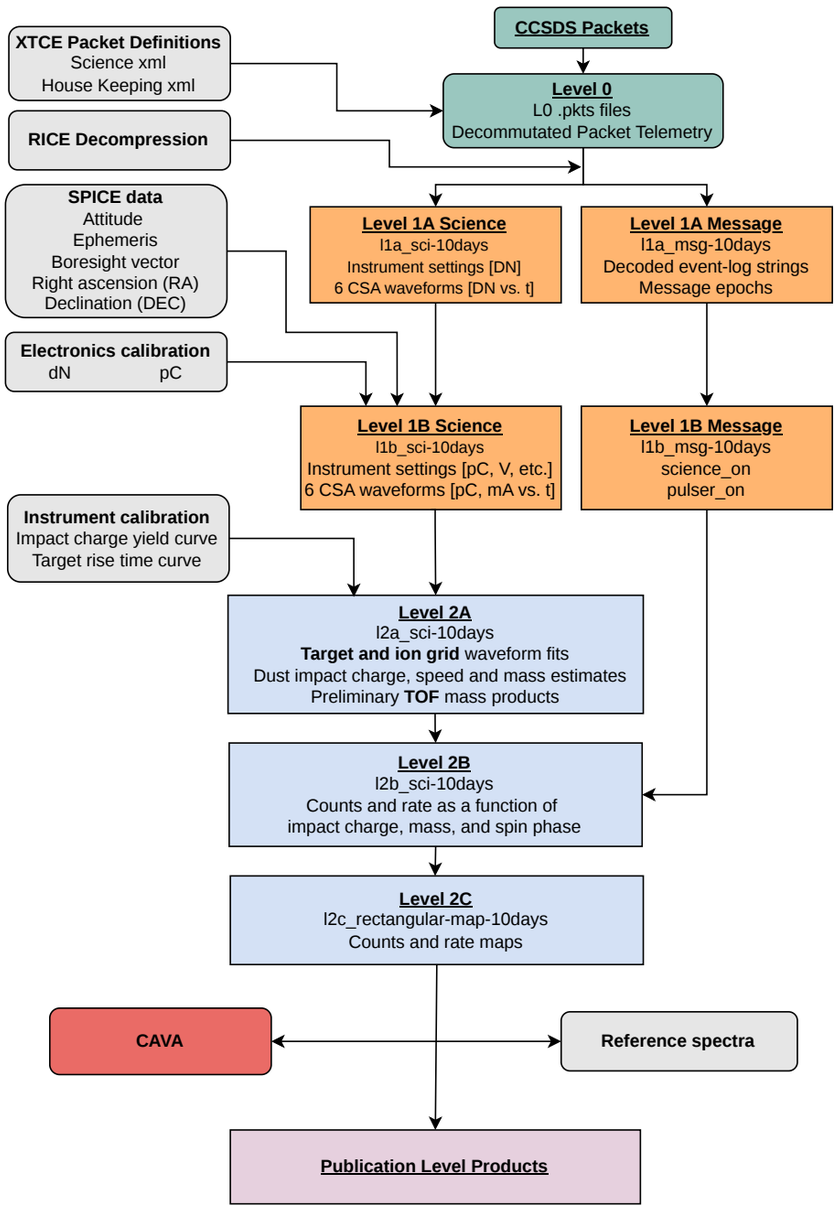


Figure 4.1: The IDEX science data pipeline processing flowchart. Level 1 data products are given in orange, level 2 data products in light blue, and the necessary auxiliary inputs in grey along the sides.

4.2 Data Processing Structure

The IDEX pipeline is implemented as a sequence of Python processing modules, with each module ingesting one data level and producing the next. The principal processing scripts are:

- `idex_l0.py`, which decommutates raw packet files using the IDEX XTCE definitions;
- `idex_l1a.py`, which assembles L0 packet data into event-level science, message, and catalog-list products;
- `idex_l1b.py`, which converts L1A products into engineering-unit science and state products;
- `idex_l2a.py`, which applies calibration and waveform-fitting routines to generate event-level dust-impact quantities;
- `idex_l2b.py`, which produces higher-level rate and map products.

Each processing stage has a defined input and output product. In general, the input to a stage is the output of the preceding stage, along with any required ancillary data. These ancillary inputs include XTCE packet definitions for decommutation, calibration files for waveform interpretation, and spacecraft geometry products such as SPICE kernels, spin-phase information, and ephemeris data. The output of each stage is written as an IMAP-compliant data product with associated metadata and CDF attributes.

The pipeline is Python-based and is designed to run within the IMAP Science Data Center processing environment rather than relying on mission-specific manual processing steps.

The pipeline is supported by automated test scripts corresponding to the processing modules, such as `test_idex_l1a.py`, `test_idex_l1b.py`, and `test_idex_l2a.py`. These tests check expected outputs, edge cases, CDF creation, calibration behavior, and known validation data. The project-level testing requirement is to maintain at least 90% automated test coverage so that changes to parsing, calibration, metadata, or science-product generation are exercised before release.

4.3 Dependencies and Ancillary Inputs

Each IDEX processing level depends on the data product from the preceding level and, where needed, a small set of packet-definition, calibration, geometry, or configuration files. The primary dependencies are summarized below by the first processing level where they are required.

4.3.1 Product-Window and Metadata Dependencies

- **IDEX 10-day processing-window table:** `idex_10_day_CDF_names.csv`. This table defines the start and end dates for IDEX 10-day products and is used to assign product windows and name output files.
- **CDF metadata and attribute definitions:** IMAP CDF attribute files for IDEX. These metadata definitions provide product-level and variable-level attributes used when writing IMAP-compliant CDF products.

4.3.2 L0 Dependencies

- **XTCE science packet definition:** `idex_science_packet_definition.xml`. This file defines the science packet structure used during decommutation, including the science packet type field, waveform payload fields, and FPGA metadata-header fields.
- **XTCE housekeeping/event-message packet definition:** `idex_housekeeping_packet_definition.xml`. This file defines the housekeeping and event-message packet structure, including event-message timing, event identifiers, and parameter-byte fields.

4.3.3 L1A Dependencies

- **Event-message rendering dictionary:** `idex_evt_msg_parsing_dictionaries.json`. This file provides the lookup and formatting information used to convert event-message identifiers and parameter bytes into readable message strings.

4.3.4 L1B Dependencies

- **Engineering-unit conversion and variable-unpacking table:** `idex_variable_unpacking_and_eu_conversion.csv`. This table defines the bit masks, shifts, and conversion coefficients used to unpack selected instrument settings and convert raw digital numbers into engineering units.
- **SPICE kernels:** mission SPICE kernels. These are used to obtain spacecraft position, velocity, pointing, and coordinate-frame information at the event epoch.
- **Spin data:** mission spin table/product. This input is used to determine the spacecraft spin phase at the event epoch.
- **Ephemeris and attitude data:** mission geometry products, accessed through the SPICE and pointing utilities. These provide the spacecraft state and pointing context attached to the L1B science product.

4.3.5 L2A Dependencies

- **L2A rise-time calibration curve:** `imap_idex_l2a-calibration-curve-t-rise_20250101_v002.csv`. This file provides the calibration coefficients used to relate fitted target rise time to dust-impact speed.
- **L2A charge-yield calibration curve:** `imap_idex_l2a-calibration-curve-yield-params_20250101_v001.csv`. This file provides the charge-yield calibration coefficients used with the impact charge and speed estimate to calculate dust mass.
- **Atomic mass table:** `atomic_masses.csv`. This table provides the reference ion or elemental masses used when constructing the preliminary time-of-flight mass scale.

4.3.6 L2B Dependencies

- **L2A science product:** one L2A science CDF spanning the IDEX 10-day processing window. The L2B code uses the event-level `dust_hit_flag`, event geometry, spin phase, and fitted charge and mass estimates when calculating the count products. The currently published agnostic count and rate products use the dust-hit flag and event context; the charge- and mass-binned products remain withheld.
- **L1B event-message product:** one L1B message CDF with the `msg-10days` descriptor for the same processing window. The `science_on` transition records are used to calculate the science-acquisition on-time that normalizes the L2B rates. The message rows with unknown state values are ignored.
- **L2B metadata definitions and fixed bin definitions:** IDEX CDF attributes provide the L2B variable and global metadata. The L2B implementation defines the spin-phase, impact-charge, and dust-mass bin edges internally and does not require an additional calibration file or external geometry product.

4.4 Data Volume Expectancy

The estimates for the expected IDEX instrument science data volume are derived from simulations of known IDP and ISD populations. Figure 4.2 depicts counts for ISD (red/blue) and IDP (black) particles expected to be measured by IDEX during the mission.

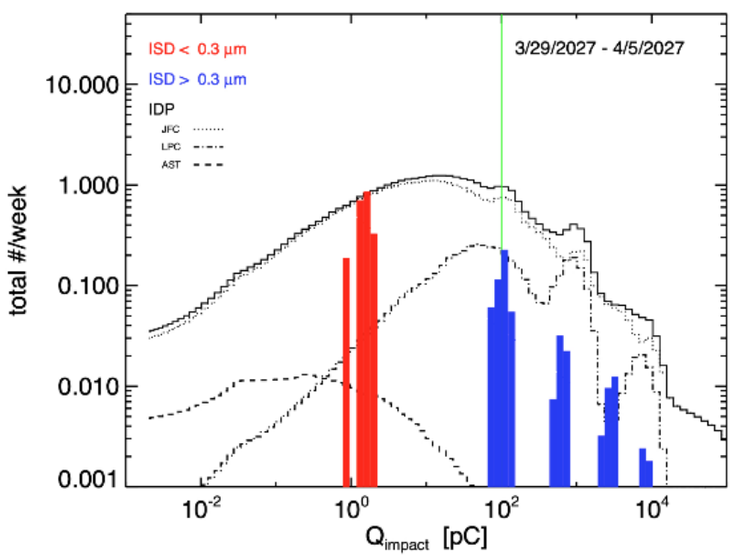


Figure 4.2: Expectations for IDEX's ISD and IDP measurements during the mission.

From this simulation, IDEX is expected to measure 16 events per day on average. Using these estimates in conjunction with the bitmap in Figure **??**, we can estimate the weekly data volume

expectancy for IDEX during the mission. This has been carried out for each of the science data product levels, as depicted in Table 4.1.

PRODUCT	PRODUCT STANDARD	DESCRIPTION
LEVEL 0	Packet	288 Kilobits per event * 16 Events per day * 7 events per week = **40,852 Kilobits per week**
LEVEL 1A	Raw	40 voltages, currents and temperatures tracked in DN (40*12 = 1,280 bits), 264,192 bits for all 6 signals, so 265,472 per event * 7 * 16 = **29,733 Kilobits per week**
LEVEL 1B	Raw	Conversion to Voltage does not introduce new volume, **29,733 Kilobits per week**
LEVEL 1C	Reduced	2 double words for each charge + 81,920 bits for TOF spectra = 81,984 bits per event * 7 * 16 = **9,183 Kilobits per week**
LEVEL 2	Calibrated	1 Voltage array + 1 double word for mass + up to 12 double words for mass index = 82,336 bits per event * 7 * 16 = **9,222 Kilobits per week**
LEVEL 3	Derived	Up to 12 mass lines and their relative abundances = 24 double words = 768 bits per event * 7 * 16 = **87 Kilobits per week**
CALIBRATION	Ancillary	Library of laboratory mass spectra of candidate minerals, SPICE kernels for spacecraft state vector and attitude

Table 4.1: Expectations for IDEX's weekly data volume throughout the mission, organized by data product level.

4.5 CCSDS to Level 0: `idex_l0.py`

4.5.1 Packet Decommutation

The `idex_l0.py` module performs the first software step after receipt of CCSDS packet files. It decommutes the packet stream using the IMAP processing packet utilities and appropriate XTCE packet definitions, then returns the decoded packet contents to downstream processing.

The function `decom_packets()` defines separate XTCE files for science packets and housekeeping packets:

- `idex_science_packet_definition.xml`
- `idex_housekeeping_packet_definition.xml`

Science packets are decoded with `packet_generator()`, while housekeeping packets are decoded with `packet_file_to_datasets()`.

4.5.2 Science and Housekeeping Separation

The science and housekeeping packet streams are handled separately because the standard dataset conversion does not work for IDEX science packets due to branching logic in the science XML definition. Therefore, `idex_l0.py` returns three objects:

1. a list of decommutated science packets,
2. a dictionary of raw housekeeping datasets indexed by APID,
3. a dictionary of derived housekeeping datasets indexed by APID.

At this stage, the code does not construct science events, decode waveform arrays, apply timing corrections, or create final L1A products. It only converts packet bytes into named telemetry fields.

Output

At the L0 stage, packet files may contain multiple IDEX packet types, including both science and housekeeping packets. These packets remain stored together as packet-level `.pkts` files organized by data time range; e.g. `imap_idex_l0_raw_20260101_v001.pkts`. The separation between science, event-message and housekeeping content occurs during decommutation and later L1A processing through APID selection and the appropriate XTCE packet definitions, rather than through separate L0 files for each content type.

4.6 Level 0 to Level 1A Processing: `idex_l1a.py`

4.6.1 Ten-Day Product Assembly

The `idex_l1a.py` module processes one or more L0 packet files into L1A `xarray.Dataset` products. The top-level function `idex_l1a()` sorts the input packet files, parses each file with `PacketParser`, groups datasets by product type, concatenates files across the requested 10-day window, sorts by epoch, removes duplicate epochs, and keeps the latest file version when duplicates are present.

The resulting products are filtered to the requested 10-day interval using TTJ2000 nanosecond epoch values.

4.6.2 L1A Product Types

The `PacketParser` class produces two possible products from the decommutated L0 data:

- `l1a_sci-10days`: processed science waveform events,
- `l1a_msg-10days`: rendered event-message log entries,

Only event messages are produced at L1A from the raw housekeeping dataset.

4.6.3 Science Packet Classification and Event Grouping

Science packets are grouped into dust events using the `SCI0TYPE` field. The implemented science type map is:

1=First/Header Packet, **2**=TOF High, **4**=TOF Low, **8**=TOF Mid, **16**=Target Low, **32**=Target High, **64**=Ion Grid

A first packet creates a new `RawDustEvent`. Subsequent waveform packets are associated with that active event using the event number. The stable event key is built from the transmit timestamp fields and event number, rather than from the event number alone. If waveform packets arrive before their header packet, the code raises an error because event context is missing.

4.6.4 Event Time Reconstruction

For science events, the event epoch is reconstructed from the FPGA header timestamp. The 32-bit coarse seconds counter is split across two 16-bit fields:

$$t_{\text{coarse}} = (\texttt{IDX__TXHDRTIMESEC1} \ll 16) + \texttt{IDX__TXHDRTIMESEC2}. \tag{4.1}$$

The fine time is stored in 20-µs units:

$$t_{\text{fine}} = 20 \times 10^{-6} \texttt{IDX__TXHDRTIMESUBS}. \tag{4.2}$$

The reconstructed mission elapsed time is therefore

$$t_{\text{MET}} = 2^{16} \texttt{IDX__TXHDRTIMESEC1} + \texttt{IDX__TXHDRTIMESEC2} + 20 \times 10^{-6} \texttt{IDX__TXHDRTIMESUBS}. \tag{4.3}$$

The code converts this MET value to TTJ2000 nanoseconds using `met_to_ttj2000ns()`.

4.6.5 Trigger Delay and Time-Array Construction

The L1A code reconstructs relative waveform time axes using the pre-trigger block fields and the selected TOF sample delay. The high-rate and low-rate sample spacings are defined as

$$\Delta t_{\text{HS}} = \frac{1}{260}\ \mu\text{s}, \qquad \Delta t_{\text{LS}} = \frac{1}{4.0625}\ \mu\text{s}. \tag{4.4}$$

Each high-rate block contains 512 samples, while each low-rate block contains 8 samples. The code extracts pre-trigger block counts from `IDX__TXHDRBLOCKS`, applies the offset-by-one convention, and computes:

$$t_{\text{LS,trig}} = \Delta t_{\text{LS}} \left(N_{\text{pre,LS}} + 1\right) 8, \tag{4.5}$$

$$t_{\text{HS,trig}} = \Delta t_{\text{HS}} \left(N_{\text{pre,HS}} + 1\right) 512 - \Delta t_{\text{HS}} \left(N_{\text{delay}} - 1\right). \tag{4.6}$$

The delay value is selected from `IDX__TXHDRSAMPDELAY`. This field contains separate 10-bit delay values for high-gain, mid-gain, and low-gain TOF channels. The active delay is selected using bits in `IDX__TXHDRTRIGID`.

Trigger-Delay Selection Priority

The lower ten bits of `IDX__TXHDRTRIGID` determine which TOF delay is used. If multiple TOF trigger bits are set, the code selects the High-gain delay first (bit 0), the Low-gain delay second (bit 1), and the Mid-gain delay third (bit 2). If none of these bits is set, the High-gain delay is used by default.

The final time arrays are constructed as

$$t_{\text{LS}}[i] = i\Delta t_{\text{LS}} - t_{\text{LS,trig}}, \tag{4.7}$$

$$t_{\text{HS}}[i] = i\Delta t_{\text{HS}} - t_{\text{HS,trig}}. \tag{4.8}$$

4.6.6 Waveform Fragment Assembly and Duplicate Handling

Each science waveform channel is packetized into fragments. The L1A code stores fragments by science type and fragment offset before assembling complete waveform bit strings. Exact duplicate fragments are ignored. If two fragments occupy the same science type and offset but have different lengths, the longer fragment is preferred. If two same-length fragments disagree, the event is marked as conflicting and skipped.

After fragment assembly, each waveform bit string is converted into integer samples.

Waveform Decoding

The six science waveform products are decoded into integer sample arrays:

- `TOF_High`,
- `TOF_Low`,
- `TOF_Mid`,
- `Target_High`,
- `Target_Low`,
- `Ion_Grid`.

High-rate TOF waveforms are interpreted as 32-bit words containing 2 padding bits followed by three 10-bit samples. The final four high-rate samples are removed for uncompressed data.

Low-rate target and ion-grid waveforms are interpreted as 32-bit words containing 8 padding bits followed by two 12-bit samples.

If the event is marked as compressed, the waveform is decoded with Rice-Golomb decompression instead of direct bit slicing.

4.6.7 Metadata Preservation and AID Correction

The L1A science dataset preserves the header telemetry fields as event metadata variables. One field is intentionally replaced: `SCI0AID` is skipped because it is not updated properly by the flight software. Instead, `TXHDRFSWAIDCOPY` is renamed to `aid` and used as the acquisition identifier in the output dataset.

4.6.8 Incomplete Event Filtering

After waveform decoding, the code checks whether each waveform has the expected length for its corresponding time coordinate. If any waveform length does not match the expected shape, the event is treated as incomplete, a warning is logged, and that event is skipped. This allows the CDF product to be created from complete events while excluding events with missing packets.

4.6.9 L1A Event Classification and Dust-Hit Detection

The L1A science classifier assigns mutually exclusive event-type flags: `noise_capture`, `pulser`, `science_event`.

The primary trigger-source field is `idx__txhdrtrigid`. Its lower 10-bit trigger-origin field contains six defined origin bits: TOF High, TOF Low, TOF Mid, Target High/low range, software trigger, and external trigger. The classifier uses bits 0–3 to identify trigger-origin channels and bits 4–5 to identify software or external triggering. The TOF channel mode fields `idx__txhdrhgtrigmode`, `idx__txhdrmgtrigmode`, and `idx__txhdrlgtrigmode` also mark their corresponding TOF gain channels active when nonzero. Thus, the active-channel set is formed from both the trigger-ID bits and the nonzero TOF trigger modes.

The trigger-level control fields are `idx__txhdrhgtrigctrl1`, `idx__txhdrmgtrigctrl1`, and `idx__txhdrlgtrigctrl1` for the three TOF gains. The classifier specifically extracts the High-gain trigger level from `idx__txhdrhgtrigctrl1` by shifting right by 22 bits and masking to its 10-bit value; this value is used for the pulser test.

Noise Capture

An event is classified as a noise capture when no trigger channels are active, or when the trigger source is software or external and the only active channel is TOF High. The active-channel and trigger-source conditions are determined from `idx__txhdrtrigid` and the nonzero TOF trigger-mode fields described above. In these cases, `noise_capture_flag`=1 and the other mutually exclusive event-type flags are zero.

Pulser

An event is classified as a pulser event when TOF High is the only active channel, `idx__txhdrhgtrigmode`=1, and the extracted High-gain trigger level is 1000 DN. In this case, `pulser_flag`=1. Pulser classification is evaluated after the noise-capture condition, so an event meeting the software or external single-High condition is classified as noise capture instead.

Science Event

An event is classified as a science event when it does not satisfy either the noise-capture or pulser conditions. In this case, `science_event_flag`=1. The `dust_hit_flag` is evaluated only for events classified as science events.

Dust-Hit Detection Criteria

If an event is classified as a science event, it is then checked by the dust-hit classifier to determine if the event a dust impact or noise trigger.

The dust-hit classifier searches the High-, Mid-, and Low-gain TOF waveforms independently. Let $x_i = x(t_i)$ be a waveform in DN, and let t_0 be its first valid sample time. For normal processing, the baseline is

$$B = \text{median}\{x_i : t_i < t_0 + 3\ \mu\text{s}\}, \tag{4.9}$$

and the robust noise width is

$$\sigma = 1.4826\ \text{median}\{|x_i - B| : t_i < t_0 + 3\ \mu\text{s}\}. \tag{4.10}$$

If this robust estimate is not positive, the standard deviation of the baseline samples is used instead. Candidate peaks are found with a minimum separation of 30 ns. The three dust-hit criteria are:

1. **Peak count and significance.** A qualifying peak i must have baseline-corrected height

   $$H_i = x(t_i) - B \geq 7\sigma \tag{4.11}$$

   and prominence

   $$P_i = H_i - \max(H_{L,i}, H_{R,i}) \geq 5\sigma, \tag{4.12}$$

   where $H_{L,i}$ and $H_{R,i}$ are the baseline-corrected values at the left and right prominence bases identified by the peak-finding algorithm. The normal rule requires at least two qualifying peaks in one gain channel.

2. **Peak width.** For each qualifying peak, define the half-height as $H_i/2$. Linear interpolation gives the times $t_{i,-}$ and $t_{i,+}$ where the waveform crosses this level on the rising and falling sides. The measured full width at half maximum is

   $$W_i = t_{i,+} - t_{i,-}. \tag{4.13}$$

   Each of the two qualifying peaks must have $W_i \geq 20$ ns.

3. **Saturation-aware width substitution.** TOF saturation is flagged when a sample reaches $0.95D_{\max}$, where $D_{\max} = 1023$ DN for the 10-bit TOF channels. If a qualifying peak is saturated, its width may be replaced by the width of the nearest qualifying peak in a lower-gain channel within 50 ns, provided that replacement peak is not saturated. High-gain peaks fall through to Mid and then Low gain, while Mid-gain peaks fall through to Low gain. Contiguous saturated regions are counted as one candidate peak.

In addition to the two-peak rule, exactly one qualifying High-gain peak is accepted when its direct, non-substituted FWHM is at least 50 ns. A gain channel is treated as having a signal-contaminated initial baseline when the median over its initial 3 μs differs from the channel's reference baseline by more than 20 DN. The affected gain is then reprocessed with reference baselines of 511 DN, 513 DN, and 514 DN for High, Mid, and Low gain, respectively, and reference noise widths of 2.9652 DN, 1.4826 DN, and 2.9652 DN. A high measured-noise estimate by itself does not invoke this fallback. The truncated-waveform fallback requires two qualifying peaks with $W_i \geq 20$ ns. Peaks are counted within each source gain, while a saturated peak width may still be supplied by a temporally matched lower-gain peak according to the saturation-aware substitution rule above.

Saturation Flags

The classifier also writes saturation flags for TOF High, TOF Mid, TOF Low, Target High, Target Low, and Ion Grid. The TOF flags use a 10-bit maximum of 1023 DN, while the low-rate channels use a 12-bit maximum of 4095 DN; in both cases the flag is set if any part of the waveform reaches 95% of the applicable maximum.

4.6.10 Event Message Processing

Event message packets are decoded from the housekeeping packet stream and converted into readable message strings. In the L1A processing code, event messages are only produced from the raw housekeeping event-message APID.

The event-message epoch is reconstructed from the event-message packet timing fields:

$$t_{\mathrm{MET}} = \texttt{elsec_evtpkt} + 20 \times 10^{-6}\texttt{elssec_evtpkt}. \tag{4.14}$$

This value is converted to TTJ2000 nanoseconds and stored as the `epoch` coordinate.

The output event-message dataset is initialized with three time-related variables:

`epoch`, `elsec_evtpkt`, `elssec_evtpkt`.

The remaining packet fields used for message construction are not retained as separate output variables in this product. Instead, they are used to construct the final readable message string.

The message text is generated by loading

`idex_evt_msg_parsing_dictionaries.json`.

Because JSON stores object keys as strings, the processing code first converts dictionary keys back to integers before using them for event ID and parameter-value lookup. The event ID field,

`elid_evtpkt`,

selects both a message template and, when available, a short log-entry name. The four parameter bytes,

`el1par_evtpkt`, `el2par_evtpkt`, `el3par_evtpkt`, `el4par_evtpkt`,

are stacked into a four-byte parameter array for each event and passed to the message renderer.

4.7 Level 1A to Level 1B Processing: `idex_l1b.py`

Level 1B processing converts the packet-derived L1A science and message products into engineering-unit products with additional event-level metadata. The processing path is selected from the input product descriptor. Science products with descriptors beginning with `sci-10days` are processed by the science L1B path, while message products with descriptors beginning with `msg-10days` are processed by the message L1B path. Unsupported descriptors are rejected.

The L1B products are constructed as `xarray.Dataset` objects. Each output dataset is initialized from the parent dataset's `epoch` coordinate, and selected variables are copied forward using name-prefix matching. Additional derived variables are added during processing. CDF global and variable attributes are loaded through the IDEX attribute helper, which combines IMAP default attributes with IDEX-specific global attributes and level-specific IDEX variable attributes.

4.7.1 L1B Science Processing

The L1B science product preserves the event structure created at L1A, but converts the waveforms to channel-specific engineering units, unpacks instrument settings, computes event dead time, derives trigger information, and appends SPICE-derived geometry and pointing quantities. The output product uses the global attribute set

`imap_idex_l1b_sci`.

The L1B science path performs the following operations:

1. unpack packed instrument-setting fields from L1A telemetry words,
2. convert waveform arrays from digital numbers to channel-specific engineering units,
3. compute event dead time from packed header fields,
4. derive trigger mode, trigger threshold, and trigger-origin labels,
5. append SPICE-derived spacecraft state, IDEX pointing, solar longitude, and spin phase,
6. convert unpacked instrument settings into engineering units.

Waveform Conversion

The six waveform arrays are converted from digital numbers to their channel-specific engineering units using fixed conversion factors:

$$X_{\text{waveform}} = \text{DN}\, C_{\text{waveform}}. \tag{4.15}$$

The TOF waveforms are reported in milliamperes (mA), while the Target and Ion Grid waveforms are reported in picocoulombs (pC). This conversion is applied directly to the L1A waveform arrays. The converted arrays retain the same event and sample dimensions as the L1A waveforms.

Table 4.2: IDEX waveform conversion factors used during L1B processing.

Channel	L1B Variable	Conversion Factor (Engineering Units/DN)	Sampling Rate (MHz)
TOF High Gain	`TOF_High`	7.50×10^{-5} mA/DN	260
TOF Mid Gain	`TOF_Mid`	2.93×10^{-3} mA/DN	260
TOF Low Gain	`TOF_Low`	1.34×10^{-1} mA/DN	260
Target High Gain	`Target_High`	1.63×10^{-1} pC/DN	4.0625
Target Low Gain	`Target_Low`	1.58×10^{1} pC/DN	4.0625
Ion Grid	`Ion_Grid`	7.46×10^{-4} pC/DN	4.0625

Instrument Setting Unpacking and Engineering-Unit Conversion

Many L1A instrument settings are stored as packed bit fields. During L1B processing, these packed fields are unpacked using the table

`idex_variable_unpacking_and_eu_conversion.csv`.

For each mnemonic, the table identifies the source variable, bit width, starting bit, and padding needed to isolate the desired field.

For a field with unsigned bit width N_{bits}, the mask is

$$M = 2^{N_{\text{bits}}} - 1. \tag{4.16}$$

The value is shifted and masked according to

$$x_{\text{unpacked}} = [x_{\text{raw}} \gg (b_{\text{start}} - b_{\text{pad}})] \ \& \ M. \tag{4.17}$$

After unpacking, the L1B dataset is passed through the general engineering-unit conversion utility. This conversion table supports both unsegmented polynomial conversion and segmented polynomial conversion. For unsegmented conversion, the engineering-unit value is computed using polynomial coefficients:

$$P(x) = \sum_i C_i x^i. \tag{4.18}$$

For segmented conversion, different coefficient sets are applied over different valid raw-DN ranges.

Therefore, L1B uses two distinct conversion mechanisms. Waveform arrays are converted by fixed channel-specific engineering-unit-per-DN constants, while instrument settings are unpacked from bit fields and then converted using the engineering-unit conversion table.

Dead-Time Calculation

Event dead time is derived from the packed L1A header field

`idx__txhdrblocks`.

Two bit fields are extracted:

$$N_{\text{shift}} = (\texttt{idx__txhdrblocks} \gg 20) \ \& \ 0b1111, \tag{4.19}$$

$$N_{\text{base}} = (\texttt{idx__txhdrblocks} \gg 24) \ \& \ 0b111111. \tag{4.20}$$

The dead time is then computed as

$$t_{\text{dead}} = N_{\text{base}}\, 2^{N_{\text{shift}}}\, \Delta t_{\text{block}}. \tag{4.21}$$

The block duration is defined from the low-rate sampling cadence:

$$\Delta t_{\text{block}} = \frac{8}{4.0625 \times 10^6} \approx 1.96923\ \mu\text{s}. \tag{4.22}$$

The result is stored as the event-indexed L1B variable `dead_time`.

Trigger Mode, Trigger Level, and Trigger Origin

L1B processing converts selected trigger fields into more usable event-level variables. For the TOF low-, mid-, and high-gain channels, the trigger mode is read from

`idx__txhdrlgtrigmode`, `idx__txhdrmgtrigmode`, `idx__txhdrhgtrigmode`.

The trigger-control words are read from

`idx__txhdrlgtrigctrl1`, `idx__txhdrmgtrigctrl1`, `idx__txhdrhgtrigctrl1`.

If the trigger mode is zero, the channel is treated as having no active trigger mode for that event. Otherwise, the mode label includes the applicable gain prefix `LG`, `MG`, or `HG`:

1 : `LGThreshold`, `MGThreshold`, or `HGThreshold`,
2 : `LGSinglePulse`, `MGSinglePulse`, or `HGSinglePulse`,
3 : `LGDoublePulse`, `MGDoublePulse`, or `HGDoublePulse`.

The threshold level is extracted from the upper ten bits of the trigger-control word:

$$L_{\text{trig}} = (\texttt{trigger_control} \gg 22) \ \& \ 0b1111111111. \tag{4.23}$$

The extracted threshold is multiplied by the corresponding TOF conversion factor, so the trigger threshold is reported in mA, the same units as the converted TOF waveform.

The trigger origin is derived from the lower ten bits of `idx__txhdrtrigid`. The implemented labels are:

0 : HS ADC0I trigger (TOF HG),
1 : HS ADC0Q trigger (TOF LG),
2 : HS ADC1Q trigger (TOF MG),
3 : LS ADC1 trigger (Target HG / low range),
4 : software trigger,
5 : external trigger.

Multiple bits may be set, in which case the labels are joined into one comma-separated trigger-origin string. If no recognized bits are set, the event is labeled as having an unknown trigger origin.

SPICE-Derived Geometry, Pointing, and Spin Phase

L1B science processing adds event-context quantities derived from SPICE and spin-table data. The L1A `epoch` coordinate is stored as TTJ2000 nanoseconds. It is first converted to ephemeris time,

$$t_{\mathrm{ET}} = \texttt{ttj2000ns_to_et}(\texttt{epoch}), \tag{4.24}$$

and then to mission elapsed time for spin-phase lookup:

$$t_{\mathrm{MET}} = \texttt{et_to_met}(t_{\mathrm{ET}}). \tag{4.25}$$

The IMAP spacecraft state is queried relative to the Sun in the default ECLIPJ2000 frame. The position components are stored as

`ephemeris_position_x`, `ephemeris_position_y`, `ephemeris_position_z`,

and the velocity components are stored as

`ephemeris_velocity_x`, `ephemeris_velocity_y`, `ephemeris_velocity_z`.

The IDEX boresight is transformed from the `IMAP_IDEX` instrument frame into the configured IDEX event reference frame. The current configured event reference frame is

`ECLIPJ2000`.

The transformed pointing vector is converted to spherical coordinates, and the resulting angular coordinates are stored as

`longitude`, `latitude`.

The solar longitude is computed separately from SPICE geometry, and the spacecraft spin phase is obtained by interpolating the spin table at the event MET. The spin phase is then converted from fractional phase to degrees:

$$\theta_{\mathrm{spin}} = 360^{\circ}\phi_{\mathrm{spin}}. \tag{4.26}$$

These SPICE and spin quantities are included for event context and downstream interpretation; they are not used to alter the L1B waveform conversion itself.

4.7.2 L1B Event-Message Processing

The `science_on` variable identifies the transitions into and out of science acquisition. It is set to 1 when the message string exactly matches

`SCI state change: ACQSETUP ==> ACQ`,

and it is set to 0 when the message string exactly matches

`SCI state change: ACQ ==> CHILL`.

Pulser State

The `pulser_on` variable identifies a validated pulser operation using two exact message strings. A pulser operation begins with the `PULSER_ON` message

`SEQ success (len=0x0580,opCodeLCDictionary(enstim))`

and ends with the `PULSER_OFF` message

`UPK stim pulser operation completed,, PulserSel=0x00000007.`

The completion message is accepted when it occurs at or after the pulser-enable epoch and no more than 5 seconds later. If the enable message occurs at epoch t_{on}, a completion message at epoch t_{off} is accepted when

$$t_{\text{on}} \leq t_{\text{off}} \leq t_{\text{on}} + 5 \text{ s}. \tag{4.27}$$

When a valid pair is found, the enable row is assigned `pulser_on`=1 and the first matching completion row within the time window is assigned `pulser_on`=0. The messages do not need to be adjacent; intervening control messages, including `susprel`, do not prevent the pulser operation from being recognized.

Message Curation and Fill Values

All message rows that do not exactly match a science transition, or do not participate in a valid pulser pair, are assigned the fill value 255 for the corresponding state variable. There is no separate `noise_on` variable in the L1B message product. Noise-capture classification is performed per science event by the L1A event flags described above, rather than from the message log.

After both state variables are constructed, rows for which `science_on`=255 and `pulser_on`=255 are removed. The resulting L1B message product therefore contains only epochs where at least one science or pulser state is explicitly identified. It is a curated state-transition product rather than a complete copy of the L1A event-message log. If no qualifying state transitions are present, no L1B message dataset is produced.

4.8 Level 1B to Level 2A Processing: `idex_l2a.py`

Level 2A processing uses the L1B science product to derive event-level dust impact quantities. The L2A code fits the Target Low, Target High, and Ion Grid waveforms, uses the fitted target rise time and impact charge to estimate target-channel velocity and mass, and uses the Ion Grid-to-target charge ratio to estimate Ion Grid velocity. The selected target charge and Ion Grid velocity are then used to estimate the corresponding dust mass. The current implementation also creates preliminary TOF mass-spectrum products, but the unvalidated TOF-derived quantities remain NaN placeholders.

The L2A output product uses the global attribute set

`imap_idex_l2a_sci`.

4.8.1 Calibration Inputs

L2A processing requires two ancillary calibration files. The first provides the rise-time calibration used to estimate velocity from target rise time. The second provides the charge-yield calibration used to estimate dust mass from impact charge and velocity. The current ancillary files contain the parameter sets in table 4.3

Table 4.3: L2A calibration parameters used by the current processing code.

Calibration	$\log A$	a_1	a_2	a_3	v_b **(km/s)**	v_c **(km/s)**	k	σ	Δ
Rise time	1.27	-0.2	-2.1	-0.37	5.3	13.3	13.3	0.28	1.33
Charge yield	0.06	2.8	5.9	4.1	13.0	22.7	8.2	0.40	1.47

4.8.2 Target and Ion Grid Signal Fits

The current L2A code fits each low-rate charge-sensitive amplifier waveform independently:

`Target_Low`, `Target_High`, `Ion_Grid`.

Future implementations will combine Target Low and Target High before fitting for optimal dynamic range. Instead, each channel is fit separately against the low-rate time array.

The fit function is

$$y(t) = C_0 + H(t - t_0)\, A \left[1 - \exp\left(-\frac{t - t_0}{\tau_r}\right)\right] \exp\left(-\frac{t - t_0}{\tau_d}\right), \tag{4.28}$$

where

- $H(t - t_0)$ is the Heaviside step function,
- t_0 is the fitted impact time,
- C_0 is the fitted constant baseline offset,
- A is the fitted pulse amplitude parameter,
- τ_r is the fitted rise time,
- τ_d is the fitted discharge or decay time.

The five fitted parameters are stored using the labels

`time_of_impact`, `constant_offset`, `amplitude`, `rise_time`, `discharge_time`.

Before fitting, the code estimates the baseline from the first 5 μs of the waveform record. The initial impact time is set to 0 μs. The initial constant offset is set to the baseline mean. The initial amplitude is selected from the largest absolute signal excursion relative to that baseline. The initial rise-time and discharge-time guesses are

$$\tau_{r,0} = 0.371\ \mu\text{s}, \qquad \tau_{d,0} = 37.1\ \mu\text{s}. \tag{4.29}$$

The fit requires the rise time and discharge time to remain positive. For target channels, the amplitude is constrained to be positive. For the Ion Grid channel, the amplitude sign may be positive or negative depending on the observed signal polarity.

Impact Charge from the Fitted Waveform

The reported impact charge is computed from the fitted waveform maximum rather than directly from the fitted amplitude parameter. After fitting, the code evaluates the analytic pulse maximum:

$$t_{\max} = t_0 + \tau_r \ln\left(\frac{\tau_d}{\tau_r} + 1\right). \tag{4.30}$$

The fitted model is evaluated at this time, and the impact charge is taken as the absolute difference between the fitted maximum and the fitted baseline:

$$Q_{\text{impact}} = |y(t_{\max}) - C_0|. \tag{4.31}$$

The fit also returns the modeled waveform, a chi-square value, and a reduced chi-square value.

For each of the three low-rate channels, the L2A product includes:

- `{channel}_fit_parameters`,
- `{channel}_impact_charge`,
- `{channel}_velocity_estimate`,
- `{channel}_dust_mass_estimate`,
- `{channel}_chi_squared`,
- `{channel}_reduced_chi_squared`,
- `{channel}_fit_results`.

4.8.3 Velocity and Mass Estimates from Target Fits

For each science event low-rate waveform fit, the pipeline attempts to derive a velocity and mass estimate from the fitted rise time and impact charge (these values are left as `NaN` for pulsers and noise-captures). The fitted rise time is converted to velocity by numerically inverting the calibration relation

$$\tau_r = f(v). \tag{4.32}$$

The calibration function is represented as a smoothly transitioning power law in log space. In general form,

$$\log_{10} y = \log_{10} A + a_1 \log_{10} v + \log_{10}\left[\left(1 + \left(\frac{v}{v_b}\right)^k\right)^{(a_2-a_1)/k}\left(1 + \left(\frac{v}{v_c}\right)^k\right)^{(a_3-a_2)/k}\right], \tag{4.33}$$

where the same functional form is used for both the rise-time calibration and the charge-yield calibration. For the rise-time inversion, y represents τ_r. For the yield calculation, y represents the charge yield.

The inversion is performed in $\log_{10} v$ using a scalar root solve over the bracket

$$-1 \le \log_{10} v \le 2, \tag{4.34}$$

corresponding to

$$0.1 \le v \le 100 \text{ km s}^{-1}. \tag{4.35}$$

If the rise time is non-finite, non-positive, or cannot be inverted within this range, the velocity and corresponding mass estimates are returned as `NaN`.

Once a velocity estimate is obtained, the charge-yield calibration is evaluated at that velocity. The measured impact charge is converted from picocoulombs to coulombs, and the dust mass estimate is computed as

$$m_{\mathrm{dust}} = \frac{Q_{\mathrm{impact}}}{Y(v)}. \tag{4.36}$$

4.8.4 Ion Grid Mass and Velocity Estimation

The Ion Grid velocity estimate, v_{IG}, is determined using the empirically calibrated relationship between the ratio of charge measured by the Ion Grid and the target, QI/QT, and impact velocity:

$$v(QI/QT) = c \cdot (QI/QT)^p + v_0. \tag{4.37}$$

Where the empirical best fit parameters are $c = 55[km/s]$, $p = -3.2$, and $v_0 = 1.5[km/s]$. The selected target charge, QT, and v_{IG} are then used with equations 4.33 and 4.36 to calculate the Ion Grid dust-mass estimate. Target High charge is preferred when it is unsaturated; Target Low charge is used when Target High is saturated or unavailable. The estimates are set to `NaN` when the Ion Grid is saturated, when no valid unsaturated target charge is available, or when the required fitted charges are invalid.

4.8.5 TOF Mass-Scale and Peak-Fit Products

The current L2A code contains a preliminary TOF mass-spectrum analysis path. It uses the `TOF_High` waveform as the TOF input. A list of reference ion masses is loaded from `atomic_masses.csv`. The uploaded mass table contains 21 reference masses, including H, H_2, C, O, Na, Mg, Al, Si, K, Ca, several Fe isotopes, and Au.

For each event, the code constructs a preliminary time-to-mass scale by comparing the measured TOF waveform to expected mass peak locations of the form

$$t_i = t_{\mathrm{offset}} + A\sqrt{m_i}. \tag{4.38}$$

A set of stretch factors is tested. For each stretch factor, a synthetic expected-peak array is generated and cross-correlated with the measured TOF waveform. The shift and stretch that maximize the correlation are then used to convert the high-rate time axis into an estimated mass scale:

$$m(t) = \left[\frac{t - t_{\mathrm{shift}}}{A}\right]^2. \tag{4.39}$$

Detected TOF peaks are identified using a prominence threshold. Around each detected peak, the code fits an exponentially modified Gaussian. The fitted TOF peak parameters are reported using the labels

`mu`, `sigma`, `lambda`.

For each fitted peak, the code also computes the area under the fitted curve, the chi-square value, and the reduced chi-square value.

The TOF path also computes a signal-to-noise ratio using a pre-impact baseline window:

$$-7\ \mu\mathrm{s} \le t \le -5\ \mu\mathrm{s}. \tag{4.40}$$

It also computes `tof_peak_kappa`, the signed mean residual between detected peak masses and their nearest integer mass values.

The TOF path also computes:

- `tof_snr`, based on a pre-impact baseline window from -7 to -5 μs,
- `tof_peak_kappa`, the signed mean residual from the nearest integer mass positions on the preliminary mass scale,
- `tof_peak_area_under_fit`,
- `tof_peak_fit_parameters`,
- `tof_peak_chi_square`,
- `tof_peak_reduced_chi_square`,
- `mass_scale` and `mass`.

However, these TOF-derived outputs are intentionally not released as validated science quantities in the current version. After the product variables are created, the code overwrites the TOF peak-fit products, TOF SNR, TOF kappa, and mass-scale variables with `NaN`. This preserves the product schema while preventing unvalidated TOF fitting results from being interpreted as finalized L2A science data.

4.8.6 Current NaN Placeholder Block

For the current release, the following TOF and mass-spectrum L2A variables are explicitly filled with `NaN` after they are created:

- `tof_peak_area_under_fit`,
- `tof_peak_chi_square`,
- `tof_peak_fit_parameters`,
- `tof_peak_kappa`,
- `tof_peak_reduced_chi_square`,
- `tof_snr`,
- `mass`,
- `mass_scale`.

This NaN block is intentional and applies to the unvalidated TOF mass-spectrum products. The Ion Grid velocity and dust-mass estimates are not part of this unconditional NaN block. They are calculated from the fitted Ion Grid charge and the best available unsaturated target charge, with Target High preferred and Target Low used as a fallback when Target High is saturated or unavailable. If a Target Low, Target High, or Ion Grid waveform is saturated, that channel's `impact_charge`, velocity estimate, and dust-mass estimate are set to `NaN`; its fit parameters and fit results remain available for diagnostics. For non-science events, the velocity and mass estimates are set to `NaN`, while fitted impact charges remain available for diagnostics.

The Ion Grid estimates are masked to `NaN` for non-science events, when the Ion Grid waveform is saturated, when both target gains are saturated or lack a finite fitted charge, or when the fitted Ion Grid or target charge is non-finite or non-positive. Thus, valid science events with suitable unsaturated fits can retain populated `ion_grid_velocity_estimate` and `ion_grid_dust_mass_estimate` values.

4.8.7 Future Work: Combined Target Waveform Fits

The current L2A implementation fits `Target_Low` and `Target_High` independently. A future version is expected to combine the two target gain stages before fitting. The intended approach is to use the high-gain target channel where it remains unsaturated and to use the low-gain target channel where the high-gain signal saturates or loses dynamic range. Both channels would first be baseline corrected and converted into common charge units, after which a combined target waveform could be constructed for a single target fit.

The combined target fit would allow a single best estimate of target impact charge, rise time, and decay time to be reported for each event, rather than separate low-gain and high-gain estimates. The product will also include a flag to indicate the validity or quality of fit in future releases.

4.8.8 Future Work: Combined TOF Waveform Fits

The current L2A TOF path uses `TOF_High` as the TOF fitting input. A future version is expected to improve this by combining information across the TOF high-, mid-, and low-gain channels. As with the target channels, the goal is to use the best unsaturated gain range for each portion of the waveform or to construct a combined TOF waveform with improved dynamic range.

Once validated, the combined TOF workflow is expected to support:

- a more robust time-to-mass conversion,
- improved peak detection across saturated and low-amplitude regions,
- EMG or other peak-shape fits to identified ion peaks,
- peak-area estimates for mass-spectrum interpretation,
- quality metrics such as SNR, reduced chi-square, and mass-scale alignment.

The current TOF variables remain in the L2A product as placeholders, but their values are filled with `NaN` until this fitting path is sufficiently validated. The product will also include a flag to indicate the validity or quality of fit in future releases.

4.8.9 L2A Output Summary

The current L2A science product contains three categories of variables.

First, it preserves selected timing and SPICE context from L1B, including the low- and high-rate time arrays and the event-level SPICE arrays needed for geometry and pointing interpretation.

Second, it contains fitted low-rate waveform products for:

`Target_Low`, `Target_High`, `Ion_Grid`.

For each channel, the product includes fit parameters, impact charge, fit results, and fit-quality statistics. Target-channel velocity and mass estimates are included, and Ion Grid velocity and

mass estimates are included when the event is a science event and the required fitted charges and saturation conditions are valid.

Third, it contains TOF and mass-spectrum variables that define the intended L2A mass-analysis product structure. In the present release, these TOF-derived values are placeholders and are filled with `NaN`. They are retained so that future validated TOF products can be added without changing the overall L2A product structure.

4.9 Level 2A to Level 2B and Level 2C Processing: `idex_l2b.py`

The current `idex_l2b.py` module creates the L2B science product and an accompanying L2C rectangular sky-map dataset in the same processing step. It receives the L2A science dataset, the L1B message dataset, and the start date of the ten-day accumulation window. The L2B and internally generated L2C datasets use the same window epoch and event-message on/off information for calculating the accumulation time. The L2C dataset is currently suppressed from formal publication.

4.9.1 Spin-Phase Assignment

The event-level `spin_phase` used by L2B is calculated upstream in L1B. The L1B processing obtains spacecraft spin phase by interpolating the mission spin table at each event epoch; the fractional phase is converted to degrees in the range 0–360°. L2B does not recalculate spin phase from the waveform data or assign a separate phase to each dust peak. Instead, each event with `dust_hit_flag`=1 is assigned to a spin-phase bin using its event-level L1B/L2A `spin_phase` value.

The four spin-phase bins are centered on the four 90° quadrants. To place the bin boundary at ±45° around zero phase, L2B shifts the phase by 45° and wraps it modulo 360°:

$$\phi' = (\phi + 45^\circ) \bmod 360^\circ. \tag{4.41}$$

The shifted phase is then assigned to the intervals $[0^\circ, 90^\circ)$, $[90^\circ, 180^\circ)$, $[180^\circ, 270^\circ)$, and $[270^\circ, 360^\circ)$. Equivalently, in the original phase coordinate the bins are $[315^\circ, 360^\circ) \cup [0^\circ, 45^\circ)$, $[45^\circ, 135^\circ)$, $[135^\circ, 225^\circ)$, and $[225^\circ, 315^\circ)$. The output coordinate labels are the corresponding bin midpoints 45°, 135°, 225°, and 315°.

4.9.2 Rectangular Spatial Mapping and Binned Products

Only events with `dust_hit_flag`=1 contribute to the spatial maps. Event longitude is wrapped into $[0^\circ, 360^\circ)$, latitude is clipped to $[-90^\circ, 90^\circ]$, and events without finite longitude and latitude are omitted from the agnostic map. The remaining events are accumulated on a rectangular longitude–latitude grid with 6° spacing in the configured IDEX event reference frame. The L2C `counts_map` contains one count histogram for the full ten-day window, and `rate_map` is obtained by dividing that histogram by the science acquisition on-time.

The code also calculates spin-phase and spatial histograms binned by impact charge and dust mass. These calculations use the Target Low `impact_charge` and `dust_mass_estimate` for dust-hit events. Charge values use fixed bin edges from 10^{-1} through 10^{4} pC, and mass values use the fixed mass-bin edges defined in `idex_l2b.py`; values outside the configured ranges are clipped to the nearest boundary before histogramming. The charge- and mass-binned L2B and L2C products are currently replaced with fill values or `NaN` pending validation, while the agnostic spin-phase and rectangular-map products remain populated.

Laboratory for Atmospheric and Space Physics
University of Colorado Boulder

4.9.3 Science On-Time and Rate Calculation

Science acquisition on-time is calculated from the L1B `science_on` transitions with values of 0 or 1; rows with the fill value 255 are ignored. The message times and transitions are sorted and duplicate epochs are removed before the on-time calculation. The calculation tracks the full half-open accumulation interval

$$[t_{\text{window,start}}, t_{\text{window,end}}).$$

Each state is extended from its message time to the next state transition, and the final state is extended through the end of the ten-day window. If no state is available exactly at the window start, the implementation inserts a synthetic initial state opposite to the first observed transition. Thus, an initial transition to science-on implies that science was off before that transition, and an initial transition to science-off implies that science was on before that transition.

The resulting science on-time is

$$T_{\text{on}} = \sum_j \mathbb{1}(s_j = 1)(t_{j+1} - t_j), \tag{4.42}$$

where s_j is the science acquisition state for each interval. The total tracked time is

$$T_{\text{total}} = \sum_j (t_{j+1} - t_j). \tag{4.43}$$

The `on_seconds` value computed and used by L2B is T_{on}.

Only events with `dust_hit_flag`=1 contribute to the L2B counts. For spin-phase bin k, the agnostic count is

$$N_k = \sum_i \mathbb{1}(\texttt{dust_hit_flag}_i = 1)\,\mathbb{1}(\phi_i \in k)\,. \tag{4.44}$$

The corresponding agnostic rate is the count divided by science acquisition on-time:

$$R_k = \frac{N_k}{T_{\text{on}}}. \tag{4.45}$$

If either total tracked time or science on-time is missing or zero, the agnostic rate variables are filled with `NaN`. The charge- and mass-binned rate paths use a negative sentinel and a quality flag when on-time is invalid; the current release subsequently withholds those charge- and mass-binned products. The agnostic spin-phase counts and rates remain available.

4.10 Calibration and Maintenance

Calibration products maintained as ancillary files are not hard-coded algorithm constants; some channel conversion factors and empirical coefficients are defined directly in the processing code. New calibration files will receive a new versioned filename and the processing configuration should point to the newest file version. If a calibration file is updated existing products can be regenerated by rerunning the affected levels. L2A products are affected by rise-time and yield calibration updates. L1B products are affected by waveform and engineering-unit conversion updates. Validation tests will be rerun after any calibration update.

The instrument has on-board pulsers to inject each CSA with programmable levels of known charges to test their engineering-unit conversions. These pulser injection results will be periodically manually reviewed to monitor the channel-specific conversion from DN to engineering units.

4.11 Data Validation and Testing

The IDEX processing pipeline is supported by an automated test suite that validates the major processing stages from packet decommutation through L2A product generation. These tests are not intended to document every implementation detail individually; instead, they provide broad verification that the pipeline produces correctly structured data products, preserves expected values, handles known edge cases, and writes standards-compliant CDF files.

The test suite uses a combination of unit tests, regression tests, validation-file comparisons, and error-handling checks. Shared fixtures provide representative IDEX L0 packet files, L1A and L1B validation files produced by the IDEX team, calibration files, and mocked SPICE outputs where external kernels or spin-table data are not the subject of the test. This allows the tests to focus on the behavior of the IDEX processing logic while keeping the results reproducible.

At the L0 and L1A levels, the tests verify that CCSDS packet decommutation produces the expected number of science events and event-message records. They also compare selected waveform arrays against IDEX-team-validated reference outputs, confirm that compressed and uncompressed science packets decode consistently, and check that duplicate, incomplete, or conflicting packet fragments are handled as intended. The IDEX event-flag tests additionally cover trigger-based event classification, 95% saturation flags, saturated-peak width handling, multi-gain peak detection, the broad single-peak exception, and the truncated-waveform baseline fallback. These tests are especially important because the L1A stage is responsible for assembling packet fragments into complete event-level waveform products.

At the L1B level, the tests verify engineering-unit conversion, waveform units, instrument-setting unpacking, trigger-mode and trigger-origin decoding, event dead-time calculation, SPICE-data attachment, L1B message-state reduction, and CDF file generation. The L1B tests also compare SDS-generated variables against independent IDEX-team validation data where available, while skipping variables known to differ because of time-system conventions or mocked SPICE quantities.

At the L2A level, the tests check the current science-analysis functions, including calibration-file loading, time-to-mass scaling, TOF signal-to-noise calculations, peak-fit handling, smooth power-law calibration behavior, rise-time-to-velocity inversion, target/ion-grid waveform fitting, and dust mass estimation. The tests also verify that the unvalidated TOF mass-spectrum variables remain `NaN`, while Ion Grid velocity and mass estimates are populated when their input charges and saturation conditions are valid and are masked when those conditions are not met.

CDF generation is also tested directly. The tests confirm that valid products can be written successfully and that invalid CDF metadata or malformed variables raise errors. This provides an additional validation layer beyond numerical correctness: the output products must also satisfy the metadata and formatting requirements needed for archive-ready CDF files.

As a project-level software quality requirement, the IDEX processing pipeline is expected to maintain at least 90% automated test coverage. This coverage requirement helps ensure that future changes to packet parsing, waveform conversion, calibration logic, CDF metadata, or derived science products are exercised by the test suite before release. In practice, this means new pipeline logic should be accompanied by corresponding tests or validation updates so that the code base remains both scientifically traceable and operationally reliable.

Appendix A

LASP Packets

The **generator** method from the **parser.py** script in LASP Packets.

```
1 def generator(self, binary_data: bitstring.ConstBitStream, parse_bad_pkts: bool = True,
      skip_header_bits: int = 0, root_container_name="CCSDSPacket", ccsds_headers_only: bool =
      False, yield_unrecognized_packet_errors: bool = False, show_progress: bool = False):
2     """Create and return a Packet generator.
3     Creating a generator object to return allows the user to create many generators from a
      single Parser and reduces memory usage.
4     ...
```

Appendix B

IDEX Science Packet Definition

The first 100 lines of the IDEX Science Packet definition are shown below.

```
<?xml version="1.0" encoding="UTF-8"?>
<xtce:SpaceSystem xmlns:xtce="http://www.omg.org/space/xtce" name="IDEX">
  <xtce:Header classification="BuildType=FLIGHT,CreatedBy=XTCEEditor" date="Created
    =2023/01/12 15:27:45" version="DocumentVersion=FSW Build ,DocumentVersion=20190109
    v1,LASPXTCESchemaVersion=1.2,XTCEEditorVersion=0.47"/>
  <xtce:TelemetryMetaData>
    <xtce:ParameterTypeSet>
      <xtce:IntegerParameterType signed="false" name="VERSION_Type">
        <xtce:UnitSet/>
        <xtce:IntegerDataEncoding encoding="unsigned" sizeInBits="3"/>
      </xtce:IntegerParameterType>
      <xtce:IntegerParameterType signed="false" name="TYPE_Type">
        <xtce:UnitSet/>
        <xtce:IntegerDataEncoding encoding="unsigned" sizeInBits="1"/>
      </xtce:IntegerParameterType>
      <xtce:IntegerParameterType signed="false" name="SEC_HDR_FLG_Type">
        <xtce:UnitSet/>
        <xtce:IntegerDataEncoding encoding="unsigned" sizeInBits="1"/>
      </xtce:IntegerParameterType>
      <xtce:IntegerParameterType signed="false" name="PKT_APID_Type">
        <xtce:UnitSet/>
        <xtce:IntegerDataEncoding encoding="unsigned" sizeInBits="11"/>
      </xtce:IntegerParameterType>
      <xtce:IntegerParameterType signed="false" name="SEQ_FLGS_Type">
        <xtce:UnitSet/>
        <xtce:IntegerDataEncoding encoding="unsigned" sizeInBits="2"/>
      </xtce:IntegerParameterType>
      <xtce:IntegerParameterType signed="false" name="SRC_SEQ_CTR_Type">
        <xtce:UnitSet/>
        <xtce:IntegerDataEncoding encoding="unsigned" sizeInBits="14"/>
      </xtce:IntegerParameterType>
      <xtce:IntegerParameterType signed="false" name="PKT_LEN_Type">
```

```
        <xtce:UnitSet/>
        <xtce:IntegerDataEncoding encoding="unsigned" sizeInBits="16"/>
      </xtce:IntegerParameterType>
      <xtce:FloatParameterType name="SHCOARSE_Type">
        <xtce:UnitSet>
          <xtce:Unit>dn</xtce:Unit>
        </xtce:UnitSet>
        <xtce:IntegerDataEncoding encoding="unsigned" sizeInBits="32"/>
      </xtce:FloatParameterType>
      <xtce:FloatParameterType name="SHFINE_Type">
        <xtce:UnitSet>
          <xtce:Unit>dn</xtce:Unit>
        </xtce:UnitSet>
        <xtce:IntegerDataEncoding encoding="unsigned" sizeInBits="16"/>
      </xtce:FloatParameterType>
      <xtce:FloatParameterType name="CHECKSUM_Type">
        <xtce:UnitSet>
          <xtce:Unit>dn</xtce:Unit>
        </xtce:UnitSet>
        <xtce:IntegerDataEncoding encoding="unsigned" sizeInBits="32"/>
      </xtce:FloatParameterType>
      <xtce:IntegerParameterType name="IDX__SCI0AID_Type">
        <xtce:UnitSet/>
        <xtce:IntegerDataEncoding encoding="unsigned" sizeInBits="32"/>
      </xtce:IntegerParameterType>
      <xtce:IntegerParameterType name="IDX__SCI0TYPE_Type">
        <xtce:UnitSet/>
        <xtce:IntegerDataEncoding encoding="unsigned" sizeInBits="8"/>
      </xtce:IntegerParameterType>
      <xtce:IntegerParameterType name="IDX__SCI0CONT_Type">
        <xtce:UnitSet/>
        <xtce:IntegerDataEncoding encoding="unsigned" sizeInBits="8"/>
      </xtce:IntegerParameterType>
      <xtce:IntegerParameterType name="IDX__SCI0SPARE1_Type">
        <xtce:UnitSet/>
        <xtce:IntegerDataEncoding encoding="unsigned" sizeInBits="13"/>
      </xtce:IntegerParameterType>
      <xtce:EnumeratedParameterType name="IDX__SCI0PACK_Type">
        <xtce:UnitSet/>
        <xtce:IntegerDataEncoding encoding="unsigned" sizeInBits="1"/>
        <xtce:EnumerationList>
          <xtce:Enumeration value="0" label="DS"/>
          <xtce:Enumeration value="1" label="EN"/>
        </xtce:EnumerationList>
      </xtce:EnumeratedParameterType>
      <xtce:EnumeratedParameterType name="IDX__SCI0FRAG_Type">
        <xtce:UnitSet/>
        <xtce:IntegerDataEncoding encoding="unsigned" sizeInBits="1"/>
```

```
        <xtce:EnumerationList>
          <xtce:Enumeration value="0" label="DS"/>
          <xtce:Enumeration value="1" label="EN"/>
        </xtce:EnumerationList>
      </xtce:EnumeratedParameterType>
      <xtce:EnumeratedParameterType name="IDX__SCI0COMP_Type">
        <xtce:UnitSet/>
        <xtce:IntegerDataEncoding encoding="unsigned" sizeInBits="1"/>
        <xtce:EnumerationList>
          <xtce:Enumeration value="0" label="DS"/>
          <xtce:Enumeration value="1" label="EN"/>
        </xtce:EnumerationList>
      </xtce:EnumeratedParameterType>
      <xtce:IntegerParameterType name="IDX__SCI0EVTNUM_Type">
        <xtce:UnitSet/>
        <xtce:IntegerDataEncoding encoding="unsigned" sizeInBits="16"/>
      </xtce:IntegerParameterType>
      <xtce:IntegerParameterType name="IDX__SCI0CAT_Type">
        <xtce:UnitSet/>
        <xtce:IntegerDataEncoding encoding="unsigned" sizeInBits="8"/>
```

4.6.1 Validation

4.7 Lyman-α

GLOWS Lyman-α data product definitions and processing algorithms are embedded below

GLOWS data products

M. Bzowski*[1], M. Strumik[1], I. Kowalska-Leszczyńska[1], M. A. Kubiak[1], R. Wawrzaszek[1], K. Ber[1], and P. Orleański[1]

[1]CBK PAN, Bartycka 18a, 00-716 Warsaw, Poland

Revision 4.4.7, July 25, 2025

Abstract

This memo presents data products from GLOWS, with justifications. The most important parameters related to data taking and data structures are presented in Table 0.1. Note that some of the parameters are configurable in flight (marked with superscript c). Shown are presently adopted values for launch time. Changing all or one of them results in a change in the magnitude of dependent parameters.

The document is organized as follows. A **general introduction** to the GLOWS instrument can be found in Section 1. Brief summary of **onboard-processing-related issues** can be found in Section 2. Short discussion of **ground processing** is given in Sections 3 and 4. In Sections 5—11 more details, rationales, and discussions of tradeoffs are provided. Detailed description of data products is given in Sections 12 and 13.

Contents

1 Introduction **5**

2 Outline of onboard processing for IMAP GLOWS (science-team view) **6**
2.1 Overview of onboard processing . . . 7
2.2 Types of data generated onboard and transferred in telemetry . . . 7
2.3 Direct events . . . 7
2.4 Histograms . . . 8
2.5 Ancillary onboard-collected data . . . 9

3 A draft of data ground-processing algorithm for IMAP GLOWS from Level-0 to Level-2 **9**
3.1 Objective . . . 10
3.2 Input for Level-0-to-Level-2 ground-processing pipeline . . . 10
3.3 Ground-processing pipeline from Level-0 to Level-2 – overview . . . 11
3.3.1 Overview of histograms . . . 11
3.3.2 Overview of direct events . . . 11
3.3.3 Organization of GLOWS data – "per pointing" . . . 13
3.4 Level-0 data products . . . 14
3.4.1 Level-0 Histograms . . . 15
3.4.2 Level-0 Direct Events . . . 16
3.5 Level-0 to Level-1A processing . . . 19
3.5.1 Level-0 to Level-1A processing: histograms . . . 19
3.5.2 Level-0 to Level-1A processing: direct events . . . 19
3.6 Level-1A data products . . . 20
3.7 Level-1A to Level-1B processing . . . 21
3.7.1 Level-1A to Level-1B processing: histograms . . . 21
3.7.2 Level-1A to Level-1B processing: direct events . . . 22
3.8 Level-1B data products . . . 23
3.9 Level-1B to Level-2 processing . . . 23
3.9.1 Level-1B to Level-2 processing (histograms only) . . . 23
3.10 Level-2 data products . . . 28

*M. Bzowski, bzowski@cbk.waw.pl

Table 0.1

What	Denotation	Magnitude	Reference
IMAP day length (time btwn spin ax.change)	$T_{\text{IMAP day}}$	$0.5 \leq 1.0\,\text{day} \leq 3.0$ day	Eq. (1)
IMAP spin period	P_{IMAP}	15 s, inside (14.63, 15.38) s	Eq. (2)
number of IMAP spins per block[c]	n_{block}	8, (between 1 and 256)	Eq. (14)
number of bins per histogram (per spin)[c]	n_{bin}	3600, (between 225 and 3600)	Eq. (22)
number of bins per histogram (per spin) science[d]	$n_{\text{bin}}^{\text{lores}}$	90	
number of bits to code direct events[c]	k_{word}	15 bits	Eq. (6)
bin width (hi-res)	b	0.1° (between 0.1° and 1.6°)	Eq. (21)
typical GLOWS counting rate [e]	s_{mean}	600 cps	Eq. (13)
maximum expected counting rate	s_{max}	2 000 cps	Eq. (25)
typical counts per block	C_{block}	$72\,000 \pm 268.3$	Eq. (15)
typical number of blocks per day	N_{block}	720, between 702 and 738[a]	Eq. (17)
extreme numbers of blocks per day[b]	$\lfloor N_{\text{block}} \rfloor, \lceil N_{\text{block}} \rceil$	(351, 2215)	Eq. (18)
nominal time per bin	t_{bin}	$4167\,\mu$s	Eq. (23)
maximum counts per bin	c_{max}	66.67	Eq. (26)
number of bits per histogram bin	d	8 bits	Eq. (27)
average data rate for histograms (no overhead)	D	240 bps (bits per second)	Eq. (28)
expected number of DEs/IMAP day	C_{day}	5.184×10^7	Eq. (5)
GLOWS counter frequency (GLOWS clock resolution)	f_{counter}	2×10^6 Hz $= 2$ MHz	Eq. (3)
number of blocks per day for the telemetry	T_{dirEv}	48	Eq. (??)
azimuth of the GLOWS boresight in the s/c frame	ψ_{GLOWS}	TBD	TBD

[a] given the margin for the spin period for the nominal IMAP day length
[b] due to possible extremely short or extremely long IMAP days
[c] in-flight configurable
[d] configurable on the ground
[e] corresponds to the sensitivity 1 cps/R; facilitates rescaling for any actual GLOWS sensitivity; affects C_{block}, C_{day}, T_{dirEv}, which scale linearly as a function of cps/R

3.11 Python-script bundle provided by the GLOWS team . . . 30
3.12 Settings/parameters/input for ground-processing pipeline (ancillary files) . . . 30
3.13 Validation data sets . . . 31
3.13.1 Validation Set 1 . . . 31
3.14 Comments . . . 32

4 A draft of data ground-processing algorithm for IMAP GLOWS for Level-3 32
4.1 Inputs for Level-3 ground-processing pipeline (MS) . . . 32
4.2 Level-3 ground-processing pipeline – overview (MS) . . . 34
4.3 Level-2 to Level-3A processing (MS) . . . 34
4.4 Level-3A data products (MS) . . . 34
4.5 Initializer for Level-3B and higher levels (MS) . . . 38
4.6 Level-3A to Level-3B processing (IKL) . . . 39
4.7 Level-3B data products (IKL) . . . 40
4.8 Level-3B to Level-3C processing (IKL) . . . 41
4.9 Level-3C data products (IKL) . . . 42
4.10 Level-3B/C to Level-3D processing (IKL+MK) . . . 42
4.11 Level-3D data products (IKL) . . . 43
4.12 Level-3D to Level-3E processing (IKL+MK) . . . 43
4.13 Level-3E data products (IKL+MK) . . . 45
4.14 Test scripts in Python/Mathematica . . . 45
4.15 Settings/parameters for ground-processing pipeline . . . 45
4.16 Comments . . . 49

5 Sources of the observed signal 49

6 What the data system must guarantee 50

7 Characteristics of the observed signal 50

8 Operation modes 51
8.1 Normal science operations . . . 52
8.2 Regular in-flight tests . . . 53
8.2.1 Regular in-flight HV gain tests . . . 53
8.2.2 Regular comparation voltage test . . . 53
8.2.3 Regular threshold voltage test . . . 53
8.3 Ground processing for DE (direct-event) data . . . 53

9 Direct Events 54
9.1 Executive summary on direct events . . . 54
9.1.1 Direct-events collection . . . 54
9.1.2 File format for onboard storage . . . 55
9.1.3 Regular daily downlinking: selection of blocks . . . 55
9.1.4 On-demand downlinking . . . 55
9.1.5 Direct-events telemetry content . . . 56
9.2 The volume of DE data for downlinking . . . 56
9.3 Selection of direct events data for downlinking . . . 60

10 Histograms **61**
10.1 Executive summary on histograms . . . 61
10.1.1 Histogramming algorithm . . . 61
10.1.2 Histogram-related parameters . . . 61
10.1.3 File format for onboard storage . . . 61
10.1.4 Downlinking, histogram-telemetry content . . . 61
10.1.5 Spin-phase angle . . . 62
10.2 Block length: defined by particle background removal capability . . . 62
10.3 Bin widths: defined by requirements for calibration from stars . . . 63
10.4 Histogram-generation algorithms . . . 64
10.4.1 Data binning and histogram generation . . . 64
10.4.2 Statistical χ^2 testing – method . . . 68
10.4.3 Histograms vs. modeled lightcurves – a comparison . . . 68
10.4.4 Distribution of histograms-lightcurve residuals . . . 70
10.4.5 Statistical χ^2 testing . . . 71
10.5 Bit rate for the histograms . . . 72
10.6 Effective offset of the spin angle . . . 73

11 Ancillary onboard-collected data **74**
11.1 Executive summary on ancillary onboard-collected data . . . 74
11.1.1 Ancillary-telemetry content . . . 74
11.1.2 Ancillary-data encoding . . . 74
11.2 Formulas for ancillary-data average and variance . . . 74
11.3 Event signals on board . . . 75
11.4 On-board encoding and ground decoding of measured quantities . . . 75

12 Data products L0-L2 **77**
12.1 On-board storage . . . 78
12.1.1 Proprietary GLOWS on-board data . . . 78
12.1.2 Data expected in the general IMAP telemetry stream . . . 78
12.2 Ancillary data collected onboard by GLOWS . . . 79
12.2.1 Times . . . 79
12.2.2 Ancillary parameters . . . 79
12.3 Flags . . . 80
12.3.1 On-board generated bad-time flags for histograms . . . 80
12.3.2 Bad-time flags added during ground processing to individual histograms . . . 81
12.3.3 Bad-angle flags added during ground processing to individual histograms . . . 81
12.3.4 Daily-histogram flags (Level-2) . . . 82
12.3.5 Flags for direct events . . . 82
12.4 Raw data and Level 0 . . . 82
12.5 Level 1A: unpacked telemetry blocks . . . 82
12.5.1 Telemetry blocks for histograms HB (Level-1A) . . . 82
12.5.2 Telemetry blocks for direct events DE (Level-1A) . . . 83
12.5.3 Telemetry blocks for housekeeping HK . . . 83
12.6 Level 1B: unpacked telemetry + relevant HK and ancillary info . . . 83
12.6.1 Ancillary data from general IMAP telemetry . . . 84
12.6.2 Data structure for histograms HB (Level-1B) . . . 84
12.6.3 Data structure for direct events DE (Level-1B) . . . 85
12.7 Ground-processing pipeline from Level-1B to Level-2 . . . 85
12.7.1 Initial culling – identifying bad-time intervals . . . 86
12.7.2 Advanced culling against issues for the entire block histograms . . . 87

12.7.3 Co-adding block-accumulated high-resolution histograms . . . 88
12.7.4 Computing the daily count rate . . . 88
12.7.5 Calibration for computing the helioglow intensity in Rayleigh units . . . 89
12.7.6 Bad-angle masking . . . 89
12.7.7 Uncertainties . . . 90
12.8 Level-2: helioglow intensity in physical units . . . 90

13 Data products Level-3 **91**
13.1 Ground-processing pipeline from Level-2 to Level-3a . . . 92
13.1.1 Rebinning high-resolution lightcurve into low-resolution lightcurve . . . 92
13.1.2 Culling – masking star-contaminated bins . . . 92
13.1.3 Estimating extra-heliospheric background . . . 92
13.1.4 Estimating time-dependent background . . . 93
13.1.5 Uncertainties of the low-resolution lightcurve . . . 94
13.2 Level-3a: daily low-resolution lightcurve of Lyman-α photon flux with estimates of backgrounds . 94
13.3 WawHelioIon-MP . . . 94
13.3.1 Method . . . 94
13.3.2 Training sets: ionization rate . . . 95
13.3.3 Training sets: light curves . . . 95
13.3.4 Reconstruction . . . 95
13.3.5 Vantage points selection . . . 95
13.3.6 Model parameters file . . . 95
13.4 SOHO/SWAN Cross-calibration . . . 95
13.5 Relevant ionization processes . . . 95
13.6 Photoionization rate . . . 96
13.7 Normalization to the solar wind measurements in the ecliptic plane . . . 96
13.8 Solar energy flux . . . 96
13.8.1 Latitudinal invariant . . . 97
13.8.2 Solar wind density and speed profiles . . . 97
13.8.3 OMNI2 database . . . 97
13.9 L3D initial structure . . . 97
13.9.1 Source flags . . . 98
13.10 Survival probabilities . . . 98
13.10.1 General description . . . 98
13.10.2 Running the programs . . . 99
13.10.3 Output text file . . . 102

14 Coordinate frames **102**
14.1 Instrument frames . . . 102
14.1.1 Instrument frame for science (SPICE) . . . 102
14.1.2 MICD instrument frame . . . 104

15 Concluding remarks **104**

Change log **107**

1 Introduction

GLOWS (GLObal solar Wind Structure) is one of experiments on a NASA mission IMAP (Interstellar Mapping and Acceleration Probe, McComas et al., 2018), scheduled for launch into a Lissajous orbit around the Lagrange point L1 in 2025 . The objective of GLOWS is to investigate the global heliolatitude structure of the solar wind

and its evolution during the solar cycle. Additionally, GLOWS investigates the distribution of interstellar neutral hydrogen (ISN H) and the solar radiation pressure acting on ISN H.

The objectives of GLOWS are accomplished by observation of the heliospheric backscatter glow of ISN H (the helioglow). The helioglow is created by resonant excitation of ISN H atoms within several au from the Sun by the intense solar electromagnetic radiation in the Lyman-α waveband 121.567 nm. The H atoms move in this region collisionless and thus immediately after excitation of the photons from the Sun, they re-emit them in random directions. Those re-emitted photons form the helioglow. The intensity of the helioglow observed at $\sim$ 1 au varies across the sky, dependent on the location of the observer; it is on the order of 180–900 Rayleigh (*GLOWS Signal Evolution Report*, Kowalska-Leszczynska et al., 2021).

The density and atom velocities of ISN H are governed on one hand by the solar radiation pressure in the Lyman-α line and solar gravity, and on the other hand by ionization losses. The responsible ionization processes include charge exchange between ISN H atoms and charged particles forming the solar wind particles (mostly protons and alpha particles), photoionization by solar radiation with wavelengths shorter than the threshold for H ionization at $\sim$ 91.2 nm, and, within 1–2 au from the Sun, by impact-ionization by solar wind electrons (Bzowski et al., 2013). The solar wind features a latitudinal structure that evolves during the cycle of solar activity. During low activity, it has a region of relatively slow and dense outflow ($\sim$ 400 km s^{-1}, $\sim$ 5 protons cm^{-3} at 1 au) in a heliolatitude band around solar equator. At polar heliolatitudes, the solar wind is fast ($\sim$ 750 km s^{-1}) and rarefied ($\sim$ 2.5 protons cm^{-3} at 1 au; McComas et al., 2000). The structure of the helioglow varies during the cycle of solar activity. Because of the two different regimes of the solar wind, the intensity of the rate of charge exchange between the solar wind particles and ISN H atoms varies with heliolatitude, which results in forming a characteristic 3D structure of ISN H density. This structure is reflected in the sky distribution of the helioglow. Thus, by observing the sky distribution of the helioglow at all heliolatitudes, it is possible to infer the latitudinal structure of the solar wind and by monitoring the evolution of the helioglow sky distribution over a time interval between the minimum and the maximum of solar activity, one can monitor the evolution of the solar wind structure (Bzowski et al., 2003).

GLOWS scans a small circle in the sky, centered at a point offset by 4° from the Sun towards lower ecliptic longitudes. The diameter of the field of view of the instrument is $\sim$ 3.31° FWHM (*PSF Report*, Strumik, 2020b; Bzowski et al., 2022). After a day of observations, the spin axis of IMAP is redirected to maintain the 4° offset from Sun's center, and the strip of the sky observed by GLOWS accordingly shifts in the sky. A product of daily observations is a lightcurve of the helioglow intensity, collected from the scanning circle and composed of registered counts of the instrument, accumulated in bins organized by spin angle of the spacecraft. The modulation of the lightcurve depends on one hand on the structure of the solar wind, and on the other hand on the location around the Sun from which the observations are taken. The set of observations collected during a prolonged time enables determining the latitude structure of the solar wind.

The GLOWS detector is a non-imaging single-pixel Lyman-α photometer, effectively a photon counting instrument. It is conceptually based on the TWINS/LaD photometer (Nass et al., 2006; McComas et al., 2009), originally designed to observe the terrestrial exospheric resonant Lyman-α glow. The instrument includes a collimator with a baffle, a spectral filter, and a channeltron (CEM) detector. They are connected to the electronics block, responsible for collecting the event pulses and binning them for downlinking to the ground. The instrument is designed and assembled in the Space Research Centre PAS (CBK PAN).

This document presents data structures planned for the GLOWS data processing pipeline, with an extended discussion of the rationale for relevant system parameter selection. We present data structures used in the processing from raw telemetry packets to calibrated science data (lightcurves of the helioglow). The structure of data and data structures in the instrument memory are presented elsewhere.

2 Outline of onboard processing for IMAP GLOWS (science-team view)

This section contains a brief description of onboard processing as seen by the GLOWS Science Team. The main purpose is to provide a brief summary with links to other sections of this document, where details are discussed. Engineering-oriented discussion is provided in a separate document (reference needed).

A **general introduction** to the GLOWS instrument can be found in Section 1. **Signal sources** are discussed in Section 5. **Requirements for GLOWS data system** are discussed in Section 6.

2.1 Overview of onboard processing

- **Measurement principle, direct-events definition.** Incoming photons within the GLOWS field of view are transmitted through the optical entrance system and hit the surface of the channeltron electron multiplier (CEM). Onboard electronics will measure impulses generated by photon-initiated avalanches of electrons in the CEM. Impulses of an appropriate amplitude and length are registered as direct Events (DEs, see Section 11.3). A short discussion on direct events is given below in Section 2.3.
- **Histogramming.** Photon detection times (i.e., direct events) recorded by GLOWS are histogrammed onboard in the spin-angle domain (see Section 10.4). The histograms with $n_{\rm bin}$ bins are accumulated over spin blocks containing $n_{\rm block}$ spin periods. The default values of $n_{\rm bin}$ and $n_{\rm block}$ are given in Table 0.1. Short discussion on histograms is given below in Section 2.4.
- **GLOWS operation modes (including calibration procedures)** are discussed in Section 8 and summarized in Table 2.1 below. The default initial high-voltage settings have been determined during laboratory

Table 2.1: GLOWS operation modes

Operation mode	Comments/Remarks	Related sections
Normal science operations	basic regular daily operations	Section 8.1
In-flight voltage tests	regular, once per month	Section 8.2.1
Initial calibration and high-voltage ramp-up	during the commissioning phase	beginning of Section 8

pre-launch tests. The initial calibration will be tested via high-voltage ramp-up procedures during the commissioning phase after launch (see Section 8). Normal science operations involve day and night modes, as discussed in Section 8.1. Regular in-flight voltage tests are anticipated to determine the optimum operation voltages and other event-detection parameters (see Section 8.2.1).

- **Types of data generated onboard** are listed in Table 2.2 and briefly discussed in Section 2.2 below. A more detailed discussion of the data types is provided at the beginning of Section 3.
- **Telemetry, downlinking priority**. Onboard-generated histograms and direct events are packed into telemetry packets containing also some ancillary data (e.g., block-averaged spin period, instrument temperature, CEM voltage, etc.), described briefly in Section 2.5. Histograms generated onboard are the main highest-priority data product and all of them must be downlinked to the ground. On the contrary, direct events are supporting data and only a portion of them will be downlinked subject to the bit rate available for GLOWS. For direct events there are two types of transfers, the regular daily transfers having a lower priority than the on-demand transfers.

2.2 Types of data generated onboard and transferred in telemetry

Onboard-processing software generates types of data described in Table 2.2. Ancillary onboard data (e.g., block-averaged spin period, instrument temperature, etc.), described briefly in Section 2.5 below, are not listed here as a separate category because they are assumed to be included in the HB, DE, and HK data. Housekeeping and diagnostic data are normally expected to be out of the scope of the Science Team work, but may be useful in an abnormal/emergency situation.

2.3 Direct events

Direct events are understood as timestamps of photon detection events and their durations (pulse lengths). A brief description of direct events in the context of onboard processing is provided above in Section 2.1. A more general discussion of direct events is provided in Section 9, which is summarized in Section 9.1.

Table 2.2: Types of data generated by GLOWS onboard-processing software

Type of data	Comments/Remarks	Related sections
Histograms (HB)	main science data	Sections 10, 12.4-12.7
Direct Events (DE)	used onboard for histogramming, considered as supporting data in ground processing	Sections 11.3, 9, 12.4-12.6
Housekeeping data (HK)		Section 12.5.3, beginning of Section 3
Diagnostic data		beginning of Section 3

- **Direct-events collection**. Direct events are collected over entire observation days (including day and night modes discussed in Section 8.1). After downlinking, direct events can be histogrammed on the ground. See Section 9.1.1 for more details.
- **File format for onboard storage**. Direct events are stored onboard in one-second sectors stacked into one-minute files. Individual spins and blocks of spins (the same blocks that are used for histogramming) can be identified with the time resolution corresponding to the sectors, extracted from instrument memory and sent by telemetry to the ground. Direct events are stored onboard compressed as time differences as discussed in Section 9.1.2, only the first direct event in a given second will be stored as the full time stamp. Available onboard memory and partitioning scheme guarantee a retention time of ∼24 days, which enables an emergency on-demand downlinking.
- **Regular daily downlinking: selection of blocks**. Direct events from a given observation day are sent by telemetry on the next observation day (i.e., Spin Axis Pointing in the IMAP lingo). Blocks with the maximum and minimum number of counts are identified and downlinked. Other blocks for downlinking are evenly distributed over a given observation day, the order of downlinking is determined using the bisection method (see Section 9.3). For the minimum and maximum block, also adjacent blocks (preceding and following) are transferred to the ground. A direct-event block for downlinking is composed of full seconds of direct events during which a requested histogram was collected. The regular daily downlinking has a lower priority than on-demand transfers. The allocated telemetry band allows for downlinking of DEs for $\sim$ 13 histograms per observation day for the mean counting rate 3.37×600 cps, expected based on simulations and ground calibration. Section 9.1.3 describes the regular downlinking process a more detail.
- **On-demand downlinking**. "Historical" blocks of direct events that are stored onboard can be downloaded with telemetry commands. This option should be considered as the last resort in an emergency situation, when ground analysis of onboard-generated histograms reveals serious issues. Telemetry command determine start second and offset for a given block of DE seconds to be downlinked to the ground. By default, it is planned that direct-event data ensembles downlinked in this mode correspond to a selected histogram with adjacent seconds. The on-demand transfers have a higher priority than the regular daily transfers of direct events, but a lower priority than the histogram transfers. See Section 9.1.4 for more details.
- **Direct-events telemetry content**. In Section 3.4.2, a list of items in unpacked telemetry for direct events (Level-0/Level-1A data product) is discussed. See Sections 3.4.2, 9.1.5, and 12.5.2 for more details.
- **Daily amount of downlinked direct events**. Section 9.2 presents an assessment of the number of blocks (histograms) for which direct events are downlinked daily. The minimum and maximum blocks plus the adjacent blocks make 6 blocks. The bandwidth available for GLOWS during normal science operations allows for 7 more blocks, which makes 13 blocks in total.

2.4 Histograms

Histograms are understood as lightcurves of the photon flux intensity along the scanning circle, computed from direct events accumulated in bins organized by spin angle of the spacecraft. A brief introduction to histogramming

in the context of onboard processing is provided above in Section 2.1. A more detailed discussion is provided in Section 10), which is summarized in Section 10.1.

- **Histogramming algorithm.** Algorithm 2 in Section 10.4 was selected as more convenient for implementation. The histogram is generated once after the current block end is detected. The time and status messages broadcast by IMAP to the instruments are expected to contain the estimated spin phase, which is critical for histogramming.
- **Histogram-related parameters**. Histograms with n_{bin} bins are accumulated over time intervals corresponding to blocks of n_{block} spins. The onboard-histogram resolution (i.e., the default value of n_{bin}) is adjustable in flight and determined by the science team based on considerations discussed in Section 10.3. The spin-block length (i.e., the default value of n_{block}) results from particle-background-removal capability as discussed in Section 10.2. Each histogram bin is encoded on $d = 8$ bits, the default value of d is determined in Section 10.5. The adopted default values of all histogram-related parameters are given in Table 0.1. See Section 10.1.2 for more details.
- **(Lack of) Onboard storage**. The histograms are not stored in the GLOWS memory but immediately after generation sent out to the main IMAP SSR memory for downlinking during DSN contacts.
- **Downlinking, histogram-telemetry content**. The flight software guarantees downlinking of all onboard-generated histograms to the ground as the highest-priority functionality. Section 3.4.1 contains a list of expected items in unpacked telemetry blocks (Level-0/Level-1A data product). See Sections 3.4.1, 10.1.4, and 12.5.1 for more details.
- **Spin-phase angle**. The spin-phase angle provided by the IMAP observatory in time and status messages is used for histograms generated onboard. However, GLOWS-boresight-azimuth-corrected values of the spin angle are used in higher-level ground-generated data products (Level-2 and Level-3A). See Sections 10.1.5 and 10.6 for more details.

2.5 Ancillary onboard-collected data

Some onboard-collected data are additionally included in the histogram and direct-events telemetry packets. These data include times (GLOWS and IMAP clocks) and over-block averages and variances of the temperature, CEM voltage, spin period, and length of event impulse. A more detailed discussion can be found in Section 11.

- **Ancillary-telemetry content**. Sections 3.4.1 and 12.2 contain expected ancillary-data items in unpacked telemetry blocks for histograms (Level-0/Level-1A data product). To enable direct-event-based histogramming on the ground, direct-events CCSDS packets contain ancillary data (`data_every_second` structure) as used by the histogramming algorithm. See Table 3.2 and Section 11.1.1 for more details.
- **Ancillary-data encoding**. Generally, ancillary data collected onboard will be encoded as integer numbers. The onboard-encoding and ground-decoding procedures are discussed in Section 11.4. In particular, Equations (40) and (44) will be used for encoding-decoding purposes with conversion coefficients summarized in Table 11.1. See Section 11.1.2 for more details.

3 A draft of data ground-processing algorithm for IMAP GLOWS from Level-0 to Level-2

This section is intended to contain a brief description of data products from Level-0 to Level-2. Extended studies/analyses for these levels are expected to be included in Sec. 12, where early ideas on data structures are covered as well. Higher-level data products are described in Sec. 4.

Details of instrument operations (the process of data acquisition and the histogram forming onboard, unpacking the telemetry, etc.) are discussed in Sec. 8. This section is based on the *Draft Data Processing Report* (Bzowski et al., 2020), which is inserted in this document and appropriately adapted to connect with later sections of this document.

The data that GLOWS puts into the IMAP telemetry are the following:

1. Science data (the histograms; this is the main topic of this section)

2. Supporting data (Direct Events)
3. Housekeeping data (HK), with the following subcategories:
   - HK Full (full HK data packet)
   - HK Brief, including health flags and baseline HK parameter values that are likely to be used in science data analysis
4. Diagnostic data, including
   - Flight Software Memory Dump
   - Flight Software Boot Report

This section focuses on items 1 and 2. Items 3 and 4 are described in a separate engineering document.

3.1 Objective

The objective of the Level-0-to-Level-2 processing discussed in Sec. 3 is to provide a calibrated daily lightcurve of the photon flux in physical units (Rayleighs) based on the observed daily count numbers. Direct events (supporting data) are processed from Level-0 to Level-1B. Sources of the expected signal are discussed in Section 5. Requirements for the data system are discussed in Section 6.

3.2 Input for Level-0-to-Level-2 ground-processing pipeline

1. **GLOWS-instrument telemetry**

   Daily series of histograms (by default $n_{\rm bin} = 3600$, see Section 10.3 and Table 0.1) with the observed counts as a function of the spin angle, accumulated during a block of IMAP spins (by default $n_{\rm block} = 8$, see Section 10.2 and Table 0.1). The count number in the i-th bin of the histogram is denoted here by H_i, i going from 1 to $n_{\rm bin}$. Each bin has an associated spin angle $\psi_i = 360^\circ/n_{\rm bin}(i - 1/2) = 0.1^\circ(i - 0.5)$, which means that the left edge (not the center!) of the first bin is set to $\psi = 0$.

   The histograms are supplemented by **onboard-collected ancillary information** on the observation time (see Section 12.2.1) and the voltage, filter temperature, spin period, mean length of the event impulse (see Section 12.2.2).

   Direct events. GLOWS telemetry includes also photon detection times (so-called direct events), which are understood as supporting data. Direct events can be histogrammed on the ground to obtain ground equivalent of block-accumulated histograms that are normally generated onboard. Due to telemetry limits only a small part of all direct events collected onboard will be downlinked to the ground.

2. **Ancillary data** (expected to be provided by the SDC/POC/MOC during ground-processing of GLOWS data)

   Additional ancillary parameters that were not collected by the GLOWS instrument, but are included in the general IMAP telemetry or expected to be provided by IMAP SOC . These parameters characterize the spin period (recorded at a high time cadence and possibly corrected in ground postprocessing), position-angle offset for GLOWS, spin-axis orientation, satellite position and velocity, etc. See Section 12.1.2

3. **Input provided by the GLOWS team**

   Some pre-defined input will be provided by the GLOWS team to SDC in the form of files to be used in the ground-processing pipeline. These items are listed below. Generally for GLOWS it is important to distinguish between **bad times** (meaning that a given block is problematic as a whole, see Sec. 12.7.1) and **bad angles** (meaning that individual histogram bins are problematic, see e.g., Sec. 12.7.6).

   Maps (catalogs) of UV point sources (e.g., stars) and excluded regions (e.g., galactic belt) will be provided by the GLOWS team in the form of files (see items 1 and 3 in Sec. 3.12), possibly updated

during the mission. GLOWS scanning-circle points (histogram bins) located close to the points in the maps will be marked by bad-angle flags in GLOWS data products. The bad-angle bins are expected to be identified in the SDC ground-processing pipeline using an algorithm provided by the GLOWS team as described in Section 12.7.6.

Bad-time/bad-angle flag arrays (see item 4 in Section 3.12) are planned to be provided by the GLOWS team if any problematic blocks will be identified by the instrument team. These flag arrays are expected to give the instrument team the possibility of marking bad-time/bad-angle blocks in future releases of data products.

Suspected-transient-event flag arrays (see item 5 in Section 3.12) are planned to be provided by the GLOWS team as pointing to bins possibly strongly affected by transient events (e.g., a comet passing close to the Sun). The flag arrays will be handled similarly to bad-time/bad-angle flag arrays described above.

Conversion table (see item 2 in Sec. 3.12) for ancillary parameters (such as temperature, voltage, spin period, pulse length) that are collected onboard as integers. Using the table, onboard units are converted to physical units. The conversion can be by a simple linear relation, but for some quantities (e.g., temperature) it can be a nonlinear relation that requires more parameters except for the temperature, where the relation can be nonlinear. The conversion methods are described in Section 11.4, including squared quantities, encoded as integer numbers.

Calibration factor to convert cts/s measured by the instrument to physical units of Rayleighs (see item 6 in Sec. 3.12 and Section 12.7.5). The calibration factor will be provided by the GLOWS team before launch (based on ground calibration) and possibly updated during the mission (using in-flight calibration), if needed.

Pipeline settings (processing parameters) (see item 9 in Section 3.12) are required for the ground-processing pipeline to be defined by the GLOWS team. These parameters include, e.g., set of active flags for bad times and bad angles, angular distance for exclusion regions, and other parameters.

3.3 Ground-processing pipeline from Level-0 to Level-2 – overview

We present here an overview of the ground data-processing pipeline, additional information can be found in Section 12.

The high-level flowchart shown in Figure 3.1 presents the ground-processing pipeline for the science data from the GLOWS instrument. The flow of information is visualized for various levels of histogram data products and direct-events-related products.

3.3.1 Overview of histograms

Histograms are generated onboard by the flight software. Timestamps of direct events are collected by the flight software, which implies registration in the time domain. The software keeps track of GLOWS-clock readings for incoming PPS/ITF packets and the spin-phase information in time and status messages. This makes it possible to relate GLOWS-clock time with the spin-phase angle and use this information to generate histograms in the spin-phase domain.

More information on the histogramming algorithm can be found in Sections 2.4 and 10.4.

3.3.2 Overview of direct events

Direct Events (DE) are not used in the regular science analysis. They are rather considered as Supporting Data that provide more technical information on operations of the instrument and allow for an in-depth analysis of the signal in search for things such as the presence or absence of a noise (white or colored), which is not expected but may turn out to be present, for estimation of the instrument dead time (and its evolution during the mission, which is not expected, but who knows), etc. Downloaded direct events cover only a small portion of all direct events collected by the instrument but they are suitable to be fed into a ground version of the on-board GLOWS

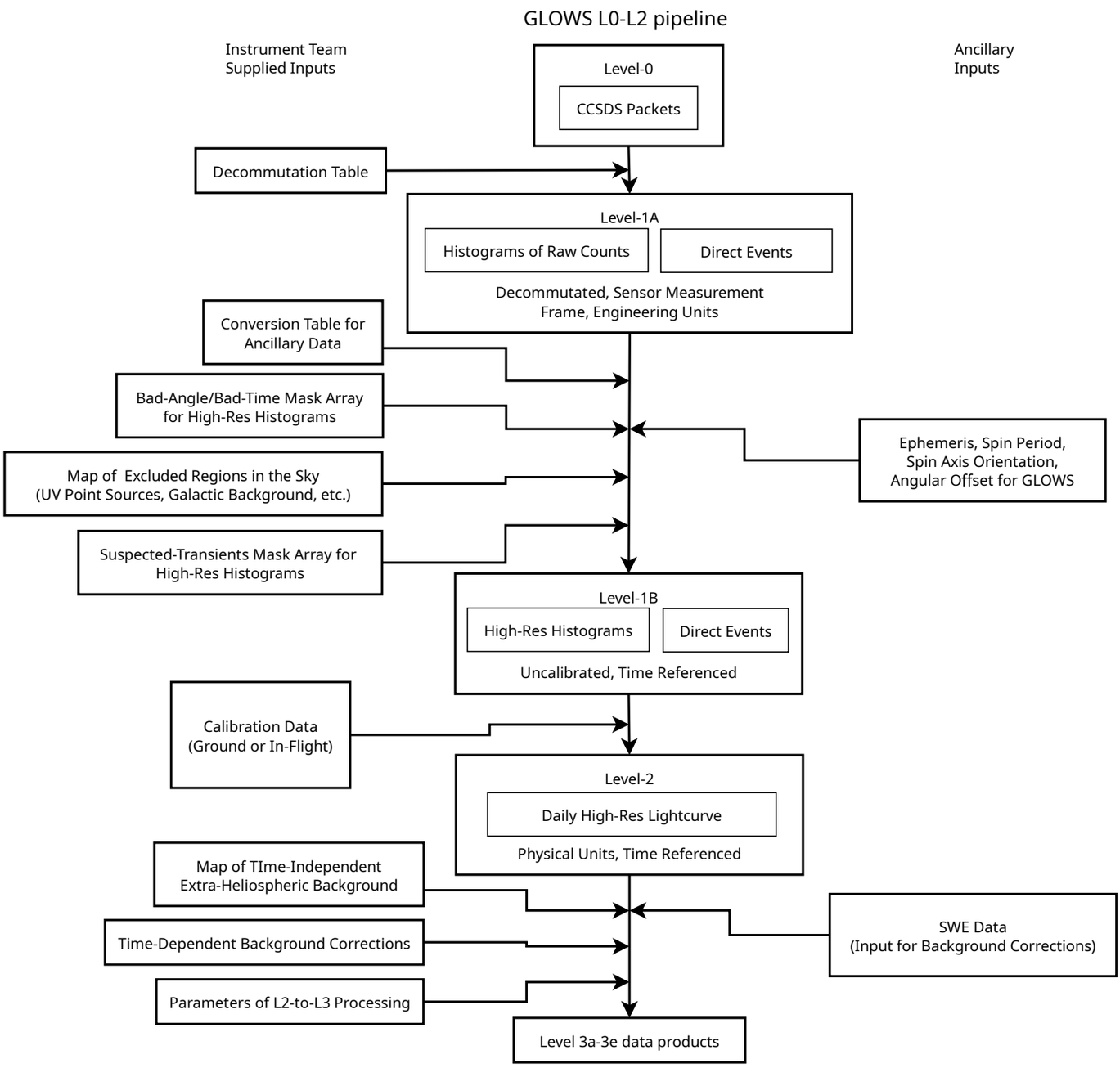


Figure 3.1: Ground-processing flowchart for IMAP/GLOWS from Level-0 to Level-2. Daily Hi-Res Lightcurve at Level-2 should be understood as accumulated over a given observational day (i.e., a time interval when the IMAP spin axis pointing is nominally fixed). A similar flowchart for Level-3+ pipeline is shown in Fig. 4.1.

software and production of the histograms, which subsequently can be fed into the regular data pipeline. Not planned as a regular operation, rather in contingency, in case of unexpected events, etc.

Selection of direct events for downlinking. A portion of DE will be regularly downloaded for ground analysis of instrument operation during science operations. An individual DE datum is the event registration time. DEs are sent in chunks containing one second of data. They will be grouped in blocks spanning over the time range of $n_{\rm block}$-spin histogram (the boundary seconds also include data from the outside of the given block). By default, data from the time interval between one spin axis repointing maneuver and another will be analyzed to identify blocks with the biggest and the smallest count numbers $C_{\rm block,max}$ and $C_{\rm block,min}$, respectively. With these two blocks identified, the data intervals centered at these two blocks will be defined. These two intervals will be composed of $2k_{\rm DE}+1$ blocks, centered at the blocks with $C_{\rm block,max}$ and $C_{\rm block,min}$ counts. The magnitude of $k_{\rm DE}$ is adopted as $k_{\rm DE}=1$, but can be changed if necessary during the mission. These intervals will be downlinked anyway.

This selection leaves DE intervals equivalent to 13 blocks corresponding to $n_{\rm bin}$-spin histograms to be downloaded daily within the telemetry bandwidth available for GLOWS (Section 9.3). Within this limit, the blocks to download are selected as follows. The blocks corresponding to max- and min-counts histograms plus the adjacent blocks make 6 blocks. The bandwidth available for GLOWS during normal science operations allows for 7 more blocks, which makes 13 blocks per observational day in total. The order of downlinking the 7 blocks is determined using the bisection method (see Section 9.3).

In addition, some blocks may be downloaded on-demand, i.e., a ground command lists the blocks that the GLOWS team wants to be downloaded. These blocks are downloaded with the higher priority than the automatically-selected blocks discussed above. A resumption of the DE blocks selected automatically using the algorithm described above is performed after downloading the on-demand blocks.

Both regular daily transfers of DE and on-demand transfers are organized in dumps containing an integer number of seconds. For the daily transfers the direct-event dumps contain the photon detection times from three adjacent histogram blocks, with full-second margins at the begining and the end. Therefore the direct-event dumps need to be filtered on the ground by block-start and block-end times for histograms to obtain ground equivalents of histograms generated onboard by the GLOWS instrument. For on-demand transfers DE packets may have different lenght in seconds, depending on parameters of the telecommand used for selection of time intervals for downlinking.

3.3.3 Organization of GLOWS data – "per pointing"

In terms of the concept of operations (CONOPS) for the IMAP satellite the discussion presented in this section is based largely on GSWG on Nov 16, 2023. SDC-related issues were discussed during SDWG on Nov 16, 2023.

Generally two types of maneuvers will be performed for IMAP: daily repointing and ΔV (which includes trajectory-correction maneuvers TCM, station-keeping maneuvers SKM, and spin-rate adjustments).

GLOWS data products from Level-1A up were agreed to be organized in observational days on fixed-pointing basis. A pointing counter is expected to be run by POC/MOC/SDC, which is increased at each daily-repointing or ΔV maneuver. The repoint information is added to the UTC time field in data-product file names. Details of the file name convention (including repoint information) are described in the SDC documentation.

GLOWS histograms. The following definitions of the start/end time for observational days will be used:

- Daily repointing. By default HV bias on GLOWS is not decreased for daily repointing maneuvers. Thus histograms are collected continuously (i.e., also during the observational night). POC/MOC provide the repointing start time t_0 (it occurs 60 minutes after the repointing maneuver flag RMF is raised). RMF is cleared 34 minutes after t_0. Then IMAP-Lo pivot motion begins, its duration varies from 2.5 to 12.5 minutes (see Figure 8.1). However, note that during ΔV maneuvers the instrument is turned off as discussed below.
  - Level-0. Level-0 is organized on per-pointing basis in the SDC processing pipeline. The SDC software uses pointing-based WebPODA queries to download Level-0 data for further processing. MET field from CCSDS header is used by POC/MOC to decide which pointing a given histogram or DE packet belongs to. Since histograms are sent out by the instrument within seconds after their generation,

the CCSDS-MET-based rule is expected to work correctly for them. DE packets are sent out by the instrument with a delay, which implies that additional operations in the pipeline are needed to properly associate DE timestamps with the pointing number in SDC data products.

  - Level-1A/1B are organized by observational days (on per-pointing basis) similarly to Level-0.
  - Level-2 is also organized by observational days (on per-pointing basis). However only a subset of Level-1B histograms is used for computations of daily Level-2 histogram, because a number of histograms around the IMAP repointing maneuver is excluded as possibly affected by the maneuver (see item 2 in Section 3.9.1 for details).

- GLOWS is powered off during ΔV maneuvers. The power-offs can last two hours or even more, thus a natural gap appears in GLOWS histograms for this type of maneuvers. RMF is expected to be set and cleared after ΔV maneuvers. Note that, e.g., spin-rate adjustments may only slightly change the spin axis pointing, thus the question if ΔV maneuvers are considered as repointings is not trivial. Since GLOWS data processing in SDC is organized based on the official repointing table provided by POC/MOC, the definition of observational days in official data products for GLOWS is based on this table. The definition may change by the GLOWS team if found necessary during the mission.

Possible influence of IMAP-Lo pivot motion (expected after some repointings) on GLOWS histograms will be investigated during the mission.

Direct events. These are supporting data devised to be used by scientists in non-automatic processing. Similarly to histograms, the direct events will organized on per-pointing basis.

3.4 Level-0 data products

It is assumed that Level-0 data is a file `imap_glows_l0_raw_{date}-repoint{repoint number}_v{version}.pkts` containing a binary stream of CCSDS packets with headers for a given observational day. Observational day as a whole is understood as the time interval between two consecutive IMAP repointing maneuvers. APID field in CCSDS header (see Table 3.1) is used to distinguish between different packets (histograms, direct events, housekeeping, telecommands, etc.). Packets with APID=1480 (0x5c8) contain histograms, while APID=1481

Table 3.1: Brief description of 80-bit CCSDS header (Level-0 data).

No.	Item	number of bits	Comments/Remarks
1	`CCSDS_VER`	3	CCSDS Packet Version Number
2	`CCSDS_TYPE`	1	CCSDS Packet Type Indicator
3	`CCSDS_SEC_HDR_FLAG`	1	CCSDS Packet Secondary Header Flag
4	`CCSDS_APID`	11	CCSDS Packet Application Process ID
5	`CCSDS_GRP_FLAG`	2	CCSDS Packet Grouping Flags
6	`CCSDS_SSC`	14	CCSDS Packet Sequence Count
7	`CCSDS_PKT_DATA_LN`	16	CCSDS Packet Length
8	`CCSDS_MET`	32	CCSDS Packet 2nd Header Coarse Time (SCLK)

(0x5c9) identifies direct events. Packets with other APIDs are ignored by the SDC processing algorithm for GLOWS.

3.4.1 Level-0 Histograms

Each CCSDS packet consists of the 80-bit header described in Table 3.1 followed by packet data, which for GLOWS histograms (APID=0x5c8) contains the fields listed below in this section. The first uppercase name refers to the telemetry definition in the sheet `P_GLX_TMSCHIST` of the file `TLM_GLX_YYYY_MM_DD.xlsx`, while the second lowercase name refers to the same quantity in test Python scripts developed by the GLOWS team and provided to the SDC. The fields in the histogram CCSDS packet are as follows.

1. `STARTID` or `first_spin_id_in_block`, length in bits: 32. Ordinal number of the first IMAP spin ID in the block.
2. `ENDID` or `diff_spin_id_in_block`, length in bits: 16. Difference of the last ID in the block with respect to the first ID. Note that the name `ENDID` can be misleading in this context, but it is used here for consistency with the telemetry definition file `TLM_GLX_2023_05_22.xlsx`.
3. `FLAGS` or `histogram_validity_flags`, length in bits: 16. Flags for extra information (e.g., test or normal operation) see Sec. 12.3.
4. `SWVER` or `software_version`, length in bits: 24. Version of flight software used for generation of histogram.
5. `SEC` or `imap_start_time_second`, length in bits: 32. Seconds of IMAP-clock start time for the histogram block, specified as a number of IMAP seconds since start from IMAP epoch as defined in GI ICD, see Sec.12.2.1.
6. `SUBSEC` or `imap_start_time_subsecond`, length in bits: 24. Subseconds of the IMAP-clock start time for the histogram block. Subsecond field is computed by GLOWS flight software onboard by interpolation based on GLOWS-internal-clock readings. The maximum number of subseconds is 2000000. See Sec.12.2.1.
7. `OFFSETSEC` or `imap_diff_second`, length in bits: 16. Seconds of IMAP-clock end-time offset for the histogram block. See Sec. 12.2.1.
8. `OFFSETSUBSEC` or `imap_diff_subsecond`, length in bits: 24. Subseconds of the IMAP-clock end-time offset for the histogram block. The maximum number of subseconds is 2000000. See Sec. 12.2.1.
9. `GLXSEC` or `glows_start_time_second`, length in bits: 32. Seconds of GLOWS-clock start time for the histogram block. Value read from internal SCIENCE timer of GLOWS. See Sec. 12.2.1
10. `GLXSUBSEC` or `glows_start_time_subsecond` length in bits: 24. Subseconds of the GLOWS-clock start time for the histogram block. Value read from internal SCIENCE timer of GLOWS. The maximum number of subseconds is 2000000. See Sec. 12.2.1.
11. `GLXOFFSEC` or `glows_diff_second`, length in bits: 16. Seconds of the GLOWS-clock end-time offset for the histogram block. Value read from internal SCIENCE timer of GLOWS. See Sec. 12.2.1.
12. `GLXOFFSUBSEC` or `glows_diff_subsecond`, length in bits: 24. Subseconds of the GLOWS-clock end-time offset for the histogram block. Value read from internal SCIENCE timer of GLOWS. The maximum number of subseconds is 2000000. See Sec. 12.2.1.
13. `SPINS` or `number_of_spins_per_block`, length in bits: 8. Number of spins in the histogram. Taken from configuration parameters of GLOWS flight software and included in the science telemetry to cross-verify the values of item 2 during ground processing.
14. `NBINS` or `number_of_bins_per_histogram`, length in bits: 16. Number of bins in the histogram.

15. `TEMPAVG` or `filter_temperature_average`, length in bits: 8. Block-averaged mean filter temperature encoded as unsigned integer, see encoding in Eq. (37).

16. `TEMPVAR` or `filter_temperature_variance`, length in bits: 16. Variance of filter temperature encoded as unsigned integer, see encoding in Eq. (43).

17. `HVAVG` or `hv_voltage_average`, length in bits: 16. Block-averaged HV voltage on the channeltron encoded as unsigned integer, see encoding in Eq. (37).

18. `HVVAR` or `hv_voltage_variance`, length in bits: 32. Variance of the HV voltage on the channeltron, encoded as unsigned integer, see encoding in Eq. (43).

19. `SPAVG` or `spin_period_average`, length in bits: 16. Block-averaged spin period used in onboard histogramming encoded as unsigned integer, see encoding in Eq. (37).

20. `SPVAR` or `spin_period_variance`, length in bits: 32. Variance of spin period, encoded as unsigned integer, see encoding in Eq. (43).

21. `ELAVG` or `pulse_length_average`, length in bits: 8. Block-averaged length of event impulse, encoded as unsigned integer, see encoding in Eq. (37).

22. `ELVAR` or `pulse_length_variance`, length in bits: 16. Variance of event-impulse length, encoded as unsigned integer, see encoding in Eq. (43)

23. `EVENTS` or `number_of_events`, length in bits: 32. The total number of events in histogram.

24. `HISTTAB` or `histogram`, length in bits: `number_of_bins_per_histogram*8`. Histogram array, block-accumulated count numbers for bins evenly distributed on the GLOWS scanning circle. IMAP spin angle values ψ are used here instead of GLOWS position angle ψ_{PA}, see Sec. 10.6.

Bytes should be read as big-endian. For block-averaged quantities the formulas for the average and variance are discussed in Sec. 11.2.

3.4.2 Level-0 Direct Events

Direct events are downlinked in packets containing one second of data. If the number of direct events is large and one second of data exceeds the size limit for CCSDS packets, a given portion of data is split into multiple packets.

After the 80-bit CCSDS header described in Tab. 3.1, in packets with APID=0x5c9, the direct event data are included with the fields listed below in this section. The first uppercase name refers to the telemetry definition in the sheet `P_GLX_TMSCDE` of the file `TLM_GLX_YYYY_MM_DD.xlsx`, while the second lowercase name refers to the same quantity in test Python scripts developed by the GLOWS team and provided to the SDC. The fields in the direct-event CCSDS packet are as follows.

1. `SEC` or `imap_start_time_second`, length in bits: 32. IMAP-clock start time (full second) for direct events in the packet, specified as the number of IMAP seconds from IMAP epoch as defined in GI ICD, see Sec.12.2.1.

2. `LEN` or `number_of_de_packets`, length in bits: 16. Number of packets containing a given second of data. It is > 1 if a given portion (one second) of data is split into multiple CCSDS packets.

3. `SEQ` or `seq_num_of_de_packet`, length in bits: 16. Number of a given CCSDS packet in a sequence of multiple CCSDS packets containing one second of data splitted.

4. `DATA` or `de_data`, length in bits: variable (even number smaller than the max size of CCSDS packet). Direct event data, detailed description is given below.

The field number 4 may have different structure depending on the values of the fields 2 and 3.

If both `LEN/number_of_de_packets` and `SEQ/seq_num_of_de_packet` are zeros, then a given packet does not contain any useful data. Such packet may appear, e.g., when a requested second of DE was not found in the instrument memory.

If `LEN/number_of_de_packets` is not zero but `SEQ/seq_num_of_de_packet` is equal to zero (a single packet or the first packet in a sequence), the field `DATA/de_data` contains the following items:

1. `data_every_second` structure, length in bits: 320. See Table 3.2 for details.
2. the first direct event (during the current second of direct events) encoded as the full timestamp, length in bits: 64. See Table 3.3 for details.
3. sequence of direct events (length in bits: variable) encoded in two possible ways:
   (a) compressed direct events saved as time offset (16 or 24 bits) + impulse length (8 bits). See Table 3.4 for more details.
   (b) saved as the full timestamp (including impulse length, see Table 3.3) if a time offset relative to the previous event is too large to be encoded on 24 bits.

Table 3.2: Description of data-every-second structure used by the GLOWS histogramming algorithm onboard and attached to each second of direct events downlinked in CCSDS packets. Item names refer to test Python scripts developed by the GLOWS team.

Level-0 (also Level-1A), direct events: content of data-every-second structure			
No.	Item	Size in bits	Comments/Remarks
1	`imap_sclk_last_pps`	32	IMAP seconds for the last PPS
2	`glows_sclk_last_pps`	32	GLOWS seconds for the last PPS
3	`glows_ssclk_last_pps`	32	GLOWS subseconds for the last PPS
4	`imap_sclk_next_pps`	32	IMAP seconds for the next PPS
5	`catbed_heater_active`	8	flag
6	`spin_period_valid`	8	flag
7	`spin_phase_at_next_pps_valid`	8	flag
8	`spin_period_source`	8	flag
9	`spin_period`	16	uint encoded value, see Sec. 11.4
10	`spin_phase_at_next_pps`	16	uint encoded value, see Sec. 11.4
11	`number_of_completed_spins`	32	provided onboard by IMAP to GLOWS
12	`filter_temperature`	16	uint encoded value, see Sec. 11.4
13	`hv_voltage`	16	uint encoded value, see Sec. 11.4
14	`glows_time_on_pps_valid`	8	flag
15	`time_status_valid`	8	flag
16	`housekeeping_valid`	8	flag
17	`is_pps_autogenerated`	8	flag
18	`hv_test_in_progress`	8	flag
19	`pulse_test_in_progress`	8	flag
20	`memory_error_detected`	8	flag
21	`zero_padding`	8	filling up to even number of bytes

If `seq_num_of_de_packet` is larger than 0 (and `number_of_de_packets` is larger than 1), it means that multiple-packet splitting occurred and a given packet is a continuation of the previous one. Then it contains

Table 3.3: Description of full timestamp for direct events. Sequence of items is from the most significant bits. Item names refer to test Python scripts developed by the GLOWS team.

Level-0, direct events: content of full timestamp structure			
No.	Item	Size in bits	Comments/Remarks
1	`marker`	2	0x0 means full timestamp
2	`seconds`	30	seconds of the GLOWS clock
3	`impulse_length`	8	length (in 50-ns units) of an impulse associated with the current direct event
4	`multi_event`	1	Flag equal to True if event is marked by FPGA as multi event. According to KPLabs it is currently not used by GLOWS flight software and always set to False.
5		2	not used bits, according to the flight software provider they are not always necessarily set to 0
6	`subseconds`	21	subseconds (ticks) of the GLOWS clock

Table 3.4: Description of time offset for direct events. Sequence of items is from the most significant bits. Item names refer to test Python scripts developed by the GLOWS team.

Level-0, direct events: content of time offset structure			
No.	Item	Size in bits	Comments/Remarks
1	`marker`	2	0x2 means 2-byte encoding, 0x3 – 3-byte encoding
2	`offset`	14 or 22	time offset (GLOWS-clock ticks) of the current direct event relative to the previous direct event
3	`impulse_length`	8	length (in 50-ns units) of impulse associated with the current direct event

only a sequence of direct events (item 3 in the list above), which is an extension of the direct events from the previous packet. Note that the splitting process is performed at the layer of bytes (not at the layer of direct events), so a given direct event may be splitted between two subsequent CCSDS packets. Therefore, it is convenient in the first step to merge splitted packages into one, and then in the second step parse the binary stream to identify encoding for each direct event and decode it into full timestamp using the previous event.

For full timestamps or time offsets, two most significant bits define `marker` (see the first item in Tabs. 3.3 and 3.4), which contains information about the number of bytes used for encoding a given direct event. The value 0x0 denotes the full timestamp, 0x2 – two bytes (14=16-2 bits for the offset), 0x3 – three bytes (22=24-2 bits for the offset).

The CCSDS packets are required to have even number of bytes. So if the number of bytes is odd for a given direct-event packet, then zero-byte padding is applied at the end.

Bytes should be read as big-endian.

3.5 Level-0 to Level-1A processing

GLOWS processing from Level-0 to Level-1A generally consists in decommutating CCSDS packets with APIDs 0x5c8 and 0x5c9 from the binary stream and saving the content of the packets as a human-readable data structure. Level-1A data are understood as unpacked telemetry blocks.

3.5.1 Level-0 to Level-1A processing: histograms

The processing consists in converting the 24 fields listed in Sec. 3.4.1 (Level-0 binary stream) into a human-readable data structure (Level-1A).

One of bad-time filters for GLOWS histograms is based on comparison of the total numbers of counts in a given block-accumulated histogram with the daily average (deviations by n-sigma and more are interpreted as being beyond daily statistical error). This type of flagging will be performed between Level-1A and Level-1B but to do this, the daily average number of the total counts in block-accumulated histogram needs to be known a priori. Therefore, it is convenient to save the total number of counts for each block when generating Level-1A data for a given observational day, compute the daily average and use this saved information later during generation of Level-1B data.

The onboard flags are simply copied (encoded as unsigned integer) to Level-1A structure for histograms. An additional flag (`is_generated_on_ground`) is also attached at this stage to indicate whether a given histogram was generated onboard or on the ground (i.e., from downlinked direct events).

3.5.2 Level-0 to Level-1A processing: direct events

The processing consists in converting the four fields SEC, LEN, SEQ, DATA listed in Sec. 3.4.2) (Level-0 binary stream) into a human-readable data structure (Level-1A). This can be achieved in the following steps:

1. The field `LEN/number_of_de_packets` makes it possible to check if a given second of direct events was splitted into multiple packets. If so, it is convenient to merge the fields `DATA/de_data` from the splitted packets into one binary stream before any further processing. It is assumed in the next steps that splitted packets are merged into one data stream.

2. Read `data_every_second` structure (320 bits, see Tab. 3.2) from the `DATA/de_data` binary stream.

3. Read the full timestamp (64 bits, see Tab. 3.3) of the first direct event in the `DATA/de_data` binary stream.

4. Read the sequence of time offsets or full timestamps by following the two steps below in a loop:

   (a) Read one byte which allows us to determine the value of the 2-bit `marker` (see the first item in Tabs. 3.3 and 3.4). This marker determines the additional number of bytes to be read after (0x0 – 7 bytes, 0x2 – 1 byte, 0x3 – 2 bytes) and tells us if we are reading a timestamp (0x0) or an offset (0x2 or 0x3).

(b) Read the additional bytes from step 4(a), which encode (together with the 6 least significant bits of the first byte) either the offset or the full timestamp. The bytes containing the full timestamp can be decoded using Tab. 3.3, and the offset can be decoded using Tab. 3.4. If the offset is read, then add it to the previous timestamp to get the current timestamp.

3.6 Level-1A data products

Listing of the fields of Level-1A data structure is provided in Tab. 3.5 for histograms and in Tab. 3.6 for direct events.

Table 3.5: Brief description of GLOWS Level-1A histogram-binned data product (see Sec. 12.5 for details). Level-1A data are understood as unpacked telemetry blocks. A given histogram is accumulated over n_{block} spins and contains n_{bin} bins. Item names refer to test Python scripts developed by the GLOWS team.

Level 1A: high-resolution histograms of photon counts vs. spin angle		
No.	Item	Comments/Remarks
1	`first_spin_id_in_block`	ID of the first IMAP spin in the block (histogram identifier)
2	`last_spin_id_in_block`	ID of the last IMAP spin in the block
3	`block_header`	header
3.1	`flight_software_version`	copied from Level-0
3.2	`ground_software_version`	set by ground software
3.3	`pkts_file_name`	name of Level-0 data file (input file for Level-1A)
3.4	`seq_count_in_pkts_file`	sequence counter (per APID) in pkts (Level-0) file
4	`glows_start_time`	start time (GLOWS clock) of the block
5	`glows_end_time_offset`	end-time offset (GLOWS clock) for the block
6	`imap_start_time`	start time (IMAP clock) of the block
7	`imap_end_time_offset`	end-time offset (IMAP clock) for the block
8	`number_of_spins_per_block`	n_{block} [b]
9	`number_of_bins_per_histogram`	n_{bin}
10	`histogram`	array of block-accumulated count numbers
11	`number_of_events`	total number of events/counts in histogram
12	`filter_temperature_average`	block-averaged temperature, uint encoded[a], see Eq. (37
13	`filter_temperature_variance`	variance of the temperature, uint encoded[a], see Eq. (43)
14	`hv_voltage_average`	block-averaged HV voltage on CEM, uint encoded[a], see Eq. (37
15	`hv_voltage_variance`	variance of the HV voltage on CEM, uint encoded[a], see Eq. (43)
16	`spin_period_average`	block-averaged spin period, uint encoded[a], see Eq. (37
17	`spin_period_variance`	variance for the spin period, uint encoded[a], see Eq. (43)
18	`pulse_length_average`	block-averaged impulse length, uint encoded[a], see Eq. (37
19	`pulse_length_variance`	variance for the impulse length, uint encoded[a], see Eq. (43)
20	`flags`	onboard flags + `is_generated_on_ground` flag
20.1	`flags_set_onboard`	copied from Level-0 (`histogram_validity_flags`)
20.2	`is_generated_on_ground`	set by ground software to `false` if histogram generated onboard

[a] all quantities that are averaged and require a unit are integer-value-encoded as described in Sections 11.1.2 and 11.4

[b] taken from configuration parameters of GLOWS FSW and included in the science telemetry to cross-verify the values of items 1 and 2 during ground processing

Times (GLOWS-clock and IMAP-clock based) are kept at Level-1A in the same convention as at Level-0, i.e., as integer-seconds and integer-subseconds.

Ancillary quantities that are encoded onboard as unsigned integers are still kept as integers at Level-1A. The

Table 3.6: Brief description of GLOWS Level-1A direct-events data product. Level-1A data are understood as unpacked telemetry blocks. Item names refer to test Python scripts developed by the GLOWS team.

Level 1A: direct events		
No.	Item	Comments/Remarks
1	`header`	
1.1	`ground_software_version`	set by ground software
1.2	`pkts_file_name`	name of Level-0 data file
1.3	`seq_count_in_pkts_file`	sequence counter (per APID) in pkts (Level-0) file
2	`imap_start_time_seconds`	start time, IMAP clock
3	`number_of_de_packets`	number of packets containing one second of direct events
4	`data_every_second`	structure defined in Tab. 3.2 without `zero_padding` field
5	`direct_events`	array of direct events, structure of each direct event is described in Tab. 3.7

Table 3.7: Structure of single direct event at Level-1A.

Level 1A: single direct event data structure		
No.	Item	Comments/Remarks
1	`seconds`	GLOWS-clock seconds
2	`subseconds`	GLOWS-clock subseconds (clock ticks)
3	`pulse_length`	length (in 50-ns units) of impulse associated with the current direct event

encoding details are discussed in Sec. 11.4.

3.7 Level-1A to Level-1B processing

3.7.1 Level-1A to Level-1B processing: histograms

This processing stage for histograms includes:

1. Converting IMAP and GLOWS times for the start and end of blocks from integer-second/integer-subsecond format to a float with integer part representing seconds and decimal part representing subseconds
2. Decoding onboard-collected flags (`flags_set_onboard` at Level 1A) from integer-encoded value to a simple human-readable structure of bad-time flags
3. Copying the value of `is_generated_on_ground` flag from Level-1A
4. Bad-time masking: generating additional ground-processing-based bad-time flags
5. Bad-angle masking: generating histogram flag array containing information about bad angles
6. Converting integer-encoded values of ancillary parameters (temperature, spin period, HV voltage, pulse length) to physical units. The averages are decoded in a straightforward way. The variances are first decoded and then the standard deviation is computed. Conversion table is provided by the GLOWS team.
7. Adding the averages and standard deviations of ancillary data provided by SDC (spin period, spin axis orientation, IMAP ephemerides, position-angle offset for the GLOWS instrument), see Sec. 11.2 for formulas
8. Generating an IMAP-spin-angle grid for histogram bin centers

At Level-1B two spin period estimations are anticipated. It is assumed that the real-time information on spin phase from the IMAP star tracker will be used by GLOWS during histogramming onboard, which defines the first spin period value (downlinked in the GLOWS telemetry, item 17 in Table 3.8). However, the resulting spin-period value computed onboard by GLOWS processing unit may have substantial uncertainties as compared to a more accurate spin-period value that may be inferred assuming the constancy of the period on time scales much longer than the block interval. Therefore, the instrument team anticipates a possibility of computing a value of the spin period based on the information available during ground processing, using the assumption of constancy or corrections provided by MOC/POC/SOC. This is the ground value (item 21) in Table 3.8.

Bad-angle masking algorithm. There are several reasons why a given bin in a Level-1A histogram can be classified as bad. Tab. 3.11 lists bad-angle flags. Brief summary of the flags:

1. `is_close_to_uv_source`: a given bin is close to a bright UV point source, e.g., a star
2. `is_inside_excluded_region`: a given bin is inside a sky region, which was excluded by the instrument team due to strong expected background that cannot be accurately estimated
3. `is_excluded_by_instr_team`: a given bin was excluded by the GLOWS team as a result of analysis of the observations
4. `is_suspected_transient`: a given bin was marked by the instrument team as most likely affected by transient events, e.g., a comet

For `is_close_to_uv_source` the GLOWS team will provide an ancillary file with data needed to identify bins affected by bright UV sources (see item 3 in Sec. 3.12).

For `is_inside_excluded_region` the GLOWS team will provide a set of directions in the sky that densely cover regions to be excluded (e.g., in the proximity of the galactic plane, see item 1 in Sec. 3.12). The ground processing software needs to check if a given bin in a histogram is closer than `angular_radius_for_excl_regions__deg` (angular distance in degrees predefined in item 9 in Sec. 3.12). If a given bin is closer, an appropriate flag needs to be set to 1, otherwise 0.

Computations of `is_close_to_uv_source` and `is_inside_excluded_region` flags have been implemented in Python scripts provided by the GLOWS team (see Sec. 3.11) using `search_around_sky()` function from `astropy` Python module. This approach allows to compare quickly 3600 histogram-bin positions in the sky against thousends of points defining masked regions and find indexes of bins to be masked.

For the flags `is_excluded_by_instr_team` and `is_suspected_transient`, the GLOWS team will provide two separate ancillary files (see items 4 and 5 in Sec. 3.12) that will contain a list of `unique_block_identifiers` for Level-1B histograms (see Tab. 3.8) and arrays, which contain the flag values 0/1 for all bins of a given histogram. The ground processing software needs to copy the flag values from the ancillary files to the data products. If a given Level-1B histogram is not listed in the ancillary files, the flags are to be to set to 0 by default. The GLOWS team has implemented such algorithm in Python scripts shared with the SDC.

Sec. 12.7.6 contains further clarifications on the bad-angle masking.

3.7.2 Level-1A to Level-1B processing: direct events

This processing stage for direct events includes:

1. Converting IMAP and GLOWS times for the start and end of blocks from integer-second/integer-subsecond format to a float with integer part representing seconds and decimal part representing subseconds
2. Grouping onboard-collected flags included in `data_every_second` structure (see Tab. 3.2) into one sub-structure called `flags`.
3. Converting integer-encoded values of ancillary parameters (temperature, spin period, spin phase, HV voltage) to physical units. Conversion table is provided by the GLOWS team.

4. Converting direct events at Level-1A into variables `direct_event_times` containing timestamps of direct events as floats (GLOWS-clock seconds with decimal part) and `direct_event_pulse_lengths` containing pulse lengths in the physical units of μs TBC.

3.8 Level-1B data products

The listing of the fields of Level-1B histogram data products is provided in Tab. 3.8, details of the header are in Tab. 3.9, bad-time flags are listed in 3.10, and bad-angle flags are listed in 3.11.

The listing of the fields of Level-1B direct-event data products is provided in Tab. 3.12. Automated processing of direct events in the SDC ends at Level-1B.

3.9 Level-1B to Level-2 processing

3.9.1 Level-1B to Level-2 processing (histograms only)

This section describes Level-1B to Level-2 processing for the histograms and it is expected to be consistent with Sec. 12.7, which presents detailed discussion of processing steps and also some early ideas and the intentions of the GLOWS Science team. The Level-1B-to-Level-2 processing includes:

1. Identifying good times, i.e., Level-1B blocks that pass quality criteria defined in a flag mask provided by the GLOWS team (`active_bad_time_flags` section in pipeline settings, item 9 in Sec. 3.12). Conversely bad times are defined as Level-1B blocks that have not passed the criteria. The mask simply says which bad-time flags from Tab. 3.10 are to be taken into account during block rejection. An additional data structure is anticipated here for counters providing information how many times blocks were rejected due to having the true value for a given flag. This structure is expected to keep track of main reasons why blocks are rejected during accumulated over the entire observational day.

2. During accumulation over the entire observational day only histograms with times from $t_0^n + \Delta_0$ to $t_0^{n+1} - \Delta_1$ should be included, where n and $n+1$ denote two subsequent observational days and t_0 is the repointing start time. The time interval $(t_0^n + \Delta_0,\, t_0^{n+1} - \Delta_1)$ defines observational day for GLOWS, while $(t_0^n - \Delta_1,\, t_0^{n+1} + \Delta_0)$ represents so-called GLOWS night.

   Values of the offsets Δ_0 and Δ_1 are generally related to SCSUNRISE and SCSUNSET parameters used by the flight software (see Figure 8.1 and Section 8.1). The two parameters control the time interval around the repointing time t_0 for which `is_night` flag (see item 30.7 in Table 3.10) in GLOWS histograms is raised onboard. Pipeline settings file provided by the GLOWS team (item 9 in Sec. 3.12) defines additionally ground processing parameters `sunrise_offset` and `sunset_offset`. The parameters are understood as corrections to the flight software settings for `is_night` flag. If changes of `is_night` flag are identified in a sequence of Level-1B histograms, then during computations of Level-2 histogram:

   - `is_night` $0 \to 1$ transition should be shifted by `sunset_offset` histograms
   - `is_night` $1 \to 0$ transition should be shifted by `sunrise_offset` histograms.

   Therefore, the following behavior is expected:

   - if `sunrise_offset`$= 0$ (`sunset_offset`$= 0$) then no corrections are needed relative to `is_night` transition set onboard
   - if `sunrise_offset`> 0 (`sunset_offset`> 0) then night extends (shortens) by `sunrise_offset` (`sunset_offset`) histograms relative to `is_night` $1 \to 0$ (`is_night` $0 \to 1$) transition set onboard
   - if `sunrise_offset`< 0 (`sunset_offset`< 0) then night shortens (extends) by `sunrise_offset` (`sunset_offset`) histograms relative to `is_night` $1 \to 0$ (`is_night` $0 \to 1$) transition set onboard

Table 3.8: Brief description of GLOWS Level-1B histogram-binned data product (see Sec. 12.6 for details). Relative to Level 1A, the additional items at Level 1B include the information obtained from general IMAP telemetry: spacecraft location/attitude and spin period characteristics. Also measured onboard-encoded GLOWS parameter values (i.e., times, temperature, CEM voltage, spin period, event-impulse length) included in Level 1A are decoded at the transition to Level 1B using Tab. 11.1. Item names refer to test Python scripts developed by the GLOWS team.

Level 1B: high-resolution histograms of photon counts vs. spin angle with spacecraft location/attitude and spin-period information included		
No.	Item	Comments/Remarks
1	`block_header`	header, see Tab. 3.9
2	`unique_block_identifier`	`YYYY-MM-DDThh:mm:ss` based on IMAP UTC time
3	`glows_start_time`	GLOWS clock, subseconds as decimal part of float, see Sec. 12.2.1
4	`glows_end_time_offset`	GLOWS clock, subseconds as decimal part of float, see Sec. 12.2.1
5	`imap_start_time`	IMAP clock, subseconds as decimal part of float, see Sec. 12.2.1
6	`imap_end_time_offset`	IMAP clock, subseconds as decimal part of float, see Sec. 12.2.1
7	`number_of_spins_per_block`	n_{block}
8	`number_of_bins_per_histogram`	n_{bin}
9	`histogram`	array of block-accumulated count numbers
10	`number_of_events`	total number of events/counts in histogram
11	`imap_spin_angle_bin_cntr`	IMAP spin angle ψ for bin centers, see Sec. 10.6
12	`histogram_flag_array`	array of bad-angle flags for histogram bins, see Tab. 3.11
13	`filter_temperature_average`	block-averaged value, decoded to Celsius degrees using Eq. (40)
14	`filter_temperature_std_dev`	standard deviation (1σ), decoded to Celsius degrees using Eq. (44)
15	`hv_voltage_average`	block-averaged value, decoded to volts using Eq. (40)
16	`hv_voltage_std_dev`	standard deviation (1σ), decoded to volts using Eq. (44)
17	`spin_period_average`	block-averaged onboard value, decoded to seconds using Eq. (40)
18	`spin_period_std_dev`	standard deviation (1σ), decoded to seconds using Eq. (44)
19	`pulse_length_average`	block-averaged value, decoded to μs using Eq. (40)
20	`pulse_length_std_dev`	standard deviation (1σ), decoded to μs using Eq. (44)
21	`spin_period_ground_average`	block-averaged value computed on ground, see Sec. 12.6.1
22	`spin_period_ground_std_dev`	standard deviation (1σ), see Sec. 12.6.1
23	`position_angle_offset_average`	block-averaged value in degrees, see Sec. 10.6 and 12.6.1
24	`position_angle_offset_std_dev`	standard deviation (1σ), see Sec. 10.6 and 12.6.1
25	`spin_axis_orientation_average`	block-averaged spin-axis ecliptic longitude $\langle\lambda\rangle$ and latitude $\langle\phi\rangle$ in degrees, see Sec. 12.6.1
26	`spin_axis_orientation_std_dev`	standard deviation(1σ): $\Delta\lambda$, $\Delta\phi$ for $\langle\lambda\rangle$, $\langle\phi\rangle$; see Sec. 12.6.1
27	`spacecraft_location_average`	block-averaged Cartesian ecliptic coordinates $\langle X\rangle$, $\langle Y\rangle$, $\langle Z\rangle$ [km] of IMAP; see Sec. 12.6.1
28	`spacecraft_location_std_dev`	standard deviations (1σ) ΔX, ΔY, ΔZ for $\langle X\rangle$, $\langle Y\rangle$, $\langle Z\rangle$, see Sec. 12.6.1
29	`spacecraft_velocity_average`	block-averaged values $\langle V_X\rangle$, $\langle V_Y\rangle$, $\langle V_Z\rangle$ [km/s] of IMAP velocity components (Cartesian ecliptic frame); see Sec. 12.6.1
30	`spacecraft_velocity_std_dev`	standard deviations (1σ) ΔV_X, ΔV_Y, ΔV_Z for $\langle V_X\rangle$, $\langle V_Y\rangle$, $\langle V_Z\rangle$, see Sec. 12.6.1
31	`flags`	flags for extra information see Tab. 3.10 see Sec. 12.3

Table 3.9: Brief description of GLOWS Level-1B header (item 1 in Tab. 3.8) for histograms. Item names refer to test Python scripts developed by the GLOWS team.

Level 1B, histograms: header		
No.	Item	Comments/Remarks
1	`block_header`	
1.1	`flight_software_version`	copied from Level-1A
1.2	`ground_software_version`	set by ground software
1.3	`pkts_file_name`	name of Level-0 data file (copied from Level-1A)
1.4	`seq_count_in_pkts_file`	sequence counter (per APID) in pkts (Level-0) file
1.5	`l1a_file_name`	name of Level-1A input file
1.6	`ancillary_data_files`	names of ancillary data files used for processing

Table 3.10: Brief description of GLOWS Level-1B **bad-time** flag structure (item 30 in Tab. 3.8) for histograms. Item names refer to test Python scripts developed by the GLOWS team. GLOWS uses a convention for bad-time flags, where false value corresponds to normal conditions and true value indicates a problem.

Level 1B, histograms: bad-time flag structure		
No.	Item	Comments/Remarks
30	`flags`	see Sec. 12.3 for detailed flags description
30.1	`is_pps_missing`	set onboard
30.2	`is_time_status_missing`	set onboard
30.3	`is_phase_missing`	set onboard
30.4	`is_spin_period_missing`	set onboard
30.5	`is_overexposed`	set onboard
30.6	`is_direct_event_non_monotonic`	set onboard
30.7	`is_night`	set onboard
30.8	`is_hv_test_in_progress`	set onboard
30.9	`is_test_pulse_in_progress`	set onboard
30.10	`is_memory_error_detected`	set onboard
30.11	`is_generated_on_ground`	copied from Level-1A
30.12	`is_beyond_daily_statistical_error`	requires meta file with total count numbers in blocks (generated at Level-1A)
30.13	`is_temperature_std_dev_beyond_threshold`	
30.14	`is_hv_voltage_std_dev_beyond_threshold`	
30.15	`is_spin_period_std_dev_beyond_threshold`	
30.16	`is_pulse_length_std_dev_beyond_threshold`	
30.17	`is_spin_period_difference_beyond_threshold`	

Table 3.11: Brief description of GLOWS Level-1B **bad-angle** flag structure (item 11 from Tab. 3.8) for histograms. This type of flags is set as an array (see item 12 in Tab. 3.8), where each element corresponds to one histogram bin. Item names refer to test Python scripts developed by the GLOWS team. GLOWS uses a convention for bad-angle flags, where false value corresponds to normal conditions and true value indicates a problem. See Sec. 12.3 for detailed flags description.

Level 1B, histograms: bad-angle flag structure		
No.	Item	Comments/Remarks
1	`is_close_to_uv_source`	see Sec. 3.7.1
2	`is_inside_excluded_region`	see Sec. 3.7.1
3	`is_excluded_by_instr_team`	see Sec. 3.7.1
4	`is_suspected_transient`	see Sec. 3.7.1

Note, that during detection of `is_night` transitions one should exclude Level-1B histograms, where `is_hv_test_in_progress` flag is raised. This flag is related to monthly calibration tests, where time-tagged loads of commands are used. Due to specific way of commanding for the GLOWS instrument, the command loads may cause fake transitions in `is_night` flag.

3. Adding good-time Level-1B histograms from a given observational day to get daily raw histogram of the same resolution as at Level-1B

4. Adding exposure times for good-time Level-1B histograms to get daily exposure times

5. Setting bad-angle flags for daily histogram using an active-flag mask provided by the GLOWS team

6. Computing daily-averaged count rates from raw histograms (daily count numbers) and exposure times

7. Applying a calibration factor to convert the daily-averaged count rates into photon-flux estimation in Rayleigh units

8. Computing daily averages and standard deviation of all ancillary parameters (i.e. items from 13 to 30 in Tab. 3.8). The daily average is computed as the mean of block averages. The daily standard deviation is computed as the spread of block averages (to account for possible drifts of ancillary parameters).

9. Generating angular grids for bin centers: spin angle, ecliptic longitude, and ecliptic latitude. The spin angle at Level-2 is defined as measured from the northermost point of the GLOWS scanning circle (i.e., the GLOWS position angle ψ_{PA} should be used here instead of the IMAP spin angle values ψ used at Level-1B). See Sec. 10.6.

It is assumed here that all histogram data for a given observational day (time interval between repointing maneuvers) are provided in one pkts file at Level-0. Thus one Level-0 pkts file is assumed to correspond directly to one Level-2 file.

Bad-angle masking for Level-2. Flags in Level-1B defined in Tab. 3.11 and discussed briefly in Sec. 3.7.1 are generally intended to simply propagate bin-by-bin to Level-2 when adding block-accumulated histograms. In the pipeline settings file (see item 9 in Sec. 3.12) the GLOWS team provides a binary mask (section `active_bad_angle_flags`) saying which flags from Level-1B are active for bin exclusion in Level-2. By default all bits in the active-flag mask will be set to true value, so all flags are to be active for copying from Level-1B to Level-2. However, it should be implemented as configurable, depending on settings included in the ancillary file. The expected behavior is that inactive flags have zeroes set in Level-2 even if they are not zeroed in Level-1B.

Table 3.12: Brief description of GLOWS Level-1B direct-event data product. Item names refer to test Python scripts developed by the GLOWS team.

Level 1B: direct events		
No.	Item	Comments/Remarks
1	`header`	
1.1	`ground_software_version`	set by ground software
1.2	`pkts_file_name`	name of Level-0 data file (copied from Level-1A)
1.3	`seq_count_in_pkts_file`	sequence counter (per APID) in pkts (Level-0) file
1.4	`l1a_file_name`	name of Level-1A input file
1.5	`ancillary_data_files`	names of ancillary data files used for processing
2	`unique_identifier`	`YYYY-MM-DDThh:mm:ss` based on IMAP UTC time
3	`imap_time_last_pps`	IMAP clock, subseconds as decimal part of float, see Sec. 12.2.1
4	`imap_time_next_pps`	IMAP clock, subseconds as decimal part of float, see Sec. 12.2.1
5	`glows_time_last_pps`	GLOWS clock, subseconds as decimal part of float, see Sec. 12.2.1
6	`number_of_completed_spins`	copied from `data_every_second` at Level-1A
7	`filter_temperature`	decoded to Celsius degrees using Eq. 39
8	`hv_voltage`	decoded to volts using Eq. 39
9	`spin_period`	decoded to seconds using Eq. 39
10	`spin_phase_at_next_pps`	decoded to degrees using Eq. 39
11	`flags`	copied from Level-1A
11.1	`is_catbed_heater_active`	
11.2	`is_spin_period_valid`	
11.3	`is_spin_phase_at_next_pps_valid`	
11.4	`is_spin_period_source`	
11.5	`is_glows_time_on_pps_valid`	
11.6	`is_time_status_valid`	
11.7	`is_housekeeping_valid`	
11.8	`is_pps_autogenerated`	
11.9	`is_hv_test_in_progress`	
11.10	`is_pulse_test_in_progress`	
11.11	`is_memory_error_detected`	
12	`direct_event_glows_times`	array of times for direct events, GLOWS clock, subseconds as decimal part of float, see Sec. 12.2.1
13	`direct_event_pulse_lengths`	array of pulse lengths [μs] for direct events

3.10 Level-2 data products

This section describes the content of GLOWS Level-2 data products for histograms and it is expected to be consistent with Sec. 12.8, which presents some early ideas on Level-2 and the intentions of the GLOWS Science team. The listing of the fields of Level-2 data structure for histograms is provided in Tab. 3.13, details of the header are in Tab. 3.14 and daily-lightcurve fields structure is shown in 3.15.

Table 3.13: Brief description of GLOWS Level-2 histogram-binned data product (see Sec. 12.8 for details). The product contains daily lightcurve of photon flux in physical units (Rayleighs) along the scanning circle of GLOWS. Information on spacecraft location/attitude and spin period characteristics is included as inherited from Level 1B and averaged over a given observation day. Resolution of the lightcurve is the same as for Level-1B histograms. Item names refer to test Python scripts developed by the GLOWS team.

Level 2: daily lightcurve of photon flux in physical units		
No.	Item	Comments/Remarks
1	`header`	header for Level-2 histograms (see Tab. 3.14)
2	`identifier`	unique Level-2 histogram identifier (number of pointing, i.e., observational day number)
3	`start_time`	UTC start time of a given observational day
4	`end_time`	UTC end time of a given observational day
5	`daily_lightcurve`	arrays for observational-day-accumulated lightcurve (see Tab. 3.15)
6	`filter_temperature_average`	observational-day-averaged filter temperature [Celsius deg]
7	`filter_temperature_std_dev`	standard deviation for filter temperature [Celsius deg]
8	`hv_voltage_average`	observational-day-averaged channeltron voltage [volt]
9	`hv_voltage_std_dev`	standard deviation for channeltron voltage [volt]
10	`spin_period_average`	observational-day-averaged spin period [s] (onboard value)[a]
11	`spin_period_std_dev`	standard deviation for spin period [s]
12	`pulse_length_average`	observational-day-averaged pulse length [μs]
13	`pulse_length_std_dev`	standard deviation for pulse length [μs]
14	`spin_period_ground_average`	observational-day-averaged spin period [s] (ground value)[a]
15	`spin_period_ground_std_dev`	standard deviation for spin period [s]
16	`position_angle_offset_average`	observational-day-averaged GLOWS angular offset [deg]
17	`position_angle_offset_std_dev`	standard deviation for GLOWS angular offset [seg]
18	`spin_axis_orientation_average`	observational-day-averaged spin-axis ecliptic longitude $\langle\lambda\rangle$ and latitude $\langle\phi\rangle$ [deg]
19	`spin_axis_orientation_std_dev`	standard deviation for spin-axis longitude and latitude [deg]
20	`spacecraft_location_average`	observational-day-averaged Cartesian ecliptic coordinates $\langle X\rangle$, $\langle Y\rangle$, $\langle Z\rangle$ [km] of IMAP
21	`spacecraft_location_std_dev`	standard deviation for ecliptic coordinates [km] of IMAP
22	`spacecraft_velocity_average`	observational-day-averaged values $\langle V_X\rangle$, $\langle V_Y\rangle$, $\langle V_Z\rangle$ of IMAP velocity components [km/s] (Cartesian ecliptic frame)
23	`spacecraft_velocity_std_dev`	standard deviation for IMAP velocity components [km/s]
24	`bad_time_flag_occurences`	numbers of occurences of blocks for each bad-time flag during observational day

[a] From two values (onboard- and ground-computed) of the spin period available at Level 1B we anticipate to use here the onboard-computed value, provided that everything goes as expected and differences between the onboard- and ground-computed values are relatively small. Tentatively, for the expected spin phase uncertainty $\sim$0.2°, the difference is expected to be smaller than $(0.2/360)(\langle P_{\rm GLOWS}\rangle + \langle P_{\rm IMAP}\rangle)/2$, where $\langle P_{\rm GLOWS}\rangle$ is the mean spin-period value computed onboard and $\langle P_{\rm IMAP}\rangle$ is the mean value computed on the ground.

Table 3.14: Brief description of GLOWS Level-2 header (item 1 in Tab. 3.13). Item names refer to test Python scripts developed by the GLOWS team.

Level 2: header		
No.	Item	Comments/Remarks
1	`header`	
1.1	`flight_software_version`	copied from Level-1B
1.2	`ground_software_version`	set by ground software
1.3	`pkts_file_name`	name of Level-0 file for a given observational day (copied from Level-1B)
1.4	`ancillary_data_files`	list of ancillary files used for generation of Level-1B and Level-2 data
1.5	`number_of_l1b_files_used`	number of good-time Level-1B files used for generation of Level-2 data
1.6	`number_of_all_l1b_files`	number of all Level-1B files for observational day

Table 3.15: Brief description of GLOWS Level-2 daily-lightcurve structure (item 5 in Tab. 3.13). Item names refer to test Python scripts developed by the GLOWS team.

Level 2: daily-lightcurve structure		
No.	Item	Comments/Remarks
5	`daily_lightcurve`	items 5.1-5.8 listed below are arrays with n_{bin} elements
5.1	`spin_angle`	values of spin angle [deg] (measured from the north) for bin centers
5.2	`photon_flux`	observational-day-averaged photon flux [Rayleigh]
5.3	`raw histogram`	raw daily counts in lightcurve bins [cts]
5.4	`exposure_times`	exposure times for bins [s]
5.5	`flux_uncertainties`	statistical uncertainties for photon flux [Rayleigh]
5.6	`histogram_flag_array`	flags for bins (see Sec. 3.9.1 and Tab. 3.11)
5.7	`ecliptic_lon`	ecliptic longitude of bin centers [deg]
5.8	`ecliptic_lat`	ecliptic latitude of bin centers [deg]
5.9	`number_of_bins`	number of bins n_{bin} in lightcurve

3.11 Python-script bundle provided by the GLOWS team

The GLOWS team developed a number of test Python scripts for processing GLOWS data from Level-0 to Level-2. The scripts are organized in a test ground-processing pipeline invoked by a shell script. Ancillary files (instrument team input) discussed in Sec. 3.12 are also included in this package.

The scripts are used to process CCSDS packets from Level-0 validation data sets prepared by the GLOWS team and provided to the SDC. The scripts generate JSON files for all levels of GLOWS data products. Data from the JSON files have been analyzed and visualized by the GLOWS team. The JSON files are then compared in a rigorous way (number vs number) with the content of CDF files generated by the SDC as a part of validation process for GLOWS data products generated by the SDC.

Looking into the source code in the scripts (and/or asking the GLOWS team) is presumably the best way of understanding the intentions of the instrument team, when something in this document needs clarification.

3.12 Settings/parameters/input for ground-processing pipeline (ancillary files)

Variable parameters needed for ground processing, like a flag-related mask, conversion factors for the temperature, calibration data, HV-dependence of the sensitivity, etc., will be defined in separate files. These files will be posted by the GLOWS team to SDC, so that they can be used in the automated processing pipeline. Currently anticipated list of the files is as follows:

1. `imap_glows_l1b-map-of-excluded-regions_YYYYMMDD_vXXX.dat` contains a map of excluded regions (e.g., proximity of the galactic plane) defined by points in the sky (ecliptic coordinates J2000)

2. `imap_glows_l1b-conversion-table-for-anc-data_YYYYMMDD_vXXX.json` contains parameters of the conversion formulas for onboard collected data (temperature, spin period, spin angle, HV voltage, pulse length) from integer-encoded value to physical units

3. `imap_glows_l1b-map-of-uv-sources_YYYYMMDD_vXXX.dat`: contains a map of UV sources (stars) defined by points in the sky (ecliptic coordinates J2000). This file contains three columns: longitude, latitude, and masking radius. The masking radius can be generally different for each source depending on its brightness.

4. `imap_glows_l1b-exclusions-by-instr-team_YYYYMMDD_vXXX.dat` contains Level-1B unique block identifiers
(`YYYY-MM-DDThh:mm:ss`) and arrays of 0/1 masks for masking Level-1B-histogram segments if any issues are found by the GLOWS team

5. `imap_glows_l1b-suspected-transients_YYYYMMDD_vXXX.dat` contains Level-1B unique block identifiers (`YYYY-MM-DDThh:mm:ss`) and arrays of 0/1 masks for masking Level-1B-histogram segments that are likely to contain substantial transient signals (e.g., regions in the sky affected by cometary signal). These masks are provided by the GLOWS team.

6. `imap_glows_l2-calibration_YYYYMMDD_vXXX.dat` contains calibration data, i.e., cps-per-R factor. This file contains two columns: `start_time_UTC` and `cps_per_R`. A given value of `cps_per_R` applies from a time specified in the `start_time_UTC` column until the next time in this column. The last value in the `start_time_UTC` column defines open-ended time interval.

7. `imap_glows_l3a-map-of-extra-helio-bckgrd_YYYYMMDD_vXXX.dat`: contains an all-sky map of extra-heliospheric (time-independent) background. Ecliptic coordinates J2000 are used. This file contains three columns: longitude, latitude, and background estimate. HEALPix grid is used to obtain all-sky coverage. This file is used for the L2-to-L3a processing.

8. `imap_glows_l3a-time-dep-bckgrd_YYYYMMDD_vXXX.dat`: each row contains Level-3a lightcurve identifier (number of pointing), start time for a given Level-3a lightcurve (`YYYY-MM-DDThh:mm:ss`), and an array of corrections (nominally 3600 bins) span on a spin angle grid provided in the header. Linear interpolation

should be used to map the background corrections from 3600 bins onto the grid in a given Level-3a file. These background corrections are to be provided by the GLOWS team.

9. `imap_glows_lxx-pipeline-settings_YYYYMMDD_vXXX.json` contains parameters for the ground-processing pipeline (thresholds, bad-time flags to be activated, bad-angle flags to be activated, number of bins in Level-3a, etc.)

Examples of the files are included in the python-script bundle described in Sec. 3.11.

3.13 Validation data sets

The GLOWS team prepared data sets for validation of the SDC processing pipeline. The data sets are provided as `imap_glows_l0_raw_{date}-repoint{repoint number}_v{version}.pkts` files containing binary streams of CCSDS packets intended to be used as input for the SDC processing pipeline. The Level-0 data are organized on "per-pointing" basis as expected by the SDC.

The Level-0 validation files are included in subsequent versions of the Python-script bundle (see Section 3.11) provided by the instrument team to the SDC. For a given Level-0 validation set, corresponding JSON files from Level-1A to Level-3A are provided with the expected output. As discussed in Section 3.11, the JSON files are intended to be compared with the content of CDF files generated by the SDC.

3.13.1 Validation Set 1

The data set was provided to the SDC in `data_l0` subdirectory of a zip archive `data_products_cbk_implementation_2025-07-25_validation_set_1.zip`. JSON output files generated by the GLOWS team from Level-1A to Level-3A have been provided in this archive as well. Plots illustrating content of the JSON files are also included. The data set contains 5 pointings (observational days).

The first three pointings come from tests of GLOWS EQM illuminated by UV light from a deuterium lamp in a vacuum chamber using an EGSE developed by the GLOWS engineering team. Therefore they represent data generated by real device (fully equivalent to GLOWS flight model) and real flight software (v. 3.0.1). Histogram and direct event CCSDS packets are included in the binary stream that was obtained from GSEOS TLM relay during a testing session. Histograms are flat due to lack of UV beam modulation with the simulated spin phase. This is an important difference relative to in-flight data, where strong modulations in histograms are expected. The count rate slowly drifts on time scales of hours. The data set additionally contains monthly calibration tests, seen in the data as drops of the count rate and variations of the HV bias during time intervals when `is_hv_test_in_progress` flag is raised.

Pointings 4 and 5 represent purely synthetic CCSDS packets generated by a python script. Simulations of the helioglow have been performed using the WawHelioGlow model and expected signal from stars was added. Based on the simulated lightcurves direct events were generated using a pseudo-random generator (with modulated exponential distribution of time offsets between events). Then the DE were histogrammed (by a python script, not the flight software) and put into the CCSDS data structure together with synthetic ancillary data. Only histograms are included, no DE packets are expected for the last two observational days. This part of data includes modulation of the signal in histograms as expected in flight for DOY ∼105 for solar min and max.

In summary, the two parts provide a combination of two pieces of data:

- pointings 1-3: histograms and direct events from the actual GLOWS-flight-model-equivalent device and flight software but without a realistic modulation of the histograms with the spin angle
- pointings 4-5: only histograms with a realistic modulation of the signal but at the expense of purely synthetic character of the data

Both pieces of data are provided as CCSDS packets that can be used as input in the SDC pipeline. Expected output (from Level-1A to Level-3A) generated by the GLOWS team has been provided as well.

3.14 Comments

1. This algorithm provides at Level-3 a quick-look calibrated flux of the Lyman-α helioglow. It uses very simple recipes and, consequently, removes data that potentially might be rescued after some in-depth analysis. The GLOWS team plans to do this analysis during the mission. In Phases C-D, more sophisticated analysis methods may be developed that potentially can be automated and then be used at the IMAP SDC.

2. It is important to note, that the histograms at Level-1A and Level-1B are organized by IMAP spin angle (used for histogramming onboard). Conversion to the GLOWS position angle is done at Level 2. This conversion is done by subtracting the GLOWS effective angle defined in Eq. (30) and subsequently applying the `modulo[., 360°]` function. More details can be found in Sec. 10.6.

3. The HK data likely needed for in-depth science analysis certainly include the optical filter temperature and its variation, as well as the HV setting. Other parameters may be added in the future as a result of ground tests performed during Phase C (e.g., channeltron temperature).

4. The process of identifying bad-time intervals with a strong background signal is currently anticipated rather to be based purely on statistical testing of data from the GLOWS instrument only. The tests described in Sec. 12.7.1 are devised to identify those blocks, where the total number of counts exceeds certain statistics-based thresholds. However, data from other instruments (e.g., electron fluxes measured by IMAP/SWE or high-energy cosmic rays measured by IMAP/HIT) may be very useful in identifying periods of increased background. The GLOWS team plans some studies aimed at potential use of other-IMAP-instrument data in identifying bad-time intervals. However, it is not anticipated to include other-IMAP-instrument data in the data-processing pipeline for GLOWS performed between Level-0 and Level-2. The other-IMAP-instrument data can be used for generation of Level-3 or higher levels of data products.

5. The daily lightcurves (Level-2 or Level-3) can be mapped on the sky, if needed, based on the knowledge of the spacecraft spin axis and the radius of the GLOWS scanning circle.

4 A draft of data ground-processing algorithm for IMAP GLOWS for Level-3

This section contains a brief description of Level-3 data products. Extended studies/analyses for Level-3 are expected to be included in Sec. 13. Lower-level data products are described in Sections 3 and 12.

4.1 Inputs for Level-3 ground-processing pipeline (MS)

1. **Level-2 data product** with the high-resolution lightcurve that includes all photon-flux contributions (helioglow + stars + other backgrounds). This input contains also all arrays with flags needed to masking bins in the low-resolution lightcurve in Level-3a.

2. **Inputs supplied by the GLOWS Instrument Team**

   - Corrections for extra-heliospheric sources: time-independent map of the background (mainly diffuse galactic background, in the ecliptic frame J2000; see Section 5)
   - Background corrections: time dependent corrections provided by the GLOWS team for every daily lightcurve to correct for, e.g., comets
   - Bad-day list: based on analysis of the SOHO/SWAN observations, the GLOWS team expects that some observational days can be so strongly affected by backgrounds (e.g., caused by solar flares, CMEs, etc.) that they should be excluded from processing in the SDC pipeline. By default, observational days are marked as good days. The list of days to be excluded from the processing is provided by the GLOWS team.

- WawHelioIon-MP parameters: for converting the helioglow lightcurve into the daily ionization rates
- UV anisotropy factor: for calculations related to the solar EUV output in Level-3B–E processing
- Parameters for Level-3B–C processing: for conversion of the helioglow lightcurve into the ionization rates and then into solar wind plasma speed and proton density structure.
- Parameters for Level-3D processing: for computation of the solar wind parameters history from Level-3b and Level-3C data products, WawHelioIon model, and external dependencies (Lyman-α, OMNI)
- Parameters for Level-3E-related computations: for computation of the ENA survival probabilities from Level-3D data products

3. **Internal dependencies** which include:

- SWE data products: energy spectrum, presumably Level-2; see *Notes on the electron background* in Section 13.1.4 for details. SWE data are planned to be used in Level-2-to-Level-3A processing (as needed for background corrections).
- SWAPI data products: moments of the distribution functions for solar wind protons and alphas. SWAPI data are used in the processing pipeline at many steps from Level-3A to Level-3D.
- Averaged spin axis data product: a data product provided by the SDC to ensure that all ENA instruments and GLOWS use exactly the same spin axis directions for all IMAP pointings. The averaging should be performed over the time intervals when the IMAP spin axis is fixed because both GLOWS and ENA instruments organize their data products on fixed-pointing basis. This common spin axis is needed because averaging over different good times sets for different instruments instruments can cause small differences between the averaging results.

HIT data products are an optional dependency for GLOWS. This question will be a part of GLOWS science analyses during the mission. If a method GLOWS background estimation based on of HIT data is derived, it will be incorporated into the GLOWS processing pipeline. Then our L3a product would depend on HIT.

4. **External dependencies**

- F10.7 index
(`https://lasp.colorado.edu/lisird/data/penticton_radio_flux`) is needed for calculation of the photoionization rate of interstellar H and subsequent decomposition of the total ionization rate into its charge-exchange and photoionization components during production of Level-3B data
- Composite Lyman-α time series
(`https://lasp.colorado.edu/lisird/data/composite_lyman_alpha`) is needed for calculation of radiation pressure in the calculation of ENA survival probabilities at Level-3E.
- OMNI2 database
(`https://omniweb.gsfc.nasa.gov/html/ow_data.html`) is needed because GLOWS algorithms are fine-tuned on historical solar wind data from this database. Therefore, SWAPI and SWE data need to be recalibrated to OMNI2 before using them in the GLOWS processing pipeline.

The F10.7 index and composite Lyman-α are both available via official LASP APIs (see the links). The data are updated on close to daily basis, with a small delay of the order of one or two days. So this dependency is not expected to generate significant delays in the GLOWS Level-3 processing. Since time averaged quantities are used in the processing, even if F10.7 or composite Lyman-α are not updated for one or two weeks, we the processing software will still be able to generate reasonably accurate GLOWS Level-3 data products.

As a contingency planning, the F30 index (`http://solar.nro.nao.ac.jp/norp/data/daily/`) can be used as a replacement for F10.7. The OMNI2 database can be used as a replacement for SWAPI and SWE data if they are not available for some reasons.

4.2 Level-3 ground-processing pipeline – overview (MS)

We present here an overview of the ground data-processing pipeline, additional information can be found in Section 13.

The high-level flowchart shown in Figure 4.1 presents the ground-processing pipeline for the science data of the GLOWS instrument. The flowchart shows the flow of information from Level-2 to Level-3E.

4.3 Level-2 to Level-3A processing (MS)

Objective: Level-3A defined as daily low-resolution lightcurve of the Lyman-α photon flux

- Brief description: low-resolution lightcurve of the photon flux (in the Rayleigh units) accumulated over the entire observation day. Nominally 90 bins (before masking), but the number of bins is a configurable parameter defined in the pipeline-settings file (item 9 in Section 3.12). The lightcurve represents modulation of the Lyman-α photon flux along the GLOWS scanning circle as a function of the spin angle (so in the despun frame). Bins contaminated by stars are masked. Uncertainties and exposure times are included. An estimate of background is provided. By subtraction of the background from the total-intensity lightcurve one can obtain a lightcurve that is expected to contain only the helioglow signal.
- Instrument team supplied inputs: parameters for L2 to L3A processing (see item 9 in Section 3.12), a time-independent map of the extra-heliospheric background (see item 7 in Section 3.12), time-dependent background corrections (see item 8 in Section 3.12)
- Internal dependencies: GLOWS L2, SWE data products (energy spectrum, one-minute cadence, presumably Level-2; see *Notes on the electron background* in Section 13.1.4 for details)
- External dependencies: none

Processing from Level-2 to Level-3A involves:

- Rebinning the daily lightcurve to a lower resolution (see Section 13.1.1), nominally $n_{\mathrm{bin}}^{\mathrm{lores}} = 90$ bins 4°wide, but the masking process leads effectively to a smaller number of bins
- Masking out bins affected by strong background that is difficult to estimate accurately (e.g., proximity of bright point UV sources, some "excluded" regions close to the galactic equator, etc.). The procedure is described in Sections 13.1.1 and 13.1.2 and based on the quality flags Q_m determined from Level-1B/Level-2 flags listed in Table 3.11. Note that the lightcurve-related arrays listed in Table 4.3 have $n_{\mathrm{bin}}^{\mathrm{lores}} - n_{\mathrm{masked}}$ elements, i.e., the masked bins are simply removed from the lightcurve.
- Estimation of the extra-heliospheric background, see Section 13.1.3
- Estimation of a time dependent background, see Section 13.1.4
- Estimation of statistical uncertainties, see Section 13.1.5

The final result of Level-2 to Level-3a processing is described in Sections 4.4 and 13.2.

4.4 Level-3A data products (MS)

This section describes the GLOWS Level-3a data products for histograms and it is expected to be consistent with Section 13.2, where intentions of the GLOWS science team are discussed. The listing of the fields of Level-2 data structure for the histograms is provided in Table 4.1, details of the header are in Table 4.2, and the structure of the fields of the daily lightcurve is shown in Table 4.3.

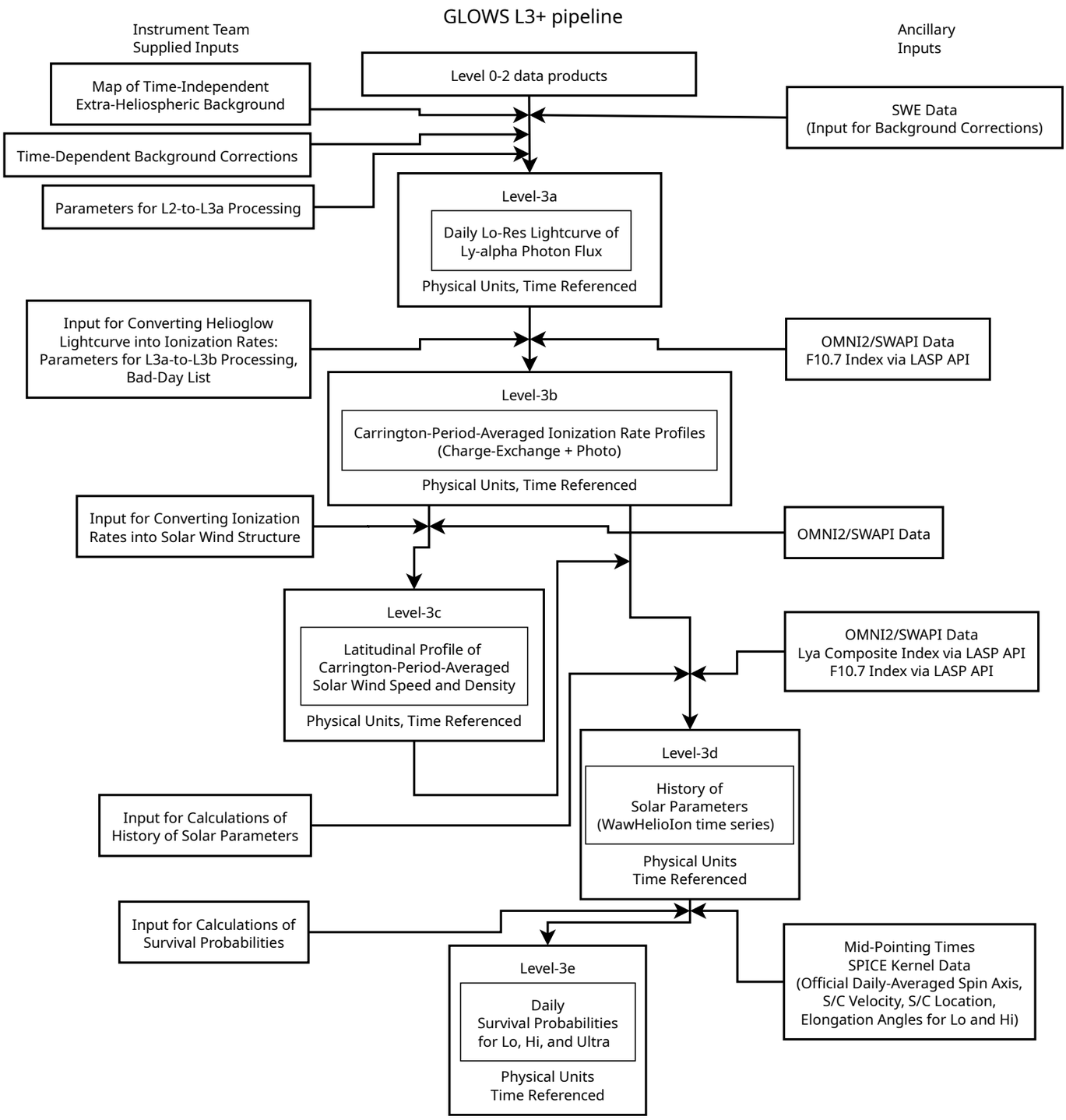


Figure 4.1: Ground-processing flowchart for IMAP/GLOWS for Level-3 data products. Referring to a given data product as "Daily" means that it is accumulated/averaged over a given spin axis pointing (i.e., a time interval when the IMAP spin axis pointing is nominally fixed). A similar flowchart for the pipeline from Level-0 to Level-2 is shown in Fig. 3.1.

Table 4.1: Brief description of the GLOWS Level-3A data product (see Section 13.2 for details). The product contains a daily lightcurve of the photon flux in the physical units (Rayleighs) collected along the GLOWS scanning circle. Information on the spacecraft location/attitude, spin period, and other average and standard deviation characteristics is inherited from Level 2. The resolution of the lightcurve is lower than that for Level-2 histograms. Stars are masked out and estimates of background corrections are provided. Item names refer to a Python-script bundle developed by the GLOWS Team.

Level-3A: daily low-resolution lightcurve of photon flux in physical units		
No.	Item	Comments/Remarks
1	`header`	header for Level-3a histograms (see Table 4.2)
2	`identifier`	unique Level-3a histogram identifier (number of pointing, i.e., observational day)
3	`start_time`	UTC start time of a given observational day
4	`end_time`	UTC end time of a given observational day
5	`daily_lightcurve`	arrays for observational-day-accumulated lightcurve (see Table 4.3)
6	`filter_temperature_average`	observational-day-averaged filter temperature [Celsius deg]
7	`filter_temperature_std_dev`	standard deviation for filter temperature [Celsius deg]
8	`hv_voltage_average`	observational-day-averaged channeltron voltage [volt]
9	`hv_voltage_std_dev`	standard deviation for channeltron voltage [volt]
10	`spin_period_average`	observational-day-averaged spin period [s] (onboard value)
11	`spin_period_std_dev`	standard deviation for spin period [s]
12	`pulse_length_average`	observational-day-averaged pulse length [μs]
13	`pulse_length_std_dev`	standard deviation for pulse length [μs]
14	`spin_period_ground_average`	observational-day-averaged spin period [s] (ground value)
15	`spin_period_ground_std_dev`	standard deviation for spin period [s] (ground)
16	`position_angle_offset_average`	observational-day-averaged GLOWS pos.ang. offset [deg]
17	`position_angle_offset_std_dev`	standard deviation for GLOWS pos.ang. offset [deg]
18	`spin_axis_orientation_average`	observational-day-averaged spin-axis ecliptic longitude $\langle\lambda\rangle$ and latitude $\langle\phi\rangle$ [deg]
19	`spin_axis_orientation_std_dev`	standard deviation for spin-axis longitude and latitude [deg]
20	`spacecraft_location_average`	observational-day-averaged Cartesian ecliptic coordinates $\langle X\rangle$, $\langle Y\rangle$, $\langle Z\rangle$ [km] of IMAP
21	`spacecraft_location_std_dev`	standard deviation for ecliptic coordinates [km] of IMAP
22	`spacecraft_velocity_average`	observational-day-averaged values $\langle V_X\rangle$, $\langle V_Y\rangle$, $\langle V_Z\rangle$ of IMAP velocity components [km/s] (Cartesian ecliptic frame)
23	`spacecraft_velocity_std_dev`	standard deviation for IMAP velocity components [km/s]

Table 4.2: Brief description of GLOWS Level-3a header (item 1 in Tab. 4.1). Item names refer to a Python-script bundle developed by the GLOWS Team.

Level-3A: header		
No.	Item	Comments/Remarks
1	`header`	
1.1	`flight_software_version`	copied from Level-2
1.2	`ground_software_version`	set by ground software
1.3	`pkts_file_name`	name of Level-0 file for a given observational day (copied from Level-2)
1.4	`ancillary_data_files`	list of ancillary files used for generation of Level-3a (and levels before)
1.5	`l2_input_file_name`	name of Level-2 file used as input data

Table 4.3: Brief description of GLOWS Level-3a daily-lightcurve data structure (item 5 in Table 4.1). Item names refer to a Python-script bundle developed by the GLOWS Team.

Level-3A: daily low-resolution lightcurve data structure		
No.	Item	Comments/Remarks
5	`daily_lightcurve`	items 5.1–5.7 listed below are arrays with $n_{\mathrm{bin}}^{\mathrm{lores}} - n_{\mathrm{masked}}$ elements
5.1	`spin_angle`	values of spin angle [deg] (measured from the north) for bin centers
5.2	`photon_flux`	observational-day-averaged photon flux [Rayleigh]
5.3	`raw histogram`	raw daily counts in lightcurve bins [cts]
5.4	`exposure_times`	exposure times for bins [s]
5.5	`flux_uncertainties`	statistical uncertainties for photon flux [Rayleigh]
5.6	`ecliptic_lon`	ecliptic longitude of bin centers [deg]
5.7	`ecliptic_lat`	ecliptic latitude of bin centers [deg]
5.8	`extra_heliospheric_bckgrd`	extra-heliospheric background estimates for bin centers [Rayleigh]
5.9	`time_dependent_bckgrd`	time-dependent background estimates for bin centers [Rayleigh]
5.10	`number_of_bins`	number of bins $n_{\mathrm{bin}}^{\mathrm{lores}} - n_{\mathrm{masked}}$ in lightcurve

4.5 Initializer for Level-3B and higher levels (MS)

At the transition from Level-3A to Level-3B a cadence change occurs from the daily (per-pointing) cadence to the Carrington rotation (CR) period. Additionally, in Level-3B and higher levels a complex set of internal (SWAPI) and external (OMNI2, Lyman-α Composite Index, F10.7 index) dependencies appears. For these reasons, a special triggering mechanism and dependency checks are needed for Level-3B and higher-levels processing. They must take into account the actual CR and update dates for the external dependencies.

The list of important events on the timeline includes: CRs (every ∼27.4 days), DSN contacts (every ∼3 days), update dates for the external dependencies (every week or a couple of weeks). These events are not expected to be synchronized in any way.

The GLOWS team proposes implementing an initializer for the Level-3B and higher-levels processing. The initializer has the following tasks:

- suspend the processing for Level-3B and higher-levels until the next CR time t_{nextCR} (the time can be computed upfront, see, e.g., the function `jd_fm_Carrington()` in the Python script bundle for Level-3B provided by the GLOWS team)
- if $t > t_{\mathrm{nextCR}}$ then download external dependencies
- make checks on the downloaded external dependencies and internal dependencies if they all contain at least one data entry time tagged with $t > t_{\mathrm{nextCR}}$ (the internal and external dependencies are defined as items 3 and 4 in Section 4.1)
- if the conditions listed above are not satisfied, the initializer should send a report/notification to the instrument team with information which dependencies are not met
- if the conditions listed above are satisfied, the initializer should archive the downloaded external dependencies, trigger the processing for Level-3B and higher-levels, send a report/notification to the instrument team about successful execution

Various comments/remarks on the initializer:

- the initializer should be invoked after each DSN contact (every $\sim$ 3 days) when a new telemetry chunk becomes available
- it is expected that most initializer executions will not result in new data product files, a sucessful generation of data product files is expected approximately once per CR period
- the reports/notifications mentioned above are expected to explain the instrument team the reasons why a given invocation of the initializer has not resulted in new data product files
- the initializer is expected to use an internal dependency tracker developed by the SDC
- dependencies should be defined in such a way that generation of Level-3B and higher levels is fully synchronized, i.e., if Level-3B is generated then all higher-level data products are generated as well
- the initializer is expected to give the GLOWS team ∼56 days (2 CRs) of time (after measurements of a given L3a lightcurve) to update the bad day list. It may happen that no new bad days will be added for a given CR. A given day is good by default (if not listed in the bad day list), so there is no need to check the bad day list by the initializer.
- the proposed initializer is expected to ensure traceability/reproducibility of data products, but requires the SDC to store the directories with the external-dependency files for every CR (∼200 MB per month)
- retro updates of external dependencies are not problematic in this approach. L3b-L3d pipeline always uses the most recent version of external dependencies by default.

4.6 Level-3A to Level-3B processing (IKL)

Objective: Level-3B defined as ionization rate profiles averaged over Carrington period

- Brief description: profiles of the ionization rate of interstellar H as well as the contributing charge-exchange and photoionization rates, provided as functions of the heliographic latitude (range: $-90° : 90°$, resolution: $10°$). Computed using the stationary-atom approximation. The connection between the daily lightcurve and daily ionization rate profile is defined by a set of parameters obtained by using WawHelioIon-MP model (details of the method can be found in Porowski and Bzowski (2024) and Section 13.3). Retrieval of the ionization rate profile from a lightcurve is performed using pre-defined matrix operations. Matrices valid for a set of pre-defined vantage points are provided as one of the ancillary files by the science team (13.3.6). After each Carrington rotation, science team provides a text file with a list of bad days that are not good enough for further analysis. The the daily ionization rate profiles qualified as good are averaged and passed to the next step of data processing.
- Instrument team supplied inputs: parameters for L3A to L3B processing, bad-day list, WawHelioIon-MP parameters, UV anisotropy profiles
- Internal dependencies: GLOWS Level-3A, SWAPI (moments of the solar wind proton distribution function: density, bulk velocity, temperature, alpha particle content), SPICE kernels (s/c – Sun distance needed for adjustment of the solar wind density to 1au)
- External dependencies: F10.7 index via LASP API, OMNI2 solar wind parameters (plasma speed, proton density, and α-particles abundance)

Processing from Level-3A to Level-3B involves:

- checking if the gaps in the light curve are not too big (see Sec. 13.3.3)
- removing the extraheliospheric and time dependent backgrounds
- re-calibrating the GLOWS lightcurve to the SWAN units (since WawHelioIon-MP is tuned to SWAN data) (see Section 13.4)
- light curve decomposition into a truncated Fourier series (the order depends on the vantage point) using one of the regression methods
- performing Principal Component Analysis (PCA) by applying matrices from WawHelioIon-MP model (see Section 13.3.1)
- calculation of the PCA coefficients of the ionization rate profiles
- calculation of the daily ionization rate profile using the obtained coefficients and base functions provided in the WawHelioIon-MP parameter file (see Figure 4.2)
- averaging of the daily ionization rate profiles over Carrington rotation period
- rescaling of the averaged ionization rate profile so that the magnitude of the equatorial bin equals to the sum of the sum of the Carrington-averaged photoionization rate and charge exchange rate obtained from averaging of the solar wind equatorial speed and density obtained from in-situ measurements, adjusted to 1 au (see Section 13.7)
- decomposition of the ionization rate profile into charge exchange and photoionization profiles. Photoionization value in the equatorial bin is calculated from the F10.7 radio flux measurements (see Section 13.6) and then modulated by the profiles of UV anisotropy factor provided by the instrument team. The charge exchange profile is calculated by subtracting the photoionization rate profile from the ionization rate profile.

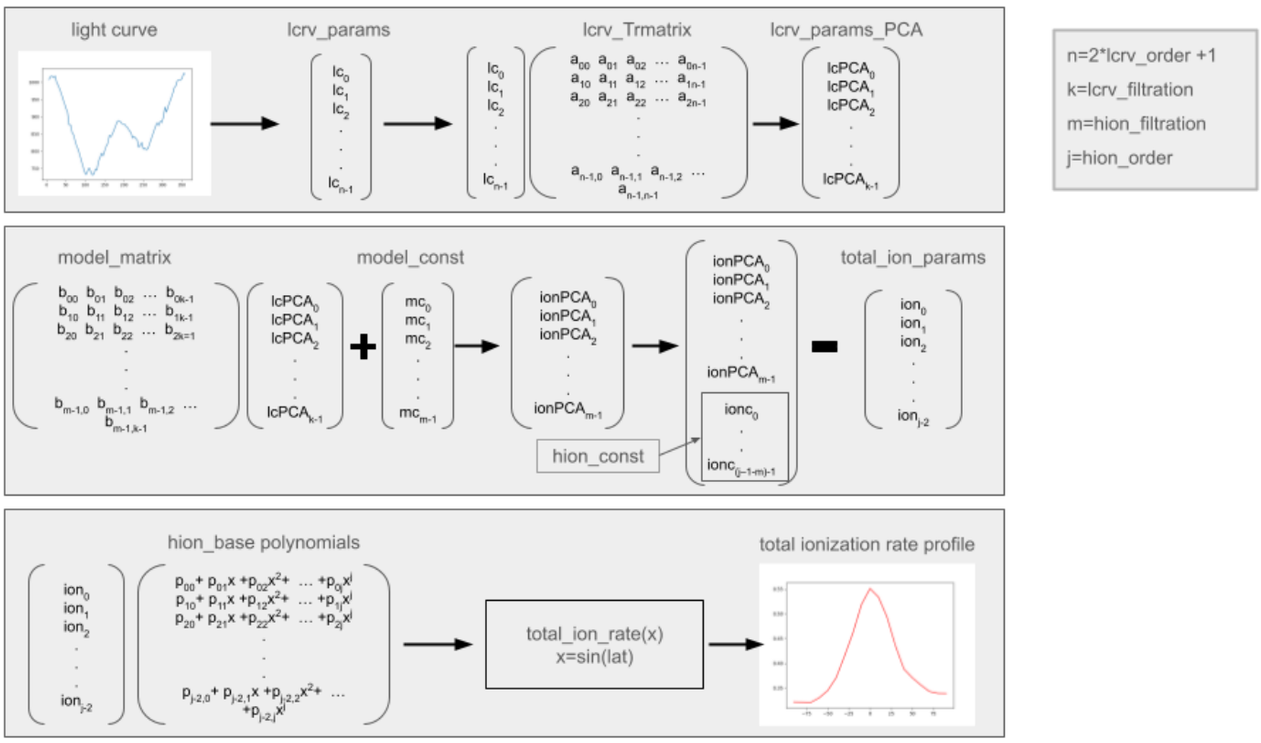


Figure 4.2: Scheme of the mathematical operations needed to convert a lightcurve into ionization a rate profile.

4.7 Level-3B data products (IKL)

Level-3B data product is Carrington period-averaged profiles of quantities related to ionization of neutral H atoms. Ionization rate will be provided in physical units [s^{-1}] with a 10° angular resolution in heliographic latitude. The product will be given as a 4 heliolatitudinal profiles:

- a sum of the charge exchange rate in the stationary atom approximation and the photoionization rate
- charge exchange rate in the stationary atom approximation
- photoionization rate
- UV anisotropy factor

Table 4.4: Brief description of GLOWS Level-3B data product. The product contains ionization rate, charge exchange, photoionization rate, and UV anisotropy profiles averaged over 1 Carrington rotation period. Item names refer to a Python-script bundle developed by the GLOWS Team.

Level-3B: Carrington averaged ionization rate profiles.		
No.	Item	Comments/Remarks
1	`header`	header for Level-3B profiles (see Table 4.5)
2	`date`	UTC averaged time (depends on input L3A files not excluded from the analysis)
3	`CR`	Carrington rotation number
4	`ion_rate_profile`	arrays for ionization rate profiles obtained from the lightcurve (see Tab. 4.6)
5	`uv_anisotropy_factor`	UV anisotropy factor

Table 4.5: Brief description of GLOWS Level-3B header (item 1 in Tab. 4.4). Item names refer to a Python-script bundle developed by the GLOWS Team.

Level-3B: header		
No.	Item	Comments/Remarks
1	`header`	
1.1	`software_version`	set by ground software
1.2	`filename`	name of the file
1.3	`ancillary_data_files`	list of ancillary files used for generation of Level-3B
1.4	`external_dependecie`	list of external files used for generation Level-3B
1.5	`l3a_input_file_name`	name of Level-3A files used as input data for generation Level-3B

Table 4.6: Brief description of GLOWS Level-3B Carrington ionization rate profile structure (item 4 in Table 4.4). Item names refer to a Python-script bundle developed by the GLOWS Team.

Level-3B: ionization rate profile structure		
No.	Item	Comments/Remarks
4	`ion_rate_profile`	
4.1	`lat_grid`	latitudinal grid [deg]
4.2	`sum_rate`	averaged ionization rate profile obtained from lightcurve [s^{-1}]
4.3	`ph_rate`	averaged photoionization rate profile [s^{-1}]
4.4	`cx_rate`	averaged charge exchange rate profile (stationary atom approximation) [s^{-1}]
4.5	`sum_uncert`	averaged ionization rate profile uncertainty [s^{-1}]
4.6	`ph_uncert`	averaged photoionization rate profile uncertainty [s^{-1}]
4.7	`cx_uncert`	averaged charge exchange rate profile uncertainty [s^{-1}]

4.8 Level-3B to Level-3C processing (IKL)

Objective: Level-3C defined as heliolatitudinal profile of Carrington-period-averaged solar wind speed and density

- Brief description: proton density and bulk velocity as functions of the heliographic latitude (range $-90°$: $90°$, resolution $10°$)
- Instrument team supplied inputs: parameters for L3B-to-L3C processing
- Internal dependencies: GLOWS Level-3B, SWAPI (moments of the distribution function: density, bulk velocity, temperature)
- External dependencies: OMNI2 time series data (plasma speed, proton density and α-particles abundance in the ecliptic plane)

Processing from Level-3B to Level-3C involves:

- reading and processing solar wind parameters in the ecliptic plane (at first from OMNI2 database (see Sec. 13.8.3))
- calculating solar energy flux (latitudinal invariant) (see Sec. 13.8) using solar wind parameters measured in the ecliptic plane. The invariant is averaged over long time interval of the order of 1 year (precise value will be given in the pipeline settings file).
- calculating the solar wind plasma speed and proton density at each latitude by solving a set of two equations (see Sec. 13.8.2).

4.9 Level-3C data products (IKL)

Level-3C data products are the solar wind plasma speed and proton density as a function of heliographic latitude. The parameters are adjusted to a distance of 1 au and have angular resolution of 10° in heliographic latitude. Plasma speed is in km/s, while proton density in cm^{-3}. The adjustment is done assuming that the speed is distance invariant (i.e., no change) and the density drops with the square of solar distance.

Table 4.7: Brief description of GLOWS Level-3C data product. The product contains plasma speed and proton density profiles averaged over 1 CR period. Item names refer to a Python-script bundle developed by the GLOWS Team.

Level-3C: Carrington period-averaged solar wind plasma speed and proton density profiles		
No.	Item	Comments/Remarks
1	`header`	header for Level-3C profiles (see Tab. 4.8)
2	`date`	UTC averaged time set in Level-3B
3	`CR`	Carrington rotation number set in Level-3B
4	`solar_wind_ecliptic`	solar wind parameters in the ecliptic plane averaged over 1 CR (see Table 4.9)
5	`solar_wind_profile`	arrays for solar wind parameter profiles obtained from the ionization rate profiles (see Table 4.10)

Table 4.8: Brief description of GLOWS Level-3C header (item 1 in Table 4.7). Item names refer to a Python-script bundle developed by the GLOWS Team.

Level-3C: header		
No.	Item	Comments/Remarks
1	`header`	
1.1	`software_version`	set by ground software
1.2	`filename`	name of the file
1.3	`ancillary_data_files`	list of ancillary files used for generation of Level-3C
1.4	`external_dependecie`	list of external files used for generation Level-3C
1.5	`l3b_input_file_name`	name of Level-3B files used as input data for generation Level-3C

Table 4.9: Brief description of GLOWS Level-3C Carrington solar wind parameters values in the ecliptic plane (item 4 in Table 4.7). Item names refer to a Python-script bundle developed by the GLOWS Team.

Level-3C: averaged solar wind parameters in the ecliptic plane		
No.	Item	Comments/Remarks
4	`solar_wind_elciptic`	
4.1	`plasma_speed`	averaged solar wind plasma speed in the ecliptic plane [km s^{-1}]
4.2	`proton_density`	averaged proton density in the ecliptic plane adjusted to 1 au [cm^{-3}]
4.3	`alpha_abundance`	averaged α-particles to protons ratio in the ecliptic plane

4.10 Level-3B/C to Level-3D processing (IKL+MK)

Objective: Level-3D defined as history of latitudinal profiles of solar wind parameters (WawHelioIon time series) needed in the calculations of survival probabilities.

- Brief description: set of arrays with the history of latitudinal profiles of solar parameters on a common, regular time grid with Carrington-rotation period resolution

Table 4.10: Brief description of GLOWS Level-3C: structure of Carrington-averaged profiles of solar wind parameters (item 5 in Table 4.7). Item names refer to a Python-script bundle developed by the GLOWS Team.

	Level-3C: structure of profiles of solar wind speed and density		
	No.	Item	Comments/Remarks
profile	5	`solar_wind_profile`	
	5.1	`lat_grid`	latitudinal grid [deg]
	5.2	`plasma_speed`	averaged profile of solar wind plasma speed [km s^{-1}]
	5.3	`proton_density`	averaged profile of proton density adjusted to 1 au [cm^{-3}]

- Instrument team supplied inputs: parameters for Level-3B/C to Level-3D processing
- Internal dependencies: GLOWS Level-3B, GLOWS Level-3C, SWAPI
- External dependencies: Lyman-α composite flux via LASP API, F10.7 index via LASP API, OMNI2 (for electrons, optionally SWE)

Processing from Level-3B/C to Level-3D involves:

- read initial L3D structure based on WawHelioIon model (see Section 13.9)
- read solar parameters for the current Carrington rotation period:
  - `L3b:uv_anisotropy_factor`
  - `L3b:ion_rate_profile:ph_rate`
  - `L3c:solar_wind_profile:plasma_speed`
  - `L3c:solar_wind_profile:proton_density`
  - `L3c:solar_wind_ecliptic:plasma_speed`
  - `L3c:solar_wind_ecliptic:proton_density`
  - `L3c:solar_wind_ecliptic:alpha_abundance`
  - `external_dependencies:lya`
- interpolate on Carrington rotation centers
- update the text files by appending to the initial files
- generate Level-3D CDF file

4.11 Level-3D data products (IKL)

The Level-3D data product is in two forms: a CDF file described in Table 4.11 and a set of text files described in Table 4.15. These text files are used in the Level-3E processing and have the same header and structure as the set of ancillary files delivered by the instrument team (see Section 13.9).

4.12 Level-3D to Level-3E processing (IKL+MK)

Objective: Level-3E defined as daily survival probabilities for Lo, Hi, Ultra

- Brief description: arrays with the survival probabilities of the incoming energetic neutral atoms (ENAs) as a function of the ENA energy, arrival direction, and time (geometry details to be agreed with the Lo, Hi, and Ultra teams)
- Instrument team supplied inputs: parameters for L3e processing

Table 4.11: Brief description of GLOWS Level-3D data product. The product contains a history of latitudinal profiles of the solar parameters: plasma speed, proton density, UV anisotropy factor, photoionization rate, Lyman-α flux, and electron density. Item names refer to a Python-script bundle developed by the GLOWS Team.

Level-3D: History of the solar parameter profiles (WawHelioIon time series).		
No.	Item	Comments/Remarks
1	`header`	header for Level-3D profiles (see Tab. 4.12)
2	`lat_grid`	latitudinal grid for profiles [deg]
3	`cr_grid`	time grid with Carrington rotation period resolution. Bins are set in the middle of each CR [CR]
4	`time_grid`	UTC time corresponding to the Carrington grid centers [decimal years]
5	`solar_params`	latitudinal arrays of solar parameters history (see Tab. 4.13)
6	`flags`	source flags for selected solar parameters

Table 4.12: Brief description of GLOWS Level-3D header (item 1 in Table 4.11). Item names refer to a Python-script bundle developed by the GLOWS Team.

Level-3D: header		
No.	Item	Comments/Remarks
1	`header`	
1.1	`software_version`	set by ground software
1.2	`ancillary_data_files`	list of ancillary files used for generation of Level-3D
1.3	`external_dependecie`	list of external files used for generation Level-3D
1.4	`l3b_input_file_name`	name of Level-3B files used as input data for generation Level-3D
1.5	`l3c_input_file_name`	name of Level-3C files used as input data for generation Level-3D

Table 4.13: Brief description of GLOWS Level-3D history of Carrington-averaged solar parameters (item 5 in Table 4.11). Item names refer to a Python-script bundle developed by the GLOWS Team.

Level-3D: solar parameters history		
No.	Item	Comments/Remarks
5	`solar_params`	
5.1	`plasma_speed`	solar wind plasma speed profile [km s^{-1}]
5.2	`proton_density`	proton density profile [cm^{-3}]
5.3	`uv_anisotropy`	UV anisotropy factor profile [dimensionless]
5.4	`photoion`	photoionization rate in the ecliptic plane [s^{-1}]
5.5	`lya`	composite solar Lyman-α flux [ph cm^{-2} s^{-1}]
5.6	`electron_density`	solar wind electron density in the ecliptic plane [cm^{-3}]

Table 4.14: Brief description of GLOWS Level-3D flags (item 6 in Table 4.11). Item names refer to a Python-script bundle developed by the GLOWS Team.

Level-3D: source flags		
No.	Item	Comments/Remarks
6	`flags`	
6.1	`plasma_speed`	solar wind plasma speed source flags
6.2	`proton_density`	proton density source flags
6.3	`uv_anisotropy`	UV anisotropy factor source flags

Table 4.15: Brief description of GLOWS Level-3D Carrington solar parameters history in text format. Items are descriptors in the official SDC file naming scheme `https://imap-processing.readthedocs.io/en/v0.5.0_a/development-guide/style-guide/naming-conventions.html`

Level-3D text files descriptors		
No.	Item	Comments/Remarks
1	`plasma-speed`	item 5.1 in Tab. 4.13
2	`proton-density`	item 5.2 in Tab. 4.13
3	`uv-anisotropy`	item 5.3 in Tab. 4.13
4	`photoion`	item 5.4 in Tab. 4.13
5	`lya`	item 5.5 in Tab. 4.13
6	`electron-density`	item 5.6 in Tab. 4.13

.

- Internal dependencies: GLOWS Level-3D, SPICE kernels (spacecraft position, velocity vector, IMAP-Lo inclination angle), official spin axis pointing averaged for a given observation day (i.e., time interval between repointings)
- External dependencies: None

profile

Processing from Level-3D to Level-3E involves:

- generation of the ionization files in the txt format from L3D data product that are required by the `survProb*` executable (see items 5-10 in Tab. 4.17)
- generation of the command line parameters required by the survProb* executable (see Table 4.16)
- run executable for each detector: `survProbLo,survProbHi,survProbUltra`

Detailed description of the code, how to run it and summary of the error messages are presented in Sections 13.10.1 and 13.10.2.

4.13 Level-3E data products (IKL+MK)

Level-3E data product is a survival probability files for a specific instruments. The CDF variables are defined based on text output produced by the `survProb*` executable (see Section 13.10.3).

4.14 Test scripts in Python/Mathematica

Python-script bundle for the Level-0 to Level-2 processing (described in Section 3.11) was extended to generate Level-3a JSON files. The files show how the GLOWS team envisions the data products. The content of the Level-3A JSON file is expected to be fully consistent with Tables 4.1, 4.2, and 4.3.

Further extensions of the Python-script have been developed by the GLOWS team to generate Level-3B, Level-3C, Level-3D, and Level-3E data products.

4.15 Settings/parameters for ground-processing pipeline

The full list of ancillary files (referred to as *Instrument Team Supplied Inputs* in Fig. 4.1) is provided in Section 3.12. Items from the general list used specifically for the Level-2 to Level-3A processing include:

- item 6 – the calibration coefficient in Level-3a lightcurve as a configurable parameter
- item 7 – all-sky map of extra-heliospheric (time-independent) background

Table 4.16: Command-line parameters for the survival probability programs survProb*

Input from the command line for the survProb* programs		
No.	Item	Comments/Remarks
0	example	`./survProbLo 20090101_000001 2009.00000 0.983305 100.5761 0.00 -29.7745 -5.5893 -0.0008 280.57619 0.000 90.0`
1	time in IMAP format	IMAP time identification, in the format YYYYMMDD_HHMMSS. Must be a 15-character string.
2	time_point	time as decimal year (first 10 digits used in the name of output file), range=[1800:2070]. Center of the time interval pointing.
3	R of SC	spacecraft location: distance from the Sun in AU, range [0:routs_end] (Table 13.4:line 7)[a]
4	long of SC	spacecraft location: ecliptic longitude J2000 [°] in the solar-inertial reference frame, range [0:360][a]
5	lat of SC	spacecraft location ecliptic latitude J2000 [°] in the solar-inertial reference frame, range [-90:90][a]
6	Vx	spacecraft velocity relative to the Sun [km/s], ecliptic Cartesian system: x component. Range: $\sqrt{V_x^2 + V_y^2 + V_z^2} < 60$ km/s. Applies to Vx, Vy, and Vz[a]
7	Vy	spacecraft velocity relative to the Sun [km/s], ecliptic Cartesian system: y component[a]
8	Vz	spacecraft velocity relative to the Sun [km/s], ecliptic Cartesian system: z component[a]
9	alpha Axis	ecliptic longitude J2000 of the IMAP spin axis [°] (pointing close to the Sun), range [0:360][b]
10	beta Axis	ecliptic latitude J2000 of the IMAP spin axis [°] (pointing close to the Sun), range [-90:90][b]
11	elongation	For Lo and Hi: the angle between the spacecraft spin axis and the instrument boresight. For Lo: the actual elongation for a given spin axis pointing; range: [60:165]. For Hi: either 90 (for IMAP-Hi90) or 135 (for IMAP-Hi45]). For Ultra: the radius of the avoidance circle, i.e., the angle between the spin axis of the spacecraft and the border of the calculation region. Inside that circle, near the Sun, there will be no calculations of prob. of surv. Range [10:180].

a From SPICE exactly for time_point.

b Average over the time pointing interval.

Table 4.17: Input files for the programs survProb*

Input files for the prob. of. surv. program		
No.	Item	Comments/Remarks
0	example file list in `ionization.files.dat`	`lyaSeriesV4_2021b.dat`, `speed3D.v01.Legendre.2021b.dat`, `density3D.v01.Legendre.2021b.dat`, `phion_Hydrogen_T12F107_2021b.dat`, `swEqtrElectrons5_2021b.dat`
1	`tessXYZ8.dat`	Just for IMAP-Lo: HealPix grid in Cartesian coordinates, based on tesselation 8, used for collimator integration in IMAP-Lo. No header. Columns: x y z
2	`tessAng16.dat`	Just for IMAP-Ultra: HealPix grid in spherical coordinates [°] based on tessellation 16, used for spatial grid on the sky. No header. columns: colatitude, longitude
3	Energy Grid	Energy grid in [keV], in the spacecraft frame. For each energy the probability is calculated separately. Files specific for individual instruments: `EnGridLo.dat`, `EnGridHi.dat`, `EnGridUltra.dat`. No header. The length of files is flexible, but must be within [5:80]. Columns: Energy.
4	`ionization.files.dat`	A list of all ionization-related files needed to run the calculations. No header. The content of this file is listed below. The length of the file is 6.
5	lyaSeries	Time series of the total solar Lyman-α flux, time resolution 1 CR, magnitude range [1e11:1e12]. Header 30 lines. Columns: time [y], flux [ph cm^{-2} s^{-1}]
6	solar_uv_anisotropy	Latitudinal modulation factor for the solar Lyman-α flux and photoionization rate. Range [0.6:1.5] Columns: time [y], mod_fac(lat=-90°), mod_fac(lat=-80°), ..., mod_fac(lat=0°), ..., mod_fac(lat=90°), CR (Carrington rotation number)
7	speed3D SW	Latitudinal profiles of solar wind speed [km s^{-1}], time resolution 1 CR, range [100:1200]. Header 30 lines. Heliolatidudal grid is fixed at range [-90°:90°] with step 10°. Columns(21): time [y], speed(lat=-90°), speed(lat=-80°), ..., speed(lat=0°), ..., speed(lat=90°), CR (Carrington rotation number)
8	density3D SW	Latitudinal profiles of solar wind number density [cm^{-3}], time resolution 1 CR, range [0:30]. Header 30 lines. Columns: time [y], density(lat=-90°), density(lat=-80°), ..., density(lat=0°), ..., density(lat=90°), CR (Carrington rotation number)
9	phion_Hydrogen	Time series of equatorial hydrogen photoionization rate [s^{-1}], time resolution 1 CR, range [0.5e-7:4e-7]. Header 30 lines.
10	swElectrons	Time series of the equatorial number density of solar wind electrons, time resolution 1 CR, range [0:25]. Header 30 lines. columns: time [y], density [cm^{-3}]

Table 4.18: Brief description of GLOWS Level-3E data product for IMAP-Lo and IMAP-Hi. The product contains survival probabilietes.

Level-3E: Survival probability for IMAP-Lo and IMAP-Hi		
No.	Item	Comments/Remarks
1	`header`	header for Level-3E (see Table 4.20)
2	`date`	UTC time
3	`instrument`	instrument name for which calculation were done
4	`elongation`	elongation angle of the instrument set in item 3 [°]
5	`energy_grid`	energy grid for a specific instrument [eV]
6	`spin_angle`	angle along the circle in the sky centered at the direction of the IMAP spin axis, counted anticlockwise off the the nearest point to the ecliptic north pole anticlockwise
7	`surv_prob`	array with survival probability (size: len(`energy_grid`) x len(`spin_angle`))
8	`surv_prob_v0`	array with survival probability for a s/c velocity equal to 0 (size: len(`energy_grid`) x len(`spin_angle`))

Table 4.19: Brief description of GLOWS Level-3E data product for IMAP-Ultra. The product contains survival probabilietes.

Level-3E: Survival probability for IMAP-Ultra		
No.	Item	Comments/Remarks
1	`header`	header for Level-3E (see Tab. 4.20)
2	`date`	UTC time
3	`instrument`	instrument name for which calculation were done
4	`energy_grid`	energy grid for a specific instrument [eV]
5	`coord_grid`	(longitude, latitude) of the healPix grid points
7	`surv_prob`	array with survival probability (size: len(`energy_grid`) x len(`coord_grid`))
8	`surv_prob_v0`	array with survival probability for a s/c velocity equal to 0 (size: len(`energy_grid`) x len(`spin_angle`))

Table 4.20: Brief description of GLOWS Level-3E header (item 1 in Tab. 4.18 and Table 4.19). Item names refer to a Python-script bundle developed by the GLOWS Team.

Level-3E: header		
No.	Item	Comments/Remarks
1	`header`	
1.1	`software_version`	set by ground software
1.2	`ancillary_data_files`	list of ancillary files used for generation of Level-3E
1.5	`l3d_input_file_name`	name of Level-3D files used as input data for generation Level-3E

- item 8 – time-dependent background corrections for bins of Level-3A lightcurves
- item 9 – pipeline settings: includes the number of bins

Items for the Level-3A-to-Level-3E processing

- `imap_glows_bad_days_list_vXXX.json`: list of bad days when daily light curve is not good enough for further analysis
- `imap_glows_WawHelioIonMP_vXXX.json`: parameters of the WawHelioIon-MP model that converts ligtcurve into ionization rate profile
- `imap_glows_uv-anisotropy-<tag>_vXXX.dat`: solar UV anisotropy factor profile history
- `imap_glows_p-density-<tag>_vXXX.dat`: proton density profile history
- `imap_glows_sw-speed-<tag>_vXXX.dat`: plasma speed profile history
- `imap_glows_lya-<tag>_vXXX.dat`: composite Lyman-α irradiance history
- `imap_glows_phion-<tag>_vXXX.dat`: photoionization rate in the ecliptic plane history
- `imap_glows_e-density-<tag>_vXXX.dat`: electron density in the ecliptic plane history (calculated from the proton and α-particles density - assuming charge quasi-neutrality of the solar wind)

4.16 Comments

5 Sources of the observed signal

The sources of the signal observed by GLOWS are discussed in the *GLOWS Entrance System Writeup* (Bzowski et al., 2021). Briefly, they include

1. The heliospheric backscatter glow in the Lyman-α line,
2. Reflections of flares and active regions at the Sun's surface off the interplanetary hydrogen,
3. Solar Lyman-α emission scattered on interplanetary dust
4. The glow of energetic neutral atoms (ENAs)
5. Extraheliospheric (EH) sources: (stars, Milky Way, quasars etc.), planets, and comets,
6. Stray light from strong EUV sources in the sky,
7. Particle background.
8. Black counts.

Out of these signal components, science analysis is planned on (1), and all the other ones need to be identified and subtracted. (5) is planned to be used for calibration, so that the global long-time evolution of (1) can be distinguished from effects of the expected gradual loss of sensitivity of the detector during observations. (4) may become a subject of scientific analysis.

6 What the data system must guarantee

GLOWS is its own

- science instrument,
- star sensor, and
- background monitor.

The design of the instrument does not facilitate distinguishing between event counts due to photons and the charged particles within the instrument. Contributions to the event counts downlinked to Earth have to be sorted out during data analysis. Therefore, the design of the data products must guarantee the following objectives:

1. identification and removal of unwanted particle background,
2. identification and removal of the contribution from extraheliospheric sources,
3. tracking the day-to-day evolution of signal from selected calibration stars when they are in the FOV,
4. binning on the ground of the pure-heliospheric glow signal into 90 well defined spin angle bins (without smearing etc.)

7 Characteristics of the observed signal

Predictions on the observed signal during various times during the year and during various phases of the solar activity cycle are presented in the *GLOWS signal evolution report* (Kowalska-Leszczynska et al., 2021). The counting rate due to the helioglow is expected to be between $\sim$ 200 and $\sim$ 1000 cps (counts per second), and for the brightest star about 1000 cps (TBC). Hence, the maximum signal that must not saturate the detector is $\sim$ 2000 cps (TBC).

Singular stars will be seen as peaks superimposed on the lightcurve observed during spin. Since the nominal diameter of the FOV is $\sim 8^\circ$ (the transmission coefficient at this distance is equal to 0.01 (based on Figure 22 in the *Baffle design report*, Kaźmierczak et al. (2021), and the *PSF Definition Report*, Strumik (2020b)), a star would be visible during $\sim$ 8 consecutive observation days, in the absence of the helioglow. Of course, the helioglow will swamp the signal during several days at the beginning and end of the visibility period. The magnitude of the peak of the star signal will be proportional to the angular distance of the star from the boresight; this feature will be used to measure the total visible brightness of calibration stars. However, stars will be seen as asterisms, i.e., more than one star will frequently be in the FOV. The data system must ensure a resolution sufficient to identify these cases.

The signal from the helioglow is expected not to significantly change over spin angle ranges characteristic of individual stars. However, in addition to point-like stars, the Milky Way will be visible in the sky, not resolved into individual stars. Rather, it will form an arc-like region of enhanced emission, similar in shape to the IBEX ribbon. Its width is on the order of 30°. The Milky Way signal is currently modeled as a part of unresolved H source contribution (Strumik et al., 2020; Strumik, 2020a). The data system should enable to identify and remove the Milky Way component on the ground, or at least to mask it without unnecessary loss of useful information. Due to a narrower profile of its spectral sensitivity, the signal measured by GLOWS is expected to be less contaminated by contribution from stars as compared with SOHO/SWAN. This, however, makes the process of star-based calibration more challenging.

In addition to the helioglow and stars, a particle background is expected. The intensity is TBD, which will likely be possible to estimate only after launch. This component of the signal is expected to be bursty. In the data, it will be visible as non-directional fluctuations in the total count rate measured during one or several spins of the spacecraft. The data products must ensure detection of the particle background at a percent level.

The observations will be performed during *IMAP days*, i.e., time intervals of a fixed spin axis pointing. The spin axis will be repositioned every 24 h (MRD), with possible deviations of −0.5 day, +3 days. Hence the length of IMAP day $T_{\text{IMAP day}}$ will be

$$0.5\,\text{day} \le T_{\text{IMAP day}} = 1.0\,\text{day} \le 3.0\,\text{day}. \tag{1}$$

The lightcurves will be collected spin after spin, accumulated in *blocks* of several spins, and binned. Blocks will be *grouped* to facilitate rebinning within individual blocks to account for possible irregularities in tagging the spin phase by the spacecraft. The counts are expected to feature a statistical scatter following the Poisson probability distribution. In the absence of a bursty background, the signal is expected not to vary from one spin to another, excluding the statistical scatter. The spin rate of the IMAP spacecraft is expected to be 4 ± 0.1 rpm (revolutions per minute); hence, the orbital period P_{IMAP} will be

$$14.63\,\text{s} \le P_{\text{IMAP}} = 15.00 \le 15.38\,\text{s}. \tag{2}$$

The stability of the spinning rate, or the spinning rate reported by the spacecraft, needs to be possible to verify based on GLOWS observations. Based on IBEX experience, possible issues include problems with identifying the spin phase, related variations in the reported beginnings of individual spins, possible small drift of the spacecraft spin axis, which may affect the peak heights of the stars and thus bias the calibration stars photometry, possible nutation/precession of the spacecraft and/or a misalignment of the spacecraft rotation axis and its z-axis.

The binning scheme is presented in Section 10.4.

Time keeping on-board[1] The mission clock onboard IMAP counts seconds past an epoch 00:00:00 UTC on 1 January 2010, as the time reference for commands and telemetry. The mission clock has a resolution of 48 bits and a $3\,\sigma$ accuracy $\pm 50\,\mu$s. This information is distributed to all instruments, including GLOWS once per second (1 PPS), with an accuracy $\pm 30\,\mu$s. The mission time will be aligned with the UTC time within ±500 ms (3σ) after ground post-processing. (this paragraph TBC)

Attitude and spin information[2] The measured attitude of GLOWS will be known to 0.15°, 3σ, single axis, relative to the heliocentric inertial frame (EMOJ200) during science operations after ground processing. The spin period estimate in flight will be stable to $\pm 8000\,\mu$s, distributed at 1 PPS to the instrument.

On the ground, the attitude and spin information will be available at a 10 Hz cadence[3]. The uncertainty of the spin and attitude information in these data will be 0.1°(understood as 1σ). (1σ or 3σ? TBC)

8 Operation modes

GLOWS will perform initial calibration and high voltage ramp up during the commissioning phase of the mission. Afterward, it will perform normal science operations. However, during the normal science operations three additional tests are performed approximately monthly: the test of sensitivity vs high-voltage setting (the HV test). the comparation voltage test (comparation test), and the threshold voltage test (threshold test). From the viewpoint of operations and collected data, these are normal observations.

The GLOWS data products reflect the following modes of operations:

1. Normal science operations
2. Regular in-flight tests (high-voltage, comparation voltage, and threshold voltage, performed at regular intervals during normal operations)
3. Initial calibration and high voltage ramp-up (expected to be performed at first powering on after launch, then at restarting after drastic mishaps, operations during commissioning, etc.)

[1] Based on information from the Payload Engineer Susan Pope, relayed by Roman Wawrzaszek in an e-mail of September 27, 2019; file Requirements_MRD_L2 Draft 08-19-2019.

[2] Same source as for the time keeping.

[3] Information provided at the IMAP Technical Meeting, APL, March 28 – April 1, 2022.

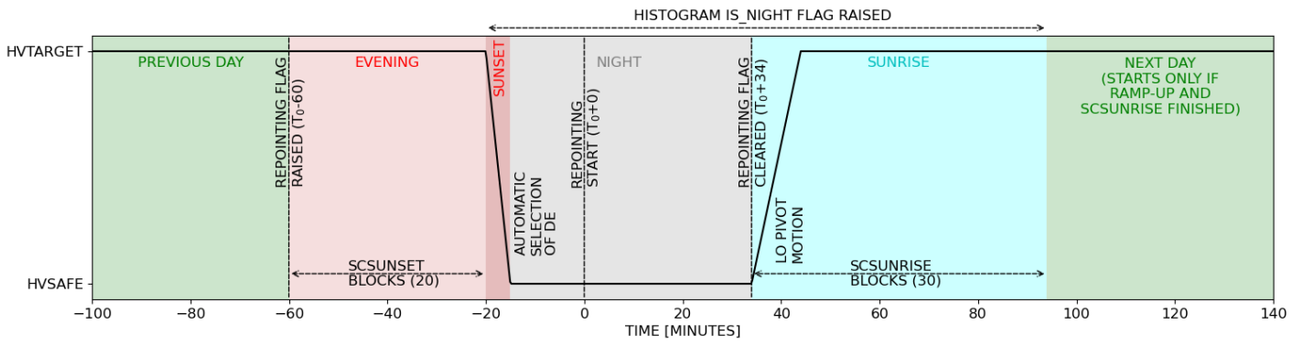


Figure 8.1: *nightTimeLine* A sequence of GLOWS state transitions at the turn of observation days (pointings). See Section 8.1 for explanations.

The on-board data structures, registered during normal science ops (including the aforementioned tests) are identical during the tests and outside the tests. Data collected during commissioning also maintain this format.

Organization of data onboard is irrelevant for the purpose of this document and is not discussed here. What counts are the data downlinked in the telemetry packets and at the lowest level of the processing pipeline, they are just unpacked telemetry packets.

As the processing advances and reaches increasing Data Product Levels, more products appear. In normal science ops, the baseline data structure is that for an individual histogram (Section 12.6, block histogram H_i). At the next level, data culling begins and on one hand, data structures related to culling are introduced (BT), on the other hand, and histograms are aggregated into daily histograms. It may be that because of culling, some of them will be missing. In that case, a BT structure must be nevertheless available to facilitate the user to identify the reason for rejection of a data subset. Details are presented in Section 12.7.1.

8.1 Normal science operations

In the following, we discuss normal science ops. Measurements are taken continuously, without ramping down the voltage on the detector during daily spin-axis repositioning maneuvers, however the system is prepared for ramping down the voltage if deemed needed in flight and this resulted in the need of implementation of a sequence of transitioning from one observation day to another through a sequence of states, presented in Figure 8.1.

Preparations for the spin axis repositioning maneuvers involve turning on catbed heaters for control thrusters 1 hour before starting a given maneuver. At this, a flag `RepointingPending` is set by the spacecraft. GLOWS is still in the **Day Mode** but enters the **Evening state** and starts counting down 20 spin blocks (corresponding to $\sim$ 40 minutes; in-flight configurable) that are still attributed to the current observation day. Data collection and histograming are performed out normally. After this time interval, GLOWS sets the flag `IsNight`, enters the **Night Mode**, and transitions into the **Sunset state**. The HV can now be[4] decreased or switched off. Once the HV ramp-down procedure is completed, GLOWS switches on the **Night state** and remains in it until the `Repointing Pending` flag is cleared by the spacecraft 34 minutes after the maneuver is initiated.

At this, GLOWS transitions into **Sunrise state** and the HV is ramped up to the normal operational value. The procedure to ramp up the voltage is always invoked, even though the target voltage is planned to be identical to the night-time voltage and in fact the voltage is not being changed. The instrument continues to be in the **Night Mode** but the data are collected normally. The **Sunrise state** continues for 30 spin blocks (in-flight configurable) and is subsequently switched off. This additional waiting time is added to allow for damping of spin axis instabilities after IMAP-Lo pivot platform activity. repointing the IMAP-Lo pivot platform. GLOWS

[4]This is implemented as a launching a procedjure to ramp down the HV to a magnitude given in the configuration file. The Night state target setting can be identical to that for the Day state, which results in maintaining the HV setting unchanged and continuing data collection during Night state. At the time of this writing (March 17, 2025), this is default. Maintaining the voltage unchanged does not change the flag behavior: the flag IsNight is set ON.

prefers to stay in the **Sunrise state** during this operation because it may involve instabilities of the IMAP rotation axis pointing, which are unwanted during GLOWS science ops.

When the instrument is in the **Night Mode**, the AppSW analyzes the numbers of event counts in the histograms collected during the observation day just completed to determine the histograms with the minimum and maximum numbers of counts and prepares a list of DEs for downlinking to ground during the following observation day.

During the `RepointingPending` time interval, GLOWS still records DEs and histograms. Data gathered during this time can be used for the estimation of the dark current for the instrument, if the decision is made to ramp down the voltage. Even though the voltage is not ramped down in the standard operations procedure, it is preferable to maintain the Night and Day Modes to clearly separate observations when some activities on the spacecraft that potentially can disturb the spinning of the spacecraft are underway. The system of flags for the GLOWS telemetry data (histogram and direct-event packets) contains the flag `IsNight` that informs about the current mode (Day or Night), when a given set of measurements was obtained. Histograms and direct-event packets contain the HV-settings information, which allows to distinguish further if HV was maintained, decreased, or switched off completely in the Night Mode.

Measurements stop and HV is taken out (ramped down) during station keeping maneuvers; once they are completed, HV is ramped up gradually, using a predefined slope of the voltage in time. Precautions in the ramping up of HV are taken after safings and other mishaps; in these cases, the procedure used at the first power-on will be performed (TBC).

8.2 Regular in-flight tests

8.2.1 Regular in-flight HV gain tests

The data structures for HV gain tests are identical to normal science data structures. Gain tests will consist of reducing the voltage to a predetermined level and continuing observation during $N^{\mathrm{HV}}_{\mathrm{block}}$ spin blocks. Subsequently, the voltage will be increased in $N^{\mathrm{HV}}_{\mathrm{step}}$ steps to a level HV_{MAX} exceeding by a certain margin the original setting and the measurements will be executed for the same amount of time. It is expected that the brightness of the strip of the sky observed by GLOWS will not change during the test, so the total number of counts registered for each HV setting should vary only due to the varying sensitivity of the channeltron. Consequently, the parameter of interest here is the total number of counts per block.

In practice, however, (1) the brightness of the sky may change a little (a few percent at most), (2) there might occur a burst of particle background counts, (3) something currently not predicted may appear. This is in addition to the normal statistical scatter of the number of counts. Since ramping of HV is done gradually, a change of HV after a given block results in a variable HV setting during a non-negligible portion of the subsequent block. This block is unsuitable for the instrument sensitivity and science analysis and needs to be flagged. The capability to inspect the histograms collected during the gain tests is needed, and therefore it seems advisable to use the same data structure as for the normal science ops, with the gain test flag `is_hv_test_in_progress` set on.

Detailed description of the gain-test scenario can be found in a calibration-plan document (reference needed).

8.2.2 Regular comparation voltage test

8.2.3 Regular threshold voltage test

8.3 Ground processing for DE (direct-event) data

A portion of Direct Events is downloaded as described in Sections 9 and 12.5 and used as supporting data for ground analysis of instrument operation. The DE data can be processed by ground software to generate histograms by using Algorithms 1 or 2 in a similar manner as the histograms generated onboard. However, the DE data structures corresponding to individual histograms must be appropriately clipped in time to precisely correspond to the times for which the on-board histograms were collected. This clipping must be done because the DE on-board data portions correspond to full time seconds. The ground-generated histograms will have

the same angular resolution and accumulation time as the onboard-generated histograms. A data structure for the ground-generated histograms equivalent to Level-1A is created, which makes it possible to further process the ground-generated histograms by the standard ground-processing pipeline for histograms, as described in Sections 12.6–12.7. The headers of data structures at all levels contain information whether a given histogram was generated onboard or on the ground. This is given by the flag `is_generated_on_ground`.

GLOWS uses the onboard 1PPS-spin-phase information to compute the IMAP spin-phase values at a 1-second cadence measured by the IMAP clock, but DE are registered using the GLOWS internal clock. Keeping track of the GLOWS clock relative to the IMAP clock makes it possible to relate the GLOWS-clock readings with spin-phase values and consequently perform binning of the DE data in the spin-phase domain onboard. However, Algorithm 1 assumes histogram-bin incrementing at 1PPS, which means that to reproduce onboard-generated histograms on the ground with the full precision, we need to know the full history of the GLOWS clock vs. IMAP clock at a 1-second cadence. Such clocks-related data are not downlinked, thus ground-based histogram generation for DE uses clock-related information from the data structures defined in Section 12.5. This means that the relative state of the GLOWS clock with respect to the IMAP clock is known on the ground with the cadence corresponding to one block (approximately 2 minutes). This is the reason why it was decided to use Algorithm 2 for binning ground-generated histograms, which assumes histogram-bin incrementing once per block. The IMAP telemetry contains a time series of IMAP-clock values and the corresponding spin-phase values at at least 1 second cadence. This information can be potentially used in the GLOWS ground-histogram generating process, which would make it possible to use Algorithm 1. Still, however, the full-precision relation between readings of the GLOWS and IMAP clocks is available only onboard and hence is not possible to be fully reproduced during ground processing of DE. However, since the daily-accumulated drift of the GLOWS clock relative to the IMAP clock is expected to be negligible (TBC), no statistically-significant difference is expected between the onboard- and ground-generated histograms.

9 Direct Events

In this section, a thorough discussion on direct events is provided. An executive summary is provided in Section 9.1. The volume of Direct Event data available for downlinking, which depends on the length of data word used in the memory, is estimated in Section 9.2. A strategy for prioritizing Direct Event blocks for downlinking is described in Section 9.3.

9.1 Executive summary on direct events

This subsection contains a summary of Section 9, while other subsections usually contain extended studies and discussions of particular topics. This subsection is expected to contain up-to-date information on decisions made in internal discussions of the GLOWS team. Note that updates of this subsection may likely imply updates of Section 2.3.

9.1.1 Direct-events collection

Collection process. Direct events are collected over entire observation days, including the Day and Night Modes, discussed in Section 8.1. Direct events are collected and saved in the instrument memory. After downlinking, direct events can be histogrammed on the ground.

GLOWS vs. IMAP clock. The GLOWS clock is not synchronized regularly with the IMAP clock, but GLOWS-clock timestamping of the incoming 1PPS packets is performed with the jitter/delay < 300 ns, which should fix the question of correspondence between the GLOWS and IMAP clocks. Both GLOWS and IMAP readings are sent in the science telemetry packets.

The timestamps for direct events are measured nominally by the GLOWS internal clock with the time resolution of 0.5 μs. Downlinked science telemetry contains block-start and block-duration readings from both GLOWS and IMAP clocks to enable synchronization of the GLOWS spin blocks with the IMAP general-telemetry data available on the ground. More details are discussed in Section 12.1.1.

Memory faults for DE. Possible GLOWS memory faults resulting from radiation may cause random changes of timestamps for DE. The probabilities of such events are still TBD but believed to be very low. The occurrence of memory faults should be marked by an appropriate flag for a given sector of DEs and in the corresponding histograms generated onboard. Generally, the histogramming algorithm is designed to be not sensitive to memory faults.

9.1.2 File format for onboard storage

Onboard-storage system. The timestamps of DEs and DE durations are stored onboard in data files. Individual spins and blocks of spins (the same blocks that are used for histogramming) can be identified with the time resolution sent by telemetry to the ground, i.e., with the resolution of full seconds.
File format. Section 9.2 describes in detail various considerations/studies related to encoding/compression of direct events by saving them in the instrument memory as time differences rather than full timestamps. Based on these studies, it was decided that the time-difference-based format will be used for storing direct events onboard and in the telemetry. The full timestamp (GLOWS-clock) is stored only for the first event of a given one-second sector. For the next events within the one-second sector, time offsets relative to the previous direct event are stored. The event coding scheme presented in Section 9.2 is used. The default length of word for encoding direct-event time differences is 16 bits (integer multiple of byte), and will be dynamically increased when an overflow situation is detected by the onboard software.

In addition to the time stamp, each event has its duration coded as an 8-bit number (see Section 11.3).
Memory size. Available onboard memory will guarantee a storage time longer than a month, which enables an emergency on-demand downlinking. However. The on-board storage is divided into 32 partitions. Each partition covers $\sim$ 18 hours due to the adopted addressing scheme. If during that time more DEs than the volume of the current partition is gathered (unlikely), then the excess DEs over the partition volume are not stored.

9.1.3 Regular daily downlinking: selection of blocks

Selection of blocks. Direct events from a given observation day will be sent by telemetry on the next observation day. This approach is adopted because blocks with the maximum and minimum number of events need to be identified and downlinked, which is only possible after a given observation day came to its end. Additionally, this approach allows us to better organize transfers of other selected direct-events blocks in such a way that blocks scheduled for downlinking different to the min/max blocks are evenly distributed over the given observation day.

The number of blocks to be downlinked is dynamically determined depending on the available bit rate (after securing the higher-priority transfers of histograms and on-demand-direct-events blocks). It is assumed that for each nominal requested block, the neighboring (preceding and following) blocks will also be transferred to the ground, which gives effectively a triplet of adjacent blocks for each block nominally selected for downlinking. Since DE are organized onboard into one-second sectors, the triplets will be slightly longer than the intervals resulting from zero-spin-phase-transition times. Therefore, direct event blocks will require a trimming in ground processing.
Ordering of block transfers. The ordering of block transfers should guarantee an even daily coverage if daily telemetry unexpectedly ends earlier. To that end, the bisection method (daily first, daily last, daily middle, etc.) discussed below in Section 9.3 will be used to determine the block order for downlinking.
More info, priorities. Section 9.3 presents a more detailed insight into the selection process for direct events. The regular-daily downlinking has a lower priority than the histogram and on-demand transfers.

9.1.4 On-demand downlinking

On-demand downlinking addresses data collected during individual time seconds (full seconds). However, on-demand DEs need to correspond to individual block histograms. Therefore, the user specifies the histograms for which DEs are requested and a ground software determines the corresponding time seconds, as mentioned in 2.3. Since sectors with full seconds of data are downloaded, and the time boundaries of the histograms are not the full seconds, some excess DE data are thus be downloaded.

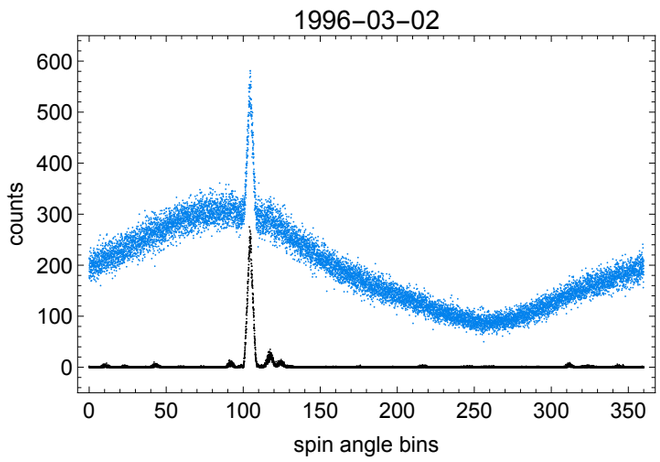


Figure 9.1: *exampleTimeSeries* An example 1-hour time series of the total signal virtually observed by GLOWS on March 3, 1996 using the XN filter (blue) and the signal solely from stars (black). The Monte Carlo time series of direct events was binned into 0.1° spin angle bins. Figure source: `timeStamps2019-10-31.nb` at `imap/GLOWS/timestamps`.

Based on the list of requested histograms, a list of requested contiguous intervals of seconds is compiled and uplinked to the instrument. The flight software maintains a list of seconds for downliking. DE data corresponding to this list are downlinked at top priority. Resumption of the regular scheme of DE downlinking will occur once the on-demand list is empty. The Science Team will generate a list of requested histograms, understood as a list of histograms for which the corresponding DEs are to be downloaded.

9.1.5 Direct-events telemetry content

In Section 12.5.2, a list of expected items in unpacked telemetry for direct events (Level-1A data product) is discussed. The flight software must guarantee that all the items will be included in science-telemetry CCSDS packets for direct events.

It is assumed that telemetry files will be organized similarly to onboard files used for storing direct events. Namely, the full timestamp will be stored only for the beginning of a given sector, while direct events will be stored as time differences. All events will have the associated event durations; see Section 11.3. The structure of the telemetry files should guarantee the possibility of extracting data for individual spin periods and blocks of spins.

9.2 The volume of DE data for downlinking

The frequency of the GLOWS event counter is

$$f_{\text{counter}} = 2\,\text{MHz} = 2 \times 10^6\,\text{Hz}, \tag{3}$$

which implies that the minimum time between registered events (equivalent to the instrument dead time) is

$$t_{\text{dead}} = 0.5\,\mu\text{s} = 5 \times 10^{-7}\,\text{s}. \tag{4}$$

The expected number of events per day is

$$C_{\text{day}} = 86400\,\text{s} \times s_{\text{mean}} = 5.184 \times 10^7\,\text{cts}. \tag{5}$$

M. Strumik performed Monte Carlo simulations of a 1-hour series of observations for a day when a bright star is visible. The basis for the simulations were simulations of the helioglow signal for this day, performed by

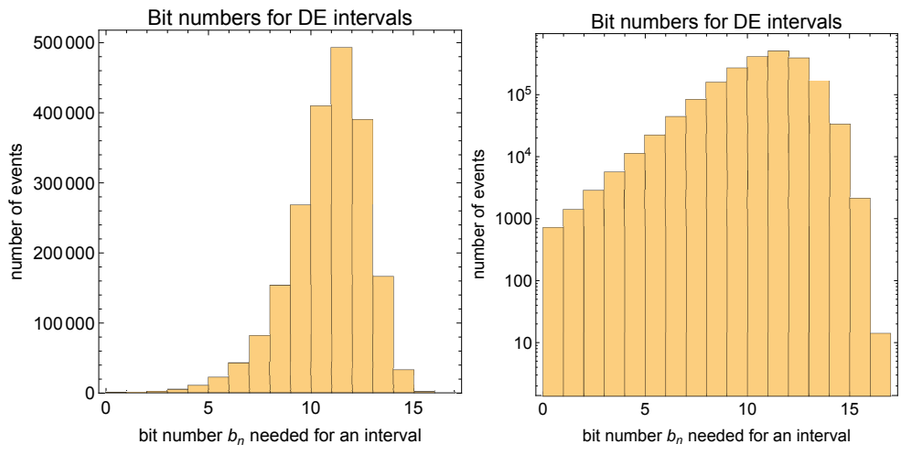


Figure 9.2: *bitsPerInterval* Histogram of the number of bits needed to code the DE time intervals, for the simulation shown in Fig. 9.1. The left panel shows the histogram in the linear scale, the right panel presents the same histogram in the semi-log scale. Note the relatively large number of very short intervals. Also note there are 14 intervals at the right-hand side of the histogram that must be coded in as many as 16 bits, i.e., the interval length is on the order $2^{16} - 1 = 65535$ ticks (~ 0.033) s. Figure source: notebook `timeStamps2019-10-31.nb` at `imap/GLOWS/timestamps`.

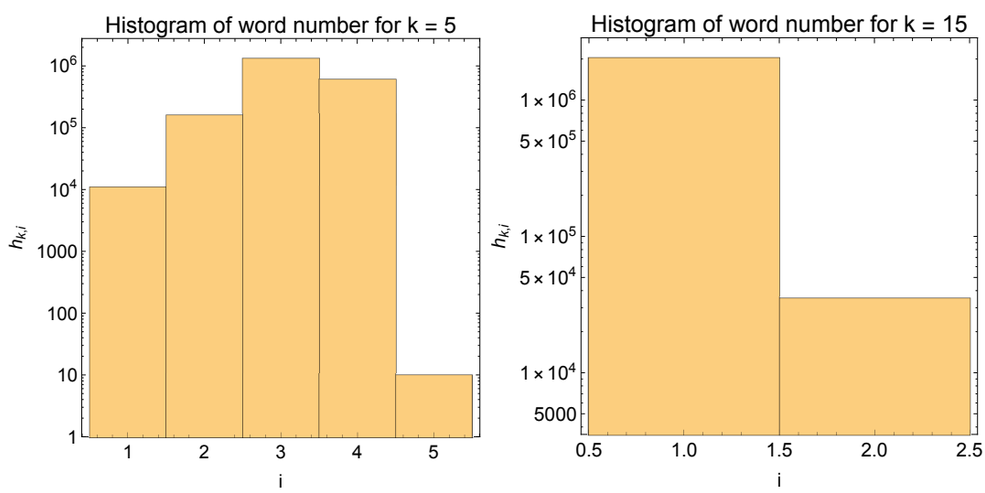


Figure 9.3: *wordHistogram* Histogram H_k of the number of k-words needed to downlink the time series shown in Fig. 9.1 for $k = 5$ (left panel) and $k = 15$ (right panel). The histogram values $h_{k,i}$ are calculated from Eq. 8. The source notebook identical as in Fig. 9.2.

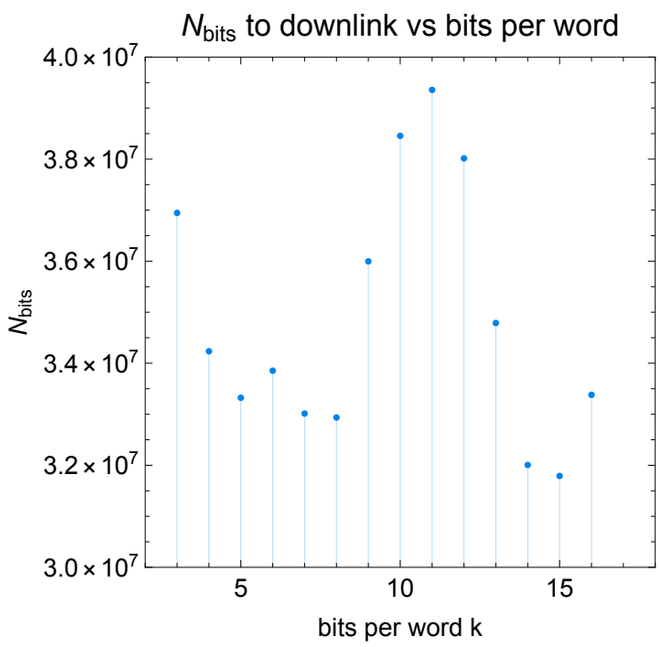


Figure 9.4: *totalBitsVsBitsPerWord* The number of bits that must be downlinked for 1 h of GLOWS observations, shown as a function of the length of k-words used to code the time intervals between individual events, calculated based on the MC simulation presented in Fig. 9.1. Note that the intensity of the signal used in the simulation corresponds to the XN filter, planned for GLOWS, with the minimum guaranteed transmissivity assumed (see the upper panel in Fig.10, Bzowski et al., 2019). The most likely emissivity is greater by approximately a factor of 1.5, which may modify the optimum k-word length by one bit. Figure source: notebook `timeStamps_2019-10-31.nb` at `imap/GLOWS/timestamps`.

M.A. Kubiak using the WawHelioGlow model (Kubiak et al., 2021), and simulations of the EH contribution, performed for this date by I. Kowalska-Leszczyńska. Both the helioglow and the star simulations are presented in the collimator document (Bzowski et al., 2019). The simulations[5] binned into 0.1° spin angle bins are presented in Fig. 9.1.

The events are registered as integer numbers, coded in words of several bits. One of the bits is used as an overflow flag. When the number of clock ticks to store exceeds the capacity of the word, the overflow bit is set and the remainder of the counts is written in another word. If the number of ticks exceeds the capacity of two words, another word is added etc. For the word length of k_{word} one can register n_{word} ticks of the clock:

$$n_{\mathrm{word}} = 2^{k_{\mathrm{word}}-1} - 1. \tag{6}$$

The -1 in the exponent exists because one bit of the k-word is used to mark the overflow. If set, the system is informed that this k-word must be connected with the subsequent one. A given natural number number n is coded in b_n bits:

$$b_n = \lceil \log_2(n+1) \rceil \,, \tag{7}$$

where $\lceil\ \rceil$ means the ceiling function, i.e., the smallest integer greater than or equal to the given number. For the word length k_{word}, the number of words needed to code the same number n is given by the following expression:

$$w_{n,k} = \lceil \log_{2^{(k-1)}}(n+1) \rceil \ \text{ or } \ w_{n,k} = 1 \,\text{for}\ \ n \in \{0,1\} \tag{8}$$

For the clock frequency given in Eq.(3), one needs the following number of bits to code the number of clock ticks between the following events:

[5]Results of the MC simulations are located in the directory `imap/GLOWS/timestamps`; the *Mathematica* notebook to process them is `timeStamps.nb`, in the same directory.

- 21 bits every second
- 25 bits every spin (assuming the spin period is ≤ 16.7772 s)
- 38 bits for one day
- 46 bits for one full year
- 51 bits for a 30-year interval

Event coding will be done relative to the beginning of the day. For downlinking, the first event will be sent in full-length (i.e., as a 38-bit word, TBC), and subsequently differences between the times of events will be coded. The question is, what the optimum word length k_{word} is to be used; the optimization goal is to reduce the data volume to downlink. The optimized k_{word} value is established based on a numerical experiment. A 1-h interval of observations was simulated as a series of randomly spaced events, as illustrated in Fig.9.1.

The intervals between the simulated events were encoded using k-words with k varying from 3 to 16, and the total number of bits that must be downlinked for those different word lengths were obtained. The differences between times of subsequent events were expressed in clock ticks corresponding to the planned frequency of the GLOWS clock, defined in Eq. 3. A histogram of the number of bits needed to code these differences is presented in Fig. 9.2. Subsequently, the numbers of k-words $w_{n,k}$ needed to code each of them were calculated using Eq. 8. The resulting time series of $w_{n,k}$ was then histogrammed for k values ranging from 3 to 16; the histograms H_k were series of $h_{k,i}$. The largest spread between the minimum and maximum number of k-words needed to code the time differences was obtained for $k = 3$; the minimum number obtained was $i_{\min} = 1$ and the maximum number was $i_{\max} = 9$. For $k \geq 10$, the number of words needed to code the time differences was $i_{\min} = 1$ and $i_{\max} = 2$.

The number of bits N_{bits} needed for downlinking the results was obtained from the formula:

$$N_{\text{bits}} = \sum_{i=i_{\min}}^{i_{\max}} h_{k,i}\, i\, k. \tag{9}$$

Histograms of k-words needed for two example values $k = 5$ and $k = 15$ are shown in Fig. 9.3. An estimate of the optimum length k_{word} was obtained by minimization of N_{bits} vs k. The results are presented in Fig. 9.4. The conclusion is that the lowest bit rate needed for downlinking the time tags to the Earth is obtained for the word length equal to 15:

$$k_{\text{word}} = 15\,\text{bits}. \tag{10}$$

This value of k_{word} should be understood as the base word length, i.e., a certain part of time tags will be encoded in k_{word}-bit words, but the other part of time tags will have to be encoded using two k_{word}-bit words, thus in general, the average word length for encoding the time tags will be larger than k_{word} bits.

An assessment of the equivalent number of histograms in direct events possible to downlink daily given the available bandwidth and its use by other data follows.

Adopted parameter values

total bandwidth = 1200 [bps]
histogram size = 8×3670 [bits] (3600 bits for histogram + 60 bits for other histogram data + 10 bits for CCSDS header)
histogram cadence = 120 [s]
housekeeping size = 8×142 [bits]
housekeeping cadence = 30 [s]
autonomy size = 96 [bits]
autonomy cadence = 1 [s]
bits per DE after compression = 3×8 [bits]
expected count rate = 3.37×600 [cps]
observation day duration = 86400 [s].

Calculations

histogram bandwidth = histogram size/histogram cadence [bps]
housekeeping bandwidth = housekeeping size/housekeeping cadence [bps]
autonomy bandwidth = autonomy size/autonomy cadence [bps]
DE bandwidth = total bandwidth − histogram bandwidth − housekeeping bandwidth [bps] (we neglect autonomy, which is not included in the 1200 bps bandwidth)
DE per histogram = histogram cadence × expected count rate
DE size per histogram = DE per histogram × bits per DE after compression [bits]
number of DE blocks daily = DE bandwidth × observation day duration / DE size per histogram

Results

total bandwidth [bps] 1200.00
histogram bandwidth [bps] 244.67
housekeeping bandwidth [bps] 37.8
autonomy bandwidth [bps] 96.00
DE bandwidth [bps] 917.47
DE per histogram 242640.00
DE size per histogram [bits] 582 3360.00
number of DE blocks daily 13.61[6]
Thus,

$$T_{\mathrm{dirEv}} = 13. \tag{11}$$

The downlinked series of direct events is used to inspect the blocks flagged as suspect of particle background in the ground analysis, and to verify the data binning, which is based on spin phase and timing information from the spacecraft. Effectively, this enables using GLOWS as a star sensor, measuring the spin phase based on star observation, similarly as it is done on IBEX in the ground analysis carried out for time intervals where on-board spin pulse synchronization is not maintained.

9.3 Selection of direct events data for downlinking

Selection of the intervals for downlinking is by default made on-board, with a capability to override it by parameters in the command files. By default, data collected in the Day Mode for the time interval between two spin axis repointing maneuvers are analyzed during the following night to identify blocks with the biggest and the smallest count numbers $C_{\mathrm{bl,max}}$ and $C_{\mathrm{bl,min}}$, respectively. With these two blocks identified, the data intervals centered at these two blocks are defined. These two intervals are composed of $2k_{\mathrm{DE}} + 1$ blocks, centered at the blocks with $C_{\mathrm{bl,max}}$ and $C_{\mathrm{bl,min}}$ counts. The magnitude of k_{DE} is adopted $k_{\mathrm{DE}} = 1$. These intervals will be downlinked anyway.

This selection leaves a bandwidth for downlinking T_{reg} intervals

$$T_{\mathrm{reg}} = T_{\mathrm{dirEv}} - 2(2k_{\mathrm{DE}} + 1) = T_{\mathrm{dirEv}} - 4k_{\mathrm{DE}} - 2 = 7 \text{ blocks} \tag{12}$$

for downlinking. The remaining DE series for downlinking are organized in sets of blocks with the length of $2k_{\mathrm{DE}} + 1$, distributed uniformly during the day. $T_{\mathrm{reg}}/(2k_{\mathrm{DE}} + 1)$ gives ~ 14 sets per day, i.e., one set of three blocks worth of DE data every 1.7 h. k_{DE} will be configurable in flight. The sequence of the blocks to download will be determined as follows.

The blocks are numbered from 1 to T_{dirEv}. The programmed sequence of blocks to download is this: $(\frac{1}{2}\,T_{\mathrm{dirEv}}, 1, T_{\mathrm{dirEv}}, \frac{1}{4}\,T_{\mathrm{dirEv}}, \frac{3}{4}\,T_{\mathrm{dirEv}}, \frac{1}{8}T_{\mathrm{dirEv}}, \frac{3}{8}\,T_{\mathrm{dirEv}}, \frac{7}{8}\,T_{\mathrm{dirEv}}, \frac{5}{8}\,T_{\mathrm{dirEv}}, ...)$, until the maximum available number of blocks is selected. The observation time interval is covered approximately evenly, with data from both halves of the observation time interval downlinked.

Adopting this idea requires a careful programming of the sets for downlinking. Direct events are organized into sets related to individual IMAP spins on-board (Sections 12.1 and 12.5). For regular downlinking, these files will be taken in groups corresponding to the n_{block}-spin blocks. The algorithm must determine whether or

[6] source: maro@ms-laptop: /work/imap/*direct_events_packets_per_day*.

not the "absolutely required" blocks with the minimum and the maximum counts are inside the two selected groups and adjust the other block sets accordingly. The requirement to download the blocks in sets of $2k_{\mathrm{DE}}+1$ consecutive blocks creates the necessity to address the situations when a given block is at the beginning or at the end of a group, or is the first or the last during the day. Also, regardless, the on-board algorithm must be able to handle a situation when a group is incomplete, i.e., the observation day ended (the spin axis was repointed) before the current group or block was finished.

10 Histograms

10.1 Executive summary on histograms

This subsection contains a summary of Section 10, while other subsections usually contain extended studies and discussions of particular topics. This subsection is expected to contain up-to-date information on decisions made in internal discussions of the GLOWS team. Note that updates of this subsection may likely imply updates of Section 2.4.

10.1.1 Histogramming algorithm

Algorithm selection. Two algorithms are considered in Section 10.4 for histogram generation onboard the GLOWS instrument. In the algorithms, the process of incrementing the histogram bins occurs at different moments in time. In algorithm 1, the incrementing of histogram bins is performed on a regular basis every time a new 1PPS frame is received (i.e., every second). By contrast, in the algorithm 2, the incrementing of histogram bins is done once per spin block (i.e., once per n_{block} spin periods, nominally ~ 120 s). It was decided to use Algorithm 2. The flight software verifies every second if the end-of-block flag has been raised and if so, it starts histogramming the events collected during the time interval corresponding to the just-finished block of events.
Onboard vs. on-the-ground histogramming. The 1PPS frames will contain the estimated spin phase at the time of the 1PPS arrival to the instrument. This makes it possible to link internal GLOWS-clock ticks with the spin-phase values, and thus we can determine the spin phase for direct events. Therefore, histogramming in the spin-angle domain is generally possible onboard, but it critically depends on the availability of the spin-phase information from the IMAP observatory.

10.1.2 Histogram-related parameters

Parameter values. Histograms with n_{bin} bins are accumulated over blocks containing n_{block} spin periods. The onboard-histogram resolution (i.e., the default value of n_{bin}) is determined by in-flight calibration procedures based on selected stars as discussed in Section 10.3. The spin-block length (i.e., the default value of n_{block}) results from the particle-background-removal capability, as discussed in Section 10.2. Each histogram bin will be encoded on d bits, the default value of d is determined in Section 10.5. The adopted default values of all histogram-related parameters are given in Table 0.1.
In-flight parameter adjustments. The parameters n_{bin} and n_{block} are expected to be configurable in flight, while the parameter $d = 8$ bits is fixed. The GLOWS instrument will likely be loosing its sensitivity with time. Configurable parameters n_{bin} and n_{block} are expected to provide enough flexibility in adjusting the maximum number of counts per bin and block to be comparable to the value of c_{max} parameter given in Table 0.1 and discussed in Section 10.5. This value of c_{max} can be encoded on 8 bits with a proper overflow margin.

10.1.3 File format for onboard storage

The histograms are not stored in individual files but sent directly to the telemetry).

10.1.4 Downlinking, histogram-telemetry content

The flight software must guarantee downlinking all onboard-generated histograms to the ground as the highest-priority functionality. Section 12.5.1 contains a list of expected items in unpacked telemetry blocks (Level-1A

data product). The flight software must guarantee that all the items are included in the science telemetry CCSDS packets; this concerns both the histograms and the onboard-collected ancillary data.

10.1.5 Spin-phase angle

Uncorrected spin-phase angle provided by the IMAP observatory in the 1PPS packets are used for the histograms generated onboard. However, the value of the spin angle corrected for the azimuth of the GLOWS boresight is used in the ground-generated data products (from Level-1B on), as discussed in Section 10.6.

10.2 Block length: defined by particle background removal capability

The block length is adopted based on the requirement to enable detection of bursty backgrounds at a level of $\sim 1\%$. If a burst of background occurs, it will be registered during a certain amount of time, resulting in an increase in the total count number during the bursty observation block. It can be detected statistically, as a statistically significant increase in counts accumulated during this block in comparison with the mean value of the count number per block observed during a day. Assuming a typical counting rate

$$s_{\mathrm{mean}} = 600\,\mathrm{cps}, \tag{13}$$

for a block of

$$n_{\mathrm{block}} = 8\,\mathrm{spins}, \tag{14}$$

the total counts per block C_{block} will be

$$C_{\mathrm{block}} = s_{\mathrm{mean}}\, P_{\mathrm{IMAP}}\, n_{\mathrm{block}} = 72\ 000 \pm 268.3, \tag{15}$$

where the 1-σ uncertainty is the statistical scatter characteristic of the Poisson distribution:

$$\Delta C_{\mathrm{block}} = \sqrt{C_{\mathrm{block}}}. \tag{16}$$

Hence, the 1-σ statistical scatter of the total counts per block will be 0.37%. The total number of blocks during a nominal IMAP day is

$$\begin{aligned} N_{\mathrm{block}} &= \frac{86400\,\mathrm{s}}{P_{\mathrm{IMAP}}\, n_{\mathrm{bin}}} \\ 701.982 &\leq N_{\mathrm{block}} = 720 \leq 738.209. \end{aligned} \tag{17}$$

Taking the shortest IMAP day and the slowest spin period and the longest IMAP day and the fastest spin rate (Eqs (1) and (2)), we obtain the extreme minimum and maximum number of blocks per IMAP day:

$$\begin{aligned} \lfloor N_{\mathrm{block}} \rfloor &= 351 \\ \lceil N_{\mathrm{block}} \rceil &= 2215. \end{aligned} \tag{18}$$

A false alarm is rejecting legitimate (i.e., not background-affected) data because of exceeding the threshold due to statistical fluctuation. Approximating the Poisson probability distribution with the normal distribution with the mean value equal to the number of counts and the standard deviation equal to the square root of the mean number of counts one can easily calculate the false alarm probability and the background detection level for an adopted threshold value. Setting the false alarm threshold $q_{\mathrm{fa}} = n_{\mathrm{fa}}\,\sigma$ one obtains the false alarm probability equal to

$$p_{\mathrm{fa}} = \int_{q_{\mathrm{fa}}}^{\infty} \mathsf{N}[0,1](x)\,dx, \tag{19}$$

where $\mathsf{N}[0,1](x)$ is the function of probability density for the normal distribution with the mean value equal to 0 and the standard deviation equal to 1.

Adopting an alarm threshold $q_{\rm fa} = 3\sigma$, the likelihood of false alarm $p_{\rm fa} = 1.35 \times 10^{-3}$: this is the probability of a fluctuation exceeding the 3-σ threshold. Thus, it is expected that $1.35 \times 10^{-3} \times 720 \simeq 1$ legitimate (i.e., no-background) block is rejected per day. With this threshold, the background detection limit is equal to $3\Delta C_{\rm block}/C_{\rm block} \simeq 0.011$, i.e., a background at a level of 1.1% of the mean signal. Adopting this criterion implies that a background with the total count number less than the threshold value goes undetected, i.e., maximum of 1.1% of the mean counts per block non-legitimate counts: $72\,000 \times 0.011 \simeq 800$ can go undetected while $1/720 \sim 0.14\%$ of blocks with legitimate (background-free) data are rejected.

Adopting the threshold for background detection of $q_{\rm fa} = 4\sigma$ one obtains the false alarm likelihood $p_{\rm fa} = 3.17 \times 10^{-5}$, i.e., one false alarm per 44 days, but the background detection limit increases to 1.5% of the mean signal strength. The actual threshold to be used in the analysis is TBC, but clearly, adopting the block length of 8 spins enables a successful and sufficient background detection.

It must be noted that the proposed procedure is only effective for a bursty background, with relatively rare bursts. Any slowly-varying background cannot be statistically resolved on a daily basis. It may likely be identified in the analysis by correlating of the count variations with data from other instruments, particularly the electron detector and high-energy ion detector. This topic, however, is outside the scope of this document.

The assessment of the false alarm probability presented above is a simplification because the number of counts is given by the Poisson probability distribution, not the normal distribution. However, while the estimate done using the normal distribution does not depend on the magnitude of the count number (provided the count number is high enough to justify using the normal distribution), estimates for the Poisson distribution do depend on the number of counts. Adopting $C_{\rm block}$ as in Eq. 15 one obtains $p_{\rm fa} = 1.37 \times 10^{-3}$ for $q_{\rm fa} = 3\sigma$ and $p_{\rm fa} = 3.29 \times 10^{-5}$ for $q_{\rm fa} = 4\sigma$. The probability of registering *fewer* counts than the limit are equal to 1.33×10^{-3} for the Poisson statistics vs 1.35×10^{-3} for the normal statistics; for for $q_{\rm fa} = 4\sigma$, the latter two values are 3.04×10^{-5} vs 3.17×10^{-5}.

Conclusion: the extreme count threshold is

$$3\sigma \leq q_{\rm fa} \leq 4\sigma \tag{20}$$

10.3 Bin widths: defined by requirements for calibration from stars

Stars are used by GLOWS as standard candles for calibration (selected subset of all stars visible to GLOWS) and to verify the stability of spin phase and the orientation of the FOV in the sky.

With the spin axis direction changed daily by $\sim 1^\circ$ and the full diameter of the GLOWS FOV $\sim 6.8^\circ$, a star is expected to be within the FOV for ~ 7 consecutive days, crossing the FOV at a different distance from the boresight each day. Because the collimator attenuates the brightness of objects off its boresight, the height of the lightcurve peaks due to the passage of a star across the GLOWS FOV will be reduced proportionally as a function of the minimum elongation of the star from the boresight on a given day. Therefore, GLOWS will never observe the full visible brightness of a star because no star will ever go precisely through the center of the FOV (see the collimator memo). The absolute apparent brightness of stars, needed to establish changes in the absolute calibration of GLOWS, will be determined from analysis of daily variations of the peak height: with the positions of the stars in the sky precisely known, and with the geometric location of the GLOWS scanning circle in the sky known, one can calculate the minimum elongation of the star for a given day. With observations from several days, one can establish a brightness – elongation relation, which can subsequently be extrapolated to 0 elongation and thus yield the absolute visible brightness of a given star.

However, this quantity may be affected by possible irregularities in the spin axis orientation (nutations, drifts) and in the spin phase determination. To facilitate analysis of these effects, a sufficient spin angle resolution of the data histograms is needed on one hand, and a sufficient statistics on the other hand. Therefore, an appropriate balance is needed to be established with the requirement of an appropriate time resolution for eliminating the particle background.

The resolution of the data histograms, i.e., the histogram bin width b, is currently set at

$$b = 360^\circ/n_{\rm bin} = 0.1^\circ \tag{21}$$

which makes

$$n_{\rm bin} = 3600\,{\rm bins}. \tag{22}$$

The time $t_{\rm bin}$ spend on observing one bin during one spin will just be:

$$\begin{aligned} t_{\rm bin} &= P_{\rm IMAP}/n_{\rm bin} \\ 4065\,\mu{\rm s} &\leq t_{\rm bin} = 4167\,\mu{\rm s} \leq 4272\,\mu{\rm s}, \end{aligned} \tag{23}$$

depending on the actual spin period (Eq. 2).

10.4 Histogram-generation algorithms

This section describes histogram-generation algorithms for GLOWS onboard processing.

Direct events are binned on-board in the spin-phase domain. Spin phase is calculated in sync with the spin phase information that is broadcast to the instruments at 1 PPS. This means that the histograms are generated on-board by *the spacecraft spin angle*. Re-adjustment of the spin phase so that phase 0 is at the northernmost bin is performed during ground processing. The spin phase is readjusted by the angle equal to the azimuth $\psi_{\rm GLOWS}$ of the GLOWS boresight in the IMAP reference system. The magnitude of $\psi_{\rm GLOWS}$ is TBD.

We need to generate histograms with $n_{\rm bin}$ per spin, distributed uniformly over the spin phase. The histograms count the occurrence of photon detection events for different phases of the satellite rotation. Using an appropriate calibration factor, the histogram counts can be directly transformed into the intensity of the signal along the scanning circle in the Rayleigh units. The histogram-generation code is executed as an independent thread. A separate thread is responsible for the registration of the photon detection times (direct events). The histogram-generation thread runs in parallel with the registration thread. Once per second, the histogram-generation thread checks if the block-finished flag has been raised. If not, it waits for another second. If yes, then it performs histogramming of the just-finished block and lowers the flag after histogramming is completed.

10.4.1 Data binning and histogram generation

The 1PPS frames are assumed to provide us with a sequence of times τ_i (measured by the GLOWS clock with the resolution of 0.5 μs) and spin-phase estimates ψ_i (estimated value at the 1PPS arrival time), where i is a daily 1PPS counter. The GLOWS instrument registers photon detection times $t_j^{\rm DE}$, where j is a direct event counter. We need to compute histograms $H_{k,m}$ accumulated over spin blocks extending over a time interval $[t_k^{\rm B1}, t_k^{\rm B2})$, where k is a daily block counter and $1 \leq m \leq n_{\rm bin}$ is the index of a given histogram bin. Each block consists of $n_{\rm block}$ spin periods, $1 \leq l \leq n_{\rm block}$ is the spin period counter within a given block (see Section 10.2, Eq. 14).

The main source of uncertainties seems to be related to the accuracy of the spin-phase estimation by IMAP the satellite star tracker, which amounts to $\sigma = 0.2^\circ/3$ (which corresponds to 2778 μs in the time domain for the nominal spin period of 15 s). Other uncertainties (the resolution of the GLOWS internal clock – 0.5 μs, the time of distribution of the 1PPS frame to GLOWS – 10 μs) are two or more orders of magnitude smaller than the spin-phase uncertainty. Therefore, we anticipate that the spin-phase uncertainty will dominate errors in the histogram-generation procedure.

We assume here that there is an independent procedure find_tDE($t_{\rm min}$,$t_{\rm max}$) that can be called to obtain indexes $j_1 \leq j \leq j_2$ of direct events within a given time interval $[t_{\rm min}, t_{\rm max})$, i.e., $t_{\rm min} \leq t_j^{\rm DE} < t_{\rm max}$. Since the histogram-generation algorithms described below are assumed to be executed as an independent thread, a separate step may be required before calling find_tDE() that will synchronize the histogram-generation thread with an independent direct-event-registration thread. Such synchronization step is necessary to avoid a situation when the procedure find_tDE($t_{\rm min}$,$t_{\rm max}$) is called, but for the last element $t_{j_{\rm max}}^{\rm DE}$ of the array of already-registered direct events we have $t_{\rm max} > t_{j_{\rm max}}^{\rm DE}$. It seems to be reasonable to require that all calls of find_tDE() should occur for $t_{\rm max} < t_{j_{\rm max}}^{\rm DE}$, because it guarantees that the array of registered direct events is properly filled. We assume below that the thread synchronization is done inside the procedure find_tDE(), i.e., this procedure checks whether $t_{\rm max} < t_{j_{\rm max}}^{\rm DE}$ and if not, it waits for this condition to be satisfied, with a possible retry timeout to account for the possibility of hitting the end of a given observation day.

The algorithm needs to handle somehow the start and the the end of a given observation day. The algorithms assume that 1PPS frames contains the phase wrapped to $[0°, 360°)$. We assume that at the beginning of an observation day we wait doing nothing until the first phase jump is detected. Then the first histogram-generation block for this day starts. At the end of a given observation day, typically the last 1PPS frame will be received somewhere inside of a block. It seems to be reasonable to reject the last incomplete histogram, if it has been accumulated only over a part of a block. For this purpose, in the algorithms described below we include a list of legit histograms H_k^{legit}.

It seems to be reasonable to assume that the satellite spins with a constant angular speed during normal operations. Therefore, since the spin phase will increase at a constant rate, we can use the linear interpolation for the estimation of the spin phase. We also assume that we will receive at least one 1PPS frame per spin period. If it does not happen, histograms should be generated using an emergency mode discussed in Section **??**. All times in the algorithm are assumed to be measured by the GLOWS internal clock with the resolution of 0.5 μs from the beginning of a given observation day.

We consider here two algorithms for generation of GLOWS histograms. In Algorithm 1, incrementing of histogram bins is done every time at receiving of a new 1 PPS frame, so approximately 120 times per block (assuming $n_{\text{block}} = 8$ and the nominal spin period of 15 s). In Algorithm 2 we keep track of the increasing number of spin periods within a block, but incrementing of the histogram bins is done only once per block, when the times of the block start and its end are known. Mathematical-style pseudocodes for the algorithms are presented below, $\lfloor \cdot \rfloor$ denotes the floor operation.

Algorithm 1 Histogram-generation algorithm for GLOWS with histogram-bin incrementing at 1PPS

$i = 1$ ▷ initialize the 1PPS counter
$k = 0$ ▷ initialize the block counter
while $i < i_{\max}$ **do** ▷ we iterate over all 1PPS frames until the end of the observation day
  if $i = 1$ **then** continue ▷ we do nothing waiting until we have at least two 1PPS frames
  if $k = 0$ and $\psi_i > \psi_{i-1}$ **then** continue ▷ we do nothing waiting for the first phase jump
  if $k = 0$ **then** ▷ the first phase jump detected for a given observation day, we initialize the first block
    $l = 0$ ▷ we set the spin-period counter to 0 to mark the start of the first block
    $k = 1$ ▷ we set the block counter
    $\phi = \psi_i + 360$ ▷ auxiliary variable, we have $\psi_i < \psi_{i-1}$ here so for interpolation we need to add 360
    $t_k^{\mathrm{B1}} = (\tau_i - \tau_{i-1})(360 - \psi_{i-1})/(\phi - \psi_{i-1}) + \tau_{i-1}$ ▷ block start time, linear interpolation
  else ▷ normal daily operation after initialization of the first block
    if $\psi_i < \psi_{i-1}$ **then** $l = l + 1$ ▷ phase jump detected, we increment the spin-period counter
    if $l \le n_{\mathrm{block}}$ **then** ▷ we are still entirely within the current block
      if $\psi_i < \psi_{i-1}$ **then** $\phi = \psi_i + 360$ ▷ auxiliary variable, phase-jump case
      else $\phi = \psi_i$ ▷ auxiliary variable, no phase jump
      (j_1, j_2)=find_tDE(τ_{i-1}, τ_i) ▷ find indexes $j_1 \le j \le j_2$ for which $\tau_{i-1} \le t_j^{\mathrm{DE}} < \tau_i$
      for $j = j_1$ to j_2 **do** $\psi_j^{\mathrm{DE}} = (\phi - \psi_{i-1})(t_j^{\mathrm{DE}} - \tau_{i-1})/(\tau_i - \tau_{i-1}) + \psi_{i-1}$ ▷ direct-event phases
      for $j = j_1$ to j_2 **do**
        if $\psi_j^{\mathrm{DE}} > 360$ **then** $\psi_j^{\mathrm{DE}} = \psi_j^{\mathrm{DE}} - 360$ ▷ wrapping the phase
      for $j = j_1$ to j_2 **do** $m_j^{\mathrm{DE}} = \lfloor n_{\mathrm{bin}} \psi_j^{\mathrm{DE}} / 360 \rfloor + 1$ ▷ compute indexes of histogram bins to increment
      for $j = j_1$ to j_2 **do** $H_{k,m_j^{\mathrm{DE}}} = H_{k,m_j^{\mathrm{DE}}} + 1$ ▷ increment histogram bins
    else ▷ we are partially outside of the current block
      $\phi = \psi_i + 360$ ▷ auxiliary variable, we can be sure it is the phase-jump situation
      $t_k^{\mathrm{B2}} = (\tau_i - \tau_{i-1})(360 - \psi_{i-1})/(\phi - \psi_{i-1}) + \tau_{i-1}$ ▷ block end time, linear interpolation
      (j_1, j_2)=find_tDE$(\tau_{i-1}, t_k^{\mathrm{B2}})$ ▷ find indexes $j_1 \le j \le j_2$ for which $\tau_{i-1} \le t_j^{\mathrm{DE}} < t_k^{\mathrm{B1}}$
      for $j = j_1$ to j_2 **do** $\psi_j^{\mathrm{DE}} = (360 - \psi_{i-1})(t_j^{\mathrm{DE}} - \tau_{i-1})/(t_k^{\mathrm{B2}} - \tau_{i-1}) + \psi_{i-1}$ ▷ direct-event phases
      for $j = j_1$ to j_2 **do** $m_j^{\mathrm{DE}} = \lfloor n_{\mathrm{bin}} \psi_j^{\mathrm{DE}} / 360 \rfloor + 1$ ▷ compute indexes of histogram bins to increment
      for $j = j_1$ to j_2 **do** $H_{k,m_j^{\mathrm{DE}}} = H_{k,m_j^{\mathrm{DE}}} + 1$ ▷ increment histogram bins
      if k=1 **then** $H_k^{\mathrm{legit}} = 1$ ▷ initialize a list of legit histograms, i.e., accumulated over a full block
      else append$(H_k^{\mathrm{legit}}, k)$ ▷ append current histogram number to the list of legit ones
      $l = 0$ ▷ we set the spin-period counter to 0 to mark the start of the next block
      $k = k + 1$ ▷ we increment the block counter
      $t_k^{\mathrm{B1}} = t_{k-1}^{\mathrm{B2}}$ ▷ end time of the current block becomes the start time of the next block
  if l=0 **then** ▷ steps related to initialization of a new block
    (j_1, j_2)=find_tDE$(t_k^{\mathrm{B1}}, \tau_i)$ ▷ find indexes $j_1 \le j \le j_2$ for which $t_k^{\mathrm{B1}} \le t_j^{\mathrm{DE}} < \tau_i$
    for $j = j_1$ to j_2 **do** $\psi_j^{\mathrm{DE}} = \psi_i (t_j^{\mathrm{DE}} - t_k^{\mathrm{B1}})/(\tau_i - t_k^{\mathrm{B1}})$ ▷ compute direct-event phases
    for $j = j_1$ to j_2 **do** $m_j^{\mathrm{DE}} = \lfloor n_{\mathrm{bin}} \psi_j^{\mathrm{DE}} / 360 \rfloor + 1$ ▷ compute indexes of histogram bins to increment
    if k=1 **then** allocate$(H_{k,m})$ ▷ allocate histogram array for the first block of a given observation day
    else append(allocate$(H_{k,m})$) ▷ allocate and append histogram array for the next block
    for $m = 1$ to n_{bin} **do** $H_{k,m} = 0$ ▷ fill the new histogram up with zeros
    for $j = j_1$ to j_2 **do** $H_{k,m_j^{\mathrm{DE}}} = H_{k,m_j^{\mathrm{DE}}} + 1$ ▷ increment histogram bins
    $l = 1$ ▷ set the spin-period counter
  $i = i + 1$

Algorithm 2 Histogram-generation algorithm for GLOWS with histogram-bin incrementing once per block

$i = 1$ ▷ initialize the 1PPS counter
$k = 0$ ▷ initialize the block counter
while $i < i_{\max}$ **do** ▷ we iterate over all 1PPS frames until the end of the observation day
  if $i = 1$ **then** continue ▷ we do nothing waiting until we have at least two 1PPS frames
  if $k = 0$ and $\psi_i > \psi_{i-1}$ **then** continue ▷ we do nothing waiting for the first phase jump
  if $k = 0$ **then** ▷ the first phase jump detected for a given observation day, we initialize the first block
    $l = 1$ ▷ we set the spin-period counter to 1 to mark the start of the first block
    $k = 1$ ▷ we set the block counter
    $\phi = \psi_i + 360$ ▷ auxiliary variable, we have $\psi_i < \psi_{i-1}$ here so for interpolation we need to add 360
    $t_k^{\mathrm{B1}} = (\tau_i - \tau_{i-1})(360 - \psi_{i-1})/(\phi - \psi_{i-1}) + \tau_{i-1}$ ▷ block start time, linear interpolation
    allocate($H_{k,m}$) ▷ allocate histogram array for the first block of a given observation day
    for $m = 1$ to n_{bin} **do** $H_{k,m} = 0$ ▷ fill the new histogram up with zeros
  else ▷ normal daily operation after initialization of the first block
    if $\psi_i < \psi_{i-1}$ **then** $l = l + 1$ ▷ phase jump detected, we increment the spin-period counter
    if $l > n_{\mathrm{block}}$ **then** ▷ we are partially outside of the current block
      $\phi = \psi_i + 360$ ▷ auxiliary variable, we can be sure it is the phase-jump situation
      $t_k^{\mathrm{B2}} = (\tau_i - \tau_{i-1})(360 - \psi_{i-1})/(\phi - \psi_{i-1}) + \tau_{i-1}$ ▷ block end time, linear interpolation
      (j_1, j_2)=find_tDE($t_k^{\mathrm{B1}}, t_k^{\mathrm{B2}}$) ▷ find indexes $j_1 \le j \le j_2$ for which $t_k^{\mathrm{B1}} \le t_j^{\mathrm{DE}} < t_k^{\mathrm{B2}}$
      for $j = j_1$ to j_2 **do** $\psi_j^{\mathrm{DE}} = n_{\mathrm{block}} 360 (t_j^{\mathrm{DE}} - t_k^{\mathrm{B1}})/(t_k^{\mathrm{B2}} - t_k^{\mathrm{B1}})$ ▷ direct-event unwrapped phases
      for $j = j_1$ to j_2 **do** $\psi_j^{\mathrm{DE}} = \psi_j^{\mathrm{DE}} - \lfloor \psi_j^{\mathrm{DE}}/360 \rfloor 360$ ▷ wrapping the phase
      for $j = j_1$ to j_2 **do** $m_j^{\mathrm{DE}} = \lfloor n_{\mathrm{bin}} \psi_j^{\mathrm{DE}}/360 \rfloor + 1$ ▷ compute indexes of histogram bins to increment
      for $j = j_1$ to j_2 **do** $H_{k,m_j^{\mathrm{DE}}} = H_{k,m_j^{\mathrm{DE}}} + 1$ ▷ increment histogram bins
      if k=1 **then** $H_k^{\mathrm{legit}} = 1$ ▷ initialize a list of legit histograms, i.e., accumulated over a full block
      else append(H_k^{legit}, k) ▷ append current histogram number to the list of legit ones
      $l = 1$ ▷ we set the spin-period counter to 1 to mark the start of the next block
      $k = k + 1$ ▷ we increment the block counter
      $t_k^{\mathrm{B1}} = t_{k-1}^{\mathrm{B2}}$ ▷ end time of the current block becomes the start time of the next block
      append(allocate($H_{k,m}$)) ▷ allocate and append histogram array for the next block
      for $m = 1$ to n_{bin} **do** $H_{k,m} = 0$ ▷ fill the new histogram up with zeros
  $i = i + 1$

If the 1PPS phase is provided as assumed, we always have $t_k^{\mathrm{B2}} = t_{k+1}^{\mathrm{B1}}$, thus formally we do not need to keep track of t_k^{B2}. Keeping both t_k^{B1} and t_k^{B2} makes sense if we decided to detect missing-phase-zero events and tried to initialize new block immediately after detection of such event.

There are some repeating steps in the algorithms described above that can be wrapped into functions. However, for readability reasons we do not do it here, it is up to a programmer to decide if functions are useful during implementation of the algorithms.

In the next subsection, we describe the χ^2 statistical test that is used in the next subsections for statistical testing of the histogram generation algorithms presented above.

10.4.2 Statistical χ^2 testing – method

The χ^2 statistical test is based on the following quantity

$$\chi^2 = \sum_{j=1}^{n_{\mathrm{bin}}} \left[\frac{(b_j - s_j)}{\sigma_j^{\mathrm{b}}} \right]^2 , \tag{24}$$

where b_j represents results of measurements with uncertainties σ_j^{b} and s_j denotes a model. The quantity χ^2 is a random variable distributed according to the chi-quare distribution with $n_{\mathrm{bin}} - 1$ degrees of freedom. We can compute the so-called reduced value $\chi^2_{\mathrm{dof}} = \chi^2/(n_{\mathrm{bin}} - 1)$, which is a random variable with the mean value $\langle \chi^2_{\mathrm{dof}} \rangle = 1$ and the standard deviation $\sigma_{\chi^2_{\mathrm{dof}}} = \sqrt{2/(n_{\mathrm{bin}} - 1)}$.

Since χ^2_{dof} represents a reduced deviation of the measurements relative to the model (in other words, a deviation from the model per degree of freedom), its value can be used to determine the goodness of fit. This can be checked by using the ratio $(\chi^2_{\mathrm{dof}} - 1)/\sigma_{\chi^2_{\mathrm{dof}}}$. Usually a rule is adopted that for $|(\chi^2_{\mathrm{dof}} - 1)/\sigma_{\chi^2_{\mathrm{dof}}}| > 3$ the model is rejected, otherwise we accept it. Large negative values of the ratio $(\chi^2_{\mathrm{dof}} - 1)/\sigma_{\chi^2_{\mathrm{dof}}}$ (or equivalently χ^2_{dof} much smaller than 1) may indicate that the uncertaintes σ_j^{b} are overestimated.

10.4.3 Histograms vs. modeled lightcurves – a comparison

We use the following procedure to test the histogram generation algorithms described above. Using simulated maps, we compute a smooth lightcurve s representing the heliospheric glow signal and a contribution from point-sources (resolved and unresolved) along the scanning circle. From the synthetic lightcurve we generate timestamps of direct events, where time intervals between the timestamps are randomly drawn from an exponential distribution modulated by the shape of the lightcurve. Lightcurve-based counting rate (in cts/s units, computed for the same phase values as the centers of the histogram bins) is denoted hereafter by s_m. For a given time interval T of the histogram accumulation, the expected number of counts can be computed as $G_m = s_m T/n_{\mathrm{bin}}$. We can compare generated histograms $H_m = \sum_{k=1}^{n_{\mathrm{accum}}} H_{k,m}$ with the theoretical lightcurve G_m, where n_{accum} is the number of blocks over which the histogram is accumulated.

In the simulations discussed below we assume the spin period equal to 15.38 s, which is the upper limit for the IMAP rotation period according to the requirements discussed in Eq. (2). To simulate the uncertainty of the spin phase provided by 1PPS, we add a Gaussian noise with $\sigma = 0.2°/3$ to an exact phase computed from the generated timestamps and the spin period. Below, we analyze two time intervals T for the accumulation of histograms: $\sim$2 and $\sim$12 hours. For the spin period considered here, it translates to $n_{\mathrm{accum}} = 60$ and 351 blocks, correspondingly. The case $n_{\mathrm{accum}} = 351$ corresponds to the minimum expected length of the observation day for GLOWS. The values of $n_{\mathrm{bin}} = 3600$ and $n_{\mathrm{block}} = 8$ were used in the simulations presented below, in agreement with Equations (22) and (14).

Figure 10.1 shows simulated histograms H_m^{60blks} accumulated over $n_{\mathrm{accum}} = 60$ blocks by Algorithms 1 and 2 for the simulated signal modulation for September 5, 1996. Similar comparison for the histograms H_m^{351blks} accumulated over $n_{\mathrm{accum}} = 351$ blocks is shown in Figure 10.2. Visual inspection of the plots shows a good agreement between the histograms and the smooth lightcurve. The effect of decrease of the Poisson-noise statistical scatter is clearly seen in the plots when we change n_{accum} from 60 to 351 blocks. Naturally, the number of counts in the bins increases with the number of blocks accordingly.

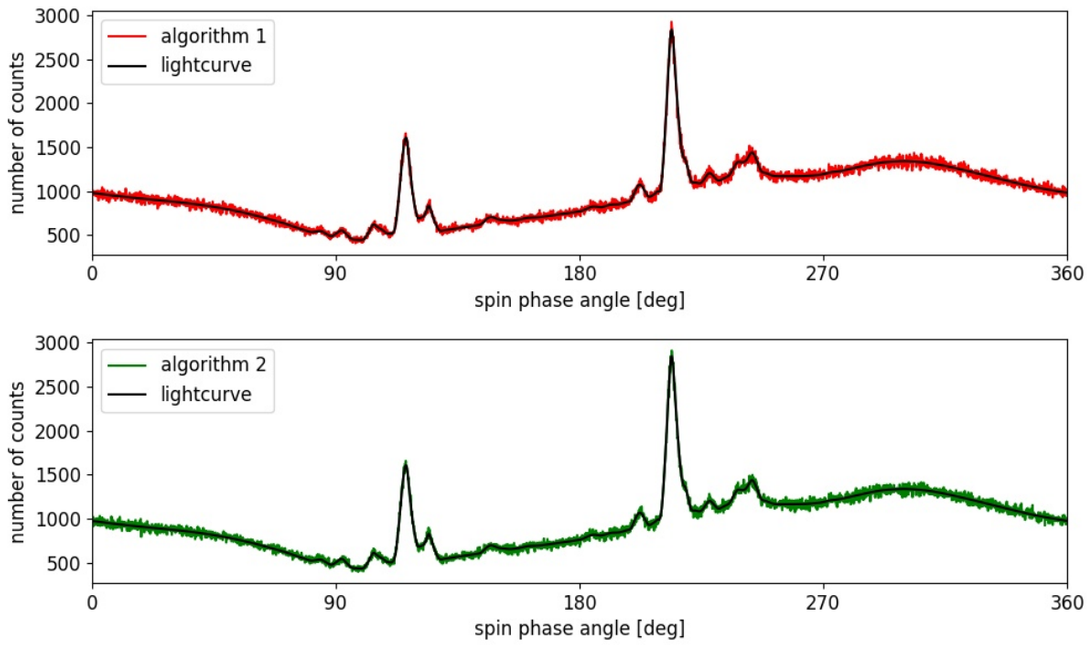


Figure 10.1: *histogramTest60blocks* Histograms obtained by Algorithms 1 (red) and 2 (green) for the simulated signal modulation for September 5, 1996. The histograms $H_m^{60\text{blks}}$ accumulated over 60 blocks ($\sim$2 hours) are compared with a simulated smooth lightcurve G_m (black line) for this day.

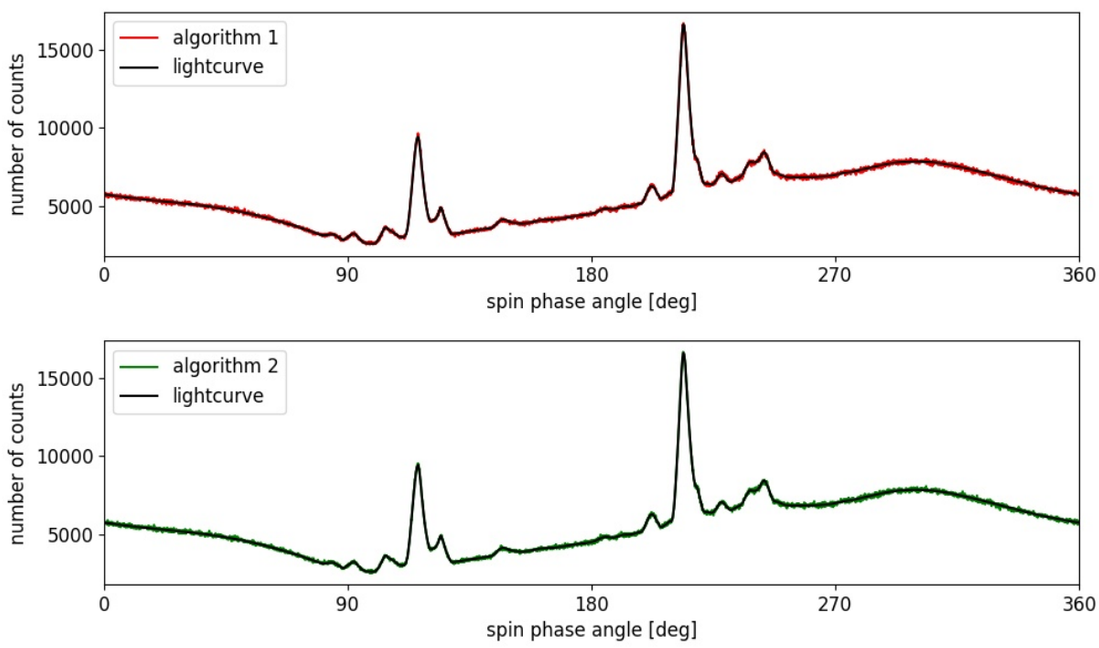


Figure 10.2: *histogramTest351blocks* The same type of comparison as in Figure 10.1 but for histograms $H_m^{351\text{blks}}$ accumulated over 351 blocks ($\sim$12 hours).

10.4.4 Distribution of histograms-lightcurve residuals

In Figure 10.3 we show distributions of the normalized residuals $(H_m^{60\text{blks}} - G_m)/\sqrt{G_m}$ between the simulated histograms and the smooth lightcurve. We use here 100 independent random 60-block samples obtained for different values of a random seed in the pseudorandom-number generator. Since for a large number of counts the Poisson distribution can be approximated by the Gaussian distribution, the normalized residuals are expected to be approximately standard-normal distributed (the mean value equal to zero, the standard deviation equal to one). The comparison of the distributions of the residuals with the standard normal distribution presented

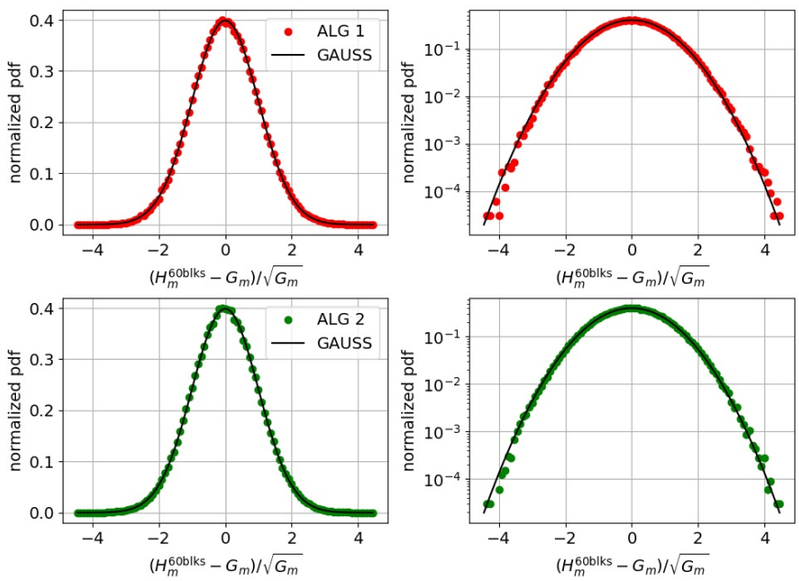


Figure 10.3: *fig:residuaDistr60blocks* Distributions of the residuals $(H_m^{60\text{blks}} - G_m)/\sqrt{G_m}$ for Algorithms 1 (red) and 2 (green) for the simulated signal modulation for September 5, 1996. The distributions are compared with the standard normal distribution (black line). In the left panels linear vertical scale is used, while in the right panels the vertical scale is logarithmic to better visualize the behavior of tails of the distributions.

in Figure 10.3 shows that the distributions are indeed close to the standard-normal case. Formal χ^2 testing of the distribution normality gives $\chi^2_{\text{dof}} \approx 1.01$ for both Algorithms 1 and 2, at the $\sigma_{\chi^2_{\text{dof}}} \approx 0.14$ for the two cases (the residua distribution was computed for 100 bins). Therefore, in terms of the ratio $(\chi^2_{\text{dof}} - 1)/\sigma_{\chi^2_{\text{dof}}}$ we get 0.07, which formally confirms that the normalized residuals are approximately standard-normal distributed. One should note, however, that this conclusion comes from a simple χ^2 testing. In fact, the tails of the residuals distributions are slightly but systematically shifted to the right with respect to the standard normal distribution (see panels on the right in Figure 10.3). This can be explained as an inheritance from the Poisson distribution. If more stringent tests based on the skewness and kurtosis are applied, like e.g. D'Agostino-Pearson test, this shift in distribution tails results in rejection of the normality hypothesis.

A similar analysis as in Figure 10.3 but performed for residuals computed over 351 blocks is presented in Figure 10.4. Generally, the same conclusions as for the 60-block residual analysis hold also for the 351-block case. Formal χ^2 testing of the normality of the distribution gives very similar parameter values to the previously analyzed case, suggesting that the residuals for the 351-block case are approximately standard-normal distributed. In the previous paragraph we discussed a slight systematic shift relative to the standard normal distribution, which is, however, much smaller in Figure 10.4. In fact, this is fully consistent with our expectations, because the convergence of the Poisson to the normal distribution is a function of the number of counts, which is obviously higher for the histogram accumulation over 351 blocks as compared with the 60-block case.

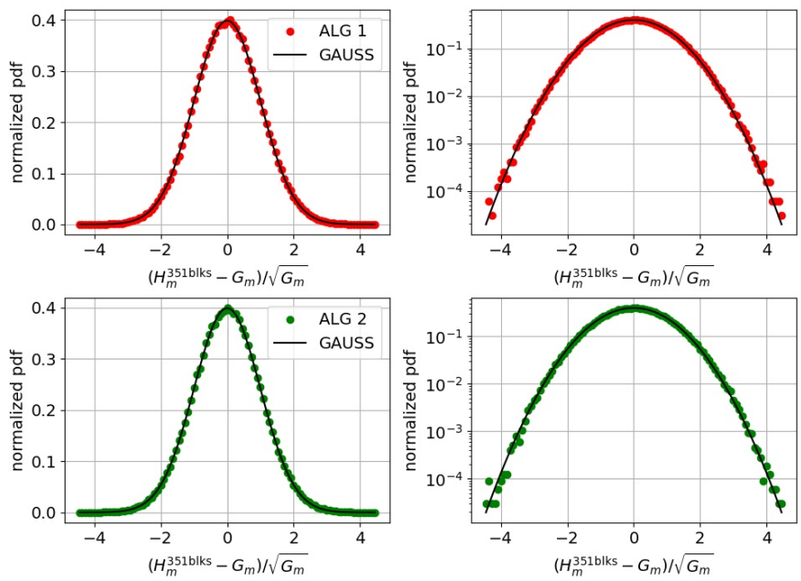


Figure 10.4: *residuaDistr51blocks* The same type of comparison as in Figure 10.3 but for distributions of the residuals $(H_m^{351\text{blks}} - G_m)/\sqrt{G_m}$ computed over 351 blocks.

10.4.5 Statistical χ^2 testing

We also performed statistical χ^2 testing of the histograms $H_m^{60\text{blks}}$ and $H_m^{351\text{blks}}$ against the exact lightcurve G_m. Results of the analysis are presented in Figure 10.5. For this purpose we generated 100 independent

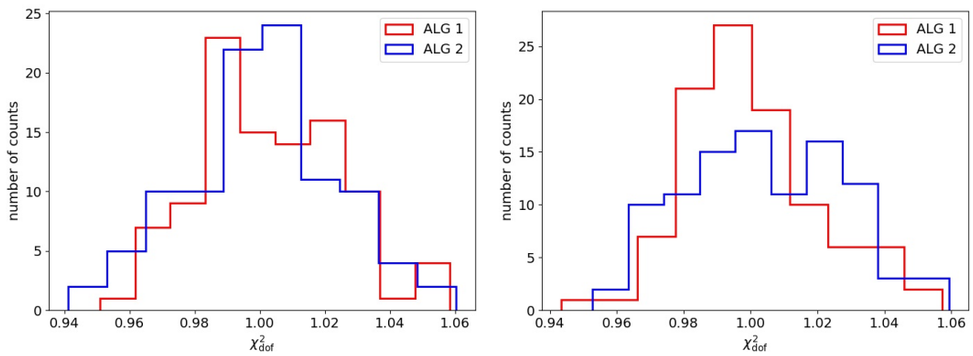


Figure 10.5: *chisq60-351blocks* Distributions of the χ^2_{dof} parameter characterizing the fit between a given sample histogram $H_m^{60\text{blks}}$ (or $H_m^{351\text{blks}}$) and G_m.

pseudorandom samples for the 60-block and the 351-block cases. The samples are obtained for different values of a random seed in the pseudorandom-number generator. For each sample we compute the reduced χ^2_{dof} parameter as characterizing the fit between a given sample histogram $H_m^{60\text{blks}}$ (or $H_m^{351\text{blks}}$) and G_m. Figure 10.5 shows the distribution of the values of the reduced parameter χ^2_{dof} for 100 pseudorandom samples for histograms accumulated over 60 and 351 blocks. The magnitudes of the χ^2_{dof} parameter generally extend from ~ 0.94 to ~ 1.06. For the 60-block histograms, the mean values over 100 samples are 1.00221 and 1.00019 for Algorithms 1 and 2, correspondingly. For the 351-block histograms, the mean values are 1.00051 and 1.00379 for the two algorithms. Therefore, the mean values are very close to the expected value of 1. The standard deviations over 100 samples are 0.02212 and 0.02318 for the 60-block histograms, while for the 351-block histograms they are

0.02050 and 0.02346 for the two algorithms. The standard deviations are very close to the expected value 0.02357 as computed from the formula $\sigma_{\chi^2_{\rm dof}} = \sqrt{2/(n_{\rm bin}-1)}$ discussed above.

In view of the testing results presented above, the two proposed algorithms for histogram generation correctly reproduce the signal modulation along the scanning circle. They are quite similar in terms of their accuracy measured as a goodness-of-fit, i.e., the agreement between the generated histograms and the smooth lightcurve that was used for generation of synthetic direct events. Therefore, the selection of one of the algorithms for implementation in the onboard processing software of GLOWS can be solely based on engineering-related specifics of the hardware and software design for the GLOWS processing unit.

One could expect that Algorithm 1 is less prone to spin-phase error, since incrementing histogram bins occurs more often than in Algorithm 2, which should lead to faster averaging out of random spin-phase errors. However, this statement is correct for one-block histograms, which are not planned to be considered in scientific analysis at any point. We anticipate using histograms accumulated over a large number (at least tens) of blocks, which makes the spin-phase error possible to be averaged out also in Algorithm 2, as confirmed by the statistical testing results presented above. Algorithm 2 is simpler than Algorithm 1, thus it is less prone to programming bugs.

10.5 Bit rate for the histograms

The capacity of the data product must guarantee conversion of the maximum expected signal, with some margin. It is expected that the peak intensity to be registered is equal to

$$s_{\rm max} = 2000\,{\rm cps}. \tag{25}$$

One obtains the maximum count number per bin in a block equal to

$$c_{\rm max} = s_{\rm max}\, P_{\rm IMAP}\, n_{\rm block}/n_{\rm bin} = 8.33\,{\rm counts/bin/spin} \times n_{\rm block} = 66.67\,{\rm cts/bin/block} \tag{26}$$

This implies that $c_{\rm max}$ must be coded using at least $d = 7$ bits. Adding for safety one more bit:

$$d = 8\,{\rm bits}, \tag{27}$$

this implies the volume of data per day D is

$$D = d\, n_{\rm bins}\, N_{\rm block} = 20\,736\,000\,{\rm bits\ per\ day} = 240\,{\rm bps}, \tag{28}$$

excluding the time tags for individual blocks, the protocol overhead, and the housekeeping allocation.

Since the data rate may be reduced during the mission because of the inevitable reduction in the sensitivity of the detector, the magnitude of d will be adjustable in flight. Reducing d results in a decrease in the data volume. If, however, it is detected during the ops that histograms become saturated, it will be necessary to increase d. With the current GLOWS data rate limit of 1200 bps, it is possible to increase d to $d = 10$ (not likely to happen).

With this data binning scheme, all registered data will be downlinked to the Earth. The remainder of the bandwidth will be used to transfer a portion of direct events. This is needed to verify the precision of the binning scheme.

In order to measure the location (spin angle) and the height of the peak of the calibration stars one must suppress the statistical scatter. The peak shape is approximately described by an analytic four-parameter formula, which will be fit to the data. This fitting will be done after subtraction of the estimated signal due to the helioglow. Subtracting the helioglow signal does not result in reducing the absolute statistical uncertainty of the remaining count numbers. Therefore, to safeguard the statistical uncertainty at a sufficiently low level, one must stack data from many blocks. However, to that end it is necessary to keep the bins precisely aligned among the histograms from different blocks, also those pretty much separated in time during the observation day. In the following, the format of Direct Events data is defined and the data volume possible to downlink using the available telemetry bandwidth is calculated.

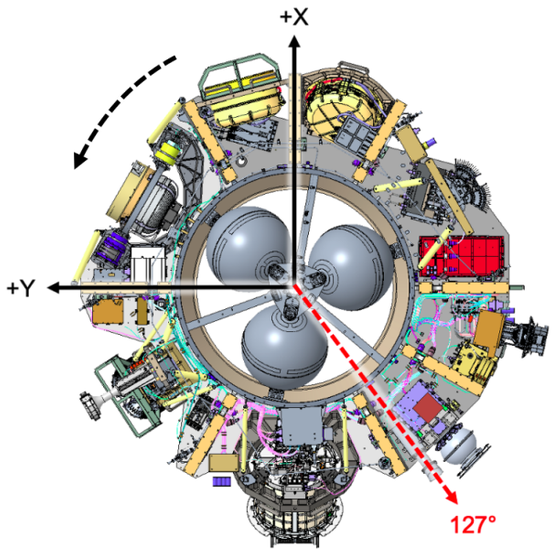


Figure 10.6: Azimuth of the GLOWS boresight in the IMAP frame. The red dashed line is aligned with the GLOWS boresight and the black dashed line shows the rotation direction. Note that the +Z axis is directed out of the page toward the reader, thus the rotation direction is counter-clockwise. It changes to the clockwise rotation when looking along +Z axis directed toward the page (or from the spacecraft to the Sun).

10.6 Effective offset of the spin angle

Based on the IMAP design, the azimuth of the GLOWS boresight in the IMAP reference system is $\psi_{\rm GLOWS} = 90 + 127 = 217^\circ$ measured from the X axis as illustrated in Fig. 10.6. The precise value of this angle including assembly inaccuracies is to be measured TBD.

According to the GI ICD, the definition of the IMAP spin angle ψ provided to the instruments onboard is as follows: "The zero degree spin phase angle is defined as the direction at which the Y-axis crosses the plane parallel to the EMOJ2000 ecliptic plane at the spacecraft orbital location, as the Y-axis is moving from North to South assuming the observatory is rotating with a +Z rotation". For science analyses, the GLOWS team prefers to use a spin angle in the same rotation direction as ψ but measured from the northernmost point of the GLOWS scanning circle. This angle is denoted here by $\psi_{\rm PA}$ (referred to in this document also as the position angle on the scanning circle).

Conversion between the spin angle ψ and the angle $\psi_{\rm PA}$ can be done using the formula:

$$\psi_{\rm PA} = \mathrm{mod}[\psi - \psi_{\rm G,eff}, 360^\circ], \tag{29}$$

where $\psi_{\rm G,eff}$ is an effective offset angle. Fig. 10.6 suggests that for $\psi = 0^\circ$ we have $\psi_{\rm PA} = \psi_{\rm GLOWS} = 217^\circ$, thus

$$\psi_{\rm G,eff} = 360^\circ - \psi_{\rm GLOWS} + \delta\psi_{\rm G,eff}, \tag{30}$$

where $\delta\psi_{\rm G,eff}$ is the mean variation in a given histogramming block. Generally, it is expected that values of $\delta\psi_{\rm G,eff}$ can be determined on the ground based on the full ancillary information available from the SOC.

Although the GLOWS azimuthal angle $\psi_{\rm GLOWS}$ will be measured after assembling the instrument to the spacecraft, it can change after launch because of dynamical loads. The measurement accuracy is also expected to be no better than $\sim 0.1^\circ$. It is also possible that precession and nutation may affect slightly the conversion between ψ and the angle $\psi_{\rm PA}$. The precession and nutation effects are estimated to be small with their angular amplitude smaller than 0.25° (understood as 3σ) and projection of this amplitude on the spin-angle direction is expected to be even smaller.

The conversion between ψ and the angle $\psi_{\rm PA}$ is planned to be performed in the ground processing pipeline. Generation of block-accumulated histograms at L1B involves the averaging over several spin periods as resulting from histogramming onboard. Science analyses will be performed on L2 and L3a daily lightcurves/histograms, where the accumulation/averaging period is even longer. Therefore, the precession and nutation effects are expected to be averaged out to even smaller values than discussed above.

Generally, all effects included in $\delta\psi_{\rm G,eff}$ are expected to be small. The instrument team decided to us the formula (29) without corrections, i.e., assuming $\delta\psi_{\rm G,eff} = 0$. Observations of stars by the GLOWS instrument give a possibility of verifying these assumptions. Such analyses are planned during the mission.

GLOWS data products in Levels 1B (Tab. 3.8), 2 (Tab. 3.13), and 3A (Tab. 4.1) have variables related to the position angle angle offset. Following the discussion presented above, `position_angle_offset_average` should be set to $\psi_{\rm G,eff} = 360^\circ - \psi_{\rm GLOWS}$ and `position_angle_offset_std_dev` should be set to 0. These values may be changed during the mission if needed.

Conversion between the spin/position angle $\psi_{\rm PA}$ of the GLOWS boresight and ecliptic coordinates of the centers of the GLOWS histograms is defined in Strumik (2018).

11 Ancillary onboard-collected data

11.1 Executive summary on ancillary onboard-collected data

This subsection contains a summary of Section 11, while other subsections usually contain extended studies and discussions of particular topics. This subsection is expected to contain up-to-date information on decisions made in internal discussions of the GLOWS team. Note that updates of this subsection may likely imply updates of Section 2.5.

11.1.1 Ancillary-telemetry content

Ancillary data. Apart from direct events and histograms, some additional data is collected onboard and then included in histogram and direct-events telemetry packets. The data include times (GLOWS-clock and IMAP-clock readings) and spin-block averages and variances of: the temperature, CEM voltage, spin period, length of event impulse (see Section 11.3). The data are recorded by the GLOWS instrument as time series with a time resolution much higher than the spin block length. However, for telemetry blocks we need one value per block, thus the recorded quantities need to be averaged.

Averages and variances. Explicit formulas for computations of ancillary-data averages and variances are discussed in Section 11.2.

Telemetry content. Section 12.2 contains the expected ancillary-data items in unpacked telemetry blocks for histograms (Level-1A data product). The flight software must guarantee that all the items are included in science telemetry. To enable direct-event-based histogramming on the ground, the direct-event CCSDS packets must contain the same ancillary data as the histogram CCSDS packets.

11.1.2 Ancillary-data encoding

If more details are needed with respect to "Ancillary-data encoding" subsection in Section 2.5, they should be added here.

11.2 Formulas for ancillary-data average and variance

To avoid possible confusion, explicit formulas for the average value and variance are discussed in this subsection.

We assume that we have a quantity T_i (e.g., temperature, voltage, etc.), which is a function of time measured onboard with a much higher resolution as compared with the spin-block length. Then the value averaged over

the block is defined as

$$\langle T \rangle = \frac{1}{N} \sum_{i=1}^{N} T_i, \tag{31}$$

where N is the number of readings of T_i within the time interval corresponding to a given block containing n_{block} spins.

The block variance of the quantity T is defined as follows

$$\Delta T^2 = \langle T^2 \rangle - \langle T \rangle^2, \tag{32}$$

where both the quantity-squared average $\langle T^2 \rangle$ and the quantity average $\langle T \rangle$ are computed using Equation (31). The standard deviation is defined as the square root of variance

$$\Delta T = \sqrt{\Delta T^2} \tag{33}$$

and is assumed in this document to be an estimator of the 1σ spread or uncertainty.

11.3 Event signals on board

An event is registered on-board when the electronics detects an increase in the voltage from the CEM detector that exceeds a certain threshold value. The voltage is sampled at fixed time intervals and consequently, the duration of a voltage increase is a discrete number. When the measured duration exceeds a certain limit, alarm is raised because this situation is interpreted as saturation because of the excessive counting rate. Similarly, alarm is raised when event rate exceeds a certain predefined frequency; this is to protect the CEM in a situation of direct illumination by the Sun or a similar unwanted condition.

The expected length of the event signal L_k will be statistically distributed. Details of this distribution are TBD; they can only be obtained from measurements. It is expected that the mean duration of the event signal for Lyman-α photons δL_{LyA} will feature a characteristic spread magnitude. This quantity is defined as the second central moment of the event length sample:

$$\delta L_{\text{LyA}}^2 = \langle L_k^2 \rangle - \langle L_k \rangle^2, \tag{34}$$

where $\langle . \rangle$ denotes arithmetic mean (see Equation 31).

It is expected that the typical signal duration depends on the energy of the particle impacting at the CEM. In particular, the length of the signal is expected to be different for solar wind electrons, for high-energy charged particles (cosmic rays etc.), and for other particles able to trigger the channeltron. In space, the statistics of the event lengths collected during a block includes events due to all possible sources. Knowing the expected length of a photon-event signal and having that actually measured, one can verify if the measured average length statistically agrees with that expected. If not, this may be used to assess the contribution from unwanted signal sources, i.e., the observation background.

Details are TBD; in particular, the characteristics of the signal length distribution for Lyman-α photons, for electrons with the energies typical for solar wind, etc. Anyway, the signal length statistics will be included in science data products.

11.4 On-board encoding and ground decoding of measured quantities

GLOWS will measure several quantities in addition to Lyman-α photon events, like CEM voltage, filter temperature etc., and times. In this section, we discuss digital encoding of these measured quantities and subsequent decoding them into physical units.

Let us take a quantity T. We expect it to be within certain limits: $T_{min} \leq T \leq T_{max}$, expressed in physical units. We want to encode it so that it is coded as an integer value using n_T bits. The encoded quantity is τ, and the relation between T and τ is

$$\tau = \frac{T - T_{min}}{T_{max} - T_{min}} \cdot (2^{n_T} - 1). \tag{35}$$

Since τ is an integer number, we assume that the floor operation (the greatest integer less than or equal) will be used in the computations of τ. The quantity τ will be put into the telemetry stream as an n_T-bit integer value. For the measurements that are lower or higher than the respective boundary limits, the algorithm will set T to the minimum or maximum allowable value.

To decode τ and express it in physical units as T, one needs to calculate:

$$T = \tau \frac{T_{max} - T_{min}}{2^{n_T} - 1} + T_{min}. \tag{36}$$

Eq. (35) is a linear equation

$$\tau = AT + B, \tag{37}$$

with the coefficients A, B that can be precalculated and stored as a lookup table for ground processing of coefficients specific for all relevant quantities, including times, periods, temperatures, and voltages using the formulae:

$$\begin{aligned} A &= \frac{2^{n_T} - 1}{T_{max} - T_{min}} \\ B &= -T_{min} \frac{2^{n_T} - 1}{T_{max} - T_{min}} = -T_{min} A. \end{aligned} \tag{38}$$

Note that the decoded quantity of Eq. (36) will still take discrete values, with 2^{n_T} different magnitudes possible.

Decoding returns a decoded quantity T_d, where in general $T_d \neq T$, and will be performed using the following equation:

$$T_d = (\tau - B)/A \tag{39}$$

Some of the quantities measured in flight will be averaged before encoding and putting into the telemetry stream as $\langle T \rangle$. For these quantities, we want an assessment of its spread. To that end, we will also calculate mean square of this quantity $\langle T^2 \rangle$. With this, the spread can be calculated as $\Delta T = \sqrt{\langle T^2 \rangle - \langle T \rangle^2}$. The quantity to be put into the telemetry will be a square of the spread, defined as $\langle T^2 \rangle - \langle T \rangle^2$ and calculated on board.

Simple algebra shows that the onboard-measured values can be encoded identically as individual quantities and decoding them also goes identically:

$$\langle T \rangle_d = (\langle \tau \rangle - B)/A. \tag{40}$$

For the spread: on-board, we will average the squares of the encoded quantities:

$$\tau_i^2 = (AT_i + B)^2 = A^2 T_i^2 + 2ABT_i + B^2. \tag{41}$$

Clearly, averaging will return

$$\langle \tau^2 \rangle = A^2 \langle T^2 \rangle + 2AB\langle T \rangle + B^2. \tag{42}$$

Calculating the spread we obtain:

$$\Delta\tau^2 = \langle \tau^2 \rangle - \langle \tau \rangle^2 = A^2 \left(\langle T^2 \rangle - \langle T \rangle^2 \right). \tag{43}$$

With this, one can obtain

$$\Delta T_d^2 = \Delta\tau^2 / A^2. \tag{44}$$

The conclusion is that we need to downlink the mean encoded quantity τ as a n_T-integer number and the encoded quantity $\Delta\tau^2$ as an $2n_T$-integer value. Since the spread is a priori unknown, we believe it is recommended to use the full $2n_T$-integer range here[7].

The conversion factors A, B for the relevant quantities and the lengths of the words to use are specified in Table 11.1. These values are generally TBC by cross-validation with appropriate engineering documents (references needed). Generally, n_T (number of bits for encoding) is obtained by analysis of the required accuracy and range, then it is rounded up to multiples of bytes.

Comments and remarks for each row in Table 11.1:

[7] It seems feasible to develop an algorithm to code ΔT_d^2 using n_T bits without loss of accuracy but whether or not it is worthwhile to invest time and effort to develop this and save a few bytes per histogram is TBD.

Table 11.1: Conversion coefficients for converting entries in the histogram data structures HB from the on-board to the physical units. Conversion is done using Equations 39 for the quantities and 44 for their spreads squared. A, B are obtained from Equation 38.

No.	Quantity	Description	$T_{\min}$	$T_{\max}$	T unit	n_T	A	B	Remarks
1	$\langle T_{f,i} \rangle$	filter temperature	-30	80	°C	8	$\frac{2^8-1}{110}$	$30A$	See 1
2	$\langle \Delta T^2_{f,i} \rangle$	filter temp. spread			$(°C)^2$	16			See 2
3	$\langle \mathrm{HV}_i \rangle$	HV voltage	0	56012.8205128	V	16	1.17+4.285e-13	0	See 3
4	$\langle \Delta \mathrm{HV}^2_i \rangle$	HV voltage spread			V^2	32			See 4
5	$\langle P_i \rangle$	spin period	0	20.9712	s	16			See 5
6	$\langle \Delta P^2_i \rangle$	spin period spread			s^2	32			See 6
7	ψ_i	spin phase	0	360	deg	16			See 5
8	$\langle L_i \rangle$	event (pulse) length			μs TBC	8			See 7
9	$\langle \Delta L^2_i \rangle$	event length spread			μs^2 TBC	16			See 8

1. We assume that 12-bit values from ADC will be converted to 8-bit values at the expense of the resolution. In fact, presumably a nonlinear dependence is here, which may require a lookup table for accurate decoding.
2. Estimated max spread for 8-bit value gives 16 bits.
3. We assume that 12 bits from ADC will be rounded up to 16 bits (note that in params.xlsx there are 8 bits, but during a discussion on Feberuary 4, 2022 it was agreed that 12/16 bits are the correct numbers). The 12-bit value will be converted to 16-bit value without resolution change, so $T = 3500$ V corresponds to $\tau = 4095$. This means that $T_{\max} = 3500(2^{16} - 1)/(2^{12} - 1) \approx 56012.8205128$ V.
4. Estimated max spread for 16-bit value gives 32 bits
5. This is consistent with GI ICD
6. Estimated max spread for 16-bit value gives 32 bits.
7. TBC means that 8-bit encoding is likely to be adopted here, but it may happen that the full-resolution GLOWS-clock ticks will not be used as a unit (if max event length turns out to be longer than 255 ticks).
8. Estimated max spread for 8-bit value gives 16 bits.

12 Data products L0-L2

This section is intended to describe only L0—L2 data products. It was created by the GLOWS Team at an early stage as a writeup of various considerations on the data products. Later, when the data-product plans were better crystallized, Section 3 was written and it turned out to be easier to maintain for detailed technical description of the data-product content. Therefore, the most up-to-date data-product content can be found in Section 3, while this section explains certain details and preliminary ideas. If some definitions from this section and Section 3 are not in agreement, Section 3 presumably contains the most up-to-date information. However, this section describes more accurately the intentions of the GLOWS Science Team, thus disagreements between this section and Sec. 3 should be alarming.

In the following, we discuss data structures and processing for regular science operations. Data structures used for housekeeping and special modes (HV tests, commissioning) are discussed elsewhere.

This is based on `GLOWS data products v2.docx`, version of June 26, 2020, which is hereby being updated and extended.

12.1 On-board storage

In this section, we briefly present the data collected by GLOWS on-board and those relevant for processing of the GLOWS measurements that are collected by the IMAP spacecraft and downlinked to the ground outside the content of the GLOWS telemetry stream.

12.1.1 Proprietary GLOWS on-board data

Science-related data collected on-board are the DE time stamps and HB histograms corresponding to blocks of n_{block} IMAP spins.

The DE data are stored onboard in chunks corresponding to 1 second of observations. The content of the data is the event time and impulse length, which can be considered in some sense as the event duration. The HB data are stored in separate files, each file corresponding to an individual histogram[8]. Alignment of these files with each other onboard and subsequently on the ground is performed based on the GLOWS internal-clock time.

At the beginning of each "day" (where the "day" corresponds to a time interval with a fixed spin axis pointing, after the daily axis shifting), the IMAP and GLOWS clocks (times) are saved in their respective full resolution. It is expected that the GLOWS clock will not need be restarted during flight, unless rebooting (power off/power on) is performed, the instrument or the spacecraft goes into safe mode, and in case potential mishaps of TBD nature. Even if they occur, we want the GLOWS clock to pick up where it stopped. Aligning of the GLOWS clock with the mission (IMAP) clock will or will not be performed, TBD. Even after cold restart, the GLOWS time needs to pick up more or less where it was just before the mishap/power down. Alternatively, we may restart the GLOWS clock based on the available IMAP time. The GLOWS clock will be free-running, i.e., no synchronization with the IMAP clock will be performed.[9]

12.1.2 Data expected in the general IMAP telemetry stream

In the processing scheme provided in the following sections, it is assumed that the following information is available from the general IMAP telemetry, not specific to the GLOWS data stream, or from the Mission Operations Center:

1. IMAP attitude at 1 PPS (the information broadcast on-board to the instruments)[10]:
   (a) IMAP time $t_{l,\text{PPS}}$ in the IMAP clock units
   (b) IMAP attitude at 1 PPS, i.e., either:
      – spin axis orientation J2000 (longitude, latitude) = $(\lambda_{l,\text{ax,PPS}}, \phi_{l,\text{ax,PPS}})$ for the time $t_{l,\text{PPS}}$
      – spin phase $\psi_{l,\text{ax,PPS}}$ for this time
      – spin phase change rate $\dot{\psi}_{l,\text{ax,PPS}}$
   (c) or, alternatively, the 3D attitude of the IMAP spacecraft 3D and its change at the time $t_{l,\text{PPS}}$
      – J2000 ecliptic coordinates (longitude, latitude) of the IMAP z-axis $(\lambda_{z,l,\text{IMAP,PPS}}, \phi_{z,l,\text{IMAP,PPS}})$
      – the rate of change of the above: $(\dot{\lambda}_{z,l,\text{IMAP,PPS}}, \dot{\phi}_{z,l,\text{IMAP,PPS}})$
      – J2000 ecliptic coordinates (longitude, latitude) of the IMAP x-axis $(\lambda_{x,l,\text{IMAP,PPS}}, \phi_{x,l,\text{IMAP,PPS}})$
      – the rate of change of the above: $(\dot{\lambda}_{x,l,\text{IMAP,PPS}}, \dot{\phi}_{x,l,\text{IMAP,PPS}})$;

[8] It is TBD if the histogram are actually stored in the GLOWS file system or sent directly to the telemetry without saving them to the file system.

[9] TBC!!!

[10] This information will be available on the ground with a higher resolution, so it is potentially possible to use this higher resolution, if needed, in the data assembled on the ground.

the position and the rate of change of the y-axis are welcome but not strictly necessary

2. IMAP state vector (location and velocity) relative to the Sun at $t_{l,\mathrm{PPS}}$
3. IMAP state vector (location and velocity) relative to the Earth $t_{l,\mathrm{PPS}}$
4. IMAP thruster operation flag. The details here are TBD but GLOWS must know if during a given second the IMAP thrusters fired or not (regardless how long). As far as it is known today, there will be the thruster heater flag set ON, but no other information on the thruster operation will be broadcast to the instruments.
5. Anything else?

The data extracted from this telemetry stream will be appropriately processed and the results inserted into the GLOWS data products. The IMAP state vectors mentioned above are expected to change slowly during science ops within a give observation day and listing them at 1 PPS is an overkill. However, the data system is expected to provide a reliable information on the IMAP state vectors for every spin block.

12.2 Ancillary data collected onboard by GLOWS

Apart from direct events and histograms, some additional data are collected onboard by the GLOWS instrument and then included in the histogram and direct-events telemetry packets. This type of data will be included in the GLOWS data products. This section defines the ancillary data structures.

12.2.1 Times

Each histogram telemetry packet corresponds to a block of n_{block} IMAP spin periods. The following structure defines the block-start and block-duration times:

1. start time $t_{i,\mathrm{start}}$, 32(seconds) + 24(subseconds) = 56 bits, GLOWS clock
2. end time offset Δt_i, 16(seconds) + 24(subseconds) = 40 bits, GLOWS clock
3. start time $\tau_{i,\mathrm{start}}$, 32(seconds) + 24(subseconds) = 56 bits, IMAP clock
4. end time offset $\Delta\tau_i$, 16(seconds) + 24(subseconds) = 40 bits, IMAP clock

Downlinked histogram telemetry packets need to contain time readings from both the GLOWS and IMAP clocks for most accurate synchronization of the GLOWS spin blocks with the IMAP general-telemetry data available on the ground. More details are discussed in Section 12.1.1.

This block of data is included in the telemetry blocks for histograms HB. Downlinked direct-event packets are identified by IMAP-clock seconds. Onboard the GLOWS instrument and at Levels-0/1A, the times are integer numbers. At Level-1B times are converted to floats with subseconds as decimal part of seconds. At Level-2 and higher levels, the times are converted to the J2000 (or UTC) time.

12.2.2 Ancillary parameters

The data include: temperature, CEM voltage, spin period, spin phase, length of event impulse (see Section 11.3). The data are recorded by the GLOWS instrument as time series with a time resolution much higher than the spin block length. However, for telemetry blocks we need one value per block, thus the recorded quantities need to be averaged. Explicit formulas for computation of averages and variances of ancillary-data are discussed in Section 11.2.

Telemetry blocks of the ancillary parameters for the histograms include:

1. mean filter temperature $\langle T_{f,i}\rangle$ (once per histogram, arithmetic average over the histogram time, read every second)

2. variance $\Delta T_{f,i}^2 = \langle T_{f,i}^2 \rangle - \langle T_{f,i} \rangle^2$ (Levels 0/1A) or standard deviation $\Delta T_{f,i} = \sqrt{\Delta T_{f,i}^2}$ (Levels 1B and higher) of the filter temperature
3. mean CEM voltage at $\langle \mathrm{HV}_i \rangle$
4. variance $\Delta \mathrm{HV}_i^2 = \langle \mathrm{HV}_i^2 \rangle - \langle \mathrm{HV}_i \rangle^2$ (Levels 0/1A) or standard deviation $\Delta \mathrm{HV}_i = \sqrt{\Delta \mathrm{HV}_i^2}$ (Levels 1B and higher) of the CEM voltage
5. mean spin period $\langle P_i \rangle$ (the value that is computed onboard and used by the GLOWS instrument during histogramming; if the spin-phase information is not available onboard, the nominal period of 15 s is used here, as discussed in Section **??**)
6. variance $\Delta P_i^2 = \langle P_i^2 \rangle - \langle P_i \rangle^2$ (Levels 0/1A) or standard deviation $\Delta P_i = \sqrt{\Delta P_i^2}$ (Levels 1B and higher) of the spin period (if the spin-phase information is not available onboard, and a default spin-period value is used, then zero is set here)
7. mean length of the event impulse $\langle L_i \rangle$ (block-averaged)
8. variance $\Delta L_i^2 = \langle L_i^2 \rangle - \langle L_i \rangle^2$ (Levels 0/1A) or standard deviation $\Delta L_i = \sqrt{\Delta L_i^2}$ (Levels 1B and higher) of the event-impulse length

Note that referring above to the variance or standard deviation means that at level 1B and higher levels in the ground-processing pipeline the variance is replaced with the standard deviation.

This block of ancillary data is included also in the telemetry blocks for histograms HB. Onboard GLOWS and at Levels 0/1A, the ancillary data are integer numbers encoded using the formalism described in Section 11.4. At level 1B and higher levels, the ancillary data are included as decoded values in physical units. The units are as follows:

- temperature [Celsius degrees]
- CEM voltage [Volts]
- spin period [seconds]
- length of event impulse [microseconds] TBC

12.3 Flags

This section defines a system of flags holding extra information collected onboard and obtained during ground processing. The GLOWS Team distinguishes between bad-time flags regarding histogram as a whole and bad-angle flags concerning individual histogram bins.

12.3.1 On-board generated bad-time flags for histograms

The flags are stored in a 16-bit integer field within the HB data structure. The following items are in the GLOWS histograms sent by telemetry[11]:

1. number of missing PPS greater than 0
2. number of missing time status messages grater than 0
3. number of missing spin phases greater than 0
4. number of missing spin periods greater than 0

[11] Based on e-mail from Tomasz Martyniak (KPLabs) sent on October 10, 2022

5. overexposure in at least one of the bins occurred
6. non-monotonic event counter greater than 0
7. histogram collected during Night Mode
8. HV test in progress
9. pulse test in progress
10. memory error detected

The remaining 6 bits are currently void and will be pre-initialized with 0. The flags are listed in Tab. 3.10 together with flags set on the ground.

12.3.2 Bad-time flags added during ground processing to individual histograms

For ground-processing data products, the system of flags described in the previous section will be extended with additional information, added to individual histograms:

1. on-board vs on-the-ground processing flag: it informs if the histogram (at Levels 1B and higher) was generated on-board by the flight software or on the ground from DE data.
2. flag based on comparison of the total numbers of counts in a given block-accumulated histogram with the daily average (deviations by n-sigma and more are interpreted as beyond daily statistical error), see the end of Sec. 10.2
3. threshold value for the standard deviation of the filter temperature exceeded
4. threshold value for the standard deviation of the HV voltage exceeded
5. threshold value for the standard deviation of the spin period exceeded too high; see Section 12.2.2, 6.
6. threshold value for the standard deviation of the spin pulse length exceeded
7. external information on exceeding a background threshold (TBC)

These flags will be attached during ground processing and thus can be provided as a part of a human-readable data structure, immediately after the decoded onboard-generated flags defined in Section 12.3.1. All flags can be preserved in this structure. The full list of bad-time flags (set onboard and on the ground) is provided in Tab. 3.10.

12.3.3 Bad-angle flags added during ground processing to individual histograms

These flags inform that:

1. a given bin is close to a point source
2. a given bin is close or inside a masked/excluded region defined by the instrument team
3. a given bin was excluded by the instrument team for a given Level-1B unique block identifier
4. a given bin is suspected by the instrument team to contain a substantial contribution of a transient signal (e.g., of cometary origin) for a given Level-1B unique block identifier

These flags are used in the ground-processing pipeline at Levels-1B and 2 in the form of a histogram flag array of the same size as histograms, i.e., a separate flag set is used for each histogram bin.

The bad-angle flags are listed in Tab. 3.11.

12.3.4 Daily-histogram flags (Level-2)

Level-1b histograms with bad-time flags raised are excluded from summation leading to Level-2.

Currently defined flags for daily histograms are bad-angle flags in the form of histogram flag array based on the flags of the parent block histograms in Level-1b. Bad-angle flags from Level-1b propagate to Level-2. If a given flag in a bin is True in any histogram of Level-1b, it is also equal to True at Level-2. It is TBC if Level-2 needs any other system of flag.

12.3.5 Flags for direct events

Direct events downlinked to the Earth contain the `data_every_second` structure used onboard by the histogramming algorithm. This structure contains flags listed in Tab. 3.2.

12.4 Raw data and Level 0

Raw data are understood as raw telemetry containing possibly overlapping data sets and communication artifacts.

Level-0 data are unprocessed instrument data without communication artifacts (e.g., synchronization frames, communications headers, and duplicate data are removed). These data consist of binary CCSDS packets with CCSDS headers.

A brief description of the structure of **CCSDS packets** is included at the beginning of Section 3.4.

A detailed technical description of science telemetry for **histograms** is included in Section 3.4.1.

A detailed technical description of science telemetry for **direct events** is included in Section 3.4.2.

12.5 Level 1A: unpacked telemetry blocks

Level 1A data are extracted from CCSDS packets and should be understood as full-resolution, uncalibrated, time-referenced data.

DE telemetry packets are identified by IMAP-clock seconds (from epoch defined by GI ICD). This information is also included in the histogram HB packets, so it makes it possible to generate independently histograms on the ground from direct events even in an emergency situation when reasonable histograms cannot be generated onboard and sent by telemetry to the ground (see Section **??**).

12.5.1 Telemetry blocks for histograms HB (Level-1A)

Telemetry block for an i-th histogram means data included in GLOWS telemetry blocks but without data included in the general IMAP telemetry (e.g., ephemeris, attitude data). All ancillary-data items are in the internal GLOWS units (integer numbers). This GLOWS-telemetry-based data structure contains:

1. histogram identifier k_i^{first}; the content codes ID of the first IMAP spin in the block
2. ID of the last IMAP spin in the block k_i^{last}
3. block header h_i (a series of text strings with the information on the version of flight software, version of ground software used for unpacking, the Level-0 files used for generation of the Level-1A file, etc.)
4. data structure containing time readings (block-start and block-duration) from both the GLOWS and IMAP clocks as defined in Section 12.2.1
5. number of spin periods in block $n_{\text{block},i}$ (will not be changed during an observation day)
6. number of bins per spin $n_{\text{bin},i}$ (will not be changed during an observation day)
7. histogram H_i (count number): $n_{\text{bin},i}$ slots, collected over $n_{\text{block},i}$ spins, each slot d bits (see Eq. 27), the histogram is arranged by the IMAP spin angle ψ (see Sec. 10.6)
8. total number of events in the histogram

9. GLOWS ancillary parameters (characterizing the instrument temperature, CEM voltage, spin period, length of event impulse) defined in Section 12.2.2 and encoded as integers using a formalism described in Section 11.4; note that the variance is used here as a spread measure at Level 1A
10. data structure with extra-information flags defined in Section 12.3

Detailed technical listings of Level-1A data (unpacked telemetry items) for histograms are included in Tab. 3.5.

12.5.2 Telemetry blocks for direct events DE (Level-1A)

Both regular daily transfers of DE and on-demand transfers are organized in chunks containing one second of data. For the daily transfers the direct-event dumps contain the photon detection times from three adjacent histogram blocks, with full-second margins at the beginning and the end. Therefore, the direct-event dumps need to be filtered on the ground by block-start and block-end times for the histograms to obtain ground equivalents of the histograms generated onboard by GLOWS. For on-demand transfers, DE packets may have different length in seconds, depending on the parameters of the telecommand used for selection of time intervals for downlinking.

Therefore, DEs are organized by time intervals in seconds, and the following structure is used for a DE 1-second chunk at Level-1A:

1. header with information on the version of the ground software used for processing, the name of Level-0 data file, the number of CCSDS packet in the Level-0 data file
2. start time, IMAP-clock seconds (from epoch defined in GI ICD)
3. number of DE packets in a series
4. sequence number of a given DE packet in a series
5. Direct Events chunk containing data compressed by the algorithm described in Sec. 9.2

Detailed technical listings of Level-1A data (unpacked telemetry items) for direct events are included in Tab. 3.6. Note that the content of data-every-second structure (see Tab. 3.2) used by the GLOWS histogramming algorithm onboard is attached to each second of direct events downlinked in GLOWS telemetry. It is expected to provide all information needed to generate histograms on the ground from direct events downlinked in the telemetry.

12.5.3 Telemetry blocks for housekeeping HK

Telemetry blocks for GLOWS HK are defined in a separate document `TLM_GLX_2023_06_22.xlsx` maintained by the GLOWS Engineering Team.

12.6 Level 1B: unpacked telemetry + relevant HK and ancillary info

Unpacked GLOWS telemetry will be compiled with IMAP HK and other information. The most relevant information from the spacecraft seem to be

- the history of the location of the spacecraft in space,
- the history of the spin axis pointing.
- the history of spacecraft spinning (IMAP times and spin phases)

The raw HB data include histograms for individual blocks and ancillary data from the spacecraft, as a separate data structure. Some of the information in the data structures will be redundant. The objective is to avoid overloading data structures with too much information on one hand (the histograms) but to facilitate consulting the ancillary data on the other hand, should such a need appear.

The items are now being converted from internal GLOWS units to physical units; the exception is the helioglow intensity, which at this phase of the processing is still in the form of counts in the histogram bins. Generally, the conversion will be done using

12.6.1 Ancillary data from general IMAP telemetry

At Level-1B, additional data from the general IMAP telemetry are included in the GLOWS data products. The data structure to be included as additional information in Level-1B data products is the following:

1. mean spin period $\langle P_{\mathrm{IMAP},i} \rangle$ for the duration of the block, obtained from the general IMAP telemetry available during ground processing
2. standard deviation of the mean spin period $\Delta P_{\mathrm{IMAP},i}$; computed during ground processing using general IMAP-telemetry data
3. mean offset of the GLOWS position angle $\langle \psi_{\mathrm{G},i} \rangle$
4. mean spread of the offset of the GLOWS position angle $\Delta \psi_{\mathrm{G},i}$
5. $\langle \lambda \rangle, \langle \phi \rangle$ – average J2000 longitude and latitude of the spin axis
6. spreads $(\Delta \lambda_i, \Delta \phi_i)$ of the longitude and latitude of the spin axis over the time interval of the histogram; the spreads are computed as standard deviations
7. spacecraft location information (TBD, most likely X_i, Y_i, Z_i – the Cartesian heliocentric coordinates in the ecliptic reference system, obtained from spacecraft telemetry or ground processing[12])
8. uncertainties $\Delta X_i, \Delta Y_i, \Delta Z_i$ for the spacecraft location; the spreads are computed as standard deviations
9. spacecraft velocity information (TBD, most likely $V_{X_i}, V_{Y_i}, V_{Z_i}$ – the Cartesian heliocentric components in the ecliptic reference system, obtained from the spacecraft telemetry or ground processing[13])
10. uncertainties $\Delta V_{X_i}, \Delta V_{Y_i}, \Delta V_{Z_i}$ for the spacecraft velocity components; the spreads are computed as standard deviations

Table 3.8 contains the final form of the listing of ancillary data discussed above. The formulas for calculation of the averages and spreads are provided in Section 11.2.

The data structure described above is expected to be included in Level-1B data-product files. However, the data structure contains only averages and spreads of full time series from general IMAP telemetry that will be available on the ground. Perhaps it would be useful to define a data structure with full time series as separate files that could however be easily linked to regular Level-1B data-product files.

12.6.2 Data structure for histograms HB (Level-1B)

The data structure for **histogram** H_i comprises:

1. block header $h_{i,\mathrm{hdr}}$ (a series of text strings with the information on the files used, software used, processing time etc., TBD
2. unique block identifier $H_{i,\mathrm{ID}}$, likely based on on-board GLOWS or IMAP time (TBD); we want to be able to refer to individual histograms easily sorted in time and to be able to quickly check the existence of gaps between histograms (missing data, data rejected/not downloaded because they were collected during spin axis repointing etc.). The naming system must not be disrupted by potential resets on board.
3. data structure containing time readings (block-start and block-duration) from both the GLOWS and IMAP clocks as defined in Section 12.2.1; at Level-1B no conversion is anticipated, i.e., the same structure is used for times at Level-1A and 1B

[12] TBC; perhaps it is too early in the data pipeline for inserting this information, if it is not readily available at the time of download. Definitely, if not now, must be added later on, i.e., to Level 2 etc. data

[13] TBC; perhaps it is too early in the data pipeline for inserting this information, if it is not readily available at the time of download. Definitely, if not now, must be added later on, i.e., to Level 2 etc. data

4. number of spins in block $n_{\text{block},i}$
5. number of bins per spin $n_{\text{bin},i}$
6. the histogram H_i (count number vs spin angle): $n_{\text{bins},i}$ slots, collected over $n_{\text{block},i}$ spins, each slot d bits (see Eq. 27). The histogram is rearranged relative to Level 1A by changing the IMAP spin angle ψ to the GLOWS position angle ψ_{PA} (see Eq. (29)).
7. GLOWS ancillary parameters (characterizing the instrument temperature, CEM voltage, spin period, length of event impulse) decoded to physical units as described in Section 12.2.2; note that the standard deviation is used here as a spread measure
8. ancillary parameters (characterizing the spin period, position-angle offset, spin-axis orientation, satellite position and velocity) from general IMAP telemetry as described in Section 12.6.1
9. data structure with extra-information flags defined in Section 12.3
10. anything missing?

We do not anticipate currently any initial calibration at Level-1B. HB data will simply contain raw count numbers for full-resolution histogram bins accumulated over spin blocks.

Detailed final technical listings of Level-1B items for histograms are included in Tabs. 3.8, 3.9, 3.10, 3.11.

12.6.3 Data structure for direct events DE (Level-1B)

The DE data structure must enable reproducing the corresponding HB data structure on the ground[14].

In the course of work on the definition of directs events it turned out that the specific flight-software implementation forces direct events to be packed into one-second chunks. At Level-1A (unpacked telemetry) naturally the same approach is used. At Level-1B this way of organizing the direct-event files is maintained. A post-processing software producing histograms on the ground from downlinked direct events needs to organize the Level-1B direct event products into histogram blocks.

Detailed final technical listing of Level-1B items for direct events is included in Tab. 3.12.

Additional questions:

When exactly ground-generated histograms will be produced?

Can we generate a sensible Level-2 for DE?

12.7 Ground-processing pipeline from Level-1B to Level-2

This section is supposed to provide a more extended discussion of issues described in Sec. 3.9.

Level-2 data product is understood here as representing the lowest level of research-grade scientific data. It is supposed to be conceptually equivalent to SOHO/SWAN measurements, with the caveat that it contains signal modulation along the GLOWS scanning circle instead of all-sky maps. Level-2 represents the lightcurve of the photon flux (in Rayleigh units) measured by GLOWS including all components occurring in nature (helioglow + stars + background; see Section 5). Level-2 has the same angular resolution as the histograms at the lower levels but is accumulated over a longer period of time, namely the fixed-satellite-spin-axis-pointing time intervals, which we call observation days. Level-2 data product is called here a lightcurve (a signal in physical units modulated along the GLOWS scanning circle) to distinguish it from histograms (that contain count numbers).

The Level-2 data product contains also mask arrays carrying both the flags set onboard and the flags set during ground processing of lower-level data products for GLOWS. The purpose of the masks is to mark problematic bins but the signal values are kept at Level-2 as they are (i.e., not zeroed or nan'ed).

The final list of processing steps from Level-1b to Level-2 is included in Sec. 3.9.1. In subsequent sections we discuss some details related to the list included in in Sec. 3.9.1.

[14] *We need to check if the content of this structure is sufficient to perform this task.*

12.7.1 Initial culling – identifying bad-time intervals

At the end of Section 12.6, we have the telemetry unpacked and compiled with the HK and ancillary information. Now we start culling the data, i.e., identifying data intervals unsuitable for analysis. We introduce a data structure defining the bad time intervals (**BT**). Data from these intervals are rejected from further analysis. The criteria for qualifying as bad time will be developed in the future. Most likely, as the analysis progresses along the data pipeline, the bad time list will be extended. Quite likely, the BT list may be branched for different applications/purposes (TBC).

The BT structure is composed of a time-sorted list of records that includes items for all successfully downloaded and unpacked telemetry blocks. The idea is to address all histogram items separately. This facilitates rejecting entire histograms (all bins to reject) or only portions of them. Hence, each histogram bin has its own field that is filled with an appropriately defined flag. The system to construct the flag is now TBD.

The elements to consider at the construction of BT data structures are the following.

- All blocks that have been downloaded must be accounted for in the BT data structure
- The system must be manageable, i.e., the files are text and must not be too long
- The structure of the files must be prone to machine processing but also human-readable
- The data structure must enforce registering the versioning information, as well as the history of processing; most likely, the culling of data will be done in several consecutive steps and it must be evident from the information in the file which of these steps have been performed using which version of the processing software
- The system of data processing will be deployed and run at the SOC[15] without human interaction (fire & forget); hence the need to log essential information during the process.

Hence, a BT data structure covers one IMAP day of observations. Within the daily BT, the data are organized into spin blocks, and an atom of the BT structure is a spin block.

A BT record is composed of the identifier of the first bad block and the last bad block in a bad time series, and a wide commentary field to specify the reason for rejection and a signature of the rejector. A rejector may be a software program used to filter the data or an individual person in the case when manual culling becomes necessary. Anyway, the reason for rejection must be specified, preferentially in a standardized (but human-readable) way, i.e., standard text strings for various rejection conditions rather than numerical flags.

The Bad Times BD_k data structure (daily) comprises

1. file header $H_{\mathrm{BT},k}$ (content TBD)
2. block identifier $H_{i,\mathrm{ID}}$
3. a list of n_{bin} flags specifying the quality of individual bins. Will be pre-initialized to 0, which means 'keep it'. Rejection because of various reasons will be given in such a way that identification of all possible reasons is possible based on a given flag

Initial culling includes:

1. Identifying good (error-free) telemetry blocks
2. Identifying blocks collected during prohibited times (PT)

The list of Prohibited Times (PT) is constructed based on predetermined criteria. This list will evolve as the instrument and mission development progresses. Presently, Prohibited Times include the time intervals of:

1. Night mode and maneuvering (all kinds of, but mostly those, when HV on the detector is ON and the instrument registers counts); flag MNVRN=ON

[15] IMAP Science Operations Center

2. GLOWS gain tests (these times, however, need to be marked up separately to enable the analysis of results of these tests); flag GAINTEST=ON

3. Known conditions when observations are unsuitable, based on information from the IMAP telemetry and from flags in the GLOWS telemetry blocks, presently TBD; flag(s) IMAPBT=ON; each reason for bad times will have its own code. Basically, these conditions include issues given in Section 12.3.1. However some of those conditions might be given a waiver, e.g., the double memory error or IMAP or GLOWS clocks not fully accurate, TBD.

The flags will be organized in integer-like data structures. The decision which of the raised flags are given a waiver will be made by the GLOWS Science Team based on in-flight experience. This choice will be coded in the filters supplied by GLOWS to ISOC in the form of filter files. These files will contain the filter defined as an integer number, which during filtering will be subjected to logical AND procedure with the flags parameter in the histograms. The filters will be version-controlled.

After initial culling, we start calculating count rates and we introduce their uncertainties. As analysis progresses (i.e., along the pipeline), these quantities will evolve (starting from the simple Poissonian uncertainty, through uncertainties due to uncertainties due to corrections for instrument aging, star removal, binning uncertainty etc.)

It is expected that particle background may lead to an artificial elevation of the signal level measured by GLOWS. This contamination is expected to occur in the form of bursts of finite length in time. Rejection of the particle-background-contaminated blocks will be performed by finding those blocks for which the total number of counts per block is larger than

$$C_{\text{block}} + n_{\text{reject}}^{\text{upper}} \sqrt{C_{\text{block}}}, \tag{45}$$

where C_{block} is the expected total number of counts per block. Sec. 10.2 provides a more detailed discussion related to Eq. (45). Since the mean (i.e., scanning-circle averaged) helioglow signal level depends on the position of the observer and the solar-cycle phase, the value of the parameter C_{block} will be determined on a daily basis. The value $n_{\text{reject}}^{\text{upper}}$ that determines the rejection threshold will be probably set between 3 and 4 (TBD). Blocks for which the total number of counts per block is higher than the threshold defined in Eq. (45) will be included in bad-time list of blocks. The lower rejection limit

$$C_{\text{block}} - n_{\text{reject}}^{\text{lower}} \sqrt{C_{\text{block}}} \tag{46}$$

will be applied to block-accumulated GLOWS histograms, unless analysis of actual data shows that such blocks occur in agreement with statistical expectations.

At this point, we have identified and listed those bad-time intervals for which blocks are rejected as a whole. Therefore, we are able to identify good-time blocks that are processed further in the next step described in the next section. The set (list) of good-time blocks is denoted hereafter by $\mathbb{K}$.

At this point, we have a list of good-time blocks. The initial culling process is finished.

12.7.2 Advanced culling against issues for the entire block histograms

At this phase of the processing, the data products will be filtered against exceeding predefined thresholds by selected parameters, like spin period and its spread, impulse length and its spread, filter temperature and it spread, etc., as well as against issues related to the quality of the spacecraft attitude detected on-board.

At this stage, the on-board measured mean quantities and their variances will be tested for staying within their prescribed limits and not showing evidence for large variations during accumulation of the given histogram. Exceeding theses limits by at least one of these parameters will result in rejection of the given block, with appropriate extension of the Bad Times matrix.

The logic will be: IF outside the prescribed limits THEN reject ELSE IF the variance larger than prescribed a limit (perhaps relative to the parameter value, TBD), THEN reject ELSE keep.

The Bad Times matrix will be updated accordingly.

The limits for all parameter values and the variances values will be provided to ISOC by the GLOWS team in separate files for each of the conditions based on experience. The limits will be version-controlled and time-stamped (with the validity interval defined) because some of those limits might be varying with time due to natural reasons (e.g., raising the CEU voltage because of the natural aging of the instrument). On the other hand, some of the limits might be changed based on the increasing experience and evolving views of the GLOWS Team; since this would be a qualitative change, them the version would also need to be changed.

Filtering against these conditions will result in raising appropriate flags in the block histograms Level 1B. Subsequently, the Bad Times list will be appended with the time interval for this block.

At the end of filtering, based on the downlinked block histograms and the Bad Times list, a list of qualified histograms will be compiled in oirder to hand it to the routine calculating the daily histogram (see Section 12.7.3).

Some of these conditions might turn out to be mute, i.e., filtering against them might turn out to be unnecessary. In this case, the filtering might be turned off by specifying very liberal threshold and boundary conditions, so that all histograms are given a pass based on this given criterion.

12.7.3 Co-adding block-accumulated high-resolution histograms

Having the block-accumulated high-resolution histograms $H^{\text{block}}_{k,m}$ we can add them together within a given observation day (i.e., the time interval between repointing maneuvers) according to the following formula

$$H_m = \sum_{k \in \mathbb{K}} H^{\text{block}}_{k,m} \tag{47}$$

to obtain the daily-accumulated high-resolution histogram H_m. The sum is computed over the previously-determined list $\mathbb{K}$ of good-time blocks.

Assuming an approximately constant angular rate of satellite spinning over one block, the exposure time of one high-resolution bin $H^{\text{block}}_{k,l}$ can be computed as

$$\Delta^{\text{block}}_{k,m} = \frac{n_{\text{block}} \langle P_{\text{GLOWS},k} \rangle}{n_{\text{bin}}}, \tag{48}$$

where k is a given block number and $\langle P_{\text{GLOWS},k} \rangle$ is the spin period averaged over this block.

To keep track of the exposure times for H_m, it is useful to define the following quantity

$$\Delta_m = \sum_{k \in \mathbb{K}} \Delta^{\text{block}}_{k,m}, \tag{49}$$

that is actually the sum of exposure times of good high-resolution histogram bins $H_{k,l}$ that were co-added to obtain the number of counts in a given bin of the daily-accumulated histogram H_m.

12.7.4 Computing the daily count rate

The daily-accumulated high-resolution histogram H_m is obtained by co-adding high-resolution bins within one observational day as described in the previous subsection. The blocks selected for accumulation are chosen based on predefined selection criteria using flag arrays associated with histograms. The flags contain onboard-collected information and determined-on-the-ground information, e.g., exceeding predetermined thresholds on spreads of selected ancillary parameters.

The quantity Δ_m contains the exposure times for H_m. Therefore, the daily-averaged counting rate S_m can be computed as

$$S_m = \frac{H_m}{\Delta_m}. \tag{50}$$

The counting rate S_m should be understood as describing the modulation of the signal along the GLOWS scanning circle in cts/s units.

A procedure of computing a count-rate uncertainty σ^{s}_m is discussed below in Section 12.7.7.

12.7.5 Calibration for computing the helioglow intensity in Rayleigh units

Having the count rate S_m (in cts/s units) along the scanning circle we need a conversion factor α to compute the helioglow intensity (i.e., the photon flux in the Rayleigh units). We adopt here an approach similar to that applied in the TWINS/LAD detector Nass et al. (2006), which is a heritage instrument for GLOWS.

Laboratory measurements performed in the PTB synchrotron facility using the GLOWS flight model allow us to determine the quantum efficiency QE [cts/photon] for the detector (for the Lyman-α wavelength of 121.6 nm). It should be understood as the ratio of the counts number per one incoming photon (averaged over the GLOWS FOV) for the detector as a whole (i.e. with filter, collimator, grounding grid, etc.). Measurements of the PSF function performed in the PTB and CBK give us an estimate of the effective solid angle Ω [sr]. The area A [cm^2] of the CEM can be determined from its diameter. We define $L_{1\mathrm{R}} = 10^6/(4\pi)$ photons s^{-1} cm^{-2} sr^{-1} as the radiance corresponding to the photon flux density of 1 Rayleigh. We finally get the calibration factor

$$\alpha_0 = L_{1\mathrm{R}} \times QE \times A \times \Omega = 3.37 \quad [\mathrm{cps/R}] \tag{51}$$

for $QE = 0.0041$ cts/photon, $\Omega = 0.00416$ sr, $A = 5.067$ cm^2, and cps=cts/s. For the TWINS/LAD detectors the conversion factor was $\alpha_{\mathrm{TWINS}} \approx 2$ cps/R.

The calibration factor presented above was obtained for the following GLOWS electronics settings: HV_0=1600 V, $THRS_0$=1.74 V, $COMP_0$=3.2 V. HV denotes here the high voltage set on the instrument HVPS, $THRS$ is a discrimination threshold for electronic pulses associated with photon detection events, and $COMP$ is a comparator voltage for measuring the length of pulses associated with photon detection events. Generally, we expect that the calibration/conversion factor $\alpha(HV, THRS, COMP, t)$ is a function of the voltages mentioned above and time (to account for sensor aging effects). We assume the following general form

$$\alpha(HV, THRS, COMP, t) = \alpha_0 \times f(HV, THRS, COMP, t) \quad [\mathrm{cps/R}] \tag{52}$$

By t_0 we understand the time of performing the calibration in the PTB, thus $f(HV_0, THRS_0, COMP_0, t_0) = 1$. The function $f(HV, THRS, COMP, t)$ will be determined from laboratory measurements (performed during ground calibration in the PTB and during tests in the CBK) and regular gain tests that will be performed during the mission. The dependence on the time t will be determined by tracking stars seen in the GLOWS FOV during the mission. Formally, $f(HV, THRS, COMP, t)$ may contain a separate constant term that can be attributed to the effects of background. If a dependence of the calibration factor on the temperature will be found during the mission, the GLOWS team will try to characterize it by analysis of obtained measurements.

Using the conversion factor $\alpha(HV, THRS, COMP, t)$ we can compute the intensity I_m of the helioglow in Rayleigh units

$$I_m = S_m \times \alpha(HV, THRS, COMP, t). \tag{53}$$

The calibration factor $\alpha(HV, THRS, COMP, t)$ will be provided to the SDC by the instrument team as described in item 6 in Sec. 3.12.

12.7.6 Bad-angle masking

Brief description of bad-angle flags is included in Sec. 3.7.1 and Tab. 3.11. This section contains some additional comments and clarifications.

The helioglow signal observed by GLOWS will be typically contaminated by point sources (mainly stars) that are seen as localized peaks on the lightcurve as shown, e.g., in Figures 10.1 and 10.2. Using observations from IUE and other missions, the GLOWS team is preparing a sky map of bright point sources within the spectral sensitivity range of the GLOWS instrument. A catalog of bright point sources (including their J2000 ecliptic positions in the sky and masking radiuses depending on their brightness) will be provided by the GLOWS team by the beginning of the mission and possibly updated later during the mission, if found necessary.

Based on the angular radius of the GLOWS scanning circle, spin phase and the block-averaged J2000 ecliptic longitude and latitude of the spin axis, the positions of the bins in the sky can be computed. This makes it possible to compute the angular distance between a given bin position and a given item in the bright-point-source catalog. This distance will be compared with a pre-defined threshold (determined by the width of the

PSF function for GLOWS) which we refer to as masking radius. If the distance is smaller than the threshold, a given bin will be marked as bad, i.e., point-source-contaminated. The information about bad bins will be stored in a bin-quality array associated with a given histogram.

The masking radiuses will be set for each star separately depending on its brightness. Generally, for the brightest sources the radius is anticipated to be approx. 4 deg. The smaller brightness, the smaller radius will be applied, but it should always be larger than a certain limit value 0.2-0.6 deg (larger than the expected 3σ for the nutation). The catalog of bright UV point sources needed for the `is_close_to_uv_source` flag will contain probably hundreds of sources. Identification of stars that will need to be masked is under way. This needs to be done in conjunction with analysis of the expected signal because a star of a given brightness can potentially be harmful in a region of the sky with a low helioglow intensity, but not in a region where the glow is bright.

Apart from stars, it seems to be necessary to define excluded regions in the sky where there is a more diffuse contamination difficult to estimate. For the `is_inside_excluded_region` flag, the most universal way of defining to-be-masked regions in the sky is presumably by providing a set of points in the sky that densely cover regions to be excluded (e.g., proximity of the galactic plane). Such approach makes the problem of region-masking similar to star-masking and similar algorithm can be used for the two purposes. The parameter `angular_radius_for_excl_regions__deg` will be probably set to the half of the nominal radius of the GLOWS FOV for the excluded-region-masking purposes.

12.7.7 Uncertainties

The uncertainties of the helioglow intensity will be the statistical (Poisson) scatter, scaled similarly as re-scaling the counting numbers in individual bins to intensities in Rayleighs. The data correlation matrix at this phase of processing is thus diagonal (TBC). In the reality, the helioglow observed in individual bins features bin-to-bin correlations but they will be addressed at Level-3.

The uncertainty of the intensity in one bin will be given by appropriate scaling of the statistical scatter of the observed count number in that bin. For the count number H_m, the uncertainty σ^s_m of count rate S_m is given by

$$\sigma^s_m = \frac{\sqrt{H_m}}{\Delta_m}, \tag{54}$$

and the uncertainty σ^I_m of the intensity in the Rayleigh units by:

$$\sigma^I_m = \sigma^s_m \times \alpha(HV, THRS, COMP, t). \tag{55}$$

Since the factor $\alpha(HV, THRS, COMP, t)$ has its own uncertainty σ_α, this needs to be acknowledged in the uncertainty system. However, we do not modify the heteroscedastic uncertainties of the helioglow intensity given in Equation (55) because from the global point of view, the uncertainty σ_α has a systematic character (albeit perhaps changing with time) and needs to be addressed in the global uncertainty system.

12.8 Level-2: helioglow intensity in physical units

The most up-to-date listing of GLOWS Level-2 data product is included in Sec. 3.10. The material presented here should be consistent with Sec. 3.10.

The intensity I_m is the basic Level-2 science-data product for GLOWS. This will be the intensity of the measured signal in the form of a light curve in the high-resolution bins. We anticipate the Level-2 data structure to contain:

1. header (a series of text strings with the information on the files used, software used, processing time, etc)
2. Level-2 histogram identifier
3. start time (UTC)
4. end time (UTC)

5. helioglow intensity vs. position angle along the scanning circle I_m (in Rayleighs; $1 \leq m \leq n_{\rm bin}$)
6. uncertainty of the intensity $\sigma^{\rm I}_m$ (in Rayleighs)
7. exposure times Δ_m (in seconds)
8. average longitude and latitude of the spin axis over the time interval of the histogram
9. spreads for the average longitude and latitude (standard deviation 1σ)
10. spacecraft location information (TBD, most likely X_i, Y_i, Z_i – the Cartesian heliocentric coordinates in the ecliptic reference system)
11. spreads ΔX_i, ΔY_i, ΔZ_i for the spacecraft location (standard deviation 1σ)
12. spacecraft velocity information (TBD, most likely $V_{X_i}, V_{Y_i}, V_{Z_i}$ – the Cartesian heliocentric coordinates in the ecliptic reference system)
13. spreads ΔV_X, ΔV_Y, ΔV_Z for the spacecraft velocity (standard deviation 1σ)
14. average filter temperature over the time interval of the histogram
15. spread of the filter temperature (standard deviation 1σ)
16. average channeltron voltage over the time interval of the histogram
17. spread of the average channeltron voltage (standard deviation 1σ)
18. average spin period over the time interval of the histogram
19. spread of the average spin period (standard deviation 1σ)
20. average offset of the GLOWS position angle
21. spread of the average GLOWS position angle (standard deviation 1σ)
22. average length of the event impulse
23. spread of the average length of event impulse (standard deviation 1σ)

A procedure of computing the uncertainty $\sigma^{\rm I}_m$ is discussed Section 12.7.7.

High-resolution histograms at Level 2 are needed to enable masking out star-contaminated bins, preserving as much not-contaminated data as possible. This will be done at transition from Level-2 to Level-3, but this is subjected to in-depth science analysis. Nevertheless, Level-2 product can be used in science analysis provided that a researcher addresses the issue of multiple signal sources and all kinds of backgrounds. The IMAP Data Level Definitions say that Level 2 should "represent the lowest level of research grade scientific data". From the point of view of helioglow analyses, a daily-accumulated histogram seems to be consistent with the definition and requirements for the GLOWS instrument.

All items within this data structure are in physical units. Angles are expressed in decimal degrees, times either in seconds (e.g., spin period-related items), or (like dates) as a year + decimal DOY. This latter approach facilitates quick recognition of absolute time during the mission, the ordinal number of a daily data set, and a time difference, like identifying time spans related to Carrington rotations etc.

13 Data products Level-3

This section is intended to describe only Level-3 data products. Similarly to Section 12 it is intended for extended studies/analyses, but for Level-3. A brief description of the Level-3 data products is provided in Section 4.

13.1 Ground-processing pipeline from Level-2 to Level-3a

13.1.1 Rebinning high-resolution lightcurve into low-resolution lightcurve

At the end of the initial culling process (i.e., at Level-2), we obtain a high-resolution daily-accumulated lightcurve, where each bin in the lightcurve has an associated quality flag. Using the quality flag, bad bins can be identified. Rebinning the high-resolution lightcurve S_l (where $1 \leq l \leq n_{\rm bin}$ is the bin number) into a low-resolution lightcurve s_m requires adding up good bins within an appropriate range of the indexes l for a given index m (where $1 \leq m \leq n_{\rm bin}^{\rm lores}$). The low-resolution histograms will contain $n_{\rm bin}^{\rm lores}$ bins (before masking), where $n_{\rm bin}^{\rm lores}$ should be chosen in such a way that $n_{\rm bin}$ is an integer multiple of $n_{\rm bin}^{\rm lores}$. We currently anticipate $n_{\rm bin} = 3600$ and $n_{\rm bin}^{\rm lores} = 90$, possibly (but unlikely) to be modified. The ratio $n = n_{\rm bin}/n_{\rm bin}^{\rm lores}$ is the nominal number of the high-resolution bins that must be co-added to merge them into one low-resolution bin, according to the formula

$$h_m = \sum_{l=1}^{n} H_{l+(m-1)n} Q_{l+(m-1)n}. \tag{56}$$

The quantity h_m is the daily-accumulated number of counts in a given low-resolution bin, and $H_{l+(m-1)n}$ is a high-resolution bin defined in Eq. (47). The quality-flag array $Q_{l+(m-1)n}$ for a given high-resolution lightcurve contains 0 for bad bins and 1 for good bins. They are determined from Level-1b bad-angle flags listed in Table 3.11 and discussed in Sections 12.3.3 and 12.7.6.

The high-resolution exposure times Δ_i (see Eq. (49)) are co-added similarly (accounting for the quality flags) in the following way

$$\delta_m = \sum_{l=1}^{n} \Delta_{l+(m-1)n} Q_{l+(m-1)n}. \tag{57}$$

to obtain the exposure times δ_m for low resolution bins.

The daily-accumulated low-resolution count rate s_m is finally obtained as

$$s_m = h_m/\delta_m. \tag{58}$$

This operation is possible only for bins with $\delta_m \neq 0$. The calibration procedure presented in Section 12.7.5 (discussed there for the Level-2 high-resolution lightcurve) needs to be applied to the count rate s_m to obtain the photon flux in Rayleigh units for the low-resolution lightcurve.

The calibration factor $\alpha(HV, THRS, COMP, t)$ is provided to the SDC by the instrument team as described in item 6 in Section 3.12.

13.1.2 Culling – masking star-contaminated bins

Some bins in the low-resolution histogram discussed in Section 13.1.1 have the null value of the exposure time δ_m after co-adding corresponding high-resolution bins (due to zero values of the quality flag $Q_{l+(m-1)n}$ in the high-resolution bins, see Eq. (57)). These bins need to masked out by simply removing them from the Level-3a lightcurve.

13.1.3 Estimating extra-heliospheric background

Methods of estimating physical backgrounds and extra-heliospheric sources needs to be developed. It is anticipated that this type of background will contain several components:

- unresolved UV point sources (see Strumik et al. (2020))
- dim resolved stars (because dim sources are not included in the UV sources catalog discussed in Section 12.7.6)
- diffuse emissions (presumably localized in the proximity of the galactic plane) resulting from scattering of photons from the stars on molecular clouds, dust, etc.

IUE, SOHO/SWAN and TD1-Stellar Ultraviolet Flux Survey observations and modeling are planned to be used to estimate the background. This type of background is expected to be constant in time (if we neglect possible variability of stars), thus can be computed as a sky map (ecliptic coordinates J2000, HEALPix pixelization scheme), from which the background can be computed by interpolation for a particular lightcurve in Level-3A.

The sky map with estimates of the background is provided by the instrument team to the SDC as an ancillary file in the format described in item 7 in Section 3.12. Since the estimate is done by the instrument team and possibly influenced by their specific views it seems reasonable not to subtract it from the photon flux at Level-3A, but rather to provide it as a separate array. This enables data users to apprehend that the photon flux comes directly from the GLOWS measurements, and the background is estimated by the instrument based on other measurements/models. During Level-3A-to-Level-3B processing, this background is to be subtracted from the photon flux, so it should be provided in the Rayleigh units for convenience.

13.1.4 Estimating time-dependent background

Due to their time variability, estimates of this type of background need to be provided by the instrument team to the SDC (as an ancillary file) separately for each observational day. This background contains the following components:

- corrections for the electron background (will be estimated during the mission by analysis of correlations between GLOWS and SWE measurements)
- corrections for variable stars (to be determined during the mission if really needed)

Development of methods for estimation of this background is still in progress. Similarly to the extra-heliospheric background discussed in Section 13.1.3, we do not plan to subtract the time-dependent background from the photon flux at Level-3a, but rather provide it as a separate array. During Level-3a to Level-3b processing, this background is to be subtracted from the photon flux, so it should be provided in the Rayleigh units for convenience.

Notes on the electron background. Generally, unwanted correlations may appear between the GLOWS signal and SWE electron fluxes for high energy electrons. However, currently there is no data obtained in the past on which the correlations could be investigated. During a meeting on October 30, 2024 with the SWE and SWAPI teams, the GLOWS team obtained the following information on SWE measurements:

- Level-2 (perhaps Level-1b) data product for SWE will contain the so-called energy-angle spectrum provided on a one-minute cadence
- the flux of electrons will depend on the energy, bin angle, and polar angle
- the range of energies is: 20 eV – 5 keV
- in Level-3, pitch-angle distribution will be provided (with separate characteristics for core, halo, strahl, and superhalo populations)
- moments of the VDF are generally problematic for electrons (due to complicated VDF?); density estimates being very uncertain, temperature more reliable, bulk velocity small as compared to the thermal speed

During the meeting on October 30, 2024, the GLOWS team asked also about the dependence of the Dr Sjuts CEMs sensitivity on the energy of electrons. SWE team pointed out to Dr Sjuts materials, where the sensitivity is shown to be relatively flat in the energy range 10 eV - 100 keV and negligible below 10 eV.

Based on all the information, the GLOWS team plans to investigate the GLOWS vs. SWE correlations at the beginning of the mission and derive a method for estimating the background corrections if needed. The dependence of the electron flux on the angles is planned to be neglected in the first step and only correlations between the GLOWS signal and electron fluxes in energy bins will be analyzed.

The final corrections are planned to be computed by the GLOWS team and provided to the SDC in the file format described in item 8 in Section 3.12.

13.1.5 Uncertainties of the low-resolution lightcurve

The statistical uncertainty is computed similarly to the high-resolution case discussed in Section 12.7.7. Eqs. (54) and (55) are fully applicable, with H_m replaced with h_m and Δ_m with δ_m. The Level-3a data product only contains the statistical uncertainty for the photon flux. Other uncertainties are estimated to be small or have a systematic character.

We currently assume that the uncertainty for δ_m (determined by the uncertainty of the spin period $\langle P_{\mathrm{GLOWS},k}\rangle$) is negligibly small as compared with the Poisson-statistical-scatter error for h_m. Therefore, we do not include it in the uncertainty estimations. If this assumption turns out to be incorrect during the mission, the uncertainty for δ_m should be accounted for using appropriate uncertainty-propagation formulas.

The calibration factor $\alpha(HV, THRS, COMP, t)$ has its own uncertainty σ_α, which was determined by the GLOWS team before launch and will be updated during the flight. This is a systematic uncertainty, which correlates all bins for a given observational day. A possible dependence of the instrument sensitivity on the instrument temperature, only possible to be identified after launch, may introduce additional systematic uncertainties.

Additional uncertainties of the photon flux are related to the uncertainties in the spin axis pointing. The magnitudes of the uncertainties of the spin axis pointing and other relevant factors are given in the data products.

The model of the backgrounds has its own uncertainties, which need to be developed. They will be compiled with the uncertainty of the data product during the science analysis. In data product documentation, they will only be mentioned to consider by data users.

13.2 Level-3a: daily low-resolution lightcurve of Lyman-α photon flux with estimates of backgrounds

Detailed listings of items/variables included in Level-3a data product are provided in Section 4.4. In this section, we provide some additional comments why the Level-3a data product is constructed the way it is.

Resolution. The high resolution of 0.1°in Level-2 and lower levels is needed to resolve accurately stars for sensitivity degradation tracking. Since the helioglow intensity is a slowly-varying function in the sky, a much lower resolution is required for its studies. Additionally, the effective diameter of the GLOWS FoV is $\sim 4°$, which introduces some correlations between signal values in bins of the high-resolution lightcurve. Analyses performed by the GLOWS team suggested that dividing the scanning circle into nominally 90 bins (4°each) provides a good basis for deriving the heliolatitudinal modulation of the total ionization rate at Level-3b.

Cadence. Analyses performed by the GLOWS team suggest that the $\sim$ 24-hour cadence related to the regular IMAP repointing maneuvers is sufficiently small to track the helioglow variations due to changes in the H-atoms ionization in the proximity of the Sun. It is also sufficiently large to obtain sufficiently large numbers of counts that give a small statistical scatter.

Physical unit. The GLOWS team uses the Rayleigh unit, which has been commonly used on many missions (e.g., Mariner 10 UVS, SOHO/SWAN, TWINS/LAD, and many others) to describe diffuse emissions in the sky similar to the helioglow.

Coordinate frame. The GLOWS team prefers to use the ecliptic frame J2000. Analyses of SOHO/SWAN observations showed it is a convenient choice for this type of studies.

Masking. The masking procedure is required as a pre-processing step to obtain later a part of the signal directly related to the helioglow.

13.3 WawHelioIon-MP

The detailed discussion of the method is presented by Porowski and Bzowski (2024). (TBD)

13.3.1 Method

General description of the method (very short, the most important points) (TBD)

13.3.2 Training sets: ionization rate

Ionization rate from IPS - how profiles are prepared (those actually used) (TBD)

13.3.3 Training sets: light curves

Light curves from SWAN data - how they were selected and prepared, which one are good enough (gaps from stars etc.) (those actually used) (TBD)

13.3.4 Reconstruction

How well we can reconstruct ionization rate, stability and accuracy of the method, how big gaps in the data are acceptable and why (TBD)

13.3.5 Vantage points selection

How many, where, why? TBD

13.3.6 Model parameters file

Structure of the json file that will be delivered TBD

13.4 SOHO/SWAN Cross-calibration

How the cross-cal of GLOWS with SWAN is done (TBD)

13.5 Relevant ionization processes

Ionization of the hydrogen atom can be caused by various processes (Bzowski et al., 2013). In the following subsections, we present some general background about them.

One of the ionization reactions, the so called photoionization, is due to an interaction of a H atom with a photon that carries enough energy to eject the electron.

$$\mathrm{H} + \nu \rightarrow \mathrm{H}^{+}_{\mathrm{PUI}} + \mathrm{e}. \tag{59}$$

The energy of the impacting photon must be above the ionization threshold, which in the case of hydrogen is $E_{\mathrm{th}} = 13.6$ eV. It means that we are interested in photons with the wavelength shorter than $\lambda_{\mathrm{th}} = 91.2$ nm. The rate of this reaction per H atom depends on the instantaneous solar EUV flux and drops with the square of solar distance. The products of the reaction are a free electron and a proton, which typically has a different velocity than the ambient plasma, becoming a pickup ion.

Photoionization concerns all H atoms in the heliosphere, both interstellar neutral H, which are the source population for the helioglow observed by GLOWS, and energetic neutral atoms (ENAs), for which GLOWS calculates the survival probabilities. The rate is independent of the atom kinetic energy.

Another relevant reaction is charge exchange between (H) atoms and protons (p):

$$\mathrm{H} + \mathrm{p} \rightarrow \mathrm{H}^{+}_{\mathrm{PUI}} + \mathrm{H}_{\mathrm{ENA}}. \tag{60}$$

In this reaction, a collision between a H atom and a proton results in a transfer of electron from the H atom to the proton, which becomes a neutral H atom. At the collision speeds characteristic for the inside of the heliosphere, this reaction goes without momentum exchange between the collision partners. Since the former H atom, which has just been stripped of its electron, has typically a different velocity to that of the ambient plasma, it becomes picked up by the magnetic field frozen in the ambient plasma and becomes a pickup ion $\mathrm{H}^{+}_{\mathrm{PUI}}$. The former proton – now a H atom – maintains its original velocity but now, being neutral, is no longer bound by the ambient magnetic field and runs away freely as an energetic neutral atom (ENA). Since ENAs have typically

velocities comparable to that of the solar wind ions, they are Doppler shifted away from the spectral range of the solar Lyman-α line and thus do not contribute to the helioglow. From this viewpoint, charge exchange is a loss reaction for the ISN H gas, which is the source population for the helioglow. For charge exchange between ENAs and solar wind protons, formally the charge exchange is not a loss process because the number of ENAs in the global population does not change. However, the resulting ENA has a different energy and velocity direction than the original one, and from this view point, the original ENA flux, for which one wants to calculate ionization losses, is reduced due to this reaction.

The rate of charge exchange per H atom at a given location in the heliosphere is given by the local density of protons $n_{\rm p}$, collision speed $v_{\rm rel}$, and the cross section for the reaction $\sigma_{\rm cx}(v_{\rm rel})$, which depends on relative velocity of the reaction partners:

$$\beta_{\rm cx} = n_{\rm p}\, v_{\rm rel}\, \sigma_{\rm cx}(v_{\rm rel}). \tag{61}$$

The solar wind proton density is assumed to drop with the square of solar distance and the solar wind speed to be constant and directed antisolar-wise. For ISN H atoms, it can be assumed that the relative speed for the collision is equal to that of the solar wind speed (the so-called stationary atom approximation). For the ENAs, the relative speed must be calculated by subtraction of the velocity vectors of the collision partners: $v_{\rm rel} = |\boldsymbol{v}_{\rm ENA} - \boldsymbol{v}_{\rm SW}|$. This approximation works well because the thermal spread of the solar wind speed is very small relative to the radial expansion speed.

13.6 Photoionization rate

Bzowski et al. (2013) showed that photoionization rate at 1 au is correlated with radio flux F10.7 (Tapping, 2013). The photoionization rate for hydrogen is calculated using Equation 3 in Sokół et al. (2020), which we repeat here for convenience:

$$\beta_{\rm ph} = -2.9819 \times 10^{-8} + 2.416 \times 10^{-8} f_{\rm F10.7}^{0.4017}. \tag{62}$$

The F10.7 radio flux is available via the LASP service: `https://lasp.colorado.edu/lisird/data/penticton_radio_flux`. In the original data set, the radio flux is measured 3 times a day (if there are no issues). In our analysis, we use daily measurements taken near local noon, and average them over Carrington rotation period. In the absence of the noon observations, we use what is available for the given day.

13.7 Normalization to the solar wind measurements in the ecliptic plane

The ionization rate profile that we obtain from the observed GLOWS lightcurve is affected by various calibration factors. In order to be consistent with the in-situ measurements of the solar wind parameters in the ecliptic plane, we normalize our profile before further analysis. Using the OMNI2 or SWAPI data, we calculate the charge exchange rate in the ecliptic plane averaged over Carrington rotation period

$$\beta_{\rm cx,ecl}^{\rm CR} = \langle \sigma_{\rm cx}(v_{\rm ecl})\, v_{\rm ecl}\, n_{\rm p,ecl} \rangle, \tag{63}$$

where $\sigma_{\rm cx}^{\rm CR}$ is the charge exchange cross-section, $v_{\rm ecl}$ and $n_{\rm p,ecl}$ are plasma speed and proton density measured in the ecliptic plane at a high time resolution, and $\langle . \rangle$ means averaging over Carrington period.

The Carrington period-averaged photoionization rate in the ecliptic plane $\beta_{\rm ph,ecl}^{\rm CR}$ is calculated using the approach presented in Section 13.6.

The ionization rate profile retrieved directly from the lightcurve $\beta(\Theta)$ is scaled by division by the equatorial bin value and then multiplication by the sum of the charge exchange and photoionization rates in the ecliptic calculated above:

$$\beta_{\rm norm}^{\rm CR}(\Theta) = \frac{\beta(\Theta)}{\beta(\Theta = 0)} \times \left(\beta_{\rm cx,ecl}^{\rm CR} + \beta_{\rm ph,ecl}^{\rm CR}\right), \tag{64}$$

13.8 Solar energy flux

13.8.1 Latitudinal invariant

The solar wind structure (density and speed) varies with heliographic latitude and the solar cycle phase. During solar minimum there is a clear difference between the slow solar wind emitted from the equatorial regions of the Sun and the fast solar wind observed at higher latitudes up to solar poles. While the solar activity increases during the solar cycle, the fast and slow solar winds are mixing and there is no clear latitudinal structure. Analysis of the data from the Ulysses mission by Le Chat et al. (2012) showed that the solar energy flux is a latitudinal invariant (although it is changing in time):

$$\xi(\Theta) = \rho(\Theta)v(\Theta)\left(\frac{1}{2}v^2(\Theta) + \frac{GM_\odot}{R_\odot}\right) = const., \tag{65}$$

where $\rho(\Theta)$ is the solar wind density (protons and α particles combined) and $v(\Theta)$ is the solar wind speed (we assume that protons and α particles have the same speed). G is the gravity constant, and $M_\odot$, $R_\odot$ are the solar mass and radius, respectively. Using this relation, latitudinal profiles of solar wind speed retrieved from the lightcurves, and measurements of solar wind speed and density in the ecliptic plane, we can calculate the latitudinal profiles of solar wind density.

In the ecliptic plane, the solar wind density and latitudinal invariant can be expressed as

$$\rho(\Theta = 0) = n_p(\Theta = 0)m_p + pn_p(\Theta = 0)m_\alpha = n_p(\Theta = 0)(m_p + pm_\alpha), \tag{66}$$

and the flux of solar mechanical energy as

$$\xi(\Theta = 0) = \rho(\Theta = 0)v(\Theta = 0)\left(\frac{1}{2}v^2(\Theta = 0) + \frac{GM_\odot}{R_\odot}\right) \tag{67}$$

where n_p is the protons concentration, m_p is the proton mass, p is the protons to α particles ratio, and m_α is the α particle mass. All of the above mentioned quantities are measured in the ecliptic plane and can be obtained from OMNI2 data base. GLOWS analysis reliquaries smooth, average over long periods values, therefore we will use OMNI2 data at the beginning of the mission, and then we will use SWAPI measurements.

13.8.2 Solar wind density and speed profiles

Calculating solar wind density and speed profiles requires solving set of 2 equations:

$$\xi(\Theta) = \xi(\Theta = 0) \tag{68}$$

$$\beta_{cx}(\Theta) = \sigma_{cx}\left(v(\Theta)\right) n_p(\Theta)v(\Theta), \tag{69}$$

where $\beta_{cx}(\Theta)$ is the Carrington rotation period averaged charge exchange rate profile (Level-3B data product) and σ_{cx} is the charge exchange cross section calculated using a formulae from Swaczyna et al. (2025)

$$\sigma_{cx}(E) = 10^{-16} \times \frac{A_1 \ln(A_2//E + A3)}{1 + A_4E + A_5E^{A_6} + A_7K^{A_8}} \tag{70}$$

where: E is the energy of the atom in keV, $A_1 = 4.8569$, $A_2 = 21.906$, $A_3 = 31.487$, $A_4 = 0.12018$, $A_5 = 4.1402 \times 10^{-6}$, $A_6 = 3.7524$, $A_7 = 8.8476 \times 10^{-12}$, and $A_8 = 6.1091$.

13.8.3 OMNI2 database

13.9 L3D initial structure

Survival probabilities calculations require a long history of the solar parameters. Therefore, the instrument team provides a set of initial text files with a long history of these parameters calculated using the WawHelioIon model (well tested and frequently used in the past; Bzowski et al., 2013; Porowski et al., 2022, 2023).

Items 1-3 in Table 13.1 have 22 columns: time [decimal year], value(-90°), value(-80°), ..., value(90°), CR, flag Items 4-6 in Table 13.1 have 3 columns: time [decimal year], value(0°), CR

Table 13.1: Brief description of initial solar parameters history. Item names refer to a descriptor in the official SDC file naming scheme `https://imap-processing.readthedocs.io/en/v0.5.0_a/development-guide/style-guide/naming-conventions.html`

Level-3D solar parameters history: initial files based on WawHelioIon model		
No.	Item	Comments/Remarks
1	`plasma-speed-<tag>`	solar wind plasma speed profile [km s^{-1}]
2	`proton-density-<tag>`	proton density profile [cm^{-3}]
3	`uv-anisotropy-<tag>`	UV anisotropy factor profile
4	`photoion-<tag>`	photoionization rate in the ecliptic plane
5	`lya-<tag>`	composite total solar Lyman-alpha irradiance
6	`electron-density-<tag>`	solar wind electron density in the ecliptic plane

13.9.1 Source flags

Items 1-3 in Table 13.1 high level products that are developed by Warsaw group for many years. They involve sophisticated modelling and external data usage. The models as well as the source data were changing during time and will probably evolve in the future. To distinguished between different approaches, we defined a source flag composed of 5 digits (FFMMI). The first two digits (FF) represents a family of the solutions, the next two digits indicate specific model, and the last digit will be 0 if the data are based on actual measurements or 1 if they are based on interpolation. A list of used flags with they descriptions is currently under development.

13.10 Survival probabilities

13.10.1 General description

Survival probabilities of energetic neutral H atoms (H ENAs) are the probabilities that an ENA is not ionized during its travel from the outer boundary of the system, defined as a Sun-centered sphere with a radius r_{End}, to IMAP. The theory of calculation of ENA survival probabilities is presented in Bzowski (2008). The probabilities are calculated using three FORTRAN programs dedicated to the three IMAP ENA instrument: `survProbLo`, `survProbHi`, and `survProbUltra` for IMAP-Lo, IMAP-Hi, and IMAP Ultra, respectively. These programs calculate the probabilities for a series of carefully selected instrument boresight directions for a grid of ENA energies in the spacecraft-inertial reference frame. The calculations are performed based on information on the ionization (loss) rates of H ENAs obtained from analysis of lightcurves from the GLOWS instrument.

Calculation of survival probabilities $w(t_0, \boldsymbol{r}_0, \hat{\boldsymbol{l}}, E)$ for a given boresight direction $\hat{\boldsymbol{l}}$ and an ENA energy E in the IMAP-inertial reference frame for the IMAP locus in the solar frame $\boldsymbol{r}_0$ at a time t_0 goes as follows:

1. Calculation of the velocity of impact at IMAP for an ENA incoming from the direction $\hat{\boldsymbol{l}}$ at a given time t_0 and kinetic energy E in the spacecraft-inertial reference frame

2. Conversion of the atom impact velocity from the spacecraft-inertial to the solar-inertial reference frame and calculation of the state vector of this atom at the moment of impact t_0. To that end, the IMAP velocity vector and the radius-vector relative to the Sun $\boldsymbol{r}_0$ are needed.

3. With the state vector taken as the initial condition for integration, numerical tracking of the atom trajectory $\boldsymbol{r}(t, x, y, z)$ backwards in time from the impact locus $\boldsymbol{r}_0$ to the outer boundary at a distance from the Sun r_{End}. The backtracking is performed by numerical solution of the equation of motion. The atom moves in the solar gravity field and under a radiation pressure force, which varies with time as a function of the solar Lyman-α flux. Details of the radiation pressure model are given by Kowalska-Leszczynska et al. (2020).

4. Calculation of the exposure $\varepsilon(t_0, \boldsymbol{r}_0, \hat{\boldsymbol{l}}, E)$ of the ENA to ionization losses between the spacecraft at $\boldsymbol{r}_0$ and the outer boundary r_{End}, by numerical integration along the atom trajectory of the local ionization rate

$\beta(t, \boldsymbol{r})$, which varies as a function of time, solar distance, and heliolatitude:

$$\varepsilon(t_0, \boldsymbol{r}_0, \hat{\boldsymbol{l}}, E) = \int_{t_0}^{t(r_{\mathrm{End}})} \beta(t, \boldsymbol{r}(t))\, \mathrm{d}t. \tag{71}$$

The integration goes backwards in time from t_0 to the time $t(r_{\mathrm{End}})$ of reaching by the test atom the boundary distance r_{End}. Information on the instantaneous heliolatitude of the test atom is coded in the instantaneous vector $\boldsymbol{r}(t)$. For integration backwards in time, the exposure value ε is a negative number. The ionization rate β is calculated using GLOWS data products L3d and the instantaneous atom velocity $\mathrm{d}\boldsymbol{r}/\mathrm{d}t$.

5. Calculation of the survival probability

$$w(t_0, \boldsymbol{r}_0, \hat{\boldsymbol{l}}, E) = \exp(\varepsilon(t_0, \boldsymbol{r}_0, \hat{\boldsymbol{l}}, E)). \tag{72}$$

The survival probability programs `survProb*` use a common core module for calculation of the survival probabilities for individual boresight directions. They operate on energy grids specific for their dedicated instrument. They use time histories of latitudinal profiles of solar wind speed and density (the GLOWS L3d product) as well as time series of the photoionization rate of H at 1 au and the solar wavelength-integrated Lyman-α flux obtained from external sources. The baseline time resolution of these products is 1 Carrington rotation period in time and 10° in heliolatitude. During calculation of the exposures defined in Equation 71, the SW density, speed, and photoionization rate are bilinearly interpolated to the instantaneous time t and heliolatitude $\phi(t)$ calculated from the instantaneous radius-vector $\boldsymbol{r}(t)$.

The differences between the **survProb*** programs consist in their approach to the impact direction grids and integration of the probabilities over their respective field of views. **survProbLo** and **survProbHi** calculate the probabilities for the boresight directions evenly distributed along the actual scanning circles of their respective instruments for each IMAP pointing (Table 4.16:lines 9–11). **survProbUltra** calculates the probabilities on a HealPix grid of directions defined in the ecliptic J2000 coordinates (with a circumsolar gap, Table 4.17:line 2).

The probability product of **survProbHi** and **survProbUltra** is just the probability calculated using Equation 72.

The probability product of **survProbLo** for a given boresight $\hat{\boldsymbol{l}}$ is obtained from numerical integration of the probabilities over the IMAP-Lo collimator field of view, weighted by the IMAP-Lo collimator transmission function $\mathrm{PSF}_{\mathrm{Lo}}(\boldsymbol{\varpi})$, where $\boldsymbol{\varpi} = \hat{\boldsymbol{l}}' - \hat{\boldsymbol{l}}$, $\hat{\boldsymbol{l}}$ is the boresight direction and $\hat{\boldsymbol{l}}'$ is a direction within the collimator field of view. With the normalization condition $\int_{\mathrm{FoV}} \mathrm{PSF}_{\mathrm{Lo}}(\hat{\boldsymbol{l}}' - \hat{\boldsymbol{l}})\, \mathrm{d}\hat{\boldsymbol{l}}' = 1$, the probability for IMAP-Lo is calculated as:

$$w_{\mathrm{Lo}}(\hat{\boldsymbol{l}}) = \int_{\mathrm{FoV}} \mathrm{PSF}_{\mathrm{Lo}}(\hat{\boldsymbol{l}}' - \hat{\boldsymbol{l}})\, w(\hat{\boldsymbol{l}}')\mathrm{d}\hat{\boldsymbol{l}}'. \tag{73}$$

In practice, numerical integration is replaced with a finite sum, with the directions $\hat{\boldsymbol{l}}'$ taken as the centers of HealPix pixels within the IMAP-Lo field of view for a grid with the north pole coincident with the boresight direction $\hat{\boldsymbol{l}}$.

13.10.2 Running the programs

The survival probability programs are run with command-line parameters, as follows:

```
./survProbLo time_in_IMAP_form time_point R_SC long_SC lat_SC Vx Vy Vz alpha_Axis beta_Axis elongation
```

For an example command line and discussion of individual parameters and their ranges, see Table 4.16. The program first verifies if the number of command-line parameters is correct. If not, it displays an error message and exits. Subsequently, the program verifies if the magnitudes of the parameters are within the allowable ranges and returns an error message and exits if any of them is not. In this case, a message which parameter was violated and the relevant allowable range are displayed.

Input files The **survProb*** programs require input files for the time histories of:

- solar Lyman-α flux
- latitudinal modulation factor for the solar Lyman-α flux and photoionization rate
- latitudinal profiles of the solar wind density at 1 au
- latitudinal profiles of the solar wind speed at 1 au
- photoionization rate of hydrogen at 1 au at the solar equator
- density of the solar wind electrons at 1 au at the solar equator

The list of these files to use is obtained by the program by reading the file `ionization.files.dat`.

The **survProbLo** program uses a collimator transmission function. For integration over this function (Equation 73) a Healpix tesselation file `tessXYZ8.dat` is used (Table 4.17:line 1).

The **survProbUltra** program calculates the survival probabilities for directions distributed in the sky at the centers of HealPix pixels, tesselation 16 (Table 4.17, line 2), defined in the file `tessAng16.dat`.

The **survProbHi** program does not need any tesselation file.

All three programs require an energy grid file. The energy grids are defined in the files `EnGridHi.dat`, `EnGridLo.dat`, and `EnGridUltra.dat` (Table 4.17, line 3). The energy grid system is defined as homogeneous for the entire energy range of all IMAP ENA cameras. The grids for individual programs are subsets of the global grid. There are energy overlaps between the instruments, which was taken into account in the definitions of the instrument-specific grids.

The global energy grid is regular in the logarithmic scale, and the energies are defined in keV. The adopted ranges for the individual energy grids are the following:

- Lo: [0.01:4.00]
- Hi: [0.374:19.58]
- Ultra: [2.37:356.0].

The survival probability programs calculate the probabilities for the energies they find in their respective `EnGrid*.dat` files. There must be at least 5 energy entries in each of these files.

If the parameter values in the ionization files are outside of the relevant testRanges, the program returns an error message and information for which parameter this violation has occurred and exits.

Error information The program running with right parameters return exit status code by 0 to the shell. If there occurs an error, the exit status code returned to the shell is different than 0.
The program used with incorrect parameters generates error information. There are three basic sources of errors, as follows:

1. command line – the number of the arguments of the command is fixed. Calling the programs with a different number of arguments generates an error message. Each of the arguments is separately checked. The arguments must be within their respective ranges. The range for each argument is shown in Table 4.16.
2. problem with an input file – the programs read several input files. Each of the entries in the input files is checked if it is in the correct range. The ranges of all values are shown in Table 4.17.
3. lengths of the tables – the tables (arrays) inside the program have fixed maximum lengths. If the program finds the length of an array read-in from an input file outside the table length, an error will show up.
4. time validity – one of the program's command-line arguments specifies the time for which the calculations will be performed. If the requested time is earlier than the range of data available in the ionization files, the program will use the first available value as a constant until the actual data appears. If the requested time is later than the available data range in the ionization files, the program will return an error.

Table 13.2: Error information

Error information		
No.	Item	Comments/Remarks
	command line	Error: Not enough arguments given in command line. You need to give 11 arguments: time_imapForm(1) decimal_time(2) r(3) long_SpaceCraft(4) lat_SpaceCraft(5) Vx(6) Vy(7) Vz(8)(Spacecraft) Axis:long(9) lat(10) elongation(11)
	command line	Error: Wrong IMAP time format. Should be YYYYDDMM_HHMMSS, length should be 15, and is 14
	command line	Error: Wrong decimal time given 1009.000000 It must be in range [1800:2700]
	command line	Error: Wrong distance of the Spacecraft to the Sun -1.000000 It must be in range [0: 90.000000]
	command line	Error: Wrong longitude of the Spacecraft. It must be in the spherical ecliptic coordinates, in deg, in range [0:360], and it is -90.57619428
	command line	Error: Wrong latitude of the Spacecraft. It must be in the spherical ecliptic coordinates, in deg, in range [-90:90], and it is 100.000000
	command line	Error: Wrong velocity of the Spacecraft. It must be in the Cartesian ecliptic coordinates, in km/s, in range around 30km/s, and it is Vabs= 79.97006 Vx Vy Vz= -79.77450 -5.58930 -0.00080
	command line	Error: Wrong longitude of the spin axis. It must be in the spherical ecliptic coordinates, in deg, in range [0:360], and it is -280.5761983
	command line	Error: Wrong latitude of the spin axis. It must be in the spherical ecliptic coordinates, in deg, in range [-90:90], and it is 180.00000
	command line	Error: Wrong elongation angle. It must be in deg, in range [40:180], and it is 234.9999
	problem with the file	Error: file with list of all-ionization related files ionization.files.dat has incorrect length. It must be 6, and is 4
	problem with the file	Error: file with Itot has incorrect values inside: 606.7014 The offending file name: speed3D.v01.Legendre.2021b.dat
	problem with the file	Error: file with SW speed has incorrect values inside: 2.81044 The offending file name: density3D.v01.Legendre.2021b.dat
	problem with the file	Error: file with SW density has incorrect values inside: 1.031826357E-007 The offending file name: phion_Hydrogen_T12F107_2021b.dat
	problem with the file	Error: file with photoionization rates has incorrect values inside: 5.67645011 The offending file name: swEqtrElectrons5_2021b.dat
	problem with the file	Error: file with electrons has incorrect values inside: 606.7014 The offending file name: speed3D.v01.Legendre.2021b.dat
	length of the table	Error: the file with the energy grid is too short, shorter than : 5
	length of the table	Error: file with Itot is too long. Table for that value is 2000 long.
	length of the table	Error: file with SW speed is too long. Table for that value is 2000 long.
	length of the table	Error: file with SW density is too long. Table for that value is 2000 long.
	length of the table	Error: file with photoionization rates is too long. Table for that value is 2000 long.
	length of the table	Error: file with electrons is too long. Table for that value is 2000 long.
	time validity	Error: file with photoionization is too short. Last time in it is: 2021.6186039726019. The offending file name: `phion_Hydrogen_T12F107_2021b.dat`

13.10.3 Output text file

Each of the programs **survProb*** generates one output text file. The file names are composed of instrument-specific prefixes (`probSur.Imap.Lo, probSur.Imap.Hi, probSur.Imap.Ultra`) and strings representing the parameters described in line 1 of Table 13.3. The content of the files is presented in Table 13.3. The content of the file headers is presented in Table 13.4.

Table 13.3: Output files from the survival probability programs

Output files for the prob. of. surv. program		
No.	Item	Comments/Remarks
0	example:	`probSur.Imap.Lo_20090101_000001_2009.000_60.00.dat` `probSur.Imap.Lo.V0_20090101_000001_2009.000_60.00.dat`
1	name of files	prefixes for the instruments: `probSur.Imap.Lo, probSur.Imap.Hi, probSur.Imap.Ultra` Strings in the file names: (1) IMAP time identifier (Table 4.16:line 1), (2) decimal year (3) time (Table 4.16:line 2) (4) elongation (Table 4.16:line 11) Note: there is no elongation in the Ultra file name
2	V0 in filename :	The version of files with the velocity of SC set to zero. If program gets: Vx=Vy=Vz=0 (Table 4.16:line 6-8), it will automatically add `V0` to the prefix
3	header	Header length 200 lines. For header description see Table 13.4.
4	columns for Lo and Hi: spin_angle prob_of_surv(energy_grid)	spin_angle - angle along the circle in the sky centered at the direction of the IMAP spin axis, counted anticlockwise off the the nearest point to the ecliptic north pole anticlockwise TBC survival probabilities on instrument-specific energy grids, see Table 4.17:line 3)
5	columns for Ultra: longitude latitude	longitude, latitude, survival probabilities for the Ultra-specific energy grid J2000 ecliptic longitude [°] of the direction based on HealPix tesselation, based on the file in Table 4.17,line 2 J2000 ecliptic latitude [°] of the direction based on HealPix tesselation, based on the file in Table 4.17,line 2)

14 Coordinate frames

14.1 Instrument frames

It is important to differentiate between two different instrument frames for GLOWS. A frame convenient for science is defined below in Sec. 14.1.1. A different frame, convenient for mechanical-interface-related discussions is described below in Section 14.1.2.

14.1.1 Instrument frame for science (SPICE)

Definition: GLOWS Z axis along the GLOWS boresight, but pointing in the opposite direction wrt the boresight. GLOWS Y axis (pointing anti-sunward) in the plane defined by the GLOWS boresight and the Z axis of the

Table 13.4: Headers for the output files from the survival probability programs

Headers for the output files from the survival probability programs		
Line	Item	Comments/Remarks
1	length	200 lines
2	author	Marzena A. Kubiak
3	cmd.line descriptor	description of the parameters that are copied from the command line
4	parameters copied from the command line	Table 4.16, lines: 2–8
5	ident.of.day.IMAP, elongation/avoidance circle	Table 4.16:lines: 1, 11
6	spin axis direction	J2000 ecliptic longitude, latitude [°]
7	routs_end	distance to the boundary of tracking the test atoms [AU]
8	collim. tessel. for Lo spatial tessel. for Ultra	spatial grid for integration over the collimator (Table 4.17:line 1) spatial grid of directions on the sky used for Ultra (Table 4.17:line 2)
9	code version, date of calculations	
11-17	description of the input parameters	Table 4.16:lines: 1-11
19	flag_atom	species descriptor, H = hydrogen
29	Ly_a_Profile	model of the solar Lyman-α profile used
30	flag_Itot	solar Lyman-α time series file name (Table 4.17:line 5)
31-32	v_SW, n_SW	names of the files with solar speed (v) and density at the equator (n; Table 4.17:line 7-8)
33	photoionization rate series file	name of the file with the photoionization rate time series (Table 4.17:line 9)
34	sigma_SW	reference to the cross section function for charge exchange between H atoms and protons
35	electron flag	electron ionization rate function and name of file with electron density at the equator (Table 4.17:line 10)
36	SW_lati	heliolatitudinal function of solar wind
37	phot_lati	heliolatitudinal modulation of photoionization, the same as for Lyman-α anisotropy parameter (range [0.7:1.1]),
41-196	ionization & radiation pressure information	detailed information about ENA ionization-related files, copied from files in Table 4.17:lines 5-10
197	energy grid	list of energies. Different length for different instrument (Table 4.17:line 3)
198	definition of spin_angle	
200	column description	

IMAP body frame. GLOWS uses the right-handed frame, which determines the direction of the GLOWS X axis. See Fig. 14.1.

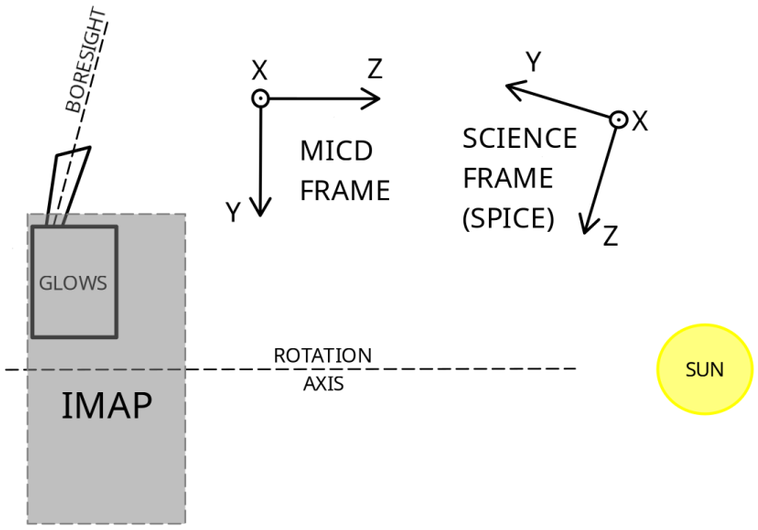


Figure 14.1: Definition of directions in the science (SPICE) instrument frame and the MICD instrument frame. The two frames are co-rotating with the satellite body. Centers of the frames are randomly located in this figure.

Boresight vector: (0, 0, -1) in this frame.

14.1.2 MICD instrument frame

Definition: Z axis perpendicular to the mounting plane, where the instrument is accomodated. X axis perpendicular to EBOX PCBs. This is a right-handed frame, which determines Y axis direction.

Fig. 14.2 shows the definition of the "mechanical" frame as illustrated in the MICD document (Kowalski, 2020).

15 Concluding remarks

This is a living document and at the time of this writing must not be regarded as a complete description of the planned system of data processing for GLOWS. The present content drives the processing of the telemetry data to a minimum level enabling scientific analysis of the results: daily lightcurves converted to physical units (Rayleighs) based on ground calibration.

In the future, several important elements will be added, including, among others

1. Point-source data product, suitable for photometric analysis of detected point sources. It will contain full-resolution portions of the histograms (accumulated over several n_{spin} blocks) with the contribution from the helioglow subtracted, organized in sequences of several observation days. This product will be a basis for determining the brightness of known stars and to tracking the apparent changes of this brightness, that are likely to occur because of instrument aging. The analysis will result in re-calibration of the instrument with time

2. Temperature-sensitivity data product, suitable for analysis of an optimum temperature to maximize the ratio of the signal from the helioglow to the signal from extraheliospheric sources. This data product will be developed using observations collected during the temperature tests. The data product will also be used to re-calibrating the observations to the conditions of a nominal temperature for the GLOWS filter that will be determined at a later date based on lab testing.

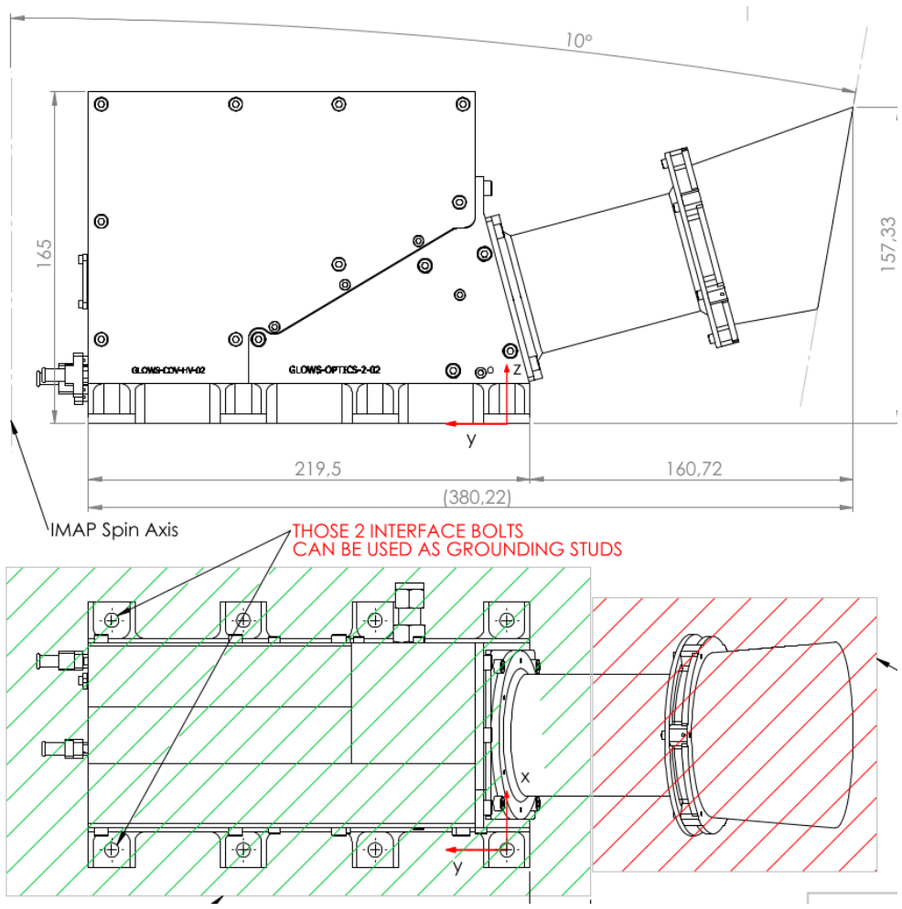


Figure 14.2: Definition of the MICD instrument frame (copied from MICD document Kowalski (2020)).

3. HV-sensitivity data product, suitable for analysis of the sensitivity of GLOWS as a function of HV setting, suitable for selecting the optimum HV setting.

4. A flight-calibrated data product, where results of in-flight tracking of the absolute calibration of GLOWS based on the temperature and HV tests, as well as analysis of photometric observations of stars will be implemented

5. A histogram-from-DE data product, compiled from DE data downlinked to Earth, intended for a comparison with equivalent HB-products downlinked from the spacecraft; the intention is to study the operation of the on-board algorithms, potential abnormalities etc. The purpose is analytic rather than for scientific analysis of the signal.

This list will likely be extended in the future.

References

Bzowski, M. (2008). Survival probability and energy modification of hydrogen Energetic Neutral Atoms on their way from the termination shock to Earth orbit. *A&A*, 488:1057–1068.

Bzowski, M., Ber, K., Strumik, M., and Wawrzaszek, R. (2020). A draft of data ground-processing algorithm for IMAP GLOWS. Technical Report GLOWS-CBK-SPEC-2020-11-02-030-v1.3, CBK PAN, Warsaw, Poland.

Bzowski, M., Mäkinen, T., Kyrölä, E., Summanen, T., and Quèmerais, E. (2003). Latitudinal structure and north-south asymmetry of the solar wind from Lyman-α remote sensing by SWAN. *A&A*, 408:1165–1177.

Bzowski, M., Sokół, J. M., Tokumaru, M., Fujiki, K., Quémerais, E., Lallement, R., Ferron, S., Bochsler, P., and McComas, D. J. (2013). Solar parameters for modeling the interplanetary background. In Quémerais, E., Snow, M., and Bonnet, R., editors, *Cross-Calibration of Far UV Spectra of Solar Objects and the Heliosphere*, number 13 in ISSI Scientific Report, pages 67–138, doi 10.1007/978–1–4614–6384–9_3. Springer Science+Business Media.

Bzowski, M., Strumik, M., Kowalska-Leszczynska, I., and Wawrzaszek, R. (2019). Spectral sensitivity and the collimator transmission for GLOWS. Expected count rates from the helioglow and extraheliospheric sources. Technical Report TBD, GLOWS Science Team, CBK PAN, Warsaw, Poland.

Bzowski, M., Strumik, M., Kowalska-Leszczynska, I., and Wawrzaszek, R. (2021). Spectral sensitivity and the collimator transmission for GLOWS. Expected count rates from the helioglow and extraheliospheric sources. Technical Report GLOWS-CBK-RP-2020-12-16-041-v3.3, GLOWS Science Team, CBK PAN, Warsaw, Poland.

Bzowski, M., Strumik, M., Kowalska-Leszczynska, I., and Wawrzaszek, R. (2022). Spectral sensitivity and the collimator transmission for GLOWS. Expected count rates from the helioglow and extraheliospheric sources. Technical report, GLOWS Science Team, CBK PAN, Warsaw, Poland.

Kaźmierczak, P., Strumik, M., and Wawrzaszek, R. (2021). Baffle design process. Technical Report GLOWS-BaffleReport:v5.0, GLOWS Science Team, CBK PAN, Warsaw, Poland.

Kowalska-Leszczynska, I., Bzowski, M., Kubiak, M. A., and Sokół, J. M. (2020). Update od the solar lyα profile line model. *ApJS*, 247:62.

Kowalska-Leszczynska, I., Bzowski, M., Kubiak, M. A., and Strumik, M. (2021). Expected evolution of the GLOWS signal during a year and solar activity cycle. Technical Report GLOWS-CBK-RP-2020-12-07-038-v1.2, GLOWS Science Team, CBK PAN, Warsaw, Poland.

Kowalski, T. (2020). GLOWS mechanical interface control drawing. Technical Report GLOWS-CBK-DWG-2020-08-25-019-v4.6, GLOWS Science Team, CBK PAN, Warsaw, Poland.

Kubiak, M. A., Bzowski, M., Kowalska-Leszczynska, I., and Strumik, M. (2021). WawHelioGlow: a model of the heliospheric backscatter glow. I. Model definition. *ApJS*, 254:16.

Le Chat, G., Issautier, K., and Meyer-Vernet, N. (2012). The solar wind energy flux. *SoPh*, 279:197–205.

McComas, D., Christian, E., Schwadron, N., Fox, N., Westlake, J., Allegrini, F., Baker, D., Biesecker, D., Bzowski, M., Clark, G., Cohen, C., Cohen, I., Dayeh, A., Decker, R., de Nolfo, G., Desai, M., andH.A. Elliott, R. E., Fahr, H., Frisch, P., Funsten, H., Fuselier, S., Galli, A., Galvin, A., Giacalone, J., Gkioulidou, M., Guo, F., Horanyi, M., Isenberg, P., Janzen, P., Kistler, L., Korreck, K., Kubiak, M. A., Kucharek, H., Larsen, B., Leske, R., Lugaz, N., Luhmann, J., Matthaeus, W., Mitchel, D., Moebius, E., Ogasawara, K., Reisenfeld, D., Richardson, J., Russell, C., Sokół, J., Spence, H., Skoug, R., Sternovsky, Z., Swaczyna, P., Szalay, J., Tokumaru, M., andP. Wurz, M. W., Zank, G., and Zirnstein, E. (2018). Interstellar Mapping and Acceleration Probe (IMAP): A new NASA mission. *SSRv*, 214:116.

McComas, D. J., Allegrini, F., Baldonado, J., Blake, B., Brandt, P. C., Burch, J., Clemmons, J., Crain, W., Delapp, D., Demajistre, R., Everett, D., Fahr, H., Friesen, L., Funsten, H., Goldstein, J., Gruntman, M., Harbaugh, R., Harper, R., Henkel, H., Holmlund, C., Lay, G., Mabry, D., Mitchell, D., Nass, U., Pollock, C., Pope, S., Reno, M., Ritzau, S., Roelof, E., Scime, E., Sivjee, M., Skoug, R., Sotirelis, T. S., Thomsen, M., Urdiales, C., Valek, P., Viherkanto, K., Weidner, S., Ylikorpi, T., Young, M., and Zoennchen, J. (2009). The Two Wide-angle Imaging Neutral-atom Spectrometers (TWINS) NASA mission-of-opportunity. *SSRv*, 142(1–4):157–231.

McComas, D. J., Barraclough, B. L., Funsten, H. O., Gosling, J. T., Santiago-Munoz, Goldstein, B. E., Neugebauer, M., Riley, P., and Balogh, A. (2000). Solar wind observations over Ulysses first full polar orbit. *J. Geophys. Res.*, 105:10419–10433.

Nass, H. U., Zoennchen, J. H., Lay, G., and Fahr, H.-J. (2006). The TWINS-LAD mission: Observations of terrestrial Lyman-α fluxes. *ASTRA*, 2:27–31.

Porowski, C. and Bzowski, M. (2024). WawHelioIonMP: A semiempirical tool for the determination of latitudinal variation in the ionization rate of interstellar hydrogen and the solar wind. *ApJ*, 967:57.

Porowski, C., Bzowski, M., and Tokumaru, M. (2022). A new 3D solar wind speed and density model based on interplanetary scintillation. *ApJS*, 259:2.

Porowski, C., Bzowski, M., and Tokumaru, M. (2023). On the general correlation between 3D solar wind speed and density model and solar proxies. *ApJS*, 264:11.

Sokół, J. M., McComas, D. J., Bzowski, M., and Tokumaru, M. (2020). Sun-Heliosphere Observation-based Ionization Rates Model. *ApJ*, 897:179.

Strumik, M. (2018). Mathematics for transformation between spin angle and ecliptic coordinates. Technical report, GLOWS Science Team, CBK PAN, Warsaw, Poland.

Strumik, M. (2020a). Contribution from unresolved point sources for GLOWS. Technical Report GLOWS-CBK-TN-2020-09-30-028-v1.0, GLOWS Science Team, CBK PAN, Warsaw, Poland.

Strumik, M. (2020b). Zemax-simulation-based point spread function for modeling point-source contribution to the IMAP/GLOWS measurements. Technical Report GLOWS-CBK-TN-2020-09-30-027-v1.0, GLOWS Science Team, CBK PAN, Warsaw, Poland.

Strumik, M., Bzowski, M., Kowalska-Leszczynska, I., and Kubiak, M. A. (2020). Inferring contributions from unresolved point sources to diffuse emissions measured in UV sky surveys: General method and SOHO/SWAN case study. *ApJ*, 899(1):48.

Swaczyna, P., Bzowski, M., and Kubiak, M. A. (2025). Production and loss processes of hydrogen energetic neutral atoms in the heliosphere from 5 ev–500 keV. *ApJS*, 277(1):17.

Tapping, K. F. (2013). The 10.7 cm solar radio flux ($f_{10.7}$). *Space Weather*, 11:1–13.

Change log

References to numbered items (sections, equations etc.) are made using the numbers from the version being modified.

July 25, 2025 [MS]
This completes Version 4.4.7

1. TBDs and TBCs addressed and/or removed in Section 3
2. Section 3.13 added with the description of the first "official" Level-0 data set for validation of SDC data products

4.7.1 Validation

4.8 Error Estimation

4.9 Quality Flags

IMAP/CMAD 5

Data Accessibility and Usage

5.1 IMAP Guidelines for Data Usage

The terms for distribution and use of the IMAP data products are specified in the NASA Heliophysics Science Data Management Policy document, and are summarized here in terms of the IMAP mission. These guidelines govern both the production and distribution of scientific data sets by the IMAP program, and also use of the IMAP data by the science community and general public, and are summarized below.

- IMAP data products are open to all scientists and the public (Users).
- There are no proprietary periods associated with any of the validated IMAP data products.
- Users shall have timely access to the scientifically useful data and analysis tools that are equivalent to the level that the IMAP science working team uses.
- Users should contact the IMAP Principal Investigator (PI) and the relevant IMAP instrument leads and co-investigators early in an analysis project to consult on the appropriate use of instrument data or model results.
- Users who wish to publish results derived from IMAP data should directly involve the IMAP PI and/or Instrument Leads and team members as appropriate in the analysis and are encouraged to offer co-authorship. Co-authorship may be declined.
- Users should heed the caveats of investigators as to the interpretation and limitations of data or model results. Important caveats should be included in the publication, even if co-authorship is declined. Data and model version numbers should also be specified, ideally pointing to a specific Digital Object Identifier (DOI) for ease of citation.
- Users should acknowledge the sources of data used in all publications, presentations, and reports using an appropriate DOI. Appropriate acknowledgement to institutions, personnel, and funding agencies should be given.
- Users should provide the IMAP PI and instrument lead Co-Is a copy of each manuscript that uses IMAP data upon submission of that manuscript for consideration of publication. Upon publication, the citation should be transmitted to the PI and any other providers of data.
- Users should widely distribute, to interested parties, their conference abstracts, presentations, and publications.
- Users should make tools of general utility and/or value-added data products widely available to the community, and to notify the IMAP PI of such utilities or products, having clearly labeled the product as being different from an original IMAP produced data product.

5.1.1 Participation and Authorship on Papers

Invitations for authorship should err on the side of being too inclusive instead of not inclusive enough, especially earlier in the mission. At a minimum, all IMAP team member-led papers should *invite* the Science Leadership Team, relevant Theme Team lead(s), and instrument lead(s) for any instruments' data used. Further, to ensure accurate use of CAVA, papers using significant CAVA-generated analysis should consider inviting the CAVA science lead, Jamey Szalay. Lead authors should also generally consider inviting one of more theory team members in order to see if/how they can contribute and strengthen the study.

All coauthors must participate in, review, comment on, try to help improve, and generally agree with the results of the paper; this is done by positively responding to the lead author's request(s). If no (or an inadequate) reply is received from a potential author by the date requested by the lead author, they will be removed from the author list, and the paper should be submitted without them.

5.1.2 Coordination of Science Topics Across the IMAP Team

The three Theme Teams help brainstorm and develop ideas for crosscutting science on IMAP, but do not manage who leads which studies and papers. Instead, once initially developed, ideas/proposals for topics should be sent to Dave and Matina, who will update and maintain the overall science project/paper list, They, with help from the others in the Science Leadership Team, will also manage deconflicting topics as

needed. Team members are only be able to "reserve" one topic at a time and need to make good progress and to publish in a timely manner in order to retain priority on that topic.

Early career participants (students, postdocs, etc.) are a very important part of the IMAP team, but each must be sponsored by a senior Co-I or Instrument lead, who is then responsible for overseeing them and ensuring that their efforts and use of data are fully consistent with these team guidelines. The Science Leadership Team must sign off on such participant data access and studies.

5.1.3 Coordination of IMAP Data Sharing with Outside Collaborators

Data sharing outside the IMAP team is strongly discouraged before the data has been internally validated. Any scientific use or publication of IMAP data (including non-public I-ALiRT data) by people outside the IMAP team must be OK'ed by and coordinated through the Science Leadership Team, who will work with Theme Team leads, instrument leads, and others as needed to identify IMAP science participants and coauthors.

5.2 Data Access

IMAP data are available at the IMAP Science Data Center website:
https://imap-mission.com/

5.3 Data Processing Software

IMAP's library of data processing software is available at this Zenodo repository:
https://zenodo.org/records/23574248

5.4 Data Usage Guidelines and Caveats

5.4.1 Summary of Latest Release

IMAP 01-Nov-2026 Release Notes Summary

Compiled by: Jonathan Niehof, 27-Oct-2026

imap_codice_l3a_hi-direct-events
Major version 2, Oct. 8, 2026 - Add incident_ion_energy and use to calculate estimated_mass.

imap_glows_l2_hist
Major version 2, Oct. 8, 2026 - Use corrected spin tables and SPICE kernels for spin axis and spin phase.

imap_glows_l3a_hist
Major version 2, Oct 8, 2026 - Pad `spin_angle` dimension to 90. Use corrected SPICE kernels for spin axis and spin phase.

imap_glows_l3b_ion-rate-profile
Major version 2: Use CR midpoint as `epoch` and a single `epoch_delta` variable instead of `epoch_delta_minus`/`epoch_delta_plus`. Add new `mean_time` variable. Remove `lat_grid_delta` to support plotting. Pad `used_l3a` to 50 entries.

imap_glows_l3c_sw-profile
Major version 2: Use CR midpoint as `epoch` and a single `epoch_delta` variable instead of `epoch_delta_minus`/`epoch_delta_plus`. Add new `mean_time` variable. Remove `lat_grid_delta` to support plotting.

imap_glows_l3d_solar-hist
Major version 2: Add quality flag to indicate CRs beyond the last L3b CR, which are filled with copies of the last valid data.

imap_glows_l3e_survival-probability-hi-45
Major version 2, Oct. 8, 2026 - Add `epoch_delta`, `energy_delta_plus`, and `energy_delta_minus` to support plotting. Add quality flags for L3d data copied from a previous CR and the use of predicted ephemeris. Quality flags are propagated from the nearest two L3d data points. Use corrected SPICE kernels for spin axis and spin phase.

imap_glows_l3e_survival-probability-hi-90
Major version 2, Oct. 8, 2026 - Add `epoch_delta`, `energy_delta_plus`, and `energy_delta_minus` to support plotting. Add quality flags for L3d data copied from a previous CR and the use of predicted ephemeris. Quality flags are propagated from the nearest two L3d data points. Use corrected SPICE kernels for spin axis and spin phase.

imap_glows_l3e_survival-probability-lo
Major version 2, Oct. 8, 2026 - Add `epoch_delta`, `energy_delta_plus`, and `energy_delta_minus` to support plotting. Add quality flags for L3d data copied from a previous CR and the use of predicted ephemeris. Quality flags are propagated from the nearest two L3d data points. Use corrected SPICE kernels for spin axis and spin phase.

imap_glows_l3e_survival-probability-ul-hf
Major version 2, Oct. 8, 2026 - Add `epoch_delta`, `energy_delta_plus`, and `energy_delta_minus` to support plotting. Add quality flags for L3d data copied from a previous CR and the use of predicted ephemeris. Quality flags are propagated from the nearest two L3d data points. Use corrected SPICE kernels for spin axis and spin phase.

imap_glows_l3e_survival-probability-ul-sf
Major version 2, Oct. 8, 2026 - Add `epoch_delta`, `energy_delta_plus`, and `energy_delta_minus` to support plotting. Add quality flags for L3d data copied from a previous CR and the use of predicted ephemeris. Quality flags are propagated from the nearest two L3d data points. Use corrected SPICE kernels for spin axis and spin phase.

imap_idex_l2a_sci-10days
Major version 2, Sept. 14, 2026 - Propagates the new event and saturation flags and uses them to suppress invalid impact charges, velocities, and masses for saturated or non-science events. Ion-grid velocity is now estimated from the ion-grid-to-target charge ratio, with mass derived from the selected target charge. Inherits the corrected IDEX-frame spin phase.
Major version 3, Oct. 8, 2026 - Use corrected spin tables and SPICE kernels for spin axis and spin phase.

imap_mag_l2_burst-dsrf
Major version 2, Oct. 8, 2026 - Use corrected spin tables and SPICE kernels for spin axis and spin phase.

imap_mag_l2_burst-gse
Major version 2, Oct. 8, 2026 - Use corrected spin tables and SPICE kernels for spin axis and spin phase.

imap_mag_l2_burst-gsm
Major version 2, Oct. 8, 2026 - Use corrected spin tables and SPICE kernels for spin axis and spin phase.

imap_mag_l2_burst-rtn
Major version 2, Oct. 8, 2026 - Use corrected spin tables and SPICE kernels for spin axis and spin phase.

imap_mag_l2_burst-srf
Major version 2, Oct. 8, 2026 - Use corrected spin tables and SPICE kernels for spin axis and spin phase.

imap_mag_l2_norm-dsrf
Major version 2, Oct. 8, 2026 - Use corrected spin tables and SPICE kernels for spin axis and spin phase.

imap_mag_l2_norm-gse
Major version 2, Oct. 8, 2026 - Use corrected spin tables and SPICE kernels for spin axis and spin phase.

imap_mag_l2_norm-gsm
Major version 2, Oct. 8, 2026 - Use corrected spin tables and SPICE kernels for spin axis and spin phase.

imap_mag_l2_norm-rtn
Major version 2, Oct. 8, 2026 - Use corrected spin tables and SPICE kernels for spin axis and spin phase.

imap_mag_l2_norm-srf
Major version 2, Oct. 8, 2026 - Use corrected spin tables and SPICE kernels for spin axis and spin phase.

imap_swapi_l3a_alpha-sw
Major version 2, Oct. 8, 2026 - Use corrected SPICE kernels for spin axis and spin phase.

imap_swapi_l3a_proton-sw
Major version 2, Oct. 8, 2026 - Use corrected SPICE kernels for spin axis and spin phase.

imap_swe_l2_sci
Major version 2, Oct. 8, 2026 - Use corrected spin tables and SPICE kernels for spin axis and spin phase.

imap_swe_l3_sci
Major version 2, Oct. 8, 2026 - Use corrected SPICE kernels for spin axis and spin phase.

5.4.2 SWAPI

SWAPI Data Usage Guidelines and Caveats for the Preliminary Data Release

IMAP SWAPI Data Release Notes:

L1/L2 data:

- *The data quality flags for L1 and L2 are named as swp_l1a_flags. It is actually L1 data quality flags and should be named as swp_l1_flags. This is a typo and will be updated in the future data release. swp_l1a_flags = 0 means the data is good.*

L3a Data:

Solar Wind Protons:

- The solar wind proton speed is lower by ~17 km/s (~3-4%) compared to other L1 spacecraft measurements (e.g., WIND, ACE, and DISCOVER). An investigation is underway to resolve this discrepancy, and the results will be included in the next data release.
- SWAPI makes 1D measurements but attempts to derive the solar wind bulk flow vector through forward modeling, using spacecraft spin. Most of the time, it succeeds in determining the bulk flow vector. However, at times, the transverse components of the bulk flow vector are flipped due to a local minimum in the solution space. A list of dates for these cases is included in the ***list of odd times for L3a data products***. This issue may be resolved through algorithm improvements in future releases.
- The transverse components of the bulk velocity are offset compared to WIND by ~1 degree. Currently, there is a known ~55 ms offset in the spacecraft spin period that is not yet reflected in the SPICE kernels used for forward modeling. The ~55 ms offset corresponds to a ~1.3-degree rotation given IMAP's ~15 s spin phase, so it is quite likely that this offset will be resolved in the next release.
- SWAPI's temperature is ~20% lower than WIND's scalar temperature. An investigation is underway about this discrepancy and may be resolved in the future.
- The solar wind proton data product is flagged when the temperature is > 500,000 K. This is especially the case when the solar wind is hot enough to go through the open aperture, e.g., downstream of the shock. This issue will be fixed in the second data release.
- The solar wind proton density is lower by ~20% on average compared to WIND. This is within ~20% uncertainty of the lab measurements used to normalize SWAPI's instrument response. The uncertainty may be reduced in the future using sophisticated modeling of the instrument.

Solar Wind Alphas:

- The alpha bulk speed is ~2.5% lower on average compared to WIND. Investigation is underway to resolve this discrepancy.
- The alpha temperature is ~20% lower on average compared to WIND's scalar temperature.

- The alpha/proton ratio is ~20% higher on average compared to WIND. This is within the >20% uncertainty of the lab measurements used to normalize SWAPI's instrument response. The uncertainty is ~20% near ~1 keV/q, and greater at other energies.
- The transverse components of the bulk velocity vector are affected by the same caveats that apply to the proton bulk velocity vector.
- The alpha peak finding algorithm may sometimes mistake a high-energy secondary proton distribution for the alphas. The user should keep an eye out for sudden drops in alpha density or increases in alpha temperature.
- The solar wind alpha products have dependencies on the MAG L2 data. Therefore, alpha data products are missing when there is no MAG L2 data.

L3b data:

The combined differential flux provided in L3B includes both protons and alphas. The same geometric factor is used for both: the flux is simply the coincidence rate divided by the geometric factor. The derived flux may be too large by 5% for alphas and interstellar pickup helium, since the geometric factor is larger for alphas by 5% in the high-energy limit.

The geometric factor is for an isotropic distribution. Thus, one may denote the reported flux J_{hot}. For an anisotropic distribution, J_{hot} represents a weighted average of the differential flux, weighted by the instrument response. If what one desires is $J_{4\pi}$, the average of the flux over solid angles for energy E, defined by

$$J_{4\pi}(E) \equiv \frac{1}{4\pi}\int_{\Omega} \mathrm{d}\,\hat{\omega}\, J(E,\hat{\omega}) = \frac{1}{4\pi}\int_0^{2\pi} \mathrm{d}\,\phi \int_0^{\pi} \mathrm{d}\,\theta\, \sin\theta \cdot J(E,\theta,\phi).$$

Then for cold plasma, such as the solar wind populations, $J_{\text{hot}} \ll J_{4\pi}$. The instrument response itself is highly anisotropic because SWAPI's sunglasses attenuate the solar wind by a factor of 10^3. Furthermore, SWAPI's angular field of view of 1.34 sr must be accounted for.

When the temperature is high enough that the distribution is wide compared to the energy resolution but still low enough that the population is fully contained within the sunglasses, a good approximation to $J_{4\pi}$ is

$$J_{4\pi} \approx J_{\text{cold}} \equiv \frac{1.34}{4\pi} \cdot 10^3 \cdot J_{\text{hot}}.$$

If one has an isotropic model phase space distribution in the solar wind frame, $f(\| \boldsymbol{v} - \boldsymbol{v}_{\text{sw}} \|)$ (where $\boldsymbol{v}_{\text{sw}}$ is the bulk velocity vector and $\boldsymbol{v}$ is an arbitrary velocity vector in the instrument frame), then they may relate it to J_{cold} by integrating over solid angles in the spacecraft frame:

$$\frac{m^2}{2E} J_{\text{cold}} \approx \frac{1}{4\pi}\int_{\Omega} \mathrm{d}\,\hat{\omega}\, f(\| \boldsymbol{v}(E,\hat{\omega}) - \boldsymbol{v}_{\text{sw}} \|).$$

Note that when the temperature is sufficiently high, a substantial fraction of the distribution may bypass the sunglasses. This is typically the case downstream of shocks. In such cases, $J_{4\pi}$ lies somewhere between J_{cold} and J_{hot}, and forward modeling with the instrument response is required to compare the model to the observations.

- **List of odd times for L3a data products** that are not reliable:
  - Solar wind protons:
    - Data with very low solar wind proton temperature are unreliable (T < 11,604 K (~1 eV)):
      - Nov 13
      - Jan 20.
    - Data with strange **oscillations on $\boldsymbol{u_T}$, $\boldsymbol{u_N}$**:
      - Nov 16, 24, 25, 26
      - Dec 04, 06, 07, 9, 17, 22, 23, 24, 27
      - Jan 01, 02, 03, 17, 28, 29
      - Feb 04, 15, 22, 24, 25
      - Mar 09, 12, 14, 23
      - Apr 02, 03, 05, 20, 30
    - The solar wind proton peak count rate is less than the alpha peak count rate for Apr 30, and the data is not reliable
  - Solar wind alphas:
    - Data with very low solar wind alpha temperature are unreliable (T < 4*11,604 K (~4 eV)):
      - Nov 10, 11, 12, 13, 18, 19
      - Dec 03, 10
      - Jan 20, 22
      - Mar 20, 21, 22
    - Data with a rapid change in alpha density, likely due to a fitting convergence issue:
      - Nov 17, 22, 24, 25
      - Dec 04, 13, 15, 16
      - Jan 03, 12, 13, 16, 17, 22, 26, 27
      - Feb 05, 06, 07, 14, 15, 22, 23
      - Mar 03, 07, 11, 14, 29
      - Apr 02, 04, 20
  - Interstellar He^+ PUIs: All the data (not going to be released for the first data release)

Description of the L3a Data flags:

Flag / Bit Definition	Variable	Description
BAD_FIT 2 ** 2 (bit 2)	swp_flags (epoch)	The fit converged but is an inaccurate representation of the data ($R^2 < 0.9$). For protons, also set if the fitted temperature exceeds 500,000 K.
FIT_ERROR 2 ** 3 (bit 3)	swp_flags (epoch)	An error occurred during the fitting process, or the fit failed to converge.
PRELIMINARY_MAG 2 ** 4 (bit 4)	swp_flags (epoch)	MAG L2 was unavailable, so MAG L1D was used instead.

Caveats for L3b:

- The energy in this data product is different from that in L2 data products.

IMAP SWAPI Data Release 2 Notes:

L1/L2 data:

- *The data quality flags for L1 and L2 are named as swp_l1a_flags. It is actually L1 data quality flags and should be named as swp_l1_flags. This is a typo and will be updated in the future data release. swp_l1a_flags = 0 means the data is good.*

L3a Data:

Solar Wind Protons:

- The solar wind proton speed is lower by ~17 km/s (~3-4%) compared to other L1 spacecraft measurements (e.g., Wind, ACE, and DISCOVER). An investigation is underway to resolve this discrepancy, and the results will be included in the next data release.
- SWAPI makes 1D measurements but attempts to derive the solar wind bulk flow vector through forward modeling, using spacecraft spin. Most of the time, it succeeds in determining the bulk flow vector. However, at times, the transverse components of the bulk flow vector are flipped due to a local minimum in the solution space. A list of dates for these cases is included in the ***list of odd times for L3a data products***. This issue may be resolved through algorithm improvements in future releases.
- SWAPI data show that the spin phase has been corrected within error (average rotation about the Sun-Earth line decreased from $0.84 \pm 0.35°$ to $-0.1 \pm 0.35°$). The average rotation angle between SWAPI and Wind flow vectors changed from $1.7 \pm 0.18°$ to $1.25 \pm 0.07°$. It is not yet clear whether the remaining ~1.25° deviation is due to residual error in the SPICE kernels, a systematic error of order of ~1° in the Wind dataset, or error introduced by the model assumptions in our fitting procedure. The details are still under investigation.
- SWAPI's temperature is ~20% lower than Wind's scalar temperature. An investigation is underway about this discrepancy and may be resolved in the future.
- The solar wind proton data product is flagged when the temperature is > 500,000 K. This is especially the case when the solar wind is hot enough to go through the open aperture, e.g., downstream of the shock. This issue will be fixed in the second data release.
- The solar wind proton density is lower by ~20% on average compared to Wind. This is within ~20% uncertainty of the lab measurements used to normalize SWAPI's instrument response. The uncertainty may be reduced in the future using sophisticated modeling of the instrument.

Solar Wind Alphas:

- The alpha bulk speed is ~2.5% lower on average compared to Wind. Investigation is underway to resolve this discrepancy.
- The alpha temperature is ~20% lower on average compared to Wind's scalar temperature.

- The alpha/proton ratio is ~20% higher on average compared to Wind. This is within the >20% uncertainty of the lab measurements used to normalize SWAPI's instrument response. The uncertainty is ~20% near ~1 keV/q, and greater at other energies.

The transverse components of the bulk velocity vector are affected by the same caveats that apply to the proton bulk velocity vector.

Interstellar He^+ PUIs:

- The density and temperature of the interstellar He^+ PUIs are obtained by fitting an isotropic filled shell distribution (Vasyliunas & Siscoe, 1986) model to 10-minute averaged data. The model has only two free parameters: cutoff speed and ionization rate.
- We use a constant background rate of 0.1 Hz for all energy bins, based on the final calibration data taken in the lab and background measurements taken during commissioning of the flight instrument following high-voltage turn-on.
- The background rate in our data product is obtained by fitting filled-shell distribution with ionization rate as free parameter and represents the combination of photoionization, electron impact ionization and charge exchange.

L3b data:

The combined differential flux provided in L3B includes both protons and alphas. The same geometric factor is used for both: the flux is simply the coincidence rate divided by the geometric factor. The derived flux may be too large by 5% for alphas and interstellar pickup helium, since the geometric factor is larger for alphas by 5% in the high-energy limit.

The geometric factor is for an isotropic distribution. Thus, one may denote the reported flux J_{hot}. For an anisotropic distribution, J_{hot} represents a weighted average of the differential flux, weighted by the instrument response. If what one desires is $J_{4\pi}$, the average of the flux over solid angles for energy E, defined by

$$J_{4\pi}(E) \equiv \frac{1}{4\pi}\int_{\Omega} \mathrm{d}\,\widehat{\omega}\, J(E,\widehat{\omega}) = \frac{1}{4\pi}\int_0^{2\pi} \mathrm{d}\,\phi \int_0^{\pi} \mathrm{d}\,\theta\,\sin\theta \cdot J(E,\theta,\phi).$$

Then for cold plasma, such as the solar wind populations, $J_{\text{hot}} \ll J_{4\pi}$. The instrument response itself is highly anisotropic because SWAPI's sunglasses attenuate the solar wind by a factor of 10^3. Furthermore, SWAPI's angular field of view of 1.34 sr must be accounted for.

When the temperature is high enough that the distribution is wide compared to the energy resolution but still low enough that the population is fully contained within the sunglasses, a good approximation to $J_{4\pi}$ is

$$J_{4\pi} \approx J_{\text{cold}} \equiv \frac{1.34}{4\pi} \cdot 10^3 \cdot J_{\text{hot}}.$$

If one has an isotropic model phase space distribution in the solar wind frame, $f(\| \boldsymbol{v} - \boldsymbol{v}_{\rm sw} \|)$ (where $\boldsymbol{v}_{\rm sw}$ is the bulk velocity vector and $\boldsymbol{v}$ is an arbitrary velocity vector in the instrument frame), then they may relate it to $J_{\rm cold}$ by integrating over solid angles in the spacecraft frame:

$$\frac{m^2}{2E} J_{\rm cold} \approx \frac{1}{4\pi} \int_{\Omega} \mathrm{d}\,\hat{\omega}\, f(\| \boldsymbol{v}(E, \hat{\omega}) - \boldsymbol{v}_{\rm sw} \|).$$

Note that when the temperature is sufficiently high, a substantial fraction of the distribution may bypass the sunglasses. This is typically the case downstream of shocks. In such cases, $J_{4\pi}$ lies somewhere between $J_{\rm cold}$ and $J_{\rm hot}$, and forward modeling with the instrument response is required to compare the model to the observations.

- **List of odd times for L3a data products** that are not reliable:
  - Solar wind protons:
    - Data with very low solar wind proton temperature are unreliable (T < 11,604 K (~1 eV)):
      - Nov 13
      - Jan 20
      - June 01
    - Data with strange **oscillations on $\boldsymbol{u_T}$, $\boldsymbol{u_N}$**:
      - Nov 16, 24, 25, 26
      - Dec 04, 06, 07, 9, 17, 22, 23, 24, 27
      - Jan 01, 02, 03, 17, 28, 29
      - Feb 04, 15, 22, 24, 25
      - Mar 09, 12, 14, 23
      - Apr 02, 03, 05, 20, 30
      - May 15, 16
      - June 12, 25
      - July 10, 23
    - The solar wind proton peak count rate is less than the alpha peak count rate for Apr 30, and the data is not reliable
  - Solar wind alphas:
    - Data with very low solar wind alpha temperature are unreliable (T < 4*11,604 K (~4 eV)):
      - Nov 10, 11, 12, 13, 18, 19
      - Dec 03
      - Jan 20, 22
      - Mar 20, 21
      - July 04, 05, 13, 28

        - Data with a rapid change in alpha density, likely due to a fitting convergence issue:
            - Nov 17, 22, 24, 25
            - Dec 04, 13, 15,16
            - Jan 03, 12, 13, 16, 17, 22, 26
            - Feb 05, 06, 07, 14, 15, 23
            - Mar 03, 07, 11, 14, 29
            - Apr 02, 04, 26
            - May 01, 07, 16
            - June 04, 17, 30
            - July 06.
    - Interstellar He^{+} PUIs: None

Description of the L3a Data flags:

Flag / Bit Definition	Variable	Description
BAD_FIT 2 ** 2 (bit 2)	swp_flags (epoch)	The fit converged but is an inaccurate representation of the data ($R^2 < 0.9$). For protons, also set if the fitted temperature exceeds 500,000 K.
FIT_ERROR 2 ** 3 (bit 3)	swp_flags (epoch)	An error occurred during the fitting process, or the fit failed to converge.
PRELIMINARY_MAG 2 ** 4 (bit 4)	swp_flags (epoch)	MAG L2 was unavailable, so MAG L1D was used instead.

Caveats for L3b:

- The energy in this data product is different from that in L2 data products.

5.4.3 CoDICE

CoDICE Data Usage Guidelines and Caveats for the 01-Nov-2026 Data Release

1. CoDICE Data Usage Guidelines and Caveats

This document describes the CoDICE operation timeline, changes, and caveats associated with each of the released CoDICE data products. In general, when using CoDICE data, please reach out to the instrument team with any questions/concerns and to ensure that the data will be used and interpreted correctly.

2. Instrument Operation Timeline and Changes

Reduced Geometric Factor Operation (RGFO) Mode

Launch Configuration: In the reduced geometric factor operation (RGFO) mode, the ratio of voltages applied to the upper and lower portion of the CoDICE ESA is reduced (normally the ratio is 1). This reduces the number of ions that can pass through the ESA section, thereby reducing the count rate on the Lo MCPs. In the launch-configuration operation of the instrument, the flight software (FSW) monitors the total counts measured by the START-A and START-B MCP over the course of a half-spin of the spacecraft (~7.5 s). If these total counts surpass a limit (tunable via onboard lookup table, LUTs), then the instrument enters RGFO mode on the next half-spin and remains in RGFO until either no-scan operation (NSO) mode is triggered or the end of the current 32 half-spin cycle. Changes to the RGFO implementation that occurred throughout commissioning are described in the table below. Note: a full ESA scan involves 32 half-spin cycle and lasts for 4 minutes.

Current Configuration: On 01/29/2026 the onboard FSW was updated with important changes to the RGFO mode. In this updated (and current) configuration, the FSW monitors the MCP count rates during each individual ESA step and spin sector measurement. If the measured count rate exceeds the updated count rate threshold, then the instrument switches to RGFO mode on the following ESA step and spin sector pair.

No-Scan Operation (NSO) Mode

Launch Configuration: In NSO mode, the ESA voltage is set to the highest value (esa step 0, ~81 keV/e) and remains at that value until the end of the current 32 half-spin cycle. In the launch configuration operation of the instrument, NSO can only be triggered while the instrument is in RGFO mode. To trigger NSO, the FSW monitors the total counts measured by the START-A and START-B MCP over the course of a half-spin. If these total counts surpass a limit (tunable via onboard LUTs), then the instrument enters NSO mode on the next half-spin and remains in NSO mode until the end of the current 32 half-spin cycle. Changes to the NSO implementation that occurred throughout commissioning are described in the table below.

Current Configuration: On 01/29/2026 the onboard FSW was updated with the same changes that were made to the RGFO mode. In this updated (and current) configuration, the FSW monitors the MCP count rates during each individual ESA step and spin sector measurement. If the measured count rate exceeds the updated count rate threshold, then the instrument switches to NSO mode on the following ESA step and spin sector pair.

Table 1. Summary of CoDICE operational changes since launch.

Period Number	Date Range	Description of Instrument Operation
P0	Launch - 11/24/2025	- RGFO triggers on total counts accumulated over half spin. If limit is surpassed, instrument enters RGFO mode on next half spin - When in RGFO mode, NSO triggers on total counts accumulated over half spin. If limit is surpassed, instrument enters NSO mode on next half spin
P1	11/24/2025 – 12/18/2025	- RGFO limit is reduced so that RGFO always triggers on half spin 0. However, ESA voltage ratio remains 1 so that the instrument does not actually operate with reduced G-factor. - NSO mode still triggers on half spin boundaries.
P2	12/18/2025 – 01/29/2026	- ESA sweep table is updated so that only 3 ESA steps are sampled per half-spin starting at ESA step 80 (576 V, 3.3 keV/e) - RGFO and NSO implementation is the same as during P1
P3	01/29/2026 – 04/03/2026	Flight Software (FSW) Update: - RGFO and NSO now trigger based on count rates measured during a single ESA step and spin sector. Trigger is based on count rate rather than total counts. Count rates are monitored at each ESA step and spin sector pair and mode switch is implemented during the following ESA step spin sector pair o Additional fields added to all COUNTS and PHA science packets: ▪ RGFO half-spin (already in COUNTS packets, only added to PHA) ▪ RGFO spin-sector ▪ RGFO e-step ▪ NSO half-spin (already in COUNTS packets, only added to PHA) ▪ NSO spin-sector ▪ NSO e-step - Hi/Lo Priority Counts packets are no longer lossy-compressed (lossless only) - Swapped Fe highQ/lowQ labels o Affects: ▪ View 0: Lo – IALiRT (label swap)

		▪ View 5: Lo – SW Species Counts (label swap) ▪ View 7: Lo – SW Angular Counts (changed selected species) • Data prior to the v1.5 FSW load were sending Species 13 (SW – Fe highQ, but was labeled as Fe lowQ) • Data after the v1.5 FSW load will send Species 14 (SW – Fe lowQ) - Enabled 2 additional species for Lo Angular Counts: o SW – He+ (View 7, ApID 0x486) o NSW – He+ (View 8, ApID 0x487) - Increased PHA allocation o Lo: 5,760 -> 11,520 events per cycle o Hi: 5,000 -> 10,000 events per cycle - Updated Hi Priority Scheme o P5 = Heavies, P4 = Helium, P3 = Protons.
P4	04/03/2026 – 09/16/2026	- Lo SCI_LUT update o Fixed indexing issue that resulted in species rates being assigned to the wrong rate box. - Lo onboard species classification LUT update o Refined mass boundaries for key species o Binned H+ data now consists of TCRs only (was DCRs during P0 – P3) - Hi onboard species classification LUT update o Corrected bug that was sending low tof events to low priority
P5	09/16/2026 – Current*	- Lo onboard species classification LUT update o Refined mass boundaries for C, O and Fe species - Hi onboard species classification LUT update o Updated mid-gain energy conversion used for onboard binning o Updated energy conversion for SSD 11 high-gain events o Optimized species classification boundaries for priority, omni, and sectored data

*Current in reference to the date of this document publication. Check with instrument team for real-time updates.

Gain Tests

The CoDICE instrument executes monthly gain tests (every 30 days) to assess the stability of the MCP detection efficiency. Each gain test takes ~4.45 hours to complete. The table below provides the start and approximate end time for each gain test since January 2026 through October 2026. **All science data acquired during these intervals should not be used for analysis.**

Timeline of CoDICE Gain Tests				
Year	**DOY**	**Date**	**Start Time (UTC)**	**End Time (UTC)**
2026	014	01/14	00:00:00	04:30:00
2026	044	02/13	00:00:00	04:30:00
2026	073	03/14	00:00:00	04:30:00
2026	104	04/14	00:00:00	04:30:00
2026	134	05/14	00:00:00	04:30:00
2026	164	06/13	00:00:00	04:30:00
2026	194	07/13	00:00:00	04:30:00
2026	224	08/12	00:00:00	04:30:00
2026	254	09/11	00:00:00	04:30:00
2026	284	10/11	00:00:00	04:30:00

* End times are approximate

3. Updates to Data Product Processing

This section describes updates to the processing code that were made between each data release. Only products that were updated are listed. No major changes were made to products that are not listed.

3.1 Release 1

Data Coverage: *February 1 2026 – April 30 2026*

3.2 Release 2

Data Coverage: *February 1 2026 – July 31 2026*

L3a_lo-direct-events:

- The *normalization* and *normalization_per_event* variables were updated to now include DCR events in the computation. These variables in previous data release versions were computed only using TCR events, which resulted in the computed event normalization value being too high.
- The computation of the *elevation_angle* variable was updated to use *apd_id* rather than the *position* variable. This variable in previous releases is not correct and should not be used.

L3a_hi-direct-events:

- A new variable named *incident_ion_energy* has been added to the data product. This variable provides an estimate of the total energy (MeV) of each event, which is derived from the deposited SSD energy. This variable is then used to compute the *estimated_mass*.
- The *estimated_mass* variable is now computed using *incident_ion_energy* rather than *ssd_energy*. The effect of this change is that the species tracks are now straight in energy-per-nuc vs mass space. Any mass and energy-per-nuc limits used to

select individual ion species events should be updated based on these new mass values.

L3b_lo-3d-vdfs:

- Release 2 includes a new data product consisting of CoDICE Lo intensities as a function of energy-per-charge, spin angle, and elevation angle. This product is formed using the Lo direct events. Further details and caveats are provided in the following section.

4. Data Product Use and Caveats

4.1 Caveats Affecting All Products

- **Spin Phase Offset:** An error related to the start tracker (ST) delay onboard the spacecraft resulted in an error in the reported spin phase of the spacecraft. This introduced an error in all of the computed spin angles for the CoDICE data. The timeline and magnitude of the resulting spin phase errors are described in Table 2 at the end of this section. ***The resulting errors in CoDICE spin angles are not corrected in the second data release and should be considered when using CoDICE data that requires analysis involving the spin angle.***

- **Coordinate System Mismatch:** IMAP is supposed to point 4 degree ahead of the sun, so at the beginning of the day the SC is repointed to 4.5 ahead of the sun and drifts to 3.5 degree ahead of Sun by the end of the day. Since launch, the SC team used inconsistent coordinate systems. The SC Star Tracker uses Ecliptic MOD but the SC was uploading instructions in Ecliptic J2000. This mismatch in coordinate systems, resulted in a 0.4 degree error in IMAP pointing 4.9-3.9 degree ahead of the Sun since launch. The timeline and resulting changes that have been implemented are summarized in Table 2 at the end of this section.

Table 2. Summary of spin phase offset and coordinate mismatches since launch

Dates	Coordinate Mismatch (SC --> Ground)	Coordinate Mismatch (Ground --> SC)	Spin Phase Offset
09/24/2025 - 07/08/2026	~0.4-degree SC-Sun pointing offset in data pipeline; data erroneously showed 3.5 to 4.5 degree SC pointing	~0.4-degree SC-Sun pointing offset; true SC pointing from ~ 3.9 to 4.9 degrees not the planned ~3.5 to 4.5	~1.0 degree offset; 200 ms ST Delay
07/08/2026 - 09/10/2026	SPICE & data pipeline corrected; data shows true 3.9 to 4.9 degree SC pointing	~0.4-degree SC-Sun pointing offset. true SC pointing from ~ 3.9 to 4.9 degrees not the planned ~3.5 to 4.5	~2.3 degree offset; 255 ms ST Delay
09/10/2026 - 09/30/2026	ACS pointing knowledge corrected; data shows true 3.5 to 4.5 degree SC pointing	True SC-Sun pointing of ~3.5 to 4.5 degrees	~2.3 degree offset; 255 ms ST Delay
09/30/2026 +	ACS pointing knowledge corrected; data shows true 3.5 to 4.5 degree SC pointing	True SC-Sun pointing of ~3.5 to 4.5 degrees	~0 degree offset; 157 ms ST Delay

4.2 Specific Data Product Use and Caveats

lo-sw-species:

The l2_lo-sw-species contains intensities measured by the sunward (sw) facing detectors (APDs 1, 2, 3, 23, 24). Counts are binned onboard based on the position determined from the delay-line circuit. These counts are then converted to intensities on ground and provided in 128 energy-per-charge steps.

Caveats and Use:

- These are **not** omni-directional intensities, rather, they represent the intensity of particles coming from the sunward direction.
- The delay-line position is not fully accurate and so a portion of sw counts are assigned non-sunward (nsw) directions. Thus, the intensities are underestimated by ~7 – 10 %. Quantification of the exact percentage is ongoing.
- When a count is measured in sunward APDs but the delay-line position corresponds to the anti-sunward direction, that event is assigned position = 25. All position 25 events are then binned into the sw-species product.
- The current onboard species identification algorithm is not fully optimized to clearly separate charge state species (Oxygen, Carbon, Iron). Thus, the intensities for the different charge state species are only estimates.
- Provided uncertainties correspond to the Poisson uncertainty in counts and are assumed symmetric.
- Onboard look-up-table (LUT) change on 04/03/2026 (P4 in Table 1)
    - Before 04/03/2026, the H+ data includes double coincidence rates (DCRs; i.e., ESA + TOF only). This was changed on 04/03/2026 via an onboard LUT load which changed the onboard binning scheme for the H+ data to only include triple coincidence rates (TCRs). The computed intensity uses DCR or TCR efficiencies for the corresponding dates, however, the DCR efficiency is not as well calibrated and therefor H+ rate/intensity is significantly reduced due to this change.
    - Before 04/03/2026, CNO+ data is not available.
    - Before 04/03/2026, most of the Lo i-ALiRT ratio data is not available. This is corrected in the 04/04 LUT load, and all Lo I-ALiRT data is available since then.

lo-direct-events:

The l2_lo-direct-events contains the measurement information for each event. These events are selected based on their priority level and only a subset of all events is downlinked during intense periods. See VAR_NOTES for the priority levels.

The l3a_lo_direct-events contain all of the variables from the l2 product, with the addition of derived mass and mass-per-charge estimates for each event.

Caveats and Use:

- Do not use events with position = 25
- When binning data, use APD ID to determine the angular direction corresponding to each event. See instrument paper for a description of APD mappings.
- TCR events are identified by type = 0. See VAR_NOTES and CATDESC for other event type definition.
- For the cleanest events (i.e., quadruple coincidence), only include events for which apd_id matches position and where apd_energy > 0.
- The TOF is automatically corrected onboard based on the delay-line position determined for each event. This introduces uncertainty in the TOF value due to the uncertainty in the delay-line position.
- The multi_event flag indicates events for which multiple APD detectors were triggered.
- **Dropped Data Packets:** The spacecraft flight software periodically drops CoDICE data packets from the telemetry sent to ground. This results in the data for that given epoch not being transmitted to ground correctly and so the resulting data in each affected data product are set to fill values during that epoch. The cause of these occurrences are currently being investigated, but preliminary analysis suggests that this occurs in < ~10 epochs per day, with a mean of ~1-2 epochs per day.

hi-omni:

The l2_hi-omni product contains omni-directional intensities for multiple ion species. The efficiencies for low energy bins are set artificially high since those energies are dominated by noise.

Caveats and Use:

- H data
    - The first 5 energy bins are noisy and should not be used.
    - Systematic uncertainty for energies [0.134, 0.190, 0.269] MeV are [84%, 67%, 33%]. For other energy channels, assume 0% systematic uncertainty.
    - Total uncertainties should combine the uncertainties provided in the CDF file (Poisson uncertainty) in quadrature.

- He3 and He4 data
    - The first 2 energy bins are noisy and should not be used.
    - Systematic uncertainty for energies [0.047, 0.067, 0.095] MeV/nuc are [58%, 24%, 10%]. For other energy channels, assume 0% systematic uncertainty.
    - Total uncertainties should combine the uncertainties provided in the cdf file (Poisson uncertainty) in quadrature.
- Systematic uncertainties for heavier ion species are much smaller and currently being assessed by the instrument team.
- See VAR_NOTES for "junk" bin definition. This contains counts that were not identified as a real ion species and should not be used.
- The mid-gain and low-gain channels are not well calibrated, so the high-energy bins are subject to scrutiny (i.e., > ~3 MeV total energy).
- Counts are binned based on mass which is computed onboard for each event and not corrected for carbon foil and SSD energy loss effects. This mostly affects the lower energy bins for lighter species (i.e., H and He).

hi-sectored:

The l2_hi-sectored product contains intensities for multiple ion species in 12 x 12 angular bins. The efficiencies for low energy bins are set artificially high since those energies are dominated by noise.

Caveats and Use:

- H data
    - The first 3 energy bins are noisy and should not be used.
    - Systematic uncertainty for the 4^{th} and 5^{th} energy bins depend on SSD. Contact instrument team for their values.
    - Total uncertainties should combine the uncertainties provided in the CDF file (Poisson uncertainty) in quadrature.
- He3 and He4 data
    - The first energy bin is noisy and should not be used
    - Systematic uncertainty for the 2^{nd} through 5^{th} energy bins depend on SSD. Contact instrument team for their values
    - Total uncertainties should combine the uncertainties provided in the CDF file (Poisson uncertainty) in quadrature.
- Systematic uncertainties for heavier ion species are much smaller and currently being assessed by the instrument team.
- The mid-gain and low-gain channels are not well calibrated, so the high-energy bins are subject to scrutiny (i.e., > ~3 MeV total energy).

- Counts are binned based on mass which is computed onboard for each event and not corrected for carbon foil and SSD energy loss effects. This mostly affects the lower energy bins for lighter species (i.e., H and He).

hi-direct-events:

The l2_hi-direct-events contains the measurement information for each event. These events are selected based on their priority level and only a subset of all events are downlinked during intense periods.

The l3a_hi-direct-events contain all of the variables from the l2 product, with the addition of estimated mass for each event.

Caveats and Use:

- Mid-gain and low-gain energy channels are not well-calibrated. These are identified by the 'gain' variable. gain = 3 -> high-gain, gain = 2 -> mid-gain, gain = 1 -> low-gain.
- TCR events are identified by type = 0 and are recommended for common usage. See VAR_NOTES and CATDESC for other event type definition.
- Counts are selected based on descending priority level, with 5 being the highest priority. Priority = 5 identifies heavy ions, priority = 4 identifies He, and priority = 3 identifies H. Lower (0, 1 and 2) priority are not TCR events.
- The multi_event flag indicates events for which multiple SSD detectors were triggered.
- The "estimated_mass" variable is computed from the "incident_ion_energy" and "energy_per_nuc" variables, which include the mass corrections for high-gain data. Mass corrections for mid- and low-gain data have not been implemented and so the species tracks for these events still sag down. This will be corrected in future releases. When identifying events based on "estimated_mass" energy-dependent mass ranges should be used and care should be given to mid-and low-gain events. For details on how to determine appropriate mass and energy ranges contact instrument team.
- Onboard look-up-table (LUT) change on 04/03/2026 (P4 in Table 1)
    - Before 04/03/2026, the onboard LUT assigned all events with raw TOF channel < 58 to priority 0. Hence, most of these events were not downlinked due to data rate limitations. This is corrected in the onboard LUT load.
- Onboard look-up-table (LUT) change on 09/16/2026 (P5 in Table 1)
    - The mid- and low-gain energy conversions used onboard were mis-classifying these events and sending them to lower priorities. Thus, there are not many mid- and low-gain events prior to this LUT upload.

- **Dropped Data Packets:** The spacecraft flight software periodically drops CoDICE data packets from the telemetry sent to ground. This results in the data for that given epoch not being transmitted to ground correctly and so the resulting data in each affected data product are set to fill values during that epoch. The cause of these occurrences are currently being investigated, but preliminary analysis suggests that this occurs in < ~10 epochs per day, with a mean of ~1-2 epochs per day.

hi-pitch-angle:

The hi-pitch-angle product contains intensity as a function of energy and pitch angle for multiple ion species. These are computed from the sectored intensities.

Caveats and Use:

- These are computed from the sectored-intensities and so all of the corresponding caveats apply.
- Level 2 magnetic field data is used in these computations. In the case that level 2 mag data is not available, then level 1d mag data is used instead.

lo_partial-density, lo_charge-state-distributions:

These products are computed from the lo-sw-species product and so all caveats corresponding to the lo-sw-species apply here.

Caveats and Use:

- Since individual charge state species are not currently well-resolved, the corresponding charge-state-ratios and abundance ratios are not reliable.
- Contact instrument team for reliable charge state and abundance ratios.

lo-3d-vdfs:

This product provides 3D distributions of H, He^{+}, He^{++}, and O^{6+} intensities as a function of energy-per-charge, spin angle, and elevation angle. They are computed using the l3a lo direct events. The data is binned based on apd_id and the counts are normalized based on the measured priority counts. The angles provided are relative to the DSRF coordinate system, where elevation angle is measured from the spacecraft spin axis and spin angle is measured from the DSRF +X axis.

Caveats and Use:

- This product is formed using TCR events and does not require position to match apd_id. It is possible to obtain 'cleaner' events by requiring the apd_id to match the position when binning the events into angular bins. However, this is not currently implemented in this product.
- Provided uncertainties correspond to the Poisson uncertainty in counts and are assumed symmetric.
- During RGFO the measured count rate is significantly reduced (by a factor of ~10) and the FOV is deflected. ***Thus, significant care should be taken when interpreting data acquired during RGFO mode. Contact CoDICE team when working with RGFO data.***

5.4.4 HIT

HIT Release Notes

1. Release 2 - YYYY-MM-DD Data range: 2026-05-01 - 2026-07-31

   - Science data products released: L0 (raw), L1a (counts-standard), L1b (standard-rates, summed-rates), L2 (standard-intensity, summed-intensity)
   - Due to updates required to look-up tables, higher-level (L1a, L1b, L2) data from 2026-05-01 - 2026-05-19 are derived from ground processing of pulse-height data, instead of flight software. Data from after 2026-05-19 - 2026-07-31 is from FSW. Several small updates are still required in the look-up tables that will further refine L2 data in following releases.
   - Transitions between dynamic threshold states (e.g., 2026-07-31 11:18 DT0 → DT1, 2026-07-31 15:44 DT1 → DT0, 2026-07-31 18:25 DT0 → DT1) produce 1-minute (single interval) spikes/dips dependent on whether the instrument is increasing in dynamic threshold state, or decreasing. This is due to a 1-minute offset between when the dynamic threshold change is activated and when it is reported. These are artifacts that will be removed in the next data release.

2. Release 1 - 2026-08-07 Data range: 2026-02-01 - 2026-04-30

   - Science data products released: L0 (raw), L1a (counts-standard), L1b (standard-rates, summed-rates), L2 (standard-intensity, summed-intensity)
   - Due to updates required to look-up tables, all released higher-level (L1a, L1b, L2) data are derived from ground processing of pulse-height data, instead of flight software.

5.4.5 SWE

SWE Data Public Release Notes: Level 3 Caveats

1. Quality flags for SWE L3 are set during L3 data processing and are time varying.

   - Nominal ("Good") when swe_flags is equal to 0 for a given time interval.
   - Bit 2 (FALLBACK_POTENTIAL_ESTIMATE, value 4): set if the spacecraft potential could not be determined from SWE measurements because the potential is below the SWE energy range. If set, then spacecraft_potential is set to 2.5 V, which may lead to erroneous moments values.
   - Bit 3 (BACKUP_SPLINE_UNRESOLVED, value=8): set if the breakpoint finding algorithm requires fall back to a spline method approach and the spline method fails.
   - Bit 4 (POTENTIAL_FIT_UNCONVERGED, value=16): set if the fit to determine the spacecraft potential (breakpoint between photoelectrons and core electrons) fails, requiring fall back to the spline method approach.
   - Bit 5 (BREAKPOINT_FIT_UNCONVERGED, value=32): set if the fit to determine the core-halo breakpoint fails, requiring fall back to the spline method approach.
   - Bit 6 (ULTRA_HV_OFF, value=64): set if any of IMAP Ultra deflectors are turned off. Nominal is when IMAP Ultra deflectors are turned on. (May still be "good" if no other flags are set.) (Not Yet Implemented)
   - Bit 7 (TEMPERATURE OUTLIER, value=128): set if any temperature product yields a value found to be an extreme statistical outlier, like a spike removal routine.
   - Bit 8 (PRELIMINARY MAG, value=256): set if MAG L1D is used for acquiring the magnetic field direction instead of the nominal MAG L2 product. (Products that do not require MAG are "Good", and products that do require MAG may not be nominal.)
   - Bit 9 (FALLBACK_SWAPI_SPEED, value=512): set if solar wind velocity vector is unresolved, but solar wind speed is provided by SWAPI L3A.
   - Bit 10 (NEGATIVE_MOMENT, value=1024): set if any density or temperature moments are negative, which is unphysical.
   - Bit 11 (UNPHYSICAL_PSD, value=2048): set if any PSD values are unphysically large (>1e-19).
   - Bit 12 (FALLBACK_CALIBRATION_EXTRAPOLATED, value=4096): set if LAST_CAL_INTERVAL from L2 Quality Flags is not nominal, meaning that detector gains were extrapolated from the most recent in-flight gain test and thus may not be up-to-date
   - Bit 13 (PREDICTIVE_EPHEMERIS, value=8192): set if the Predictive Ephemeris is used instead of the nominal Reconstructed Ephemeris. (Not Yet Implemented)

2. There are many times when the UNPHYSICAL_PSD flag (Bit 11, value 2048) is set. This does not typically mean that the PSD is greater than 1e-19 at all energies and angles. Instead, extrapolation of the PSD after transforming to the solar wind reference frame can lead to erroneously large PSD values at the lowest and/or highest energy bins. Therefore, even though this flag is set, most parameters at this time may still be valid, including the < 1e-19 PSD values and the electron temperature moments. However, these large, extrapolated values of PSD can lead to spikes in the calculated moments, particularly the integrated moments. The SWE team is investigating ways to improve this extrapolation to minimize these "bad" extrapolated values.

3. Although electron density and velocity parameters are provided, electron moments calculations are very dependent on the spacecraft potential and thus have large uncertainties. We thus strongly recommend using SWAPI ion measurements to determine solar wind speed, velocity, and density. SWE measurements are appropriate to use for electron temperatures and the partial densities of core and halo electron populations.

4. Minor signature of High frequency periodicity in integrated moments (integrated temperatures and densities).

    - At times, a high frequency periodicity is observed in SWE integrated moments parameters. This is typically observed at times when the spacecraft potential at SWE is forced to +2.5V (Quality flag value 4), or if either the spacecraft observed at SWE or the core-halo breakpoint are set using the fallback spline method (Quality flag value 8, 16, 32. The periodicity arises because the adjustment of the energy bins based on the breakpoints is set to a constant, rather than following real changes in the electron distribution, leading to the oscillatory effect in the integrated moments. The fitted moments are less susceptible to these small shifts in the energy bins, so they do not exhibit such behavior as clearly, if at all. We recommend examining both the integrated and fitted moments to determine if variations in the integrated moments are reflected in the fits or not before targeted analysis on such features.

5.4.6 MAG

Level 2 MAG magnetic field measurements are generally of reasonable quality. Some artifacts remain, associated with spacecraft signals, the determination of both spin plane and spin axis offsets, and angles and gains in the calibration matrices.

Some classes of time periods with significant artifacts are flagged in the quality flag metadata within the released CDF files and users should always consult these flags when using the MAG data. The MAG quality flags are as follows:

Quality Flag	Description
0	Good data
1	Bad data; not suitable for science

If the quality flag is raised to indicate poor quality data, the quality bitmask can be consulted for additional information. The quality flag being raised will always be accompanied by a non-zero value of the quality bitmask. The quality bitmasks are indexed from bit 0 – 7, where bit 0 refers to the least significant bit. The bitmasks are defined as follows:

Quality Bitmask Bit	Description	Additional Information
0	Data is sourced from secondary sensor	The IMAP Magnetometer has two in flight sensors. Data is sourced from the primary sensor, which is further away from the spacecraft in order to reduce the impact of spacecraft interference. If the data in this file has instead been sourced from the secondary sensor, this bit will be raised.
1	Thruster firing signals have been removed	IMAP undergoes a daily thruster firing, that generally occurs at approximately 10:00 UT. A cleaning process attempts to clean these signals from the data but the cleaning may be imperfect. This bit indicates that thruster firing signals are being removed from the data, and can be used to distinguish thruster firings from surrounding science.
2	Spacecraft interference impacts these data	This flag encompasses general spacecraft signals which are not cleaned and have an impact on the data. It is raised for between 3-6 hours around Trajectory Correction Maneuvers to indicate the poor quality data. It is also used to indicate the movement of the IMAP-Lo pivot platform, which generally occurs at approximately 10:35 UT and is accompanied by signals in the data. The bit is raised while the pivot platform is in motion.
3	Instrument signals have been removed	This bit is raised when signals from instruments have been removed from the data.
4 - 7	Reserved for in-flight calibration	These bits are currently unused, and are reserved for future calibration.

Some particular types of artificial signals which users might encounter are described below.

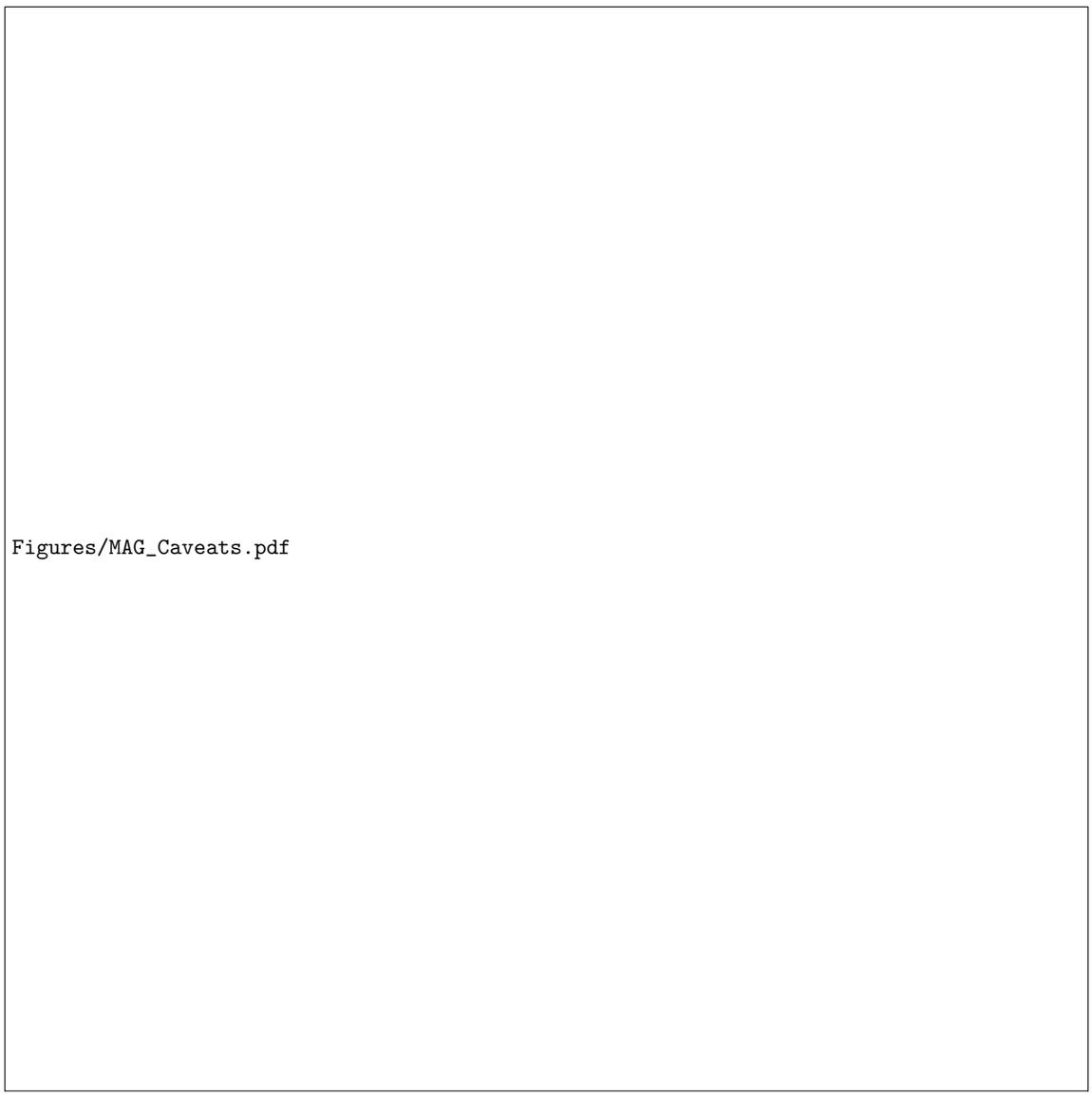


Figure 5.1: Artificial signals due to thruster firings visible in MAG burst mode L2 data.

Thruster Firings

The IMAP spacecraft spin axis is repointed, typically daily around 10:00 UT. An additional related activity occurs one hour beforehand, around 09:00 UT. At each of these times, a series of short but large spacecraft fields are produced: the precise sequence varies between days depending on which thrusters are fired. These times are flagged in the quality data as a quality flag value of 1, and bit 1 raised in the quality bitmask and users should always check these flags. The artificial fields in the normal mode L2 data products are removed effectively, but significant signals can sometimes remain in the burst mode files. Users should be wary of all sharp signals in the data, which can be confused with physical signals such as solitons, mirror modes or other ion-scale phenomena. An example event is shown in Figure 5.1.

Trajectory Correction Maneuvers (TCMs)

TCMs occur every one or two months and consist of a long sequence of thruster firings. These signals are not currently cleaned from the L2 data and result in very obvious, long sequences of sharp, large field pulses, such as that shown in Figure 5.2. Users should note that some isolated signals can also occur outside the main sequence of firings.

It is best not to analyze data during TCMs. These events are flagged in the quality metadata as a quality flag value of 1, and bit 2 raised in the quality bitmask .

IMAP-Lo Pivot Platform Movement

The IMAP-Lo instrument pivot platform moves into different positions, generally once a day at 10:35 UT, with the motion lasting approximately 6 minutes. It produces a magnetic field signal when in motion that is not necessarily easily detectable in the time series, and that is not cleaned from the data. The pivot platform motion is flagged in the quality metadata as a quality flag of 1, and bit 2 is raised in the quality bitmask.

Spin Axis Offset

The IMAP spacecraft spin axis is approximately aligned with the GSE and GSM X axes and the RTN R axis. The precise value of the remaining artificial field in this direction is challenging to quantify with a

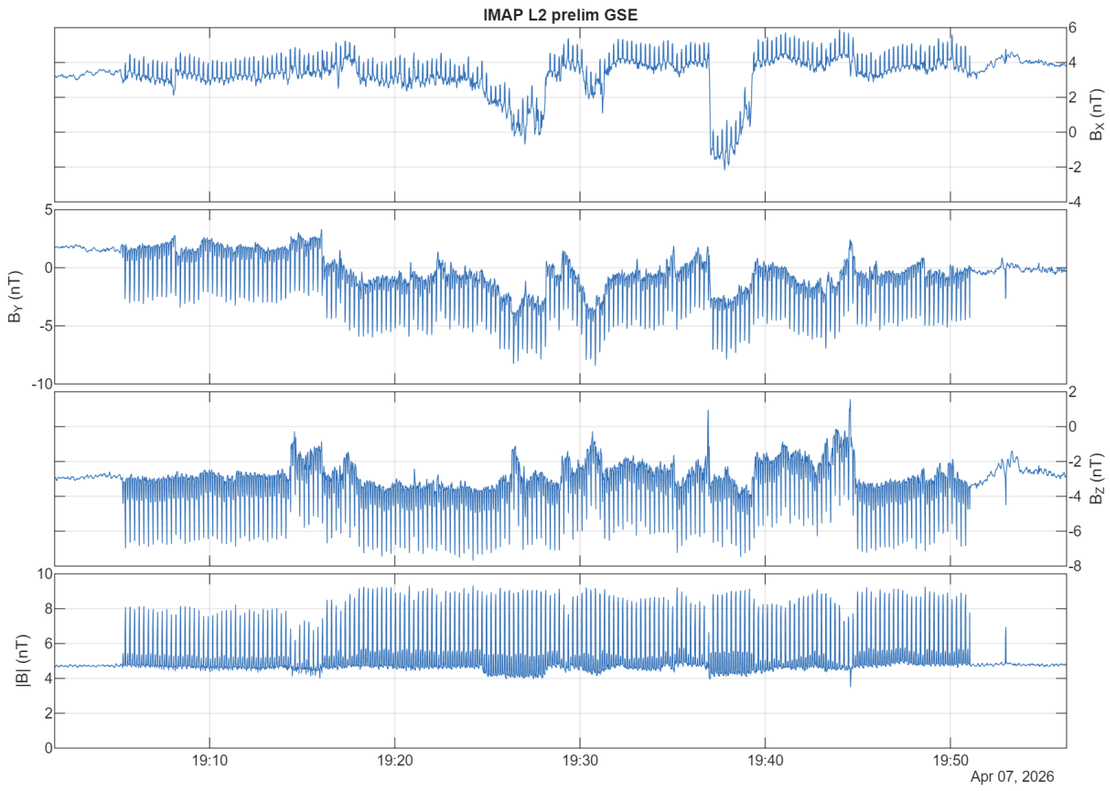


Figure 5.2: Magnetic field signals from a trajectory correction maneuver.

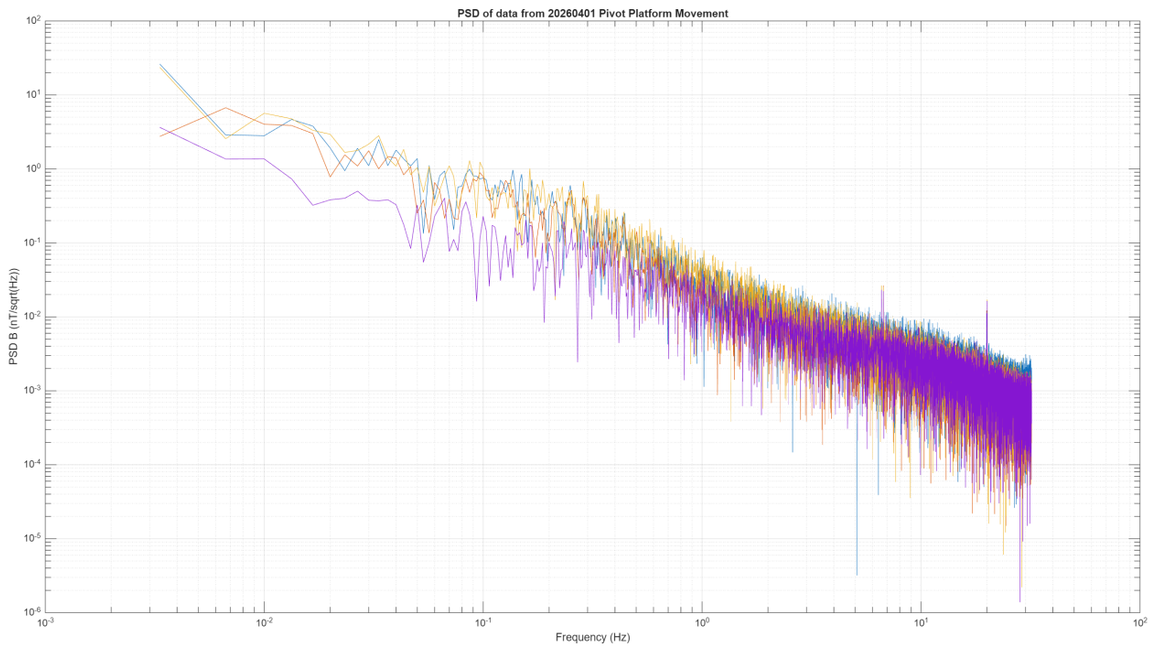


Figure 5.3: Power spectral density during an IMAP-Lo pivot platform maneuver.

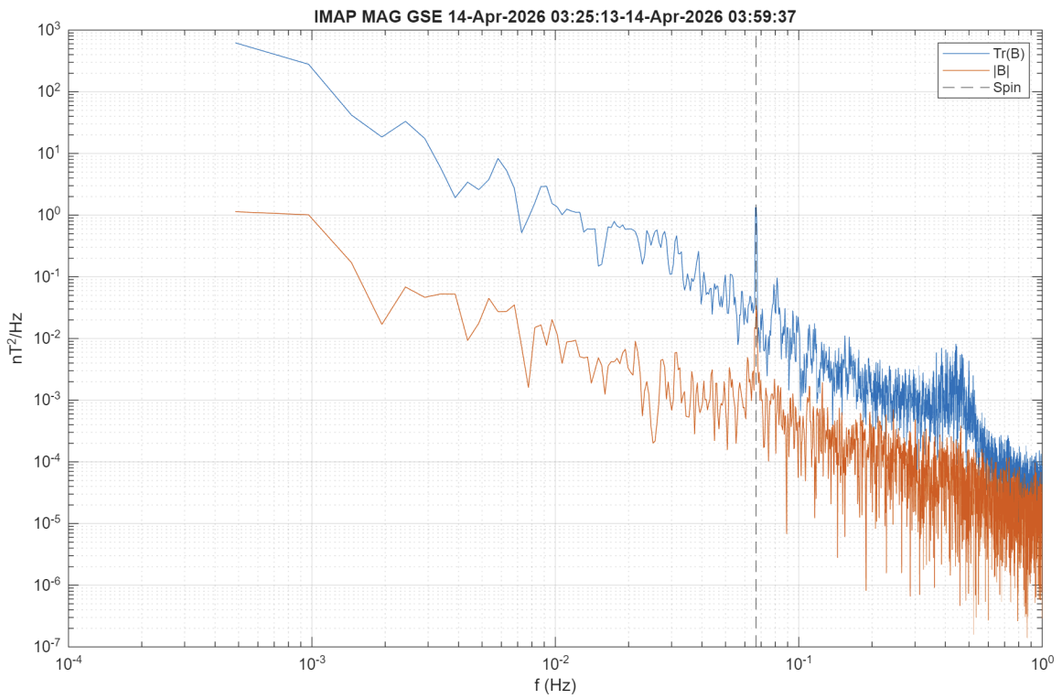


Figure 5.4: Spin tone in the field component (blue) and magnitude (red) spectrum The spin period is marked by a dashed vertical line.

precision better than 0.1nT and there is evidence that at times the uncertainty can be larger, perhaps up to 0.5nT. Users should therefore take care when considering the absolute field value in this direction.

Incorrect spin axis values effectively result in a near-DC shift in the field in this direction. Some science impacts of this can include:

- Incorrect estimates of $|\mathbf{B}|$ and hence physical parameters such as ion gyroradii and gyroperiods, plasma beta etc.
- Incorrect estimates of the magnetic field direction by up to 10 deg for typical interplanetary magnetic field strengths, and much more in very low field regions. This can result in issues when calculating anisotropies, for example field-aligned particle anisotropy, turbulence anisotropy.
- Field-transverse fluctuations can be folded into the field magnitude, resulting in apparently higher power fluctuations: users estimating spectra of $|\mathbf{B}|$ fluctuations should take special care.
- Comparison between spacecraft: a fixed shift between two spacecraft can result in significant errors when estimating cross-correlations, structure functions, current densities, and so on.

Spin Tone

The IMAP spacecraft has an approximately 15s spin period. Errors in estimates of the spin plane spacecraft fields, as well as in the calibration matrix, can result in spin "tone" – narrowband signals in the two spin plane field components (approximately GSE and GSM Y and Z, and RTN T and N) as well as the field magnitude.

Since variations in $|\mathbf{B}|$ on spacecraft scales of tens of seconds are typically smaller than in the field components due to the dominance of Alfvenic fluctuations, spin tone can often be most easily seen in the magnitude time series or power spectrum.

IMAP MAG data has long periods where spin tone is low, but there are periods where it is significant; an example is shown in Figure 5.4.

Users should take care when considering fluctuations near the spin period. Possible science impacts include:

- Errors in estimates of the total fluctuation power and spectral index. This can affect the component spectrum and is typically a larger effect for the magnitude spectrum for the reasons described above.
- Misidentification with physical phenomena, especially ion cyclotron waves. The proton cyclotron period is typically rather shorter than that of the 15s spacecraft spin period, but it can reach this low. More significantly, heavy ion species, most notably alphas, can often have gyroperiods in this range. An example is shown in Figure 5.5 where, without care, one could interpret the spin tone peak as being due to heavy ions.

It is important to note that the amplitude of the spin tone signal can vary significantly and it can be present in the data in a way that is sometimes quite hard to determine from the time series. Calculation of a power spectrum, or a dynamic spectrum plot including that of the field magnitude, is recommended in order to identify intervals where spin tone is present.

Spin tone can also be present during high field regions such as coronal mass ejections, perhaps due to uncertainties in the gain and alignment angle determinations in the calibration matrix, where it can be clear due to the low level of natural variability. An example is shown in Figure 5.6.

5.4.7 IMAP-Lo

5.4.8 IMAP-Hi

5.4.9 IMAP-Ultra

5.4.10 IDEX

IDEX Data Public Release Notes

IDEX data release notes report embedded below

IDEX Data Release Note

IMAP IDEX Team

September 17, 2026

IDEX Data Release Note

This release note provides important context for the current IDEX data products. The IDEX data processing pipeline remains under active development, and the products included in this release should be interpreted as preliminary. More complete analyses, improved event classification, and additional higher-level products will be included in later data releases as the pipeline matures.

Users should apply discretion when interpreting Level 2A waveform-fit products and the derived mass and velocity estimates. The Level 2A pipeline fits target and ion-grid waveform products and reports derived quantities where possible; however, a successful waveform fit or a reported mass/velocity estimate does not guarantee that the fitted waveform was produced by a dust grain impacting the target.

At the time of this release, the pipeline provides event-classification flags separating noise events, calibration events, and science events. Additionally, it applies a preliminary algorithm to flag candidate dust impacts among the science events.

Level 2B products include overall candidate dust-impact counts and rates without mass or charge binning. Mass- and charge-resolved count and rate products remain populated with fill values pending further validation.

Level 2C products are not included in this release. This means that mapped impact-rate products are intentionally excluded from the present delivery. This higher-level product will be included in a later release after the event-classification and rate-generation portions of the pipeline have been further validated.

Candidate Dust Event Times:

The following list is manually curated and should supersede the list of events identified by the pipeline's `dust_hit_flag`.

- 2025-11-26T12:13:02.034
- 2025-11-27T22:06:54.656
- 2025-11-28T04:16:30.823
- 2025-11-29T12:08:45.148
- 2025-12-08T22:56:16.731
- 2025-12-15T08:08:06.712
- 2025-12-24T17:33:10.743
- 2025-12-25T08:46:51.620
- 2025-12-28T23:17:20.464
- 2026-01-19T07:17:00.560
- 2026-01-20T00:43:32.355
- 2026-01-20T03:48:38.168
- 2026-01-23T08:22:41.791
- 2026-01-25T08:57:31.271
- 2026-01-25T11:55:08.610
- 2026-01-26T11:18:42.839
- 2026-01-29T09:21:05.848
- 2026-02-07T10:31:07.632
- 2026-02-16T04:32:41.694
- 2026-02-16T16:00:38.906
- 2026-02-19T11:04:38.181
- 2026-02-20T15:32:46.369
- 2026-02-21T22:24:50.175
- 2026-02-26T18:10:39.310
- 2026-03-01T00:59:37.352
- 2026-03-01T12:12:45.870
- 2026-03-02T06:00:28.459
- 2026-03-03T06:38:51.617
- 2026-03-05T13:10:21.236
- 2026-03-11T22:00:17.311
- 2026-03-13T12:48:39.704
- 2026-03-18T20:54:15.109
- 2026-03-19T11:44:59.331
- 2026-03-21T03:32:18.201
- 2026-04-01T08:18:25.610
- 2026-04-01T14:00:04.706
- 2026-04-03T04:40:18.974
- 2026-04-05T12:10:34.141
- 2026-04-07T16:39:25.104
- 2026-04-08T03:25:49.047
- 2026-04-13T05:47:45.666
- 2026-04-14T20:11:03.836
- 2026-04-18T16:50:08.651
- 2026-04-19T15:03:43.920
- 2026-04-25T09:28:57.536
- 2026-04-28T21:06:38.583
- 2026-05-03T09:58:37.611
- 2026-05-03T13:46:00.621
- 2026-05-04T10:43:29.425
- 2026-05-10T01:57:15.475
- 2026-05-10T07:49:20.669
- 2026-05-10T19:11:45.259
- 2026-05-18T13:54:28.936
- 2026-05-18T20:16:20.527
- 2026-05-19T09:17:07.136
- 2026-05-20T11:07:27.171
- 2026-05-20T15:04:50.503
- 2026-05-21T12:45:24.951
- 2026-05-25T06:17:36.984
- 2026-05-25T15:55:07.187
- 2026-05-27T11:30:01.659
- 2026-05-28T04:02:41.131
- 2026-05-31T14:02:41.254
- 2026-06-06T21:35:05.965
- 2026-06-09T21:39:45.774
- 2026-06-13T12:36:17.815
- 2026-06-17T06:32:35.891
- 2026-06-21T13:47:23.167
- 2026-06-29T19:54:48.191
- 2026-07-05T17:01:57.359
- 2026-07-07T02:22:52.969
- 2026-07-07T04:32:19.009
- 2026-07-08T02:12:27.486
- 2026-07-11T01:29:44.225
- 2026-07-12T09:14:36.150
- 2026-07-12T23:11:03.239
- 2026-07-14T23:06:05.728
- 2026-07-15T14:05:07.808
- 2026-07-20T08:24:02.652
- 2026-07-23T16:19:51.204
- 2026-07-24T09:27:09.005
- 2026-07-26T06:53:36.693
- 2026-07-28T18:15:16.697
- 2026-07-29T08:24:52.499
- 2026-07-29T18:55:25.571
- 2026-07-31T21:10:45.485

- 2026-07-31T21:57:08.942
- 2026-08-02T03:00:33.828
- 2026-08-05T09:18:06.140
- 2026-08-14T07:08:46.316
- 2026-08-14T12:37:45.962
- 2026-08-15T07:12:03.941
- 2026-08-15T15:14:42.406
- 2026-08-20T09:11:13.402
- 2026-08-30T11:00:24.721
- 2026-09-01T13:55:32.384
- 2026-09-02T06:41:42.183
- 2026-09-02T11:14:13.302

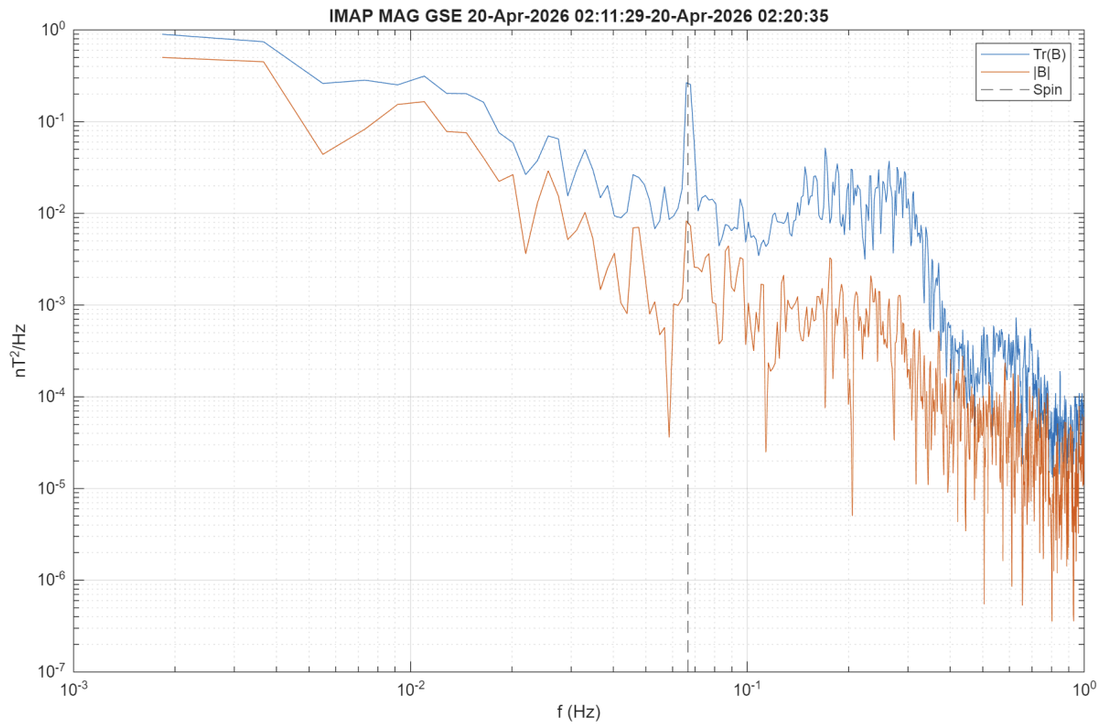


Figure 5.5: An interval with spin tone which could be misinterpreted as ion cyclotron waves driven by heated ions. Note the proton ion cyclotron peak at a period of around 5 seconds.

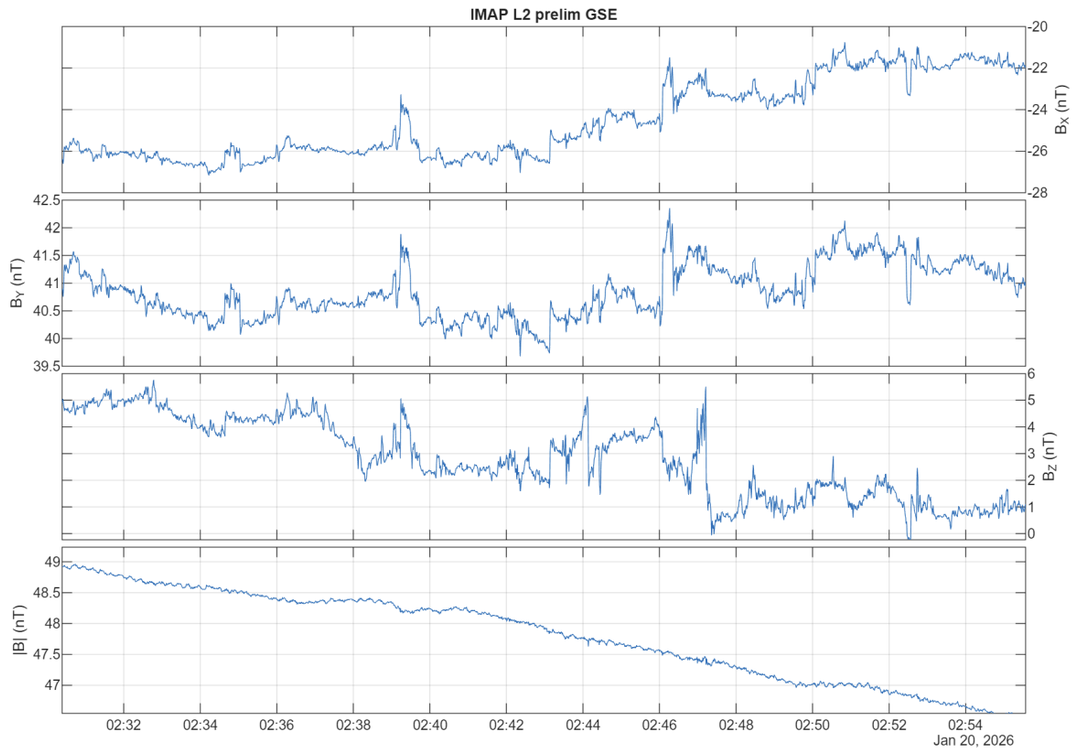


Figure 5.6: Spin tone, especially clear in the field magneitude (bottom panel), during high field magnitudes within a coronal mass ejection.

5.4.11 GLOWS

GLOWS Data Public Release Notes

IMAP/GLOWS Data Release 2
PI: Maciej Bzowski (bzowski@cbk.waw.pl)
Changes in the data products since Release 1

1. Spin axis coordinate system correction
Due to an issue with the IMAP ACS identified after DR1, the parameter spin_axis_orientation_average in GLOWS L1b, L2, and L3a data products had a systematic offset in longitude by +0.36 deg in DR1. In DR2, corrected SPICE kernels have been used and the spin_axis_orientation_average reports the corrected longitude.

Formally the ACS issue affects also the latitude reported in the parameter spin_axis_orientation_average, but the latitudinal offset is negligibly small ($\sim 0.003°$).

2. Spin phase offset correction
Another issue with the IMAP ACS resulted in offsets of the IMAP onboard spin angle relative to an adopted convention, where the crossing of the ecliptic plane by Y axis of the IMAP SPACECRAFT frame marks the spin phase equal to 0. The offset values are 1 deg before July 8, 2026 and $\sim 2.3°$ after that date. GLOWS L0 and L1a data products do not include explicit values of the onboard spin angle, but the histograms included there should be understood as affected by the issue. GLOWS L1b data product includes the parameter imap_spin_angle_bin_cntr which represents explicitly the IMAP onboard spin angle and thus both the spin angle and histogram at L1b are affected by the ACS issue. In GLOWS science-grade L2 and L3a data products the parameter spin_angle represents a spin angle measured from the northernmost point at the GLOWS scanning circle. It is computed by subtracting a GLOWS-specific spin offset (parameter position_angle_offset_average) from the onboard spin angle imap_spin_angle_bin_cntr included in the L1b data product. The values of position_angle_offset_average in GLOWS L1b, L2, and L3a data products have been corrected both in DR1 and DR2.

Therefore, the parameter spin_angle at L2 and L3a reports corrected spin angle values measured from the northernmost point at the GLOWS scanning circle both in DR1 and DR2.

3. WawHelioIon-MP model
In Release 2, we used a new version of the WawHelioIon-MP model, which converts observed lightcurves into ionization rate profiles (Porowski & Bzowski 2024a). The model is based on machine learning techniques. In the current version, the training set of SOHO/SWAN lightcurves has been extended and the list of analysed sectors has been updated. Additional repotins included in the L3b/c analysis:
CR2306: 91-97
CR2306: 83-90

4. L3d: parent files
The list of parent files used to generate the L3d data product (solar wind parameter history) has been updated. Previously, only the L3b and L3c files used to generate the last record in the L3d file were listed. The current version lists all L3b and L3c files used to calculate the L3d records based on GLOWS data.

IMAP/CMAD A

Appendix: Definitions and Notation

Definitions and Notation for the IMAP mission are provided in the Appendix of the IMAP mission paper [McComas et al., 2025]. *Any additional Definitions and Notation adopted after that paper are added to this section.*

IMAP/CMAD B

Appendix: Acronyms

Acronyms for the IMAP mission are provided in the Appendix of the IMAP mission paper [McComas et al., 2025]. *Any additional acronyms adopted after that paper are added to this section.*

Bibliography

M. Bzowski et al. GLObal solar Wind Structure (GLOWS). *Space Science Reviews*, December 2025.

E. R. Christian et al. The High-energy Ion Telescope (HIT) for the Interstellar Mapping and Acceleration Probe (IMAP) mission. *Space Science Reviews*, December 2025.

H. O. Funsten et al. The Interstellar Mapping and Acceleration Probe High energy (IMAP-Hi) neutral atom imager. *Space Science Reviews*, December 2025.

M. Gkioulidou et al. The IMAP-Ultra energetic neutral atom (ENA) imager. *Space Science Reviews*, December 2025.

M. Horányi et al. Interstellar Dust Experiment (IDEX) onboard NASA's Interstellar Mapping and Acceleration Probe (IMAP). *Space Science Reviews*, December 2025.

T. S. Horbury et al. The IMAP Magnetometer. *Space Science Reviews*, December 2025.

S. A. Livi et al. The Compact Dual Ion Composition Experiment (CoDICE) for the IMAP mission. *Space Science Reviews*, December 2025.

D. J. McComas et al. Interstellar Mapping and Acceleration Probe: The NASA IMAP Mission. *Space Science Reviews*, December 2025.

J. S. Rankin et al. Solar Wind and Pickup Ion (SWAPI) instrumnet on NASA's Interstellar Mapping and Acceleration Probe (IMAP). *Space Science Reviews*, December 2025.

N. Schwadron et al. The IMAP-Lo instrument. *Space Science Reviews*, December 2025.

R. M. Skoug et al. The Solar Wind Electron (SWE) instrument for the Interstellar Mapping and Acceleration Probe mission. *Space Science Reviews*, December 2025.